427+475=902p

N63-15114 - N63-15159

(N63-15114 & N63-15137 → Book I
(N63-15138 & N63-15159 → Book II

TID-7652

Code-3

Proceedings of the Symposium
on the

Protection Against Radiation Hazards in Space

held in
Gatlinburg, Tennessee
November 5-7, 1962

BOOK 1

UNITED STATES ATOMIC ENERGY COMMISSION
Division of Technical Information

Case 53

LEGAL NOTICE

TID-7652
PHYSICS

PROCEEDINGS OF THE SYMPOSIUM ON THE

PROTECTION AGAINST RADIATION HAZARDS IN SPACE

Gatlinburg, Tennessee

November 5-7, 1962

BOOK 1: Radiation Environment in Space
Effects of Space Radiation on Radiosensitive Objects
Biological Effects of Space Radiation

BOOK 2 : Shielding Against Space Radiations

Sponsored by:

Oak Ridge National Laboratory

Manned Spacecraft Center, NASA

American Nuclear Society

FOREWORD

The realization in recent years that outer space is traversed by high-energy radiations has caused man to reevaluate the feasibility of manned or even instrumented exploration outside our atmosphere. Fortunately, it is possible to determine the nature and intensities of these radiations and to produce similar radiations on earth by means of accelerators. Thus we can learn how to attenuate them and to design capsules which afford protection against them. Of course this protection carries a weight penalty so that there is a premium on optimizing the shield design. Many groups in the United States are engaged in research to this end, and it was the purpose of this symposium to bring these groups together so that they could exchange information. To make the meeting more comprehensive, sessions on the nature of the radiations and their effects on people and things were included. However, the major part of the meeting was devoted to discussions on shielding research, comprising theoretical calculations and experiments carried out mainly with high-energy accelerators. The symposium committee feels that the aims of the symposium were met and that progress in space research program was greatly accelerated thereby.

Symposium Committee

Committee Members

E. P. Blizard, Chairman
Oak Ridge National Laboratory

C. D. Zerby
Oak Ridge National Laboratory

Wright Langham
Los Alamos Scientific Laboratory

Wilmot N. Hess
Goddard Space Flight Center

W. L. Gill
Manned Spacecraft Center
National Aeronautics and Space Administration

J. Warren Keller
National Aeronautics and Space Administration
Washington

Fred C. Maienscheim
Oak Ridge National Laboratory

PROGRAM AND CONTENTS

BOOK 1

Session C

BIOLOGICAL EFFECTS OF SPACE RADIATIONS

Robley D. Evans -- Chairman
Massachusetts Institute of Technology

BOOK 2

Session D

SHIELDING AGAINST SPACE RADIATIONS

Clayton D. Zerby -- Chairman
Oak Ridge National Laboratory

Session E

SHIELDING AGAINST SPACE RADIATIONS (continued)

H. J. Schaefer -- Chairman
U. S. Naval School of Aviation Medicine

Session F

SHIELDING AGAINST SPACE RADIATIONS (continued)

T. F. Foelsche -- Chairman
Langley Field, NASA

THE MISSION OF MAN IN SPACE

Homer E. Newell
Director, Office of Space Sciences
National Aeronautics and Space Administration

Introduction

This meeting on Protection Against Radiation Hazards in Space is a timely one. It comes at a time when world-wide attention has been drawn to the subject by the striking effects of artificial radiation belts on some unmanned satellites. It takes place against a background of growing programs and far-reaching plans for scientific research, practical applications, and manned flight and exploration in space.

The first years of the Space Age have demonstrated clearly that unmanned spacecraft can play a significant role in man's quest for knowledge and human advancement. On the scientific side, Explorers, Pioneers, Mariner, Ranger, Sputniks, and Luniks have already yielded a wealth of knowledge, answering many important scientific questions. The future is bright for these electromechanical extensions of man's presence beyond the earth, especially when increased payload capacity permits us to launch Surveyors to the moon and Voyagers to the planets.

TIROS, Telstar, and Transit have shown how effective unmanned satellites can be in weather surveillance, for long range communications, and as navigational aids. The outstanding success of the TIROS research satellite gives full assurance that the Nimbus and Aeros operational satellites to come will advance weather surveillance, forecasting, and research far beyond their previous status. Telstar, a private venture of AT&T, speaks for itself, and it, too, presages a bright future for the application of satellite technology to human advancement.

All these, and other examples of the effectiveness and usefulness of unmanned satellites and deep space probes, testify to their worth. It follows as a corollary that the matter of providing these inanimate servants of mankind with protection against radiation hazards of the space in which they must operate is worthy of careful attention. Protection, through shielding, overdesign (or perhaps under the circumstances one should say "adequate design"), modified demands on components or systems, substitution of suitable components for unsuitable ones, or avoidance of hazardous regions or times, must be worked out in theory and in practice to make most effective use of the space opportunities that lie before us. And this is a part of the subject of the present meeting.

But what about protection for man, himself? If he would just stay at home on earth where some people think he belongs, the problem would be solved. You recall the old chestnut about the man with the broken leg. His pal, rushing into the doctor's office, in his excitement could hardly tell the doctor what the trouble was. Finally, breathlessly, he managed to get out with, "Doctor, what do you do about a man who has broken his leg in two places?" To which the doctor replies, "Tell him to stay out of those places!"

Well, the easiest way to protect a man from the radiations in space is to keep him out of space. And, indeed, there are many who insist that that would be the best all-around course of action. They say that we don't need man in space; that everything we wish to accomplish out there can be done with unmanned vehicles and equipments; and that in fact it would be cheaper to do it without man.

I don't agree. No matter how you design and build, you won't be able to put man's discernment, judgment, versatility, and adaptability in space except by putting the man himself there. The more complex the mission, and the farther from the earth it must be carried out, the greater will be the need for that human versatility and insight and adaptability. At some point in complexity and distance from the earth, it will actually become cheaper to use the man than to build the mechanical substitute. Some, who have studied the matter, assert that the switchover occurs between the moon and the nearest planet.

At any rate, this is no longer an open question. Man has already gone out into space. He is going to go out again, and then again. This nation is committed in dead seriousness to placing a man on the moon in the present decade, and thousands of people are tackling this most difficult of all mankind's ventures with a determination to bring it about.

It is quite to the point, therefore, to ask what will he do out there? What is there for him to do in space anyway? With your permission I should like to explore with you now, this very question, and to review the lengthy list of reasons why man should go out into space, thereby requiring the protection that you are gathered here to discuss.

Scientific Exploration

First a few general statements. It is clear that the very first thing that man will do in space, on the moon, and on the planets, will be to explore. Whether systematized or not, whether planned or incidental, every look he takes, every glance will be exploration. And if he is an accurate observer, all of it will be science. Each bit of information, each observation, each new phenomenon or object noted, will be listened to and seized upon avidly by the scientific community.

Following this initial scientific exploration, based on the first-look results, specific investigations will be designed and carried out. Later, although right now many, indeed most, of them cannot be foreseen, there will be many practical applications, both civilian and military, of the new space knowledge and technology, and of the human ability to move about in space.

Man in Orbit

Man in orbit acquires a perspective in which to view the earth that cannot be achieved on the ground or from the lower atmosphere. Already small beginnings have been made by the Mercury pilots in the area of scientific observations from orbit. In these early days when the principal concern is with the struggle to fly at all in space and return safely, the scientific exploration necessarily received little attention. But as confidence and ability develops, the man in an earth-orbiting satellite will be able to devote more and more attention to such matters as observations of weather patterns, the airglow, the aurora, the zodiacal light, the Gegenschein, the sun's corona, and other astronomical objects.

At some time in the development of the space program, it will be important to send aloft scientists to do their own observing. It is important, therefore, that the scientific community begin to give careful thought not only to the scientific tasks to be done in orbit, but also to how they are to be done, and by whom. If scientists themselves are to go into orbit to do science there in person, these scientists must receive appropriate training for survival, for performance of their duties as members of the spacecraft crew, as well as in how to carry out their scientific investigations under the unusual conditions of space and space flight. At some appropriate time such scientists must be introduced into the NASA astronaut training program.

Actually more thought seems to have gone into the research that a man might do in person on the moon, than in a satellite orbiting about the earth. This is due in part to President Kennedy's commitment of the nation to the landing of a man on the moon within the present decade. It is due also in part to the fact that the moon is clearly an explorable body in the same sense as the earth is. One can easily see in the mind's eye men walking around, looking, poking here and there in search of interesting and important finds, picking up specimens for later study in the laboratory, taking pictures, making field tests, drilling holes, implanting instruments and automatic observing stations, and in general doing the many things that an exploration geophysicist might do on earth. It is also due in part to the fact that many of the questions of current scientific interest concerning the earth, its atmosphere, the sun, and astronomical problems are already being attacked with vigor and promise by means of unmanned satellites and probes.

But there are enough valuable scientific observations for a scientist in orbit to make, that are already apparent, that it behooves the sceintific community to pursue the subject further with vigor. We have mentioned a little earlier some of the geophysical and astronomical

observations that a man in a satellite might make. In addition, man himself, in orbit, is an important subject of scientific study. Indeed, when large orbiting laboratories can be put into operation there will be opportunity to conduct, under the same conditions of careful control and with same close personal attention that one gives in the laboratory on the ground, biological experiments on the effects of weightlessness, radiation, new periodicities, and other conditions strange to terrestrial life. In such a laboratory, fundamental and applied research, and perhaps even some of the development, of closed ecological systems can be carried out under the very conditions under which they will be required to operate. For example, those systems to be used on manned planetary missions, will have to operate for years without failure. In an orbiting laboratory such a system could be given a life test that would be fully meaningful and in which one could place some confidence.

When man has learned to move about freely in space, especially when he is able to move around outside the spacecraft or space station that serves as his home base in space, there will be many activities that he can pursue. One of these will be engineering and construction in space. At the present time, space engineering is carried out on the ground. The engineered object, if it is a space vehicle or a spacecraft, is placed in orbit after the engineering has been accomplished. In this approach, man stays on the ground, and sends his engineered object out into space. Much has been accomplished by this approach, in the form of scientific satellites and space probes, weather satellites, communications satellites, navigation satellites, and military applications of space technology, and even manned satellites.

But one day man will do some of his engineering and building right out in space. A lot of this activity may perhaps be more properly referred to as construction and maintenance, but the novelty of the problems and the environment to be faced will be such that for a long time to come the constructors and the maintainers will actually have to be engineers in the true sense of the word.

One can foresee the need to assemble in space large laboratories, huge antenna systems, stations to serve as staging areas for interplanetary flight, and even space vehicles for making flights to the planets and into deep space.

It may be necessary to form the reflecting surfaces for astronomical telescopes under the conditions of weightlessness under which they are to operate so as to eliminate distortions that would be introduced by forming them on the ground under 1 g and then launching them into orbit.

Considering the tremendous expense that one must anticipate for the construction of huge observatories and laboratories of the future, it may well prove to be far cheaper to provide human maintenance and repair, than to rebuild and launch a new satellite every time an old one has ceased to function. In fact, in many cases it may not be just a matter of maintenance and repair. By replacement of instruments in an orbiting observatory it may be possible to update at relatively low cost a basically expensive facility.

This newly developed ability to engineer, inspect, build, maintain, renovate, and carry out complex logistics operations in space, will also have military value. In the matter of military applications of space, informed thought appears to have gone full circle. At first, years ago, although opinions varied, the general thought was that space provided an overwhelming military potential, and that he who dominated space would dominate the world. This was followed by a reaction period, during which the general thought swung to the opinion that perhaps there was very little of military value in space. At the present time, there are few who would deny that space does offer possibilities for many important military applications. I would venture to predict that in time engineering in space will form an important segment of the sum total of manned operations in space for military purposes.

Man on the Moon

One of the most important reasons for placing a man on the moon is to carry out a scientific investigation of that body. The moon is of especial interest to the scientist for a number of reasons.

We know that the solar system was formed about 4.5 billion years ago, but we do not know how it was formed, and this problem has been the subject of much speculation and thought for centuries. The investigation of the origin of the solar system is a project of the greatest scientific interest,one to which the exploration of the moon can contribute significantly.

The moon will play a special role in this investigation because it is a body whose surface has preserved the record of its history for a much longer period than the earth, and probably much longer than Mars and Venus as well. On the earth, the atmosphere and the oceans wear away surface features in 10 to 50 million years. Mountain-building activity turns over large areas of the surface in about the same time. There is little left on the surface of the earth of the features that existed several hundred million years ago. The same is probably true of Mars and Venus. But on the moon there exist no oceans and very little atmosphere to destroy the surface. Also, inspection of the moon's surface in a telescope shows few signs of the mountain-building activity which distorts and defaces the surface of the earth so rapidly.

Thus the moon's surface will carry us back very far into the early history of the solar system, perhaps not back to the birth of the sun and planets, but certainly billions of years back --- much longer than the 10 to 20 million years to which we are limited on the earth.

Not only the lunar surface, but also the internal structure of the moon may provide a clue to the early history of the solar system and the birth of the planets.

One of the theories for the creation of the planets, popular until recent times, held that the solar system was created during a near collision between our sun and another star, in which the gravitational forces between these two massive bodies tore huge streams of flaming gas out of each. As the intruding star receded, the masses of gas which happened to be near the sun were captured by it into orbits in which they eventually cooled and solidified to form the planets. If such a collision was the manner of formation of the solar system, then the moon and planets must have been molten at an earlier stage in their histories. In that event, the iron in their interiors would melt and run to the center to form a dense core.

Another theory holds that the planets were formed out of pockets of condensation in the du t surrounding our sun during the early stages of its lifetime. We know that stars themselves are almost certainly formed in this way, by condensation of pockets of interstellar gas and dust which happened to be somewhat denser than their surroundings. It seems likely that additional subcondensations could have developed in the tenuous matter surrounding the sun before the central condensation had proceeded to its final stages; and that the moon and planets were eventually formed from these subcondensations.

Large bodies like the earth have enough radioactive uranium inside them to produce melting of iron simply through the heat generated in nuclear decays. Therefore, the existence of a dense core of iron in the interior of the earth does not prove the validity of the collision theory, or disprove the theory of condensation. However, the moon is smaller and colder, and will provide a much better indication than the earth, as to which of the two theories on the origin of the solar system is correct.

The necessary observations and measurements obviously cannot all be made just by man's standing on the moon and looking around. But a giant step will have been taken when the first scientist on the moon does look around and begins to zero in on the most likely answers, and more importantly, can determine the most promising courses to follow for obtaining the answers. Before that time some data will have been obtained by means of unmanned spacecraft, Rangers and Surveyors, but the full power of the lunar science effort will not be brought to bear until man and instrument together tackle the problems to be solved.

This subject was discussed at length at the Space Science Summer Study conducted at the State University of Iowa, under NASA sponsorship, this past summer. Most of the participants felt that the first scientist-astronaut to be landed on the moon should be a geologist. His first job should be to look -- and think. There was considerable discussion about the qualifications of this first scientist on the moon. The thought was brought out that this man should be a top notch, first rate scientist. As an illustration, it was pointed out that it took a Darwin to make the voyage of the Beagle the historic success that it was. If one wants to be quantitative about it, one might say that the difference between sending

a run-of-the-mill scientist, or a non-scientist given special supplementary training in science, to the moon to look around, and sending a Darwin there is a matter of many many orders of magnitude in what returns are realized from the venture. Of course, the problem is to find a Darwin who can also become an astronaut, and is willing to.

The question of how man will do science on the moon is one that is worthy of much thought. One approach is that already mentioned, namely, to send scientists to the moon. Another is to train the astronauts to look for anticipated objects and phenomena and to try to be alert to the unanticipated ones and report them accurately. Still a third might be to have an astronaut-scientist team in which the astronaut on the moon is linked with the scientist on the earth by means of radio and television. In two-way conversation, the astronaut receives guidance from the scientist who sees through the television what the astronaut sees. By questioning the astronaut, the scientist can get additional details from the man on the moon about objects that appear to be of special significance.

At any rate, the scientific observer on the moon will have plenty to keep him busy. As mentioned, the first thing he should do is look and think. He should examine the surface, note the various geologic formations, select appropriate samples to bring back to earth, and take pictures. Eventually, although very likely not on the first trip, he should conduct measurements of surface properties, radioactivity, temperature and heat flow, seismic activity, etc., bringing with him the necessary instruments to accomplish these tasks. At some time, he will begin to use the moon as a base for a variety of observations, some of them not necessarily of the moon itself. Studies of the librations of the moon can give a great deal of information about the internal construction of the moon, but other astronomical investigations may well concern the sun and stars. For example, the other side of the moon has been pointed to as ideal for setting up a radio astronomy observatory. Also there may be great value in observations of the earth, particularly atmospheric phenomena, from the moon.

At first this observing from the moon as a base may well be done with automatic or semi-automatic equipment emplaced on the moon by the men who go there, supplementing other such observatories that were landed on the moon by unmanned spacecraft. Eventually, however, manned bases, including scientific observatories, will probably be established.

We have already said that the first scientist to land on the moon should probably be a geologist. Because of the construction work that will in time take place on the moon, it is also desirable that among the early lunar explorers there be a civil engineer. His job also will be to look and think, and collect data for the day when construction of supply depots, radiation shelters, roads, landing areas, large bases, and observatories will take place.

Already it is certain that when man does do engineering and building on the moon, he will do it under conditions far different from those encountered on the earth. The gravity will be only one-sixth of that met with on earth while the lack of an atmosphere, bombardment by meteoritic particles, the constant presence of the interplanetary radiations, the

tremendous range of temperatures, the possible presence of dust that may be more than just a nuisance, unusual conditions of electrostatic charging, etc., will confront him with problems that will tax his ingenuity and skill to the utmost.

When manned lunar bases or observatories go into operation, it will be necessary to have worked out a plan for maintaining the supply lines to them. The required logistics and operational support to the endeavor will make an Antartic expedition look like a grade school exercise in comparison.

All of this will require, of course, that an adequate scheme for protecting the men involved from the radiations of space will have been worked out, and put into use.

Man Around the Moon

Doubtless man will circumnavigate the moon, even go into orbit around it, before making a landing. At any rate, this is the present U. S. plan. During such maneuvers, prior to landing, man can make preliminary observations. Such observations will be needed to support the ultimate landing on the lunar surface, particularly those that reveal the character of the surface and permit one to select suitable landing sites. They will also be of scientific value. Of especial importance will be pictures that can be taken from the circumnavigating or orbiting spacecraft.

After man has landed and established a base on the moon, a lunar orbiting space station carrying one or more human observers can be used in conjunction with the observatory on the ground for further scientific exploration of the moon. For some time to come, the lunar satellite approach may be easier than lunar surface transportation for a global survey of the moon.

Interplanetary Space

On the way to the moon or the planets, man must traverse the space between earth and them. Although much of the investigation of these regions will doubtless best be done by intrumented space probes, nevertheless man will again have the opportunity to look about and search for the unexpected. Most of his observational opportunities will be astronomical in character. The zodiacal light, the Gegenschein, the sun's corona, the atmospheres of the planets, new views of the bodies of the solar system, can come under new scrutiny. In addition, man can continue observations on himself, under conditions of isolation not producible in any other fashion.

Man on the Planets

The investigation of the moon and planets by satellites, deep space probes, and manned exploration, serves to broaden the horizons of the geophysicst tremendously. A little thought will show that the techniques and experience that must be called upon in investigating these bodies must be those of the geophysicist. Moreover, as one goes forward with these lunar and planetary investigations, the student of the earth should find the broadened perspective provided by increased knowledge about the moon and planets a powerful lever to use in prying loose some of the secrets of the earth itself. Indeed, it is in recognition of these facts that the American Geophysical Union just recently voted to establish a new Section on Planetary Science.

The experience gained in manned exploration of the moon will no doubt serve as a basis for beginning the manned exploration of the planets. There will be many similarities, and many differences. Among the latter are the considerably greater distances that must be traversed, the longer times that man must spend out in the lonely voids of space, and the existence of atmospheres on the planets.

The ability to send measuring instruments to the moon and planets, and eventually to visit them in person, permits man to study directly more than one sample of the material of which the universe is composed, and more than one sample of the bodies of the universe. It is possible that the scientist may also have the opportunity to study more than one sample of physical life in the universe.

Certainly one of the most exciting possibilities in space exploration is that indigenous life may be found there. The most likely candidate, as you know, is Mars, where balloon observations in the infrared have detected emissions characteristic of the carbon-hydrogen bond. While this does not prove the existence of life on Mars, it is most certainly highly provocative. For this reason, preparations are going forward with various types of instruments to search for living forms on the Red Planet. These will be carried in fly-bys and landers as soon as we are able to provide the necessary transportation.

All the data available at present would indicate that there is little likelihood of life on Venus. Various radioastronomical observations of the planet indicate that the surface temperatures are in the vicinity of 600°K., well over the boiling point of water. These temperatures are in themselves discouraging enough, but when taken in conjunction with probably very high pressures existing on Venus (exceeding 20 atmospheres at the surface) it seems most likely that the entire planetary surface is bathed in a searing atmosphere, and that there is no chance of life there. The biologists insist, however, that there may yet be life on Venus, existing in the cooler upper atmosphere. Balloon samplings are being made of the earth's upper atmosphere to search for organisms that

might be living there. Results from these investigations may shed additional light on how much of a point the biologists have in connection with Venus.

It does not appear likely that there are living forms on the surface of the moon, because of the lack of an atmosphere, the lack of any observable water, and the extreme temperature ranges to which the lunar surface is subjected. Some believe, however, that there might be living forms existing at some distance below the hostile lunar surface. But even if there are no living forms on the moon, other biologists point out that the moon is still of interest in that it may carry the residue of previously living forms or possibly material that is in the nature of precursors to life. Controversy rages on this issue, with some scientists categorizing this reasoning on the part of the biologists as absolute nonsense. But the biologists can counter with the observation that if they should be right, walking all over the moon with dirty feet, or plastering it with dirty material, can destroy a once-in-forever opportunity to make exobiological studies that may have great bearing on our understanding of terrestrial life.

At any rate it seems clear that we must be careful about what we do in the case of Mars. A suggestion was made at the SUI Space Science Summer Study that Mars be made an ecological preserve, where steps are taken to protect the planet from undesirable contamination. According to the suggestion, Mars would be investigated in such a manner as to protect the interests and needs of the biologists who wish to search for and study any living forms or traces of life that might exist there. This proposal also included the suggestion that, although Venus and the moon not be considered as ecological preserves, care be taken to minimize their contamination.

Of course, if Mars is to be maintained as an ecological preserve, this can be done only by international cooperation, specifically, at the present time between the U. S. and the U.S.S.R.

One might mention in passing, that those who are concerned about possible contamination of our neighbors in space through the introduction of terrestrial organisms, also point to the possible danger of back contamination of the earth by the introduction of extraterrestrial organisms. Careful thought must be given to this problem, and in due time appropriate steps taken to remove any risks that are judged unacceptable.

When man reaches out toward the planets, who can say where it will all end? Your imaginations can explore this question as well as mine. Manned bases, observatories, landings on the satellites of planets, such as those of Jupiter or Saturn, artificial orbiting observatories about the different planets, and many other such things are in the realm of possibilities that the far distant future holds out to man. One even hears mention of the possibility of modifying the atmosphere of Mars to

make it less hostile or even almost habitable. This might be accomplished by the introduction of suitable biological agents to the planet, after the initial search for and investigations of indigenous life have been made.

But these speculations can serve us no real good here except to indicate that the field of space is wide open as far into the future as we can now see, and that the path to the planets leads farther than man can peer from his present position on the earth, at this point in time.

Conclusion

I am sure that I haven't made any startling revelations to you, or carried our subject any further in thought than you could have done, or perhaps have already done. But, hopefully, this little review of the things that man can look forward to doing in space, will serve the good purpose of showing clearly that it is indeed desirable to find ways of protecting man against the radiation hazards of space, so that he may go out into space in pursuit of his destiny.

Paper A-1

Brief Note on the Radiation Belts of the Earth

by

J. A. Van Allen
State University of Iowa

There are many different aspects to the radiation belts of the earth which may engage one's interest. This note is intended to present a brief graphical summary of one of these aspects, namely, the positional dependence of the absolute intensity of several selected components of the trapped particle population.

One of the earliest findings was that there are two distinct "belts" of trapped particles in the geomagnetic field -- an inner belt whose outer boundary is approximately the "magnetic shell" which crosses the equator at 1.8 earth radii from the center of the earth; and an outer belt which lies between this shell and one which crosses the equator at approximately 12 earth radii [Van Allen and Frank, 1959a]. The properties of the radiation in the respective

belts were found to be quite different [Van Allen and Frank, 1959b] [Van Allen, Ludwig, and McIlwain, 1959].

In subsequent work of a more comprehensive nature, using a variety of instruments carried by satellites, rockets, and space probes, it has become clear that the structure of the trapping region is quite complex and in fact that there are as many different structure functions as they are components of the trapped radiation to be considered. The concept of a two-belt structure has persisted, though it has now assumed a rather different significance than the original one. The distinctive general characteristic of the inner belt is now regarded as its relative time-stability whereas the distinctive general characteristic of the outer belt is its large and rapid time-variability. (Orders of magnitude change in intensity of selected components within times of the order of days and even of hours.) The magnetic shell which crosses the equator at 1.8 earth radii continues to represent the approximate interface between inner and outer zones. Despite the great time variability of particle populations and energy spectra in the outer zone, there has been observed during the past four years a remarkable tendency for it to relax back to a more or less standard state during prolonged periods of geomagnetically quiet conditions. The accompanying figures represent an effort to depict four sample structure functions

which are moderately well known and which give an abridged view of present knowledge. Each of these figures is a geomagnetic-meridian cross-section of the earth and of its near-astronomical environment. The semicircle at the left is the cross-section of the solid earth and the linear scale is in units of earth radii (6371 km). The contours are labeled by the value of omnidirectional intensity of the component specified in the caption. The distribution of particles in three dimensions is understood to be obtained by the rotation of the structure function shown about the vertical axis.

Figure 1 is considered to have a good level of reliability. It is based primarily on data from Explorer IV and from Pioneers III and IV (see references cited above). The omnidirectional intensity of protons having $E > 30$ MeV has its peak value at 1.4 earth radii on the equator and is about $3 \times 10^4/cm^2$ sec; beyond 2 earth radii it is less than $10/cm^2$ sec and may be much less than this beyond 4 earth radii.

Figure 2 is based in large part on the data from Pioneers III and IV (cited above), from Explorer VI [Arnoldy, Hoffman, and Winckler, 1960] [Fan, Meyer, and Simpson, 1961] [Rosen and Farley, 1961], and from Explorer XII [O'Brien, Van Allen, Laughlin, and Frank, 1962]. Values as high as 10^5 to $10^6/cm^2$ sec are sometimes found in the

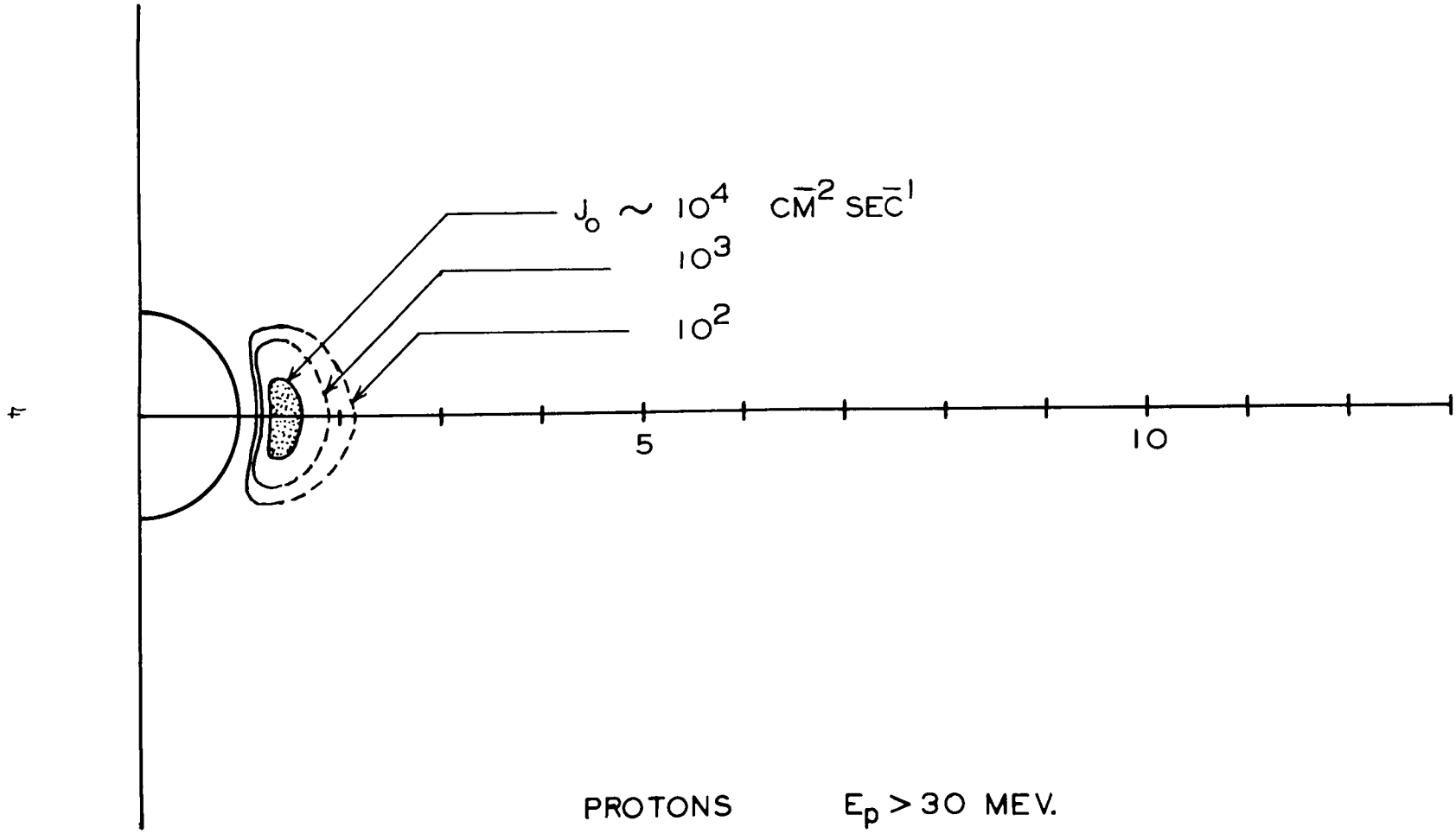

Fig. 1

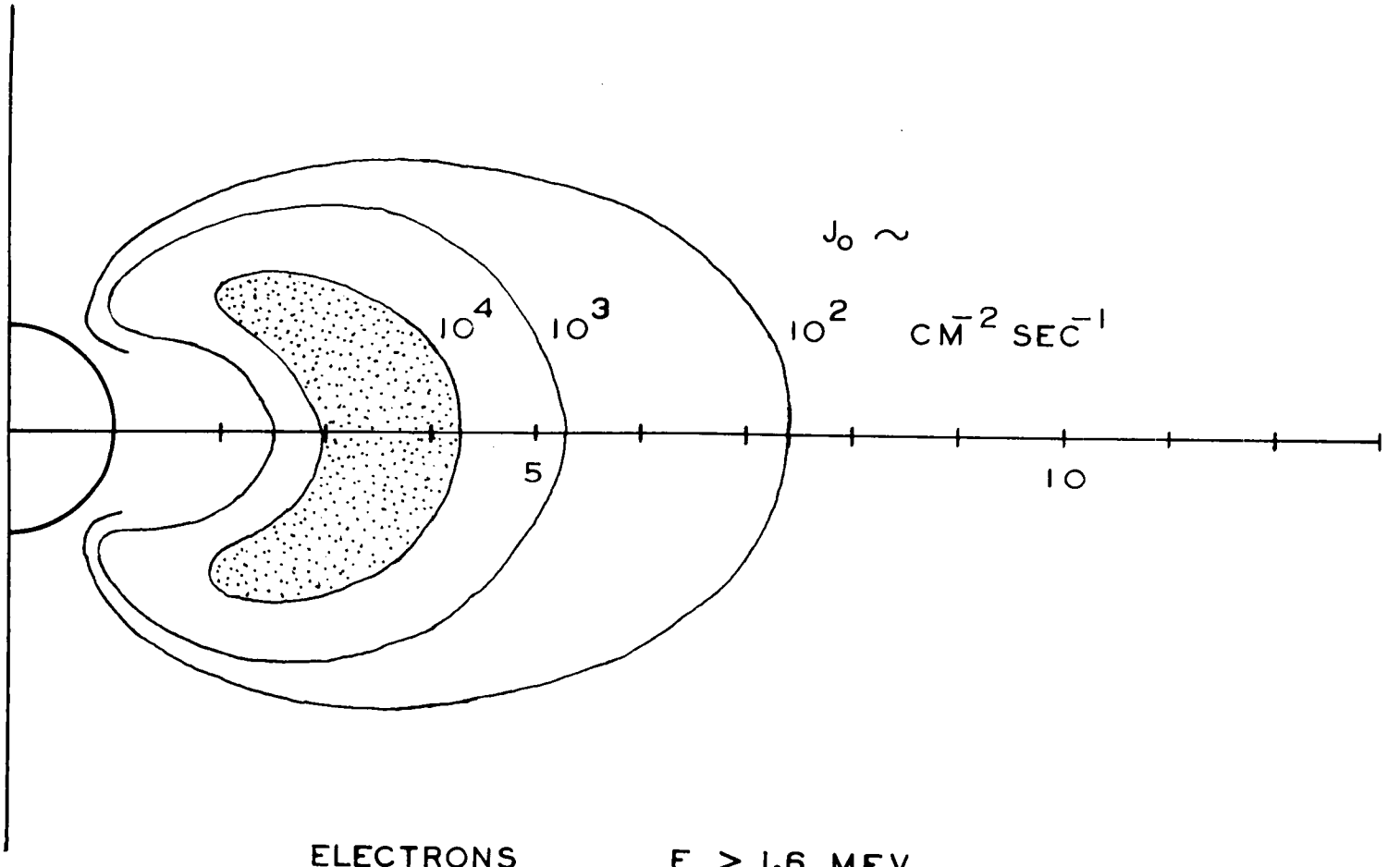

Fig. 2

vicinity of 4 earth radii. On other occations, the intensity of electrons of E > 1.6 MeV drops below the plotted values by as much as two orders of magnitude. The values shown in Figure 2 are intended to be representative of quiet conditions. The maximum intensity near 3.5 earth radii under such conditions is of the order of $10^5/cm^2$ sec. A comprehensive survey is currently underway with Explorer XIV [Van Allen and Frank, 1962], whose apogee is at 16.4 earth radii and whose perigee is at an altitude of about 400 km.

The structure function of Figure 3 for protons of energy $0.1 < E < 5$ MeV is an attempt on the part of the present author to represent the observations of Bame, Conner, Hill, and Holly [1961], Naugle and Kniffen [1962], and most importantly those of Davis and Williamson [1962], the latter with Explorer XII. Further extensive surveys are currently underway with Explorer XIV and Explorer XV.

Figure 4 synthesizes low altitude observations with Injun I [O'Brien, Laughlin, Van Allen, and Frank, 1962] and extensive observations with Explorer XII in a highly eccentric orbit [O'Brien, Van Allen, Laughlin, and Frank, 1962] [Rosser, O'Brien, Van Allen, Frank, and Laughlin, 1962]. Again there are marked time variations. Current observations with Explorer XIV are confirming the general character of Figure 4 and are contributing definitive new knowledge

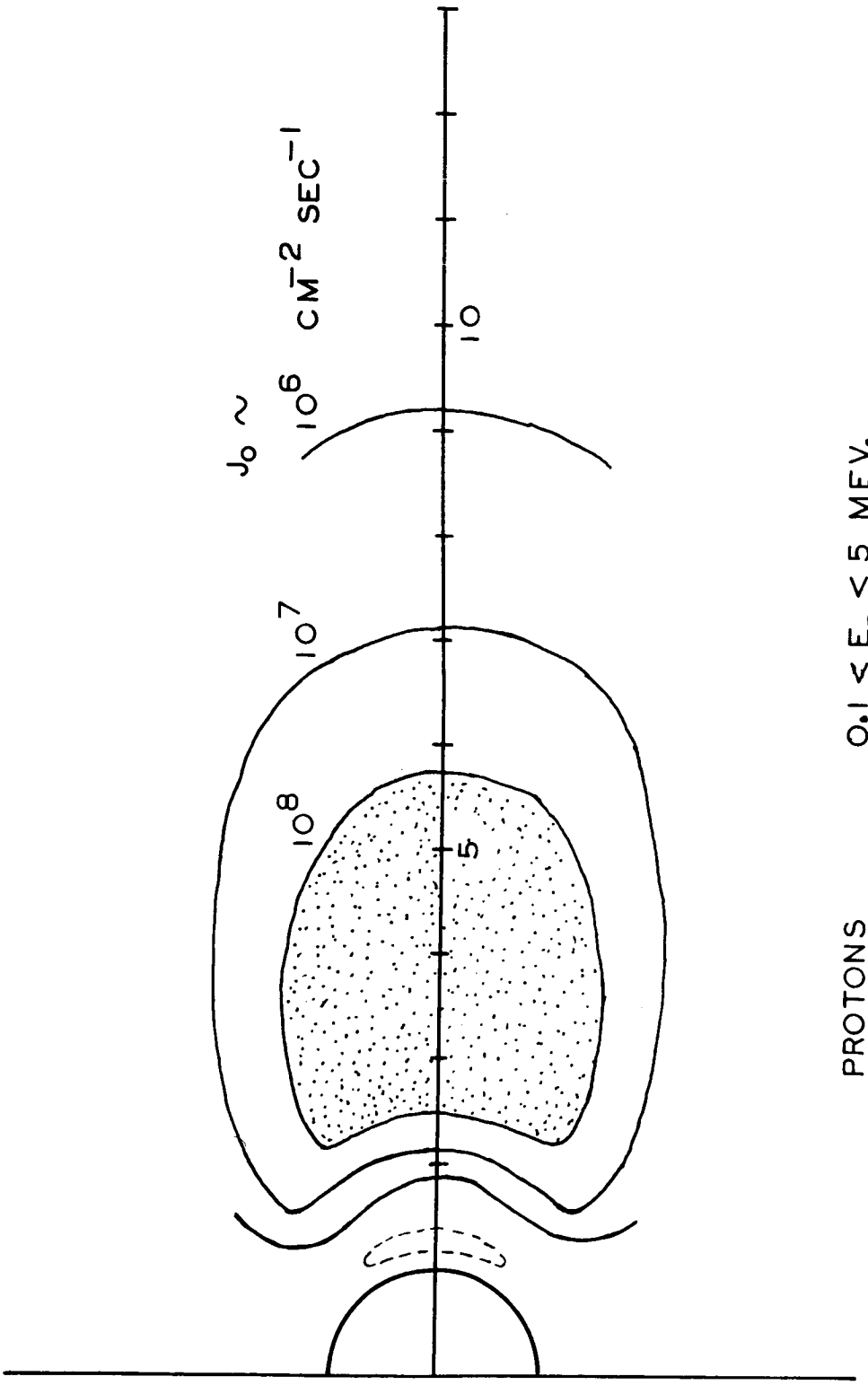

PROTONS $0.1 < E_p < 5$ MEV.

Fig. 3

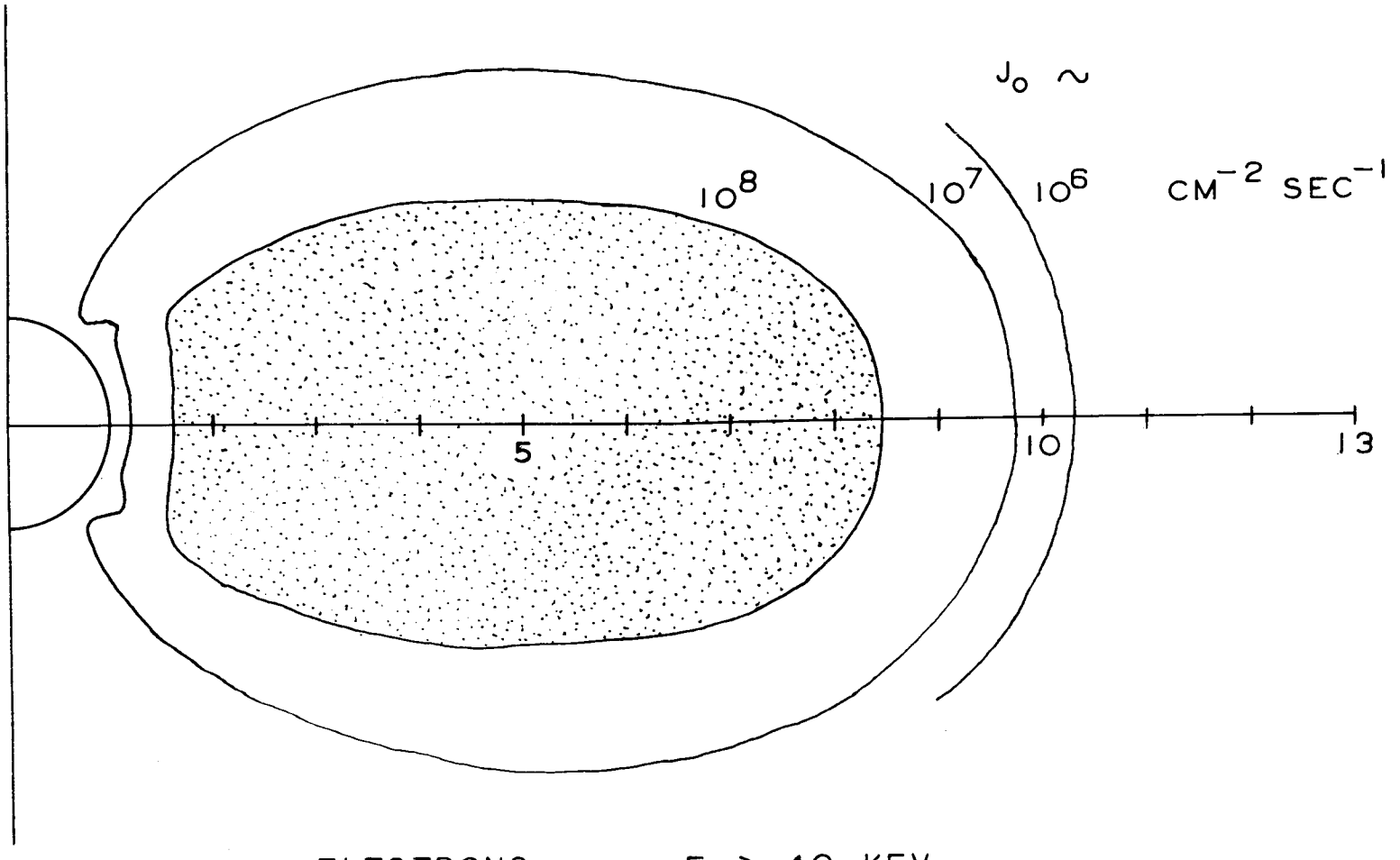

Fig. 4

on the omnidirectional intensity of electrons having $E > 40$ keV as well as those having $E > 250$ keV and those having $E > 1.6$ MeV [Van Allen and Frank, 1962].

For an earlier review of a more comprehensive character, the reader is referred to a paper in the Proceedings of the International Astronomical Union [Van Allen, 1962]

REFERENCES

Arnoldy, R. L., R. A. Hoffman, and J. R. Winckler, "Observations of the Van Allen Radiation Regions during August and September 1959, Part 1", J. Geophys. Research 65, 1361-1375 (1960).

Bame, S. J., J. P. Conner, H. H. Hill, and F. E. Holly, "Protons in the Outer Van Allen Belt", J. Geophys. Research 67, 1628 (Abstract) (1962).

Davis, L. R. and J. M. Williamson, "Low-Energy Trapped Protons", Third International Space Science Symposium and COSPAR Plenary Meeting, Washington, D. C., April 30-May 9, 1962.

Fan, C. Y., P. Meyer, and J. A. Simpson, "Dynamics and Structure of the Outer Radiation Belt", J. Geophys. Research 66, 2607-2640 (1961).

Naugle, J. E. and D. A. Kniffen, "The Flux and Energy Spectra of the Protons in the Inner Van Allen Belt", Journal of the Physical Society of Japan Vol. 17 Supplement A-II, 1962, International Conference on Cosmic Rays and the Earth Storm Part II, pp. 118-122.

O'Brien, B. J., C. D. Laughlin, J. A. Van Allen, and L. A. Frank, "Measurements of the Intensity and Spectrum of Electrons at 1000-Kilometer Altitude and High Latitudes", J. Geophys. Research 67, 1209-1225 (1962).

O'Brien, B. J., J. A. Van Allen, C. D. Laughlin, and L. A. Frank, "Absolute Electron Intensities in the Heart of the Earth's Outer Radiation Zone", J. Geophys. Research 67, 397-403 (1962).

REFERENCES (continued)

Rosen, A. and T. A. Farley, "Characteristics of the Van Allen Radiation Zones as Measured by the Scintillation Counter on Explorer VI", J. Geophys. Research 66, 2013-2028 (1961).

Rosser, W. G. V., B. J. O'Brien, J. A. Van Allen, L. A. Frank, and C. D. Laughlin, "Electrons in the Earth's Outer Radiation Zone", J. Geophys. Research 67 (in press).

Van Allen, J. A., "Dynamics, Composition and Origin of the Geomagnetically-Trapped Corpuscular Radiation", Proceedings, International Astronomical Union, 1962 (in press).

Van Allen, J. A. and L. A. Frank, "Radiation Around the Earth to a Radial Distance of 107,400 Kilometers", Nature (London) 183, 430-434 (1959).

Van Allen, J. A. and L. A. Frank, "Radiation Measurements to 658,300 Km with Pioneer IV", Nature (London) 184, 219-224 (1959).

Van Allen, J. A. and L. A. Frank (Private Communication, 1962).

Van Allen, J. A., C. E. McIlwain, and G. H. Ludwig, "Radiation Observations with Satellite 1958 Epsilon", J. Geophys. Research 64, 271-286 (1959).

Paper A-2

An Evaluation of the Radiation Hazard Due to Solar Cosmic Rays

by
W. R. Webber and P. S. Freier*

Introduction

Although the characteristics of the galactic cosmic radiation have been recognized and investigated in detail for many years, the ability of the sun to produce large bursts of energetic particles was discovered only in 1946 (Reference 1) and the arrival of this solar cosmic radiation at the earth has been studied in detail only since 1956. In the ten years preceding the solar cosmic ray event of February 23, 1956, there were only four cases of an increase of cosmic ray intensity at the earth (as measured at ground-level by ionization-type detectors) that could be related to solar activity. Therefore the idea became widespread that these events were quite rare.

The introduction of the neutron monitor in 1949 (Reference 2) somewhat improved the sensitivity of the ground-level measurements, but the real breakthrough came recently with particle counters and emulsions flown in balloons, satellites, and space probes. In addition, it has been found that the solar particle bursts may be detected indirectly through their effects on the absorption of VHF cosmic noise in the ionospheric D-layer over the polar caps - called polar cap absorption (PCA).

From the studies of solar particle bursts over the last few years by this wide variety of techniques, a reasonably complete picture of these events is beginning to emerge (Reference 3). The cosmic ray particles ejected from the sun are known to be primarily protons with typically steep energy spectra and

*University of Minnesota

ranging in energy from less than 10 Mev to a few Bev. Such cosmic ray particles may be present near the earth in detectable numbers a significant fraction of the time (5 - 10 percent), exceeding the normal galactic cosmic ray intensity for a much smaller period of time (~ 1 percent) and occasionally for intervals of one or two days, reaching intensities many thousands of times greater than the galactic cosmic ray intensity.

The intensity-time, directional, spectral, and charge characteristics of the solar cosmic rays differ considerably from event to event. For example, some events may contain a relatively large fraction of high-energy particles, thus producing a rare effect in a sea-level detector; but, on the other hand contain few low energy particles, thus giving a small integrated particle intensity. The latter characteristic causes the event to be classified as a relatively small one. Other important dissimilarities exist from event to event, and for this reason we shall catalog some of the more important ones individually. However, we may define certain general characteristics - common to all events - which may aid in understanding these events.

The Intensity-Time Profile

A typical event will have a set of intensity-time profiles, one for each energy, such as those shown in Figure 1 . Certain times characterize each profile:

1. The onset-delay time is defined as the time from the maximum of the visual flare intensity to the arrival of the first particles at the earth. This time is variable from event to event and is strongly energy-dependent, the higher energies arriving first. Onset-delay times may vary from a few

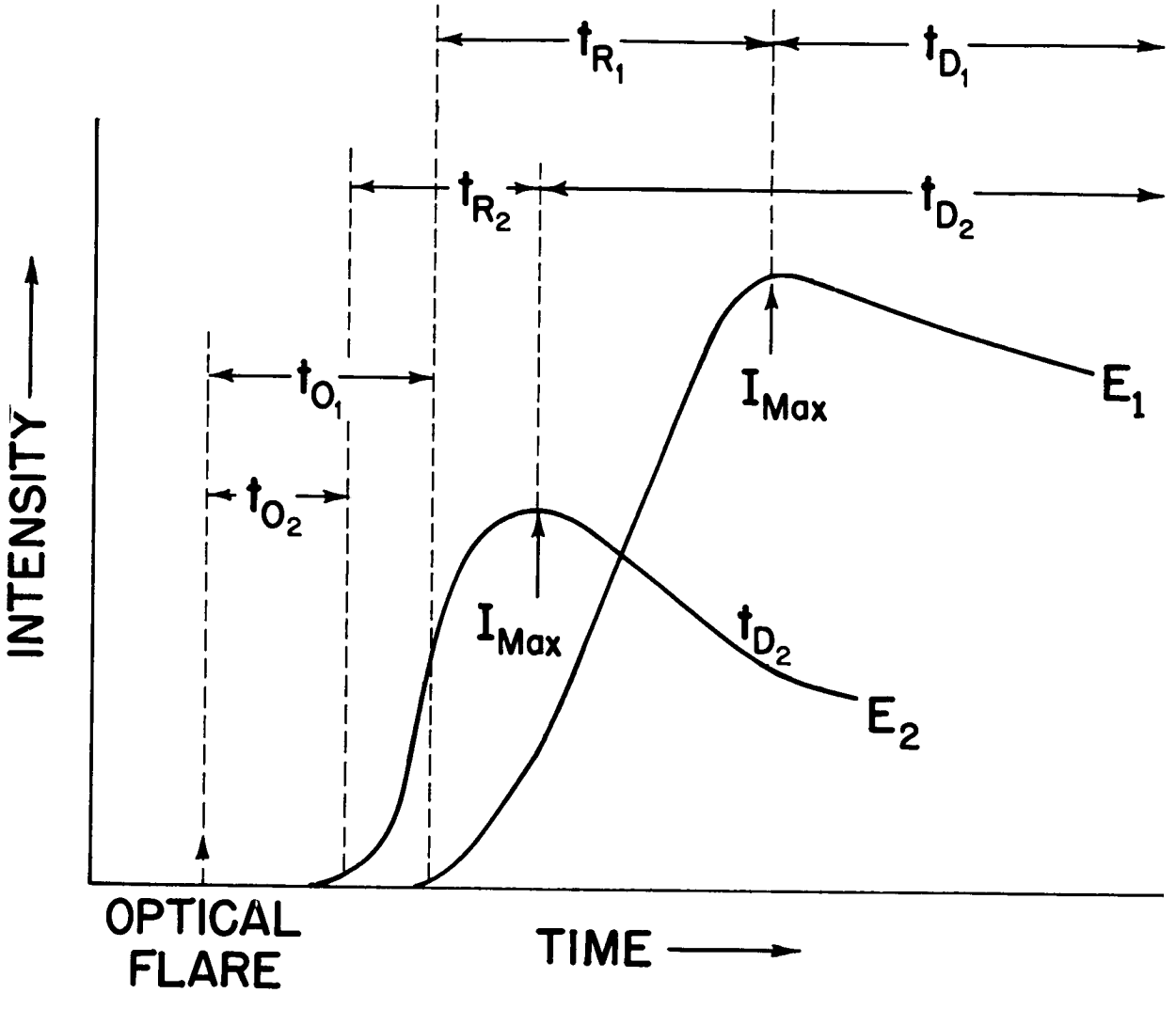

Figure 1 - Intensity-time profiles for a typical event. Curve E_2 represents the arrival of particles of energies that are high in comparison with the energies of the particles represented by curve E_1. T_{O_1} and T_{O_2} are onset-delay times; T_{R_1} and T_{R_2}, rise times; and T_{D_1} and T_{D_2}, decay times.

minutes for high energy particles in some events to many hours for low energy particles in other events.

2. The rise time is defined as the time interval from the first arrival at the earth of particles of a particular energy to the time at which maximum intensity of these particles is attained. This time also varies from event to event and is strongly energy-dependent, the higher energies reaching maximum intensity first. These times are usually related to the onset times in a particular event, and may range from a few minutes for high energy particles in some events to many hours for low energy particles in other events.

3. A growing body of evidence indicates that the decay of the intensity of the particles above a particular energy is exponential at most times and over a wide range of energies (Reference 3). Thus we may define a characteristic decay time t_D and write the following equation for the intensity of flare particles with energies greater than some energy E at some time t after the maximum intensity $I_{Max}(E)$ attained:

$$I = I_{Max}(E)\, e^{-t/t_D}.$$

The time t_D itself is a function of energy being smaller for higher energies and is variable from event to event. It may be changed during the course of an event by the arrival at the earth of a changed interplanetary field configuration, such as might be evidenced by a magnetic storm or other magnetic activity. The decay time may range from 3-4 hours for high energy particles in some events to 2-3 days for low energy particles in other events.

Anisotropies in the Flare Particles

For the most part the solar flare particles arrive at the earth very

nearly isotropically (within $\pm$ 5-10 percent) and the aforementioned intensity-time characteristics refer to this isotropic radiation. Frequently, however, significant anisotropies exist in the direction of arrival of solar flare particles in the earth's vicinity. In particular, the particles appear to arrive from a highly preferred and fairly narrow direction in space. Such directional radiation is usually of short duration compared to the isotropic part; however, unusually high intensities may occur in the preferred direction for periods of a few minutes. It is also possible to define onset-delay, rise, and decay times for this directional radiation.

The Energy Spectrum of the Flare Particles

It is obvious from the foregoing discussion on the intensity-time characteristics of the flare particles and from the energy-dependence of each of the parameters involved that there is no unique energy spectrum for any one event. The spectrum measured in a single event will depend upon the specific time in the event at which the measurements are made. The problem of determining a useful and meaningful representation of the solar flare particle spectrum has been one of the most difficult connected with the study of the flare particles. Usually the differential number spectrum of the flare particles has been expressed either as a power law energy spectrum eg $\frac{dJ}{dE} = \frac{K_1}{E^{n_1}}$ or as a power law rigidity spectrum eg $\frac{dJ}{dP} = \frac{K_2}{P^{n_2}}$ (the rigidity of a particle $\equiv P = \frac{pC}{Ze}$ where p is the particle momentum, C the velocity of light, e the unit charge, and Z the charge number of the particle). When either of these representations is used n_1 (or n_2) is a function of both energy (or rigidity) and time (eg n_1 or n_2 is usually smaller for lower energies or rigidities causing a bending over of the spectrum - also n_1 or n_2 increase with time after

the onset of an event thus resulting in a steepening of the particle spectrum with time).

Because the energy or rigidity interval viewed in any one measurement is usually quite narrow, it is possible to represent reasonably well the number spectrum of solar flare particles as a power law energy or rigidity spectrum with a constant n over the interval of measurement. This does not prove to be a useful representation over the entire range of rigidities involved in the solar outburst, however.

After a careful examination of the data from a large number of events which were difficult to interpret if the solar particle spectrum were considered to be power laws in either energy or rigidity we have reached the conclusion that a one parameter system best defines the spectra of the solar flare particles (Reference 4). This one parameter system is an exponential rigidity spectrum of the form $\frac{dJ}{dP} = (\frac{dJ}{dP})_o e^{-P/Po(t)}$. $P_o(t)$ is a characteristic rigidity which in a single event is a function of time only - decreasing as the event progresses. Its value and time dependence may vary from event to event, however. Such spectra apply to all rigidities providing the time is a few times the normal delay time for particles of a particular energy arriving from the sun.

The above conclusion is reached only after a considerable modification of our interpretation of solar particle spectra from measurements made during balloon ascents and particularly after a considerable reinterpretation of the intensities and spectra of low energy solar flare particle from riometer measurements. The grounds for these modifications are discussed in detail in reference 4.

With such spectra it is not necessary to "artificially" bend over the power law spectra at lower energies - the effect of an exponential spectrum

is the same as a "bent over" power law. A comparison of the time development of a typical solar cosmic ray spectrum during an event using the two representations is shown in Figure 2. Typical initial values of the "characteristic" rigidity may range from ~ 300 MV in events with very flat spectra containing many high energy particles to ~ 50 MV in events with very steep spectra containing many low energy particles and producing strong radiowave absorption.

Charge Composition of the Flare Particles

The particles emitted in a solar flare burst are predominantly protons, but in each event, to a greater or lesser degree, particles heavier than protons appear to be present - predominantly alpha particles but including nuclei in the CNO group at least (references 5 and 6). To date these heavier particles have actually been observed during six solar cosmic ray events, by only one or two spot measurements during each event. In addition these measurements may represent intensity integrals of solar particles over several hours. It is useful, however, to define a characteristic ratio of the protons to the heavier nuclei present in a particular event eg P/a = proton-alpha particle ratio. This characteristic ratio apparently varies from event to event. The P/a ratio may be from as high as 40 to as low as 1 in different events, and the P/CNO ratio may vary from 10^2 to 10^3. This ratio appears to be constant as a function of rigidity since both the alpha particles and heavier nuclei seem to also be best represented by an exponential rigidity spectrum. As far as total particle numbers are concerned, the heavier nuclei in solar flares are probably, on the average, relatively less abundant than the heavier nuclei in the galactic radiation.

Specific Features of Important Solar Cosmic Ray Events and Related Solar Flares

During the period 1956-1961 nearly 50 solar cosmic ray outbursts have been recorded at the earth by a wide variety of techniques. These events display

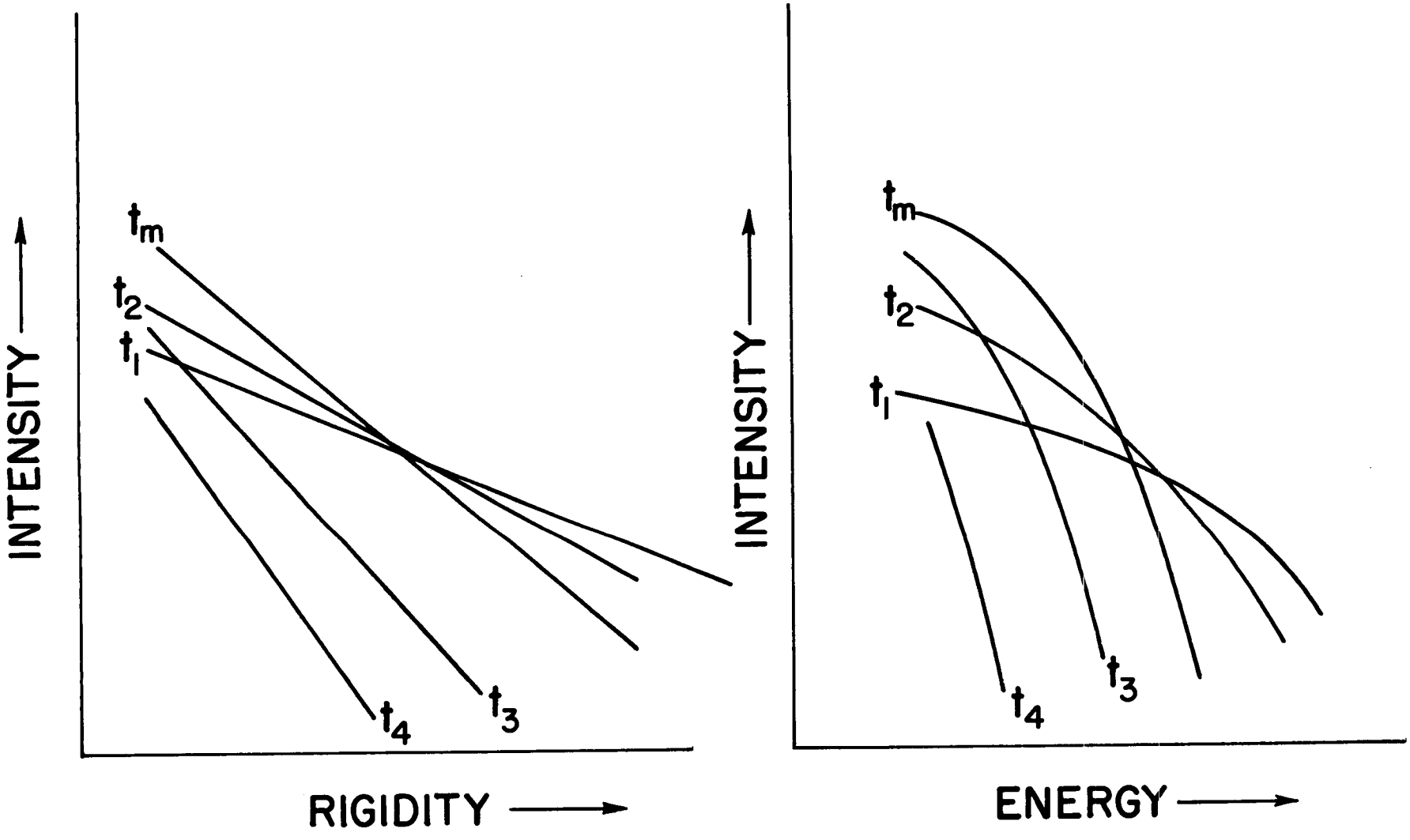

Figure 2 - Typical power law energy and exponential rigidity spectra obtained at different times (T_1 T_2 T_m T_3 T_4) during a single event.

an enormous variation (10^4 - 10^5) of integrated particle intensities for the duration of the outbursts. Of these events, approximately 30 of the largest - those with minimum integrated intensity of 10^{-6} particles/cm^2 at energies greater than 30 Mev observed at the earth - have been selected for discussion here. These events are comparable to the integrated intensity of galactic radiation for one week; the smaller events obviously do not contribute appreciably to the enhancement of the cosmic ray intensity near the earth. Prior to 1956 it was not possible to make a size estimate on any of the solar cosmic ray events; therefore, these events are not included, although undoubtedly many important ones occurred. The identification of a solar cosmic ray event by radiowave absorption (riometer) data alone is not regarded as sufficient to make a specific size estimate. In fact, size estimates based on the relative radiowave absorption may be grossly misleading, since the absorption may in many instances be produced by solar cosmic rays of much lower energy than the 30 Mev lower limit selected, or by auroral electron effects. (The chosen lower energy limit represents a penetration of about 1 gm/cm^2.)

Rough size estimates have been made when direct measurements of solar cosmic ray intensities at the top of the atmosphere or in space near the earth were available at one time during the event. Detailed estimates of intensity-time characteristics, spectral distribution, and size have been made only when a number of direct measurements of solar cosmic ray intensities and/or spectra exist at the top of the atmosphere or in space near the earth for a particular event.

By referring to Table I, we may elaborate more critically on some features of specific solar flares and related cosmic ray events. First we note that although 30 separate events are cataloged over the six-year period, they occur in only 16 different active centers. During the last three years (1959-1961) this tendency is even more pronounced, for 18 separate events have been associated with only 5 different active centers. The active centers associated with these flares were usually already well developed when they appeared at the east limb of the sun. Only once did the same active center continue to produce large cosmic ray events during its subsequent appearance on the visible hemisphere of the sun. From four of these active centers (McMath Plage Numbers 3400, 5269, 5925 and 6171) have come over 90 percent of all of the solar cosmic rays/observed at the earth in the last six years. with energy $\geq$30 Mev

From Table 1, we note that, of the 30 events listed, 22 have been from flares in the sun's western hemisphere and 8 from the eastern. Of the 10 largest events, 6 have come from flares in the western hemisphere and 4 from flares in the eastern. Finally, from the 5 active regions that have produced 18 of the cosmic ray flares in the last three years, 11 of the flares have occurred while the active center was in the western hemisphere; and 7 in the eastern. Of these five active regions, the four major ones have been in the northern hemisphere and the remaining one in the southern.

From the above statistics we can say that for cosmic-ray-producing flares as a whole, there is a greater likelihood of observing cosmic rays at the earth when the flare is in the sun's western hemisphere. This situation suggests that on the average a greater fraction of the particles produced are received at the earth when the flare is nearest the west limb of the sun. A large,

Table I
Solar Flare and Cosmic Ray Data Relating to the Major Solar Cosmic Ray Outbursts Occurring During the Years 1956-1961

	Solar Flare Data					Cosmic Ray Data										
						Onset and Rise Time (hours)		Decay Time (hours)		Peak Intensity**		Characteristic	Integrated Intensity		Integrated Skin dose***	
Date	Importance	Heliographic Position (degrees)	Time of Optical Maximum	Maximum RF Emission*		>30 Mev	>100 Mev	>30 Mev	>100 Mev	>30 Mev	>100 Mev	Po (MV)	>30 Mev	>100 Mev	>30 Mev	>100 Mev
1956 Feb 23	3+	N22 W74	0340	20,000 at 0341		6-8	3-4	30	16	6,200	5,000	325	6.5×10^8	3.2×10^8	120	28
1956 Aug 31	3	N16 E16	1241			No detailed estimate possible							3×10^7		10	
1957 Jan 20	3+	S25 W30	1120							2,000-3,000	100-200		3×10^8	10^7	60	1.2
1957 Jul 03	3+	N14 W40	0740			No detailed estimate possible							1×10^7		3	
1957 Aug 29 to 31	(uncertain flare, possibly two events)									200-300	~10		5×10^6		15	
1957 Oct 20	3+	S26 W45	1642			No detailed estimate possible							1×10^7		3	
1958 Feb 09	2+	S12 W14	2142			No detailed estimate possible							5×10^6		1.5	
1958 Mar 23	3+	S14 E78	1005	10,000 at 1004				(40)	(20)	1200-1500	~50		2×10^8	5×10^6	50	0.7
1958 Jul 07	3+	N25 W08	0115	2,000 at 0112				32	16-20	1500-2000	~80		3×10^8	7×10^6	80	1.0
1958 Aug 16	3+	S14 W50	0440	6,200 at 0442		10		18		200			2×10^7		4	
1958 Aug 22	3	N18 W10	1448			10-12	3-4	20	8-12	500	20		5×10^7	1×10^6	20	0.15
1958 Aug 26	3	N20 W54	0027	6,700 at 0025		~9		(12)		1,100			5.3×10^7		17	

1959	May 10	3+	N23 E47	2118	~10,000	18-22	12-48	22	10-14	6,000-8,000	1,000	60	7×10^{8}	7.5×10^{7}	170	10
	Jul 10	3+	N22 E70	0222	15,000 at 0224	30-40	18-20	40	20	4,000	1,200	90	8.8×10^{8}	1.0×10^{8}	148	11
	Jul 14	3+	N16 E07	0349	6,300 at 0352	16-20	12-16	18	9-12	10,000-12,000	1,200	70	1.1×10^{9}	6.3×10^{7}	177	7.4
	Jul 16	3+	N08 W26	2145	6,500 at 2200	12-14	4-5	30	18	6,000-8,000	1,500	110	8.1×10^{8}	1.3×10^{8}	125	19
1960	Apr 01	3	N12 W10	0859		2-3	<1	12	4-6	50	6		2.7×10^{6}	1.5×10^{5}	0.6	0.001
	Apr 05	2+	N10 W61	0245	~8,000 at 0203			12		40			2×10^{6}		0.7	
	Apr 28	3	S05 E34	0130		8-10	3-4	18 24	8	300	20		2.5×10^{7}	7×10^{5}	6	0.08
	May 04	3+	N14 W90	1020		2-3	<1	8	4	200	40	300	7×10^{6}	7×10^{5}	16	0.07
	May 06		uncertain flare							50-100			5×10^{6}		1.5	
	Sep 03	3	N18 E88	0110	12,000 at 0108	12-16	7-9	32	26	240	60		4×10^{7}	7×10^{6}	4	0.6
	Nov 12	3+	N27 W02	1329	10,000 at 1329	12-16	8-10	18-24	14-18	12,000	2,500	145	1.4×10^{9}	3.5×10^{8}	205	33
	Nov 15	3+	N30 W32	0221	14,000 at 0227	10-16	3-5	16-20	8-12	6,000	2,400	135	5.2×10^{8}	1.2×10^{8}	100	12
	Nov 20	3	N28 W113	2020		3-4	~1	10-16	4-6	1,000	4,000		6×10^{7}	6×10^{6}	15	0.7
1961	Jul 11	3	S06 E32	1700	2,500	8-10	4	22-26	18	20	3		2×10^{6}	3×10^{3}	0.5	0.03
	Jul 12	3+	S07 E22	1030	7,500	8-12	6	16-20	12	120	15	50	1.0×10^{8}	1.6×10^{6}	10.5	.29
	Jul 18	3+	S06 W60	1010	5,000	6-10	2-3	24	12	2,500	600	135	2.1×10^{8}	4.8×10^{7}	27	3
	Jul 20	3+	S07 W90	(1600)	2,500	4-6	1.5	6-8	3	300	70		9×10^{6}	1.2×10^{5}	2.5	0.2
	Sep 28	3	N14 E30	2223								250	2.2×10^{5}	9.7×10^{4}	0.5	0.15

*Max Emission in range 3,000-10,000 Mc in units of 10^{-22} w/(m^2-cps)
**In units of particles/(cm^2/sec) or particles/cm^2 in free space (4π) x integrated intensities
***In units of rad (1 rad = 3.2×10^{7} (particles/cm^2) x average specific ionization in units of 1.6 Mev)

important cosmic-ray event is almost equally likely to arise from a flare in the western or eastern hemisphere. However, a distinct northern hemisphere preference is noted.

The correlation between the peak RF emission in the frequency range between 3,000 and 10,000 Mc/s during the flares, and the size of the cosmic ray event at the earth is sufficiently good that we can use the values of this peak RF emission to make fairly useful statements regarding the integrated size of the cosmic ray event. If the peak RF emission in this range exceeds $10{,}000 \times 10^{-22}$ w/m^2-cps, about 50 times normal, the integrated intensity of solar cosmic rays at energies above 30 Mev at the earth will generally exceed 10^8 particles/cm^2 (i.e., exceed the average yearly integrated intensity of galactic cosmic rays). If the peak RF emission in this range exceeds $3{,}000 \times 10^{-22}$ w/m^2-cps, the cosmic ray event will still be important and the integrated intensity of particles at energies greater than 30 Mev at the earth will usually exceed 10^7 particles/cm^2. If the peak emission in this range is less than 1,000 to 2,000 $\times 10^{-22}$ w/m^2-cps, the cosmic ray event is usually not a major one.

Turning now to the characteristic intensity-time profiles of the solar cosmic rays as observed in the earth's vicinity, we see that the average initial delay from the time of the peak optical (and radio) emission until the first arrival of the isotropic component of solar particles at the earth (for particle energies above 100 Mev) is about 1/2 hour for flares in the western hemisphere and about 1-1/2 hours in the eastern. The average rise times for the particles with energies $>$100 Mev are 2-3 hours and 6-8 hours for the western and eastern hemispheres respectively. The onset and rise times

for the isotropic component of particles with energies above 30 Mev are longer by a factor of 2 in each event, but otherwise show the same characteristics.

A detailed examination of the rise-time characteristics for particles with energies above 100 Mev during a number of events reveals that this increase in solar particle intensity may be closely approximated by

$$I = I_{Max}(E)\, e^{-t/t_R},$$

where t_R is the characteristic rise time and t is measured from the time of peak intensity $I_{Max}(E)$ back to the time of the flare. In view of our previous statements t_R will be a function of the energy of the particles and also of the position of the flare on the sun.

The decay of intensity of the solar flare particles near the earth, like the onset characteristics, appears to be related in some lesser degree to the position of the flare on the sun. Thus, the time scales of the decays will be related to the time scales of the onsets just discussed, although there is not a strict one-to-one correspondence between these features. A detailed examination of the decay characteristics of a number of events reveals that the decay may be closely approximated by

$$I = I_{Max}(E)e^{-t/t_D},$$

where t_D is the characteristic decay time which depends on the energy and probably to some extent also on the flare's location; and t is measured from the time of the peak intensity $I_{Max}(E)$ to later times in the event. For particle energies greater than 100 Mev, t_D ranges from 10 to 20 hours in 15 of the 18 events in which it was possible to determine a characteristic decay time. There is some tendency for the longest characteristic decays to be associated with flares near the sun's east limb; and the three shortest decays, with

characteristic times less than 10 hours, are all associated with flares occurring near the west limb (and in active centers which had previously produced cosmic rays). Consequently, there is the aforementioned relation between t_R and t_D. The average for the 18 events, considering particle energies greater than 100 Mev, is $t_D/t_R = 4$ with extremes from 1.5 to 6. The characteristic decay times for particles with energies exceeding 30 Mev are about twice as long as for particles with energies exceeding 100 Mev. A similar ratio for t_D/t_R also exists for the lower energy particles, since t_R for the latter is also twice t_R for particles with energies greater than 100 Mev.

The utilization of the characteristically similar intensity-time behavior for events having widely differing peak intensities and occurring at different locations on the sun permits a fairly dimple estimate of the total integrated intensities of particles with energies greater than 30 Mev and those with energies greater than 100 Mev in space near the earth. Thus for J, the total integrated intensity in an event, we have

$$J\ (>E) = \int_{-\infty}^{0} I_{Max}\ (>E)\ e^{-t/t_R}\ dt + \int_{0}^{\infty} I_{Max}\ (>E)\ e^{-t/t_D}\ dt$$

$$= (t_R + t_D)\ I_{Max}\ (>E),$$

The appropriate $J_{Max}(>E)$ is determined from the measured spectra in each event and a study of the variation of Jo and the characteristic rigidity Po with time during the event.. This data may be found in reference 4. We should point out that the $I_{Max}(>E)$ derived here are considerably lower than previous estimates, particularly at the lower energies. This is due to a number of

reasons - the main ones being - (1) the adaption of the exponential rigidity spectrum for the solar particles (2) the use of ionospheric parameters that predict a larger radiowave absorption for a given solar particle intensity - or conversely a lower solar particle intensity for a given (measured) radiowave absorption (reference 7) (3) the modification of the solar particle spectra deduced from balloon ascent measurements.

The total skin or free-space doses evaluated for each event depend only on the total integrated particle intensity/cm^2 and the average specific ionization (relative to the minimum ionization) of each particle. Meanwhile, the average specific ionization per particle depends on the characteristic rigidity describing the spectrum of the radiation. As we have noted, this characteristic rigidity varies over the course of a single event, being largest at earlier times and smallest at later times. However, an average value over the course of an event has been deduced and we use this value to obtain the average specific ionization per particle of the radiation. For $I_{Max}(>30 Mev)$, this specific ionization ranges from about 8 times minimum for characteristic rigidity $\sim$ 50 MV to about 3 times minimum for characteristic rigidity $\sim$ 300 MV, assuming the incident radiation to be composed of protons only. For I_{Max} ($>$100 Mev) these values are $\sim$ 4 times minimum and 2 times minimum respectively. (The minimum ionization is 1.6 Mev/gm-cm^2 in air or 2.6 x 10^{-6} erg/gm-cm^2. Since one roentgen equals 83.7 ergs/gm of air, an integrated intensity of 3.2 x 10^7 particles/cm^2 of minimum ionization produces a dose of one roentgen.)

The total skin or free space doses evaluated for each event are presented in Table I along the peak particle intensities $>$30 Mev and 100 Mev and the total integrated particle intensities over the entire event above these energies.

Summary of Solar Cosmic Ray Events in Relation to Dose Rates Obtained in Space

The main objective of this summary of solar cosmic ray events is, of course, to attempt an evaluation in general terms of the radiation hazard in space presented by these events. It seems reasonable to evaluate the hazard in terms of the integrated dose of galactic radiation, for this radiation forms an almost constant background in space - and one so penetrating that reasonable shielding considerations have little effect on the intensity of the radiation. The free-space galactic particle intensity varies from 1.5 particles/cm^2-sec near sunspot maximum to about 4 particles/cm^2-sec near sunspot minimum. The integrated weekly rates are thus roughly 1×10^6 and 2.5×10^6 particles/cm^2 respectively; the yearly rates range from 5×10^7 to 1.2×10^8 particles/cm^2. (Assuming an average specific ionization about 3 times minimum for these galactic particles, the integrated weekly dose ranges from 0.1 to 0.25 rad and yearly dose from 5 to 12 rad.)

In Table 2 the yearly integrated intensities of solar particles above 30 and 100 Mev are compared with the total integrated intensity of galactic particles for the years 1956-1961. Over this six-year period the integrated intensity of solar cosmic rays with energies greater than 100 Mev and greater than 30 Mev are respectively, about 2.5 and about 15 times the total integrated galactic intensity. Most of the solar cosmic ray intensity occurs during the three particular years 1956, 1959, and 1960. In fact, most of the solar cosmic ray intensity comes from the solar events associated with only three active centers; McMath Plage 3400 for the February, 1956 event; 5269 for July, 1959; and 5925 for November, 1960. The remaining events during this six year period contribute only 0.2 and 2 times the integrated galactic cosmic ray intensity above 100 Mev

Table 2

Yearly Integrated Intensities of Solar Cosmic Rays with Energies Above 30 and 100 Mev and of Galactic Cosmic Rays

Year	Number of Events	Solar Cosmic Rays Integrated Intensity (particles/cm^2)		Galactic Cosmic Rays Integrated Intensity (particles/cm^2)
		30 Mev	100 Mev	
1956	2	7×10^8	3.2×10^8	1×10^8
1957	4 or 5	4×10^8	1.0×10^7	7×10^7
1958	6	7×10^8	1.0×10^7	6×10^7
1959	4	3.6×10^9	3.4×10^8	6×10^7
1960	8	2×10^9	5.0×10^8	8×10^7
1961	5	3.2×10^8	6.0×10^7	1×10^8
TOTAL	30	7.2×10^9	1.2×10^9	4.7×10^8

and 30 Mev respectively. A study of the smaller events not individually listed here reveals that, even if the frequency of these events is 20 to 30 a year, the integrated yearly intensity of solar cosmic rays with energies greater than 30 Mev from these events is not likely to exceed that from galactic cosmic rays. Thus we can state that during a time scale of one year - neglecting the three largest events - the integrated intensities of solar cosmic rays with energies above 30 Mev and of galactic cosmic rays are comparable; and with a reasonable minimum shielding of only 2 to 3 gm/cm^2 the yearly average dose from solar cosmic rays is less than that from galactic cosmic rays (i.e., less than 12 rad).

Thus, the problem of radiation exposure from solar cosmic ray outbursts would reduce to the problem of such exposure from the few largest events. The total integrated dose from these events may present a problem, the seriousness of which depends on the amount of shielding - as can be seen from the doses due to particles with energies above 30 and 100 Mev (Table 1). The two largest sequence of events, those of July 1959 or November 1960 produced integrated skin doses from particles with energy >30 Mev of ~ 450 rad and 300 rad respectively. Such would be the doses under slightly more than 1 g/cm^2 of shielding. For 10 g/cm^2 shielding corresponding to particles 100 Mev the doses would have been ~ 40 rad and 45 rad respectively for these "most dangerous" events.

The statistics relating to the frequency of occurrence of the largest events are, of course, very limited - 6 events in 6 years, or an average of one event every year producing a dose >100 rad (or 3 events producing a dose >200 rad) during six years from particles >30 Mev. Only one of these events would have been observable by the techniques used prior to 1950, when four events were recorded in about 10 years of observation. If we assume then that the techniques in operation during this period could detect one out of three events of truly major importance, about 12 such events may have occurred during the 10 year period. These considerations are undoubtedly crude but they are the best available at present. Combined with the recent, more definitive data, they suggest that on the average of once every year an active region appears that will ultimately emit one or more major cosmic ray bursts. Although dozens of smaller events may occur during such a period, they are relatively unimportant in consideration of the overall integrated solar cosmic ray intensity.

It is quite certain that the appearance of active regions producing major cosmic ray bursts is not strongly correlated with the maximum in the eleven-year cycle of solar activity. During the recent maximum, 1957-58, no such major cosmic ray bursts were recorded, and the yearly integrated solar cosmic ray intensities at energies greater than 30 and 100 Mev were lower than for adjacent years of lower solar activity. From the limited number of large events available for study it appears that they are most frequent during periods of increasing and, particularly, decreasing solar activity, with the periods near maximum and minimum relatively free from such events. In other words, in periods of increasing or decreasing solar activity the frequency of potentially dangerous cosmic ray outbursts may be greater than one per year and, in periods near maximum or minimum, less than one per year.

REFERENCES

1. Forbush, S. E., "Three Unusual Cosmic-Ray Increases Possibly Due to Charged Particles from the Sun," Phys. Rev. 70(9 and 10):771-772, November 1 and 15, 1946.

2. Adams, N., "A Temporary Increase in the Neutron Component of Cosmic Rays," Phil. Mag. 41:503-505, May 1950.

3. Webber, W. R., "Time Variations of Low Energy Cosmic Rays during the Recent Solar Cycle," in: Progress in Elementary Particle and Cosmic Ray Physics, ed. by J. G. Wilson and S. A. Wouthuysen, Amsterdam: North-Holland Publ. Co., Vol. 6, 1962 (In Press).

4. Freier, P. S. and Webber, W. R., "Exponential Rigidity Spectra for Solar Flare Cosmic Rays," J. Geophys. Res. (in press).

5. Fichtel, C. E. and Guss, D. E., "Heavy Nuclei in Solar Cosmic Rays," Phys. Rev. Letters 6 (9):495-497, May 1, 1961.

6. Biswas, S., Freier, P. S., and Stein, W., "Solar Protons and α Particles from the September 3, 1960 Flares," J. Geophys. Res. 67(1):13-24, January 1962.

7. Webber, W. R. "The Production of Free Electrons in the Ionospheric D Layer by Solar and Galactic Cosmic Rays and the Resultant Absorption of Radio Waves," J. Geophys. Res. 67(12):3991-4006, 1962.

COMPOSITION OF SOLAR COSMIC RAYS

C. E. Fichtel
Goddard Space Flight Center
Greenbelt, Maryland

Introduction

Having Dr. Webber's previous paper as an excellent summary of the general properties of solar cosmic rays, this report can begin at once with the treatment of one particular aspect of these solar particles, namely their composition.

The energetic solar particles arriving at the earth after some major disturbances on the sun are known to consist primarily of hydrogen nuclei. There are, however, smaller quantities of other nuclei which appear to be present in every event, since every time an observation has been made in the appropriate energy range they have been seen when the general intensity of the event was sufficiently high to expect to be able to detect them on the basis of their abundances in other events. In addition, there is also some relatively limited knowledge on electrons and γ radiation. Within the scope of the present incomplete knowledge, then, the relative abundances of these less plentiful components, namely helium nuclei, heavier nuclei, electrons, and γ-rays, will be given.

Helium Nuclei

Beginning with helium, the second most abundanent nuclear species, it is realized at once that care must be taken in how the helium to proton ratio is defined. Firstly, since these two nuclear species have different charge to mass ratios, they will not have the same rigidity[1] if they have

[1] Rigidity, R, is defined by the equation $\frac{cP}{Z}$, where c is the velocity of light, P is the total momentum, and z is the charge in units of the proton charge.

the same velocity. For example, a helium nucleus with a total kinetic energy of 200 MeV. has the same energy per nucleon as a proton of 50 MeV., but the same rigidity as a proton of 187 MeV. Further, an examination of the particle spectra as a function of energy per nucleon, rigidity, or possibly other variables must be made to determine whether or not they have the same or different spectra.

Because protons and helium nuclei that are in the same energy per nucleon interval, or equivalently the same velocity interval, also are in the same particle range interval, it seems worthwhile to look at the energy per nucleon spectra first since for shielding purposes range is the most significant parameter. In general, the helium nuclei spectrum has a steeper slope than that of the protons. This feature has been seen on several occasions [2,3,4], every time a measurement was possible. Typical examples[3] are shown in figs. 1 and 2. On the other hand when the spectra are plotted in terms of rigidity, R, they are always found to be similar.[2,3,4,5] A typical example of similar rigidity spectra[3] is shown in figure 3. Webber and Freier[5] have shown that proton spectra can be represented very

---

[2]S. Biswas, P. S. Freier, and W. Stein, J. of Geophys. Research 67, 13 (1962)

[3]S. Biswas, C. E. Fichtel, and D. E. Guss, "A Study of Hydrogen, Helium, and Heavy Nuclei in the November 12, 1960 Solar Cosmic Ray Event", to be published in the Physical Review.

[4]S. Biswas, C. E. Fichtel, D. E. Guss, and C. J. Waddington, private communication.

[5]Drs. Biswas, Freier, Ney, and Stein have made many measurements which are summarized in P. S. Freier and W. R. Webber, "Exponential Rigidity Spectra for Solar Flare Cosmic Rays", submitted to J. of Geophys. Research

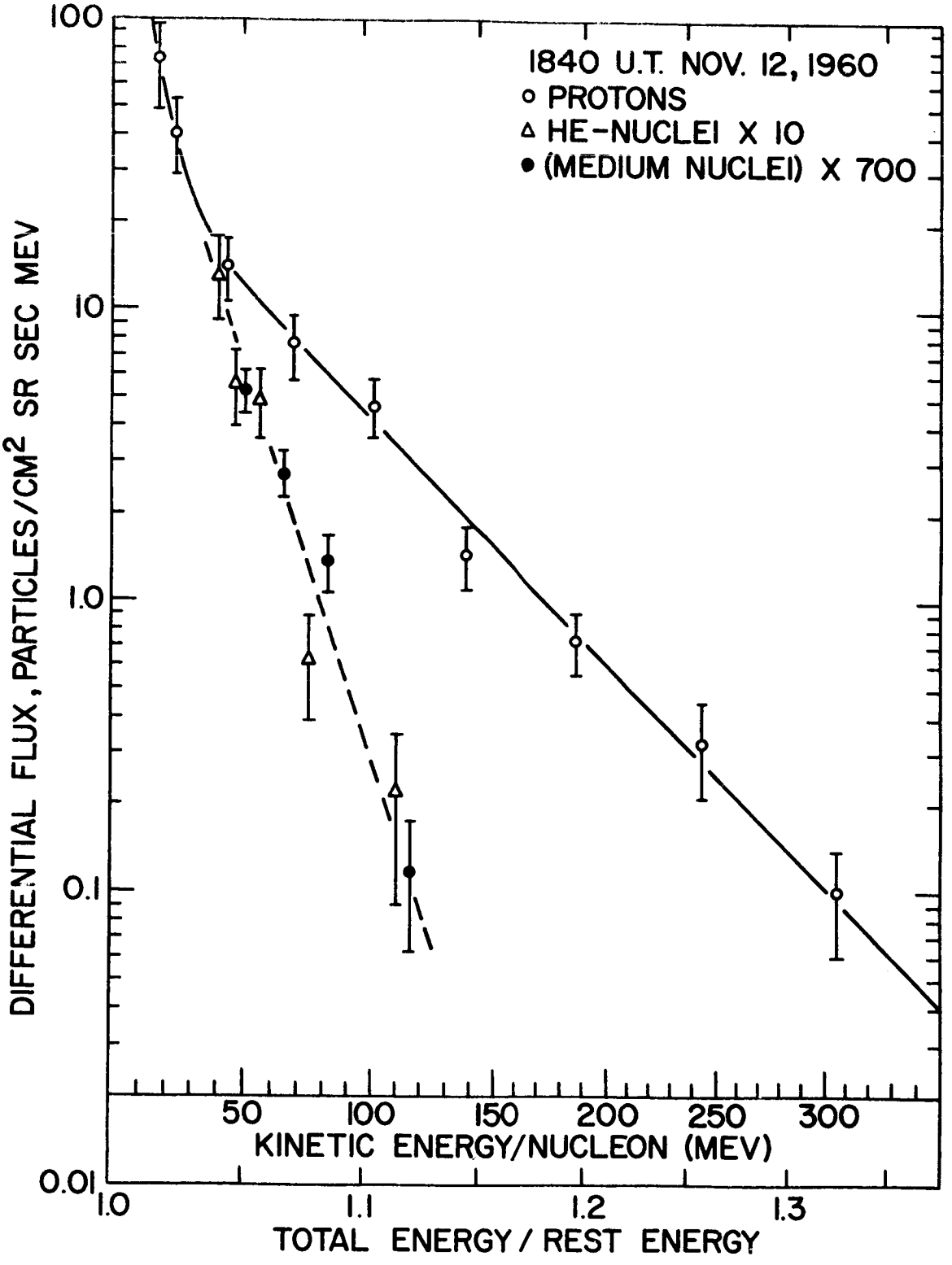

FIG. 1: Energy spectra for solar particles at 1840 U.T., NOV. 12, 1960.[3]

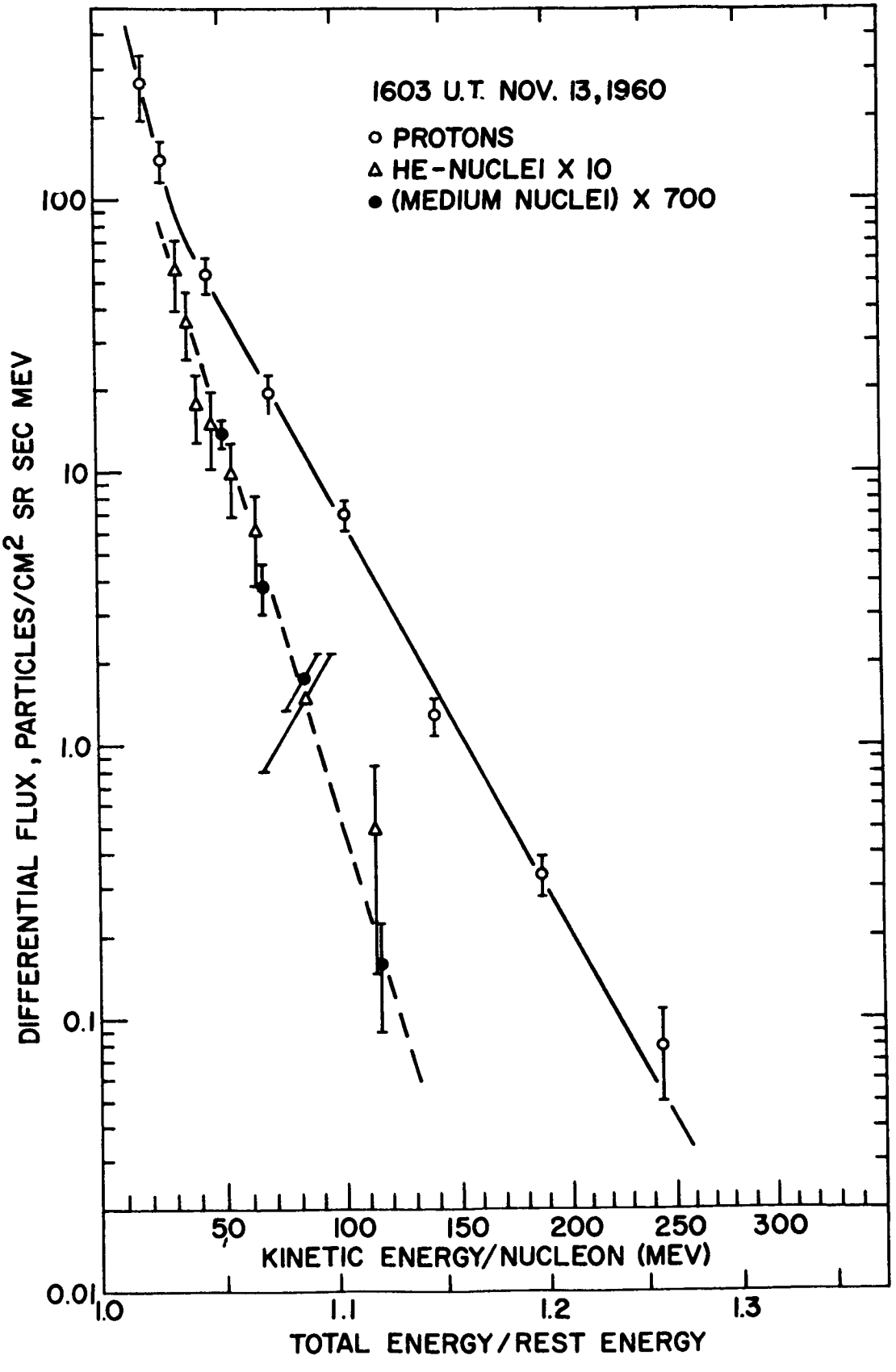

FIG. 2: ENERGY SPECTRA FOR SOLAR PARTICLES AT 1603 U.T., NOV. 12, 1960.[3]

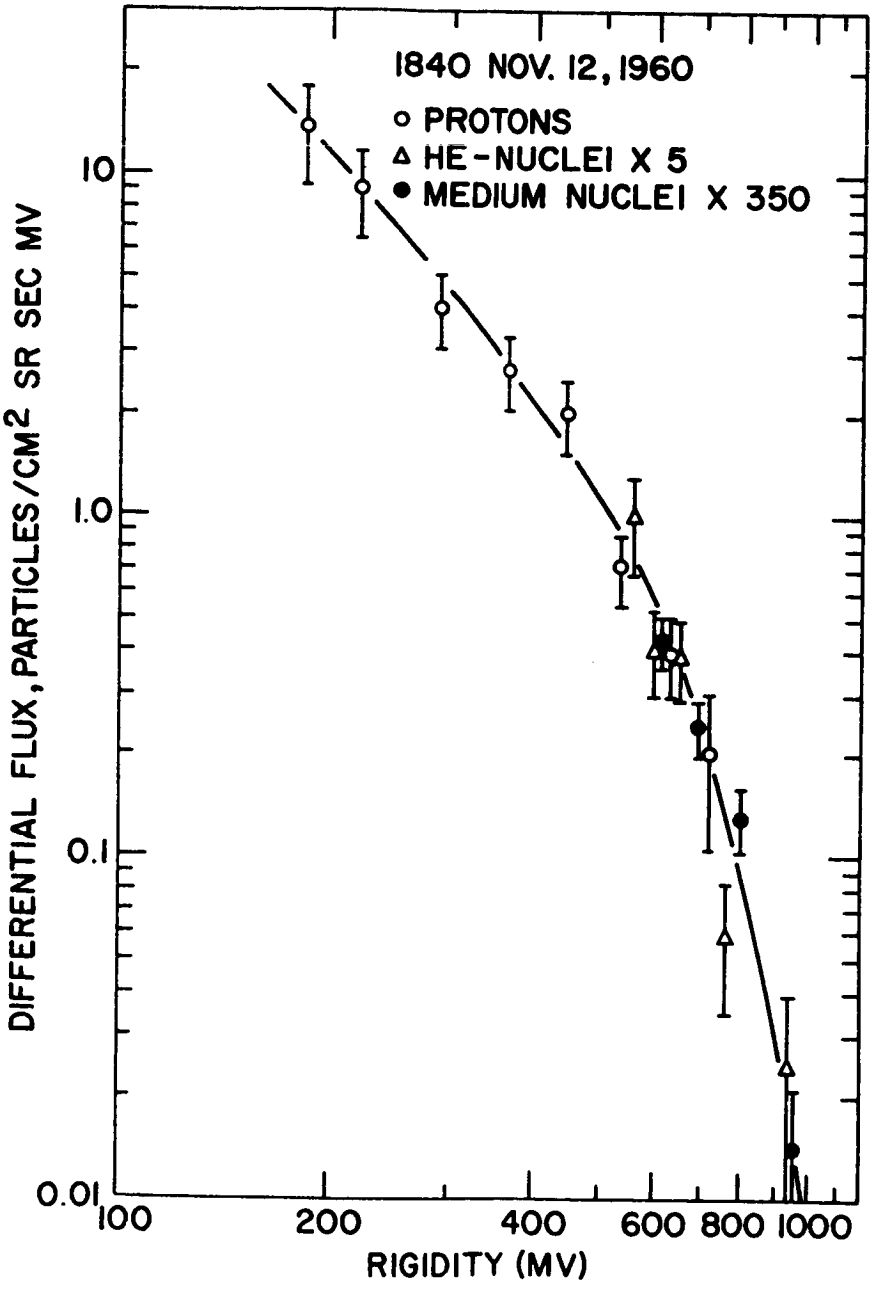

FIG. 3: RIGIDITY SPECTRA FOR SOLAR PARTICLES AT 1840 U.T., NOV. 12, 1960.[3]

well in general by an expression of the form

$$dJ/dR = J_o \exp(-R/R_o) \qquad (1)$$

where dJ/dR is the differential rigidity flux and J_o and R_o are constants. Further, since the helium nuclei have the same shape this expansion will also represent the helium nuclei with the same R_o, but a different J_o.

When proton to helium ratios are compared, however, it is found that, although the helium and hydrogen nuclei seem to have the same rigidity spectrum, the ratio of the two components in the same rigidity interval varies greatly from one event to another and at different times in one event. For example, at approximately MV rigidity, the proton to helium ratio has varied from $\geq$ 50:1 to 1:1. A list of some of the ratios that have been observed by Biswas, Freier, Ney, Stein[2,5], Fichtel, Guss[3], and Waddington[4] is given in Table I. A more complete list can be found in the indicated references. It should perhaps be noted that not all of the data in Table I correspond to the same rigidity interval; however, since the rigidity spectra are the same, it seems justified to compare all of the ratios listed, especially since the rigidity intervals are not very different.

On the other hand, there is now some evidence to indicate that for a given velocity interval the proton to helium ratio is similar in each event, although not exactly the same. In this case, however, the interval must be specified since the ratio of the hydrogen to helium nuclei varies with energy per nucleon. The proton to helium ratio is typically bound

to vary from about twenty at 40 MeV./nucleon to a few hundred at 120 MeV./nucleon. These ratios are not exactly the same from one event to another or even with time in an event, but the limited data available does seem to indicate that they are typical.

Heavy Nuclei

Turning now to the heavy nuclei, that is those with a nuclear charge greater than three, present evidence indicates that the energy per nucleon spectra of the various multiply charged nuclei are the same[3,4]. Further, since all of the multiply charged nuclei of interest have essentially the same charge to mass ratio, if their energy per nucleon spectra are the same their rigidity spectra will be also. These features are shown for typical cases in figures 1, 2, and 3. The relative abundances among the heavy nuclei taken in the same energy per nucleon intervals have been found to be the same each time a measurement was made, namely five times in two events. The helium to medium nuclei ($6 \leq Z \leq 9$) ratio has been measured in three events and found to be the same each time within uncertainties[3,4]. The composition for the same energy per nucleon intervals is given in table II below with a base of ten having been chosen for oxygen. It is seen that the medium nuclei are the most abundant among the heavy group and are about one-sixtieth as abundant as helium. Notice also in table II that the abundances are similar to those in the sun and different from those of galactic cosmic rays.

Although the heavy nuclei are easily stopped because they are of very low energy and high charge, they should perhaps not be completely ignored

TABLE I

PROTON TO HELIUM RATIOS IN THE SAME RIGIDITY INTERVALS

$\sim$ 1200 U.T., July 11, 1959[5]	1.4 ± 0.2
$\sim$ 1800 U.T., July 12, 1959[5]	5.0 ± 0.8
$\sim$ 2130 U.T., May 5, 1960[5]	≥ 50
$\sim$ 1400 U.T., Sept. 3, 1960[3]	31
$\sim$ 2000 U.T., Sept. 4, 1960[3]	19
1840 U.T., Nov. 12, 1960[3]	5 ± 1
1603 U.T., Nov. 13, 1960[3]	1 ± 0.2
1951 U.T., Nov. 16, 1960[4]	1.7 ± 0.5
0339 U.T., Nov. 18, 1960[4]	1.7 ± 0.5
$\sim$ 1630 U.T., July 18, 1961[6]	6 ± 1

TABLE II

RELATIVE ABUNDANCES WITH A BASE OF 10 FOR OXYGEN

Nuclei	He	Li,Be,B	C	N	O	F	Ne	$11 \leq Z \leq 18$
Solar Cosmic Rays*	1100	< 0.2	6	$\lesssim 2$	10	< 0.3	1.5	1.3
Sun +	?	< 0.01	6	1	10	< 0.01	?	1
Galactic Cosmic Rays*	360	11	18	$\lesssim 8$	10	$\lesssim 1$	3	9

*The uncertainty in the values in this line varies from 10% to about 30%

+The uncertainty in the values in this line is of the order of a factor of 1.5 to 2.

if relatively thin shields will be used. For example, the flux of medium nuclei that would penetrate 2 gm/cm^2 of aluminum was nearly 10^2 particles/(m^2.sr.sec.) for more than a day in the Nov. 12, 1960 event, and all of them would be of the low energy, or "ending", variety.

At a few times for periods of the order of ten to twenty minutes, Kurnosova et al[6] have seen increases in the counting rate of the higher dE/dx channels of their Cirenkov detectors flown on satellites which they interpret as short term increases of relativistic heavy nuclei associated with solar disturbances. These increases, however, represent an integral particle flux which is quite small compared to the daily average of relativistic heavy nuclei in the same charge region, and, therefore, they do not need to be considered as an additional hazard.

Electrons

We come now to the next component, electrons. The abundance of very energetic electrons is expected to be small due to the high rate of energy loss by synchtrotron radiation at large relativistic energies; so, even if there were large numbers of these energetic electrons initially, they would soon lose their energy.

Although the flux of very energetic solar electrons is known to be relatively small, appreciably less than the proton component, positive

---

[6] Kurnosova, L. V., L. A. Razorenov, and M. I. Fradkin, "Short-Term Increases of the Cosmic Ray Intensity Associated with the Solar Activity", Journal of the Physical Society of Japan 17, Supplement A-II, 315 (1962); Iskusstvennye Sputnik: Zeml: No. 6, 132 (1961); Iskusstvennye Sputnik: Zeml: No. 12, 31 (1962)

evidence for electrons does exist for at least one event.[7] In this case, the flux of electrons greater than 100 MeV. was only 0.04 el./ (cm^2 sr sec), or a few percent of the proton flux in the same kinetic energy region.

Relatively large fluxes of low energy electrons, kinetic energy < 1 MeV., have also been seen on occasions. Hoffman et al[8] saw 3×10^6 el/ (cm^2 sr sec) between 10 and 35 KeV. for about ten minutes on Sept. 30, 1961, associated approximately with the arrival of the sudden commencement. Except for that period the flux was less than the detectable limit of 2×10^5 el/(cm^2 sr sec).

γ-Rays

At the present time, the information on high energy electromagnetic radiation is very limited. There have been at least two events observed in which the energy flux was estimated to be of the order of 10^7 ev/ (cm^2 sec) for less than five minutes, with the average kinetic energy in the range of 20 to 500 KeV.[9,10] Several other events with a smaller total

---

[7] P. Meyer and R. Vogt, Phys. Rev. Letters 8, 387 (1962)

[8] R. A. Hoffman, L. R. Davis, and J. M. Williamson, "0.1 to 5 MeV. Protons and 20 KeV. Electrons at 12 Earth Radii during Sudden Commencement on 30 September 1961," submitted to the J. of Geophys. Research.

[9] L. E. Peterson and J. R. Winckler, J. of Geophys. Research 64, 697 (1959)

[10] J. R. Winckler, T. C. May, and A. J. Mosley, J. of Geophys. Research, 66, 316 (1961)

energy flux above 20 KeV have also been observed.[11, 12] All of the events seem to be of short duration, although in some cases the period of observation was not long enough to permit a determination of the length of the event. The shape of the energy spectrum seems to vary appreciably from one event to the next. There have also been several negative results, that is cases where γ-rays were not detected although a rather large flare was seen on the sun.

[11] K. A. Anderson and J. R. Winckler, J. of Geophys. Research 67, 4103 (1962)

[12] T. A. Chubb, H. Friedman, and R. W. Kreplin, J. of Geophys. Research 65, 1831 (1960)

Paper A-4

DETAILS OF INDIVIDUAL SOLAR PARTICLE EVENTS*

by
Carl E. Fichtel, Donald E. Guss, and K. W. Ogilvie

INTRODUCTION

This paper attempts to present a time history of the intensities and energies of solar cosmic ray particles detected at or near the earth. Ideally it would be desirable to show the complete energy spectrum of the proton component in these events as a function of time. Upon consideration of the incomplete information and uncertainties involved in the measurements, however, we see that this can only be done approximately. Regions of time and energy which have not been adequately surveyed can be described only by interpolation and, to some extent, by extrapolation. The goal is to remain within a factor of 2 of the real intensity at all times. Frequently the accuracy attained is very much better.

This survey begins with the event on February 23, 1956 – the first one for which there is an estimate of both the low and high energy flux components. All of the largest events from that date to the present and some of the smaller ones for which particularly complete data are available have been selected for examination. All events for which there was a riometer reading in excess of 10 db (indicating a particle flux greater than about 600 particles/cm^2-ster-sec for particles with energies above 20 Mev) have been included. Also any event with a high energy component sufficiently large to be detected on the neutron monitor has been studied. Events for which less than 10 db of absorption was detected on the riometer and no detectable neutron monitor increase was observed have, in general, been included only if there were other data from detectors flown on balloons and satellites.

The description of the various detectors used to study the solar particles will be followed by a discussion of the individual events in order to emphasize the interesting features and the variety of geophysical effects occurring from time to time. The descriptions will be followed by diagrams giving the integral flux as a function of time above specified energies and energy spectra at various times during the event. Finally, an imaginary event will be presented which is just large enough to include all the types of events observed.

* Reprinted from Goddard Space Flight Center External Document Number X-611-62-122

DETECTORS

The Riometer

The riometer measures the signal strength of extraterrestrial radio noise (References 15 and 16). During solar particle events the bombardment of the earth by energetic charged particles increases the electron density in the upper atmosphere causing absorption of the extraterrestrial noise and a consequent decrease in the signal measured at the ground (Reference 17). The particles primarily responsible for this absorption are protons in the 20-200 Mev kinetic energy range. Owing to the earth's magnetic field these particles can enter only at high latitudes; hence, this phenomenon is termed polar cap absorption (PCA). Thus at high latitudes, a riometer permits continuous monitoring of the intensity of protons in this energy range.

Magneto-ionic theory shows that, if the riometer observation frequency, ω, is much greater than both the critical frequency of the ionosphere and the longitudinal component of the magnetic gyrofrequency, the absorption for a vertically incident plane wave is found by integrating the following equation over the height of the ionosphere:

$$A = 0.46 \int \frac{N\nu}{\nu^2 + \omega^2} \, dh \, , \tag{2-1}$$

where A is the absorption in decibels, N the electron density, ν the electron collision frequency, and h the altitude in centimeters. The electron density at any height is related to the electron production rate q by the equation

$$N = q^{1/2} \left[(1 + \lambda) \alpha_e \right]^{-1/2} \, , \tag{2-2}$$

where α_e is the effective recombination rate for electrons and λ is the negative-ion to electron ratio. By substitution of Equation 2-2 into Equation 2-1, we then get the following equation.

$$A = 0.46 \int q^{1/2} \left[\nu \left(\nu^2 - \omega^2 \right)^{-1} (1 + \lambda)^{-1/2} \alpha_e^{-1/2} \right] dh \, . \tag{2-3}$$

During a PCA event, the electron production rate at any altitude is directly proportional to the total rate of energy loss by ionization of solar protons at that altitude. Equation 2-3, then, is a relation between the absorption measured by a riometer and the intensity and energy spectrum of the particles causing the PCA. For spectra of the same shape Equation 2-3 also predicts that the absorption in decibels is directly proportional to the square root of the particle intensity, provided the quantity in the brackets is independent of q.

During the daytime this is indeed the case to a high degree of accuracy, but there is a somewhat important dependence of λ on q during times of darkness.

Because of the photo-detachment effect of sunlight on the ionosphere, the absorption during a PCA is much stronger during the day than at night. A calculation by Reid (Reference 18), based on currently accepted values for the atmospheric parameters, yields a value of about 3 for the ratio of day to night absorption at an observing frequency of 30 Mc for a particular spectrum shape. Observations indicate that the average ratio is about 4, but that it can vary considerably and is sometimes as large as 10 or 12. The riometer provides its most useful information during the daylight hours and conversion of nighttime absorption readings to effective daytime absorption readings must be approached with some caution.

By the nature of its response, the riometer absorption is a function of geomagnetic latitude. However, the riometer records from College, Alaska; Churchill, Canada; and Thule, Greenland, generally show approximately the same absorption, though the cutoff energies for protons calculated by Quenby and Webber (Reference 19) are 113, 6.4, and approximately 0 Mev., respectively. Here it was assumed that the absorption from these stations was equivalent, and absorption values from stations other than Churchill were used when needed.

In order to calculate the expected absorption during a PCA the particle spectrum, intensity, and directionality must be known. The radiation causing the PCA is generally assumed to be isotropic over the upper hemisphere; and this is a good approximation a few hours after the flare causing the event. The electron production rate must be determined from the spectrum shape and intensity, and Equation 3 integrated. This has been done by a number of authors (References 17, 18, and 20) for specific times in specific events where some spectral details have been determined experimentally.

To find the spectral shape and intensities of solar particles from the observed absorption is a more ambiguous process, and several assumptions must be made. A calculation by Brown and Weir (Reference 20) shows that for protons with energies greater than 100 Mev, the predicted absorption is very insensitive to the shape of the energy spectrum and depends primarily upon the particle intensity. A similar calculation by Bailey (Reference 17) indicates that the same is true for particles in the energy range between 20 and 100 Mev. For protons with energies at the top of the atmosphere less than about 20 Mev the effectiveness for producing absorption is a rapidly decreasing function of energy, because protons of these energies ionize primarily at altitudes where the electron collision frequency is small.

From a series of rocket shots during PCA's in the fall of 1960 the energy spectra and intensities of protons were obtained down to energies below 20 Mev for a variety of riometer absorption intensities (References 21 and 22). The results indicated that for these events, the shape of the energy spectrum does not remain constant to very low energies. If the shape

of the energy spectrum is expressed by means of a power law

$$dN(E) = CE^{-\gamma}dE \,, \qquad (2\text{-}4)$$

then the exponent γ is a decreasing function of energy. Because of this and the fact that protons with energies below 20 Mev are less effective in producing absorption, it was assumed that the absorption at the times of the rocket shots was determined by the intensity of particles with energies greater than 20 Mev. The proton intensity at energies greater than 20 Mev is plotted against the observed absorption on the 30 Mc riometer at Churchill in Figure 2-1. This curve was subsequently used to obtain the PCA-determined particle intensities for the other events studied here. The extremum lines shown in Figure 2-1 indicate the uncertainty in the riometer readings alone and do not reflect the uncertainty in the resulting particle intensities, which is estimated to be about a factor of 2.

The shape of the energy spectrum for most solar particle events shows that the primary contribution to the absorption is from protons in the energy range below 100 Mev, since the

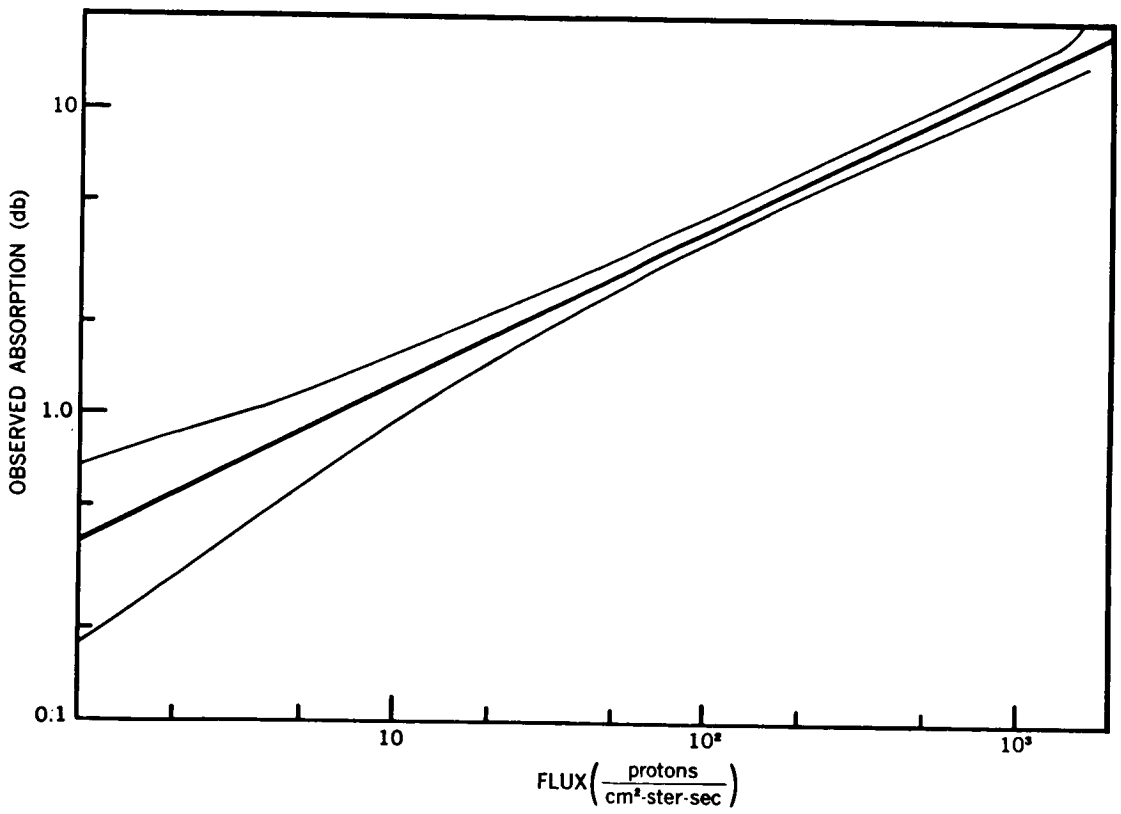

Figure 2-1—Proton flux versus riometer absorption

particle intensity above this energy is negligible by comparison, except for times early in the events. If the energy spectrum at higher energies is known, a knowledge of the absorption data makes it possible to show something of the nature of the spectrum as well as the intensity below 100 Mev. For example, the proton flux was measured during the daylight hours of July 13, 1961 by nuclear emulsions on a balloon flight at Churchill. The intensity with energies above 78 Mev was 1.6 P/cm^2-ster-sec, and between 78 and 230 Mev $\gamma = 5.5 \pm 0.3$. Extrapolating this spectrum back to 20 Mev would result in an intensity $7.9 \times 10^{+2} P/cm^2$-ster-sec which, from Figure 3, corresponds to an absorption of 11 db. However, the observed absorption on the 30 Mc polar riometer at Churchill was equal to or greater than 15 db during the entire flight, while that on the 27.6 Mc riometer at College varied from 14.5 to 17.5 db. This indicates that the shape of the spectrum did not change appreciably down to energies below 20 Mev. It must be noted that, although particles below 20 Mev become increasingly less effective at producing absorption, there would be 16 times as many particles between 20 and 10 Mev as there are above 20 Mev if γ did not decrease with energy.

The interpretation of riometer absorption in terms of particle intensities is complicated by two other problems: the superposition of auroral absorption upon the PCA; and the occurence of anomalous but real changes in absorption.

At stations within the auroral zone riometers show auroral absorption as well as the PCA. College lies near the maximum of the auroral absorption zone, and Churchill at the northern edge. Usually the auroral absorption can be at least partially eliminated since it appears as absorption spikes superposed upon the generally smoothly varying PCA. Leinbach and Reid (Reference 23) suggested that the PCA is best represented by the minimum absorption recorded over a period of several hours when auroral absorption is present.

During a number of PCA events anomalous decreases of absorption have been observed immediately following a sudden commencement. These have been discussed by J. Ortner, et al. (Reference 24). Leinbach (Reference 25) has also noted the occurrence, on some occasions, of *mid-day recoveries* at College, and on at least one occasion this phenomenon was observed at Churchill. These seem best attributed to local changes in the geomagnetic cutoff or local changes of the characteristics of the absorption layer rather than to a change in the intensity of the particles causing the event.

Increases in absorption have also been observed near the time of a sudden commencement (Reference 24). Recently, it was found that the sudden increase in absorption immediately preceding a sudden commencement following the flare of September 28, 1961 was coincident with an increase in the intensity of very low energy particles as observed by the satellites Explorer XII (Reference 27) and Injun I (Reference 3) (1961 υ and 1961 $o2$, respectively).

In general, it is assumed herein that the PCA is a smoothly varying function of time, although a sustained increase in absorption following a sudden commencement is interpreted

as an increase in particle intensity. "Spikes" are generally interpreted to be auroral absorption or due to local manipulation of the ionization causing the absorption rather than actual fluctuations in particle intensity.

In calculating particle intensities, the daytime values of absorption from the 30 Mc riometer at Churchill were used whenever possible. During periods of particular interest a factor of 4 was used to convert nighttime absorption to effective daytime absorption unless this procedure seemed unreasonable. At several periods of importance the absorption records from College, Barrow, and Thule were used. These riometers record a higher absorption before saturating than does that at Churchill. In all cases it was assumed that there was no effective cutoff operating at any of these stations.

Webber (Reference 3) has also calculated particle intensities from riometer records for several events. The absorption for a 30 Mc riometer and for a differential rigidity* spectrum of the form

$$dN(R) = CR^{-6}dR \qquad (2\text{-}5)$$

was calculated in a manner similar to that of Bailey (Reference 17) but with the more recent values for the atmospheric constants. He then used these curves to calculate the particle intensities as a function of time for a number of PCA events. In Figure 2-1, the transformation from db to particle intensities agrees quite well with the values obtained by Webber and the differences in particle intensity are results of differences in interpretation of the absorption. The most notable difference occurs for the event of February 23, 1956. Before the sudden commencement Webber assumed a proton cutoff of 113 Mev at College, Alaska. In this paper, we assume that there is no effective cutoff at College and that the absorption increase following the sudden commencement is attributable to an increase in very low energy particles similar to that observed on September 28, 1961.

The Neutron Monitor

The neutron monitor (Reference 28) consists of an extensive structure in which BF_3 neutron proportional counters are surrounded by an arrangement of lead and paraffin blocks. A high energy proton or neutron passing through this lead has a high probability of undergoing an interaction similar to a *star* in a nuclear emulsion; and some of the reaction products will be neutrons. These neutrons are slowed down in the paraffin by collisions with hydrogen nuclei, which are then detected by the counters. Thus the detected particles are, for the most part, secondaries to the nucleonic component of the cosmic radiation at sea level. Consequently, the neutron monitor is more sensitive to primary particles of rigidity in the range 1 to 2 Bv than any other sea level monitor. The neutron method of detecting cosmic ray intensity

*Rigidity is defined by the equation R = pc/z, where R is the particle rigidity, p its momentum, z its charge, and c the velocity of light.

changes also has the advantage that the necessary corrections for meteorological effects can be made accurately, as cannot be done, for instance, with a meson detector.

We can write (Reference 29), the following relation between the counting rate of a monitor and the primary spectrum:

$$N(R,x,t_0) = \int_{R_0}^{\infty} S(p,x) \frac{dJ(R,t)}{dR} dR \ . \qquad (2\text{-}6)$$

Here the counting rate – a function of rigidity, time, and the depth of the detector in the atmosphere – is obtained from the primary differential spectrum J by multiplying dJ for a rigidity interval dR by a function S(p,x), and integrating over a range of rigidity from R_0 to infinity. The quantity S, called the specific yield function, gives the number of secondary particles detected in a neutron monitor at any given atmospheric depth as a function of primary particle rigidity. It depends upon the composition of the primary radiation, and henceforth we shall assume that this remains constant. R_0, the lowest primary rigidity incident at the top of the atmosphere, is a function of the geomagnetic coordinates of the detector. Atmospheric absorption causes S to go to zero for R less than about 1 Bv independently of the influence of the earth's magnetic field. In Figure 2-2 S is plotted in terms of R.

Thus, if particles in the rigidity range from about 1 Bv upwards are isotropically incident upon the earth, a network of neutron monitors set up at points with known R_0 permits something to be learned about their energy spectrum, since S is known. This situation is complicated by at least two effects. If the source of the particles is localized in space in a region surrounding the sun, for example, we cannot assume in general that the particles are incident isotropically. In fact, anisotropic incidence usually occurs early in the solar event; later isotropy can usually be assumed. An intense magnetic storm can change the magnetic threshold rigidity R_0 and this must also sometimes be taken into account.

The motion of particles toward the earth from the sun has been studied by many authors (References 30 and 31), and we now have a fair knowledge of the effects which occur. These are discussed in detail in Chapter 3.

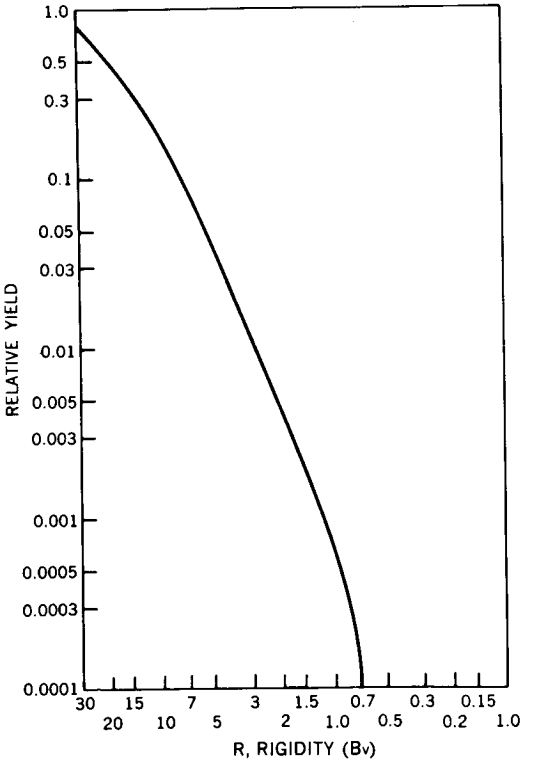

Figure 2-2—The specific yield function

In Figure 2-3 the times of these events are superimposed upon a plot of smoothed sunspot numbers (Reference 32). Even making allowance for the increase in the number of detecting stations during the past solar cycle it seems, in contrast to the PCA, that there is a definite tendency for flares producing a large flux of particles in the Bv rigidity range to occur during the increase and decrease of sunspot activity rather than during the maximum. At present there is no explanation for this tendency.

Using the neutron monitor record we can determine easily the percentage increase in the rate at any time during an event. The background rate is caused by the galactic cosmic rays which are always incident upon the earth. If we use the known spectrum of these particles and the specific yield functions*, we can obtain from Equation 2-6 a quantity proportional to the rate due to particles having rigidities above R_0. A similar calculation made with various assumed or measured spectra for the flare particles gives a quantity proportional to the additional rate due to flare particles. A difficulty arises in that the primary spectrum varies with time over the solar activity cycle (References 33 and 34) but an approximate correction can be made for this. Various relevant assumed spectra and threshold rigidities have been employed in Table 2-1 to show the intensity increase required above rigidity R_0 (in units of the normal cosmic ray background above R_0) to double the counting rate of a neutron monitor. We shall use these figures and the primary spectrum variations to deduce intensities in the rigidity range from the observed counting rate increases. By using the figures in the second column for interpreting rate increases of neutron monitors situated at points where the

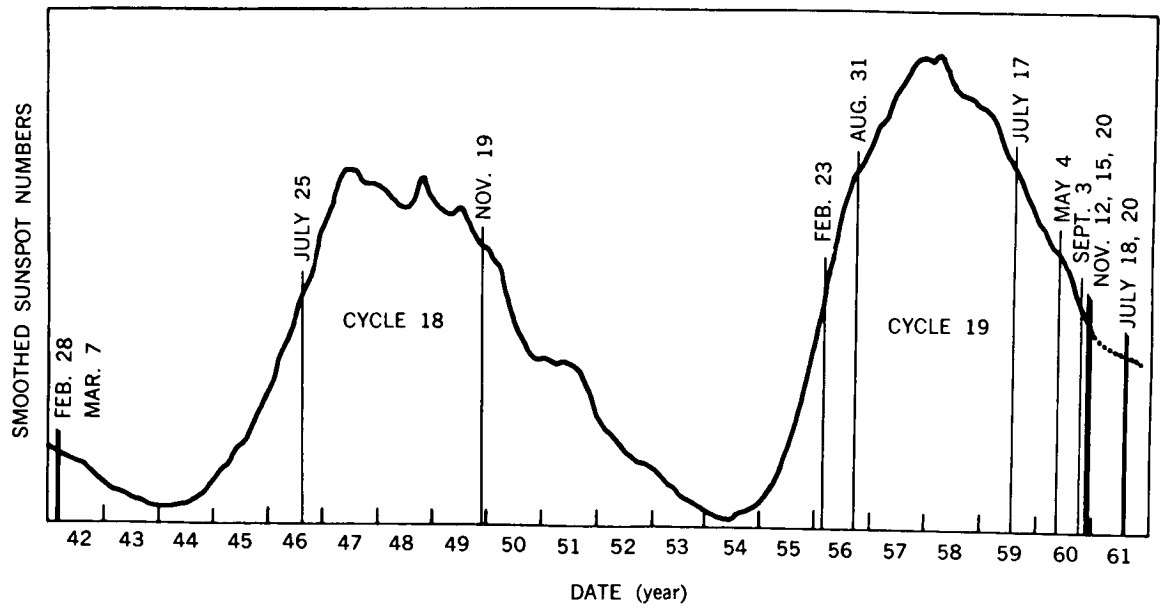

Figure 2-3—Distribution of cosmic ray events detected at sea level as a function of the solar cycle

*Obtained by using the revised specific yield function $s' \nu n$ in Figure 2-2.

Table 2-1

The Radiation Increase Required above Rigidity R_0 (in Units of Normal Cosmic Ray Background above R_0) to Double the Counting Rate of the Neutron Monitor

Differential Spectral Exponent	Intensity Increase			
	R_0 = 1 Bv	R_0 = 2 Bv	R_0 = 3 Bv	R_0 = 5 Bv
4	10	17	24	40
5	12	31	62	160
6	13	45	130	—

cutoff rigidity is less than 1 Bv, we make the assumption that they are not affected by the additional particles present. Thus a 5 percent increase in the rate of a high latitude neutron monitor(R_0 = 1 Bv) indicates, if the incident spectrum is $1\text{-}p^6$, an incident flux of $0.05 \times 13 \times J_0 = 0.05 \times 13 \times 0.23$ (in February 1956) = $0.150/cm^2$-ster-sec, in addition to the background above 1 Bv. The minimum increase that can be detected with certainty is less than 5 percent, and probably about 2 percent. This figure depends to some extent on the monitor involved and upon geophysical conditions. For example a confusing situation might arise if the increase in flux occurs during a Forbush decrease. At such times the diurnal variation in rate becomes large and irregular in phase and might conceivably obscure a slow change due to solar emitted particles.

The procedure outlined above for determining the intensity of particles away from the earth, requires two approximations. First, there is the question of the primary spectrum referred to above; and second, the specific yield function has been extrapolated from 2 Bv to 1 Bv – a region of critical importance with steep spectra. In deducing the spectra the assumption is made that the intensity of the radiation in the asymptotic cones of acceptance is the same; this is difficult to check, but probably true. It seems likely that the intensities given here are accurate to at least a factor of 2. The largest contribution to the error arises from the uncertainty in the knowledge of the spectral exponent.

Direct Primary Particle Detectors

Some information on solar cosmic rays has been obtained directly from particle detectors flown on balloons, sounding rockets, and satellites. Balloon borne experiments have provided valuable information on the intermediate energy interval (between approximately 80 and 500 Mev) for protons. The lower limit of the energy interval is determined by the air cutoff – usually of the order of 6 gm/cm^2. The upper energy limit is set by the difficulty of obtaining anything but an integral flux above that energy with the detectors used and the fluxes observed.

The detectors used on these flights can be divided into three very broad groups: nuclear emulsions; simple omnidirectional or wide-angle counters; and complex electronic systems including both a small solid angle and fine energy discrimination. Nuclear emulsions have the advantage of yielding an excellent energy spectrum and permitting one to determine the charge composition, but have the disadvantage of not providing time variation information throughout a flight. Simple counters do provide time resolution, when other factors such as balloon altitude variations are not present; but it is difficult to deduce good quantitative flux values because of the absorber variation as a function of solid angle and, in some cases, the lack of sufficient knowledge about the energy spectrum. However, an estimate of the energy spectrum can sometimes be obtained by observing the counting rate as a function of altitude during ascent and by using atmospheric absorption information. In addition, for some flights, nuclear emulsion data exist for a time interval included in the counter record and may therefore be used as an absolute flux calibration for the counting rates. Unfortunately, there have been only a few balloon flights with electronic experiments capable of energy resolution, so information from this source is limited.

For balloons flown where the geomagnetic particle rigidity cutoff is normally greater than that caused by the residual atmosphere, there is the additional problem of time dependent magnetic field effects, which permit varying percentages of the total particle flux to reach the detector. At the present, it is not possible to construct a model, based upon existing data, which gives the actual percentages of transparency as a function of energy and time in the event. In practice, fortunately, at Minneapolis, where many of the measurements were made, the cutoff often seems either to be the same as during geomagnetically quiet times or not to exist for energies greater than the air cutoff. However, this difficulty has limited the degree to which the proton energy spectra of solar cosmic ray events can be described in quantitative detail.

Sounding rockets with recoverable payloads provide a means of studying these events above the earth's atmosphere with both electronic counters and nuclear emulsion techniques. Data from these payloads provide information on the proton energy spectrum down to a fraction of an Mev, and detailed charge composition measurements exist for three of the events to be included in the present analysis. This method provides only a sampling of the radiation at a few times during the event; however, it does help to calibrate those instruments which do record time variations, such as the riometer.

Finally, electronic experiments in satellites outside the Van Allen belts can give a detailed time history of the energy spectrum down to very low energies. However, not until Explorer XII was launched on August 15, 1961 did such a system exist; and at present, data giving the detailed history of the proton energy spectra are available only for the September 28, 1961 event. Previous satellites have provided integral fluxes above an energy cutoff, determined from the counting rate of a single detector under a known amount of material. These results have been used in developing the history of several of the events discussed in this report.

From several of the previously mentioned sources, it has been determined that protons are by far the most abundant nuclei in these events. In the same energy/nucleon interval (and hence the same range interval), helium nuclei are less abundant than hydrogen nuclei by a factor of 20 or more. Nuclei with a charge greater than 3 are more scarce than protons in the same energy/nucleon interval by a factor of a few thousand at low energies (40-100 Mev) and probably by a larger factor at higher energies.

HISTORY AND ENERGY SPECTRA OF EVENTS

In the diagrams of spectra presented here a solid curve indicates that the detailed energy spectrum has been obtained directly. A dashed curve indicates an interpolation between these data and the integral flux at 20 Mev deduced from PCA measurements*. In the time variation curves a solid line represents the particle intensity greater than 20 Mev; a dotted portion of the curve represents an extrapolation, and a blank space represents a portion for which a reasonable interpolation could not be made. This time variation curve normally was obtained from riometer results which were generally in agreement with satellite data at those times when a valid comparison could be made. The only exception is the latter portion of the May 4, 1960 event, for which information from a satellite-borne counter was available, but no riometer data. A dashed curve represents neutron monitor results, and a dot-and-dash curve represents the variation of intensity above 100 Mev. The zero of time represents the time of the beginning of the flare, and it should be noted that there is a change of scale at 12 hours.

0331 UT February 23, 1956

The February 23, 1956 flare produced the largest intensity of particles yet observed in the Bv range. However, the riometer observations show that the intensity of low energy particles was an order of magnitude smaller than in many other solar particle events (Figure 2-4). There is only a single counter measurement (Reference 35) indicating an intensity at Minneapolis (threshold 0.81 Bv) 4-5 times normal at 2030 UT on the 23rd.

A great deal of work has been done on the neutron monitor observations of this event, and we shall summarize these with a view to finding the intensity, the spectrum, and their variation with time. The spectrum of particles at various times has been derived by examination of the latitude effect (Table 2-2).

Pronounced impact zone effects were seen during the first 10 minutes of the event (References 37 and 38) but isotropy may be safely assumed for much later times after 0400, at least in space close to the earth. The first spectrum refers to the direct radiation; that is to say radiation received in the primary impact zone, which covered most of

*It must be remembered that a very high intensity of particles with energy below 20 Mev can appreciably increase the riometer absorption. In such cases the particle intensity as deduced from Figure 2-1, if interpreted as an integral intensity above 20 Mev must be considered as an upper limit. The events of April 29, 1960 and May 6, 1960 are probably examples of this effect.

Table 2-2

February 23, 1956 High Energy Observations

Source	Energy Threshold	Time from Flare	Diff. Rigidity Spectrum
Pfotzer	1 Bv	20 min.	p^{-4}
Simpson	1.6 Bv	2 hr. 20 min.	p^{-6}
		20 hr.	p^{-7}

*Reference 36
†Reference 37

Europe at the time. The storage region was not filled up at that time, but the steeper spectra observed later refer to radiation stored in that region. If we now apply our results to these observations, we arrive at the data given in Table 2-3. Thus an expression for the integral rigidity spectrum containing the best available information for the period from 0400 UT to 1000 UT is $150/p^5\ t^{-3/2}$ with R in Bv above 1 Bv, and t in hours from 0400 UT. Simpson (Reference 37) has established that the neutron monitor rate at Chicago and other stations decayed according to a $t^{-3/2}$ law between 0430 and 1000 UT ($t = 0$ at 0350 UT), and exponentially thereafter with a decay constant of about 8 hours.

Table 2-3

February 23, 1956 High Energy Intensities

Time from Flare (min.)	Station	Threshold (Bv)	Diff. Spectrum	Integral Intensity above Threshold $\left(\frac{\text{particles}}{\text{cm}^2\text{-ster-sec}}\right)$
20	Leeds	1.77	$1/p^4$	150
40	Chicago	1.6	$1/p^6$	160
50	Ottawa	1.05	$1/p^6$	90*
150	Chicago	1.6	$1/p^7$	34

*The inconsistency between Ottawa and Chicago may be due to the late arrival of particles at low energies.

The peak intensity for particles with energies greater than 20 Mev, as deduced from the riometer observations at College (Reference 15) by using the curve of Figure 2-1, is radically different from the value at 30 Mev determined by Webber and Malitson†; the

†Chapter 1.

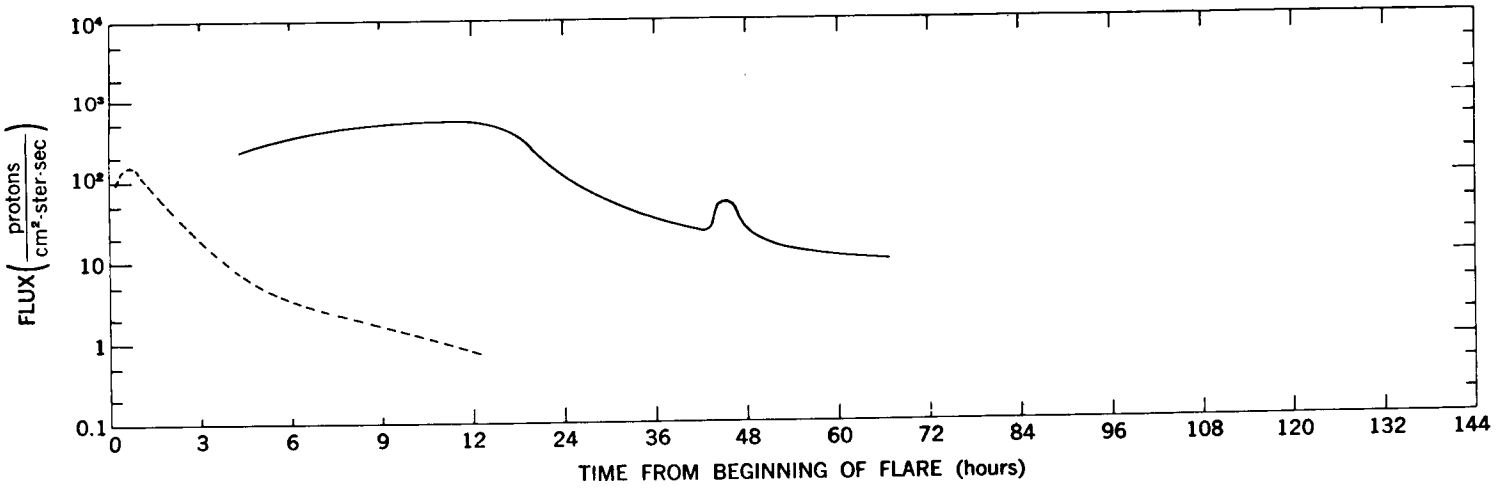

(a) Time history

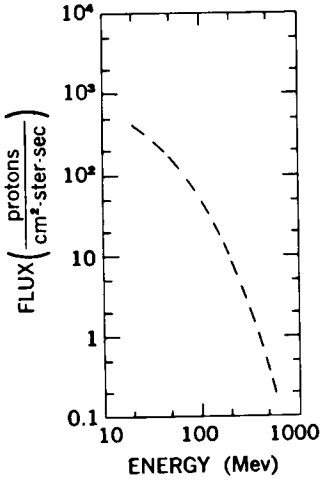

(b) Energy spectrum at 2030 UT (+17 hours)

Figure 2-4—The February 23, 1956 event

difference results from a difference in interpretation. Here it is assumed that the geomagnetic cutoff at College is not appreciably different from that at Churchill. This, indeed, seems to be the case during all other events for which comparisons are available. The interpretation here is that the event was large at high energy and small at low energy — similar to that of September 3, 1960 or July 18, 1961.

A small increase in absorption preceded the sudden commencement on February 25th and this was interpreted as an increase in particle intensity similar to that of the Explorer XII observations (Reference 26).

1030 UT August 29, 1957

In the August 29, 1957 event (Figure 2-5) a PCA lasted for 49 hours, reaching a maximum of 8 db at Churchill (Reference 39). There was no neutron monitor increase and also no increase detected at balloon altitudes between 1400 UT (Reference 40) on the 29th, an hour after the start of the PCA, and 0600 UT on the 30th. Such a detector could have found an increase of 10 percent, and from this fact it can be shown that the exponent γ of a spectrum $N = N_0 E^{-\gamma}$ must have been of the order of 6 or more and that this spectrum must have persisted down to at least 20 Mev.

0947 UT March 23, 1958

The PCA began within a few hours after the flare (Reference 41). At the time of the sudden commencement, 1540 UT on the 25th, there was a rapid increase in the PCA to about 12 db. This was probably a consequence of an intensity increase at low energies of the type observed by Bryant et al. (Reference 26) with instruments flown in Explorer XII on September 28, 1961. There was no detectable neutron monitor increase, but at 0700 UT on March 26th a lower limit of 0.07 ± 0.01 particle/cm^2-ster-sec (between 120 and 180 Mev), was determined by balloon measurements at Minneapolis (Reference 42). Probable variations of

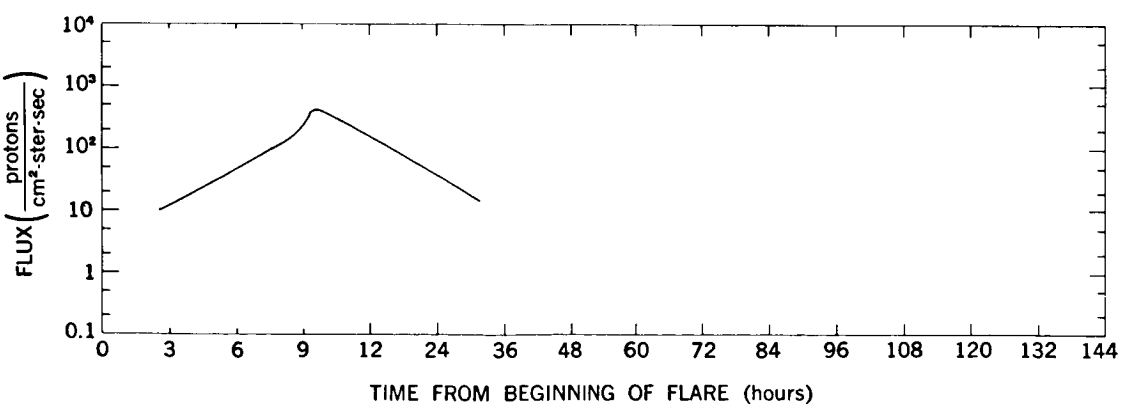

Figure 2-5—The time history for August 29, 1957 event

the magnetic threshold during the flight prevent anything more than the determination of a lower limit to the flux or an upper limit of 4 to the exponent of the integral energy spectrum in the 20-200 Mev interval.

0020 UT July 7, 1958

The flare produced a PCA reaching as much as 17 db at Kiruna (Reference 43) at 0400 UT on July 8th. No neutron monitor increase was observed, but balloon measurements were made by Russian workers at Kiruna (References 44 and 45). At an atmospheric depth of 10 gm/cm^2 the intensity was 4 times normal at 1000 UT on July 8th, when the riometer absorption was 18 db, and returned to normal by 1500 UT when the riometer absorption was 13 db (Figure 2-6). In this instance it is hard to reconcile the balloon and riometer results, but it is evidence for a very steep spectrum. It is possible that the energy spectrum was so steep that, if the second balloon were under a few gm/cm^2 more atmosphere than the first, the difference in counting rate could be caused by the differences in the cut-off energy determined by the air above the balloon.

0433 UT August 16, 1958

For this event only riometer data, showing a maximum absorption greater than 15 db, are available. Because an energy spectrum cannot be constructed from riometer data alone, no figure is presented for this event.

1428 UT August 22, 1958

This event is characterized by a steep spectrum and no detectable neutron monitor increase (Figure 2-7). The solar particles were observed by means of balloons (Reference 46) and by the Explorer IV (1958ϵ) satellite (Reference 47). At Churchill, after only 1 hour, the intensity of protons with kinetic energies above 100 Mev was 20 times normal; and the subsequent rapid fluctuations until 1900 UT were probably due to fluctuations in particle emission. The spectra exhibited are derived from the balloon and satellite observations. A direct determination at 0500 UT on August 23rd gives an approximate integral energy spectrum proportional to $1/E^{3.5}$ above 100 Mev; and the satellite results support the validity of extrapolating this energy spectrum to 30 Mev. Measurements made on Explorer IV (References 47 and 48) give integral fluxes, above 30 and 40 Mev, at three times during the event, which are consistent with the riometer observations (Reference 39).

0005 UT August 26, 1958

For this event only riometer data showing a maximum absorption greater than 15 db, are available*. Because an energy spectrum cannot be constructed from riometer data alone, no figure is presented for this event.

*Chapter 1.

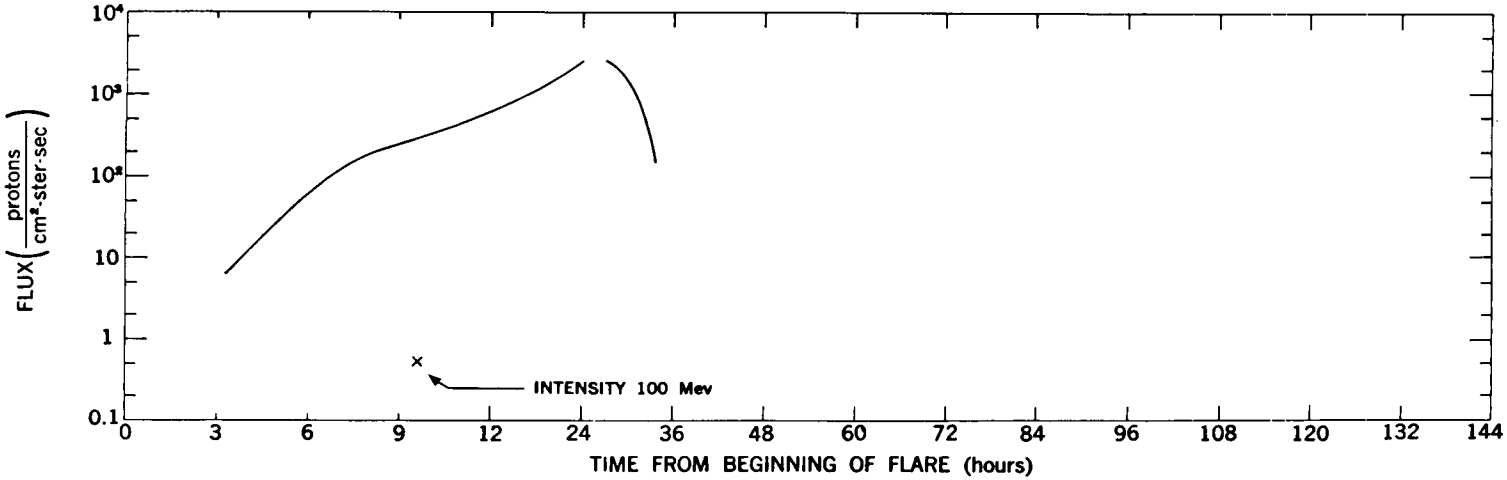

(a) Time history

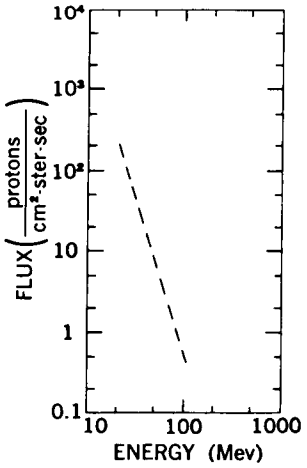

(b) Energy spectrum at 1000 UT
(+9-2/3 hours)

Figure 2-6—The July 7, 1958 event

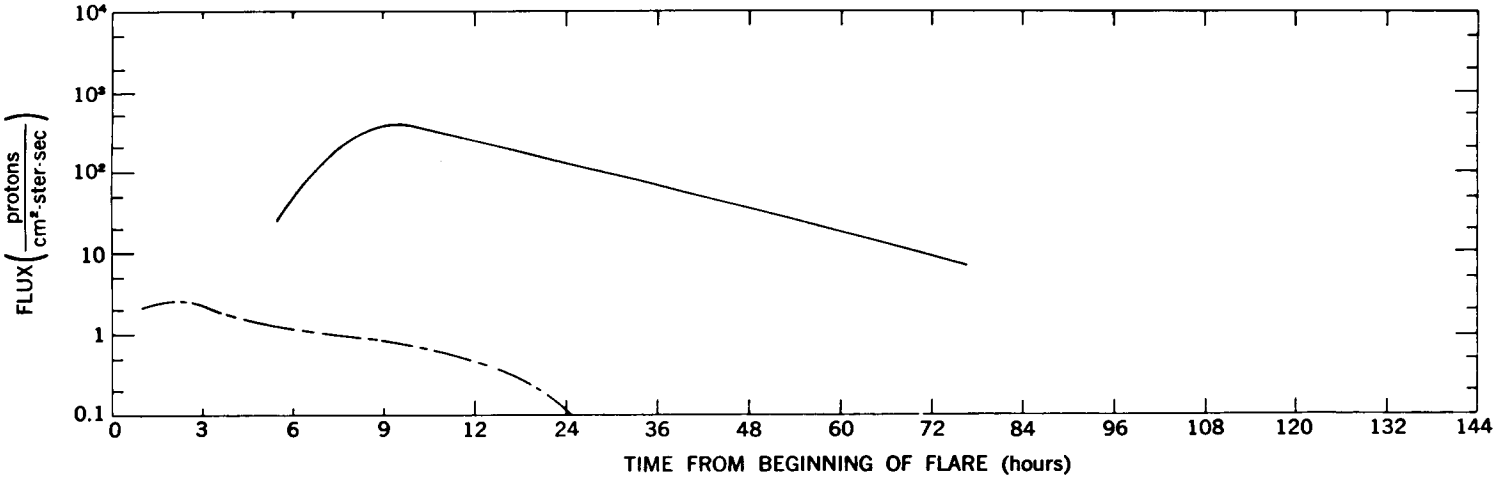

(a) Time history

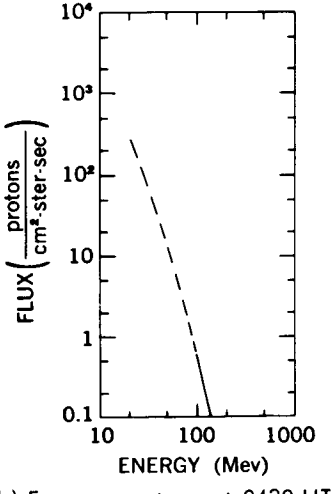

(b) Energy spectrum at 0430 UT (+14 hours)

Figure 2-7—The August 22, 1958 event

2101 UT May 10, 1959

Energy spectra were obtained at balloon altitudes during the period of 0400 to 1600 UT on May 12, 1959 at Minneapolis, by the University of Minnesota (References 49, 51, and 51). However, balloon observations by Charakhch'yan, et al. (Reference 44) show that during the latter portion of this time only a fraction of the total particle flux reached Minneapolis, so that only the energy spectrum at 0640 UT has been shown (Figure 2-8). The PCA began about 5 hours after the flare, reached an absorption maximum in excess of 12 db at Longyearbyen, and recovered over a period of several days (Reference 52).

The July 1959 Events

The complex series of events occurring during July 1959 are the subject of a monograph published by UGGI (Reference 53). In brief, a series of three great solar flares, occurring before 0210 UT July 10th, at 0319 UT July 14th, and at 2118 UT July 16th, caused a series of three large solar cosmic ray events (Figures 2-9, 2-10 and 2-11). The last of the flares also produced particles in a range of energies and in a quantity detectable by neutron monitors. The absorption showed increases to greater than 20 db for all three of the events, as recorded by the 27.6 Mc riometer at College (Reference 23); the riometers at Barrow (Reference 23), Thule (Reference 23), and Churchill (Reference 54), are in general agreement with these maximum values.

The neutron monitor increase has been discussed by McCracken and Palmeira (Reference 14) who point out the very slow rate of rise, and the isotropic nature of the flux at the energies detected by the neutron monitors. High latitude monitors detected an increase at about 0300 UT on the 17th and, between 0800 UT and 1200 UT, recorded an increase of about 6 percent for particles above 1 Bv. If we take a differential spectrum (Reference 53) of the form $1/p^6$, a particle intensity of $0.06 \times 13 \times 0.09 = 0.07$ particles/cm^2-ster-sec ($P > 1$ Bv) is implied. This is consistent with the fact that stations with thresholds above 1.2 Bv did not see an increase.

The neutron monitor records show no additional particles–even at the highest latitudes–after about 1800 UT on the 17th. If we assume a steepening of the spectrum of $1/p^6$, and that a 1 percent increase would have been detected, the intensity above 1 Bv was less than $0.01 \times 13 \times 0.09 = 0.0012$ particles/cm^2-ster-sec.

A number of balloon flights provided particle data in the intermediate energy range. Information from Freier (Reference 49), Winckler, et al. (Reference 55), Webber (Reference 56), Brown and D'Arcy (Reference 57), and Anderson and Enemark (Reference 40), have been combined to give energy spectra at four times during the July 10th event and twice during each of the other two, as well as relatively complete histories of the integral flux above 100 Mev.

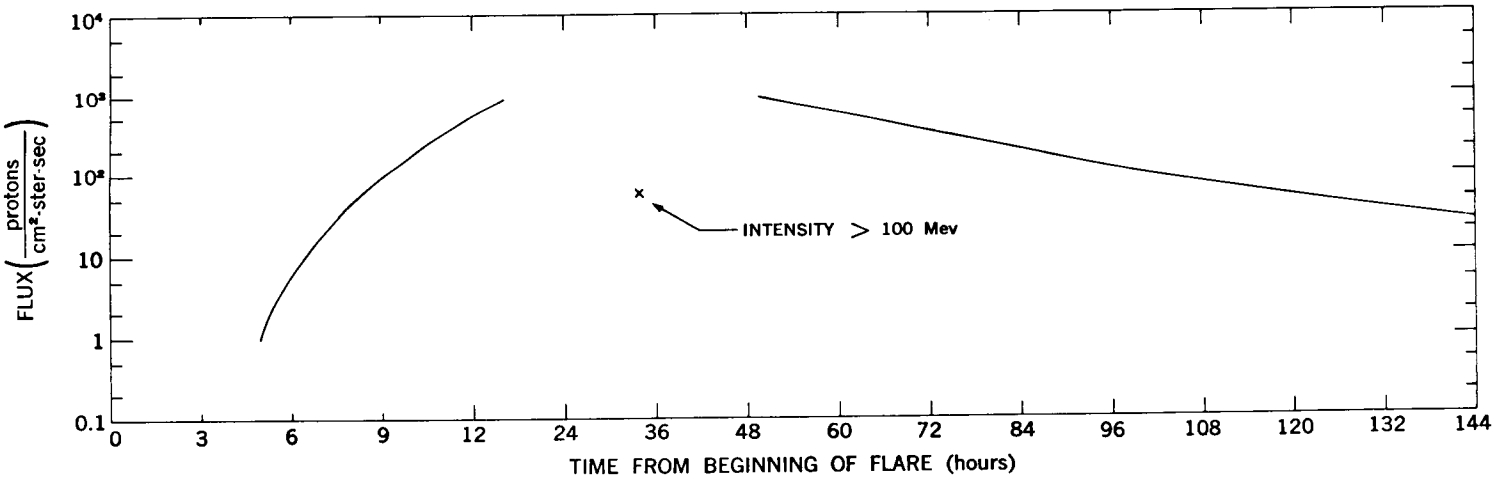

(a) Time history

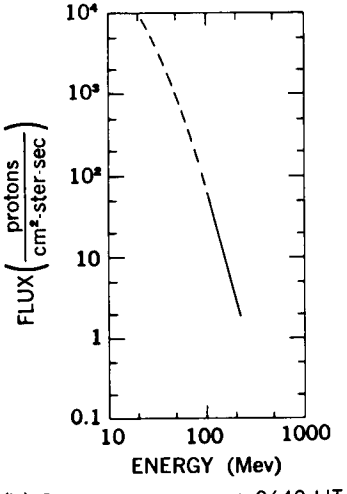

(b) Energy spectrum at 0640 UT (+34 hours)

Figure 2-8—The May 10, 1959 event

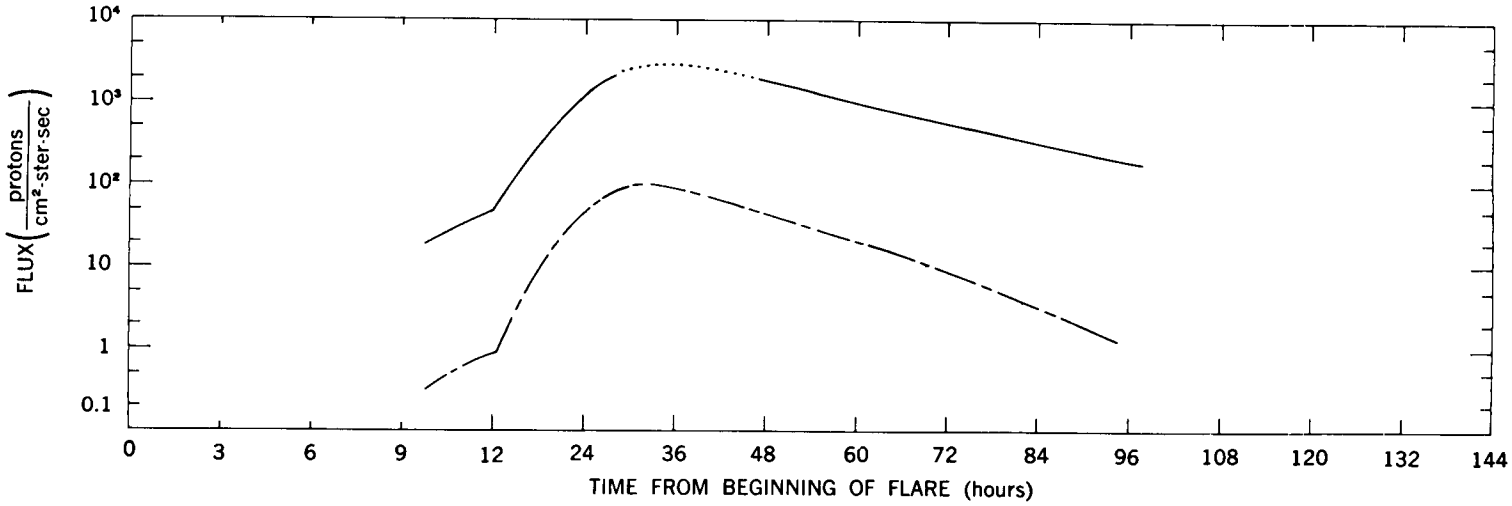

(a) Time history

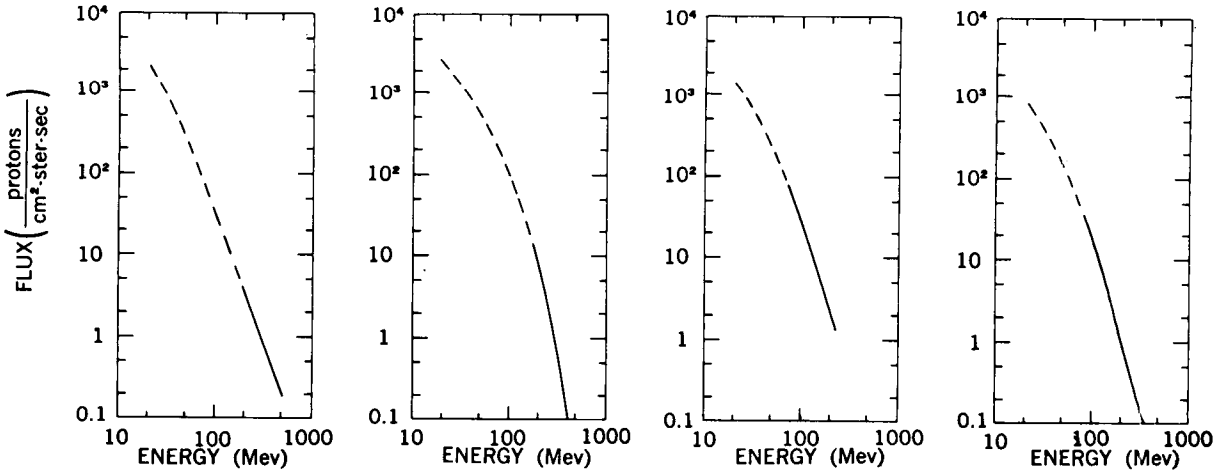

(b) Energy spectra at 0800 UT (+30 hours); 1200 UT (+34 hours); 0700 UT (+53 hours); and 1800 UT (+64 hours)

Figure 2-9—The July 10, 1959 event

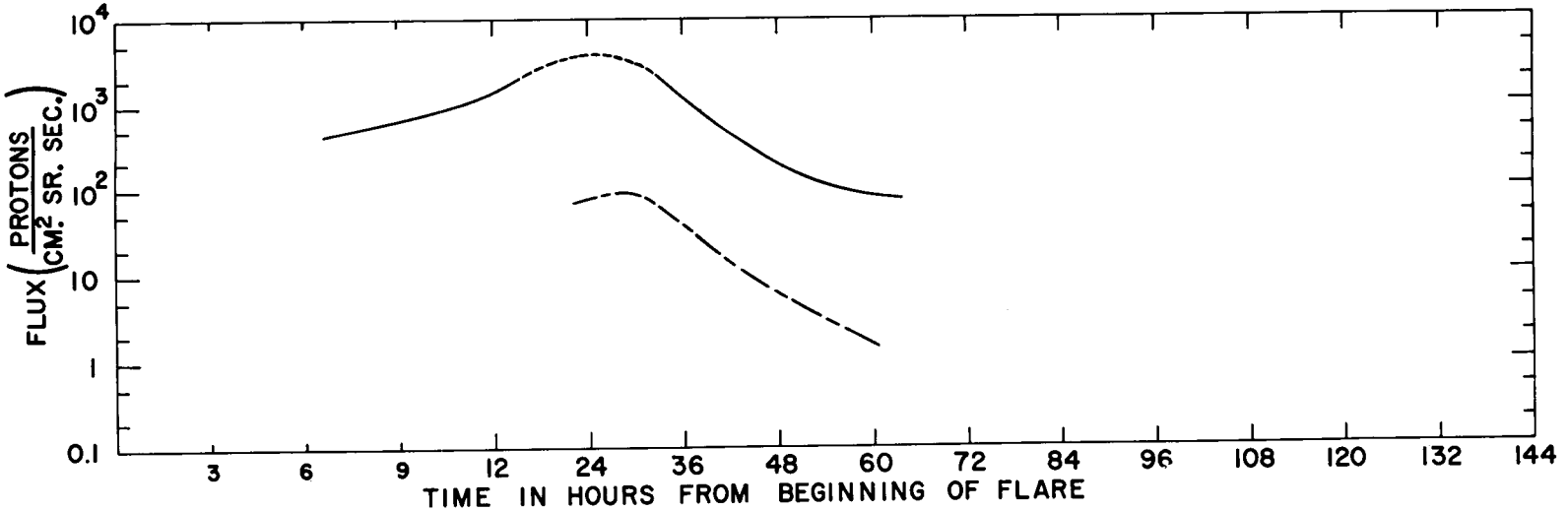

(a) Time history

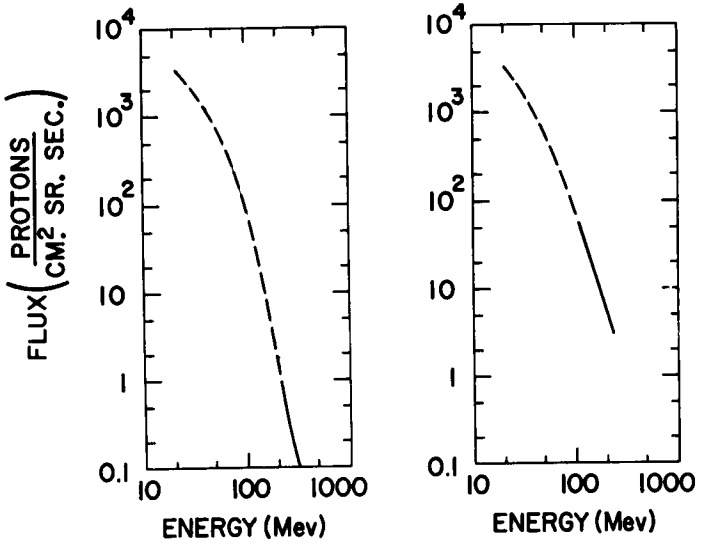

(b) Energy spectra at 0500 UT (+25-1/2 hours) and 1042 UT (+31 hours)

FIGURE 2—10 — THE JULY 14, 1959 EVENT

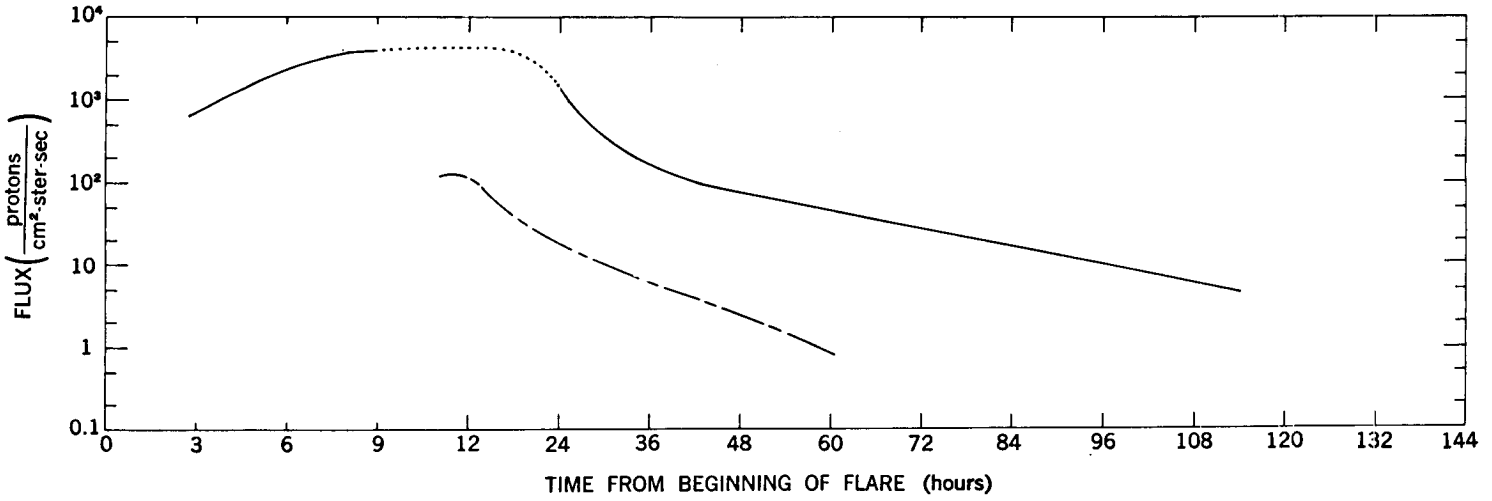

(a) Time history

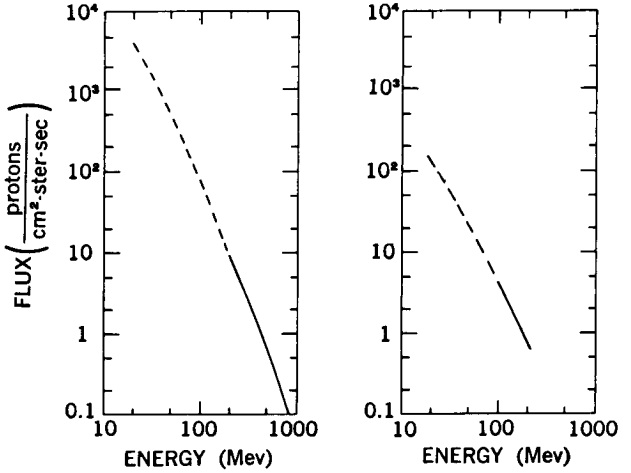

(b) Energy spectra at 1200 UT (+14-3/4 hours) and 1510 UT (+42 hours)

Figure 2-11—The July 16, 1959 event

0138 UT April 29, 1960

The riometers at College (Reference 41), Thule (Reference 41), and Churchill (Reference 54) were in essential agreement during this event and showed a maximum absorption of about 13 db on April 30th at about 0600 UT (Figure 2-12). Several readings from the Explorer VII (1959ι 1) (Reference 58) counters during the period 1800 UT April 29th through 0100 UT April 30th at L values* where the full intensity was often seen in other events indicated flux values more than an order of magnitude lower than those inferred from the riometer data. This shows that either the satellite was situated in a position where the minimum energy observable due to geomagnetic effects was larger than the nominal threshold energy of the detectors (18 and 30 Mev) or that there was a large component at energies below 18 Mev.

1000 UT May 4, 1960

This event, observed at sea level by neutron monitors, falls into the category of *rapid risers* and shows pronounced impact zone effects. The intensity in the impact zones started to rise at 1030 ±1 UT, and reached maximum at 1040 ±2 UT, with a differential spectrum of about p^{-4} (Figure 2-13). Outside the impact zones the intensity began to rise at 1035 UT and reached maximum at 1048 ±2 UT, with a differential spectrum varying approximately as p^{-5}. The neutron monitor at Deep River detected particles arriving directly and observed an increase of 3.5 times at maximum, which implies an intensity of $3.5 \times 12 \times 0.1 = 4.5$ particles/cm^2-ster-sec above 1 Bv. This quantity checks within a factor of 2 with the increase recorded at the Jungfraugoch where the threshold is 3.6 Bv; the agreement provides some confidence in the spectrum. The decay above 1 Bv can be approximated by an expression of the

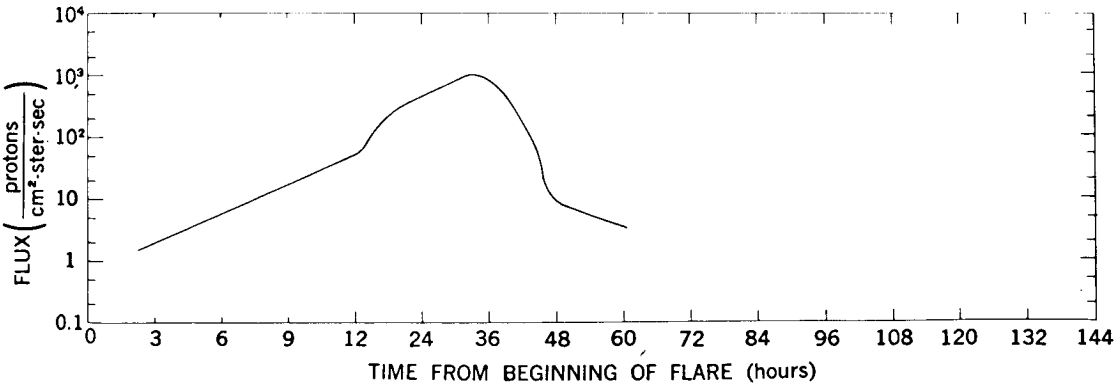

Figure 2-12—The time history of the April 29, 1960 event

*The distance called the "L value" is the radius (in earth radii) at which the magnetic line of force to which it refers crosses the equatorial plane.

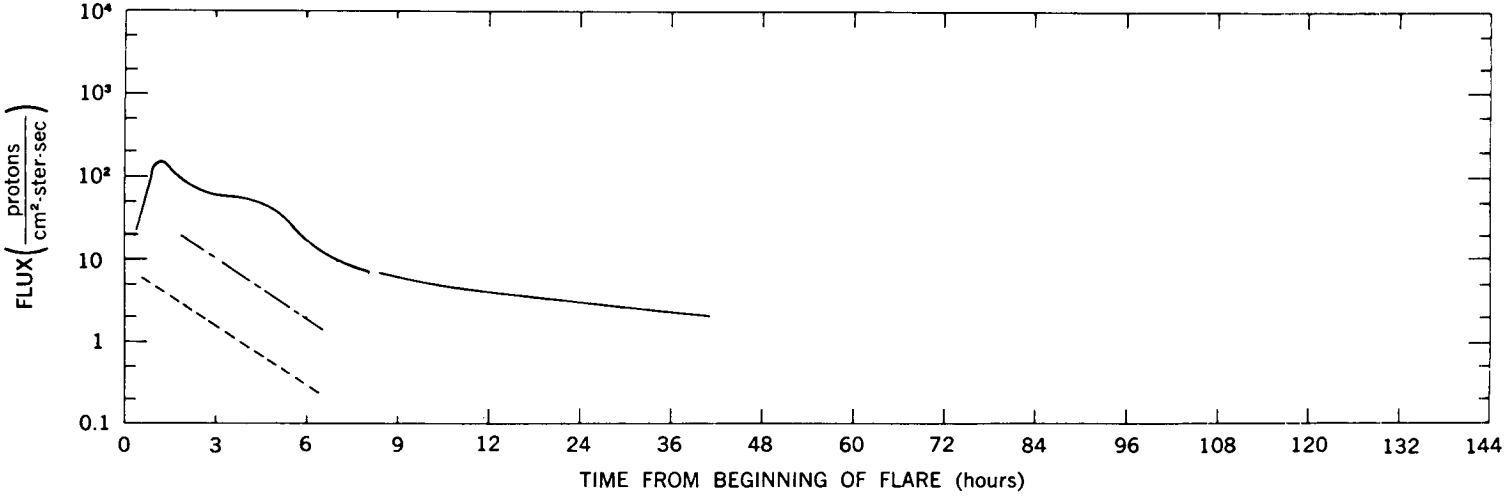

(a) Time history

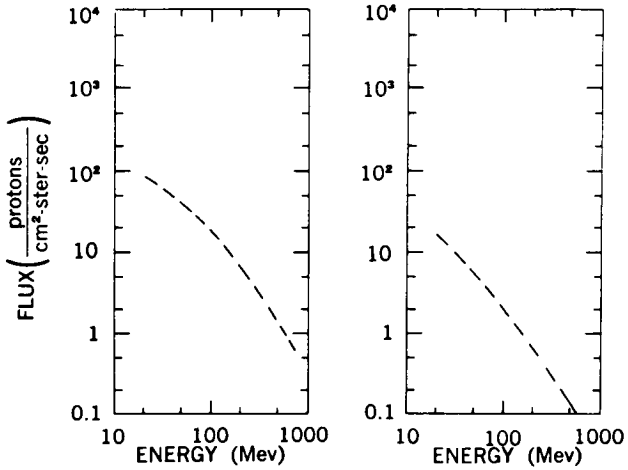

(b) Energy spectra at 1220 UT (+2 hours) and 1630 UT (+6 hours)

Figure 2-13—The May 4, 1960 event

form $N = N_0 e^{-t/t_0}$ with t_0 = 2 hours. J. R. Winckler et al. (Reference 59), at 1630 UT on May 4th, found a flux above 1 Bv with detectors flown on balloons, which is in excellent agreement with the flux inferred by neutron monitor data.

The riometer data from Thule (Reference 41) showed a rapid increase to a maximum absorption of about 5 db two hours after the start of the flare. The riometers at College (Reference 41) and Churchill (Reference 54) were in darkness at that time. Following the maximum, the three riometers were in agreement, and the inferred particle intensity agreed with the State University of Iowa (SUI) Explorer VII data (Reference 58) obtained from 10 to 32 hours after the flare.

1404 UT May 6, 1960

The riometers at College (Reference 41), Churchill (Reference 54), and Thule (Reference erence 40) showed agreement for this event, with a maximum absorption of about 13 db, forty hours after the flare (Figure 2-14). Again there is disagreement with the SUI Explorer VII data (Reference 54), probably for the same reasons discussed in connection with the event of April 29, 1960.

0037 UT September 3, 1960

In this interesting event the solar emission, due to a class 3 flare at 17°N 87°E on the sun, occurred during the transit to the earth of distrubances from two previous flares. A slowly rising isotropic flux was detected, which caused an increase of about 2 percent in the neutron monitor rate at Deep River at 0900 UT (Reference 32). Rockets launched from Churchill at 1400 UT and 1700 UT measured a spectrum steepening towards high energies (Reference 21), which could be approximated in differential form $1/p^{3.3}$ between 0.15 and 0.7 Bv (Figure 2-15). If we assume that $1/p^6$ is appropriate above 1 Bv, then the intensity at the time of maximum was about 0.05 particles/cm^2-ster-sec. Winckler (References 55, 60, and 61) deduced an integral spectrum $2 \times 10^7 E^{-3.1}$ (E in Mev) from balloon

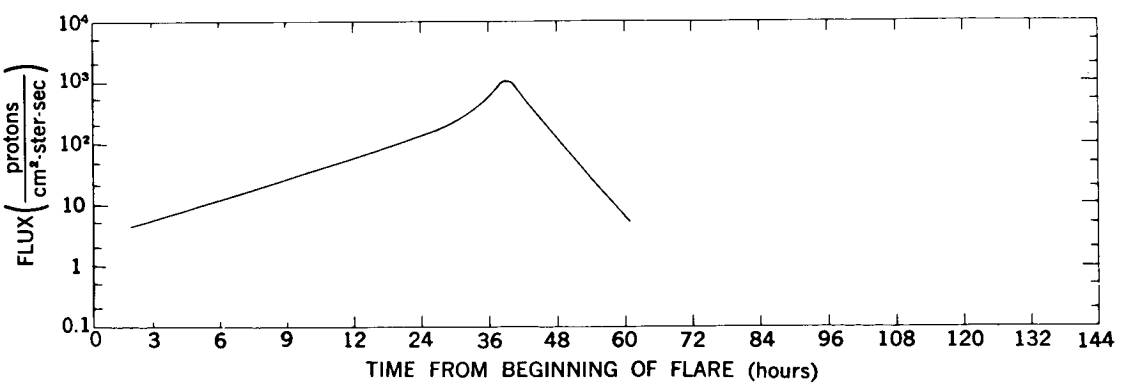

Figure 2-14—The time history of the May 6, 1960 event

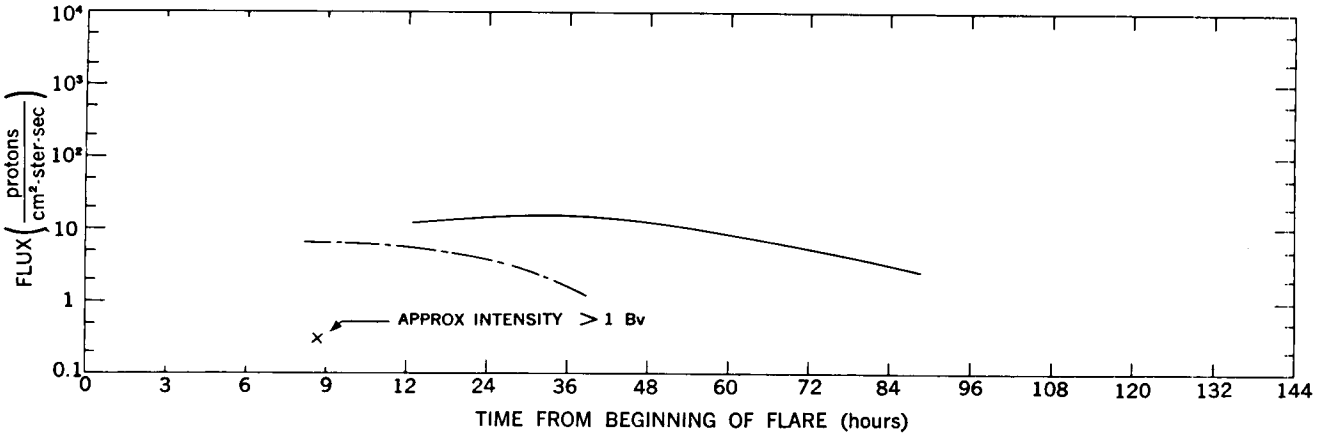

(a) Time history

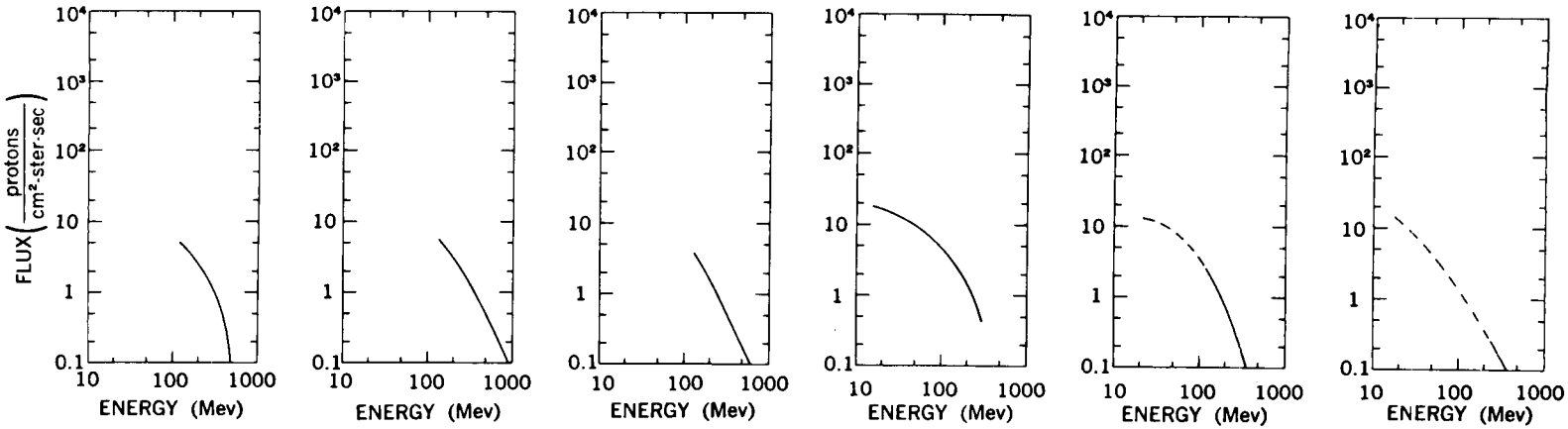

(b) Energy spectra at 0900 UT (+8 hours); 1000 UT (+9 hours); approximately 1230 UT (+12 hours); 1408 UT (+13-1/2 hours); 0000 UT (+23 hours), and 1615 UT (+39-1/2 hours)

Figure 2-15—The September 3, 1960 event

measurements at Minneapolis and Churchill at about 1730 UT. This is in fair agreement with the intensity value given above, as are the results of Biswas et al. (Reference 5). In the energy region from 22 to 67 Mev the intensity remained the same between 1400 and 1700 UT. We know from the behavior of the low energy particles producing the cosmic noise absorption that the decay of the event at these energies was very slow; and examination of the emulsion measurements at 1 Bv at Minneapolis showed that the high energy flux decayed by a factor of almost 10 in about 30 hours.

The PCA observations indicated a very flat spectrum, consistent with that found by the rocket emulsion measurements. In addition the measurements of Explorer VII (Reference 58) are in agreement with the intensities inferred from riometer absorption.

1322 UT November 12, 1960

This event was a complicated one in which two separate maxima are displayed at high latitudes by the neutron monitor records. Figure 2-16 shows the records of the Deep River neutron monitor for the month of November 1960 showing the coordinates of the important flares. It has been postulated (References 62 and 63), that the flares occurring on the 10th and 11th produced plasma fronts, and these were in transit towards the earth when the flare on the 12th produced an injection of high energy particles. Thus, detectors on the earth sampled the intensity of solar particles for six hours before and several hours after the passage of a front which generated a large magnetic storm and a very rapid Forbush decrease. In addition to the neutron monitor and riometer data, detailed energy spectra were

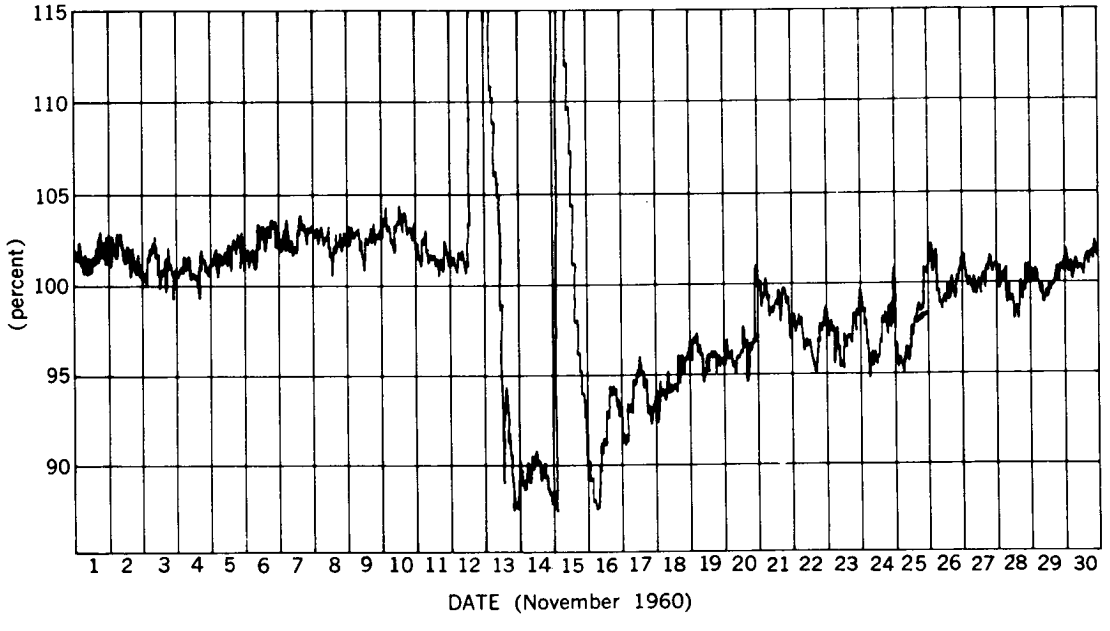

Figure 2-16—November, 1960 neutron monitor data from Deep River

obtained at three times during this event by the reduction of data from sounding rockets fired from Churchill (References 63 and 64). These spectra for the November 12 event are shown in Figure 2-17. The low energy component between 20 and 80 Mev was seen to increase markedly between 1840 and 2330 UT in agreement with the riometer data. Between 2330 UT on November 12 and 1603 UT on November 13, the high energy component continued to decline as indicated by the curve deduced from neutron monitor data between about 2000 UT on November 12 and 0400 UT on November 13.

For this event Lockwood and Shea (Reference 65) have performed calculations similar to those reported here; and this permits a check on our procedure for finding the flux above the atmosphere corresponding to a given neutron excess. Lockwood and Shea find a spectrum of the form p^{-6} between 1600 and 1630 UT on November 12, and deduce a differential spectrum for protons which corresponds to 2.9 particles/cm^2-ster-sec above 1.25 Bv. Our calculation leads to $0.85 \times 21 \times 0.11 = 2.0$ particles/cm^2-ster-sec above 1.25 Bv.

Further confirmation can be found from the results of the measurements made at 1840 UT by a NASA rocket launched from Churchill just before the earth entered the trapping region (Reference 65). From the emulsion measurements, Fichtel and Guss found an intensity above 680 Mv of 24 particles/cm^2-ster-sec, and a slope of about -6 for the integral rigidity spectrum. Assuming this slope to continue, the intensity above 1 Bv would be 3.5 particles/cm^2-ster-sec. It is difficult to obtain a rate of decrease with time which has much meaning over a wide rigidity range. After 1900 UT Manzano et al. (Reference 66) found a decrease proportional to $t^{-2.3}$ and a sudden increase in the decay rate at 1000 on November 13th.

0200 UT November 15, 1960

After the first hour, during which particles were incident principally from a direction about 50° west of the earth-sun line and the intensity rose rapidly, a regular decline set in at high energies. The maximum of the neutron monitor increase at high latitudes indicates an intensity of approximately 3 particles/cm^2-ster-sec above 1.25 Bv, assuming a $1/p^6$ differential rigidity spectrum. Lockwood and Shea deduced a differential rigidity spectrum of $10^2 p^{-6}$ for P in the range 1-7 Bv. This leads to an intensity above 1.25 Bv of 6.5 particles/cm^2-ster-sec at the time of the maximum, which is in fair agreement with the calculation made here.

The riometer data indicate that the maximum flux of particles above 20 Mev occurred about twenty hours after the flare (Reference 41), and was almost 10^4 particles/cm^2-ster-sec (Figure 2-18). Detailed energy spectra were available early in the event from balloon borne equipment (Reference 6) and later in the event from sounding rockets (References and). The Explorer VII (Reference 58) data agree with the other data obtained to within a factor of 2. A relatively fast decline is observed late in the event, with the decay following a law of the form $1/T^n$, with T = 0 at the time of the flare and n perhaps as large as 3 (Reference 67).

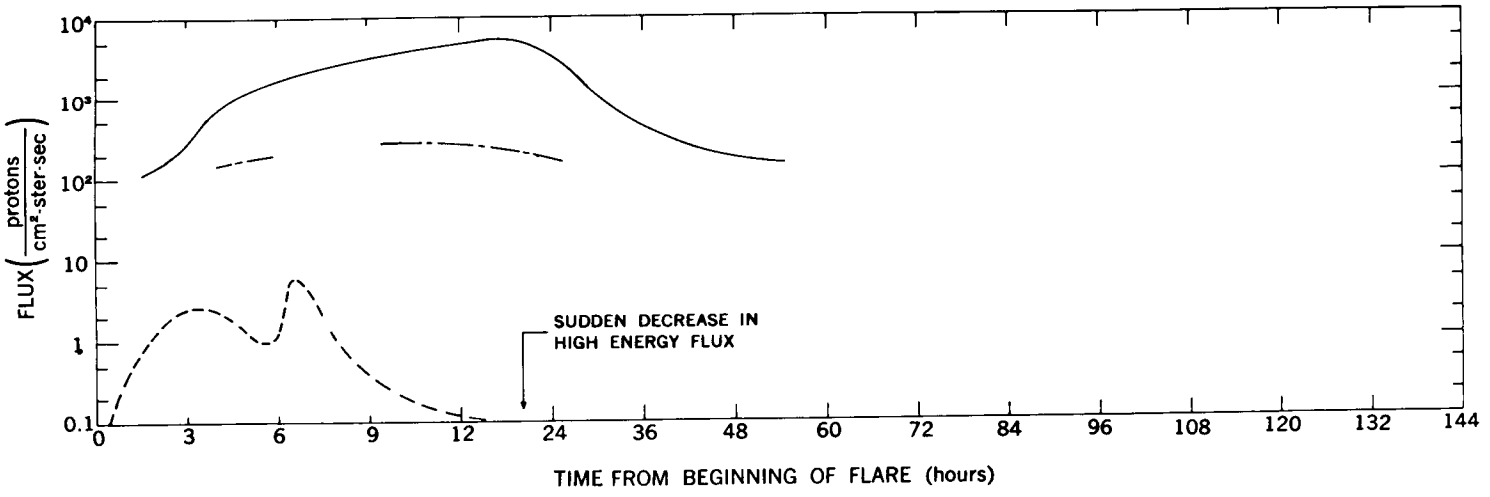

(a) Time history

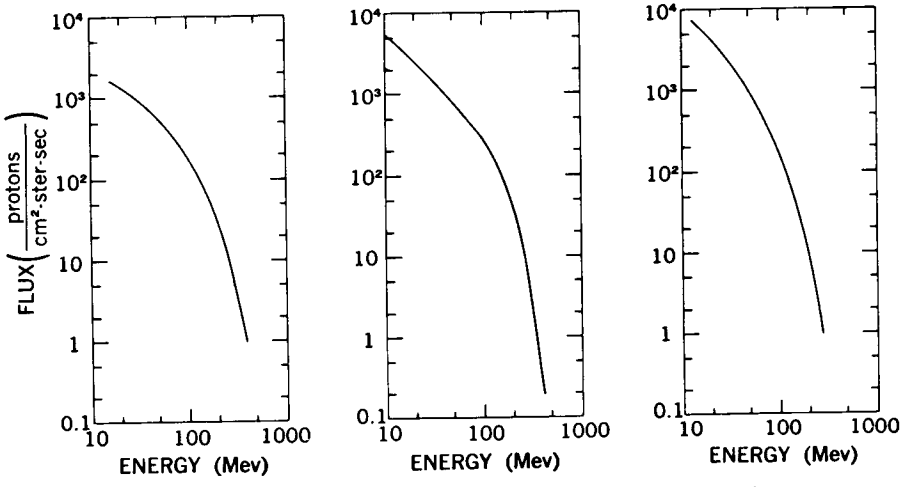

(b) Energy spectra at 1840 UT (+5 hours); 2330 UT (+10 hours); and 1603 UT (+26-1/2 hours)

Figure 2-17—The November 12, 1960 event

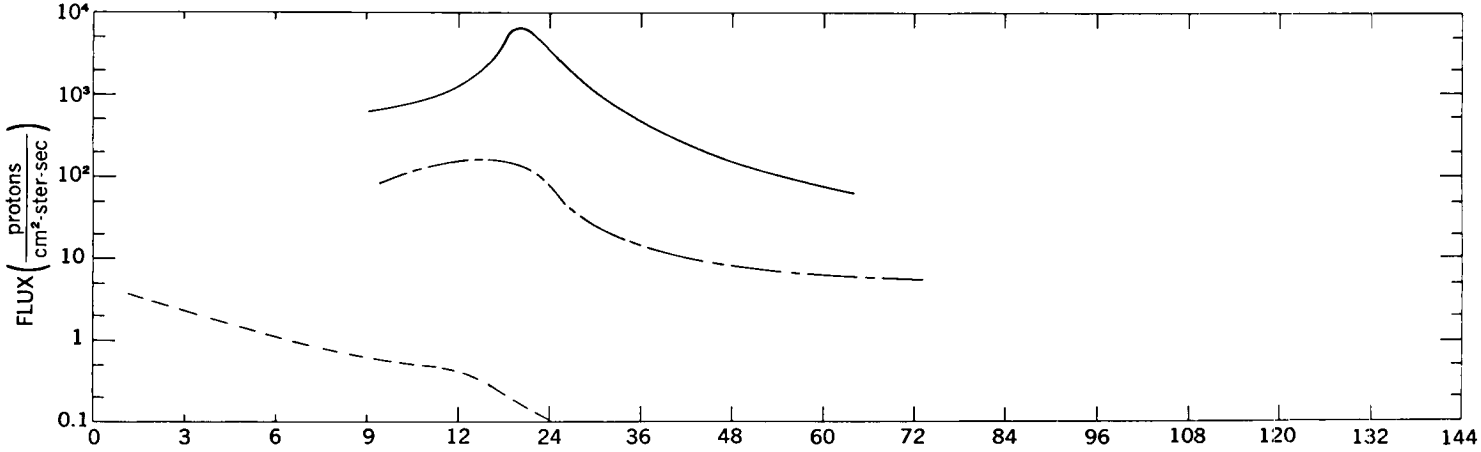

(a) Time history

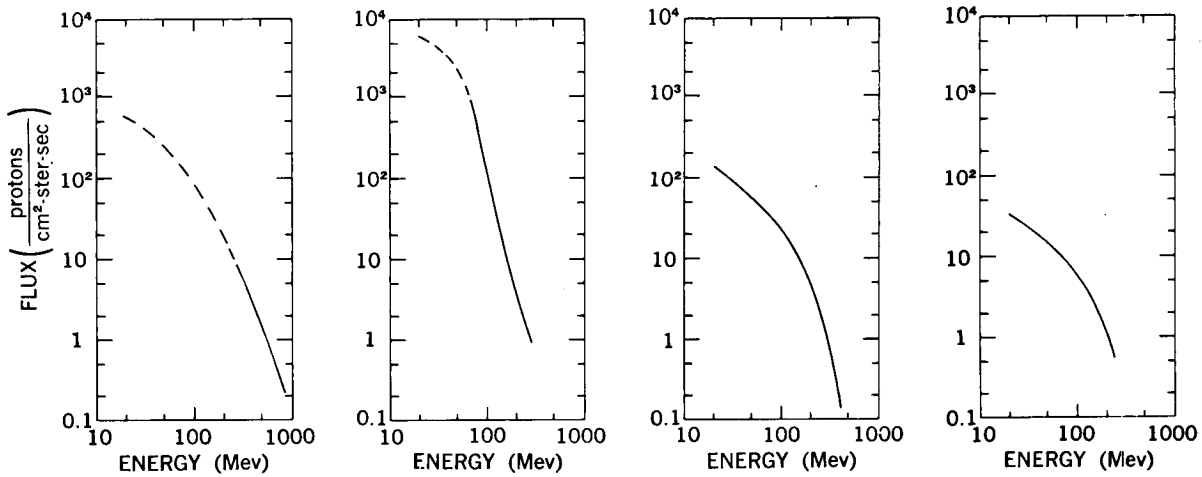

(b) Energy spectra at 1130 UT (+9-1/2 hours); 2200 UT (+20 hours); 1600 UT (+38 hours); and 0340 UT (+74 hours)

Figure 2-18—The November 15, 1960 event

November 20, 1960

On November 20th there was another solar event; the flare was from the same region as the flares associated with the November 12th and 15th events which, by then, was just around the western limb of the sun. The increase at neutron monitor energies was small and took about one hour to reach its maximum value, 5 percent above background, at Deep River (Reference 20). An increase of the order of 1/2 to 1 percent occurred at points with a threshold rigidity of 3 Bv, indicating a very flat spectrum. The riometer increase was also relatively small, indicating that the integral intensity of particles above 20 Mev did not exceed 100 particles/cm^2-ster-sec.

July 12, 1961

The integral flux of particles greater than 20 Mev, as determined by the absorption detected on the riometer (References 41 and 54), increased relatively slowly early in the July 12, 1961 event and reached a maximum shortly after the sudden commencement – 24 hours after the flare (Figure 2-19). From nuclear emulsions flown on a balloon near Churchill, Guss and Waddington (Reference 68) obtained an energy spectrum averaged over a 10 hour period centered about 26-1/2 hours after the flare*, when the intensity was greatest. From Figure 2-19, we see that the integral proton energy spectrum is very steep at this time, of the order of $1/E^{4.5}$, in the energy range from 78 to 140 Mev. Based on the riometer data, we conclude that it must have remained approximately that steep to energies below 20 Mev. From geiger counter observations on another balloon at a slightly lower altitude (Reference 69) and the riometer data, it is known that the energy spectrum was at least this steep during the entire period around maximum intensity.

0930 UT July 18, 1961

This event is presumed to be associated with the 3+ flare at 0930 UT on July 18, 1961 because of the relatively rapid flux increase shortly thereafter as detected by neutron monitors and the riometers at various northern stations. There were, however, two major flares shortly before this time, a class 3 flare at 0505 UT and a class 2 flare at 0805 UT, which may have contributed particles to the event. Unlike the previous event on July 12, the riometer absorption for this event shows a rapid rise almost to the maximum value within about two hours (Figure 2-20). In addition, there was a detectable particle flux in excess of about 450 Mev as shown by the neutron monitor increase. There was a balloon in the air from 1305 to 1918 UT on July 18th carrying nuclear emulsion (Reference 71). A combination of this, the riometer, and the neutron monitor data permits the determination of an energy spectrum early in the event. On the basis of the neutron monitor and riometer records, as well as the behavior of other events, it is reasonable to assume that the energy spectrum

*Data obtained from the Injun satellite (Reference 70) is in general agreement with this interpretation.

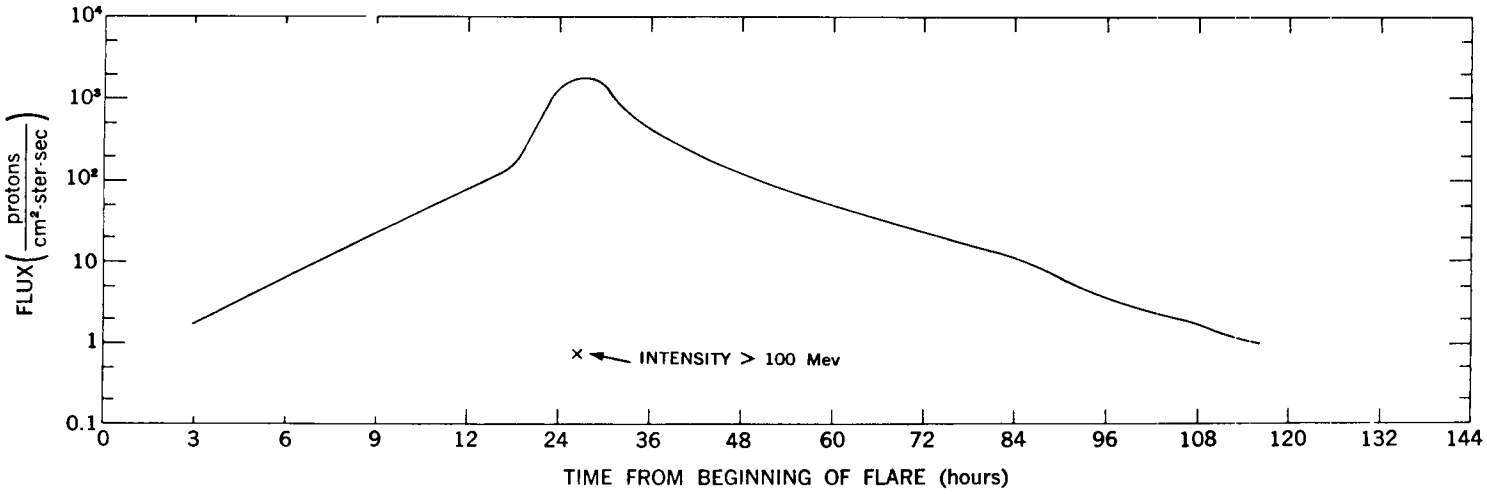

(a) Time history

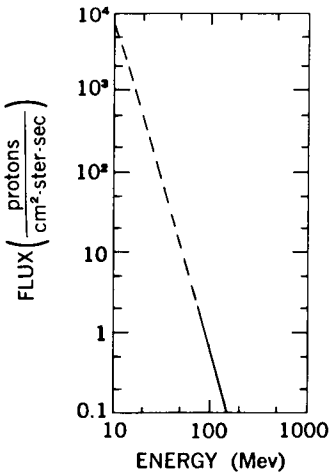

(b) Energy spectrum at 1300 UT (+27 hours)

Figure 2-19—The July 12, 1961 event

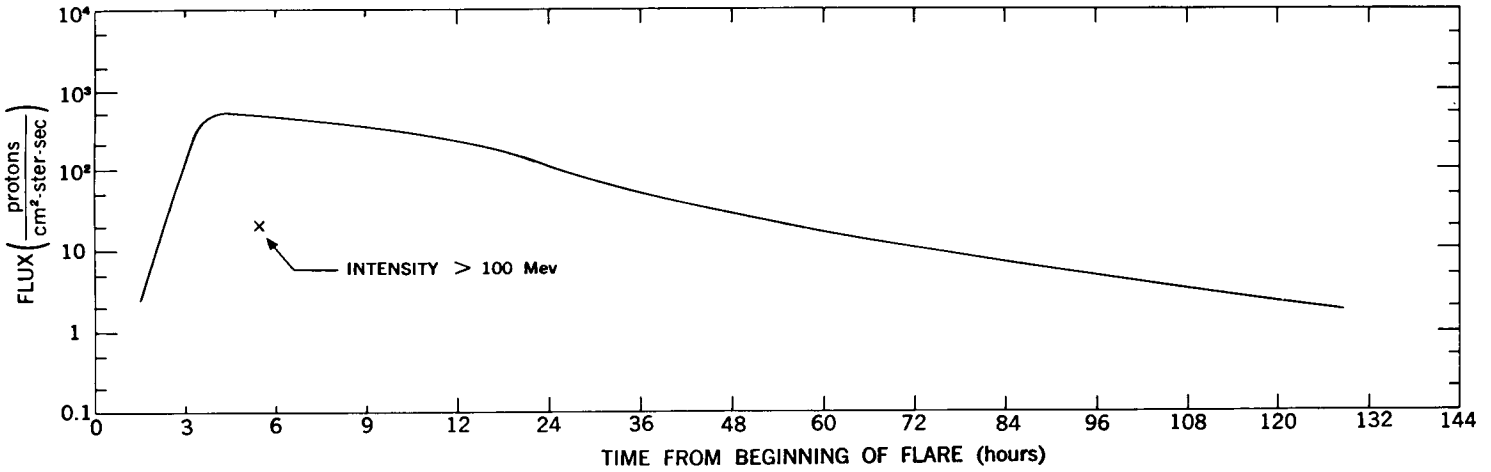

(a) Time history

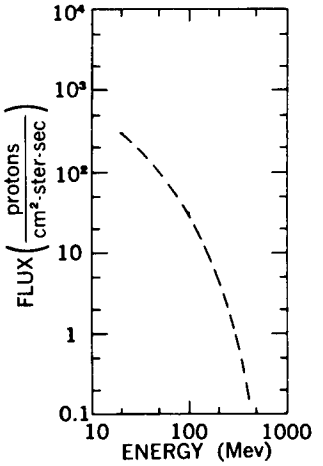

(b) Energy spectrum at 1600 UT (+6-1/2 hours)

Figure 2-20—The July 18, 1961 event

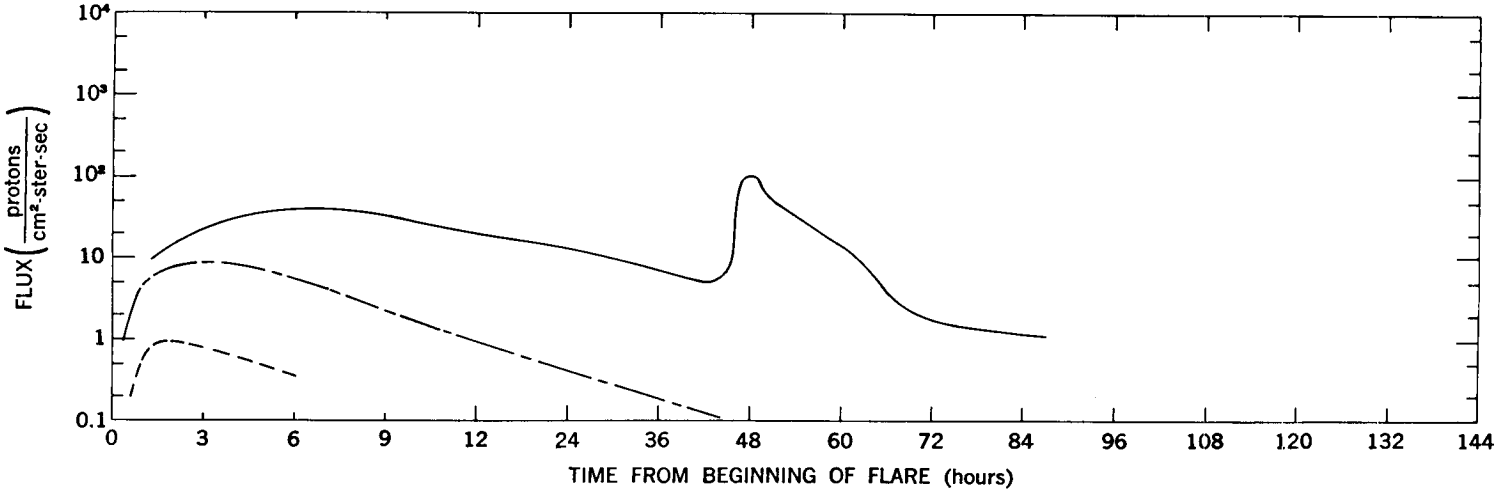

(a) Time history

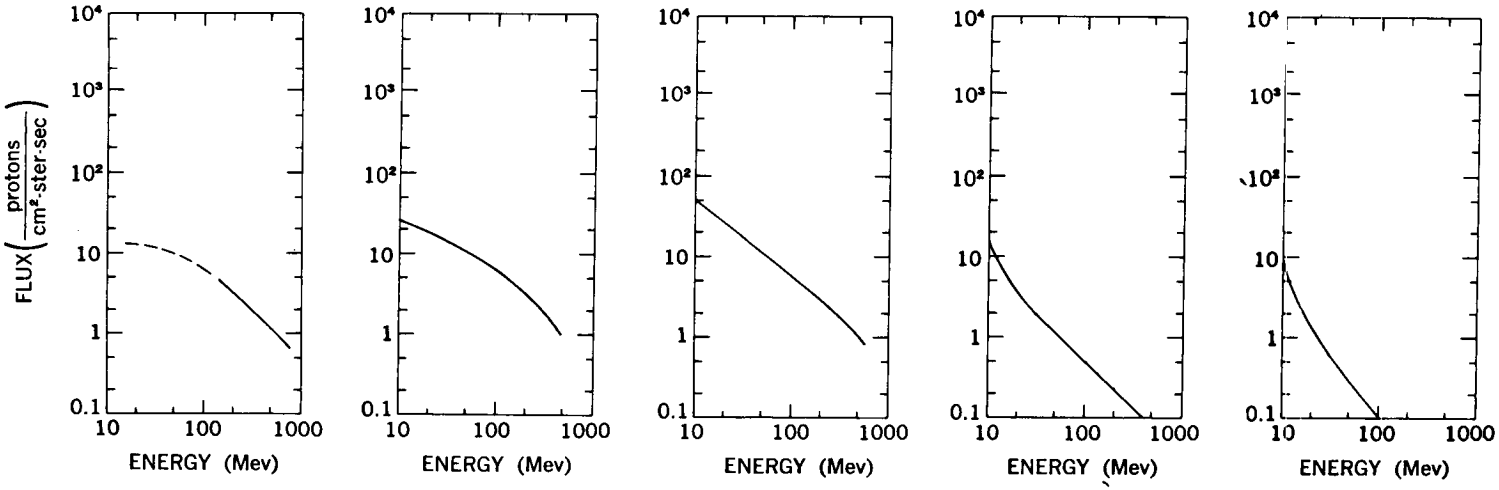

(b) Energy spectra at 2330 UT (+2-1/2 hours); 0140 UT (+4-1/2 hours; 0410 UT (+7 hours); 1730 UT (+20 hours); and 1902 UT (+46 hours)

Figure 2-21—The September 28, 1961 event

steepened with time for the first twelve or more hours of the event. The integral flux above 20 Mev had already begun to decline six hours after the event began.

2115 UT September 28, 1961

The September 28, 1961 event is the first for which there is a detailed energy spectrum, as a function of time from 10-1000 Mev, for a large fraction of the event (Figure 2-21). The data was obtained from instruments flown on Explorer XII by D. A. Bryant et al. (Reference 26). The flare presumed to be associated with the event began at approximately 2215 UT, September 28 and reached its maximum intensity at about 2230 UT. The slope of the integral energy spectrum progressively increased with time in the low energy region until it was approximately as steep as that at high energies. Then there was a general decay with relatively little change in spectral shape above about 30 Mev. In the energy region from 1.5-30 Mev the flux was seen to increase markedly around the time of the sudden commencement and remain at a high level for several hours (References 26 and 72). The fluxes obtained by D. A. Bryant et al. (Reference 26) and O'Brien et al. (Reference 72) in the low energy region are found to be in agreement, within expected uncertainties, with each other and with the fluxes deduced from the riometer absorption curve.

Imaginary Envelope Event

In Figure 2-22 the curves of proton flux as a function of time were drawn so that the integral flux above the indicated energy level would be just slightly larger than in any event ever observed at the corresponding time from the beginning of the flare. Although this imaginary event is based on the best available data, there is, of course, the strong possibility that some past events have been bigger. Also, some future solar outbursts may very well have larger effects.

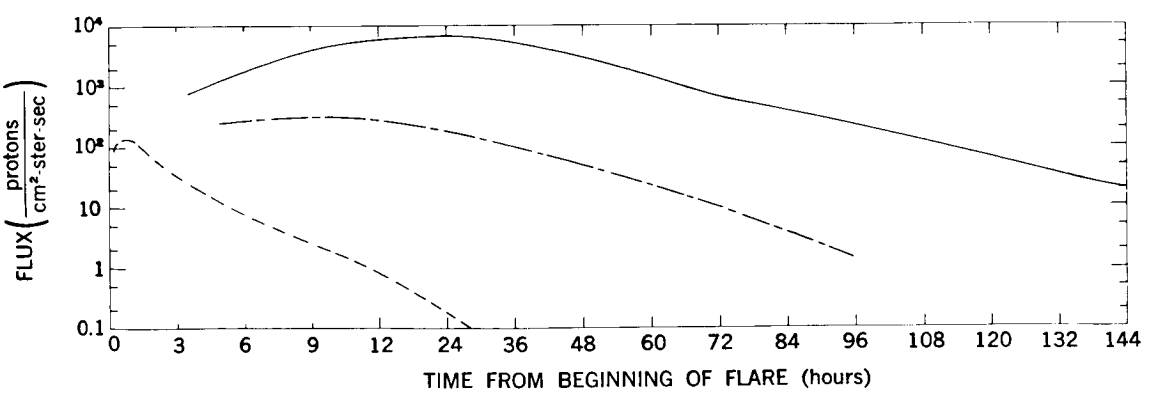

Figure 2-22—The time history of an imaginary envelope event which includes all the types of events observed

ACKNOWLEDGMENTS

The authors are happy to acknowledge the contributions of the following people, many of whom were kind enough to permit the inclusion of unpublished data: P. D. Bhavsar; S. Biswas; D. A. Bryant; L. L. Cline; U. Desai; P. S. Freier; T. R. Hartz; H. Leinbach; W. C. Lin; F. B. McDonald; E. P. Ney; B. J. O'Brien; G. C. Reid; W. Stein; J. A. Van Allen; E. L. Vogan; W. R. Webber; J. R. Winckler.

REFERENCES

1. Forbush, S. E., "Three Unusual Cosmic-Ray Increases Possibly Due to Charged Particles from the Sun," *Phys. Rev.* 70(9 and 10):771-772, November 1 and 15, 1946.

2. Adams, N., "A Temporary Increase in the Neutron Component of Cosmic Rays," *Phil. Mag.* 41:503-505, May 1950.

3. Webber, W. R., "Time Variations of Low Energy Cosmic Rays during the Recent Solar Cycle," in: *Progress in Elementary Particle and Cosmic Ray Physics*, ed. by J. G. Wilson and S. A. Wouthuysen, Amsterdam: North-Holland Publ. Co., Vol. 6, 1962 (In Press).

4. Fichtel, C. E. and Guss, D. E., "Heavy Nuclei in Solar Cosmic Rays," *Phys. Rev. Letters* 6(9):495-497, May 1, 1961.

5. Biswas, S., Freier, P. S., and Stein, W., "Solar Protons and α Particles from the September 3, 1960 Flares," *J. Geophys. Res.* 67(1):13-24, January 1962.

6. Ney, E. P. and Stein, W., "Solar Protons in November 1960," in: *Proc. Internat. Conf. on Cosmic Rays and the Earth Storm, Kyoto, September 1961. II. Joint Sessions*, Tokyo: Physical Society of Japan, 1962, pp. 345-353.

7. Dodson, H. W., "Observation of Loop-Type Prominences in Projection Against the Disk at the Time of Certain Solar Flares," *Proc. Nat. Acad. Sci.* 47(7):901-905, July 15, 1961.

8. Kundu, M. R. and Haddock, F. T., "A Relation Between Solar Radio Emission and Polar Cap Absorption of Cosmic Noise," *Nature* 186(4725):610-613, May 21, 1960.

9. Hachenberg, O. and Krüger, A., "The Correlation of Bursts of Solar Radio Emission in the Centimetre Range with Flares and Sudden Ionospheric Disturbances," *J. Atmos. Terrest. Phys.* 17(1/2):20-33, December 1959.

10. Bachelet, F., Conforto, A. M., and Iucci, N., "Solar Flares with Type IV Radioburst and Transient Phenomena of Cosmic Rays," in: *Space Research, Proc. 1st Internat. Space Sci. Sympos., Nice, January 1960*, Amsterdam: North-Holland Publ. Co., 1960, pp. 662-664.

11. Thompson, A. R. and Maxwell, A., "Solar Radio Bursts and Low-Energy Cosmic-Rays," *Nature* 185(4706):89-90, January 9, 1960.

12. Boischot, A. and Denisse, J.-F., "Les Émissions de Type IV et l'Origine des Rayons Cosmiques Associés aux Éruptions Chromosphériques," *Comptes Rendus, Academie des Sciences* (Paris) 245(25):2194-2197, December 16, 1957.

13. Peterson, L. E. and Winckler, J. R., "Gamma-Ray Burst From a Solar Flare," *J. Geophys. Res.* 64(7):697-707, July 1959.

14. McCracken, K. G. and Palmeira, R. A. R., "Comparison of Solar Cosmic Ray Injections Including July 17, 1959, and May 4, 1960," *J. Geophys. Res.* 65(9):2673-2683, September 1960.

15. Little, C. G. and Leinback, H., "Some Measurements of High-Latitude Ionospheric Absorption Using Extraterrestrial Radio Waves," *Proc. IRE* 46(1):334-348, January 1958.

16. Little, C. G. and Leinback, H., "The Riometer — A Device for the Continuous Measurement of Ionospheric Absorption," *Proc. IRE* 47(2):315-320, February 1959.

17. Bailey, D. K., "Abnormal Ionization in the Lower Ionosphere Associated with Cosmic-Ray Flux Enhancements," *Proc. IRE* 47(2):255-266, February 1959.

18. Reid, G. C., "A Study of the Enhanced Ionization Produced by Solar Protons during a Polar Cap Absorption Event," *J. Geophys. Res.* 66(12):4071-4085, December 1961.

19. Quenby, J. J. and Webber, W. R., "Cosmic Ray Cut-Off Rigidities and the Earth's Magnetic Field," *Phil. Mag.* 4(37):90-113, January 1959.

20. Brown, R. R. and Weir, R. A., "Ionospheric Effects of Solar Protons," *Arkiv för Geofysik* 3:523-529, 1961.

21. Davis, L. R., Fichtel, C. E., et al., "Rocket Observations of Solar Protons on September 3, 1960," *Phys. Rev. Letters* 6(9):492-494, May 1, 1961.

22. Ogilvie, K. W., Bryant, D. A., and Davis, L. R., "Rocket Observations of Solar Protons during the November 1960 Event," in *Proc. Internat. Conf. on Cosmic Rays and the Earth Storm, Kyoto, September 1961. II. Joint Sessions,* Tokyo: Physical Society of Japan, 1962, pp. 317-319.

23. Leinbach, H. and Reid, G. C., "Polar Cap Absorption During the Solar Cosmic Ray Outbursts of July 1959," in: International Union of Geodesy and Geophysics, *Symposium on the July 1959 Events and Associated Phenomena, Helsinki, July 1960,* Paris: Institut Géographique National, 1960, pp. 145-150.

24. Ortner, J., Leinbach, H. and Sugiura, M., "The Geomagnetic Storm Effect on Polar Cap Absorption," *Arkiv för Geofysik* 3:429-434, 1961.

25. Leinbach, H., "Some Observations of Daytime Recoveries During Polar Cap Absorption Events," *Arkiv för Geofysik* 3:427, 1961 (Abstract).

26. Bryant, D. A., Cline, T. L., et al., "Results from the Goddard Cosmic Ray Experiments on Explorer XII," Presented at Explorer XII Symposium, Goddard Space Flight Center, January 1962.

27. Van Allen, J. A., Frank, L. A., et al., "Coordinated Injun I—Explorer XII Observations of Solar Cosmic Rays, 28 September to 4 October 1961," Presented at Explorer XII Symposium, Goddard Space Flight Center, January 1962.

28. Simpson, J. A. and Fenton, K. B., "The Neutron Monitor," Univ. Chicago, 1955 (unpublished).

29. Webber, W. R. and Quenby, J. J., "On the Derivation of Cosmic Ray Specific Yield Functions," *Phil. Mag.* 4(41):654-664, May 1959.

30. Schlüter, A., "Störmer Orbits of Low Energy," *Supplemento al Nuovo Cimento* 8(2):349-357, 1958.

31. Carmichael, H. and Steljes, J. F., "Review of Recent High Energy Solar Particle Events Including November 1960," Atomic Energy of Canada Ltd., AECL-1387 (CRGP-1056) October 30, 1961; Also *Proc. Internat. Conf. on Cosmic Rays and the Earth Storm, Kyoto, September 1961. II. Joint Sessions,* Tokyo: Physical Society of Japan, 1962, pp. 337-344.

32. McCracken, K. G., "The Cosmic-Ray Flare Effect. 1. Some New Methods of Analysis," *J. Geophys. Res.* 67(2):423-434, February 1962.

_____, "The Cosmic-Ray Flare Effect. 2. The Flare Effects of May 4, November 12, and November 15, 1960," *ibid.,* pp. 435-446.

_____, "The Cosmic-Ray Flare Effect. 3. Deductions Regarding the Interplanetary Magnetic Field," *ibid.,* pp. 447-458.

33. McDonald, F. B. and Webber, W. R., "The Variation of the Cosmic Ray Intensity During a Solar Cycle," in: *Space Research: Proc. 1st Internat. Space Sci. Sympos.,* Nice, January 1960, ed. by H. K. Bijl, Amsterdam: North-Holland Publ. Co., 1960, pp. 968-981.

34. Fenton, A. G., Fenton, K. B., and Rose, D. C., "The Variation of Sea Level Cosmic Ray Intensity Between 1954 and 1957," *Can. J. Phys.* 36(7):824-839, July 1958.

35. Winckler, J. R., "Cosmic-Ray Increase at High Altitude on February 23, 1956," *Phys. Rev.* 104(1):220, October 1, 1956.

36. Pfotzer, G., "On the Separation of Direct and Indirect Fractions of Solar Cosmic Radiation on February 23, 1956 and on the Difference in Steepness of Momentum Spectrum of These Two Components," *Supplemento al Nuovo Cimento* 8(2):180-187, 1958.

37. Meyer, P., Parker, E. N., and Simpson, J. A., "Solar Cosmic Rays of February 1956 and Their Propagation through Interplanetary Space," *Phys. Rev.* 104(3):768-783, November 1, 1956.

38. Dorman, L. I., "Cosmic Ray Variations," Moscow: State Publishing House for Technical and Theoretical Literature, 1957; Translation prepared by Technical Documents Liaison Office, Wright-Patterson Air Force Base, 1958.

39. Jelly, D. H., "Compiled Data for Polar Cap Absorption Events Observed at Churchill, June 1957 to June 1960," Canada, Defence Res. Telecommunications Establ. Rept. No. 1062, May 1961.

40. Anderson, K. A. and Enemark, D. C., "Observations of Solar Cosmic Rays Near the North Magnetic Pole," *J. Geophys. Res.* 65(9):2657-2671, September 1960.

41. Leinbach, H., Private Communication.

42. Freier, P. S., Ney, E. P., and Winckler, J. R., "Balloon Observation of Solar Cosmic Rays on March 26, 1958," *J. Geophys. Res.* 64(6):685-688, June 1959.

43. Hultqvist, B., Aarons, J., and Ortner, J., Effects of the Solar Flares of 7 July 1958," *Tellus* 11(3):319-331, August 1959.

44. Charakhch'yan, A. N., Tulinov, V. F., and Charakhch'yan, T. N., "Large Cosmic-Ray Intensity Fluctuations in the Stratosphere," *Zhurnal Eksperimental'noi i Teoreticheskoi Fiziki* 38(4):1031-1036, April 1960 (in Russian); Translation in *Soviet Physics—JETP* 11(4):742-746, October 1960.

45. Rymko, N. P., Tulinov, V. F., and Charakhch'yan, A. N., "A Case of a Sharp Increase in Cosmic-Ray Intensity in the Stratosphere," *Zhurnal Eksperimental'noi i Teoreticheskoi Fiziki* 36(6):1687-1689, June 1959 (in Russian); Translation in *Soviet Physics—JETP* 9(6):1202-1203, December 1959.

46. Anderson, K. A., Arnoldy, R., et al., "Observations of Low-Energy Solar Cosmic Rays from the Flare of 22 August 1958," *J. Geophys. Res.* 64(9):1133-1147, September 1959.

47. Van Allen, J. A., McIlwain, C. E., and Ludwig, G. H., "Radiation Observations with Satellite 1958 ϵ," *J. Geophys. Res.* 64(3):271-286, March 1959.

48. Rothwell, P. and McIlwain, C., "Satellite Observations of Solar Cosmic Rays," *Nature* 184(4681):138-140, July 18, 1959.

49. Freier, P. S., Private Communication.

50. Winckler, J. R. and Bhavsar, P. D., "Low-Energy Solar Cosmic Rays and the Geomagnetic Storm of May 12, 1959," *J. Geophys. Res.* 65(9):2637-2655, September 1960.

51. Ney, E. P., Winckler, J. R., and Freier, P. S., "Protons from the Sun on May 12, 1959, *Phys. Rev. Letters* 3(4):183-185, August 15, 1959.

52. Eriksen, K. W., Holt, O., and Landmark, B., "A Note on the Polar Absorption Event of 11-18 May 1959," *J. Atmos. Terrest. Phys.* 18(1):78-81, April 1960.

53. International Union of Geodesy and Geophysics, "Symposium on the July 1959 Events and Associated Phenomena, Helsinki, July 1960," Paris: Institut Géographique National, 1960.

54. Hartz, T. R. and Vogan, E. L., Private Communication.

55. Winckler, J. R., Bhavsar, P. D., and Peterson, L., "The Time Variations of Solar Cosmic Rays during July 1959 at Minneapolis," *J. Geophys. Res.* 66(4):995-1022, April 1961.

56. Webber, W. R., Private Communication.

57. Brown, R. R. and D'Arcy, R. G., "Observations of Solar Flare Radiation at High Latitude During the Period July 10-17, 1959," *Phys. Rev. Letters* 3(8):390-392, October 15, 1959.

58. Lin, W. C. and Van Allen, J. A., Private Communication; Also, Lin, W. C., "Observation of Galactic and Solar Cosmic Rays from October 13, 1959 to February 17, 1961 with Explorer VII (Satellite 1959 Iota)," State Univ. of Iowa SUI-61-16, August 1961 (Thesis submitted for M. S. degree).

59. Winckler, J. R., Masley, A. J., and May, T. C., "The High-Energy Cosmic-Ray Flare of May 4, 1960. 1. High-Altitude Ionization and Counter Measurements," *J. Geophys. Res.* 66(4):1023-1027, April 1961.

60. Winckler, J. R., Bhavsar, P. D., et al., "Delayed Propagation of Solar Cosmic Rays on September 3, 1960," *Phys. Rev. Letters* 6(9):488-491, May 1, 1961.

61. Winckler, J. R., Bhavsar, P. D., et al., Private Communication.

62. Steljes, J. F., Carmichael, H., and McCracken, K. G., "Characteristics and Fine Structure of the Large Cosmic-Ray Fluctuations in November 1960," *J. Geophys. Res.* 66(5):1363-1377, May 1961.

63. Ogilvie, K. W., Bryant, D. A., and Davis, L. R., "Rocket Observations of Solar Protons during the November 1960 Events, 1," *J. Geophys. Res.* 67(3):929-937, March 1962.

64. Biswas, S., Fichtel, C. E., and Guss, D. E., Private Communication.

65. Lockwood, J. A. and Shea, M. A., "Variations of the Cosmic Radiation in November 1960," *J. Geophys. Res.* 66(10):3083-3093, October 1961.

66. Manzano, J. R., Santochi, O. R., et al., "Cosmic Ray Phenomena during the November 1960 Solar Disturbances," *Notas de Fisica* 7(3):25-43, 1961.

67. Davis, L. R. and Ogilvie, K. W., "Rocket Observations of Solar Protons during the November 1960 Events; 2," *J. Geophys. Res.* 67(5):1711-1716, May 1962.

68. Guss, D. E., and Waddington, C. J., Private Communication.

69. Winckler, J. R., *Internat. Conf. on Cosmic Rays and the Earth Storm, Kyoto, 1961.*

70. Pieper, G. F., Bostrom, C. O., and O'Brien, B. J., "Detection of Low-Energy Solar Protons by Injun Satellite in July, 1961," Private Communication.

71. Fichtel, C. E., Guss, D. E., and Waddington, C. J., Private Communication.

72. O'Brien, B. J., and Van Allen, J. A., Private Communication.

73. Simpson, J. A., "Cosmic-Radiation Neutron Intensity Monitor," in: *Annals of the International Geophysical Year,* London: Pergamon Press, 1957, Vol. IV, pp. 351-373.

74. Jory, F. S., "Selected Cosmic-Ray Orbits in the Earth's Magnetic Field," *Phys. Rev.* 103(4):1068-1075, August 15, 1956.

75. Firor, J., "Cosmic Radiation Intensity-Time Variations and Their Origin. IV. Increases Associated with Solar Flares," *Phys. Rev.* 94(4):1017-1028, May 15, 1954.

76. Finch, H. F. and Leaton, B. R., "The Earth's Magnetic Field — Epoch 1955.0," *Monthly Not., Roy. Astronom. Soc. Geophys. Suppl.* 7(6):314-317, November 1957.

Paper A-5

INFORMATION ON SOLAR PROTON EVENTS (PCA's) DEDUCED FROM RADIO OBSERVATIONS

D. K. Bailey
National Bureau of Standards, Boulder

Solar proton events (SPE's) are generally described (parochially) by ionospheric workers as polar-cap absorption events (PCA's) and (oddly) by cosmic-ray workers as solar cosmic-ray events. Ionospheric workers, using their traditional tool, the probing radio wave, in quite untraditional ways have been able to contribute in the last decade a considerable quantity of information about the nature and occurrence of these events. Moreover, the radio observations have been made continuously at fixed positions, whereas observations with particle detectors in balloons, rockets, and satellites are conspicuously lacking in continuity, either in space or time. Ground-based cosmic-ray monitors, while operating continuously, detect less than one-fifth of the events that are of interest in connection with the problem of radiation hazards in space.

The radio techniques do not observe directly the incoming protons, but rather observe the effects on the propagation of waves resulting from the abnormal ionization produced by the incoming protons in a height region from about balloon ceiling (30 km) to the E layer (110-120 km). This abnormal ionization is most important between about 45 and 85 km insofar as its influence on radio waves passing through it is concerned. Radio observations are capable of yielding quantitative information, not only about the onset and duration times of individual events but also, if carried on simultaneously at several suitably placed locations and with more than a single frequency, about departures from isotropy of the arriving protons and about the instantaneous spectrum and thus its time variation.

Until recently the radio techniques employed in the study of solar proton events have involved equipment that was designed for other purposes, and often only accidentally situated in favorable geographic positions. Thus one of the potentially most sensitive radio techniques, that of measuring phase and amplitude over short, high-latitude paths at low and very low frequencies, has scarcely been employed. On the other hand, because of great interest in the polar ionosphere and in auroral effects, there has been for many years, but especially during and since the IGY, an excellent network of high-latitude ionosondes and a fair network of fixed-frequency riometers. Some of the most valuable and certainly the most extensive and continuous observations have been obtained as a by-product of the desire of the USAF to have a communications system in the North Atlantic and Greenland region that would be immune to the aurorally associated polar blackouts. This system employing ionospheric-scatter propagation consists of five links, three of which have ionospheric midpoints inside the polar cap. The two remaining have ionospheric midpoints well outside the auroral zone but still in high latitudes. Continuous data, beginning in January, 1954, from several or all of the links of this system have been made available and have been analyzed for PCA events. Prior to January, 1954, similar

data exist from fewer links operating for the most part at higher and somewhat less sensitive frequencies. These earlier data extend the continuous period of study back to late 1951. Thus an entire solar cycle has been examined by the ionospheric-scatter technique.

The interpretation of this long series of ionospheric-scatter observations is continuing. It has been clarified by the simultaneous observations of certain of the more recent solar-proton events by riometers, and especially by particle detectors operated at high latitude at both balloon and rocket altitudes.

In order to assess and therefore to make sound decisions concerning the radiation hazard posed by solar-proton events, it is necessary to know their characteristics at the top of the polar atmosphere, or more generally in space at a distance from the earth such that the earth and its magnetic field no longer significantly affect the flux. Thus it is necessary to know:

1. The frequency of occurrence of solar proton events in relation to the solar cycle,

2. The statistics of occurrence of SPE's of different magnitudes described in terms of the evolution of their energy spectra from onset to the end of the period of detectability,

3. The statistics of the significant departures from nearly pure proton fluxes,

4. The statistics of departure from isotropy in space as indicated (a) at and near sunspot maximum, by differences in onset characteristics at different locations, and (b) at and near sunspot minimum, by evidence of impact zones and by evidence of much reduced "storage,"

5. The predictability of discrete events, and

6. The limitations on predictability.

The PCA observations by the ionospheric-scatter technique provide sound answers to (1) and partial answers to (2) and (4). They do not at present contribute much toward an answer to (3). Taken together with other solar observations they permit answers to (5) and (6). These latter answers, however, will perhaps not be well received. The nature of these various answers and partial answers will be described.

Paper A-6

STATISTICAL PREDICTION OF SOLAR PROTON EVENTS

James B. Weddell
North American Aviation, Inc., Downey, Calif.

Abstract

A method of correlating solar flares in time with several indices of activity of solar regions is described. The method determines the probability of occurrence of a flare if each of two indices exceeded given limits, and the average time between measurement of these indices and the outbreak of the flare. Significant correlations are listed; the most important is the tendency for major flares to occur in the second passage across the solar disk of regions exceeding 2000 millionths of the solar hemisphere in area, and which gave rise to small flares during their first passage. These criteria permit prediction of 69% of class 3 flares at least 14 days in advance. Flare positions have been correlated with the magnetic field in active regions. The field near the sites of flares tends to be frozen into the solar atmosphere to a greater extent than other portions of the field.

Introduction

The ability to predict the emission of energetic protons from the sun may eliminate or reduce the shielding requirements of manned space vehicles. If such prediction is to be useful, it must cover a time interval at least long enough for the crew to terminate their mission and return to earth after a warning of danger is made. The prediction method should seldom give false alarms which prevent space flights during periods free from solar proton events.

One present technique[1] uses sunspot penumbral areas to predict major solar flares, with which proton events are sometimes associated. This method permits flare prediction for only three days at a time. Another method[2], based on the areas and durations of calcium plage regions, gives five-day forecasts of "safe" periods during which no flares will occur. The areas and durations of many plage regions are such that safe periods cannot be forecast, although no flare actually occurs; the fraction of predicted safe time is thus greatly reduced near maxima of solar activity. Both of these methods are concerned only with observations made during a single rotation of the sun.

---

[1] K.A. Anderson, "Preliminary Study of Prediction Aspects of Solar Cosmic Ray Events," NASA Technical Note D-700, (April 1961).
[2] J.W. Evans, Private communication.

Correlation Method

We have developed a method of correlating the occurrence of flares with combinations of several indices of solar activity measured by arbitrary times before a flare. By simultaneously correlating several characteristics of a solar active region, we can more nearly identify the necessary and sufficient conditions for a major flare or proton event. By relating the times of occurrence of flares to the times of observation of the corresponding active regions during previous rotations of the sun, we open the possibility of predicting flares three weeks or more in advance.

Solar activity indices studied thus far include the area, central intensity, and duration of calcium plages, the duration of 200-Mcs and 3300 - Mcs radio noise emission from active regions[3], and the longitudinal component of the magnetic field in active regions. The area and duration of flares and their accompaniment by proton events have been considered. Published sources of data are listed as references[4-7].

To illustrate the correlation method by a hypothetical example, let A and B be two quantitative measures of active solar regions (e.g., the area of a plage region and its brightness temperature in 3300 - Mcs radio emission). Let a_1, a_2, ... , a_n be the magnitudes of A measured at times t_1, t_2, ..., t_n; let b_{n+1}, b_{n+2}, ..., b_{2n} be the magnitudes of B measured at times t_{n+1}, t_{n+2}, ..., t_{2n} . Some measurements of A and B may have been simultaneous. Let f_{2n+1}, f_{2n+2}, ..., f_{3n} be the magnitudes of some aspect of a flares (e.g., its area) measured at times t_{2n+1}, t_{2n+2}, ..., t_{3n}. We require:

$$t_{2n+K} > t_{n+K} \geqslant t_K,$$

$$1 \leqslant K \leqslant n.$$

The probabilities of the following events are calculated:

P(A,F): A is followed by a flare (i.e., in the region at which phenomenon A was observed).

P(B,F): B is followed by a flare.

$P(A \cap B,F)$: A is followed or accompanied by B, and B is then followed by a flare.

[3] G. Swarup, "Stanford Microwave Spectroheliograms for 1960 July," Stanford University, Stanford, Calif. (March 1962).

[4] "Compilations of Solar-Geophysical Data," Central Radio Propagation Laboratory, National Bureau of Standards, Boulder, Colo., (July 1957 to date, monthly).

[5] H.W. Dodson and E.R. Hedeman, "IGY Working List of Solar Flares," Mc Math-Hulbert Observatory, Pontiac, Mich., (1962).

[6] "Quarterly Bulletin on Solar Activity," Eidgenössiche Sternwarte, Zürich, Switzerland, (1917 - 1956).

[7] "Cartes Synoptiques de la Chromosphère Solaire et Catalogue de la Couche Superieure," Observatoire de Meudon, Paris, (1917 - 1956).

Lower limits a', b', and f' may be placed on a, b, and f. For example, the probability may be calculated that plages at least as large as 2000 millionths of the solar hemisphere have brightness temperatures at 3300 Mcs of at least 10^5 deg K, and that if so these regions are sites of flares at least as large as 10 sq deg.

Considering the j sets of observations for which $a_i \geq a'$, $b_{n+i} \geq b'$, $f_{zn+i} \geq f'$, the r.m.s. average time differences

$$\bar{t}_A = \left[\frac{1}{j} \sum_{i=1}^{j} (t_{2n+i} - t_i)^2 \right]^{\frac{1}{2}} , \qquad (2)$$

$$\bar{t}_B = \left[\frac{1}{j} \sum_{i=1}^{j} (t_{2n+i} - t_{n+i})^2 \right]^{\frac{1}{2}} , \qquad (3)$$

and the respective standard deviations

$$\sigma_A = \left[\frac{1}{j} \sum_{i=1}^{j} (t_{2n+i} - t_i - \bar{t}_A)^2 \right]^{\frac{1}{2}} , \qquad (4)$$

$$\sigma_B = \left[\frac{1}{j} \sum_{i=1}^{j} (t_{2n+i} - t_{n+i} - \bar{t}_B)^2 \right]^{\frac{1}{2}} \qquad (5)$$

are calculated. In our example, we find the r.m.s. average times between flares and the measurement of plage areas, and between flares and the measurements of radio brightness temperature, as well as the standard deviations of these times.

If $P(A \cap B, F) > 1/2$, $\bar{t}_A > 2\sigma_A$, and $\bar{t}_B > 2\sigma_B$, we consider that a statistically significant positive correlation exists, and that observations of A and B permit prediction of flares at least for time in advance.

Results

The following results have been obtained up to October 1962 on the basis of about 350 flares of class 2 and greater during 1958 through 1961:

1. The fraction of flares of class 2 and greater occurring at plages making at least the second passage across the disk was 0.67. The average time of the flare was 27 ± 4 days after the central meridian passage of the plage on the rotation previous to the flare.

2. The fraction of class 3 and 3+ flares occurring at plages making at least the second passage was 0.78.

3. The fraction of flares of class 2 and greater occuring at plages larger than 2000 millionths of the solar hemisphere was 0.91.

4. The fraction of flares of class 2 and greater occuring at plages which had been the sites of flares of any class during the previous rotation was 0.88.

Preliminary Prediction Method

If a plage region is the site of any flare during its first passage across the disk, and has an area of at least 2000 millionths of the solar hemisphere at its first central meridian passage, a warning of a major flare during the next rotation may be issued. This warning will include about 60% of flares of class 2 and greater, and 69% of class 3 and 3+ flares. Flares which occur by coincidence at other regions will increase the apparent accuracy of the warning.

The "false alarm" frequency of this prediction method has not been evaluated. The original warning covers the interval between the 21st and the 35th day after it is issued. When the active region reappears on the east limb of the sun on the 21st day following its first central meridian passage, the warning may be cancelled if either

(a) The plage area is smaller than 2000 millionths of the solar hemisphere, or

(b) the active region is free from sunspots.

Such cancellations reduce the effect of false alarms on the fraction of time during which space flight may be undertaken.

Relationship of Flares to Magnetic Field

The prediction method just tentatively proposed fails to predict a significant fraction — about 30% — of class 3 and 3+ flares. It may result in frequent false alarms, since some large active regions which are sites of flares during their first passage across the solar disk may not give rise to major flares during subsequent rotations. This method predicts flares rather than proton events, but it is known that some major flares are not associated with energetic protons near the earth. In order to overcome these limitations and to gain physical insight into the role of proton events in the total process of solar activity, we have begun a correlation of proton-event flares and other large flares with solar magnetic fields.

Solar magnetograms[8] obtained at Mount Wilson Observatory[9] were reproduced. The solar magnetograph measures the component of the magnetic field at the reversing layer in the observer's line of sight. Isogauss curves, or lines of constant magnetic field, were constructed from the magnetrograms. The position of a major flare associated with a given active region was translated in heliographic longitude to compensate for solar rotation between the time of occurrence of the flare and the time of measurement of the magnetic field.

---

[8]H.W. Babcock and H.D. Babcock, Publ. Astron. Soc. Pacific 71, 165 (1959).
[9]H.W. Babcock, Astrophys. J. 118, 387 (1953).

Figure 1 is a typical family of isogauss curves of a single active region. Two flares which occurred within a few days of the date of the magnetogram are shown; the crosses indicate the translated points at which the flares broke out, and the circles have areas equal to the maximum extent of the flares. It is not surprising that the points of outbreak of the flares lie very nearly on the line of zero longitudinal magnetic field. This is in accord with the observation of Severnyi[10] that flares break out beneath the highest points of dark filaments and loop prominences; these points correspond to zero radial magnetic field. Near the center of the solar disk, the radial and longitudinal components of the field are equivalent.

Figure 2 is the family of isogauss curves. Curves of the same region that was shown in Fig. 1, but measured during the previous solar rotation; this was the first passage of the region across the disk. The translated flare positions are also shown, and they again lie near the line of zero longitudinal magnetic field. This shows that the line of zero field in the vicinity of the flare sites is stationary relative to the material of the reversing layer. The other parts of the line of zero field, as well as the isogauss curves of non-zero field, exhibit marked displacement and distortion in the course of one solar rotation.

Let us list some alternative conditions which could cause parts of the line of zero field to be stationary in the ionized gaseous medium containing the field. An approximate condition for a magnetic field to be frozen into a plasma is that the magnetic Reynolds number[11]

$$R_m = \mu \sigma u L \gg 1 \qquad (6)$$

where μ is the magnetic permeability, σ is the electric charge density, u is the transport velocity of the plasma, and L is the length such that

$$\frac{F_m}{F_d} = \frac{JBL}{\rho u^2} \qquad (7)$$

In Eq. 7, F_m is the magnetic force exerted on the plasma, F_d is the dynamic force exerted on the plasma due to gravity, pressure gradients, and radiation pressure; J is the electric current density, induced in the plasma by its motion in the field, B is the magnetic field intensity, and ρ is the mass density of the plasma. Now

$$J = K \sigma u B \quad , \qquad (8)$$

where K is a constant, so

$$R_m = \frac{F_m \rho \mu u^2 K}{F_d B^2} \qquad (9)$$

Since the plasma is in approximate dynamic equilibrium near the flare sites, F_m and F_d are comparable in magnitude and their ratio varies slowly with position

[10] A.B. Severnyi, Soviet Astron. 1, 668 (1957).
[11] J.E. Drummond, "Plasma Physics," pp. 172-3 McGraw-Hill Book Co.,

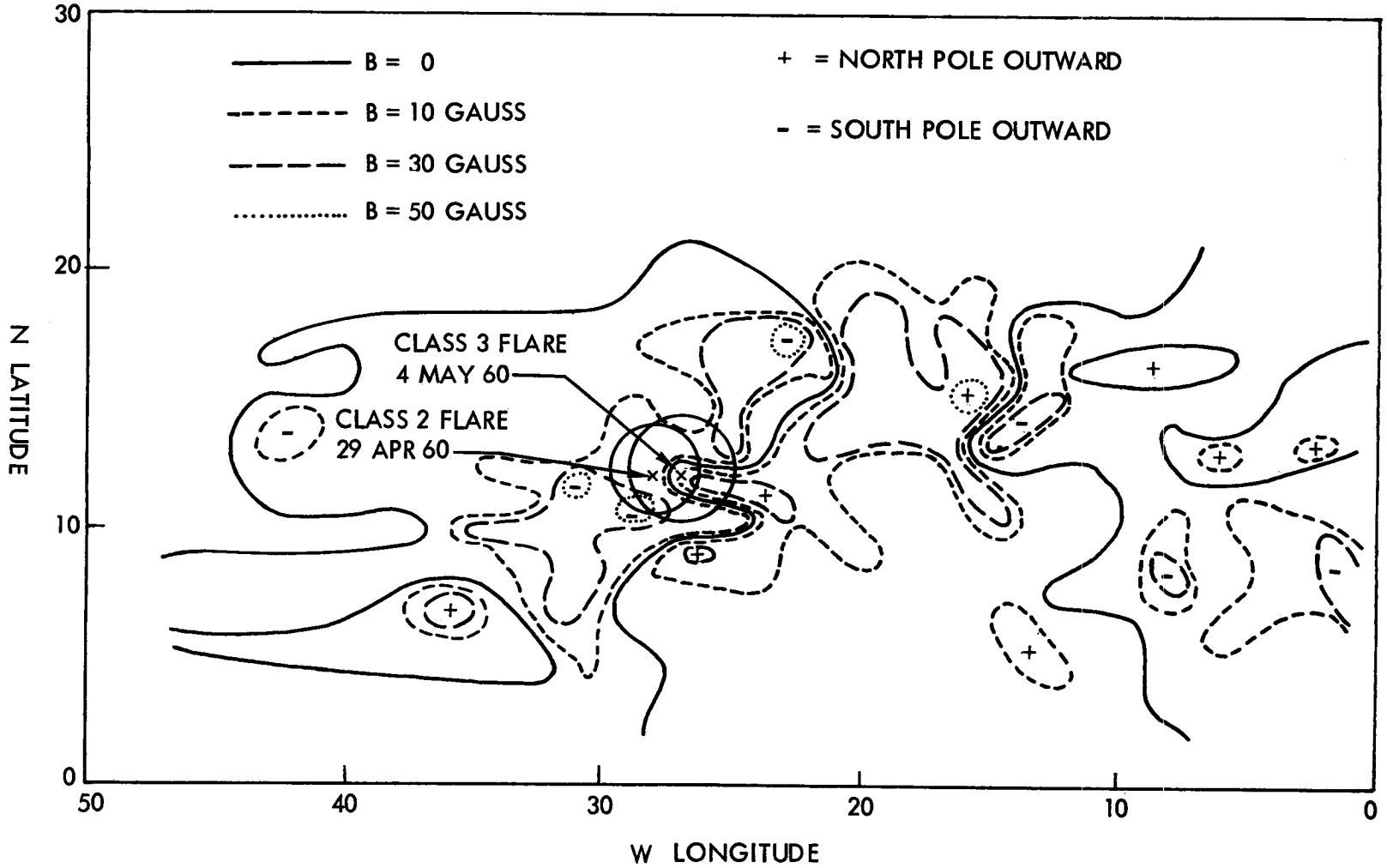

Figure 1. Isogauss Curves of McMath Region 5642. 29 April 1960

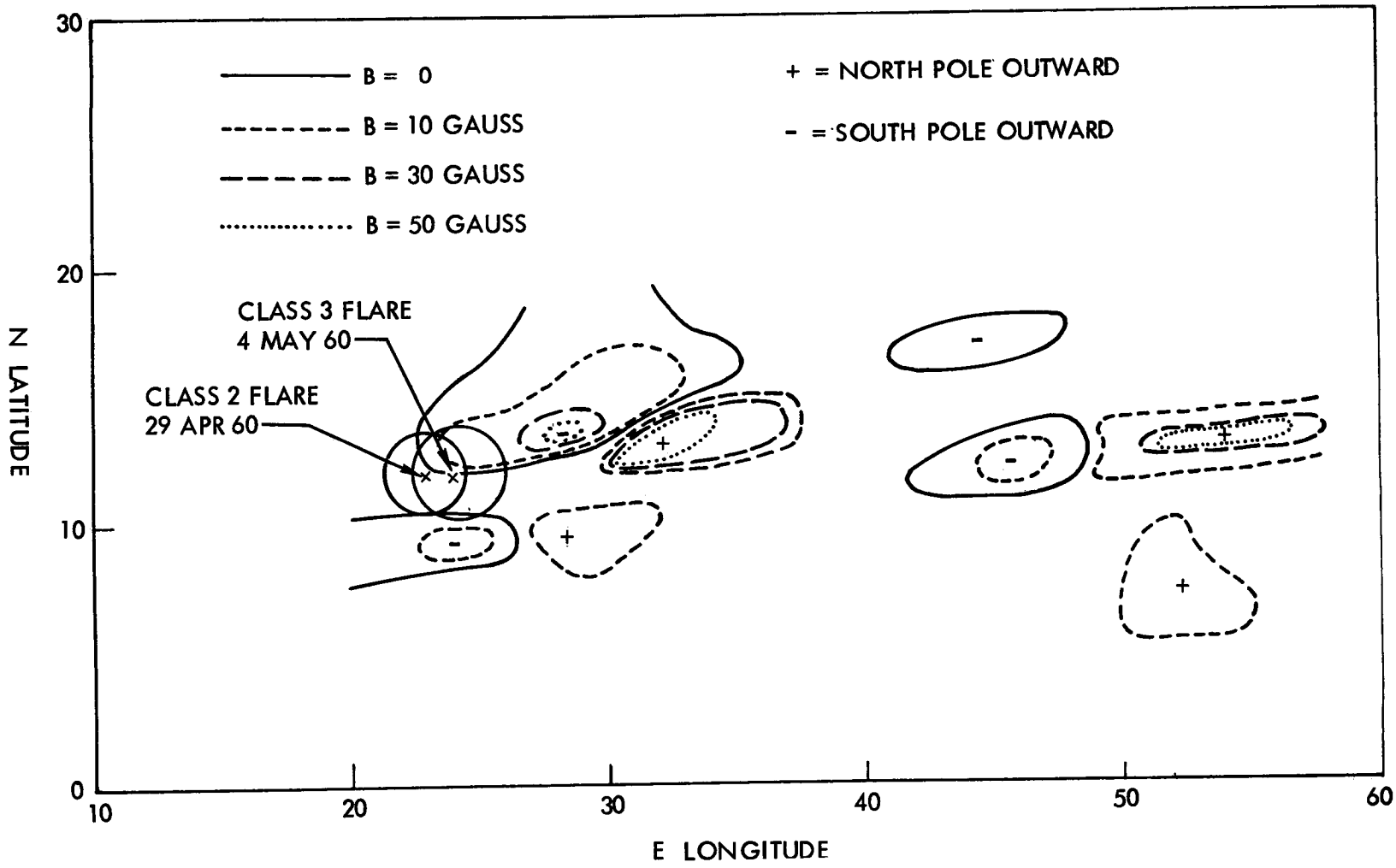

Figure 2. Isogauss Curves of McMath Region 5616, 29 March 1960

and time. If B is small, R_m is obviously large. But the total magnetic field is not necessarily small along lines where the longitudinal component of the field is zero. The transport velocity of the plasma is small, as evidenced by its rather steady participation in the rotation of the sun. The remaining way in which R_m can be large is for the plasma density ρ to be large.

Measurement of the transverse component of the magnetic field, or of the density in the reversing layer and lower chromosphere, would shed much light on this problem. Magnetograms of regions near the limb measure the component of the field tangential to the sun and in the line of sight. These magnetograms can be compared to those of the same region near the central meridian. If it is assumed that the field is essentially constant in magnitude and direction for 5 or 6 days, two of the three components of the field can be inferred.

It must be pointed out that the correlation of flare positions with magnetic field patterns does not yet include a statistically significant number of cases. The magnetic characteristics which are conducive to major flares or to proton events remain to be identified. The further study of magnetism in active solar regions is expected to improve the prediction of proton events and to increase our understanding of the behavior of the sun.

Acknowledgements

The author is indebted to Robert Howard of Mount Wilson Observatory, who made available the original magnetograms. He appreciates valuable discussions with Helen Dodson of Mc Math-Hulbert Observatory, and John W. Evans and Edward Dennison of Sacramento Peak Observatory.

Paper A-7

COMMENTS ON THE PRODUCTION OF SOLAR HIGH ENERGY PARTICLES

M. C. Chapman, R. E. Fortney, and M. R. Morrison
Northrop Space Laboratories

Abstract

A general qualitative model for the production of solar high-energy particles (SHEP) which can explain several observed flare phenomena is used in the analysis of a specific flare event. The model, incorporating the work of several Russians and Americans, explains the occurrence of solar radio emission,the initial anisotropic and later isotropic distribution of flare particles, Forbush decreases in cosmic ray intensity, decreases in cosmic radio noise, and fluctuations in the earth's magnetic field due to solar flare particles. Also qualitatively explained are such phenomena as the occurrence of shock waves during flare events, observed surges in the active region, and movement of magnetic "bumps" before the start of the flare. The model may be briefly described as follows: magnetic fields in active region contain "bumps" which move toward nodal points in the field. A conversion of energy can occur by the annihilation of magnetic fields and the contraction of the conducting medium. This contraction results in a shock wave which propagates opposite to the flow of gas. High temperatures behind the shock wave allow thermonuclear reactions to occur, producing particles which are further accelerated by the moving magnetic walls. The plasma between the magnetic walls is expelled perpendicular to the compression and carries "frozen-in" fields with it into the upper chromosphere or corona. This extended field-plasma-particle region constitutes the magnetic trap above the region from which it was generated, and determines the spectra of particles leaking from it. Energetic particles accelerated by the shock fronts fill the region and cause it to expand with an increase of energy; however, the high energy particles are not easily trapped and can escape, decreasing the energy and causing the trap to contract. This contraction will lead to further acceleration of the remaining particles. The non-equilibrium fluctuation will continue until particle diffusion does not change the energy sufficiently to cause large scale variations in

15122

pressures. The initial ejection of the high energy particles could occur in fast bursts, after which the trapping region would assume a quasi-equilibrium configuration; a slower diffusion of less energetic particles will now occur. The trap, situated in the magnetic fields of the active region, is carried out into space by the solar corpuscular streams; as the region moves outward the volume increases (perhaps eventually encompassing the earth) and the field strength decreases, so that the trapping effectiveness is reduced and the particles escape easily into the stream.

Introduction

In commenting on the production of high energy particles from the sun, one is led to a reverse analogy using the case of particle accelerators here on earth. The accelerators were developed over a period of years and are well understood, while the particles emerging from the beam target are still being investigated. In the case of solar flares we have information on the particles from the beam after it strikes the target (the earth), however, the method of accelerating these particles is still not well understood.

This paper will present a model for the production of high energy particles from flares on the sun, and using published experimental data, will show the consistency of the model with observations.

Sections will be devoted to background information on solar physics, production of SHEP (solar high energy particles), and experimental verification.

Background

A brief discussion of the sun is now presented as background information on the environment in which flares occur.

It is convenient to divide the sun into four concentric regions with more or less well-defined properties (Figure 1); [1] these are the interior, the photosphere, the chromosphere, and the corona. The interior may be

---

1. Goldberg, L., "The Sun," Science in Space, Chap.VI, National Academy of Sciences - National Research Council, Washington, D.C., 1960.

subdivided further into (a) a core, in which radiant energy is produced by thermonuclear reactions, predominantly near the center, and through which it travels by radiative transfer toward the outside; and (b) a convective layer which extends to just below the visible exterior and is probably no more than 1/5 the radius thick. The temperature, pressure, and density decline through the interior from extremely high values at the center to relatively low values at the visible surface.

The photosphere is the apparent surface from which practically all optical radiation comes. The radiation contains contributions from many different layers, but its intensity is approximately equal to that radiated by the gas at an optical depth of one. At one A.U. a layer of unit optical depth seen edge-on subtends less than 1" of arc, and therefore appears sharp. The continuous spectrum of this radiation is a mean of near black-body radiation whose temperature ranges from perhaps 4500°K to 7500°K; the resulting blended spectrum resembles that of a black body near 6000°K at the center of the disk, while near the limb, along oblique lines of sight where the contribution of the deeper, hotter layers is proportionately less, the continuous spectrum corresponds to a lower temperature. The effective temperature which most nearly matches the continuous spectrum of sunlight integrated over the whole visible disk is about 5750°K.

The photosphere appears to be mottled with small areas slightly hotter and brighter than their surroundings and having a mean lifetime of several minutes. These granules appear to be regions where currents emerge with upward velocities of the order of 1 km/sec. The photosphere also is the region where sunspots and faculae are located.

The chromosphere is a thin transition region lying between the relatively cool outer layers of the photosphere and the million-degree corona. It is extremely inhomogeneous, and small volumes are far from being in a steady state. The normal structure of the chromosphere consists of fairly closely packed spicules - small jet-like prominences with lifetimes of the order of several minutes and upward velocities of the order of 20 km/sec - whose tops reach a height of roughly 10,000 km. The appearance of the chromosphere in the light of H-α has been compared to a prairie fire. There is little uniformity of opinion for a model of the chromosphere except perhaps on the following: the region below 6000 km is complex and inhomogeneous, probably comprising cells of high and low temperature, perhaps as different as 30,000° and 4000°; in the upper chromosphere the temperature rises steadily and rapidly to several hundred thousand degrees at the base of the corona. There is no sharp division between the top of the chromosphere and the base of the corona

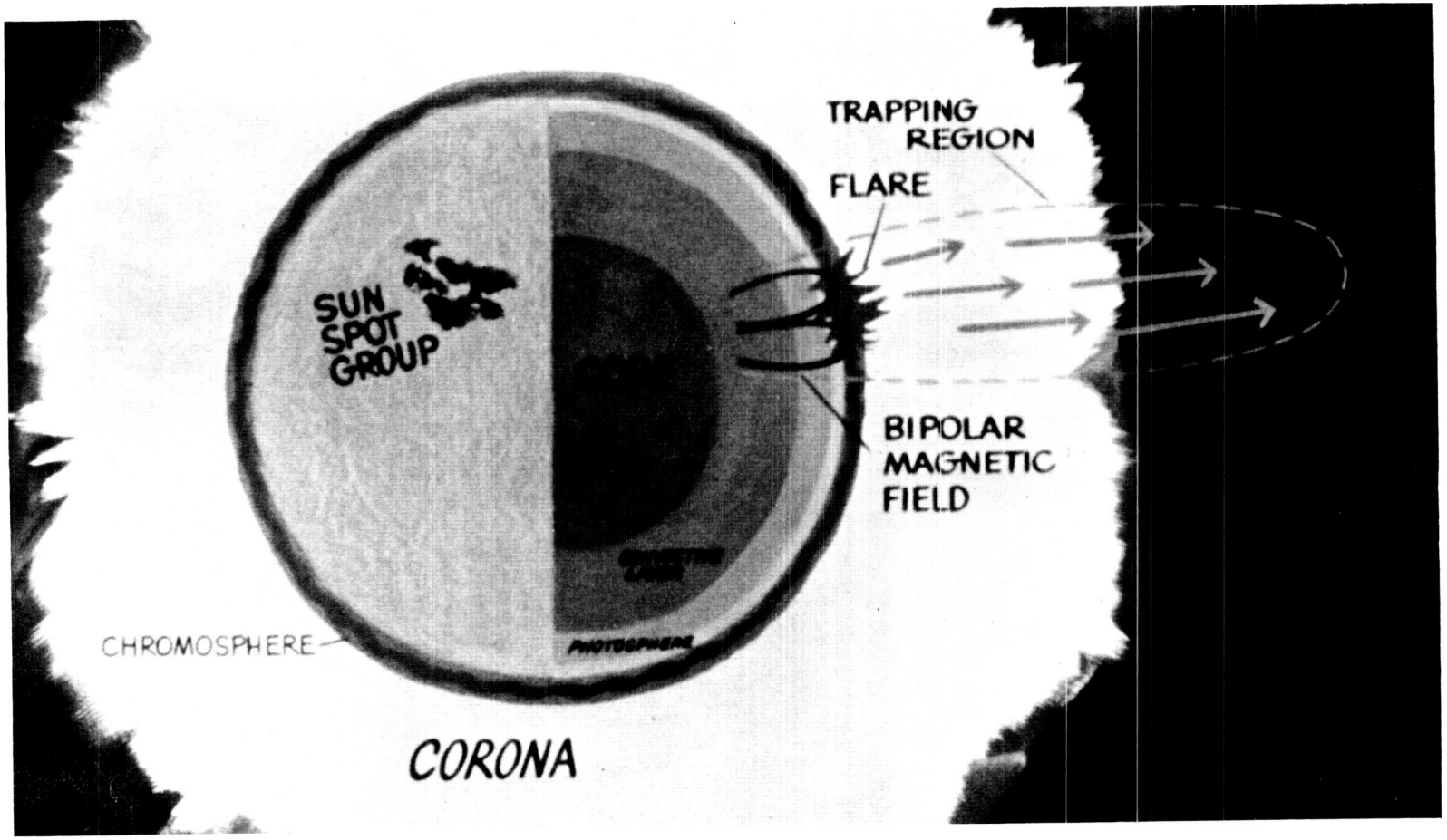

Figure 1. Structure of the Sun

since the tops of spicules sometimes project into the corona. Types of activity associated most closely with the chromosphere are flares, plages, and prominences.

The corona is the very tenuous outer atmosphere of the sun, which can be traced out into space for a distance of several solar radii. The intensity of coronal light is approximately 10^{-6} of the total sunlight, and most of this is continuous radiation from the photosphere scattered by electrons of the corona. Most of the sun's x-radiation originates in the corona and in certain active regions of the chromosphere. The kinetic temperature of the corona is of the order of $10^{6}{}^{o}$K.

The corona exhibits a considerable amount of both regular and irregular structure. The regular structure goes through a cycle in phase with the 11-year activity cycle, such that at sunspot minimum the corona shows broad extensions above the equatorial region and fine striated streamers fanning out from each pole, while at sunspot maximum the structure is more nearly the same over equator and pole, with polar streamers less pronounced. The corona also shows localized inhomogeneities, such as regions of greater radio opacity, and "hot spots" over regions of obvious activity in the chromosphere.

The sun's magnetic field can be approximated as an axisymmetric dipole field with a mean intensity in the photosphere of the order of 1-2 gauss. The field is assumed to be generally radial at the orbit of the earth, but at a distance somewhere between the orbits of Mars and Jupiter, it is assumed to become disordered from spiralling due to the sun's rotation.

All internal lines of force are assumed to lie in a relatively thin submerged layer at a depth of the order of 0.1 R that stretches between $\pm$ 55^{o} latitude. H. W. Babcock[2] has shown how the magnetic lines of force are twisted due to the sun's rotation and then are floated to the surface of the photosphere and emerge as bipolar magnetic regions. These regions are associated with sunspots and may exist in varying forms of complexity. Therefore the sunspots themselves are classified according to these magnetic fields: α = unipolar, β = bipolar, γ = complex, and $\beta\gamma$ = semicomplex. The following is a qualitative description of the four basic spot types.

α : Unipolar groups are single spots or groups of spots having the same magnetic polarity.

β : Bipolar groups in their simplest form consist of two spots of opposite polarity. Often the bipolar group is a stream of spots.

---

2. Babcock, H. W., "The Topology of the Sun's Magnetic Field and the 22-Year Cycle," Mount Wilson and Palomar Observatories, Carnegie Institute of Washington, California Institute of Technology, 1960.

$\beta\gamma$: Semicomplex groups have bipolar characteristics, but no clearly marked dividing line between the spots of opposite polarity

γ : Complex groups have polarities so irregularly distributed that they cannot be classified as bipolar; sharply bounded regions of opposite polarity sometimes exist within the same penumbra.

The sunspots and their associated magnetic fields furnish the environment for the catastrophic disturbances known as solar flares. The flare occurs usually with a sudden onset near the neutral point (boundary) between two opposing spot-connected fields where the local field intensity is close to zero.[3] The region occupied by the flare expands during the lifetime of the flare ($\simeq 10^3$ sec), with velocities of several km/sec, and may attain linear dimensions of 10^{10} cm, and it is assumed that the depth of the region is of the order of 5×10^8 cm. Thus, a flare volume may be $V \approx 5 \times 10^{28}$ cm^3.

The energy radiated by the flare may best be described in the following breakdown:

- The visible radiation has been observed to be of the order of magnitude of $10^{27} - 10^{28}$ ergs.
- The energy of X-radiation has been observed to be also $\approx 10^{27} - 10^{28}$ ergs.
- The energy carried away by SHEP's is approximately $10^{31} - 10^{32}$ ergs.
- The energy release from decreases in magnetic field gradients in the flare region is roughly $10^{27} - 10^{28}$ ergs.
- The thermal energy is of the order of $10^{27} - 10^{28}$ ergs.

---

3. Chapman, M. C., and Morrison, M. R., A Summary of Natural Particulate Radiation in Space, ASD-TDR-62-606, p. 35 (1962).

A short development of solar flare phenomena as seen from the earth, would be as follows (Fig. 2).[4] The flare is observed usually at time 1 hour to emit light in the optical, ultraviolet, and X-ray regions of the electromagnetic spectrum (Profile 1). These emissions rise rapidly to a peak and then die off within a few hours. At the same time, bursts of high frequency radio emission are observed (Profile 2), exhibiting approximately the same rise and decay profile as the optical emissions. Low frequency emissions (Profile 3) also occur in burst form and with a total intensity rise time similar to the previous effects, but the maximum of the profile is longer and the decay in time is slower, persisting for as long as 12 hours.

Solar high energy particles (SHEP) are observed to arrive over the poles of the earth some time after the electromagnetic observations of the flare event, this delay being due to propagation times greater than that required for electromagnetic radiation. The SHEP intensity (Profile 4) is observed to have a sharp rise time with irregular fluctuations near the maximum, and then to decay slowly with time; the effects still being observed for periods as long as days.

Profile 7 shows that the earth's magnetic field is undisturbed by the previously discussed effects (Profiles 1 through 4). However, at some time which may be 24 hours after the observed flare, the geomagnetic field suffers violent fluctuations. This effect is due to a solar plasma of low energy charged particles (protons and electrons) colliding with the earth's field, and causing it to contract, deform and spring back. The effect of the perturbed geomagnetic field on SHEP arrival is indicated in Profile 4. The structure observed at times 30 through 38 hours depicts the arrival of SHEP over regions on the earth at low latitudes, where they were previously forbidden due to the geomagnetic cutoff of the particles.

The galactic cosmic ray intensity (Profile 5) follows the same general form as does the earth's magnetic field. The decrease in cosmic ray intensity is caused by the particles being deflected by magnetic fields "frozen" in the solar plasma. Thus, when the solar plasma has reached the earth's field and perturbed it, many of the galactic cosmic rays in the vicinity of the earth cannot penetrate both the plasma and the field, and the previously observed intensity decreases. As the solar plasma passes the earth, both the geomagnetic field and the cosmic ray intensity recover and approach normal levels.

The cosmic radio noise (Profile 6) is affected by arrival of three emissions from the sun, i.e., ultraviolet and X-rays, SHEP, and solar plasma. Since these radio emissions must penetrate the ionosphere, the conditions there greatly influence their propagation. Coincident with the

---

4. Ibid., p. 32-35.

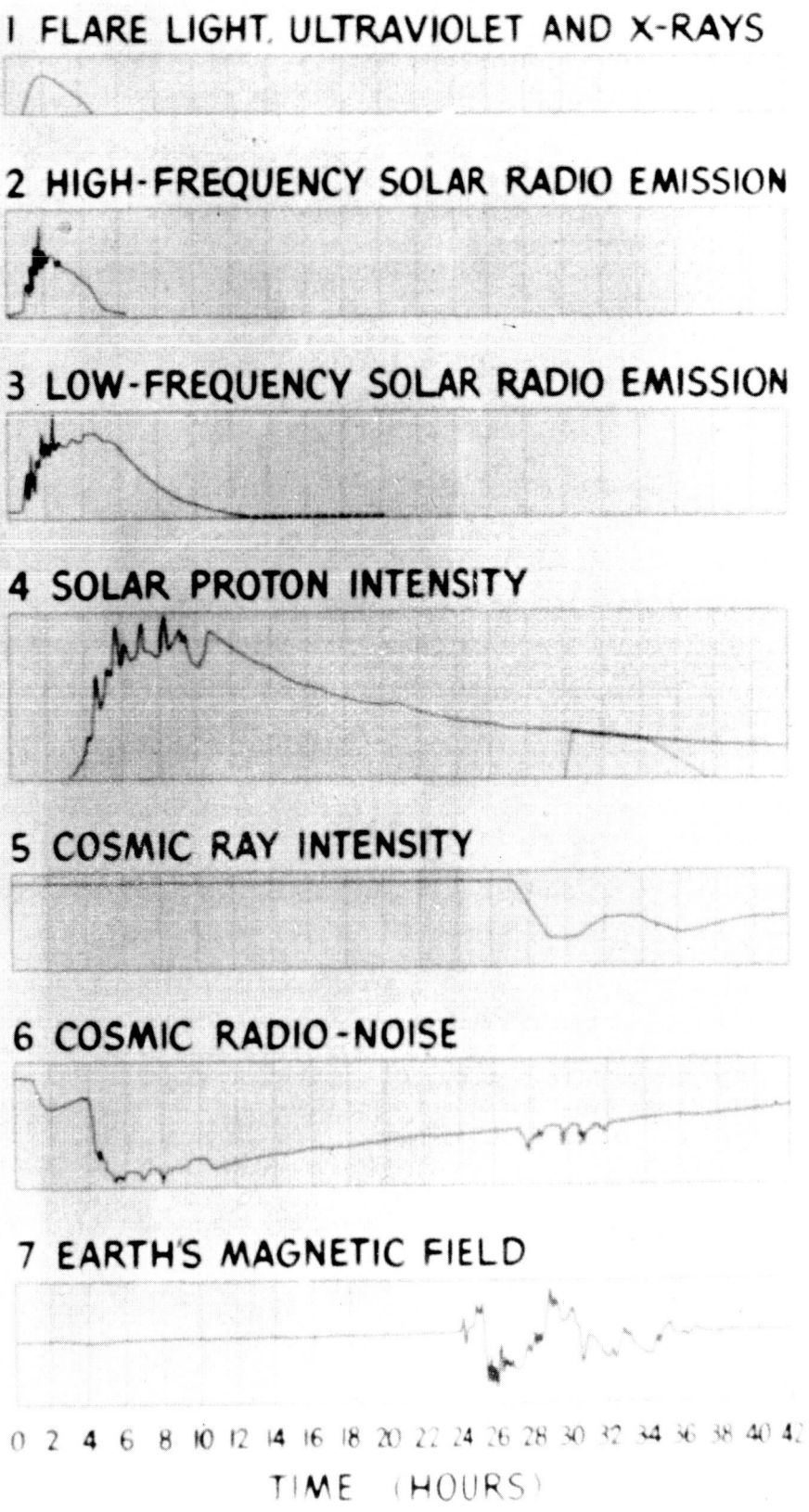

Figure 2. Development of a Solar Flare Event

emission of X-rays from the sun (allowing for a time of flight to the earth of 8 minutes), the reception of cosmic radio noise is decreased (times 1 through 4 hours). This is due to the increase in ionization in the ionosphere caused by the solar ultraviolet and X-rays, making it more opaque to transmission of the radio signals. This opacity is further increased by the arrival of the SHEP (times 4 through 24 hours) which produce additional ionization. The fine structure fluctuations in the recovery of the radio noise reception (times 27 through 32 hours) is due to the solar plasma disturbing the field and allowing additional particles to be dumped into the ionosphere, producing more ionization and thus increased opacity.

It can be seen that solar flare events produce varied geophysical phenomena and greatly influence the space environment, and with the advent of space exploration, flares are being studied with increased interest due to the radiation hazard they present to both manned and unmanned space flight.

SHEP Production Model

A. Energy Conversion

The flare event has its "roots" deep in the photosphere, actually occurs in the chromosphere, and extends into the corona. The flare processes that occur in the photosphere are not well known; however, it is thought that either ring currents are generated which rise into the chromosphere, or mutual destruction of magnetic fields leads to the observed chromospheric effects. The result of either of these two processes is a change in the configuration of chromospheric magnetic fields. Obviously, emergence of ring currents will produce this effect. However, the self-destruction of fields is a very attractive hypothesis, and could occur in the following manner.[5] Two tubes of a magnetic field could combine under favorable conditions, resulting in a destruction of a part of the field. These conditions require that two tubes collide such that the transverse components of the fields are parallel, and the longitudinal components antiparallel. If the gas conditions are favorable for field diffusion, i.e., low temperature and ionization, then the "inner" transverse field would diffuse and result in a decrease of the magnetic pressure in the gas, which would then contract due to the greater "external" magnetic field pressure. If this process were to occur in the chromosphere where the gas density is low and the internal field pressure is a large part of the total internal pressure, the destruction of this field would allow contraction and heating of the region. This heating would increase the conductivity and thus inhibit the magnetic field diffusion. This restriction does not occur in the photosphere, where the particle density is high and thus the internal thermal energy is greater than the internal field energy. These fields are relatively free to diffuse, and large contractions of the region will not result. However, since the chromospheric fields are rooted in this region, a relatively small

---

5. Shabanskii, V. P. "On the Origin and Evolution of Solar Flares and the Generation of Cosmic Rays in Them," Soviet Astronomy - AJ, Vol. 5, No. 5, March-April 1962.

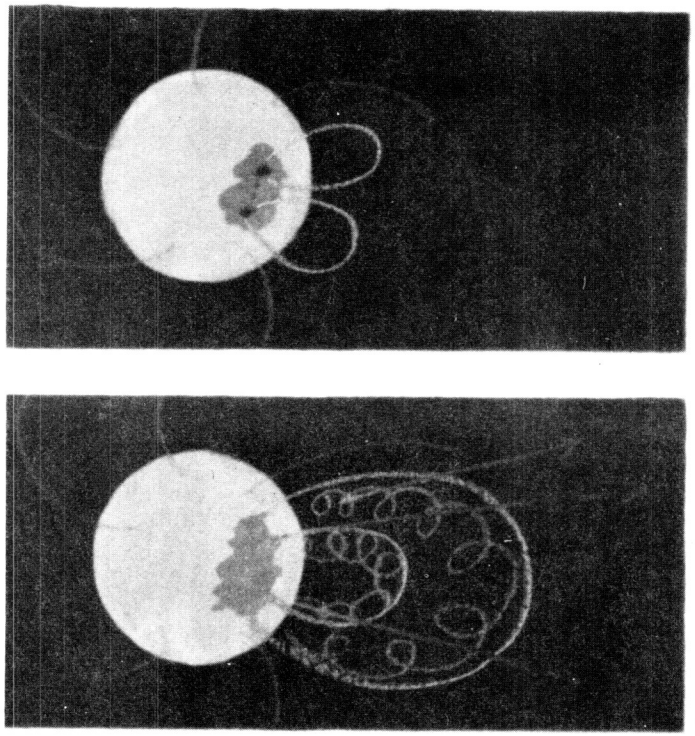

Figure 3. SHEP Production Model

change in magnetic field in the photosphere will induce a change in the chromospheric field, and due to lower gas densities, significant contraction of a region can be produced.

The protrusion of the flux tubes into the chromosphere results in sunspot magnetic fields of different polarities. The complexity of these fields results in several maxima and neutral points in the region. The plasma near a neutral point is in an unstable condition, the gradient of the magnetic pressure will tend to compress the region, and the region resists this compression by the gas pressure.

If the field gradient is high initially, then the compression forces increase more rapidly than the opposing gas pressure, and the pinch effect can occur.[6] However, before the compression proceeds very far, shock waves can be produced on either side of the neutral plane. Pressure discontinuities behind the shock waves, which propagate toward each other, tend to retard the compression. As the shock wave passes, the plasma expands behind it, leading to an increase in the flare area. The shock waves collide and are reflected; in collision, impulsive heating results in temperatures of 10^7 ^oK, which can sustain thermonuclear reactions. The chromospheric region normally exhibits temperatures of $\lesssim 10^4$ ^oK, and densities of $\sim 10^{13}$ cm^{-3}, as opposed to the photosphere where temperatures are lower and densities higher ($\sim 10^{17}$ cm^{-3}). The flare may last $> 10^3$ seconds, and have expansion velocities of 10^3 km sec^{-1}. The initial magnetic fields diffuse and are dispersed during this process, leading to different distributions after a flare.

The heated region where thermonuclear reactions can occur supplies the injection source for high energy particle accelerations. The reactions produce helium nuclei and protons with energies of $\sim$4 Mev and $\sim$3 - 14 Mev, respectively. It is necessary that the majority of the particles to be accelerated be injected with some sufficiently high initial energy, since the particle undergoing accelerations must gain energy in the face of retarding, or loss, mechanisms. The plasma (or gases) in the chromosphere and corona of the sun are sufficiently dense so that an accelerated particle loses energy through an "ionization" process in traversing them. Since ionization loss is a decreasing function of increasing particle energy, a low energy particle may suffer such great ionization losses that the acceleration process may never dominate. The rate of energy gain of a particle from acceleration processes rises approximately log linearly with particle energy, whereas the ionization loss decreases according to a power law. Thus, if a particle is injected with an energy greater than the intersection of these curves, it will always experience a net gain in energy. Also, it is true that, for equal charge, a particle of sufficiently greater mass can experience a net acceleration gain without injection, since the energy loss curve will be shifted toward higher energies.

---

6. Severnyi, A. B., "Nonstationary Processes in Solar Flares as a Manifestation of the Pinch Effect."

The accelerations occur when a particle is reflected between magnetohydrodynamic shock waves converging toward a neutral point. The particle will then be accelerated by successive reflections until it escapes the system. This mechanism could lead to a 100% increase in the energy of a relativistic particle in approximately 50 collisions if the front has a velocity of 10^3 km sec^{-1}.[7]

The plasma contained by the moving magnetic "walls" is not only compressed, but is also ejected from the region transverse to the motion of the walls. The plasma is "squeezed" both out of the region into the corona, and into the deeper parts of the sun. The outward streaming plasma carries with it energetic particles and frozen magnetic fields, and rises into the magnetic field region above the seat of the flare in the sunspot.

B. Trapping Region

The fields above sunspot groups during flares reach values of hundreds of gauss; thus, the expelled plasma and energetic particles push out into this field, forming a trapping region. Calculations of particle radii of curvature show that this region has sufficient field strength to trap Bev particles. The pressure of the expelled plasma causes the region to swell and extend outward from the sun. However, the very high energy particles do not remain trapped, but leak out of the trap. This then decreases the internal energy, and the region contracts. The contraction leads to additional acceleration of the remaining particles, of which the higher energies readily escape. Thus the region experiences a fluctuation until the energy of the remaining particles falls to a value such that they do not escape readily. If a rough dipole form is assumed for the trapping field, then the diffusion of particles out of this can be shown to be of the form

$$W_D = \frac{\nabla H}{H} \quad \frac{\beta^2 c^2}{W}$$

where W is the gyro frequency of the particles.

It has been shown that the energy spectrum of the particles can be calculated from a method similar to that used in galactic cosmic ray investigations.[5] The differential energy spectrum of the escaped particles is of the form $N(E) = CE^{-\alpha}$, where α has been calculated to be ≈ 3.5 for early stages of a flare. However, as the fluctuations cease, the lower energy particles will show a different spectrum due to perturbations from surrounding low strength fields. The trapping region now continues to push out against the sunspot field, with particles leaking out, and thus

7. Ginzburg, V. L., "Cosmic Rays on the Earth and In the Universe," Soviet Physics Uspekhi, Vol. 4, No. 4, January-February, 1962.

SHEP PRODUCTION

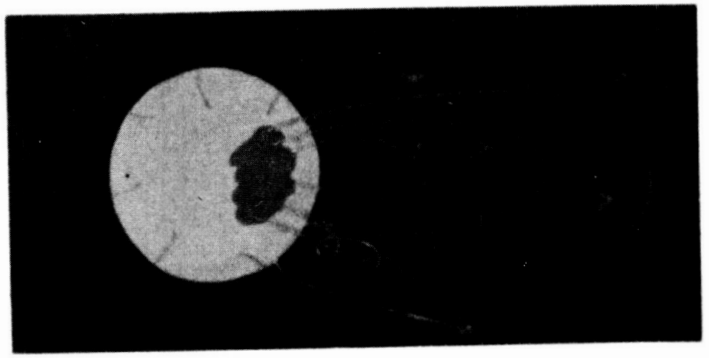

QUASI-EQUILIBRIUM TRAPPING REGION WITH START OF SLOW DIFFUSION OF PARTICLES OUT OF TRAP. EXTENSION OF TRAPPING REGION INTO RADIAL FIELD LEADING TO ISOTROPIC DISTRIBUTION OF LEAKAGE PARTICLES

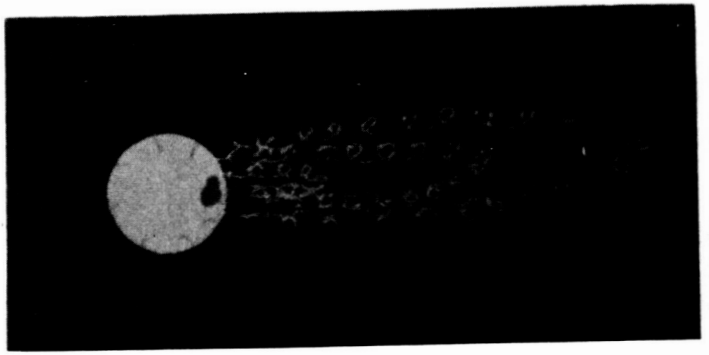

TRAPPING REGION EXTENDING TO THE ORBIT OF THE EARTH GIVING ISOTROPIC DISTRIBUTION OF PARTICLES. MAGNETIC FIELDS OF TRAP NOW AFFECT INTERPLANETARY CONDITIONS FOR FURTHER FLARE EVENTS.

Figure 4. SHEP Production Model

the internal energy decreases (assuming the source has ceased). However, the volume contained by the fields (which are still rooted in the photosphere) has increased, and thus the trapping effectiveness decreases as the field strength decreases.

Particles in the Mev energy range could be trapped for significant lengths of time, during which they lose energy through collision losses in the plasma. The rate of change of velocity for fast protons in hydrogen plasma can be expressed as a function of the plasma density and temperature. A lifetime for a high energy particle, defined as the time required for the particle to lose one-half of its energy, can be obtained from this expression, and is given as [8]

$$t_{\frac{1}{2}} = 0.64\, v^3\, mM \left\{ 12\,\pi e^4 N \ln \frac{2mv^2}{e^2} \left(\frac{kT}{4\pi N e^2} \right)^{\frac{1}{2}} \right\}$$

where N,T are the plasma density, temperature; m and M are the electron and proton masses, and v is the particle velocity. If the particle velocity is equal to, or less than, the average velocity of the plasma electrons, then v should be replaced by v_e. At a density of 10^7 cm^{-3}, and temperature of 10^5 K, the lifetime of a 10 Mev proton is approximately 41 hours. Thus the concept of a trapping region which contains energetic particles and allows them to leak out in time is consistent with particle energy lifetimes in the coronal regions.

The trap is expanded into the corona and space by the pressure of the energetic particles within the region. This region continues to propagate through space, loosely guided by the radial field of the sun, or perhaps flowing along a path swept out by a previous event. Thus, west limb flare particles usually reach the earth sooner than do those from east limb flares; in fact, it is difficult for east limb flares to produce significant radiation at the earth. Since the velocity of propagation of the region is dependent upon the internal pressure (as well as the field), the delay time of magnetic storm onset at the earth is related to the number of high energy particles produced.

The early stages of the flare event, which produce the initial high energy particles and "squeeze" out the plasma from between the moving magnetic walls, could lead to an initial anisotropic distribution of high energy particles. These particles, if of very high energy, could penetrate the magnetic trap relatively easily, and escape into space to be loosely guided by the general radial field. As the event progresses, the higher energy particles are lost and the region expands, with the lower energy particles escaping after many deflections. Thus the initial high energy particle anisotropy should decay into low energy isotropy. The

---

8. Fireman, E. L., "Density of the Solar Flare Plasma," Smithsonian Astrophysical Observatory, (Private Communication).

balance of this anisotropic - isotropic stage should be a function of the energy of particles produced, the configuration and strength of the magnetic trap and the frozen-in fields, and the perturbations due to irregularities in the interplanetary field. The front of this extended trapping region could eventually reach the earth, resulting in a Forbush decrease of galactic cosmic rays, and the onset of a magnetic storm. At this time, due to the energy dependence of the diffusion of the particles out of the region, the trap should contain a preponderance of low energy particles.

Experimental Verification

Observations pertinent to verification of the model will be discussed in this section. The model predicts that the delay in arrival of the SHEP will differ from that of direct propagation due to trapping in the region above the flare. Thus, the flux-energy spectrum should charge in time as the particles escape from the trap. Evidence for this phenomenon is presented in Figure 5, which shows the data of Bryant.[9] The first particles to arrive are of high energy and low intensity; as the event progresses the spectrum changes, becoming more intense and steeped to low energies. Variations in the specific spectra can be expected for various flare events; however, the general feature of a buildup in flux and steepness of spectra should hold. It should be noted that portions of the spectra might not be observed for an event, such as perhaps an east limb flare, if propagation conditions are such that the particles are guided past the earth at one time, whereas the earth might move into their path at another time during the event. The shift of the intensity maxima to lower energies is shown in Figure 6 for the flare of 28 September 1961. The maxima are seen to shift to lower energies as time increases. The time integrated differential flux-energy spectra, normalized to 1 proton/cm^2 steradian with energy greater than 100 Mev is shown in Figure 7 for the flare of 28 September 1961. This curve can be approximated by a power law of the form

$$N(E) = CE^{-\alpha}$$

where α has been observed to change for various events. However, this is of the form that one would expect from considerations of the flare accelerations and trapping region.

---

9. Bryant, D. A., et al., "Solar Cosmic Rays Following the Flare of September 28, 1961," Paper at American Geophysical Union Meeting, Washington, D.C., (April 1962).

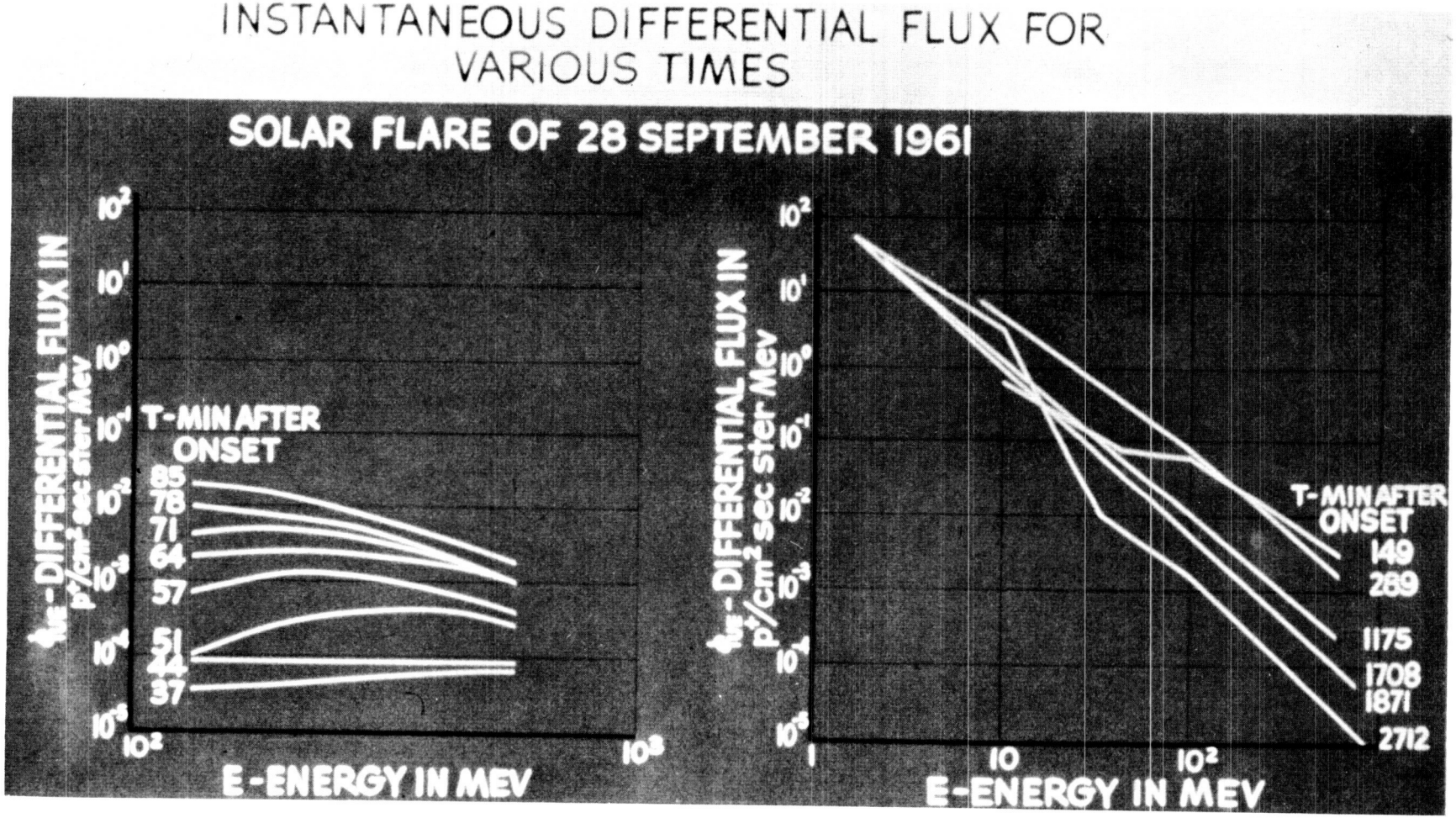

Figure 5. Solar Flare Flux - Energy Spectra

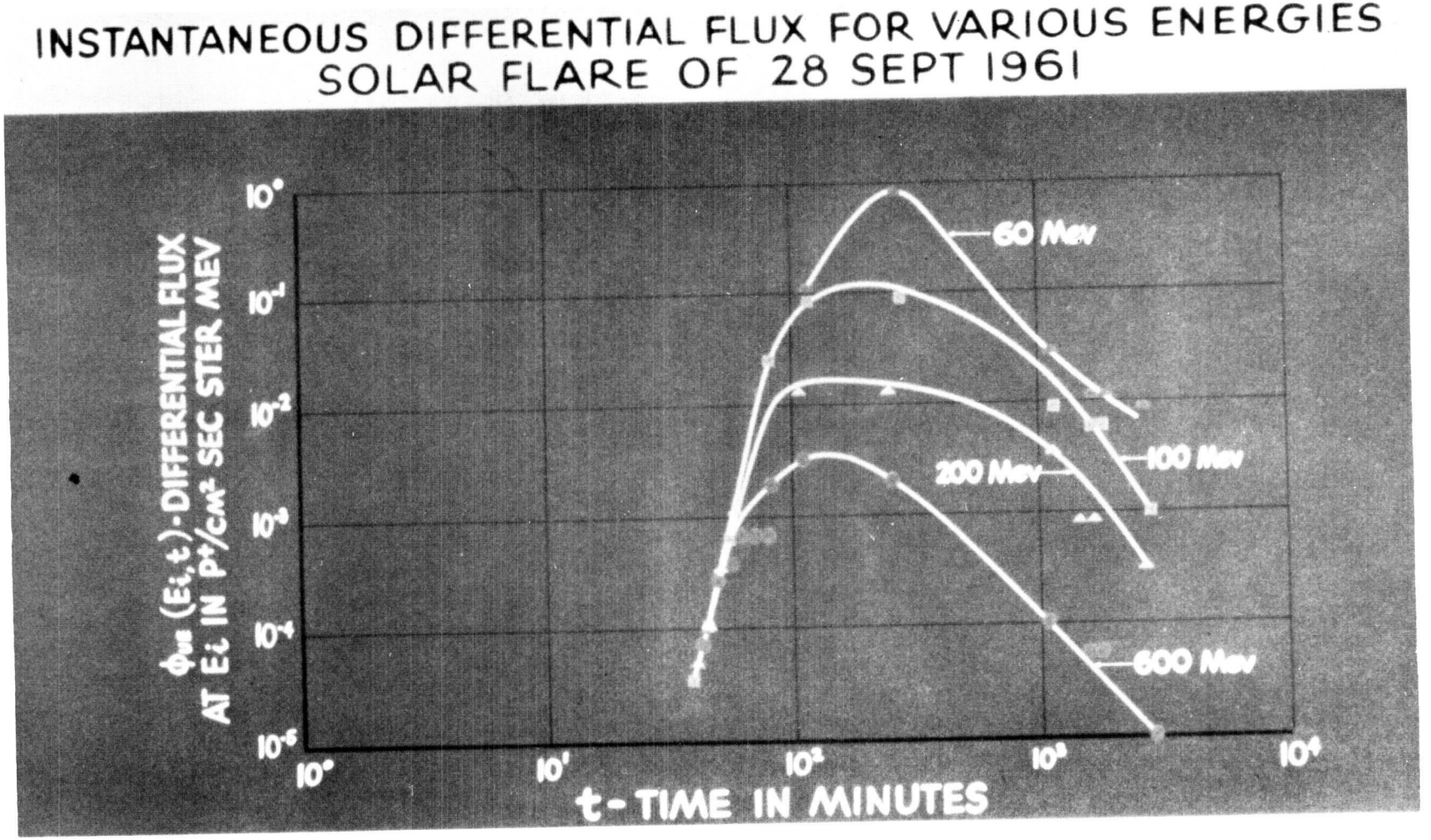

Figure 6. Solar Flare Intensity Maximum

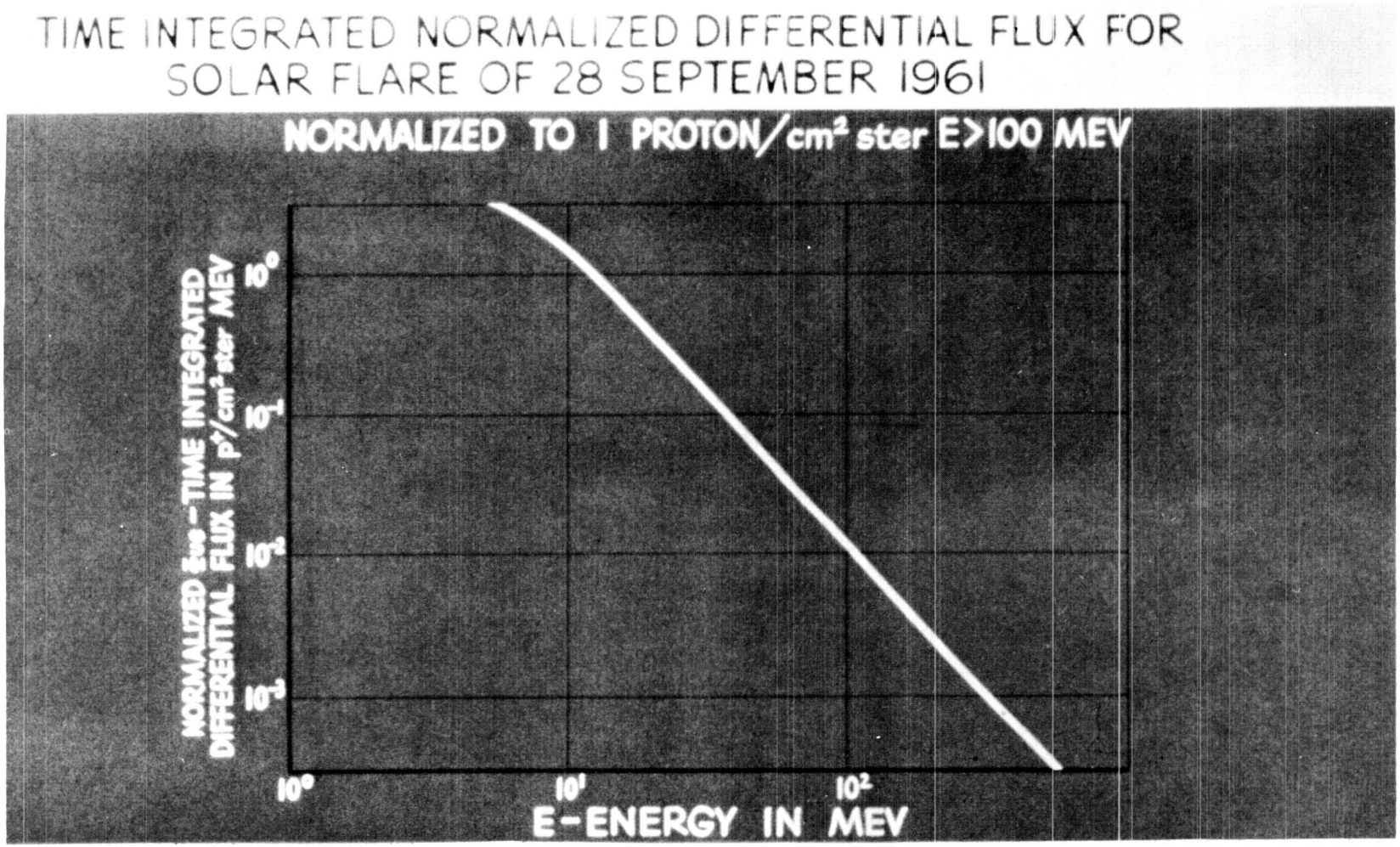

Figure 7. Time Integrated Solar Flare Spectrum

Much work has been done with radio astronomy and the radio noise from the sun has been classified into types. Some of these types have been found to correspond to radiations from particles in the chromosphere and corona can be correlated with flare events.

The following table lists the types of radio noise and the particle radiations that are believed to cause the noise.[10]

Solar Radio Noise

Type	Characteristic Duration	Probable Cause
Centimeter	Minutes	Synchrotron radiation from relativistic electrons.
Type II	Minutes	Excitation of coronal plasma oscillations by high energy particles that are probably trapped in a magneto-dynamic wave.
Type III	Seconds	Excitation of coronal plasma oscillations by high energy particles that pass through the corona freely.
Type IV	Hours	Synchrotron radiation from relativistic electrons.
Type V	Minutes	Excitation of coronal plasma oscillations by particles ejected during a flare. The particles rapidly diffuse from trapping region.
Radio Storms	Days	Excitation of coronal plasma oscillations by particles ejected during a flare. The particles slowly diffuse from trapping region.

As can be seen from the table, the kinds of particles causing the specific types of radio emission can be determined. Thus, Types II, II, V and Radio Storms agree well with a model which predicts a trapping region following a flare event. Types II and III correspond to the high energy particles that are not trapped in the region while type V and radio storms can be correlated to the diffusion of medium and low energy particles from the trap.

---

10. Denisse, J. F., "Solar Radio Phenomena and Their Physical Interpretation," NASA TT F-72, September 1961.

The change in magnetic field configuration of a sunspot group during a flare event has been observed by Gopasyuk,[11] in which he was able to distinguish "humps" of magnetic field intensity. Assignments of isogauss contours and magnitude of displacement have been made, which show, in general, that the displacement is in the direction of flare nodes (neutral points), and that these displacements do not occur in the absence of flare events. These field changes are consistent with the early stages of the flare event when compression and gas movements are in evidence. It has also been observed [12] that strong magnetic fields (hundreds of gauss) are carried thousands of kilometers above the edge of the solar disk. These fields correspond to the trapping region fields which are carried outward by the expelled plasma and energetic particles.

The observation of polar cap absorption verified another feature of the model, which discusses propagation from the sun to the earth. It has been observed [13] that SHEP stream into the polar cap regions some time after the flare occurs. At some later time, after the onset of the magnetic storm, the flare region produced another flare, and these new protons arrived much faster at the poles than did the initial protons from the first flare. This corresponds to the second flare particles following the path "carved out" by the preceding flare's trapping region, which remains rooted in the sun, but extended out and encompassing the earth. The presence of the plasma cloud near the earth results in a Forbush decrease in galactic cosmic rays, which became more severe when the plasma cloud was preceded by SHEP, than when no SHEP were observed. It is the presence of these SHEP in a flare event which makes possible the carrying-out of large magnetic fields from the sun, resulting in a strong Forbush decrease. To sum up, a SHEP flare will exhibit shorter storm delay time, lower SC amplitude, and stronger Forbush decrease than will a non-SHEP flare.

---

11. Gopasyuk, S. I., Variations of the Magnetic Field and Sunspot Configurations During Solar Flares - A Determination of the Total Energy of Flares, Soviet Astronomy - AJ, Vol. 5, No. 2, September-October 1961.

12. Severnyi, A. B., "Generation of Flares by Varying Magnetic Fields on the Sun," Soviet Astronomy - AJ, Vol. 5, No. 3, November-December 1961.

13. Dvoryashin, A.A., et al., "Active Solar Regions and Their Corpuscular Emission," Soviet Astronomy - AJ, Vol. 5, No. 3, November-December 1961.

The shock waves produced by the change in field gradient and subsequent compression of the flare region have been photographed.[14] The photographs clearly show the shock waves moving through the active region, and the region expanding. Also, through an ingeneous technique, a wavelength shift is used to show plasma ejected toward the earth in a color different than that for plasma falling back into the region. Thus the ejection of a plasma during the bright phase of a flare event has been directly photographed.

The anisotropy of the initial radiation arriving at the earth from a flare has been observed.[15] This early anisotropy seemed to come from a source located approximately 50^{o} to the west of the earth sun line, (Figure 8), which corresponds to the initial high energy particles escaping immediately from the flare trap,and being loosely guided to the earth by the spiralled field of the sun. It was observed for one event that the anisotropic SHEP arrived in bursts, which would correspond to the early fluctuations of the non-equilibrium trapping region above the flare site. The anisotropic phase of SHEP arrival is observed to vary in time, which is consistent with varying production and trapping conditions on the sun; the anisotropy decays into isotropy in a matter of minutes to a few hours.

Spectroscopic observations of flare phenomena[12] lends evidence for emission of a stream of radiating plasma having a velocity of the order of 10^{3} km sec^{-1}. These observations are of wings of hydrogen emission lines, upon which asymmetric "whiskers" are imposed. The investigations of these profiles yield good first approximations due to doppler broadening, but better agreement is obtained if velocity gradient broadening is used. Thus direct observations consistent with fast particle stream motion, both in and out of a flare region, have been made.

---

14. Ramsey, H. E., Lockheed California Company (Private Communication)

15. McCracken, K.G., "The Cosmic Ray Flare Effect," Jour.of Geophys.Res., Vol. 67, No. 2, February 1962.

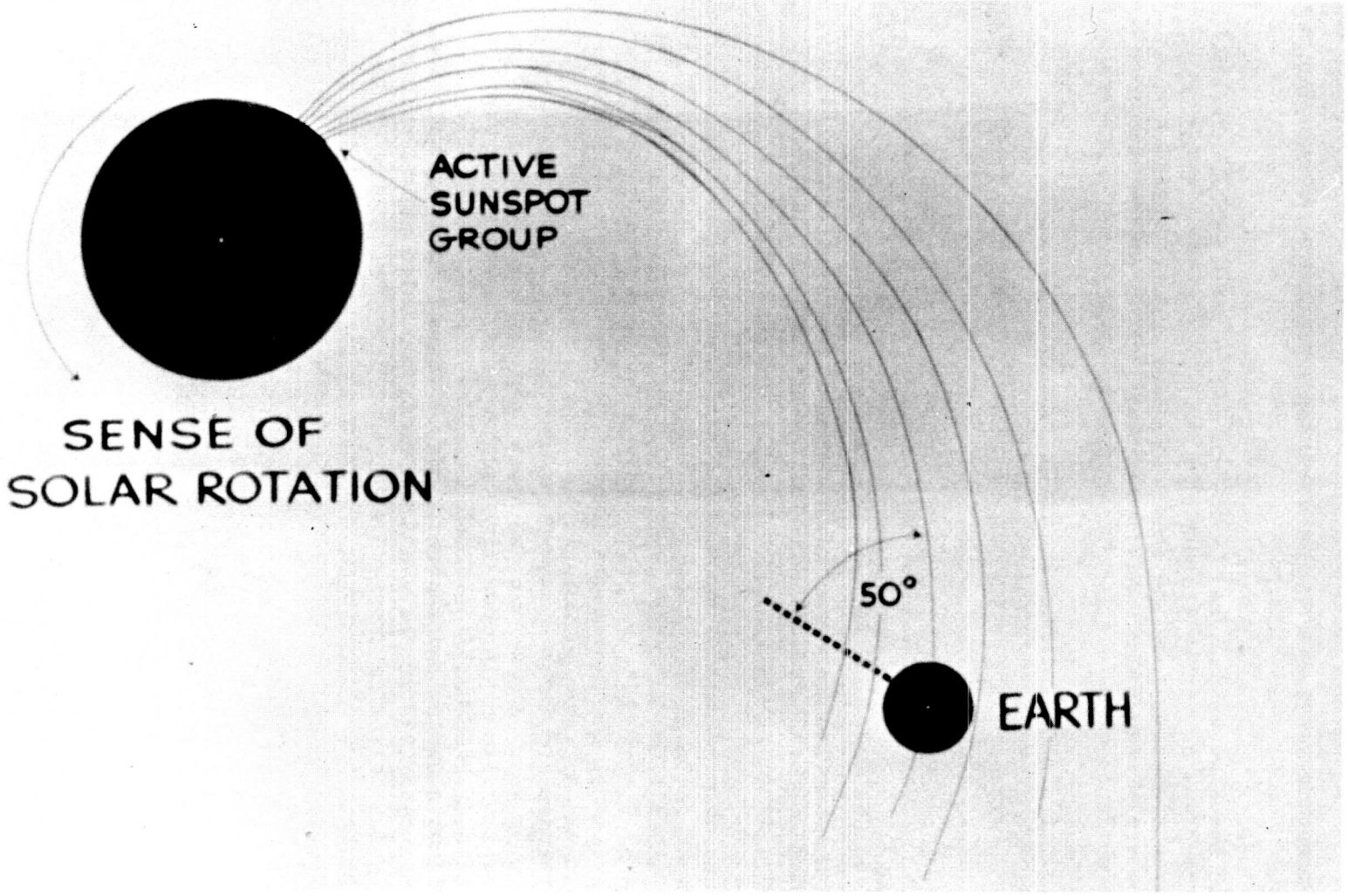

Figure 8. Solar Flare Anisotropy

Paper B-1

RADIATION DAMAGE TO SOLAR CELLS

J. A. Baicker and P. Rappaport
RCA Laboratories
Princeton, N. J.

Abstract

The construction, operation, and performance characteristics of solar cells are described. The radiation damage process is discussed, and details of proton and electron damage to silicon cells presented. The degradation of the photovoltaic current-voltage characteristics and the spectral response is shown, and a comparison made of various types of solar cells, including silicon, gallium arsenide and cadmium sulfide. Differences between p/n and n/p silicon cells are discussed and explained in terms of basic properties of the radiation defects.

I. Introduction

When solar cells were first suggested as space power supplies it was expected, based on cosmic ray intensities, that their operating lives would extend for thousands of years. However, with the discovery in 1958 of the Van Allen radiation belts it was recognized that solar cell lifetimes would be reduced to months or even less in the most intense regions. For many of the low energy electrons and protons in these belts simple quartz or sapphire shielding over the solar cells could be quite effective. Now, with the creation of the artificial radiation belt, the solar cell damage problem is quite serious and under some conditions the conventional solar cell may last for only days. This is a result of the large number of relatively high energy electrons that were produced by the high altitude bomb blast, and against which solar cells cannot be easily shielded. In this paper we will discuss solar cell radiation damage, and discuss how some of the deleterious effects may be counteracted.

First, we will describe the operation of solar cells and discuss the physical phenomena that occur when they are subjected to high energy particle radiation. The latest damage data for electrons and protons will be presented, with the general conclusion that solar cells will continue to be quite useful as space power supplies.

It is well-known that solar cells are among the most vulnerable components used in space vehicles. This is true for two reasons: (1) solar cells require long minority carrier lifetimes for efficient operation, and the lifetime is the most sensitive to radiation of all semiconductor properties, and (2) they are mounted on the exterior of the satellite in an exposed position with at most a minor amount of transparent shielding.

II. Description of Solar Cells

Several papers such as Chapin et. al.[1], Prince[2], and Rappaport[3] describe the solar cell. The basic operation is illustrated in Fig. 1. A wafer of n-type silicon is fired so as to produce a shallow-diffused surface layer of p-type silicon, and ohmic contacts are applied to both n and p regions.* When the cell is illuminated, photons with energy greater than the energy gap of the silicon generate electron-hole pairs both in the surface and base regions of the cell. These pairs are free to diffuse through the material, and those minority carriers that reach the vicinity of the space charge region near the junction are swept across the junction by the electric field. The collected carriers constitute an electric current, and can generate a voltage across an external load. Fig. 2 illustrates the typical junction i-V characteristics in the dark and under illumination. The shaded area is the region in which power is delivered to a load; notice that the cell operates with the junction biased in the forward direction, while the current flows in the reverse direction.

The spectral response of a solar cell having a 1 micron junction depth is shown in Fig. 3. The base response characteristically goes to zero at both long and short wavelength limits. This can be understood as follows: at long wavelengths the light photons have insufficient energy to produce pairs, and at the short wavelength extreme the optical absorption constant is so large that the light is totally absorbed in the 1 micron surface layer, and cannot penetrate into the base region. The surface response goes to zero at long wavelengths and approaches a constant value in the short wavelength limit, when the light is all absorbed at the surface of the cell in a layer that is thin compared with both the junction depth and the minority carrier diffusion length in the surface layer.

---

* The abbreviation p/n will be used to designate cells having n-type base material and p-type surface layers, and n/p for the reverse.

1. D. M. Chapin, C. S. Fuller and G. L. Pearson, J. Applied Phys. 25 676 (1954).

2. M. B. Prince, J. Applied Phys. 26 534 (1955).

3. P. Rappaport, RCA Review 20 373 (1959).

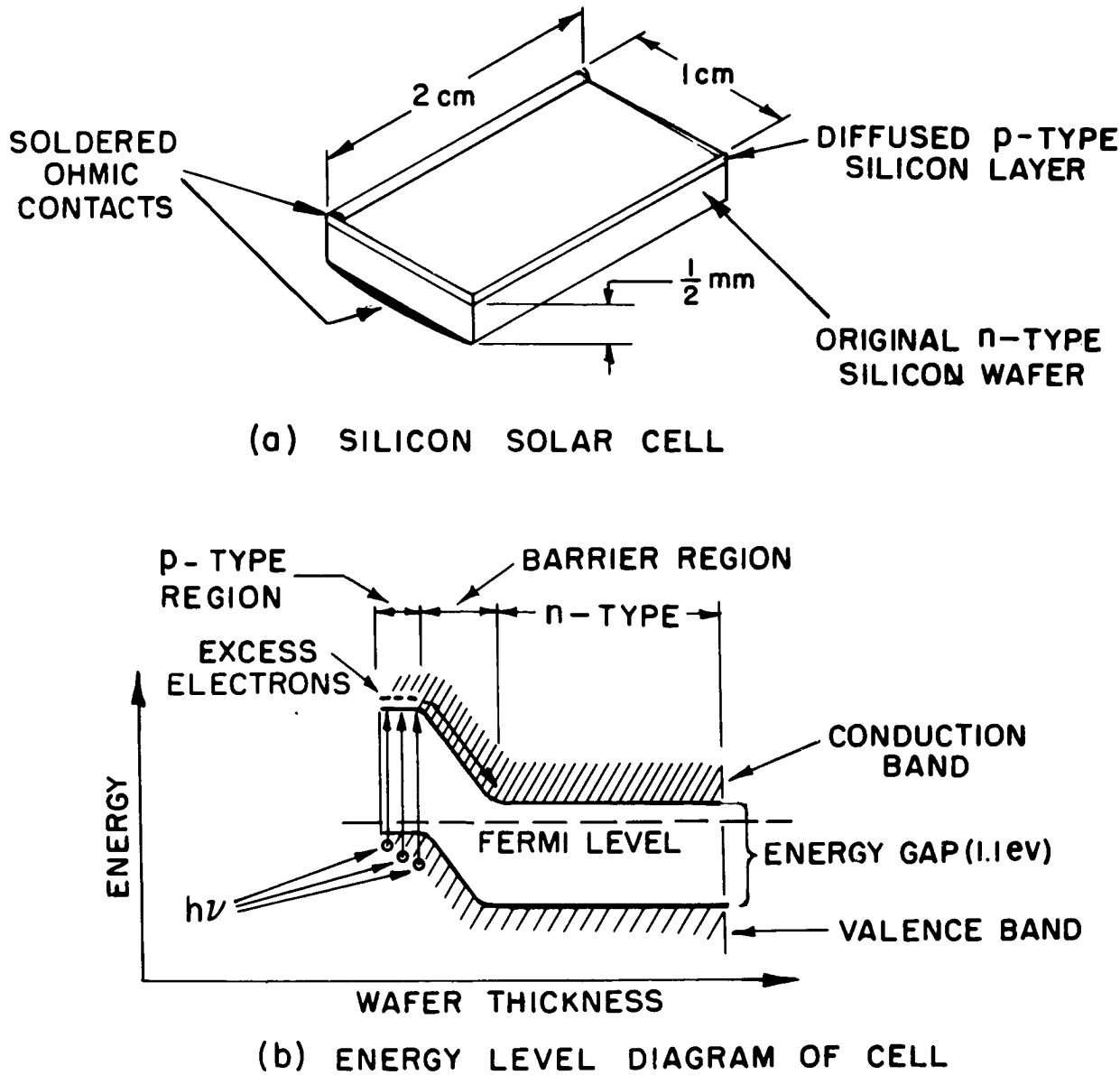

FIG. 1 Schematic diagram of a solar cell.

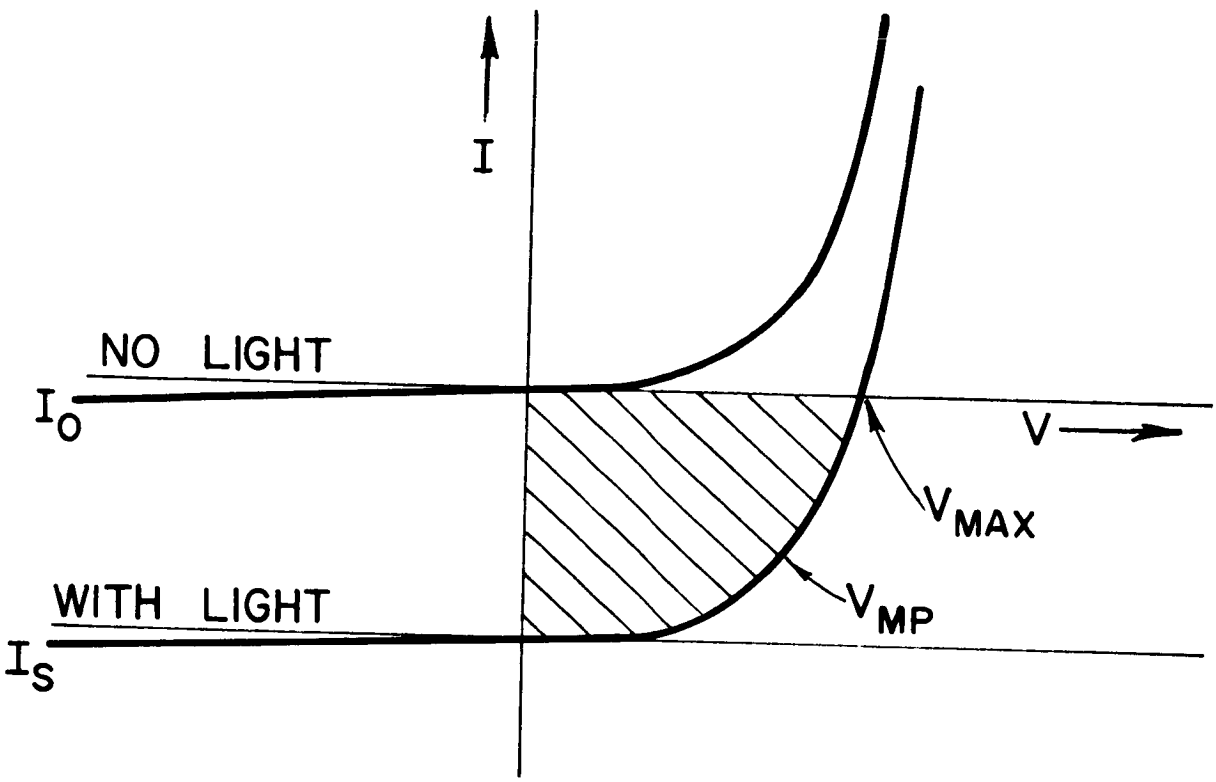

FIG. 2 Current-voltage characteristic of a solar cell.

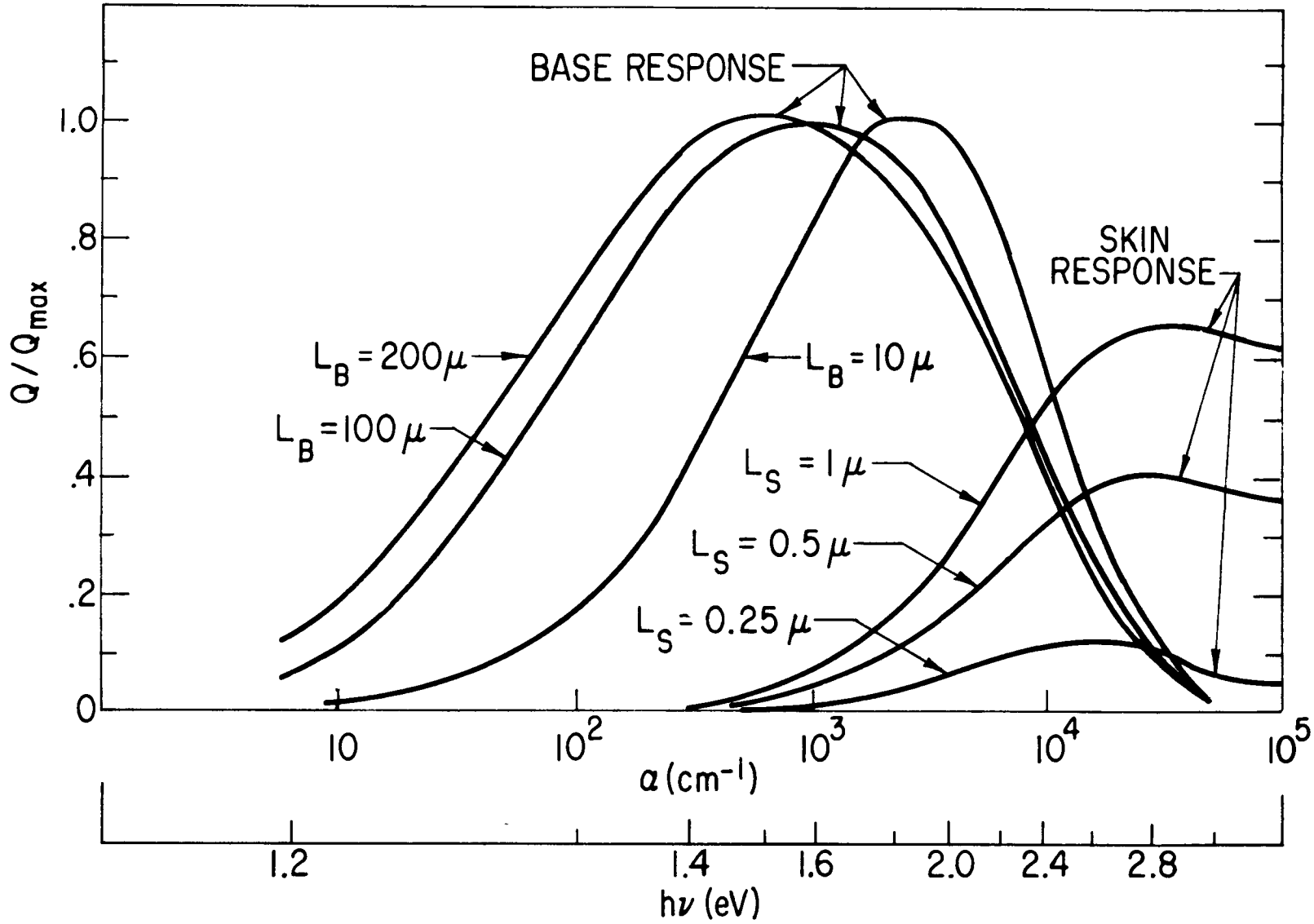

FIG. 3 Theoretical spectral response of a solar cell with a one-micron deep junction.

Figure 4 shows a typical spectral response curve, showing how it can be resolved into base and surface contributions. Note that the surface response is much smaller than the base response, a characteristic of practically all silicon cells. This is caused by two circumstances; (1) the optical absorption spectrum of silicon is such that for both sunlight and tungsten light over 75% of the radiant energy is absorbed in the base of the cell, and (2) the minority carrier diffusion length in the highly-doped surface layer is less than 1 micron, compared with 100 microns or more in the base.

This feature does not occur in solar cells made of other materials, such as gallium arsenide, for example.

The possibility of increasing the surface response by reducing the junction depth has been explored by several workers in the field. In addition to increasing the overall conversion efficiency the added surface response has the effect of shifting the peak of the spectral response towards the blue, and hence these cells are sometimes called "blue-shifted" cells.

Cells with 1/4 micron junction depths have been made; their surface response is considerably greater than the standard 1 micron junction depth cells, but the thin surface layer adds to the series resistance of the cells, and the overall efficiency is reduced. The series resistance loss can be minimized by providing a conducting grid on the surface.

Some of the performance characteristics of silicon solar cells are:

Efficiency in sunlight	10-11%	
Efficiency in tungsten light	13-14%	
Open-Circuit voltage	0.55 volt	Illuminated with 100 mw/cm^2
Short-circuit current	25-30 ma/cm^2	

III. Damage Process

It is evident that a solar cell requires a long minority carrier diffusion length for its efficient operation. With care in manufacture the diffusion length in the base is approximately 100μ. Upon bombardment with high energy particles silicon atoms are displaced from their normal lattice positions. The resulting lattice defects may act as recombination centers for electrons in the conduction band or holes in

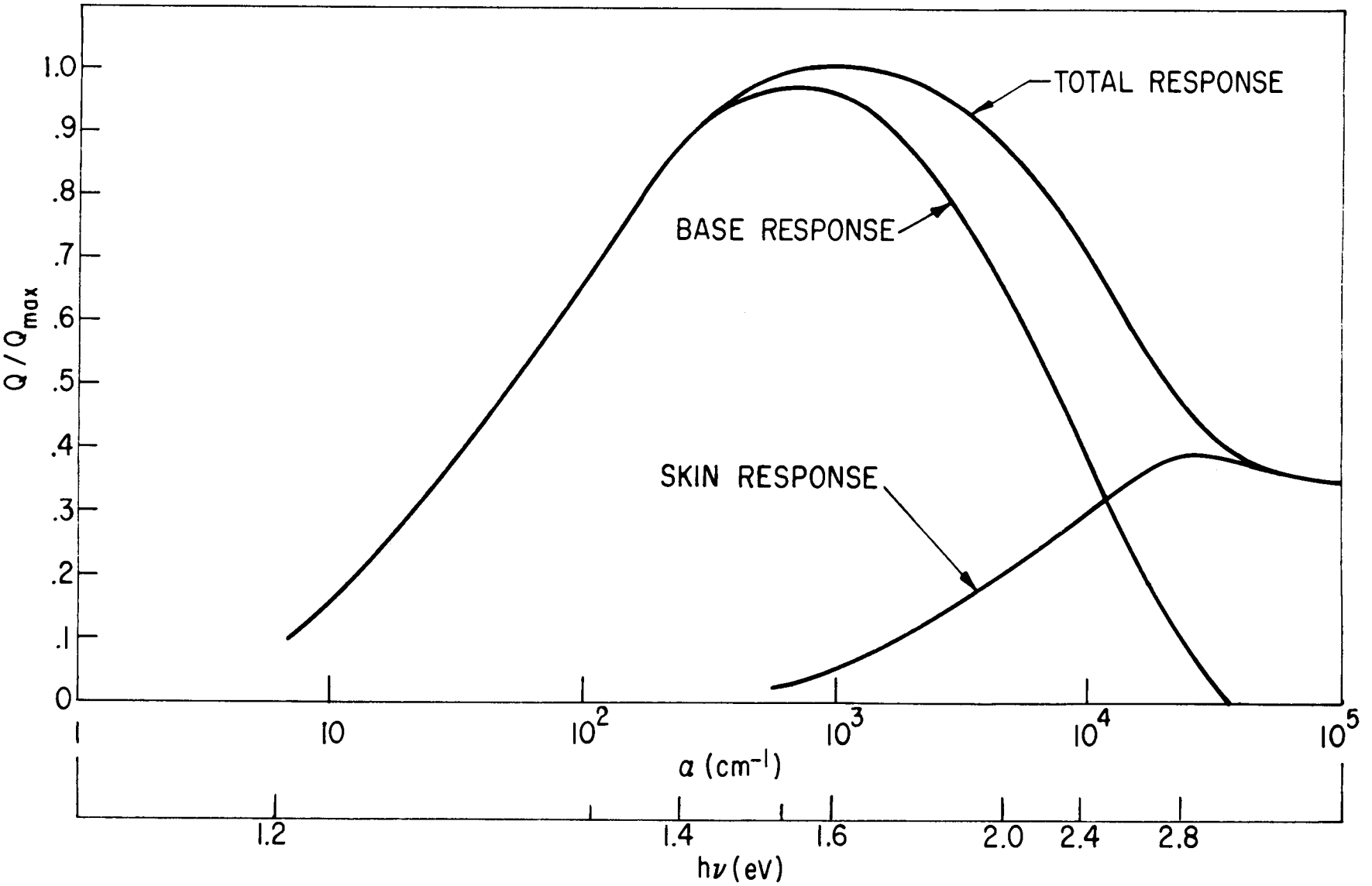

FIG. 4 Typical spectral response for a silicon solar cell.

the valence band, depending on whether the silicon is p-type or n-type. The recombination process occurs as the center first captures a minority carrier and subsequently captures a majority carrier. One electron-hole pair is annihilated in the process, and the center is left in its original charge state. The lifetime of excess carriers, τ, is reduced by the introduction of recombination centers according to the equation

$$\frac{1}{\tau} = \frac{1}{\tau_o} + N_r \sigma_r v f \qquad (1)$$

where τ_o is the lifetime before irradiation, σ_r is the recombination cross section, v is the thermal velocity of the minority carriers, N_r is the recombination center density and f is a statistical occupancy factor that is near unity in most practical cases. The diffusion length $L = (D\tau)^{1/2}$, where D is the diffusion constant, is reduced accordingly.

The first sign of damage to a cell is a reduction of the diffusion length in the base material. The diffusion length being very short in the surface region, it requires a much heavier irradiation before surface damage can be seen. As Fig. 3 shows, the red response will be the first to be affected; red light generates carriers deep in the cell, and a long diffusion length is required for collection.

IV. Results

Figure 5 shows a typical family of i-V curves before and after a number of successive irradiations. The principal loss is to the cell current; the voltage decrease is much smaller. Fig. 6 shows a typical spectral response before and after irradiation; as expected, the degradation is greatest at long wavelengths. The shallow-junction ("blue-shifted") cells are more radiation resistant than the standard cells because of their greater base response in the blue as well as their greater surface response.

The output is shown as a function of total irradiation in Fig. 7, for standard p/n and n/p silicon cells under electron and proton bombardment. The electron fluxes required for a 25% degradation in the conversion efficiency are shown as a function of electron energy in Fig. 8, for standard one-micron junction depth p/n and n/p cells. (4-8)

4. W. L. Brown and G. L. Pearson, BTL Technical Memornadum, April 1960 (unpublished).
5. P. Berman, Transitron Electronic Corp. Report. Oct 1960 (unpublished).
6. R. G. Downing Space Technology Labs Report, TR 60-0000-04057 Feb. 1960 (unpublished).
7. J. A. Baicker and B. W. Faughnan, J. Applied Phys 33 3271 (1962).
8. J. J. Wysocki and J. Scott-Monck, Personal Communication.

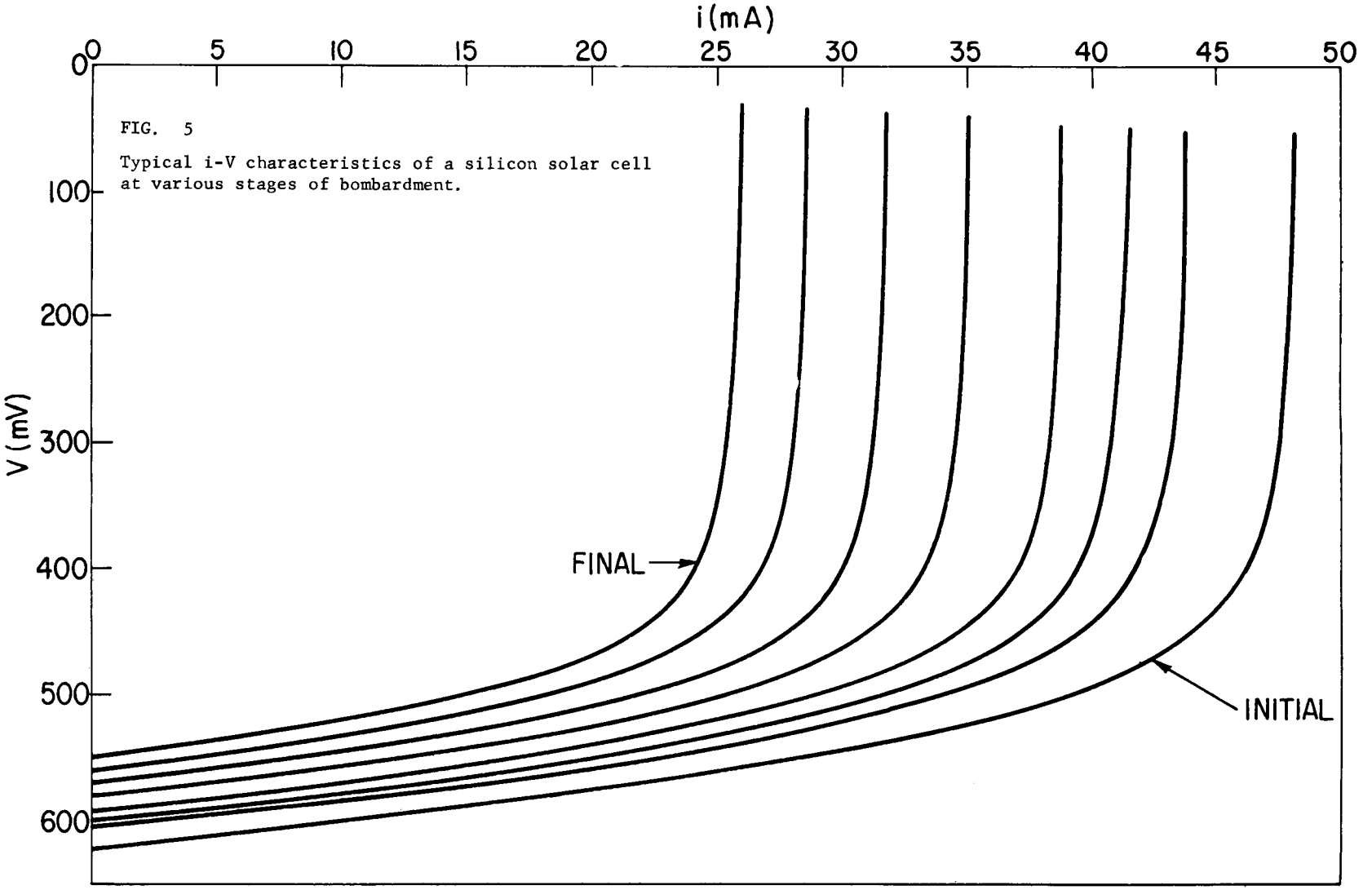

FIG. 5

Typical i-V characteristics of a silicon solar cell at various stages of bombardment.

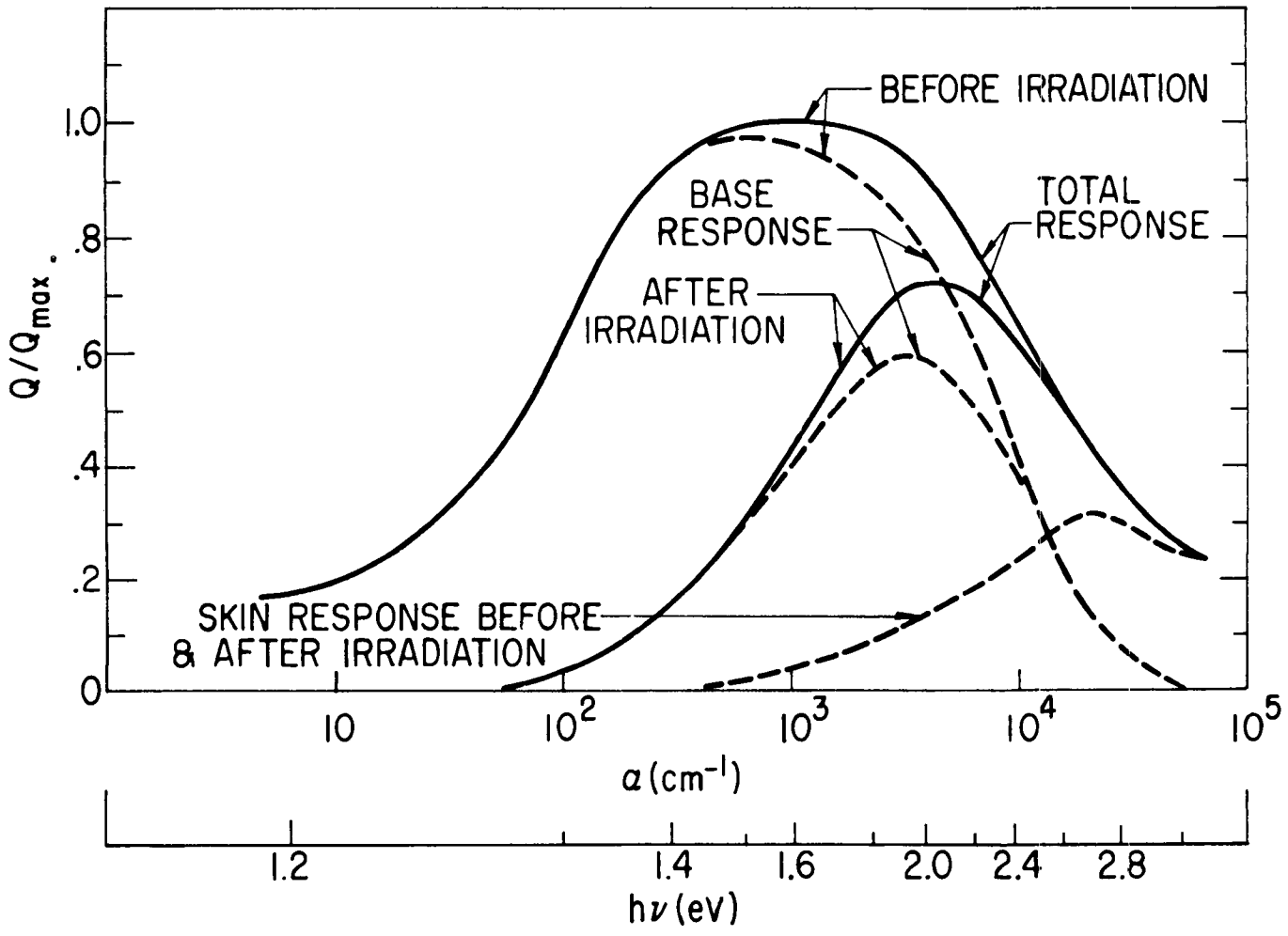

FIG. 6 Spectral response of a silicon solar cell before and after irradiation.

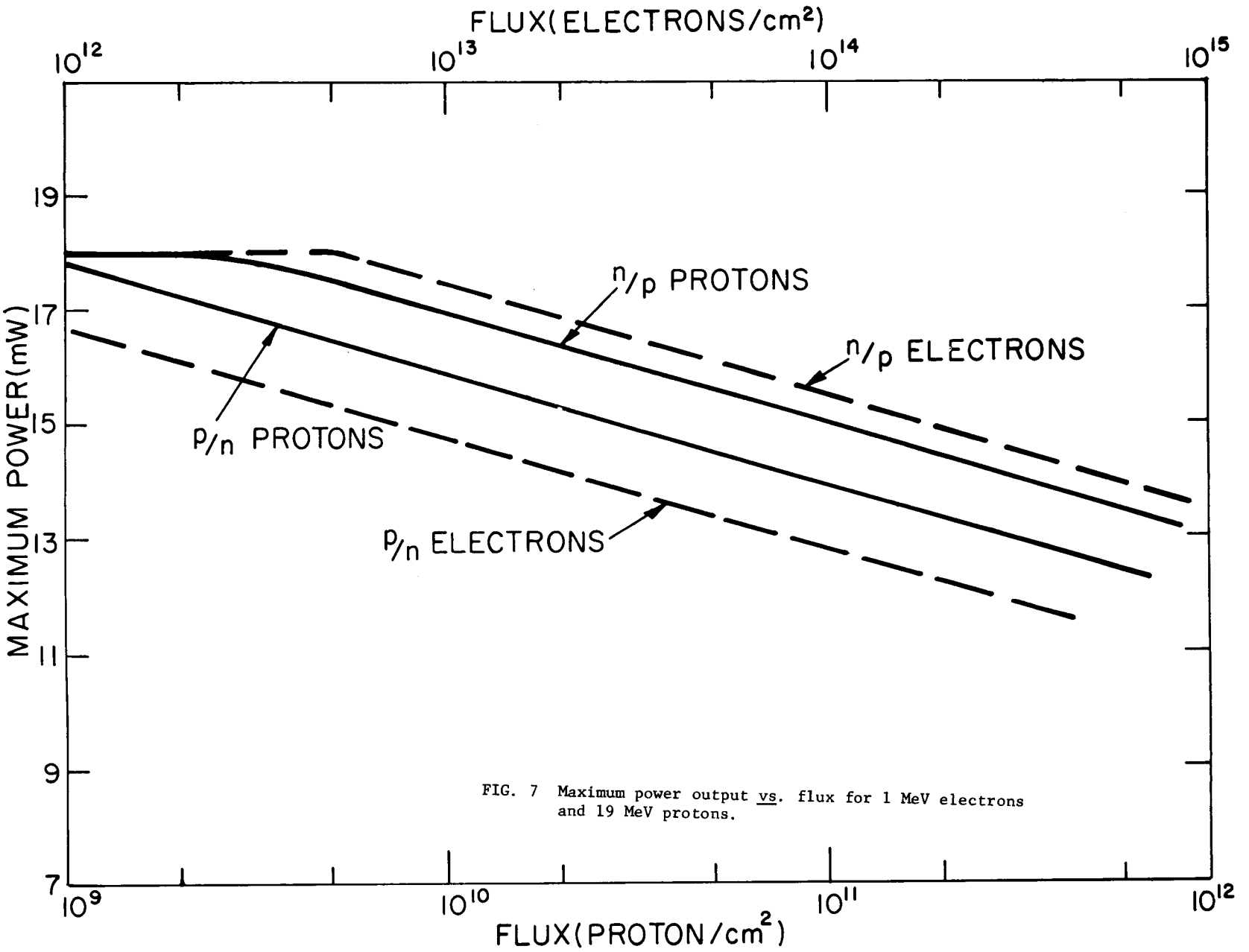

FIG. 7 Maximum power output vs. flux for 1 MeV electrons and 19 MeV protons.

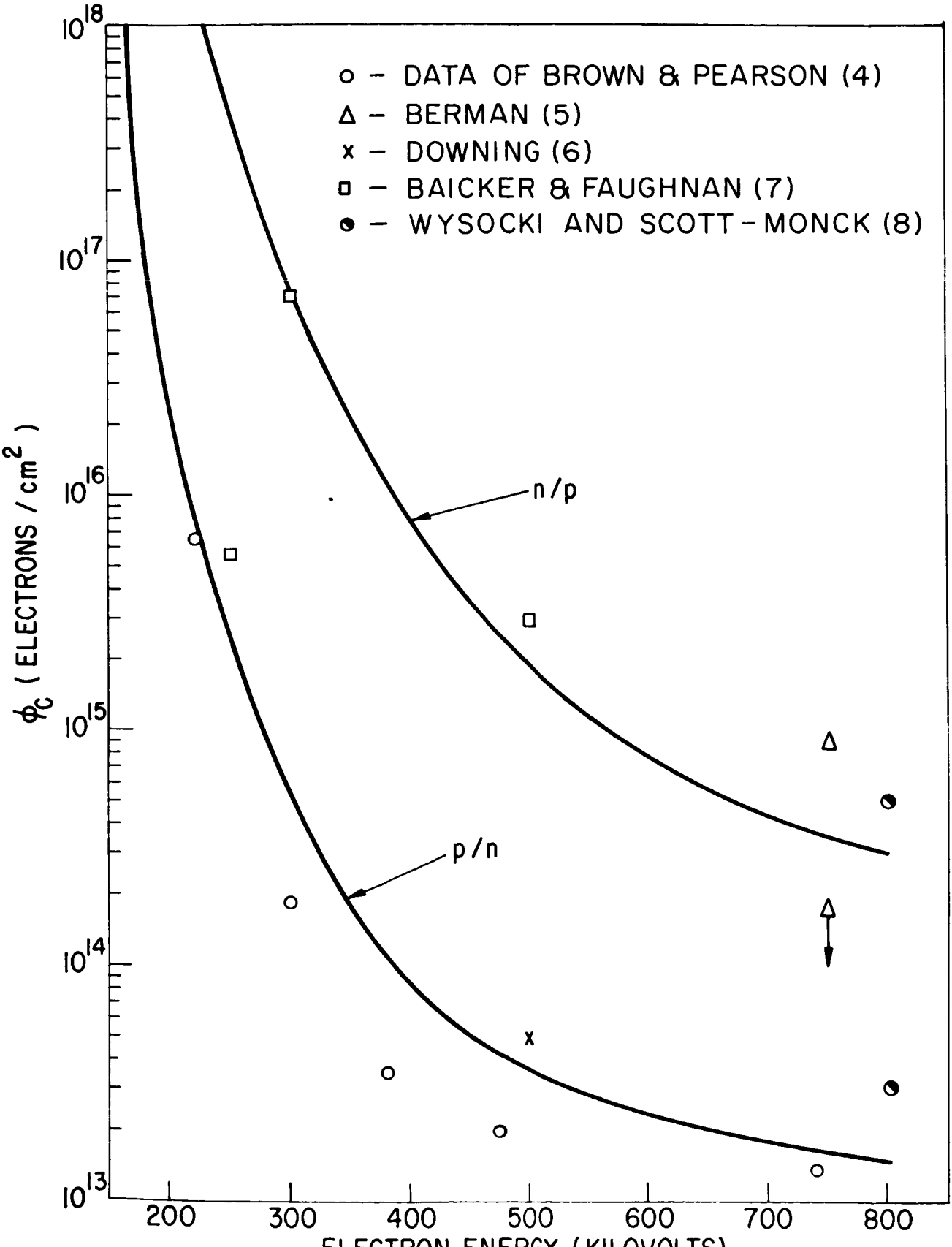

FIG. 8 Electron flux required for 25% power loss for standard p/n and n/p silicon solar cells vs. bombarding energy.

There has been considerable conjecture regarding the large difference between p/n and n/p silicon cells. This phenomenon is a result of the basic character of the recombination centers which are produced by bombardment. The simplest type of recombination center has two different charge states, one neutral and the other charge state either positive if the center is a net donor or negative if the charge state is a net acceptor. As a result of the coulomb forces a donor-like center will have a large electron-capture cross section when it is in its positive charge state, and it will have a relatively much smaller hole capture cross section when in its neutral charge state. If both donor-like and acceptor-like centers are present, the recombination process in n-type silicon will tend to be dominated by the net acceptors and in p-type by the net donors, barring enormous differences in the concentrations of the two different species. There is now substantial evidence that a multiplicity of different defects are produced in silicon by irradiation and the dominant recombination centers are indeed different in n-type and p-type silicon. They are produced in different concentrations, and have different minority capture cross sections, and it would in fact be purely coincidence if the radiation damage rates were the same in both types of silicon.

The energy dependence of the damage rate under proton bombardment is shown in Fig. 9. There should really be two curves, one for p/n and the other for n/p cells, with about a factor of 3 or 4 separating them, but the fluctuations within any given group of apparently identical cells in nearly a factor of 10, and so only an average curve is shown.

Shielding Effectiveness

Since the July 9th nuclear explosion which is generally conceded to have injected large numbers of energetic electrons into trapped orbits there has been a rapid deterioration of power on satellites traveling in the radiation region with one notable exception, the Bell Telstar. The Telstar system was different from the others on two accounts: it utilized n/p silicon cells for the first time and each cell was protected by a moderate amount of transparent shielding (30 mils of sapphire). The question of just how effective the 30-mil shield is, is rather difficult to answer, for either proton or electron fluxes, (for different reasons). In the proton case it isn't too difficult to calculate what will happen to a monoenergetic beam passing through a relatively thin layer of shielding. The difficulty occurs

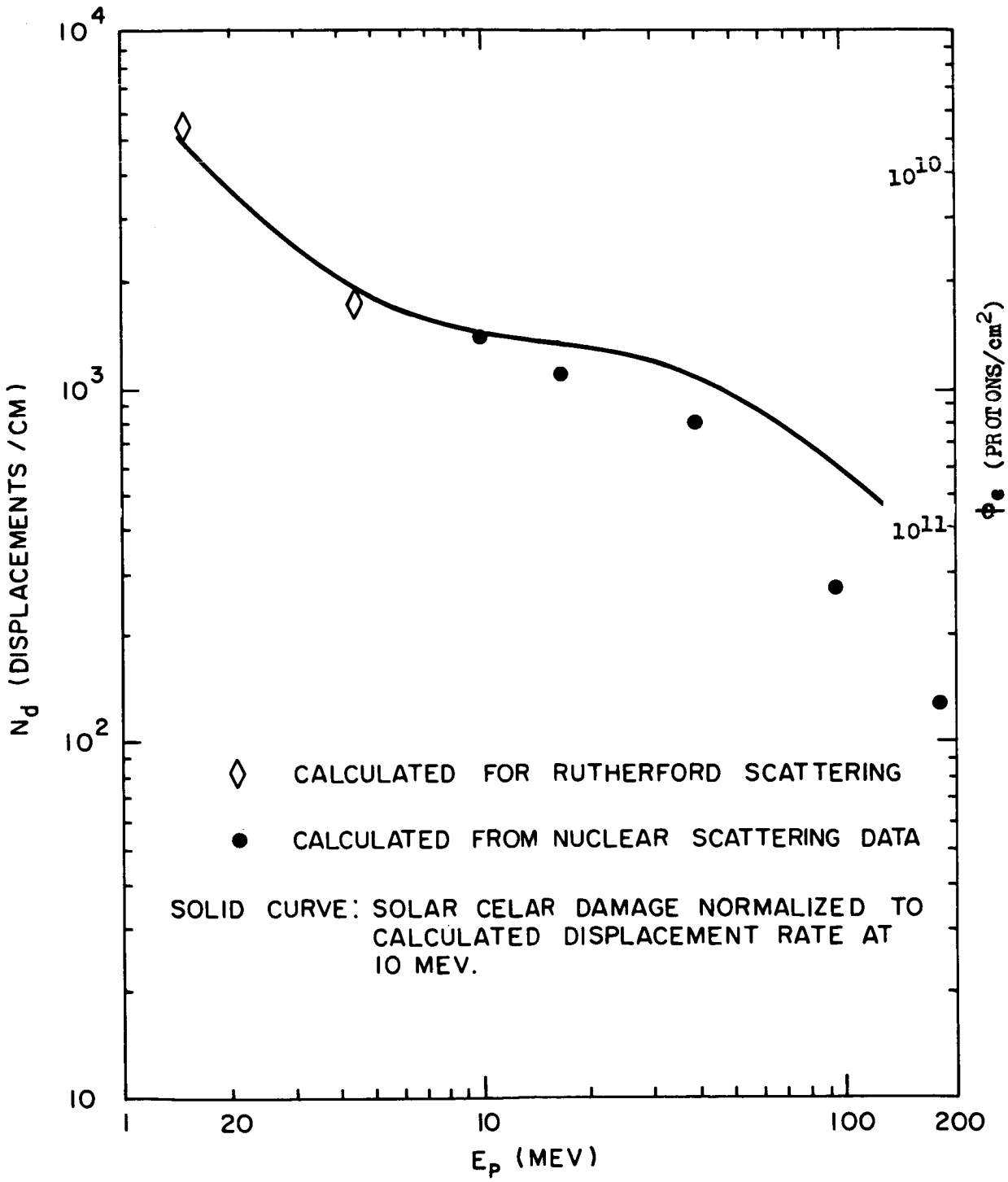

FIG. 9 Relative proton damage rate vs. bombarding energy.

because the proton spectrum has not been measured down to sufficiently low energies to account for the entire damage-producing flux. The energy spectrum increases very rapidly at low energies, and as Fig. 9 indicates the low-energy protons are at least as important to an unprotected cell as the high-energy protons. If we make the arbitrary assumption that the intensity is constant from zero to 10 Mev, and then drops off in a manner as reported by Freden and White and Naugle and Kniffen at higher energies, then we would conclude that 10 mils of sapphire would reduce the proton damage by roughly a factor of 10. A 30-mil sapphire shield would reduce the proton damage by a factor of 200, on the same assumption regarding the low energy spectrum. If, as one would suspect, the intensity continues to increase below 10 Mev the improvement due to shielding will be even greater than these figures.

In the electron case the shielding question is more difficult to answer. Electrons are not slowed down in as uniform a fashion as protons are, and there is even more diversity among the reported electron fluxes than among the proton fluxes. For a "fission-electron" spectrum such as was trapped after the Johnston Island explosion the shielding effectiveness will not be nearly as great as the approximate figures given above for the proton case. It has been estimated that the shielding reduces the damage by only a factor of two in the electron flux.[9] The principal advantage of the Telstar over the earlier satellites has come about through the use of n/p solar cells.

V. Gallium Arsenide

Photovoltaic effects are seen in practically all semiconductors, and many have been considered for energy conversion purposes. Of these, gallium arsenide and cadmium sulfide are the nearest to being practical (i.e., competitive with silicon).

Gallium arsenide photovoltaic cells are similar to silicon cells in construction. A wafer of n-type material has a p-type surface layer roughly 1μ deep. The principal difference between silicon and gallium arsenide is a consequence of the optical absorption spectra of the two materials. In GaAs the absorption constant rises very steeply above the fundamental edge, and as a result all of the carriers are generated in a very shallow layer ($\sim$ 1 micron) in the p-type surface. This is in constrast with silicon where the optical absorption rises more slowly and light can penetrate deeply into the base region. Solar cells with 10% solar conversion efficiency have been made using gallium arsenide,

9. W. L. Brown, Personal Communication

and since the active region of the cells is confined to the shallow surface layer a higher flux of damaging radiation is required to affect the output of these cells than is required for comparable silicon cells. The difference between the spectral response before and after irradiation for gallium arsenide and silicon is shown in Fig. 10.

Cadmium sulfide photovoltaic cells are the latest addition to the family, and since the exact mechanism for their operation isn't understood the present discussion will be qualitative. Cadmium sulfide cells are quite different from either gallium arsenide or silicon cells; a thin evaporated polycrystalline layer of n-type cadmium sulfide is deposited on a conducting backing, either metal or glass with a transparent conducting film, the materials being chosen to effect an ohmic contact. A surface layer of copper is deposited on top of the cadmium sulfide, and produces a surface barrier type junction.
In addition to the obvious difference in construction, the method of operation is different from silicon and GaAs. Light which is below the fundamental absorption edge can pass through the cadmium sulfide and strike the copper interface, where it is absorbed and produces carriers by a process which may be similar to photoemission. In contrast with silicon and GaAs little or no carrier diffusion is required, and hence the device is extremely difficult to damage. The maximum efficiency obtained up to now is in the neighborhood of 4-5%.

A comparison of the damage susceptibility of the various types of solar cell is given in Table I. The figures are all related to standard silicon p/n cells. The actual flux required for a given degradation can be obtained from Figures 8 and 9. Fig. 7 gives detailed numbers for 1 MeV electrons and 19 MeV protons.

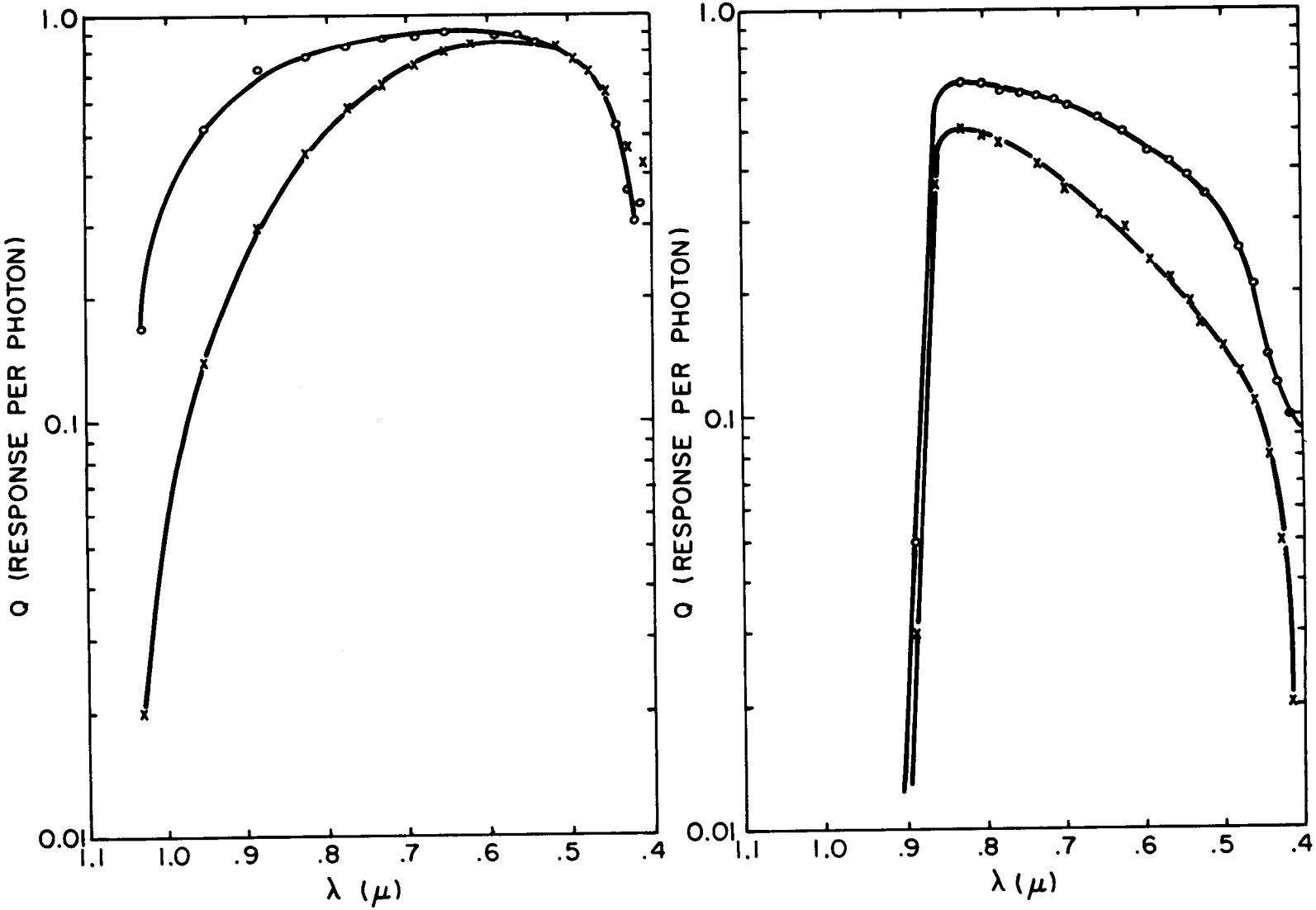

FIG 10 Comparison of the spectral response of a silicon and a GaAs solar cell before and after irradiation.

TABLE I

Comparison of Solar Cell Damage Rates
Relative Fluxes Required for Equivalent Degradation

Each Line Has Been Separately Normalized

	SILICON				GaAs
	Standard		Shallow Junction		
	(p/n)	(n/p)	(p/n)	(n/p)	
.5 MeV electrons	1	40			
1 MeV "	1	40	1.3	50	50
6 MeV "	x		1	10	100
1.8 MeV protons	1	4			60
8 MeV "	1	3			
19 MeV "	1	4		20	80
95 MeV "	1			10	60

VI. Summary

It is obvious from this discussion that there are still a number of gaps in our understanding of the radiation damage problem as it applies to semiconductor devices in general. We know very little about the physical identify of the radiation defects in silicon, and nothing about the defect centers in GaAs. There is a continuing effort at RCA and elsewhere to provide some of the answers, which we hope will be the first step in developing more damage-resistant devices.

SURFACE EFFECTS OF RADIATION ON TRANSISTORS*

by

D. S. Peck, R. R. Blair, W. L. Brown, and F. M. Smits
Bell Telephone Laboratories, Incorporated
Murray Hill, New Jersey

I. Introduction

A wide variety of effects of high energy radiation on semiconductor materials and devices have been recognized and studied for a number of years. The major emphasis in this field has been on effects that involve the bulk properties of semiconductors. A great deal of progress has been made in understanding the processes that control bulk radiation phenomena[1] and in understanding the implications of these phenomena for semiconductor devices.[2] Radiation effects on semiconductor surfaces also have been observed[3], and this paper is concerned with some special aspects of surface phenomena that have recently come to light. In contrast to bulk effects, the surface radiation effects are very poorly understood and in general even poorly characterized. This paper will attempt to shed a little light on these complexities and indicate a type of measurement program that has been found appropriate for dealing with devices intended for use in a radiation environment such as that of the Van Allen Belts in space. It will fall short of providing a satisfactory understanding of the processes involved.

*This paper was published in the January 1963 issue of the Bell System Technical Journal; included here with the permission of the American Telephone and Telegraph Co.

[1]Partly supported by contract with Electron Technology Laboratories, Aeronautical Systems Division of the United States Air Force Systems Command.

The paper is arranged as follows: in Section II for perspective, a brief discussion of the two broad classes of bulk radiation effects. Section III, description of the early observations that provoked the present work. Section IV, a proposed model of the basic process. Section V, results of a number of experiments carried out to test the mechanisms of the process. Section VI, characterization of effects with significant numbers of devices. Section VII, the process of testing and selection undertaken for Telstar devices. Section VIII, Summary.

II. Bulk Radiation Effects

Bulk radiation effects can be placed in two broad classes that arise from (a) hole-electron pairs produced in the crystal by ionizing radiation and (b) defects in the semiconductor lattice produced by high energy particles. These phenomena often occur together but they result from quite different interactions of radiation with the solid and they have very different consequences in semiconductors.

II.1 Hole-electron pair formation

Figure 1a illustrates the first case. Any charged particle passing through a solid produces ionization through collisions with the bound electrons. These collisions excite electrons to the conduction band and leave holes in the valence band, producing electron-hole pairs in exact analogy with the production of pairs by light. Neutrons and gamma rays also cause ionization effects through intermediate reactions that

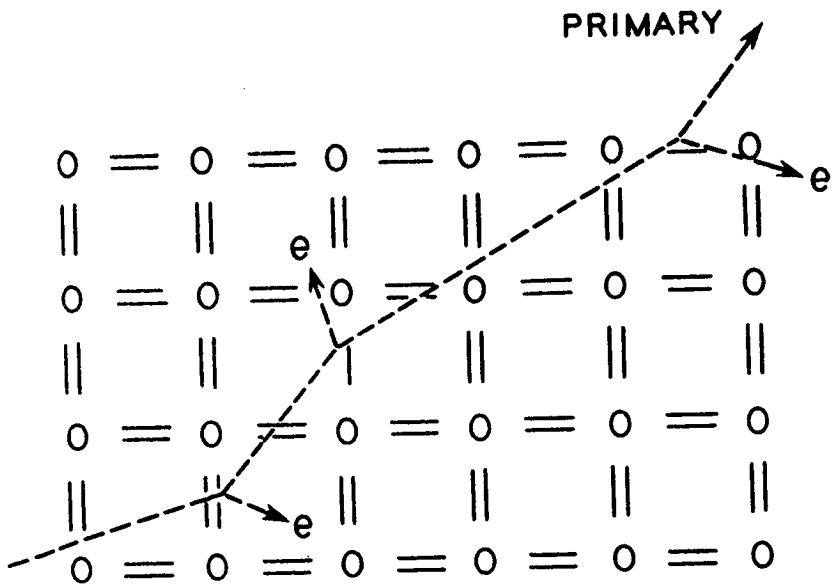

(a)

Production of hole-electron pairs by collision of a charged particle with electrons of a semiconductor.

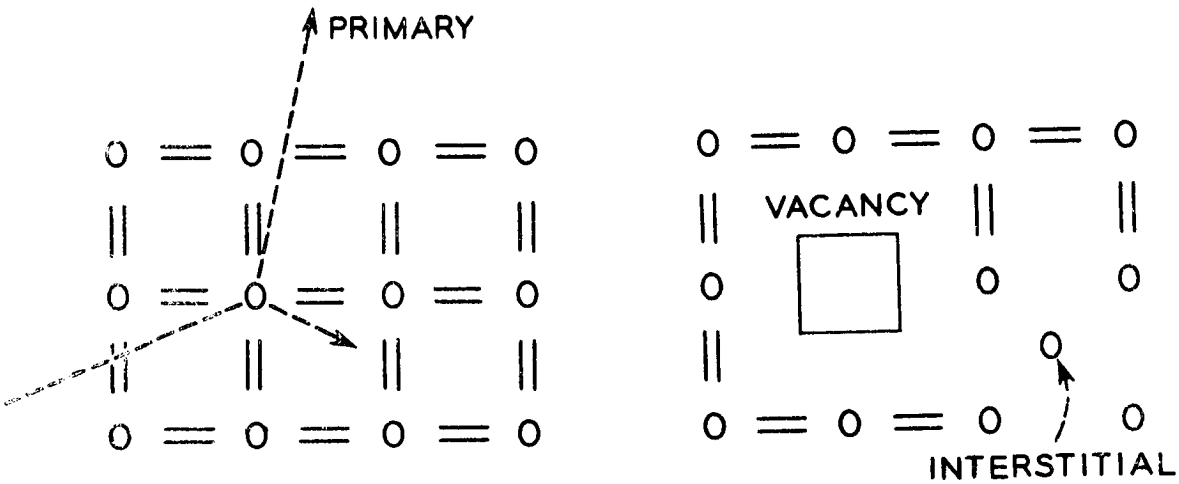

(b)

Production of lattice defects by collision of particles with the nuclei of a semiconductor.

Fig. 1

produce charged particles. As far as effects which depend on ionization are concerned, the particular particle involved is incidental; all that matters is how much energy is lost in

the solid. The number of hole-electron pairs produced is proportional to this energy loss.

The generated pairs tend to recombine with a time constant that is the conventional lifetime. Hence, all effects in this class are transient and persist only for the order of a lifetime after the excitation is removed. The pairs produced alter the conductivity of semiconducting materials. They also contribute currents in p-n junction diodes and transistors. Under pulsed ionizing radiation these effects can alter conductivities and currents by many orders of magnitude. On the other hand these effects can be very small in response to a single energetic particle and special p-n junction diodes may be required even to detect them.[4] A case of intermediate magnitude has been considered by Rosenzweig[5] who has used silicon solar cells to measure the intensity of moderate radiation fields.

II.2 Lattice damage

Figure 1b illustrates the other type of bulk radiation effect in semicondcutors that arises from collisions of energetic particles with the nuclei of the lattice. If such a collision transfers sufficient energy to the struck atom, it is capable of moving the atom from its normal lattice site to some interstitial position in the crystal. These events are rare by comparison with the ionization events of Fig. 1a, but they create permanent or at least semipermanent defects in the structure of the lattice. The most important consequence of these defects is reduction in

the carrier lifetime of the material. Increases in diode reverse current and decreases in transistor current gain are produced as functions of the time integral of the flux of particles. In contrast to the pair production of the paragraph above, this radiation damage is extremely dependent on the particular particle involved. Energetic protons, for example, are much more effective in producing damage than energetic electrons. This type of radiation effect is of major importance to the long term power conversion efficiency of solar cells in space. Detailed consideration of this problem can be found elsewhere[6].

III. The Surface Problem

Surface effects on semiconductor devices have an illustrious history of subtlety and perversity and it is no surprise to learn that radiation is an environmental factor that must be considered. Several years ago, before the present sophistication in surface processing, experiments were carried out in an attempt to characterize radiation surface effects[3] (changes in junction current, breakdown voltage, current gain, etc.). No systematic picture emerged, although surface cleanliness seemed certain to play some role.

Transistors that have evolved from refinements in junction formation and surface treatment techniques have, in the last few years, been examined in a variety of high energy neutron and gamma-ray environments. Particular attention has been given to bulk radiation damage effects on current gain

since these effects turned out to be serious (particularly for silicon) at the flux levels of current interest in the vicinity of nuclear reactors. Very substantial improvements in radiation tolerance have been found; however, no recent comprehensive work on the surface effects has been reported.

The relative stability of the characteristics of a particular type of diffused silicon transistor under radiation is illustrated in Fig. 2. The collector reverse current is displayed because it is a particularly sensitive indication of surface stability at the very low currents that are conventional in present silicon devices. The gamma ray radiation* used in this case is representative of ionizing radiation in general. The figure shows that after one hour tests with neither bias nor radiation or with either alone, the current is essentially unchanged. (Actually much longer tests under bias are conventionally made in checking device reliability with the same results as shown here.) However, when bias and gamma radiation are simultaneously applied two effects appear: there is a sudden rise in current and then an upward drift of current over many minutes. The sudden rise of about 0.02μa is largely due to ionization of the gas in the device can. The current drifts upward by another decade in the 45-minute exposure following

*Radiation dose is frequently expressed in "rads" which are a measure of the energy absorbed per unit mass of material. One rad is equivalent to absorption of 100 erg/gm. Such a dose would produce approximately 2×10^9 ion-electron pairs/cm^3 in atmospheric air or about 4×10^{13} electron-hole pairs/cm^3 in silicon.

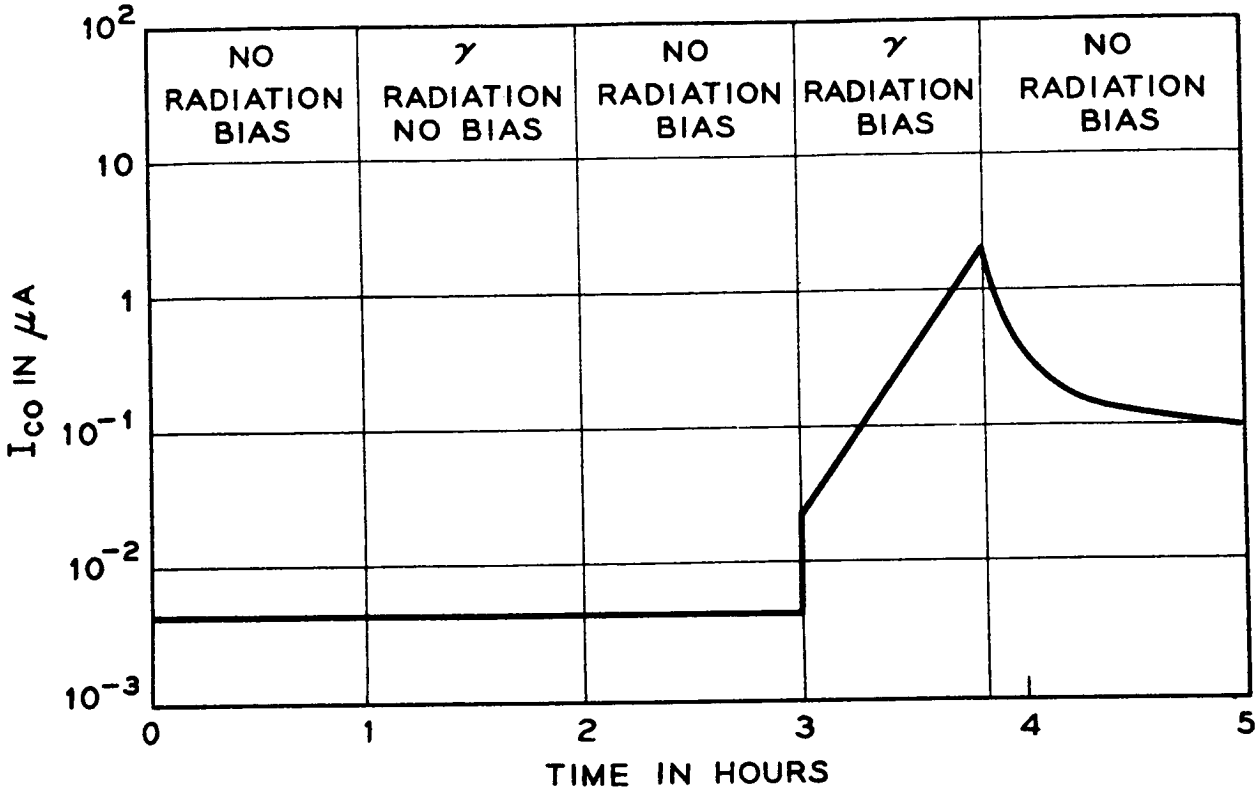

Fig. 2.

The response of I_{CBO} of a diffused silicon transistor to either radiation or bias alone or to both together. Radiation dose rate 8.5×10^5 rads/hr.

its rapid rise. When the gamma radiation is removed the current does not immediately drop back to its preirradiation value, but gradually declines and even after an hour is more than a decade too high. A drop of about 0.02μa must still occur at gamma ray turnoff, but this is so small compared with the level to which the current has drifted, that the drop is not visible.*

The drift up and the slow decay of the collector currents are surface effects produced by the radiation only when the collector junction is reverse-biased. This aspect of radiation sensitivity had not previously been reported. It represents a factor that must be considered for reliability of devices that must operate in any radiation environment including the high energy electron and proton belts found in outer space. The conclusion that these effects arise at the semiconductor surface can be reached in a number of ways. If they were bulk effects the marked influence of applied bias is quite unreasonable. Radiation defects created in a solid have been influenced by extremely high electric fields, but only to the extent of causing them to migrate very short distances in

*Ion currents to the electrical leads either in the device encapsulation or in the gamma radiation chamber pose a serious problem to measurements on devices at very low leakage currents in high radiation fields (10^5-10^6 rad/hr). It has often proved necessary to remove the device from the radiation environment momentarily for measurement. Because of recovery effects care must be taken to obtain measurements quickly and at uniform times after removal.

long times.[7] Furthermore, the decay of the effect occurs in a time that is very short for defect annealing in silicon. But more convincing is the sensitivity of the effect to the surface environment of the device inside its encapsulating can.

Figure 3 shows four typical n-p-n diffused silicon transistors of two types, each with two kinds of ambient atmosphere. Increases in collector current are observed in all four, but at quite different integrated gamma-ray doses. In both device types early current increases are associated with gas filling. In type B the evacuated device shows no measureable change until the integrated dose is in a range expected to cause substantial decreases in bulk lifetime. In this case, the influence of bias, although not shown in the figure, is practically nonexistent.

Not only is there a variation in the response depending on the gas filling of transistor cans, but there is also great variability among devices with a single type of filling. All evacuated units are slow to respond, but in the type B transistor only about half of the gas-filled units respond quickly. The other half are almost as stable as the evacuated units. This points again to a surface effect and to a broad spread in response arising from rather subtle differences in the surface chemistry. This lack of reproducibility complicates the study of the process involved and necessitates the use of statistical experiments, some of which will be reported in later sections.

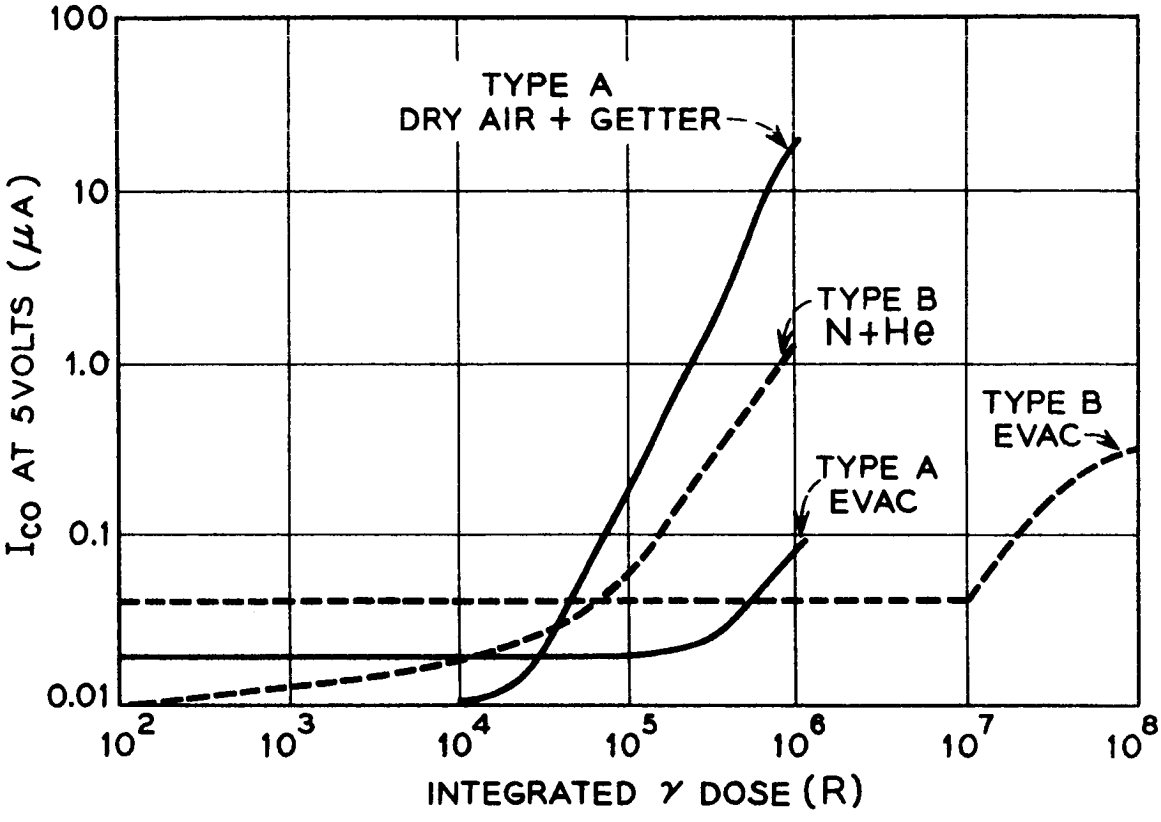

Fig. 3.

The radiation degradation of I_{CBO} of two types of diffused silicon transistors, evacuated or with gas filling. Radiation dose rate 8.5×10^5 rads/hr.

Before continuing to discuss the experimental observations we will introduce a simple model which describes some, but not all, of the effects, and provides a framework for the later discussion.

IV. A Model of the Process

Radiation, gas encapsulation, and device bias that seem to be essential to the effects shown in Section III can be combined in a simple model of the process. Fig. 4 illustrates the ingredients: the fringing field of a reverse biased collector junction on an n-p-n transistor and ions and electrons produced by gamma radiation in the gas of the encapsulation. The fringing field separates the electron-ion pairs, depositing electrons on the collector side of the junction and positive ions on the surface of the base. On both regions these charges tend to produce inversion layers at the surface, the effects being analogous for p-n-p and n-p-n devices. For simplicity only the inversion layer on the p-type base of an n-p-n transistor will be considered. A magnified view of the edge of the device might be as shown in Fig. 5. The positive ions induce an electron-rich inversion layer or "channel" on the base and in effect extend the collector region out over the base. The channel represents a grossly different surface than existed before. Since the junction between the electron-rich channel and the base material constitutes an extension of the collector-base junction, it contributes to the collector saturation current. In part this is simply because of the extra junction area. More importantly, because the channel junction is very close to the surface, the surface generation process can yield much more current per unit area than for the junction in the bulk. Furthermore, if the

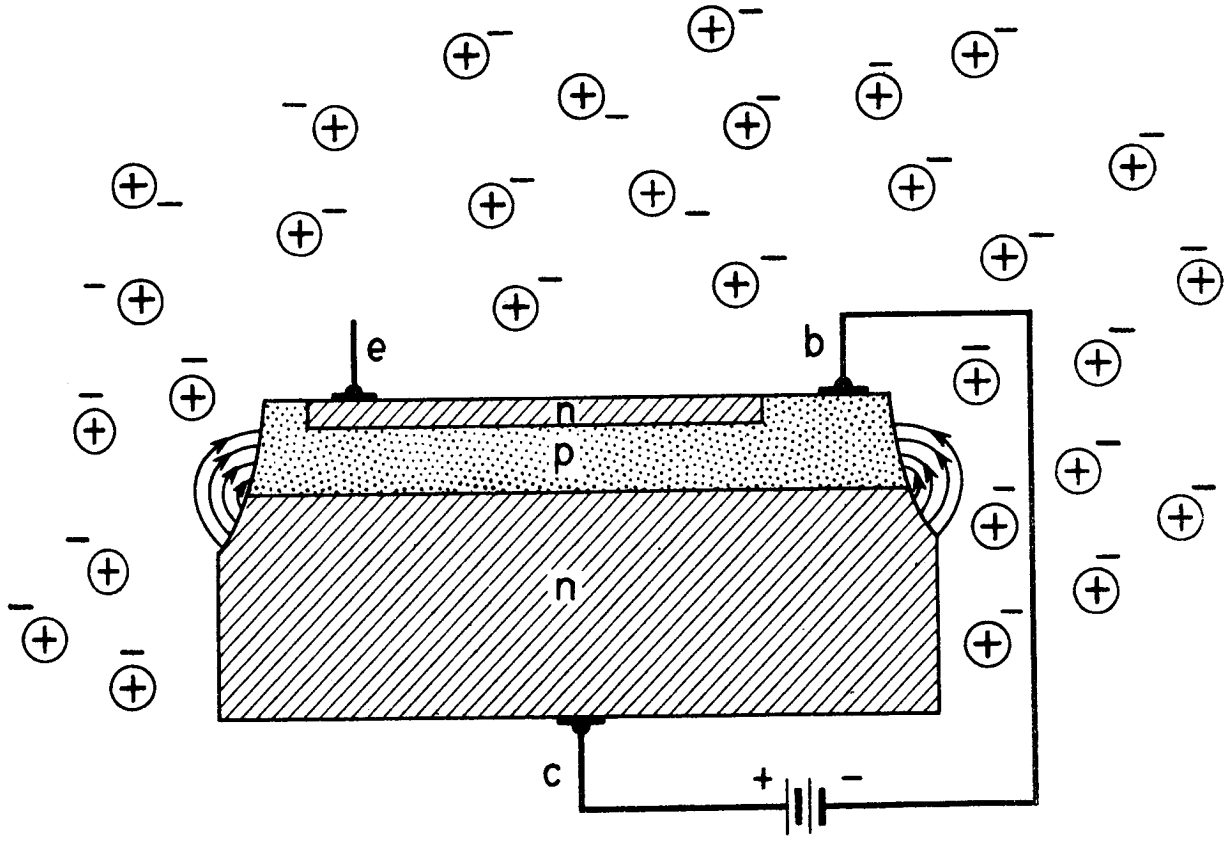

Fig. 4.

A model of a reverse biased transistor in a gas atmosphere ionized by radiation.

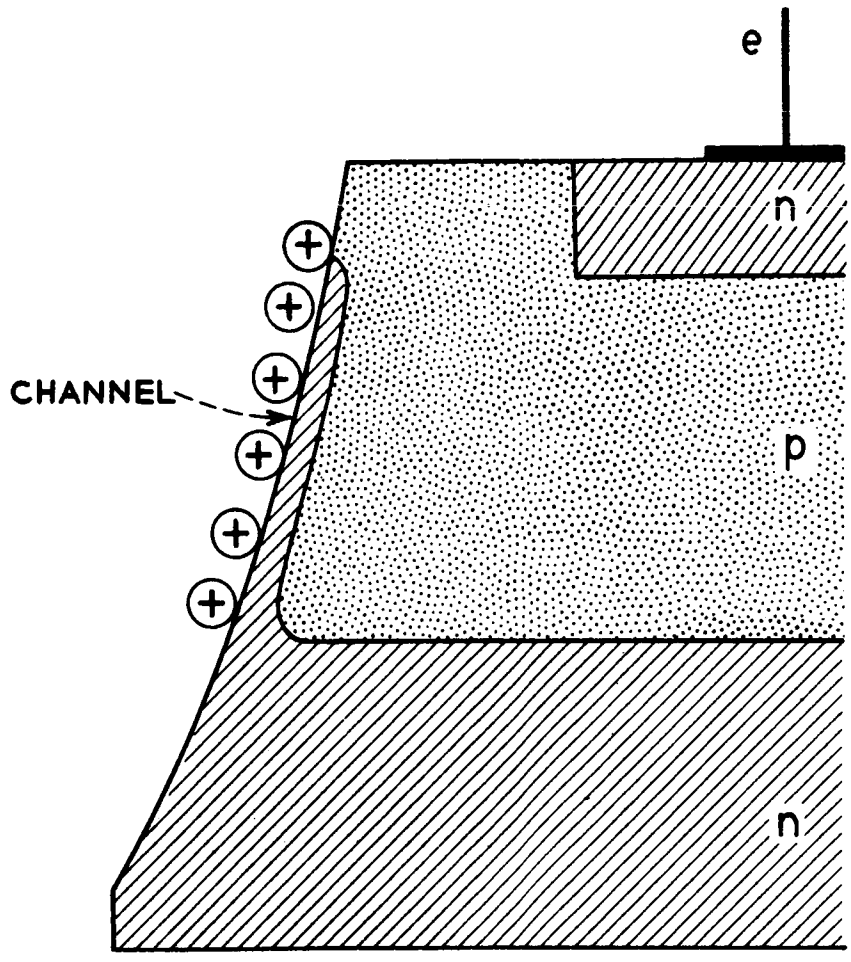

Fig. 5

Formation of a channel on the base of a transistor by + ion collection on the surface.

channel extends to the emitter it can add additional current to the collector by serving as a conducting path between the two. Channel effects on transistors and diodes have been studied previously in considerable detail[8] entirely unrelated to the presence of radiation. The basic channel characteristics of emitter-to-collector conductance, high emitter floating potential, and channel pinchoff have all been observed in connection with the present surface radiation effects on diffused silicon transistors.

We have so far considered only formation of a channel by charge collection in the collector fringing field, but a second possibility is shown in Fig. 6. In all the n-p-n diffused silicon transistors used in these experiments the collector is electrically tied to the encapsulating can of the device. Under collector reverse bias a field then exists throughout the whole can and of such a sign as to drift positive ions toward the surface of the device base. This feature can be expected to increase the ion-collection efficiency.

One may ask if there are enough ions produced in the gas of the can, by the radiation doses that have been used, to provide large channel effects. At an integrated dose of 10^4 rads (at which these effects may be substantial) and at atmospheric gas pressure (the normal device filling) a total of about 2×10^{13} ions per cc will have been produced. With a device enclosure of about 3×10^{-3} cc and a base layer area of about 10^{-3} cm^2, if all the ions were collected on the base, their concentration would be about $10^{14}/cm^2$. On typical base

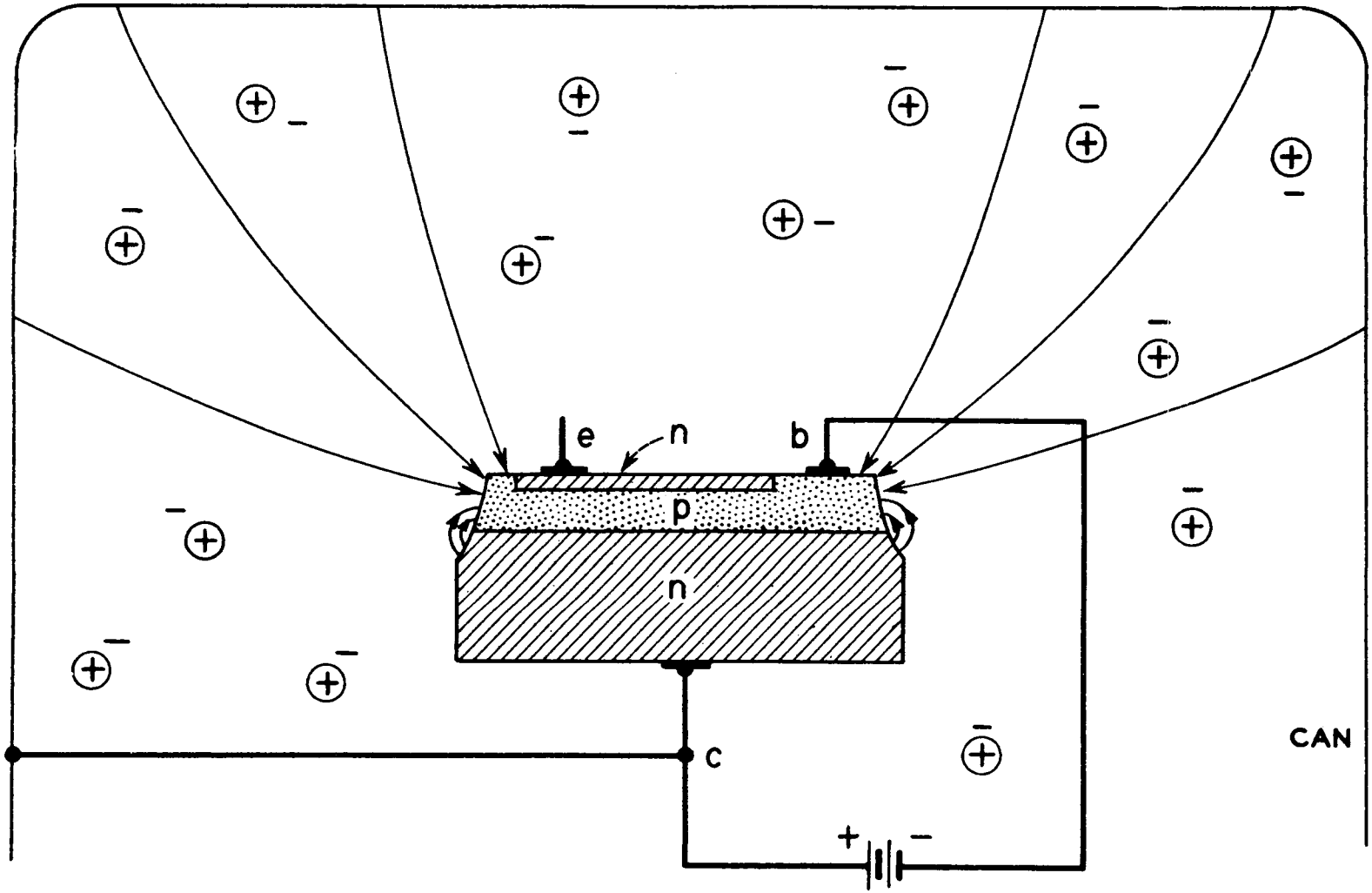

Fig. 6

The enhancement of ion collection at a transistor surface due to electron fields between the device and its encapsulating case.

material only about 10^{11} surface charges/cm^2 will be required to produce a channel. These several orders of magnitude margin are probably quite important because the efficiency of the surface charging process seems likely to be quite low. Furthermore, the process is far from a perfect charge integrator as we shall have occasion to observe in connection with reciprocity experiments in Section V.2.

The lack of reproducibility noted in Section III in connection with devices of the same type and same gas filling seems to necessitate an elaboration on the model. If ions of the gas are sufficient to produce a channel, why are there some devices with gas that are as stable as devices without? The gas ions themselves must not be the tenacious charge on the surface that forms the channel. The gas ions probably exchange their charge with residual contaminants on the device surface. Ionization of the surface contaminants directly is apparently too rare to be observed, since vacuum encapsulated devices show uniformly high surface stability. This is roughly reasonable since the probability of ionization of any single atom is estimated to be only about 10^{-5} at 10^4 rads. Even with a monolayer of residual surface contamination, the surface ion concentration would then be only about $10^9/cm^2$. Of course, if the gas ions are to do the job, they must be reasonably effective in finding and exchanging charge with the residual impurities. There seems to be margin for inefficiencies in these very rough numbers.

This model predicts a number of effects that can be tested:

1. The effect depends only on ionization, not on incident particle type.
2. The simplest form of the model suggests that the effect is cumulative and depends on total dose, not on dose rate.
3. The effect should be more pronounced at higher collector bias.
4. The electric field between the can and the semiconductor may influence ion collection.
5. The decay of the effect should be faster if the device is not under continuous bias and should be accelerated in the presence of radiation without bias.

The results of the experimental tests of these predictions are contained in the following section.

V. Tests of the Model

V.1 Ionization

If the ionization in the gas of the device encapsulation is essential, then just as in the case of the ionization effect in a semiconductor discussed in Section II.1, the type of energetic particle should not matter. The experiments in Section III were carried out with Co^{60} gamma rays which ionize through photo or Compton electrons that they produce. We have tested the model by comparing the results of 18 Mev proton irradiation with the Co^{60} gamma rays. The individual device response scatters so widely that the behavior of a number of similar devices is examined in each case. Figure 7 shows the collector reverse current versus radiation dose, for gamma rays in dashed lines and protons in solid lines. The dose is calculated simply from the amount of energy deposited in a gas (the gas of the encapsulation) by gamma rays and protons. The radiation intensity (dose per unit time) was approximately 10^6 rads/hr for the protons as well as for the gamma rays.

Within the spread of response observed, there is no significant difference between protons and gamma rays. If bulk damage in silicon were involved, one could expect a factor of 10 to 100 greater effect for the protons than for the gamma rays. (The bulk damage effect per particle comparing 18 Mev protons and 1.25 Mev gamma rays would be a factor of 10^4 to 10^5, but the scale in Fig. 7 is not particles but ionization, or energy loss, and the protons lose energy at a much higher rate

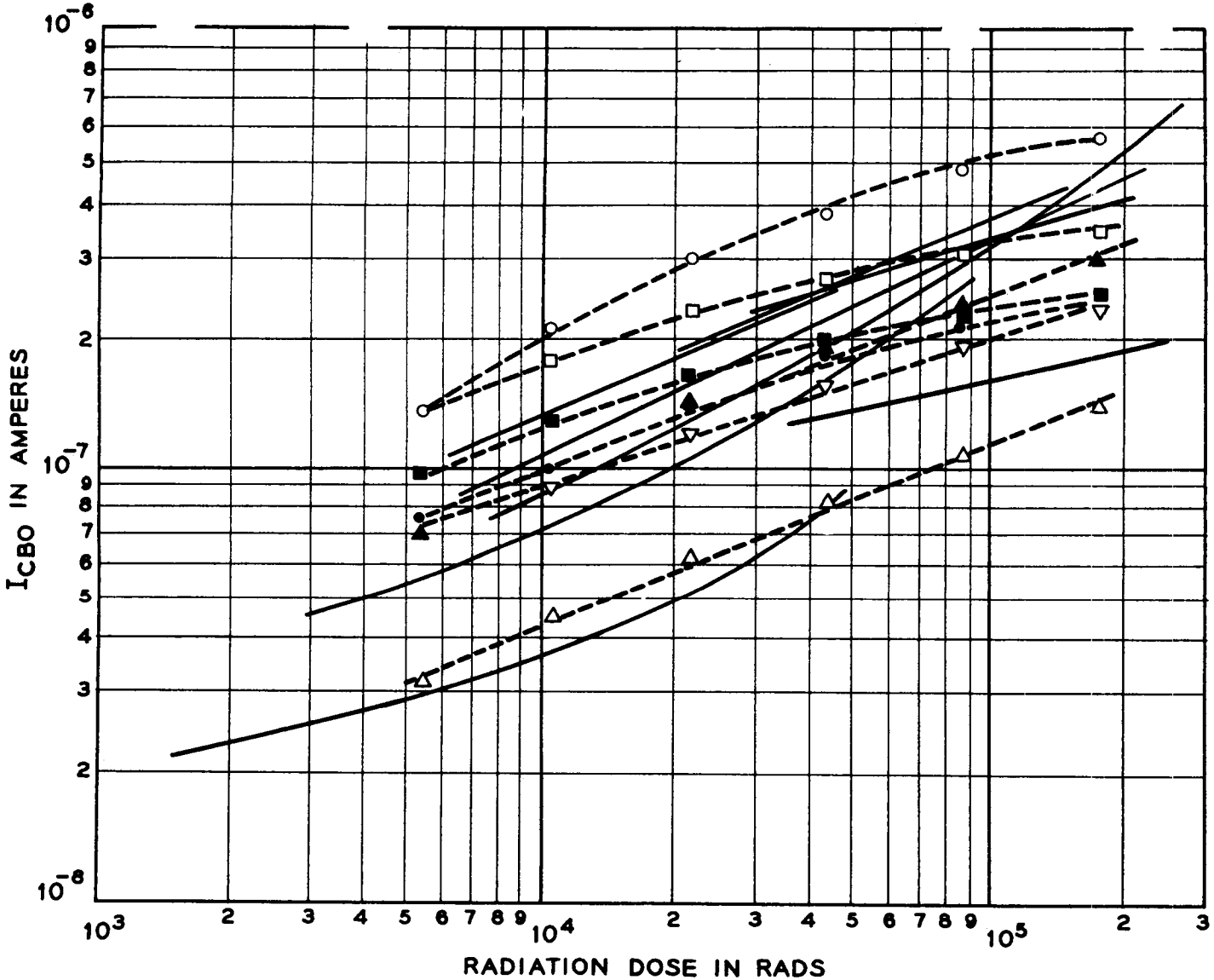

Fig. 7

Comparison of I_{CBO} changes under radiation by gamma rays (dashed lines) and protons (solid lines).

than gamma rays.) We conclude that ionization is essential to the mechanism of this surface radiation effect.

V.2 Reciprocity

The surface ionization effects may depend only on the total radiation dose or they may also depend on the dose rate. In the first case there is reciprocity between dose rate and time. Information on this point is relevant to understanding the process and is of immediate practical importance as well. The experiments are most easily performed at high dose rates, but the device reliability is also of concern in modest radiation fields.

In Fig. 2 recovery of the collector current following radiation was illustrated. The fact that recovery occurs at all when a device is removed from radiation but kept on bias proves that the observed result does not depend solely on the total dose. The ionized state of the surface at any time is not simply related to the total number of ions that have reached that surface.

Figure 8 shows the change of collector current vs. dose at two different high dose rate levels. The experiment was started at 8.5×10^5 rads/hr. After five minutes, when a dose of 7×10^4 rads had been delivered, the transistor was placed inside a lead shield that attenuated the gamma radiation by a factor of six. When a dose totaling 2.5×10^4 rads had been given the device, the attenuator was removed and the higher level radiation continued. After each attenuator change,

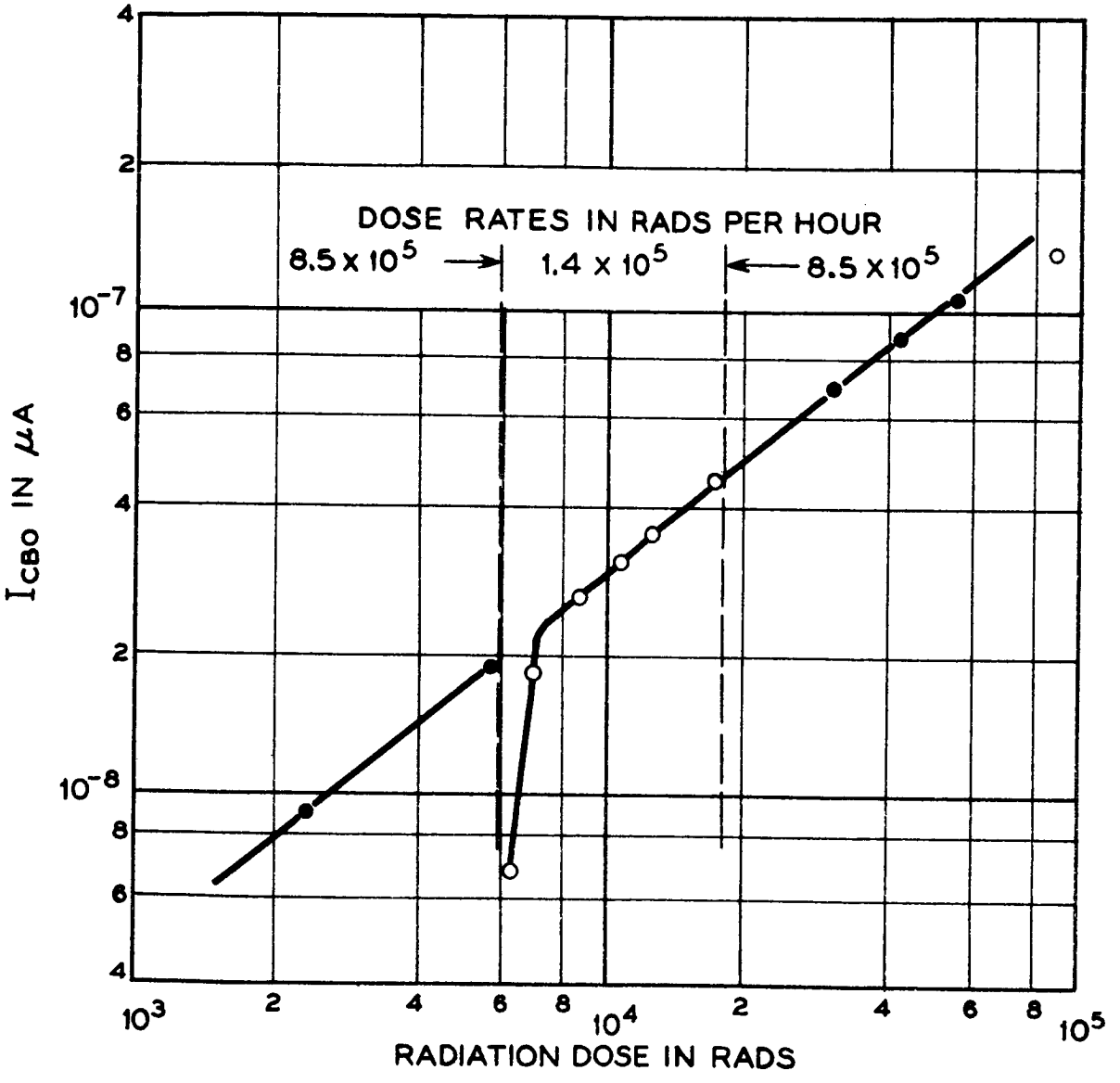

Fig. 8

Reciprocity of dose rate and time at two high radiation dose rate levels.

the collector current continues to rise in a smooth extension of the earlier portions of the curve. If the dose rate were important, the middle segment of the curve would be expected to have a different slope than the two ends. During the attenuator changes the device was out of the radiation for approximately a minute and the current had started to recover, as indicated by the first point taken at the lower dose rate. A comparable drop would have appeared at the second attenuator change, but the earliest measurement after reinsertion in the radiation field was not obtained soon enough for it to show.

The rapid re-establishment of a previous high response to radiation after some recovery from it, represents a memory in the process. This kind of memory has been seen repeatedly. Devices that were irradiated and have apparently completely recovered their original collector characteristics by standing out of radiation and even off bias, will still tend to re-establish their former response on a second radiation exposure. Even after several weeks, a device seems to retain a sensitivity to subsequent radiation as a result of an earlier exposure. There is some evidence that the memory can be removed by baking at approximately 100°C for a few hours.

The ionization produced by the radiation apparently has two functions: first, to produce some chemical species that are capable of ionization and second, to keep these species in an ionized state. The number of these centers would reflect the total radiation dose, but some minimum level of radiation would be required to keep them active.

We can draw the conclusion from Fig. 8 that, in the high-intensity region, dose is the important variable. Fig. 9 illustrates quite a different range. Here a device started its radiation history at only 10 rads/hr and established a pattern of current increase that is already determined at a dose less than 10^4 rads. Putting the device into the attenuated high-intensity source does not produce a simple continuation of the earlier curve, but rather produces a curve two and one-half orders of magnitude higher in current. This illustration is extreme and not many devices show this large a discontinuity, but essentially none give results that could be interpreted as simple reciprocity. Apparently over a dose-rate range this great, using the concept of the preceeding paragraph, the ionization-sensitive chemical entities are not fully ionized in the low radiation field.

5.3 Surface Effect vs. Collector Bias

Since the surface effects we have been considering are absent except under the simultaneous application of radiation and collector reverse bias, we expect to find that changing the bias will alter the effect. This can occur because of increases in efficiency of charge collection, but also because the increased junction field tends to bind the ions more tightly to the surface or distribute them to form a more extensive inversion region.

Figure 10 shows the effect of a sudden change in bias from 5 to 15 volts. One gains the impression that the

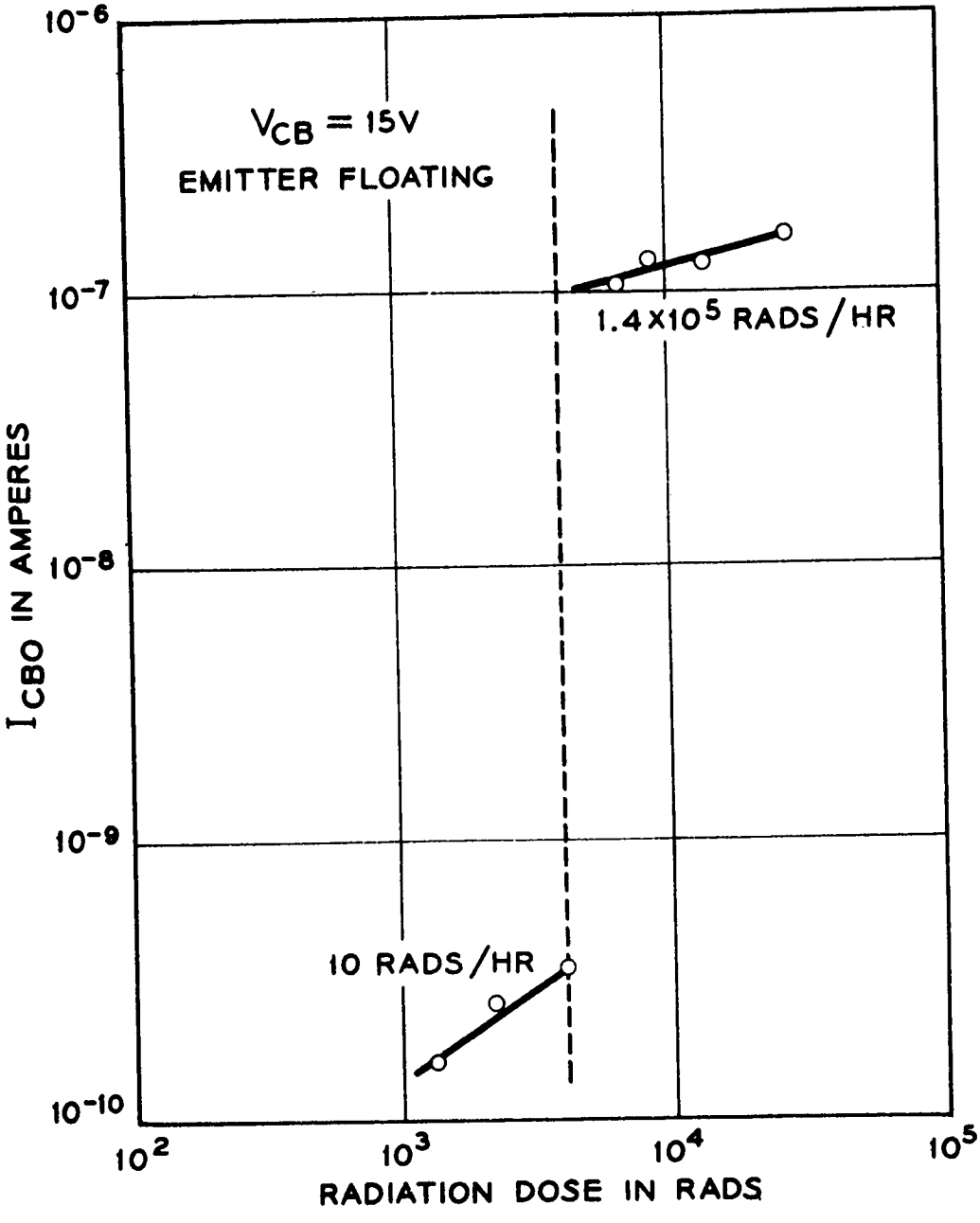

Fig. 9

Lack of reciprocity between high and low dose rates.

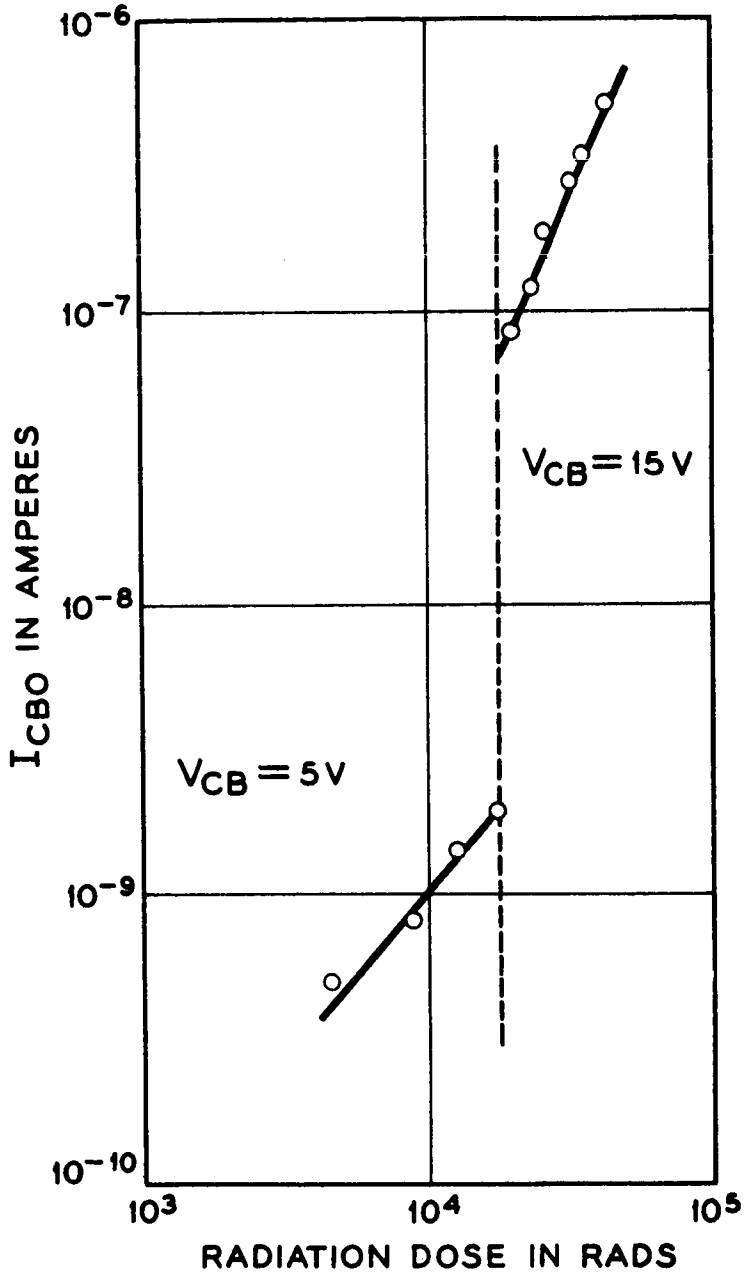

Fig. 10

Influence of change in collector bias on degradation of I_{CBO}. Dose rate 8.5×10^5 rads/hr.

current suddenly adjusts to a level and to a rate of change that are what they would have been if the entire dose had been given the device at the higher bias. If this impression is valid it would indicate that the effect at higher bias had not been retarded by the initial dose at low bias, and hence that ion collection was no different. In a plot like Fig. 10 it must be realized that the significance of the first dose rapidly diminishes in comparison with the total as one moves out along the second branch of the curve. It does seem possible to infer that a given number of ions on the surface give a larger current contribution at higher bias. Rearrangement in the new field and effective extension of the length of a surface channel can occur.

Figure 11 shows the response of transistors under radiation at different biases. Up to a dose of about 10^4 rads the current increase depends strongly on bias. Between 10^4 and 10^5 rads the slopes of the curves on this log-log plot are quite similar. Although only 4 units are illustrated in Fig. 11, the total group in the experiment was 80 and this pattern of behavior was quite consistent. Even beyond 10^5 rads where the slopes increase there is considerable uniformity between individuals and across the voltage range. This point is illustrated in a different way in Fig. 12 where the median behavior of a group of 10 to 12 devices at each bias is plotted at 6×10^3 rads and 6×10^4 rads. The pattern of bias

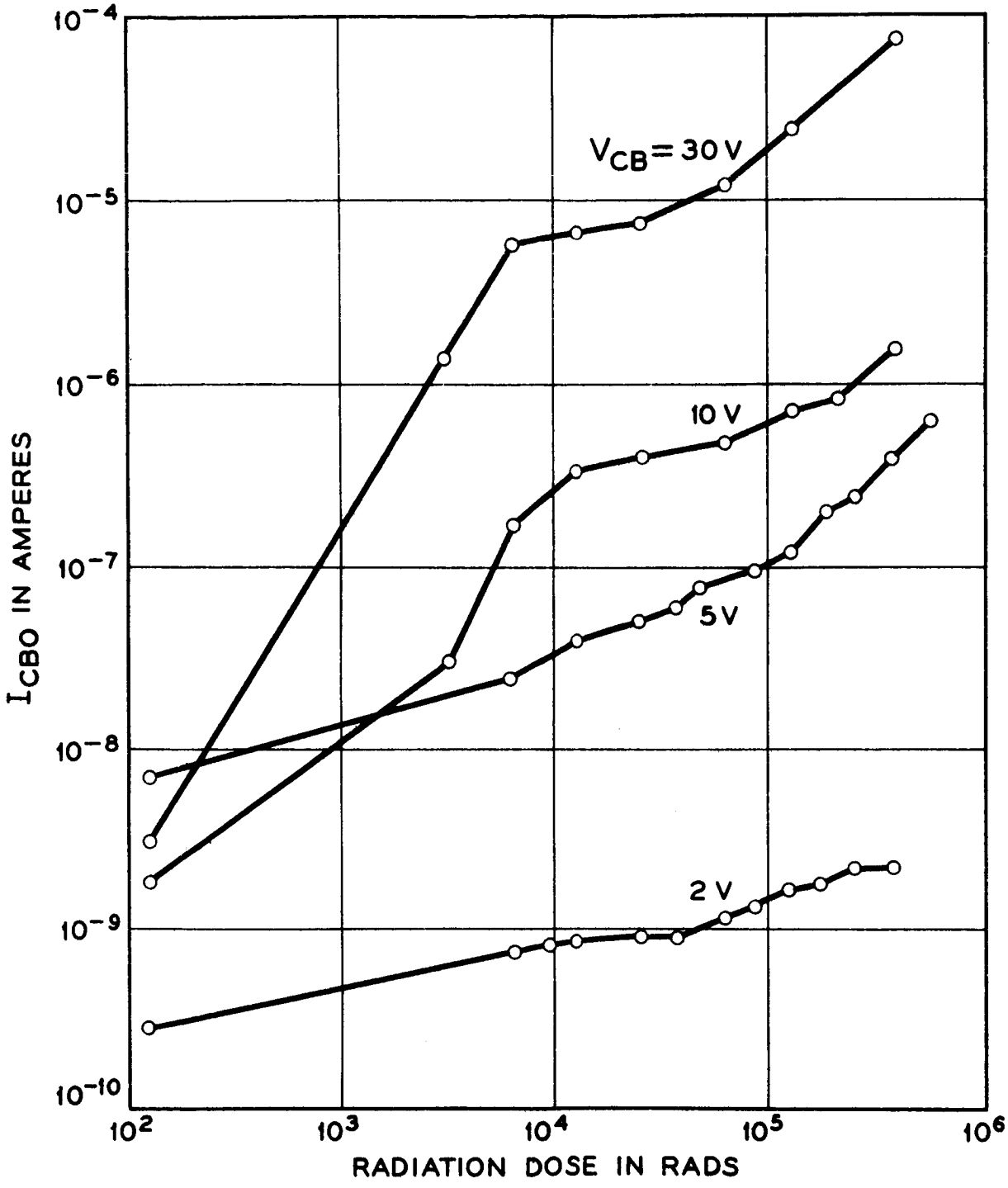

Fig. 11
Dependence of degradation in I_{CBO} on collector bias.

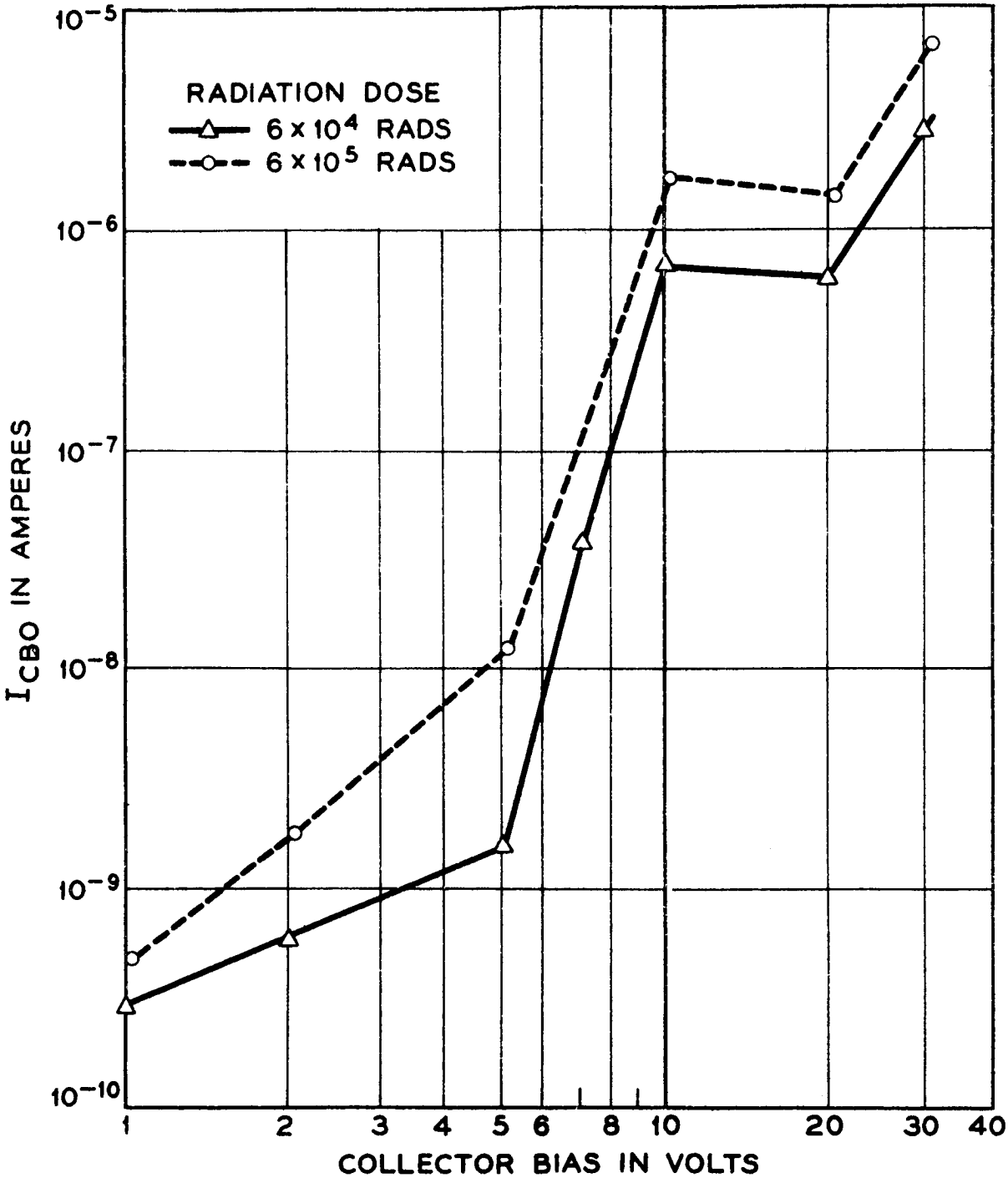

Fig. 12

Median behavior of I_{CBO} with collector bias at two integrated doses.

dependence is already established at the lower dose and is smoothly maintained after the further order-of-magnitude change in dose. The lump at 10 volts appears to be significant. If it is real, its explanation will require a clever refinement in the model.

We do indeed observe the anticipated increase in device degradation at higher bias. The consistency of the shape of the voltage dependence at doses greater than 10^4 rads strongly suggests that the dependence does not arise only from a difference in the numbers of available surface ions, but also from variation in the arrangement of ions and the influence of this arrangement on the current characteristics of the channel. The collection of charge does not seem to be the dominant variable over the voltage range examined.

Another indication that junction bias effects the arrangement of charge on a device surface is shown in Fig. 13. The characteristics observed after a total dose of about 10^7 rads and at a high dose rate may show considerable structure, depending on the rate at which the characteristic is swept out. Furthermore, the differences between the characteristics with slow and fast sweep show that rearrangements are not instantaneous. Note that here also a peak of I_{CBO} occurs in the vicinity of 10 volts.

5.4 Influence of Can Potential

It has been suggested that the electric field existing between the can and the transistor base by virtue of the bias on the collector junction may alter the collection of ions at

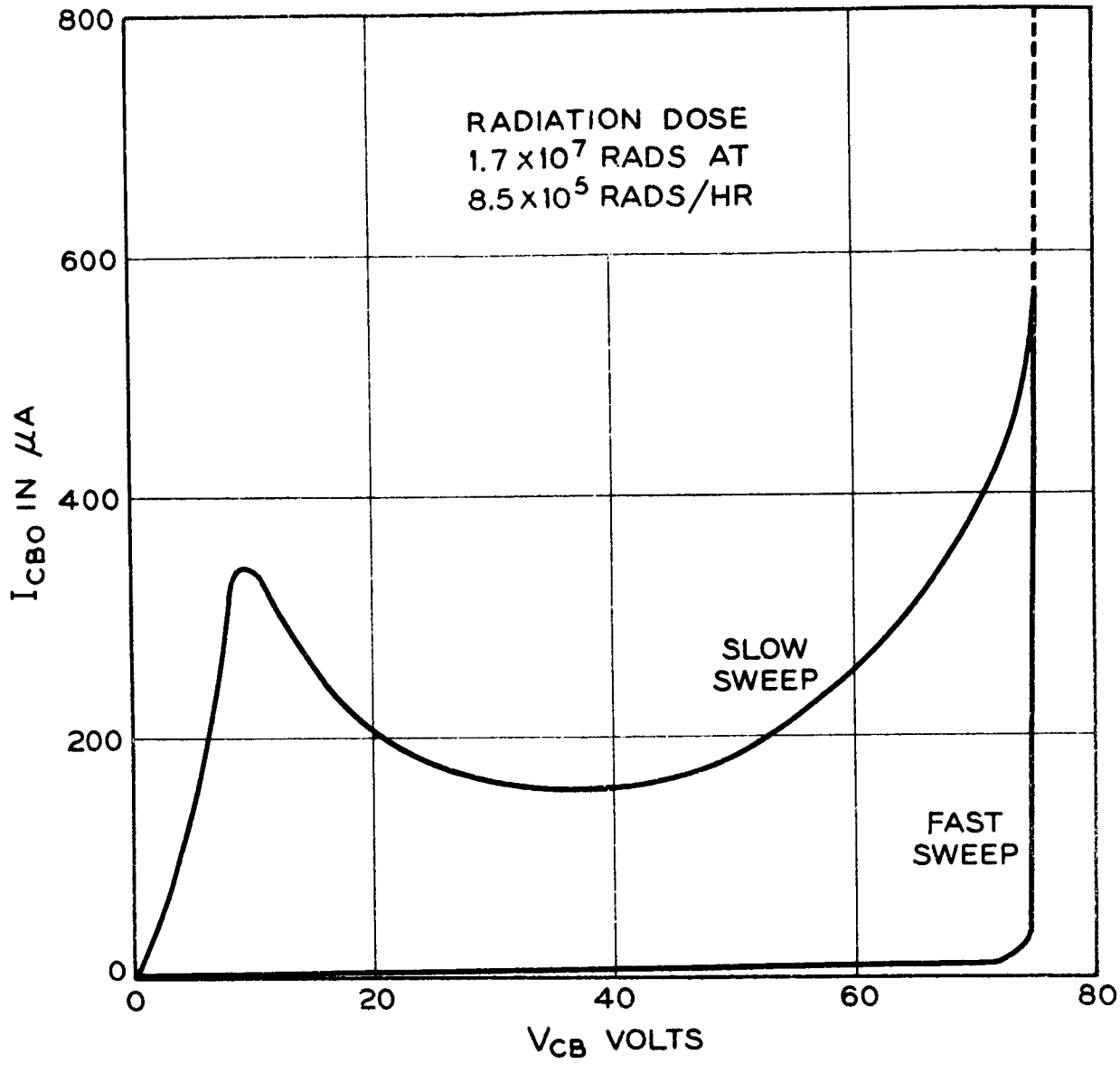

Fig. 13

Structure and drift in the reverse characteristics of a heavily irradiated transistor under radiation.

the semiconductor surface. This possibility has been examined using diffused silicon diodes, encapsulated in the same gaseous atmosphere as the diffused silicon transistors. Devices with the p-region common to the can and others with the n-region common were studied. There was no substantial difference in sensitivity to ionization in these cases. On the other hand it was found that by alteration of the device processing, devices of either polarity were insensitive. It is clear that in this case the chemical surface condition is of more vital importance than the can-to-diode bias.

No silicon transistor with reversible polarity to the can has been available, but a germanium transistor with all leads insulated from the can has been irradiated with reversal of the sign of can bias. The results are shown in Fig. 14. The device was irradiated at 8×10^5 rads/hr for one minute with the can negative with respect to the transistor base (the collector of which was continuously reverse biased) and then one minute with the can positive and so on for longer times as the irradiation proceeded. The leakage current is very clearly much more sensitive to positive potential on the can than to negative, a result consistent with the original picture of the role of positive ions in a channel on the transistor base. This experiment has been repeated several times with some lack of reproducibility. In some cases can bias makes much less difference than as shown in Fig. 14

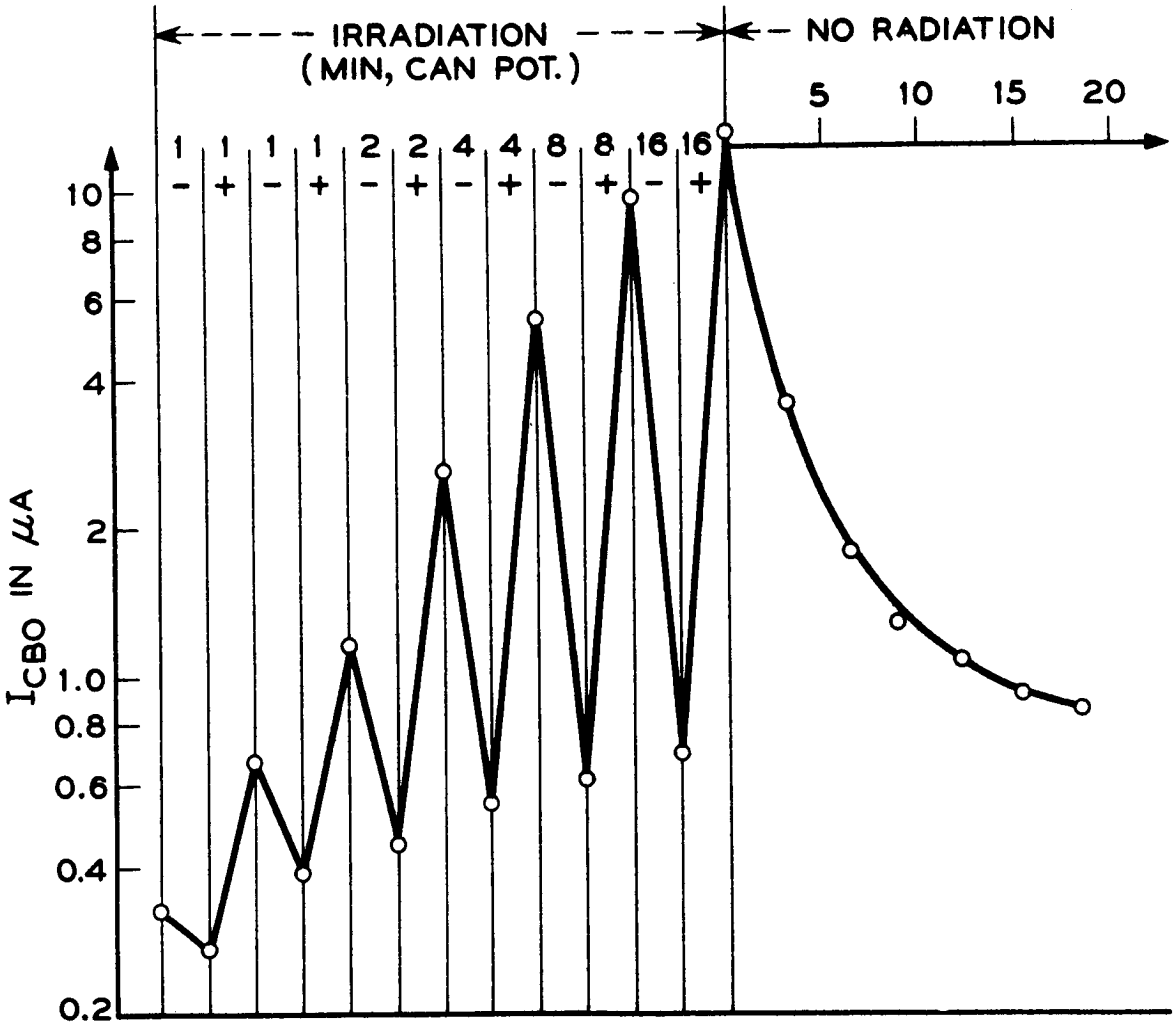

Fig. 14

The influence of the can to semiconductor potential on degradation in I_{CBO} of a germanium transistor.

and in two cases where the whole radiation effect was smaller, the dependence on can bias polarity was reversed.

There seems to be no question that the can-to-device potential can be important, but clear-cut evidence that positive ions rather than electrons (or negative ions) are always the important particle in transistor surface ionization effects has not been demonstrated.

5.5 Recovery

Recovery of the surface effects after an exposure to radiation has already been mentioned in connection with Figs. 2 and 8. The recovery is not exponential. In many cases, recovery under bias is well represented by a straight line on a log I_{CBO} vs log t plot, although the points at less than 0.5 min tend to fall below such a curve. The recovery represents a loss of charge at the surface, perhaps by neutralization from the interior in the absence of a radiation flux, but the memory effects suggest the active species do not actually leave the surface.

The comparison between recovery with and without bias is shown in Fig. 15. A transistor given a dose of 4.6×10^3 rads at 5 volts is shown, first recovering at this same bias and then recovering with the collector circuit open except momentarily for measurement. The decay is substantially accelerated in the zero bias condition. This is consistent with the idea that the ions are bound in place by the field but in its absence are free to diffuse on the

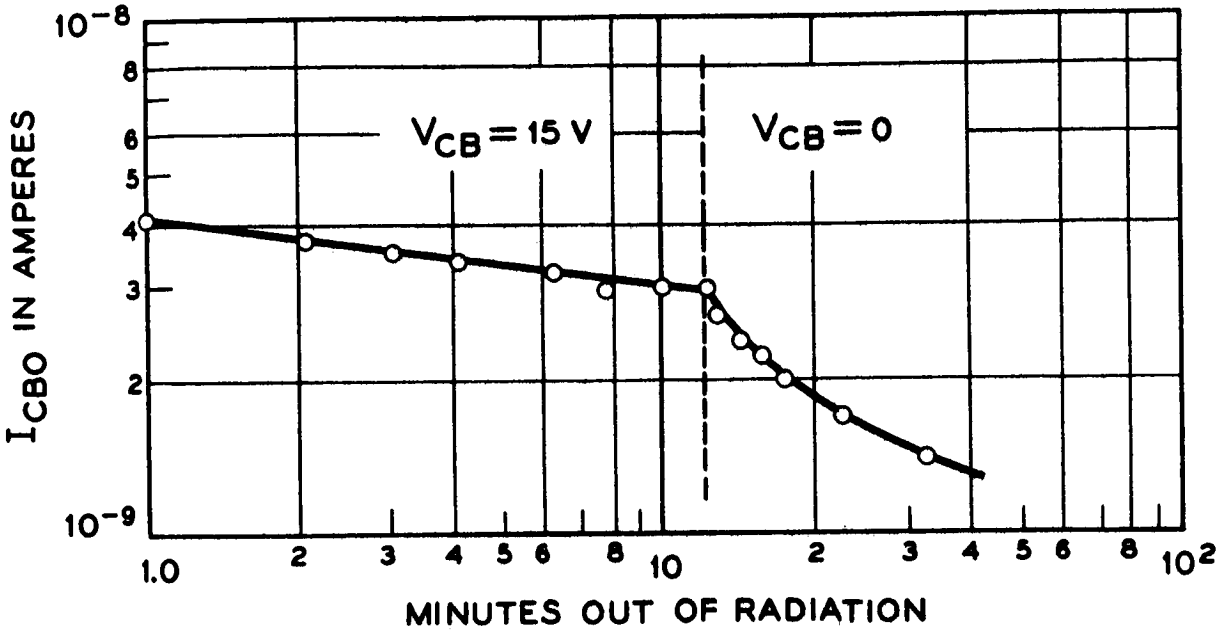

Fig. 15

Decay of the radiation effect with bias and without.

surface and will no longer be concentrated to produce an inversion layer. It has also been observed that with re-establishment of the bias the current rises before continuing its decay, suggesting that the ions are subject to recapture by the field. There is a loss in this process however, that may arise from the enhanced neutralization of the ions by electrons from the inversion layer when they are more numerous in the absence of reverse bias.

Figure 16 illustrates the effect of radiation on recovery. The upper curve was taken first and is a normal recovery with bias. The lower curve shows recovery from the same starting value in the 8×10^5 rads/hr gamma field without bias. The device is momentarily removed from radiation for measurement at 15 volts reverse bias. The recovery is substantially enhanced by the ionization in the absence of bias. This seems to be explained through neutralization of the charges on the semiconductor surface by the newly formed ions. Under bias the gas ions are directed by the junction field to strike the surface in places where they add to an inversion layer. In the absence of a field from applied bias, these ions tend to go wherever they can reduce fields produced by surface charges.

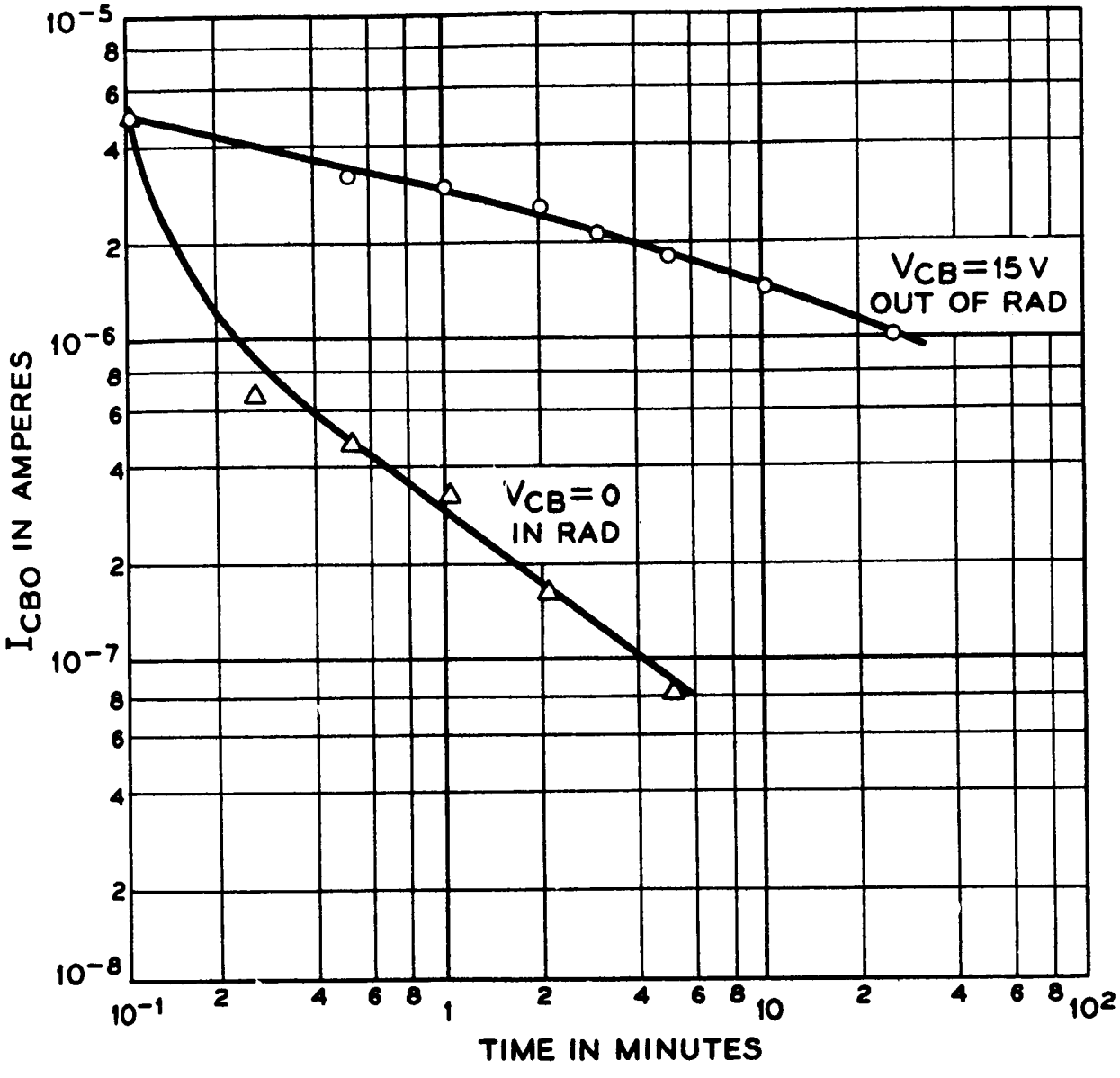

Fig. 16

Enhancement of the rate of recovery of I_{CBO} with radiation but without bias.

VI. Characterization of Effects with Significant Numbers of Devices

With the above background concerning the surface effects of ionizing radiation, and with recognition of the limited knowledge of the range of exact surface conditions existing in semiconductor devices, further tests were planned to establish the extent of the ionization effect in larger samples of devices. For the purpose of such a test program, a transistor type was selected which showed particular sensitivity to the combined effects of electrical bias and ionizing radiation. These transistors normally have quite low collector reverse currents, I_{CBO} (in the order of 10^{-10} amperes). They are therefore good subjects for study at relatively low gamma dose levels since small increases in I_{CBO} can readily be recognized. A large number of devices were available with sufficient power aging to indicate stability of characteristics, so that changes could clearly be attributed to the radiation exposure.

Although the measurements of gain of these transistors under gamma radiation indicate some change with dose, the changes are relatively smaller than those in the junction reverse current and are hence less subject to recognition of a specific pattern of change. The data presented here, therefore, relate specifically to the changes in I_{CBO}.

VI.1 Typical Pattern of Degradation with Dose

In order to determine the proper conditions for large scale evaluation, and to have some estimate of changes

to be expected, it is desirable to establish the pattern of change in characteristics. From the data presented in Section V on the various factors affecting degradation, there develops a typical pattern of degradation, at least for the type of diffused silicon transistor used, as shown in Fig. 17. In this log-log plot of I_{CBO} vs. integrated dose, four recognizable regions are indicated, an initial region of stability followed by three regions of change. The boundaries of the regions as indicated in Fig. 17 only depict representative variations and do not indicate actual limits of the device type.

As discussed in Section 5.3, the slopes of the degrading I_{CBO}'s become quite uniform among all units of this type beyond a total dose of about 10^4 rad, or beyond the variable Region 2. In Region 3 all units show slopes of approximately 1/2, and at about 10^5 rads there is a fairly distinct increase in slope, which distinguishes Region 4. Although these two regions are recognizable, they are of lesser importance in judging comparative usefulness of the devices in radiation than are the region of stability and the slope in Region 2.

The region of stability is indicated even in the early tests (see Fig. 3) and continues to show up, even at the lowest initial current levels, when the dose rate is low enough to allow measurements at sufficiently low total dose.

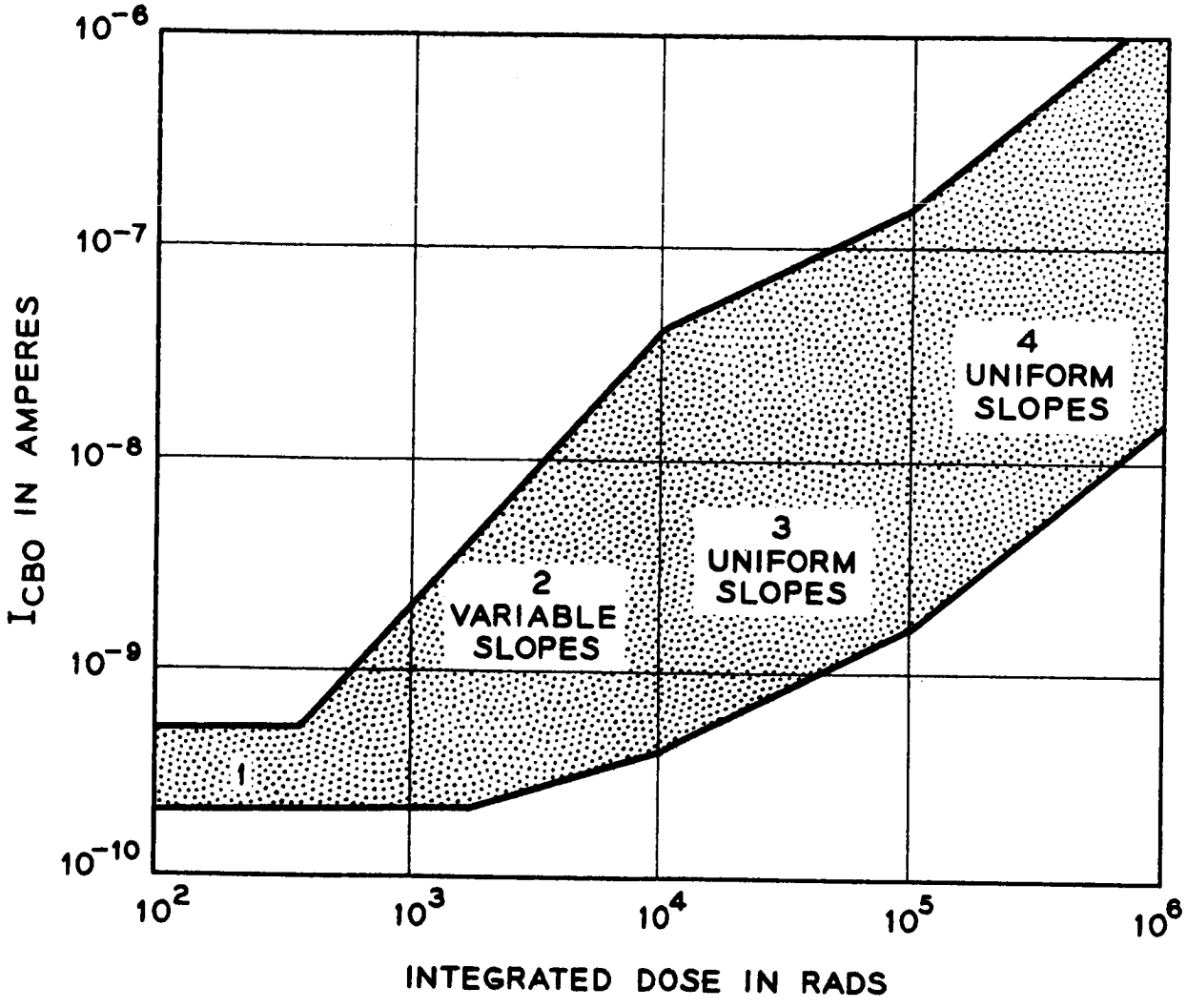

Fig. 17

The typical pattern of I_{CBO} degradation under radiation for a particular type of diffused silicon transistor.

The extent of Region 1, or the dose value at which an individual unit starts to degrade, is quite variable among units of a type, as well as between types, and is a significant point for further consideration of devices.

The transition into Region 2, where the units show a typical linear increase in log I_{CBO} with log of dose, is quite distinct in all observed cases. For this reason, data which show only the degrading slope in Region 2 (perhaps because a high dose rate causes the first measurement to be beyond Region 1) can be extrapolated with some confidence back to the preradiation value to achieve an estimate of the transition dose. Major features of Region 2 are extreme variations between individual devices of a type and considerable dependence on collector voltage. This dependence is shown in Fig. 11 by the variations in I_{CBO} values achieved at about 10^4 rad, apparently about the end of Region 2 for this type.

In general, there appears to be a consistency between Regions 1 and 2 in that those units which show the greatest change in Region 2 also tend to indicate the shortest period of stability in Region 1; and conversely, those showing smaller changes in Region 2 appear to have the longer period of initial stability. Within the range of actual initial values (from 8×10^{-11} to 2×10^{-9} amperes) however, there appears to be no correlation between the initial value and the subsequent severity of degradation.

VI.2 Distributions of Dose at Initiation of Degradation

With the recognition of the typical response of this transistor type to radiation, a question can first be asked regarding the variability in the extent of the region of stability, Region 1.

Figure 18 shows several plots of the distribution, on a normal probability scale, of the integrated dose at which degradation is initiated (the end of Region 1). The three lowest curves show the results obtained from exposure to gamma radiation at 8.5×10^5 rads/hr., 10 rads/hr., and 1 rad/hr., all with a collector bias of 15 volts and with no connection to the emitters. There appears to be only about a factor of 2 difference between the 8.5×10^5 rad/hr. and the 10 rad/hr. results. This evidence of reciprocity between the 8.5×10^5 rad/hr. dose and the 10 rad/hr. dose at the end of Region 1 is in contrast to the lack of reciprocity indicated in Fig. 9 which compares reverse currents in Region 2. On the other hand, the difference between the 1 rad/hr. and 10 rad/hr. distributions seems to indicate a breakdown of reciprocity, at this level, in the dose required to initiate degradation.

The two upper curves of Fig. 18 are obtained at 5 rad/hr. and with a forward bias on the emitters during radiation in addition to the reverse collector bias. One of these curves is on the same type (F-54273) as that of the lower distributions. The other distribution at 5 rad/hr. is

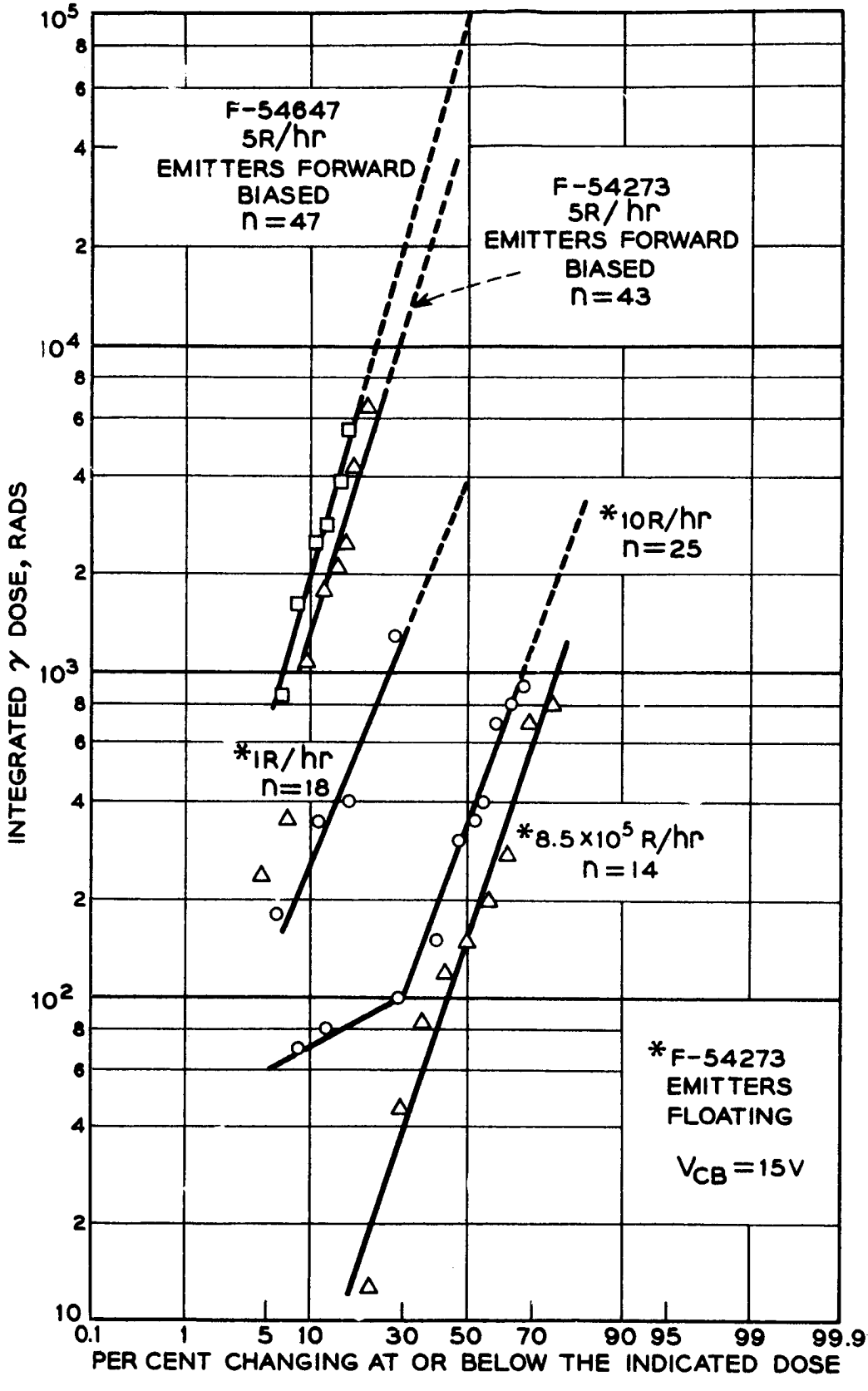

Fig. 18

Distribution of the radiation dose at initiation of degradation.

on another type (F-54647) which is basically the same but with a somewhat higher distribution of initial current gain. It would appear that the application of forward emitter bias causes an increase of roughly two orders of magnitude in the dose required for the onset of I_{CBO} degradation. This could result from the neutralization of positive charges on the surface of the base region by electrons injected into the base by the forward biased emitter.

VI.3 Distributions of I_{CBO} Increase

Figure 19 shows the distribution of the increase in collector reverse current resulting after 1.4×10^4 rads, which dose is past the completion of the variable Region 2. Here the I_{CBO}, on a log scale, is plotted on the normal probability scale. These data are on the same types of units represented in Fig. 18 and are obtained from radiation with the emitters forward biased. As in Fig. 18, the higher-gain type evidences a lesser degradation, having a longer region of stability as well as a smaller increase in I_{CBO} during Region 2. The excellent match to a log-normal distribution (except at very low currents where the data reflects the inaccuracy of measuring the difference between two nearly equal numbers) lends confidence to the interpretation that the break at the upper end of the distribution is caused by the transition into Region 3 of those units which have changed the most in the variable Region 2.

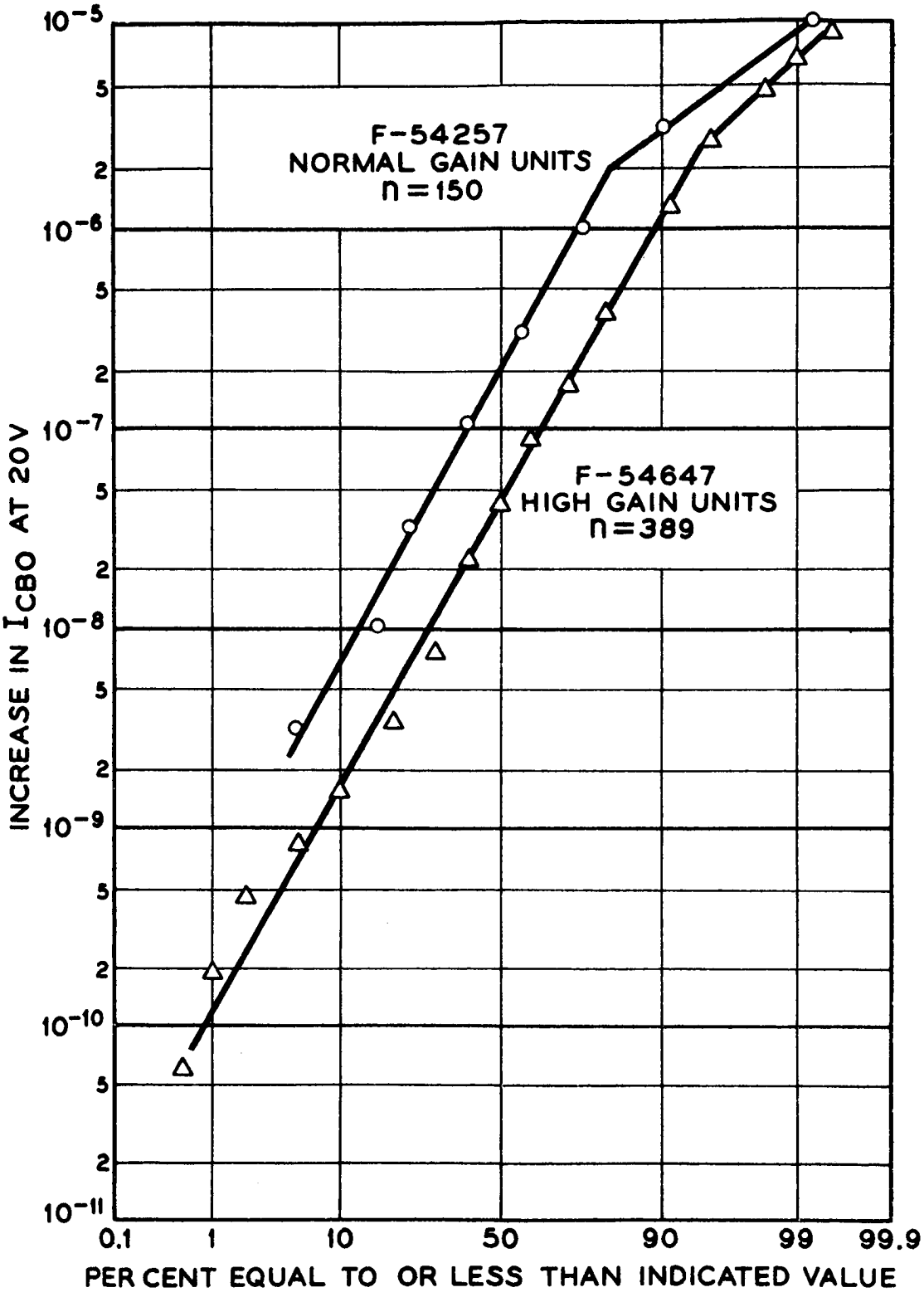

Fig. 19

Distribution of current degradation after a dose of 1.4×10^4 rad at 8.5×10^5 rads/hr.

The broad distributions of Figs. 5, 18, and 19 point up the necessity for relatively large-scale experiments in order to make valid comparisons between different test conditions or device types.

VI.4 Tests of Other Semiconductor Devices

Similar kinds of distributions and general responses to the various conditions affecting degradation under radiation have been found in other codes of diffused silicon transistors and silicon diodes which have been encapsulated with a gas filling.

Figure 20 shows, for example, the distribution of reverse current increase of a 1/4-watt diffused silicon diode after 3.7×10^4 rads at 7.4×10^5 rads/hr. The broken shape of the distribution may simply indicate that the devices did not come from a single product run. The lack of the distinct break in the distribution at high currents suggests that the transition to Region 3 may not exist, or exists at a different dose. It would appear that each type must be examined in detail for a good understanding, even empirical, of its performance under radiation.

One interesting variation to the kind of response indicated above is that of a type of silicon alloy transistor which contains a silicone grease. In this case a relatively minor degradation is observed during short periods at a high gamma dose rate, but more severe degradation occurs during

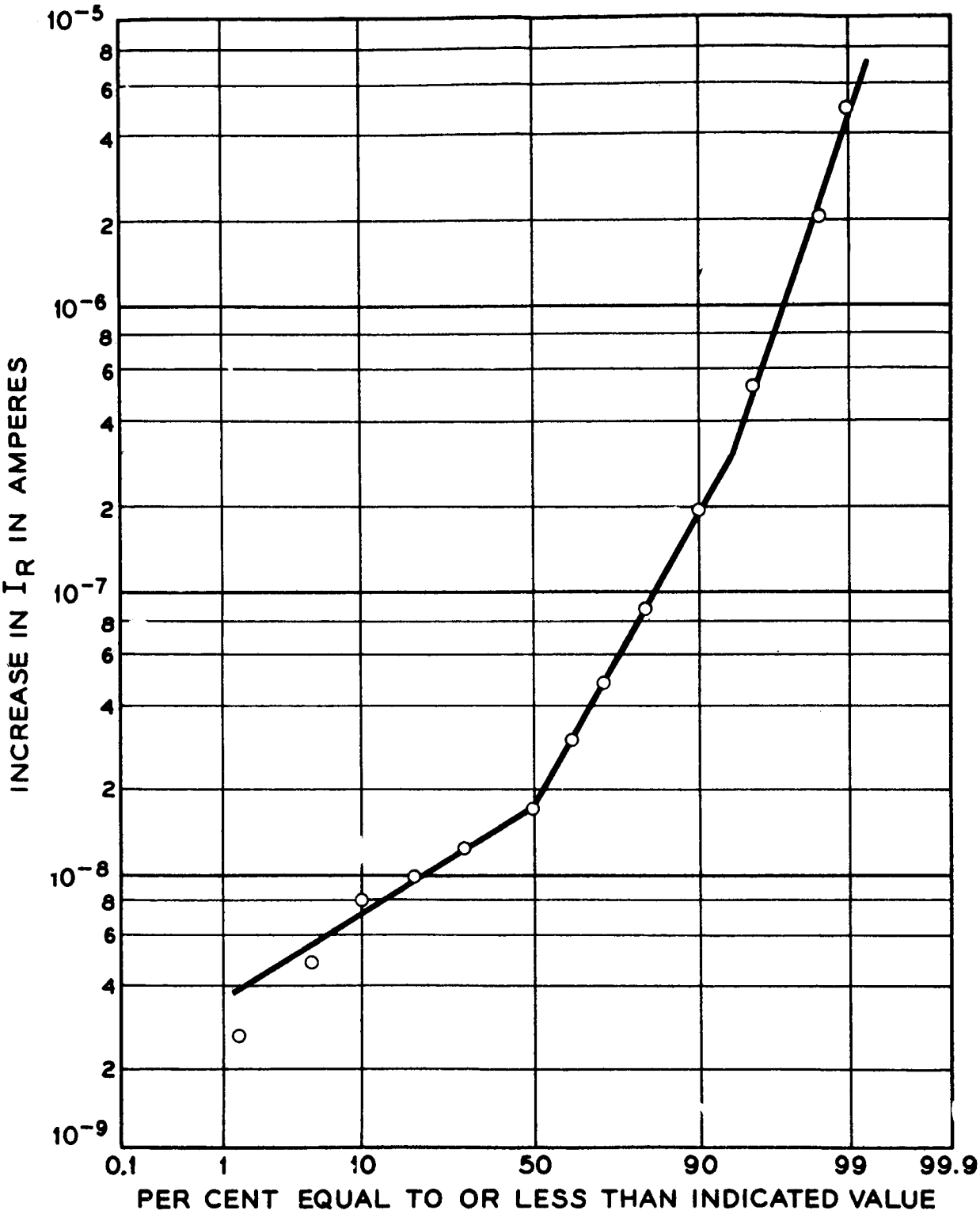

Fig. 20

Distribution of degradation of current in a type of diffused silicon diode at 3.7×10^4 rads.

the period subsequent to completion of the exposure. This is indicated in Fig. 21, a plot of collector reverse current vs. time after repeated exposures on an individual device. The device was exposed for several consecutive periods at 1.4×10^5 rad/hr, with current measurements subsequent to each exposure. The procedure was then continued at 8.5×10^5 rad/hr. Here each curve represents the I_{CBO} measurements subsequent to radiation for the total time indicated on the curve. I_{CBO} increases subsequent to the exposure, but may actually be decreased during the next exposure. After sufficient exposure, the devices evidence a saturation of the subsequent I_{CBO}, and also a saturation of the effect with continued exposure.

This saturation effect is confirmed at the 5 rad/hr. dose rate in Fig. 22, showing the I_{CBO} curves vs. integrated dose for two typical transistors of this type. Both show an eventual saturation of the curve and one shows an ultimate reduction which appears also to be typical of this type of transistor.

Several types of diffused germanium transistors have also been examined, with the general result that increases in I_{CBO} are relatively small (of the order of a factor of 3 or 4), and relatively consistent, until the dose reaches about 10^6 rads, where more drastic increases may be expected. The dependence on V_{CB} was relatively insignificant.

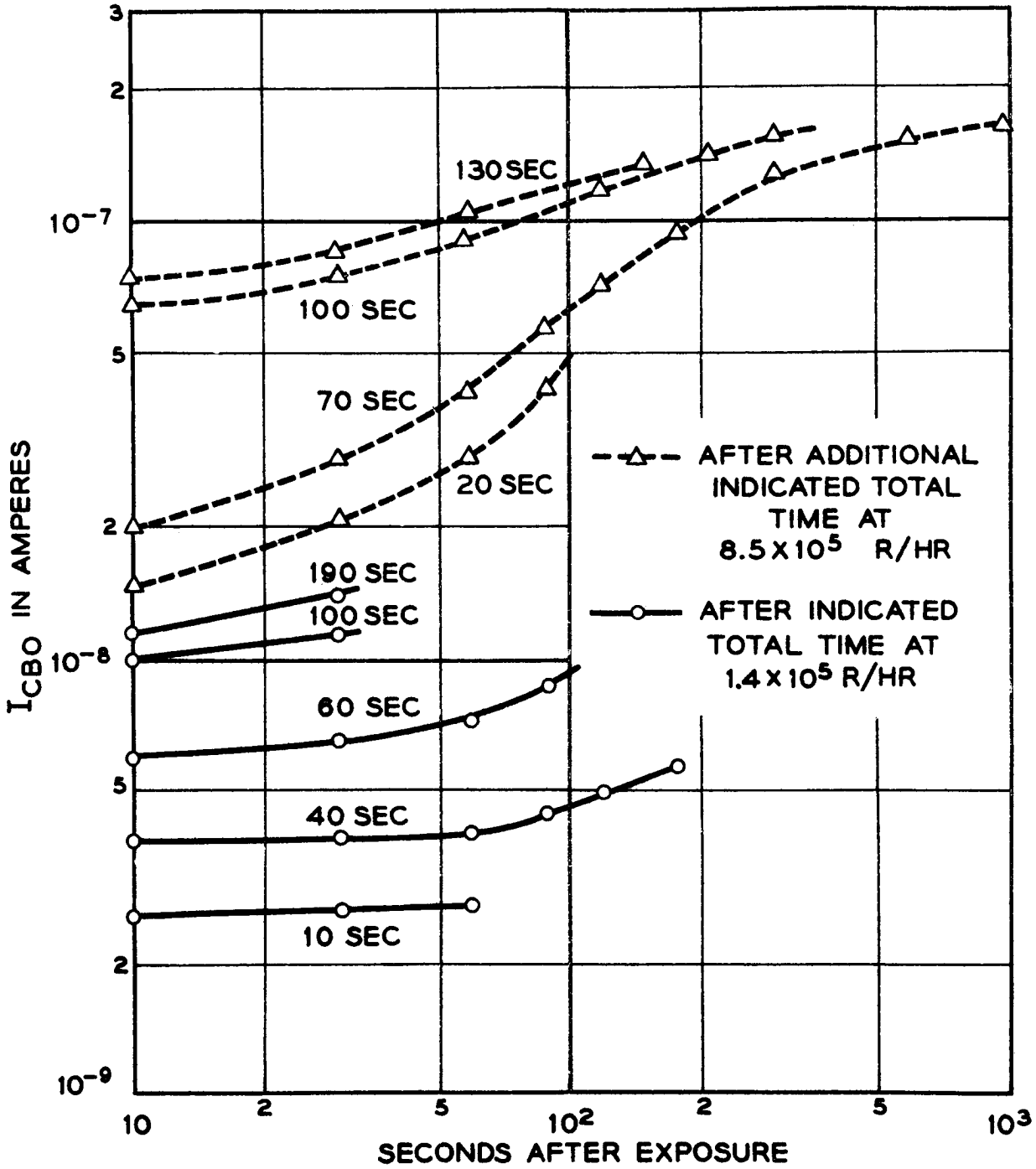

Fig. 21

The pattern of collector current response in a grease covered silicon transistor.

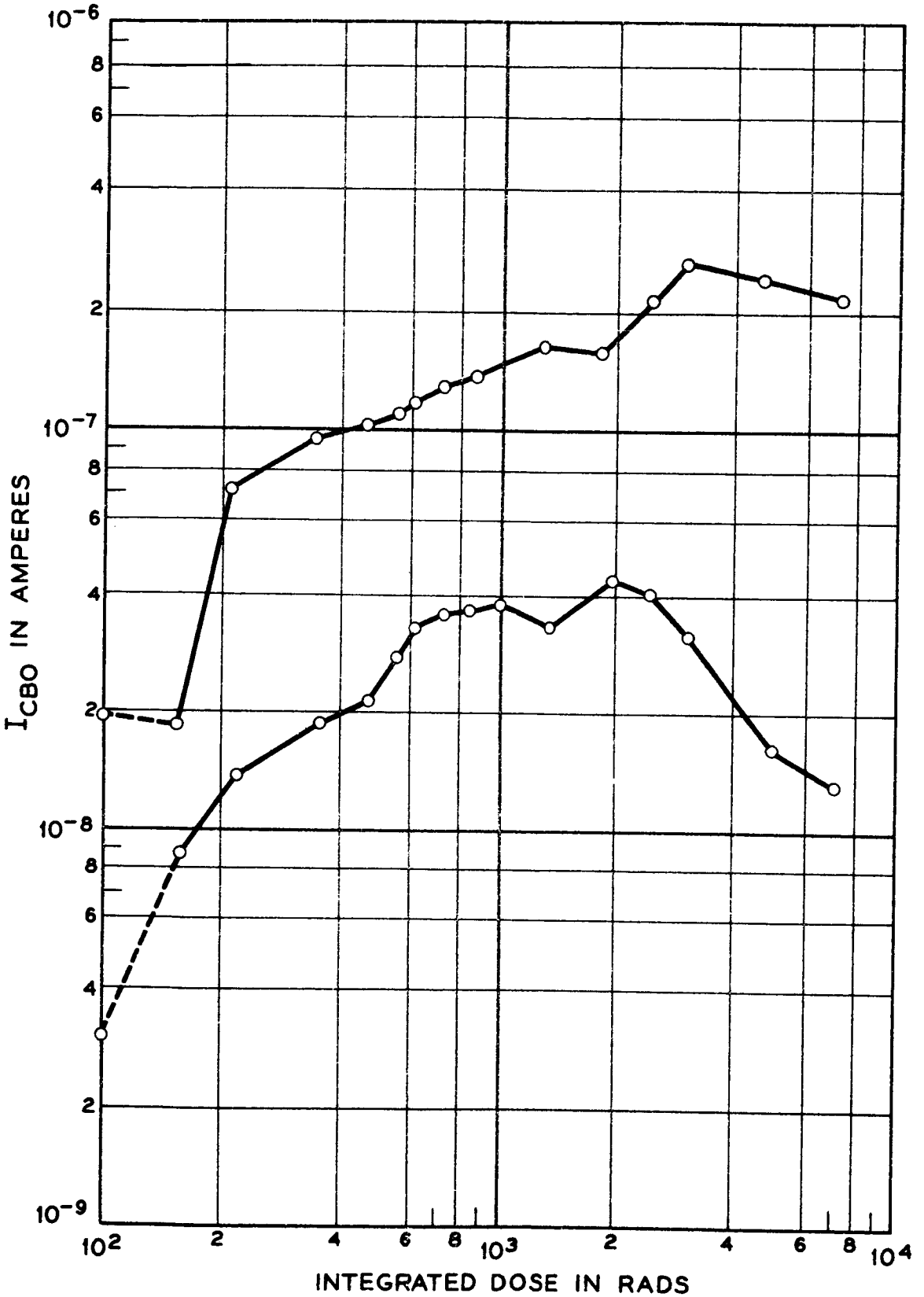

Fig. 22

The response of a grease covered silicon transistor under prolonged radiation at 5 rads/hr.

The effect of processing is evident in these types, however, with one group showing marked changes at about 10^4 rads, and another group having essentially no changes at 10^7 rads.

VII. Testing and Selection for Telstar Devices

The process of selecting the semiconductor components for use in the Telstar experimental communication satellite consisted of:

1. Qualification of design for reliability and performance as required in each application,
2. Fabrication,
3. Screening and preaging to assure satisfactory operation in the system environment,
4. Life testing,
5. Selection of the most stable devices.

At the time of recognition of surface effects from ionizing radiation (about October 1961), much of the life testing was already in process. Since the Telstar satellite was to orbit through the Van Allen radiation belt, the addition of radiation as an environmental factor was essential. Steps were therefore taken to determine the qualification of all types in the program and to study the screening and selection techniques that would be useful.

Figure 23 shows a plot of the estimated ionizing radiation intensity for components inside a satellite, as a function of the shielding of the components from the external environment. These curves refer to the ionization produced by protons only and were developed from existing estimates of the Van Allen belt particle fluxes. The upper and lower limit curves reflect the uncertainties in this estimate. For shielding thicknesses of

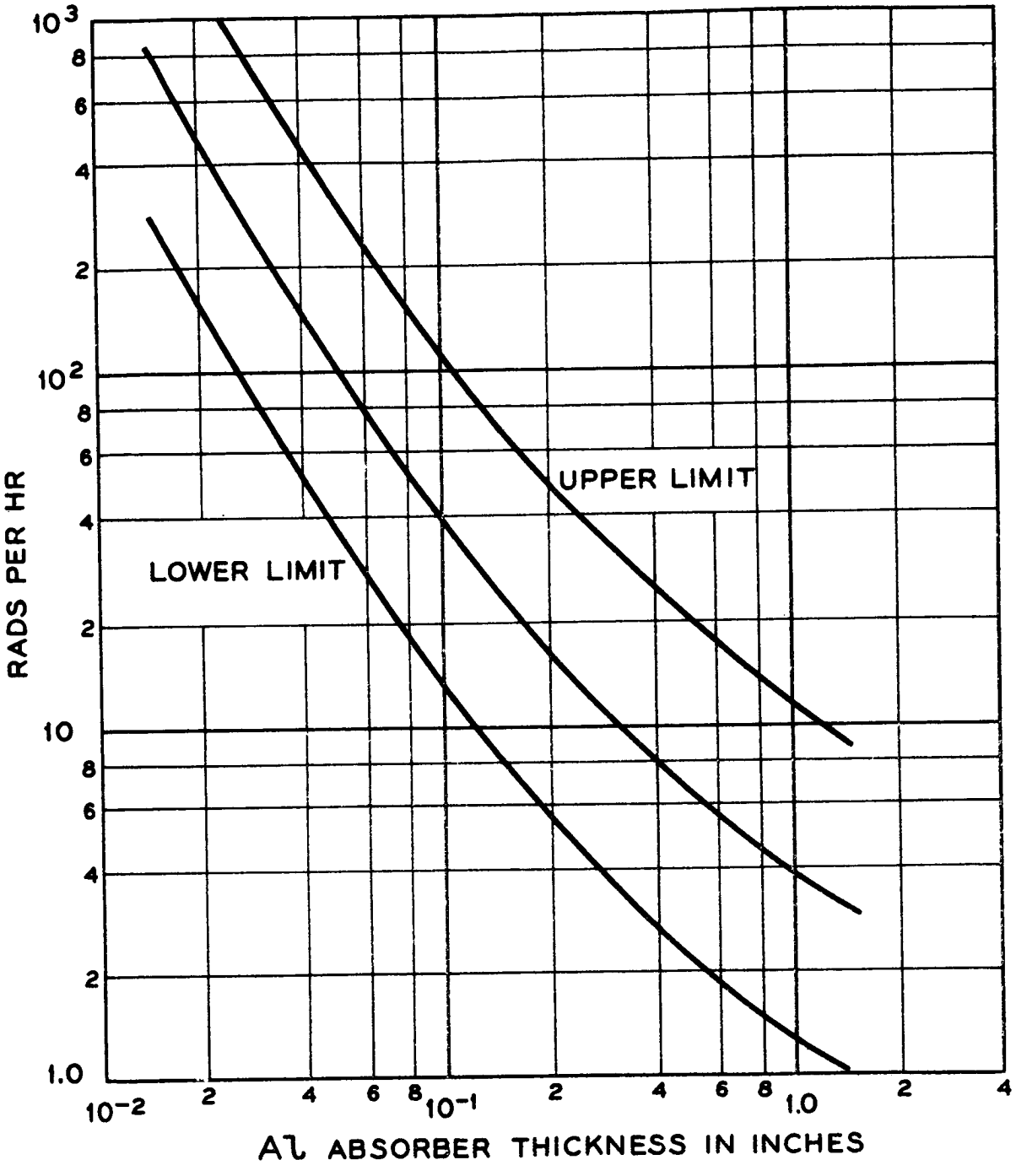

Fig. 23

The maximum radiation intensity anticipated in space due to high energy protons, as a function of the thickness of aluminum shielding.

less than 0.1 inch the electron contribution to ionization should be considered as well, but for Telstar, typical components are shielded by the equivalent of 0.5 to 1.0 inch of aluminum and only high energy protons are significant. The curves of Fig. 23 indicate that at this typical shielding, the radiation intensity would be a maximum of 10-20 rads/hr in the heart of the Van Allen belt. This results in a maximum average of 3-5 rads/hr over an entire orbit, considering Telstar's approximate 25% effective exposure to Van Allen radiation.

With this estimate of the maximum radiation environment, all device types were given a gamma exposure at 8.5×10^5 rads/hr for one minute (the equivalent of at least three months in orbit), followed by at least one week at 3 rads/hr. Any device type showing evidence of change in either condition was replaced or subjected to individual selection or screening. Device types showing no change were considered satisfactory. All of these devices were subject to a 15v reverse bias on the collector and an emitter current corresponding to the application.

The diffused silicon transistors F-54273 and F-54647 were used for experimental studies of screening and selection procedures. It is noted that the one minute dose of 1.4×10^4 rads (at 8.5×10^5 rads/hr) is not much beyond the variable Region 2 of Fig. 17 and should be very effective in providing a comparison between individuals. The study of the effectiveness of such a dose as a screening procedure was carried out through the following program:

1. Preradiation of a number of these transistors to screening exposures between 10 seconds and 6 minutes at 8.5×10^5 rad/hr and
2. Subsequent exposure at 5 rad/hr.

This permits an evaluation of the effect of the low dose rate after a screening dose.

Figure 24 shows the collector reverse current measurements of two units from this program, these being generally typical of the results of all of the devices. In this case, the measuring equipment was limited in sensitivity to about 10^{-9} amperes and the initial values prior to radiation are shown at this value although they may have been somewhat lower. Unit No. 762 is representative of those units which suffered a relatively minor increase in reverse current during the preradiation dose. During the subsequent radiation at 5 rad/hr, this unit returned quite rapidly to its original value remaining there until the dose became somewhat greater than 10^3 rads at which time it began to degrade in a fashion very similar to that expected from earlier tests. Unit No. 722 suffered a much greater change during the preradiation and took an appreciably longer time recovering toward its initial value. Before it fully recovered it reached the point of onset of final degradation and began to change quite rapidly. (A third type of response was seen in an occasional unit which degraded so severely during the preradiation that the subsequent low dose resulted in further increase in current and no recovery was evident at all.)

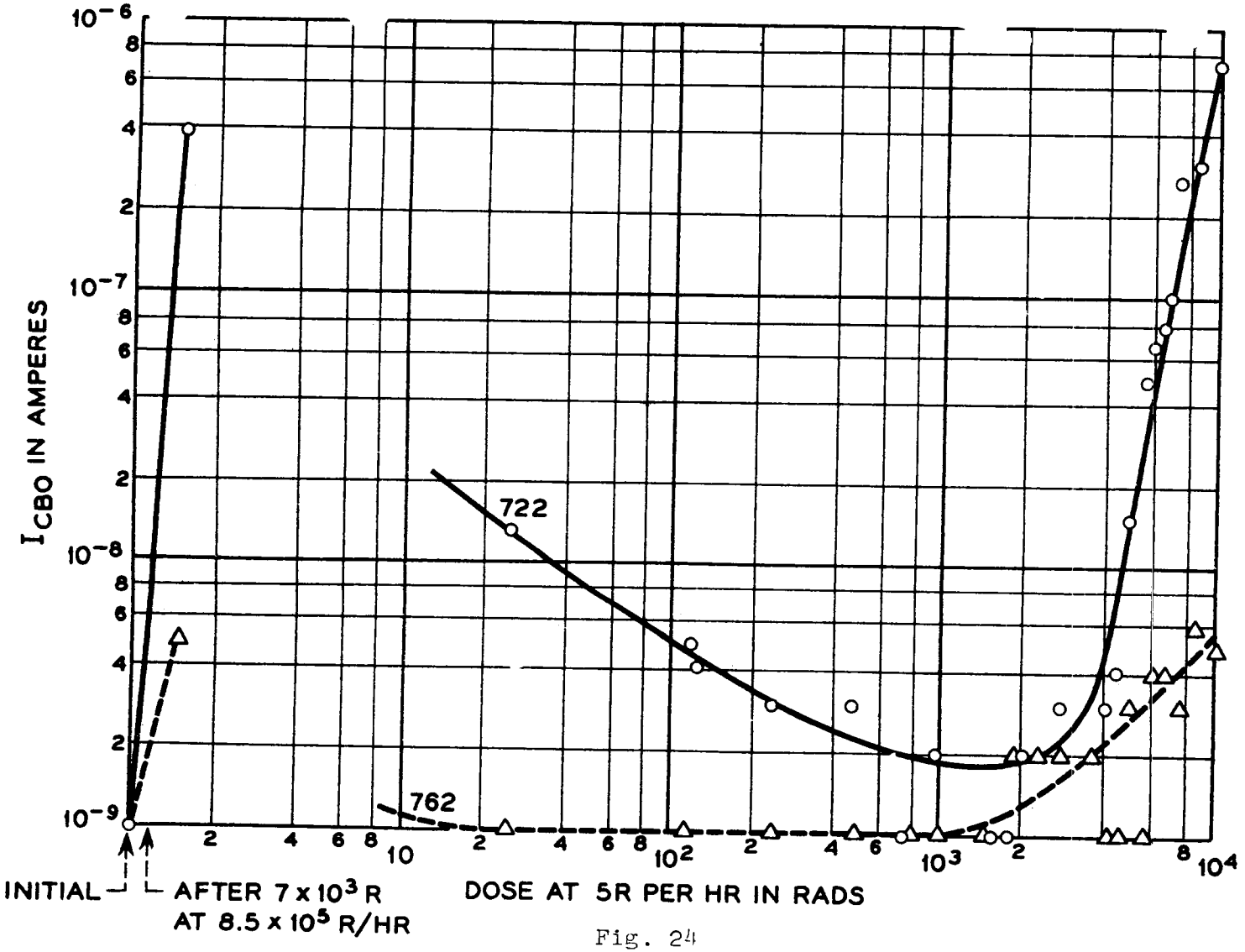

Fig. 24

The typical pattern of change in I_{CBO} in low-level radiation after a screening dose.

The influence of the screening dose on the distribution of onset of the final I_{CBO} degradation (at 5 rad/hr) is shown in Fig. 25 for four similar groups of 12 units each. One of these groups was irradiated at 5 rad/hr with no initial radiation at the high dose level. The other three groups were given an initial radiation at 8.5×10^5 rad/hr for different lengths of time to achieve the initial radiation dose indicated in the figure. It is seen that all of these distributions are essentially the same, indicating that the 5 rad/hr dose will cause a modification of the surface condition established by the high initial dose, causing the units to look eventually as if they had not received the initial dose. This is evidence of a contradiction to the principle of reciprocity of dose rate and time, in that the additional dose added at the 5 rad/hr rate does not normally cause a continuation in the degradation produced in the initial dose.

Another point of interest in Fig. 24 is the comparison of the I_{CBO} value resulting from the preradiation dose with that subsequently occurring after an equal dose at 5 rad/hr. Inspection of the two curves on Fig. 24 reveals that the currents at 7×10^3 rad are approaching those resulting from the preradiation dose. Fig. 26 shows a plot of the results of all the units so treated. The dashed line indicates the one-to-one correlation between the two current values, those points to the right of the line representing the units which during the 5 rad/hr exposure did not develop reverse currents as high as those obtained in the initial

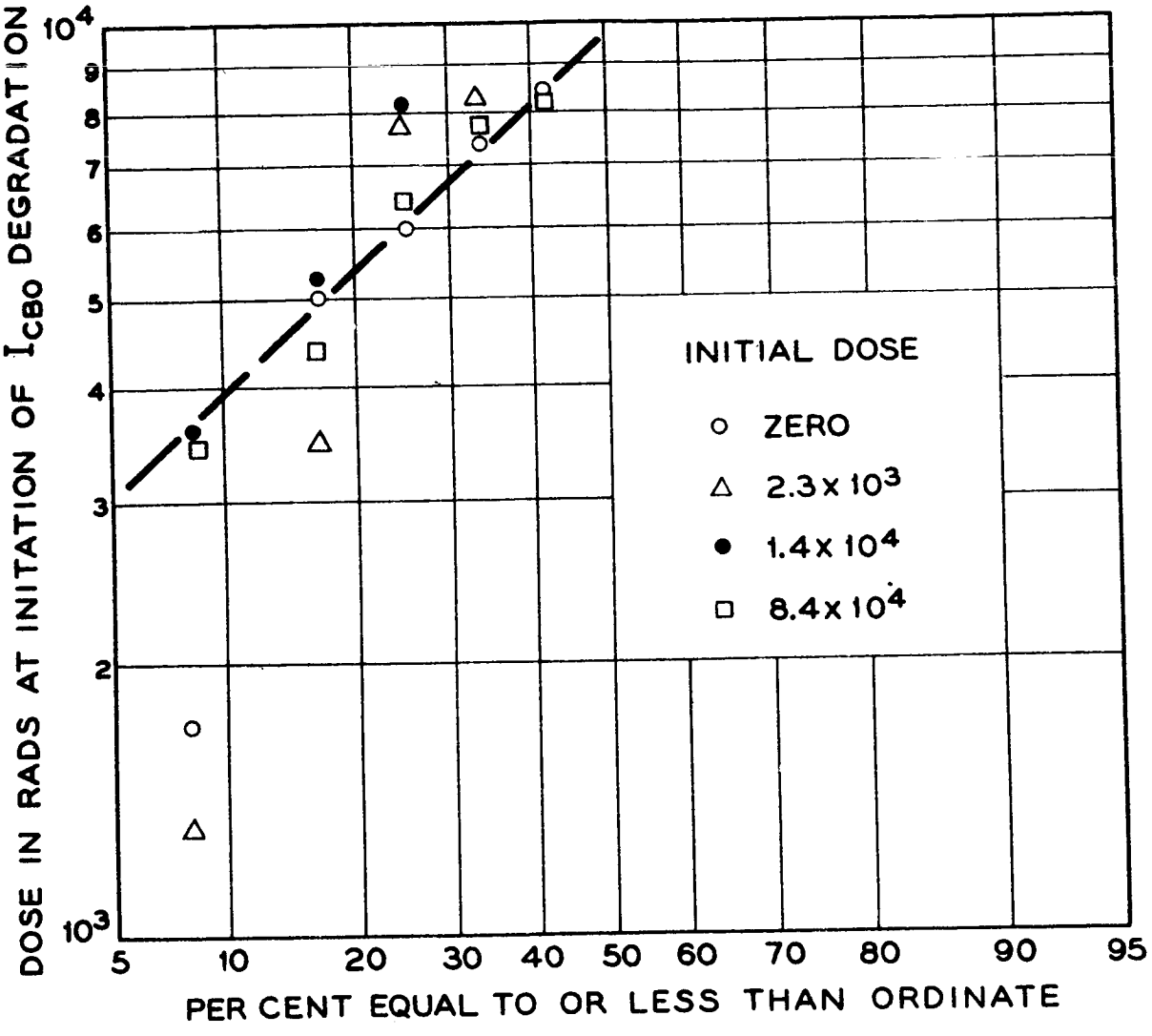

Fig. 25

Distribution in dose for initiation of degradation with and without preirradiation.

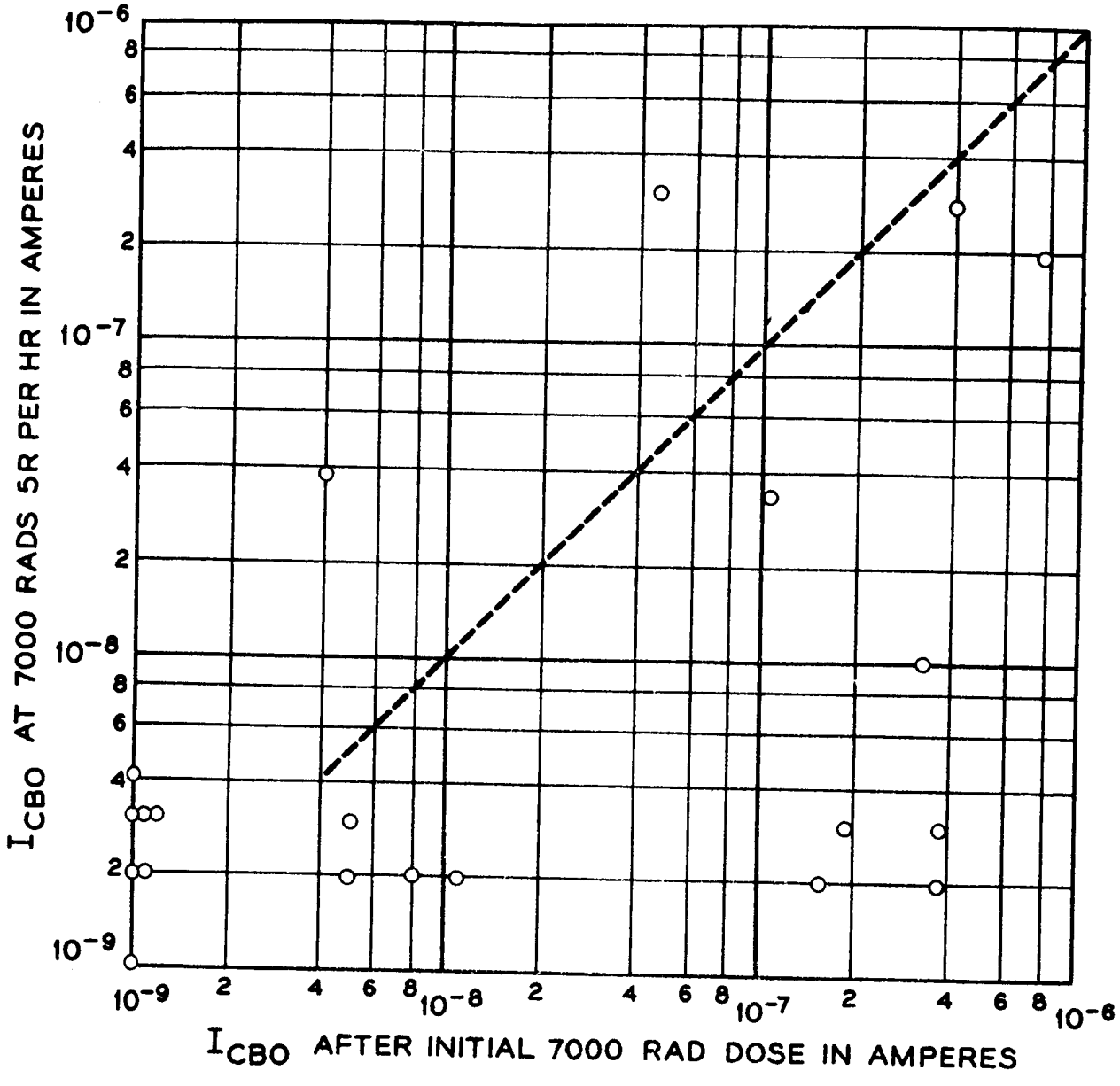

Fig. 26

Correlation of change in I_{CBO} after a screening dose at 8×10^5 rad/hr with subsequent changes at 5 rad/hr.

dose. This line was not extended below about 4×10^{-9} amperes because this was approaching the limit of sensitivity of equipment which was then in use. It is noted that all but two of the significant readings fall on the side of the one-to-one correlation line corresponding to larger changes after the preradiation dose than after the subsequent low dose rate exposure.

In some cases the lack of correlation is quite significant, the currents after the low dose rate exposure remaining below 10^{-8} amperes although quite large changes were observed after the screening dose. In these units, however, the changes in current gain after the low dose rate exposure were found to be appreciably greater than in those units which were more stable in the initial screening dose. Consequently, it is found that selecting of those units with I_{CBO} less than 10^{-8} amperes after the screening dose, would have eliminated 9 of the 10 units which subsequently degraded to either I_{CBO} values greater than 10^{-8} amperes or gains less than 50% of the initial gain. Of the 12 units good in these respects after the low dose rate exposure, only two would have been eliminated by selection following the screening dose. It is thus shown that selection on the basis of I_{CBO} after a screening dose is effective for this device type.

An indication of the effect of this screening on the distribution in degradation of I_{CBO} under low-level radiation exposure is given in Fig. 27. Both distributions are of I_{CBO}

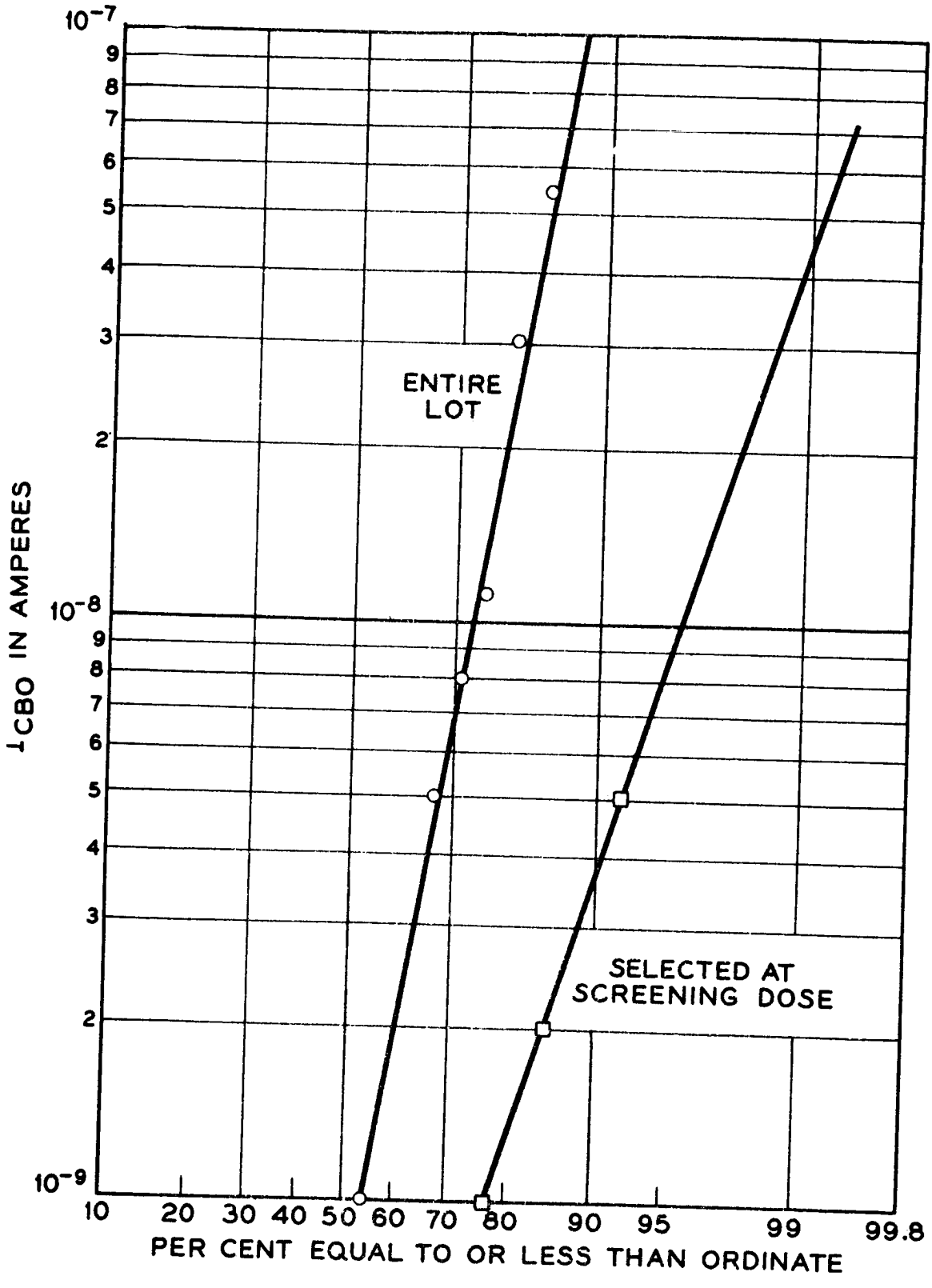

Fig. 27

Distribution of radiation response in screened and unscreened devices.

after exposure, first to 30 seconds at 8.5×10^5 rad/hr and then to 10^4 rad at 5 rad/hr. One distribution is of the entire sample of devices and the other is of only those which were selected for I_{CBO} less than 10^{-8} amperes after the initial dose. It is seen that an appreciable improvement is achieved by the screening procedure.

VIII. Summary

It has been found that changes can occur in semiconductor characteristics, because of surface effects of ionizing radiation in a device under electrical bias, at much lower doses than those required to produce surface effects in the absence of bias or to produce changes in the bulk of the semiconductor. These effects apparently arise from ionization in the gas of a device encapsulation and collection of ions on the device surface. The gas ions probably serve to produce and activate chemical species on the semiconductor which induce surface inversion layers that alter the junction characteristics. The chemical condition of the surface previous to irradiation is apparently involved in the process in a sensitive way. The effects observed depend on junction bias, envelope potential, and in many respects on total radiation dose rather than dose rate. The major features of these observations and of observations of the characteristics recovery of the surface effects after radiation under bias can be described by the ion-induced inversion layer model of the process.

In the time since the first direct observation of this effect, a comprehensive study of all types of semiconductor devices has not been attempted. Observations of several types, however, indicate that different types may respond quite differently to radiation, that the response may be quite dependent upon processing (and therefore upon production periods or batches), and that within a type the response may be quite variable between individual units.

One type of transistor was used for much of the experimental work of defining the radiation effect, and the I_{CBO} response was studied because the large changes facilitated comparative measurements. It is recognized that current gain and other surface-dependent characteristics can also be affected by radiation, and they should be observed in any evaluation of types, if critical in specific applications. It is hoped that the studies presented here will be a guide in formulating such evaluations.

It has also been found that at least some devices can be screened for sensitivity to radiation by means of a short-time, high-level dose, with correlation to subsequent low-level exposure results. Here, too, it is recognized that variations exist among types, and the usefulness of such screening operations should be evaluated for each type of interest.

It is hoped that further work will serve to provide more definitive results relating the radiation effects to a physical model and also to the surface conditions or processes contributing to the effect. These preliminary results can at least serve to expose the problem and to suggest the lines of further study and action.

Acknowledgments

The material presented here includes the contributions of many of the authors' colleagues. Of particular significance have been the efforts of E. P. Moyer, E. R. Schmid, J. Lange, of Bell Laboratories and G. L. Miller of Brookhaven National Laboratory.

REFERENCES

1. See Conference on Radiation Effects in Semiconductors. J. Appl. Phys. 30 (1959).
   G. D. Watkins, Corbitt, J. J. W., "Electron Paramagnetic Resonance of Defects in Irradiated Silicon."
2. Easley, J. W. and Dooley, J. A., "Fast Neutron Bombardment Reduction of Transistor Current Gain."
3. Proceedings of Second Conference on Nuclear Radiation Effects on Semiconductor Devices, Materials and Circuits. September 17 and 18, 1959.
4. See IRE Transaction on Nuclear Science. Vol NS-8, January 1, 1961. Solid State Radiation Detectors
5. Rosenzweig, W., "Diffusion Length Measurement by Means of Ionizing Radiation." BSTJ 41 1573 (1962).
6. Smits, F. M., Smith, K.D., Brown, W. L., "Solar Cells for Communication Satellites in the Van Allen Belt." Journal of the British Institution of Radio Engineers, 22 161 (1961).
7. Baruch, P., "Mobility of Radiation Induced Defects in Germanium." J. Appl. Phys. 32 653 (1961).
8. Kingston, R. H., "Review of Germanium Surface Phenomena." J. Appl. Phys. 27 101 (1956).

Paper B-3

NASA SPACE RADIATION EFFECTS LABORATORY

Dr. John Duberg* and Emanuel Rind**
NASA Langley Research Center

15125

Abstract

Space particulate radiation from the Van Allen belts, and from cosmic and manmade sources have energies and fluxes which have produced and are capable of producing damage in matter and living organisms which comprise space mission payloads. Laboratories in space for the study of radiation effects are not available. NASA, Langley Research Center, Virginia has proposed a ground based Space Radiation Effects Laboratory which simulates most of the particulate energy spectrum found in space and can be used in an effective, accelerated, radiation research program by means of which deleterious radiation effects can be minimized or eliminated. To achieve these results in a minimum time, a 600-Mev, proton, synchrocyclotron of proven design with variable energy and variable external beam size, as well as a 1 to 30 Mev electron accelerator with the same capabilities have been incorporated into the proposed facility. Although these devices will be used as engineering tools, provision has been made to maintain the basic research capabilities of these accelerators. This will provide three Virginia institutions of higher learning, who will operate the laboratory jointly with the Langley Research Center, with the instruments necessary to conduct a basic research program. The plan of the proposed test areas reflect the latest advances in the state of the art as it pertains to both the engineering and basic experimental requirements in flexibility, radiation background levels, shielding, and isolation. NASA, Langley Research Center, Virginia, has been engaged in particulate radiation effects research in materials, components, dosimetry, devices, and instrumentation used in space missions. These efforts have been handicapped by the limited availability of time in existing accelerators which are being used for basic physics experiments. The proposed Space Radiation Effects Laboratory will provide the necessary facilities for conducting an expanding radiation effects research program using particulate radiation which simulates the space spectrum.

*Technical Assistant to the Associate Director.
**Aerospace Technologist.

Introduction

The Langley Research Center of NASA has had a special interest in the space environment insofar as it influences the design of space vehicle systems. Scientific exploration of space has revealed a number of hostile aspects of the environment. Perhaps the most significant of these is the particulate radiation associated with cosmic rays, solar flares, and that magnetically trapped in the radiation belts. The Langley Research Center has proposed a Space Radiation Effects Laboratory in which the particulate space radiation can be simulated, accelerated testing performed, and fundamental studies made in this problem area.

Particulate Radiation in Space

A brief review of our knowledge of the particulate radiations in space is appropriate and, as cosmic rays are familiar, they are used as a basis of comparison in figure 1.[1] The cosmic ray flux is comprised of approximately 85 percent protons, 13 percent helium nucleii and the remainder, heavy ions.[2] Only the proton spectrum is shown. Although the flux is low, protons from this source attain extreme energies in the Bevs. The upper energy limit has not been determined but there is reason to believe that it is much in excess of 10^6 Bev.

The proton spectra of three solar events are shown with an indication of their time variation. The dotted portions of the curves are extrapolations. Energies of 10 Bev may be attained but flux values for these high energies are very low. Integrated, instantaneous, omnidirectional fluxes down to a few Mev may exceed 10^6 protons/cm^2/sec. The solar event of February 23, 1956 would indicate that both flux and energy decrease with time. It is more commonly believed, however, that the event of November 12, 1960 is the more likely occurrence.[3] For this event, the flux values of the lower energies increase, as those of the higher energies decrease with time.

---

[1]Trutz Foelsche, Current Estimates of Radiation Doses in Space, NASA TN D-1267, 1962.

[2]F. B. McDonald, ed., contributed by G. E. Fichtel, D. E. Guss, H. H. Malitson, K. G. McCracken, K. W. Ogilvie, and W. R. Weber, Solar Proton Manual, NASA TR R.

[3]George J. Jacobs, ed. (With Appendix A by J. R. Winckler), Proceedings of Conference on Radiation Problems in Manned Space Flight, NASA TN D-588, 1960.

The protons trapped in the inner radiation belt have omnidirectional fluxes ranging from over 10^4 protons/cm^2/sec at energies greater than 40 Mev to fluxes of the order of 10^3 protons/cm^2/sec at energies greater than 550 Mev.

It is assumed that the electron fission energy spectrum shown in figure 2 would be obtained for manmade detonations of nuclear devices. The spectrum[4] is expressed in relative differential values. If the spectrum is integrated and normalized it yields the following results: 55 percent of the electrons have energies $\leq$1 Mev and 91 percent of the electrons have energies $\leq$3 Mev. The maximum electron energy is about 7 Mev.

The recent explosion of a nuclear device produced the electron spectrum of figure 2 and these electrons have been geographically located[5] in the position shown in figure 3. The naturally trapped protons and electrons of the radiation belts as previously reported are also shown and may be used as a basis of comparison. It can be seen that the new manmade belt contributes much of its intensity in the region previously referred to as the inner belt and thus increases the radiation damage problems of low-altitude space missions. The peak intensities of the electrons of this artificial belt equal if not exceed the maxima of the natural outer region when the latter's intensities are increased by magnetic storms.

The outer region is seen to be of a transient character and has variations in flux and energy due to solar activity. By far the greatest number of these electrons have energies below 1 Mev.[6] As indicated previously, however, the manmade belt has about 45 percent of its electrons with energies between 1 and 7 Mev. The addition of any manmade trapped electron radiation may pose an even greater hazard than that which is already present from the natural belt electrons.

---

[4]R. E. Carter, F. Reines, J. J. Wagner, and M. E. Wyman. Free Antineutrinos Absorption Cross Section. II. Expected Cross Section From Measurements of Fission Fragment Electron Spectrum. Phys. Rev., Vol. 113, No. 1, p. 280-6, January 1, 1959.

[5]Artificial Radiation Belt Discussed in Symposium at Goddard Space Center, W. N. Hess, P. Nakada, Science, Vol. 138, No. 3536, October 5, 1962, pp. 53-54.

[6]B. J. O'Brien, J. A. Van Allen, C. D. Laughlin, and L. A. Frank, Absolute Electron Intensities in the Heart of the Earth's Outer Radiation Zone. Jour. Geophys. Res. (Letter to the Editor), Vol. 67, No. 1, January 1962, pp. 397-403.

A brief summary of our knowledge of particulate radiation in space is given in table I.

TABLE I.- SUMMARY OF THE PROTON AND ELECTRON SPECTRA IN SPACE

PROTON SPECTRA

Low Energy	High Energy
Energy spectra $\leqq$22 Mev as obtained from Explorer XII data: 120 Kev < E < 4.5 Mev	Energy spectra from 22 Mev to 700 Mev
Flux ($p/cm^2/sec$) = 10^7 to 10^9	Total flux $>2 \times 10^4$ $p/cm^2/sec$
	Intensity can vary by a factor of 2 to 3 with solar activity

ELECTRON SPECTRA

Low Energy	High Energy
Energy spectra <1.6 Mev	Energy spectra 1.6 < E < 6 Mev
E > 40 Kev, Flux < 10^8 $e/cm^2/sec$	Flux $\approx 2 \times 10^5$ $e/cm^2/sec$
E > 600 Kev, Flux $\geqq 5 \times 10^6$ $e/cm^2/sec$	Intensity can vary by a factor of 50 to 100 with solar activity

Electron data obtained from Explorer XII.

SOLAR FLARES

Proton energy approaches 10 Bev. Fluxes vary with maximum values between 10^5 to 10^6 $p/cm^2/sec$. The greatest intensities occur at the low-energy values.

The proton data are divided into low energy, high energy, and solar flares. The low-energy data were reported at the symposium on the scientific results of Explorer XII, January 1962, by L. R. Davis and J. M. Williamson of the NASA, Goddard Space Flight Center. The low-energy range given was from 120 Kev to 4.5 Mev. This has been extended arbitrarily to 22 Mev, the upper limit for fixed frequency cyclotrons. The integral flux in this range is between 10^7 and 10^9 protons/cm^2/sec.

The high-energy-range data were obtained with Pioneer III and Explorer VII.[7] The low end has been taken from 22 Mev and extends to 700 Mev, the integral flux being greater than 2×10^4 protons/cm^2/sec.

The maximum integral energy flux of the solar flares vary between 10^5 to 10^6 protons/cm^2/sec with energies ranging from Kevs to about 10 Bev. The natural belt electrons have their highest intensities (between 10^8 to 10^9 e/cm^2/sec) at about $2\frac{1}{2}$ to 4 earth radii as measured from the earth's center. The manmade belt electrons have peak intensities greater than 10^9 e/cm^2/sec occurring at about 1.6 earth radii. The energies of both the manmade and naturally occurring electrons extend from a few Kev to 7 Mev.

Concept of the Space Radiation Effects Laboratory

Threshold doses for functional radiation damage[8] are shown for various materials and devices in figure 4. Unfortunately, most of this data is obtained from fission radiation which neither simulates space radiation as regards energy or type of radiation. This information is still useful in that it gives relative orders of magnitude of damaging doses and provides some means for determining the fluxes needed for accelerated space radiation damage studies.

The Langley Research Center in pursuing its research program for the experimental investigation of the effects of particulate radiation on items used in space missions, found, as have other investigators, that very limited beam time is available for engineering research using high-energy proton accelerators. The existing ones are being used almost full time for basic physics research experiments. To overcome this shortcoming without interference with the high-energy physics research effort, LRC, NASA, proposed construction of a Space Radiation Effects Laboratory which would encompass most of the space particulate radiation and which would utilize proton and electron accelerators as engineering tools as well as physics instruments.

---

[7]Guido Pizzela, C. E. McIlwain, and J. A. Van Allen, Time Variation of Intensity in the Earth's Inner Radiation Zone, October 1959 through December 1960, Jour. Geophys. Res., Vol. 67, No. 4, April 1962, pp. 1235-1253.

[8]S. N. Lehr, V. J. Tronolone, and P. V. Horton, Equipment Design Considerations for Space Environment, STL/TR-60-0000-09224, Space Tech. Lab, Inc., Sept. 1960.

Since over 90 percent of the space spectrum is below 1 Bev with fluxes less than 10^6 particles/cm^2/sec, and as the needs for the facility are immediate, a survey was made of existing accelerators having energies of this range and external beams which would permit accelerated space simulation for components with volumes of at least a cubic foot. The desire was to duplicate an existing, proven, design having the necessary features for accelerated space simulation, thus saving years of development time. The choice, based on availability, was narrowed to frequency modulated cyclotrons and alternating gradient synchrotrons. The synchrocyclotron design was chosen because its external flux was adequate for our purposes, whereas the external flux of the synchrotron machine was lower by about two orders of magnitude. Considerations of down time, beam extraction and overall proven reliability were additional factors in favor of the synchrocyclotron.

Particle Accelerators

There are four synchrocyclotrons in the world with energies of about 0.6 Bev or greater. The two behind the iron curtain were not considered. The other two are the machine at Berkeley, California (0.76 Bev) and the machine at CERN, Geneva, Switzerland (0.6 Bev). The CERN machine was designed for its stated energy and incorporated the most modern concepts of the day. The Berkeley machine has been redesigned and altered to bring it up from its initial lower energies to its present level and any design improvements of it and other existing accelerators were considered in the design of the CERN machine.[9] Since the CERN machine was the most modern, met our energy and flux requirements, and had a very good operational history, it was our final choice.

CERN Synchrocyclotron

Figure 5 is a photograph of the 600-Mev proton synchrocyclotron at CERN, Geneva, Switzerland. The overall size of the magnet is 36 feet wide by 21.3 feet deep by 20 feet high. It weighs 2500 tons, and is made up of 54 blocks weighing approximately 46 tons each. The height of the beam above the floor level is 4.1 feet and the magnet gap varies between 45 and 35 cm. The coils, which are water cooled, and made of aluminum, are about 25 feet in diameter, weigh about 60 tons, and produce 0.75 megawatt of heat at 1,750 amperes. The maximum radius R of proton path (n = 0.2) = 2.27 meters. The magnetic induction at R = 2.27 meters is 1.79 webers/meters^2; and at R = 0, the magnetic

---

[9]Bengt Hedin, Design of CERN Synchro-Cyclotron Magnet, CERN 55-3, Synchro-Cyclotron Division, January 14, 1955.

induction is 1.88 webers/meter^2. The vacuum chamber and connections are made of welded stainless steel and have a volume of 23 cubic meters. This is pumped down to about 10^{-6} torr using two oil diffusion and three roughing pumps.[10]

The radio frequency system uses a water-cooled tuning fork modulator which modulates the r-f frequency between 29 and 16.5 megacycles at 55 cps.[10]

The target systems shown in figure 6, although designed basically for high-energy physics research, lend themselves readily to engineering. There are eight internal flip targets to produce neutrons at radii corresponding to energies from 110 to 600 Mev. Negative mesons are obtained by use of a suitable target on a Fermi trolley. The external proton beam is obtained by means of a magnetic channel with suitable extraction devices and is brought to focus in a beam area of 15 cm^2. The external current is about 0.3 microamp ($\approx 10^{11}$-10^{12} protons/cm^2/sec).

For the SREL, the CERN accelerator and external beam will be modified to produce variable energy and beam area. As proposed, the proton energy variation will be from 600 Mev down to as low as 100 Mev and capabilities will exist for spreading the beam from 15 cm^2 to 900 cm^2 at the target area. With the existing external beam, a year in the belt could be simulated in minutes to weeks over these target areas.

Electron Linac

Capability will also exist for accelerating electrons from 1 Mev to 30 Mev with beam current in the range of 150 microamp. These parameters will simulate the electron space environment as well as being useful for basic physics research. The beam area and energy will be variable and the linear accelerator design will be used to attain the requisite energy. Figure 7 is the accelerator section of a 10-Mev electron linac. The 30-Mev linac requires one or two additional accelerator sections.

The layout shown in figure 8 has been proposed for the SREL electron linac. The beam could be used in the linac cave or with the beam handling equipment shown, piped into the adjacent test area.

---

[10]W. Genter, K. H Schmitter, S. Kortleven, B. Bollée, and F. Krienen, The CERN 600 Mev Synchrocyclotron at Geneva, Phillips Technical Review, Vol. 22, 1960/61, No. 5, March 1961.

Plan of the Space Radiation Effects Laboratory

The floor plan of the proposed Space Radiation Effects Laboratory is divided into three major areas as shown in figure 9. These are the test and beam handling area, the test setup area, and the support building. The test and beam handling area consists of two independent target areas, the electron accelerator cave, the proton accelerator cave, and the magnet hall which will contain the beam transport and handling for the proton accelerator. The two target areas are about 30 by 30 feet and these dimensions may be changed by moving the walls. One target area is arranged for receiving a combined electron and proton beam. Sufficient area has been allowed around both accelerators which permits ready access and normal maintenance without the inconvenience of moving shielding. Very large targets may be irradiated by piping the beam directly down the magnet hall. The shielding walls are about 18 feet thick. Overhead shielding is provided to reduce skyshine. In addition the proposed arrangement of the physics test areas will isolate them in a manner to give low radiation background, thus permitting the performance of very refined experiments. The setup area allows test setups and measurements to be made without disturbance prior to installation into the target areas. Large vertical lift doors separate the target area from the setup area. The combined test and setup areas occupy approximately 37,000 square feet.

The support building is conveniently located next to the setup areas. It consists of two floors and a basement which will contain the control room and monitoring system for the accelerators, laboratory space, shop facilities, office space, counting areas, etc. The two floors have an area of about 17,000 square feet.

The section view, figure 10, is taken through the synchrocylotron cave, and shows the relationship of the test setup area with the support building and test areas. Also shown are the head room for the overhead crane and the support and pilings needed around the accelerator.

Research Program

In accord with the objectives of minimizing or eliminating the effects of space radiation on all items which comprise space missions we have outlined a research program part of which is already underway in the following areas: materials, these will include seals, cements, plastics, lubricants, solder, damping materials, phosphors, insulators, etc.; external surfaces such as coatings, transparent materials, and optical components; devices such as magnetic, electronic, and solid state; shielding will cover magnetic as well as various bulk configurations; detection encompasses design, development, testing and calibration of new detecting devices; dosimetry will include experimental studies of radiation levels and doses delivered to different

areas and constituents of space vehicles; environmental contamination will deal with the ability of radiation to produce corrosive, noxious, atmospheres, for example, ozone and nitrous oxides in closed ecological systems; sputtering phenomena; activation resulting from radiation; chemistry of elastomers and polymers; spectroscopy for the study of radiation induced changes will include nuclear magnetic resonance, electron paramagnetic resonance, infra-red and visible light, electron microscopy, X-ray techniques, and mass spectroscopy; thin films; experimental validation of theoretical studies; biological research including synergistic effects; health physics; and basic physics research.

Operation of Laboratory

The tentative operational plan for the SREL provides for William and Mary, the University of Virginia, and Virginia Polytechnical Institute organized as the Virginia Associates Research Center (VARC), to supply the operational personnel for SREL. The participating universities of VARC will also establish a basic physics research program sponsored by government grant, industry grants, or self-initiated. Other institutions requiring a facility with high-energy capability for basic research can cooperate with VARC. Programs for accelerator improvement and development may also be undertaken by VARC. The Langley Research Center will conduct the engineering, applications, and basic research phases associated with the space environment. Other NASA Laboratories, government agencies, and industry under NASA contract will operate through the Langley Research Center.

Concluding Remarks

An architect's rendering of the Space Radiations Effects Laboratory is shown in figure 11. This will be located in the city of Newport News, Virginia within 15 miles of the Langley Research Center, and will lie in a site occupying approximately 100 acres. The principal intent of the Space Radiation Effects Laboratory was to provide a facility in which investigations simulating the space environment could be performed and the results used to increase the reliability and safety of spacecraft and space missions. As the project has now evolved, the Laboratory will serve a dual function. In one capacity, it will support an engineering program aimed at increasing the reliability and safety of spacecraft and missions. In the other, it will provide our universities and colleges with the instruments by which they can conduct basic research in high-energy physics as well as expanding their graduate program in this field. Thus, by providing a facility whereby both these endeavors can be conducted concurrently, two vital needs are simultaneously fulfilled.

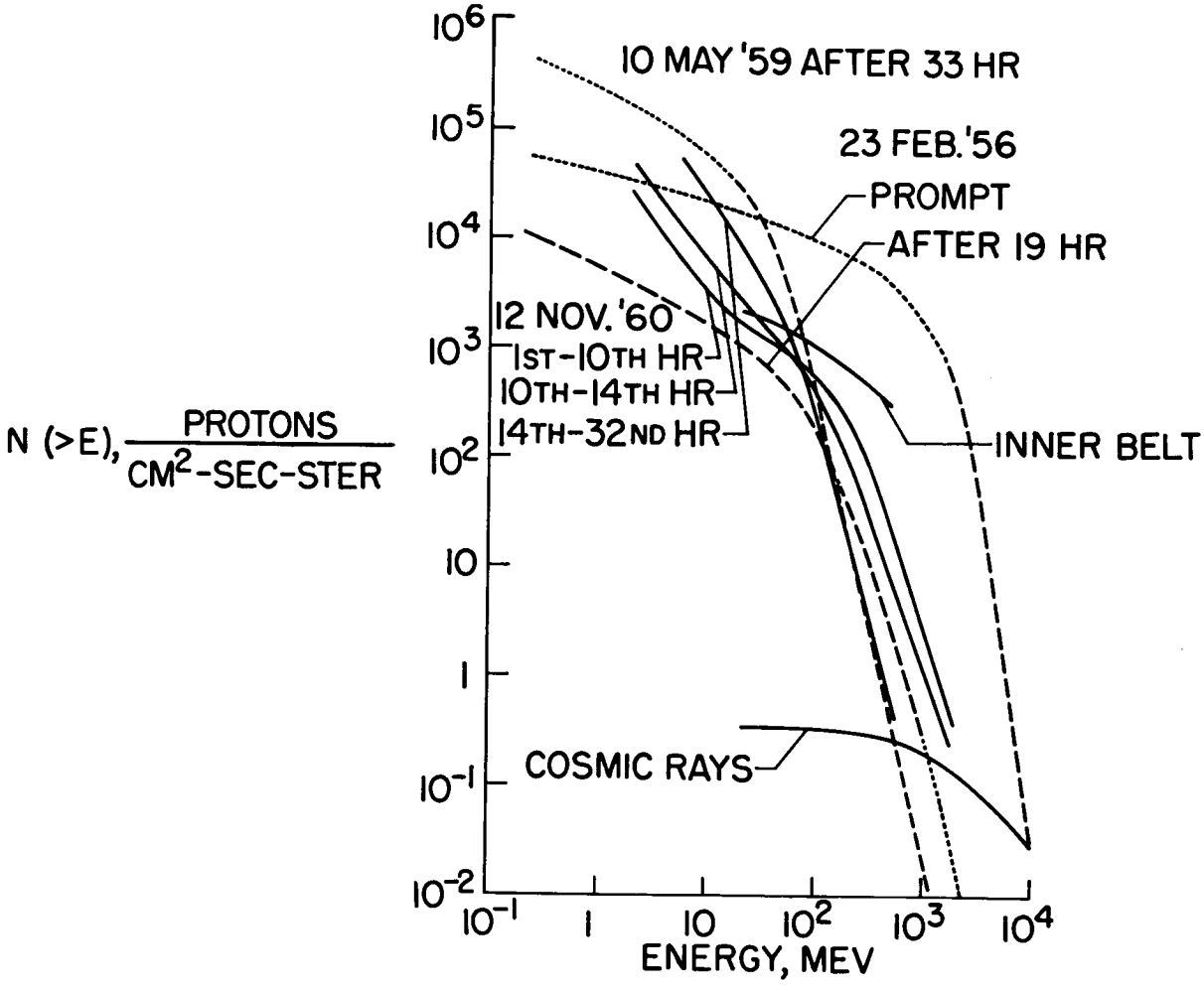

NASA

Figure 1.- The instantaneous integral energy spectra of cosmic rays, solar flare protons, and protons in the inner Van Allen belt. Dotted curves indicate extrapolations of measured data. (From ref. 1.)

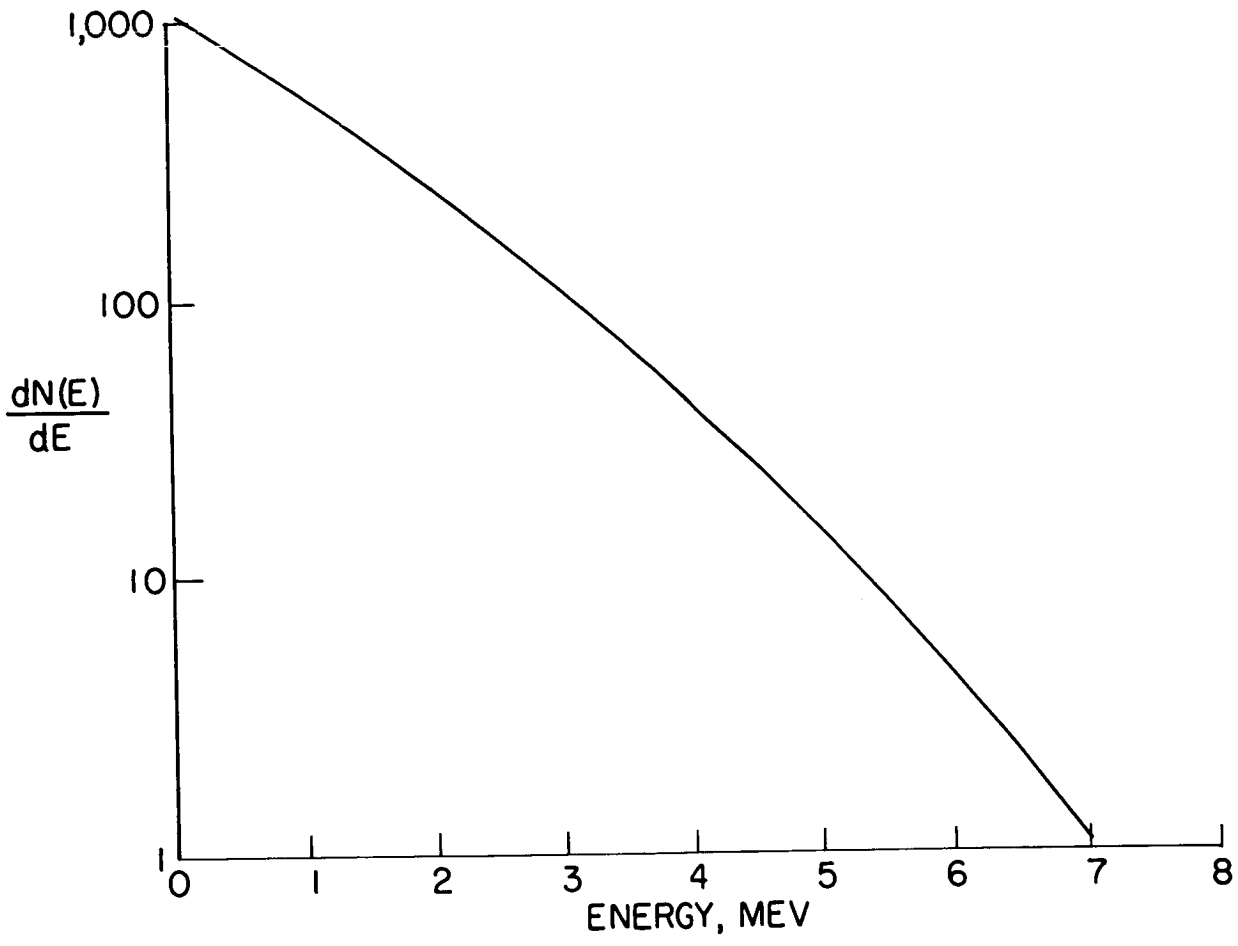

Figure 2.- Electron fission energy spectrum. (From ref. 4.)

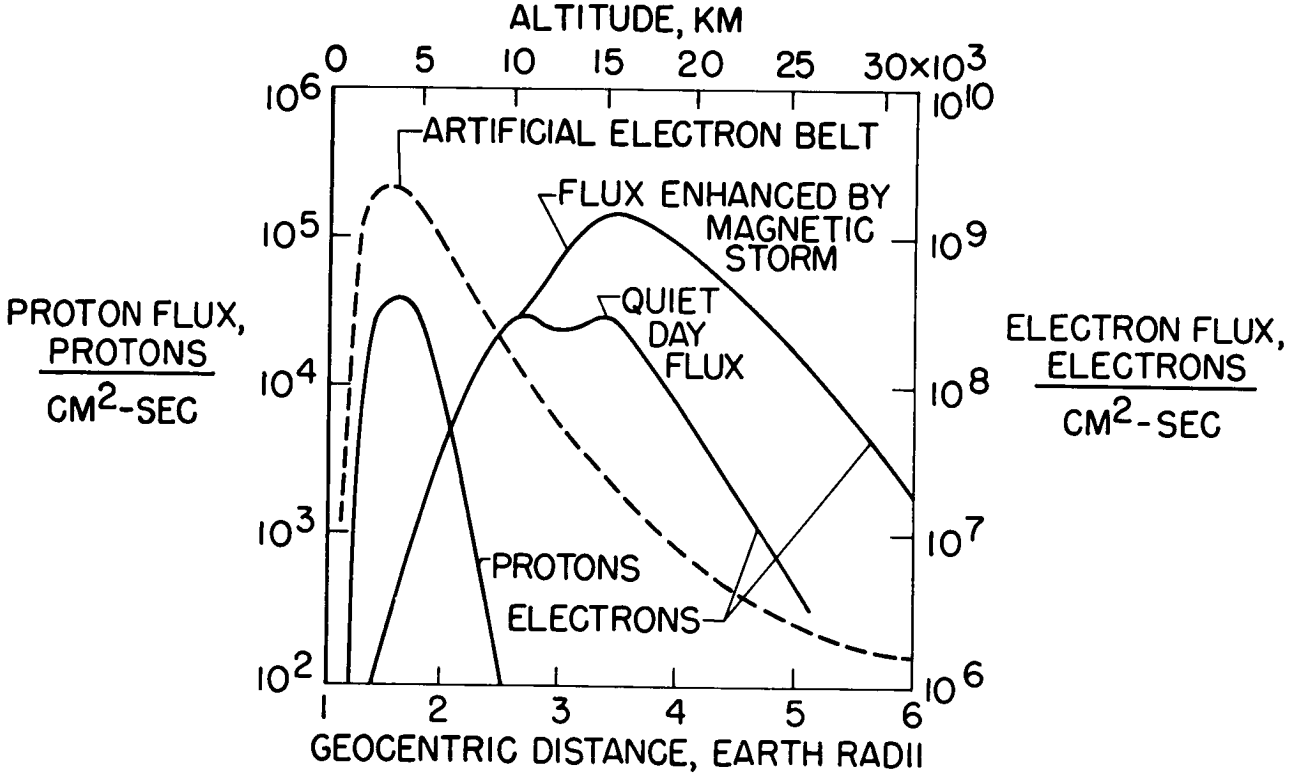

NASA

Figure 3.- Man-made electron belt shown relative to the existing electron and proton distributions. (From ref. 5.) The approximate variation of flux with geocentric distance and altitude in the plane of the geomagnetic equator is depicted.

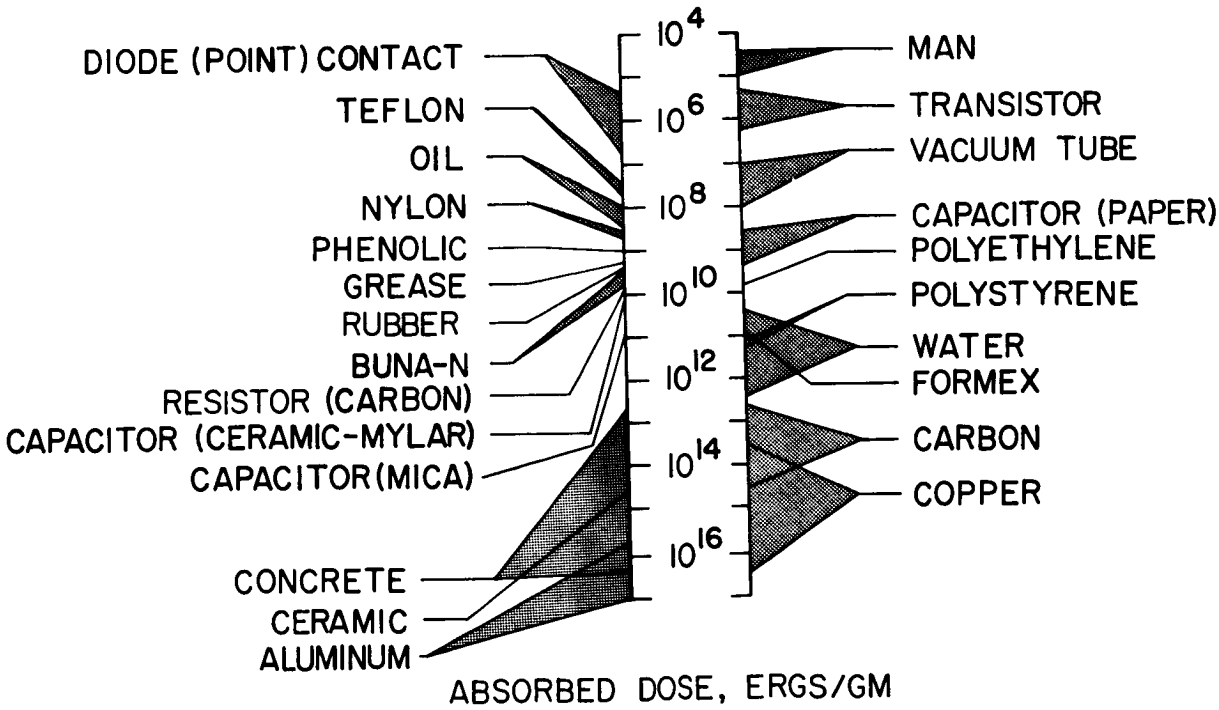

NASA

Figure 4.- Threshold dose for functional radiation damage as given in ref. 8. (Note that the absorbed dose in rads can be obtained by multiplying the dose in ergs/gm by 10^{-2}.)

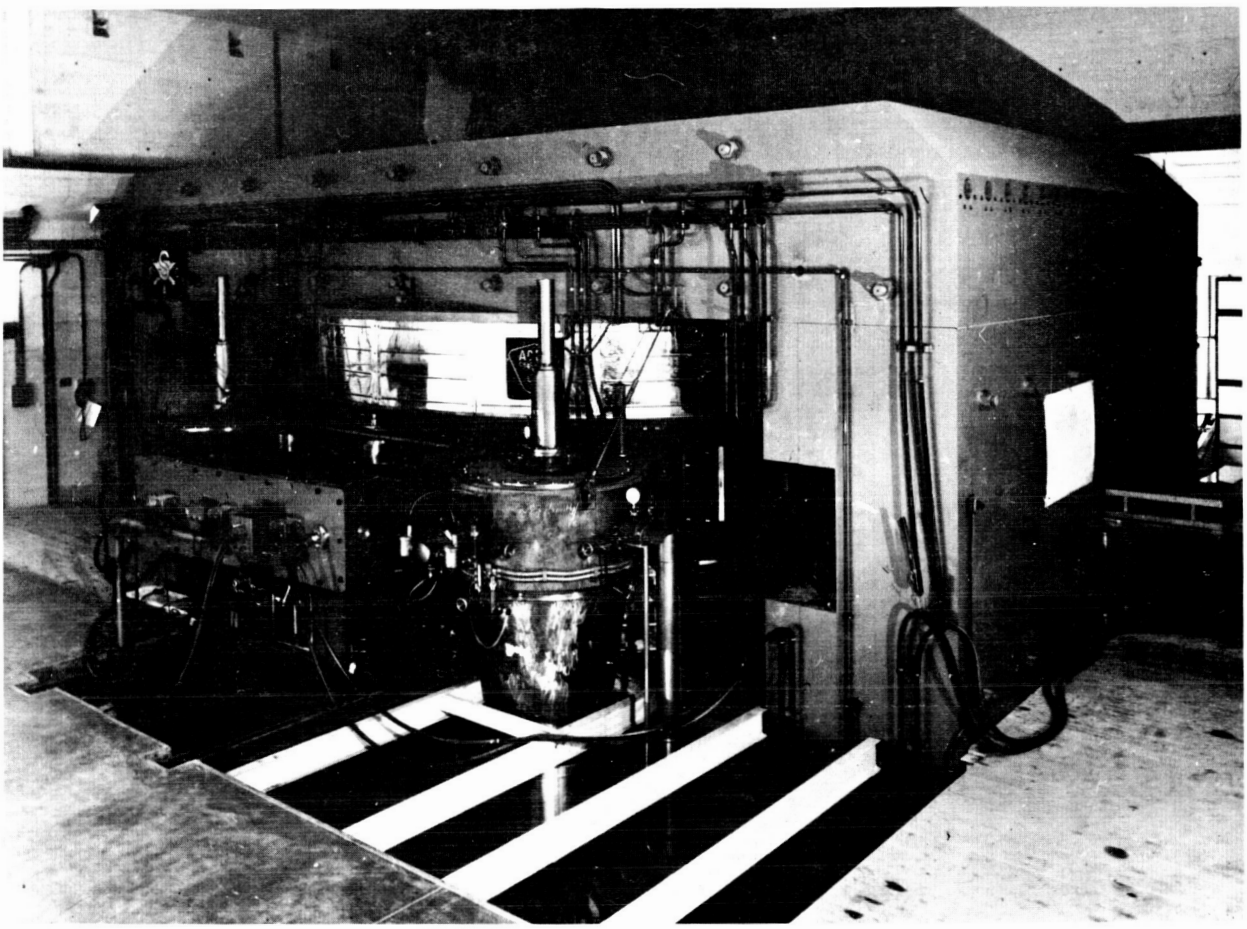

NASA
L-62-1046.1

Figure 5.- CERN 600-MEV Synchrocyclotron.

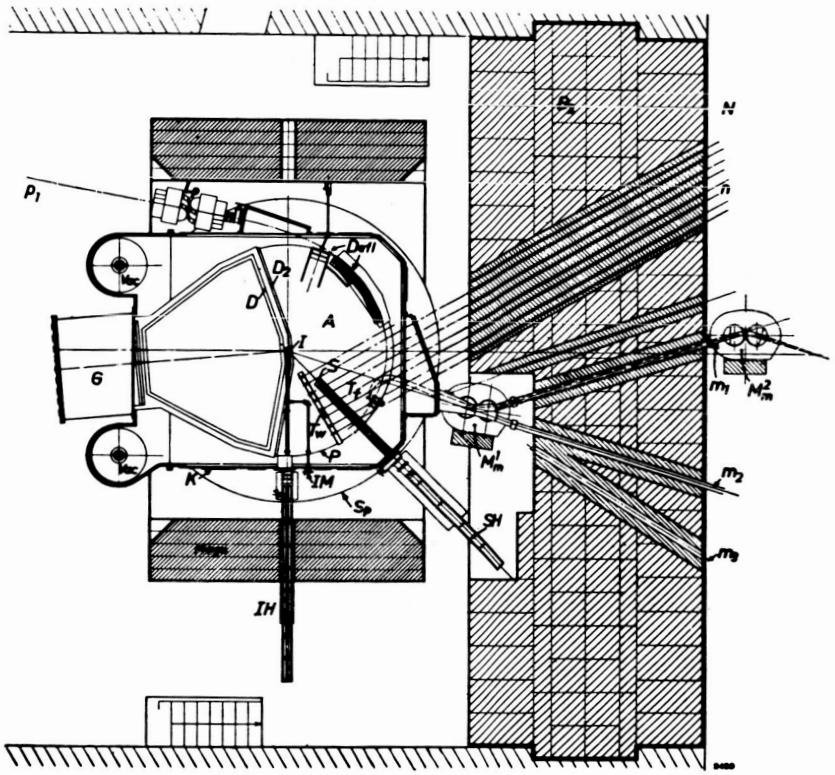

NASA

Figure 6.- Target systems for the CERN 600-MEV synchrocyclotron.

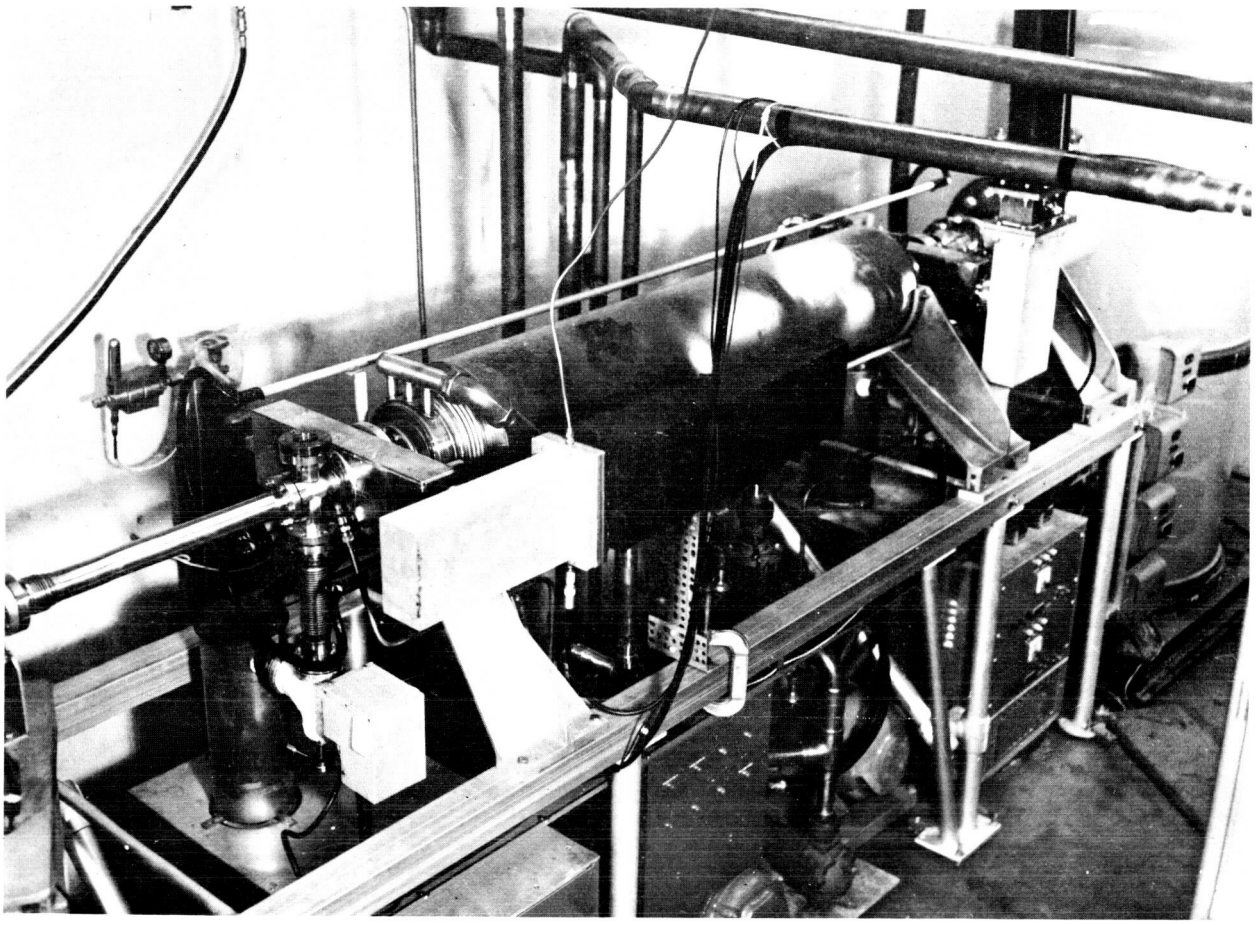

NASA
L-62-1045.1

Figure 7.- Accelerating section of a 10-MEV electron linac.

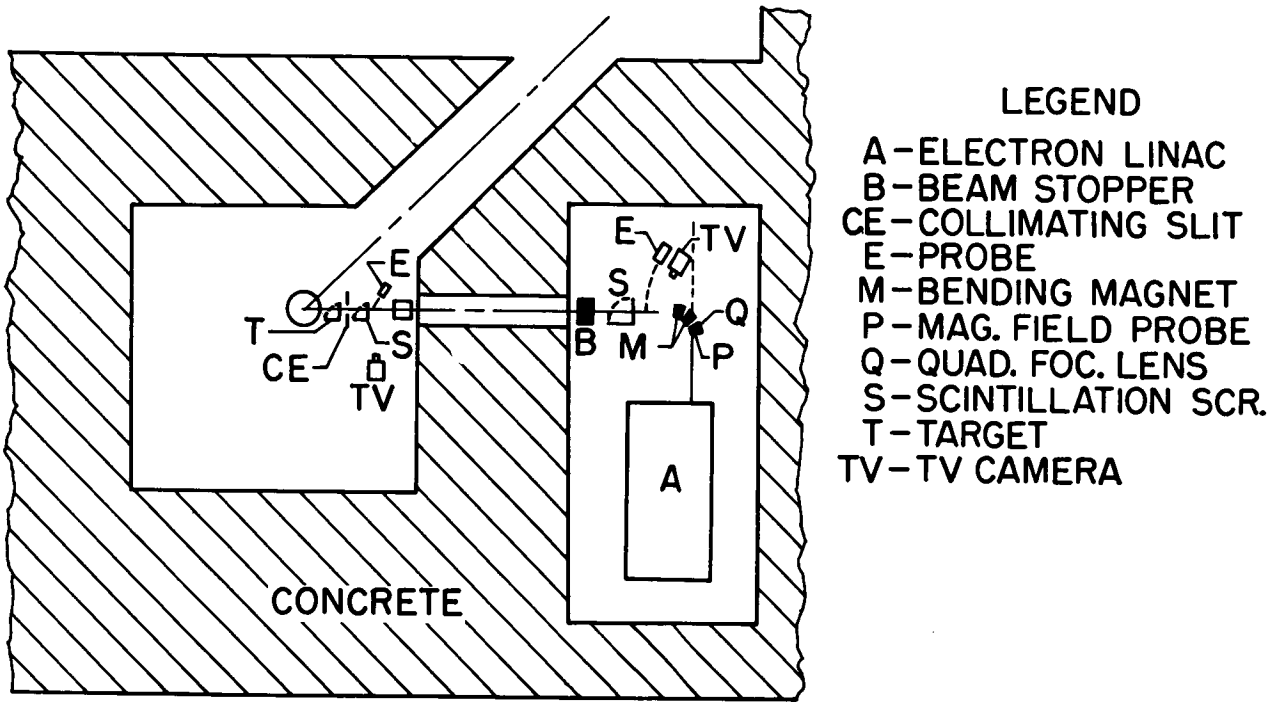

NASA

Figure 8.- Schematic of the electron linac proposed for SREL.

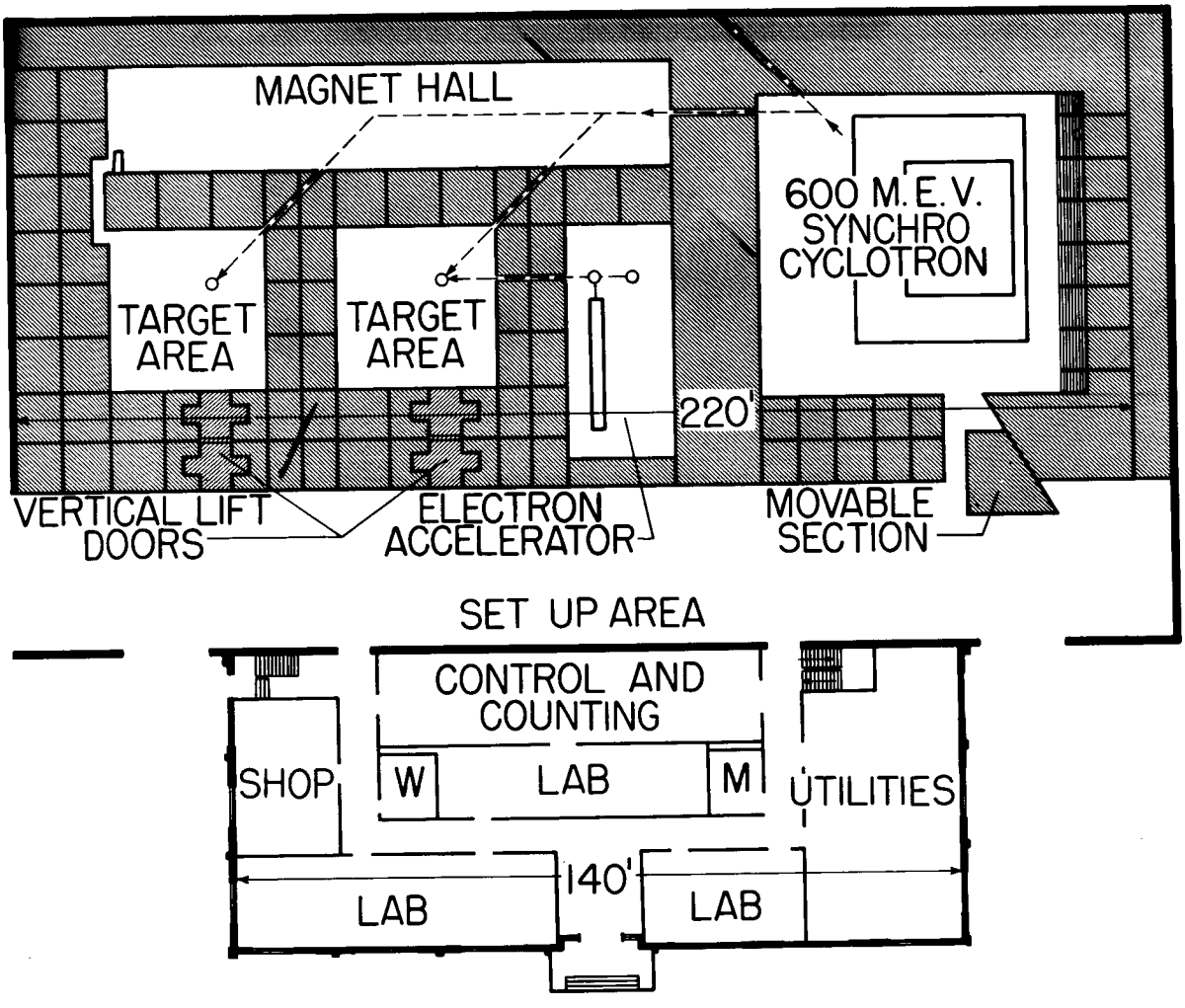

NASA

Figure 9.- Plan view of the Space Radiation Effects Laboratory.

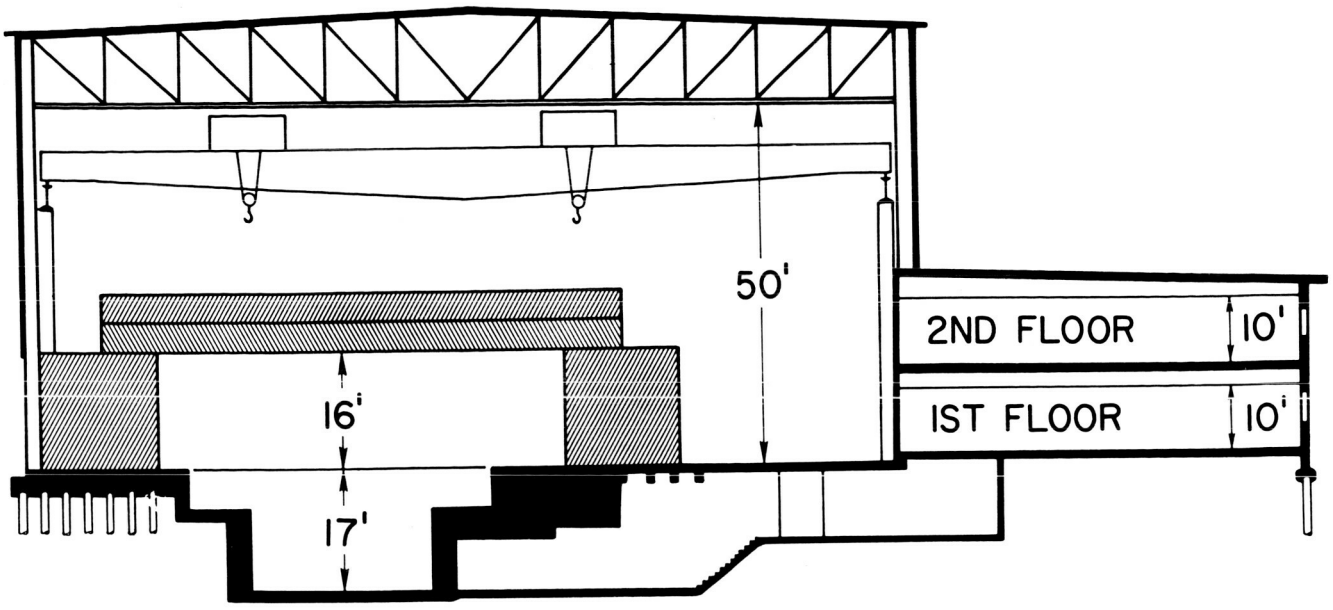

NASA

Figure 10.- Section of the Space Radiation Effects Laboratory taken through the synchrocyclotron cave.

NASA
L-62-1043

Figure 11.- Architect's perspective rendering of the Space Radiation Effects Laboratory.

Paper B-4

THE EFFECTS OF PROTONS ON SEMICONDUCTOR DEVICES

William C. Honaker*
NASA Langley Research Center

Abstract

Experimental results are presented covering the data obtained from the bombardment of several transistors with 40 and 440 Mev protons. The data indicated a proton energy as well as a transistor frequency dependence on degradation. Figures are presented showing relative degradation of transistors with integrated flux.

Introduction

The presence of high-energy protons in the earth's radiation belts and in solar flares poses a problem in the design of circuits utilizing transistors for space application. The flux above an energy of 25 Mev in the inner belt is approximately 2.5×10^4 protons/cm^2/sec with the differential energy spectrum varying as $E^{-3.4}$. The proton energy ranges up to approximately 600 Mev (refs. 1 and 2). The proton flux in an extreme solar flare may be as high as 10^6 protons/cm^2/sec. In some high-energy events the proton energies extend into the billion electron volt (Bev) range (ref. 3).

Damage produced in solids by charged-particle bombardment has been considered theoretically in references 4 and 5. Most of the theory for such damage has been arrived at by using pure-element models with no definite correlation existing with a transistor junction; thus, a definite need for experimental data exists. This report presents data obtained during experimental testing of several types of transistors. If transient damage effects such as ionization are neglected, the primary damage produced in pure silicon and germanium is the creation of Frenkel defects (vacancy-interstitual pairs). This is the vacancy created by knocking an atom from its normal lattice site and having it come to rest at an interstitual position within a lattice structure. The defects that are formed affect the electrical characteristics of a semiconductor by providing recombination and trapping sites which can reduce the number of carriers and result in a decrease in carrier lifetime (refs. 6 and 7).

---

*Aerospace Technologist.

Only a limited amount of work has been accomplished with protons in the study of radiation damage on semiconductors (ref. 8). Results of bombardment with 40 and 440 protons presented in the present report show the extent to which transistors are damaged when they are subjected to a total proton flux in the order of 10^{12} protons/cm^2. With a knowledge of the proton spectrum in the radiation belts and in solar flares, an estimate can be made of the lifetime of the various transistors subjected to these environments.

Apparatus and Procedure

University of Minnesota Test

A total of 75 transistors were irradiated with 40 Mev protons by utilizing the linac accelerator at the University of Minnesota. The accelerator is capable of producing a time-average beam current of 10^{-8} amperes (approximately 6×10^{10} protons/sec). The cross-sectional area of the proton beam is approximately 1.25 square centimeters.

The experimental setup used during irradiation tests at the University of Minnesota is shown in figure 1. The transistors were mounted in individual ports on an aluminum disk and were remotely positioned in the proton beam. A cam-controlled electric motor automatically positioned each transistor in the proton beam for 10 minutes at a beam flux rate of 3×10^9 protons/cm^2/sec or a total flux of 1.8×10^{12}. A zinc sulfide phosphor (silver activated) was placed on the aluminum disk in a position corresponding to that of the transistors and was alined with the proton-beam pipe exit. The center of the proton beam was visually located by using a closed-circuit television system to determine the location of the beam-excited portion of the phosphor. By marking the excited portion on the television monitoring screen, each transistor could be properly positioned within the marked area corresponding to the proton beam. During the experiments, the beam flux was monitored by means of a Faraday cup mounted behind the transistors. Periodic checks were made on the beam flux level through a vacant space in the aluminum disk.

During irradiation the transistors were operated in an active circuit. The transistor parameters which were monitored and recorded on a direct-writing oscillograph recorder included collector current, I_C; small-signal current gain, h_{fe}; and leakage current, I_{CBO}. The base current I_B was held constant during the irradiation. Pretest and post-test measurements on each type of transistor were made both at the Langley Research Center (LRC) as well as by the manufacturer, with the

exception of the 2N146 and 2N337 transistors for which no manufacturers' data were obtained.

Carnegie Institute of Technology Test

A total of 20 transistors were irradiated by utilizing the 440 Mev proton synchrocyclotron at the Carnegie Institute of Technology. The synchrocyclotron is capable of producing a time-average beam current of 2×10^7 protons/cm^2/sec. The cross-sectional area of the proton beam at the external port is approximately 25 square centimeters.

The method used for exposing the transistors to the beam in this experiment differed from the method used at the University of Minnesota in that the larger cross-sectional area of the beam permitted the irradiation of several transistors at the same time with each bombardment lasting approximately 6 hours. Due to the nonuniformity of the cross-sectional area of the proton beam, a profile survey was made with a scintillation counter. The positions of the various transistors in the beam were carefully determined, and total dosages were arrived at by using the beam-profile plots. The beam current was measured before and during irradiation by using a helium-filled ionization chamber mounted between the beam exit port and the specimen and operated at 2 lb/sq in. above atmospheric pressure. The transistors exposed to the beam were mounted on a bracket supported by a junction box attached to a tripod. The transistor parameters measured before, during, and after irradiation were the same as those of the University of Minnesota experiments except that no manufacturer's data were obtained. Also, the number of transistors irradiated was fewer because of the lower beam flux and the longer irradiation time.

Discussion and Results

Figure 2 shows seven 2N146 (NPN) germanium, low-frequency transistors which were irradiated with 40 Mev protons. The average change in gain was a decrease of 70 percent at a total flux of 1.8×10^{12} p/cm^2, which was found to be typical for low-frequency germanium devices. Figure 3 is a plot of six, 2N743, NPN, high-frequency silicon transistors with small signal current gain plotted against integrated proton flux. The change was about a 12-percent decrease at a total flux of 1.8×10^{12} p/cm^2 or approximately one-sixth the damage sustained by the low-frequency transistor in figure 2. In figure 4 a plot is shown of a 2N337, NPN, silicon low-frequency transistor. This device was damaged by about 85 percent of its original value after a dose of 1.8×10^{12} p/cm^2. The extent of damage was about the same as for the low-frequency germanium device.

To give an idea of the frequency dependence on transistor damage figure 5 shows a 2N1302 transistor having an alpha cutoff frequency of 0.5 megacycle and a 2N224 transistor with an alpha cutoff frequency of 4.5 megacycles. The difference in frequencies here is approximately an order of magnitude and the difference in change in gain is 20 percent. The change would be approximately the same for other orders of magnitude change in frequency but this can also vary with materials and type of junction.

The 2N1302 shown in figure 5 was one of the devices irradiated at both 40 and 440 Mev. Figure 6 shows the relative damage at these two energies for a medium frequency transistor. The relative change at the two energies at 3×10^{11} p/cm^2 was approximately a factor of 3 for this transistor. A comparison can be made between this NPN germanium device and a PNP germanium device shown in figure 7. Figure 7 is basically the same type of plot as figure 6 except that a 2N224, PNP, germanium transistor is irradiated in figure 7. The relative change in the 40 and 440 Mev bombardment again is approximately a factor of 3 at identical fluxes. Note the initial increase in gain and then a decrease. This phenomenon is noticed in PNP germanium junctions but not in NPN germanium junctions.

Table I gives a complete list of transistors bombarded with 40 Mev protons and shows the type junction, material, alpha cutoff frequency and the average change in each transistor gain at a total flux of 1.82×10^{12} protons/cm^2. The averages were arrived at using six or seven transistors at the same proton dose and the changes noted ranged from an increase of 10 percent for the 2N128 PNP germanium transistor to a decrease of 85 percent for the 2N337 NPN silicon device.

For a good comparison between NPN and PNP junction, the second transistor the 2N1302 which changes by 65 percent and the sixth a 2N1303 which changed by 23 percent are nearly the same device except for the type junction; here it is evident that the PNP junction is more resistant to proton irradiation.

In table II, if one can assume a tolerable operating level of 0.7, the original gain of a transistor and a flux of 5×10^4 p/cm^2/sec in the space environment, then the lifetime of the various transistors irradiated is given in the right-hand column which extends from 30 to 418 days.

References

1. Smith, R. V., Fisher, P. C., Imhof, W. L., and Reagan, J. B.: Midas IV Proton Measurement in the Inner Van Allen Belt. [Rep.] 3-77-62-6 (Contract AF 19(604)-8028) Nuclear Phys. Dept., Lockheed Missiles and Space Corp., Feb. 1962.

2. Freden, Stanley C., and White, R. Stephen: Protons in the Earth Magnetic Field. Phys. Rev. Letters, vol. 3, no. 1, July 1, 1959, pp. 9-11.

3. Foelsche, Trutz: Current Estimates of Radiation Doses in Space. NASA TN D-1267, 1962.

4. Seitz, Frederick, and Koehler, J. S.: Displacement of Atoms During Irradiation. Solid State Physics, Vol. 2, Frederick Seitz and David Turnbull, eds., Academic Press, Inc. (New York), 1956, pp. 305-448.

5. Mitchell, E. W. J.: The Effect of Radiation Damage on the Electronic Properties of Solids. British Jour. Appl. Phys., vol. 8, no. 5, May 1957, pp. 179-189.

6. Denny, J. M., and Pomeroy, D.: Radiation Damage and Transistor Life in Satellites. Proc. IRE, vol. 48, no. 5, May 1960, pp. 950-952.

7. Billington, Douglas S., and Crawford, James H., Jr.: Radiation Damage in Solids. Princeton University Press, 1961.

8. Hulten, W. C., Honaker, W. C., and Patterson, John L.: Irradiation Effects of 22 and 240 Mev Protons on Several Transistors and Solar Cells. NASA TN D-718, 1961.

TABLE I

RELATIVE DAMAGE TO Si AND Ge TYPE TRANSISTORS

40 MEV PROTONS - TOTAL FLUX 1.82×10^{12} CM^{-2}

TRANSISTOR	TYPE	DESCRIPTION	$f_{\alpha b}$ MC	Δh_{fe} PERCENT
2 N 859	PNP Si	ALLOY JUNCTION	17	78
2 N 1302	NPN Ge	ALLOY JUNCTION	4.5	65
2 N 224	PNP Ge	ALLOY JUNCTION	0.5	85
2 N 1305	PNP Ge	ALLOY JUNCTION	8	65
2 N 1303	PNP Ge	ALLOY JUNCTION	4.5	23
2 N 526	PNP Ge	ALLOY JUNCTION	3	65
2 N 337	NPN Si	GROWN JUNCTION	30	85
2 N 146	NPN Ge	GROWN JUNCTION	13	70
2 N 169A	NPN Ge	RATE GROWN	9	50
2 N 743	NPN Si	DIFFUSED MESA	500	12
2 N 128	PNP Ge	SURFACE BARRIER	60	+10

TABLE II

FLUX TOLERANCE $\frac{h_{fe}(\phi)}{h_{fe}(0)} = 0.7$

TRANSISTOR TYPE	MAXIMUM PROTON FLUX $(10^{11}/CM^2)$	PROTON ENERGY	SIMULATED TIME IN DAYS IN A PROTON FLUX OF 5×10^4 P/cm^2/SEC
2 N 337	1.3	40 MEV	30
2 N 224	1.5	↓	35
2 N 146	2		46.5
2 N 859	2.5		58.1
2 N 1305	5		116.3
2 N 1302	5		116.3
2 N 526	6.5		151.2
2 N 169A	7		162.8
2 N 1303	18		418.6
2 N 743	>18		>418.6
2 N 128	>18		>418.6

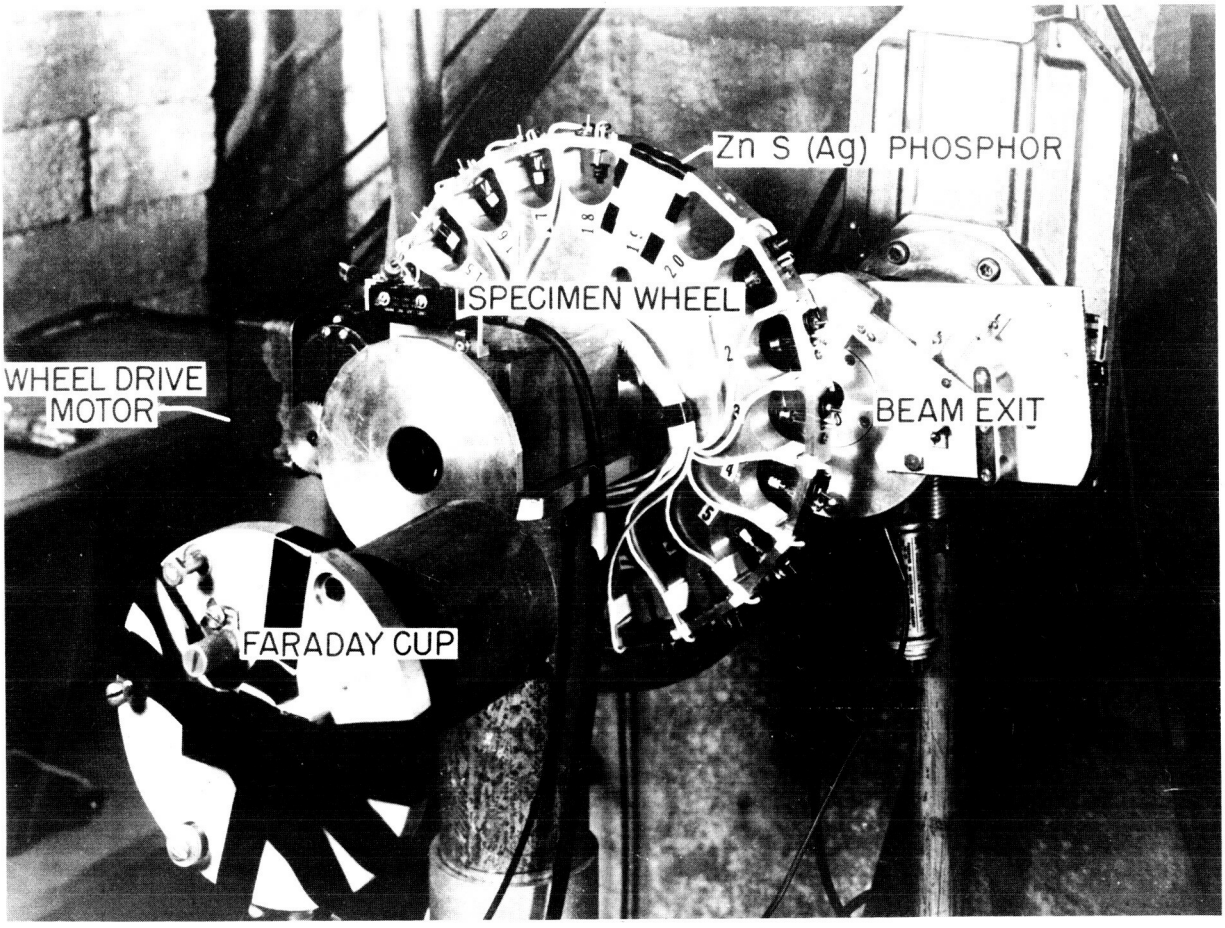

NASA
L-62-1017

Figure 1.- Transistor positioning device in the 40 Mev beam.

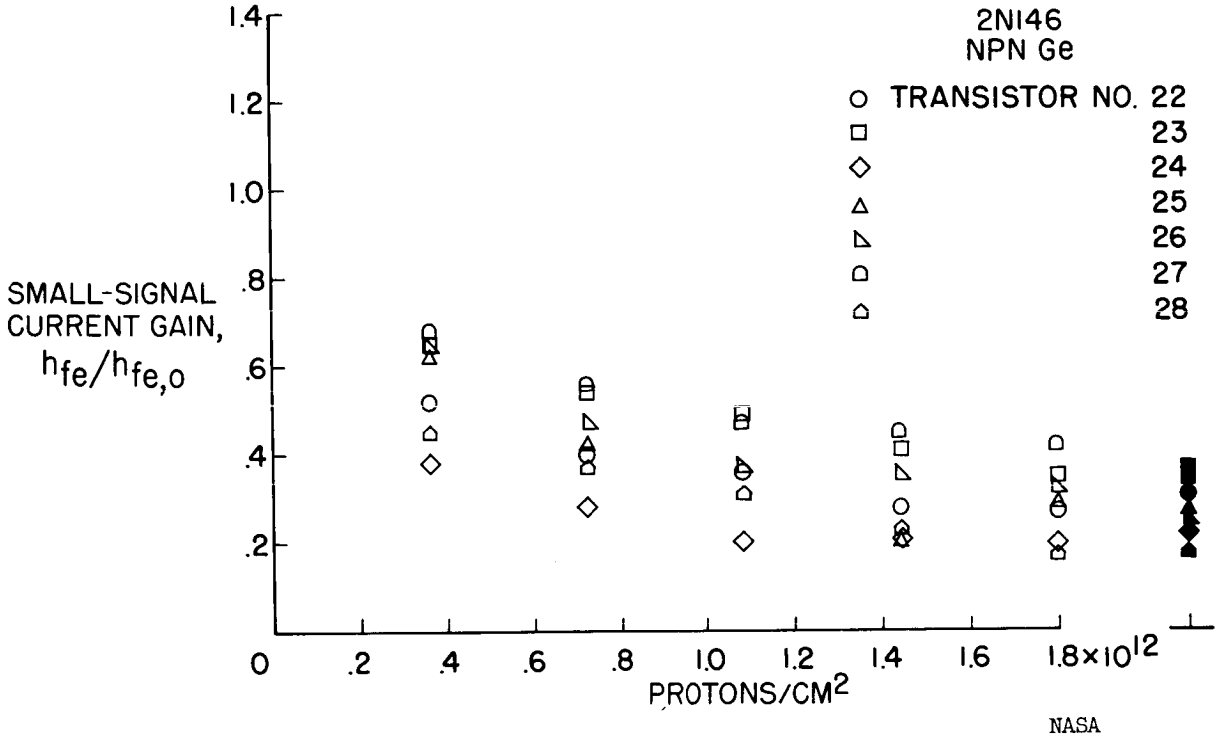

Figure 2.- 40 Mev proton damage.

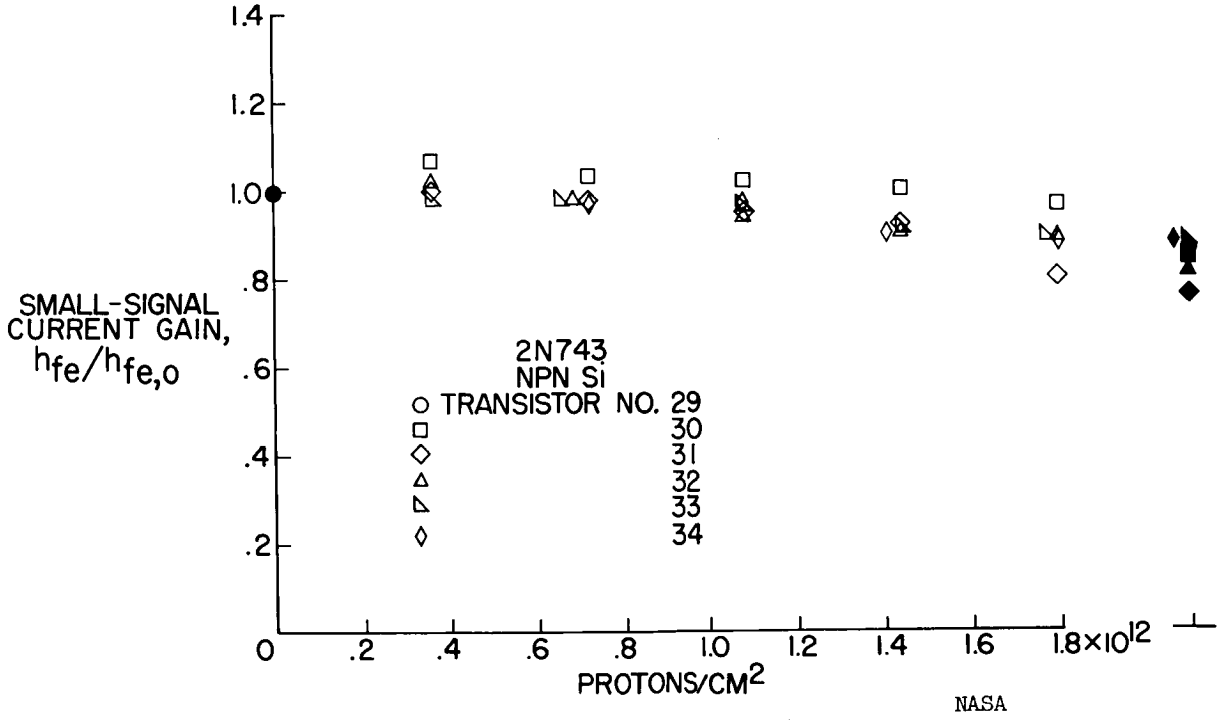

Figure 3.- 40 Mev proton damage.

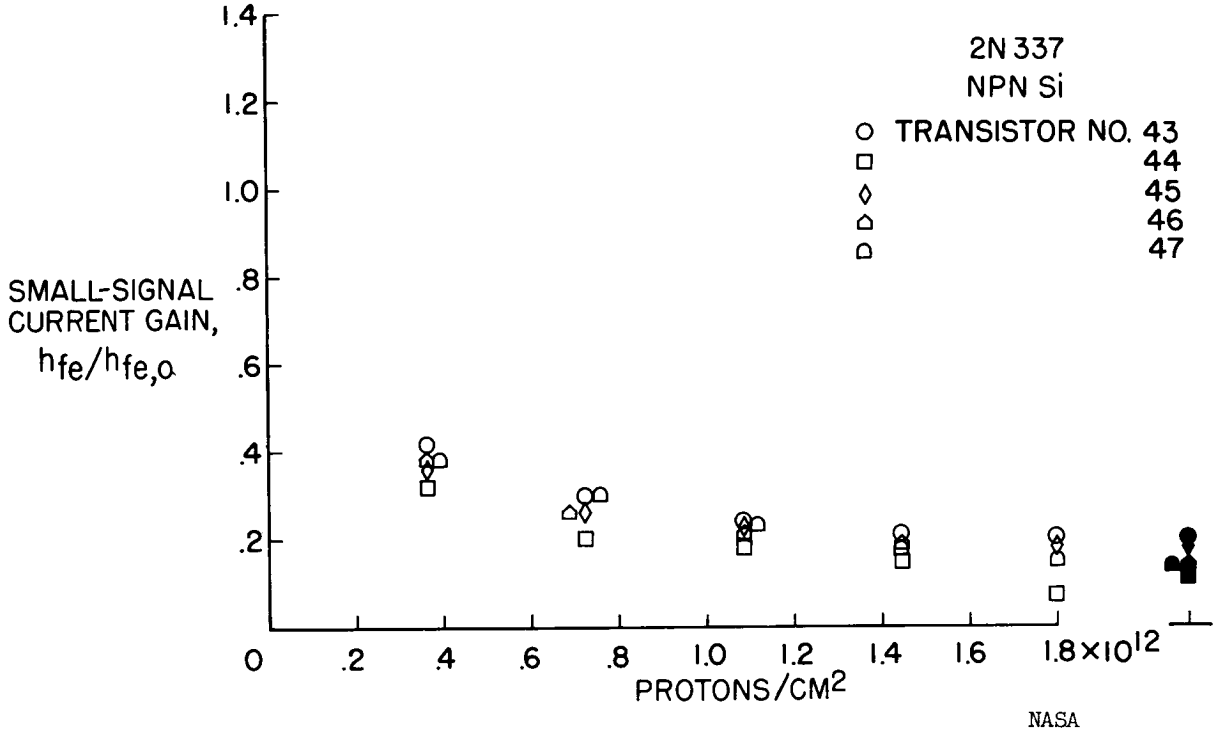

Figure 4.- 40 Mev proton damage.

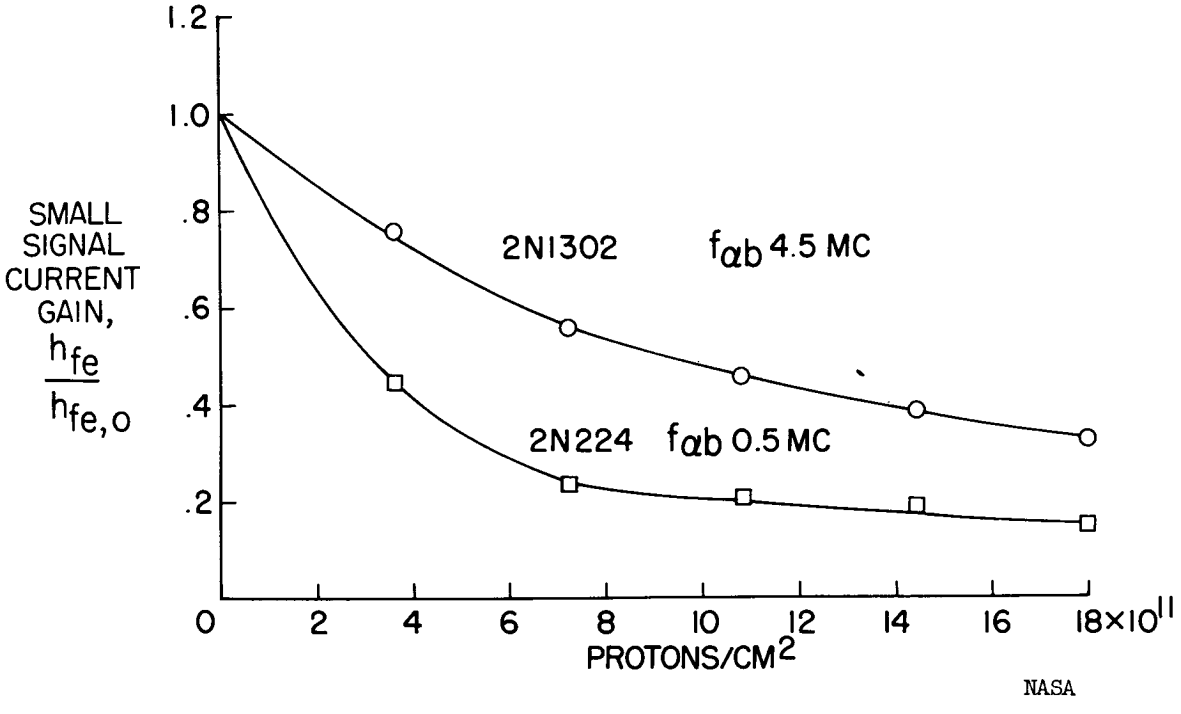

Figure 5.- Proton damage versus alpha cutoff.

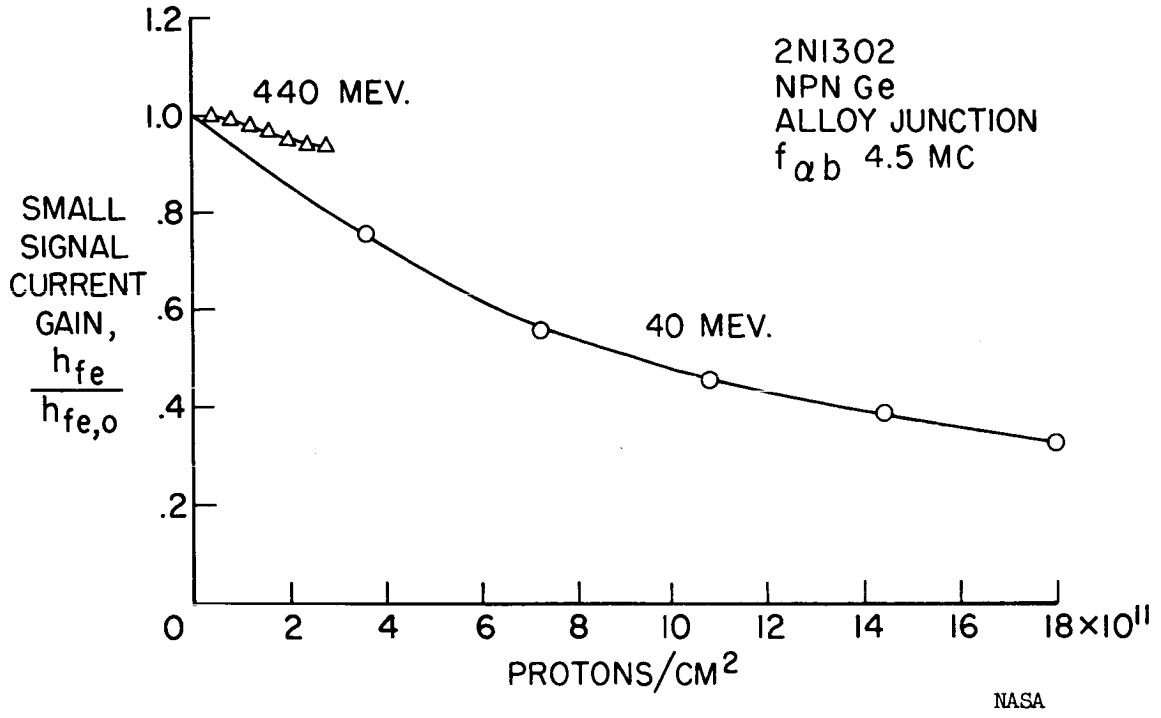

Figure 6.- Proton damage versus energy.

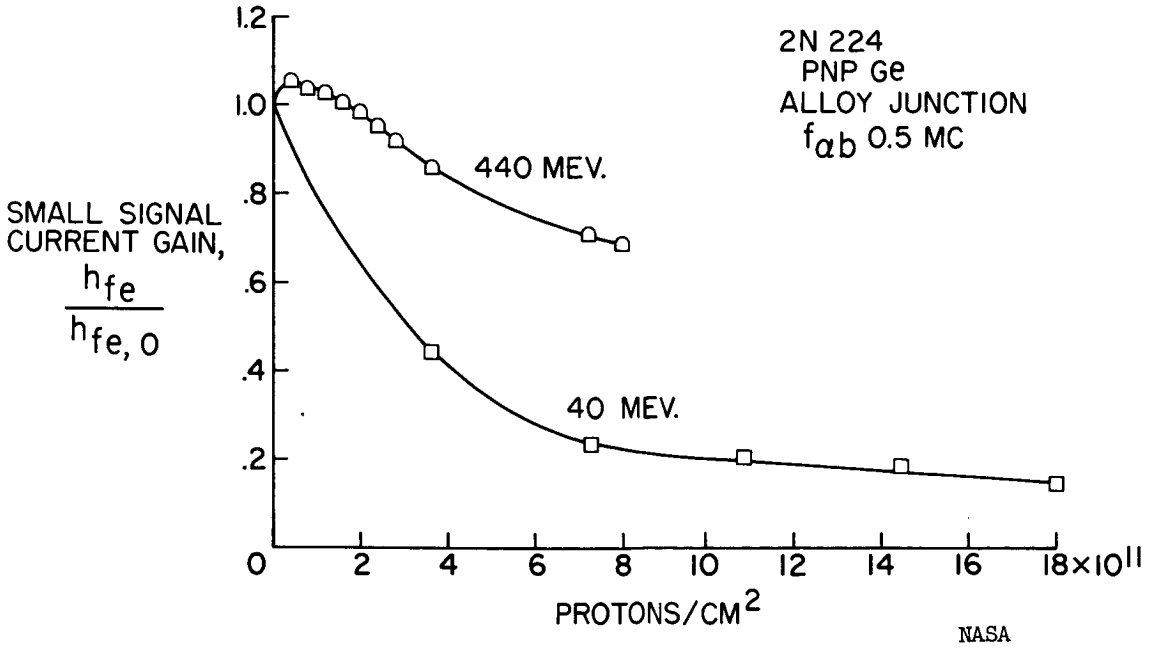

Figure 7.- Proton damage versus energy.

Paper B-5

PROTON RADIATION DAMAGE IN SEMICONDUCTOR DEVICES

D. A. Gandolfo*, D. M. Arnold*, J. A. Baicker**,
H. Flicker**, J. R. Parker*, J. Vilms**, J. Vollmer*,
Radio Corporation of America

Abstract

The objective of the present study is to interpret observed changes in transistor electrical characteristics in terms of fundamental damage in the semiconductor crystal structure and, in so doing, to predict the effects of proton bombardment. Proton and neutron displacement production rates are calculated. These are used in conjunction with neutron irradiation data and an assumed similarity of defect clusters to determine the effects of protons on transistors. Reasonable agreement with experiment is obtained. The expected lives of transistors in satellites orbiting in the inner Van Allen belt are given.

Introduction

It has become important to understand and be able to predict the extent of proton damage to semiconductor devices. Accordingly, the objective of the study reported here is to interpret the observed changes in electrical characteristics of transistors in terms of fundamental damage to the semiconductor crystal structure and in so doing, to predict the effects of proton bombardment.

The method is as follows. First, the rate of production of lattice displacements is calculated at various proton energies. Next the rate of production of lattice displacements for neutron bombardment is calculated. Finally damage constants for neutron irradiation, determined from existing data, are converted into damage constants for proton irradiation by means of the calculated displacement rates. With these, the effect of proton bombardment on transistors is computed.

*Applied Research, Camden, New Jersey
**David Sarnoff Research Center, Princeton, New Jersey

Displacement Calculations

According to the theory discussed, for example, by Seitz and Koehler[1], Dienes and Vineyard[2] and Billington and Crawford[3] the displacement production rate is given by

$$R_D = \int_{E_d}^{T_m} n_{si}\, g(T)\, \frac{d\sigma}{d\Omega}(T)\, dT \qquad (1)$$

where: R_d is the displacement density per unit flux of incident particles.

n_{si} is the number of target silicon atoms per unit volume.

$g(T)$ is the defect cascade function, i.e. the expected total number of displacements produced by a primary recoil of energy T.

$\frac{d\sigma}{d\Omega}(T)$ is the differential elastic scattering cross section.

E_d is the displacement threshold, i.e. the energy which must be imparted to a target atom to displace it from its equilibrium site.

T_m is the maximum recoil energy which may be imparted to a target atom by an incident particle with a given energy.

The variable of integration in this expression is T, the energy of the primary recoil. T is related to the energy of the incident particle, E_{inc}, and the C.M. angle, θ, through which it is deflected by

$$T = \frac{4\left(\frac{m}{M}\right)E_{inc}}{\left[1+\left(\frac{m}{M}\right)\right]^2}\ \sin^2\frac{\theta}{2} \qquad (2)$$

where m is the proton mass and M is the silicon mass.

First, the proton displacement rate will be considered. At low bombarding energies one would expect coulomb forces to dominate the proton-silicon interaction, and as will be pointed out later, the

1. F. Seitz and J. S. Koehler, Solid State Physics, (Ed. by F. Seitz and D. Turnbull) Academic Press, N. Y. 1956, Vol. 2, P. 305.

2. G. J. Dienes and G. H. Vineyard, Radiation Effects in Solids, Interscience, N. Y. 1957.

3. D. S. Billington and J. H. Crawford, Radiation Damage in Solids, Princeton University press, Princeton, 1961.

radiation damage data for protons below 10 MeV is consistent with Rutherford scattering calculations. Above 10 MeV, however, the proton-silicon interaction must be modified to include nuclear forces. The principal result is a slight, though important, enhancement of the elastic cross section mainly at large scattering angles. This enhancement does not produce an observable increase in the number of primary proton-silicon collisions, but the few extra collisions that result generally involve a large momentum transfer, on the average, and consequently a large number of secondary lattice displacements. At very high energies (above 100 MeV) a complete account of the displacement production rate requires the inclusion of a number of inelastic processess as well as elastic scattering.

In the absence of data on the scattering of protons by silicon, the proton-aluminum cross sections have been used for these calculations. The justification for this is a logical consequence of the nuclear optical model, which fits the elastic proton scattering data with considerable accuracy over the energy range from 10 to 100 MeV, and for nuclei throughout practically the entire periodic table. Since the optical model parameters are slowly varying functions of atomic weight, going from A=27 to A=28 requires practically no correction.

The proton displacement rate is shown as a function of proton energy in Fig. 1.

The solid curve shown in this figure is a compilation of silicon solar cell damage data from several sources. The two lowest-energy points shown, at 1.5 and 4.5 MeV were calculated from Rutherford scattering, and the upper five points from p+Al elastic scattering data. The solid curve has been normalized to the computed displacement rate at E_p = 10 MeV.

There are two interesting features about this figure. The first is that at proton energies as low as 10 MeV there is a perceptible contribution to the total lattice displacement rate caused by nuclear-elastic scattering. The second interesting point is that elastic scattering is sufficient to give a fairly good account of the total displacement rate for proton energies as high as 100 MeV. At 180 MeV the solar cell damage rate is 2.5 times what one would expect from elastic scattering alone.

Next, the displacement production rate for neutrons is calculated using Eq. 1, and making the same assumptions that were made in the proton displacement calculation regarding the applicability of n + Al data to silicon. The results of the calculation are given in Fig. 2 which shows the displacement rate over the energy interval, 0 to 10 MeV. The weighted average of the displacement rate for a fission spectrum is shown as $\overline{R}_{DN}$. The fission spectrum is the energy spectrum of prompt fission neutrons and is a good approximation to the energy spectrum of neutrons produced by pulsed reactors such as the Godiva and Kukla facilities.

Lifetime Damage Constant

Next attention will be turned to the electrical property of semiconductors which is most affected by radiation, namely the minority carrier lifetime. In semiconductors like germanium and silicon where direct band to band recombination is forbidden, the recombination rate is directly proportional to the number of traps or centers at which recombination can take place. The minority carrier lifetime is of course inversely related to the recombination rate; therefore, to the number of traps. According to these considerations the lifetime may be written as

$$\frac{1}{\tau} = C\, N_t\, (\varphi) \tag{3}$$

where C is related to the capture cross section of the centers for minority carriers, the energy levels of the centers, the Fermi level of the material and the thermal velocities of the carriers. C is assumed to be independent of the flux, φ. N_t is the number of traps and is, of course, a function of φ. Loferski and Rappaport[4-6] determined experimentally that the lifetime is related to the flux by

$$\frac{1}{\tau} = \frac{1}{\tau_o} + k\varphi \tag{4}$$

where τ_o is the pre-irradiation lifetime and k is the lifetime damage constant. Taking the derivative of $\frac{1}{\tau}$ with respect to φ one finds that

$$\frac{\partial\left(\frac{1}{\tau}\right)}{\partial\varphi} = C\,\frac{\partial N_t}{\partial\varphi} = k \tag{5}$$

Thus, k is simply the product of C and the rate of introduction of traps. At this point, it is assumed that the rate of introduction of traps is directly proportional to the displacement production rate. Further, it is assumed that the damage constants for protons and neutrons are related to the particle type only through the respective displacement rates. Therefore the damage constants for protons and neutrons may now be written

$$k_P = C'R_{DP};\ k_N = C'R_{DN} \tag{6}$$

4. P. Rappaport, Phys. Rev. 94, 1409(A) (1954).

5. J. J. Loferski and P. Rappaport, Phys. Rev. 98, 1861 (1955).

6. P. Rappaport and J. J. Loferski, Phys. Rev. 100, 126(A) (1955)

When C' is eliminated from Eq. 6, k_p is obtained in terms of k_N and the displacement rates

$$k_p = k_N \frac{R_{DP}}{R_{DN}} \tag{7}$$

k_N is determined from neutron irradiation experiments and R_{DP} and R_{DN} are calculated quantities.

The assumption that the damage constants are functions only of the total displacement production rates, independent of the type of particle producing the damage is an essential part of this study. However, it has been seen that for proton energies above 10 MeV nuclear-elastic scattering contributes significantly to the total displacement rate. The good agreement between the proton energy dependences of the damage rate and the displacement rate may be accounted for by assuming that all displacements are equally effective in producing electrical damage, regardless of whether they are produced in high concentration, as in the displacement spikes characteristic of nuclear-elastic scattering, or in very low concentration, as in the point defects generally characteristic of coulomb scattering.

Effects of Proton Bombardment on Transistors

Transistors and the effect of radiation induced lifetime changes on their performance will now be considered. Webster's[7] equation shows the dependence of the common emitter current gain, β, on the minority carrier lifetime

$$\frac{1}{\beta} = \frac{SA_sW}{A\,D} + \frac{\sigma_b W}{\sigma_e L_e} + \frac{1}{2}\frac{W^2}{D\tau} \tag{8}$$

where S is the surface recombination velocity, A_s is the effective area for surface recombination, W is the base width, A is the area of the conduction path, σ_b and σ_e are the conductivities of the base and emitter regions, L_e is the diffusion length in the emitter, D is the diffusion constant and τ is the minority carrier lifetime.

The first term on the right is the surface recombination term, the second is the injection efficiency term and the third is the volume recombination term. Terms one and two are assumed to be independent of the flux. Equation 8 may be rewritten, using Equation 4, to show explicitly the dependence on radiation induced lifetime changes

$$\frac{1}{\beta} = \frac{1}{\beta_o} + \alpha\varphi = \frac{1}{\beta_o} + \frac{1}{2}\frac{W^2}{D}k\varphi = \frac{1}{\beta_c} + \frac{.2}{f_{c\alpha}}k\varphi \tag{9}$$

---

[7] W. M. Webster, Proc. IRE 42, 914 (1954)

where $f_{c\alpha}$ is the alpha cutoff frequency of the device. This relationship has been checked experimentally by Messenger and Spratt[8] and Loferski[9]. In a neutron irradiation experiment where the flux is φ_N, the lifetime damage constant for neutrons, k_N, is measured. If the effect of a proton bombardment is to be calculated, $k_P\varphi_P$ must be substituted for $k_N\varphi_N$. Equation 7 shows how kp is determined from k_N and the calculated displacement rates R_{DN} and R_{DP}. Several sample calculations have been made to check the validity of the method outlined here. From the data of Puttcamp[10] of the Diamond Ordance Fuze Labs and Hicks[11], et. al. at Boeing, lifetime damage constants describing the degradation of β with neutron flux have been obtained. These have been used in conjunction with the method discussed above to compute lifetime damage constants for monoenergetic proton bombardment.

Using the damage constants thus obtained one may calculate the proton flux necessary to reduce the current gain of selected silicon transistors to a specified fraction of its initial value. The results of the calculation may be compared with the experimental results which Hulten and Honaker[12] obtained with 40 MeV protons.

Example 1: 2N743, npn mesa, $f_{c\alpha} \doteq 400$ Mc.

The data of Hulten and Honaker[12, 13](average of 6 units) showed that a flux of 1.8×10^{12} protons/cm^2 at 40 MeV reduced β to $.85\beta_o$. From Puttcamp's neutron irradiation of the 2N697, npn mesa, $f_{c\alpha} \doteq 150$ Mc, one finds

$$\alpha_N \text{ (average of 4 units)} = 1.8 \times 10^{-15} \text{ nvt}^{-1}$$

and

$$\alpha_P = \frac{150}{400} \times \frac{1000}{380} \alpha_N = 1.8 \times 10^{-15} \text{ per unit proton flux.}$$

8. G. C. Messenger and J. P. Spratt, Proc. IRE, 46, 1038 (1958)

9. J. J. Loferski, J. Appl. Phys. 29, 35 (1958)

10. Robert Puttcamp, Diamond Ordance Fuze Laboratories TR-975 (AD 270264) 27 November 1961.

11. D. A. Hicks, D. V. Keller, J. B. Robison, R. K. Durkee, J. R. Orr, B. M. Clarke, Boeing Airplane Company, Report D5-2880, 1 December 1958.

12. W. C. Hulten, "Radiation Effects of 40 and 440 MeV Protons on Transistors," Society of Aerospace Material and Process Engineers Symposium, St. Louis, May 7-9, 1962.

13. W. C. Honaker, "The Effects of Protons on Semiconductor Devices," Protection against Radiation Hazards in Space, Gatlinburg, November 5 - 7, 1962.

Using this α_p to calculate the proton flux necessary to reduce β to $.85\beta_0$ one finds

$$\varphi_{calc} = 2.2 \times 10^{12} \text{ protons/cm}^2$$

and

$$\frac{\varphi_{calc}}{\varphi_{exp}} = 1.2$$

Example 2: 2 N859, pnp alloy, $f_{c\alpha} \doteq 14$ Mc.

The data of Hulten and Honaker (average of 6 units) showed that a flux of $.7 \times 10^{12}$ protons/cm^2 at 40 MeV reduced β to $.5\beta_0$. From the neutron irradiation by Hicks et. al. of the 2N495, also a pnp alloy, with $f_{c\alpha} \doteq 35$ Mc one finds

$$k_N = 3.2 \times 10^{-7} \text{ nvt}^{-1} \text{ sec}^{-1}$$

and

$$\alpha_p = \frac{.2}{14 \times 10^6} \times \frac{1000}{380} \times k_N = 1.23 \times 10^{-14} \text{ per unit proton flux}$$

Using this α_p to calculate the proton flux required to reduce β to $.5\beta_0$ one finds

$$\varphi_{calc} = 1.5 \times 10^{12} \text{ protons/cm}^2$$

and

$$\frac{\varphi_{calc}}{\varphi_{exp}} = 2.2$$

The agreement in the case of the 2N743 is quite good. For the 2N859 it is less good but still satisfactory in light of the scatter in the proton irradiation data.

Transistors in Satellites

Having checked the method in two cases where comparable neutron and proton data exist, one may proceed to the calculation of the expected life of selected groups of transistors in a hypothetical proton flux. The flux is an idealized representation of that which might be experienced by a device aboard a satellite whose orbit is in the most intense region of the Inner Van Allen Belt. This idealized proton spectrum has been constructed from the data of Heckman and Armstrong[14] and is shown in Figure 3. The expected life of the devices has been calculated from

14. Harry H. Heckman and Alice H. Armstrong, J. Geophys. Research 67, 1255 (1962).

$$T_{(.5\beta_o)} = \frac{2D}{W^2\beta_o} \times \frac{R_{DN}}{k_N} \times \frac{1}{R_{DP}\Phi_p} \qquad (10)$$

where k_N is the average lifetime damage constant for p or n type silicon as given by Messenger and Spratt and Φ_p is the proton flux rate in particles/cm^2-sec. Results of this calculation are shown in Figure 4. Table 1 lists the type numbers and some properties of the transistors in the groups indicated by the numbers in Figure 4.

Table 1. Satellite Transistors

Group Number	W(cm.)	f_c (Mc)	Transistor Types
1	5.1×10^{-5}	> 500	2N709 2N917
2	1.02×10^{-4}	$200 < f_{c\alpha} < 500$	2N916 2N914 2N708
3	1.9×10^{-4}	$50 < f_{c\alpha} < 200$	2N718A 2N1613 2N1893 2N910
4	3×10^{-4}	$20 < f_{c\alpha} < 50$	2N1675 2N930
5	1.27×10^{-3}	$2 < f_{c\alpha} < 10$	2N560 2N657
6	2.3×10^{-3}	$.5 < f_{c\alpha} < 1.5$	2N1485 2N2016
PNP	1.2×10^{-4} 1.2×10^{-4} 1.5×10^{-4}	~ 100	2N995 2N869 2N1132

To be noted in Figure 4 is the superiority of transistors with thin bases (corresponding to high alpha cutoff frequency) and low initial current gain.

Summary and Conclusions

The displacement production rates for protons and neutrons have been calculated and used with neutron irradiation data to predict proton damage.

The lattice displacement rate produced by elastic scattering of protons has been calculated as a function of energy and compared with the observed proton damage rate for silicon solar cells. For energies up to nearly 100 MeV the agreement is quite good. As might be expected, at higher energies where nuclear reactions assume increasing importance the damage rate exceeds the displacement rate calculated from elastic scattering alone.

The effect of protons on transistors has been calculated with the use of a lifetime damage constant measured under neutron irradiation and the ratio of the calculated displacement rates. The good agreement with available data indicates that the assumptions made earlier are reasonable, and a very useful consequence follows, namely that the large amount of existing neutron damage data may be converted to proton damage information in a rather simple manner.

Acknowledgments

The authors are grateful for the assistance of Mr. Henry Harmon of the Radio Corporation of America who provided much information about the physical and electrical characteristics of the transistors considered in this study, and for that of Mr. E. Rind of the National Aeronautics and Space Administration.

This study was performed under NASA contract NASI-1654.

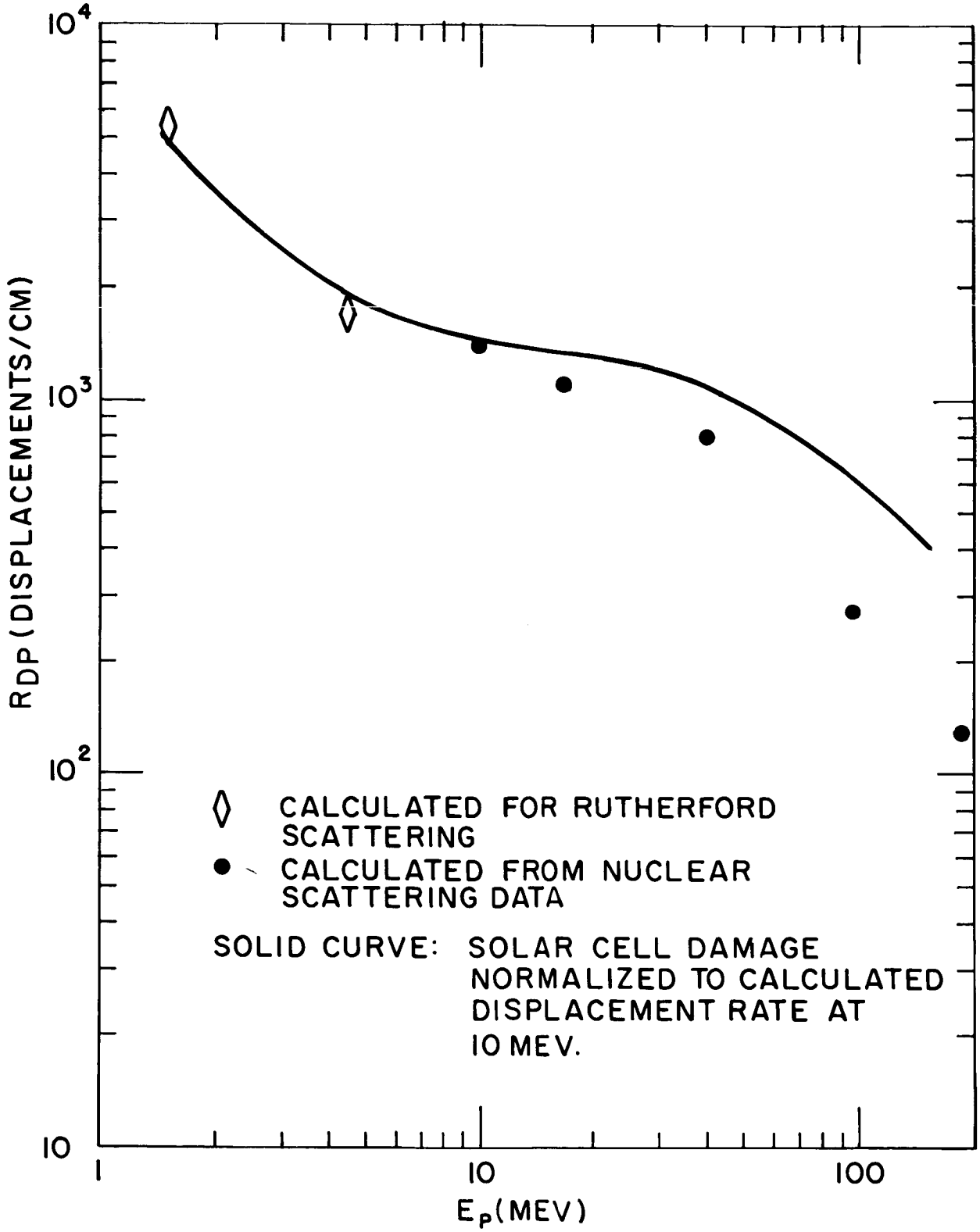

Figure 1. The number of lattice displacements, R_{DP}, per centimeter along the track of an incident proton of energy, E_P. Ionization effects by the primary recoiling silicon atom have been neglected.

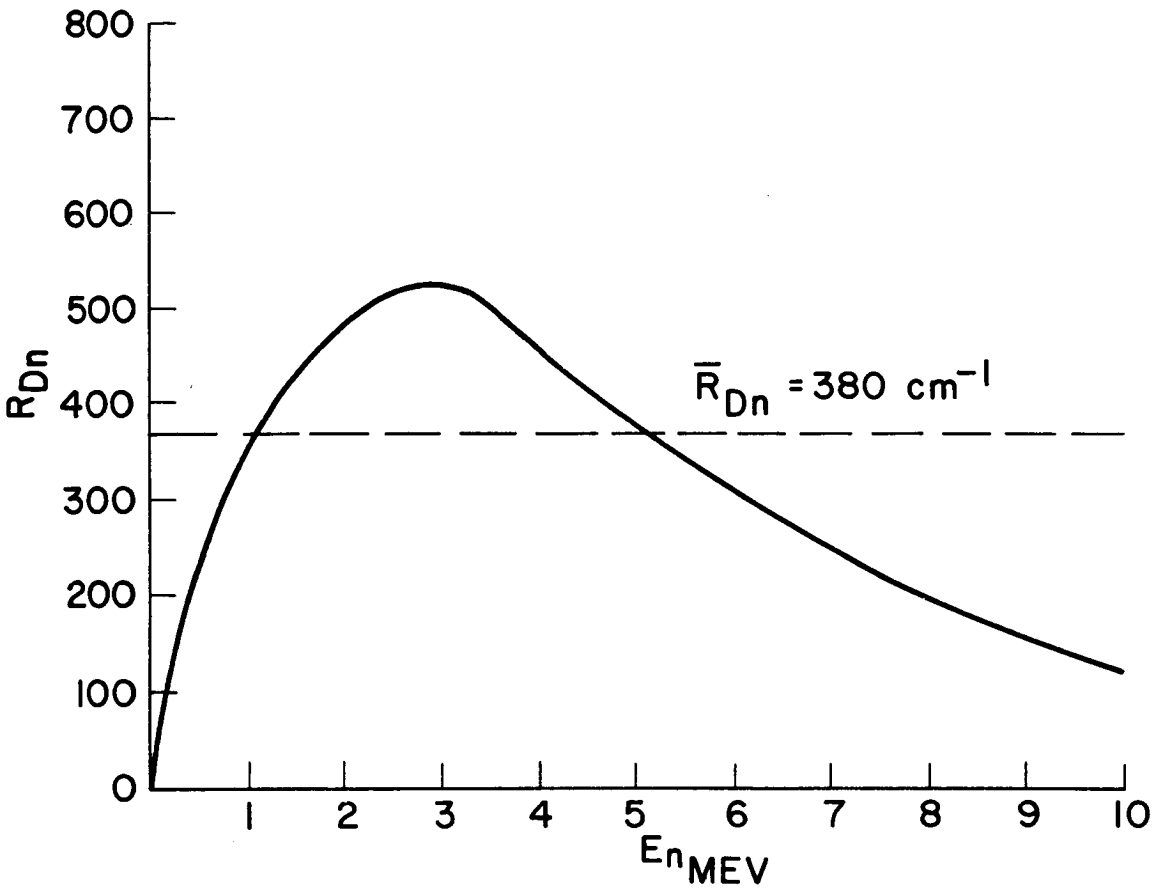

Figure 2. The number of lattice displacements, R_{DN}, per centimeter along the track of an incident neutron of energy, E_N.

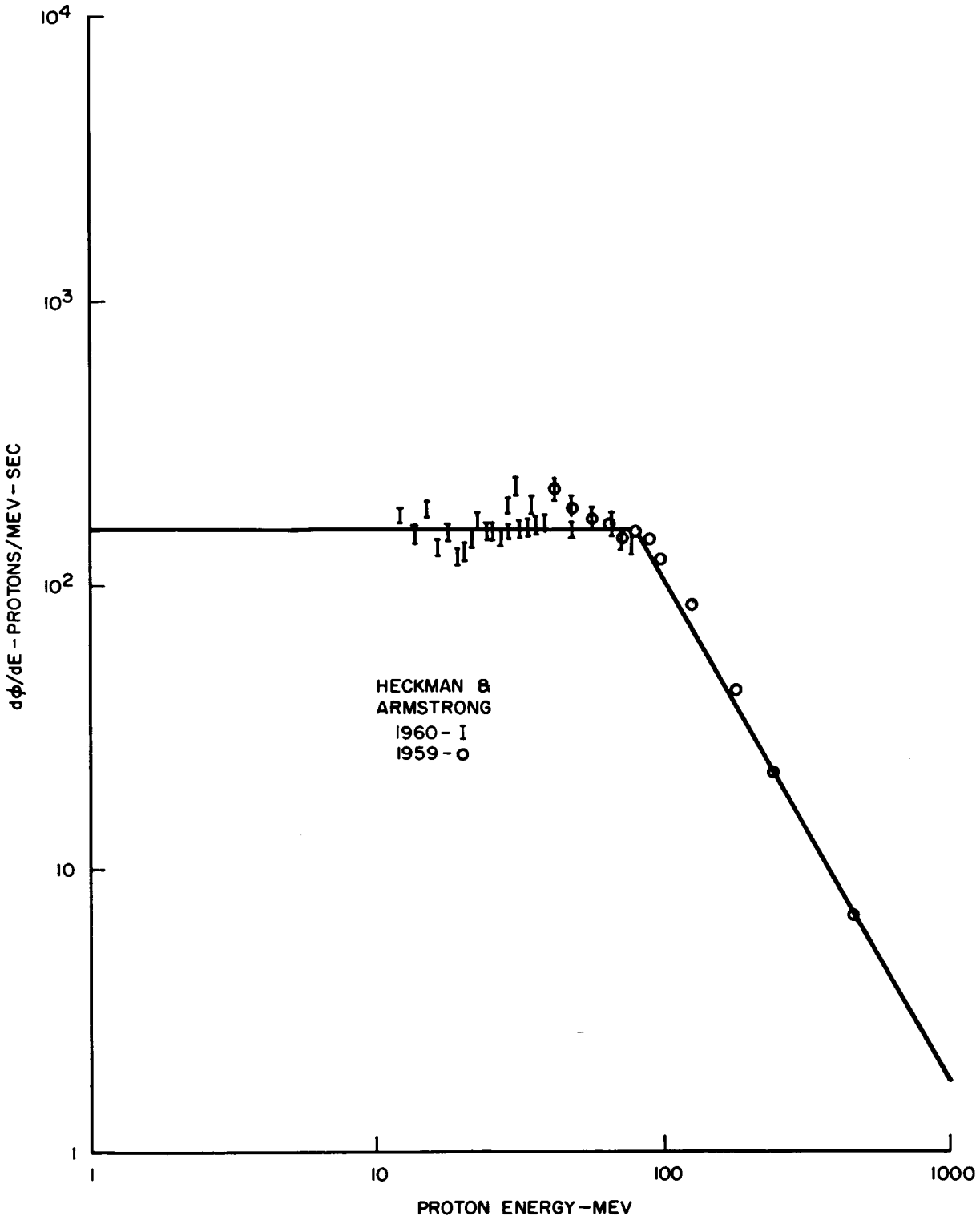

Figure 3. Idealized proton spectrum for the Inner Van Allen Belt. The shape of the spectrum is based on the data of Heckman and Armstrong,[9] but the curve has been normalized to Van Allen's total of 2×10^4 protons/cm^2-sec above 40 Mev.

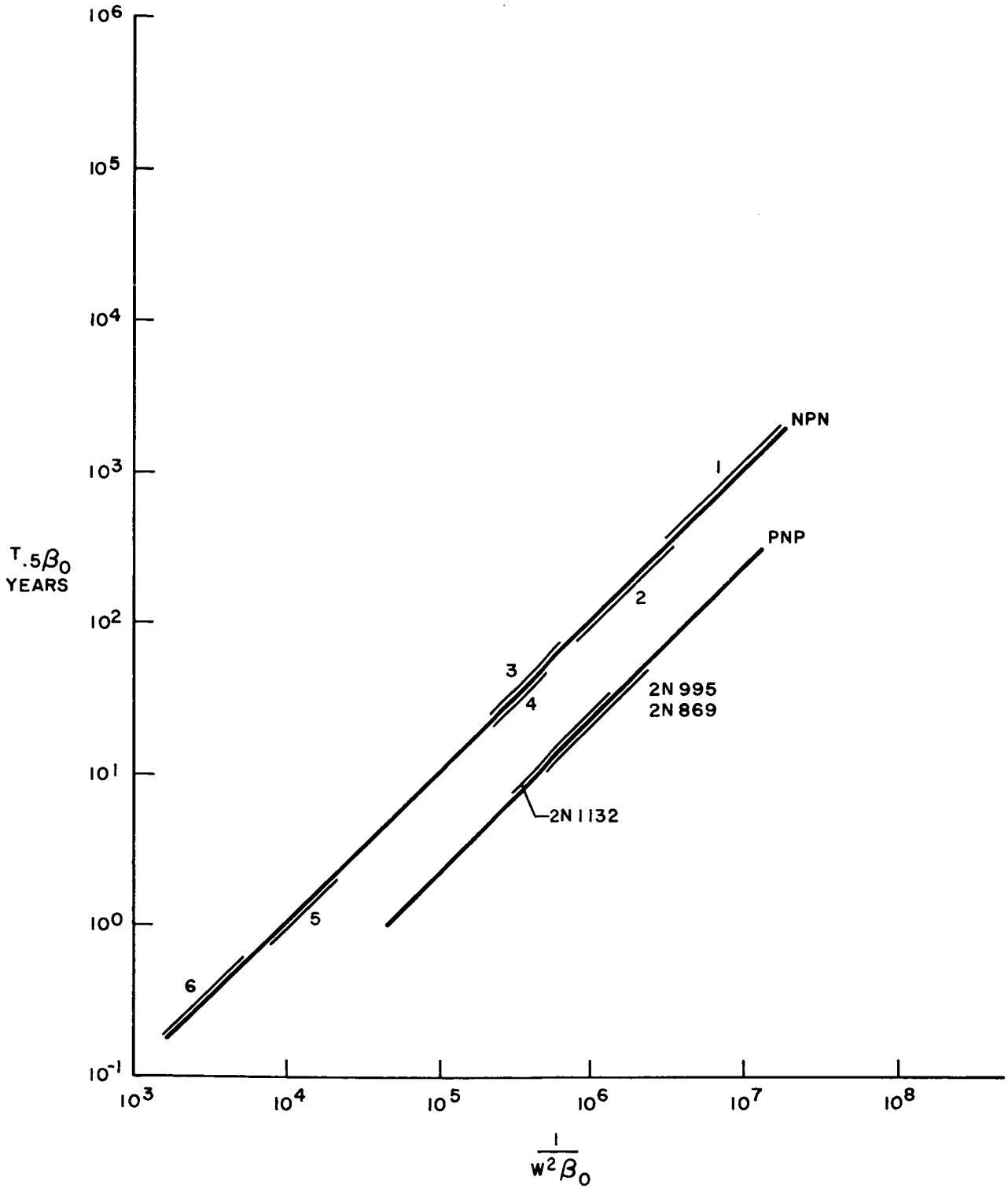

Figure 4. Time in Inner Van Allen Belt flux shown in Figure 3 for 50% reduction in current gain as a function of base width, W, and inital gain, β_0.

Paper B-6

SOLAR CELL DEGRADATION BY PROTONS IN SPACE

Richard Madey
Republic Aviation Corporation

Abstract

An analytic expression for the decrease in efficiency of a solar cell behind a protective cover glass exposed to a spectral distribution of protons is formulated on the basis that the time rate of decrease in output power is proportional to the proton dose rate absorbed at the surface of the solar cell. The decrease in the maximum power output ΔP of a solar cell exposed to protons in space is found to be

$$\Delta P = 1/2 \; P_o \ln(1 + \bar{\epsilon} L_i^2 D) , \qquad (1)$$

where D is the absorbed dose of protons at the surface of the solar cell behind a protective cover glass, and L_i is the initial value of the diffusion length of the minority carriers of the solar cell corresponding to the initial maximum power output P_i. The dependence of L_i on P_i is found from the data of Smits, Smith, and Brown[1] to be represented by

$$L_i = L_o e^{P_i/P_o} \qquad (10 \text{ mw} < P_i < 20 \text{ mw}) \qquad (2)$$

For an n-on-p cell, $L_o = 0.234$ micron and $P_o = 3.13$ milliwatts. The quantity $\bar{\epsilon}$ is a radiation damage factor averaged over the absorbed dose rate from a spectral

---

1. F.M. Smits, K.D. Smith, and W.L. Brown, "Solar Cells for Communications Satellites in the Van Allen Belt," J. Brit. IRE 22 (2), 161 (August, 1961).

distribution of protons. The energy dependence of ϵ is obtained from experimental data[2,3] on the change in the reciprocal squared diffusion length per unit integrated proton flux, I, versus proton energy E. Actually, ϵ is defined by

$$\frac{d\,(1/L^2)}{d\,I} = \epsilon \frac{dE}{dR_o} \tag{3}$$

where dE/dR_o is the specific ionization energy loss in the material of the solar cell.

The decrease in the maximum power output of an n-on-p silicon solar cell exposed to the solar flare of 12 November 1960 is calculated as a function of the thickness of protective cover glass for a power-law representation of the differential flux spectrum of the incident protons.

Introduction

Energetic protons in space bombard the active material of solar cells which supply power for satellites and space probes. Radiation damage to a solar cell results in a decrease in its power output. This degradation in the efficiency of a solar cell must be taken into account in the design of a solar cell power supply. The number of solar cells required to furnish a specified power output throughout a given mission will depend upon the decrease in power output expected during the mission. Some degradation can be prevented at the expense of additional weight by increasing the thickness of the protective cover glass. In order to be able to optimize the design of solar cell power supplies exposed to protons in space, it is useful to obtain an analytic representation for the decrease in power output of a solar cell behind a cover glass of arbitrary thickness.

---

2. W.L. Brown, "Damage to Semiconductors from Space Radiation," Presented at the American Rocket Society Space Nuclear Conference on May 3, 1961, at Gatlinburg, Tennessee.

3. W. Rosenzweig, F.M. Smits, and W.L. Brown, "Energy Dependence of Proton Irradiation Damage in Silicon," Bull. Am. Phys. Soc. II 7 (7), 437 (August 27, 1962).

Theory

Basic Assumption

In order to derive a formula for the decrease in the power output of a solar cell exposed to protons in space, we have made the assumption that dP/dt, the time rate of decrease in the output power of the solar cell, is proportional to the proton dose rate W absorbed at the front surface of the solar cell. Formally, we write

$$-\frac{dP}{dt} = F(P)\,W \tag{4}$$

where F(P) is a factor of proportionality which depends upon the instantaneous power level P of the solar cell. F(P) represents the differential decrease in power of the solar cell per unit of absorbed dose. If dP/dt is expressed in units of milliwatts/hour and W is in rads/hour, then F(P) is in units of milliwatts/rad.

Evaluation of Proportionality Factor F(P)

The proton dose rate absorbed at the surface of the solar cell behind a protective cover glass is given by the following integral:

$$W(\text{Mev/sec gm Si}) = \int \left(\frac{dE}{dR_o}\right) dR \int n'(R,\Omega)\, d\Omega\ , \tag{5}$$

where dE/dR_o is the specific ionization energy loss in Mev per gram per cm^2 of the material of the solar cell for protons of energy E, corresponding to the residual range R in the material of the cover glass. The zero subscript of dE/dR_o refers to the material of the solar cell (e.g., silicon). The differential quantity $n'(R,\Omega)\, dR\, d\Omega$ represents the number of protons emerging from the cover glass in a direction Ω in $d\Omega$ with a residual range (in the material of the cover glass) between R and R + dR.

For a spectrum of protons incident on the solar cell, the time rate of decrease in the output power is given by

$$-\frac{dP}{dt} = \int \frac{dP}{dI}\, dR \int n'(R, \Omega)\, d\Omega, \tag{6}$$

where dP/dI is the change in output power per unit time-integrated proton flux, and $dR \int n'(R, \Omega) d\Omega$ represents the number of protons

incident on the solar cell with residual ranges between R and R + dR crossing a unit area per unit time from all directions. The primed notation is used to denote that the unidirectional differential range spectrum, $n'(R, \Omega)$, at the solar cell is a degraded spectrum, the incident spectrum in space being degraded by a cover glass protecting the solar cell.

In the integrand of Eq. 6, the quantity dP/dI may be rewritten as a product of two factors:

$$\frac{dP}{dI} = \frac{dP}{d(1/L^2)} \frac{d(1/L^2)}{dI} = f(P)\, g(E), \tag{7}$$

where L is the diffusion length of the minority carriers in the material of the solar cell. The right-hand member of Eq. 7 is written in recognition of the fact that the first factor, f(P), will depend only on the power output of the solar cell and the second factor, g(E), will depend only on the proton energy.

The sensitive thickness of the solar cell is equal to the diffusion length of the minority carriers in the bulk material. The diffusion length is the average distance traveled by an excess minority carrier before recombining with a majority carrier. Values of the diffusion length range from 200 μ down to a few microns, depending upon the conductivity type, resistivity, and irradiation history of a cell.

From the data of Smits, Smith and Brown[1], the dependence of the maximum power output on diffusion length of an n-on-p solar cell may be represented by an exponential function as follows:

$$L\ (\text{microns}) = L_o\, e^{P/P_o} \qquad (10\ \text{mw} < P < 20\ \text{mw}) \tag{8}$$

where $L_o = 0.234$ micron and $P_o = 3.13$ milliwatts. In Fig. 1, this analytical representation is compared with the data of Smits et al. They measured output characteristics of 92 solar cells under electron bombardment. From their measurements, they constructed curves of median power output versus voltage under outer space illumination with the integrated electron flux and the diffusion length as parameters. The dependence of the maximum power output on diffusion length is obtained from this data.

Thus, from Eq. 8, we find that

$$f(P) \equiv \frac{dP}{d(1/L^2)} = \frac{1}{2} P_o L_o^2\, e^{2P/P_o} = \frac{1}{2} P_o L^2 \tag{9}$$

Now, let us write the energy-dependent factor as a product of two factors:

$$g(E) \equiv \frac{d(1/L^2)}{dI} = \epsilon \frac{dE}{dR_o} \tag{10}$$

where dE/dR_o is the specific ionization energy loss in the material of the solar cell, and ϵ is a radiation damage coefficient. The value of ϵ will be determined from experiment. After substituting Eqs. 7, 9, and 10 in Eq. 6, we obtain

$$-\frac{dP}{dt} = f(P) \int \epsilon \left(\frac{dE}{dR_o}\right) dR \int n'(R,\Omega)\, d\Omega. \tag{11}$$

We may rewrite Eq. 11 as follows:

$$-\frac{dP}{dt} = f(P)\, \bar{\epsilon}\, W \equiv F(P)\, W \tag{12}$$

where

$$F(P) \equiv \bar{\epsilon}\, f(P) = \frac{1}{2}\, \bar{\epsilon}\, P_o L^2 \tag{13}$$

and

$$\bar{\epsilon} \equiv \frac{\int \epsilon \left(\frac{dE}{dR_o}\right) dR \int n'(R, \Omega)\, d\Omega}{\int \frac{dE}{dR_o}\, dR \int n'(R, \Omega)\, d\Omega} \tag{14}$$

The dependence of the diffusion length on proton energy has been measured by Bell Telephone Laboratory workers[2,3] at various proton accelerators. These workers have reported their data in a plot of $d(1/L^2)/dI$ vs. proton energy. The first data of this type, reported by W.L. Brown[2], are shown in Fig. 2. Later, Rosenzweig, Smits, and Brown[3] reported similar data, shown in Fig. 3. We have shown both sets of data in a slightly different form in Fig. 4, where we have plotted ϵ vs. proton energy.

Decrease in Maximum Power Output

In order to obtain an expression for the decrease in the maximum power output of a solar cell, we integrate Eq. 12:

$$\text{Absorbed dose } D \equiv \int_{t_i}^{t_f} W dt = -\int_{P_i}^{P_f} \frac{dP}{F(P)} \equiv I(P)$$

where the subscripts i and f on the limits of the integrals denote initial and final values of the power and time. The result of integration is

$$\Delta P \equiv P_i - P_f = \frac{1}{2} P_o \ln(1 + \bar{\epsilon} L_i^2 D) \qquad (16)$$

where, from Eq. 8, L_i designates the value of the diffusion length of the minority carriers of the solar cell corresponding to the initial power P_i.

Upon substituting the values $P_o = 3.13$ milliwatts, $L_o = 2.34 \times 10^{-5}$ cm, $\bar{\epsilon} = 7.48 \times 10^{-8}$ gm/cm^2-Mev $= 4.67$ Rad^{-1}-cm^{-2}, Eq. 16 becomes

$$\Delta P \text{ (mw)} = 1.565 \ln \left[1 + 0.25 \times 10^{-8} e^{0.639 P_i} D \text{ (rads)}\right].$$

In Fig. 5, we plot the decrease in the maximum power output as a function of the absorbed dose of protons at the surface of the solar cell.

Absorbed Surface Dose Rate as a Function of Cover Glass Thickness

In order to determine the dependence of W, the proton dose rate absorbed at the surface of the solar cell, upon the thickness x in gm/cm^2 of a protective cover glass, it is necessary to integrate Eq. 5 for the dose rate. We have obtained an analytic expression relating the dose rate to the cover glass thickness on the following basis:

(a) An isotropic differential spectrum of protons is incident on a protective cover glass in plane geometry from the upper hemisphere. We represent the incident flux spectrum by a power law of the form

$$j \text{ (p/cm}^2\text{-sec-Mev)} = 2 \pi C E^{-\gamma}. \qquad (17)$$

(b) The range-energy relation for protons in matter is representable by a power law of the form

$$R \text{ (gm/cm}^2\text{)} = K E^{\alpha} \qquad (18)$$

where the constants K (gm/cm^2-Mev$^{\alpha}$) and α depend on the material.

The result of integration, written in terms of the incident flux, is

$$W \text{ (rads/hr)} = 5.76 \times 10^{-5} \frac{B(p,q)}{(1+p)\alpha \alpha_o K_o} E_x^{2-\alpha_o} j(E_x) \qquad (19)$$

where E_x is the proton energy required to just penetrate a cover glass thickness (gm/cm^2); α_o and K_o denote values for the material of the solar cell (e.g., silicon); α and K represent values for the material of the cover glass (e.g., sapphire); $B(p,q)$ is the beta function; and

$$p = (\gamma + \alpha_o - 2)/\alpha \tag{20}$$

$$q = (1 + \alpha - \alpha_o)/\alpha \tag{21}$$

Alternatively, by making use of the range-energy relationship, we may rewrite Eq. 19 directly in terms of the cover glass thickness:

$$W(t,x) = 5.76 \times 10^{-5} \frac{2\pi\, C(t)\, B(p,q)}{(1+p)\,\alpha\,\alpha_o\, K_o} \left(\frac{K}{x}\right)^p \tag{22}$$

Application to the Solar Flare of 12 November 1960

Characteristics of the Proton Spectrum

The integral proton spectrum has been measured[4] at energies as low as 2 Mev at 5 hours and 27 minutes after the peak of the optical flare on 12 November 1960. From the reported values of the spectral parameters (viz., $\gamma - 1 = 1.7 \pm 0.2$ in the energy interval from 2 Mev to 100 Mev and $N(> 2\ \text{Mev}) = 3 \times 10^4$ protons/cm^2-sec-steradian), the spectral exponent $\gamma = 2.7$ in the energy interval from 2 Mev to 100 Mev and the spectral coefficient $C(t_o) = 1.66 \times 10^5$ protons/cm^2-sec-steradian-Mev$^{\gamma-1}$ at $t_o = 5.5$ hours after the flare peak.

Absorbed Dose Rate at Time t_o

If we substitute numerical values in Eq. 22, the proton dose rate absorbed at time t_o at the surface of a silicon solar cell becomes

$$W(t_o, x) = 1.1\, x^{-1.4} . \tag{23}$$

---

4. K.W. Ogilvie, D.A. Bryant, and L.R. Davis, "Rocket Observations of Solar Protons During the November 12, 1960 Event," NASA Goddard Space Flight Center Contributions to the 1961 Kyoto Conference on Cosmic Rays and the Earth Storm. Also, K.W. Ogilvie, and L.R. Davis, "Rocket Observations of Solar Protons," presented at Forty-Second Annual Meeting, American Geophysical Union, Washington, D.C. (April 18-21, 1961).

Equation 53 is plotted in Fig. 6.

Absorbed Dose

We may estimate the integral for the absorbed dose in the approximation that the spectral exponent γ and hence the parameter p in Eq. 22 for the absorbed dose rate is independent of time t. In this approximation, the absorbed dose may be written

$$D = W(t_o, x)\ \overline{\Delta t} \tag{24}$$

where $\overline{\Delta t}$ is the effective duration of the flare. We have found $\Delta t = 2.36 \times 10^5$ seconds = 65.6 hours from the data of Fichtel, Guss, and Ogilvie[5] on the time dependence of the integral proton flux above 20 Mev.

Thus, the absorbed dose as a function of cover glass thickness $x(gm/cm^2)$ for the solar flare of 12 November 1960 is

$$D\ (rads) = 71\ x^{-1.4}. \tag{25}$$

Equation 25 is plotted in Fig. 7.

Decrease in Maximum Power Output vs. Thickness of Protective Cover Glass

Finally, the percentage decrease in maximum power output of an n-on-p silicon solar cell exposed to protons from the solar flare of 12 November 1960 is given by

$$\frac{\Delta P}{P_i} = \frac{1.565}{P_i} \ln\left(1 + 1.82 \times 10^{-7}\, e^{0.639\, P_i}\, x^{-1.4}\right) \tag{26}$$

where the powers P_i and P_f are expressed in milliwatts, and x is in gms/cm^2 of cover glass. Equation (26) is plotted in Fig. 8.

---

5. C.E. Fichtel, D.E. Guss, and K.W. Ogilvie, Private Communication.

Acknowledgements

The author gratefully acknowledges the assistance of Messrs. Howard Oringer and F. M. Sisavic in performing calculations and plotting figures.

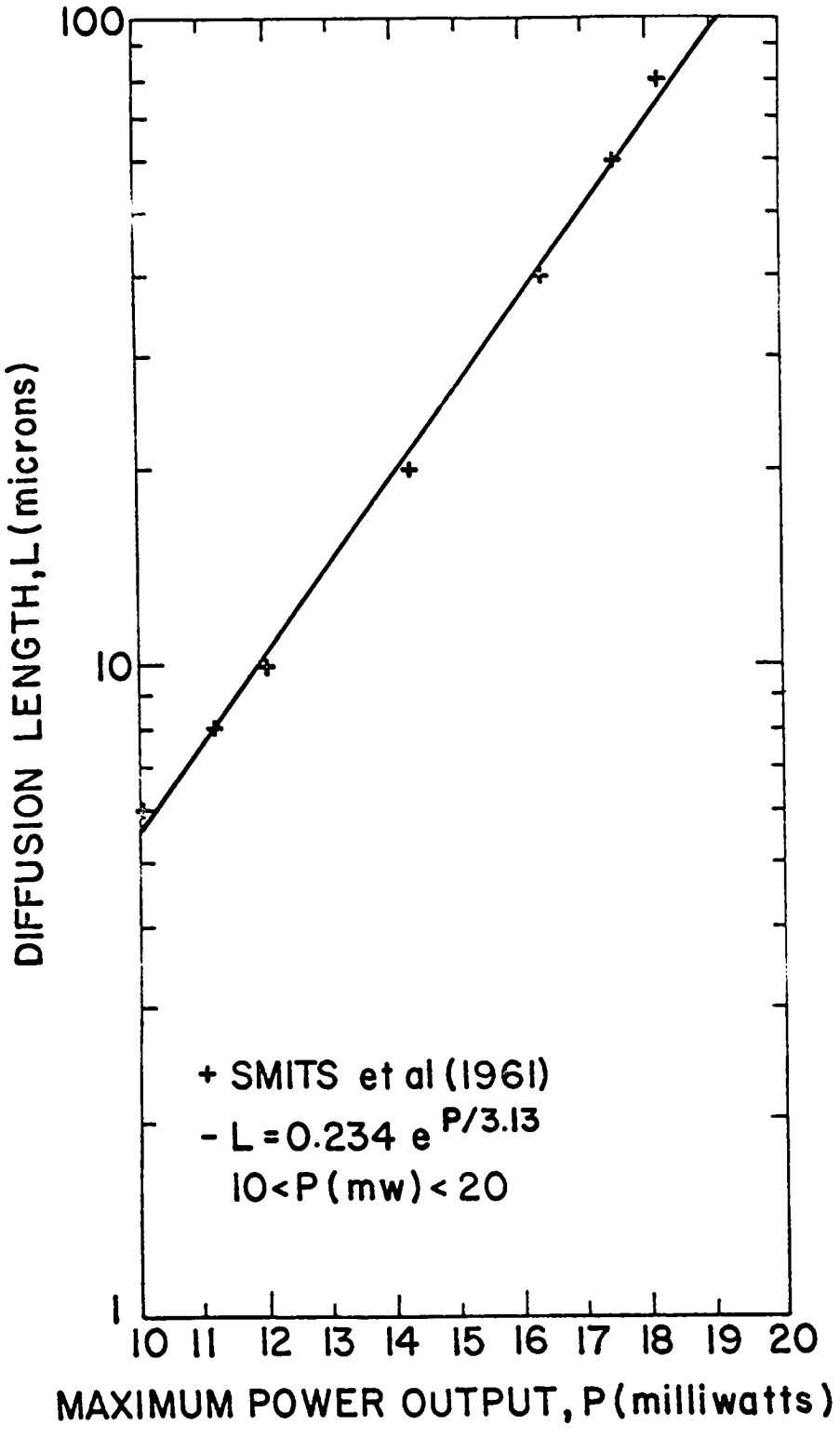

Figure 1. Diffusion Length of Minority Carriers of an n-on-p Solar Cell vs. Maximum Power Output.

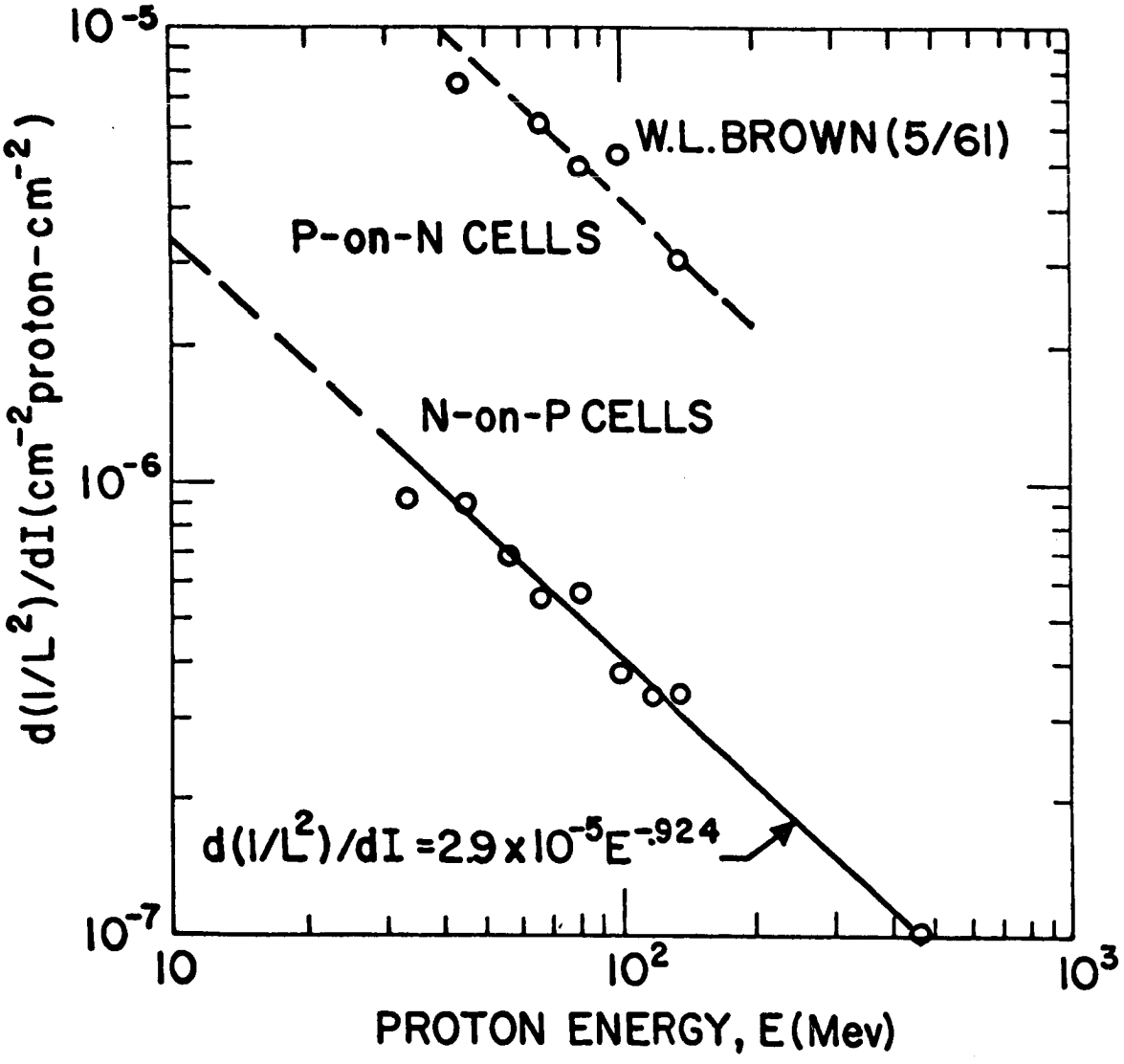

Figure 2. Change in Reciprocal Squared Diffusion Length per Unit Integrated Proton Flux for Solar Cells vs. Proton Energy. Data from W.L. Brown (May 1961).

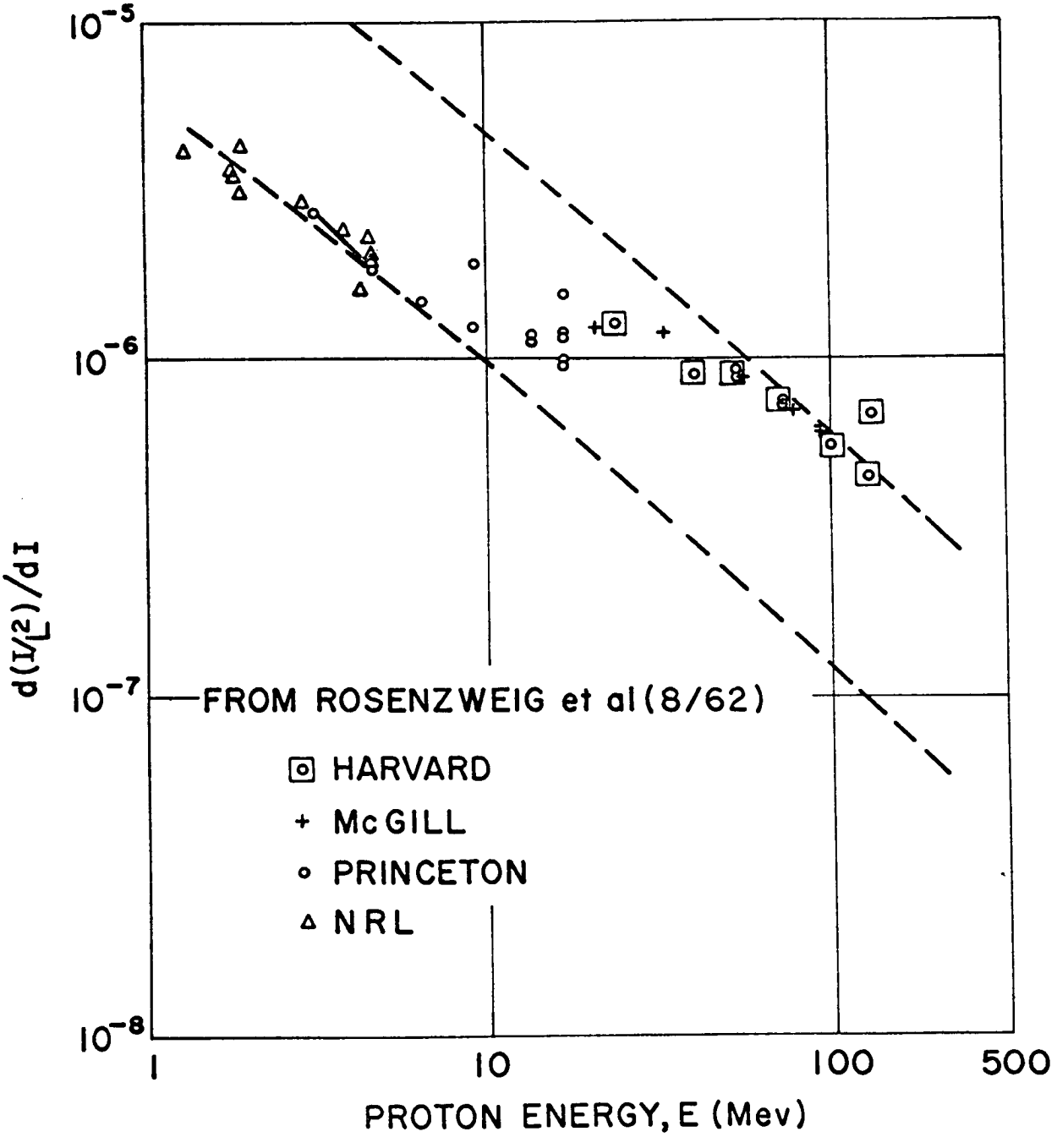

Figure 3. Change in Reciprocal Squared Diffusion Length per Unit Integrated Proton Flux for Solar Cells vs. Proton Energy. Data from Rosenzweig et al. (August 1962).

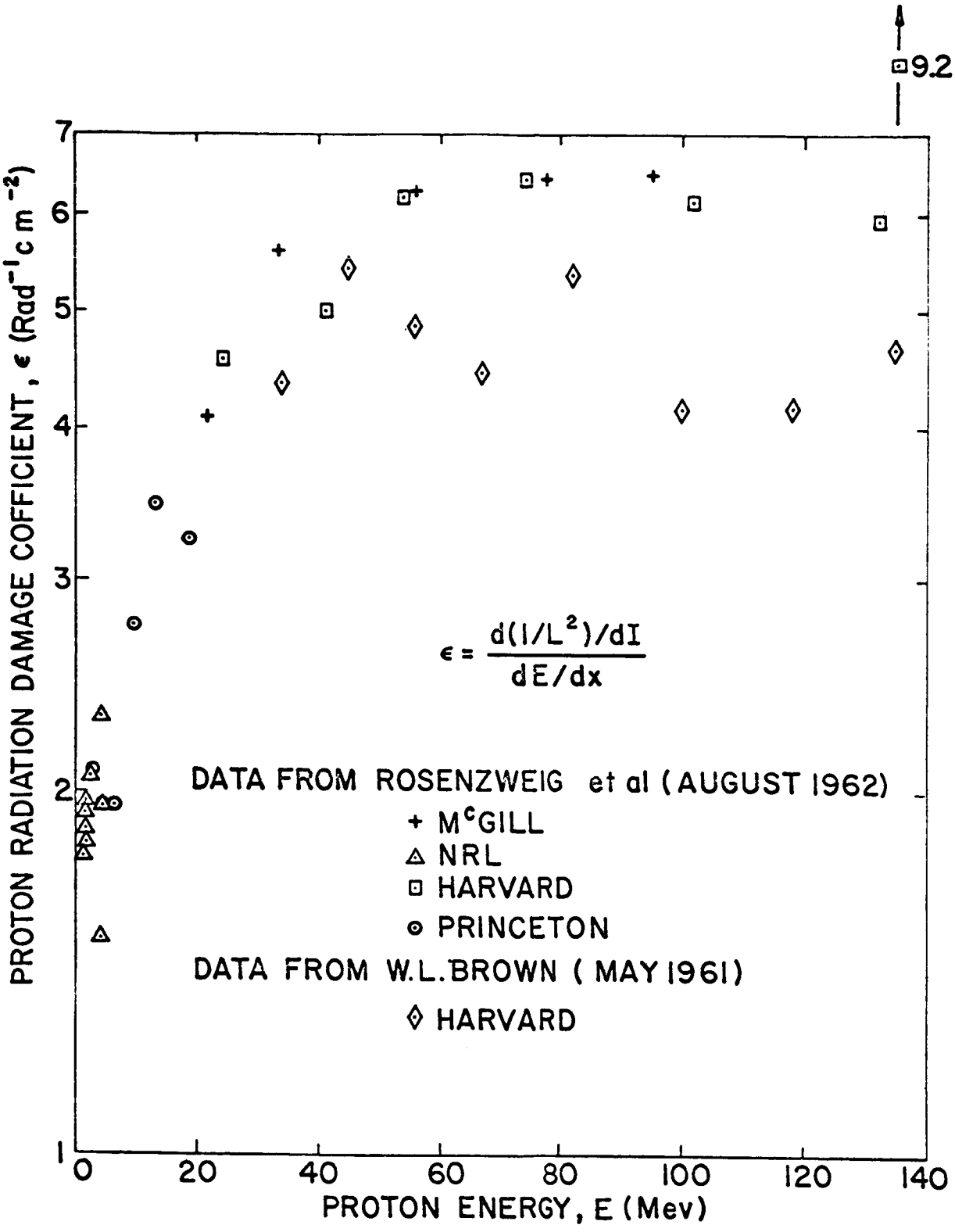

Figure 4. Proton Radiation Damage Coefficient for Solar Cells vs. Proton Energy.

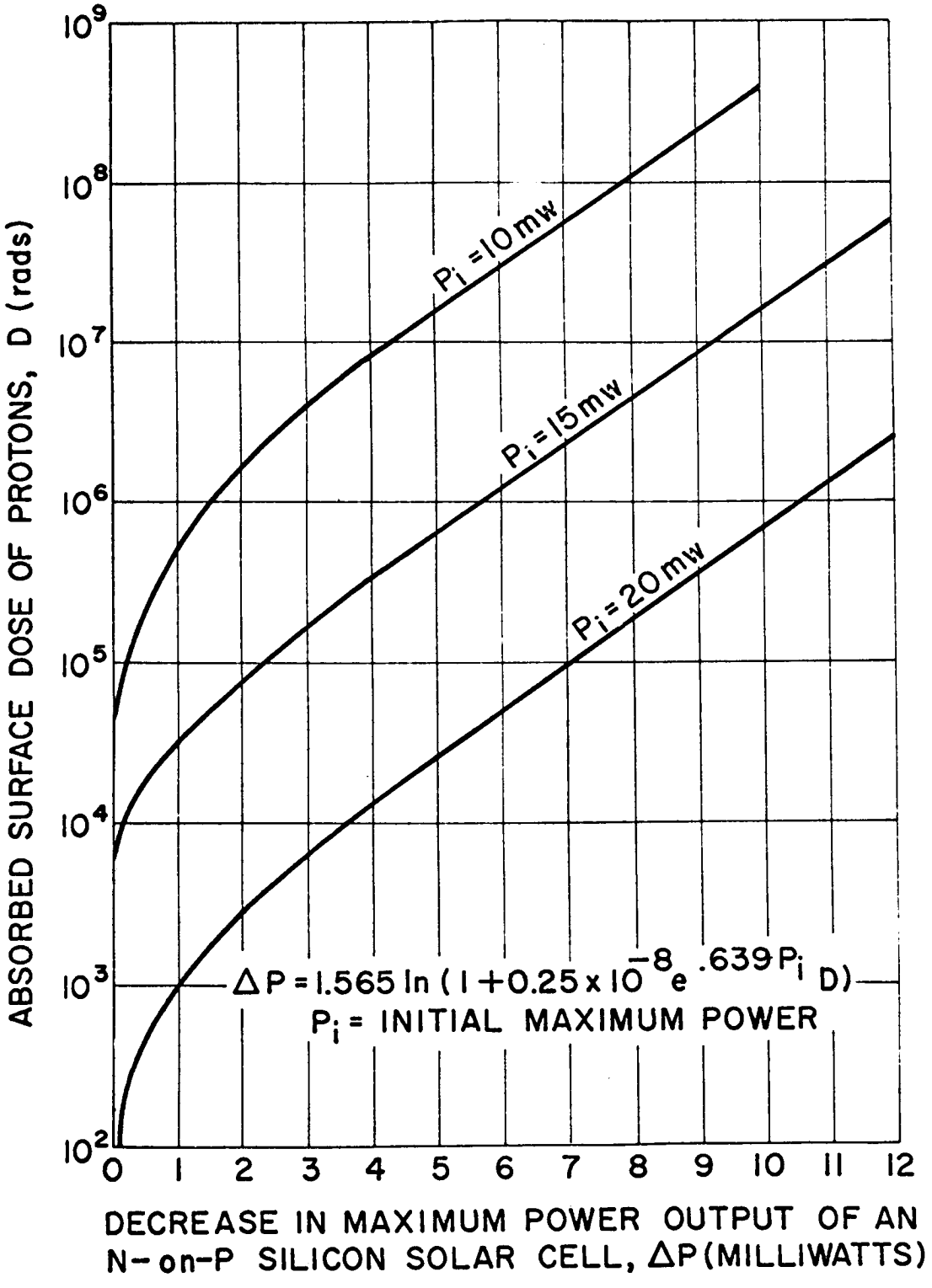

Figure 5. Decrease in Maximum Power Output of an n-on-p Silicon Solar Cell vs. Absorbed Dose of Protons at the Silicon Surface Layer Behind a Protective Cover Glass with the Initial Value of the Maximum Power Output as a Parameter.

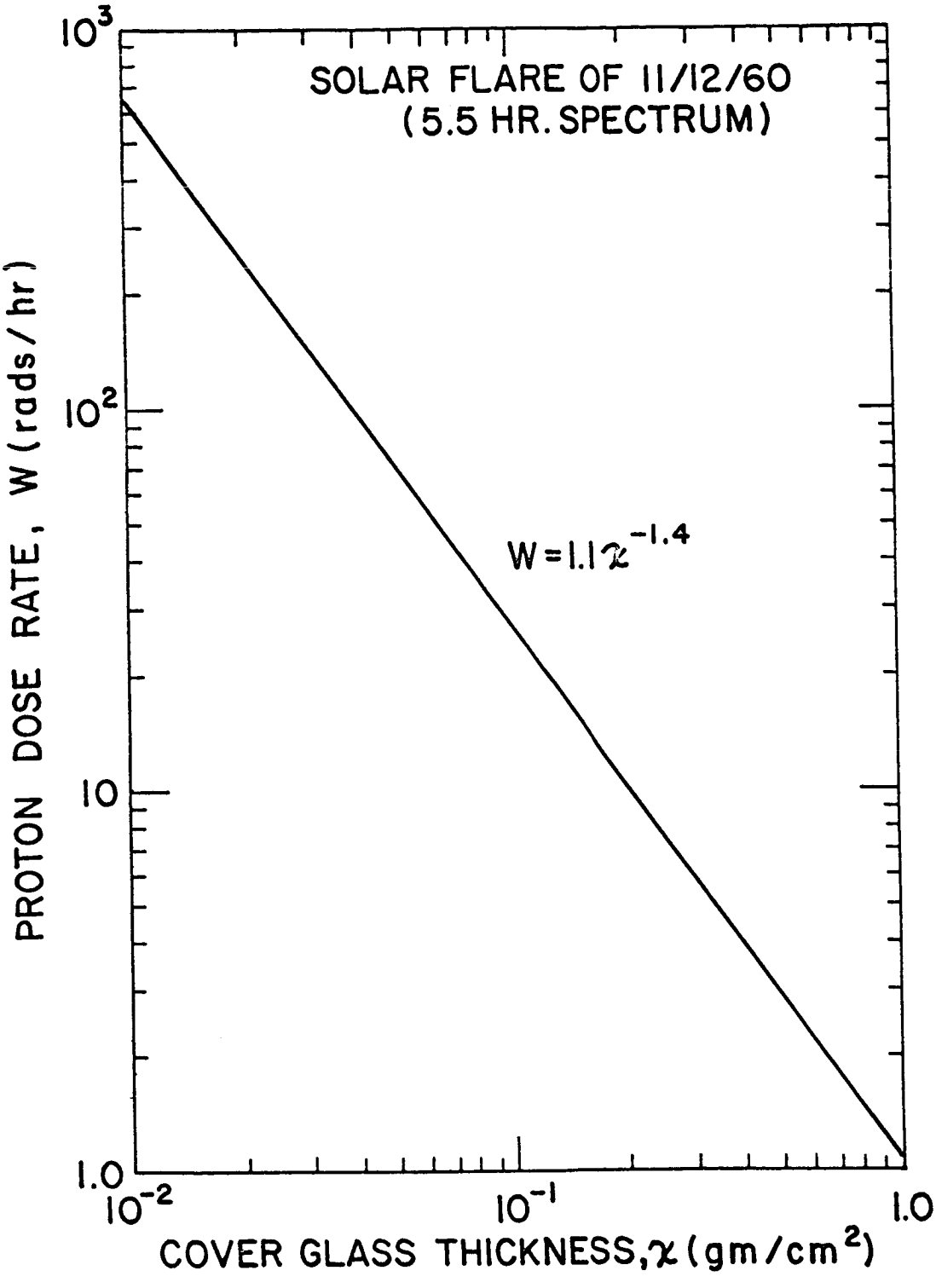

Figure 6. Proton Dose Rate (in rads/hour) from the 5.5 Hour Spectrum of the Solar Flare of 12 November 1960 vs. Thickness (in gm/cm^2) of Protective Cover Glass.

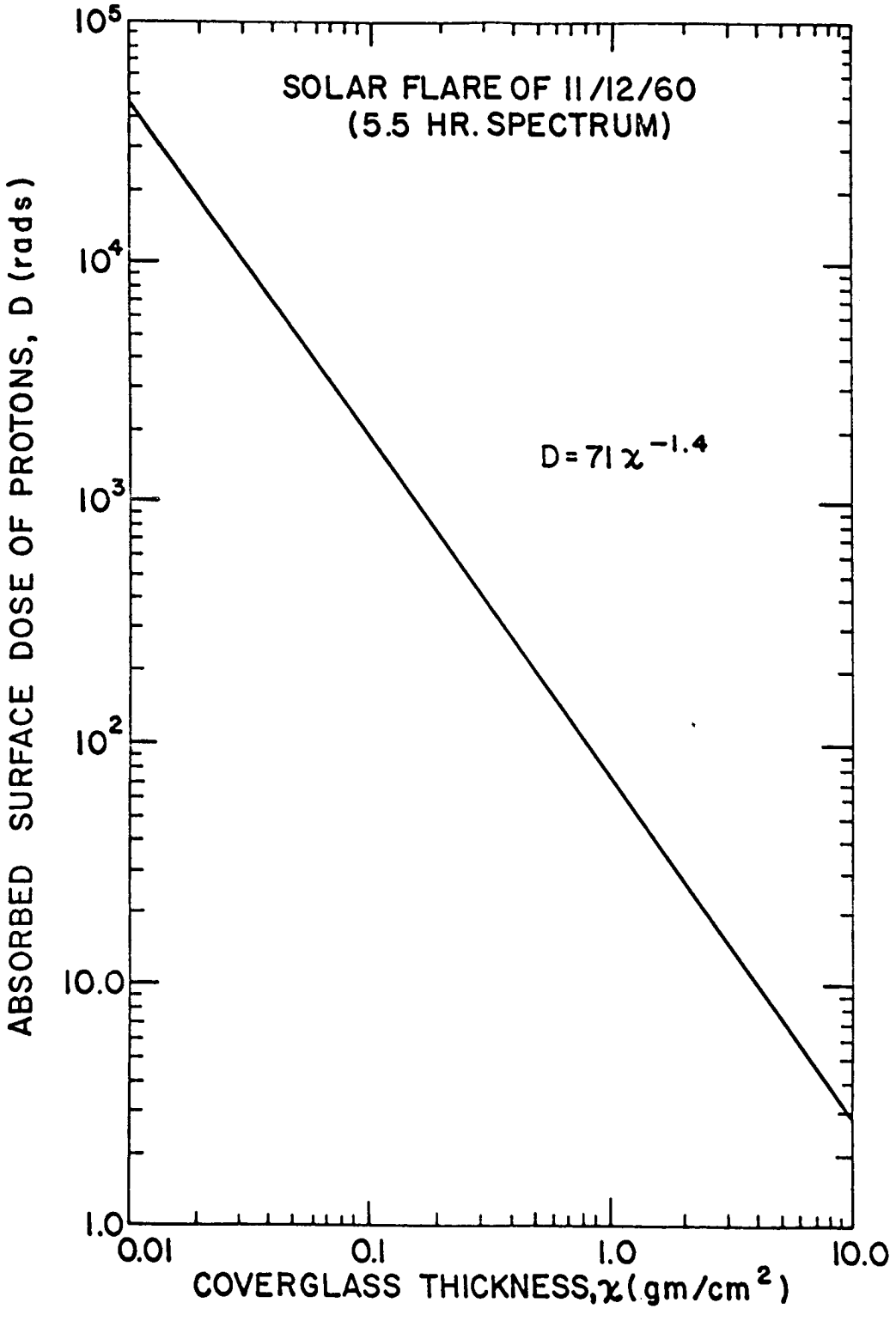

Figure 7. Surface Dose of Protons Absorbed From the Solar Flare of 12 November 1960 vs. Thickness of Protective Cover Glass.

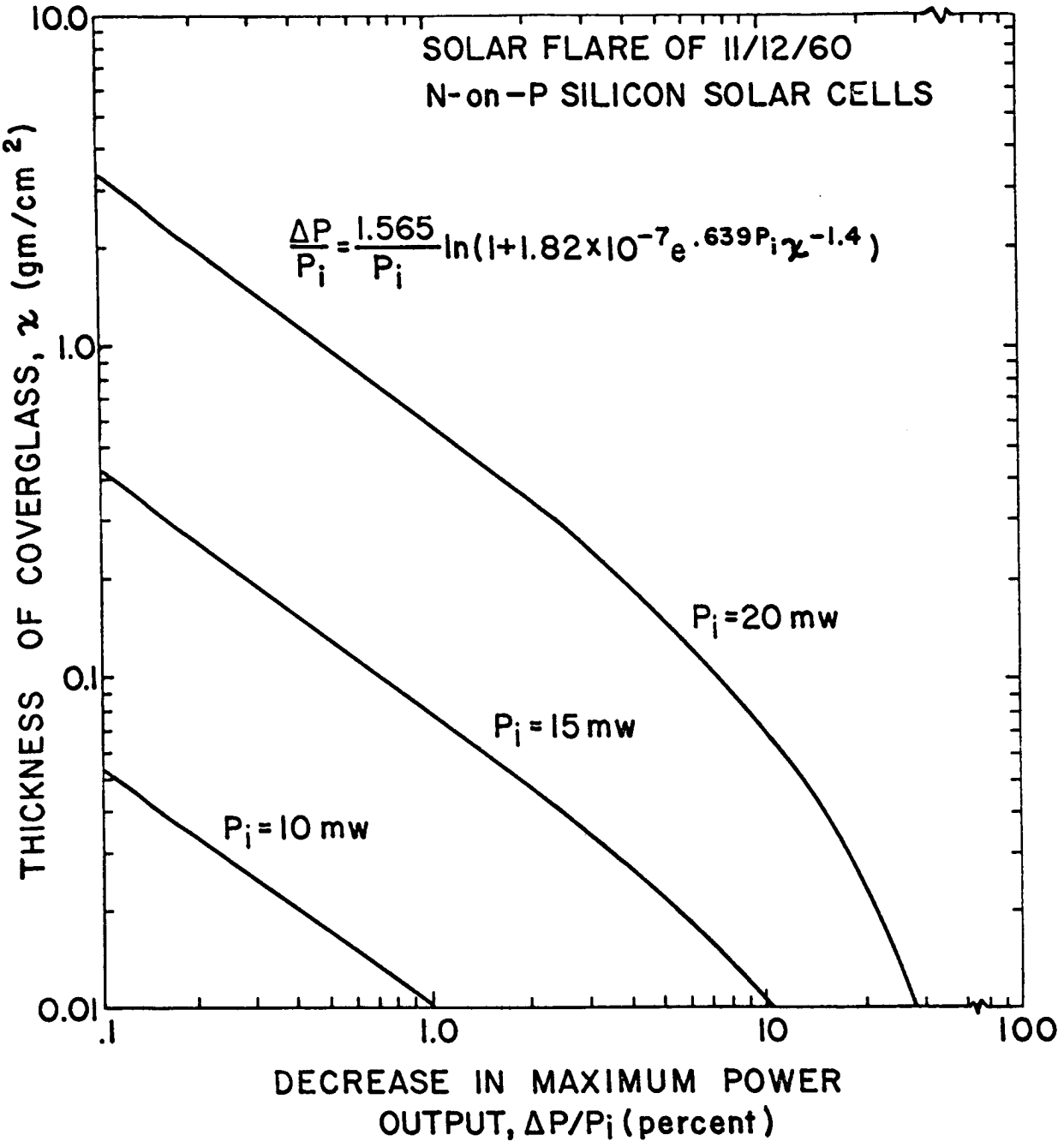

Figure 8. Decrease in Maximum Power Output vs. Thickness in gm/cm^2 of Protective Cover Glass for the Solar Flare of 12 November 1960, With the Initial Value of the Maximum Power Output as a Parameter.

Paper B-7

EFFECT OF ELECTRON IRRADIATION ON THE MECHANICAL PROPERTIES OF A COMPOSITE FOIL FOR INFLATABLE SATELLITES

Thomas G. James*
NASA Langley Research Center

Abstract

The primary effect of electron irradiation on the Echo II skin material is an increased brittleness which leads to an early and brittle failure in both the burst strength and ultimate strength tests. Severe surface damage, which occurs at doses on the order of 10^{17} e/cm^2, causes mechanical damage to the aluminum foil portion of the skin and may lead to changes in the temperature control characteristics of the surface.

Introduction

Some months after the 100-foot-diameter Echo I balloon was put into orbit, it became apparent from both optical and radar observations that the balloon was no longer a smooth sphere. Presumably the inflation gases had leaked out by this time leaving the balloon somewhat wrinkled because the 1/2-mil aluminized mylar of which it was made had no inherent stiffness. The next passive communication satellite, the 135-foot-diameter Echo II balloon, will have a much stiffer skin so that it is hoped the balloon will remain smooth and spherical after the initial inflation pressure is lost. The Echo II skin is made of 0.35-mil-thick mylar with 0.2-mil-thick aluminum glued on either side. Both outer aluminum surfaces are given an alodine coating for temperature-control purposes. (See fig. 1.)

This satellite and subsequent similar satellites will have to remain for many years in the space environment, which in this case includes the magnetically trapped radiation, both the natural Van Allen belt and the new artificial electron belt. As a result of the high-altitude nuclear explosion of July 9, 1962, Echo II, which will orbit at an altitude of about 1,000 km, will be exposed to a flux of between 10^8 and 10^9 e/cm^2/sec. The study presented herein was made in order to determine the extent to which the electron radiation part of this environment will damage the Echo II type composite foil in the course of many years in orbit. Samples of the Echo II foil were irradiated with electrons of energies up to 1.2 Mev, with total doses representing those incurred during many years in orbit.

---

*Aerospace Technologist.

Symbols

e	electron
E	modulus of elasticity, used herein as the secant modulus at 1-percent elongation, $lb/in.^2$
Kev	thousand electron volts
Mev	million electron volts
S_{ULT}	ultimate tensile stress
μa	microamperes

Tests And Equipment

Test Setup

The accelerator used in these tests was a constant-voltage cascaded-rectifier type - a Radiation Dynamics Model No. PEA-1.0 Dynamitron. This accelerator is capable of producing fluxes of electrons with intensities as great as 10 milliamperes and with kinetic energies varying from 50 Kev to 1.20 Mev. The experimental test setup is shown in figure 2. The beam enters from the accelerator at the left-hand side and passes down the beam tube through a scanning magnet which scans it vertically in the scan horn at approximately 10 cycles per second. The beam then passes into the air through a blower-cooled, 2-mil-thick titanium window. The foil sample is suspended in the beam at a distance of approximately 6 inches from the titanium window. The clamps that hold the foil are mounted approximately $1\frac{1}{2}$ inches in front of a solid aluminum support plate. The current density was measured by means of a 1- by 2-cm aluminum plate mounted on, and insulated from, the foil itself. The current captured by this small plate was measured by passing it to ground through an electrometer. The current captured by the support plate was also passed to ground through an electrometer in order to monitor the total output of the accelerator. The foil itself was grounded in order to avoid any charge-buildup effects. The kinetic energy of the electrons at the location of the foil was determined by measuring the extreme range of electrons in aluminum at this location. The uniformity of the beam intensity was determined through the use of cobalt glass dosimetry. An area of approximately 2 by 15 inches was found to be uniform to within ± 5 percent.

Mechanical Tests.- All data were obtained by means of post-irradiation tests. Six mechanical properties were studied. From the stress-strain curves measured on a Thwing-Albert Model 30LT tensile tester, the modulus of elasticity, ultimate strength, and percent elongation were determined. A standard Mullen tester was used to determine the burst strength of the skin. A Sheffield Micro-Hardness tester was used to measure the Vickers hardness of the surface of the foil. Several 1/3 cm^2 pieces of foil were weighed on a Cahn Electrobalance to determine the weight per square centimeter.

Results And Discussion

Effect of Dose Rate

Since the dose rate in these tests is necessarily higher than that in space, the initial portion of this investigation was a study of possible dose rate effects on the foils. A portion of the results of this study can be seen in figure 3. Each of the samples was given the same total dose of 3.156×10^{16} e/cm^2. This total dose, at 10^8 $e/cm^2/sec$, represents about 10 years in orbit; at 10^9 $e/cm^2/sec$, the corresponding time would be 1 year. In all cases the energy used was 1.20 Mev.

Figure 3 shows the percent change in these mechanical properties as a function of the dose rate in microamperes per square centimeter. It is apparent that dose rate has no significant effect for dose rates less than 1.12 $\mu a/cm^2$. There are, however, significant effects of dose rates much above 1.12 $\mu a/cm^2$. A dose rate of 1.12 $\mu a/cm^2$ is two or three orders of magnitude greater than the maximum dose rates in space. In general, it is seen that the damage is less for the higher dose rates. The lessened damage at high dose rates may be a result of severe heating at these dose rates; however, previously published work[1] indicates a similar trend with respect to the electrical properties of mylar. Since no significant dose rate effects are observed at a dose rate of 1.12 $\mu a/cm^2$, this value was selected for use in all subsequent tests.

Effect of Total Dose

The most significant data from the viewpoint of lifetime in the space environment is that showing the effect of total dose. Figure 4 shows the effects of total dose on the mechanical properties for an

1. The Effect of Nuclear Radiation on Elastomeric and Plastic Materials. Radiation Effects Information Center (Battelle Memorial Institute), Report No. 3, First Addendum, May 31, 1959, p. 27.

energy of 1.2 Mev. The doses shown here, at a flux level of 10^8 e/cm^2/sec, correspond to times in orbit ranging from 6 months to 50 years; at 10^9 e/cm^2/sec, the corresponding times are 18 days to 5 years. The most notable effect is a rapid degradation of the percent elongation, which is reduced by about 25 percent even at the lowest dose. This is reflected at somewhat higher doses in the early and brittle failure of both the burst strength and ultimate strength tests. The modulus of elasticity, hardness, and cot/cm^2 are essentially unchanged at least to such doses as it was possible to measure these quantities.

It will be observed that the last two points are missing for both the modulus of elasticity and hardness. The modulus of elasticity as used throughout this paper is the secant modulus at 1-percent elongation. For the two highest doses the percent elongation was less than 1 percent and, consequently, the modulus could not be measured. The degree of surface damage at these doses was such that a clean indentation could not be obtained with the microhardness tester. These surface effects will be discussed more fully in a later part of this paper.

The fact that these properties fall into two groups, one of which shows major changes and the other essentially none, is of interest since it indicates which portion of the foil has sustained the major portion of damage. It is to be noted that, in the tests of the unirradiated and lightly irradiated foils the aluminum fails long before the mylar in both the burst and tensile tests. Thus, except perhaps for the highest doses, these properties indicate almost solely the condition of the mylar. At the highest doses, there must be some damage to the aluminum, since the aluminum by itself should be able to carry about 15 percent of the initial ultimate tensile strength, whereas at the highest doses, the irradiated specimen retained only 5 percent of its tensile strength. The additional loss, however, is probably not a direct radiation effect. This point will be discussed later in this paper. On the other hand, the modulus of elasticity, which is measured in the initial portion of the stress-strain curve, and hardness, which is measured by indenting the aluminum surface, are primarily indicative of the condition of the aluminum. It will further be noticed that the aluminum surface protects the mylar from either weight loss due to outgassing or weight gain from oxidation reactions. Thus this property is primarily an indication of the integrity of the aluminum foil rather than of the mylar substrate. The conclusion, therefore, is that the mylar has sustained essentially all of the radiation damage and that the aluminum was essentially unaffected by radiation.

Surface Effects

A notable feature of the tests involving very high doses is the severe damage to the surface. A photograph of the surface after a dose

of 1.578×10^{17} e/cm^2 is shown in figure 5. This photograph is typical of the test results at all energies. The surface is seen to be markedly distorted and bubbled as a result of the internal pressure resulting from outgassing of the material in the foil. This is a radiation effect rather than a heating effect, since heating in an oven for several days at similar temperatures does not produce the same effect.

No proof has been obtained as yet as to whether the gas originated in the glue, the mylar, or both. The initial suspicion, however, points to the glue as a major factor since many of the bubbles are sharply defined on one side of the foil but only more softly defined on the other side. This asymmetry would indicate that the bubbles are not within the mylar but are rather at the interface between the mylar and the aluminum. Further tests are planned of samples prepared by vapor depositing the aluminum on the mylar without any glue as well as of samples with two sheets of aluminum foil glued together without the intermediate mylar. A comparison of the results of these tests with the present results should indicate the extent to which each portion of the foil is responsible for the outgassing.

The temperature of the balloon is determined by the optical characteristics of its surface. Thus, any change in the ratio of absorptance to emittance of the surface will affect the equilibrium temperature and could be more dangerous than the mechanical damage previously shown. The surface change shown here will doubtless produce some changes in the absorptance and the emittance. Tests are now in progress to determine the extent of these changes.

As was mentioned previously, there is some damage to the ultimate strength of the aluminum foil itself. The effect is somewhat unexpected since radiation doses of this type and magnitude do not generally affect metals. It would appear that the mechanical damage due to outgassing, rather than irradiation itself, is probably responsible for the damage to the aluminum.

Effect of Kinetic Energy

So far all of the results given herein have been for electron energies of 1.2 Mev. The electrons in space, however, encompass a broad spectrum of energies ranging from almost zero to several Mev. It is necessary to investigate all energies in this spectrum in order to obtain a reasonable picture of the effect of the space environment. Figure 6 shows the effect of kinetic energy on the results for a fixed total dose. In this case all of the samples were given the same total dose of approximately 6.31×10^{15} e/cm^2. At a dose rate of 10^8 e/cm^2/sec this total dose represents 2 years in orbit; and at 10^9 e/cm^2/sec, a little over 2 months. It will be observed that, for those properties which are affected, the degree of damage increases as the energy

decreases, except for the very lowest energy, where the electrons do not completely penetrate the foil. In studying the energy spectrum in space it is apparent that there are many more electrons with energies below 1.2 Mev than above 1.2 Mev. Thus, in assessing the damage to the material in space, it may be concluded that the increased damage potential of the lower energy electrons will probably lead to somewhat more severe damage than that demonstrated at 1.2 Mev in figure 4.

The increase in damage with lower energies is a reasonable result. It is observed that the foil is very thin so that at all energies except the lowest the electrons pass completely through the foil and thus have essentially a constant path length. In traversing this constant path the lower energy electrons, with their higher rate of linear energy transfer, deposit more energy in the foil and consequently do more damage.

Concluding Remarks

The results of this study on the effects of electron radiation on the mechanical properties of the Echo II material indicated that:

1. The primary effect of electron irradiation is an increased brittleness of the foil, resulting at higher doses in the early and brittle failure of the foil in tensile-strength and burst-strength tests.

2. Severe surface damage occurs at the highest doses used in this study. This damage results in mechanical damage to the aluminum foil.

3. The damage due to electron irradiation increases as the energy of the electrons decreases, at least until the point when electrons no longer completely penetrate the foil.

4. Dose rate effects in the material are negligible until rates at least two or three orders of magnitude higher than those in space are used.

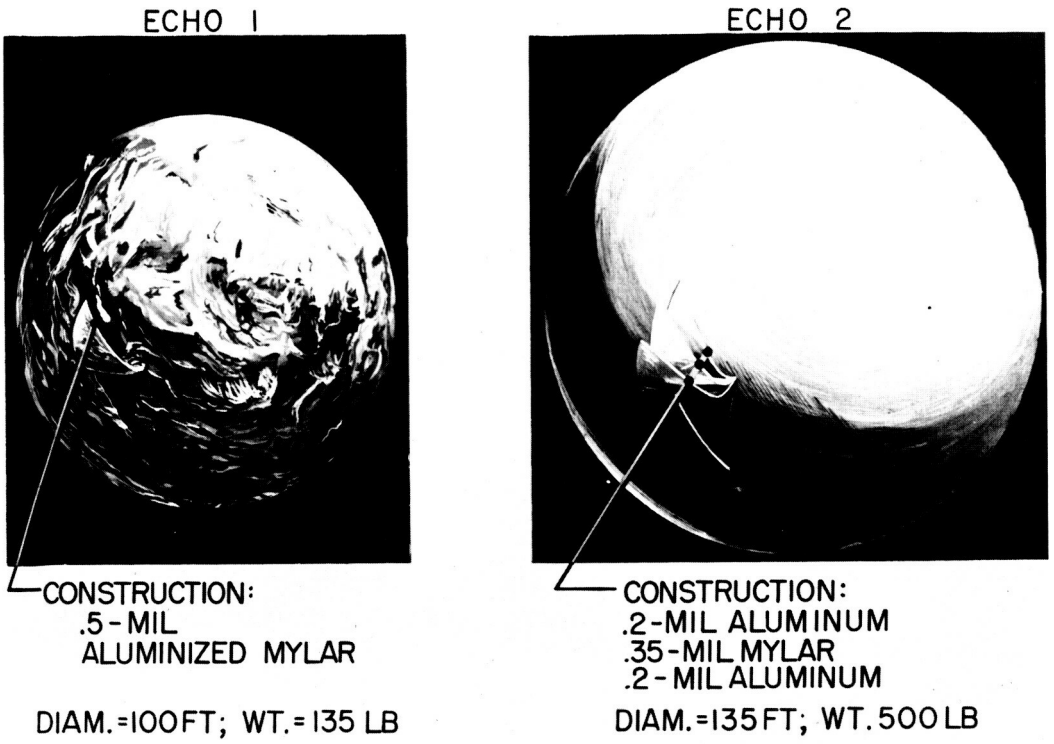

NASA
L-62-8554

Figure 1.- Construction of echo satellites.

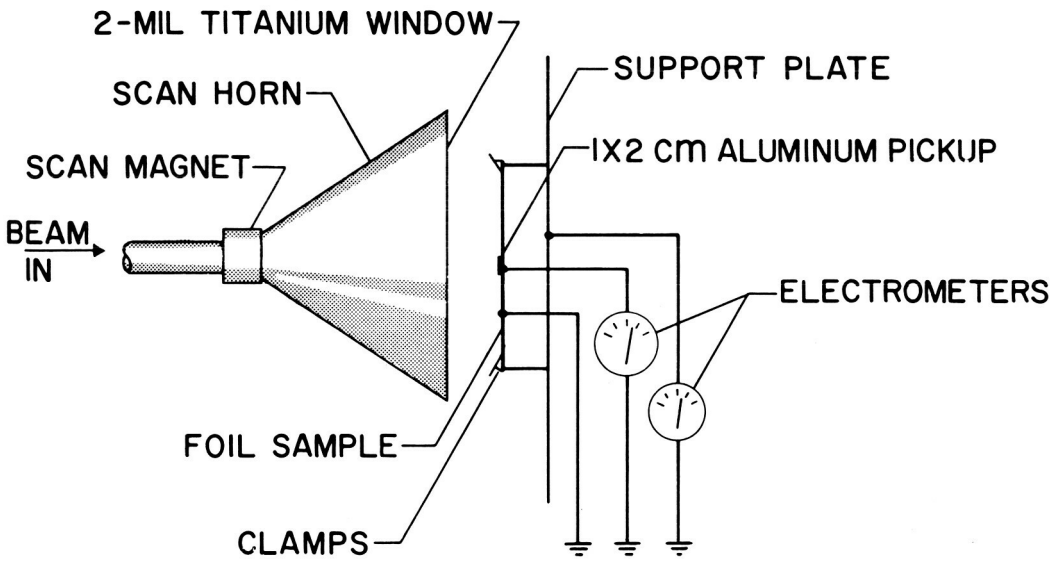

NASA

Figure 2.- Experimental arrangement.

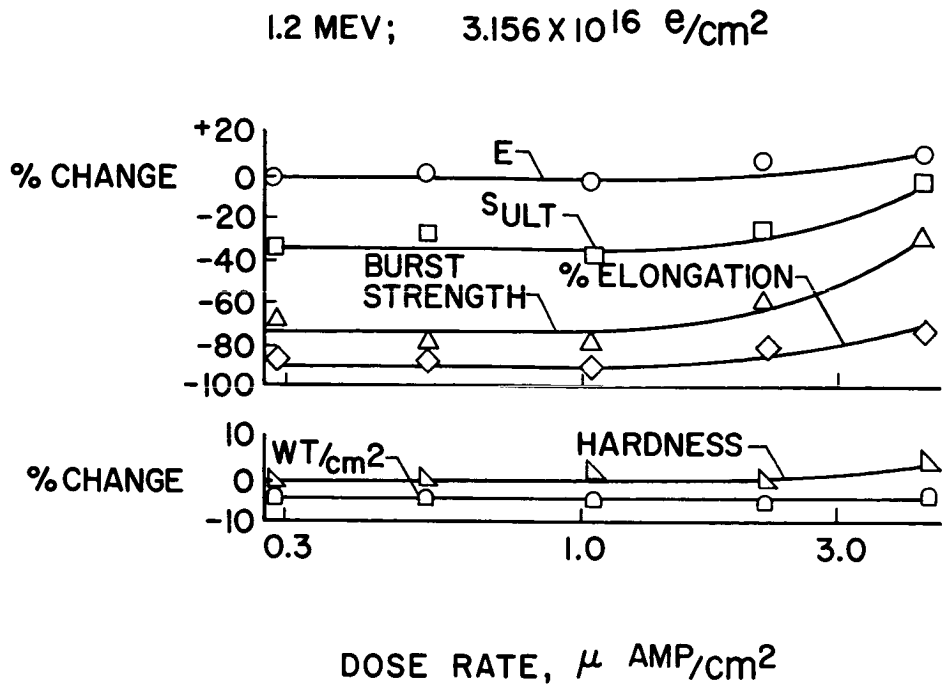

NASA

Figure 3.- Effect of dose rate.

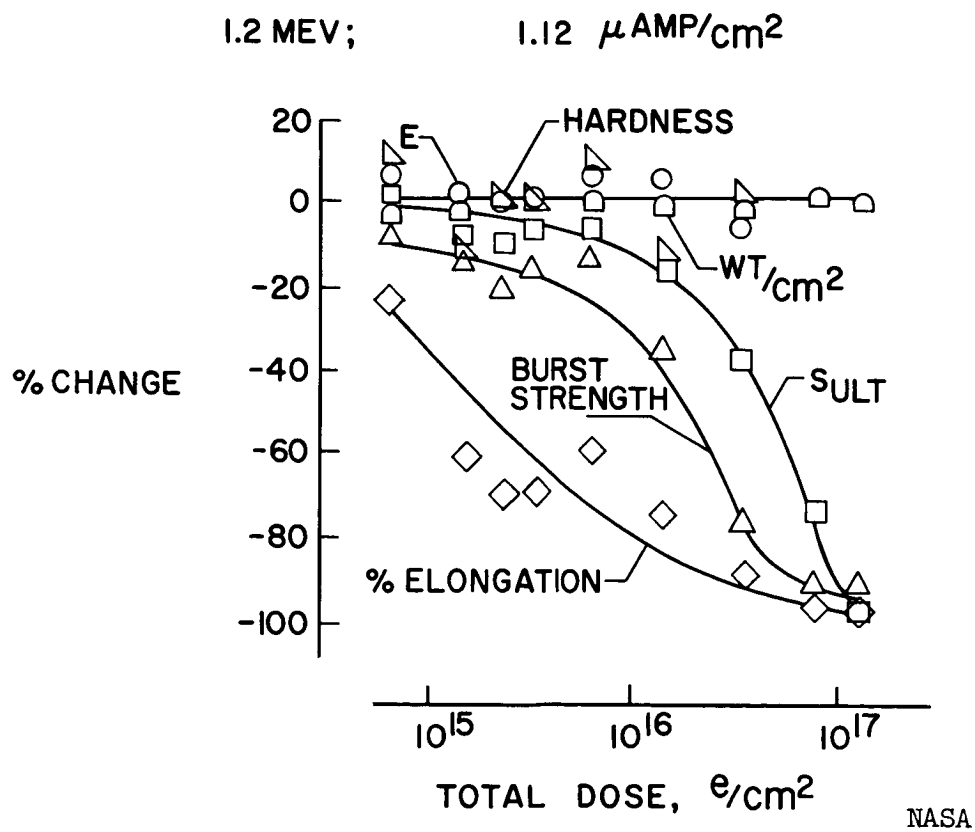

NASA

Figure 4.- Effect of total dose.

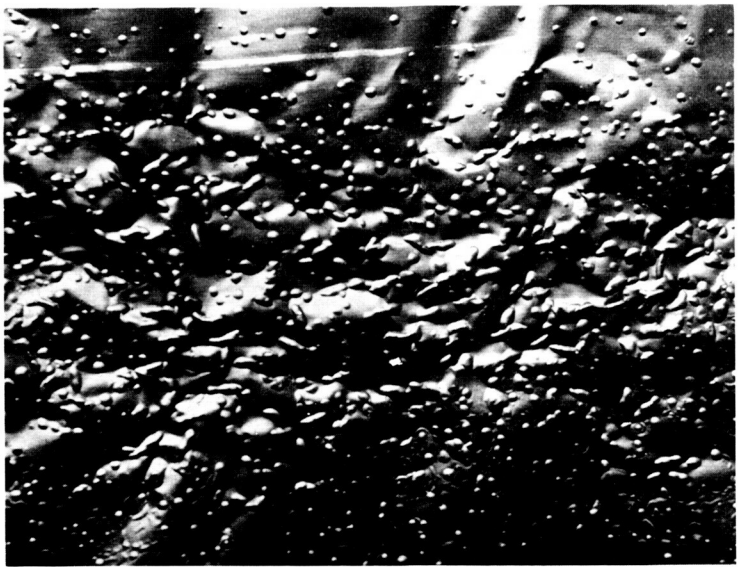

NASA

Figure 5.- Surface after 1.578×10^{17} e/cm^2.

6.31×10^{15} e/cm^2 1.12 μa/cm^2

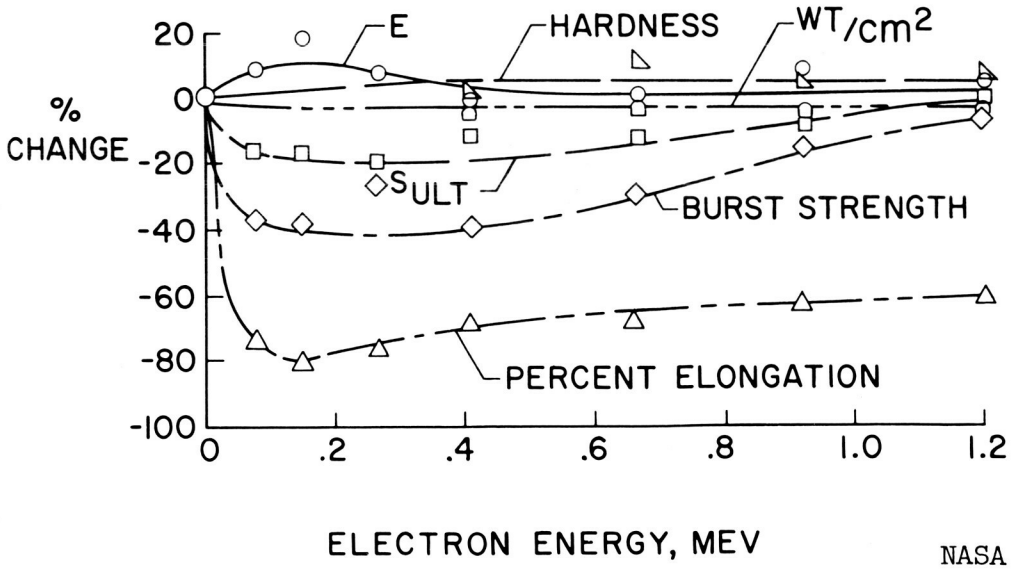

NASA

Figure 6.- Effect of electron energy.

Paper C-1

ACUTE EFFECTS OF RADIATION EXPOSURE IN MAN

J.J.Nickson,M.D.
Memorial Hospital & Sloan Kettering Institute
New York City,N.Y.

15130

Abstract

The data to be discussed today will be derived primarily from observations in man. For the most part, the events to be described will take place less than three months after the onset of the exposure. The data arises from three sorts of observation; first, those on patients who receive total body radiation in an attempt to ameliorate some ailment; second, accounts of nuclear accidents involving reactors; and third, the consequences of exposure to the events after the use or testing of nuclear weapons.

Historically, total body radiation as a medical tool was first suggested in 1907. Its use, however, may be said to have begun in 1923, and it has been used intermittently since. Medically, however, use of total body radiation may be divided into two broad components; first, when its use derives from the intent to modify a disease process itself; second, when it is used in an attempt to suppress immune mechanisms sometimes also associated with an attempt to suppress a disease process.

An acute syndrome may be divided into events associated with effects upon the function of the marrow, upon the epithelium or the gastrointestinal tract, upon the skin, and upon the central nervous system. The number of observations relating to biochemcial alterations is increasing.

These changes will be described and discussed. Major emphasis will be given to those abnormalities from which recovery may occur.

Finally, an attempt will be made to relate dose time considerations to the kinds of effects seen.

Introduction

This is clearly a large and diffuse subject. Since it is my impression that our major interest today relates to the effects noted after either total body exposure or after exposure of substantial segments of the body, information about the after-effects of radiation will be limited to those after exposure. The term "acute" is defined as those effects occurring within 30 days. It is recognized that the definition is somewhat arbitrary, but again, in the time allotted some narrowing of the area under discussion must be accepted.

Areas of Information

The information with regard to humans comes from three broad categories: patients; occupational exposure; and military usage. Data has been derived from deliberate exposure of patients, usually those suffering with malignant disease, to whom total body irradiation was given as a means of attempting to modify favorably the course of the disease. Information of this sort begins to appear in the literature in the 1920's and perhaps 50 papers have been written on the consequences of exposure of such patients. Except for the few papers since the last war, exposure was to low doses, or to low dose-time levels, and to x-rays of quite low energies, from 180 to 250 Kvp. As a consequence, the distribution of energy within the patient is inhomogenous. In the absence of detailed dosimetry, the total energy deposited varies considerably and is subject to uncertainty when one attempts to think about it today.

A second category is that following irradiation of patients to high dose levels, several hundred of roentgens in a single exposure. The radiation is given with two objectives in mind: first, to suppress the activity of the neoplastic cells, and second, to modify the immune response of the patient by suppression of the hematopoetic system, with subsequent bone marrow grafting to support life. A third category, with relatively few representatives as yet, consists of patients with non-neoplastic disease who are given radiation with the sole objective of suppressing the immune mechanism, to be followed by an organ transplant.

In general, patient exposure has been to photons only. Dosimetry, as noted above, is subject to some uncertainty. The data has the merit that the time of exposure is known with certainty. Further, in most cases and certainly in almost all recent cases, base-line laboratory values have been determined.

Occupational exposure of sufficient magnitude to be relevant here commonly has followed accidents with nuclear reactors. Wald and Thoma [1] have summarized these data. Here, the exposure to ionizing radiation is commonly a mixed one. The exact values are subject to several kinds of uncertainty. First, the absolute amount of energy absorbed is open to question. Second, the knowledge of the mixture of particulate and electromagnetic radiation is uncertain. Third, the estimation of dosage depends, at least in some of the incidents, upon assumption as to the relative biological effectiveness of the various components. Naturally, these studies commonly are not preceded by detailed baseline observations of hematologic or bio-chemical values. The individuals involved are normally healthy, or at least capable of performing a day's work

Finally, there is some information from military usage of nuclear weapons either in combat or in testing situations. Information exists from Hiroshima and Nagasaki incidents, from the exposure of the Polynesians, and from the Japanese on the Fortunate Dragon. Such information is derived from more or less random selection of the available population. No baseline studies exist. The interpretation of data may be further clouded by the presence of other kinds of trauma, frequently of sufficient magnitude by itself to cause severe illness or death of the individual.

Description of Syndrome

Three modes of death following exposure to ionizing radiation have been identified in the laboratory mammal and in man.

The first mode involves or appears to result from damage of the central nervous system and is called the "CNS" pattern, on which Dr. Langham [2] and his group have worked extensively. This occurs in mammals at dose levels of the order of tens of thousands of roentgens. In laboratory mammals, death occurs in a few hours. Convulsions are a permanent feature and are associated with profound electrolyte and fluid balance abnormalities. It seems reasonable to assume that some of the exposures at Nagasaki and Hiroshima were sufficient to induce this pattern of death. Death would have occurred before hospitalization

---

[1] N.Wald and G.E. Thoma,Jr.,Radiation Accidents: Medical Aspects of Neutron and Gamma-Ray Exposures, ORNL-2748,AEC,Oak Ridge National Laboratory, Oak Ridge Tenn.,2/21/61,pp.1-177.

[2] W.Langham,K.T.Woodward,S.M.Rothermel, P.S.Harris, C.C.Lushbaugh, and J.B.Storer, Studies of the Effect of Rapidly Delivered, Massive Doses of Gamma-Rays on Mammals, Rad.Res. 5,404,(1956).

IN MOST CASES IF NOT ALL INSTANCES. ONE LABORATORY ACCIDENT WAS FOLLOWED BY A PATTERN OF DEATH OF THIS SORT. DOSAGE ESTIMATIONS FOR THE UPPER HALF OF THE BODY WERE OF THE RIGHT ORDER.

THE SECOND OR GASTROINTESTINAL PATTERN OF DEATH OCCURS IN LARGE MAMMALS WITH DOSES OF THE ORDER OF A FEW THOUSAND ROENTGENS (1500+ R). HERE, DEATH INTERVENES AS A RESULT OF ELECTROLYTE AND FLUID LOSSES DUE TO DENUDATION OF THE GASTROINTESTINAL TRACT EPITHELIUM. DEATH USUALLY OCCURS BETWEEN FIVE TO EIGHT DAYS.

THE THIRD AND THE COMMONLY OBSERVED PATTERN OF DEATH IS A CONSEQUENCE OF INJURY TO THE HEMATOPOETIC SYSTEM. THE USUALLY GIVEN LD-50 ESTIMATES FOR MAN RELATE TO THIS PATTERN OF DEATH. AN ACCURATE LD-50/30 DAY FOR MAN IS NOT KNOWN. VALUES FOR LABORATORY PRIMATES ARE IN THE RANGE OF 450 TO 550 R. THE LD-50/30 DAY DOSE GUESSES FOR MAN USUALLY CENTER AROUND 500 R. IN EXAMINING THE EVIDENCE PREPARING FOR THE DISCUSSION TODAY, AND GIVING CONSIDERABLE WEIGHT TO RECENT STUDIES IN PATIENTS RECEIVING ABOUT 400 RADS WITH AND WITHOUT BONE MARROW GRAFT, AND ALSO TO SOME INDIRECT EVIDENCE, I HAVE COME TO FEEL THAT THE LD-50/30 DAY FOR MAN MAY WELL BY HIGHER THAN $\approx$500 R, AND MAY BE IN THE RANGE OF 650 TO 700 R.

THE CONSEQUENCE OF EXPOSURE TO DOSES OF APPROXIMATELY 500 R MAY BE SUMMARIZED AS FOLLOWS:

NAUSEA AND VOMITING, USUALLY OF SHORT DURATION, BEGINNING MINUTES OR HOURS AFTER EXPOSURE AND LASTING ABOUT 24 HOURS. FOLLOWING THIS, THE PATIENT MAY FEEL WEAK AND LETHARGIC, BUT HAS NOT SPECIFIC SYMPTOMS OR SIGNS UNTIL ABOUT THE FOURTH DAY WHEN DIARRHEA COMMONLY APPEARS. DIARRHEA MAY PERSIST FOR THREE OR FOUR DAYS AND MAY BE ASSOCIATED WITH ANOREXIA, WEIGHT LOSS, AND SIGNS OF DEHYDRATION, IF SEVERE.

FEVER RESULTING FROM INFECTION MAY DEVELOP BY THE NINTH DAY. COMMONLY, THIS IS THE RESULT OF INVASION OF THE LYMPHATIC SYSTEM AND BLOOD STREAM BY ORGANISMS NORMALLY RESIDING WITHIN THE LUMEN OF THE GASTROINTESTINAL TRACT. INFECTION DEVELOPS BECAUSE OF THE POST RADIATION SUPPRESSION OF THE IMMUNE SYSTEM, THE DECREASE OF THE WBC, AND BECAUSE OF THE LOSS OF THE EPITHELIAL BARRIER NORMALLY PRESENT.

AROUND THE TWELFTH TO FOURTEENTH DAY, IF INFECTION HAS NOT BEEN A FATAL COMPLICATION, EVIDENCES OF DISTURBANCES IN THE BLOOD'S ABILITY TO CLOT MAY APPEAR AS EVIDENCED BY PETECHIAE IN THE SKIN, NOSEBLEEDS, BLEEDING OF GUNS, AND BLOOD IN STOOL. IF BLOOD LOSS ALONE OR IN COMBINATION WITH INFECTIOUS COMPLICATIONS IS SUFFICIENT

DEATH MAY OCCUR DURING THE THIRD WEEK AFTER RADIATION. PATIENTS WHO SURVIVE THIS PERIOD USUALLY RECOVER SLOWLY, THE PERIOD OF RECOVERY LASTING SEVERAL MONTHS.

SUBLETHAL DOSAGES

PERHAPS THE BEST AND MOST ORDERLY STUDY RELATING TO THE CONSEQUENCES OF LOWER DOSES IS THAT REPORTED BY MILLER AND FLETCHER [3] IN 1961. IN THIS REPORT THE PERIODS OF OBSERVATION WERE LIMITED USUALLY TO 14 DAYS AND INVOLVED IN ALL 263 PATIENTS. THIRTY PATIENTS RECEIVED 200 R. NAUSEA AND VOMITING OCCURRED IN 17 OF THE 30 PATIENTS AND WAS SEVERE AND PERSISTENT IN ONE PATIENT ONLY. THE TYPICAL EPISODE OCCURRED ABOUT TWO HOURS AFTER IRRADIATION WAS COMPLETED. NAUSEA WAS NOTED FOR 10 TO 15 MINUTES, FOLLOWED BY VOMITING OF BRIEF DURATION. THEREAFTER THE PATIENT FELT NO FURTHER NAUSEA, AND NO MORE VOMITING OCCURRED. THE MAJORITY OF THESE PATIENTS CONTINUED THEIR NORMAL ACTIVITIES; IN A FEW INSTANCES THIS INCLUDED MANUAL LABOR.

SEVENTEEN PATIENTS RECEIVED DOSES RANGING FROM 125 TO 200 R; SEVEN OF THESE SHOWED NAUSEA AND VOMITING. EIGHTEEN PATIENTS RECEIVED 100 R; NONE SHOWED NAUSEA AND VOMITING. NONE OF THE PATIENTS RECEIVING DOSES LESS THAN 100 R SHOWED NAUSEA AND VOMITING. NONE SHOWED ANY OF THE EVIDENCES OF INFECTION OR OF HEMORRHAGIC DIFFICULTIES NOTED ABOVE.

WEAKNESS AND LETHARGY WAS NOTED IN ONLY THREE PATIENTS, ALL WERE FROM THE GROUP EXPOSED TO 200 R.

OUR EXPERIENCE WITH ABOUT 50 PATIENTS IS CONSISTENT WITH THE MILLER AND FLETCHER DATA. NAUSEA AND VOMITING HAS BEEN SEVERE IN ONLY ONE OF OUR PATIENTS; THIS WAS A PATIENT OF A VERY NERVOUS TEMPERAMENT, AND IT IS OUR BELIEF THAT THE NAUSEA AND VOMITING, WHILE IT MAY HAVE BEEN INDUCED BY THE 175 R GIVEN HER, WAS ALMOST CERTAINLY INTENSIFIED BY HER APPREHENSIONS.

HEMATOLOGIC DATA HAS BEEN OVERWHELMINGLY THE LABORATORY INDEX OF RADIATION DAMAGE TO DATE. AGAIN REFERRING TO MILLER'S AND FLETCHER'S DATA IN THE 200 R GROUP, THE WBC HAD DROPPED TO A LEVEL WITH A SIGNIFICANCE OF 0.01 BY THE SEVENTH POST-TREATMENT DAY. RED BLOOD CELL AND HEMAOGLOBIN VALUES SHOWED NO SIGNFICIANT CHANGES DURING THE PERIOD OF OBSERVATION. IN VIEW OF OUR OWN STUDIES, WHICH WILL BE COMMENTED UPON LATER, THIS IS NOT SURPRISING. LITTLE CHANGE IN THE PLATELET COUNTS WAS SEEN IN THE FIRST TEN DAYS AFTER TOTAL BODY TREATMENT.

FOR THE FOUR PATIENTS FOLLOWED LONGER THAN TEN DAYS THE PLATELET COUNTS REACHED A MINIMUM AT SEVEN WEEKS, FIVE WEEKS, FOUR WEEKS AND THREE WEEKS.

---

[3] L.S.MILLER AND G.H.FLETCHER AND H.B.GERSTNER, RADIOLOGICAL OBSERVATIONS ON CANCER PATIENTS TREATED WITH WHOLE-BODY X-IRRADIATION, RAD.RES. 8,150,(1961).

Doses of 125 to 175 r were followed by a depression in the white count with a significance of 0.01 on the seventh day. For the lymphocyte count there was a depression significance at the same level on the fourth day. The 100 r doses were followed by a fall in the lymphocyte count significant by the second day, but no significant effects was noted on the total white blood cell count. The authors concluded that doses of 100 r could be detected by the drop in the lymphocyte count; but doses below that level could not be so detected.

In our series of 11 patients, without disease of the blood forming organs, who received doses in excess of 120 r, the mean time of 50 per cent of the pre-irradiation white count was 24 days. The mean time to ten to 15 per cent of the pre-irradiation value was 31 days. Abnormal bleeding as a clinical problem is not commented upon in Dr.Fletcher's and Dr. Miller's paper. In our series abnormal bleeding occurred in several patients during the fourth week after exposure, but was a serious clinical problem in one patient only. Maximal depression of the platelet count after 100 to 175 r occurs at 20 to 30 days.

Summary and Conclusion

Radiation in sufficiently large amounts can without question produce signs and symptoms in man, primarily relating to injury to the gastrointestinal tract, and immune mechanisms, and to other evidences of suppression of hematologic function. With doses of 200 r or less in a single exposure, nausea and vomiting of relatively short duration is the only symptom which has been described. With doses of 100 r or less the probability of even nausea occurring is small and perhaps absent.

Paper C-2

LATE EFFECTS IN MAN FOLLOWING EXPOSURE TO IONIZING RADIATIONS

Douglas Grahn

Division of Biological and Medical Research, Argonne National Laboratory

The problems before the National Aeronautics and Space Administration concerning the potential biological hazards of radiation exposure are familiar ones to other agencies, such as the Atomic Energy Commission. The "late effects" or manifestations of chronic radiation injury have been of particular concern to the AEC and for the same reasons they concern the NASA; chronic injury is cumulative, though subtle and often undetected, and can be the limiting factor for individual exposure histories.

Although a considerable amount of experimental effort has been expended on late-effects problems, completely satisfactory answers are not yet available for man. This is largely due to the necessity of projecting expectations for man on the basis of experience in laboratory animals. Available direct human experience can be drawn upon, but even this can only serve to "spot check" certain predictions. At present the most thorough examination of man's response to radiation involves the Hiroshima-Nagasaki survivorship study under the jurisdiction of the Atomic Bomb Casualty Commission.[1] Other studies include the follow-up of criticality accident cases. All things considered, our information is best for doses that induce acute injury and it becomes progressively more uncertain as dose declines. Statements regarding the chronic effects of fallout radiation, for example, are almost entirely conjectural - lacking experimental validation. By and large, the same can be said for any projected effects of exposure to space radiation, with the exception that here we can be dealing with bursts of exposure to higher doses in the range of present experience.

The late effects of radiation exposure have to be examined in two broad categories; somatic and genetic. The somatic effects are those found in the irradiated individual; the genetic effects are those transmitted or transmissable to the offspring as a result of radiation-induced change in the reproductive tissues. Before discussing the biological expectations however, some comments are required concerning the physical exposure parameters.

---

[1] A research agency of the U. S. National Academy of Sciences - National Research Council supported by a contract with the U. S. Atomic Energy Commission.

Temporal and geometric aspects of exposure to space radiation

The ambient radiations in space are characterized by their heterogeneity, not only in the variety of both particulate and electromagnetic radiations but also in the energy levels of these radiations (Newell and Naugle, 1960). Since these factors are discussed elsewhere in the proceedings, my comments will be restricted to the general consequences of this heterogeneity for the hazards evaluation problem.

A heterogeneous energy spectrum of the incident radiation will produce a very non-uniform distribution of dosage in depth, if the spectrum includes a large low energy component. For photons, this would involve energies below 120-135 kvp (Grahn et al., 1956). For protons, energies generally below 100 Mev would have an inadequate range in water (Rich and Madey, 1954), and consequently wet tissue, to assure uniform depth dosage. It becomes extremely difficult to define the level of injury when the exposure dose in air may vary from two to twenty times greater than the midline tissue dose. The use of the midline dose, or other measures, such as exit dose or gram-roentgen dose, is not recommended for the definition of exposure level. There is evidence, however, to support the hypothesis that the biologically effective dose is best defined as the average dose to the bone marrow for both acute and chronic measures of injury (Grahn et al., 1956; Grahn and Sacher, 1958; Alpen et al., 1958). This problem is especially difficult when dealing with heterochromatic x or γ radiation, since absorption in bone exaggerates the non-uniformity by preferentially shielding the bone marrow. Any bremsstrahlung or secondary x or γ radiation produced by shielding or capsule materials may be in this low energy range. Protons, on the other hand, are not more effectively stopped by bone than by soft tissue, but the wide energy range for galactic and solar flare protons causes the depth dose curve to be very steep (Figure 1). As seen in Figure 1, this would lead to an extremely heterogeneous marrow dosage. In comparison to the flare proton, the geomagnetically trapped proton belt has a more uniform energy spectrum and consequently a flatter depth-dose distribution.

The actual dose in depth for any circumstance would have to be calculated from the observed differential energy spectrum; and each event is going to differ from every other event. Thus, complete monitoring of all radiation

events to which an astronaut may be exposed will be required if any sensible statements on radiation exposure stacus are to be made.

In addition to the problem of non-uniform depth dosage, there is the question of "non-random" exposure due to the extremely high local doses that will occur in cells and tissues from the passage of high energy heavy particles. In this situation, small groups of cells may be severely injured while surrounding tissue will remain unscathed. The acute and chronic effects of this type of exposure are not really understood but some comments will be made on the basis of experience with fission neutrons.

Lastly, the time pattern of exposure will be unpredictable and irregular. For example, there would be a pulse or brief period of exposure during transit of the Van Allen belts. The random occurrence of solar events would give rise to additional pulses. All of these could vary in total dose, dose rate and depth dose. Throughout a mission, there would also be a continuous low level exposure to the galactic cosmic radiation. The ultimate biological effect is known to vary with the pattern of exposure (see Figure 2 below) but because of the pulse-like nature of the exposure under discussion, it would be difficult to "assign" an individual to either a predominantly single dose exposure or continuous exposure. If the total dose remains below 50 r, it will make little difference, but it is obvious from Figure 2 that brief, single-dose, high-intensity exposures to total doses of 100 r or more can be followed by a more exaggerated chronic syndrome.

The above remarks and these below concerning somatic hazards are all based on the assumption that whole-body exposure pertains. If partial-body exposure occurs, or is deliberately planned as a protective measure, prediction of late effects becomes essentially impossible for man. The value of bone-marrow shielding as protection against both acute and chronic radiation injury is well recognized and documented for experimental animals (Thomson, 1962), but is quantitatively unevaluated for humans.

Somatic hazards

There is a variety of ways of evaluating the long term biological hazards, but the most readily quantitated measure of chronic injury is simply survival

time or life shortening. The general relationship between dose and the reduction of life expectancy is shown in Figure 2 for the mouse; the species from which we gain most of our knowledge of mammalian radiobiology. The figure indicates what might be called the limiting conditions - the exposure situations that give the maximum and minimum late effect. As indicated above, any exposure to the radiations in space during an extended mission will lie somewhere between the two extremes. If shielding is adequate so that total doses per mission are less than 50 r, late somatic effects can probably be predicted on the assumption of a continuous exposure. The expectations for man are suggested in Figure 3, according to the date and calculations of Sacher (1960) and Sacher and Grahn (1963).

The curve is described by the equation: $Y = 45e^{-1.05D}$ where Y is the predicted after-expectation of life under exposure of D roentgens per day. This relationship is exceptionally accurate for mouse populations and it is applied to man on the assumption that responses to radiation will be in proportion to the ratio of life expectancies (Sacher, 1960). In simplest terms, it states that the life shortening effect in man is about one day per roentgen, when this is accumulated in a reasonably protracted manner.

One should hasten to add that at doses probably below 0.3 r/day (for man) the actual effects are still quite unpredictable. In the mouse, for example, at comparable doses (below 10 r/day), where life shortening amounts to 15% and less, there is a great deal of variability in the response. There is extensive dependence upon environmental factors such as disease pressure, and the innate viability of the individual, (Grahn and Sacher, unpublished data).

In general, the mouse strains with shorter life expectancies tend to demonstrate little or no life shortening at doses below 10 r/day and occasionally a small increase in life expectancy over the control. Longer lived strains generally tend to show some degree of life shortening at even the lowest doses. Shorter-lived animals have the higher mortality from infectious disease and independent control samples show a wide variance of mean life expectation. The irradiated mice that are from the short-lived group may have their mortality rate from infectious disease depressed below this age-specific control, thus they

may show some over-survival. Longer-lived mice are more invariant in their normal survival times and appear to be subjected to a minimum of infectious disease pressure, whether or not they are irradiated.

It is very likely that the astronaut populations will be analogous to those mouse populations that have a better than average life expectancy and a low infectious disease incidence. In other words, they undoubtedly have a low background noise level and even at very low radiation doses, a significant signal-to-noise ratio will exist and thus some degree of chronic injury could be manifested.

The next question asked is - why does an irradiated population die sooner? Generally, chronic radiation injury is expressed by an increase in the age - specific death rates over those seen in unirradiated populations. The causes of death normally found in a population are also found in the irradiated group. There is no unique pathology associated with chronic radiation injury.

Certain causes of death are increased in incidence more than others - leukemia, for example, is readily induced by radiation. Although radiation-induced leukemia has been the subject of extensive research, the most pertinent data are still those being obtained in the Japanese survivors. A recent summary by Brill et al. (1962) substantiates earlier interpretations that above 50-100 r, the increase is linear with dose at a rate of 1 to 2 x 10^{-6}/r/year during the first 15 years post-exposure. This is an average figure for all age groups and would be slightly less for a group of adults between 30 and 40 years of age, at least for acute leukemias. The data are uncertain at doses below 50 r but tend to demonstrate a positive effect.

Radiation-induced leukemia has a phasic response pattern in time. The peak year of incidence in Japan was 1952 - seven years post-exposure - and it has been dropping steadily since then. Undoubtedly some life shortening effect will be specifically attributed to leukemia when the study is complete. Such an effect has been statistically isolated in mouse populations (Grahn, 1960).

Other neoplastic diseases are also increased following irradiation and again, early reports from the Japanese studies indicate a positive dose-response

relation for all age groups. Specifically, carcinoma of the stomach, lungs and ovaries was shown to be increased during a 20-month survey period in 1958-1959 (Hollingsworth et al., 1962).

The incidence of cataracts in the Japanese is very low (<1%) but this could be a more common sequel of exposure to space radiation due to their high LET component and high surface dose.

Earlier, it was noted that the high LET radiations may have a somewhat modified pattern of chronic injury as a result of the greater localization of energy deposition. Experience with fission neutrons indicates what can occur when geometric factors are appropriate. Nowell et al. (1958) reported that neutron exposure induces a four-fold greater incidence of stomach cancer in the mouse than does x-ray exposure (36% vs 9%). This is attributed to the fact that the mouse is small enough for the deep tissues to be largely irradiated by the high LET recoil protons from the neutron interaction. Thus, the glandular epithelium is subjected to extensive local damage along the proton track while comparable doses of x-irradiation produce a more diffuse level of injury. The cellular and local physiologic sequelae are such as to produce a higher incidence of gastric carcinoma from the neutron exposure.

This interpretation is supported by the observation that neutron induction of cell damage in the mouse's intestinal wall has an RBE of 6-8 while the concurrent acute lethal response has an RBE of 2-3 (Lesher and Vogel, 1958). In contrast, larger mammals, from the rat to the dog, do not evince the acute gastro-intestinal syndrome after fission neutron irradiation that characterizes the response of mice (Bond et al., 1956). Man would undoubtedly respond like other large mammals, since the deeper tissues would be irradiated almost entirely by thermal neutron capture gamma rays rather than by recoil protons. A more penetrating particulate radiation, such as high energy protons and heavy primaries, could produce a situation in man similar to that in the mouse exposed to fission neutrons.

The above noted case for gastric cancer induction is a clear example of a late effect that appears to be modified by the local geometric details of the energy transfer. Other cases more pertinent to space radiation exposure may be brought out if deep tissues were experimentally subjected to high LET radiations;

for example, if portions of the liver or intestine were exteriorized and exposed to charged particle beams from a HILAC.

Genetic hazards

One of the first questions that arises concerns the possibility of radiation-induced sterility. Unfortunately, good data on this point do not exist for man. What is known, along with animal experience, suggests that permanent sterility will not be induced at doses below acute lethal levels; unless a high local exposure of the gonads should occur. There may be a period of temporary sterility or reduced fertility following exposure to doses as low as 20 r, but present data from accident cases are incomplete or contradictory. One individual exposed to 12 r demonstrated a sharp reduction in sperm count (from 5×10^8/ml to 1×10^6/ml) over a period of seven months followed by an equal period of slow recovery (Hasterlik and Marinelli; 1956).

The Y-12 accident cases involved doses between 200 rad and 400 rad and some sperm counts were done (Andrews et al., 1961). Within 3 weeks, counts were low and sperm were generally non-motile. Absence of sperm, azoospermia, was noted in most of the cases for at least 9 months and reduced counts were noted at 22 months. The Vinca, Yugoslavia, accident cases, reported by Pendic (1961) and Jammet (1961) involved slightly higher doses; between 300 rad and 600 rad. Sperm counts began to decline by day 10 and within 3 months, 2 of the 4 surviving males showed azoospermia. Curiously, one individual who received a dose of 350 rad had nearly a normal sperm count 7-8 months after exposure while the other three males were azoospermic. Doses to the latter were between 400 and 600 rad. At 18 months post-exposure, one was normal, two were hypospermic and one still remained azoospermic.

While the above data are somewhat crude, the general course of events is typical of that seen in laboratory mammals; there is a pre-sterile period following irradiation, a sterile period, and a post-sterile period. The pre-sterile period in man probably lasts about 30 days. The sterile period may last months to years followed by a slow return to normal, but in some, this temporary sterility may not occur at all.

The importance of distinguishing between a pre-sterile and a post-sterile period lies in the type and frequency of mutations observed from matings in

these periods. Offspring produced in pre-sterile matings largely come from irradiated mature germ cells or spermatozoa. The mutation rate for recessive genes in these cells may be twice that observed in the spermatogonia or stem cells (Russell et al., 1958). In addition, the irradiated mature germ cells carry a high incidence of a mutational type rarely found in the immature cells - the dominant lethal. A recent survey of experimental data on dominant lethals in mice (Grahn, 1962) indicates that most act early in gestation, that the lethal effect is due to aberrant cell division and chromosome fragmentation, that the neutron: x-ray RBE is about 7, and that neutron dose-response data are linear with arithmetic dose compared to x-ray data which are more nearly linear to dose-squared. Thus, the particulate radiations of space may present an extra threat because of their dense ionization tracks and greater probability of inducing genetically lethal effects. This period of increased genetic hazard may only be of two months duration, however, according to recently reported data on the cycle of spermatogenesis in man (Heller, 1962).

Mutations observed in the post-sterile period are predominantly recessive, and about three-fourths of these may be lethal in mice (Russell and Russell, 1959) The mutation rate is lower for those mutations induced in gonia and lower still if the dose rate is less than 1 r/minute (Russell et al., 1958). Table 1 summarizes the mutation rate data in mice for the two sexes. These figures can be generally accepted as indicative of the radiation-induced mutation rate in man, at least within a factor of two. Again it can be seen that close monitoring of the exposure pattern will be required in order to assign a given exposure to the 'acute' or 'chronic' mutation rate categories.

What is the probability that a given germ cell will carry a recessive mutation? From the mouse data, this can be calculated as lying between 1 chance in 20 and 1 chance in 5, for immature germ cells following an exposure of 100 r and assuming there are 10^4 genes. Obviously, exact figures cannot be given, but the probability is certainly small for doses appreciably below 100 r. In addition, the chance of expression in the immediate offspring is probably only 1 in 25 or less (Morton et al., 1956).

Thus, there may be less than one chance in a hundred of a radiation-induced recessive mutation appearing in the first generation when the parent has

received a dose of 100 r. This seemingly low probability should not allow us to relinquish our obligation to minimize the genetic hazard.

Detrimental genes may express themselves in the population in a number of ways. These include:

a. Increase in frequency of stillbirths.
b. Shifts in sex ratio attributable to sex-linked lethal mutations.
c. Increase in mortality rate from birth to 10 years of age.
d. Increase in incidence of congenital abnormalities.
e. Decrease in life expectancy.
f. Decrease in birth weight.
g. Increase in variance of metrical traits.

The reader is referred for further detail to other reviews and reports by Grahn (1962), Neel and Schull (1956), and Stern (1960).

The major point to be made is that genetic damage can linger in the population for many generations. The probability of expression in the first generation offspring is usually low enough to produce a misleading confidence that no damage has been done. The issue will not be pressed here since the genetic hazard is probably not a major one. Most of the astronauts may be beyond median reproductive age - about 30 years - and therefore will not transmit any induced mutations. Also, this is a very small group whose genetic impact on the population will be equally small.

Assessment of hazards

The above remarks introduce the most difficult judgments of all - the value judgments on the rationalization of all of the risks involved in extended space flight missions. It is the writer's opinion that presently accepted standards of operational radiation safety for occupational and emergency situations have little meaning for these flight missions. Final judgments will depend not only on biological and medical considerations of radiation safety but also on the total complex of engineering and bioastronautics capabilities. However, it would be a pity to lose an otherwise successful mission, with all of its complications of launch, guidance and instrumentation, because of inadequate consideration of an old-fashioned hazard like radiation.

Undoubtedly, the shielding considerations should concern themselves primarily with the avoidance of acute radiation symptomatology. Any plan for the continued utilization of experienced personnel, however, will have to take chronic injury parameters into account.

In this regard, somatic endpoints are in part medically manageable so that valuable personnel need not be subjected to any maximum calculable risk; the risk based upon total absorbed dose. Genetic endpoints, in a sense, are not biologically controllable, but the hazard here is statistically manageable in that only a tiny fraction of the total reproductive population is involved.

Thus, as indicated, the judgments become almost wholly value judgments, but, fortunately, the data for establishing realistic probability statements of radiation hazards are becoming available. With these, the radiation hazards can be quantitatively evaluated along with all other risks in terms of the precautions required to insure mission success.

REFERENCES

Alpen, E. L., D. M. Jones, H. H. Hechter and V. P. Bond. 1958. The comparative biological response of dogs to 250 kvp and 100 kvp x-rays. Radiology 70: 541-550.

Andrews, G. A., B. W. Sitterson, A. L. Kretchmar and M. Bracer. 1961. Criticality accident at the Y-12 plant. In: Diagnosis and Treatment of Acute Radiation Injury. New York: Internat. Documents Service, Columbia Univ. Press, p. 27-48.

Bond, V. P., R. E. Carter, J. S. Robertson, P. H. Seymour and H. H. Hechter. 1956. The effects of total-body fast neutron irradiation in dogs. Radiation Research 4: 139-53.

Brill, A. B., M. Tomonaga and R. M. Heyssel. 1962. Leukemia in man following exposure to ionizing radiation. Ann. Internal Med. 56: 590-609.

Grahn, D. 1960. The genetic control of physiological processes: The genetics of radiation toxicity in animals. In: Radioisotopes in the Biosphere, R. S. Caldecott, Ed., Minneapolis: Univ. of Minnesota, p. 181-200.

Grahn, D. 1962. Methods in mammalian radiation genetics. In: Methodology in Mammalian Genetics, W. Burdette, Ed., San Francisco: Holden-Day.

Grahn, D. and G. A. Sacher. 1958. Chronic radiation mortality in mice after single whole-body exposure to 250, 135, and 80 kvp x-rays. Radiation Research 8: 187-194.

Grahn, D., G. A. Sacher, and H. A. Walton. 1956. Comparative effectiveness of several x-ray qualities for acute lethality in mice and rabbits. Radiation Research 4: 228-242.

Hasterlik, R. J. and L. D. Marinelli. 1956. Physical dosimetry and clinical observations on four human beings involved in an accidental critical assembly excursion. Proc. I Internat. Conf. Peaceful Uses of Atomic Energy 11: 25-34.

Heller, C. G., L. J. Matson, D. J. Moore and Y. Clermont. 1962. Rate of spermatogenesis in man determined by incorporating initiated thymidine into testes. In: Symposium on the Effects of Ionizing Radiation on the Reproduction System. In Press.

Hollingsworth, S. W., G. W. Beebe, M. Ishido and A. B. Brill. 1962. Medical findings and methodology of studies by the atomic bomb casualty commission on atomic bomb survivors in Hiroshima and Nagasaki. In: The Use of Vital and Health Statistics for Genetic and Radiation Studies. A/AC.82/Seminar, United Nations, N. Y. p. 77-100.

Jammet, H. P. 1961. Treatment of victims ot the zero-energy reactor accident at Vinca. In: Diagnosis and Treatment of Acute Radiation Injury. New York: Internat. Doc. Serv., Columbia Univ. Press, p. 83-104.

Lesher, S. and H. H. Vogel. 1958. A comparative histological study of duodenal damage produced by fission neutrons and Co^{60} γ-rays. Radiation Research 9: 560-571.

Morton, N. E., J. F. Crow and H. J. Muller. 1956. An estimate of the mutational damage in man from data on consaguineous marriages. Proc. Natl. Acad. Sci. 42: 855-63.

Neel, J. V. and W. J. Schull. 1956. The effect of exposure to the atomic bombs on pregnancy terminations in Hiroshima and Nagasaki. National Acad. Science. National Research Council Report No. 461. Washington D. D.

Newell, H. E. and J. E. Naugle. 1960. Radiation environment in space. Science 132: 1465-1472.

Nowell, P. C., L. J. Cole and M. E. Ellis. 1958. Neoplasms of the glandular stomach in mice irradiated with x-rays or fast neutrons. Cancer Research 18: 257-260.

Pendic, B. 1961. The zero energy reactor accident at Vinca. In: Diagnosis and Treatment of Acute Radiation Injury. New York: Internat. Doc. Serv., Columbia Univ. Press, p. 67-82.

Rich, M. and R. Madey. 1954. Range-energy tables. University of California Radiation Lab. Report, UCRL-2301. U. S. Atomic Energy Commission.

Russell, W. L. and L. B. Russell. 1959. The genetic and phenotypic characteristics of radiation-induced mutations in mice. Radiation Research (Suppl.) 1: 296-305.

Russell, W. L., L. B. Russell and E. M. Kelly. 1958. Radiation dose rate and mutation frequency. Science 128: 1546-1550.

Sacher, G. A. 1960. Problems in the extrapolation of long-term effects from animals to man. In: The Delayed Effects of Whole-Body Radiation. B. B. Watson, Ed., Baltimore: Johns Hopkins Press, p. 3-10.

Sacher, G. A. and D. Grahn. 1963. Survival of mice under duration-of-life exposure to gamma rays. I. Dosage-survival relations and the lethality function. In preparation.

Stern, C. 1960. Principles of Human Genetics. 2nd Ed. San Francisco: W. H. Freeman and Company.

Thomson, J. F. 1962. Radiation Protection in Mammals. New York: Reinhold Publishing Co.

TABLE 1

RADIATION-INDUCED MUTATION RATE IN MICE

(Adapted from data of W. L. Russell, ORNL)

Observed mutation rate	Sex	Cell stage	Radiation exposure
45×10^{-8}/r/gene	Male	Postgonial	Acute or chronic
21×10^{-8}/r/gene	Male	Gonial	Acute
5×10^{-8}/r/gene	Male	Gonial	Chronic
31×10^{-8}/r/gene	Female	Oocyte	Acute
4×10^{-8}/r/gene	Female	Oocyte	Chronic
0.7×10^{-5}/gene	Male and female	All stages	Unirradiated

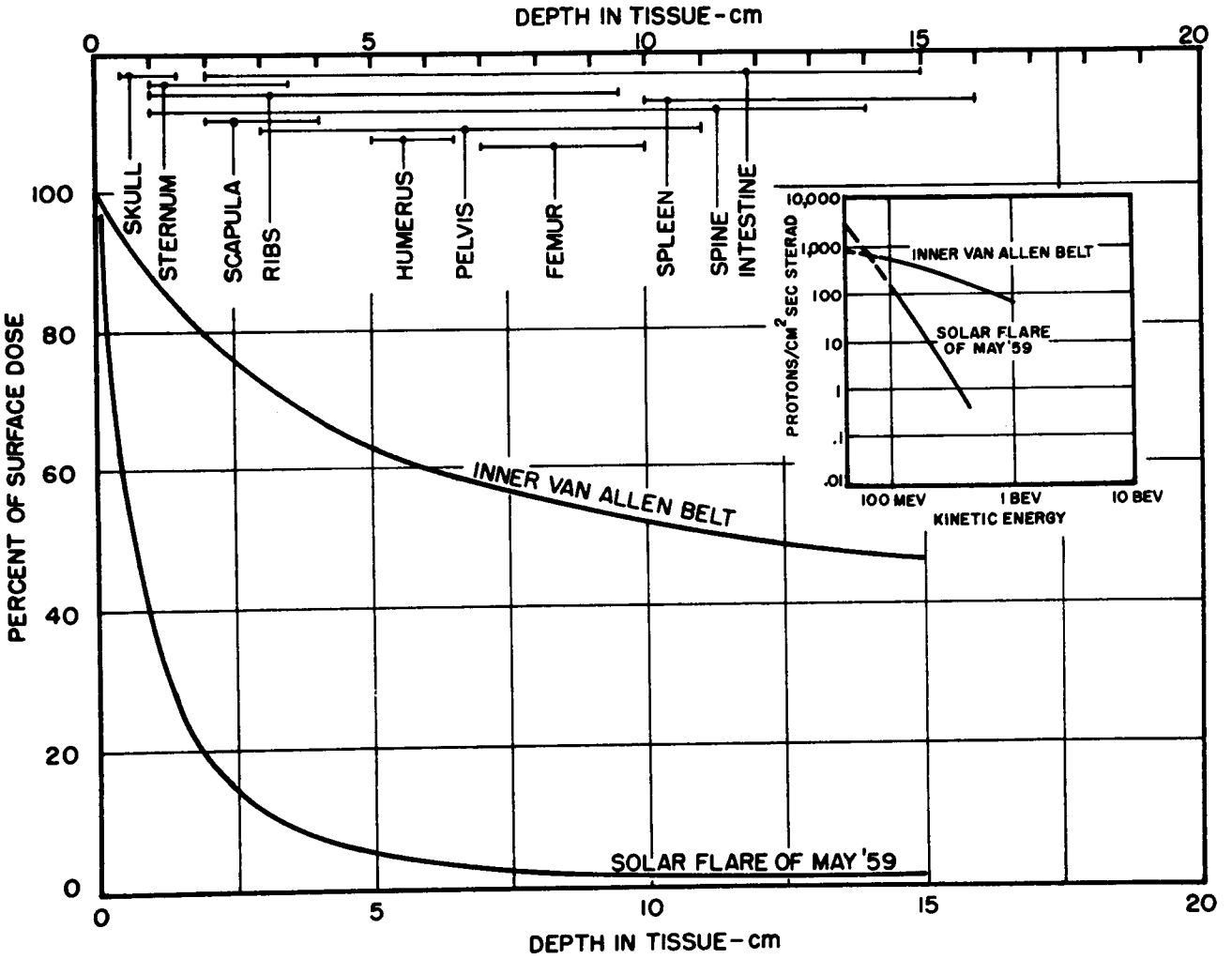

Figure 1. Depth dose as percentage of surface dose for a solar flare protons compared with inner Van Allen belt protons. Note general location of regions of active bone marrow in relation to depth dose.

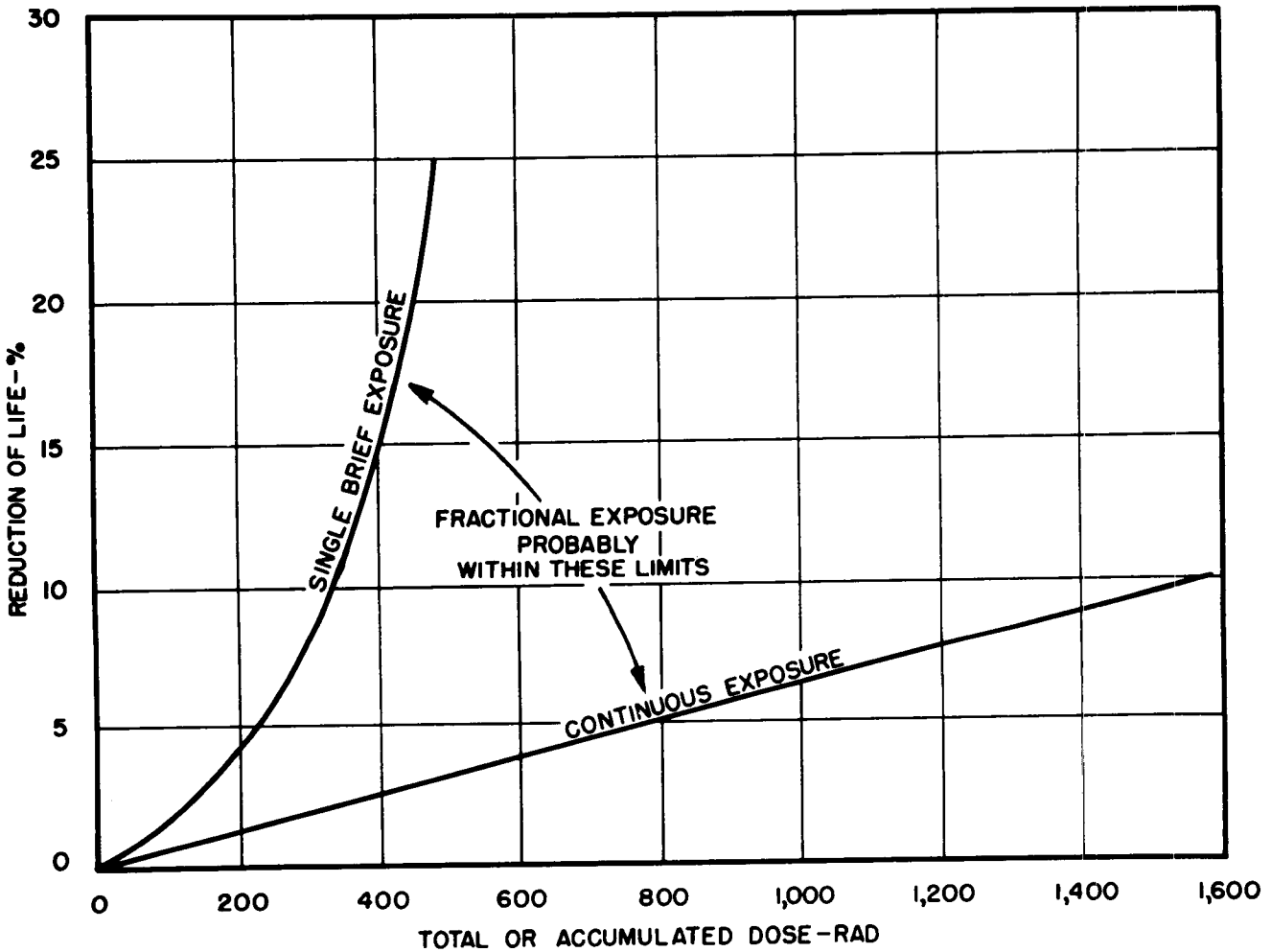

Figure 2. Idealized relation between life shortening and radiation dose for the laboratory mouse. Generally descriptive of expectations for man on the indicated basis of "percent reduction of life".

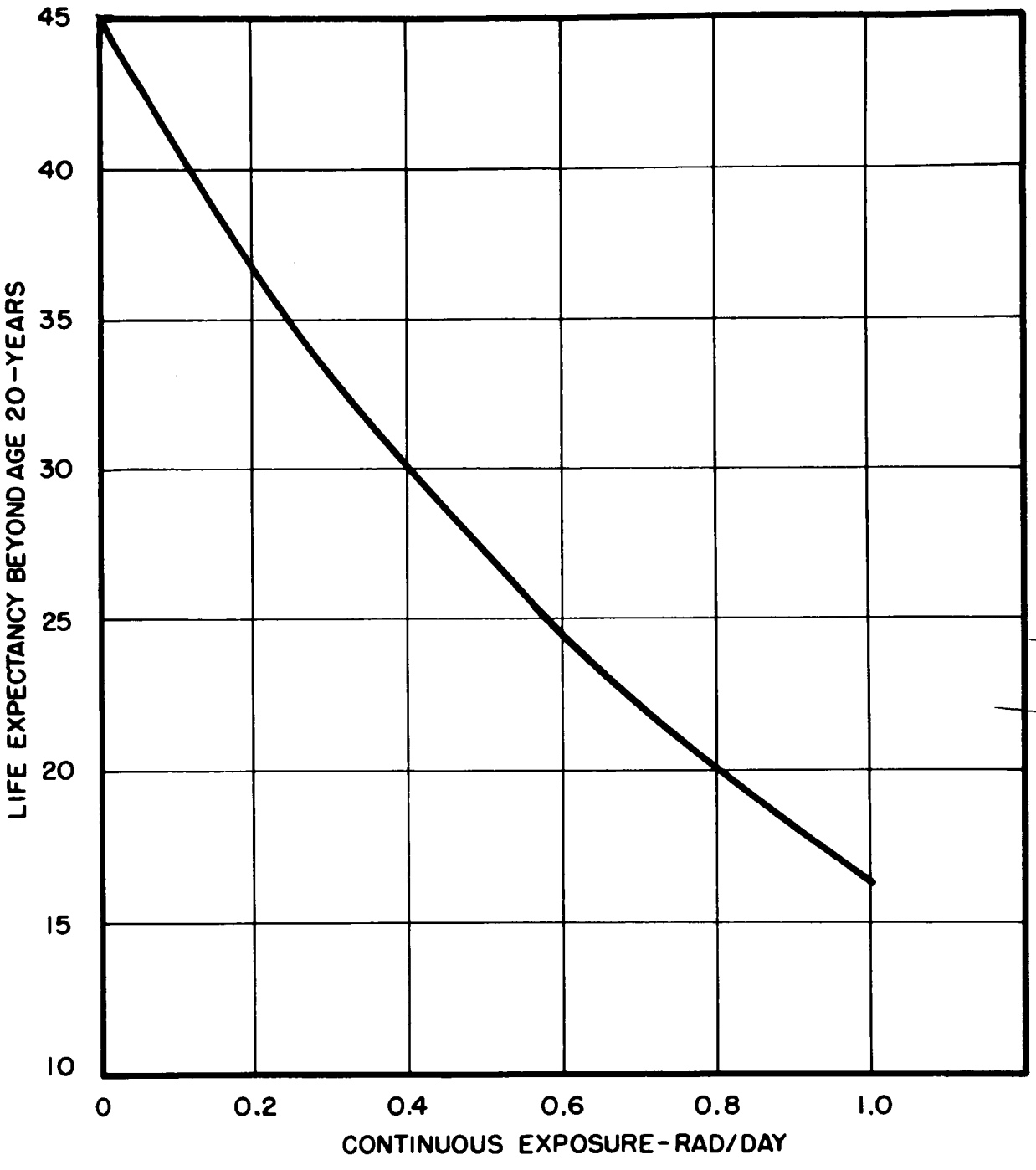

Figure 3. Prediction of life expectancy for man exposed to daily doses of radiation.

Paper C-3

17892

SOME SPECIFIC CONSIDERATIONS OF THE POTENTIAL HAZARDS OF HEAVY PRIMARY COSMIC RAYS*

Howard J. Curtis

Biology Department, Brookhaven National Laboratory, Upton, N. Y.

INTRODUCTION

The radiations of the Van Allen belts and the solar flares consist primarily of electrons and protons, the biological effects of which are reasonably well known. However, there is a very small component of the galactic cosmic rays which consists of stripped atomic nuclei of atoms as heavy as iron. The biological effects of such particles have not been extensively investigated because it is impossible to produce them in the laboratory with an energy high enough to use for mammalian experiments. Consequently it has been necessary to approach the problem by indirect methods.

The distribution of these particles is shown in Fig. 1, as estimated by Dainton et al. (1). It will be seen that most of the particles are of the very light elements and only a few heavy ones. For the elements lighter than carbon it seems safe to assume that the radiobiological effects are quite similar to those of protons or alpha particles and consequently the dose can be calculated in the usual way. Schaefer (2) has calculated this dose to be of the order of 40 m rep/day. This by itself, while it should not be ignored, would not seem to pose a very serious hazard for space travel.

* Research carried out at Brookhaven National Laboratory under the auspices of the U. S. Atomic Energy Commission.

But the particles heavier than carbon constitute a special hazard. Schaefer (2) has pointed this out a number of years ago and at that time performed much of the necessary calculation. He showed that when these heavy particles enter tissue one of two things may happen. Especially at very high energies a nuclear reaction may take place which results in a nuclear disintegration and star formation. In this the energy of the particle is widely spread throughout the tissue, and does not concentrate enough at any one spot to constitute a new type of effect. However, some of the particles, especially at low energies, slow down by interaction with the electrons of the tissue and this produces very energetic delta rays, especially near the end of the track. This leads to a very dense ionization track, and Schaefer (2) has computed that within this track, known as a "thindown," the radiation dose may be as high as 10,000 rads at the center, and decreases to low values at the edges. The track may be as much as 0.025 mm in diameter and about 1.5 mm long. Schaefer (2) has computed that there might be as many as 100 such hits per hour in an average man in interstellar space and there would be several thousand cells irradiated in each "hit." It thus appears there would be "hot spots" in the tissue in which the dose might be quite high, even though the over-all dose is quite low.

The proportion of particles which would be stopped in tissue by nuclear reactions as compared to those stopped as thindowns has been estimated by Schaefer (2) and is shown in Fig. 2 as a function of energy. It is seen that practically all particles having energies greater than 10^9 e.v./nucleon will be stopped by nuclear reactions and so need not be considered here.

The magnetic field of the earth forms an effective shield for the equatorial region of the earth for everything except a few of the most energetic of these particles. At higher latitudes more of the low energy particles will be present. Schaefer (2) has also estimated the energy spectrum of these particles at various latitudes and this spectrum is shown in Fig. 3 for 55° latitude. The extrapolation of the spectrum shown in Fig. 3 to lower energies is the spectrum for the polar region and this is also presumably the spectrum which would exist in outer space. The shaded portion of the figure shows the particles at 55° which would probably form thindowns in tissue, and at the polar regions practically all particles below 1 BEV per nucleon would form thindowns. Thus in outer space more than half of all the heavy particles would be in the energy range to produce thindown hits.

A complete discussion of shielding problems in connection with these particles is out of place here. Suffice it to say there are two facets to the shielding problem; that for the relatively low energy particles (< 1 BEV/nucleon) and that for the high energy ones. For the former, a reasonable amount of shielding, for example 6 g/cm^2 of a low molecular weight material, would only serve to make the situation worse because it would slow down the particles enough to cause more thindown tracks in a man. It would be necessary to increase the shielding to more than 20 g/cm^2 before the numbers of these thindowns would be substantially reduced. It would be equally difficult to shield against the high energy particles. Here one would rely on star formation within the material, and the cross section is independent of the energy of the particle and depends only on the nuclear cross section. Since the nuclear cross sections are relatively greater for the light elements, on a g/cm^2 basis,

light elements would be preferable for shielding here. Again it would take more than 20 g/cm^2 for effective shielding.

In order to approach the problem of the radiobiological effect of these particles from an experimental point of view it is necessary either to send biological materials to very high altitudes in the polar region, or to generate such particles in an accelerator. The latter has been accomplished only for energies up to 10 mev/nucleon and this is energetic enough only for work with single cells and tells us almost nothing about the effect in mammals. Chase (3) has sent black mice in balloons to the top of the atmosphere to observe greying of the hair in these mice. If the heavy particles are as destructive as expected, these mice should have grown a grey hair from each of the hair follicles hit by a thindown. In the 1954 series there was a very impressive increase in greying in mice flown in the polar region as compared to mice flown at lower latitudes. Fig. 4 shows a photograph of one such mouse. It is easy to see that if all the organs of the body were affected like the hair on the mouse in Fig. 4 after an exposure of only one day, space flight might be quite hazardous. However, the experiment was repeated in 1955, presumably under more rigidly controlled conditions, and no increase in greying was observed. The experiments were stopped at this point in a very inconclusive state, but with the impression that the thindowns might be quite destructive.

Other attempts have been made to measure the radiobiological effect of these particles by sending animals, including monkeys, to the top of the atmosphere with nuclear emulsions attached to them in an attempt to relate cellular damage, usually in the brain, to the thindown hits re-

corded in the emulsions. However, there are so few hits, and the geometrical considerations are so difficult, that nothing has been observed.

In order to try to get at the problem an indirect experimental approach has been developed (4). The biological effect from these particles must be due almost entirely to the delta rays which are generated by the passage of the particle, and it is these rays which cause almost all of the dense ionization of the track. From a radiobiological point of view the effect should be the same if the same ionization pattern were produced in another way. The approach used was to confine the deuteron beam from the 60" Brookhaven cyclotron in a beam which could be as small as 0.025 mm in diameter which is about the same maximum diameter for a heavy particle track. The difference would be that the particle track has maximum ionization at the center and decreases nearly to zero at the edge, while the microbeam presents a uniform ionization over the whole beam profile. By adjusting the exposure in this beam any desired ionization density could be achieved and thus any desired dosage. The experimental arrangement was such that the beam could be directed to any desired point within an accuracy of about 0.050 mm, so the part of the animal irradiated could be marked for later examination. The experimental arrangement is shown in Fig. 5 and a photograph of a mouse in position for irradiation shown in Fig. 6.

RESULTS

Irradiation of hair follicles

Since the only direct biological effect ever recorded for the heavy particles was that of greying of hair, it was felt to be important to use the greying response as one of the test objects for the microbeam

studies since this should give a direct comparison (5).

It was found to be not possible to locate an irradiated hair follicle some three months later, so the microbeam had to be modified for the study on hair. Two apertures were used. Both were formed as crossed slits, one with the slits 0.025 mm and the other 0.25 mm wide. In one of the quadrants of each aperture there was a hole 1 mm in diameter. The resulting 1 mm beam was large enough to hit many hair follicles and if the dose was more than about 500 rads, a small spot of grey hairs, the marker spot, would be visible 5 to 10 weeks later. Knowing the relationship between the spot and the slits, one can look for grey hairs along the slits.

It was found that whenever grey hairs appeared in the spot, they also appeared in the 0.25 mm slits. Further, the grey hairs were strictly confined to the region of the slits, and there was no spread of the influence of the irradiation beyond the irradiated volume. Two exposures are shown on one mouse in Fig. 7.

For the 0.025 mm slits, the results were not quite so definite because the hair follicles themselves are more than 0.025 mm in diameter so it would take a direct hit on the center to cause greying. Further, the follicles are as much as 0.2 mm apart so one would expect only a very few of them to be exactly in line. Nevertheless, whenever the spot was grey there were at least a few grey hairs along the line of the slit.

These experiments established that the threshold dose for greying is about 500 rads, and this is independent of the volume of tissue irradiated as long as the follicle is hit. This result supports Chase's results and gives a strong indication that the microbeam does simulate the

biological effect of a heavy particle.

Brain irradiation

One would expect that damage to the brain would be the greatest hazard from these particles since there are very small volumes of the brain which control very vital processes such as temperature regulation.

The microbeam was directed at the cerebral cortex of mice, and after varying periods of time up to 240 days, the mice were sacrificed and the brains examined histologically for damage (6, 7). First a wide beam 1 mm in diameter was used in order to make sure the dosage measurement was correct, since results should be predictable from x-ray experience on this broad a beam. Here it was found that at about 14,000 rads there was complete destruction of the cortex in the beam path, as predicted from x-ray work. The same dose was then administered through the 0.025 mm beam and absolutely no effect was observed at any interval. Since the maximum dose expected at the center of a heavy particle track is about 10,000 rads, it would seem that these particles would have very little effect on the brain.

It was felt to be important to find the "factor of safety" for this effect, and consequently the dose in the microbeam was increased to the point where an effect was observed. It was found necessary to go to 400,000 rads before the neurous of the brain were destroyed. These effects are illustrated in Fig. 8.

The explanation for this extreme insensitivity of the brain to a very narrow beam probably lies in the facts (a) that blood capillaries are moderately sensitive to radiation and so most radiation damage to the brain is through capillary damage. Since the capillaries are about 0.065 mm

apart in the mouse brain, the microbeam would largely miss them, and even if it did hit an occasional one, the factor of safety should be great enough to sustain this loss without damage to the neurons. (b) The neurons never undergo cell division, and it is well known that cells can withstand enormous doses of radiation if they are not required to divide. It has not yet been determined that these cells are functional, but it seems quite likely that after a dose of 10,000 rads they would be, since it takes such an enormous dose to cause destruction.

It thus appears that in this most critical organ these particles will not present a serious problem.

Irradiation of the eye

The organ next most vulnerable for the particles would be the eye. Radiation cataracts are well known, and the high LET radiations are especially effective in causing these cataracts. It could be reasoned that a thindown hit in the lens epithelium would cause a minute disruption of the lens fibers which would grow to a full cataract. Further, there is no capillary circulation in this tissue and the epithelial cells undergo cell division at a rather rapid rate. Thus the situation is quite different from that of the brain and one might expect damage at a low dose.

The microbeam was directed to the generative zone of the lens in the mouse eye and the animals were examined periodically with a slit lamp and some were sacrificed for histological examination (8). When the 1 mm beam was used cataracts were formed with doses as low as 1000 rads as expected. With the 0.025 mm beam cells which were in the beam path had a high probability of turning into a bazar cell which might lead to

a cataract. However, the beam was so small that only one or two cells were hit at a time. As these cells migrated toward the posterior pole they were sloughed off and absorbed, presumably by pressure of the surrounding normal cells. They never formed even a small cataract, so it apparently takes a cluster of abnormal cells to be stable enough to cause a persisting cataract. The dose necessary to cause abnormal cell formation by the microbeam is about the same as for the 1 mm beam.

The fact that the damage produced is independent of beam size is in accord with expectations and is in agreement with the explanation given for the action of these beams in the brain.

Here again it seems that the heavy particles will not be a serious hazard for space flight.

DISCUSSION

From these results one can estimate the effect of these heavy particles on the other organs of the body and on the body as a whole. The occasional loss of individual cells or small groups of cells in organs such as the skin which are continually undergoing cell division should be of no concern since the damaged or dead cells will be quickly replaced. The loss of individual cells in the brain or musculature is in progress continually as a normal part of the aging process. It would take a very long exposure to these heavy particles in outer space to cause a loss significantly greater than occurs spontaneously. Other organs such as the liver or kidney would likewise cause no concern. Greying of the hair seems to be the one real possibility but fortunately this is not serious. There would be some genetic

effect but this would be very minor.

It would thus seem safe to conclude that this hazard will not be very great, but the subject is important enough so it would be well to check one or two of these points by biological experiments in satellites.

SUMMARY

The ionization produced by the heavy cosmic ray particles is almost entirely highly concentrated along single tracks, and the microscopic dose in tissue within these tracks may be quite high but the overall dose rate from these particles in outer space would be very low. These particles cannot be produced in the laboratory so a microbeam of deuterons has been developed which simulates the ionization pattern of these particles. Using this microbeam on mice it is found that this type of radiation causes very little effect in either the brain or the eye, and presumably also in other vital organs. However, it will cause greying of the hair. It is concluded that this type of radiation will not cause a serious hazard for space flight.

REFERENCES

1. Dainton, A. D., P. H. Fowler and D. W. Kent. The abundance of lithium, beryllium and boron in the primary cosmic radiation. Phil. Mag. 43: 729-752 (1952).

2. Schaefer, H. J. Theory of protection of man in the region of the primary cosmic radiation. J. Aviation Med. 24: 338-350 (1954).

3. Chase, H. G. and J. S. Post. Damage and repair in mammalian tissues exposed to cosmic ray heavy nuclei. J. Aviation Med. 29: 533-540 (1956).

4. Baker, C. D., H. J. Curtis, W. Zeman and R. G. Woodley. The design and calibration of a deuteron microbeam for biological studies. Radiation Res. 15: 489-495 (1961).

5. Curtis, H. J. The effect of a deuteron microbeam on greying of hair. Radiation Res. (in press).

6. Zeman, W., H. J. Curtis, K. L. Gebhard and W. Haymaker. Tolerance of mouse brain tissue to high energy deuterons. Science 130: 1760-1761 (1959).

7. Zeman, W., H. J. Curtis and C. P. Baker. Histopathologic effect of high energy particle microbeams on the visual cortex of the mouse brain. Radiation Res. 15: 496-514 (1961).

8. Von Sallmann, L., H. J. Curtis and P. Grimes. The effect of a deuteron microbeam on the mouse crystalline lens. Arch. Ophthalmol. 67: 163-170 (1962).

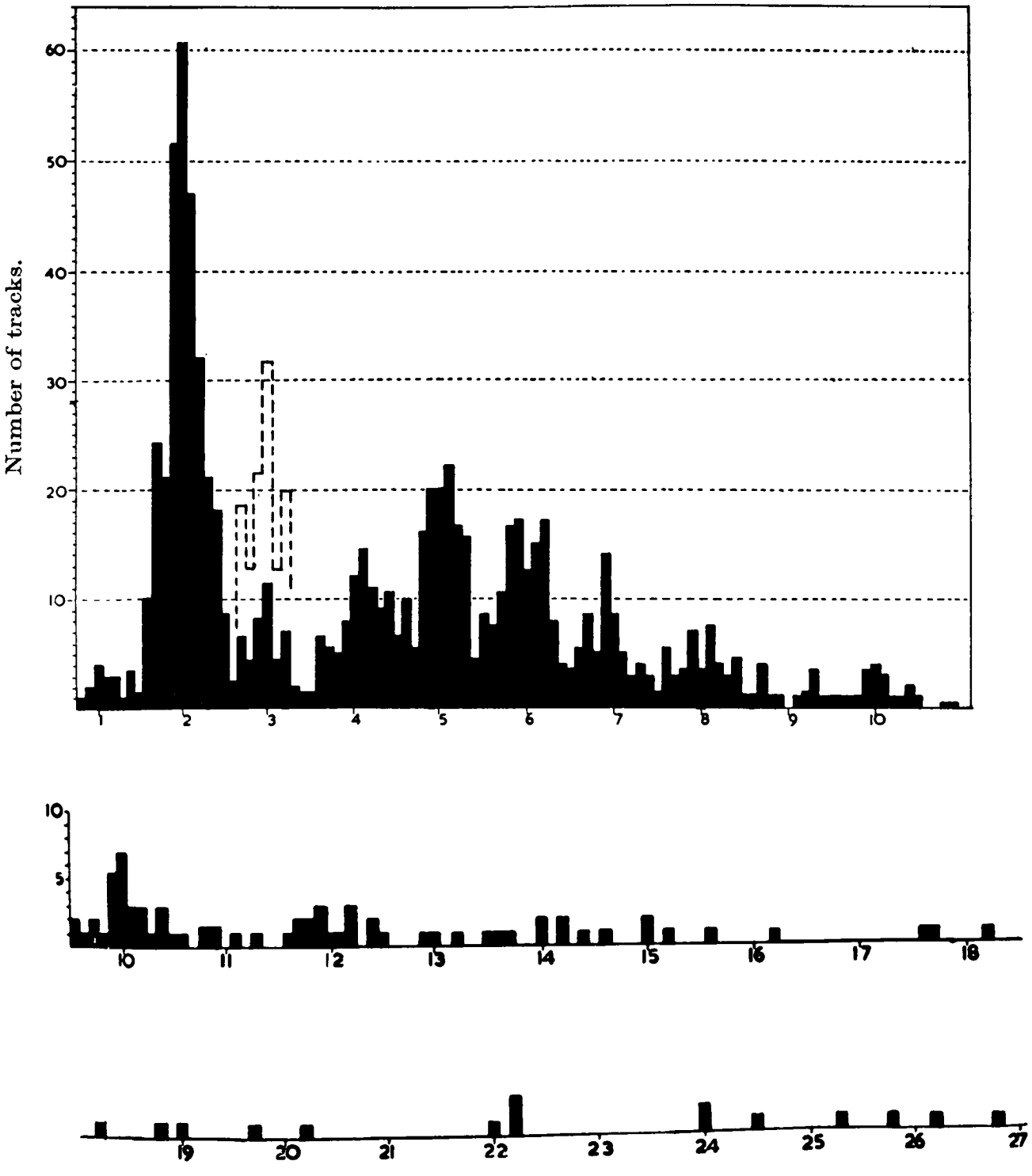

Fig. 1. Distribution of numbers of heavy particles in outer space (from Dainton, Fowler and Kent (1)).

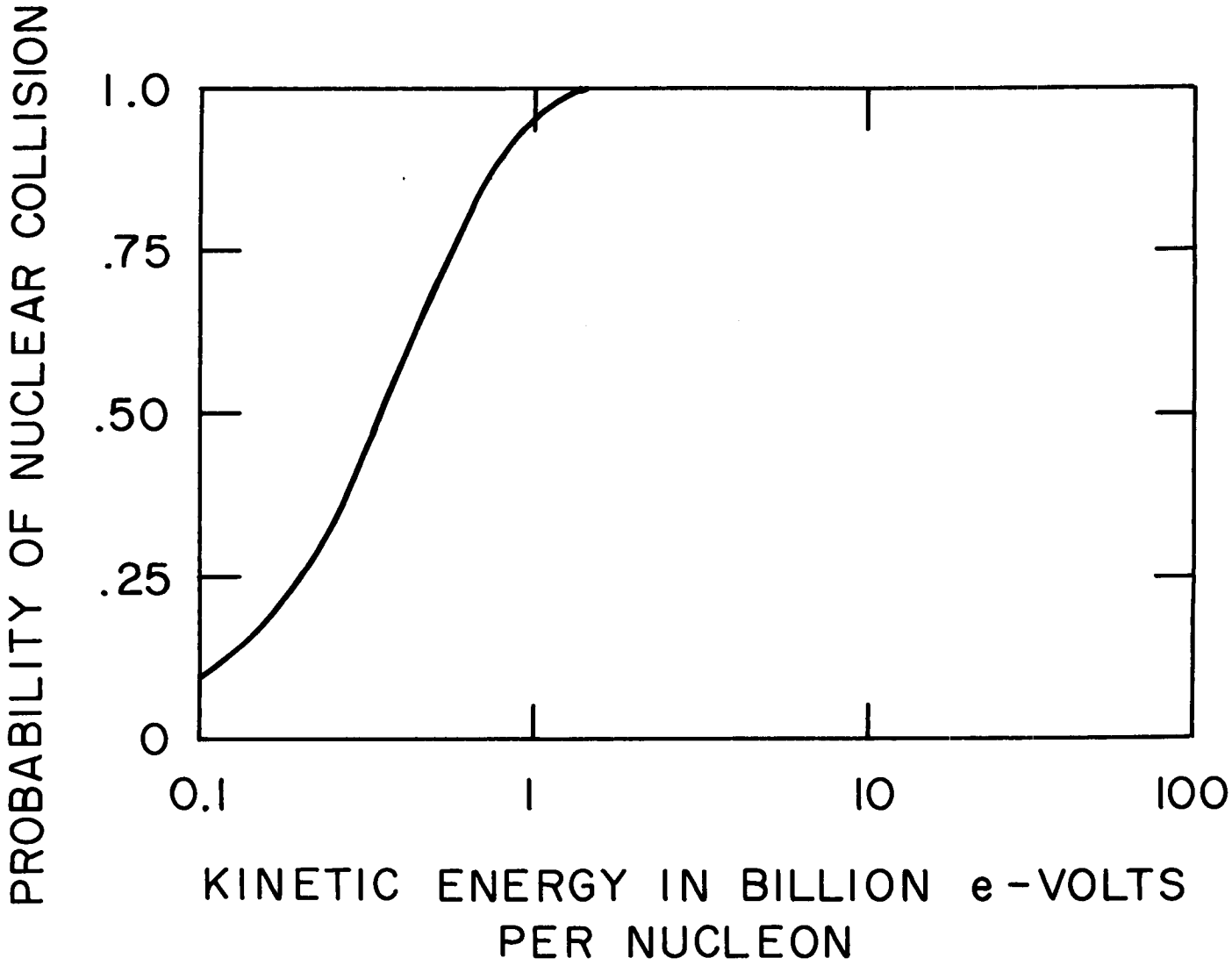

Fig. 2. Probability of a nuclear reaction as a function of energy for heavy particles (from Schaefer (2)).

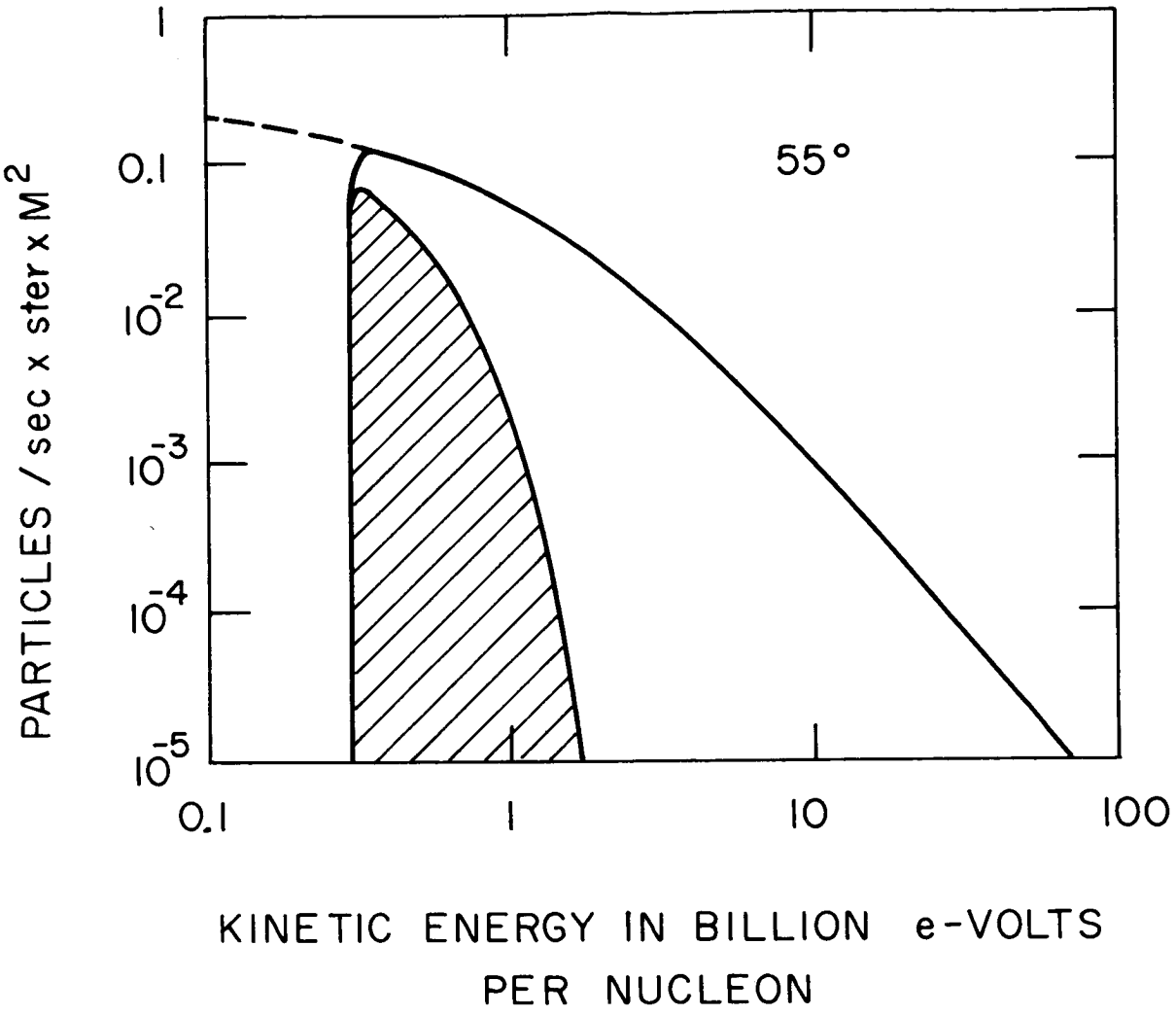

Fig. 3. Energy distribution of particles in the CNO group of primary cosmic radiation above the atmosphere at 55° latitude. The shaded portion indicates the numbers which will probably cause thindowns in tissue. At the polar region there would be no magnetic cut-off so the very low energy particles would be present, and the dotted line represents these additional particles present at the poles, and this same spectrum should hold true for outer space.

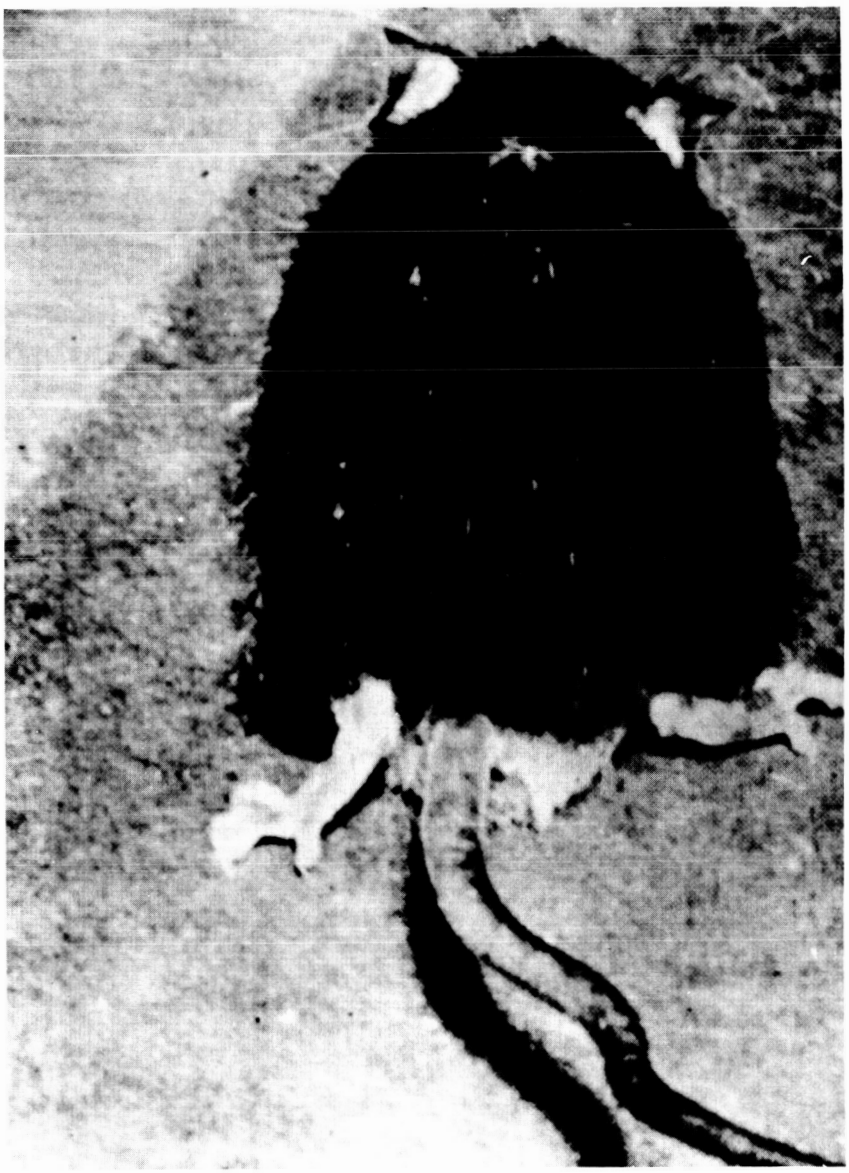

Fig. 4. Photograph of mouse exposed in balloon flight from Sault Ste. Marie in 1954 at an altitude of about 90,000 ft. for 35 hours (from Chase and Post (3)).

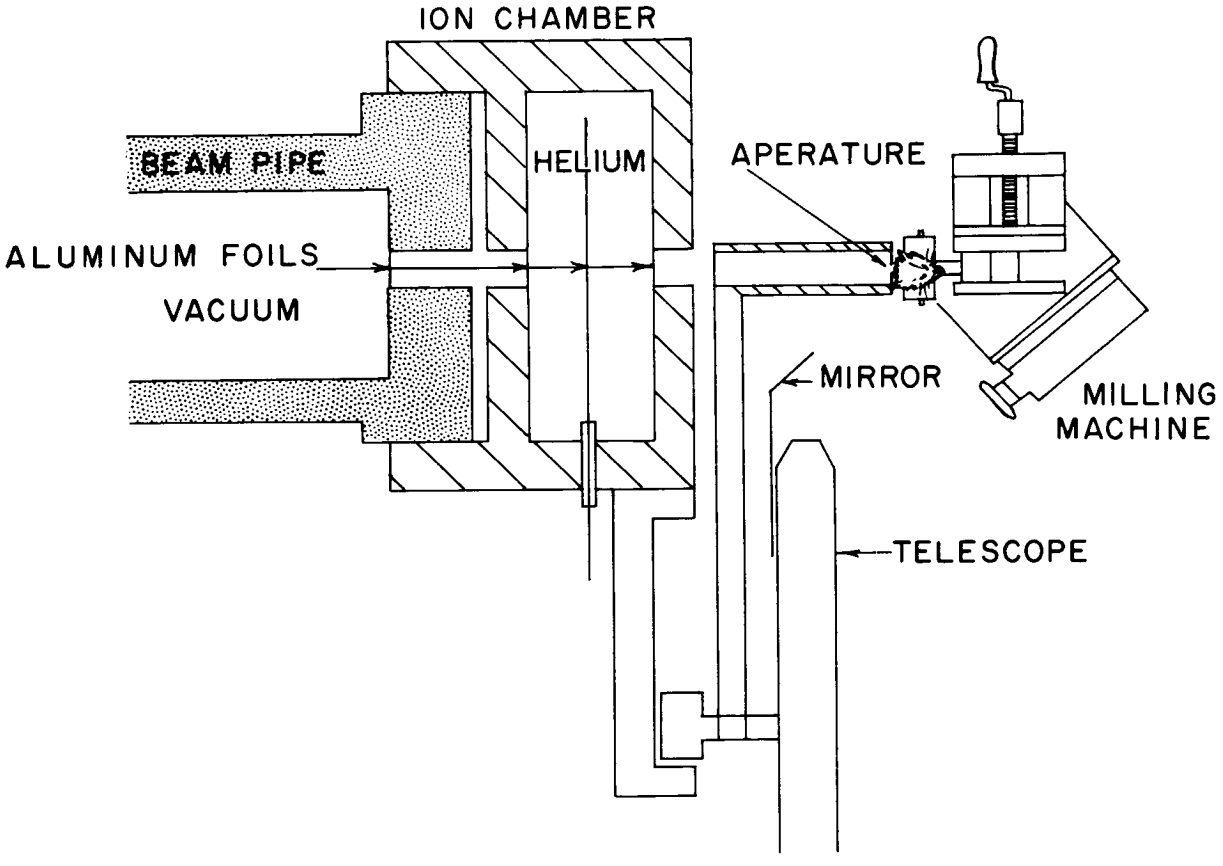

Fig. 5. Experimental arrangement for irradiation with the microbeam (from Baker, Curtis, Zeman and Woodley (4)).

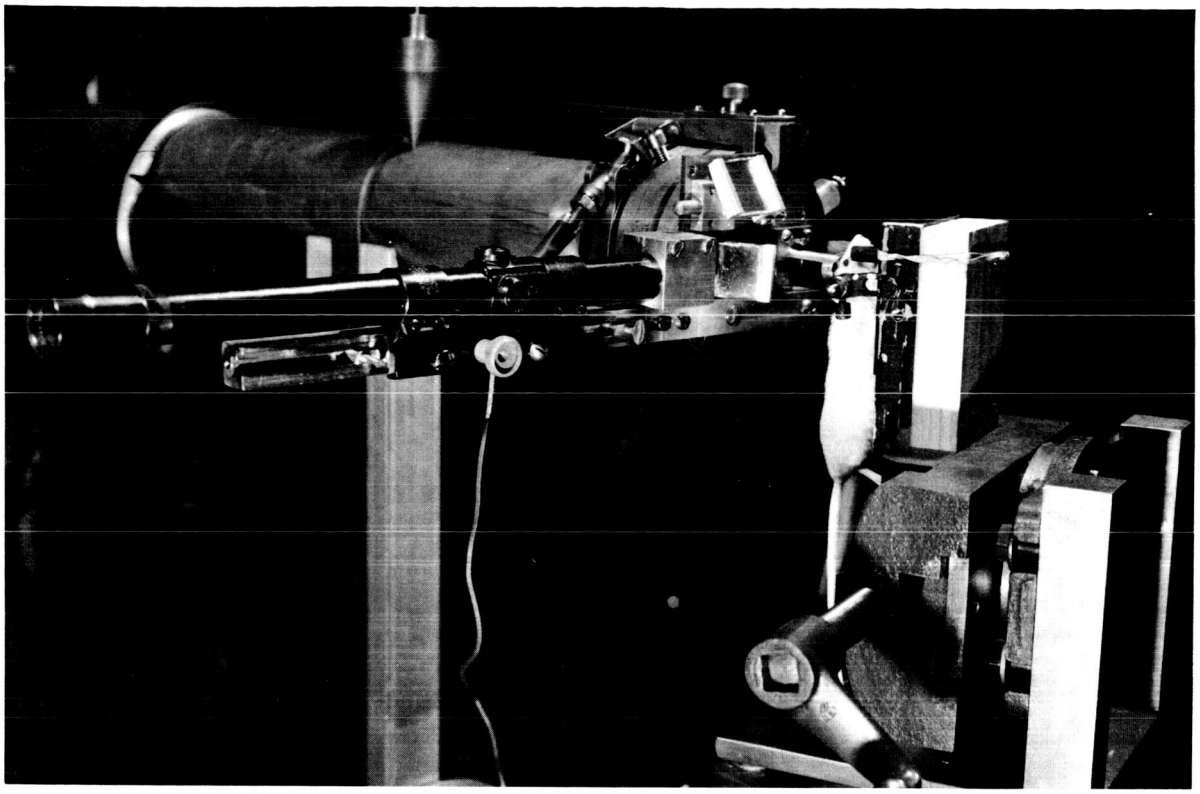

Fig. 6. Photograph of anaesthetized mouse in position for irradiation with the microbeam.

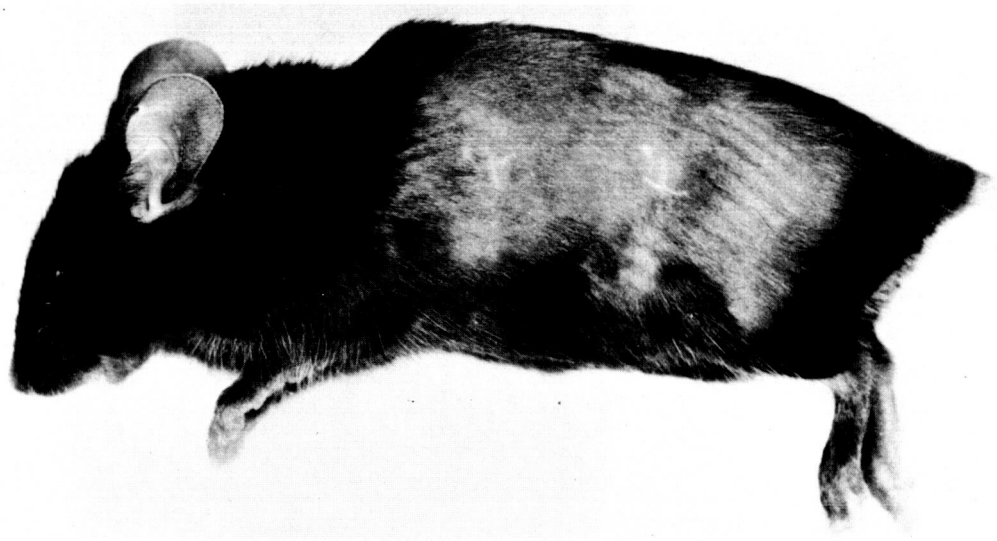

Fig. 7. Two exposures of the skin of a mouse through the 0.25 mm crossed slits with a dose of 800 rads. The marker spot is also visible (from Curtis (5)).

(A) 1 mm beam,
14,000 rads,
24 day survival.

(C) 0.025 beam,
400,000 rads,
6 day survival.

(B) 1 mm beam,
30,000 rads,
24 day survival.

(D) 0.025 beam,
400,000 rads,
24 day survival.

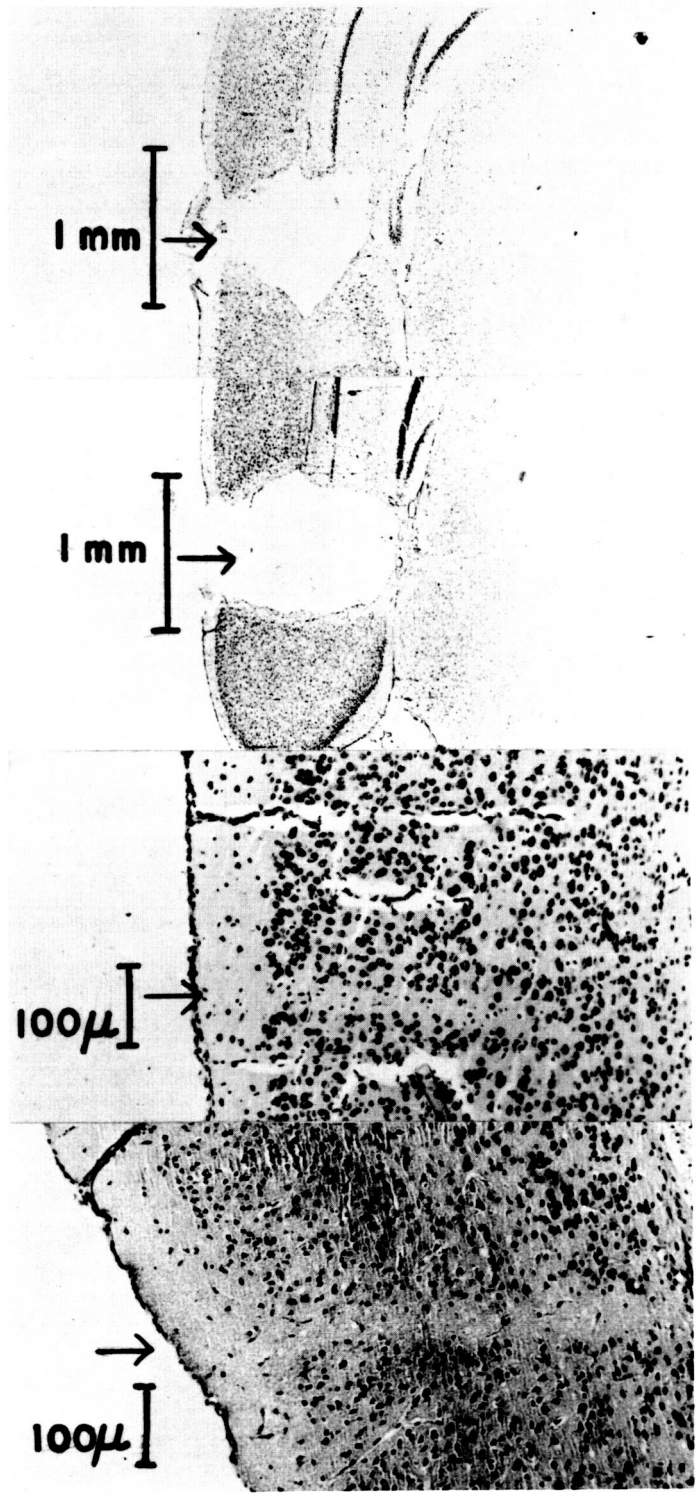

Fig. 8. Sections of mouse brain irradiated with deuteron beams. The arrows indicate the direction of the beam and the magnification can be judged from the scales (from Zeman, Curtis, Gebhard and Haymaker (6)).

Paper C-4

BIOLOGICAL EFFECTS OF HIGH ENERGY PROTONS

C. A. Sondhaus

Donner Laboratory
University of California
Berkeley, California

November 1962

ABSTRACT*

Proton fluxes of solar origin appear to constitute the main radiation hazard in space. Several semi-empirical experssions have been proposed to describe solar proton spectral energy distribution, and extensive dose calculations have been made on the basis of these estimates. Some uncertainties exist with regard to physical exposure factors, especially the variation of proton energy with time and the dependence of depth dose pattern on energy and exposure geometry. Similar uncertainties exist as to the degree of additivity of proton radiation doses both in time and with other stresses and as to differential effects between irradiated organ systems.

Since few terrestrial sources of proton radiation exist, radiobiological studies, especially on effects of high energy protons, have been rare. Existing data, which will be summarized, appear to indicate that protons of energies above about 50 Mev have an RBE close to 1, as would be expected on the basis of average LET distributions. Depth dose distribution may thus be a crucial factor determining degree of biological effect. Passage of the primary proton flux through shielding material or tissue also results in the production of secondary particles, including electrons, mesons, neutrons and recoil nuclei, as well as altering the proton energy distribution. Although it

*Presented by invitation at the Symposium on Protection Against Radiation Hazards in Space, Gatlinburg, Tennessee, November, 1962.

is to some extent possible to duplicate proton LET and depth dose geometry with gamma radiation, the secondary reactions comprise one of several reasons why biological studies with high energy proton beams are needed.

Total body irradiation of mice with 730MEV protons has yielded an RBE of 0.75 relative to 200 KVP X-rays and an $LD_{50(30)}$ dose of 775 rad for acute lethality, under conditions in which creation of secondaries was minimal and depth dose was uniform to about 5 per cent. The corresponding RBE found for splenic atrophy was about 1. In other experiments with primates, total body proton irradiation appeared to have an RBE of about 1 compared to Co^{60} gamma radiation.

Recent experimental data indicate that a peak of ionization, presumably due to secondary particles, occurs at a depth of about 30-40 gm/cm^2 when 730 Mev protons penetrate matter. Mouse studies are in progress at Berkeley to assess the radiological significance of this component. In addition, experiments with mice are under way to detect possible differences in organ mode of injury between protons and X-rays. Later series will include studies on the additivity of radiation dose and other stresses. All this work will be described.

At present, laboratory whole body exposure to a proton flux is impractical for large animals. Since exposures in space flight are almost certain to occur under omnidirectional conditions, and since a high but variable ratio of superficial to midline dose is expected to result from solar flare proton energy distributions, a means of irradiating large animals with the proton beam of the 184-inch cyclotron at Berkeley is being developed in such a way as to permit simulation of solar flare energy and geometry. Degradation of energy is brough about by a multiple Coulomb scattering target, with second-

otation of the animal around one axis normal to the beam and uniform rotation around the other, the angular dispersion produced in the emergent flux by the energy degradation process appears sufficient to generate isotropy without recourse to magnetic scanning or deflection techniques. Apparatus now under construction, which will be described, should thus permit direct experimental studies of biological effects, depth dose patterns and shielding configurations under approximately isotropic flux conditions.

BIOLOGICAL EFFECTS OF HIGH ENERGY PROTONS

C. A. Sondhaus

Donner Laboratory
University of California
Berkeley, California

November 1962

1. INTRODUCTION

It now seems quite probable that by the end of the present decade, manned lunar and deep-space flights will be a reality. These will certainly involve enorous difficulties and manifold hazards. The task which the biologist and the radiation physicist have to perform is that of developing an adequate understanding of the biologic effects of highly penetrating radiation, for it is evident that it is present everywhere in the vast reaches of space and must be reckoned with as soon as man leaves the protection of the terrestrial biosphere. Although it is not yet possible to define categorically the extent of the radiation problem in interplanetary travel, it is clear that the main component of the various space radiations is high-energy protons, particularly the intense proton fluxes which accompany visible outbursts from the sun. Because of the severe limitations in our ability to predict these phenomena or to carry enough shielding to eliminate their hazard, a basic inquiry into the biologic effects of high-energy protons is now of great practical importance.

In the relatively short time since this hazard has been known to exist, considerable effort has been expended in attempts to estimate the total dose that might be expected from proton irradiation in space. These efforts are hampered not only by the uncertainties in our physical knowledge of the energy-intensity-time relationships, but perhaps also equally by our uncertainty with regard to basic radiobiological parameters of proton exposure. It is not known, for example, whether dose rate, dose fractionation in time, combination of

irradiation with other physiological stresses, or mode of radiation injury to different organ systems in the mammal will modify biological response in the same way or to the same degree as has been found for other radiations. Such estimates as have been made are largely by calculation and extrapolation from other data, since there has been little opportunity to carry on controlled animal experiments in space and few sources of proton radiation are available for laboratory studies. It is the purpose of this paper to review some of the rather sparse experimental data which are already at hand, to summarize some experiments now in progress, and to report on some of our own work planned for the near future.

2. PHYSICAL DATA

On the basis of balloon and satellite data, Freden & White (1), Winckler (2), Bailey (3), Chupp et al (4) and others have proposed semi-empirical mathematical expressions to describe the energy and time distributions of solar flare protons. Evans (5) has presented the physical basis for a method of calculating the depth dose produced in a large volume of tissue irradiated omnidirectionally by an isotropic flux of protons of any energy or combination of energies. Schaefer, (6) using the assumed solar flare proton spectral energy distribution laws, has calculated the dose distribution in a spherical volume of tissue with and without a shield surrounding it.

Figure 1, from Schaefer, shows two of these energy distribution curves, illustrating the range of proton energy to be expected. Figure 2 shows the depth dose curves which he has calculated from these assumptions. It can be seen that great differences may exist in the distribution of dose with depth, and further that the vehicle shield or wall produces a marked hardening of the beam which penetrates it. The ratio of surface to midline dose can vary by a factor of 10 or more, depending on shield thickness and proton energy distribution. In Figure 3, an idealized set of curves of integral intensity vs time is shown, taken from the paper of Chupp, et al. It is seen that the high-energy

particles arrive earlier and persist for the shortest time; there is thus a shift of intensity with time for particles of a given energy and for the overall spectrum shape, making the net result rather complicated.

The importance of ionization density in relation to the biological effect of different radiations on mammalian tissue was realized in studies on whole mice and transplantable mouse tumors by Lawrence and others as early as 1935 (7). It was found at that time that the RBE of fast neutrons, will average linear energy transfer of about 20 Kev/μ, compared to 200 kv x-rays (average LET about 3 Kev/μ) was about 2. Since that time a number of studies have been made on the RBE of radiation with widely differing LET (8-10), and a rough pattern of the variation of RBE with LET has become evident. This is schematically indicated in the Figure 4. A few representative radiation types are marked along the abscissa at positons corresponding to their calculated average LET values. The work of a numberof investigators is summarized here, mainly from heavy particle studies on the Berkeley and Yale Hilacs together with some data on alpha particles.

The curve of RBE vs LET can apparently follow one of four different types with regard to the existence and height of a maximum, and the shape of the curve. The four rough categories are as follows: In curve I the RBE never exceeds one and decreases with increasing LET. This has been found to be the case with dry molecules, such as enzymes, and some phages and viruses for example. In the curve of type II, the RBE is found to peak at a value of about 2 for a LET between 100 and 200 keV per micron, and it falls below one thereafter. This behavior has been observed with small microbial and plant cells as well as with chromosome effects and mutations. The curve of type III shows a higher RBE than 1 for LET's of about 20 keV or higher, and again exhibits a peak in RBE in the LET range of 100 to 200 keV per micron, but this peak is now at a value of about 5. It then falls to 2 or 3 for higher LET radiation. Mammalian cells

appear to fall into this category, as do plant cells with large chromosomes, and the process of catacract formation for example. Dose rate dependence is observed here. In the type IV curve, the RBE reaches values beyond 10 at LET values of 100 or 200 keV per micron, but there are insufficient data at higher LET values to conclude even around LET values of about 10 keV per micron. This type of curve is seen with dried seeds and spores, also grasshopper heuroblasts, and the behavior seems to be related to special effects usually connected with a phase change or other physical variable.

In general, the curve of type III seems to be most pertinent to the case of human exposure to high LET radiation. Unfortunately, these data are not yet sufficient or accurate enough to draw clear-cut conclusions. It is to be expected, however, that not only dose distribution, but the distribution of LET will vary with depth in proton irradiation. Figure 5 illustrates Schaefer's calculation of the variation in specific ionization with depth in tissue for a proton beam of the energy spectrum prevailing in the inner Van Allen Belt. It is seen that the number of ion pairs produced per micron of tissue, which is related to LET, may be 5 or 10 times as high at the surface of the tissue as at the midline, depending on the thickness of the shield between the proton beam and the tissue surface.

It has been shown experimentally by J. Lyman and J. Howard in this Laboratory that ionization density builds up to a maximum value at some depth during the passage of a narrow beam of monoenergetic high-energy protons through an absorbing medium. This increase is probably due to the production of secondary protons as well as other charged particles including electrons, mesons, and recoil nuclei. At shallow depths, the ionization due to these secondary events more than compensates for the loss of ionization from reduction in primary beam intensity, the

latter caused by the inelastic collisions which produce the secondary events.

Figure 6 illustrates the effect of absorber thickness on beam ionization for lucite, lead and copper. It can be seen that the initial buildup of ionization in copper is higher than it is for lead, even though the ionization eventually falls off more rapidly. The converse is true for lucite vs lead and lucite vs copper.

These curves were obtained by placing successive layers of absorber between two ionization chambers aligned in the 730 meV proton beam of the 184-inch Cyclotron at Berkeley. They are plots of the ratio of the downstream chamber reading to the upstream chamber reading vs absorber thickness. In Figure 7, the full range of the 730 meV protons in lead is covered. A Bragg peak can be seen at the end of the range.

The prediction of secondary neutron spectra as well as other secondary particle fluxes produced by primary protons is described in the paper presented by Wallace in another session of this symposium. Of importance to the present discussion is the apparent contribution made by such secondary particle events to a dose component which is probably of high LET. This is present in addition to the calculated LET distribution of the primary proton beam whenever a thick shield or target is bombarded, and the influence of the higher LET component on biological effect needs to be evaluated under these conditions.

3. BIOLOGICAL STUDIES WITH HIGH-ENERGY PROTONS

a. Past Studies

A few studies on the biological effects of high-energy protons have been carried out in the past several years. In 1952 Tobias, et al, (11) exposed albino mice to 340 meV protons at the 184-inch Cyclotron in Berkeley, and made a

preliminary estimate of RBE, as having a value of "about 1" for $LD_{50(30)}$.

In 1960 at the Joliot-Curie Laboratory of the Institut du Radium in Paris, Bonet-Maury and collaborators (12) irradiated mice with 157 meV protons from their synchrocyclotron and determined an LD_{50} dose in eleven experiments on more than 500 animals. The proton beam was of circular cross section with a 90% isodose curve of radius 6 cm, determined photometrically by density measurement of photographic film exposed to the beam. Four mice could thus be irradiated simultaneously in thin perforated plastic tubes. It was estimated that the LET of the proton beam varied by about 10% during its passage through the animal in an anteroposterior direction. Dose rate was about 250 rad/min.

Litter-mate animals were used in the experiments. Following irradiation, the animals were weighed daily and the number of dead animals recorded. An eight-day LD_{50} dose was determined by log probit analysis.

Dosimetry of the beam was by both physical and chemical methods. An ion chamber with thin aluminum walls was used, containing air at atmospheric pressure. The total proton flux traversing the chamber during an experiment was calculated from saturation current measurement, and the isodose curves obtained photographically were then used to calculate the average flux through an individual animal and the corresponding absorbed dose. Aluminum and polyethylene mosaics were activated in the beam and the activity induced in each element was counted to check the photographic measurements. Discs of graphite were also placed with each animal and the C^{11} activity induced also served as a supplementary indication of dose. Ferrous sulphate dosimetry was also used; plastic tubes of the same size as the animals were filled with solution and irradiated in the same

way as the animals; dose measurement of optical density at 580 mμ was then made. Uniformity of dose among a group of animals was found to be within 5%.

The biological effects observed after proton exposure did not differ from those observed after exposure to x or gamma radiation: weight loss, anorexia, bloody diarrhea, etc., and reduction in general activity preceding death which occurred after the fourth day post-irradiation.

The $LD_{50(8\ day)}$ dose was found to be ± 80 rad. In order to determine an RBE, mice of the same lineage were exposed to 250 kv x-rays filtered by 0.3 mm Cu plus 2 mm Al, at a dose rate of 80 rad/min and a TSD of 46 cm. The $LD_{50(8\ day)}$ dose determined with 144 animals was 605 ± 30 rad. RBE of 157 meV protons compared to 250 kv x-rays was thus 0.77 ± 0.1. This value is close to the value of 0.7 observed for chromosome observations on vegetal cells of Allium and Vicia by Larsson and Kihlman, who used the 170 meV proton beam of the Uppsala synchrocyclotron in Sweden.

Zellmer and collaborators of the USAF School of Aerospace Medicine in San Antonio irradiated the eyes of forty-eight rhesus monkeys, macaca mulatta, with the 730 meV proton beam of the 184-inch Cyclotron at Berkeley, and found that the threshold dose necessary to produce clinical signs of injury was between 500 and 1000 rad. in comparison with Co^{60} gamma radiation an RBE of between 1 and 2 was estimated. (13).

In further experiments with primates this year, the same Air Force group, in collaboration with the Berkeley group, has studied total body radiation effects with 730 meV protons. Analysis of the data is not yet complete, but preliminary estimates indicate a $LD_{50(30)}$ of 395 rad for the 730 meV proton beam under essentially uniform exposure conditions. The dose rate was about 10 rad/min due to the scanning process

required for total body exposure of animals of this size. Figure 8 illustrates the pneumatic device which was developed by P. Bean and N. Yanni of UCLRL to enable the animal to be scanned by the small diameter beam.

Irradiation of this species with Co^{60} gamma radiation at a dose rate of the order of 100 rad/min indicated a $LD_{50(30)}$ value of 500 rad. The RBE thus appears to be around 1.4 for this end point, with most deaths occurring between seven and fifteen days post irradiation, suggesting an early bone marrow or late gut death. There is some evidence for a 20% dose buildup due to secondary particles.

These USAF primate studies are continuing with protons of other energies. 40 meV protons have been used at the University of Minnesota, 185 meV at the University of Uppsala, and 100 meV at Harvard thus far.

In a recent experiment with the 730 meV proton beam of the 184-inch Cyclotron at Berkeley, Wang, Lyman and Tobias (14) studied the RBE of 730 meV protons as compared with 200 kvp x-rays on mice following whole-body irradiation. The end points observed as indices of radiation lethality effects were a) the whole-body $LD_{50(30)}$; b) changes in spleen weight with dose following irradiation; and c) change in body weight with time after irradiation. Reproducibility of lethality experiments has been shown to be much enhanced with proper adherence to strictly controlled physical and biological experimental procedures and proper care of animals; the mice were therefore caged individually in labelled one-pint mason jars which were cleaned weekly and supplied with sterile wood shavings. Figure 9 illustrates the animal caging system. Namru strain Swiss mice white mice, random bred at the Laboratory were used--all five to seven weeks old, male

weighing 24 ± 5 grem. The mice were fed on Simonsen Laboratory white diet and water ad libitum.

Physical factors for the Phillips 200 kvp x-ray unit which was used were 200 kv, 15 ma, 0.25 cμ + 1.0 mm Al filter, for which the resulting HVL of the beam was 1.0 mm Cμ. A rotating positioning wheel was used; this is shown in Figure 10. The wheel rotated at 2.5 rpm and the dose rate delivered was 30 rad/min, as measured with a Victoreen condenser r-meter.

The proton beam was deflected from the Cyclotron, magnetically sorted and collimated by the quadrupole focussing method. After emergence from the vacuum system into the air, the protons form a nearly parallel homogeneous beam almost two inches in diameter. Slide 10 illustrates the exposure setup; a parallel plate ionization chamber of thin aluminum foils provided the dosimetry. As much as possible, the creation of secondary particles by passage of the beam through thick absorbers, as discussed earlier, was avoided in this experiment, and the ionization in the whole-mouse body was found by phantom measurements to be uniform within 5%. Dose rate was from 500 to 1000 rad/min, and each mouse was irradiated in an individual cylinder positioned in the beam by setting a wheel. In both x-ray and proton experiments twenty mice were exposed at each dose level; pre-and post-irradiation care was identical in both groups. The mice were followed for thirty days, dead animals were autopsied, and five of each group of survivors were sacrificed and the organs studied at the end of the experiment.

The resulting LD 50(30) for 730 meV protons was 775 rad, while that after 200 kvp x radiation was 580 rad (580 roentgens measured in phantom). Figure 11 shows the survival curves which were obtained. RBE of the protons relative to 200 kvp x-rays was found to be about 0.75. Since Upton et al (15) found about

the same RBE for Co^{60} gamma radiation in producing acute lethality in mice, this experiment suggests that the RBE of 730 meV protons is about the same as Co^{60} gamma rays, which is consistent with the findings that the respective LET distributions of the two radiations are quite similar.

Figure 12 shows the reduction in spleen weight observed at autopsy of those mice dead of radiation. More than 50% decrease in spleen weight occurred following similar doses of either x or proton radiation. RBE of 730 meV protons is about 1 compared to 200 kvp x-rays for splenic atrophy. More than 30-day survivors showed nearly normal spleens in both groups.

Figure 13 shows weight loss in the different dose groups with both radiations. Those mice which died always showed weight loss, in contrast to survivors. Rapidity of weight loss was directly proportional to the dose delivered. Both x and proton irradiated mice dying after irradiation showed a 25% weight loss during 13-16 days after 650-700 rads. The rapidity and degree of weight loss are an approximate index of RBE, which thus appears to be around 1 for this end point.

These results agree with the previous work cited earlier, using heavy particles with LET similar to 730 meV protons, as well as with earlier observations on high-energy deuterons. An RBE of less than 1 for 730 meV protons suggests that in spite of similar LET, the greater absorption in bone of 200 kvp x-rays may account for the lower proton RBE.

In order to study this question further, we are now beginning a series of experiments. In this study the time course of deaths is being followed in order to characterize the dominant mode of damage, with a view to distinguishing between "gut deaths" and "bone marrow deaths".

In the present study, in collaboration with J. Ashikawa, Simonsen Laboratory white Swiss mice have been used, all males 6-7 weeks old at irradiation and weighing 25 ± 4 gram. The animals were dipped on arrival and had been inoculated for ectomelia, a common problem in mouse colonies. Since dipping has been observed to produce a significant degree of spleen involution, the mice were placed in individual cages as described before and allowed to "come to equilibrium" physiologically for at least fifteen days. Diet and care were as previously described. At the time of irradiation, only those mice were selected which had gained weight or remained constant in weight.

Three dose rates were employed in the 730 meV proton irradiations: a) 1000 rad/min; b) 300 rad/min; and c) 100 rad/min. Exposure technique was as previously described. In the first two dose rate groups, total doses of 700, 800 and 900 rad were administered; in the 100 rad/min group, total doses were given of 600, 700, and 800 rad. The x-ray irradiation will be performed in two weeks. Both 100 kvp and 200 kvp irradiations are planned, at dose rates of 100 and 300 rad/min. We thus expect to allow for any dose rate effects which might appear.

Only preliminary impressions can be given here, as data is incomplete as yet. All mice irradiated in the first two dose rate groups have died within six days post irradiation. This strongly implies a predominantly gut death in these animals, with LD50 below 700 rad. This is to be compared with other experiments in which 250 kvp x-rays produced early gut death in mice only at total doses of 1200 rad whole-body; in the latter experiments, however, dose rate was presumably about 30 rad/min. An RBE for gut death somewhat higher than 1 for 730 meV protons is therefore suggested, but this may not necessarily be the case if dose rate differences are a factor. No definite conclusion can yet be drawn.

A series of additional mouse experiments is planned for the immediate future. In addition, several experiments with primates are planned in collaboration with Taketa et al of the Ames Laboratory biology group at Moffett Field. These studies will be aimed at answering several questions:

a. The transition curves for 730 meV protons indicate that a buildup of secondaries will occurr behind a shield. These are expected to have higher LET distributions than the primary beam, and hence to have higher RBE values, as previously mentioned. This effect can be studied with mouse exposures, and the first experiments will follow the present study. It should thus be possible to verify experimentally some of the effects predicted by calculation.

b. The additivity of two doses as a function of their separation in time will be studied in a further experiment, with the aim of estimating a recovery factor for high-energy protons in mice.

c. More detailed evaluation of hematopoetic criteria will also be made in future experiments. In addition, skin effects of both alpha and proton radiation will be studied as well as the degree of protection afforded by known agents. Finally, addition of other stresses such as temperature extremes or g-forces to that of radiation exposure will be studied.

4. MEDICAL CAVE MODIFICATIONS AT THE 184-INCH CYCLOTRON

The design portion of the modifications to be made on the Medical Cave at the 184-inch Cyclotron at Berkeley, California was started in February 1962. The aim of these changes was to permit high intensity proton irradiation of large animals. In order to perform whole-body radiation experiments with animals simulating solar flare radiation, two basic problems must be resolved.

The first is how to increase the beam intensity enough to give a reasonable exposure time. This can be accomplished only by the reduction of the amount of beam lost after it leaves the steering magnet. We propose to reduce the beam divergence by the use of a quadrupole magnet of large aperture (8-inch diameter) along with a larger aperture (8-inch diameter) beam tube. This will make it possible to focus the maximum number of protons on the target. This quadrupole magnet is on order. The design of the beam tube complex--including vacuum pipe, safety plug and a scattering target--is about 90% complete and about 50% of it is on order.

The second problem is one of protection of operating personnel from overdoses of radiation when such intense beams of protons are being directed into the Medical Cave. From our experience with such beams in the Physics Cave, we know that the present Medical Cave side walls must be increased to 12 feet equivalent of ordinary concrete, the back wall increased to 20 feet equivalent of ordinary concrete, the roof increased to 8 feet equivalent of ordinary concrete, and a solid shielding door provided. These increases amount to 140% for the side walls, 300% for the back wall, and 300% for the roof. Since the building is not large enough to accommodate a cave of adequate size with walls this thick of ordinary concrete, more massive material must be used so that a given amount of shielding may be obtained with thinner walls. This is being accomplished by using a U. S. Navy surplus steel and high-density aggregate concrete. The design, as shown in Figure 14, is complete, the required steel has been procured, the heavy aggregate is on order, and fabrication jobs for the required shielding blocks are out for bid.

The massiveness of the required shielding walls and the resulting increased floor loads necessitate reinforcing the floor in the Cyclotron building at the vicinity of the Medical Cave. A hydraulic-actuated door is available from the Physics Group; it requires a pit which can be provided when the floor is strengthened, and a slight modification to adjust it to the Medical Cave platform height. Designs on these modifications are complete, as are the designs of the platforms themselves, and both have been ordered.

The current schedule is to have all of the equipment available for installation by January 1963. This is based on the earliest possible shutdown, and depending on the Cyclotron schedule and overall modifications. It is estimated that a period of approximately three weeks will be required for installation.

Upon completion of the above modifications, it will be possible to irradiate up to a 300-pound animal with an alpha or proton beam under conditions simulating solar flare radiation. A whole body exposure of a large animal to an ommidirectional proton flux by use of the Cyclotron beam requires that certain criteria be met by suitable modifications in the beam characteristics. Among these are the following:

1. Beam Energy Variation

   Of several possible methods of producing variable energy proton beams, energy degradation by multiple coulomb scattering in passage through material appears to be most practical. Although intensity is lost and angular and energy dispersions are increased in a degraded beam, no modification of the accelerator magnetic field, or magnetic shielding-beam extraction techniques is required. Beam degradation thus does not

disturb the operation or construction of the cyclotron itself and experimental use can be achieved within a short time.

As scattering materials, lead, copper, aluminum, and carbon have been considered. Design calculations (16' show that degradation in graphite of the 730 meV beam to an energy of 100 meV, introduces an additional rms energy spread of less than ± 15 meV in the emergent beam, and less spread at higher degraded energies. Figure 15 shows that the rms angular dispersion of the emergent beam at this energy varies from 0.10 radian half angle for graphite to 0.36 radian for lead. Remanent intensity of the emergent beam after degradation to 100 meV is 7.5% for graphite and 16% for lead, as illustrated in Figure 16.

2. Broad Beam Geometry

In order to simulate a 4π or omnidirectional exposure, the usual narrow well-collimated beam emerging from the accelerator must be defocused or otherwise caused to diverge, or alternatively, must be made to scan the target by magnetic deflection. Here the angular dispersion introduced in the beam by scattering and energy degradation can be utilized. When combined with sinusoidal rotation of the target around one axis normal to the beam and uniform rotation around the other, the angular dispersion produced in the process of energy degradation appears sufficient to generate an isotropic exposure geometry, without recourse to magnetic scanning or deflection techniques. Figure 17 illustrates the animal rotator now under construction to serve this purpose.

It is concluded that sufficient angular dispersion is introduced by scattering in graphite to permit whole-body irradiation with target diameters up to three feet.

A hollow lucite sphere of this diameter containing an animal mounted in a frame can thus be rotated on the apparatus; Figure 18 illustrates the animal holder. The angular dispersion in graphite is low enough to compensate for its increased absorption loss at a given degraded energy, making graphite the scattering material of choice. The same conclusion is reached on the basis of the relative number of secondary neutrons produced in the scatterer, which is lowest for carbon.

The resulting proton energies and geometry of the exposure should simulate fairly adequately the solar flare condition by stepwise irradiation at several energies, thus permitting direct experimental study of biological effects, depth dose patterns, secondary production and shielding configurations.

This information will be of value not only in itself, but also in simulating space radiation exposure with Co^{60} or other radiation sources. The time available for biological research for the 184-inch Cyclotron is limited, but it is believed, nevertheless, that some important questions can be answered experimentally in regard to solar radiation problems with a relatively modest expenditure of time.

This study was supported by the National Aeronautics and Space Administration through the Atomic Energy Commission and Lawrence Radiation Laboratory, University of California.

REFERENCES

1. Freden, S.C. and R.S. White: Protons in the Earth's Magnetic Field; Phys. Rev. Letters 3, 9-10 (1959) and 3, 145 (1959).

2. Winckler, J.R.: This Symposium; see also Solar Influences on the Radiation Field in Space; Aerospace Med.32, 893-900 (1961).

3. Bailey, D. K.: Time Variations in the Energy Spectrum of Solar Cosmic Rays in Relation to the Radiation Hazard in Space; Nat'l Bureau of Standards, Boulder, Colo., 1960; see also Abnormal Ionization in the Lower Ionisphere Associated with Cosmic Ray Flux Enhancements; Proc. I.R.E. 47, 255 (1959).

4. Chupp, E.L., D.L. Dye, B.W. Mar, L.A. Oncley and R.W. Williams: Analysis of Solar Flare Hazard to Manned Space Systems; Boeing Report #D2-11608(1962).

5. Evans, R. D.: Principles for the Calculation of Radiation Dose Rates in Space Vehicles; Technical Report to the N.A.S.A.; A.D. Little Co. Report 63270-05-01, July 1961.

6. Schaefer, H. J.: Time Profile of Tissue Ionization Dosages for Bailey's Synthetic Spectrum of a Typical Solar Flare Event; U.S. Naval School of Av. Med.,Apr 4, 1962; see also Tissue Ionization Dosages in Proton Radiation Fields in Space; Aerospace Med. 31, 807-816 (1960).

7. Lawrence, J.H. and E.O. Lawrence: The Biological Action of Neutron Rays; Proc. Nat. Acad. Sci. 22, 124-133 (1936).

8. Storer, J.B., P.S. Harris, J.E. Furchner and W.H. Langham; The Relative Biological Effectiveness of Various Ionizing Radiations in Mammalian Systems; Rad. Res. 6, 188-288 (1957).

9. Fluke, D.J., A.C. Birge, J. Sayeg, T. Brustad and C.A. Tobias: Radiobiological Studies with Stripped Carbon Nuclei and Other Heavy Ions; Lawrence Radiation Laboratory Report UCRL-8078 (1958).

10. Brustad, T.: Study of the Radiosensitivity of Dry Preparations of Lysozyme, Trypsin and Deoxyribonuclease Exposed to Accelerated Nuclei of Hydrogen, Helium, Carbon, Oxygen and Neon; Rad. Res. Suppl.2, 65-74 (1960).

11. Tobias, C.A., H.O. Anger and J.H. Lawrence: Radiological Use of High Energy Deuterons and Alpha Particles; Am. J. Roent. Rad. Ther.Nucl.Med. 67, 1-27 (1952).

12. Bonet-Maury, P., A. Deysine, M. Frilley and C. Stefan: Relative Effectiveness of 151 Mev Protons; Comptes Rendus Acad. Sci.(Paris) 251, 3087-9(1960).

13. Zellmer, R.W. and R.G. Allen: Cosmic Radiation - Laboratory Observations; Aerospace Med. 32, 942-946 (1961).

14. Wang, C.C., J. Lyman and C.A. Tobias: Relative Biologic Effectiveness of 730 Mev Proton Particles for Acute Lethality in Mice; in Univ. Calif. Lawrence Radiation Laboratory Biol. & Med. Semiannual Report, Spring 1962; UCRL-10211, June, 1962.

15. Upton, A.C., F.P. Conte, G.S. Hurst and W.A. Mills: The Relative Biological Effectiveness of Fast Neutrons, X Rays and Gamma Rays for Acute Lethality in Mice (Abstract); Rad. Res. 3, 355 (1955).

16. Sondhaus, C.A. and R.W. Wallace: Solar Proton Exposure Simulation with the 184 Inch Cyclotron; Lawrence Radiation Laboratory Report UCRL-10447 (1962), (to be published); see also Wallace, R.W. and C.A. Sondhaus, This Symposium.

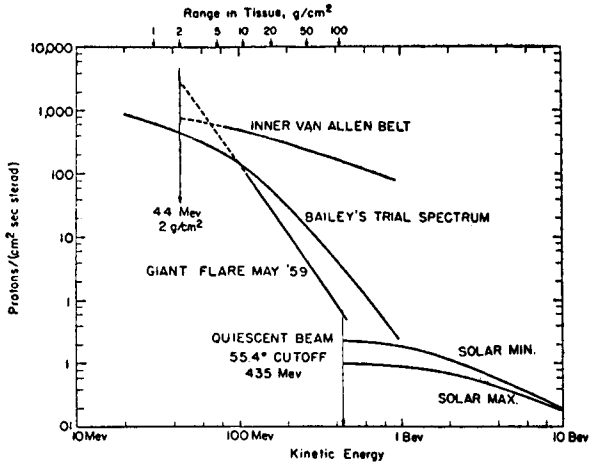

Fig. 1. Integral energy spectra of various proton radiation fields in space. Note enormous intensity of flare 59 spectrum observed at 55.4° magnetic latitude, i.e., in a magnetically forbidden region.

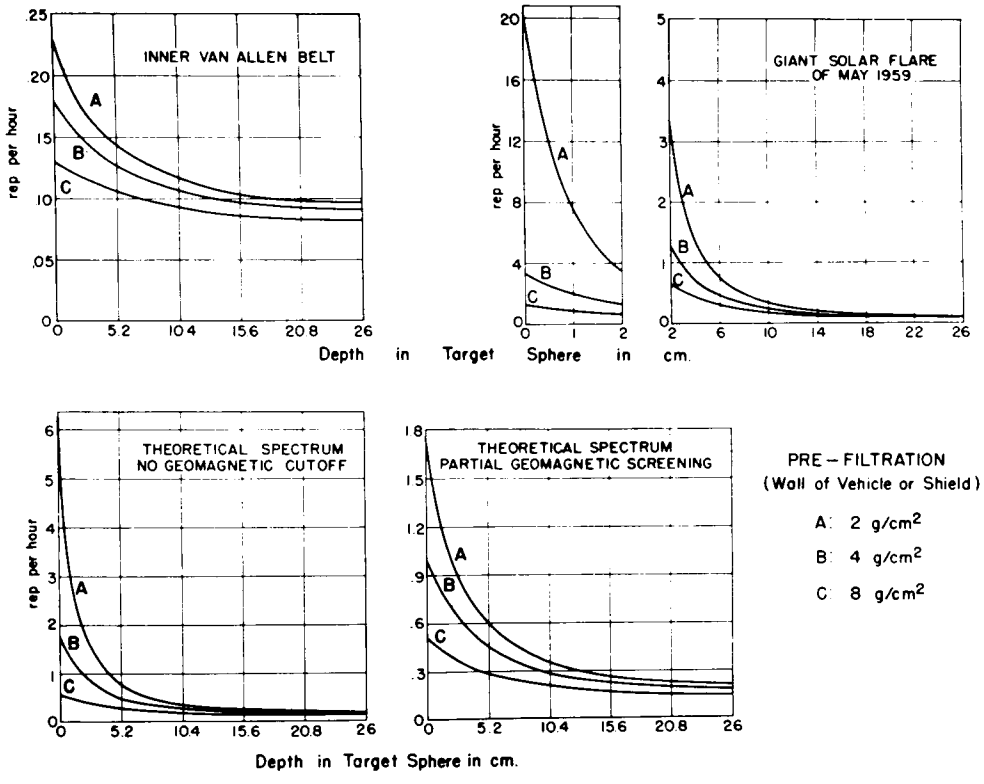

Fig. 2. Depth dose curves resulting from assumed solar flare energy distributions, as calculated for a spherical tissue volume (Schaefer).

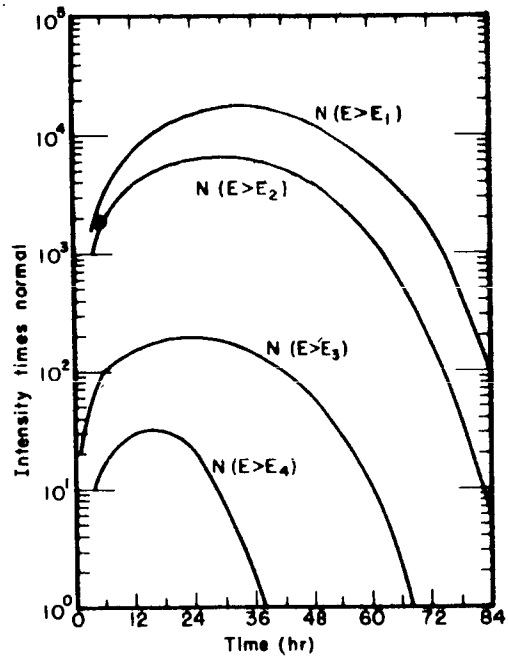

Fig. 3. Idealized set of curves of integral intensity vs. time (Chupp, et al.)

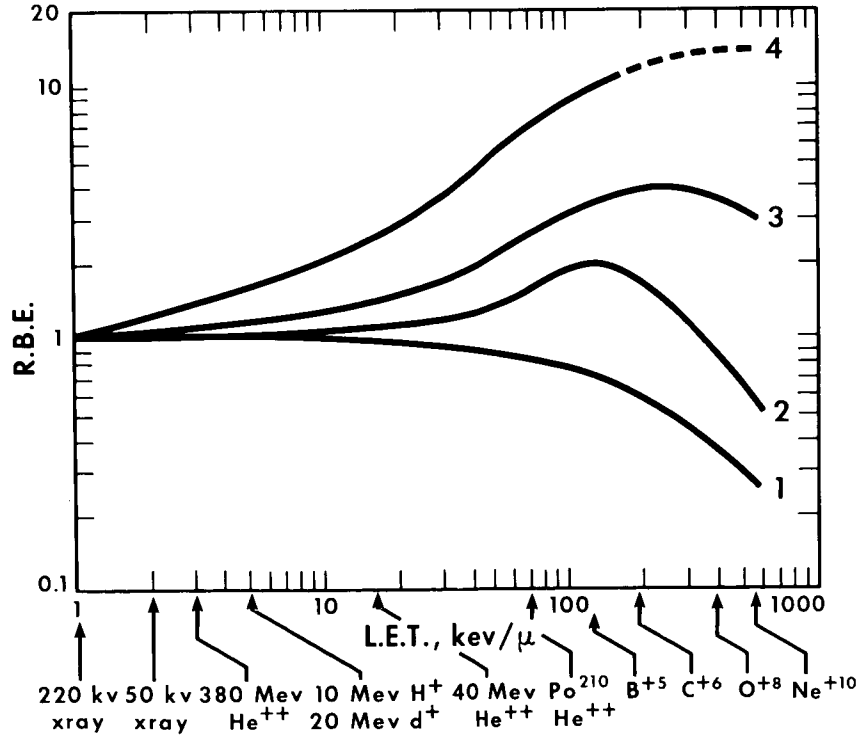

Fig. 4. Variation of Relative Biological Effectiveness with Linear Energy Transfer of radiation (idealized).

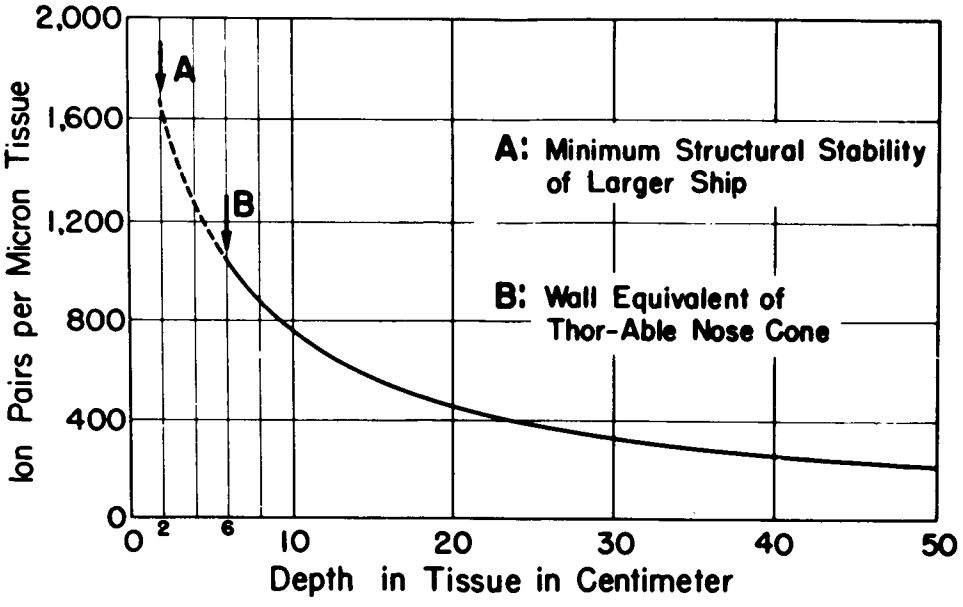

Fig. 5. Specific ionization vs. tissue depth for an assumed proton energy spectrum in Van Allen Belt (after Schaefer).

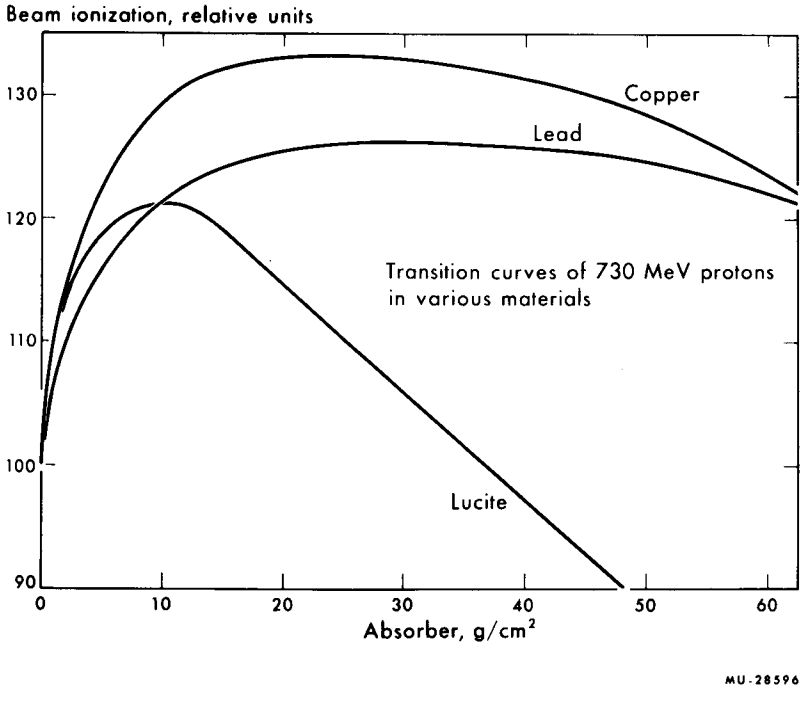

Fig. 6. Transition curves of 730 MeV protons in various materials.

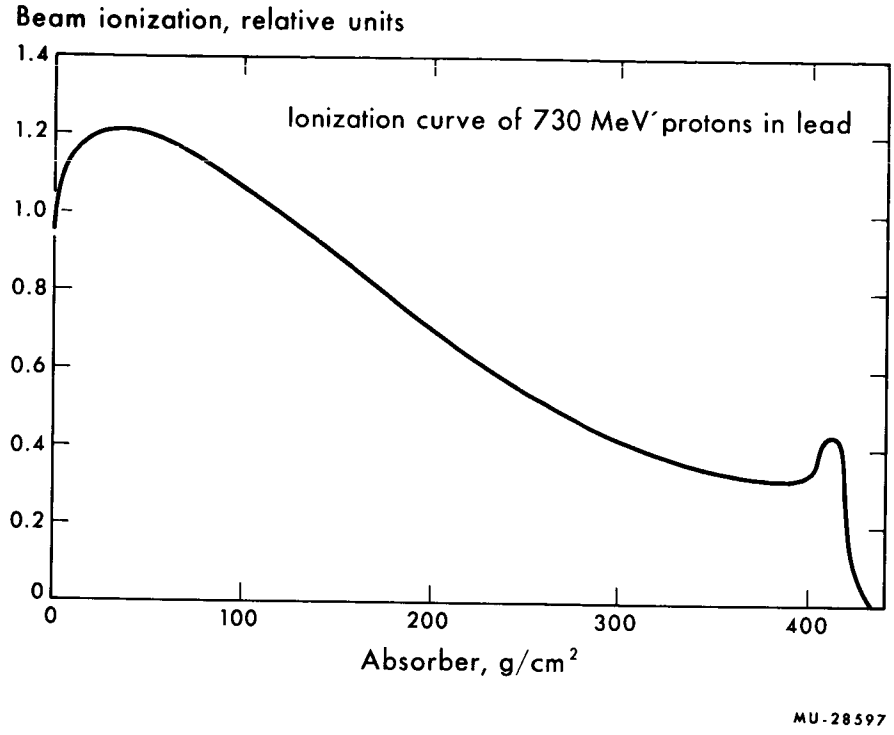

Fig.7. Transition curve of 730 MeV protons in lead - beam ionization vs. absorber thickness over full range.

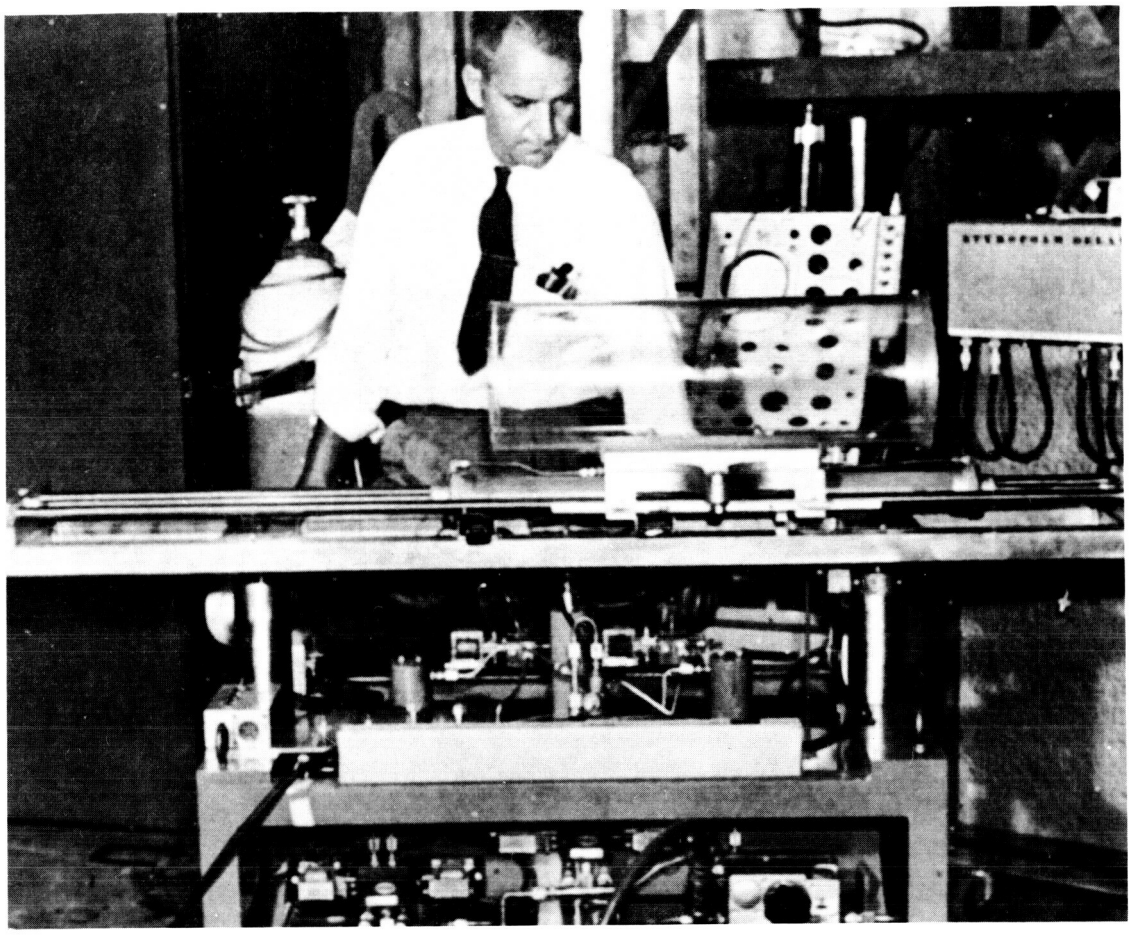

JHL-3048

Fig. 8. Pneumatically driven animal scanner for primate studies with 184" cyclotron proton beam.

JHL-3167

Fig. 9. Individual caging system for proton-irradiated mice.

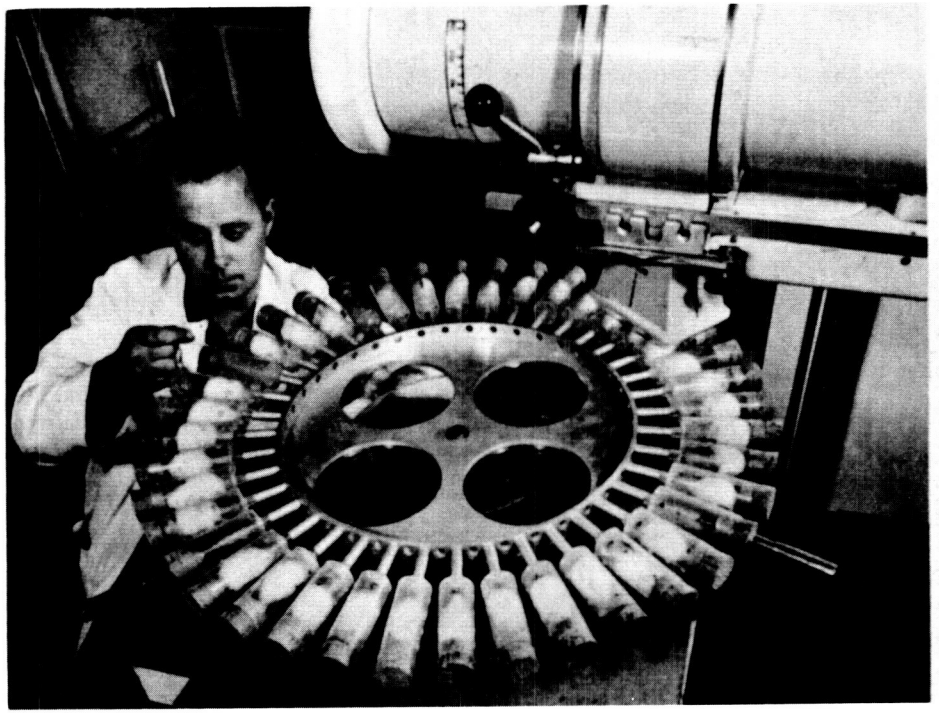

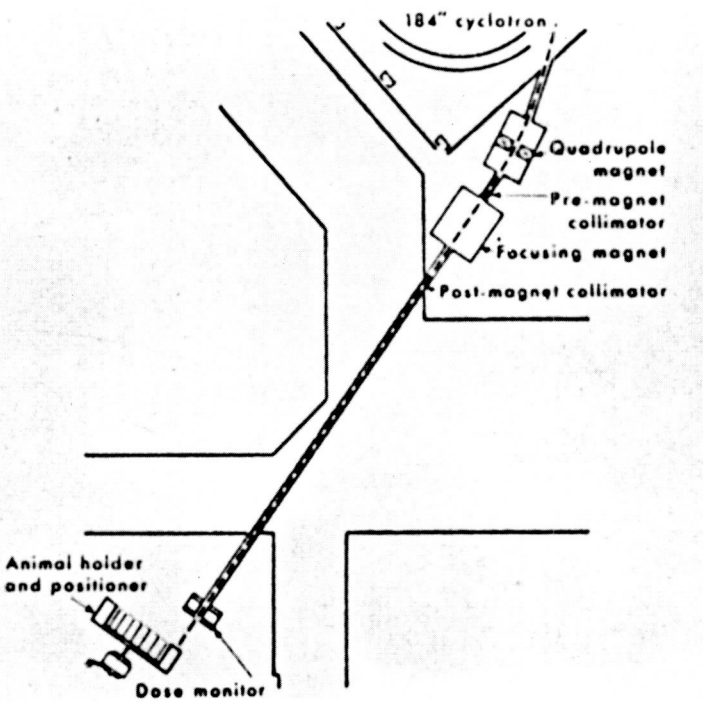

JHL-3173-C

MU 27193

Fig. 10. (Left) Mouse irradiation wheel for X ray control experiments; (Right) Exposure setup for mouse irradiation with proton beam. The X ray wheel has now been converted to a positioner to increase maximum possible dose rate during irradiation. The proton beam mouse positioner exposes the animals postero-anteriorly, the X ray positioner dorsoventrally.

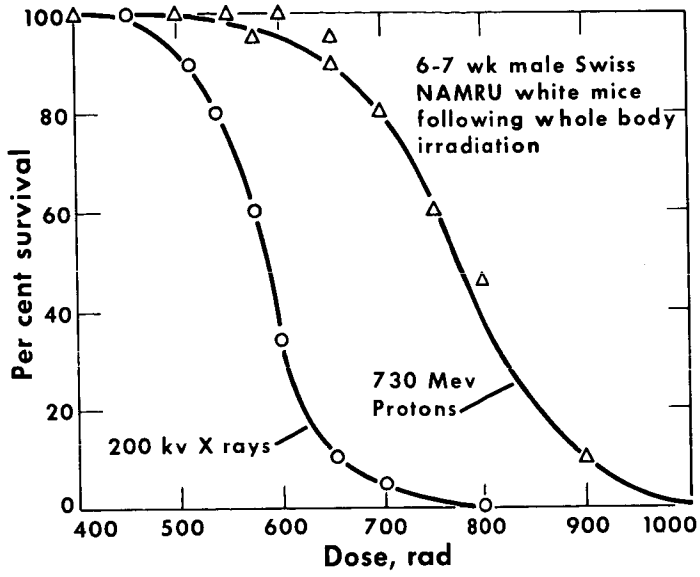

Fig. 11. Survival curves for proton irradiated and X irradiated mice.

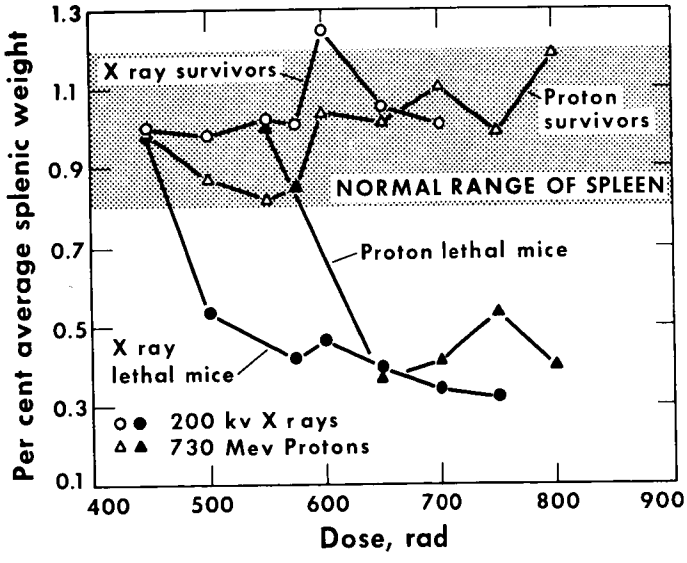

Fig. 12. Reduction in spleen weight for proton and X ray irradiated mice.

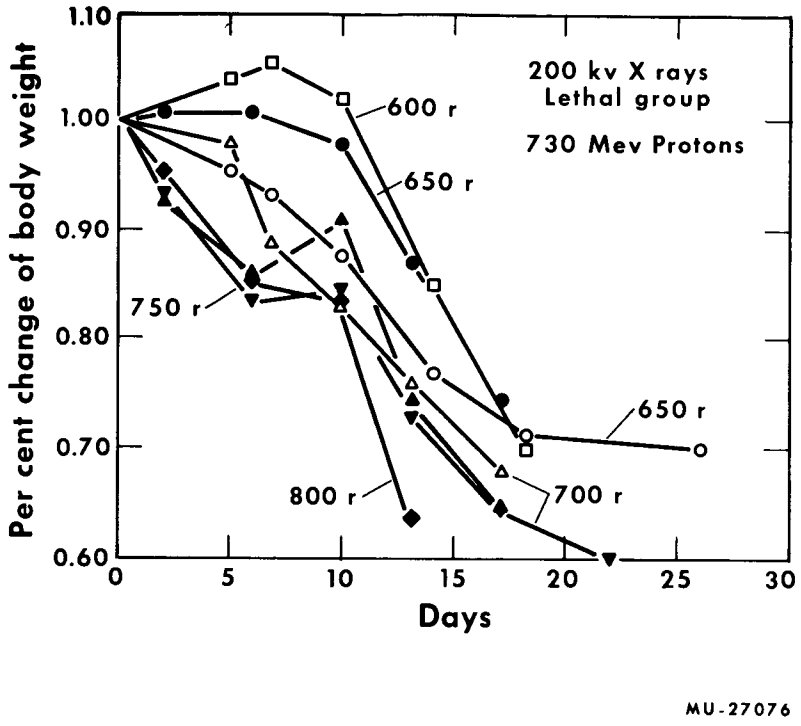

Fig. 13. Post-irradiation weight loss in proton and X - irradiated mice.

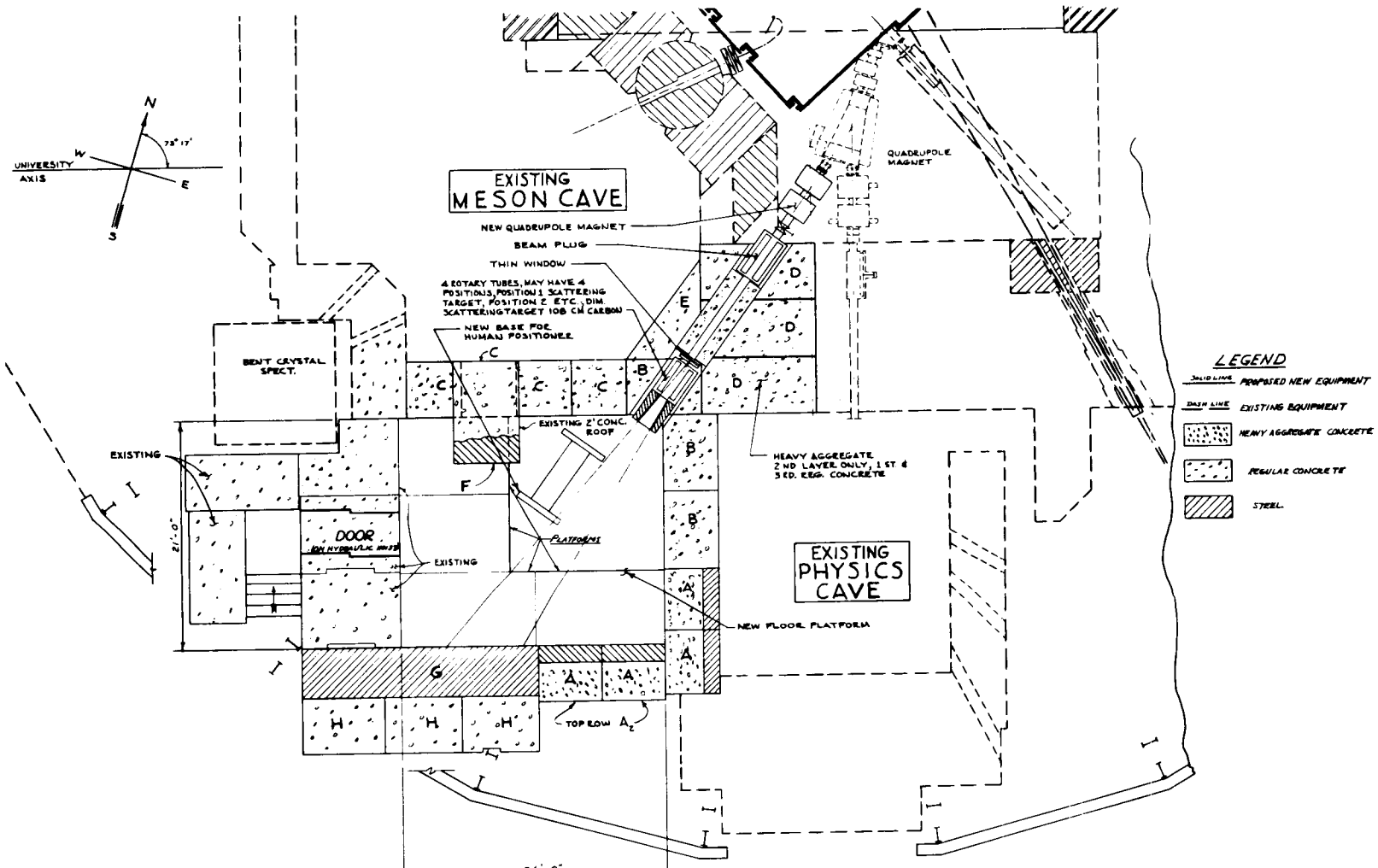

Fig. 14. Redesign of medical cave, 184 inch cyclotron, Berkeley.

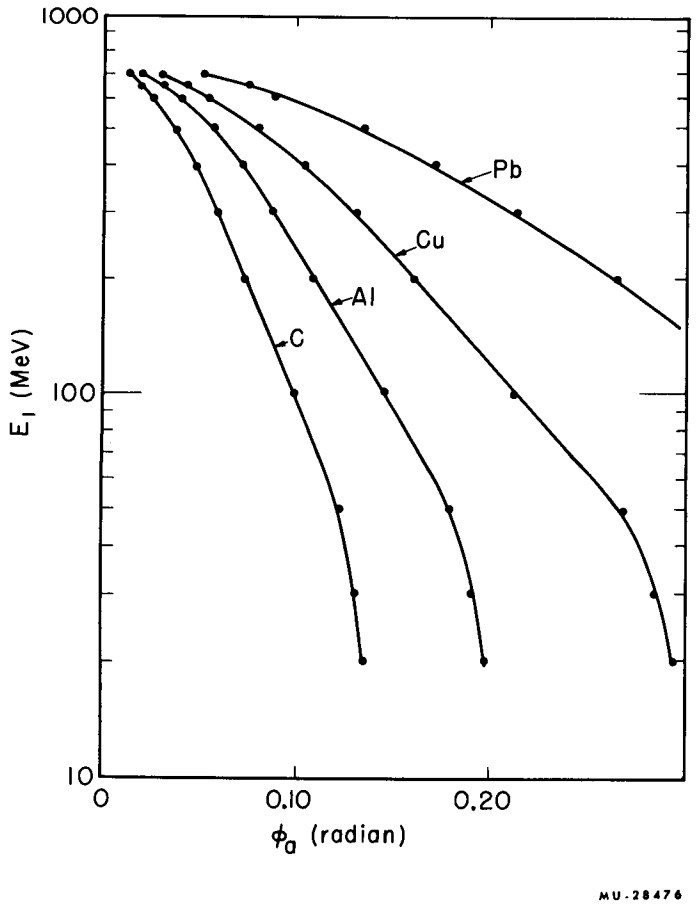

Fig. 15. Root-mean-square angular dispersion of emergent proton beam after degradation from 730 meV to 100 meV in various materials.

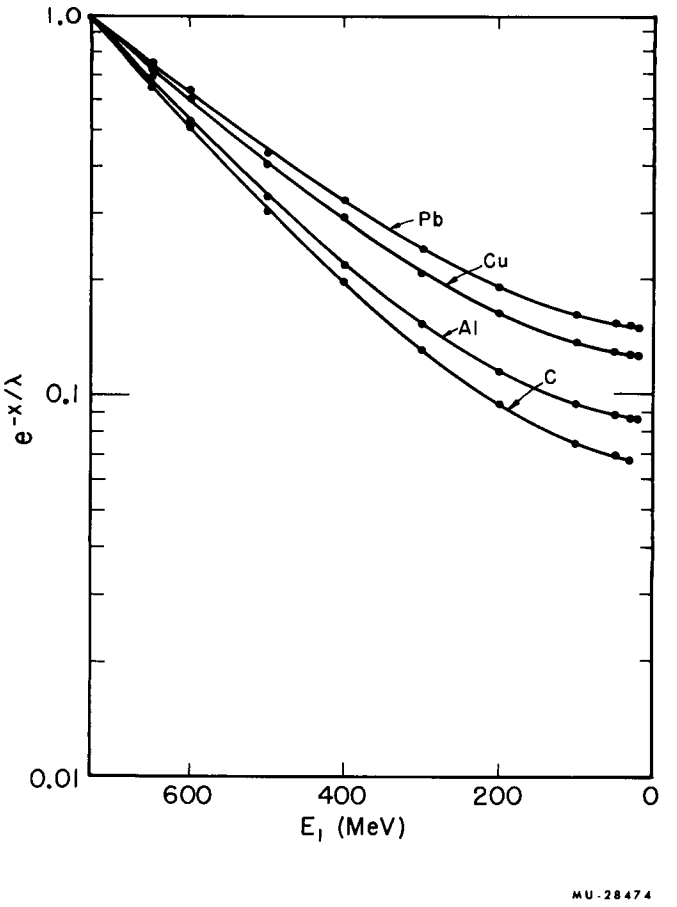

Fig. 16. Emergent proton beam intensity (fractional) after energy degradation from 730 to 100 meV in various absorbing materials.

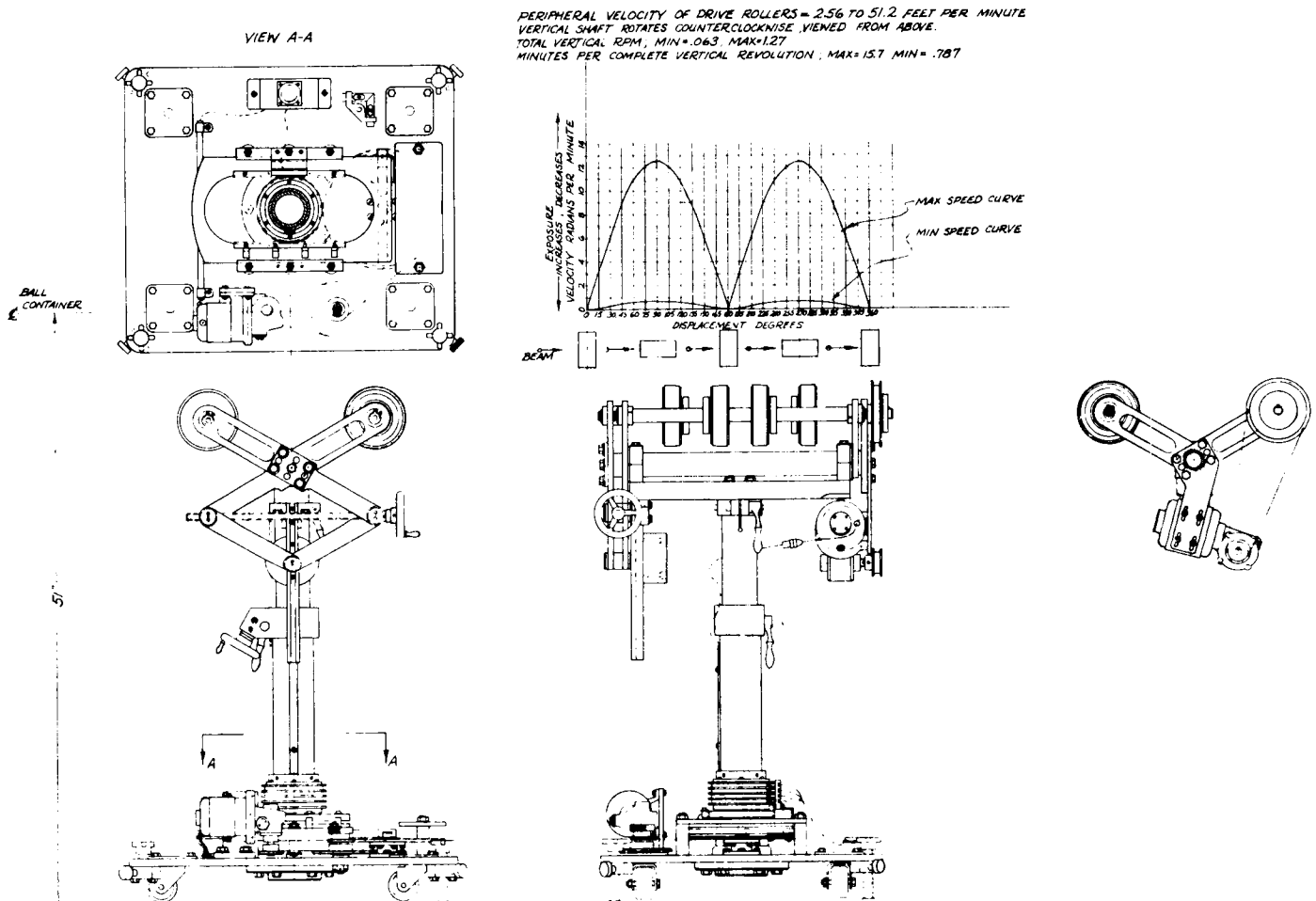

Fig. 17. Animal rotator for omnidirectional exposure of large animals to divergent, energy-degraded proton beam of 184" cyclotron, Berkeley.

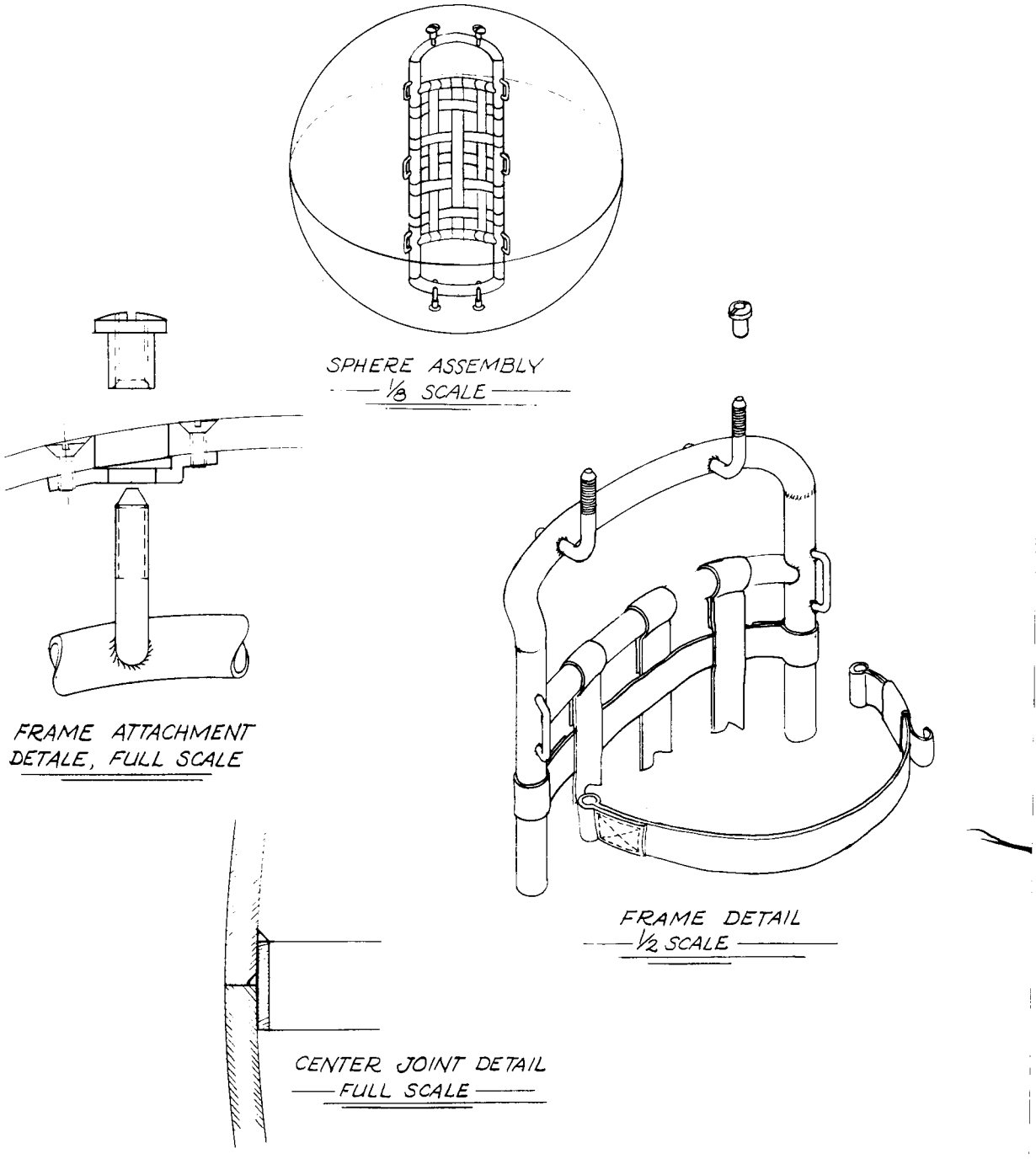

Fig. 18. Detail of animal holder, omnidirectional exposure apparatus for large animal proton irradiation.

Paper C-5 N63-15134

EFFECTS OF ACUTE RADIATION EXPOSURE ON HUMAN PERFORMANCE

R. B. Payne
USAF School of Aerospace Medicine

A literal and parsimonious interpretation of the assigned topic would allow the speaker to fulfill his obligation quite honestly in approximately four seconds, or about as long as one might require to say, "There are no effects as far as we know." But this response would leave us far from satisfied, and it would create the false impression that the problem had been studied exhaustively throughout all the critical categories of behavior under various kinds, rates, and amounts of ionizing radiation. The distressing fact is, of course, that only two systematic human studies on this subject have been reported in the Western literature, and these can scarcely be said to provide a useful grasp of the total problem.

Under the circumstances, therefore, it has seemed appropriate to broaden the empirical base of this discussion by reference to studies of lower animals. As many of you know, the Radiobiology Laboratory at Austin, Texas, operated jointly by the USAF School of Aerospace Medicine and the University of Texas, has devoted a prominent share of its energies over the past ten years to systematic studies of radiation effects on the behavior of M. mulata; and laboratories elsewhere have fed the burgeoning literature with behavioral studies of mice, rats, and dogs. Perhaps there are conditions and assumptions under which we should be willing to consider at least the infrahuman primate studies for whatever

implications they may have for the behavior of man.

First, however, there is a sense of obligation to explain the rationale for the study of behavior in a radioactive environment. What can such studies tell us that we cannot learn merely by observing the impact of ionizing radiation on the cells, tissues, and organs of the body?

Why Study Behavior?

The principal reason for sending man into the aerospace environment is to take advantage of his abilities and skills as an equipment operator, a trouble-shooter and maintenance specialist, an observer and interpreter of dynamic situations, and a maker of decisions. Mercury flights have already shown the operational flexibility which can be realized by including man as a system component, and the operational plans for such systems as Gemini and Apollo have already been modified to take advantage of this versatility. In other words, man's capabilities are operationally important and without substitute, and we must therefore be concerned about their preservation.

Man's capabilities are joint functions of many determinants, including, but not limited to, the functional properties of biological components and systems. Since biological components and systems constitute the targets of ionizing radiation, one might be tempted to argue, as indeed many have argued, that their study would provide a sufficient basis for inferences about the fate of behavior. Unfortunately, even after nearly a century of serious effort on the part of many scien-

should start with the human studies.

Human Studies

The Houston Studies

Background. The two experimental human studies were initiated in 1951 at the M.D. Anderson Hospital and Tumor Clinic of Houston, Texas, for the purpose of charting the effects of low-level ionizing radiation on some of the psychomotor capabilities relevant to the operation of aircraft. The director and staff of the hospital had long been interested in the comparative value of radiotherapy and chemotherapy for the treatment of generalized neoplastic disease, and they foresaw no valid criticism of collateral studies of biological and behavioral changes subsequent to the routine application of radiotherapy. All realized, of course, that ethical and moral considerations would necessitate compromises with some of the principles of experimental design. For example, medical considerations required that patients be assigned to treatment levels in accordance with professional judgment as to the severity of disease. Thus, the inability to employ random or stratified assignment methods virtually guaranteed some likelihood of confounding disease effects and treatment effects on the dependent variables. Further, language barriers, both of degree and kind, precluded the study of cognitive functions with available materials in which verbal comprehension occupied a central role. Despite such limitations, all agreed that the studies were feasible and desirable, and that negative results could be meaningfully interpreted and practically significant, even if

tific disciplines, we have not yet acquired more than a few of the concrete details about the way in which somatic events participate in behavior, although perhaps we have learned a great deal about the explanatory sterility of certain viewpoints. One consequence of our continued ignorance of these matters is that we are unable to forecast changes in behavior from observed changes in somatic functions with sufficient accuracy to predict the operational impact of biological damage, except, of course, under conditions of extreme insult. It is necessary, therefore, to observe and measure behavior directly in order to be able to say what is going to happen to it under specified exposure conditions. An ancillary product of such efforts may well turn out to be a better understanding of relationships between behavior and those events which occur inside the skin.

The foregoing premises have served as the foundation for modest but aggressive research efforts concentrated primarily at the USAF School of Aerospace Medicine. Such efforts have not been widespread among universities and other scientific institutions, for the resource requirements are formidable, and the monotonous occurrence of negative results soon blunts the enthusiasm of all but the most operationally minded investigators. Consequently, progress toward the achievement of a thoroughgoing research program has been slow. Many gaps are painfully evident, particularly with reference to dose dependency functions, relative behavioral effectiveness of different kinds of radiation, adequate coverage of the behavior spectrum, and the interactions of radiation effects with those of other stressors. Nevertheless a substantial amount of work has in fact been accomplished, and our review of it perhaps

the converse were not necessarily true.

Within the foregoing circumstances, two studies became possible throughout the next five years by virtue of close collaboration between the hospital and the USAF School of Aviation Medicine (Payne, 1959). The first study was concerned with the question whether a given air dose would have a greater effect when delivered in a single exposure than when delivered in a series of fractional exposures. The second study was organized as a straightforward dose-response study extending to relatively high exposure levels.

First Study. The first study was organized about the therapeutic circumstance that certain patients were treated with whole-body doses delivered in single exposures, while others were given equivalent total exposures in five equal increments separated by intervals on one hour. Psychomotor performance data obtained from both types of patients made it possible to test the prediction that performance level would be an inverse function of total dose, moreso with concentrated dosage than with temporally distributed dosage.

Subjects were male adults, usually in advanced stages of neoplastic disease not correctible by surgical intervention or localized radiation therapy. Ages ranged from 19 to 76 years.

Three well-known perceptual-motor tasks served as criteria of treatment effects. The USAF SAM Complex Coordination Test, shown in Figure 1, required the subject to coordinate the movements of a stick and rudder bar in order to match successive positions of three red lights with three green lights. Score consisted of the number of matches accomplished within standardized trial periods. The USAF SAM Two-Hand Coor-

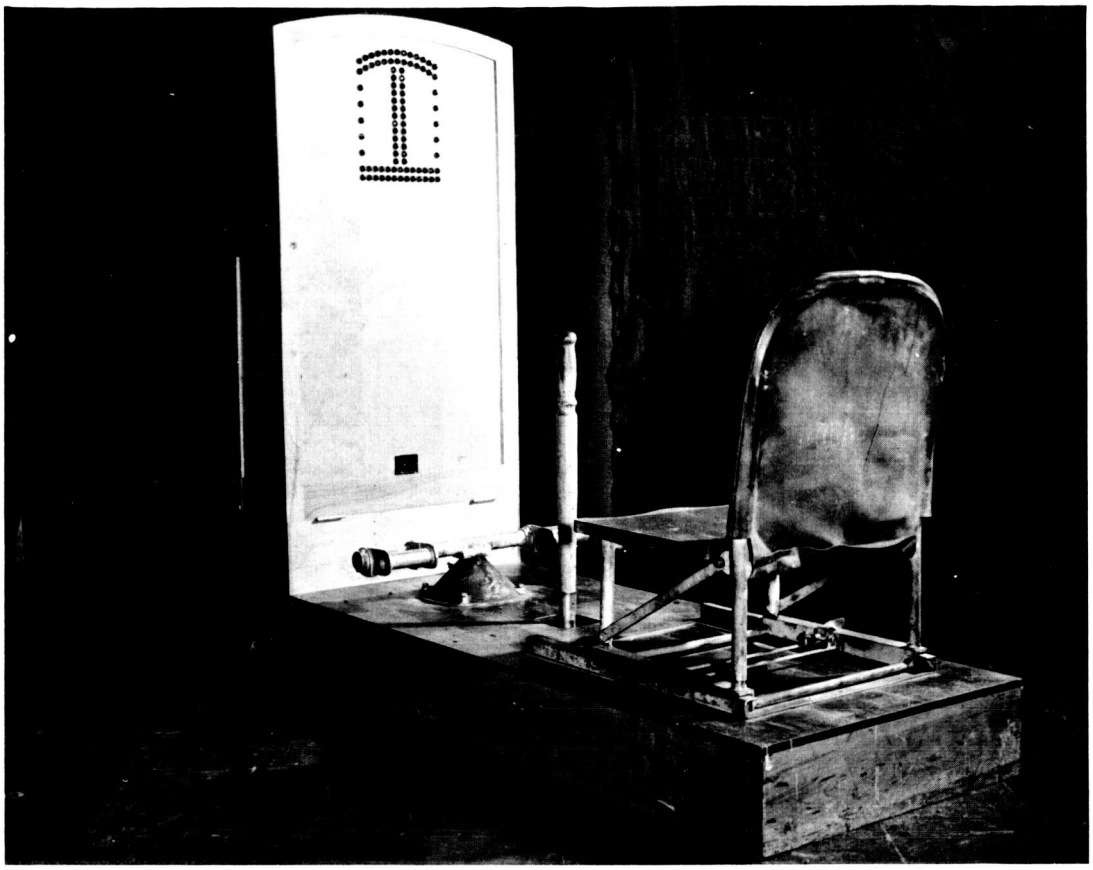

Figure 1. USAF SAM Complex Coordination Test

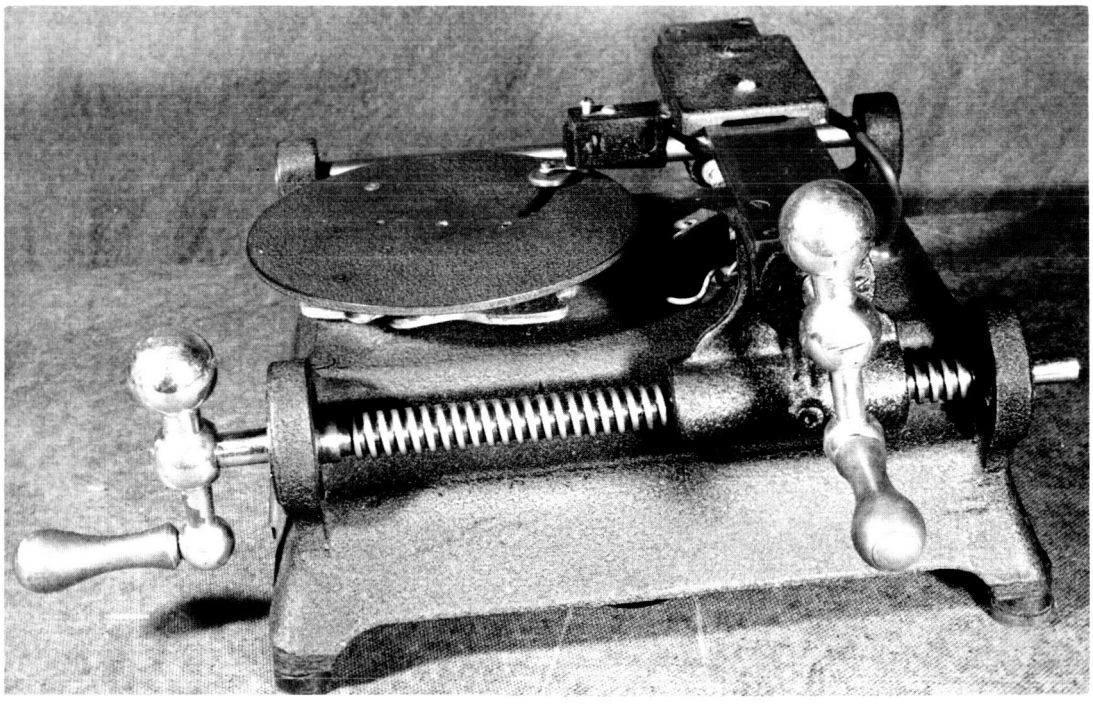

Figure 2. USAF SAM Two-Hand Coordination Test

dination Test, shown in Figure 2, required the subject to operate two lathe-like crank handles in order to keep a cursor positioned on an eccentrically moving target. Score consisted of the amount of time the pointer was on the target during standardized trial periods. Finally, the USAF SAM Rotary Pursuit Test, shown in Figure 3, required the subject to follow a rotating target with the tip of a stylus. Score consisted of time on target during standardized trial periods. All tests had been used successfully for the selection of aviation cadets during World War II, having been shown capable of accounting for a substantial portion of the variance of pilot training outcome. Thus, the behaviors under observation were relevant to flying proficiency, although they were by no means predictive of its entire factorial structure.

Three exposure levels were available for study: 15, 25, and 50 r, as measured in air at the position of a plane which bisected the patient. Each level was reached either by a single exposure or by five equal fractional exposures separated by an interval of 1 hour. Delivery was accomplished by a 400 kvp General Electric x-ray machine with Thoraeus III filtration having a half-value layer equivalent to 4.1 mm of copper. At the target distance of 300 cm, the output was approximately 0.95 r/min. One large field was used, the patient being treated in a lateral position with left and right sides alternated in proximity to the target. Air-wall ionization chambers (Farmer) were placed on the patient's skin during exposure in order to measure entrance and exit doses.

At about 0800 hours on the day of exposure, each subject was given formal test instructions and a standardized amount of preliminary practice on the three testing devices. Practice sessions were 2

minutes for the complex coordination and two-hand coordination tests, and 100 seconds (five 20-second trials separated by 10-second rests) for the rotary pursuit test. Following practice, the prescribed treatments were begun. One hour later the psychomotor testing sessions were resumed, and they were repeated thereafter at 2-hour intervals until six post-treatment sessions had been completed. Two testing sessions 8 hours apart were completed on the day following treatment. Additional testing was done on some of the subjects, but these data are not considered in the present study. Single-exposure subjects and multiple-exposure subjects within a given total exposure group were treated alike except that the latter were alternated between testing sessions and fractional treatment sessions until the five exposures had been accomplished.

Inasmuch as the performance under observation was measured early in the course of habit acquisition, two somewhat independent assessments of it were possible. The first was based simply on the total score achieved during the entire posttreatment testing sequence, while the second was an estimate of learning rate based upon the mean tangent of the angles defined by the abscissa of the performance curve and tangents drawn to successive equal segments of it. Both indexes were adjusted for multiple regression upon chronological age and pretreatment performance levels before the final analysis of posttreatment variation was performed. This adjustment had the general effect of (1) reducing the contribution of these factors and factors correlated with them (such as type and severity of disease) to posttreatment variation, and (2) increasing the precision with which final tests of significance could be made. What remained for the final analysis was the variation

attributable to the main experimental effects, their interaction, and residual differences between subjects.

Suffice it to say that only one of the six analyses (two criteria for each of three tests) provided even the slightest hint that performance was affected by the independent variables under consideration. An analysis of acquisition rate for the Rotary Pursuit Test, shown in Table 1, suggests that the effects of exposure level and method of delivery may have been correlated, i.e., the effects of treatment levels may not have been the same at all exposure levels. A plot of subclass means, shown in Figure 4, suggests that single exposures may have attenuated habit acquisition more than fractional exposures to the same levels, particularly at the highest level, in accordance with hypothesis.

Table 1. Analysis of variance of acquisition rate scores for Rotary Pursuit Test

Source	df	Mean Square	F	p
Doses	2	6.1888	< 1.00	
Methods	1	20.9941	2.05	.165
D x M	2	28.6785	2.79	.075
Error	70*	10.2589		
Total	75*			

*Reduced by 2df for regression of posttreatment scores (y) upon pretreatment scores (x) and chronological age (z).

$R_{y.xz} = .43$; $r_{zx} = -.16$; $r_{zy} = -.42$; $r_{xy} = .11$; $b_1 = .0043$; $b_2 = -.0900$

However, the probability levels associated with both methods and interaction effects are far from convincing, and the observed regressions of the two methods functions on the dosage variable are difficult to reconcile with the theoretical model.

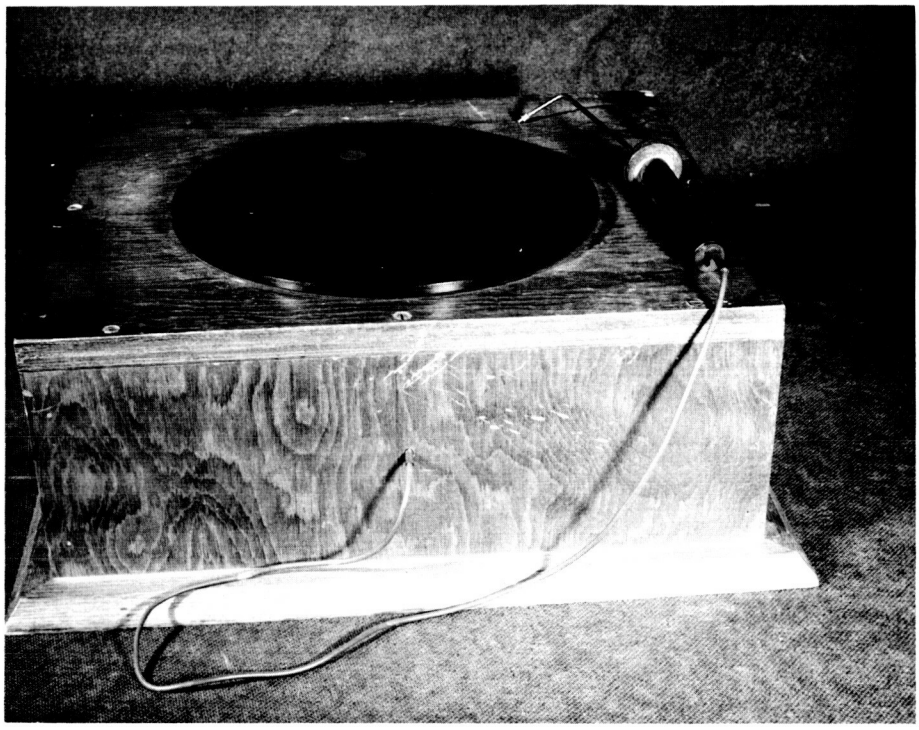

Figure 3. USAF SAM Rotary Pursuit Test

Second Study. Accumulated experience with therapeutic applications of whole-body radiation convinced the hospital staff of the wisdom of higher single doses than those which had been prescribed during the period covered by the first study. Consequently, it became possible to conduct psychomotor studies following single doses ranging from 0 to 200 roentgens (in air) in steps of 25 r, and special arrangements for hospitalization permitted the observations to extend over a period of 10 days beyond treatment.

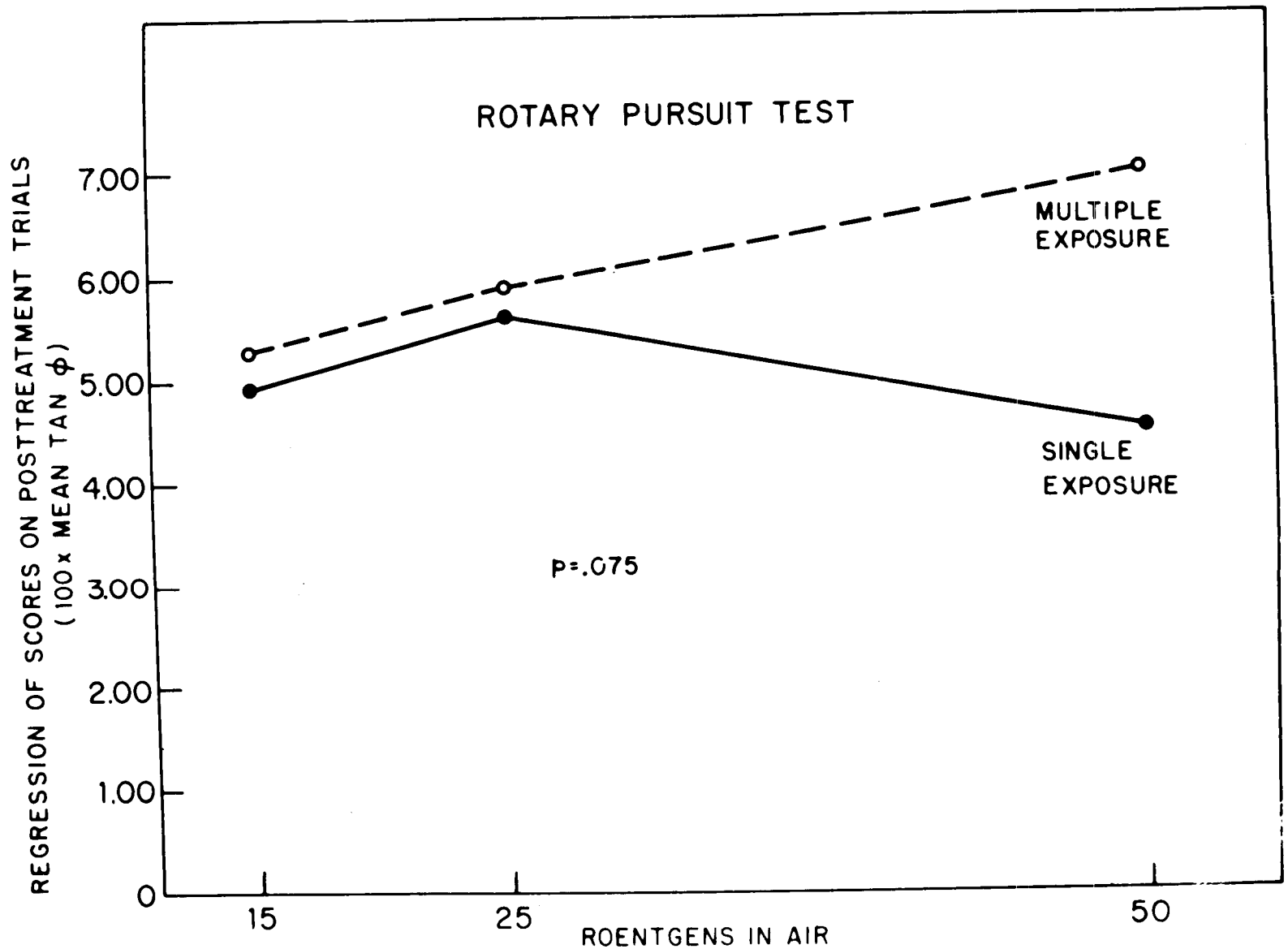

Figure 4. Rotary pursuit performance as a joint function of level and method of radiation exposure.

As before, subjects were adult males whose participation in the study was governed by their own consent and the judgment of the hospital staff. Ages ranged from 23 to 76 years. Testing devices were as previously described.

As before, patients were exposed in a lateral position with left and right sides alternated in proximity to the target. For approximately half the subjects, mostly those receiving below 75 r, the treatment was delivered as previously described. For the remainder, treatment was accomplished by a General Electric Maxitron operated at 250 kvp with a Thoraeus III filter providing half-value layer equivalent to about 3 mm of copper. Output was about 3.8 r/min. Nine exposure levels, ranging from 0 through 200 r in 25-r steps, were sampled. Each subject received his prescribed exposure in a single session.

Beginning at approximately 0800 hours each day for 4 days prior to exposure, each subject was allowed a practice session on each testing device. Practice sessions both before and after exposure were 4 minutes for complex coordination and two-hand coordination, and 300 seconds (fifteen 20-second trials separated by 10-second rests) for rotary pursuit. Exposure occurred on the morning of the fifth day. One hour later the first posttreatment testing session was held, and this was repeated each day at approximately the same time for 9 days thereafter. All subjects, including controls, were treated essentially alike except for the amount of radiation to which they were exposed.

Analyses of variation in posttreatment achievement levels for complex coordination and two-hand coordination were based on the forty one-minute performance samples obtained from each subject (10 days x 4

Table 2. Analysis of variance of adjusted posttreatment achievement levels for rotary pursuit

Source	df	Mean Square	F	p
Groups (doses)	7	23,086	< 1.00	ns
Ss treated alike	57	40,466		
Days	9	75,218	68.07	<.001
D x G	63	1,229	1.11	ns
Ss x D	513	1,105		
Trials/day	2	16,353	19.17	<.001
T x G	14	1,039	1.22	ns
Ss x T	114	853		
T x D	18	121	< 1.00	
T x D x G	126	272	1.14	ns
Ss x T x D	1,026	238		
Total	1,949*			

*Reduced by 60 df for regression coefficients, as follows: Ss treated alike (-2), Ss x D (-18), Sc x T (-4), and Ss x T x D (-36).

trials/day), while the analysis of rotary pursuit was based on the thirty 100-second performance samples from each subject (10 days x 3 trials/day). The scores of all subjects in each performance sample were adjusted for their multiple regression on chronological age and pretreatment achievement levels, and the residual variation of the

scores was then decomposed into main effects and interactions for determinations of statistical significance.

The outcomes for all testing devices are well represented by the analysis of rotary pursuit data, shown in Table 2. The highly significant variation associated with days and trials/day, when considered in conjunction with appropriate mean values, shows that significant amounts of learning occurred both within each day and from day to day. All radiation groups were essentially alike in this respect, as shown by the negligible interaction values, and there was no evidence of radiation impairment.

The data from each testing device were further analyzed in terms of the linear component of the habit acquisition curve, both within days and from day to day, but none of the analyses implicated radiation exposure as a significant source of variation. Comparable analyses were made in terms of the quadratic component of the acquisition curve. The results were negative for two-hand coordination and rotary pursuit, but those for complex coordination were significant, as shown in Table 3.

Table 3. Analysis of variance of quadratic component of scores by days for complex coordination

Source	df	Mean Square	F	p
Between radiation groups	8	.00282061	3.33	$< .01$
Within groups	58	.00084699		
Total	66			

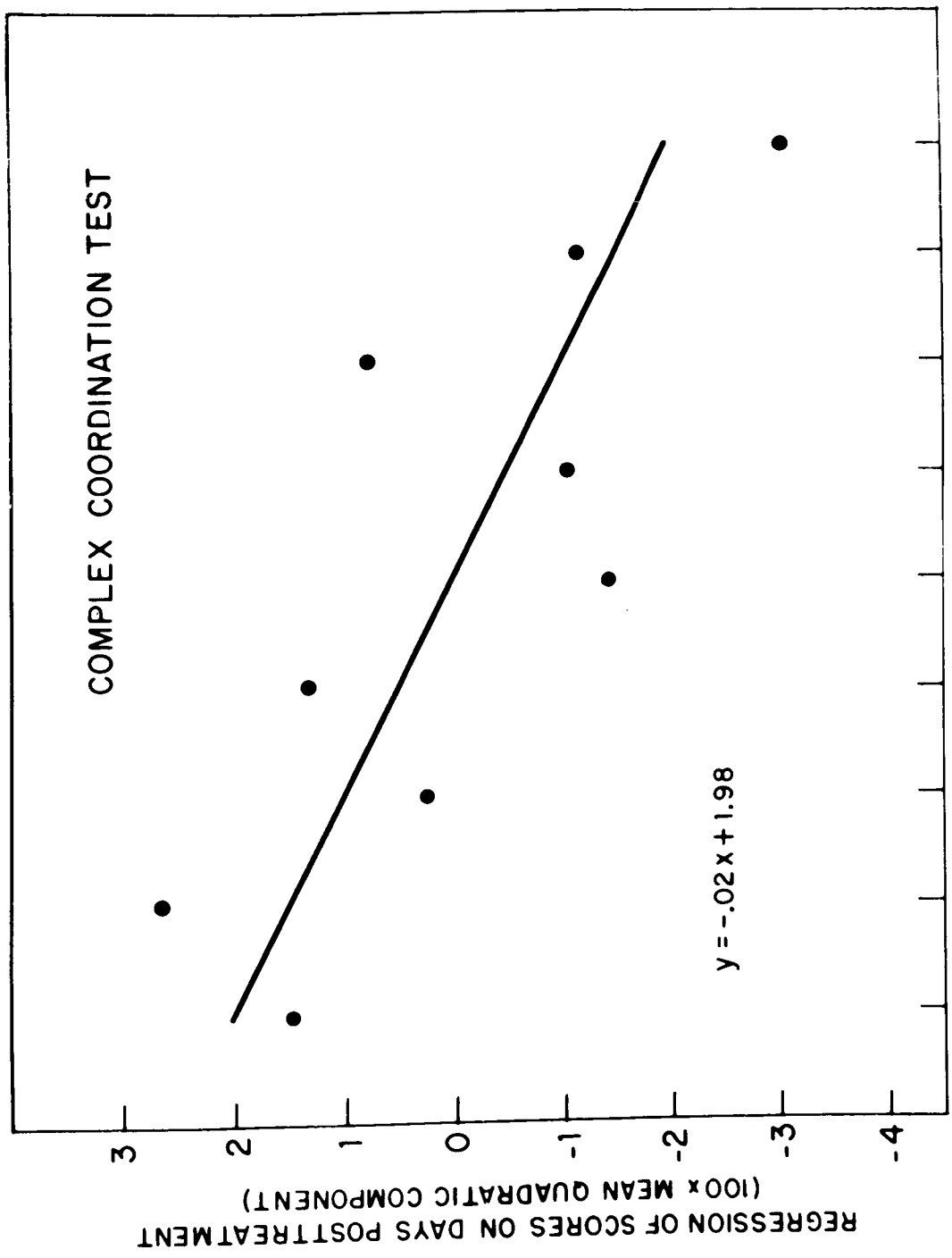

Figure 5. Quadratic component of complex coordination learning curve as a function of radiation exposure level.

A plot of the mean coefficients against exposure values, shown in Figure 5, suggests that the quadratic component of the 10-day performance curve became more negative the more intense the radiation exposure. In other words, the more intense the exposure, the more likely it was that performance was falling, rather than rising, toward the end of the 10-day period of measurement.

Except for the curvature aspect of the 10-day performance sequence for complex coordination, one can summarize these two studies by saying that there is no dependable evidence that exposure to ionizing radiation affected the variables measured. Whether this exception is a true radiation effect is debatable. It could just as well have been a disease effect, for we must presume that the prescribed exposure intensity bore some relationship to the true severity of the disease. Whatever its source, the effect probably represents progressive motoric weakness or fatigue in the operation of the spring-loaded controls rather than decrements in the cognitive aspects of the task. Finally, it seems important to re-emphasize that the application of these results to operational problems should be made with cautious regard for the medical status of the subjects and the limited relevance of experimental criteria.

Clinical Observations

Although lacking the precision of systematic experimental studies, certain observations acquired through clinical studies of bomb casualties, accidental exposures, and therapeutic experiences deserve careful

consideration because of their attention to what Furchtgott (1956) has called "behaviorally significant effects." For example, Keller (1946) noted fatigability as an almost universal complaint in his study of bomb casualties; and Gerstner (1957, 1958) commented on the appearance of listlessness, apathy, headache, and drowsiness "within a few hours" of exposure to radiotherapy. Miller, Fletcher, and Gerstner (1957) found about 50 percent of their patients showing fatigue, anorexia, and nausea shortly after radiotherapeutic exposures ranging from 125 to 175 r. Further studies of therapeutic experience by Levin, Schneider, and Gerstner (1959) observed that whole-body exposures of 150-200 r left patients asymptomatic for about an hour, but thereafter precipitated feelings of fatigue, apathy, dizziness, and headache, and produced appearances of depression and energy depletion. Thoma and Wald (1959) reported similar findings in their review of accidental exposures. Finally, Furchtgott (1952) reported studies, unavailable to him in original form, which suggested that radiation of the skin in "sub-erythemal doses" increased scotopic thresholds for several days and produced decrements in dark adaptation levels.

One, of course, cannot foresee with confidence what impact these effects might have on task performance, since high levels of training and motivation often sustain an operator to outstanding levels of achievement despite his infirmities. On the other hand, we can all agree that such effects represent potential liabilities that operators would be better off without.

The British Study

The sparse account of human studies would not be complete without reference to a recent paper by Frisby (1961). A British physician discovered one day that he had acquired a carcinoma of the tongue. As radiation therapy progressed, he came vaguely to feel that certain behavioral changes were taking place, and finally, after four weeks of this, he offered a psychologist an opportunity to study certain intellectual and perceptual functions by psychometric methods. Tests involving choice reaction time, cancellation, and fractions were administered twice daily (except Saturday and Sunday), sometimes by the psychologist and sometimes by the secretary, until a total of 6870 r had been delivered to the lesion, 5000 r to a nearby gland, and 7530 r to the skin. There was no evidence of radiation effect.

Infra-Human Primate Studies

The scarcity of human data may be regarded as compensated in part by a wide assortment of studies conducted on the infra-human primate, particularly on M. mulata. Whether such studies are truly useful depends, of course, on the validity of assumptions one makes about the phylogenetic continuity of behavioral processes. There are some who insist that there is a fundamental discontinuity between the behaviors of man and lower animals, and that little or nothing can be safely inferred about one from studies of the other. On the other hand, one should remember that such assertions are usually treated as hypotheses by those who study subhuman behavior, and the acceptance of the doctrine

before the fact would therefore seem to beg the question. Scholars in this field generally take the position that the study of lower animals promotes the understanding of human behavior to the degree that fundamental principles anticipate and embrace both sets of facts, an event which occurs more conclusively than most people today realize. From a clinical point of view it is interesting to note the conclusion drawn by Zellmer and Pickering (1960) that M. mulata demonstrates all the important aspects of the acute radiation syndrome. Diagnostic and prognostic signs (diarrhea, vomiting, purpura, anorexia, epilation, etc) occur about as frequently and with about the same latency as in humans, and the three modes of radiation death (CNS, gastrointestinal, and hematopoietic) are about as well illustrated. Thus there is a very substantial amount of conviction that M. mulata is an exceptionally suitable substitute for the human as an experimental animal. Fortunately so, for the study of lower primates permits the observation of complicated processes in their more elementary forms, and it permits the deliberate arrangement and control of a great variety of conditions for the satisfaction of experimental objectives.

Behavioral Methodology

The broad assortment of devices and techniques commonly used to study the animal's intellectual, perceptual, and motoric capabilities are described in any textbook of comparative psychology (e.g., Stone, 1951), as well as in the cited references, and any attempt to review them here would impose needlessly upon time and patience. In general, however, it may facilitate understanding to note that the investigator's

ability to observe and measure these processes entails two fundamental requirements. First, he must devise a problem the solution of which embodies the specified characteristics of such processes and falls within the anatomical and physiological capabilities of the organism. Second, he must provide an incentive which renders the solution worth the animal's effort. The rigor and precision with which he can study the processes depends in part upon the extent to which he can (a) control the environmental conditions and (b) quantify the responses in terms of their appropriateness, vigor, frequency, and latency.

The major categories of behavior which have served as focal points of research on the radiated monkey are (a) the learning and retention of discrimination habits, (b) the generalization of habits to novel situations, (c) the manipulation of environmental objects, (d) the delay of response to cues no longer present, (e) the breadth of attention to peripheral cues, (f) the solution of puzzles, (g) locomotion, and (h) free cage behavior in a comparatively unstructured environment. These categories merely represent convenient ways of classifying various aspects of the interaction between organism and environment, and one should understand that they are rigorously definable in terms of specific experimental operations.

Radiation Effects

Learning and Retention. Early systematic efforts explored the success with which the animal could reproduce discriminations which had been mastered prior to exposure. For example, Kaplan and Gentry (1954) trained animals on a serial discrimination task composed of 15 pairs of

stereometric objects, then exposed them to 1000 r of whole-body radiation delivered at 15r/min. Response evocation was rare on early post-exposure trials, but significant retention was demonstrated from 8 hours postexposure until 21 hours before death. Kaplan et al (1954) repeated the foregoing study with minor variations in which testing was resumed 24 hours postexposure and continued twice daily until the animals could no longer enter the transport cages. Although the radiated animals performed somewhat less well than controls after the third day, they exhibited significant degrees of retention virtually up to the point of collapse. Melching and Kaplan (1954) modified the procedure by requiring animals to discriminate objects in order to select an alley in which they could avoid electrical shock. Tests of retention conducted between 2 and 10 hours following the delivery of 1500 r at 34r/min were essentially negative. Rogers et al (1954) reported comparable results after exposures to 1295 r. Kaplan et al (1960), analyzing discrimination ability following massive doses of gamma radiation ranging from 1000 to 30000 r at 1000r/min, concluded that some animals were able to accept up to 5000 r without performing poorly, provided they were physically able to perform at all.

Harlow and Moon (1956) trained animals on a variety of tasks, including planometric discrimination and oddity problems, then exposed half of them to 100 r every 35 days until death. Formal testing was discontinued after the ninth exposure period for lack of survivors, but there was no evidence prior to death that radiation had degraded the ability to solve even the most complex learning problems, and animals on the verge of death maintained high performance levels until they

were so weak that overt response was no longer possible. Similarly, Riopelle, Grodsky, and Ades (1956) examined the effects of cumulative exposures adding to 2000 r on object quality discrimination only to find that the performance of radiated animals was equal to or better than that of controls.

When it became evident that the retention of simple discrimination habits was not seriously affected even by massive doses of radiation, efforts were made to devise more complicated problems and to examine the acquisition process, as opposed to the retention process, at generally lower levels of exposure. For example, eight months post-exposure to average doses up to 550 rem, Warren, Kaplan, and Greenwood (1955) trained animals to respond correctly to each of 108 pairs of multidimensional objects, then reversed the reinforcing operation so that the opposite member of each pair became the symbol of reward. Pre-reversal performance was not affected by the dosage levels; and post-reversal performance, although somewhat deficient, was not correlated with dose. McDowell and Brown (1959a) varied the cue reversal technique by rewarding the oddly colored of three objects during pre-reversal training, then rewarding the oddly shaped of the three objects during post-reversal training. Radiation exposure up to approximately 600 rem average dose failed to affect either phase of training in terms of errors committed. McDowell, Brown, and White (1961) used a comparable technique to assess the impact of massive focal radiation to the head, but with negative results.

Overall and Brown (1959) found no radiation effects when the task was one of learning to respond to the most recently rewarded position.

Later, however, Overall, Brown, and Gentry (1960) showed that the ability to learn size relationships between objects declined as a linear function of dosages which had been delivered three years prior to test (0 to 616 rep mixed neutron and gamma). Brown, Overall, and Blodgett (1959) presented consecutive discrimination problems in which both positive and negative cues in earlier series were selected at random to become negative when paired with new stimuli. Mixed neutron and gamma radiation up to 616 rep had no effect on the solution of this problem.

McDowell and Brown (1960b) adapted the Landoldt Ring principle to a series of eight problems ranging in difficulty from a 90° break to a 1° break in order to study the visual acuity of animals which had been exposed to as much as 616 rep three years earlier. All animals learned the easier problems readily, but they failed the more difficult ones in accordance with dosage received. Roughly comparable results were obtained following massive focal radiation to the head (McDowell and Brown, 1960b). However, neither set of results seemed decisive with respect to whether the deficit was a matter of visual acuity per se or planometric discrimination learning. The authors argued the former interpretation on the grounds that the easier problems were in fact learned.

Generalization of Habits. The ability to transfer principles acquired through experience with one set of problems to the solution of a new set of problems is generally regarded as a very high order of intellectual achievement. Such processes are studied in lower animals by presenting the training problem in such a way that reinforcement is

applied to all objects which have some particular feature in common, say triangularity, while nonreinforcement is applied to those objects which lack the feature. The critical test of transfer involves additional problems which incorporate some variant of the differentiated cue. Kaplan and Gentry (1953) explored the effects of radiation on this ability by comparing controls with animals that had received whole-body exposure to 400 r at about 16r/min. Half the exposed animals had their heads and spinal cords shielded. Transfer tests applied immediately postexposure as well as several months later gave no evidence of a deleterious effect. Comparable results were found with animals which had been exposed to whole-body doses as high as 616 rep (McDowell, 1960), and to focal head doses as high as 3000 r (McDowell and Brown, 1959c).

Manipulation. Leary and Ruch (1955) noted some decline in the ability to pull weights and manipulate mechanical puzzles shortly after the delivery of 200 r or more, but these effects appeared to be transient. On the other hand, Davis, McDowell, and Deter (1956) observed no important changes in manipulation ability after as much as 400 r.

Delayed Response. The measurement of an animal's ability to postpone its response to some reward or to some sign of reward following concealment from view was one of the earliest behavioristic approaches to the study of mental processes in lower animals. This process assumed considerable theoretical significance because of the implication that the animal, no longer able to sense the object, was responding to some internalized representation of it, thereby exhibiting implicit behavior remarkably like that found at the human level. Also, the amount of

delay attainable was generally correlated with phylogenetic sequence, ranging from about 10 seconds in the rat to much longer in the human. Davis, McDowell, and Deter (1956) were unable to degrade this response with acute whole-body exposures up to 400 r, and later studies involving up to about 1100 rem average dose found experimental animals performing about as well as (Davis, Elam, and McDowell, 1958) or better than (McDowell and Brown, 1958b) controls. Multiple exposures eventuating in total doses of 2000 r (Riopelle, 1959; Riopelle, Grodsky, and Ades, 1956) were likewise without effect, as were doses of 100 r given every 35 days until death (Harlow and Moon, 1956). McDowell, Brown, and White (1961) found no significant effect two years after their animals' heads had been exposed to 6000 r in two increments of 3000 r spaced 30 days apart. Harlow, Schiltz, and Settlage (1955) were able to degrade the response temporarily with 8000 r delivered to the head, but recovery was detectable four days later and was complete on the eighth day.

An unusual study worthy of note attempted to assess the impact of low-energy heavy nuclear components of primary cosmic radiation by exposing two Java monkeys to altitudes of 90 - 95M feet for 62 hours (Harlow, Schrier, and Simons, 1956). Delayed response, as well as other processes, was unaffected by this exposure, but the absence of track plate data precluded a determination of exposure level. About all one can say is that the animals were exposed to a hostile environment, and if they were hit, they were not measurably affected.

Attentiveness to Environmental Cues. Riopelle, Grodsky, and Ades (1956) were perhaps the first to suggest that the often superior performance of radiated animals represents a kind of tranquilizing

effect in which the animal is rendered less responsive to peripheral stimuli and consequently more attentive to the cues relevant to the problem presented for solution. Subsequent investigators confirmed this facilitative effect on oddity reversal problems (McDowell and Brown, 1959a), delayed response problems (McDowell and Brown, 1958b), discrimination problems (McDowell and Brown, 1958a; McDowell, Brown, and Wicker, 1959), and easier levels of the Landoldt Ring problem (Brown and McDowell, 1960). Further studies left no doubt that radiation narrowed the animal's scope of attention (McDowell, 1958; Overall and Brown, 1958; Brown, Carr, and Overall, 1958), producing as it were, a kind of "reduction in life space" (Davis, Elam, and McDowell, 1958). Although one might be tempted at first to rejoice over what might appear to be an unexpected bonus from an otherwise hostile environment, a more sober and insightful reflection on the reasons for these facilitative effects marks them as unwanted phenomena worthy of serious concern.

Miscellaneous Effects. Leary (1955) observed changes in the food preferences of animals which had been exposed to as little as 50 r, and Davis (1958) noted the persistence of such changes through at least 14 months postexposure. Several studies of free cage behavior have identified lower aggression (McDowell, Davis, and Steele, 1956) and exaggerated self-care (McDowell and Brown, 1958c, d) as consequences of whole-body doses as low as 400 r. At least one study has suggested an increase in reaction time as a function of dosage ranging from 0 to 670 rem (McDowell, Brown, and Wicker, 1961).

Summary

More than fifty studies of anthropoid behavior observed under various kinds, rates, and amounts of ionizing radiation have shown, on balance, that behavioral functions are highly resistant to acute whole-body doses well above those required to produce troublesome manifestations of acute radiation sickness. Despite this overwhelming evidence of resistance, however, several aspects of behavior are clearly not impregnable. Further effort, therefore, is required to relate such aspects both to the physical dimensions of the radiation environment and the visible damage produced in biological tissues, with particular emphasis on the modifying properties of other stressors.

From a practical and conservative point of view, any exposure intense enough to embarrass an individual's normal physiological mode should be regarded as behaviorally significant because it imposes constraints upon the convenience with which the individual can adapt to environmental circumstances. In terms of immediate effects, present knowledge suggests the acute radiation syndrome as the ruling factor in the specification of permissable acute exposure levels.

References

Brown, W. L., Carr, R. M., & Overall, J. E. The effect of whole-body radiation upon association of peripheral cues. USAF Sch. Aviat. Med. Rep., Rep. No. 58-47, 1958.

Brown, W. L., & McDowell, A. A. Visual acuity performance of normal and chronic irradiated monkeys. J. genet. Psychol., 1960, 96, 133-137.

Brown, W. L., Overall, J. E., & Blodgett, H. C. Novelty learning sets in rhesus monkeys. USAF Sch. Aviat. Med. Rep., Rep. No. 58-147, 1958.

Brown, W. L., Overall, J. E., & Blodgett, H. C. Novelty learning sets in rhesus monkeys. J. comp. physiol. Psychol., 1959, 52, 330-332.

Davis, R. T. Latent changes in food preferences of irradiated monkeys. J. genet. Psychol., 1958, 92, 53-59.

Davis, R. T., Elam, C. B., & McDowell, A. A. Latent effects of chronic whole-body irradiation of monkeys with mixed source radiation. USAF Sch. Aviat. Med. Rep., Rep. No. 57-59, 1958.

Davis, R. T., McDowell, A. A., & Deter, C. W. Performance of rhesus monkeys on selected laboratory tasks presented before and after a large single dose of whole-body x-radiation. J. comp. physiol. Psychol., 1956, 49, 20-26.

Frisby, C. B. A note on radiation treatment in relation to performance on certain tests. Brit. J. Psychol., 1961, 52, 65-70.

Furchtgott, E. The effects of x-irradiation on brightness discrimination. J. Psychol., 1952, 34, 37-41.

Furchtgott, E. Behavioral effects of ionizing radiations. Psychol. Bull., 1956, 53, 321-334.

Gerstner, H. B. Military and civil defense aspects of the acute radiation syndrome in man. USAF Sch. Aviat. Med. Rep., Rep. No. 58-6, 1957.

Gerstner, H. B. Acute clinical effects of penetrating nuclear radiation. Jour. Amer. Med. Assoc., 1958, 168, 381-388.

Harlow, H. F., & Moon, L. E. The effects of repeated doses of total-body x-radiation on motivation and learning rhesus monkeys. J. comp. physiol. Psychol., 1956, 49, 60-65.

Harlow, H. F., Schiltz, K. A., & Settlage, P. H. Effect of cortical implantation of radioactive cobalt on learned behavior of rhesus monkeys. J. comp. physiol. Psychol., 1955, 48, 432-436.

Harlow, H. F., Schrier, A. M., & Simons, D. G. Exposure of primates to cosmic radiation above 90,000 feet. J. comp. physiol. Psychol., 1956, 49, 195-200.

Kaplan, S. J. Radiation research in psychology; An analysis of techniques in maze experimentation. Psychol., Bull., 1962, 59, 153-160.

Kaplan, S. J., & Gentry, G. The effect of sublethal dose of x-radiation upon transfer of training in monkeys. USAF Sch. Aviat. Med. Proj. Rep., 1953, Proj. No. 21-3501-0003 (Rep. No. 4).

Kaplan, S. J., & Gentry, G. Some effects of a lethal dose of x-radiation upon memory. USAF Sch. Aviat. Med. Proj. Rep., 1954, Proj. No. 21-3501-0003 (Rep. No. 2).

Kaplan, S. J., Gentry, J., Melching, W. H. & Delit, M. Some effects of a lethal dose of x-radiation upon retention in monkeys. USAF Sch. Aviat. Med. Proj. Rep., 1954, Proj. No. 21-3501-0003 (Rep. No. 8).

Kaplan, S. J., Melching, W. H., Reid, J. B., Rothermel, S., and Johnson, O. Behavior. (In Pickering, J. E., Langham, W. H., & Rambach, W. A. (eds) The Effects from Massive Doses of High Dose Rate Gamma Radiation on Monkeys. USAF Sch. Aviat. Med. Rep., Rep. No. 60-57, 1960).

Keller, P. D. A clinical syndrome following exposure to atomic bomb explosions. Jour. Amer. Med. Assoc., 1946, 131, 504-506.

Leary, R. W. Food-preference changes of monkeys subjected to low-level irradiation. J. comp. physiol. Psychol., 1955, 48, 343-346.

Leary, R. W., & Ruch, T. C. Activity, manipulation drive, and strength in monkeys subjected to low-level irradiation. J. comp. physiol. Psychol., 1955, 48, 336-342.

Levin, W. C., Schneider, M., & Gerstner, H. B. Initial clinical reaction to therapeutic whole-body x-radiation - some civil defense considerations. USAF Sch. Aviat. Med. Rep., Rep. No. 60-1, 1959.

McDowell, A. A. Comparisons of distractibility in irradiated and non-irradiated monkeys. J. genet. Psychol., 1958, 93, 63-72.

McDowell, A. A. Transfer by normal and chronic whole-body irradiated monkeys of a single learned discrimination along a peripheral cue gradient. J. genet. Psychol., 1960, 97, 41-58.

McDowell, A. A., & Brown, W. L. Facilitative effects of irradiation on performance of monkeys on discrimination problems with reduced stimulus cues. J. genet. Psychol., 1958, 93, 73-78. (a)

McDowell, A. A., & Brown, W. L. Latent effects of chronic whole-body irradiation on the performance of monkeys on the spatial delayed-response problem. USAF Sch. Aviat. Med. Rep., Rep. No. 58-50, 1958. (b)

McDowell, A. A., & Brown, W. L. Some effects of nuclear radiation exposure on the behavior of the rhesus monkey. USAF Sch. Aviat. Med. Rep., Rep. No. 58-58, 1958. (c)

McDowell, A. A., & Brown, W. L. Some persisting effects of nuclear radiation exposure on the behavior of the rhesus monkey. USAF Sch. Aviat. Med. Rep., Rep. No. 58-63, 1958. (d)

McDowell, A. A., & Brown, W. L. Visual acuity performance of normal and chronic focal-head irradiated monkeys. USAF Sch. Aviat. Med. Rep., No. 59-5, 1958. (e)

McDowell, A. A., & Brown, W. L. A comparison of normal and irradiated monkeys on an oddity-reversal problem. J. genet. Psychol., 1959, 95, 105-110. (a)

McDowell, A. A., & Brown, W. L. Peripheral cue learning set in rhesus monkeys. USAF Sch. Aviat. Med. Rep., No. 59-4, 1959. (b)

McDowell, A. A., & Brown, W. L. Transfer by normal and chronic focal-head irradiated monkeys of a single learned discrimination along a peripheral cue gradient. USAF Sch. Aviat. Med. Rep., Rep. No. 59-18, 1959. (c)

McDowell, A. A., & Brown, W. L. Peripheral cue learning set in rhesus monkeys. J. genet. Psychol., 1960, 96, 129-132. (a)

McDowell, A. A., & Brown, W. L. Visual acuity performance of normal and chronic focal-head irradiated monkeys. J. genet. Psychol., 1960, 96, 139-143. (b)

McDowell, A. A., Brown, W. L., & White, R. K. Oddity-reversal and delayed-response performance of monkeys previously exposed to focal-head irradiation. J. genet. Psychol., 1961, 99, 75-81.

McDowell, A. A., Brown, W. L., & Wicker, J. E. Some effects of nuclear radiation exposure on preliminary WGTA training performance of rhesus monkeys. USAF Sch. Aviat. Med. Rep., Rep. No. 59-53, 1959.

McDowell, A. A., Brown, W. L., & Wicker, J. E. Effects of radiation exposure on response latencies of rhesus monkeys. USAF Sch. Aerosp. Med. Rep., Rep. No. 61-94, 1961.

McDowell, A. A., Davis, R. T., & Steele, J. P. Application of systematic direct observational methods to analysis of the radiation syndrome in monkeys. Percept. Mot. Skills, 1956, 6, 117-130.

Melching, W. H., & Kaplan, S. J. Some effects of a lethal dose of x-radiation upon retention (Studies of shock avoidance motivation). USAF Sch. Aviat. Med. Proj. Rep., 1954, Proj. No. 21-3501-0003 (Rep. No. 9).

Miller, L. S., Fletcher, G. H., & Gerstner, H. B. Systemic and clinical effects induced in 263 cancer patients by whole-body x-irradiation with nominal air doses of 15 to 200 r. USAF Sch. Aviat. Med. Rep., Rep. No. 57-92, 1957.

Overall, J. E., & Brown, W. L. Narrowing of attention in rhesus monkeys as a chronic effect of sublethal radiation. USAF Sch. Aviat. Med. Rep., Rep. No. 58-27, 1958.

Overall, J. E., & Brown, W. L. Response of rhesus monkeys to prohabilistic sequential dependencies. USAF Sch. Aviat. Med. Rep., No. 59-3, 1959.

Overall, J. E., Brown, W. L. & Gentry, G. V. Differential effects of ionizing radiation upon "absolute" and "relational" learning in the rhesus monkey. J. genet. Psychol., 1960, 97, 245-250.

Payne, R. B. Effects of ionizing radiation on human psychomotor skills. USAF Sch. Aviat. Med. Rep., Rep. No. 59-29, 1959.

Payne, R. B. Effects of ionizing radiation on human psychomotor skills. U.S. Armed Forces Med. Jour., 1959, 10, 1009-1021.

Riopelle, A. J. Performance of rhesus monkeys on spatial delayed response (indirect method). J. comp. physiol. Psychol., 1959, 52, 746-753.

Riopelle, A. J., Grodsky, M. A., & Ades, H. W. Learned performance of monkeys after single and repeated x-irradiations. J. comp. physiol. Psychol., 1956, 49, 521-524.

Rogers, C. M., Kaplan, S. J., Gentry, J., & Auxier, J. A. Some effects of cumulative doses of x-radiation upon learning and retention in the rhesus monkey. USAF Sch. Aviat. Med. Proj. Rep., 1954, Proj. No. 21-3501-0003 (Rep. No. 11).

Stone, C. P. (ed) Comparative Psychology (3d Edition) Englewood Cliffs (N. J.): Prentice-Hall, 1951.

Thoma, G. E., and Wald, N. The diagnosis and management of accidental radiation injury. J. occup. Med., 1959, I:8, 421-447.

Warren, J. M., Kaplan, S. J., and Greenwood, D. D. The solution of discrimination-reversal problems by normal and irradiated monkeys. USAF Sch. Aviat. Med. Proj. Rep., Proj. No. 21-3501-0003, Rep. No. 16, 1955.

Zellmer, R. W. Human ability to perform after acute sublethal radiation. Military Med., 1961, 126, 681-687.

Zellmer, R. W., & Pickering, J. E. Biologic effects of nuclear radiation in primates. USAF Sch. Aviat. Med. Rep., Rep. No. 60-66, 1960.

THE LETHAL EFFECTIVENESS OF A SOLAR FLARE-TYPE DOSE DISTRIBUTION DELIVERED TO THE RAT

K. L. Jackson

Radiation Biology Group
Bioastronautics Section
Physics Technology Department
The Boeing Company
Seattle, Washington

Abstract

An investigation of some biological effects produced by exposure of rats to a solar flare-type depth-dose distribution has been carried out. Space proton doses to bone marrow will not be appreciably attenuated by surrounding bone and, in the present study, this was simulated by use of cobalt-60 gamma radiation. Depth-dose distribution, produced in rats by a filter-rotation technique, resulted in a midline dose which was 25 per cent of the surface dose. This depth-dose is similar to that calculated for exposure of man to July 16, 1959 solar flare protons with 10 gm/cm^2 of shielding.

The 50 per cent lethal dose (LD_{50}) measured at the surface of the rat was three times greater for depth-dose exposure as compared to uniform exposure. The midline LD_{50} was less for depth-dose exposure than for uniform exposure. The depth in the body at which the depth-dose LD_{50} was equal to the uniform LD_{50} was approximately 50 per cent of the distance from the surface to the midline. The total energy absorbed at the LD_{50} was 1.5 times greater with depth-dose exposure as compared to uniform exposure. Mean survival time of decedents in the LD_{16} - LD_{84} range was significantly shorter in depth-dose exposed animals as compared to uniformly exposed animals. This suggests that depth-dose exposure produces greater injury to the intestine which was verified by measurement of intestinal weight changes.

Introduction

Interest in the biological effects resulting from whole-body exposure of mammals to a decreasing depth-dose distribution of ionizing radiation

recently has increased because space proton fields[1,2] are expected to produce this form of absorbed dose geometry[3,4]. The lethal effectiveness of decreasing depth-dose distribution down to 70 per cent of the surface dose at body-center has been discussed by Bond, et.al.[5]. However, little information is available on the lethal dose requirements for midline doses in the range of 1 to 70 per cent of the surface dose, the range expected for exposure of man to space radiation fields[4,6].

Beta irradiation of small animals has been used to produce a steep depth-dose near the body surface but this method does not produce significant doses at body-center or intermediate depths[7,8]. Interpretation of lethality and organ damage data obtained by use of low

---

1. Ney, E. P., J. R. Winckler, and P. S. Frier, Protons from the Sun, May 12, 1959. Phys. Rev. Let. 3:183-185 (1959).

2. Van Allen, J. A., and L. A. Frank, Radiation Measurements to 658,300 KM with Pioneer IV. Nature 184:219-224 (1959).

3. Dye, D. L., and J. C. Noyes, Biological Shielding for Radiation Belt Particles. J. Astronautical Sci. 7:64-70 (1960).

4. Schaefer, H. J., Further Evaluation of Tissue Depth Doses in Proton Radiation Fields in Space. U.S.N. School Aviation Medicine Research Report 17, 14 pages (May 1950).

5. Bond, V. P., E. P. Cronkite, C. A. Sondhaus, G. Imirie, J. S. Robertson, and D. C. Borg, The Influence of Exposure Geometry on the Pattern of Radiation Dose Delivered to Large Animal Phantoms. Rad. Res. 6:554-572 (1957).

6. Jackson, K. L., Influence of Solar Flare-Type Exposure Geometry on Acute Lethality: Technical Discussion and Proposed Study. Boeing Document D2-12242, 28 pages (August 1961).

7. Biological Effects of External Beta Radiation, edited by R. E. Zirkle, National Nuclear Energy Series IV-22E, McGraw-Hill Book Co., Inc., New York (1951).

8. Crook, J. C., E. V. Hulse, J. H. Mulvey, and G. J. Neary, The Acute Effects of Partial-Body Beta Irradiation of Mice. British J. Radiol. 31:477-485 (1958).

voltage X-radiation to produce a depth-dose distribution is complicated by the shielding effect of surrounding bone on marrow dose[9-12]. This appears to be an important factor in the study of biological effects produced by space proton fields since radiation doses to marrow will not be appreciably attenuated by bone[6].

In the present investigation of the effects of depth-dose irradiation of the rat, bone attenuation of marrow dose has been minimized by using cobalt-60 gamma radiation in conjunction with a filter-rotation technique. The relative depth-dose distribution studied is similar to that calculated for exposure of man to July 16, 1959, solar flare protons with 10 gm/cm^2 of shielding[6]. The advantage gained by use of gamma radiation to study depth-dose effects per se independent from RBE considerations has been discussed previously[6].

Experimental Procedure

Animals

Two-month-old, male, Sprague-Dawley rats were used in the experiments. The animals were housed four to a cage and were given water and Purina Laboratory Chow ad libitum.

---

9. Alpen, E. L., and D. M. Jones, Effects of Concomitant Superficial X-Radiation Upon the Lethal Effectiveness of 250 KVP X-Rays. Radiology 72:81-85 (1959).

10. Alpen, E. L., D. M. Jones, H. H. Hechter, and V. P. Bond, The Comparative Biological Response of Dogs to 250 KVP and 100 KVP X-Rays. Radiology 70:541-550 (1958).

11. Grahn, D., G. A. Sacher, and H. Walton, Comparative Effectiveness of Several X-Ray Qualities for Acute Lethality in Mice and Rabbits. Rad. Res. 4:228-242 (1956).

12. Report of the International Commission on Radiological Units and Measurements (ICRU) 1959, National Bureau of Standards Handbook 78, January 16, 1961.

13. Litchfield, J. T., and F. Wilcoxon, A Simplified Method of Evaluating Dose-Effect Experiments. J. Pharmacol. Exptl. Therap. 96:99-113 (1949).

Methods

A few minutes before irradiation, groups of twelve rats were anesthetized with an intraperitoneal injection of nembutal and were placed in 4.4 cm (inside diameter) cast acrylic cylinders. During irradiation the cylinders were rotated at 28 RPM about their long axes which were positioned vertically by means of the apparatus shown in Fig. 1. This technique allowed accurate positioning of the midline of the rats and caused the rats' bodies to assume a fixed cylindrical shape. In order to deliver the same midline dose to the upper, center, and lower portions of the cylinders, the long axis of a 0.5 inch diameter by 8.3 inches long (1000 C) cobalt-60 source was centered on and positioned parallel to the long axis of the cylinders.

Simultaneous exposure of six rats to a decreasing depth-dose was accomplished by rotation of the rat-containing cylinders behind wedge shaped lead filters (Fig. 1). The cross section of each filter was an isosceles triangle with an altitude of 7.5 cm and a base of 4.0 cm. The base was constructed 4 mm smaller than the diameter of the rat so that diverging rays from the source which grazed the edge of the filter at the base also grazed the surface of the rat. Because the plane of maximum thickness of the lead filter was positioned in the center of the rat (along the longitudinal axis), the midline of the rat received a low, constant dose-rate during rotation. A point on or near the surface of the rat, however, passed alternately through areas of high to low dose-rates. The net effect of such exposure geometry was to produce the depth-dose distribution shown in Fig. 2.

Simultaneous irradiation of six rats with a uniform body dose was accomplished by exposing rotating animals in the apparatus of Fig. 1 but without the use of a lead filter. In order to obtain approximately the same desired average body-surface dose-rate for the two exposure geometries, the midline to source distance for uniform and depth-dose exposure was approximately 20 inches and 10-3/4 inches, respectively. Slight adjustments of rotator positions were made to reduce the deviation of dose rate within each geometry group to less than 2 per cent of the mean.

In each series of exposures six depth-dose irradiated rats and six uniformly irradiated rats were exposed simultaneously. Because irradiation of the uniformly exposed animals required less time than was required for irradiation of the depth-dose animals, exposure of the depth-dose group was interrupted in order to remove the uniform group. The time required for removal of the uniform group was less than three minutes.

Mortality data obtained following exposure of the animals to a series of graded radiation doses were analyzed for 50 per cent lethal doses at 30 days (LD_{50}) and potency ratios by the method Litchfield and Wilcoxon[13].

FIGURE: 1

DEPTH-DOSE FILTER-ROTATION APPARATUS

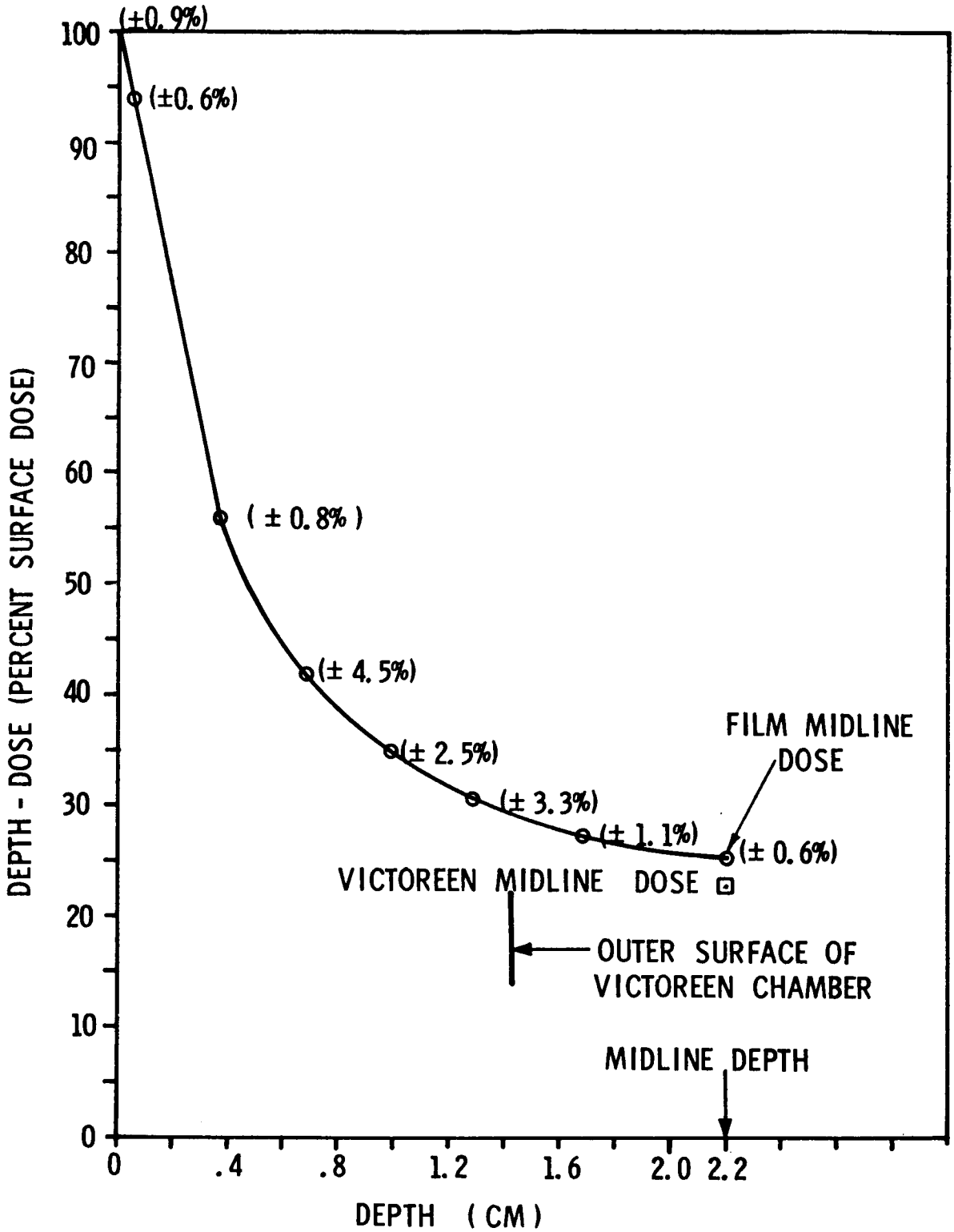

FIGURE: 2

DEPTH-DOSE PRODUCED IN RAT PHANTOM BY COBALT-60-FILTER ROTATION TECHNIQUE

In order to measure the wet weight of the small intestine, this tissue was removed under ether anesthesia and rapidly stripped free of mesenteric blood vessels, fat, and pancreas. After chilling the intestine in ice cold isotonic saline, the tissue was cut longitudinally and the luminal content was blotted away on filter paper. The intestine was rinsed in five changes of ice cold saline, reblotted on filter paper, and weighed.

Dosimetry

The primary reference for measurement of radiation doses was a #621 Victoreen 100r thimble chamber. All measurements were made with the chamber covered with a 1.3 cm thickness of pressed wood. The chamber and stem were exposed to the same radiation field. Rat phantoms were constructed from stacks of 4.4 cm diameter, 1/8 inch thick discs of pressed wood contained in the acrylic cylinders.* The tissue roentgen dose was converted to rad dose by a multiplication factor of 0.97 which is relatively constant over a considerable energy range (12).

The dose delivered to the uniformly exposed rats was determined by making a series of exposures for varying periods of time and measuring the dose with the Victoreen thimble chamber. Extrapolation of the measured dose to zero time yielded the dose delivered during the time required to raise the source to, and lower the source from, the exposure position (raise-lower-dose). Shaped lead bricks inside and below the rotators reduced the raise-lower-dose to 14.7 rad. The dose-rate with the source in the expose position was 59.6 rad/min measured at the midline of the phantom.

The dose distribution delivered to depth-dose exposed rats was measured by photographic film dosimetry using Dupont 510 film. The film loads were constructed as part of the phantom by using discs of 1/8 inch pressed wood with a circular piece of film sandwiched between the wood discs. A second strip of film was positioned in a 90 degree plane to the circular film around the outside of the wood discs. This second film was used to obtain a film density measurement near the surface of the cylinder wall. The entire film load, when sealed with black masking tape, made a tight fit in the acrylic cylinder. Micrometer measurement of masking tape, protective paper, and film thicknesses indicated the average depth of the emulsion to be 0.5 mm from the cylinder wall. The films were developed in Kodak X-Ray Developer and film densities were measured with a Macbeth-Ansco densitometer. The relationship between film density and Victoreen chamber reading was determined

*Density of the pressed wood was 1.10 gm/cm^3. The Victoreen chamber yielded the same dose in a water phantom or a pressed wood phantom when each was exposed behind a lead filter.

following simultaneous exposure of the films and thimble, each being imbedded in a pressed wood phantom and rotated in an acrylic cylinder without a lead filter. Individual standard curves relating film densities of the two films to Victoreen reading were constructed from data obtained by a series of duplicate radiation exposures.

The depth-dose distribution and dose-rate delivered to the phantom was calculated from film density measurements made at known distances from the acrylic cylinder wall following simultaneous exposure of duplicate film packs rotated behind lead filters in all depth-dose rotators. Numbers in parentheses given in Fig. 2 indicate the maximum per cent deviation from the mean of the measured dose among the six rotators. No significant buildup of the dose near the surface of the phantom was expected due to the 1/8-inch acrylic plastic wall surrounding the phantom[14]. The average dose-rate delivered to the surface of the rotating phantom, obtained by extrapolation of the depth-dose curve to the surface (Fig. 2), was determined to be 54.8 rad/min. The surface raise-lower-dose was 10.9 rad. The maximum dose-rate delivered to the surface of the phantom (measured with no rotation) was in the region of minimum lead filter thickness and this dose-rate was observed to be 189 rad/min.

Since photographic film exhibits marked energy dependence at low photon energies[15], an estimate was made of the error in dosimetry due to low energy scatter from the back of the lead filter. This error would be greatest at the center of the phantom.* Although the Victoreen chamber was too large to measure doses near the surface of the rat phantom, it could be used to determine the dose delivered to the center because in this region the dose change with depth is small over the

---

14. Burkell, C. C., T. A. Watson, H. E. Johns, and R. J. Horsley, Skin Effects of Cobalt-60 Telecurie Therapy. British J. Radiol. 27:171-176 (1954).

15. Dudley, R. A., Photographic Film Dosimetry in "Radiation Dosimetry", edited by G. J. Hine and G. L. Brownell, Academic Press, New York (1956).

* Tests made by exposure of film and Victoreen chamber behind large slabs of lead of various thicknesses indicated that the discrepancy between film and Victoreen increased with increasing thickness of lead. The discrepancy exceeded 10 per cent for slabs thicker than 5.5 cm.

dimensions of the Victoreen chamber (Fig. 2). A comparison, therefore, was made of the dose measured at the center of the phantom by the Victoreen chamber and film when these were exposed simultaneously while rotated behind a lead filter. As indicated in Fig. 2, the film registered a phantom midline dose which was 25 per cent of the surface dose and the Victoreen recorded a dose which was 23 per cent of the surface dose. Since factory calibration showed that the Victoreen chamber used reads 4.5 per cent lower for 100 KVCP X-radiation as compared to cobalt-60 gamma radiation, the error due to film energy dependence may be somewhat less than is indicated by the above test.

The total energy absorbed by a rat during depth-dose irradiation was estimated by integration of the energy delivered to a tissue cylinder by the depth-dose distribution shown in Fig. 2. The rats were assumed to be cylinders of 4.4 cm diameter with volumes equal to the body weight divided by a body density of 1.02. Graphical integration of the energy delivered was performed by summation of the mean energy delivered to a 4 mm diameter core and concentric cylinders of 2 mm wall thickness.

Results

In Experiments I and II, a total of 24 groups of six rats were exposed to graded surface doses ranging from 786 to 951 rad and 2231 to 3282 rad for uniform and depth-dose geometry, respectively. Results of analysis of mortality data obtained in these experiments are given in Table I. The surface LD_{50} values with depth-dose exposure were significantly greater than with uniform exposure and the analyses indicated the slope of dose-per cent curves in each experiment did not deviate significantly from parallelism. Therefore, potency ratios were estimated which indicate the surface LD_{50} for depth-dose exposed animals was three times greater than the LD_{50} for uniform exposure. These data also show that the midline LD_{50} for the depth-dose exposed animals was significantly lower than the midline LD_{50} of the uniformly exposed animals (Table I and Fig. 3). The LD_{50} values were numerically equal at a torso depth of 47 to 53 per cent of the distance from surface to midline (Table I and Fig. 3).

Since the dose delivered to various parts of the rat during depth-dose exposure depends upon distance of the tissue from the cylinder wall, a description of the position assumed by rats during irradiation is warranted. The trunks of the bodies made a snug fit in the cylinders and the torso was cylindrical (Fig. 1).* The end of the lower mandible was usually against the wall of the cylinder with the back of the head against the opposite cylinder wall. The fore legs were between the

*Respiration and circulation appeared normal as judged by ear color and head and thorax movements.

Table 1. Mortality Data for Rats Subjected to Uniform and Depth-Dose Exposure from Cobalt-60[a]

Experiment No.	Exposure Geometry	LD_{50} (rad)	Slope Function S	Potency Ratio at LD_{50}	Midline LD_{50} (rad)	% Depth at which Depth-Dose LD_{50} Equals Uniform LD_{50}[b]	Mean Body Weight (gm)[c]	Integral Dose (Kgrad)	Ratio of Integral Doses
I	Depth-dose	2522 (2427-2620)	1.06 (1.02-1.11)	2.99 (2.61-3.33)	631 (606-655)	47%	200	250	1.47
	Uniform	846 (831-860)	1.02 (1.01-1.04)		846 (831-860)		201	170	
II	Depth-dose	2546 (2314-2801)	1.12 (1.01-1.24)	3.21 (2.89-3.56)	636 (578-825)	54%	225	284	1.58
	Uniform	793 (763-825)	1.07 (0.71-1.59)		793 (763-825)		227	180	
III	Depth-dose	2694 (2572-2821)	1.13 (1.05-1.21)	3.18 (2.89-3.50)	673 (643-705)	53%	187	250	1.55
	Uniform	846 (833-858)	1.04 (1.02-1.06)		846 (833-858)		190	161	

[a]Values in parenthesis are 95% confidence limits.

[b]Percent of distance from surface to midline at which the LD_{50}'s for each exposure geometry were equal.

[c]Mean body weight at the time of irradiation for animals exposed within the LD_{16} to LD_{84} range.

FIGURE: 3

DOSE DISTRIBUTION AT 50% LETHALITY IN EXPERIMENT I

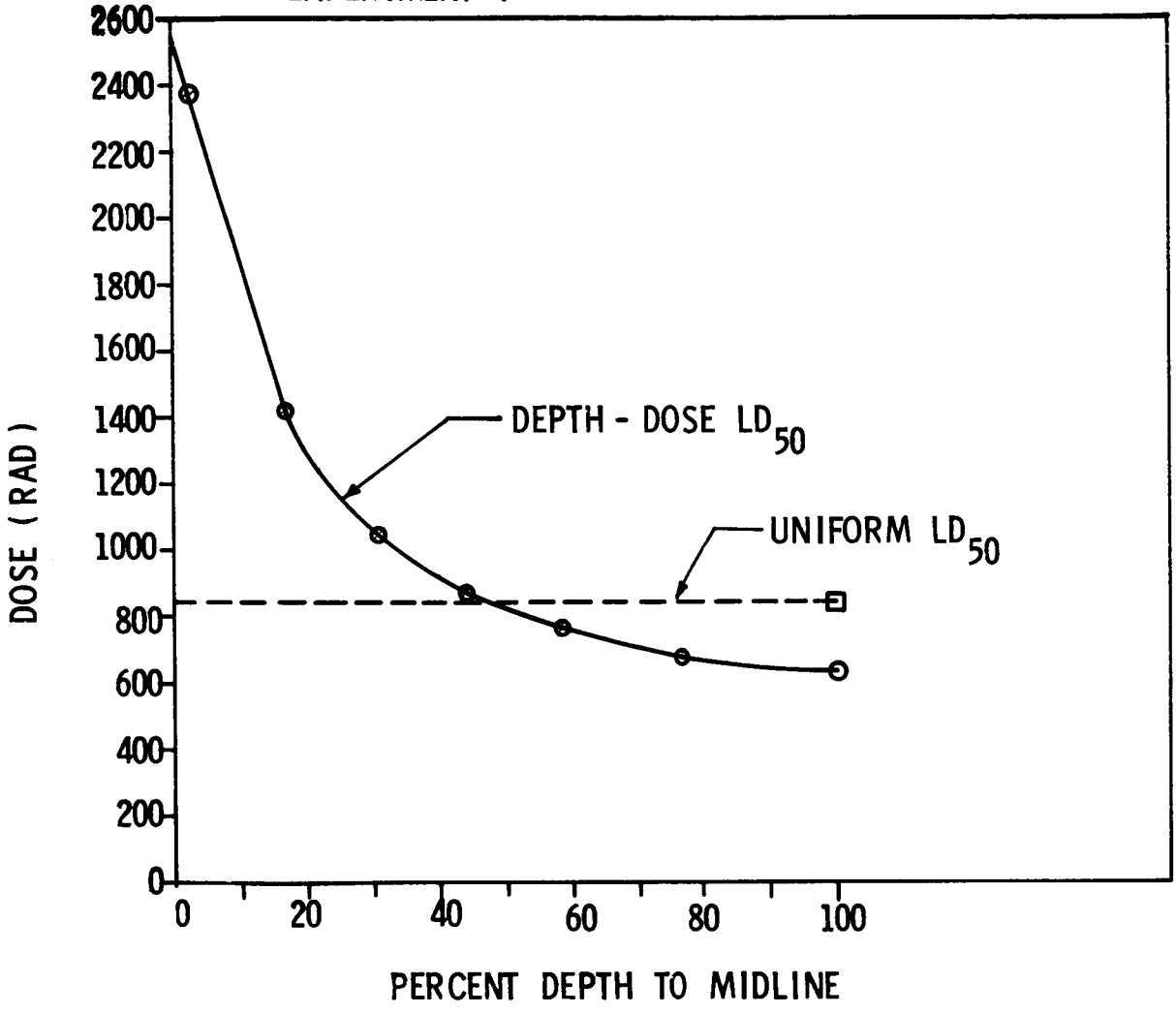

upper thorax area and the cylinder wall and the tail was coiled and generally in contact with the wall of the cylinder. The femoral portion of the hind limbs were in contact with the cylinder wall but the tibial portion varied considerably with respect to distance from the wall. Roentgenograms of a rat positioned in a cylinder showed that most of the bone structure was located near the surface of the animal but that a small amount of marrow was distributed at depths down to the midline as a result of curvature of the thoracic spine.

In order to determine if a lower dose to the tibial portion of the hind legs was responsible for any of the change in LD_{50} with depth-dose exposure, Experiment III was modified slightly. Sponge rubber pads were loosely taped between the hind legs so that in all exposures (depth-dose and uniform) the hind limbs were in contact with the cylinder walls. A total of 10 groups of twelve rats were exposed to graded surface radiation doses ranging from 820 to 897 rad and 2134 to 2910 rad. The data obtained in this experiment (Table I, Exp. III) show that positive positoning of the lower portion of the hind limbs did not decrease the depth-dose LD_{50}. The potency ratio of the LD_{50} was not significantly different from the values obtained in Experiments I and II. The estimated integral dose (Kgrad) delivered to depth-dose and uniformly exposed rats is given in Table I. At the LD_{50} the integral dose delivered to the depth-dose exposed rats was 1.5 times greater than the integ al dose delivered to the uniformly exposed rats.

All rats irradiated with depth-dose geometry in Experiments I, II, and III developed skin burns in about a 1-1/2 by 2 cm area on the thighs. This was pronounced during the third week post-exposure and epilation in the abdominal and back areas occurred during the fourth week. Body weights were followed in Experiments I and III and examination of these data revealed that mean body weight changes of animals exposed to doses within the LD_{16} to LD_{84} range did not differ significantly in the two exposure geometry groups at 1, 2, and 3 days post-irradiation. Body weights of survivors in the LD_{16} to LD_{84} range were not significantly different in the two exposure geometry groups at 30 days post-irradiation.

A difference in the mean survival times of depth-dose and uniform exposure groups, however, was detected as shown by the mean survival times given in Table II for decedents exposed to doses in the LD_{16} to LD_{84} range. These data indicate that in each experiment the mean survival time of depth-dose exposed rats was significantly less than mean survival time of the uniformly exposed rats. The median survival times were very close to the mean survival times, indicating the distributions about the means were symmetrical.

In Experiment IV intestinal weight changes as a function of time post-irradiation were measured in a group of rats irradiated with 40 per

Table 2. Mean Survival Times of Decedents Subjected to Depth-Dose and Uniform Exposures Within the LD_{16} and LD_{84} Range

Experiment No.	Exposure Geometry	Estimated Dose Range of LD_{16}-LD_{84} (rad)[a]	Range of Doses Delivered to Animals in LD_{16}-LD_{84} Range (rad)[a]	Total No. of Animals Exposed Within the LD_{16}-LD_{84} Range	No. of Decedents	Mean Survival Time (days)[b]	Probability
I	Depth-dose	2357-2658	2444-2641	12	5	10.2±0.2	< .01
	Uniform	829-864	837-860	12	6	11.7±0.2	
II	Depth-dose	2271-2854	2425-2668	12	4	10.3±1.1	.05
	Uniform	745-841	786-825	12	7	16.0±1.9	
III	Depth-dose	2381-3047	2522-2910	36	19	7.8±0.6	< .001
	Uniform	814-879	820-878	48	28	13.7±0.8	

[a]Surface doses

[b]Mean survival time ± standard error of the mean

cent of the mean surface depth-dose LD_{50} and in a second group of rats irradiated with 40 per cent of the mean uniform LD_{50} as measured in Experiments I, II and III. The doses employed were 1035 and 332 rad for depth-dose and uniform exposure, respectively. The changes observed in small intestine weight following irradiation are given in Fig. 4. These data indicate the intestinal weight loss was significantly greater in depth-dose exposed rats as compared to uniformly exposed rats on the first day ($p = .05$) and the second day ($p = .01$) following irradiation. During the recovery phase the mean intestinal weight overshoot of the non-irradiated control was greater in the depth-dose as compared to the uniformly exposed group although this difference was not significant.

Discussion

A factor which influences the magnitude of the LD_{50} in the rat is protraction of the dose due to differences in dose rate[16,17]. In the present study the time required to deliver a uniform LD_{50} was approximately 14 minutes (at 59 rad/min.) as compared to approximately 48 minutes for delivery of the depth-dose LD_{50}. An estimate of the effect of this difference in exposure time on LD_{50} can be made from data published by Logie, et. al.[17] for cobalt-60 gamma irradiation of the rat. Their data indicate that an increase in exposure time from 14 minutes (59 rad/min.) to 48 minutes would increase the LD_{50} by less than 10 per cent. In the present experiments the average surface LD_{50} and midline LD_{50} of depth-dose exposure were, respectively, 213 per cent greater and 22 per cent less than the LD_{50} of uniform exposure. Therefore, mechanisms other than dose protraction are responsible for differences observed in the lethal dose requirements of uniform and depth-dose irradiation.

It has been observed with soft X-irradiation[9-11] and confirmed in the present study that use of midline tissue dose fails to equate uniform and depth-dose LD_{50} values. The nature of the midline LD_{50} discrepancy, however, differs with cobalt-60 depth-dose and soft

---

16. Dacquisto, M. P. and E. W. Blackburn, The Influence of Delivery Rate of Whole Body 250 KV Roentgen Irradiation (30 or 3 Roentgens per Minute) on Mice, Rats, and Guinea Pigs. Am. J. Roentg. Radium Therapy Nuclear Med. 84:699-704 (1960).

17. Logie, L. C., M. D. Harris, R. E. Tatsch, and E. N. VanHooser, An Analysis of the $LD_{50(30)}$ as Related to Radiation Intensity. Rad. Res. 12:349-356 (1960).

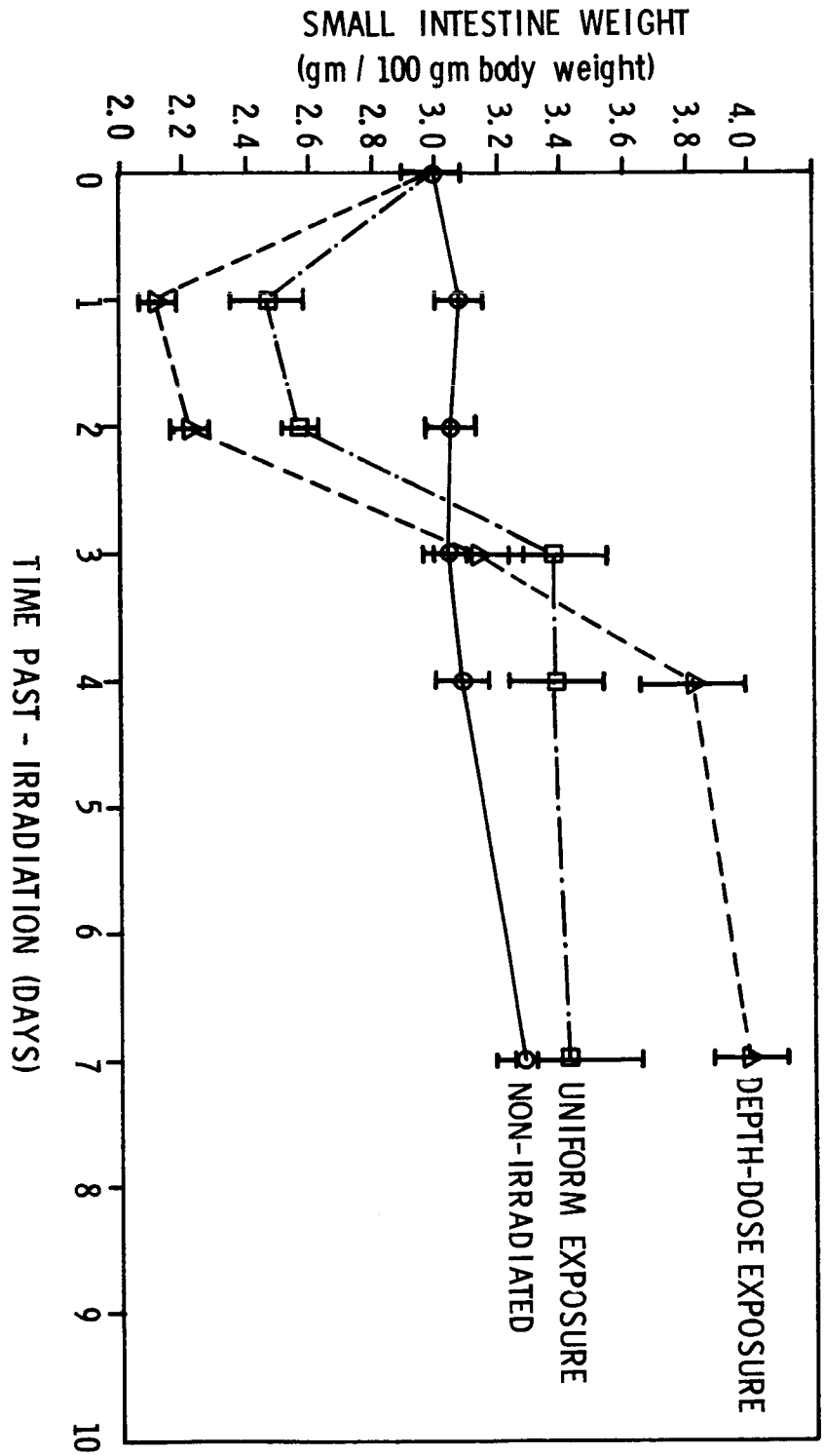

FIGURE: 4

SMALL INTESTINE WEIGHT CHANGES FOLLOWING UNIFORM AND DEPTH-DOSE IRRADIATION WITH 40% OF THE RESPECTIVE LD_{50}

X-radiation depth-dose exposure. When 80 KVP X-radiation[11], 100 KVP X-radiation[10,11] or 50 KVP X-radiation in combination with 250 KVP X-radiation[9] is used to produce depth-dose geometry, the midline LD_{50} is equal to or greater than the midline LD_{50} produced by uniform 250 KVP X-radiation. In contrast to this, in each experiment of the present study, the depth-dose midline LD_{50} was significantly lower than the uniform LD_{50} by an average of 22 per cent based on film dosimetry (and an average of 29 per cent based on Victoreen chamber measurement). The difference may be due to the marked reduction in marrow dose by surrounding bone when low voltage radiation is used[11,12] but which does not occur to an appreciable extent with high energy radiation such as cobalt-60 gamma radiation[12]. When a lethal depth-dose is produced by soft X-radiation, large soft tissue exposure as compared to uniform, hard X-ray exposure is required at marrow depths to produce sufficient injury in bone-shielded marrow. Use of soft X-radiation, therefore, results in a depth-dose midline LD_{50} which is greater than the uniform LD_{50}.

When depth-dose is produced with cobalt-60 gamma radiation, marrow receives a dose nearly equal to the soft tissue dose at the same depth in the body. As a consequence, sufficient injury to peripheral hematopoietic tissue can be produced to result in lethality without the need for a dose equal to that of uniform irradiation being delivered to the midline (Fig. 3). This is a depth-dose effect which is expected to occur with solar flare proton irradiation of man.

It is apparent from the integral dose values obtained in the present experiments (Table 1) that reduction of bone marrow shielding by use of depth-dose cobalt-60 gamma irradiation does not result in an integral dose equal to the uniform exposure integral dose. In fact, the ratio (depth-dose integral LD_{50} over uniform integral LD_{50}) of 1.5 measured in the present study is in the same range as the ratios observed for soft X-irradiation of large species where a significant depth-dose was produced; i.e., ratios of 1.3 and 2.1 for the rabbit[11] and 1.1 and 1.7 for the dog[9]. This suggests that non-uniform dose distribution, independent of bone shielding of marrow, plays an important role in the failure of the integral dose concept.

Inability of integral dose to equate uniform and depth-dose exposure is probably due to two general mechanisms: wasted energy and low doses to portions of critical organs. Some of the total absorbed energy from depth-dose exposure is wasted in tissues located closer to the surface than marrow and some energy may be wasted in critical organs maximally damaged at a lower dose than is received. Survival

of otherwise lethal gastrointestinal injury[18] or hematopoietic injury[19,20] by protection of a small portion of the critical organ system has been adequately demonstrated.

The significantly shorter survival time following depth-dose irradiation (Table 2) indicates that some factor relating to lethality is different in the two types of exposure geometry. This may result from semi-shielding of parts of the hematopoietic system during depth-dose exposure. Grahn, et.al.[11] have cited evidence, indicating that partial shielding of the hematopoietic system results in a decreased survival time. A shortened survival time, however, also suggests increased injury to the gastrointestinal tract since analyses of radiation dose-survival relationships in several mammalian species have revealed a short (3-5 day) survival time which is associated with irradiation of the intestine[21-24]. This hypothesis is strengthened by consideration of the position of the intestine in

---

18. Swift, M. N., and S. T. Taketa, Modification of Acute Intestinal Radiation Syndrome Through Shielding. Am. J. Physiol. 185:85-91 (1956).

19. Swift, M. N., S. T. Taketa and V. P. Bond, Efficacy of Hematopoietic Protective Procedures in Rats X-Irradiated with Intestine Shielded. Rad. Res. 4:186-192 (1956).

20. Alpen, E. L., and S. J. Baum, Modification of X-Radiation Lethality by Autologous Marrow Infusion in Dogs. Blood 13:1168-1175 (1958).

21. Quastler, H., Studies on Roentgen Death in Mice. I. Survival Time and Dosage. Am. J. Roentgenol. Radium Therapy 54:449-456 (1945).

22. Bond, V. P., M. N. Swift, A. C. Allen and M. C. Fishler, Sensitivity of Abdomen of Rat to X-Irradiation. Am. J. Physiol. 161:323-330 (1950).

23. Quastler, H., E. F. Lanze, M. E. Keller and J. W. Osborne, Studies on Roentgen Death in Mice. III. Acute Intestinal Radiation Death. Am. J. Physiol. 164:5456-556 (1951).

24. Cronkite, E. P., and G. Brecher, Effects of Whole-Body Irradiation. Ann. Rev. Med. 3:193-214 (1952).

the body relative to depth-dose distribution. In the peritoneal cavity the intestine is located in an approximate cylinder, which in the anterior portion is very close to the body surface. Due to this geometry a greater volume of intestine is located between the surface and half the distance to body-center than the amount of intestine located between body-center and half the distance to the surface. Calculations based on the depth-dose curve given in Fig. 2 reveal that, at the LD_{50}, the integral dose delivered to the body tissue of the rat located between the surface and half the distance to body-center was 1.7 times as great as the integral dose delivered to the same tissue by uniform irradiation. Thus, a large portion of the total intestine must have received a greater amount of energy than the same part of intestine in animals uniformly irradiated. In addition, the total body integral dose at the LD_{50} was 1.5 times as great as the uniform integral dose (Table 1) which implies that the integral dose to the total intestine was higher in depth-dose exposure as compared to uniform exposure.

Direct evidence for greater intestinal injury in depth-dose exposed rats is given by the small intestine weight changes shown in Fig. 4. The data show that when rats are subjected to the same injury as measured by mortality (i.e., 40 per cent of the respective LD_{50} for depth-dose or uniform exposure), the intestinal weight loss is significantly greater on the first two days following depth-dose exposure as compared to uniform exposure. Mean values for changes in intestine weight during the recovery phase suggest the overshoot of intestinal weight is also greater in the depth-dose exposed animals. These changes in total intestine weight are interpreted as an index of mucosa damage and recovery because previous studies with the rat have shown that total small intestine weight changes parallel mucosa weight, nitrogen, and DNA changes following irradiation[25]. An overshoot of total intestine weight, mucosa weight, and mucosa nitrogen (but not DNA) is associated with the recovery phase and in the present study the overshoot in depth-dose animals is additional evidence for greater intestinal injury following depth-dose exposure.

These data suggest that greater injury to the intestine of man may occur following solar flare proton exposure as compared to uniform body exposure. Thus, sublethal space proton depth-dose exposures may cause greater early gastrointestinal illness than has been observed following uniform exposure of humans[26].

---

25. Kay, R. E., and C. Entenman, Weight, Nitrogen and DNA Content of Small Intestine Mucosa of Rats Exposed to X-Rays. Am. J. Physiol. 197:13-18 (1959).

26. Miller, L. S., G. H. Fletcher and H. B. Gerstner, Systemic and Clinical Effects Induced in 263 Cancer Patients by Whole-Body X-Irradiation with Nominal Air Doses of 15 r to 200 r. U.S. Air Force School Aviat. Med. Report 57-92, May 1957.

Paper C-7

LET SPECTRUM AND RBE OF HIGH ENERGY PROTONS*

Hermann J. Schaefer
U. S. Naval School of Aviation Medicine

Abstract

High intensity proton radiations in space temporarily superimposed upon the ordinary cosmic ray beam have energy spectra extending from a few to many hundred Mev. Analysis of the LET spectrum of a typical flare produced proton beam shows that the bulk of the energy dissipation is effected with an LET spectrum closely resembling that of standard x-rays. A basic difference exists in the spectral region beyond 10 kev/micron tissue. Though the fractional dose in that region expressed in rad remains on the level of a few per cent, it represents a significant though not a major part of the total rem dose. It is suggested that both dose fractions be treated separately in assessing the ERD (Equivalent Residual Dose) with the recovery allowance of 2.5 per cent per day applicable only to the low LET fraction .

On the RBE of protons from terrestrial sources, a large volume of experimental data is available in the literature. In two sets of classical experiments, using protons, deuterons, and alpha particles from the Berkeley cyclotron, Tobias and co-workers[1]

---

*Opinions or conclusions contained in this report are those of the author. They are not to be construed as necessarily reflecting the views or the endorsement of the Navy Department.

1. C. A. Tobias, H. O. Anger, and J. H. Lawrence, Amer. J. Roentgenol. 67, 1 (1952).

and von Sallmann, Tobias, and co-workers[2] demonstrated the basic difference in the RBE of heavy particles in the energy range of several hundred Mev where the LET is low as compared to the terminal sections of the tracks of these particles corresponding to the energy range of a few Mev where the LET is high. Because of the low penetrating power of protons of the latter type, it is experimentally much easier to produce them indirectly as recoil protons within the specimen by means of neutron irradiation. With regard to RBE values obtained with this particular method the reader is referred to the comprehensive studies of Conger, Randolph, Sheppard, and Luippold[3] on chromosomal damage in tradescantia and of Storer, Harris, Furchner, and Langham[4] on acute effects in mammalian systems.

Proton radiations in space such as the trapped protons in the inner Van Allen Belt or flare produced solar protons are a mixture of the two types mentioned above. Already the incident beams show extremely heterogeneous energy spectra extending from a few Mev to several hundred Mev and beyond. This heterogeneity is further enhanced by the spectral degradation which occurs as the beam travels in absorber material. The RBE for space radiation protons, then, can be expected to assume an intermediate value between the lower limit of 1.0 found for protons of several hundred Mev and the much higher values up to 10 reported for neutron recoil protons.

In a previous study[5] an attempt has been made to establish theoretically a mean value for the RBE of protons in space by using the RBE/LET relationship as suggested in the official recommendations of the NCRP.[6] Quite obviously this approach leaves much to be desired from a scientific standpoint. A basic objection against it derives from the

---

2. L. von Sallmann, C. A. Tobias, H. O. Anger, C. Welch, S. F. Kimura, C. M. Munoz, and A. Drungis, A.M.A. Arch. of Ophthalm. 54, 489 (1955).

3. A. D. Conger, M. L. Randolph, C. W. Sheppard, and H. J. Luippold, Radiation Res. 9, 525 (1958).

4. J. B. Storer, P. S. Harris, J. E. Furchner, and W. H. Langham, Radiation Res. 6, 188 (1957).

5. H. J. Schaefer, Dosimetry of Proton Radiation in Space, U. S. Naval School of Aviation Medicine Project MR005.13-1002 Subtask 1, Report No. 19 (1961).

6. Permissible Dose from External Sources of Ionizing Radiation, Handbook 59, National Bureau of Standards, Washington, D. C., 1954.

fact that the LET as commonly quoted for any type of ionizing radiation merely denotes the total energy dissipated per unit length of path, yet does not convey any information on the actual spacing of the ionization events in the microstructure of the irradiated tissue. Though this is a well known fact Table 1 describes it in more detail. In the first column, selected kinetic energies of protons are listed. The second column shows the corresponding LET, the third column the maximum transferable energy to electrons, and the fourth column the range in tissue for electrons of the energies of the third column.

Table 1. Energy Dissipation Characteristics of Protons

Protons		First Order Secondary Electrons	
Kinetic Energy Mev	LET Kev/Micron Tissue	Max. Transf. Energy, Mev	Range in Tissue, Micron
100	.635	.231	556
50	1.08	.113	172
10	3.95	.022	10
1	21.35	.0022	.18

It is immediately seen that the distances over which the dissipated energy is actually spread are, for higher energies, considerably larger than one micron. For a true description of the energy dissipation, therefore, it would be necessary to carry out a complete analysis of the entire chain of events tracking down all secondaries until they come to rest. This leads to an LET spectrum rather than to a single LET value. It has been generally accepted in this type of analysis to consider an energy transfer to a secondary electron as local if an energy exchange of 100 e-volts or less is involved. The range of a 100 e-volt electron in tissue equals 0.003 micron or 30 AU (1 Angstrom Unit = 10^{-7} millimeter). The computational procedures of establishing the LET spectrum for any type of radiation is very complex. So far, such computations have been carried out only for selected types of radiations and selected energies. As an introduction to the literature, the study by Burch[7] should be consulted. For the heterogeneous proton spectra encountered in space the task is further complicated because a continuum of individual LET spectra for monoenergetic protons, covering the entire energy range of

7. P. R. J. Burch, Radiation Res. 6, 289 (1957).

interest has to be set up and then has to be integrated in order to obtain the LET spectrum of the heterogeneous beam.

An important and problematic issue in the LET analysis concerns the ranges in tissue along which a proton or electron of a certain energy maintains its local LET. The upper curve in Fig. 1 shows the local LET of protons and the lower one that of electrons as a function of residual range. It is seen that a proton maintains peak values

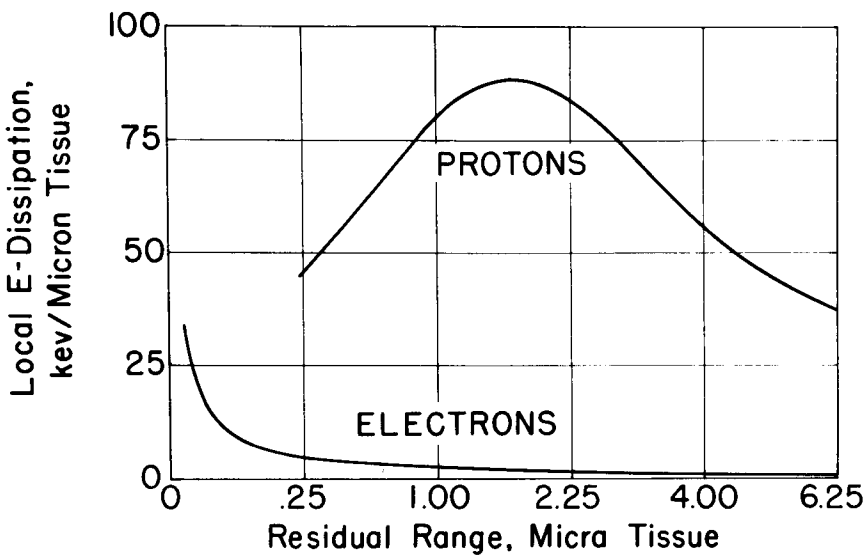

LOCAL ENERGY DISSIPATION OF PROTONS AND ELECTRONS IN THE TERMINAL SECTIONS OF THEIR TRACKS

Fig. 1

of the local LET over distances of several micra in tissue whereas an electron does so only for some 40 or 50 millimicra (400 or 500 AU). If we assume that the production of radiation damage in sensitive centers in the tissue fine structure requires penetration by an ionization column of at least several hundred AU length, the effectiveness of protons, i.e., the RBE, should be substantially greater than of electrons. This is in agreement with the experiment. It has been shown that photoelectrons of 1.3 kev are almost without effect in causing chromatid breaks due to their short range which renders them incapable of crossing the chromatid thread of about 1000 AU diameter. It is seen, then, that the concept of local energy dissipation, though it describes the microstructure of

the dose distribution much more accurately than the mean LET, has a severe limitation concerning those high LET values which are sustained only over very short distances. It is not within the scope of this treatise to discuss the microbiological significance of this difference in more detail. The reader is referred to the reviewing articles of Hutchinson,[8] Howard-Flanders,[9] and Hutchinson and Pollard.[10] In the present context, only one consequence is of importance. In establishing the LET spectra for protons in the energy interval below 1 Mev, where the local LET of the primary proton itself becomes equal to the maximum at the upper end of the LET spectrum of the electrons, the two contributions should not be added because they represent basically different types of radiation exposure for the reasons just explained. Figure 2 illustrates this

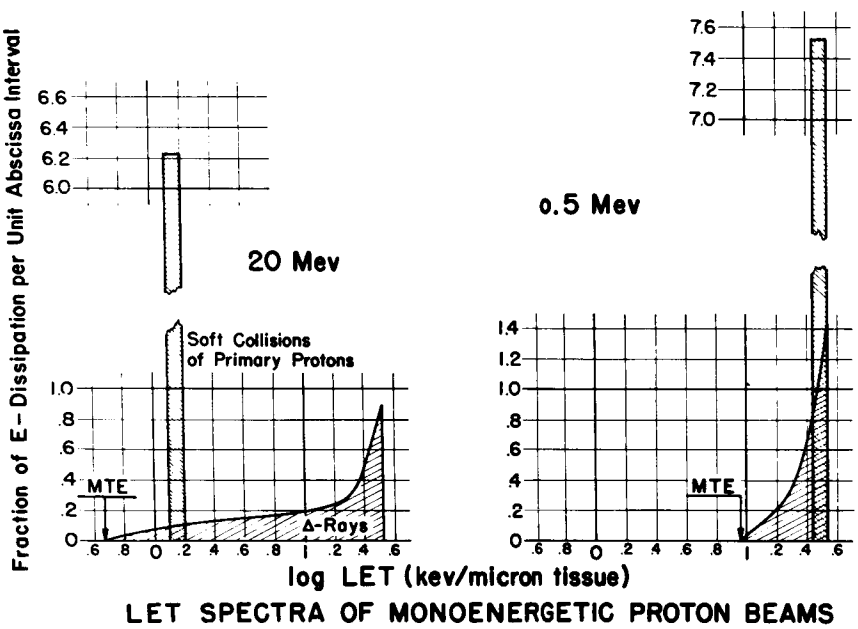

LET SPECTRA OF MONOENERGETIC PROTON BEAMS

Fig. 2

---

8. F. Hutchinson, Science 134, 533 (1961).

9. P. Howard-Flanders, "Physical and Chemical Mechanisms in the Injury of Cells by Ionizing Radiations," Advances in Biological and Medical Physics, Vol. VI, edited by C. A. Tobias and J. H. Lawrence, p. 553, Academic Press, New York, 1958.

10. F. Hutchinson and E. Pollard, "Target Theory and Radiation Effects on Biological Molecules," Mechanisms in Radiobiology, Vol. I, edited by M. Errera and A. Forssberg, Chap. 1.2, p. 71, Academic Press, New York, 1961.

graphically. Shown is at the left the LET spectrum of 20 Mev protons and at the right that of 0.5 Mev protons. The tall narrow columns represent, for both energies, the local energy dissipation of the parent proton itself, i.e., the energy imparted by the proton to electrons in so-called soft collisions in which the energy transfer does not exceed 100 e-volts. It is seen that this contribution coincides, for 0.5 Mev, with the peak LET of the secondary electrons from hard collisions. As shown above, the two contributions cannot be considered as identical nor consolidated into one spectrum.

Returning now to the original question of the RBE of a heterogeneous proton beam, we see that in integrating over the continuum of monoenergetic LET spectra for obtaining the resultant spectrum of the heterogeneous beam, only the contributions of the protons themselves should be considered. Figure 3 shows such resultant spectra for flare produced protons assuming 2 g/cm^2 (top) and 6 g/cm^2 (center) prefiltration. The bottom graph shows the LET spectrum for 220 kv x-rays as computed by Cormack and Johns.[11]

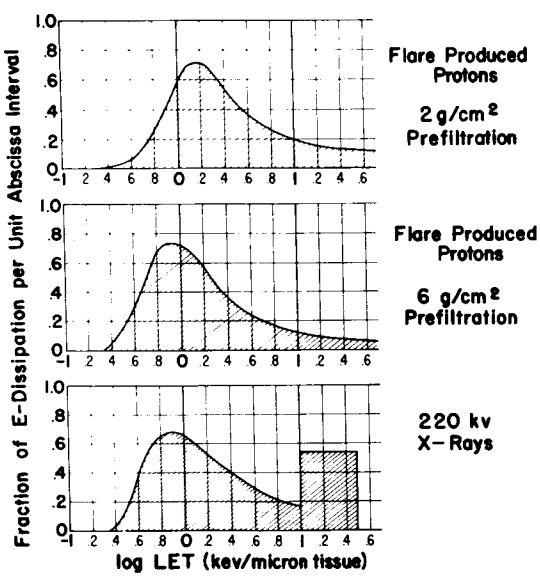

LET SPECTRA OF FLARE PRODUCED PROTONS AND OF 220 kv X-RAYS

Fig. 3

11. D. V. Cormack and H. E. Johns, Brit. J. Radiol. 25, 369 (1952).

The proton spectra, as might be expressly stated once again, show only the energy dissipation from the primary protons themselves. All secondary electrons, which receive a higher energy than 100 e-volt are disregarded. In the x-ray spectrum at the bottom, of course, all energy dissipation is due to electrons since there is no other ionizing agent present in 220 kv x-rays. The square shaped area above log LET = 1.0 is an artefact. Since the kinetics of energy dissipation below 1 kev is incompletely understood the energy dissipation in this interval is merely indicated by a square of correct total area.

As long as the comparative evaluation is limited to the LET interval below log LET = 1.0, it is interesting to note, from Fig. 3, that the two flare produced proton beams have LET spectra closely resembling that of standard x-rays. Obviously, then, this fraction representing the bulk of the total ionization dosage, should be assigned an RBE of 1.0. Beyond the point of log LET = 1.0 corresponding to an LET of 10 kev/micron tissue, however, no comparative evaluation of the proton spectra with the x-ray spectrum is allowed. This is so not just because the proton spectra in Fig. 3 do not contain the delta ray contributions, but more so for the principal reason that the high LET of the low energy delta rays are sustained over insufficient ranges for x-rays. In other words, the plateau in the x-ray spectrum beyond log LET = 1.0 represents a contribution to which an elevated RBE factor should not be assigned whereas the corresponding sections in the flare produced proton spectra represent rem doses that are substantially higher than the rad doses.

Of particular interest is a comparison of the LET spectra of flare produced protons to those of neutron produced recoil protons since the latter type radiation has been investigated by many experimenters with regard to the RBE. The center graph in Fig. 4 is identical with the center graph of Fig. 3. However, it is aligned with a lower graph showing the LET spectrum for the so-called Watt spectrum,[12] i.e., for neutron produced recoil protons from thermal fission of U-235. Again, only the energy dissipation of the protons themselves is indicated in both graphs. It is seen that, for the recoil protons, 80 per cent of the energy is dissipated at LET values in excess of the log LET = 1.0 limit in contrast to flare produced protons which dissipate more than 90 per cent of their energy at LET values below that limit. This statement pertains, of course, to the shares of the ionization dosages in rad. The rem doses of the right hand sections are substantially higher than the areas under the curves indicate.

---

12. B.E. Watt, Phys. Rev. 87, 1037 (1952).

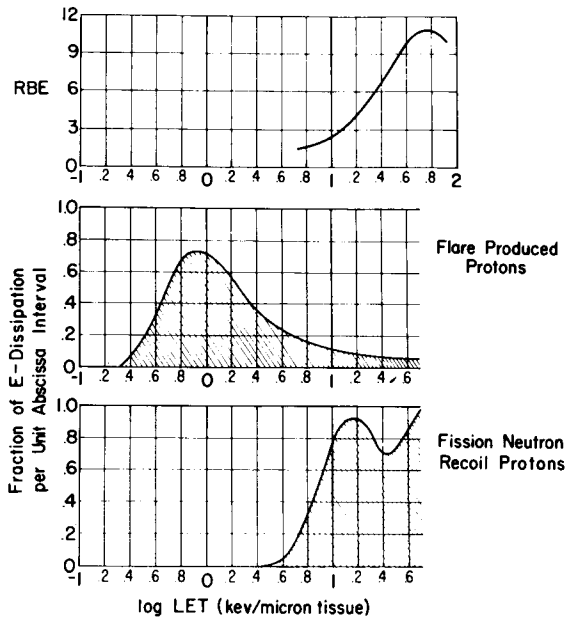

LET SPECTRA OF FLARE PRODUCED AND OF FISSION NEUTRON RECOIL PROTONS

Fig. 4

Very problematic is the question what RBE factor should be assigned to the high LET section beyond the 10 kev/micron limit. In official assessments of exposure status, it would seem proper to adhere to the Code of Federal Regulations [13] which assigns protons of the type characterized by the lower graph of Fig. 4 an RBE factor of 10. A more elaborate way, yet still using officially recommended data, would be to use the RBE/LET relationship suggested by the NCRP as mentioned above.[6] It seems of interest to point out that this latter method furnishes slightly smaller rem/r ratios if applied to the LET spectrum instead of to the mean LET value. The earlier values, therefore, and the mean values for the entire heterogeneous spectrum based thereon[5] provide a slightly larger safety margin from a radiation safety standpoint.

For reasons of scientific accuracy as well as from the practical viewpoint that the true radiation burden in a human target should be determined as closely as possible the foregoing approaches using definitions set forth in official regulations are not very

---

13. "Standards for Protection Against Radiation," Atomic Energy, Federal Regulations, Title 10, Chap. 1, Part 20, Atomic Energy Commission, 1958.

satisfactory. One has to realize, however, that a radiation which produces ionization in tissue at strictly one LET or at least at values in a narrow LET interval simply does not exist. Consequently, data on RBE factors for "monochromatic" LET values are not available. The closest approach seems to be the investigation of Conger and co-workers quoted above.[3] At least, these authors have given most careful consideration to the limitation under discussion. They arrive at an RBE/LET relationship which is shown in the upper graph of Fig. 4. It is seen that, in general agreement with the earlier estimates based on official recommendations, the critical interval of a steep rise of the RBE starts slightly below the log LET = 1.0 limit. It might also be mentioned that the data of Conger and co-workers shown in the upper graph of Fig. 4 pertain to cytological damage in tradescantia. As far as these data allow a comparison to the ones obtained by Storer and co-workers[4] on mammalian systems, the RBE for acute damage to the latter systems seems to be somewhat smaller. This again would provide for a further increase of the safety margin.

If we have arrived, in the foregoing discussion, at the conclusion that the mean LET and mean RBE furnish a total rem dose for flare produced proton radiation which closely compares to the rem dose derived from the detailed analysis of the LET spectrum, we must not lose sight of one important defect of the simplified method. We mean that it can never furnish a separate assessment of the fractional dose administered at a high LET. Though this fractional dose, assessed as ionization dose in rad, always remains on the level of a few per cent of the total ionization dose, it becomes a significant though not a major part of the total exposure after conversion into rem dose. Especially in estimates of the ERD (Equivalent Residual Dose) from repeated exposures to proton radiations in space it seems advisable to treat the two dose fractions separately allowing a recovery factor of 2.5 per cent per day only for the dose fraction whose LET spectrum closely resembles that of x-rays yet considering the high LET contribution as strictly cumulative. Another problem that comes up in this connection concerns the RBE factor that should be assigned to the high LET fraction if acute exposure or long term exposure at low dose rates is involved. Experimental evidence indicates that high LET irradiation, for the latter type of administration, shows a higher relative biological effectiveness. However, in the frame of the specific problems with which we are confronted in dealing with solar protons and the protons in the inner Van Allen Belt acute exposure seems of predominant interest. The discussion, therefore, can be terminated at this point.

Paper C-8

SOME DATA ON THE RELATIONSHIP OF RBE AND LET

W. S. Snyder
Oak Ridge National Laboratory

Abstract

The RBE of one radiation with respect to a standard radiation is usually defined as the inverse ratio of doses required to produce the same degree of a specified biological effect. It is well known that the RBE depends not only upon the quality of the radiations but also upon such conditions of exposure as dose rate, fractionation of dose, strain and condition of animals, and the biological effect studied. This paper analyzes some experimental data to obtain an indication of the dependence of RBE on LET. The cases considered include some experimental studies of effects on cells and on mice. The interpretation of such data for certain conditions of exposure in space is discussed in a preliminary way.

The relative biological effectiveness (RBE) of a radiation exposure A with respect to radiation exposure B and an end point T is usually defined as the inverse ratio of the doses $D_B(T)/D_A(T)$ required to produce the same degree of the biological effect T. The RBE of radiation dose has been found to depend upon many factors. The quality of the radiation, usually specified in terms of the rate of linear energy transfer (LET) along the tracks of the ionizing particles, is certainly one of the important factors, but it also is certain that it is not the only factor which must be considered. Many experiments have shown that dose level, dose rate, the biological end point and species used for the test, and the general situation during and after exposure may be important. Thus the RBE applicable to one exposure situation may not be applicable to another.

If we consider what the relevant conditions are likely to be for exposure during space flights of the next decade or so, it quickly becomes evident that there are a number of factors which combine to make this situation somewhat different than previous radiation exposures that man has experienced and learned to control acceptably. First of all, there is the unfamiliar nature of the radiation field -- the high-energy protons and neutrons, the mesons, and the nuclear cascade and evaporation phenomena, which are largely foreign to man's usual environment. However, there is no reason here for discouragement. Man faced a similar challenge scarcely more than 20 years ago when he had to learn to control exposure

to neutrons and exposure to a host of new radionuclides, such as Sr^{90}, Pu^{239}, etc. Then the health physicist turned to the exposure experience which had been gained with x-rays and with radium, and by judicious comparisons of the new with the old, adequate dose limits were found and a magnificent record of safety has been achieved. The concept of RBE was developed essentially for this purpose, i.e., to estimate the biological effects of the new situation in terms of previous experience with other types of radiation. There is no doubt that this is our surest course in controlling exposure in the present new situation posed by exploration of space. However, the judicious choice of RBE values for this new type of exposure will require that all factors affecting the RBE be examined and evaluated.

The RBE values appropriate for present occupational exposure may not be the same as the RBE appropriate for doses that may be incurred on certain missions in space. To use the one RBE for the other without a critical review of all the relevant factors is to betray a lack of understanding of the problem. Exposure over a working life at low dose rates may have quite different biological effects than exposure at a much higher rate for a period of a week or a month. Thus the period of exposure and the dose level must be considered as well as the LET or quality of the radiation. As a matter of fact, an Ad Hoc Committee of the ICRP on RBE has just reviewed RBE for occupational exposure and has suggested the use of other values of RBE in the case of acute accidental exposure at higher dose levels. Unfortunately, this committee did not consider the type of radiation fields likely to be encountered in space. However, those responsible for the design of the space craft and for executing the mission cannot afford to ignore the differences in exposure times and dose rates, as well as the differences in LET of the space situation as contrasted with the usual situation of occupational exposure. The success of the mission should not appear as accidental. The planning should include all fundamental aspects of the problem.

In attacking this very complicated problem, the maximum dose levels to be expected, the duration of the exposure, and the various biological effects of the exposure, all need to be taken into account. The following brief discussion of these aspects of the problem and of the bearing of LET on the problem are entirely preliminary and indicate directions of exploration rather than definitive conclusions. Although tentative, there are indications in presently available data that are quite suggestive of some conclusions. The items presented here are offered only as examples of problems where data now available suggest certain conclusions which are relevant to the problem of exposure in space and which seem to merit further study.

High energy particles, in themselves, do not seem to be a great problem. The LET is rather accurately known, and Tobias observed as long ago as 1952[1]

---

1. C. A. Tobias, H. O. Anger, and J. H. Lawrence, Am. J. Roentgenol. Ra. Therapy Nuc. Med. 67(1), 1 (1952).

that the LET on the plateau of the Bragg curve of high-energy protons, deuterons, and α particles was about that of 200 KVP x-rays and that it might be conjectured the biological effects would be similar. This has been in large part substantiated in quite a few studies of enzymes, bacteriophage, diploid yeast, and mammalian tumor cells. For example, Berry et al.,[2] in a paper now in course of publication, study the reproductive capacity of a mammalian tumor cell, P-388, irradiated in vivo by the plateau region of the tracks of 340-Mev protons or 380-Mev α particles and find a response roughly similar to that of 3-Mev x-rays, both in the oxygenated and in the anoxic condition. When the dose included sizable fractions of energy delivered from the Bragg-peak portion of the track, the effect was much more pronounced. This study is cited here mainly because a mammalian cell, irradiated in vivo, was used, but the conclusion that the biological response of very high-energy particles of low LET is, indeed, much like the response to x-rays is supported by experiments on many other biological materials.

There is also a remarkable suggestion of consistency in the biological response to the same LET from different particles. Figure 1 is adapted from a study of Fluke et al.[3] and shows phage survival cross-section as a function of LET for protons, deuterons, and ions of helium, carbon, and oxygen. It is to be recognized that the LET values used here do not include a correction for δ rays, but this should not entirely obscure the pattern that is evident. This figure illustrates also the quite common phenomenon that RBE decreases as LET increases beyond some rather high value, indicating a point beyond which energy is "wasted." The value of LET where the decrease begins to appear may vary somewhat with the type of ion and biological material, but the range does not appear to be extreme. Brustad[4] summarizes a number of such studies:

> "It has been shown that the RBE for inactivation of dry enzymes and bacteriophage (in both wet and dry states) decreases continuously with increasing LET... For all the biological systems studied thus far, however, the RBE was declining after the LET exceeded 300 kev/μ."

Another interesting pattern that is suggested relates to exposure time, i.e., to evidence, or lack of evidence, of repair processes. Andrews and Berry[5] have shown that there is no recovery between fractionated doses of fission-spectrum neutrons in their study of the mammalian tumor cells mentioned above. Berry et al. have now demonstrated that there is likewise little or no oxygen effect present in the case of fission-spectrum neutrons.[2] However, when the irradiation is by 14-Mev

---

2. R. J. Berry and J. R. Andrews, "The effect of radiation ionisation density (LET) upon the reproductive capacity of mammalian tumour cells irradiated and assayed in vivo," Unpublished.

3. D. J. Fluke, T. Brustad, and A. Birge, Rad. Res. 13, 788 (1960).

4. Tor Brustad, Rad. Res. 15, 139 (1961).

5. J. R. Andrews and R. J. Berry, Rad. Res. 16, 76 (1962).

UNCLASSIFIED
ORNL-LR-DWG. 74884

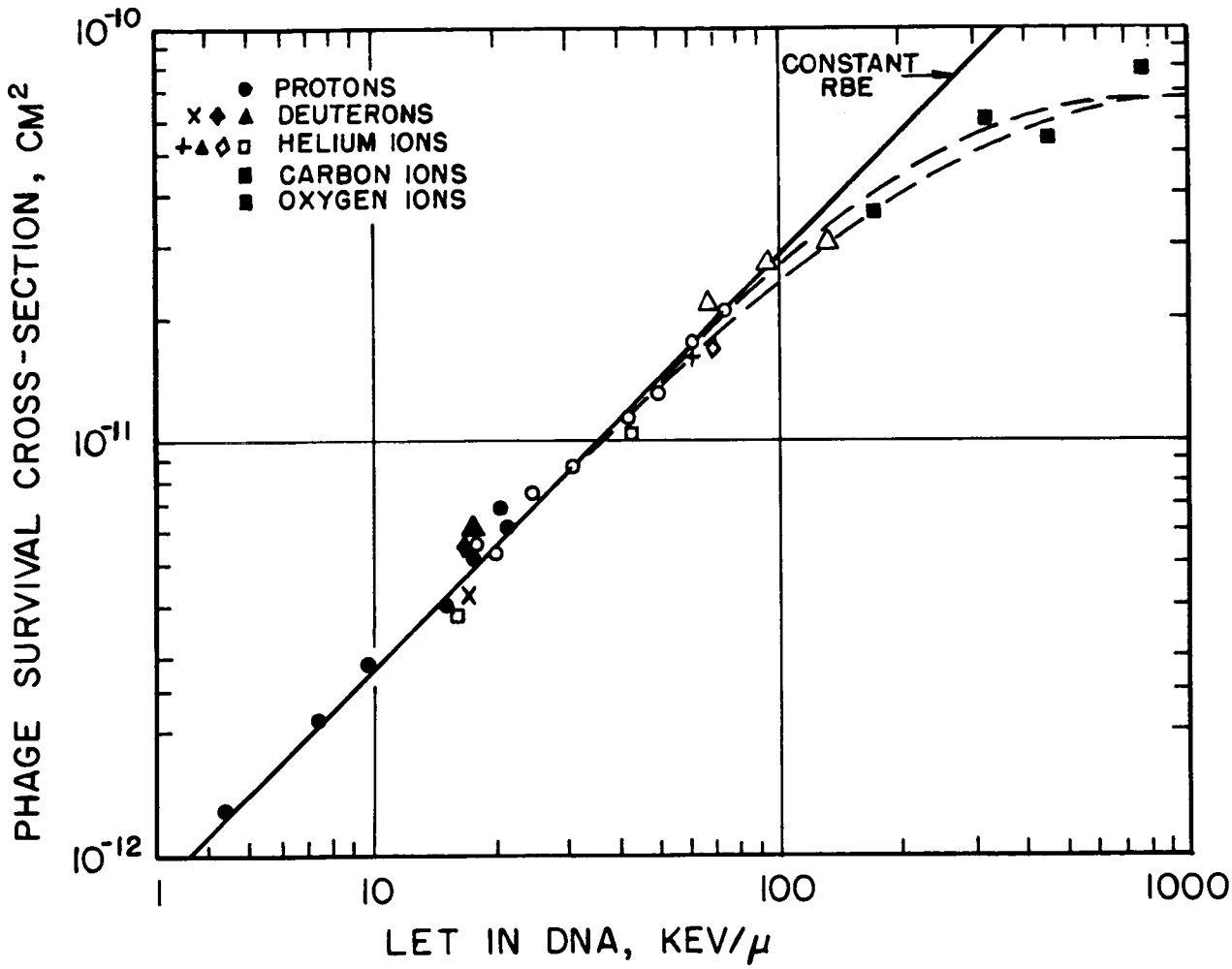

Fig. 1. RBE for Phage Survival as a Function of LET

neutrons, there is a pronounced oxygen effect, and it is probable that repair is present also. Here again the lower LET distribution of the 14-Mev neutrons seems to produce, to some extent, the type of response elicited by the classic low LET radiations. To illustrate the difference in the LET distribution of a modified-fission neutron spectrum and of monoenergetic, 14-Mev neutrons, Table 1 has been calculated using a distribution of neutron energies given by Neary[6] for a modified fission spectrum. Actually the values in Table 1 can be regarded only as qualitative since the calculation presented here represents only the first-collision dose. Nevertheless, it is apparent that there is a considerable difference in the LET distribution. The 14-Mev spectrum contains more

Table 1. Percentage of Neutron Dose in Various Ranges of LET

Neutron Source (kev/micron)	Modified-Fission-Spectrum Neutrons (% dose)	14-Mev Neutrons (% dose)
< 3.5	0.29	0.031
3.5-7	0.11	42.0
7-25	12.00	7.5
25-50	34.00	14.0
50-100	47.00	7.3
> 100	6.6	29.0

dose due to heavy-ion-recoil nuclei (range > 100 kev/μ) and less in the intermediate range of 50 to 100 kev/μ as compared with the LET spectrum of the fission neutrons. Considering the different responses reported by Berry et al., there is here, again, the suggestion that beyond a value of 100 kev/μ the RBE does not increase, but a shift of LET downward below the region of about 50 kev/μ may be significant. It should not be inferred from the above oversimplified discussion that these conclusions are firm at the present time, or that there are no problems of interpretation concerning these and other like studies. The opposite is true -- the detailed dosimetry is largely qualitative or only semi-quantitative, and there are many details and special considerations that require interpretation. Nevertheless, there is also a broad trend that is suggested by the data.

Finally, there is something that can be said concerning the influence of exposure time on the RBE. Neary[7] summarizes as follows the available data on RBE for the modified fission spectrum of neutrons as obtained using mice:

---

6. G. J. Neary, R. J. Munson and R. H. Mole, Chronic Radiation Hazards, p. 25, Pergamon Press, London, 1957.

7. Id., Ibid., p. 182.

> "Comparisons of fast neutron and gamma irradiation were made for exposure times from 24 hours to 9 months. Within this range there was no evidence that alterations in exposure time or dose rate altered the r.b.e., and published evidence to the contrary is critically examined and found wanting."

Neary also concludes that:

> "A comparison of all available information on mortality of chronically irradiated mice suggests that the r.b.e. for this effect is likely to be about 10."

The RBE he obtained for reduction of testis weight, impairment of fertility, reduction in spleen weight and in white cell count of peripheral blood were all less than 10. He concludes that:

> "Evidence was obtained that the gonads are the most sensitive organs in the mouse to chronic irradiation at very low dose rates."

Thus, there are suggestive trends in available data which offer considerable guidance in selecting RBE values appropriate for the particular conditions of exposure in space. To best interpret these trends, a more detailed knowledge of the LET spectrum obtained in the various experiments is desirable. The average LET is probably too gross a measure of radiation quality to be adequate, particularly over enormous ranges of LET. Yet much of the experimental work is reported only in terms of an average LET and needs to be reinterpreted. A more detailed knowledge of the spectrum, either by calculation along lines roughly indicated here, or by methods developed by Rossi,[8] is needed.

In summary, two conclusions have been advanced which are considered to be firmly supported by the experimental work relating to RBE:

1. The RBE to be applied for exploration in space should not be taken from currently accepted values for quite different exposure situations without a careful reassessment of all factors affecting the RBE, and LET is one, but only one, such factor. If shield weight is of critical concern, so is the question of biological effectiveness of the radiation, and the closer the design must approach critical limits of dose, the more important is the need for a careful assessment of RBE values.

2. It seems quite clear that there are many RBE values relevant to the problem and not just one value. For example, RBE's for acute effects and for long-term effects -- or for genetic damage contrasted with shortening of life -- require independent consideration.

---

8. H. H. Rossi, et al., Rad. Res. 13, 503 (1960).

The following points are not, perhaps, as firmly established, but are strongly suggested by much of the available data.

1. There is a value of LET below which the biological action of high-energy protons, α particles, etc., behave very much like x-rays. This value probably is somewhere between 25 to 50 kev/μ.

2. There is a higher range of LET values where all the heavy ions behave similarly -- lack of repair, decreasing values of RBE, etc. This value probably is about 100 kev/μ or near this value.

3. Within the exposure times, from a day to weeks or several months, as currently envisaged for space missions, the RBE probably does not vary markedly, and the values used for late effects are probably not far from those appropriate for chronic exposure. On the other hand, where acute effects are concerned, the exposure times are probably sufficiently long to allow for considerable repair of damage due to the low LET components of the dose.

TID-7652

Proceedings of the Symposium
on the

Protection Against Radiation Hazards in Space

held in
Gatlinburg, Tennessee
November 5-7, 1962

BOOK 2

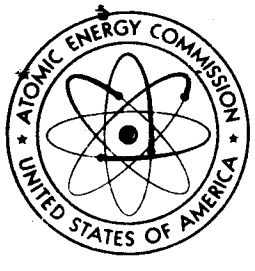

UNITED STATES ATOMIC ENERGY COMMISSION
Division of Technical Information

Code 3

LEGAL NOTICE

This report has been reproduced directly from the best available copy.

Printed in USA. This document consists of 2 books, total price $7.00. Available from the Office of Technical Services, Department of Commerce, Washington 25, D. C.

USAEC Division of Technical Information Extension, Oak Ridge, Tennessee

BOOK 2

Paper D-2

MEASUREMENTS OF SECONDARY SPECTRA FROM HIGH-ENERGY NUCLEAR REACTIONS

Karl Strauch, Harvard University

Abstract

The mechanism of the interaction of a high energy nucleon with a complex nucleus is discussed, and the various types of reaction are described. The available experimental data on secondary particles is summarized, emphasis being placed on those secondaries that might be important for shielding considerations.

Introduction

A beam of high energy neutrons passing through matter is attenuated by inelastic collisions with nuclei present in the material. A beam of high energy charged particles such as protons is attenuated by the same mechanism and in addition the proton kinetic energy decreases as the beam penetrates the material due to collisions with atomic electrons. The higher the energy of a proton, the more important is the role of nuclear collisions before the proton has reached the end of its range: about 15 percent of the protons in a 150 Mev beam will suffer an inelastic nuclear collision before stopping.

Inelastic nuclear collisions result in a variety of secondary particles with complicated energy and angular distributions. This paper uses the existing data to discuss and summarize as far as it is possible the properties of the secondary particles emitted when a high energy neutron or proton interacts with a complex nucleus. The role of secondaries must be considered in the design of shielding for space probes and capsules.

For the purpose of this paper the "high-energy" region is taken to extend from about 80 Mev to 500 Mev. Nucleons with energies higher than this limit do not appear to be present in space in sufficient number to be of importance in shielding considerations[1]. For the sake of completeness these limits will not always be used rigidly.

The probability of inelastic nuclear collisions is measured by the absorption cross section. Measurements of this cross section with both protons and neutrons exist for a variety of elements in the energy region of interest[2-5]. We will be concerned with what happens when an incident nucleon interacts with a nucleus. The general properties of secondary particles expected on the basis of the high energy reaction model will be considered first. Experimental results will then be discussed. The most recent measurements will be stressed; references to older measurements can usually be found in the more recent reports.

Reaction Mechanism

The mechanism of high energy reactions is dominated by two important facts: (1) The de Broglie wave length of the incident nucleon is small compared to the typical distance between nucleons inside the target nucleus. (2) The mean free path in nuclear matter of a high energy nucleon is of the order of the diameter of a light nucleus. The incident nucleon can thus be localized within the target nucleus, and its progress across it described by one or more nucleon-nucleon collisions inside the target nucleus.

A nucleus is a very complex system - various so called "models" exist to describe particular features of the system. The individual particle model which we will find most useful is illustrated in figure 1a. Nucleons exist in definite energy levels inside a potential well of depth V. These nucleons are not at rest, but continuously move around the well - the detailed features of this motion are characteristic of the quantum numbers describing the individual levels. The highest occupied level corresponds to a binding energy B. E. A particle of kinetic energy T_i has, after penetration inside the nucleus, a kinetic energy $T_i + V$.

[1]See papers presented in session A of this conference.

[2]R. Goloskie and K. Strauch, Nucl. Phys. 29, 474 (1962).

[3]A. F. Kirschbaum, University of California, Lawrence Radiation Laboratory report No. 1967 (1954).

[4]R. G. P. Voss and R. Wilson, Proc. Phys. Soc. 236, 41 (1956)

[5]W. P. Ball, Univ. of Calif. Lawrence Radiation Lab, report 1938 (1952).

Let us now consider the first nucleon-nucleon collision as the incident nucleon passes through the nucleus. The incident nucleon has a kinetic energy $T_i + V$ and the target nucleon has a typical momentum probability distribution which corresponds to kinetic energy values smaller than V. If during the collision the momentum transferred to the target nucleon is of the same order or smaller than typical momentum values before the collision, then the final state of the target nucleon is determined by the structure of the residual nucleus. For instance, the nucleon-nucleon collision can raise the target nucleon to an unoccupied excited level. If the incident nucleon leaves without further collision, it emerges, neglecting nuclear recoil, with a kinetic energy $T_i - E_{exc}$. The excited nucleus will return to its ground state usually emitting one or more photons with a combined energy of E_{exc}. This is called a "near-elastic" collision (figure 1b). More complicated excitations of nuclear substructures such as alpha particles or of the nucleus as a whole can also occur.

If the target nucleon receives a momentum which is large compared to typical nucleon moments inside a nucleus, then the effect of the residual nucleus on the final states is small. The collision is similar to a free nucleon-nucleon collision - only the target nucleon has an initial momentum distribution and the binding energy B.E.has to be supplied to the nucleus. If both partners have no further inelastic interactions before leaving the nucleus, they will emergy with energies of roughly $(T_i - B.E.) \cos^2 \theta$ and $(T_i - B.E.) \sin^2 \theta$ respectively where θ is the scattering angle of the incident particle. The residual nucleus can be left in an excited state which will usually decay into the ground state by emission of one or more photons. The name customarily given to this process is "quasi-elastic" collision (figure 1b).

These two simple interactions demanded that only one interaction takes place: this is fairly probably in light nuclei as long as the emerging nucleons have kinetic energies of more than 80 Mev or so. The value of the free nucleon-nucleon cross section increases rapidly below this energy as shown in figure 2[6]. Consequently the nucleon mean free path in nuclear matter decreases rapidly below 80 Mev.

In the more common case two or more collisions take place inside the nucleus and a nuclear cascade is initiated. The energy concentrated in any one nucleon decreases as the cascade progresses until all the energy which has not escaped as intermediate energy secondaries is fairly evenly distributed; the nucleon then "boils-off" this energy by emitting protons and more often neutrons in the Mev energy region. These are the "multiple collision" interactions (figure 1b).

The secondary particle spectrum that results from these processes is sketched in figure 3. Close to the elastic peak at T_{inc} are the near-elastic peaks which correspond to the level structure of the target nucleus. A fairly prominent peak at about (T_{inc} - 20 Mev) corresponds to the excitation of the dipole resonant state first observed in photoproduction. A quasi-elastic peak exists at (T_{inc} - B. E.) $\cos^2\theta$ whose width is determined by the momentum distribution of the target nucleons. The lower energy peaks ride on a rising continuum of cascade particles. Finally a low energy peak due to boil-off particles exists at about 2 Mev for neutrons or at the coulomb barrier energy if they are protons. It must be emphasized that figure 3 is presented mainly as a summary of the possible features of secondary particle spectra in high energy reactions. The relative importance of the near-elastic peaks, the quasi-elastic broad peak, the multiple collision continuum and of the boil-off peak depends strongly on the energy of the incident nucleon and the atomic number of the target nucleus. Some or all of the features sketched on figure 3 are expected for both proton or neutron secondaries with proton or neutron primaries - only the presence of the elastic peak depends on whether or not the secondary spectrum is of the same type as the incident particle.

It must also be remembered that the observation of some or all of the expected peaks in figure 3 depends critically on the experimental energy resolution.

As far as angular distribution of secondary particles is concerned, the reaction model which has been discussed suggests the following:

1. The "near-elastic" events have a strong forward peak similar to elastic scattering. Actually there might well be a dip in the extreme forward direction because of angular momentum considerations for a given excited level.

2. The "quasi-elastic" events have a distribution closely related to free nucleon-nucleon collision angular distributions in the laboratory frame.

3. Cascade particles have a general forward emission, the more pronounced the higher their energy.

4. The low energy boil-off particles are emitted isotropically.

Experimental Data

It is difficult to make detailed predictions using the reaction model discussed in the preceeding section. Phenomenological constants such as nuclear shape, well depth and mean free path must be used[7]. Those features of the secondary particles that depend on specific properties of the target or residual nucleus are especially hard to calculate. Experimental results are therefore necessary to check the validity of the general feature of the reaction model and the detailed theoretical predictions.

Low energy secondary particles will be considered first. Using 160 Mev protons, Fox and Ramsey[8] have obtained proton spectra from 5 - 23 Mev at 60°, 90° and 120° with Zn, Sn, Ta and Pb targets. Figures 4 and 5 show their results with Zn and Pb. Protons with an energy below 10 Mev are emitted isotropically, and the Coulomb barrier inhibits their emission as the target becomes heavier. Gross[9] has used 190 Mev protons to study neutron spectra from 0.5 - 12 Mev at 45°, 90° and 135° emitted by C, Al, Ni, Ag, Au and U targets. Figure 6 shows his results with U: the spectrum has the typical evaporation characteristics and appears to be isotropic - as are the spectra from the other targets. Neutron spectra at 180° have also been obtained earlier with 157 Mev protons incident on C and W targets[10]. The absolute neutron yields obtained in these experiments will be discussed below. Comprehensive studies of photons emitted in high energy nuclear reactions have become available only recently[11-13]. Using 150 Mev protons from the Harwell cyclotron, gamma ray spectra up to 7 Mev have been obtained from a variety of targets from Li to S. Absolute cross sections are also reported and will be discussed below. It is interesting to note that most of the observed gamma-rays can be identified with residual nuclei that can be reached by near-elastic or quasi-elastic collisions.

[7]See for instance paper of H. W. Bertini presented at this session.

[8]R. Fox and N. F. Ramsey, Phys. Rev. 125, 1609 (1962).

[9]E. E. Gross, University of California, Lawrence Radiation Laboratory reports No. 3330 and 3337 (1956).

[10]D. M. Skyrme and W. S. C. Williams, Phil Mag. 42, 1187 (1951).

[11]K. J. Foley, A. B. Clegg and G. L. Salmon, Nucl. Phys. 37, 23 (1962).

[12]K. J. Foley, G. L. Salmon and A. B. Clegg, Nucl. Phys. 31, 43 (1962).

[13]A. B. Clegg, K. J. Foley, G. L. Salmon and R. E. Segel, Proc. Phys. Soc. 78, 681 (1961).

Figure 7 shows the absolute yield measurements as a function of the atomic weight of the target; As checked roughly experimentally, the angular distributions of low energy secondaries are isotropic. This fact was used in calculating the absolute yields. For comparison, a plot of proton inelastic cross sections at 133 Mev[2] is also included. We see that for heavy elements the low energy neutron yield per measured collision rises to 9 - the low energy proton yield is very small. For atomic weights of 30 - 40 mass units, the yield of neutrons, protons and photons per inelastic collision is about 2, 0.8 and 0.5 respectively. These numbers can only be considered as guides - absolute cross sections, especially for neutrons and gamma rays, are hard to obtain accurately. As can be seen by comparing the 190 Mev and 157 Mev neutron yields - it seems unlikely that the differences can be accounted entirely by the difference in incident energy.

For a given target nucleus, the number of low energy particles per inelastic collision should be proportional to the average energy left in the residual nucleus after the direct cascade has terminated. This average energy can be obtained by Monte Carlo type calculations and it should therefore be possible to extrapolate with fair accuracy the above experimental results to other incident energies.

High and medium energy secondaries will be discussed next. Proton spectra will be considered first. Using 96 Mev protons, secondary protons from 40 - 96 Mev have been observed at 40° from a variety of targets from Li to Bi[14]. Figure 8 shows the C spectrum obtained in this work: besides the elastic and near-elastic peaks, there is a strong continuum. The quasi-elastic peak is too broad or too small in size to have been observed at this energy. Fig. 9 shows the Bi spectrum: the experimental resolution is too poor to resolve the near-elastic peaks and the spectrum is dominated by cascade processes. The near-elastic peaks have been studied extensively by the Upsala group[15-18] using 185 Mev protons

[14]K. Strauch and F. Titus, Phys. Rev. 104, 191 (1956).

[15]H. Tyren and Th. A. J. Maris, Nucl. Phys. 4, 637 (1957).

[16]H. Tyren and Th. A. J. Maris, Nucl. Phys. 6, 82 (1958).

[17]H. Tyren and Th. A. J. Maris, Nucl. Phys. 6, 446 (1958).

[18]H. Tyren and Th. A. J. Maris, Nucl. Phys. 7, 24 (1958).

with a variety of targets from Li to Zn.. These near-elastic secondaries are of great interest for the understanding of nuclear structure. However since they occur in only a small fraction of the total available energy range, these secondaries play a relatively small role in the total yield of secondaries. This can be seen in figure 14 on which the yield of near elastic secondaries as obtained in Upsala can be compared with the inelastic cross section. It is for this reason that near-elastic secondaries will not be considered in more detail.

Secondary proton spectra have been obtained at Berkeley with 330 Mev protons[19,20] and at Dubna with 661 Mev protons[21]. The Berkeley experiments were carried out with Li, C, Al, Cu, Cd and Pb targets, and secondary proton spectra in the energy range 50 Mev - 300 Mev were observed at 40° with all targets, and at 26°, 30° and 60° with some targets. The Dubna work was carried out with Be, C, Cu and U targets, secondary protons in the energy range of about 100 Mev - 600 Mev being observed at angles of 7°, 12.2°, 18°, 24° and 30°. Figures 10 and 11 show the Berkeley results at 40° obtained with a C and Pb target respectively. The general features of these spectra are typical of both the 300 Mev and 661 Mev results. The quasi-elastic peak dominates the secondary spectrum from light elements, while cascade particles are very important in the spectra from heavy elements. The Dubna group estimates from their results that quadi-elastic scattering at 30° varies from ≈ 60% to ≈ 9% of free nucleon-nucleon scattering when going from Be to U. Note that in both experiments the energy resolution is too poor to observe near-elastic peaks in these spectra.

---

[19]W. N. Hess and B. J. Moyer, Phys. Rev. 101, 337 (1956).

[20]J. B. Cladis, W. N. Hess and B. J. Moyer, Phys. Rev. 87, 425 (1952).

[21]L. S. Azligirey, I. K. Vzozov, V. P. Vrelov, M. G. Mescheryakov, B. S. Neganov, R. M. Ryudin and A. F. Shabudin, Nucl. Phys. 13, 258 (1959).

The Dubna work represents the most comprehensive angular study of proton secondaries from several elements. An angular region from 30° to 70° has been studied at Harvard [22] with 95 Mev protons passing through a carbon target. Figure 12 shows the results. The general forward peaking is apparent, with the higher energy secondaries being more forward peaked.

We now turn to spectra of secondary neutrons of high and intermediate energies. Because these could be obtained with internal cyclotron targets, they were some of the earliest spectra measured at Rochester with 244 Mev protons [23], at Harwell with 171 Mev protons[24] and at Harvard with 95 Mev protons[25]. A variety of targets were used. All of these measurements suffered from poor energy resolution. It might be added that neutron spectra from Be of similar poor energy resolution are scattered throughout the literature for a variety of proton energies in articles reporting experiments done with secondary neutron beams.

The development of time-of-flight methods at Harwell has permitted the observation of neutron spectra with much better energy resolution. Results with 143 Mev protons have been reported for many targets in the forward direction[26]: these show a strong charge exchange quasi-elastic peak whose relative importance decreases as the target atomic weight increases. More recent measurements with still better resolution at 95 Mev[27] show the existence of near-elastic peaks similar to those already observed with protons. The usefulness of this work will increase still further when absolute cross sections are reported, and a wider angular region is covered.

---

[22]K. Strauch and F. Titus, Phys. Rev. 103, 200 (1956).

[23]B. K. Nelson, G. Guernsey and G. Mott, Phys. Rev. 88, 1 (1952).

[24]T. C. Randle, J. M. Cassels, T. G. Pickavance and A. E. Taylor, Phil. Mag. 44, 425 (1953).

[25]J. A. Hofmann and K. Strauch, Phys. Rev. 90, 449 (1953).

[26]P. H. Bowen, G. C. Cox, J. B. Huxtable, J. P. Scanlan, J. J. Thresher and A. Langsford, Nucl. Phys. 30, 475 (1962).

[27]private communication

The measurements of intermediate and high energy secondary protons and neutrons as discussed so far have all been carried out with good angular resolution and over a limited angular region. They are very useful in checking the theoretical secondary spectra calculated with the high energy reaction model. In order to get an idea of the importance of intermediate and high energy secondaries, per inelastic collision, the neutron yield, above 45 Mev obtained with 90 Mev protons[25] have been plotted in figure 13. The results have been smoothly extrapolated to 50° and the corresponding proton yields at 40°[14] serve as a rough check of this extrapolation.

Figure 14 shows that at 90Mev there is about a 20 percent probability per inelastic collision of emitting a neutron above 49 Mev at an angle of less than 50°. It is worth noting that the cross section of near-elastic events at 185 Mev is 5 per cent or less of the absorption cross section in three elements.

Bernardini, Booth and Lindenbaum[28] have measured the number of prongs per visible interaction in emulsion. They obtain the following ratios for Ag - Br with 350 - 400 Mev protons and 300 Mev neutrons: secondary proton $E < 30$ Mev: 3.1; 30 Mev $\leq E < 100$ Mev: 0.42; $E > 100$ Mev: 0.35. These emulsion results represent probably the most reliable information available to date on the number of secondary protons/nucleon interaction.

Since photons are primarily emitted by excited nuclei after particle emission has become impossible, few photons are emitted with energies above typical particle binding energies. Special selection rules can however intervene to produce photons with energies higher than about 7 Mev: one such example is the 15.2 Mev photon emitted by carbon[29].

Only photon, proton and neutron secondaries have been discussed in detail. Deuterons, tritons, helium secondaries also exist, but as shown first by Hadley and York[30] with 90 Mev

---

[28]G. Bernardini, E. T. Booth and S. J. Lindenbaum, Phys. Rev. 85, 826 (1952).

[29]D. Cohen, B. J. Moyer, H. Shaw and C. Waddell, Phys. Rev. 96, 714 (1954).

[30]J. Hadley and H. York, Phys. Rev. 80, 345 (1950).

neutrons, their importance is relatively small. In C the number of deuterons with energies above 27 Mev per inelastic collision was found to be 0.12 and this number decreases with increasing weight of both target and secondary. More recent measurements[31,32] confirm the numerically smaller importance of heavy secondaries. Just as the nearly-elastic protons, heavy secondaries, although small in numbers are of considerable interest for nuclear structure investigations.

Conclusion

For the purpose of investigating nuclear structure, the most interesting events among the secondaries in high energy reactions are those resulting from near elastic and pure quasi-elastic processes. It is somewhat unfortunate for the purpose of this conference that the overall importance of these events is small since most of the recent work has been concentrated on picking out these events. However as has been discussed a considerable number of studies of secondary particle spectra exist and these should permit a satisfactory adjustment of the parameters needed for conventional Monte-Carlo type calculations of high energy reactions. Such calculations can of course not give features such as near-elastic peaks which depend on the detailed properties of the target or residual nucleus.

Many of the cross sections reported in the references were obtained by comparison with then accepted values of the proton-proton cross section or of reaction cross sections such as $C^{12}(p, pn)C^{11}$. The absolute values of some of these cross sections have been improved since the original work was done and when high accuracy is required, the quoted cross sections should be corrected accordingly[33].

The author wishes to thank Mr. H. W. Bertini and Dr. F. C. Maienschein for help in compiling the references.

---

[31] L. E. Bailey, University of California, Lawrence Radiation Laboratory Report 3334.

[32] P. F. Cooper and R. Wilson, Nucl. Phys. 15, 373 (1960).

[33] A recent measurement containing references to others: K. Goebel, D. Harting, J. C. Kluyver, A. Kusunegi and H. Schultes, Nucl. Phys. 24, 28 (1961).

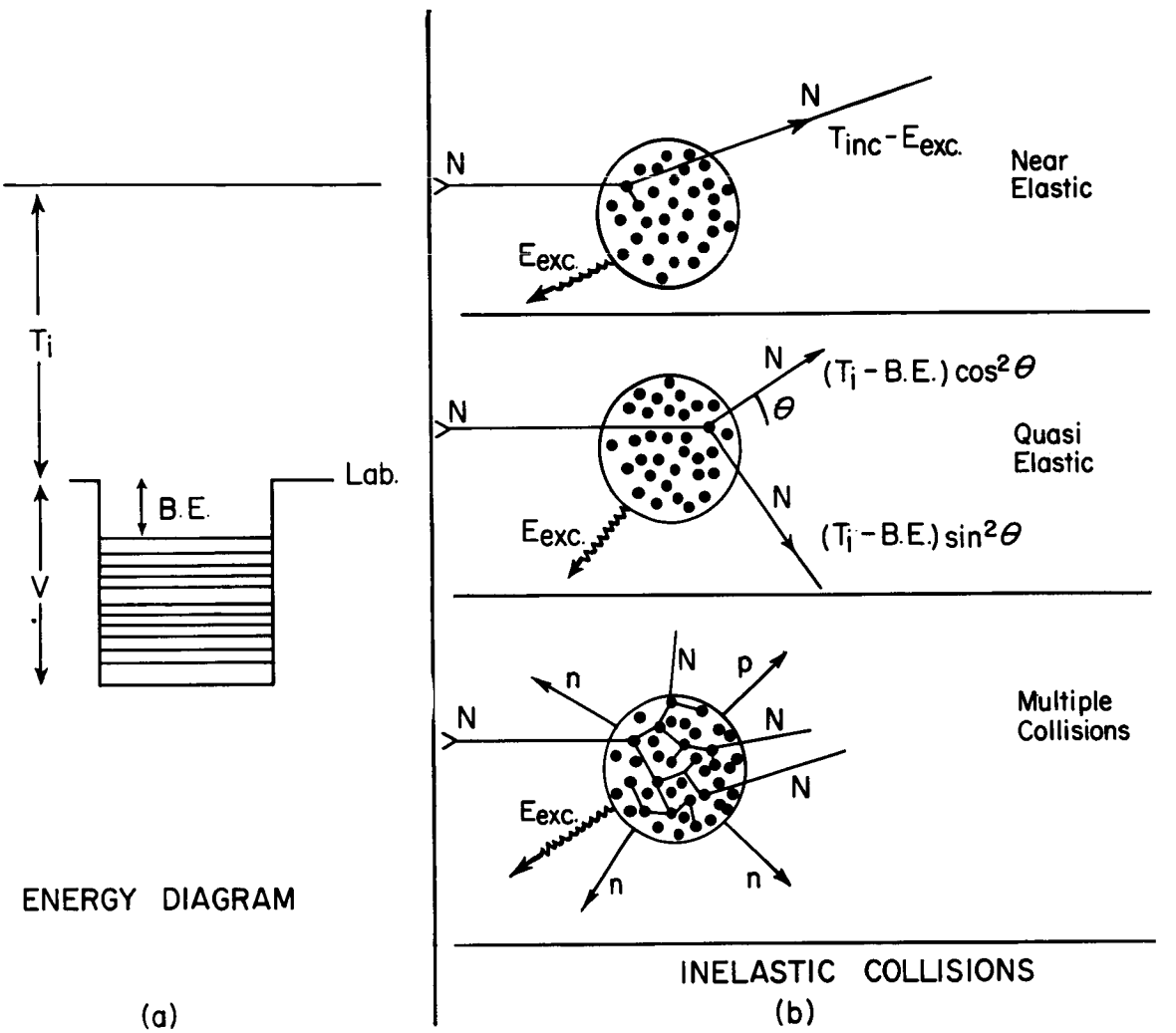

Figure 1a - Schematic representation of a nucleus using single particle model with a square well potential. Only occupied levels are shown.

1b - Schematic diagrams of possible high energy reactions. Secondary particles directly related to the incident particle are indicated by N (nucleon). Boil-off particles are indicated by n (neutron) or p (proton). Photons are represented by accordion lines.

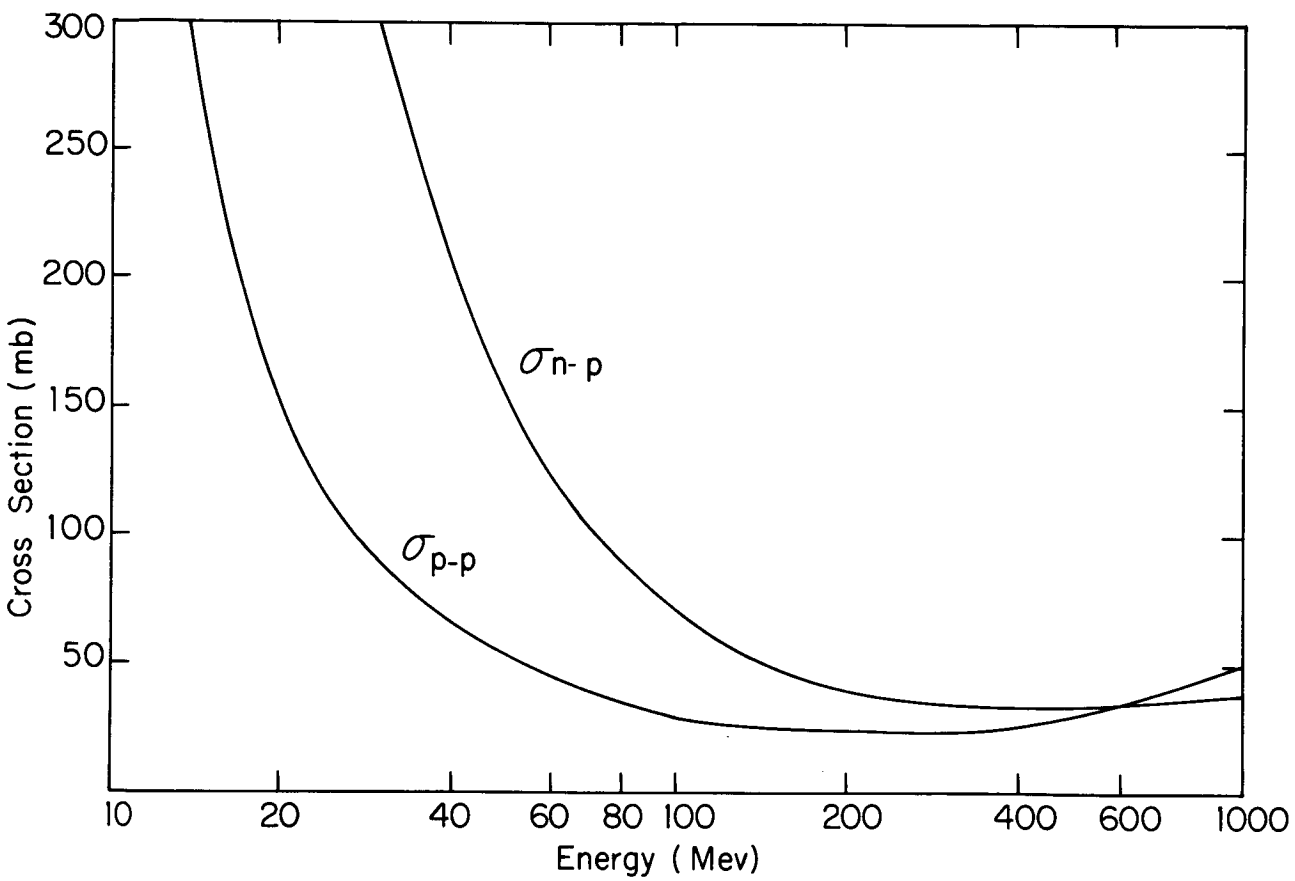

Figure 2 - Free nucleon-nucleon cross sections plotted from the summary of reference 6.

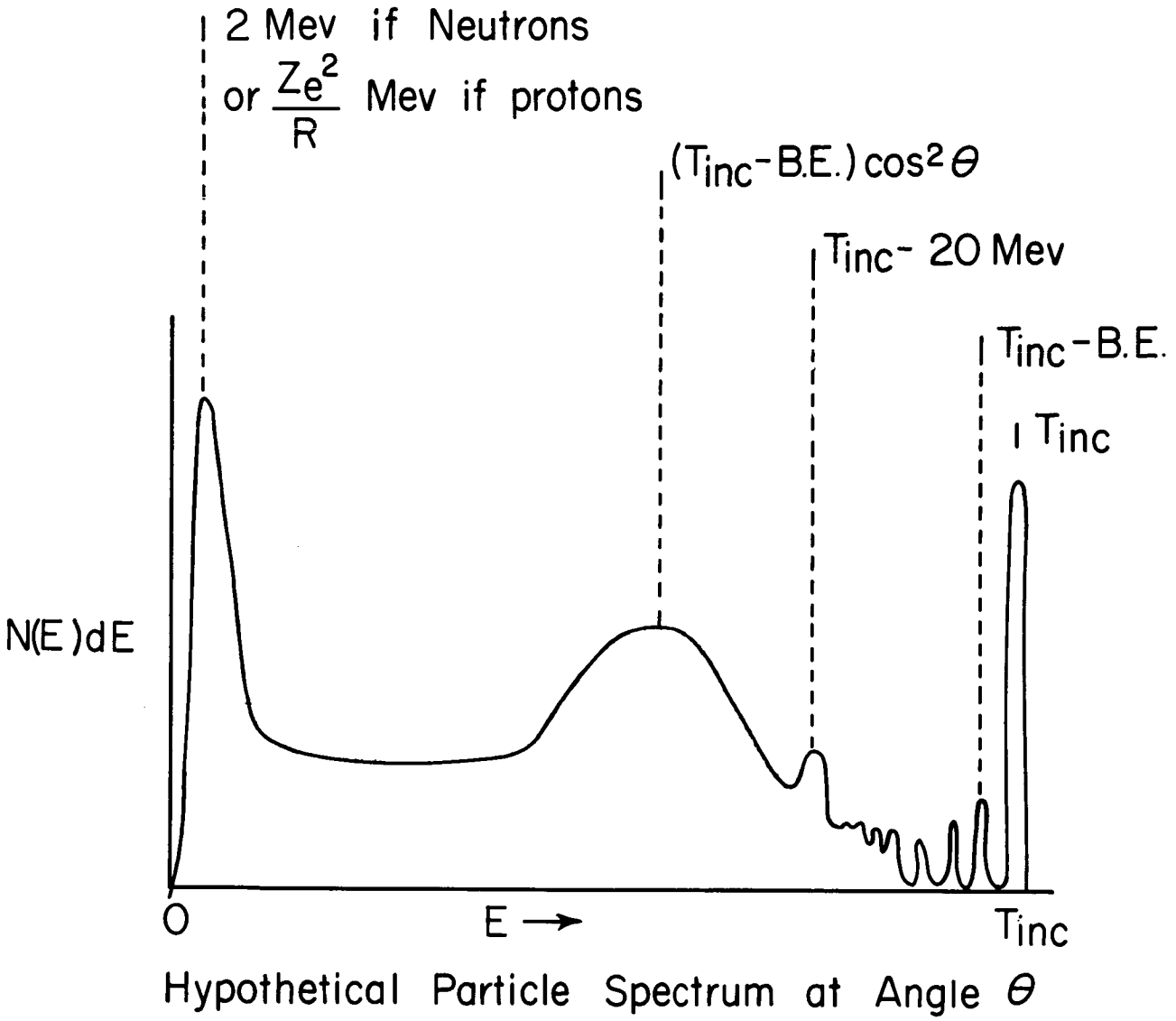

Figure 3 - Hypothetical secondary particle spectrum showing all features that might be expected.

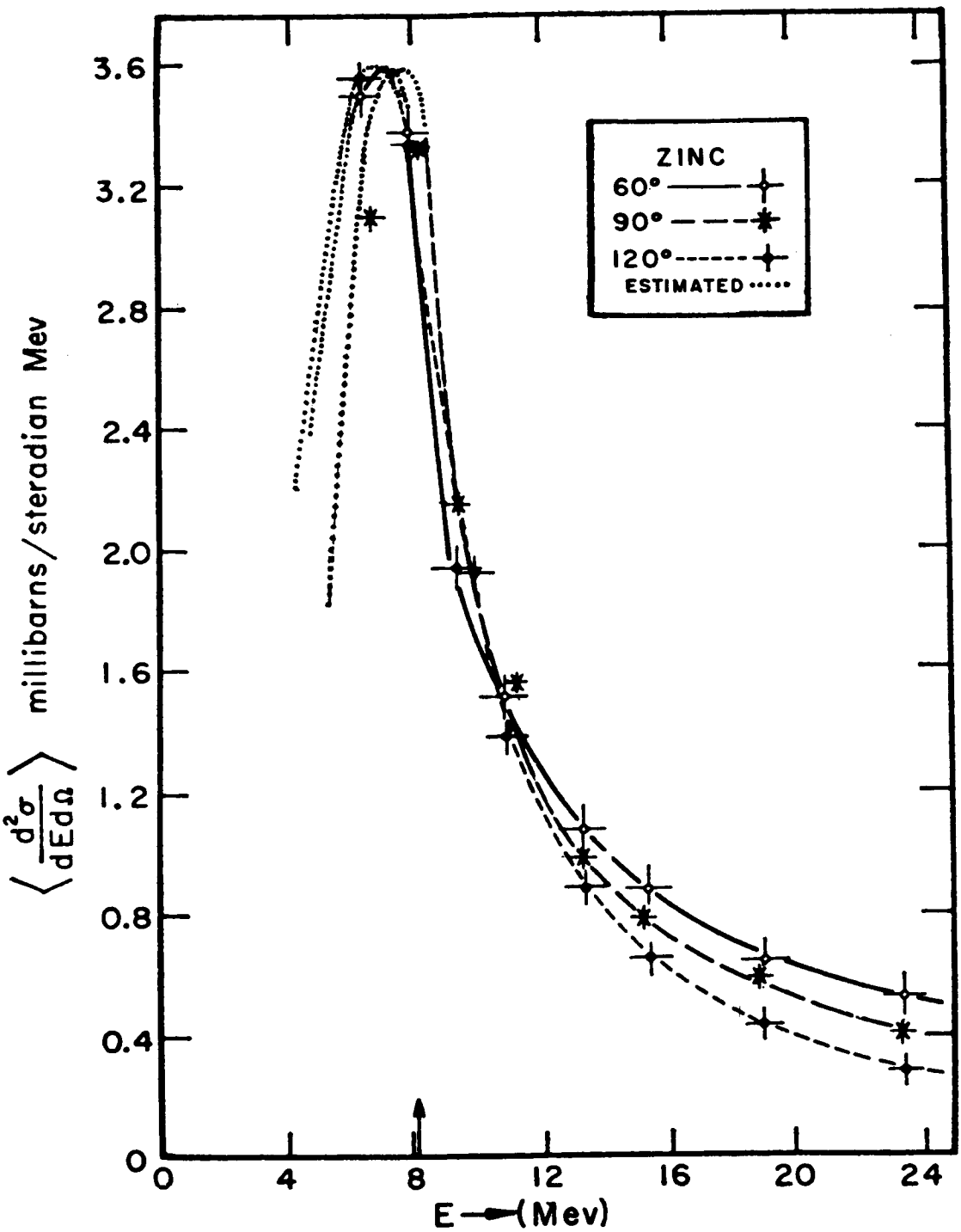

Figure 4 - Spectra of low energy protons emitted by a Zn target bombarded with 160 Mev protons (from reference 8).

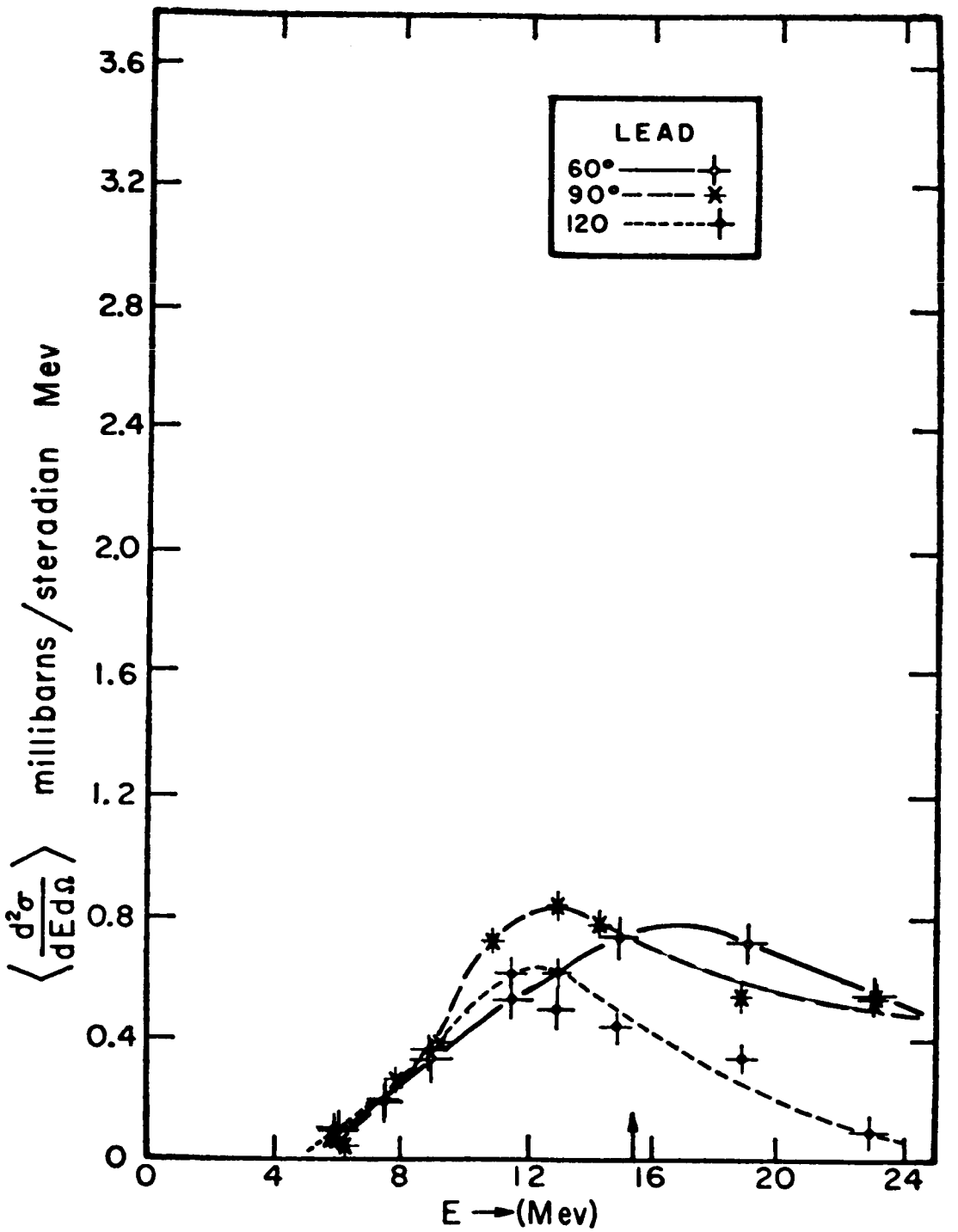

igure 5 - Spectra of low energy protons emitted by a Pb target bombarded with 160 Mev protons (from reference 8).

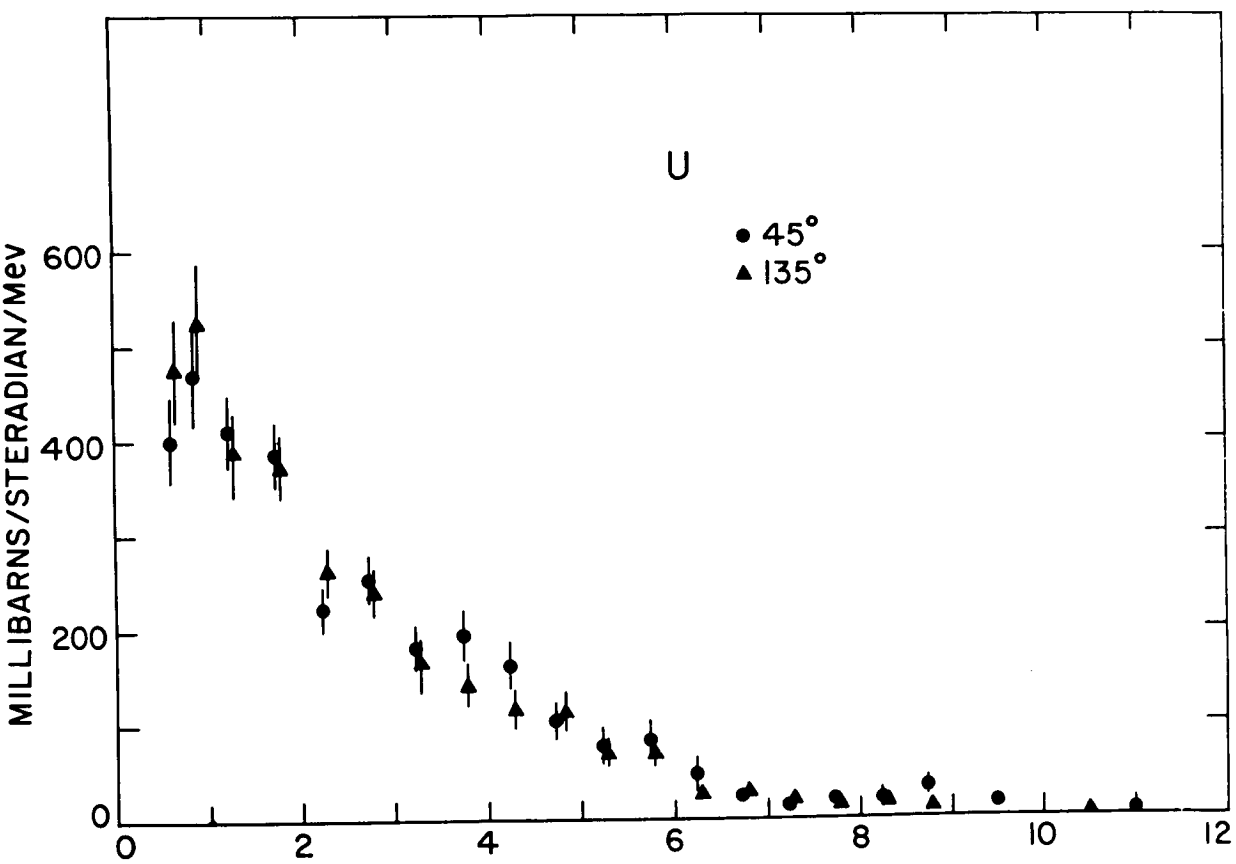

Figure 6 - Spectra of low energy neutrons emitted by an U target bombarded with 180 Mev protons (from reference 9).

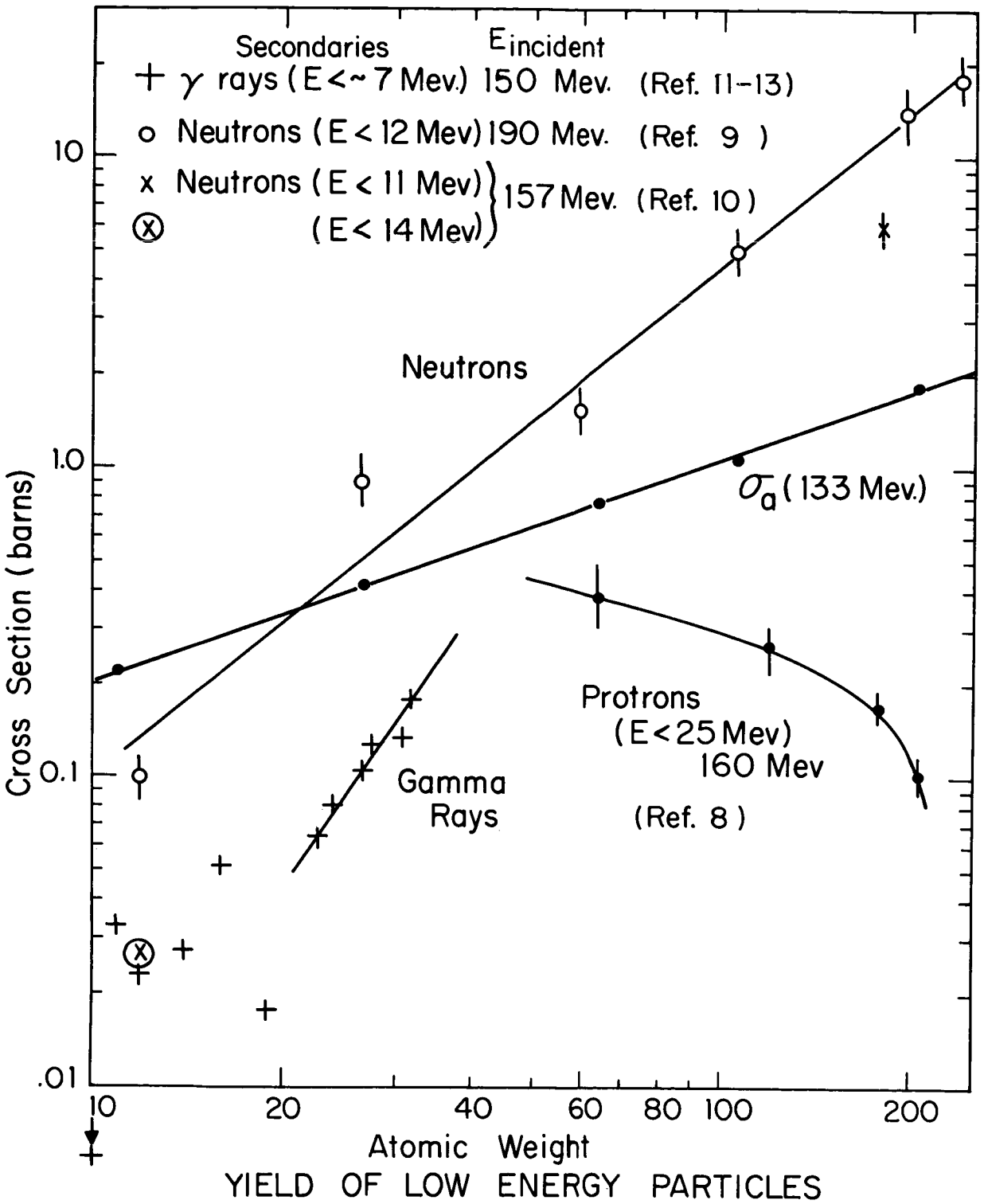

Figure 7 - Yield of low energy secondaries as a function of atomic weight. To guide the eye solid curves have been drawn in region of small scatter.

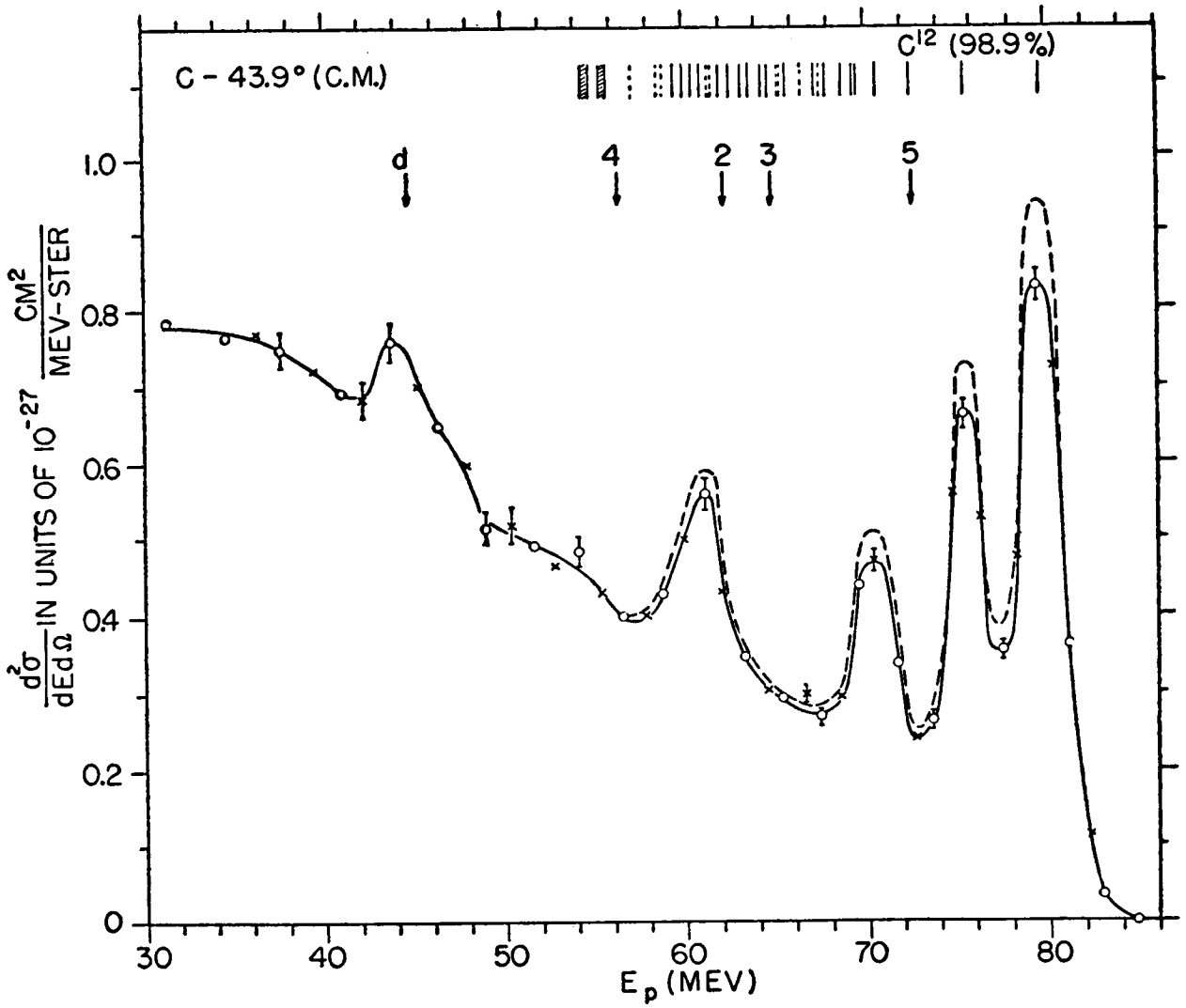

Figure 8 - Proton spectrum observed at 40° from a C target bombarded with 96 Mev protons (from reference 14 where symbols are explained).

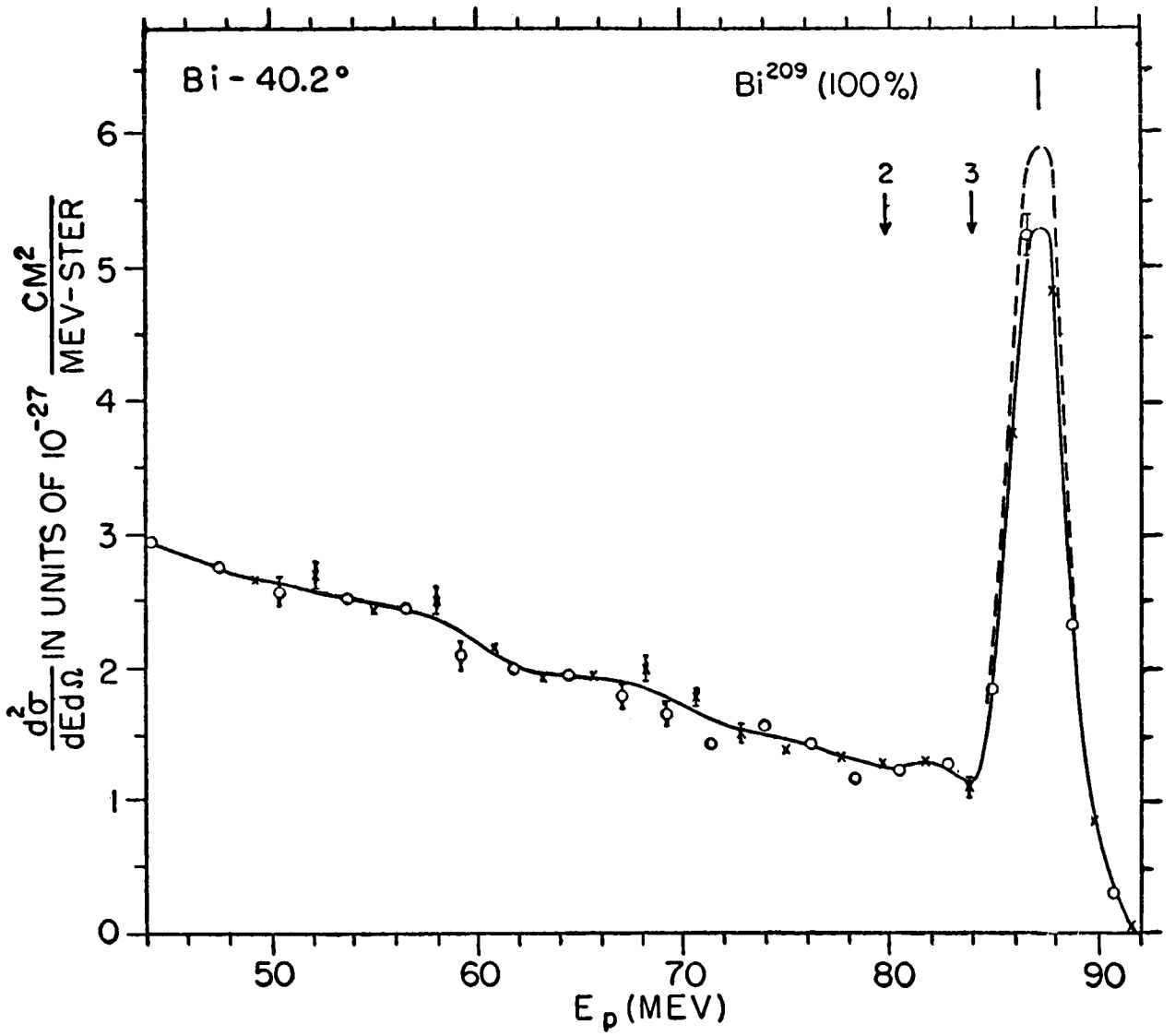

Figure 9 - Proton spectrum observed at 40° from a Bi target bombarded with 96 Mev protons (from reference 14 where symbols are explained).

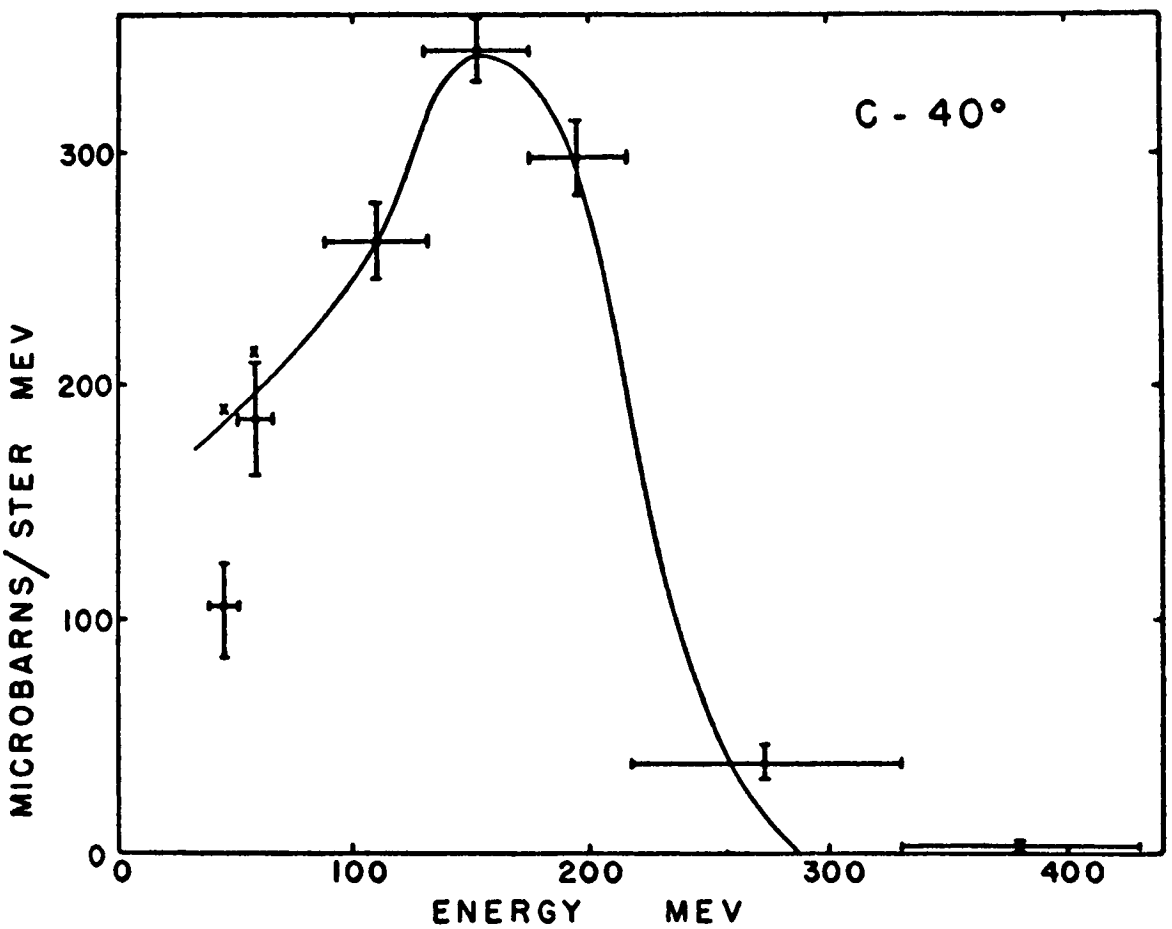

Figure 10 - Proton spectrum observed at 40° from a C target bombarded with 300 Mev protons (from reference 19).

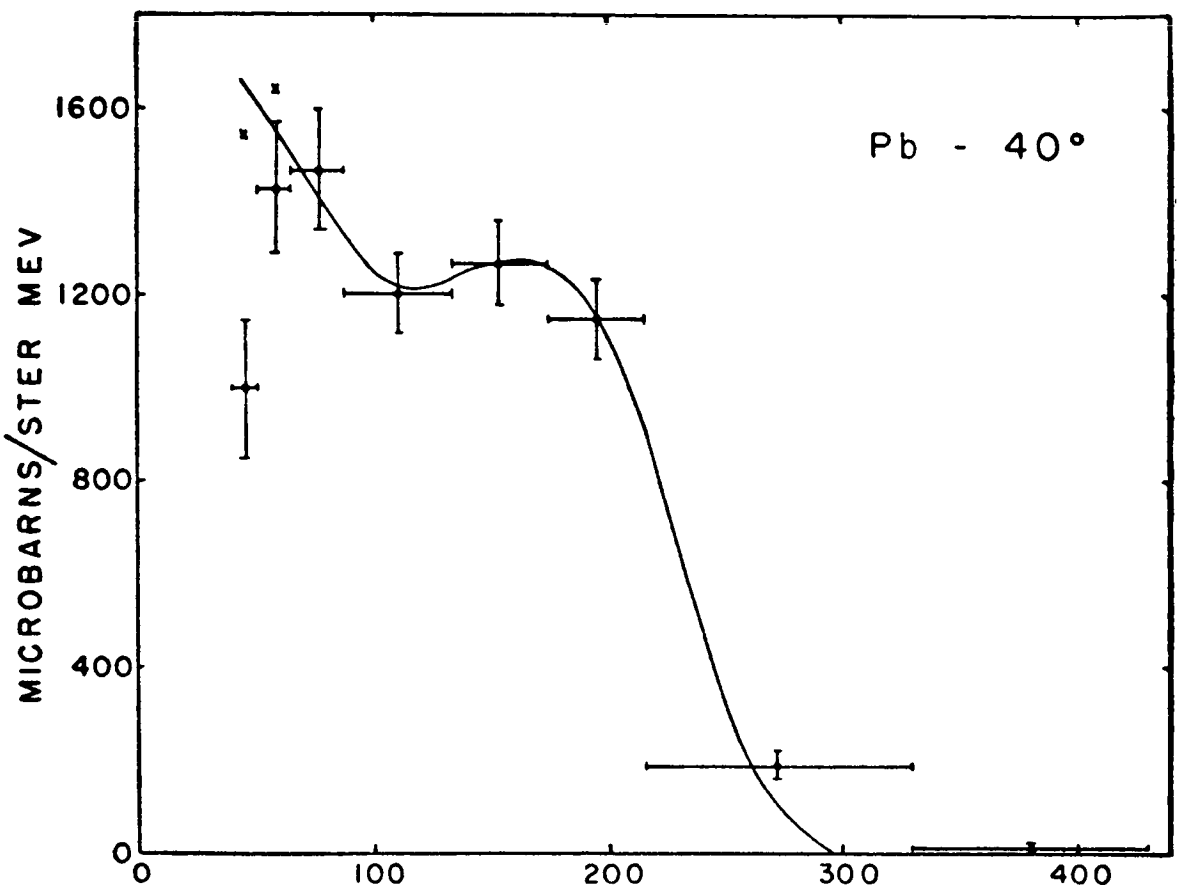

Figure 11 - Proton spectrum observed at 40° from a Pb target bombarded with 300 Mev protons (from reference 19).

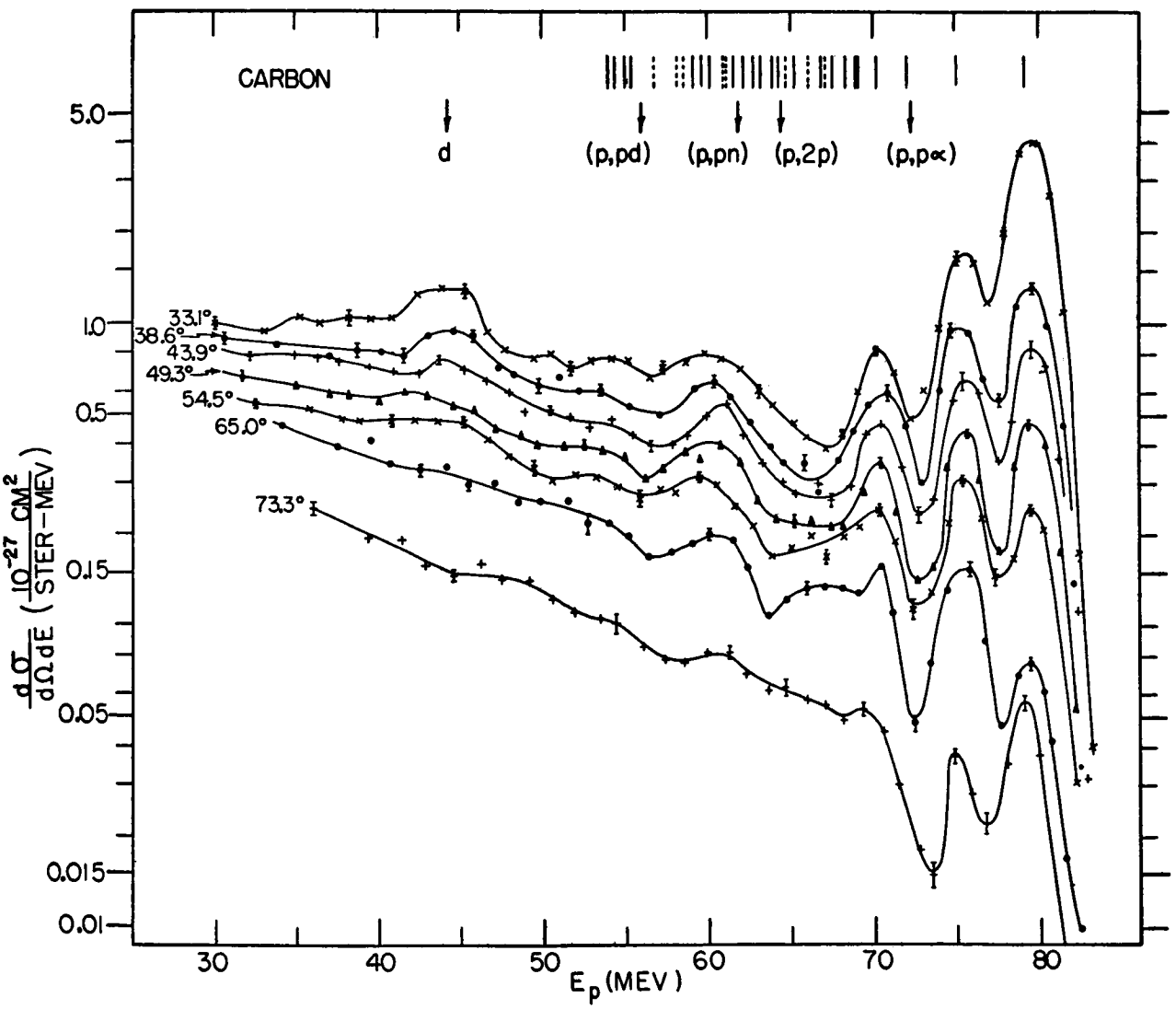

Figure 12 - Energy spectra of protons scattered from a C target bombarded with 95 Mev protons. Energy and angle values are in the p-c center-of-mass system (from reference 22).

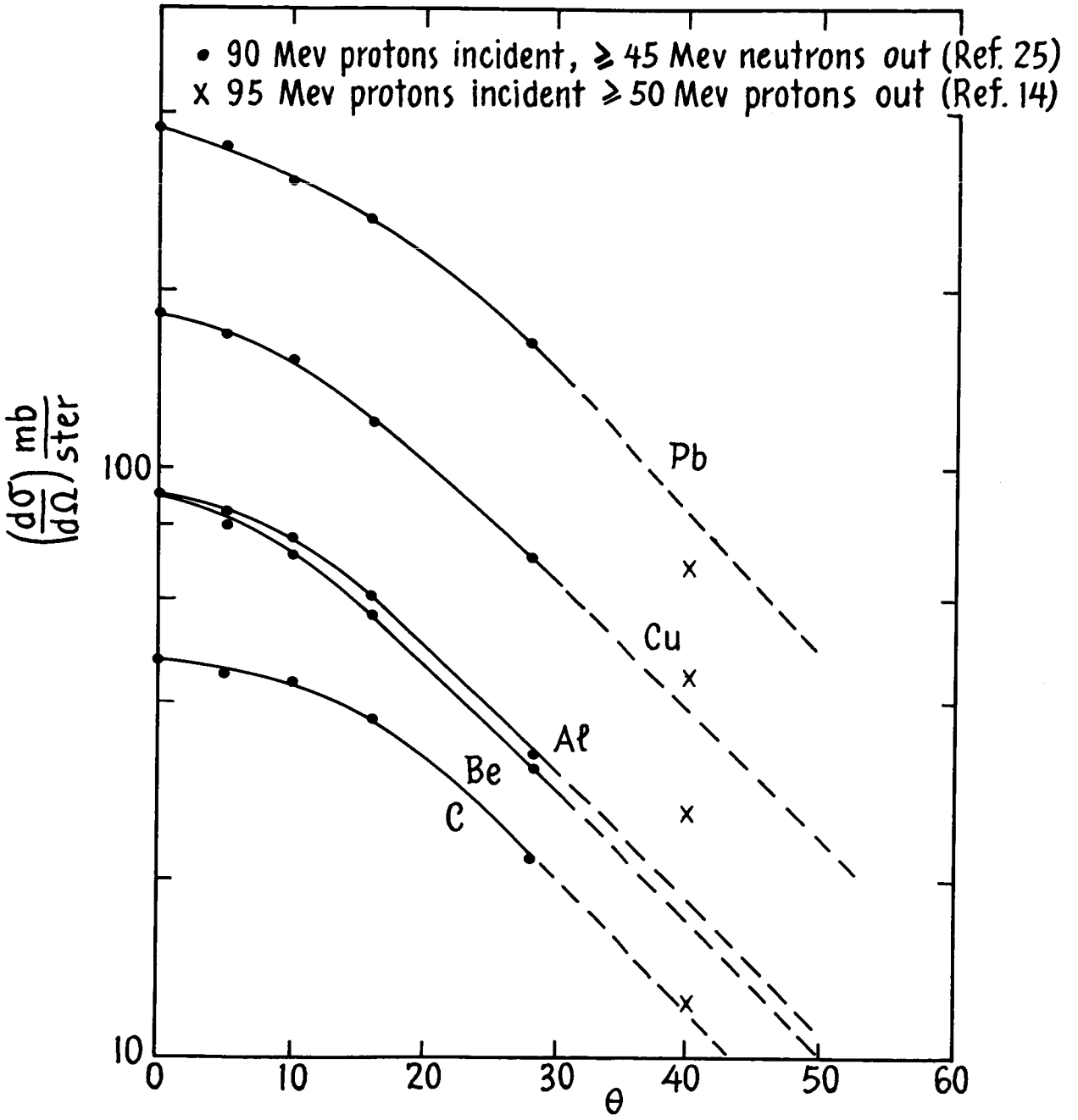

Figure 13 - Angular distribution of high energy secondaries.

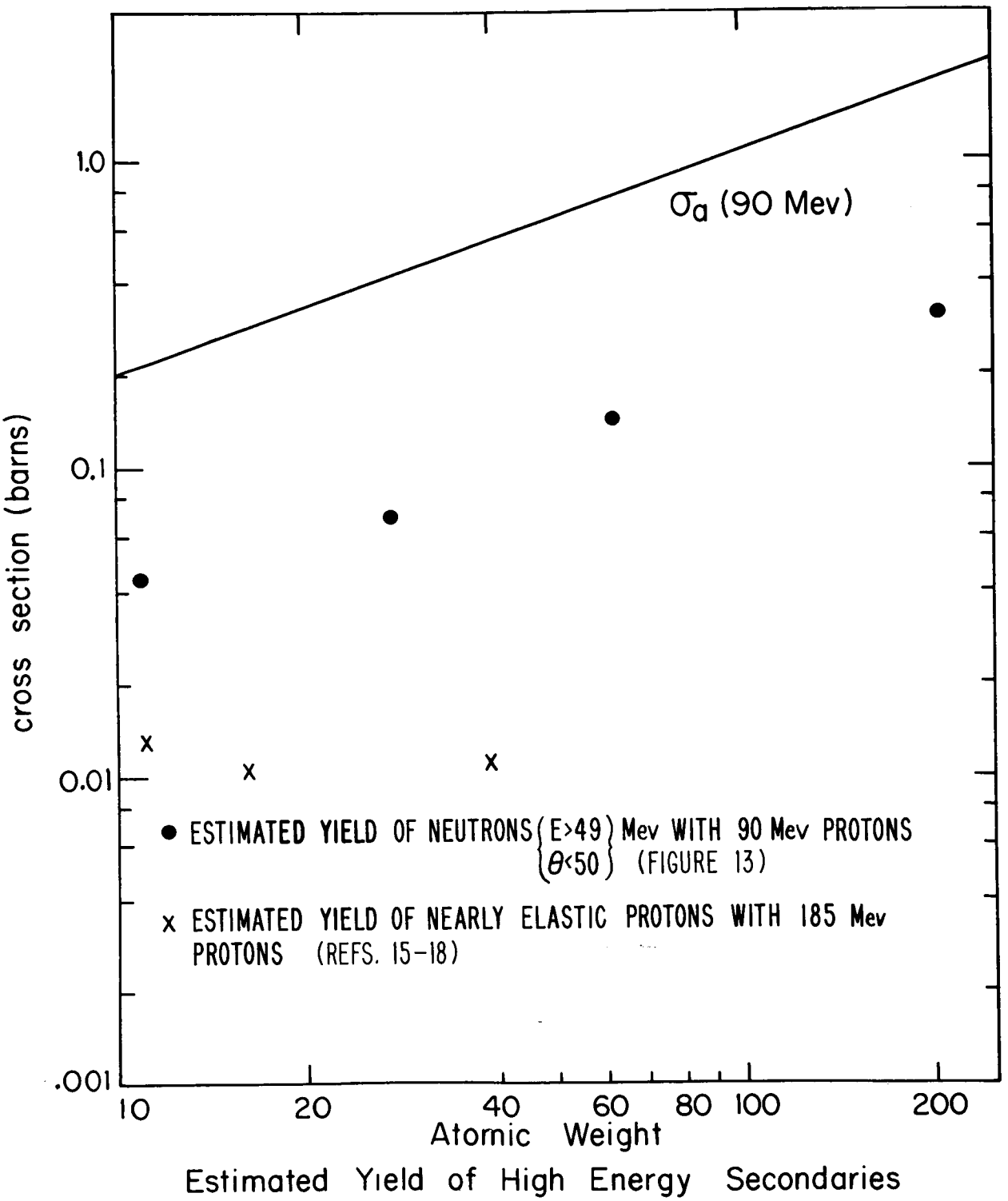

Figure 14 - Estimated yield of high energy secondaries.

Paper D-3

MONTE CARLO CALCULATIONS FOR INTRANUCLEAR CASCADES

H. W. Bertini
Oak Ridge National Laboratory

15140

Abstract

Calculations have been made for nucleons and pions incident on complex nuclei at energies where pion production is not likely (≈ 350 Mev). The interaction with the nucleus as a whole is represented by individual particle-particle collisions within the nucleus where the history of each particle involved in the collision is traced. Extensive comparisons with experiment are made to examine the limits of validity of the model. The effect of a diffuse nuclear edge is examined for certain reactions. It is demonstrated that the model can be used to predict a broad range of experimental results for incident nucleons, whereas the predictions for incident pions are not as reliable as those for nucleons when detailed information is required. It is shown that the bulk of the effects which result when a diffuse nuclear edge is used comes from the increased nuclear dimensions rather than from the edge itself. A compilation of the results for incident nucleons and pions is being prepared, and some preliminary results are presented. The calculation is also being extended to include incident-particle energies up to 2 Gev.

Monte Carlo Calculations on Intranuclear Cascades for Incident-Particle Energies from about 50 to 350 Mev

A code to calculate the reactions of high-energy particles with complex nuclei was described previously.[1,2] The code, which has been written for the IBM-7090 computer and treats incident nucleons and pions on any nucleus greater than helium, is now complete and is being used to obtain a large

1. H. W. Bertini and C. D. Zerby, Neutron Physics Div. Ann. Progr. Rep. Sept. 1, 1960, ORNL-3016, p. 235.

2. H. W. Bertini, Neutron Physics Div. Ann. Progr. Rep. Sept. 1, 1961, ORNL-3193, p. 323.

volume of data which will be illustrated in the next section. This section consists of a brief review of the code and compares some of the calculated results with experimental data.

Nuclear Model and Cross-Section Data

In the nuclear model it is assumed that for incident-particle energies of the order of 50 Mev or higher, the reactions with complex nuclei can be described in terms of particle-particle events that take place inside the nucleus. Each event gives rise to other high-energy particles which in turn make other collisions, and in this way a cascade develops inside the nucleus. These events can be calculated and the history of each particle involved can be traced by using free-particle empirical data and statistical sampling techniques.

The density distribution of nucleons inside the nucleus was made to approximate the continuously varying charge distribution obtained by Hofstadter.[3] This was done by taking three concentric spheres, one nested inside the other with individual uniform densities such that the proton density in each sphere or region corresponded to the average value of the continuous charge distribution over the same region. The region boundaries applied to neutrons as well, and the ratio of the neutron to proton density in each region was taken to be the same as the ratio of the total number of neutrons in the nucleus to the total number of protons. A few calculations were made with a constant nucleon density distribution used throughout the nucleus to determine its effect. These considerations are illustrated in Fig. 1.

In each region the nucleons were assumed to have a zero-temperature Fermi energy distribution. The binding energy of the loosest nucleon was assumed to be constant, 7 Mev, for all regions and all nucleons. The potential for nucleons inside the nucleus was taken to be 7 Mev plus the zero-temperature Fermi energy in each region. This is illustrated in Fig. 2 for a typical case.

The total free-particle cross sections that were used are illustrated in Figs. 3, 4, and 5. The differential cross sections for nucleon-nucleon collisions were taken from the work of Hess,[4] Beretta et al.,[5] and Hughes

---

3. R. Hofstadter, Revs. Modern Phys. 28, 214 (1956).

4. W. N. Hess, Revs. Modern Phys. 30, 368 (1958).

5. L. Beretta, C. Villi, and F. Ferrari, Nuovo Cimento 12, S-499 (1954).

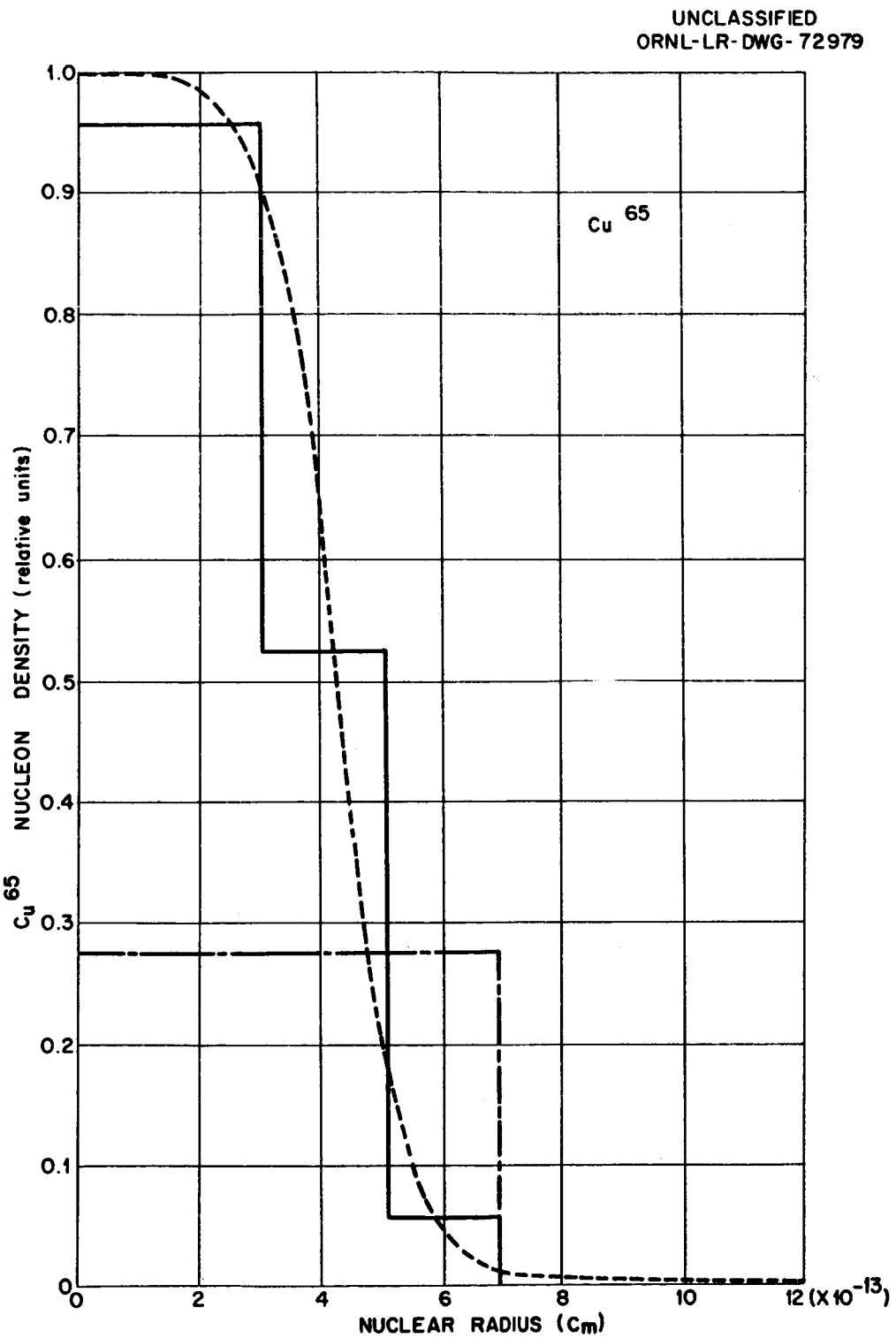

Fig. 1. Nucleon Density Distributions Within the Nucleus. Solid lines: nonuniform distribution; dot-dashed lines: uniform distribution; dotted lines: Hofstadter's curve [Rev. Mod. Phys. 28, 214 (1956)].

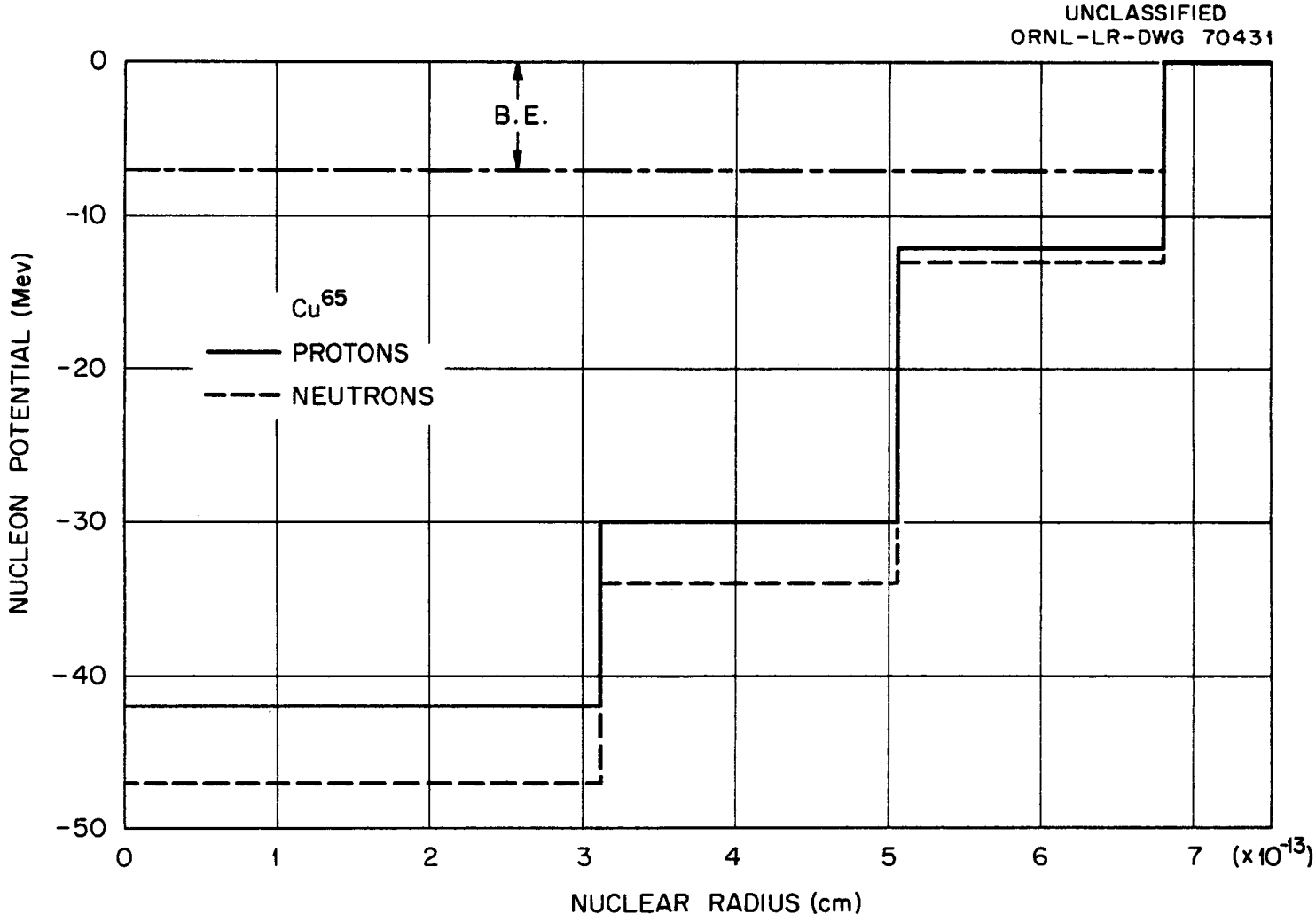

Fig. 2. Nucleon Potential vs Nuclear Radius for a Typical Nucleus. "B. E." is the fixed binding energy of the loosest nucleon.

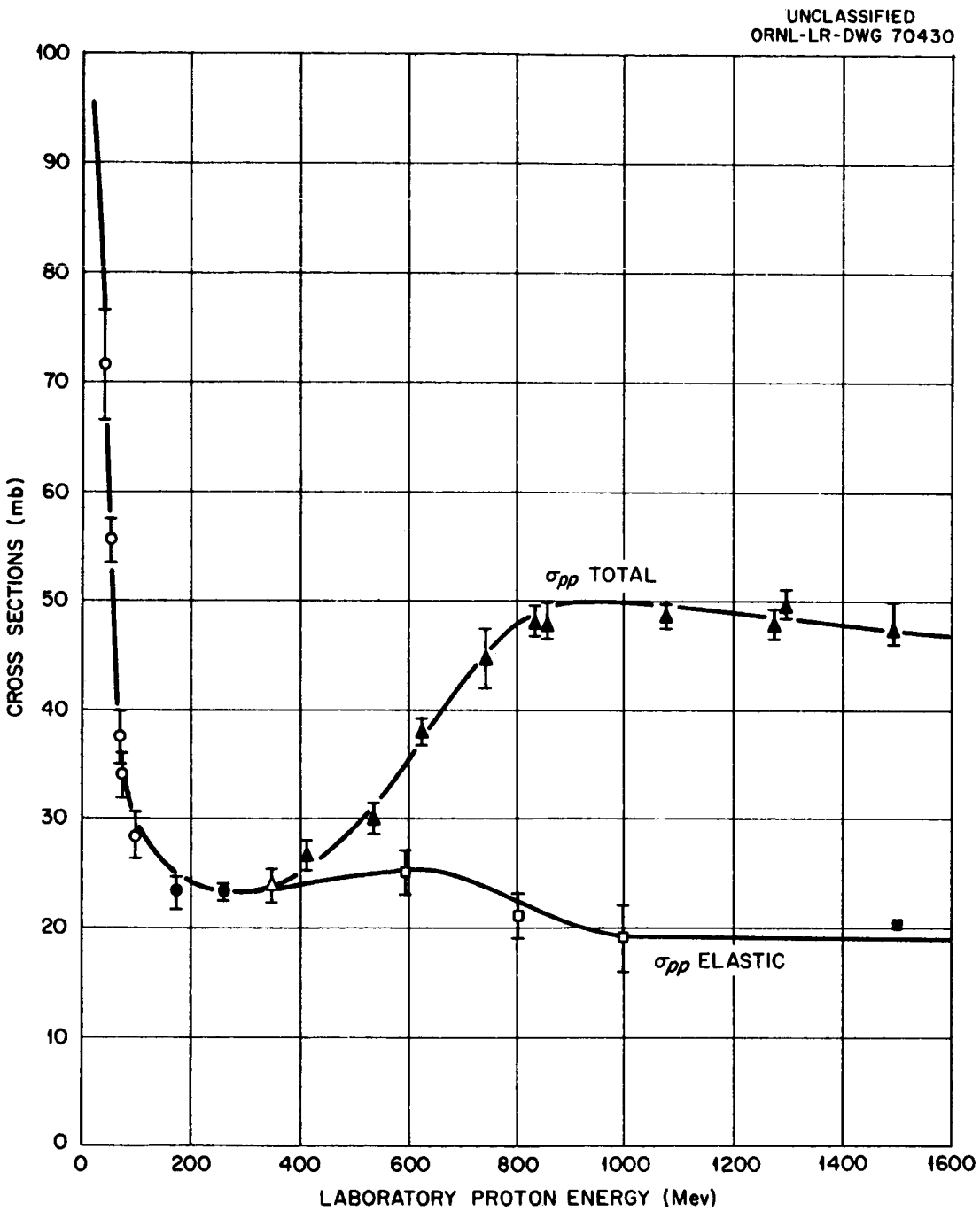

Fig. 3. Proton-Proton Total and Elastic Cross Sections vs Energy. ○ U. E. Kruse, J. M. Teem, and N. F. Ramsey, Phys. Rev. 101, 1079 (1956); ● O. Chamberlain and J. D. Garrison, Phys. Rev. 95, 1349 (L) (1954); △ O. Chamberlain, E. Segrè, and C. Wiegand, Phys. Rev. 83, 923 (1951); ▲ F. F. Chen, C. P. Leavitt, and A. M. Shapiro, Phys. Rev. 103, 211 (1956); □ L. W. Smith, A. W. McReynolds, and G. Snow, Phys. Rev. 97, 1186 (1955); ■ W. B. Fowler et al., Phys. Rev. 103, 1479 (1956).

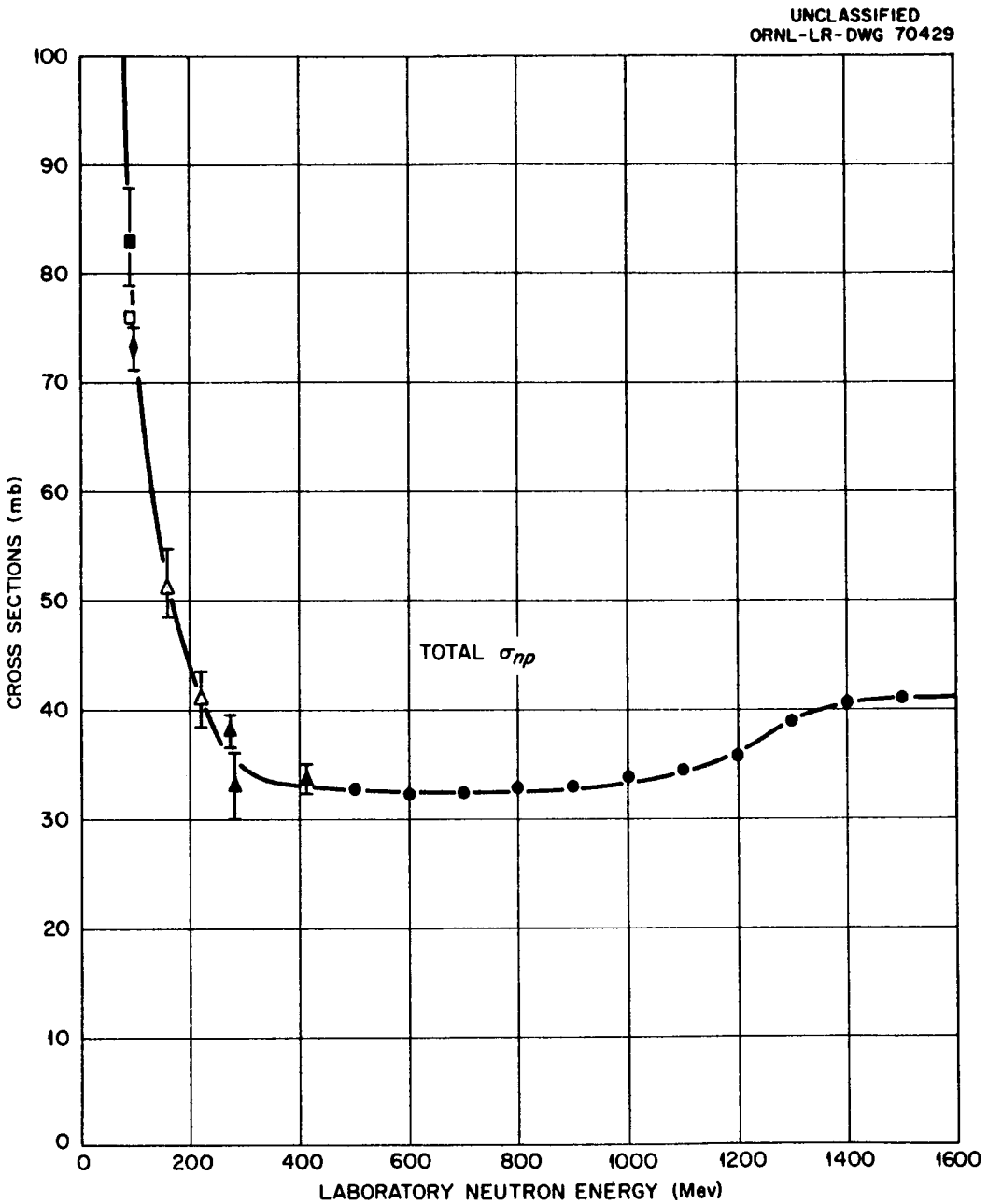

Fig. 4. Neutron-Proton Total Cross Sections vs Energy. ■ L. J. Cook et al., Phys. Rev. 75, 7 (1949); □ J. Hadley et al., Phys. Rev. 75, 351 (1949); ♦ J. DeJuren and N. Knable, Phys. Rev. 77, 606 (1950); △ J. DeJuren and B. J. Moyer, Phys. Rev. 81, 919 (1951); ▲ A. V. Nedzel, Phys. Rev. 94, 174 (1954); ● F. F. Chen, C. P. Leavitt, and A. M. Shapiro, Phys. Rev. 103, 211 (1956).

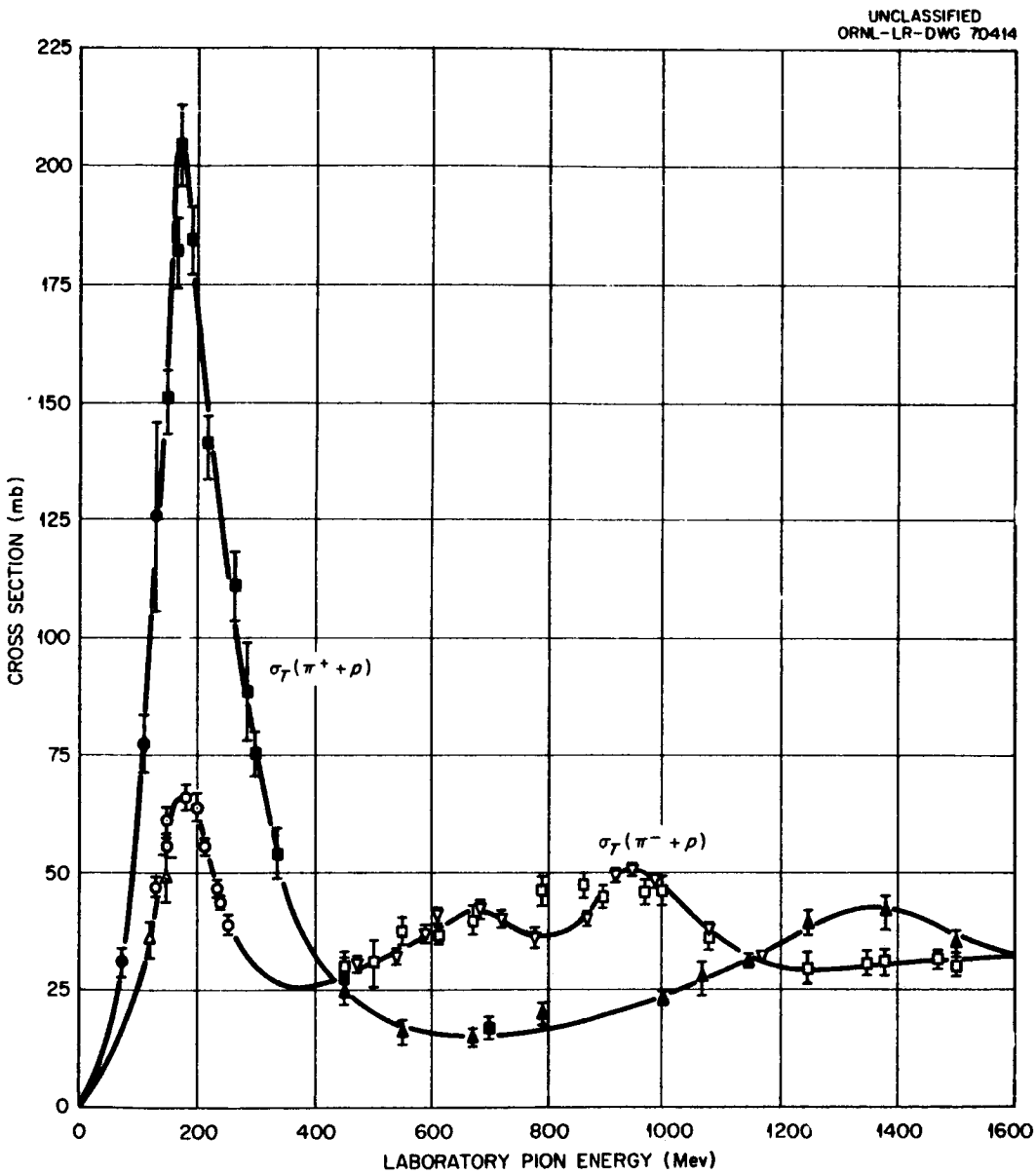

Fig. 5. π^+-Proton and π^--Proton Total Cross Sections vs Energy. ●, △ H. L. Anderson et al., Phys. Rev. 91, 155 (1953); ▩ S. J. Lindenbaum and L. C. L. Yuan, Phys. Rev. 100, 306 (1955); ▲, □ R. Cool, O. Piccioni, and D. Clark, Phys. Rev. 103, 1082 (1956); ○ J. Ashkin et al., Phys. Rev. 96, 1104 (1954); ▽ H. C. Burrowes et al., Phys. Rev. Letters 2, 119 (1959).

Schwartz.[6] The differential cross sections for pion-nucleon collisions were calculated by using the phase shifts of Orear.[7] From the results of these calculations the exchange scattering cross sections and the π^o cross sections could be deduced with the results given in Fig. 6. The numerical work of Metropolis et al.[8] was used for the pion-absorption cross section. This reaction was assumed to take place with two-particle nucleon clusters inside the nucleus. All the cross-section data were tabulated at every 20-Mev interval.

The basic sampling technique for determining the point of collision, type of collision, and momentum of the struck particle was that described by Zerby et al.[9]

Comparison with Experiment: Incident Nucleons

Table 1 contains comparisons of calculated total nonelastic cross sections with experimental data and Table 2 comparisons of the average excitation energy of the residual nucleus with calculations based on experiment. In both cases the agreement is quite good.

Figures 7 and 8 illustrate the cascade particle spectra in the forward direction for low-energy incident protons. The comparison for carbon, Fig. 7, shows one of the apparent deficiencies of the model. At higher energies this serious discrepancy in the shape of the spectrum in the forward direction is no longer manifest, as is shown in Figs. 9 and 10.

In Figs. 11-13 some comparisons at other angles are illustrated. The high-energy peaks in the experimental spectrum are due to elastic scattering, and the comparisons should be made at the energies below the peaks. Other comparisons, illustrated in Figs. 14-21, indicate low-energy peaks in some of the experimental results. These peaks are caused by nuclear evaporation, and the comparisons should be made at energies greater than about 15 Mev since evaporation is not included in the calculation. Comparisons with some of the data on emulsions are given in Figs. 22-25. Except for incident nucleon energies below 100 Mev on light- to medium-weight nuclei for particles emitted forward, the calculations indicate excellent agreement with experiment for emitted cascade particles. The angular distributions for a few reactions are given in Figs. 26-28.

6. D. J. Hughes and R. B. Schwartz, Neutron Cross Sections, BNL-325 (1958).

7. J. Orear, Phys. Rev. 100, 288 (1955).

8. N. Metropolis et al., Phys. Rev. 110, 204 (1958).

9. C. D. Zerby, R. B. Curtis, and H. W. Bertini, The Relativistic Doppler Problem, ORNL CF-61-7-20 (July 12, 1961).

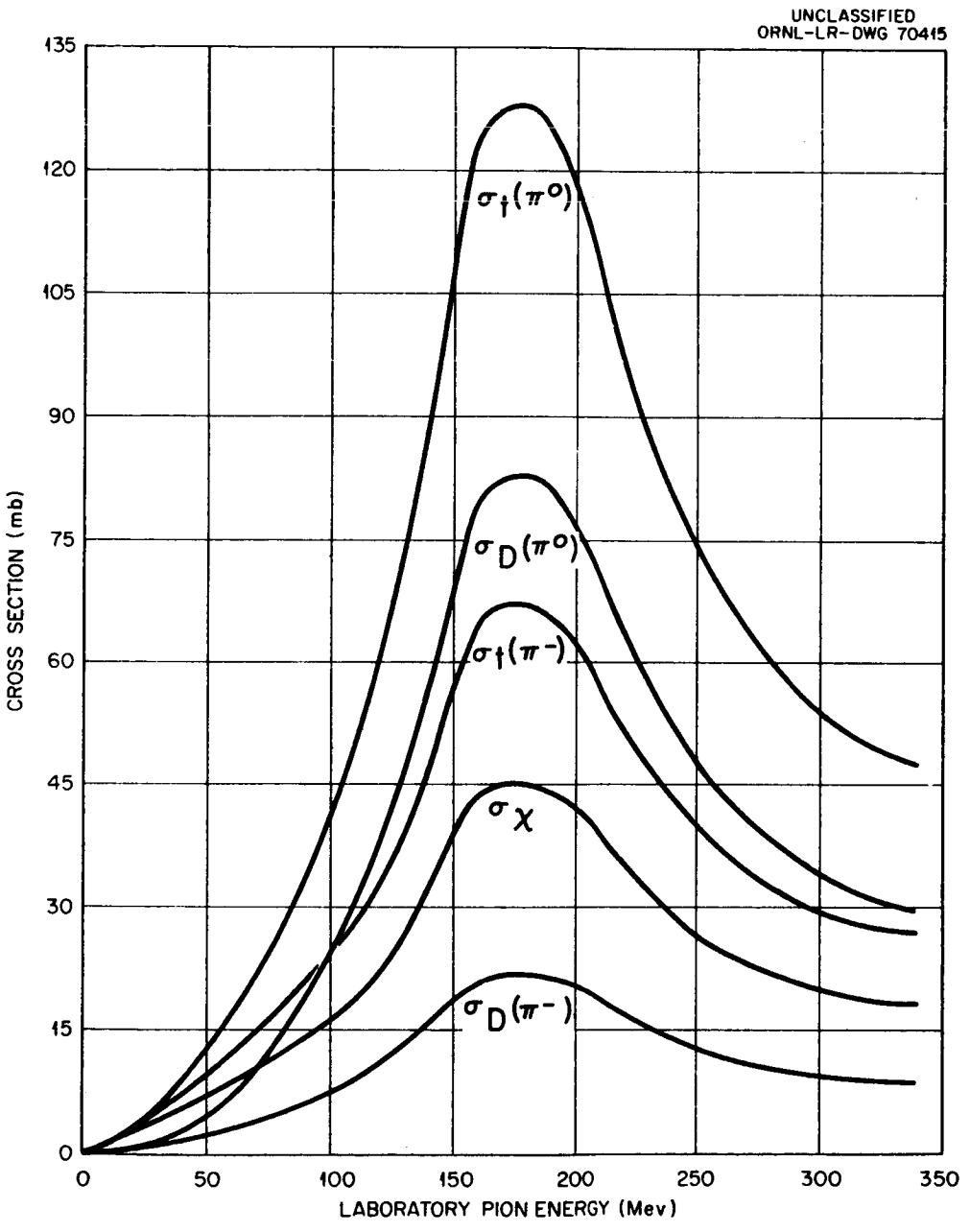

Fig. 6. Calculated Pion-Proton Cross Sections vs Pion Energy. $\sigma_t(\pi^o)$, Total cross section for π^o + p scattering; $\sigma_D(\pi^o)$, Cross section for π^o + p direct scattering; $\sigma_t(\pi^-)$, Experimental π^- + p total cross section included for comparison purposes; σ_X, Cross section for π^- + p, π^+ + n, π^o + p, and π^o + n exchange scattering; $\sigma_D(\pi^-)$, Cross section for π^- + p direct scattering.

Table 1. Calculated and Experimental Nonelastic Cross Sections for Protons and Neutrons Incident on Various Nuclei

Incident Particle	Target	Energy (Mev)	Nonelastic Cross Section (mb)	
			Calculated[a]	Experimental[b]
Proton	Be	185	187 ± 7	172 ± 17
		305	176 ± 7	151 ± 15
	Al	185	417 ± 9	408 ± 41
		305	394 ± 11	334 ± 33
	Cu	170	795 ± 23	
		185		746 ± 75
		240	747 ± 23	667 ± 67
	U	185	1825 ± 38	1900 ± 190
		305	1754 ± 28	1600 ± 160
Neutron	Be	95	217 ± 7	210 ± 8[c]
	Al	84	502 ± 16	500 ± 50[d]
		300	383 ± 11	390 ± 23
	Cu	84	825 ± 23	910 ± 50[d]
		300	725 ± 16	755 ± 33
	Pb	84	1654 ± 26	1850 ± 180[d]
		300	1552 ± 27	1720 ± 80

a. Errors shown are the limits for the standard 68% confidence interval.

b. Unless otherwise noted, all the data come from G. P. Millburn et al., Phys. Rev. 95, 1268 (1954).

c. P. E. Hodgson, Nuclear Phys. 21, 21 (1960).

d. Upper limit.

Table 2. Calculated and Experimental Average Excitation Energies for 190-Mev Incident Protons on Various Nuclei

Target	Excitation Energy (Mev)	
	Calculated	Experimental[a]
C	22	27 ± 5
Al	36	50 ± 8
Ni	59	57 ± 9
Ag	72	69 ± 12
Au	92	83 ± 17
U	95	88 ± 18

a. E. Gross, "The Absolute Yield of Low Energy Neutrons from 190-Mev Protons on Gold, Silver, Nickel, Aluminum, and Carbon," UCRL-3330 (Feb. 29, 1956); "Absolute Neutron Spectra from 190-Mev Protons on Uranium," UCRL-3337 (Mar. 8, 1956).

Table 3. Calculated and Experimental Fast Prong Distributions for Heavy Emulsion Nuclei[a]

Number of Fast Prongs	Percentage of Stars Induced			
	By 300-Mev Neutrons		By 375-Mev Protons	
	Calculated	Experimental[b]	Calculated	Experimental[b]
0	54	30 ± 4	14	29 ± 3
1	42	63 ± 5	76	60 ± 4
2	4	7 ± 2	10	9 ± 2
3	0.4	0	0.5	2 ± 1

a. Fast prongs indicate protons with energies greater than 30 Mev.

b. G. Bernardini, E. T. Booth, and S. J. Lindenbaum, Phys. Rev. 85, 826 (1952).

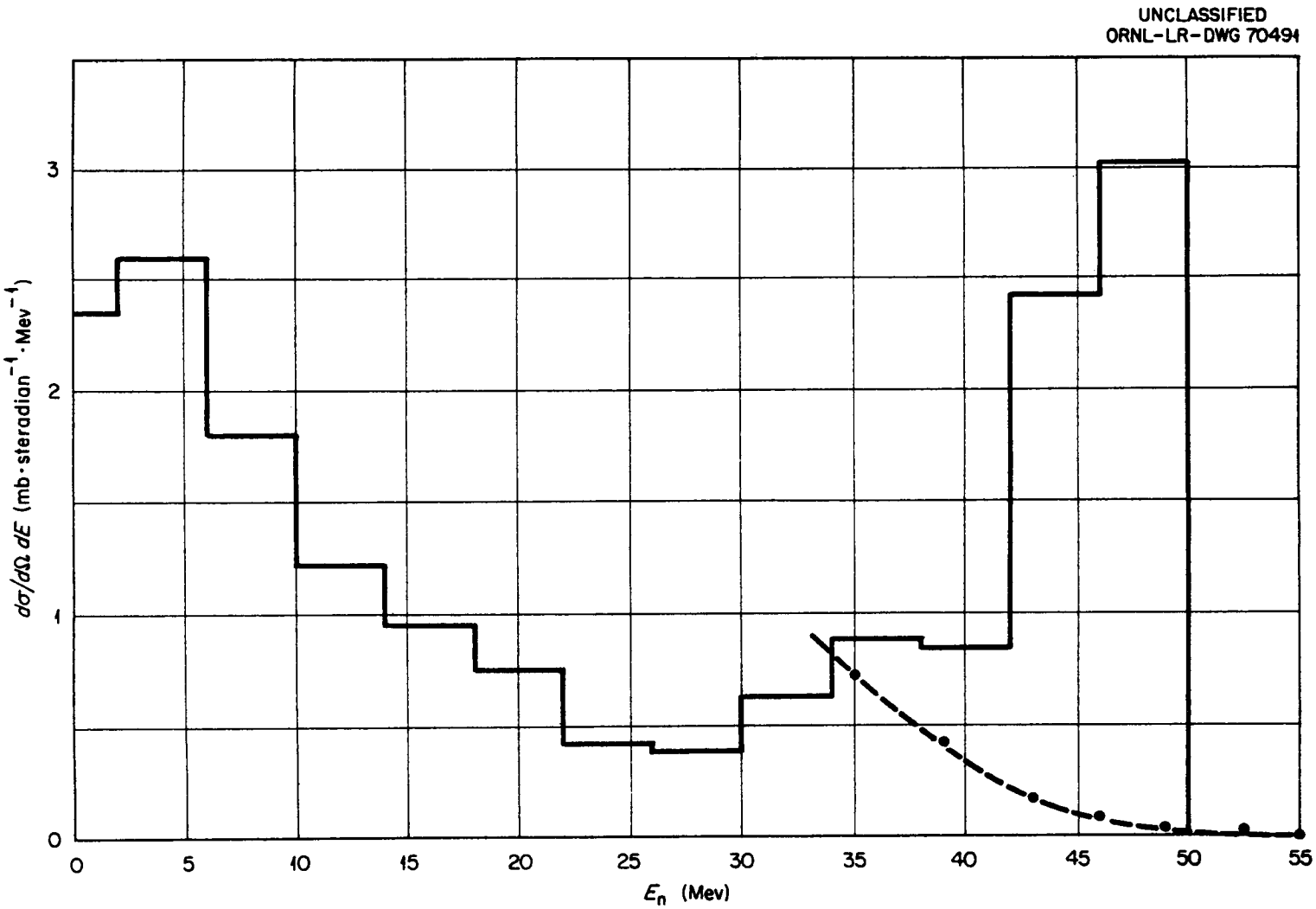

Fig. 7. Neutron Spectra at 0° from 50-Mev Protons on Carbon. Dotted curve: Hofmann's experimental results ("Neutrons Ejected from Nuclei by 50-Mev Protons," Ph.D. Thesis submitted to the Faculty of Arts and Sciences of Harvard University, Cambridge, August 1952); solid lines: calculated spectrum for neutrons emitted in the angular interval 0 to 11°.

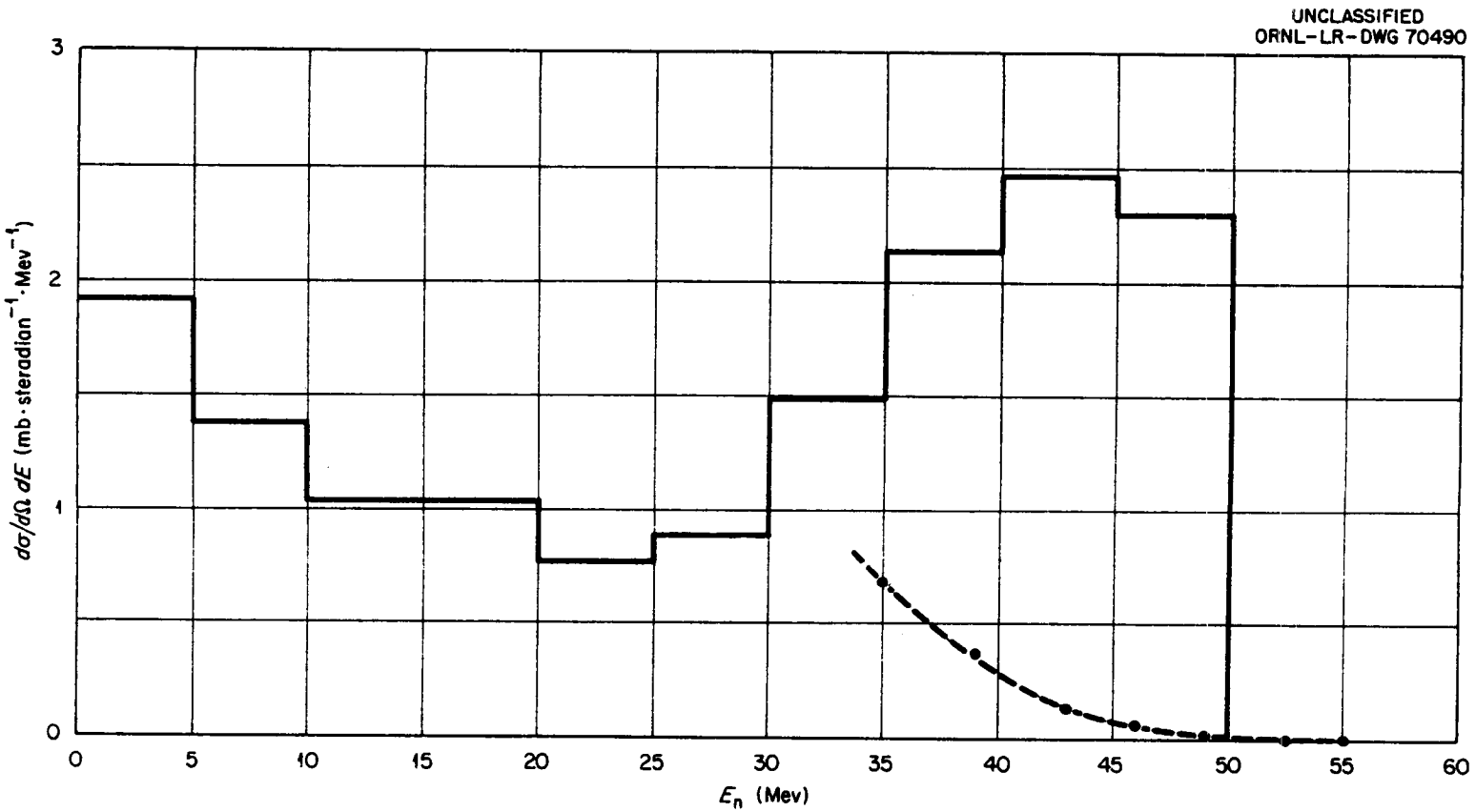

Fig. 8. Neutron Spectra at 16° from 50-Mev Protons on Carbon. Dotted curve: Hofmann's experimental results ("Neutrons Ejected from Nuclei by 50-Mev Protons," Ph.D. Thesis submitted to the Faculty of Arts and Sciences of Harvard University, Cambridge, August 1952); solid lines: calculated spectrum for neutrons emitted in the angular interval 5 to 25°.

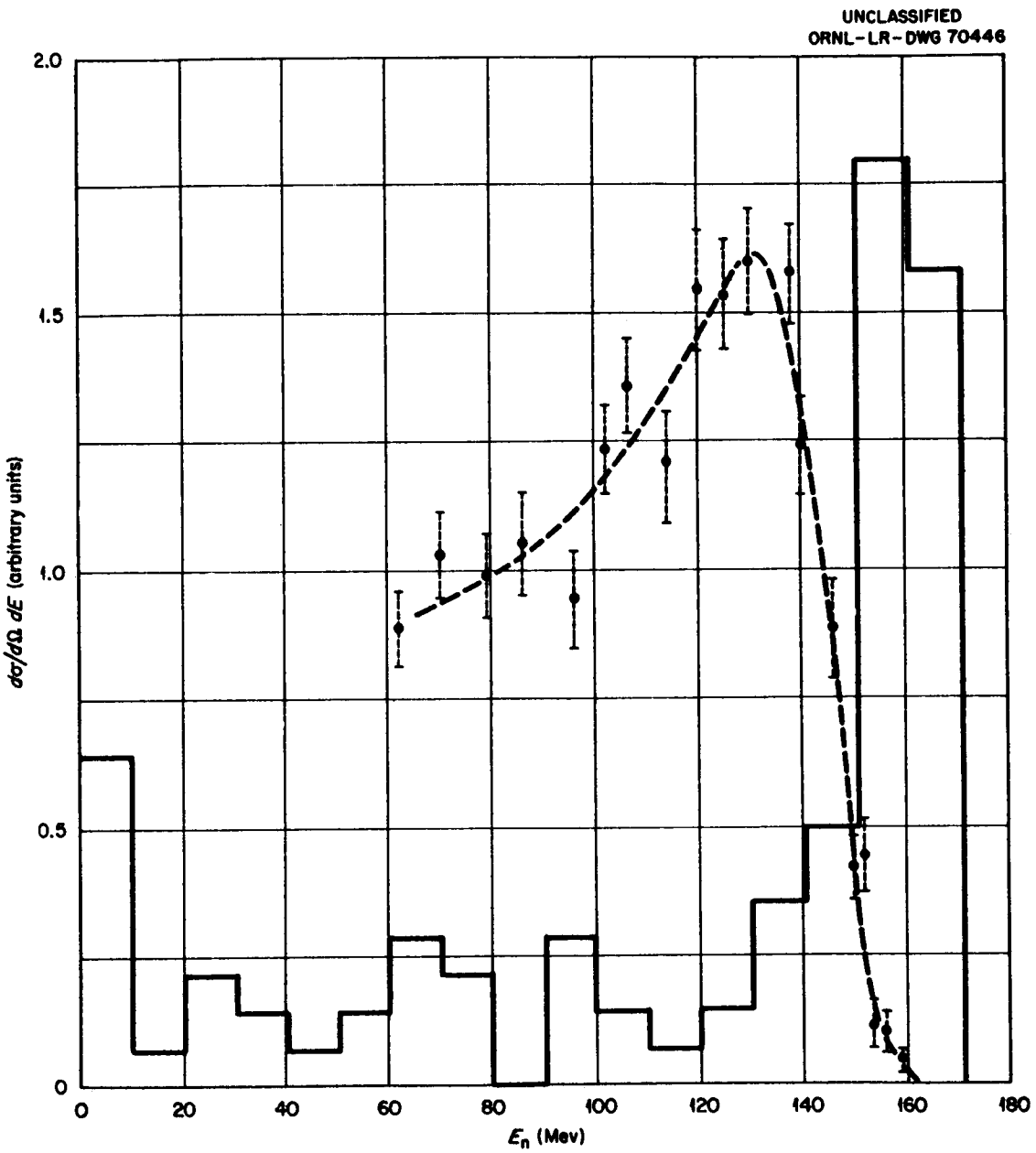

Fig. 9. Neutron Spectra at 2.5° from 171-Mev Protons on Carbon. Dotted curve: experimental results of Cassels et al. [Phil. Mag. 42, 215 (1951)]; solid lines: calculated spectrum of neutrons emitted in the angular interval 0 to 15°; ordinate units are arbitrary.

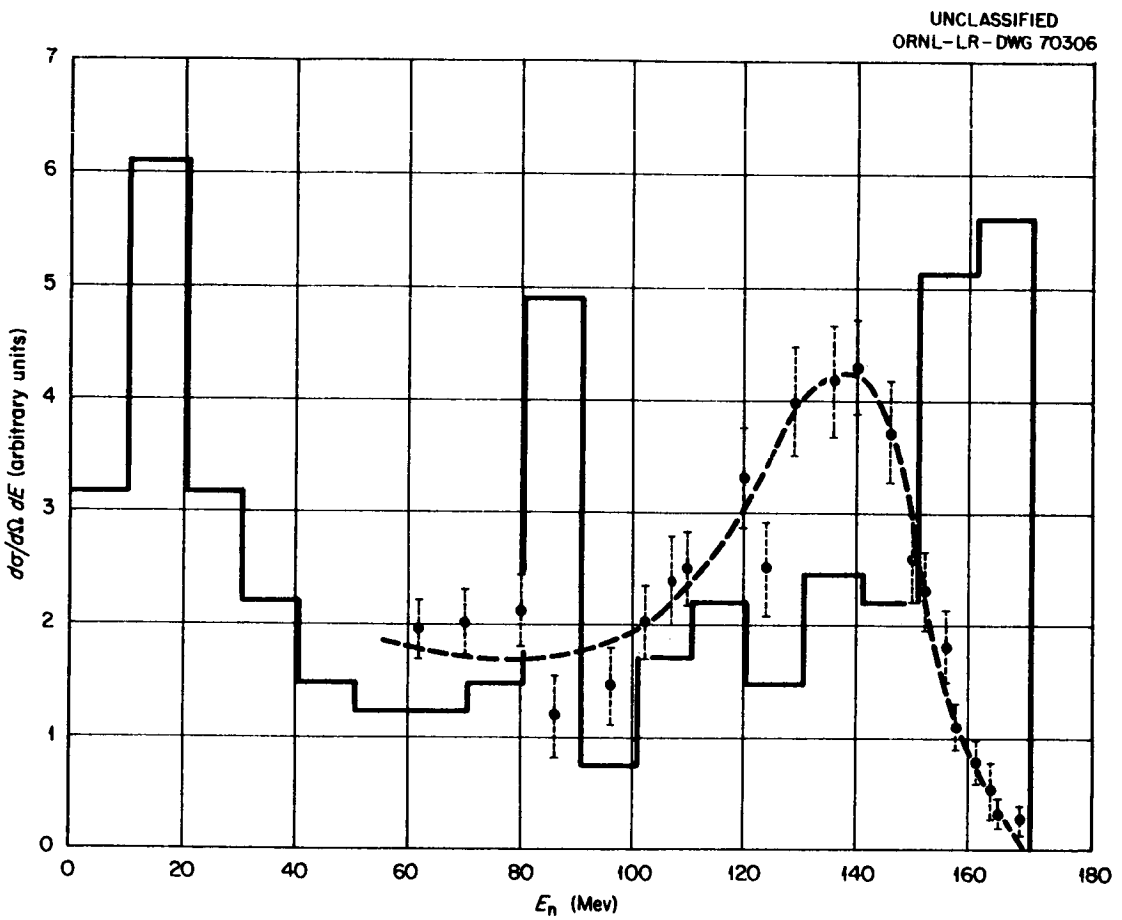

Fig. 10. Neutron Spectra at 2.5° from 171-Mev Protons on Uranium. Dotted curve: experimental results of Cassels et al. [Phil. Mag. 42, 215 (1951)]; solid lines: calculated spectrum of neutrons emitted in the angular interval 0 to 15°; ordinate units are arbitrary.

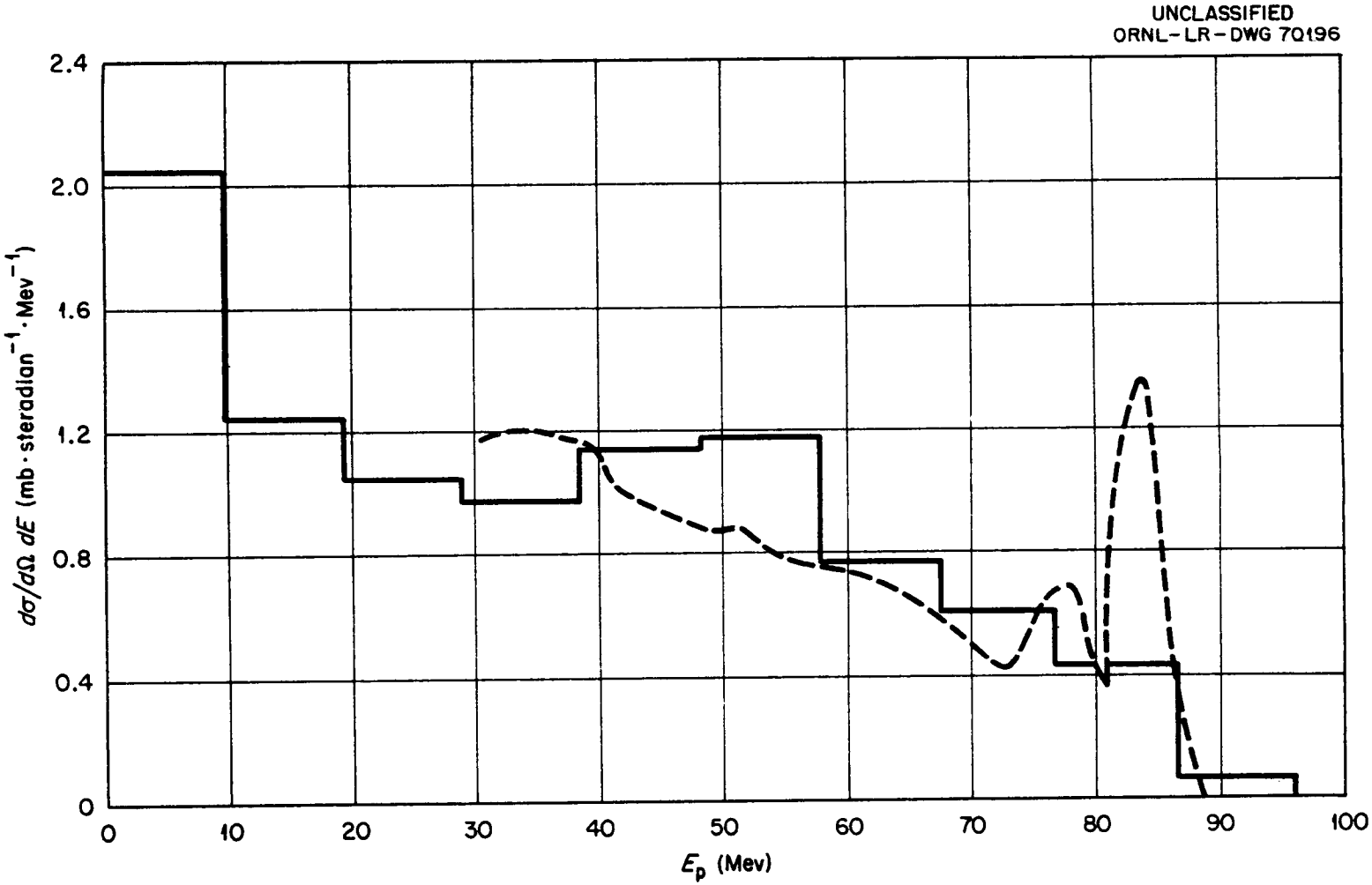

Fig. 11. Proton Spectra at 40° from 96-Mev Protons on Fluorine. Dotted curve: experimental results of Strauch and Titus [Phys. Rev. 104, 191 (1956)]; solid lines: calculated spectrum of protons emitted in the angular interval 30 to 50°.

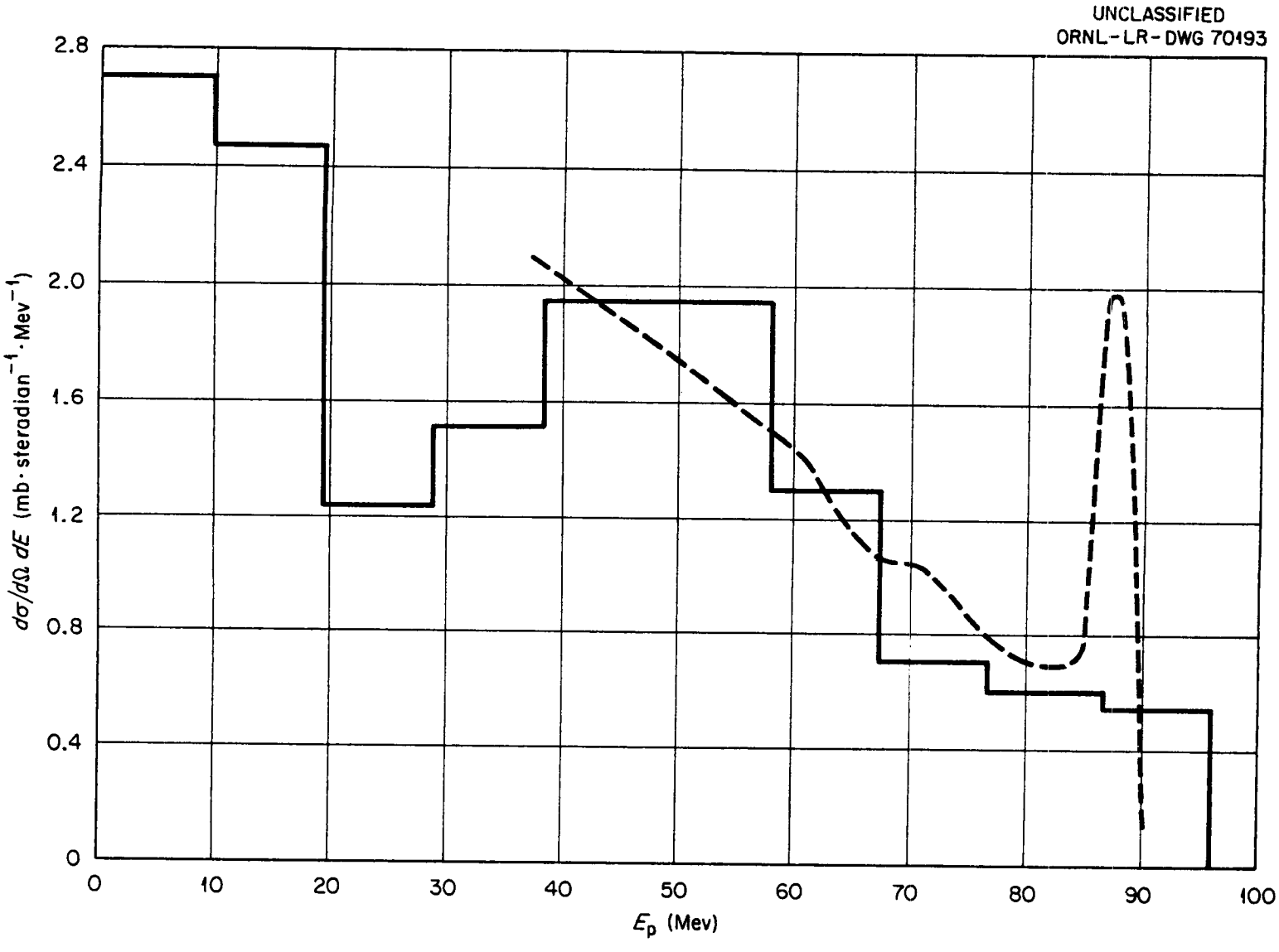

Fig. 12. Proton Spectra at 40° from 96-Mev Protons on Copper. Dotted curve: experimental results of Strauch and Titus [Phys. Rev. 104, 191 (1956)]; solid lines: calculated spectrum of protons emitted in the angular interval 30 to 50°.

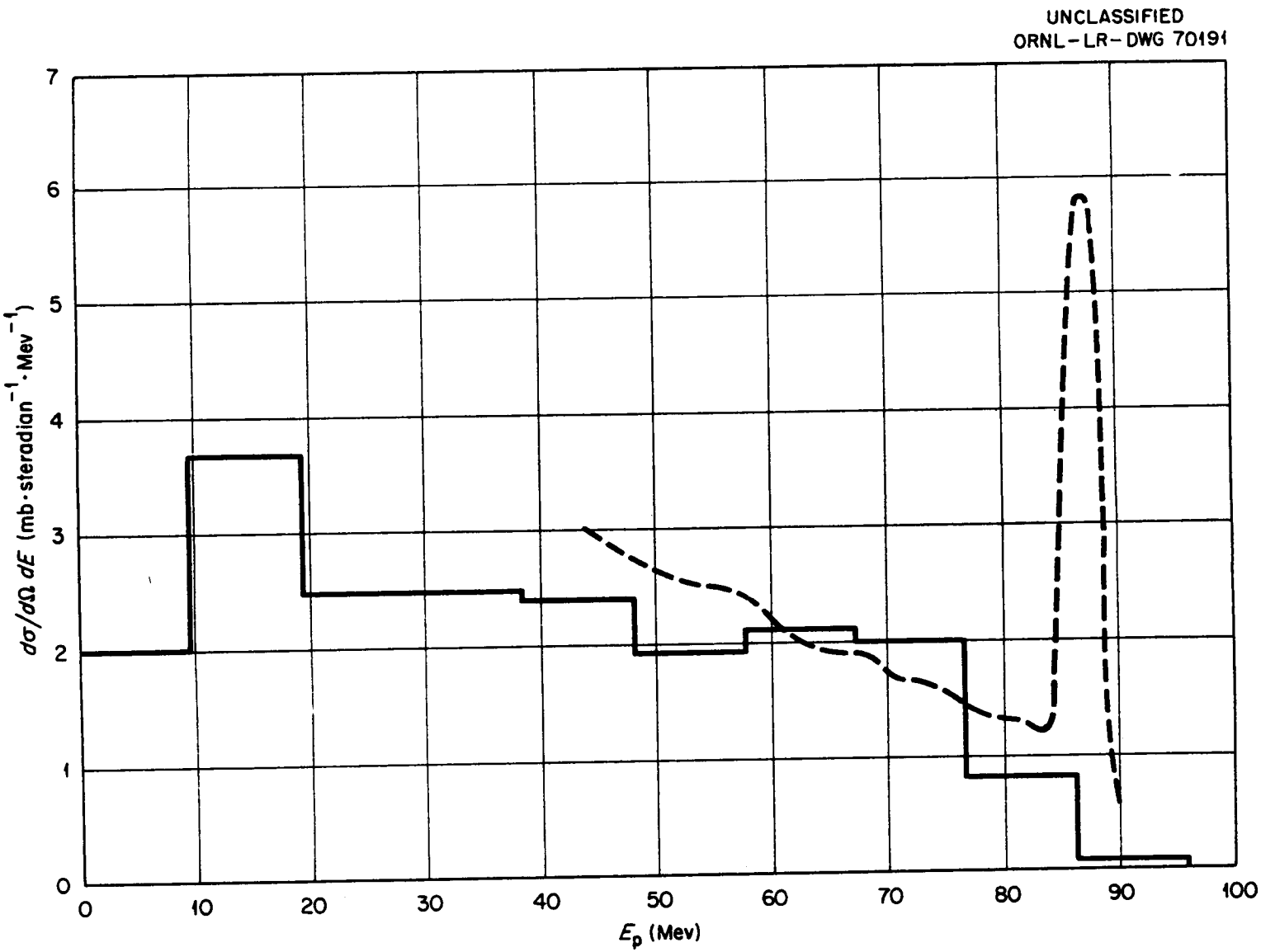

Fig. 13. Proton Spectra at 40° from 96-Mev Protons on Bismuth. Dotted curve: experimental results of Strauch and Titus [Phys. Rev. 104, 191 (1956)]; solid lines: calculated spectrum of protons emitted in the angular interval 30 to 50°.

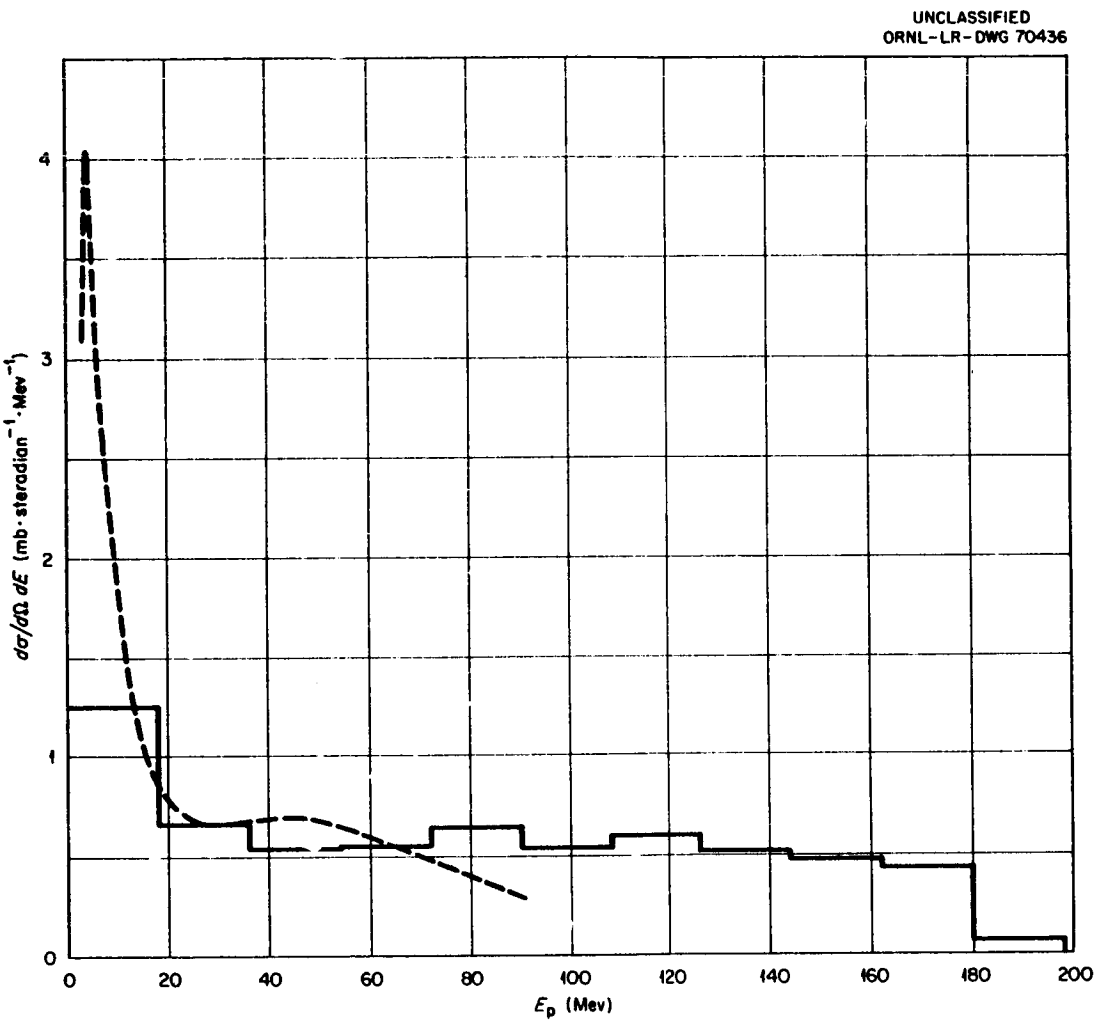

Fig. 14. Proton Spectra from 0 to 65° for 190-Mev Protons on Aluminum. Dashed curve: Bailey's experimental results ["Angle and Energy Distributions of Charged Particles from the High Energy Nuclear Bombardment of Various Elements," UCRL-3334 (Mar. 1, 1956)]; solid lines: calculated spectrum.

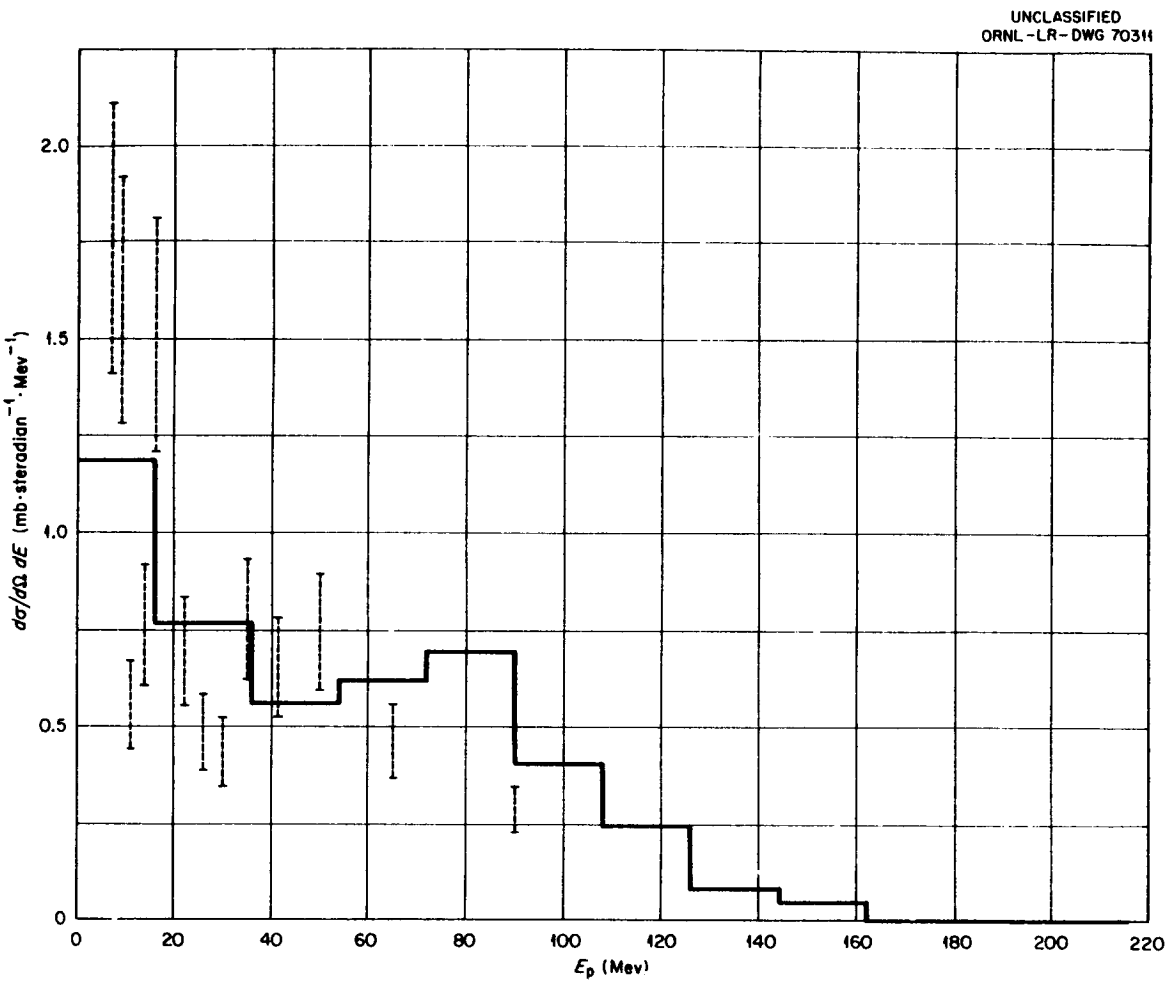

Fig. 15. Proton Spectra from 46 to 65° for 190-Mev Protons on Aluminum. Dotted lines: Bailey's experimental results (UCRL-3334); solid lines: calculated spectrum.

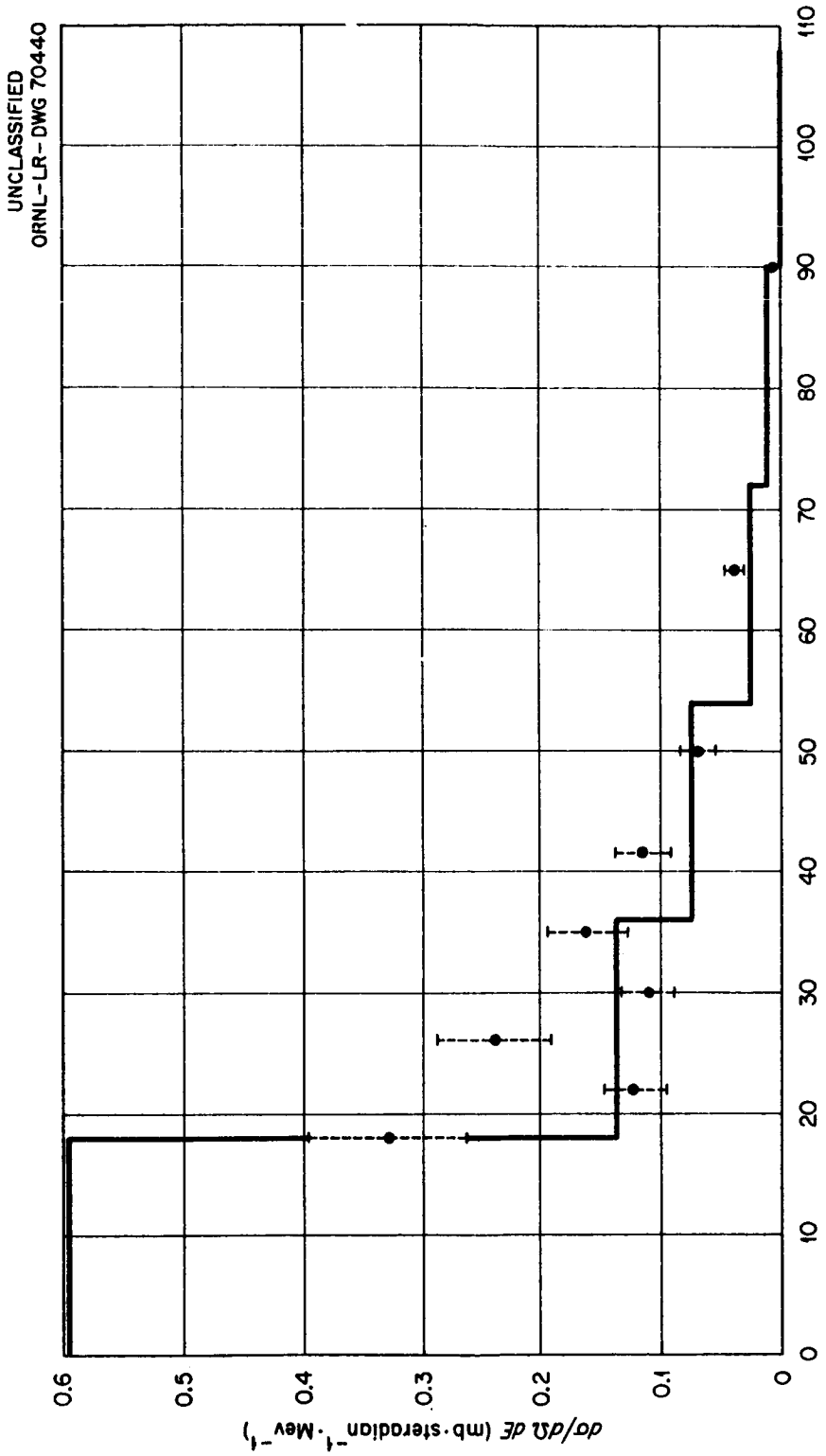

Fig. 16. Proton Spectra from 102 to 117° for 190-Mev Protons on Aluminum. Dotted lines: Bailey's experimental results (UCRL-3334); solid lines: calculated spectrum.

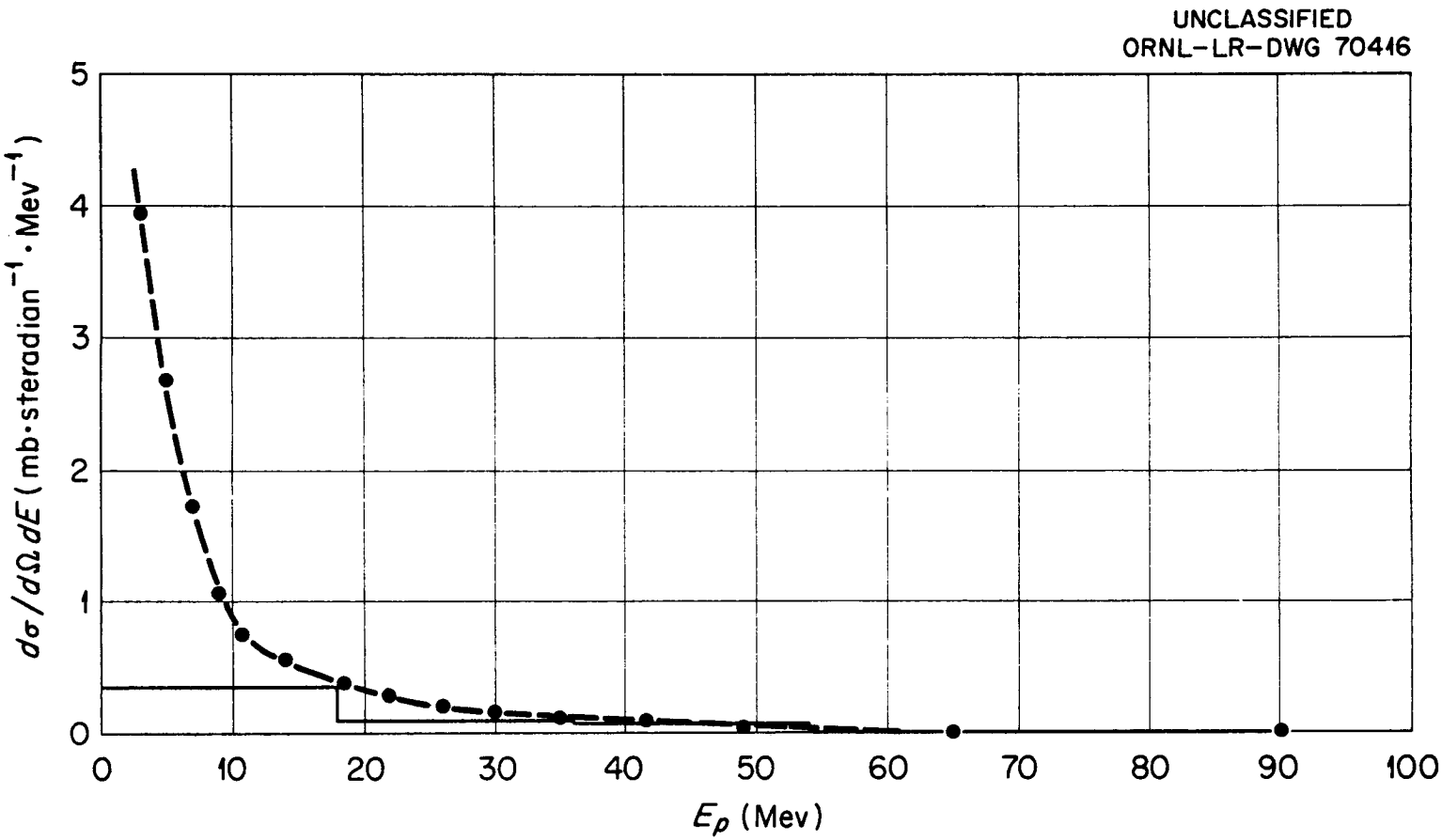

Fig. 17. Proton Spectra from 100 to 180° for 190-Mev Protons on Aluminum. Dotted curve: Bailey's experimental results (UCRL-3334); solid lines: calculated spectrum.

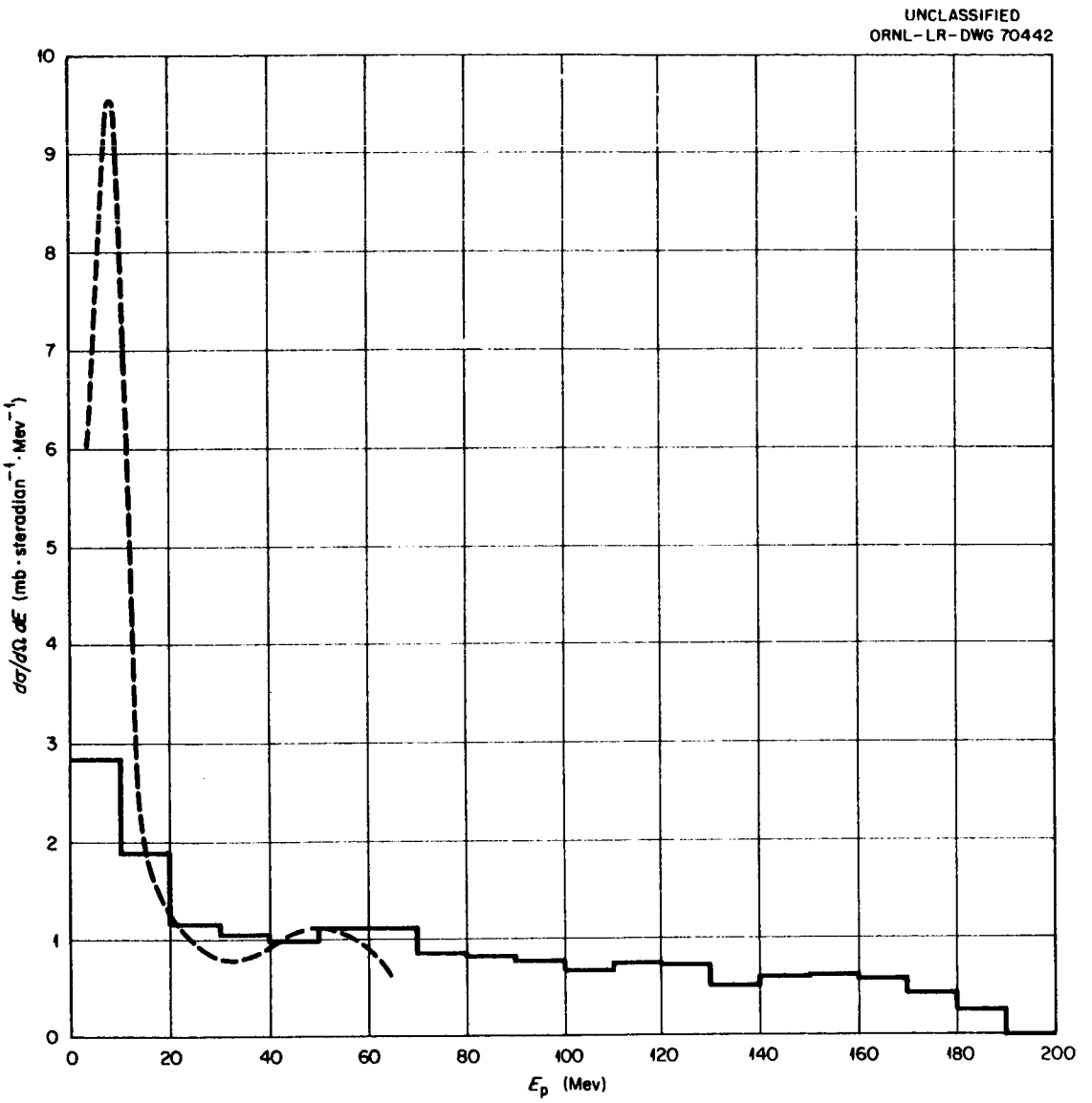

Fig. 18. Proton Spectra from 0 to 65° for 190-Mev Protons on Nickel. Dotted curve: Bailey's experimental results (UCRL-3334); solid lines: calculated spectrum.

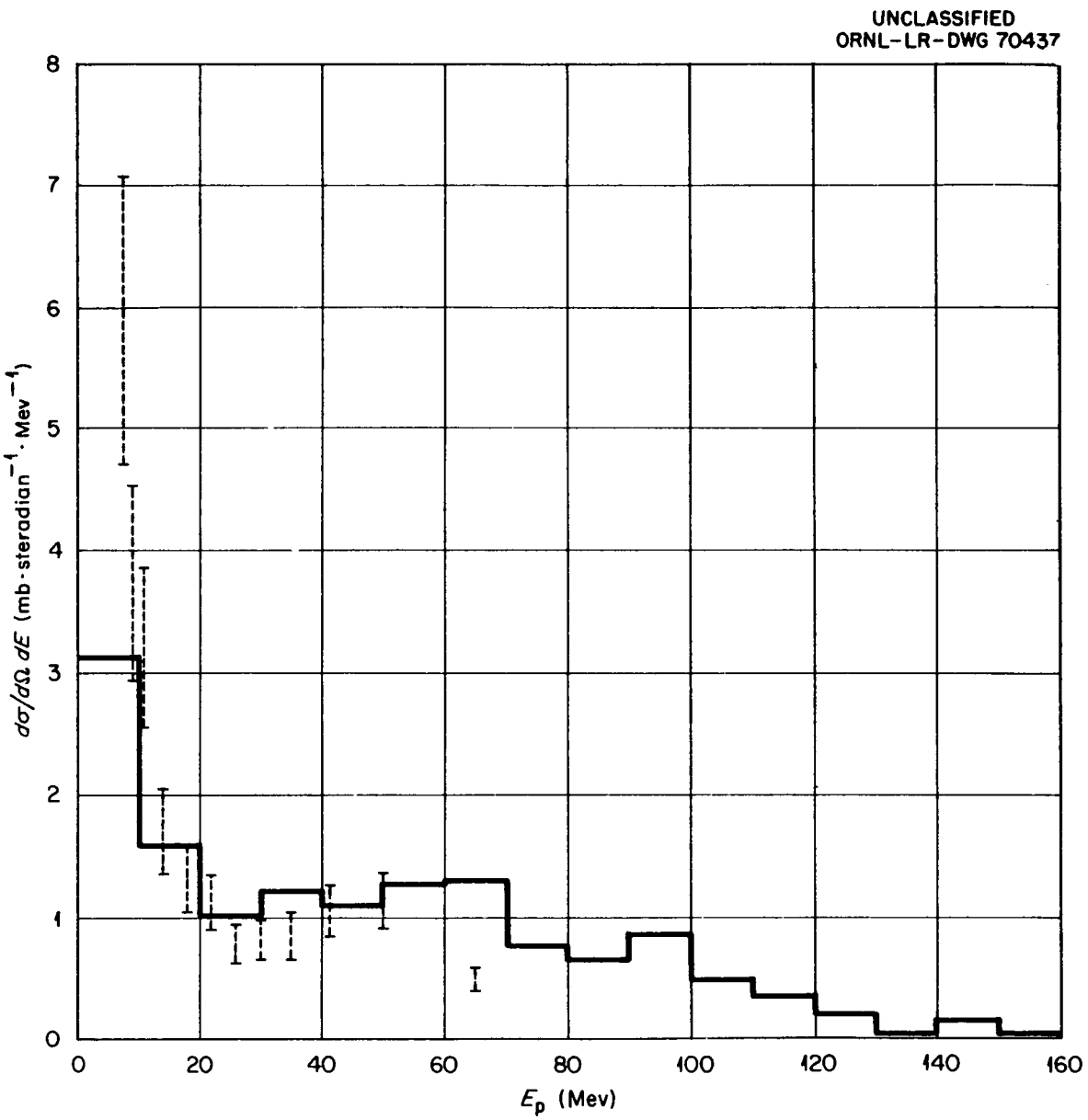

Fig. 19. Proton Spectra from 46 to 65° for 190-Mev Protons on Nickel. Dotted lines: Bailey's experimental results (UCRL-3334); solid lines: calculated spectrum.

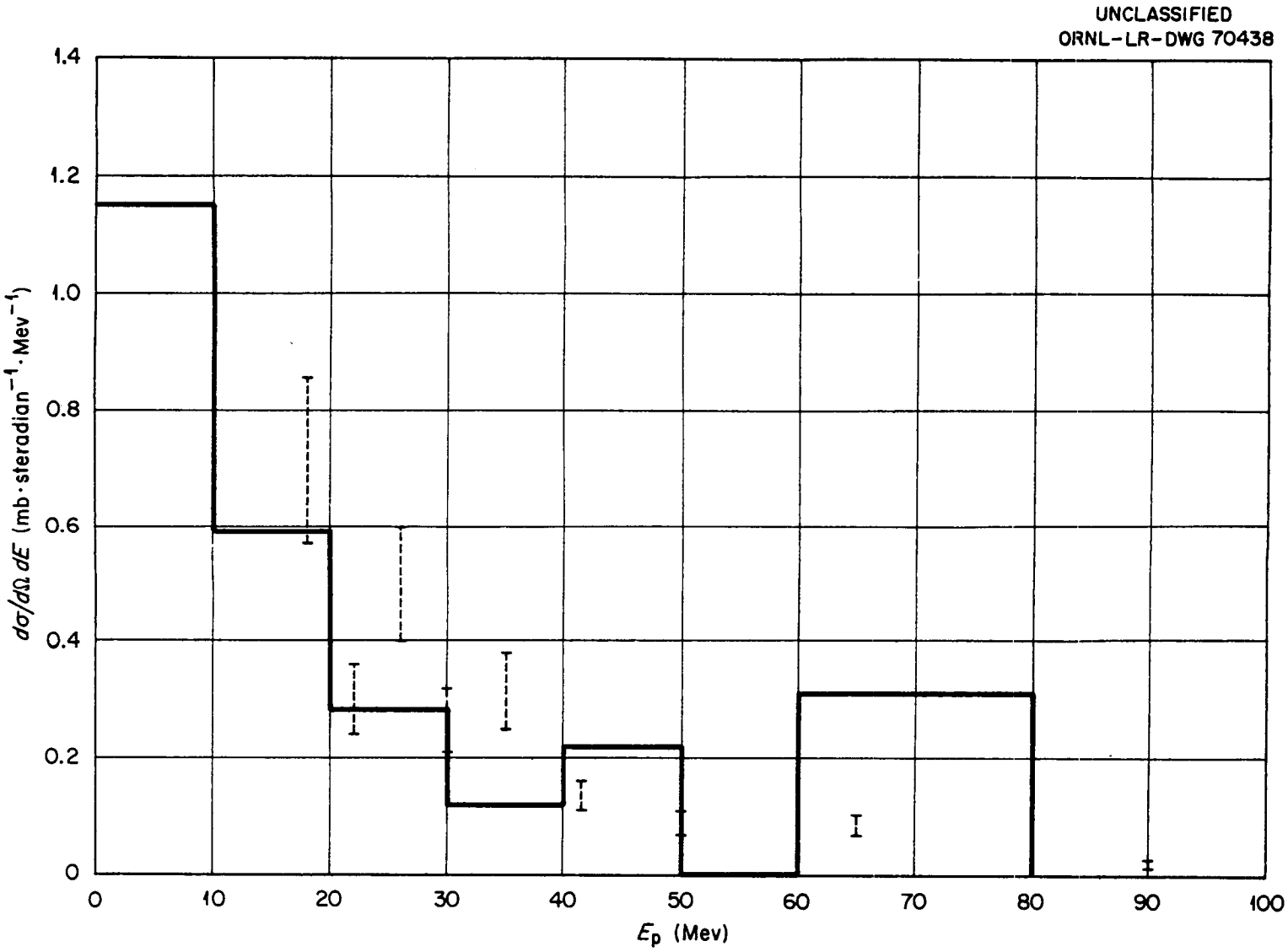

Fig. 20. Proton Spectra from 102 to 117° for 190-Mev Protons on Nickel. Dotted lines: Bailey's experimental results (UCRL-3334); solid lines: calculated spectrum.

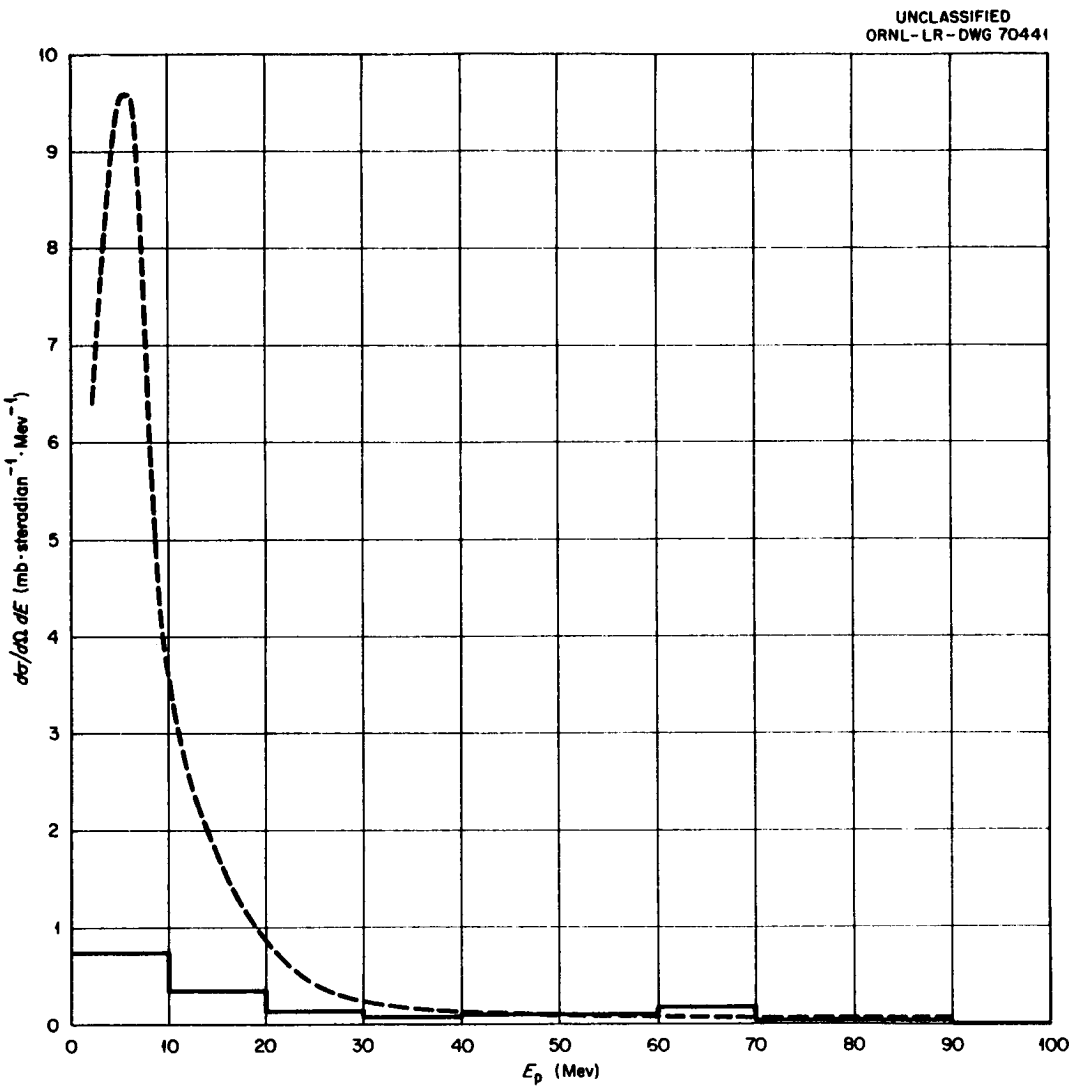

Fig. 21. Proton Spectra from 100 to 180° for 190-Mev Protons on Nickel. Dotted curve: Bailey's experimental results (UCRL-3334); solid lines: calculated spectrum.

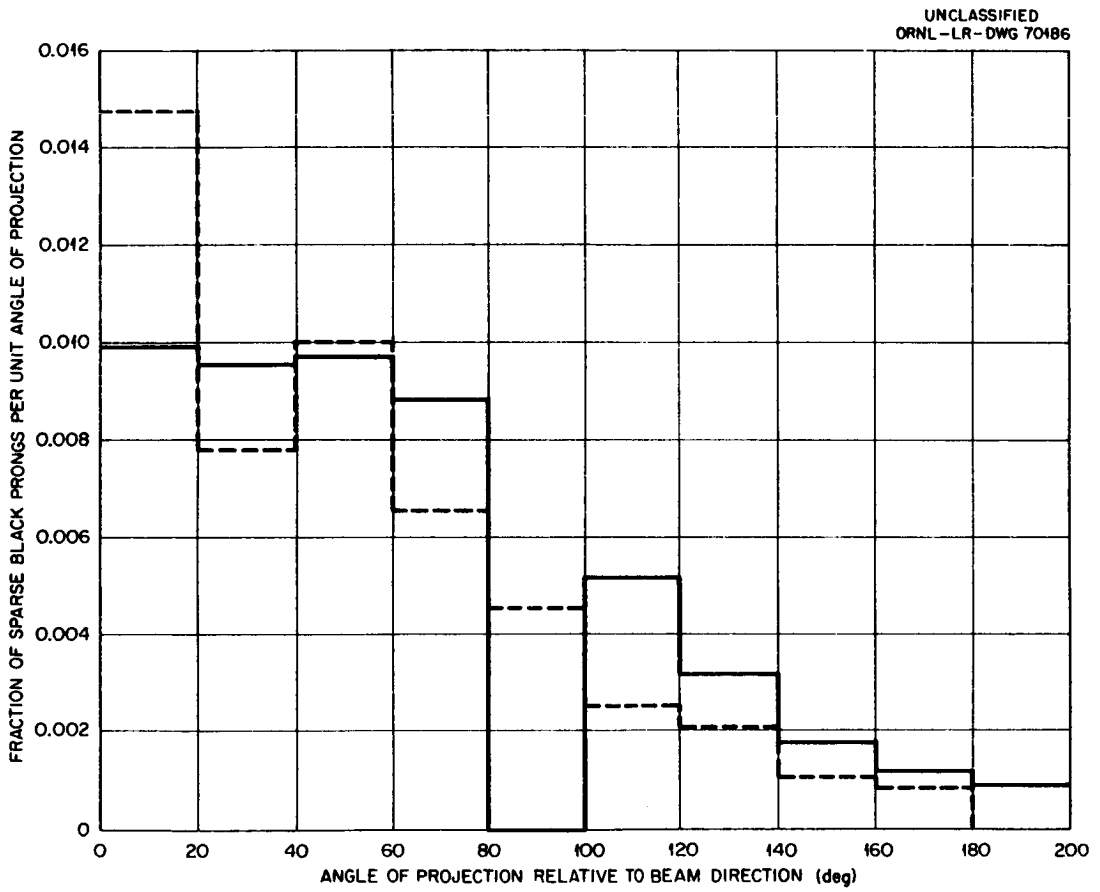

Fig. 22. Angular Distribution of Sparse Black Prongs from 375-Mev Protons on Heavy-Emulsion Nuclei. Dotted lines: experimental results of Bernardini et al. [Phys. Rev. 85, 826 (1952)]; solid lines: calculated distribution for protons emitted with energies from 30 to 100 Mev for 375-Mev protons on Ru^{100}.

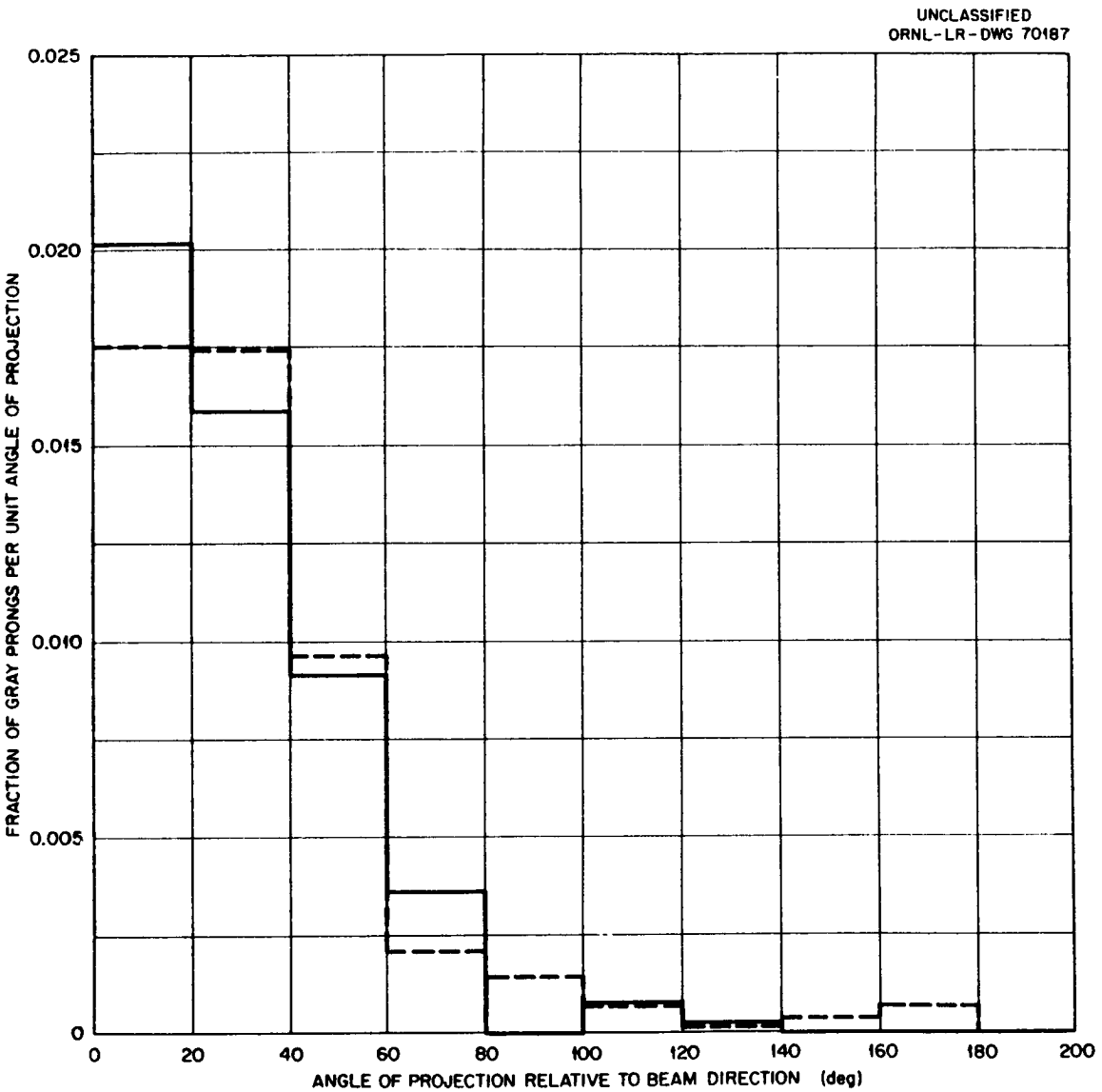

Fig. 23. Angular Distribution of Gray Prongs from 375-Mev Protons on Heavy-Emulsion Nuclei. Dotted lines: experimental results of Bernardini et al. [Phys. Rev. 85, 826 (1952)]; solid lines: calculated distribution for protons emitted with energies from 100 to 375 Mev for 375-Mev protons on Ru^{100}.

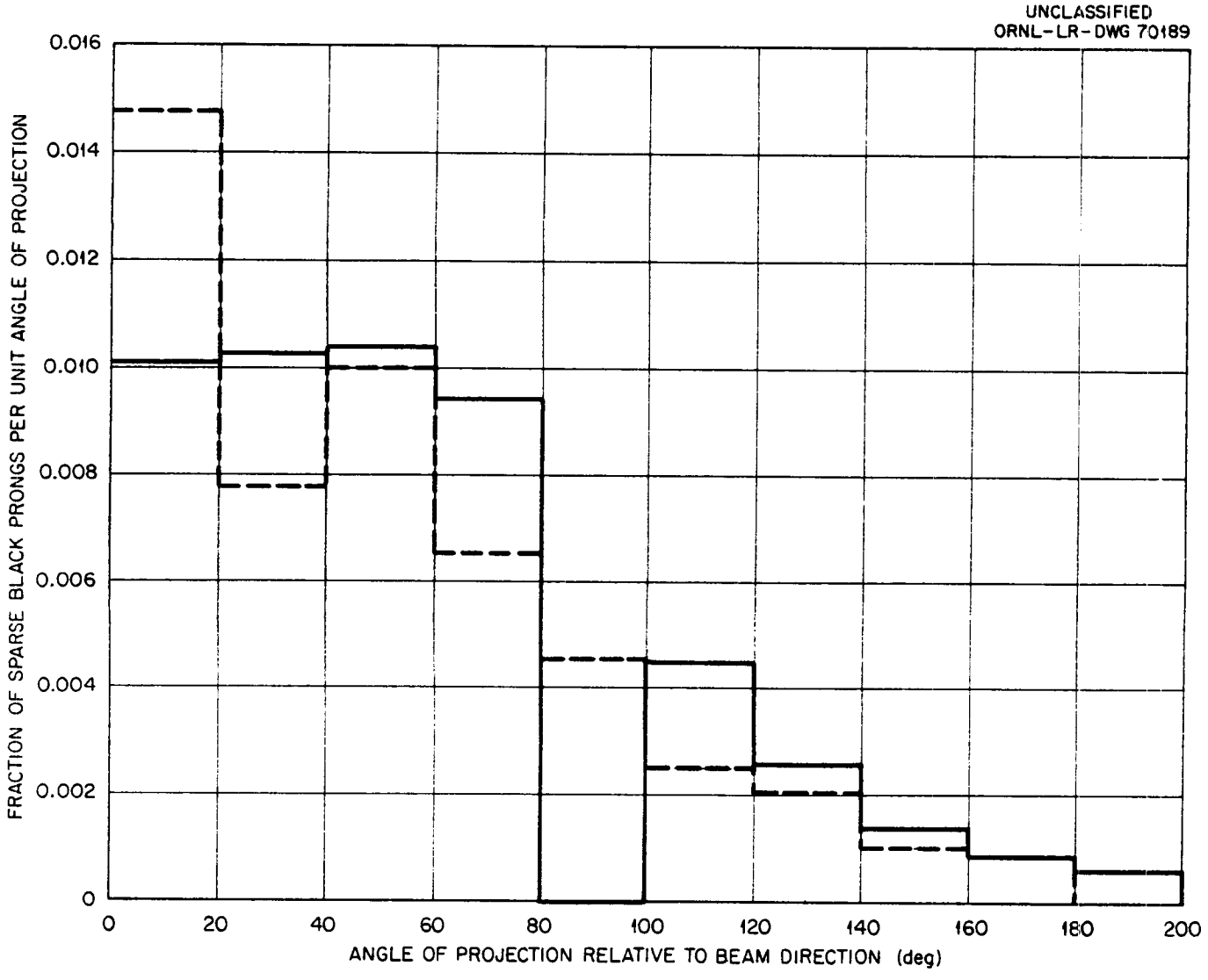

Fig. 24. Angular Distribution of Sparse Black Prongs from 300-Mev Neutrons on Heavy-Emulsion Nuclei. Dotted lines: experimental results of Bernardini et al. [Phys. Rev. 85, 826 (1952)]; solid lines: calculated distribution for protons emitted with energies from 30 to 100 Mev for 300-Mev neutrons on Ru^{100}.

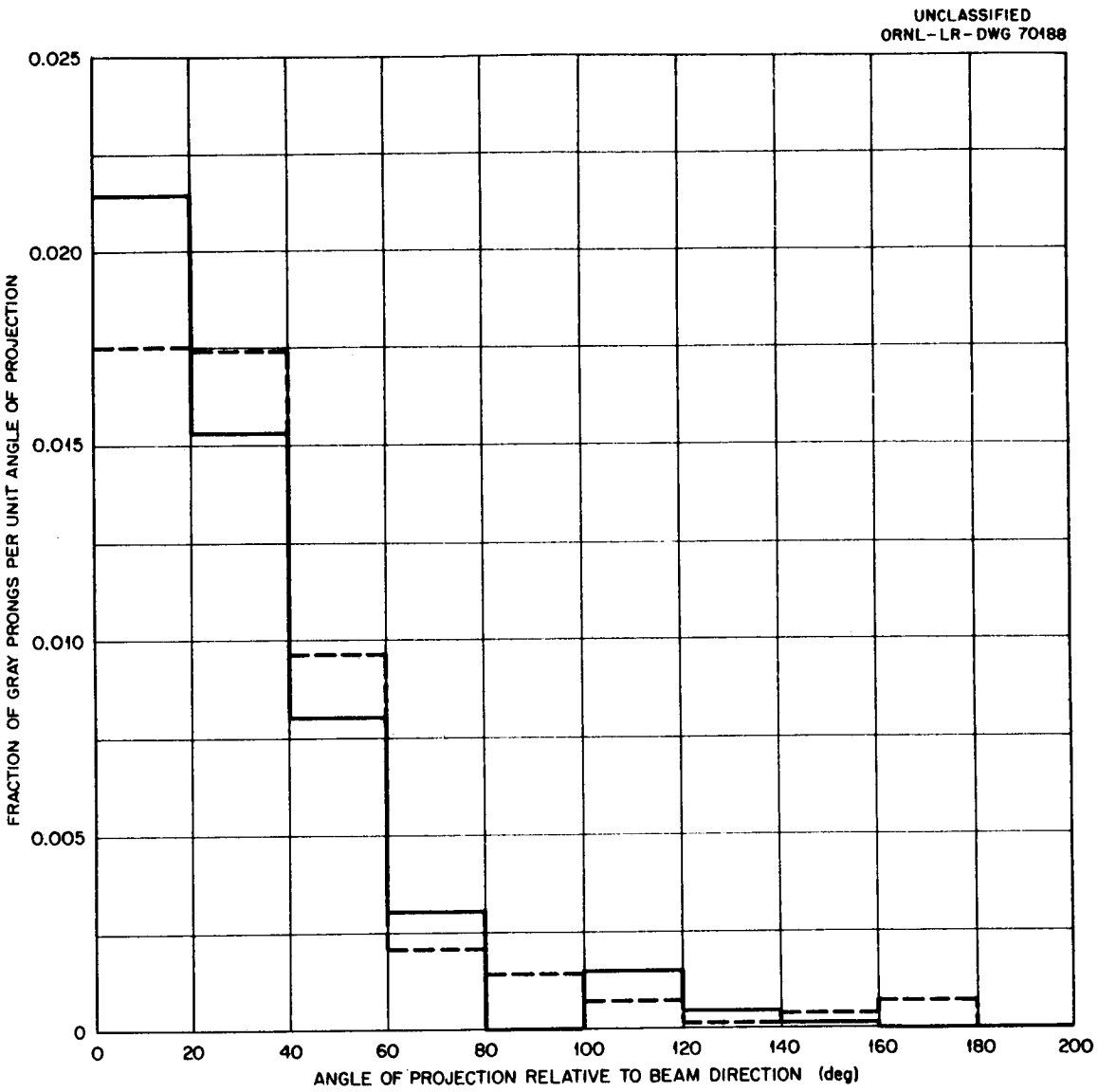

Fig. 25. Angular Distribution of Gray Prongs from 300-Mev Neutrons on Heavy-Emulsion Nuclei. Dotted lines: experimental results of Bernardini et al. [Phys. Rev. 85, 826 (1952)]; solid lines: calculated distribution for protons emitted with energies from 100 to 300 Mev for 300-Mev neutrons on Ru^{100}.

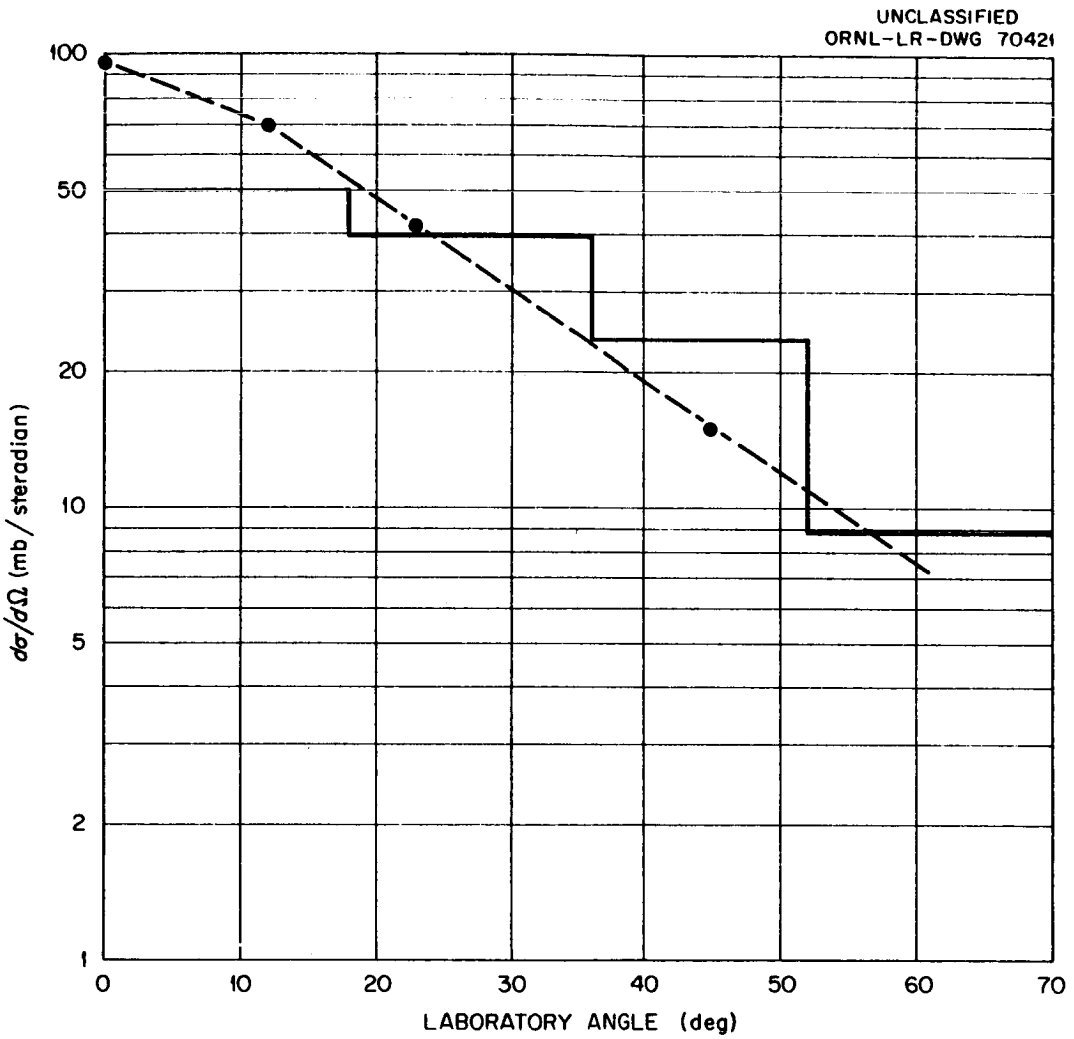

Fig. 26. Angular Distribution of Protons with Energies Greater Than 20 Mev from 90-Mev Neutrons on Carbon. Dotted lines: experimental results of Hadley and York [Phys. Rev. 80, 345 (1950)]; solid lines: calculated distribution.

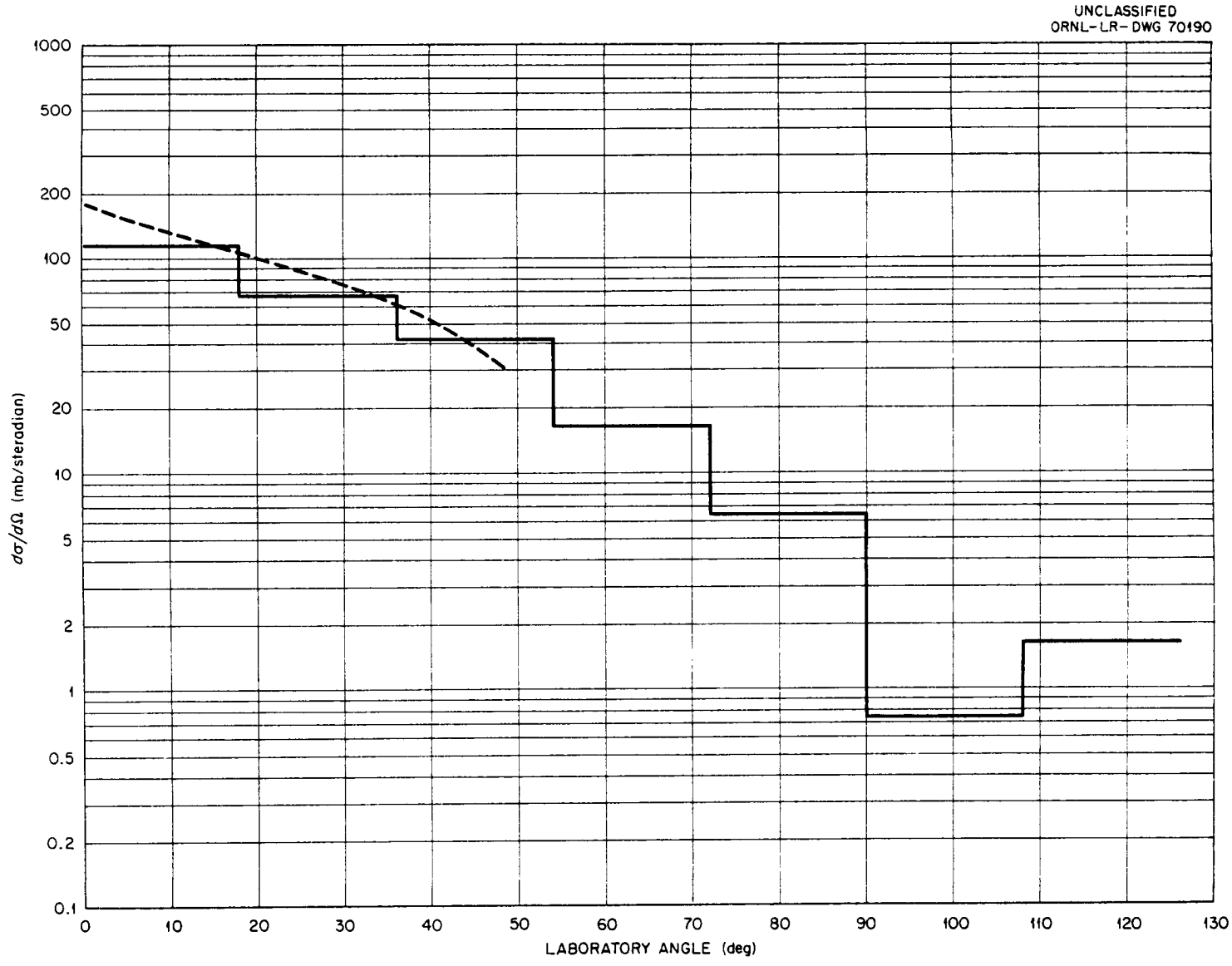

Fig. 27. Angular Distribution of Protons with Energies Greater Than 20 Mev from 90-Mev Neutrons on Copper. Dotted lines: experimental results of Hadley and York [Phys. Rev. 80, 345 (1950)]; solid lines: calculated distribution.

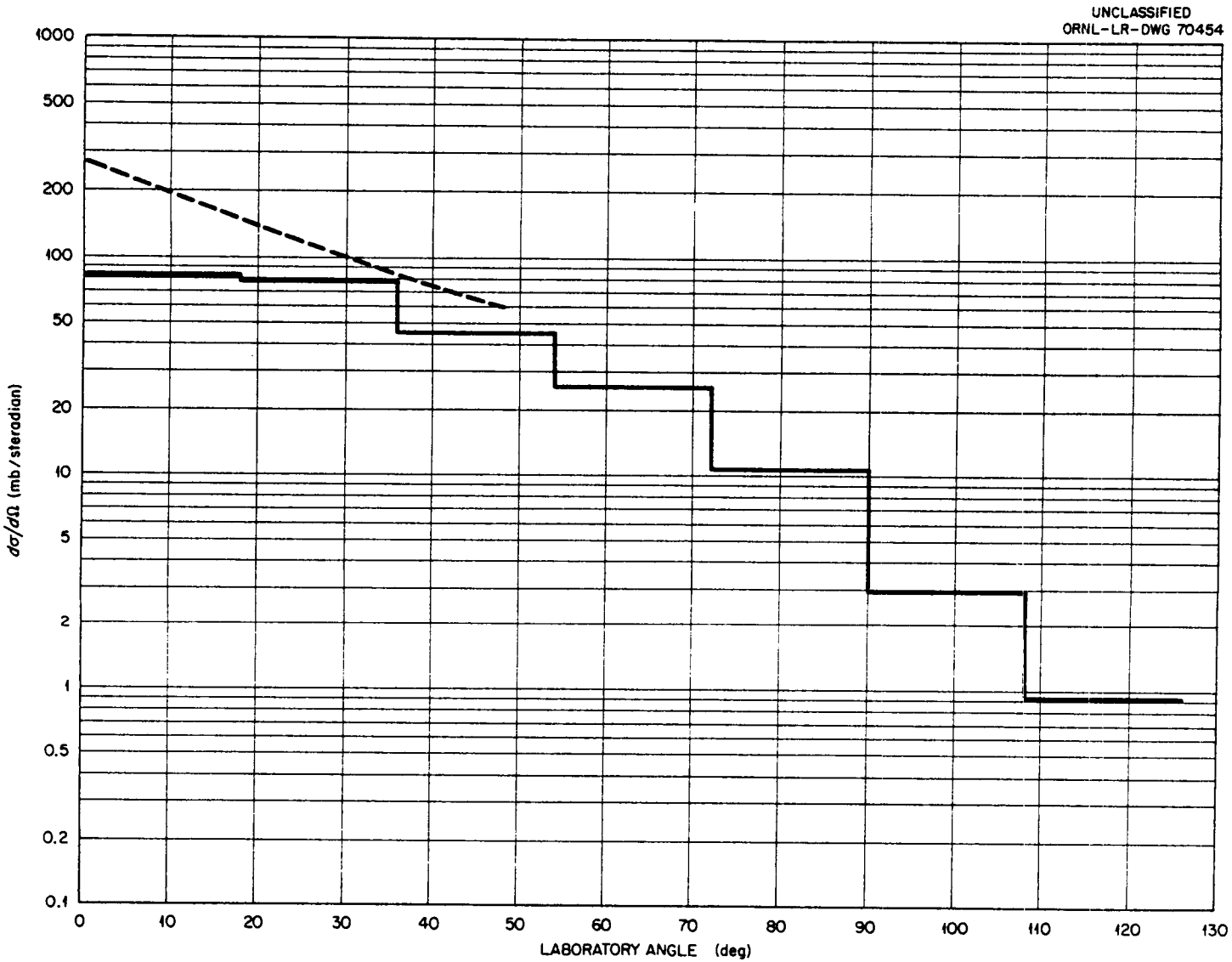

Fig. 28. Angular Distribution of Protons with Energies Greater Than 20 Mev from 90-Mev Neutrons on Lead. Dotted lines: experimental results of Hadley and York [Phys. Rev. 80, 345 (1950)]; solid lines: calculated distribution.

The calculations are compared with some experimental data on cascade particle multiplicities in Table 3. Although the agreement is not bad, the calculation does not predict the symmetry that was observed in the experiments for neutron-induced and proton-induced reactions.

Comparison with Experiment: Incident Pions

The comparison of calculated nonelastic cross sections for incident pions with experimental data is given in Table 4. The agreement is not quite so good as that for incident nucleons.

The energy spectra of nonelastically scattered pions into various angular intervals are shown in Figs. 29-33. The agreement is not bad although all the comparisons for these data are on a relative basis.

A discrepancy between the calculated data and experiments exists for nonelastic scattering at right angles and in the backward direction, as is illustrated in Figs. 34 and 35 for two different nuclear configurations. This discrepancy was observed when previous calculations of this type[9] were compared with the data obtained from use of a smaller radius nuclear model with a constant nucleon density.

The data from emulsion work are compared in Figs. 36 and 37; reasonable agreement is indicated. Other angular distributions are illustrated in Figs. 38-41. Here the calculation indicates the trends properly, but the agreement is not very good on an absolute basis.

The spectra from slow π^- absorption are compared with experimental results in Fig. 42 for a nucleus with a standard configuration and for one with a constant nucleon density distribution and a smaller nuclear radius ($r = 1.3 \times 10^{-13} A^{1/3}$). The agreement is fair and independent of nuclear configuration.

Calculated pion absorption and charge-exchange cross sections are compared with experimental values in Tables 5 and 6, respectively.

The agreement is reasonable for the absorption cross section but not very good for the charge-exchange cross section. This seems to be persistent and difficult to explain since the experiments imply a smaller cross section than the calculated values. However, the free-particle charge-exchange cross section is quite large.

In Table 7 the calculated and experimental charge-exchange plus absorption cross-section data are compared, and except for the last two entries the agreement is quite good.

Conclusions

This calculation seems to reproduce most of the experimental data for incident nucleons very well. The largest discrepancy is in the spectra of cascade particles emitted in the forward direction for small incident nucleon energies on light- to medium-weight nuclei.

Table 4. Calculated and Experimental Total Nonelastic Cross Sections for Pions Incident on Various Nuclei

Pion	Target	Energy (Mev)	Nonelastic Cross Section (mb)	
			Calculated[a]	Experimental
π^+	Li	195	324 ± 10	226 ± 18[b]
	C	185	455 ± 11	325 ± 26[b]
		270	358 ± 10	$296 \begin{smallmatrix}+35\\-28\end{smallmatrix}$[c]
	Pb	50	1563 ± 26	1620[d]
π^-	C	125	458 ± 11	308 ± 43[e]
		150	478 ± 11	430 ± 42[f]
		225	423 ± 11	346 ± 21[g]
	Al	225	653 ± 14	596 ± 30[g]
	Cu	225	1038 ± 19	1058 ± 45[g]
	Sn	225	1471 ± 20	1550 ± 70[g]
	Pb	125	2062 ± 29	2477 ± 385[e]
		150	2145 ± 29	2490 ± 160[f]
		225	1993 ± 29	2290 ± 90[g]

a. Errors indicated apply for a confidence coefficient of 68%.

b. N. I. Petrov, U. G. Ivanov, and U. A. Rusakov, Soviet Phys. -JETP (English Transl.) 10, 682 (1960).

c. W. Kan Chang et al., Soviet Phys. - JETP (English Transl.) 8, 625 (1959).

d. Calculated from the mean free path in nuclear matter given by G. Saphir, Phys. Rev. 104, 535 (1956).

e. J. O. Kessler and L. M. Lederman, Phys. Rev. 94, 689 (1954).

f. R. H. Miller, Nuovo Cimento 6, 882 (1957).

g. V. G. Ivanov et al., Soviet Phys. - JETP (English Transl.) 4, 922 (1957).

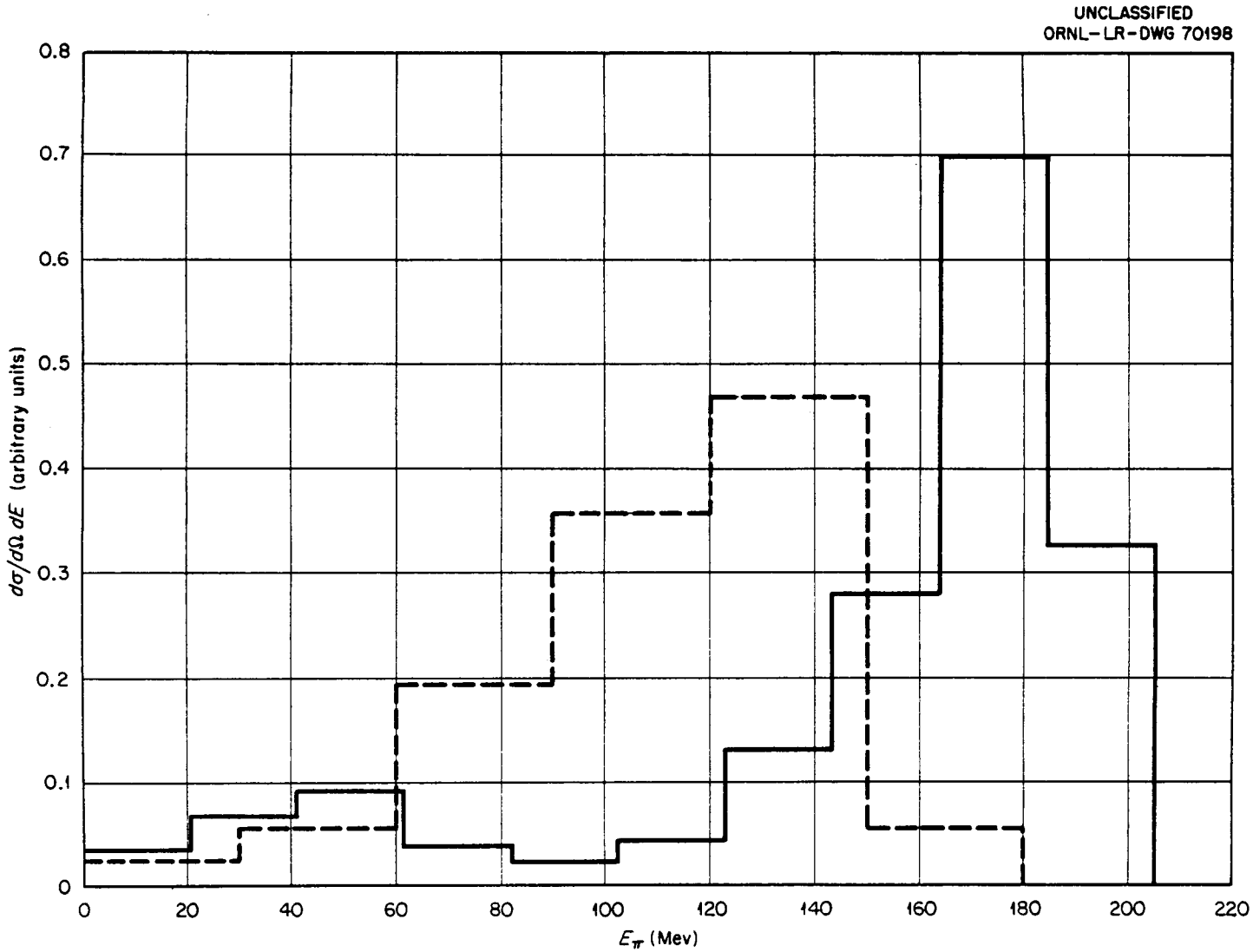

Fig. 29. Energy Spectra of Nonelastic π^+ Emitted in the Angular Interval 0 to 60° from 195-Mev π^+ on Lithium and Carbon. Dotted lines: experimental results of Petrov et al. [Soviet Phys. JETP (English Trans.) 10, 682 (1960)]; solid lines: calculated spectrum; ordinate units are arbitrary.

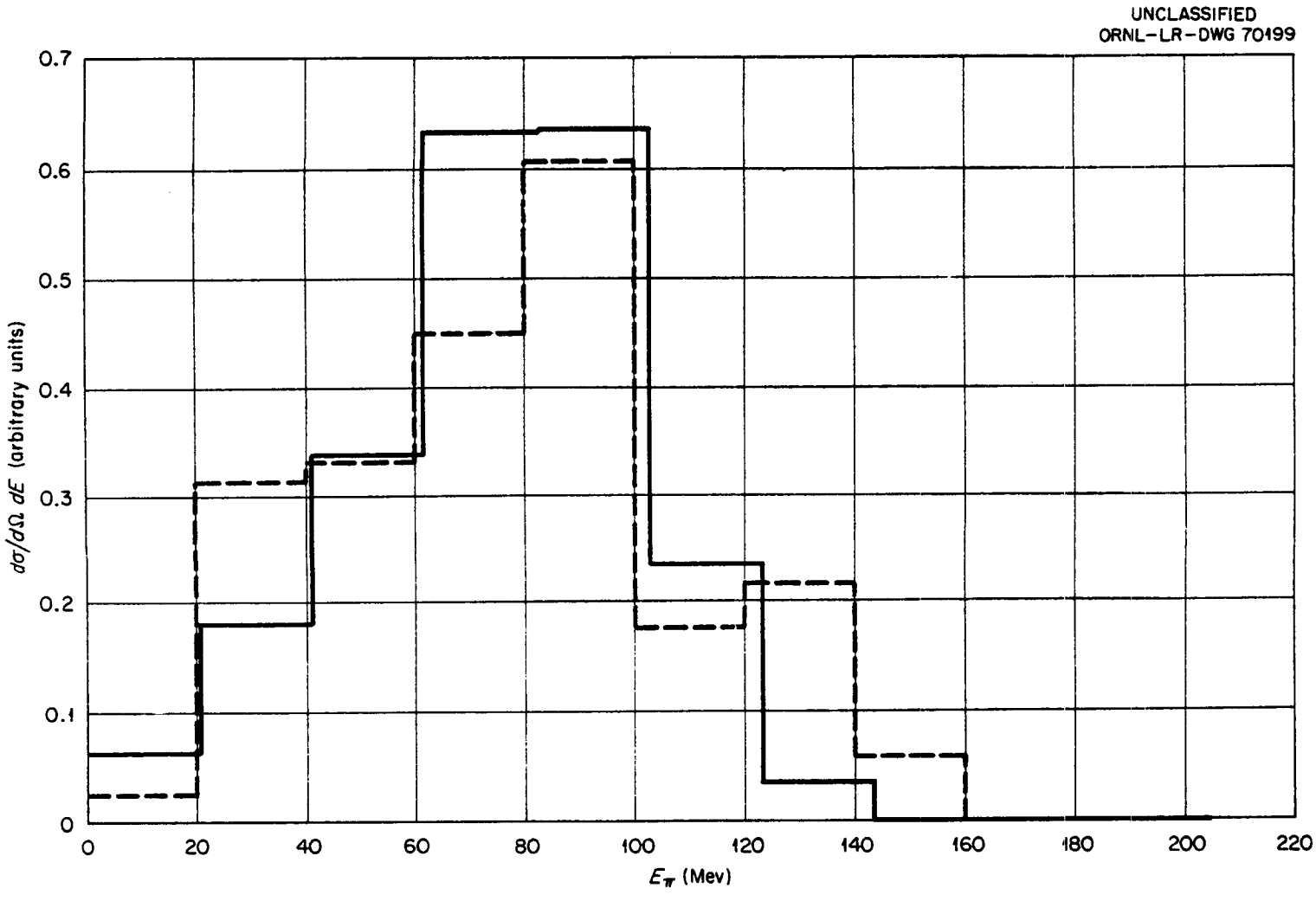

Fig. 30. Energy Spectra of Nonelastic π^+ Emitted in the Angular Interval 120 to 180° from 195-Mev π^+ on Lithium and Carbon. Dotted lines: experimental results of Petrov et al. [Soviet Phys. JETP (English Transl.) 10, 682 (1960)]; solid lines: calculated spectrum. Ordinate units are arbitrary.

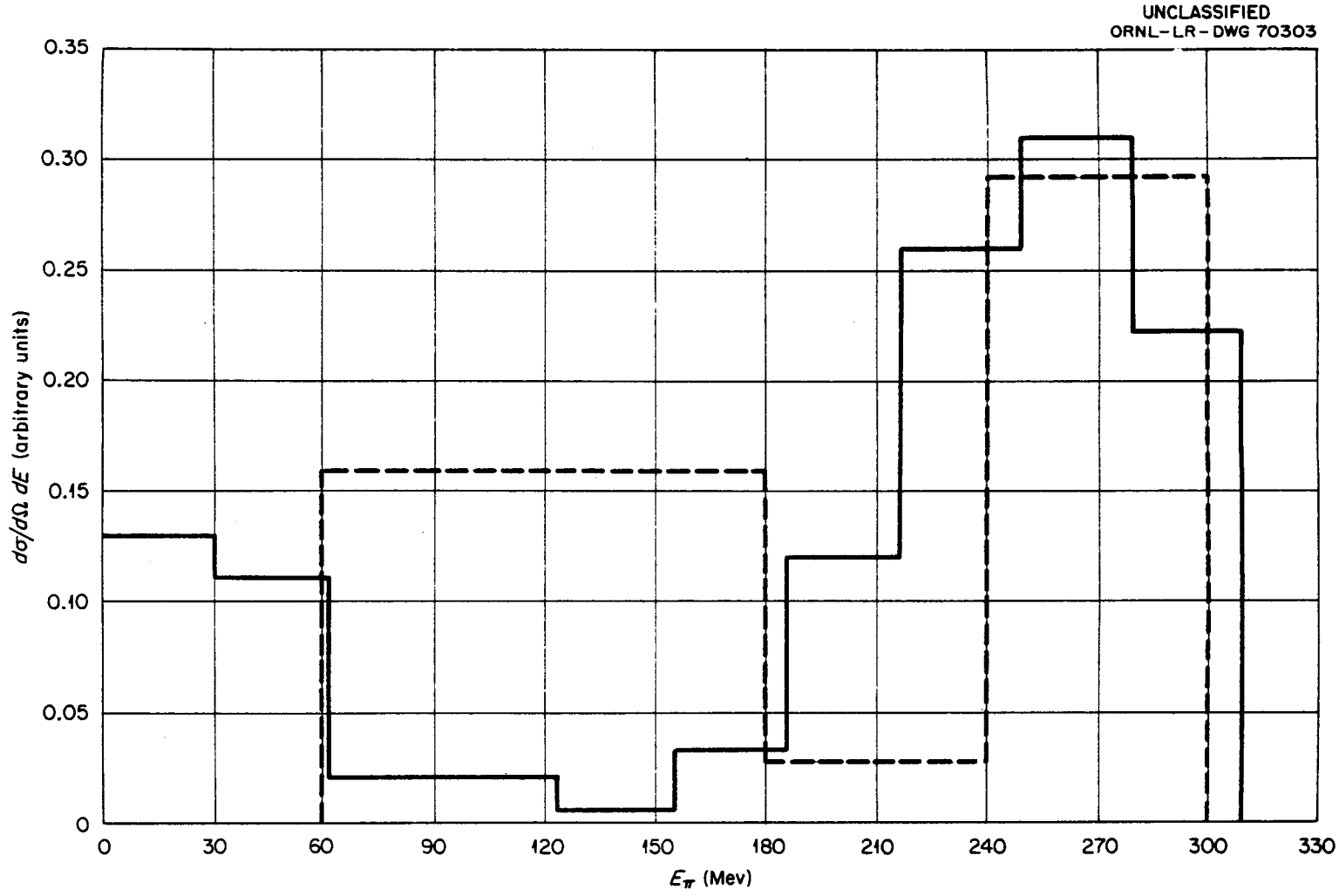

Fig. 31. Energy Spectra of Nonelastic π^- Emitted in the Angular Interval 0 to 60^o from 300-Mev π^- on Heavy-Emulsion Nuclei. Dotted lines: experimental values of Willot-Chemel [Ann. Phys. (Paris) 6, 703 (1961)]; solid lines: calculated values for 300-Mev π^- on Ru^{100}.

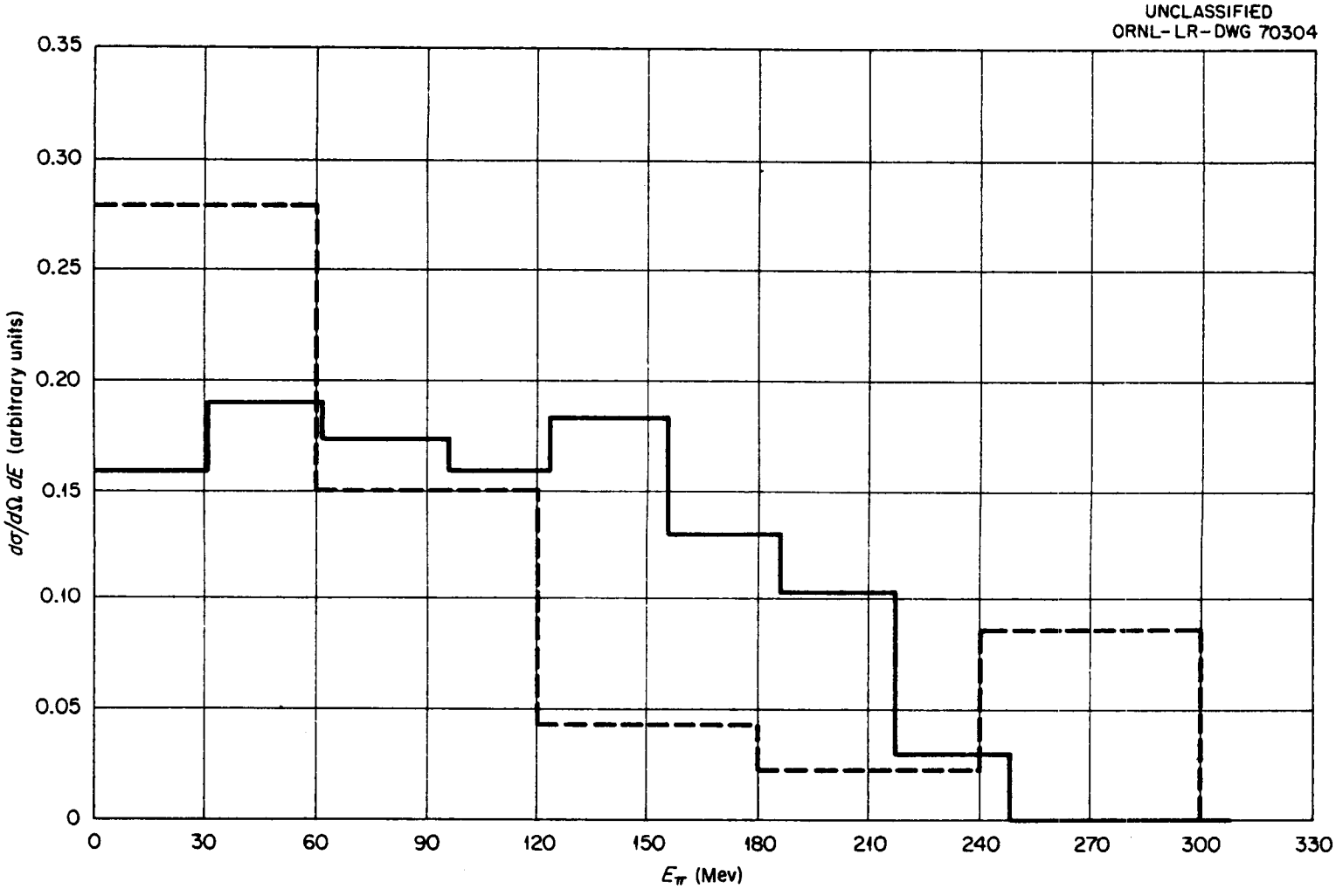

Fig. 32. Energy Spectra of Nonelastic π^- Emitted in the Angular Interval 60 to 120° from 300-Mev π^- on Heavy-Emulsion Nuclei. Dotted lines: experimental values of Willot-Chemel [Ann. Phys. (Paris) 6, 703 (1961)]; solid lines: calculated values for 300-Mev π^- on Ru^{100}.

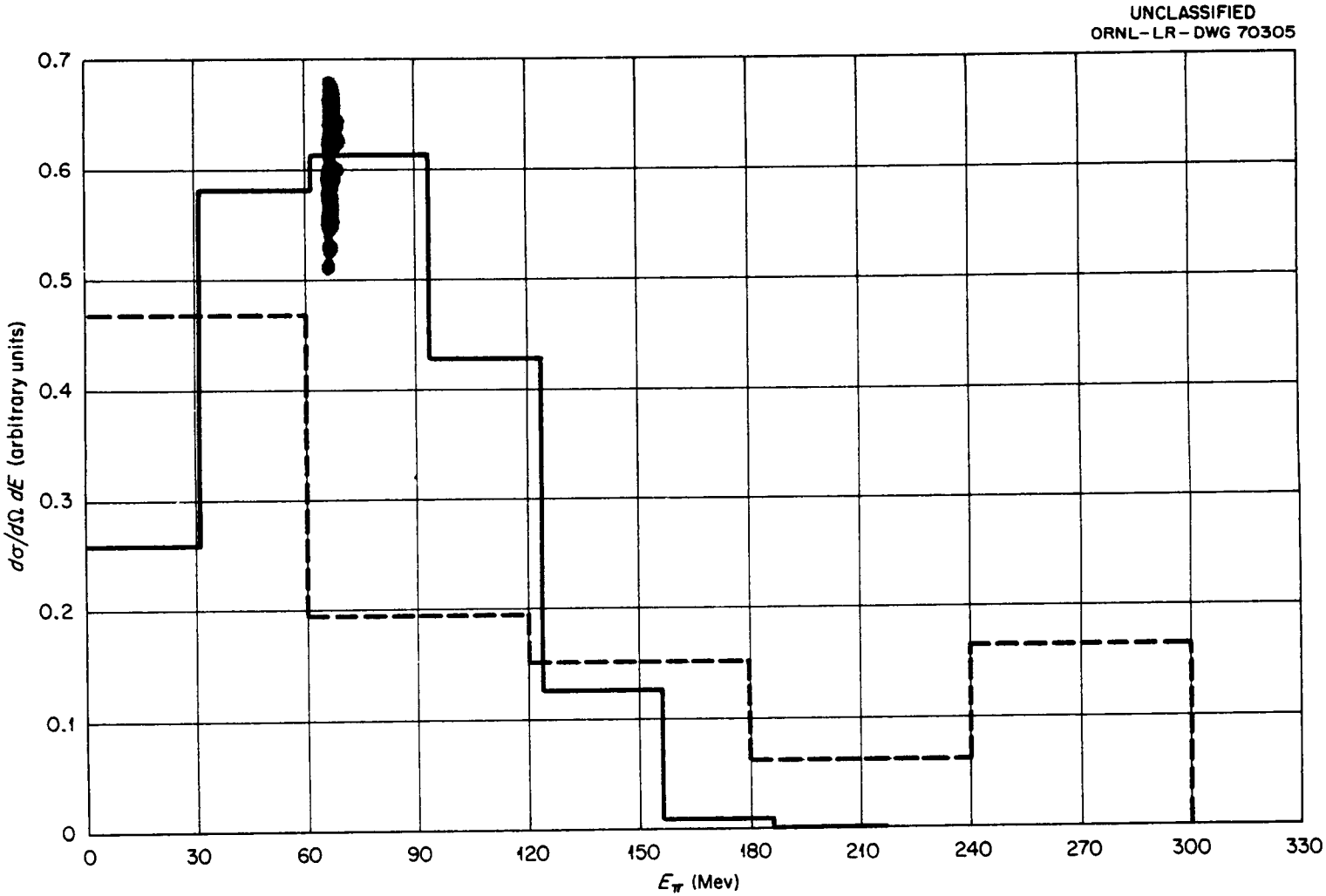

Fig. 33. Energy Spectra of Nonelastic π^- Emitted in the Angular Interval 120 to 180° from 300-Mev π^- on Heavy-Emulsion Nuclei. Dotted lines: experimental values of Willot-Chemel [Ann. Phys. (Paris) 6, 703 (1961)]; solid lines: calculated values for 300-Mev π^- on Ru^{100}.

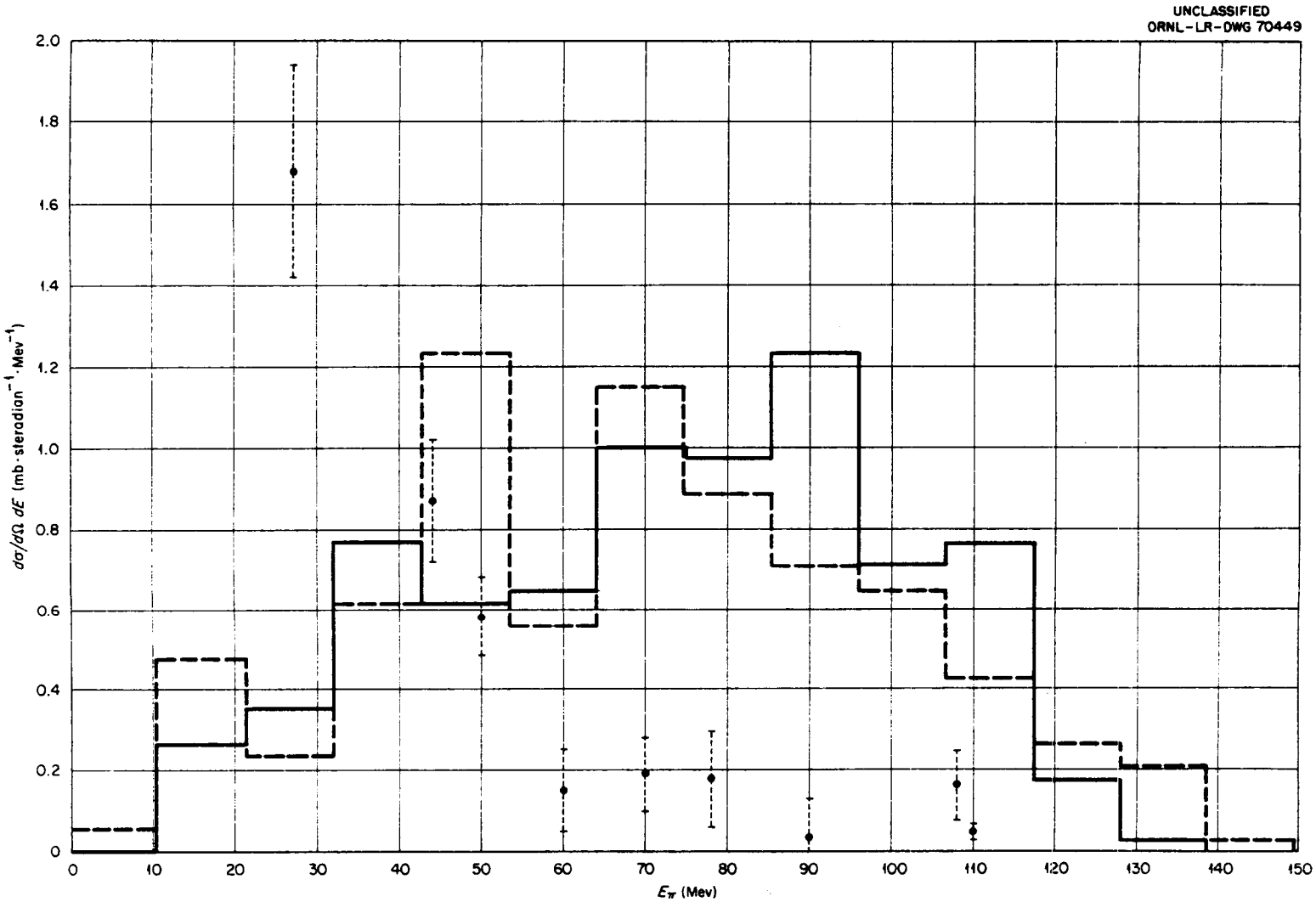

Fig. 34. Nonelastic π^- Spectra at 90° from 150-Mev π^- on Lead. Calculated spectra for π^- in the interval 78 to 102° for nucleus with medium radius. Solid lines: nonuniform nucleon density distribution within the nucleus; dotted lines: uniform density distribution; circles: Miller's experimental values [Nuovo Cimento 6, 882 (1957)].

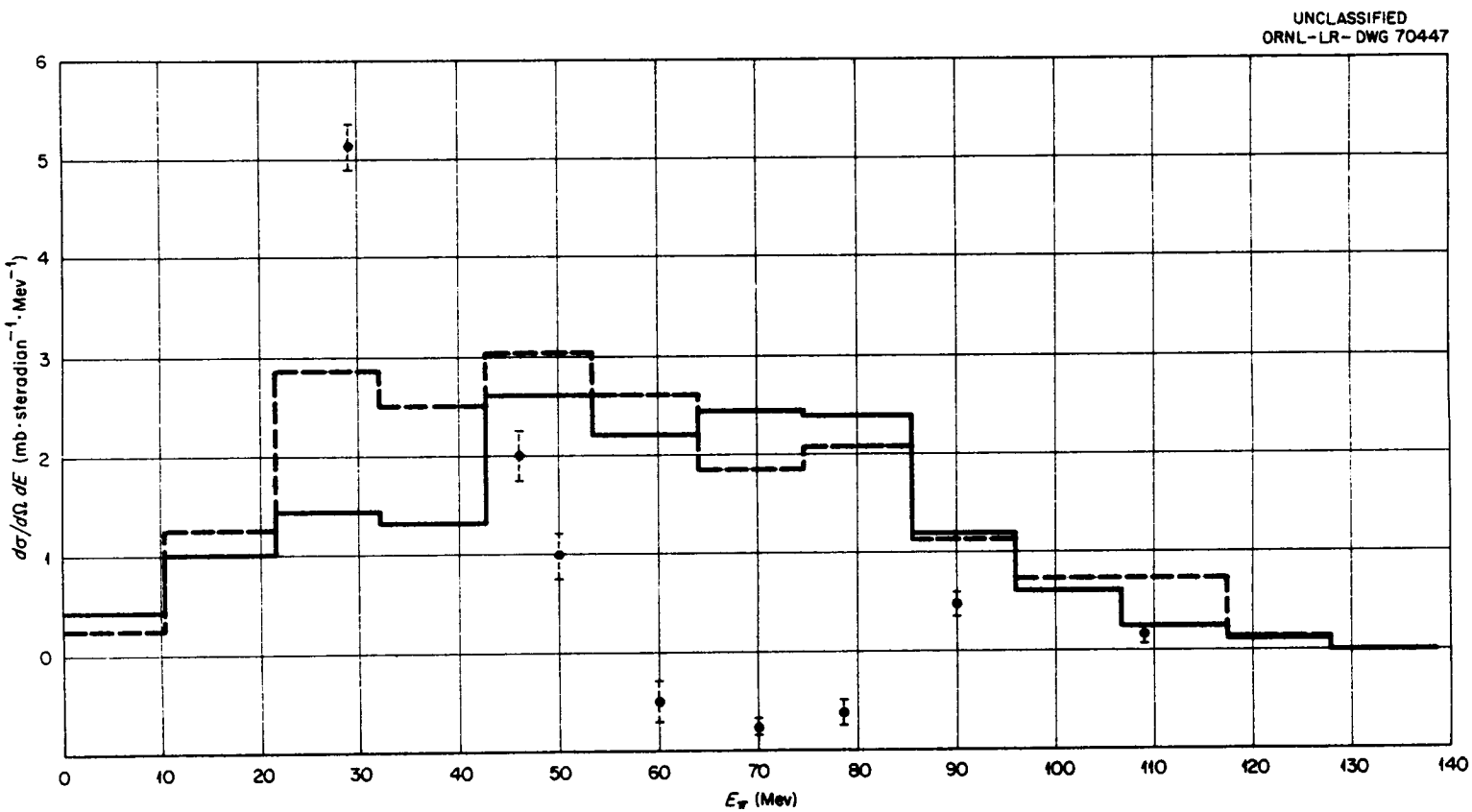

Fig. 35. Nonelastic π^- Spectra at 138° from 150-Mev π^- on Lead. Calculated spectra for π^- in the interval 130 to 148° for nucleus with medium radius. Solid lines: nonuniform nucleon density distribution within the nucleus; dotted lines: uniform density distribution; circles: Miller's experimental values [Nuovo Cimento 6, 882 (1957)].

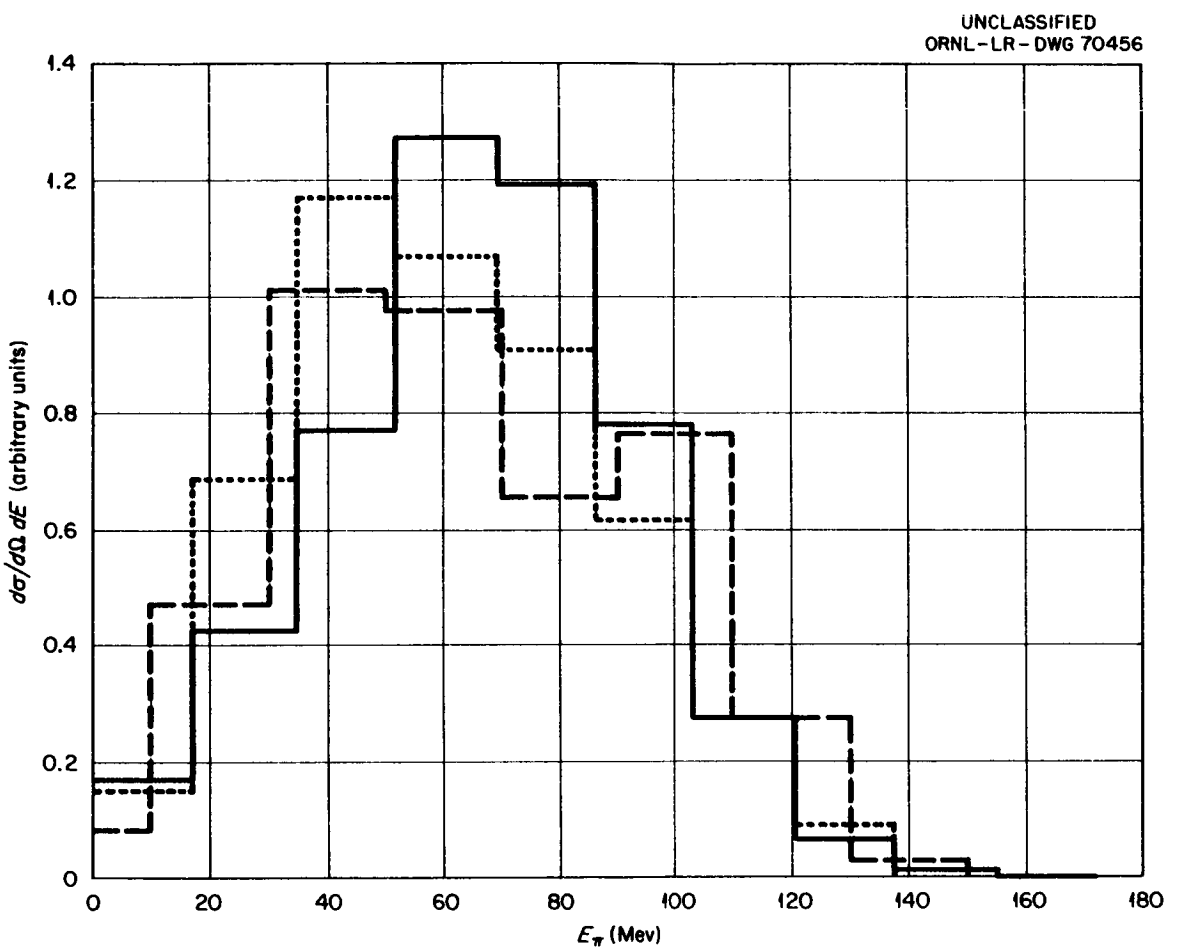

Fig. 36. Nonelastic Spectrum for π^- Emitted Into the Backward Hemisphere from 162-Mev π^- on Heavy-Emulsion Nuclei. Calculated values are for 162-Mev π^- on Ru^{100} with a medium nuclear radius. Solid lines: nonuniform nucleon density distribution within the nucleus; dashed lines: uniform nucleon density distribution; dotted lines: experimental results of Nikolskii et al. [Soviet Phys. JETP (English Transl.) 5, 93 (1957)]; ordinate units are arbitrary.

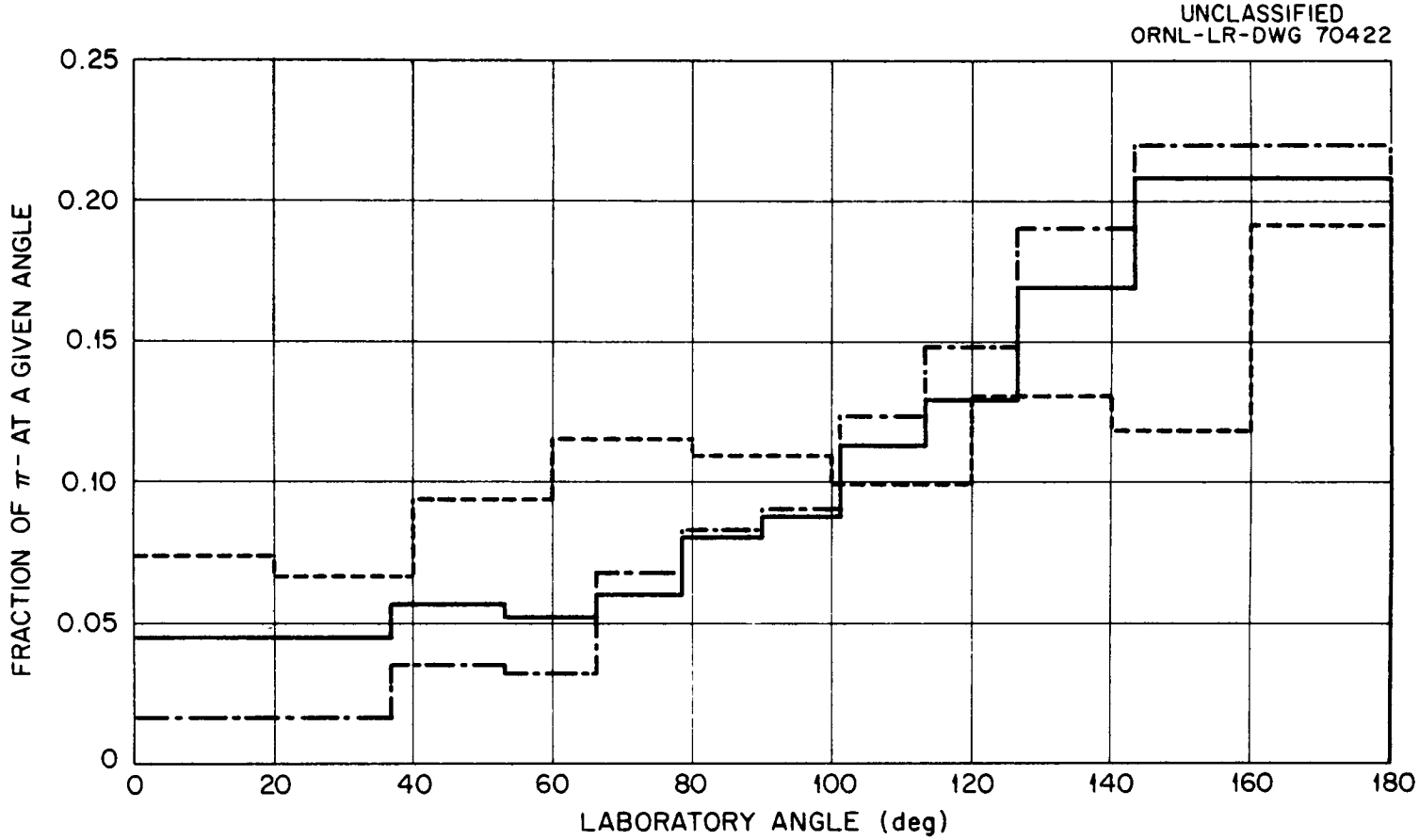

Fig. 37. Angular Distribution of Nonelastic π^- from 162-Mev π^- on Heavy-Emulsion Nuclei. Calculated distribution for nucleus with medium radius. Dotted lines: experimental values of Nikolskii *et al.* [Soviet Phys. -JETP (English Transl.) 5, 93 (1957)]; solid lines: calculated spectra for a nonuniform nucleon density distribution within the nucleus; dash-dot lines: uniform nucleon density distribution.

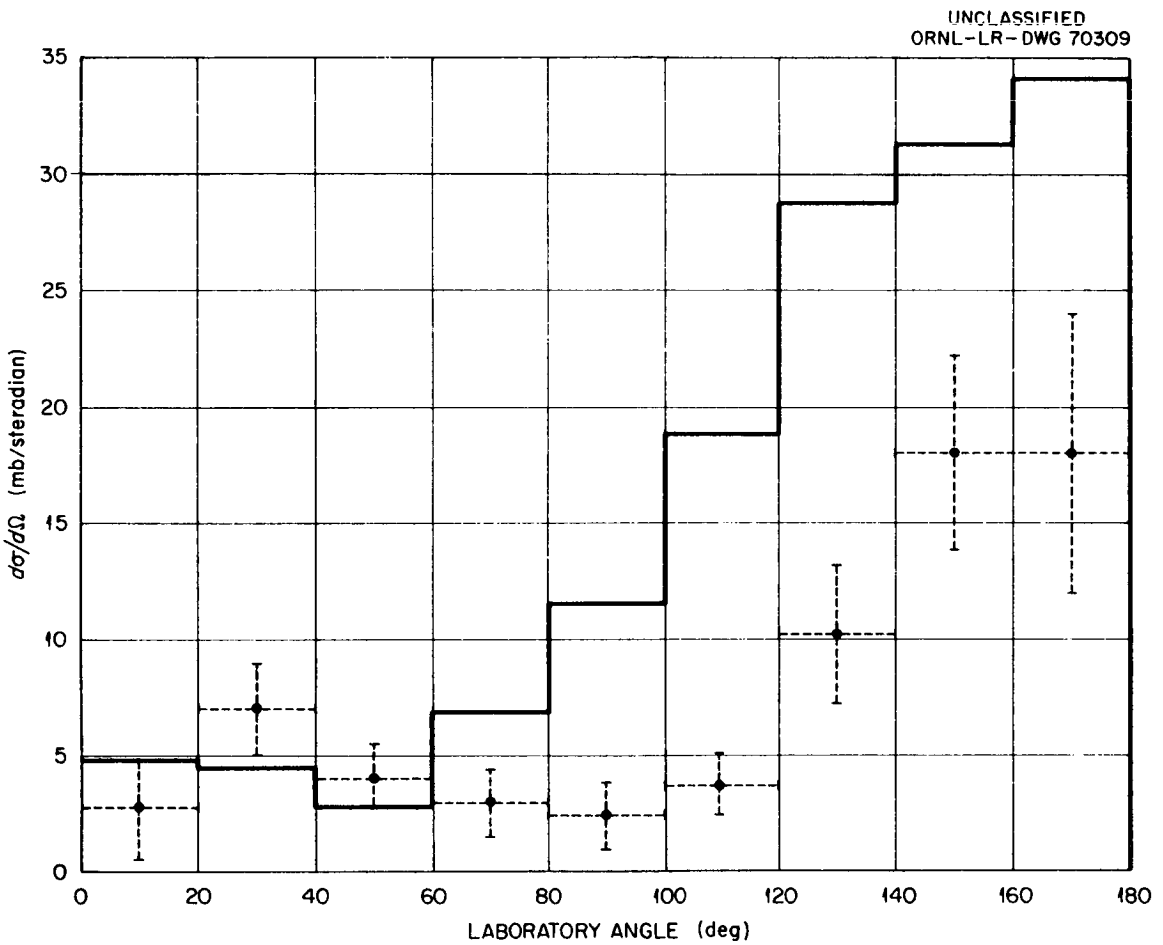

Fig. 38. Angular Distribution of Nonelastic π^- Scattered with Energy Loss Greater than 40 Mev for 125-Mev π^- on Carbon. Circles: experimental values of Kessler and Lederman [Phys. Rev. 94, 689 (1954)]; solid lines: calculated distribution.

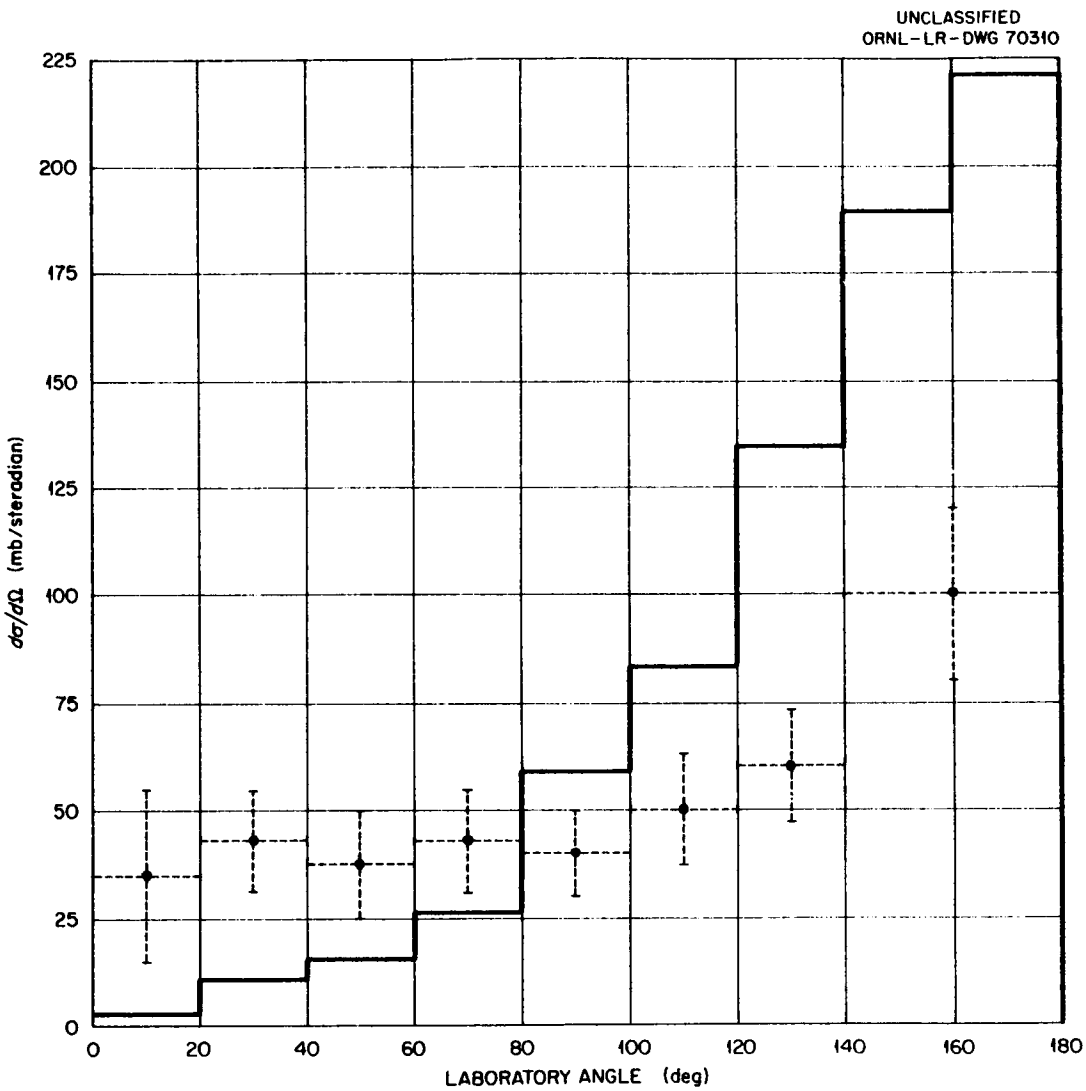

Fig. 39. Angular Distribution of Nonelastic π^- Scattered with Energy Loss Greater Than 40 Mev for 125-Mev π^- on Lead. Circles: experimental values of Kessler and Lederman [Phys. Rev. 94, 689 (1954)]; solid lines: calculated distribution.

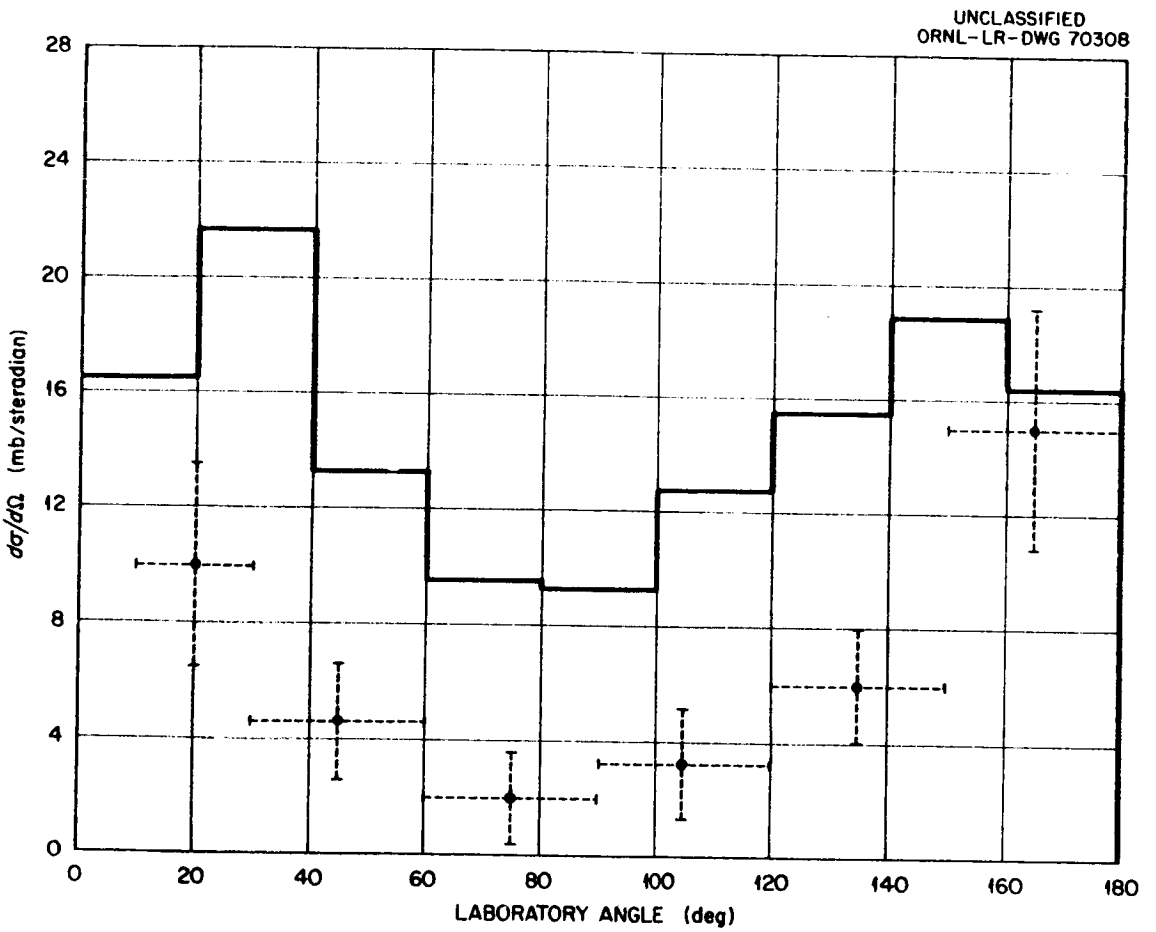

Fig. 40. Angular Distribution of Nonelastic π^+ from 195-Mev π^+ on Lithium. Circles: experimental values of Petrov et al. [Soviet Phys. -JETP (English Transl.) 10, 682 (1960)]; solid lines: calculated π^+ spectrum reduced by the ratio of the experimental to the calculated total nonelastic cross section.

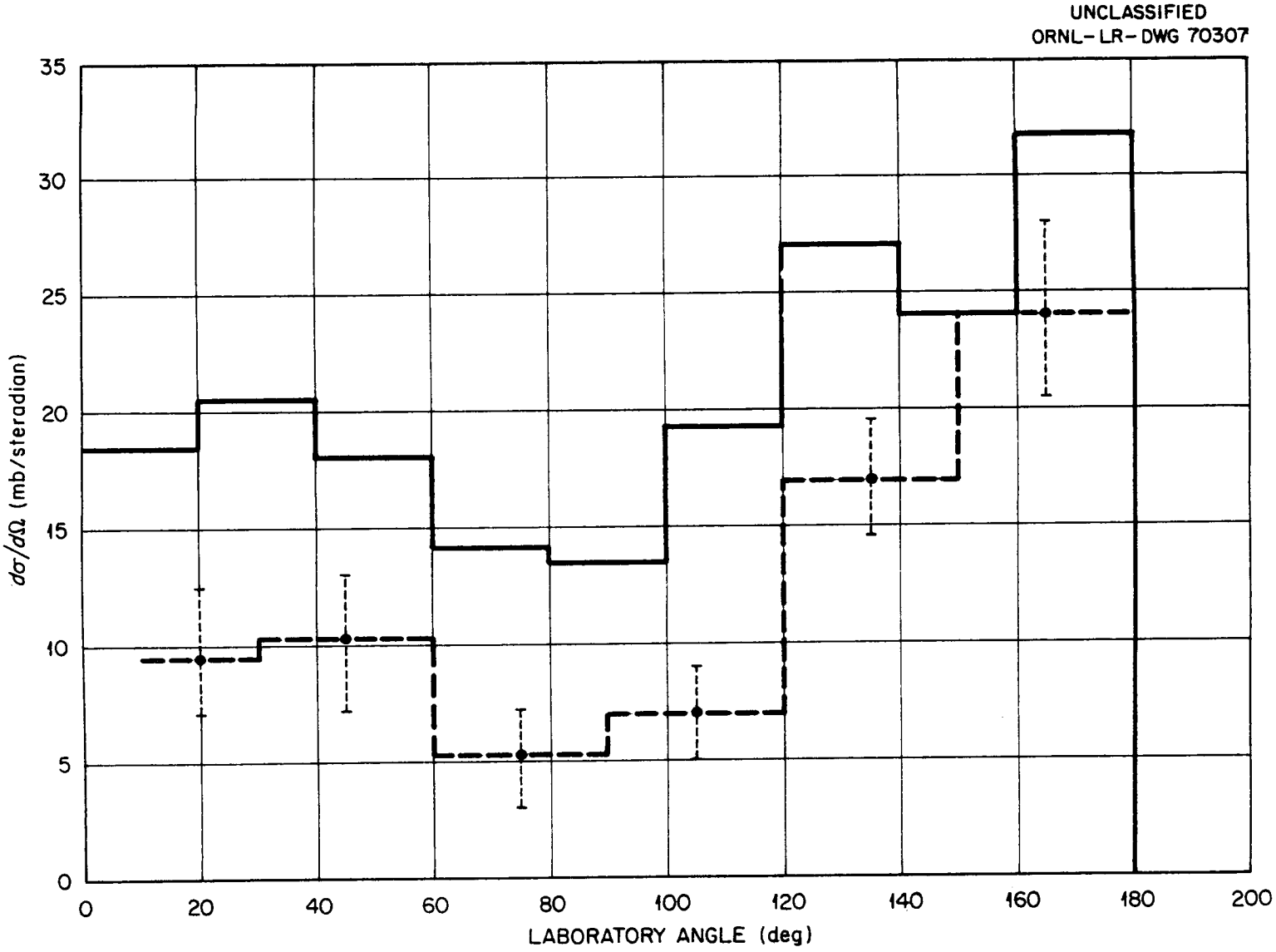

Fig. 41. Angular Distribution of Nonelastic π^+ from 195-Mev π^+ on Carbon. Circles: experimental values of Petrov et al. [Soviet Phys. JETP (English Transl.) 10, 682 (1960)]; solid lines: calculated spectrum.

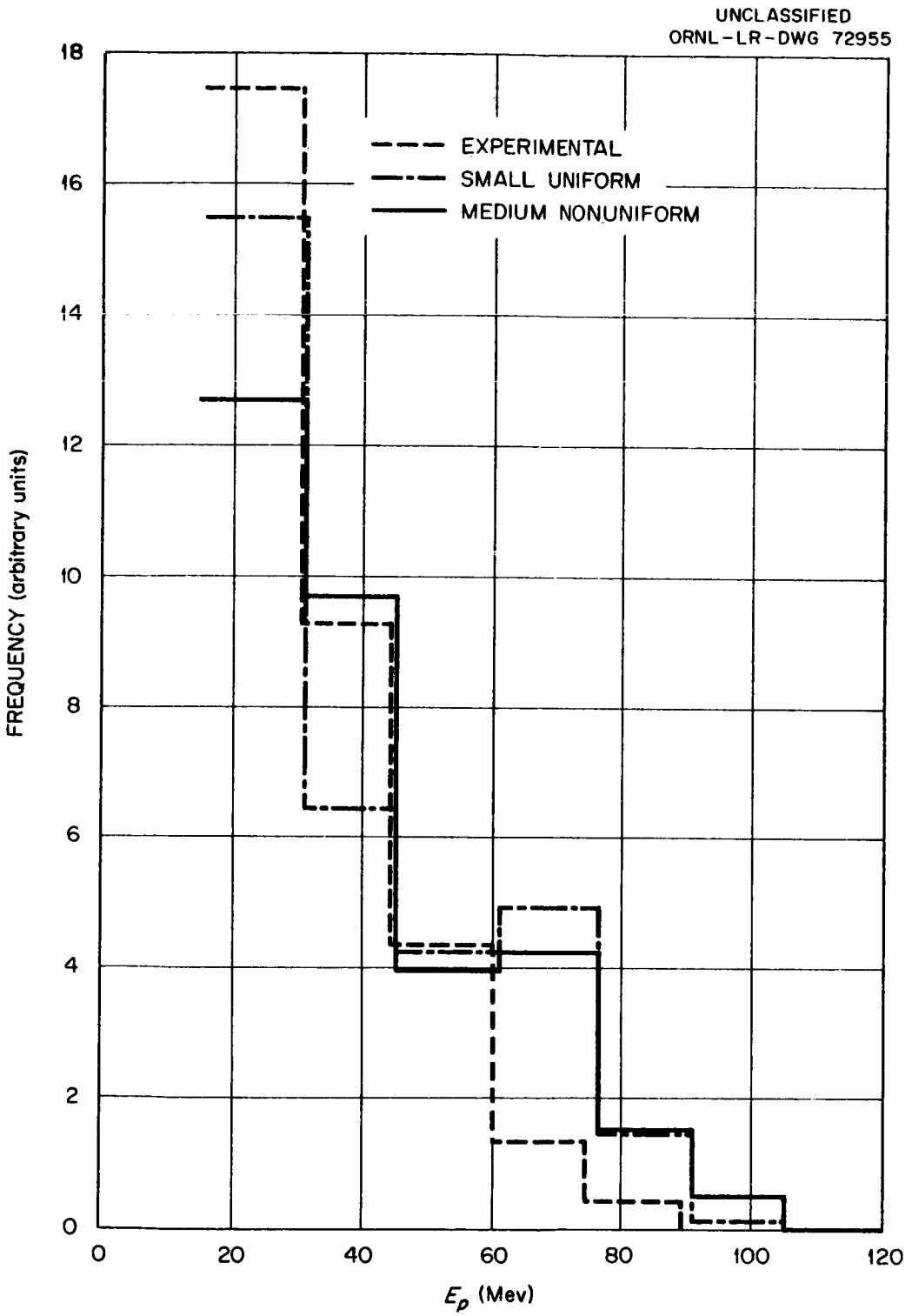

Fig. 42. Energy Spectra of Protons with Energies Greater Than 15 Mev for Slow π^- Absorption on Heavy-Emulsion Nuclei. Calculated values are for 1-Mev π^- on Ru^{100}. Solid lines: calculated spectrum for medium nonuniform nuclear configuration; dash-dot lines: calculated spectrum for small uniform configuration; dotted lines: experimental results of Azimov et al. [Soviet Phys. JETP (English Transl.) 4, 632 (1957)]; ordinate units are arbitrary.

Table 5. Calculated and Experimental Absorption Cross Sections for Pions Incident on Beryllium

Pion	Energy (Mev)	Cross Section (mb)	
		Calculated	Experimental[a]
π^+	20	58	56 ± 9
π^+	30	63	74 ± 13
π^+	40	67	96 ± 20

a. F. H. Tenney and J. Tinlot, Phys. Rev. 92, 974 (1953).

Table 6. Calculated and Experimental Charge-Exchange Cross Sections for Pions Incident on Lead and Carbon

Pion	Target	Energy (Mev)	Cross Section (mb)	
			Calculated	Experimental
π^+	Pb	50	206	27 ± 19[a]
π^-	C	125	61	$20 \,{}^{+\,20}_{-\,10}$[b]
π^-	Pb	125	215	$100 \,{}^{+\,80}_{-\,40}$[b]

a. G. Saphir, Phys. Rev. 104, 535 (1956).

b. J. O. Kessler and L. M. Lederman, Phys. Rev. 94, 689 (1954).

Table 7. Calculated and Experimental Charge-Exchange Plus Absorption Cross Sections for Pions Incident on Various Nuclei

Pion	Target	Energy (Mev)	Cross Section (mb)	
			Calculated	Experimental
π^+	Li	195	142	164 ± 16[a]
π^+	C	78	174	195 ± 20[b]
		195	205	203 ± 22[a]
		270	146	$165 \begin{smallmatrix} + 34 \\ - 22 \end{smallmatrix}$[c]
π^+	Pb	50	930	880 ± 73[d]
π^-	C	125	206	220 ± 40[e]
		150	209	192 ± 34[f]
	Pb	125	923	1840 ± 350[e]
		150	957	380 ± 310[f]

a. N. I. Petrov, V. G. Ivanov, and V. A. Rusakov, Soviet Phys. JETP (English Transl.) 10, 682 (1960).

b. R. G. Sulukvadze and D. Neagu, Soviet Phys. JETP (English Transl.) 14, 59 (1962).

c. W. Kan Chang et al., Soviet Phys. JETP (English Transl.) 8, 625 (1959).

d. G. Saphir, Phys. Rev. 104, 535 (1956).

e. J. O. Kessler and L. M. Lederman, Phys. Rev. 94, 689 (1954).

f. R. H. Miller, Nuovo Cimento 6, 882 (1957).

The data for incident pions appear to represent the gross features of the experimental data, but they can not be used to predict detailed experimental data as well as the results for incident nucleons.

Compilation of Reactions Calculated for Particles With Energies from About 50 to 350 Mev

The completion of the intranuclear cascade code makes it possible to calculate a vast quantity of data on nuclear reactions. These data are expected to be of value for all problems involving radiation from nucleons or pions in the energy range from about 50 to 350 Mev. A compilation of the data is under way and should be completed within the next three or four months.

The cases to be calculated are as follows: incident neutrons and protons with energies at 25, 50, 100, 150,...400 Mev on C^{12}, O^{16}, Al^{27}, Cr^{52}, Cu^{65}, Ru^{100}, Ce^{140}, W^{184}, Pb^{207}, and U^{238}; and incident π^+ and π^- on the same element with energies at the same intervals but extending only to 300 Mev. The calculation is valid at higher energies for incident nucleons than it is for pions because pion production for incident nucleons, which is ignored in the calculation, takes place at higher energies. The end points in the energy ranges to be used are probably beyond the limits of validity of the calculation but are included for purposes of extrapolation.

The compilation will consist mainly of tables and graphs of data from representative cases. The data for the remaining cases will be available on request. The work will include results from the cascade process alone, from the evaporation process alone,[10] and from the combined processes.

As a reminder, the cascade calculation is based on the assumption that high-energy nuclear reactions can be treated as though the interactions occur on a particle-particle basis within the nucleus. When the particle energy becomes small ($\lambda \rightarrow$ large), this assumption is no longer valid, and the reaction is assumed to be represented by the de-excitation of a highly excited nucleus, which occurs by the evaporation or "boil-off" of nucleons. In the calculations this transition is abrupt and occurs at a somewhat arbitrary energy -- the cutoff energy of the cascade calculation. However, neither the total nucleon multiplicities nor the combined cascade and evaporation spectra are very sensitive to this cutoff energy, as is illustrated in Figs.43-49. The cutoff energies used in the calculations are 1.6 Mev for Al^{27}, 4.2 Mev for Ru^{100}, and 6.7 Mev for Pb^{208}. The lower limit of the proton spectra for lead, Fig.49, is determined by the cascade cutoff energy because there is very little proton evaporation. The correct spectra would drop rapidly for energies smaller than the coulomb barrier; so some care must be exercised in using the data for similar cases. The combined neutron spectrum is illustrated in Fig.46 for Ru^{100} only since it is very similar to those for Al^{27} and Pb^{208}.

---

10. L. Dresner, EVAP - A Fortran Program for Calculating the Evaporation of Various Particles from Excited Compound Nuclei, ORNL CF-61-12-30 (Dec. 19, 1961).

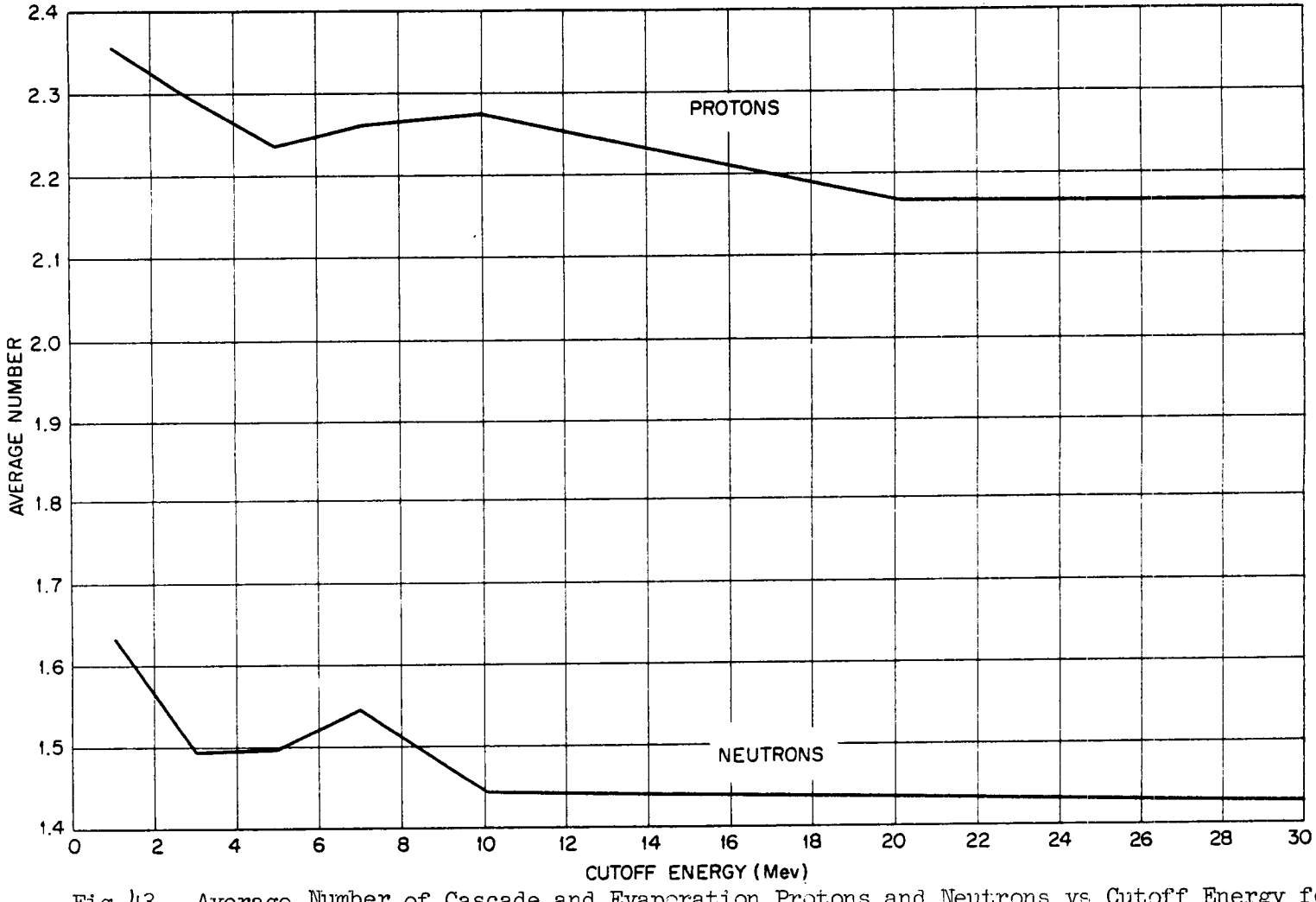

Fig. 43. Average Number of Cascade and Evaporation Protons and Neutrons vs Cutoff Energy for 150-Mev Protons on Al^{27}.

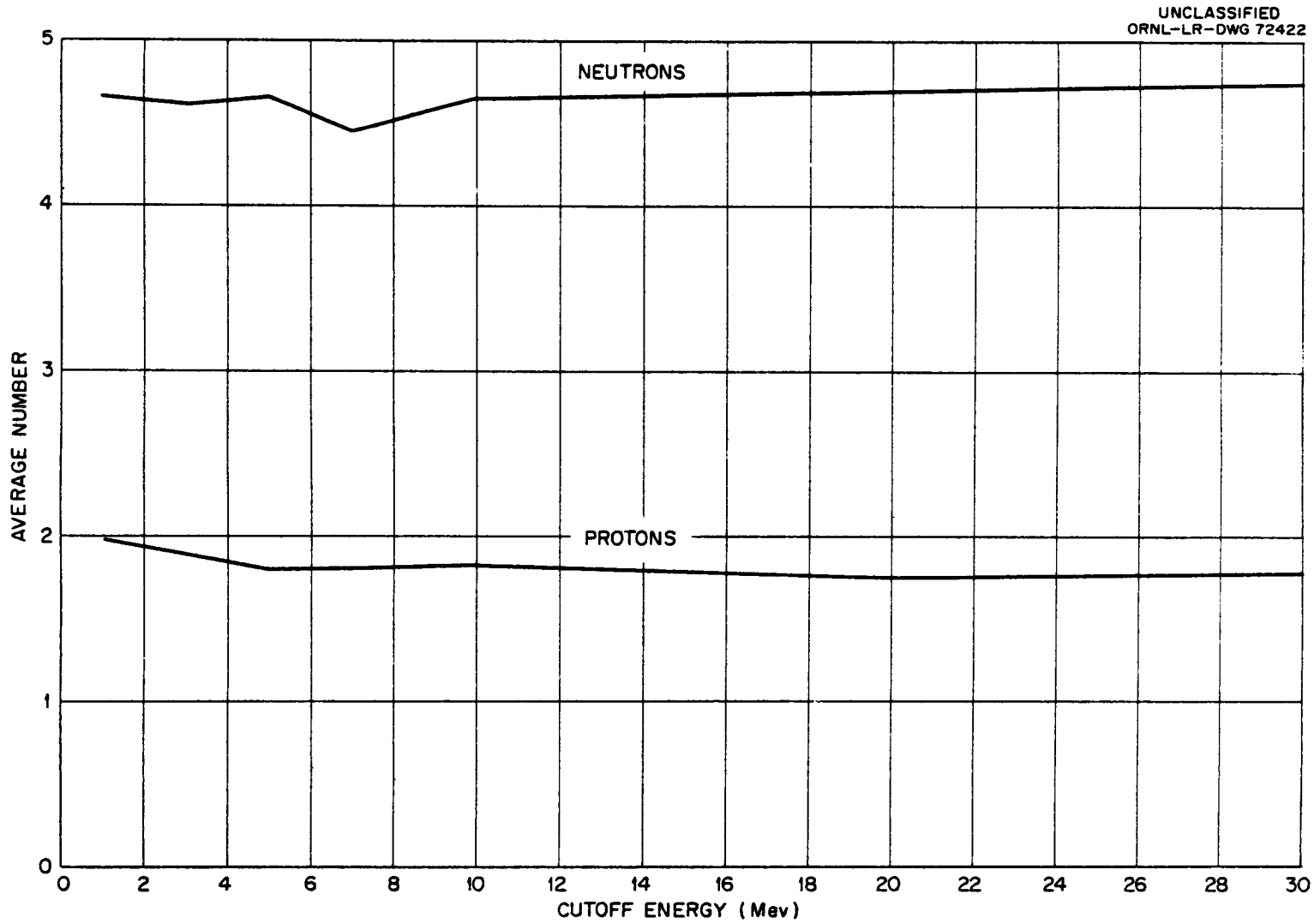

Fig.44. Average Number of Cascade and Evaporation Protons and Neutrons vs Cutoff Energy for 150-Mev Protons on $_{44}Ru^{100}$.

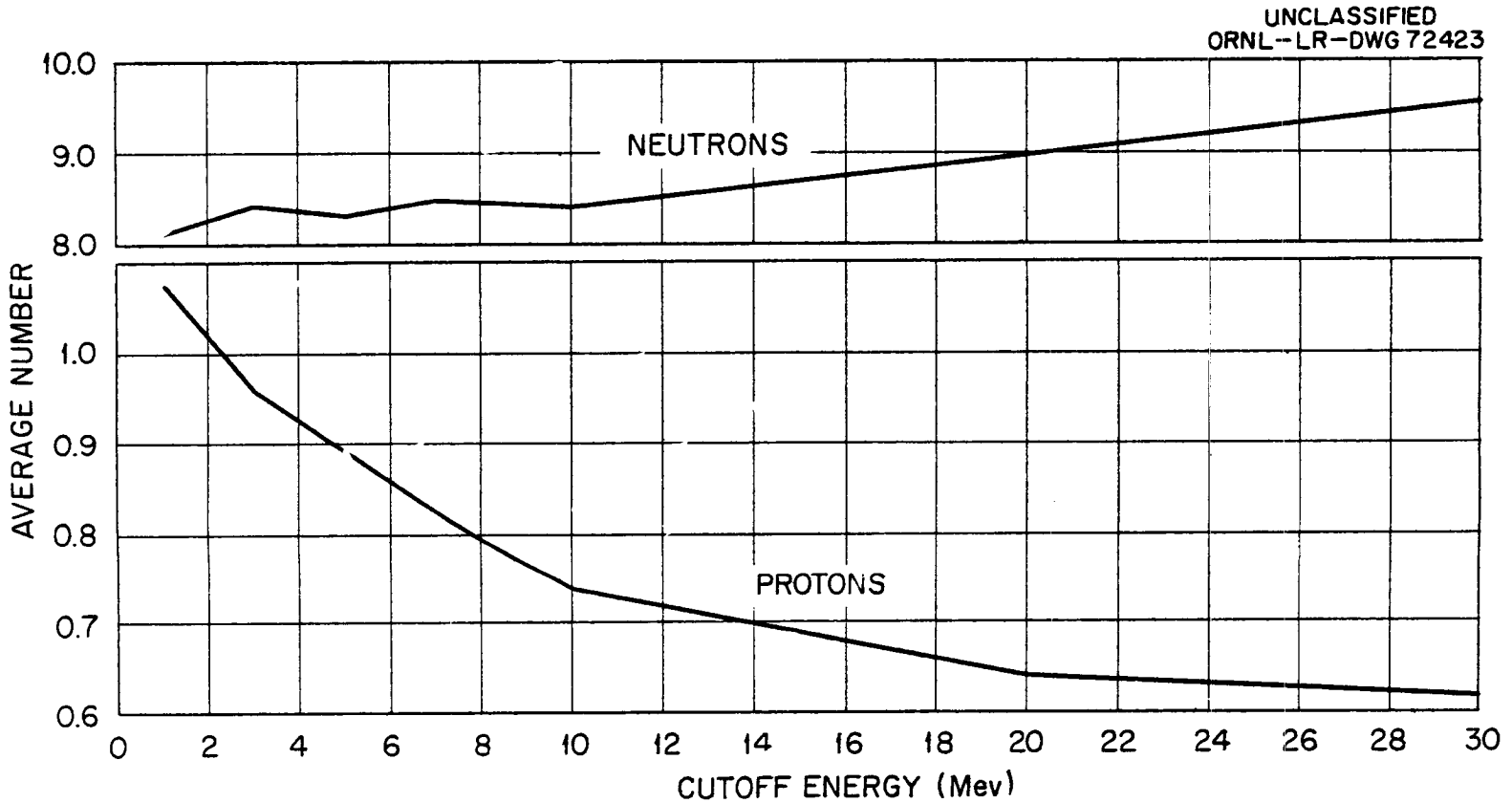

Fig.45. Average Number of Cascade and Evaporation Protons and Neutrons vs Cutoff Energy for 150-Mev Protons on $_{82}Pb^{208}$.

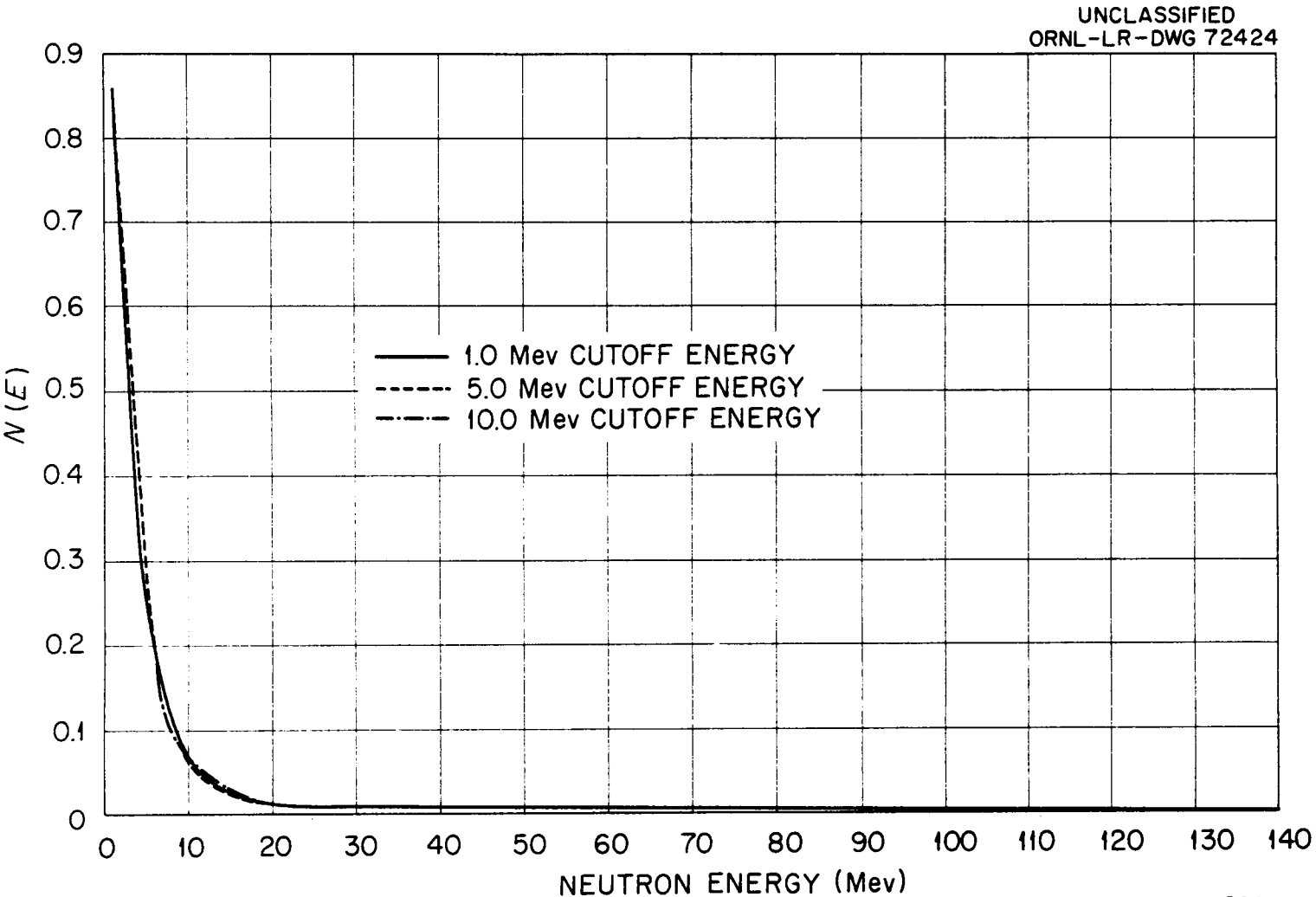

Fig. 46. Cascade and Evaporation Neutron Spectra for 150-Mev Protons on $_{44}Ru^{100}$.

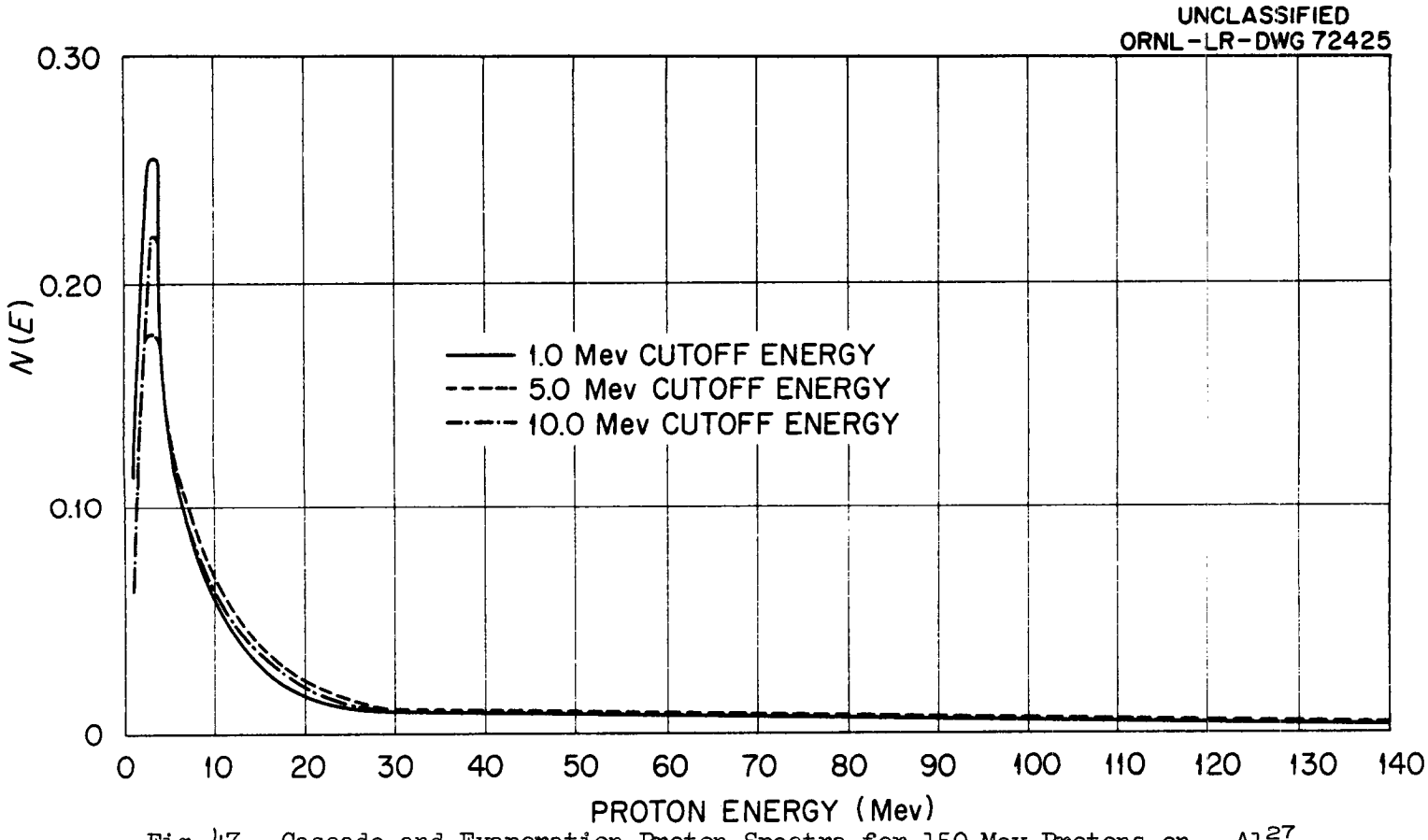

Fig. 47. Cascade and Evaporation Proton Spectra for 150-Mev Protons on $_{13}Al^{27}$.

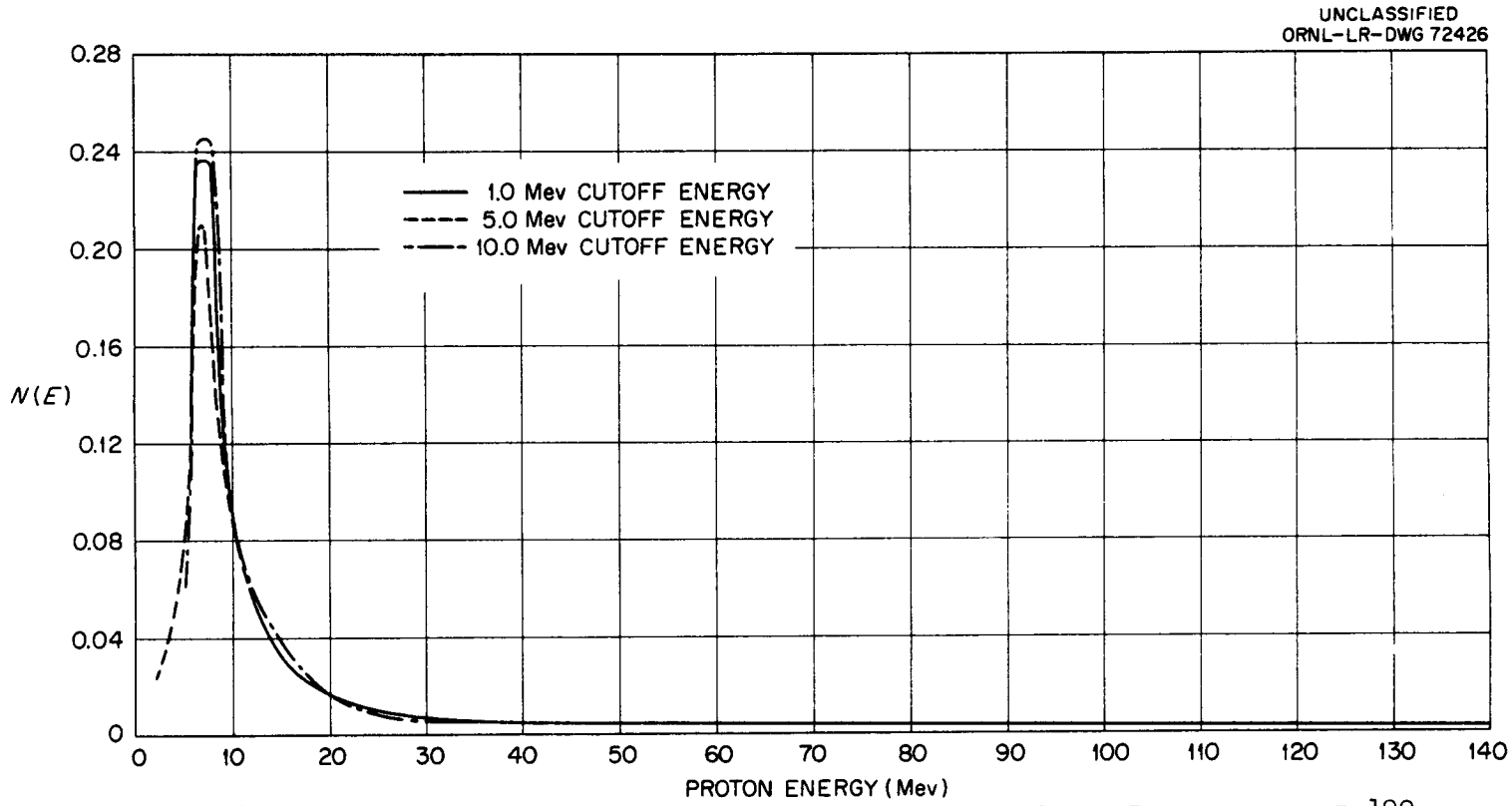

Fig. 48. Cascade and Evaporation Proton Spectra for 150-Mev Protons on $_{44}Ru^{100}$.

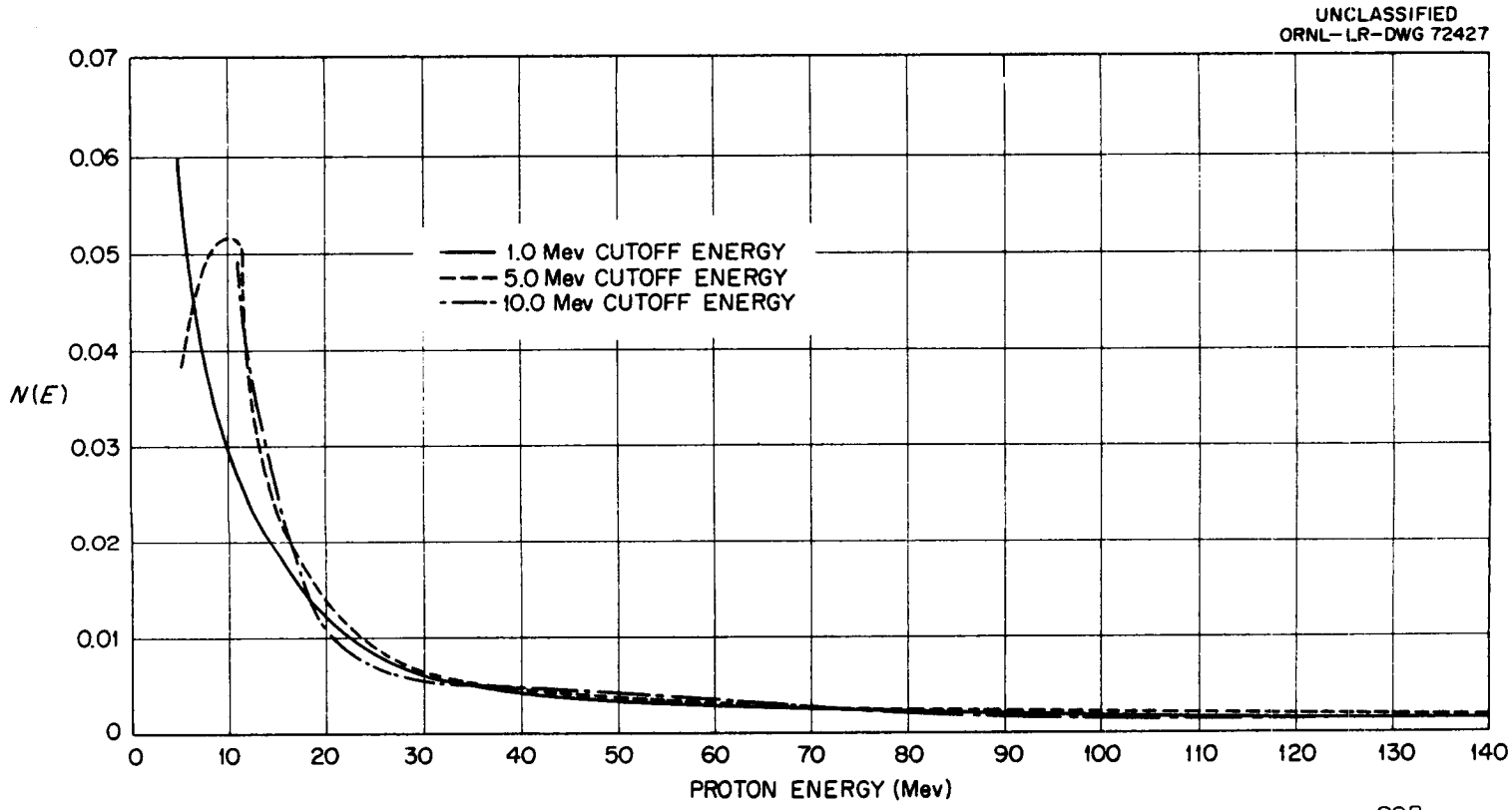

Fig. 49. Cascade and Evaporation Proton Spectra for 150-Mev Protons on $_{82}Pb^{208}$.

A list of the data that will be available on request is as follows:

I. Cascade process

A. For the cascade residual nucleus

1. Parallel and perpendicular momentum distributions and average value of each

2. Momentum distribution and average value

3. Excitation energy distribution and average value

4. Angular distribution

5. Average residual mass

B. For the emission of combinations of cascade particles

1. Cross section for each combination

2. All the distributions above for several specific combinations

C. For each type of emitted cascade particle (proton, neutron, π^+, π°, π^-)

1. Average number emitted

2. Average energy

3. Energy spectra for all angles

4. $\frac{d\sigma}{d\Omega dE}(E)$ for four angular intervals

5. Differential cross section for scattering into these intervals

6. Average energy of emission into these intervals

7. Angular distribution for all energies

8. $\frac{d\sigma}{d\Omega}(\theta)$ for three energy intervals

9. Cross section for the emission of η particles into three energy intervals (η = 1, 2, ...15)

10. $\frac{d\sigma}{d\Omega}(x)$ for the emission of two protons, where x is the angle between them

D. For incident pions

1. Pion absorption cross section

2. Pion charge-exchange cross section

E. Total nonelastic cross section for the incident particles

II. Evaporation process

A. Cross sections for the various residual nuclei following evaporation

B. For the evaporation particles (protons, neutrons, deuterons, tritons, He^3, alphas)

1. Average number

2. First, second, and third moments of the energy distribution

3. Energy distribution

III. Combined cascade and evaporation process

A. For emitted neutrons and protons

1. Average number emitted

2. Energy spectra

Figures 50-71 exemplify the type of data to be contained in the compilation. The curves drawn through the points of some of the data illustrate the general trends. The deviation of the points from the curves can be quite large in cases where the statistics are poor (Fig. 69).

Some of the data will suffer because of poor statistics, but prohibitive machine time would be involved in providing good statistics for all the data. A reasonable compromise in this respect was attempted.

Monte Carlo Calculations on Intranuclear Cascades for Incident-Particle Energies from About 50 Mev to 2 Gev

The intranuclear cascade calculation for the energy range of incident particles from about 50 to 350 Mev is being extended to higher energies. When completed, the calculation will be able to treat nuclear reactions for incident nucleons up to about 2.5 Gev and incident pions up to about 1.5 Gev.

The nuclear model will remain unchanged, but the particle-particle collisions that occur inside the nucleus will include inelastic collisions, which result in the creation of pions. Only single pion production will be considered for pion-nucleon collisions, and single or double pion production for nucleon-nucleon collisions. The 2.5- and 1.5-Gev energies are higher than the thresholds for the production of pions of greater multiplicity than will be treated in the calculation. Therefore the energy limits of validity of the calculations are nearer to 2 and 1 Gev, respectively, but the production processes which are ignored at the higher energies would constitute only about 15% of all the reactions.

The isobar model will be used for determining the type of reaction products and their angular distribution in the inelastic particle-particle

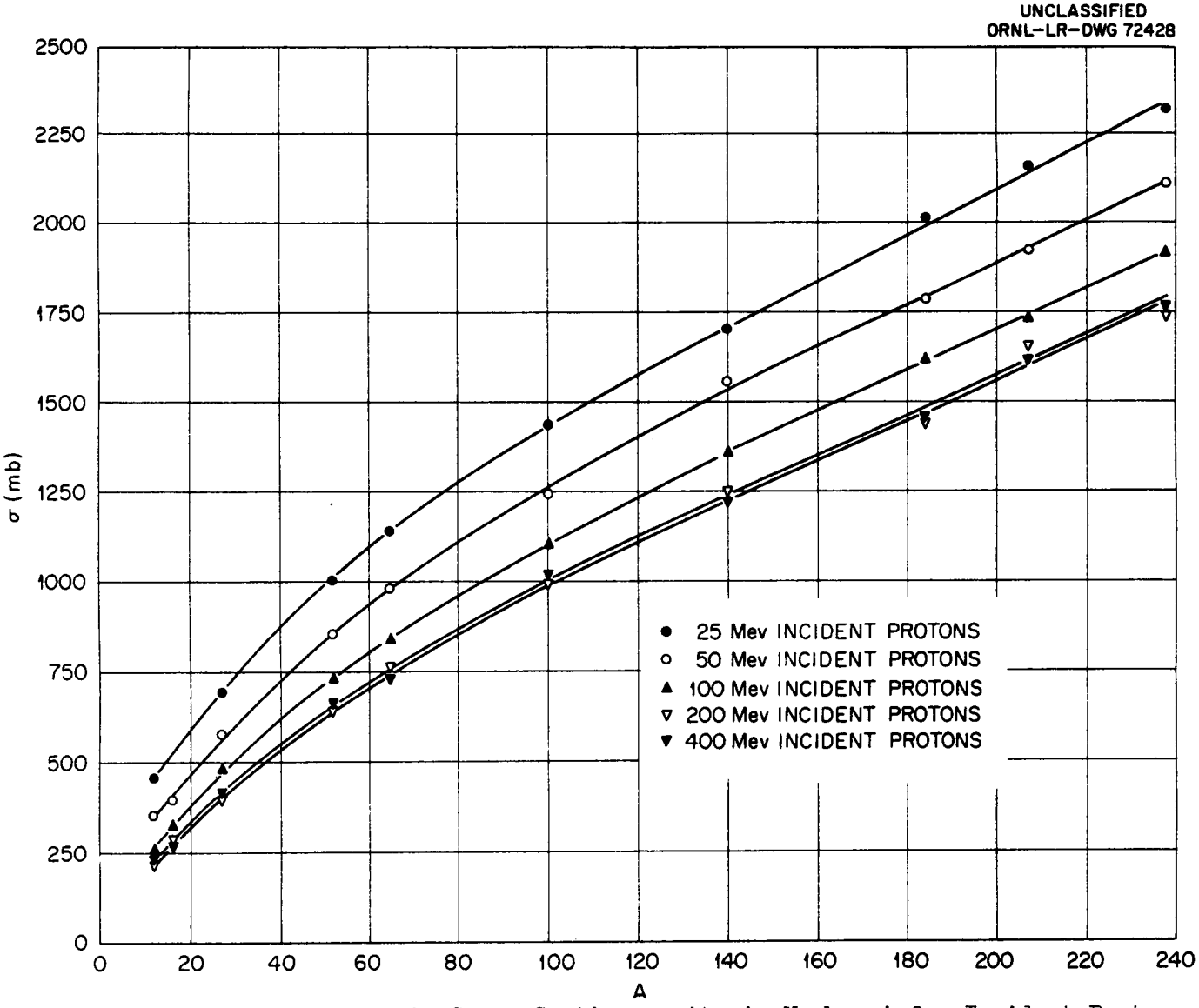

Fig. 50. Total Nonelastic Cross Section vs Atomic Number A for Incident Protons

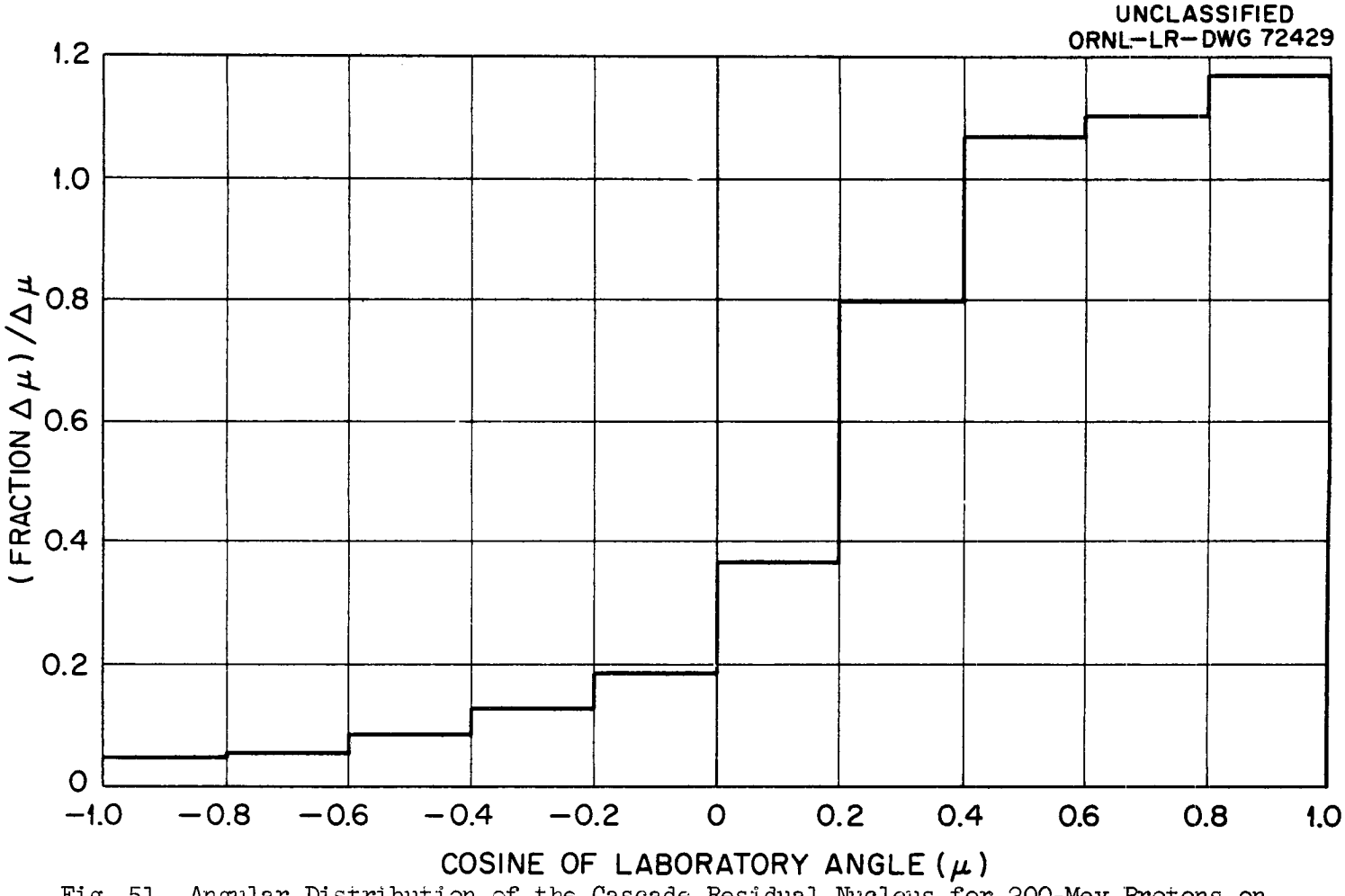

Fig. 51. Angular Distribution of the Cascade Residual Nucleus for 200-Mev Protons on Al^{27}.
[13]

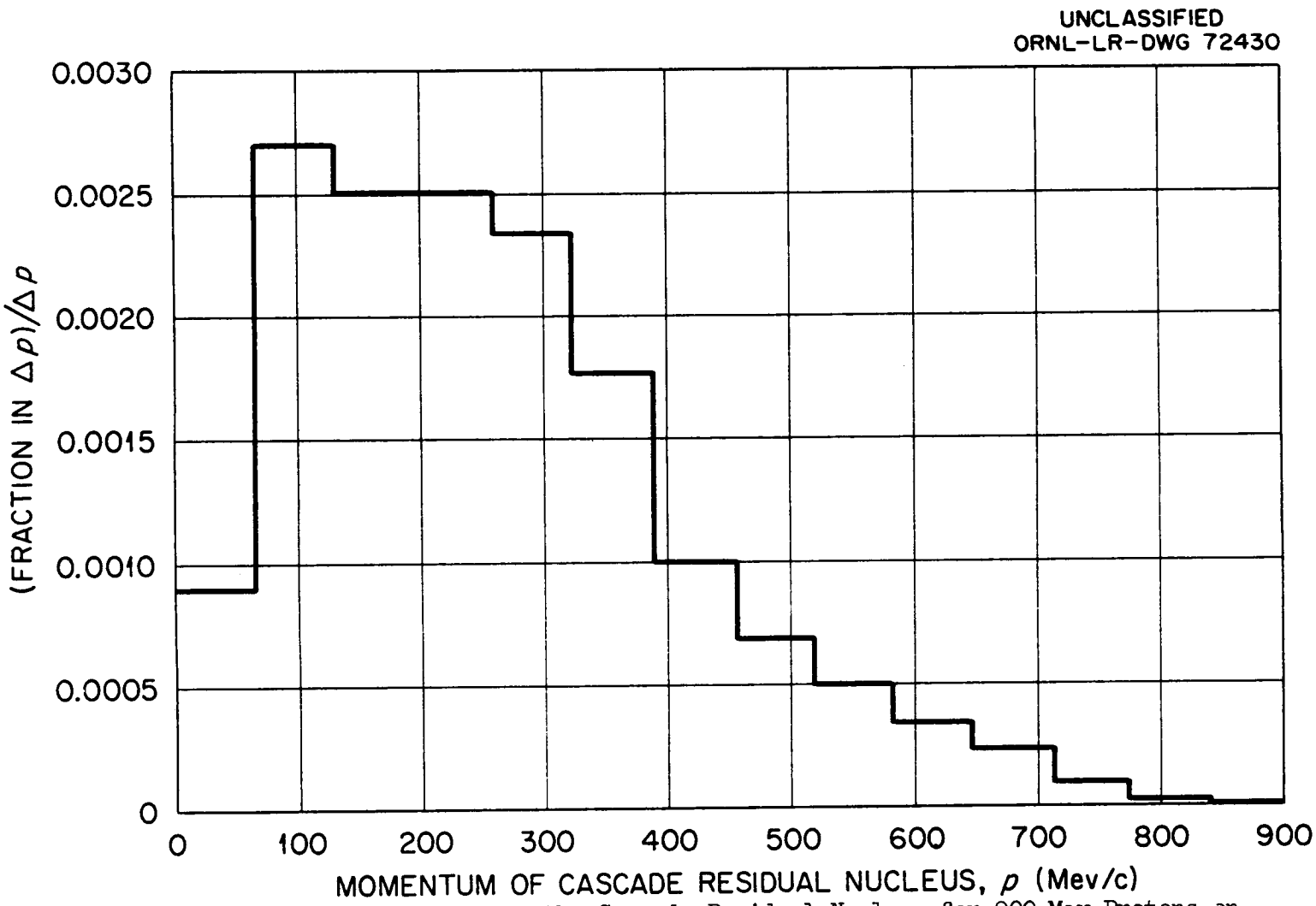

Fig. 52. Momentum Distribution of the Cascade Residual Nucleus for 200-Mev Protons on $_{13}Al^{27}$.

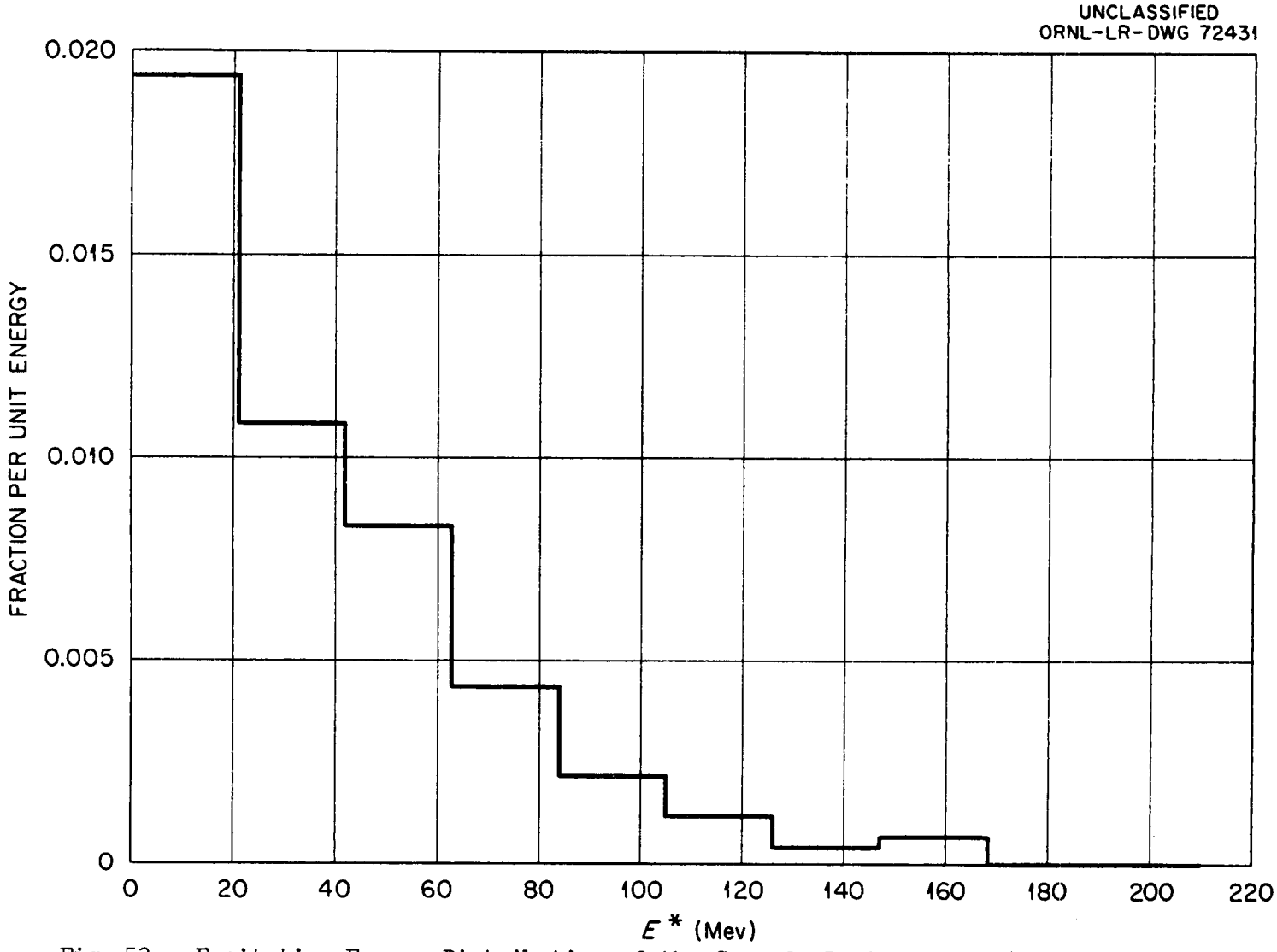

Fig. 53. Excitation Energy Distribution of the Cascade Residual Nucleus for 200-Mev Protons on Al^{27}.

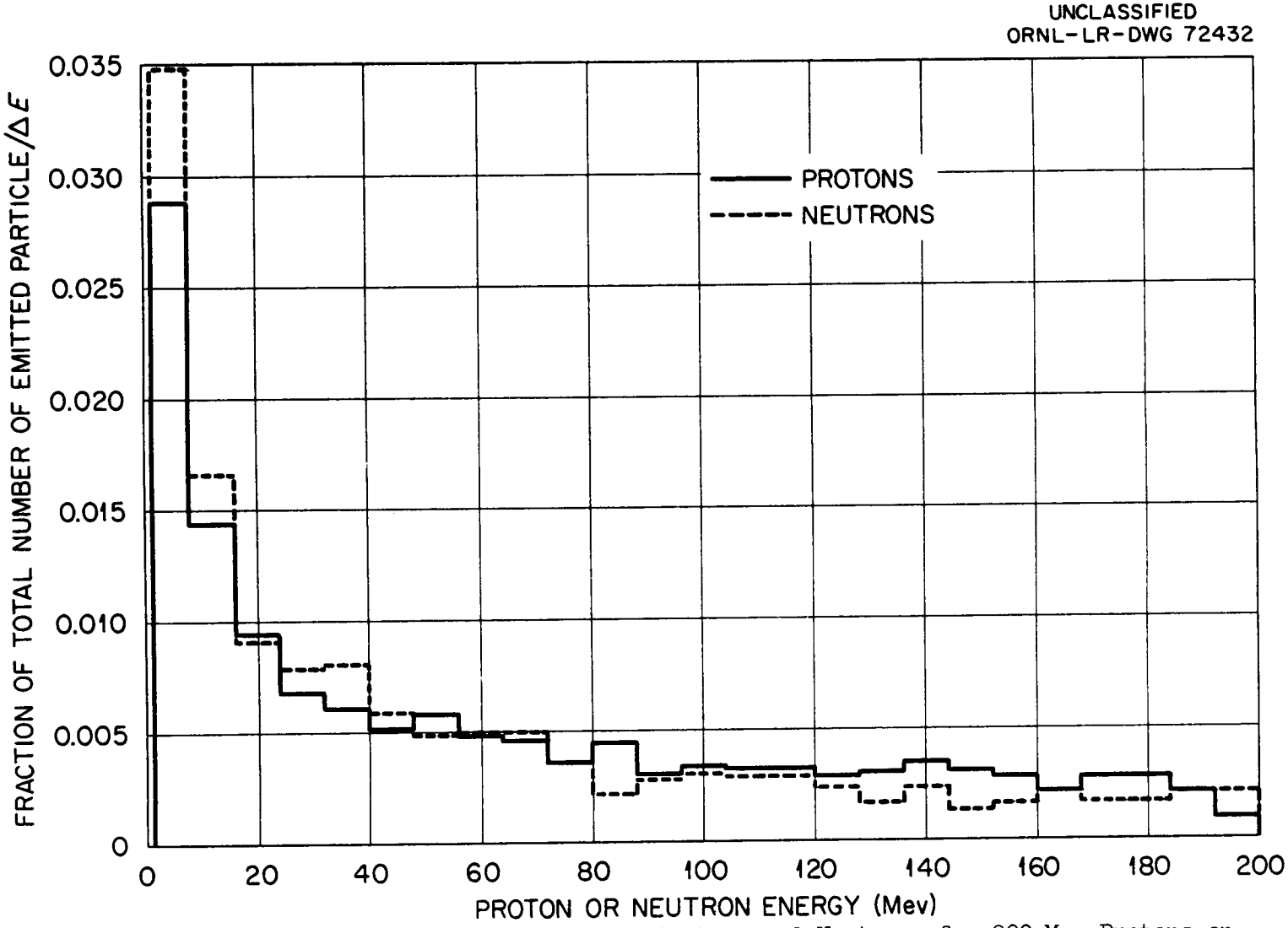

Fig. 54. Energy Spectrum of Emitted Cascade Protons and Neutrons for 200-Mev Protons on Al^{27}.

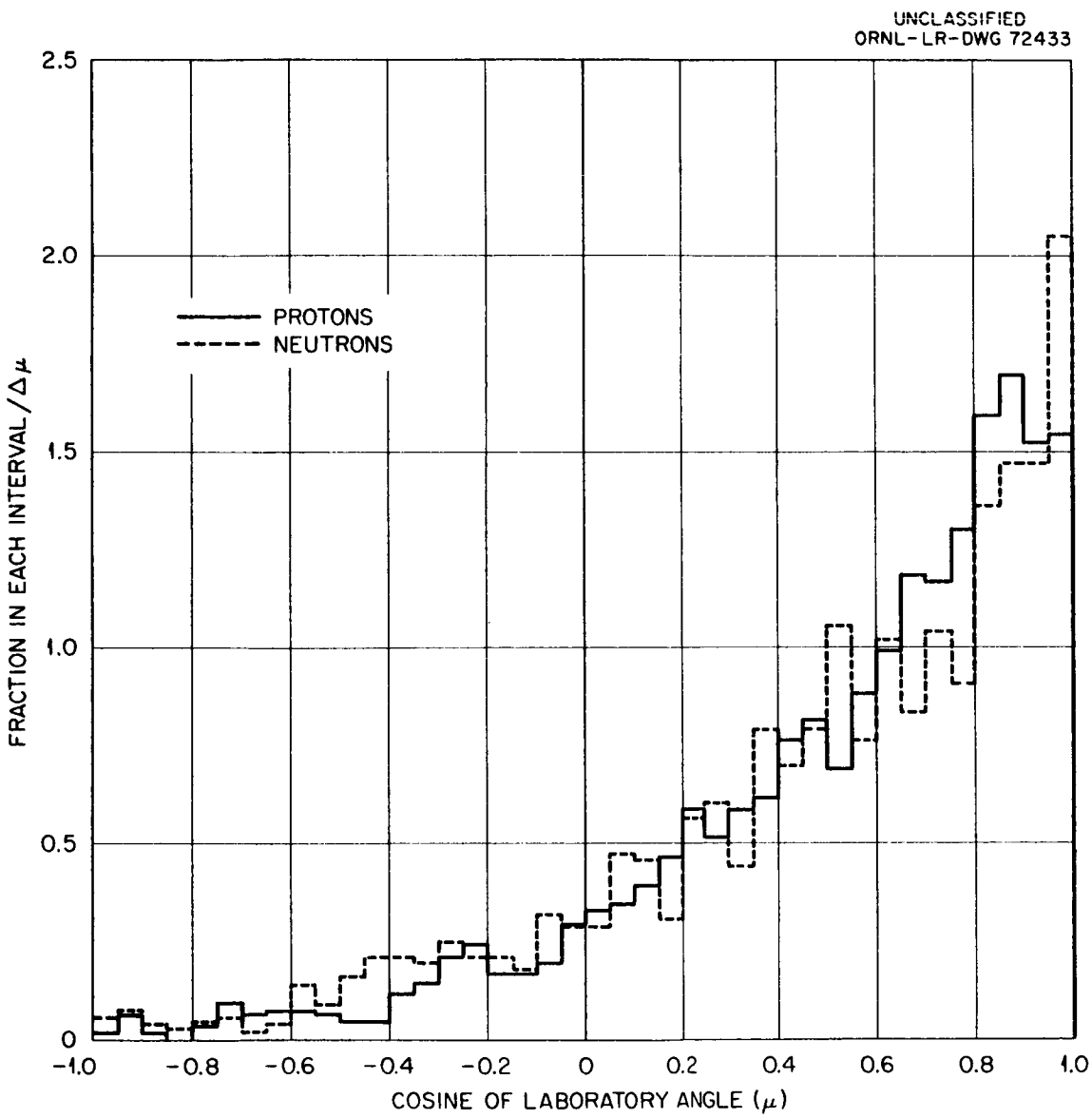

Fig. 55. Angular Distribution of Emitted Cascade Protons and Neutrons for 200-Mev Protons on $_{13}Al^{27}$.

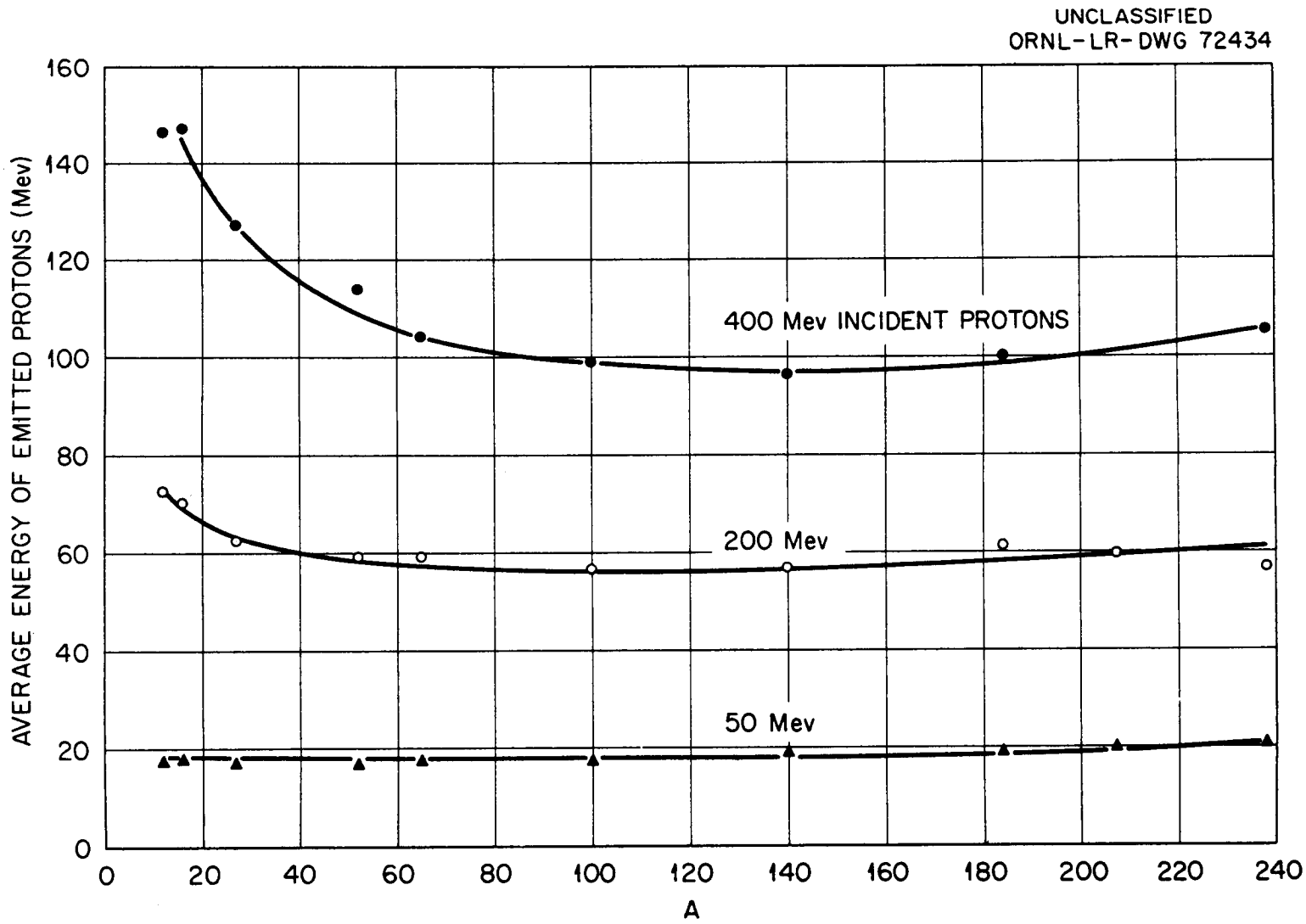

Fig. 56. Average Energy of Emitted Cascade Protons vs Atomic Number A for Incident Protons

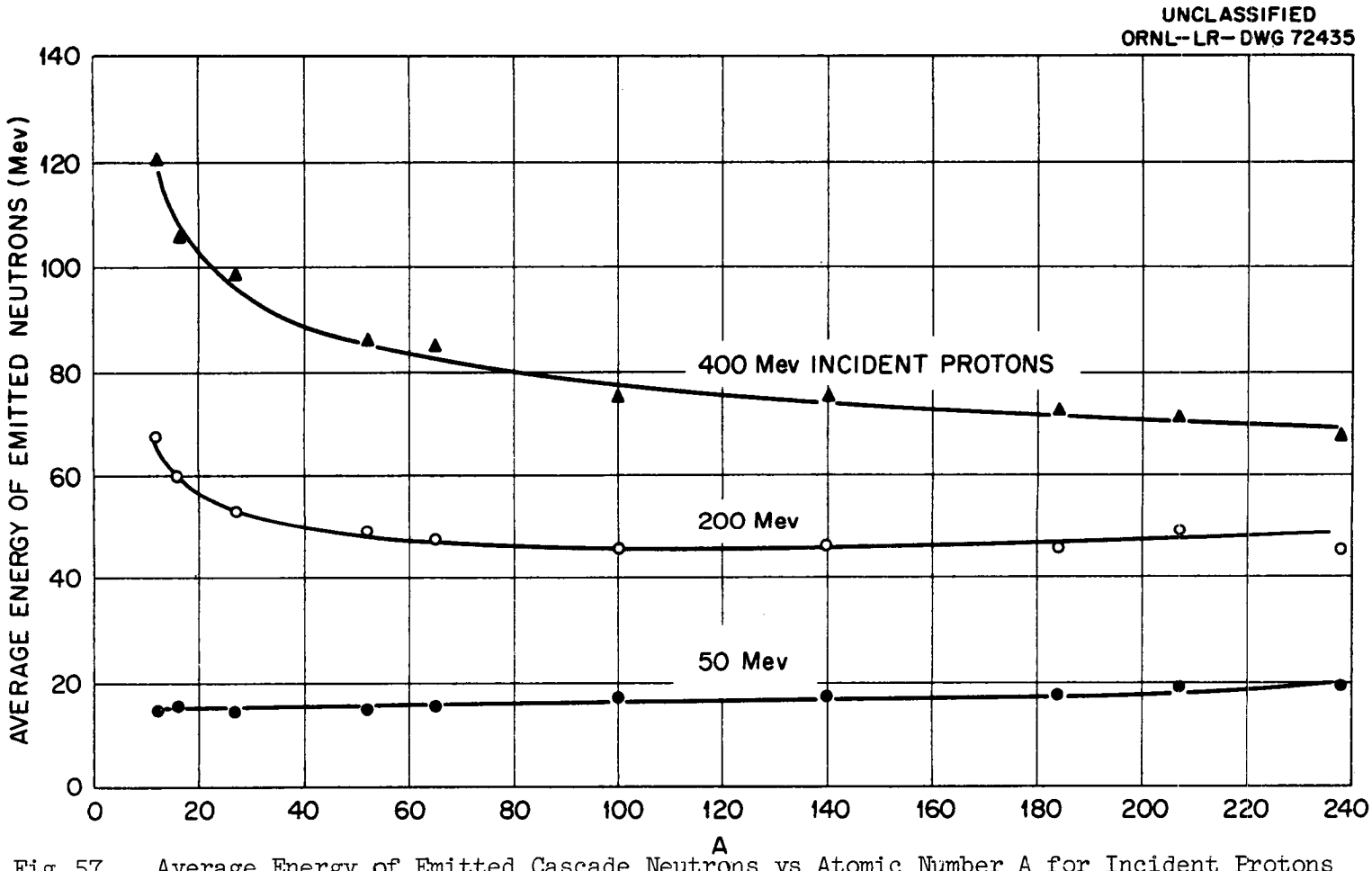

Fig. 57. Average Energy of Emitted Cascade Neutrons vs Atomic Number A for Incident Protons

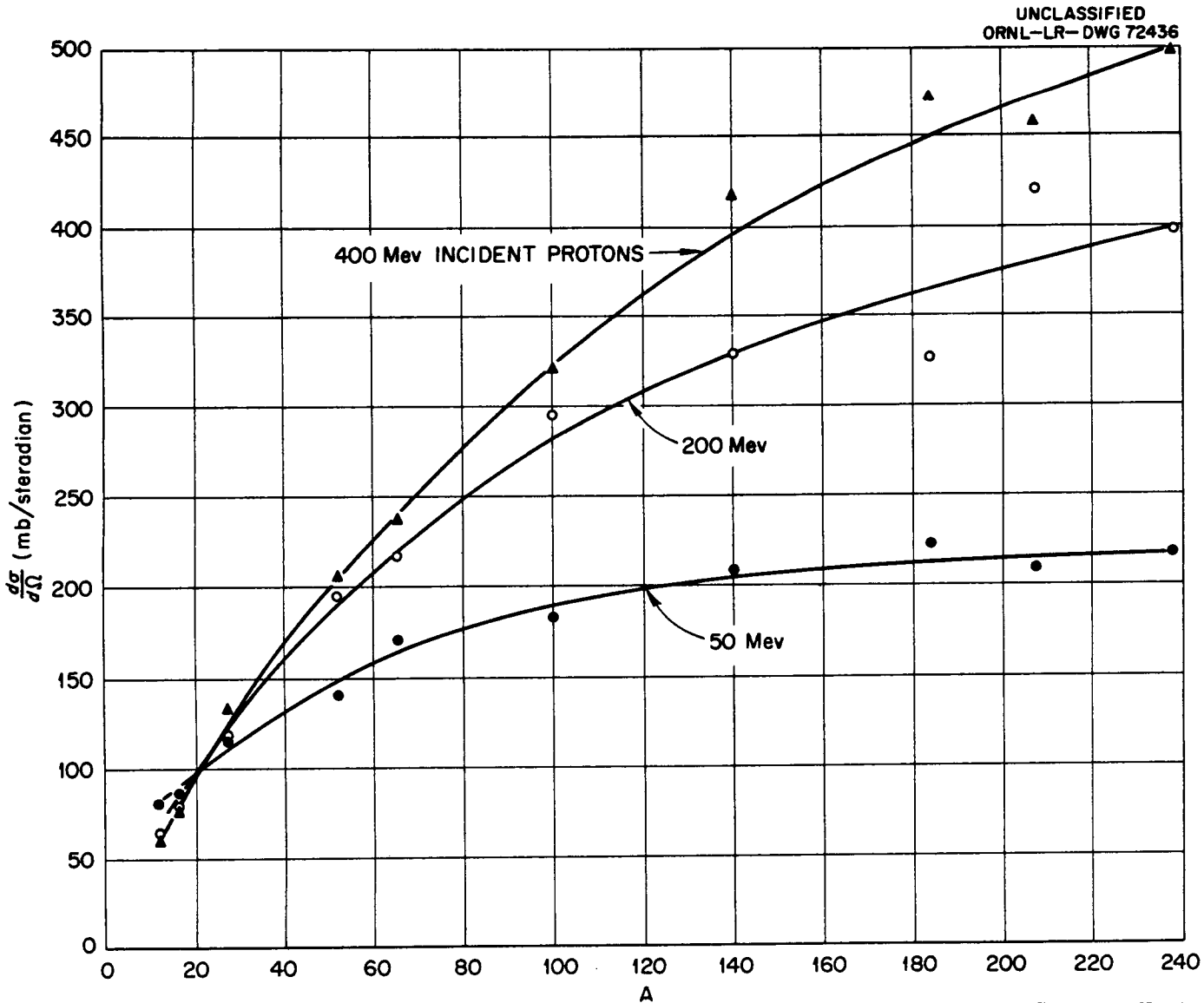

Fig. 58. Differential Cross Section vs Atomic Number A for Emission of Cascade Neutrons into the Laboratory Angular Interval 0 to 30° for Incident Protons.

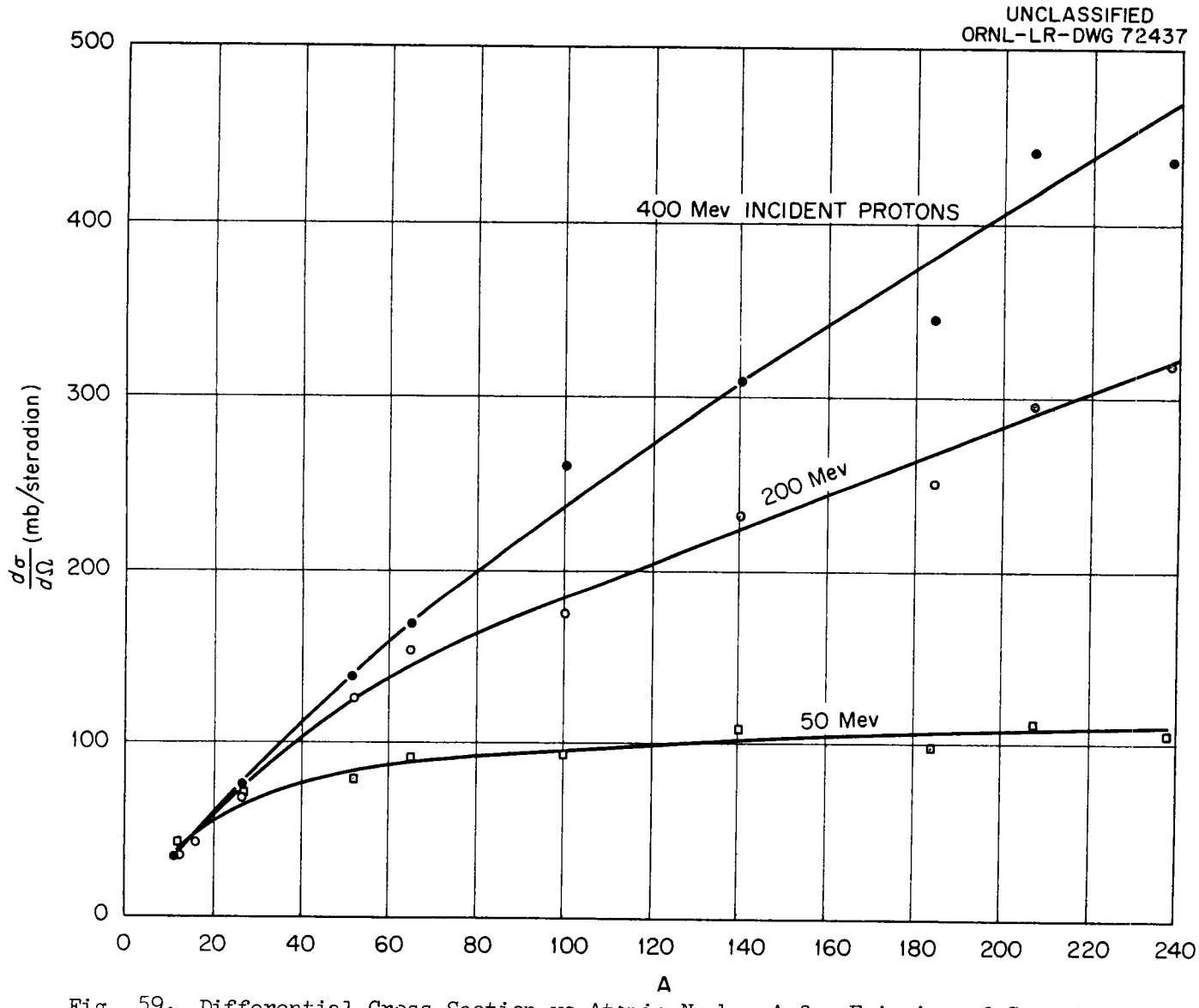

Fig. 59. Differential Cross Section vs Atomic Number A for Emission of Cascade Neutrons into the Laboratory Angular Interval 30 to 60° for Incident Protons.

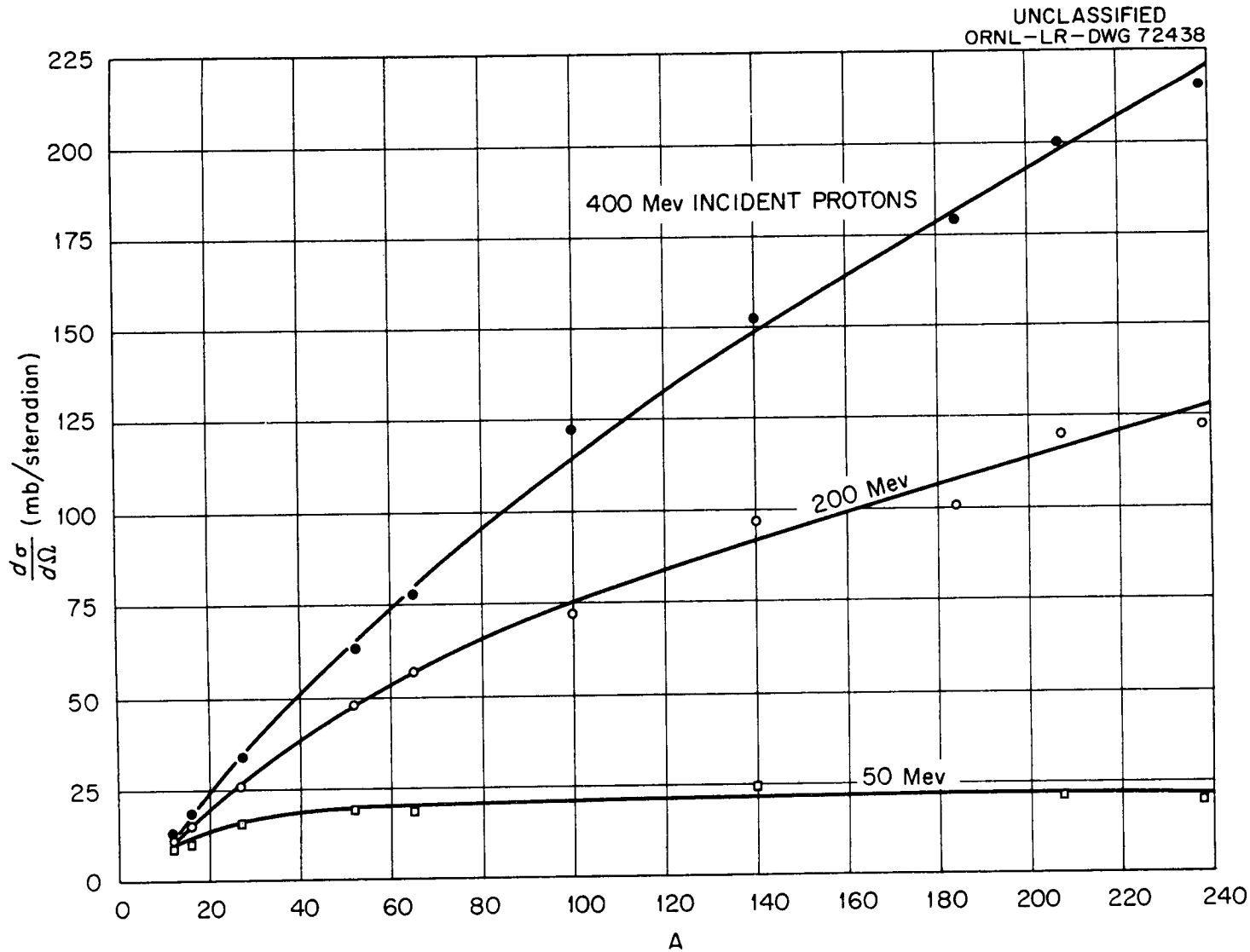

Fig. 60. Differential Cross Section vs Atomic Number A for Emission of Cascade Neutrons into the Laboratory Angular Interval 60 to 120° for Incident Protons.

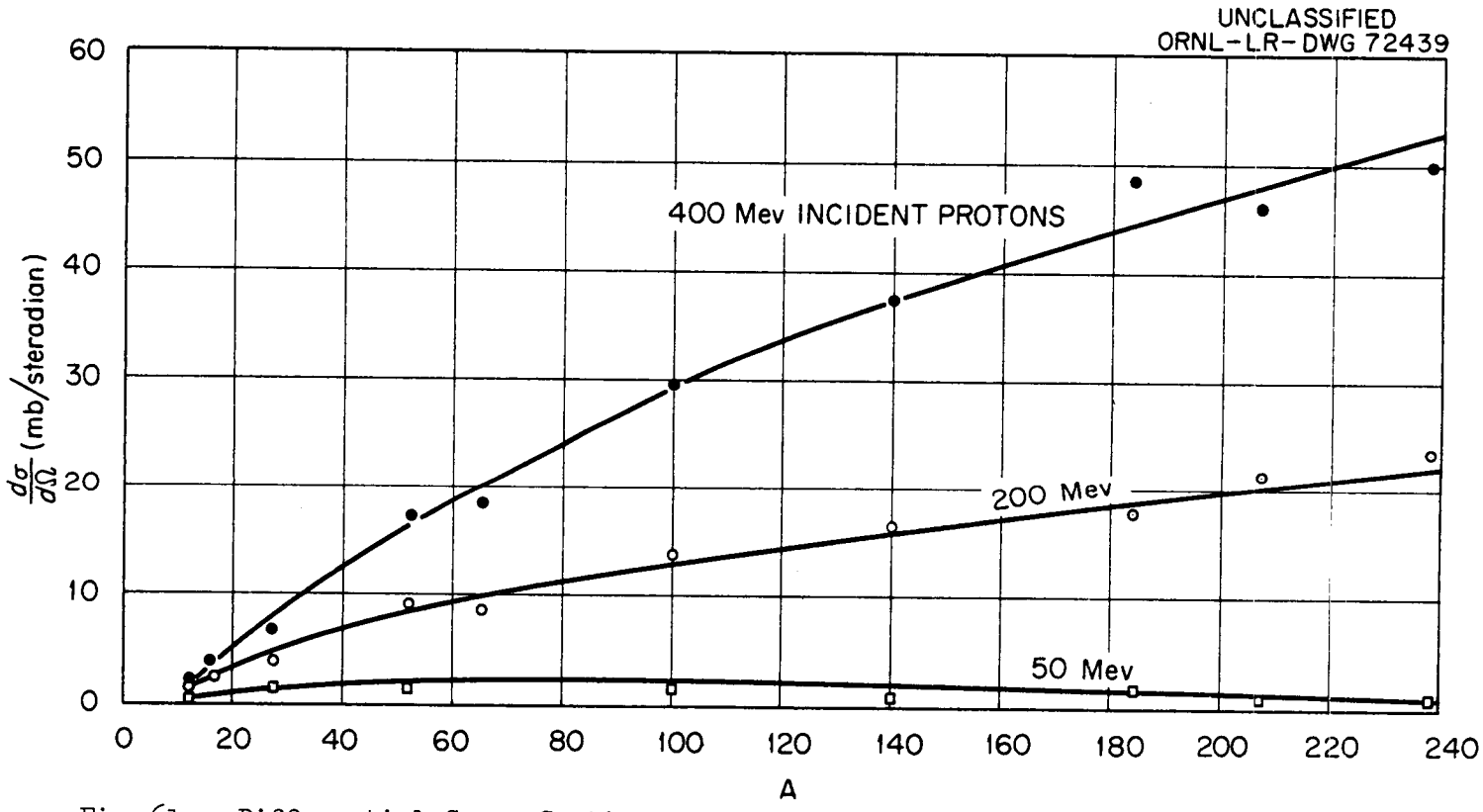

Fig. 61. Differential Cross Section vs Atomic Number A for Emission of Cascade Neutrons into the Laboratory Angular Interval 120 to 180° for Incident Protons.

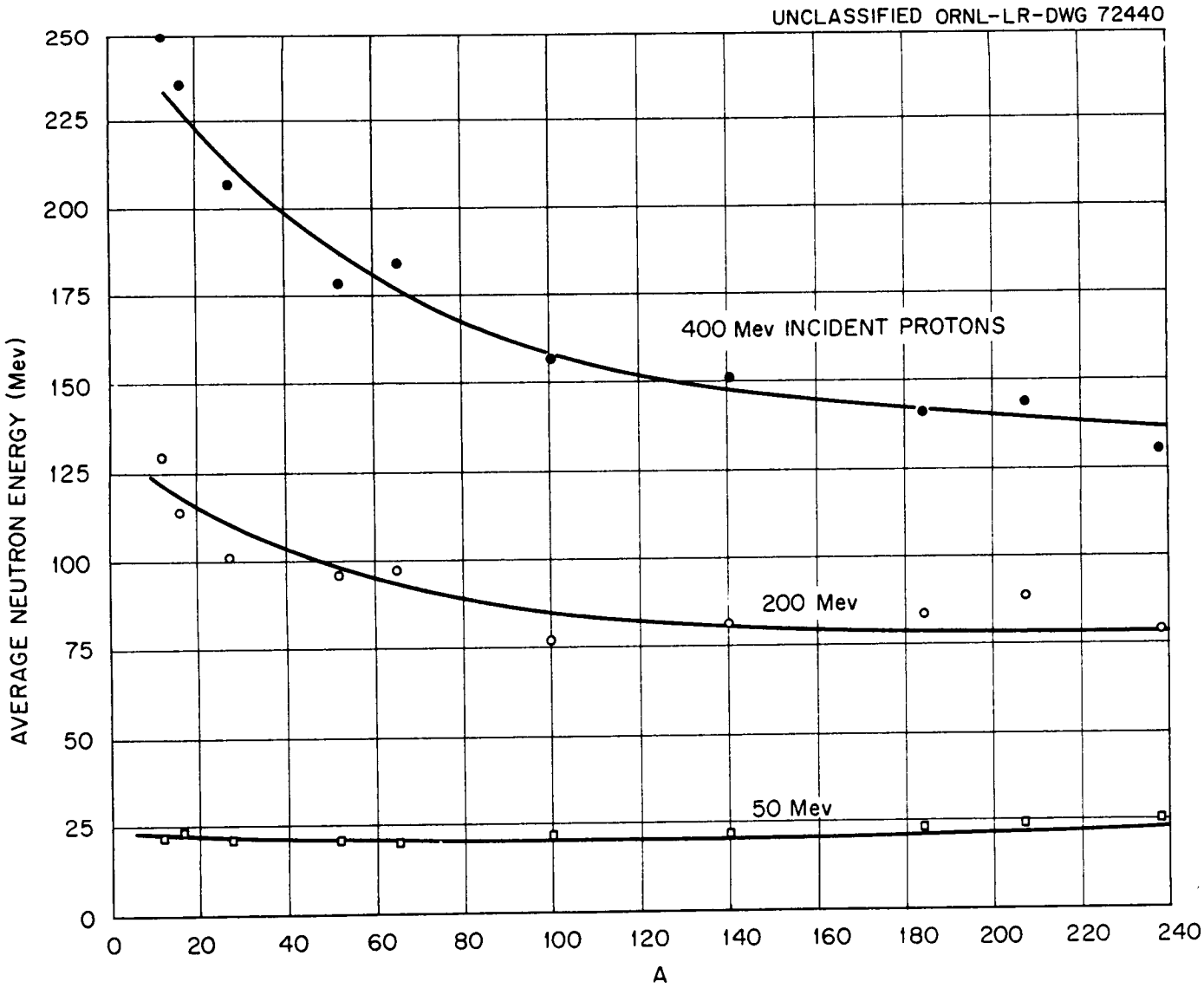

Fig. 62. Average Energy of Cascade Neutrons Emitted into the Laboratory Angular Interval 0 to 30° vs Atomic Number A for Incident Protons.

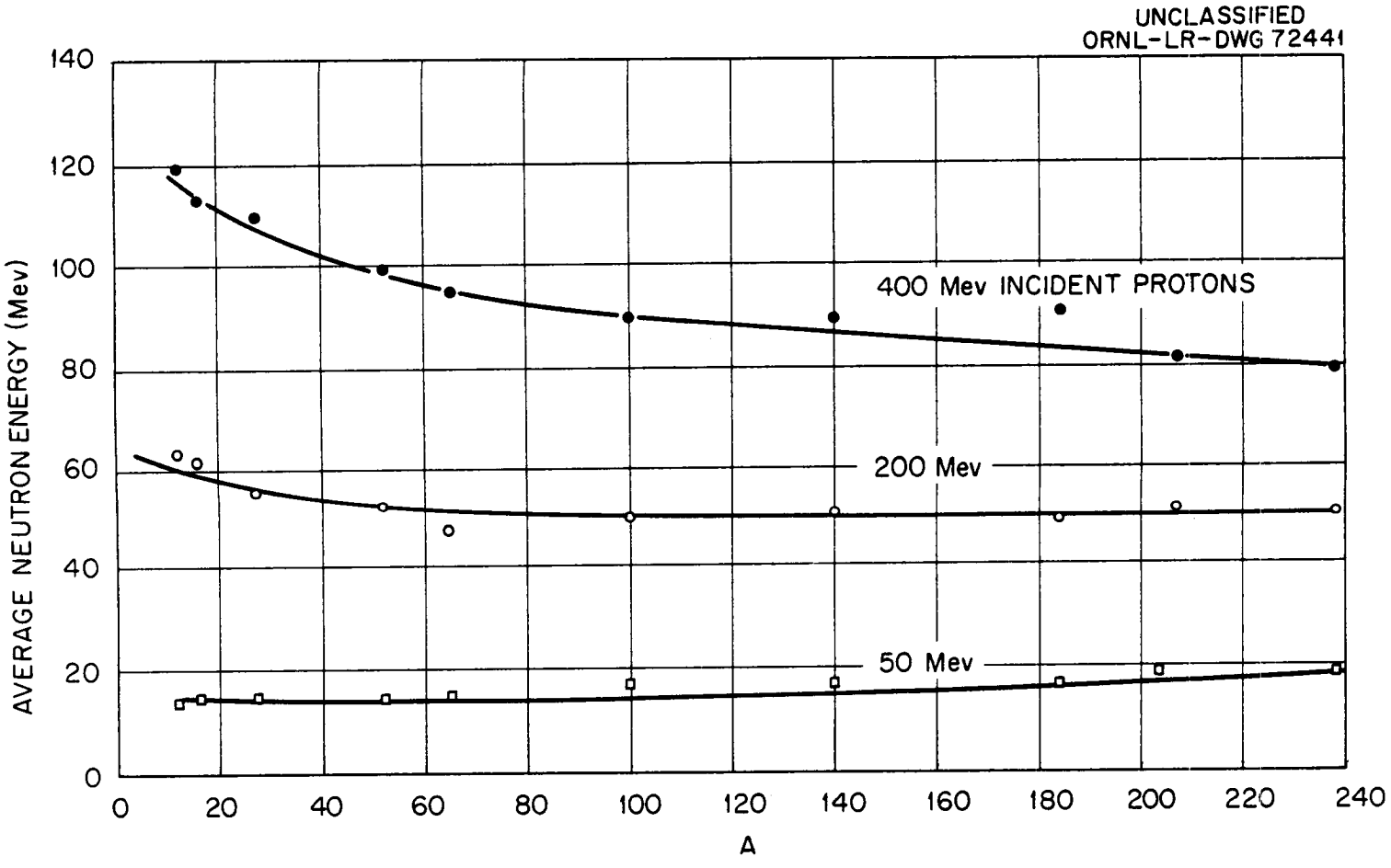

Fig. 63. Average Energy of Cascade Neutrons Emitted into the Laboratory Angular Interval 30 to 60° vs Atomic Number A for Incident Protons.

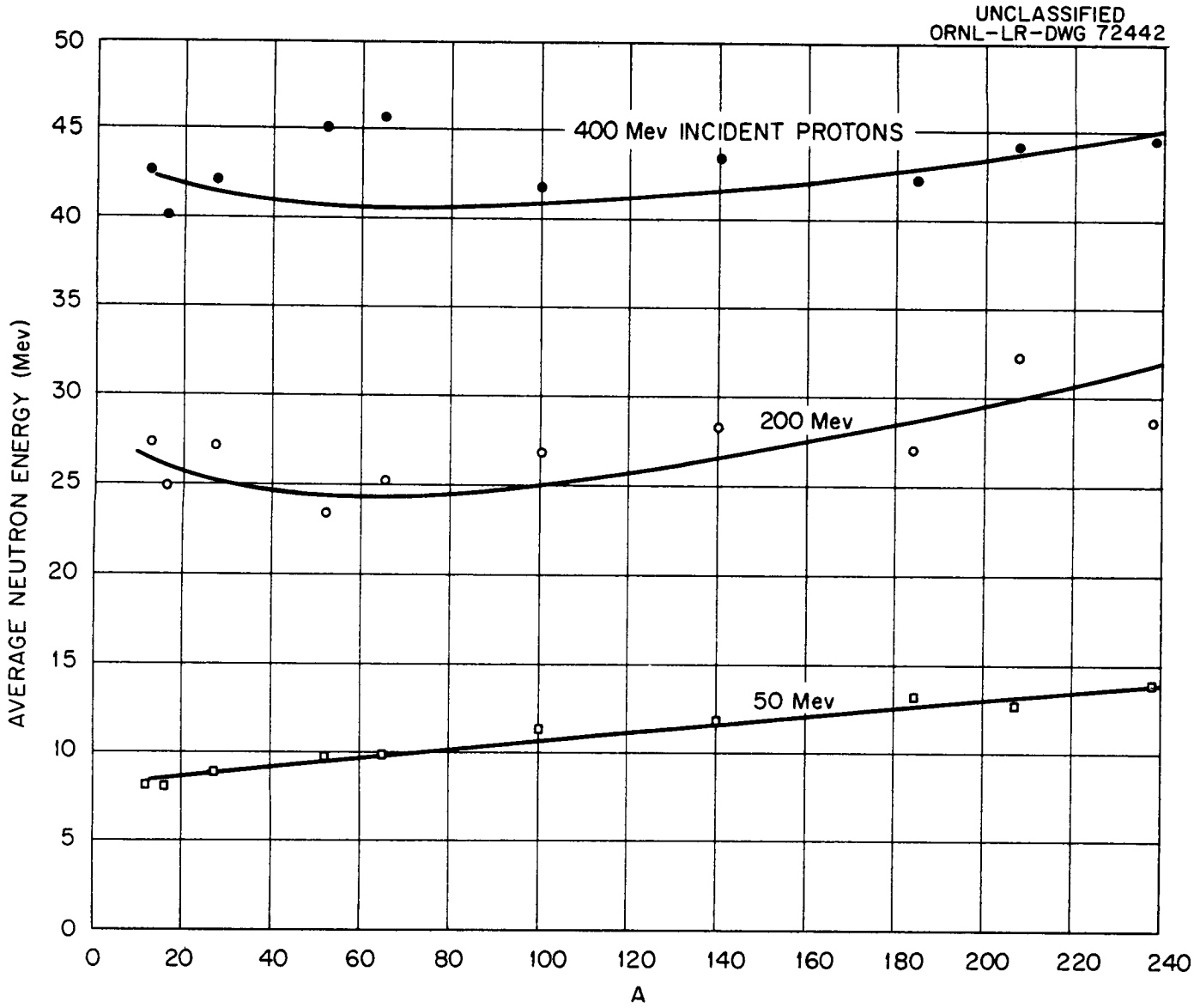

Fig. 64. Average Energy of Cascade Neutrons Emitted into the Laboratory Angular Interval 60 to 120° vs Atomic Number A for Incident Protons.

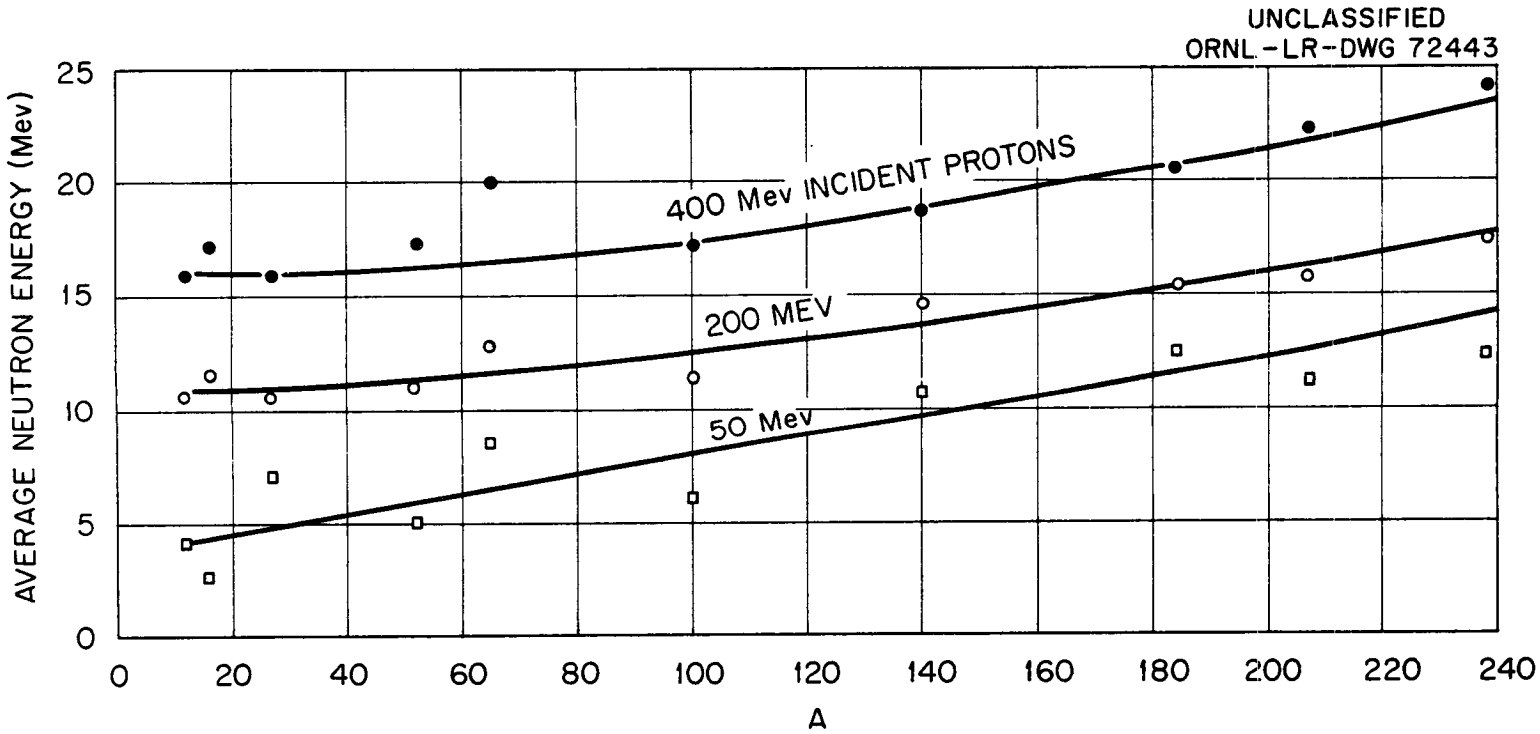

Fig. 65. Average Energy of Cascade Neutrons Emitted into the Laboratory Angular Interval 120 to 180° vs Atomic Number A for Incident Protons.

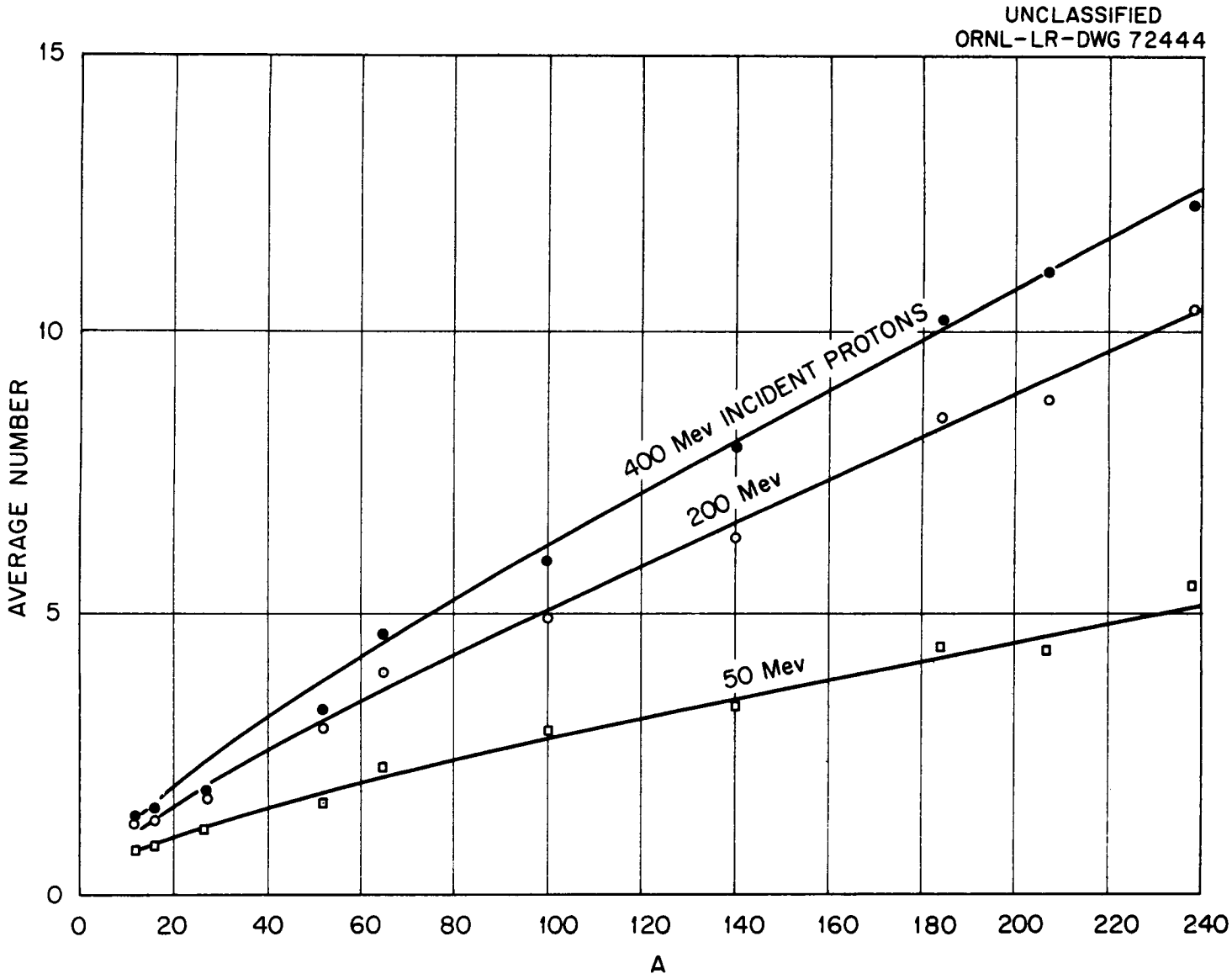

Fig. 66. Average Number of Cascade and Evaporation Neutrons vs Atomic Number A for Incident Protons.

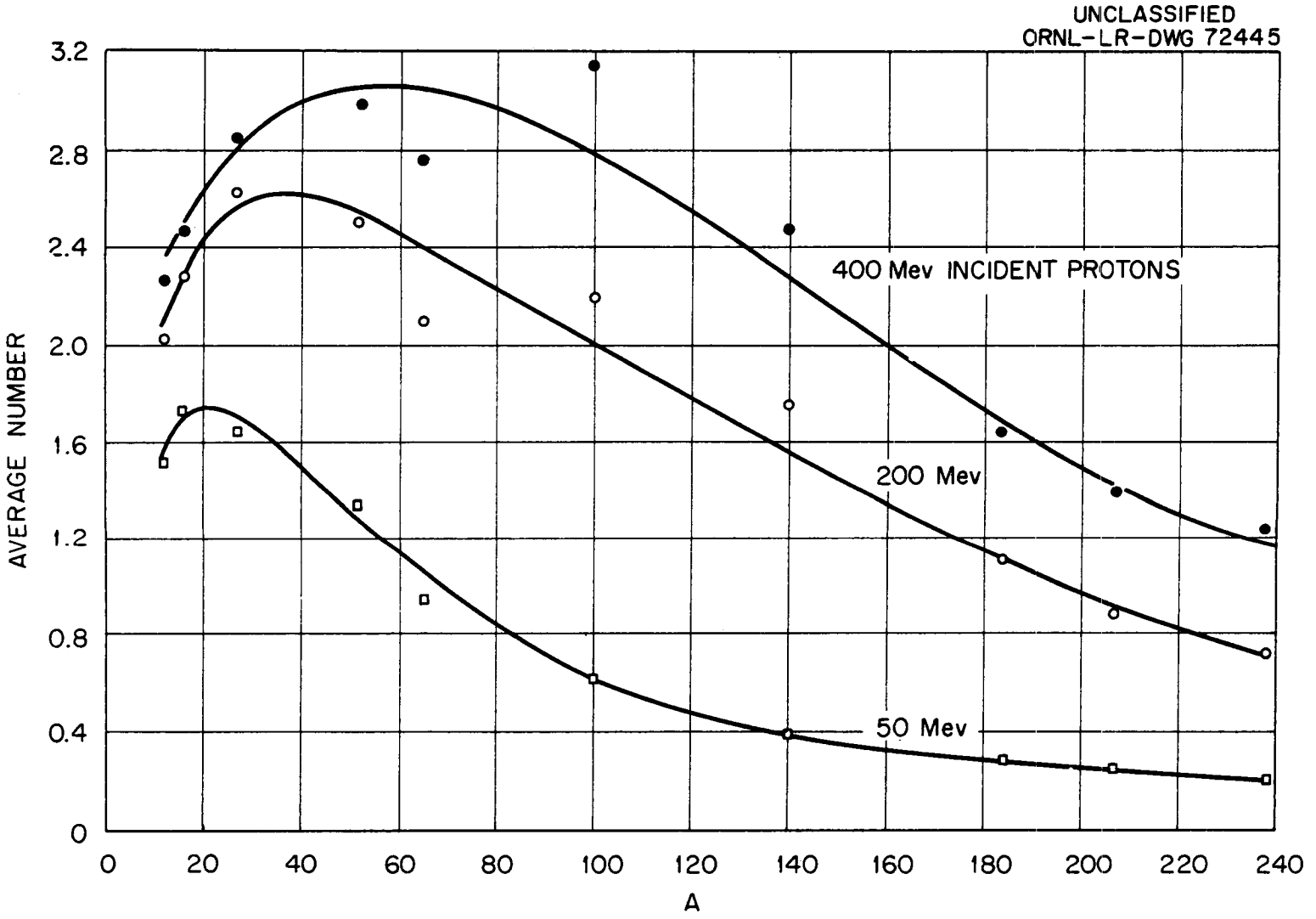

Fig. 67. Average Number of Cascade and Evaporation Protons vs Atomic Number A for Incident Protons.

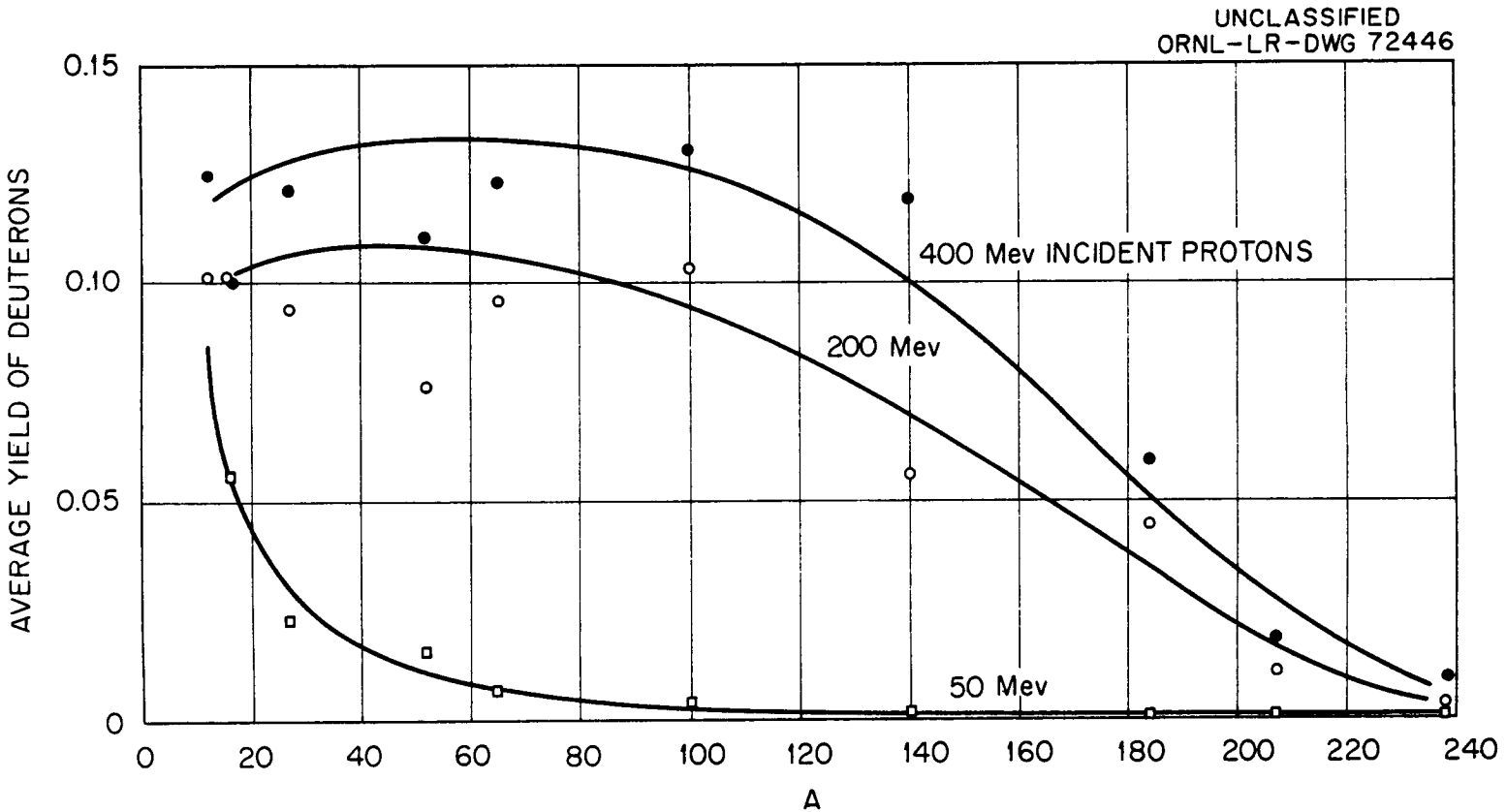

Fig. 68. Average Yield of Evaporation Deuterons per Inelastic Event vs Atomic Number A for Incident Protons.

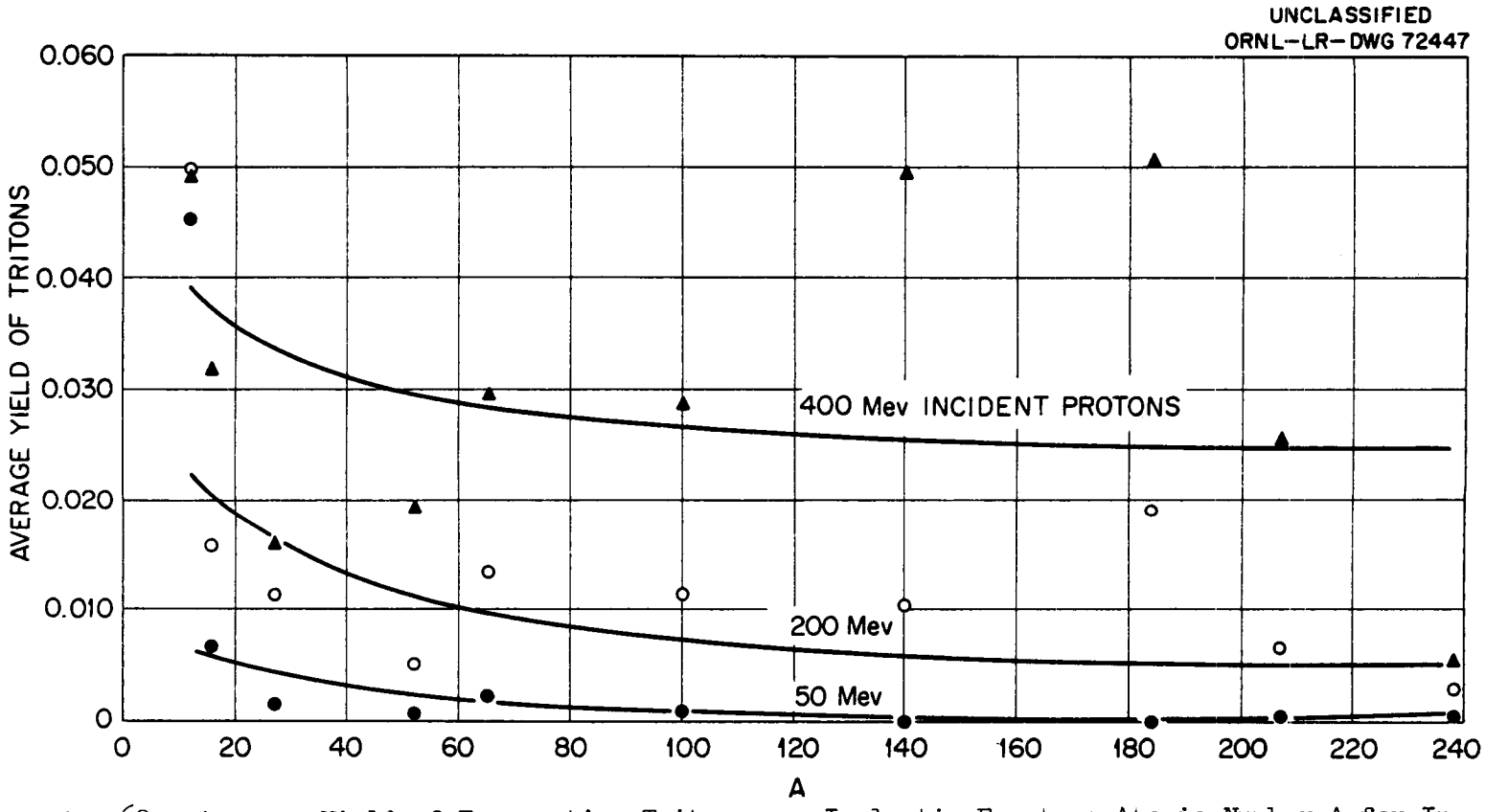

Fig. 69. Average Yield of Evaporation Tritons per Inelastic Event vs Atomic Number A for Incident Protons.

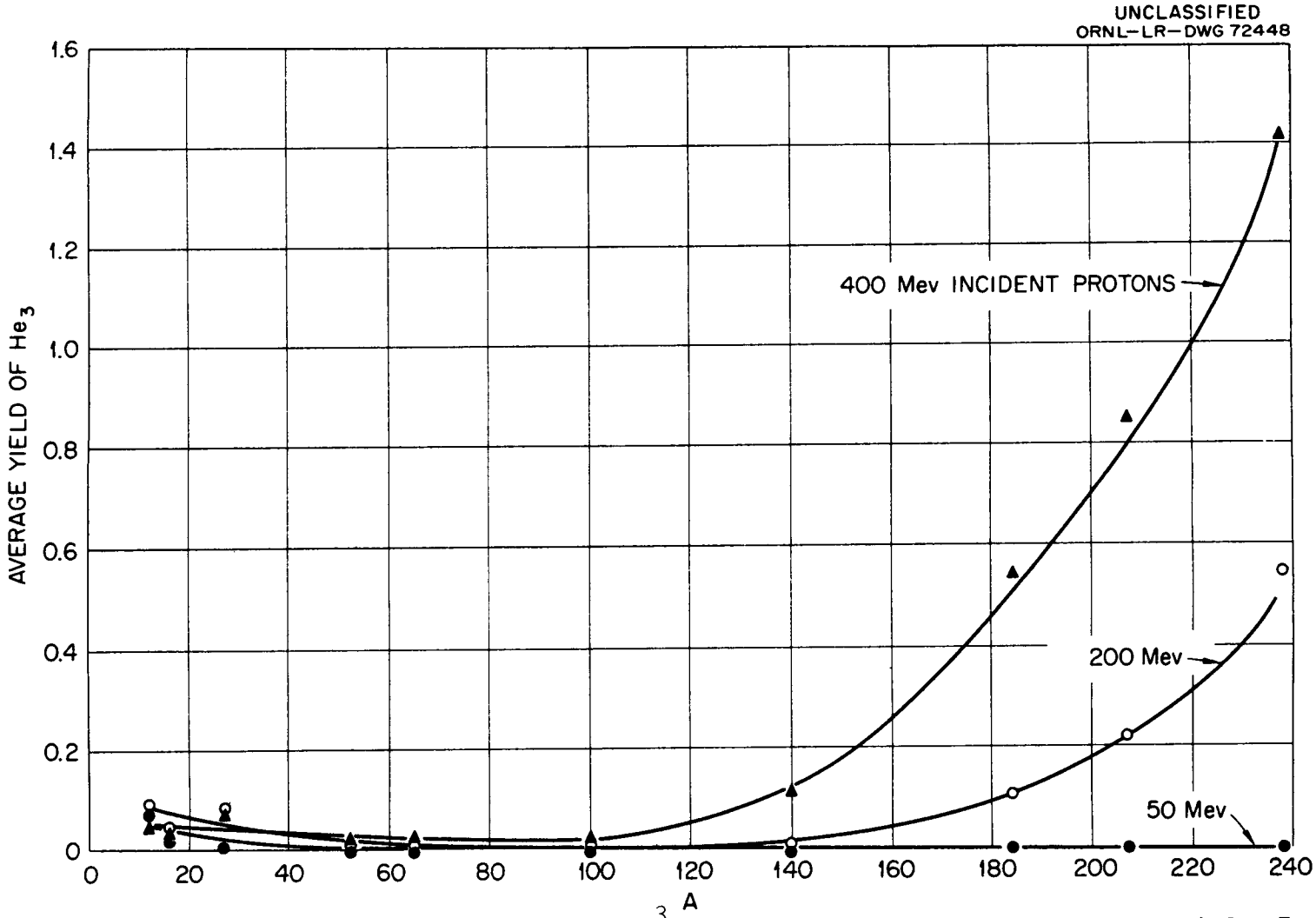

Fig. 70. Average Yield of Evaporation He^3 per Inelastic Event vs Atomic Number A for Incident Protons.

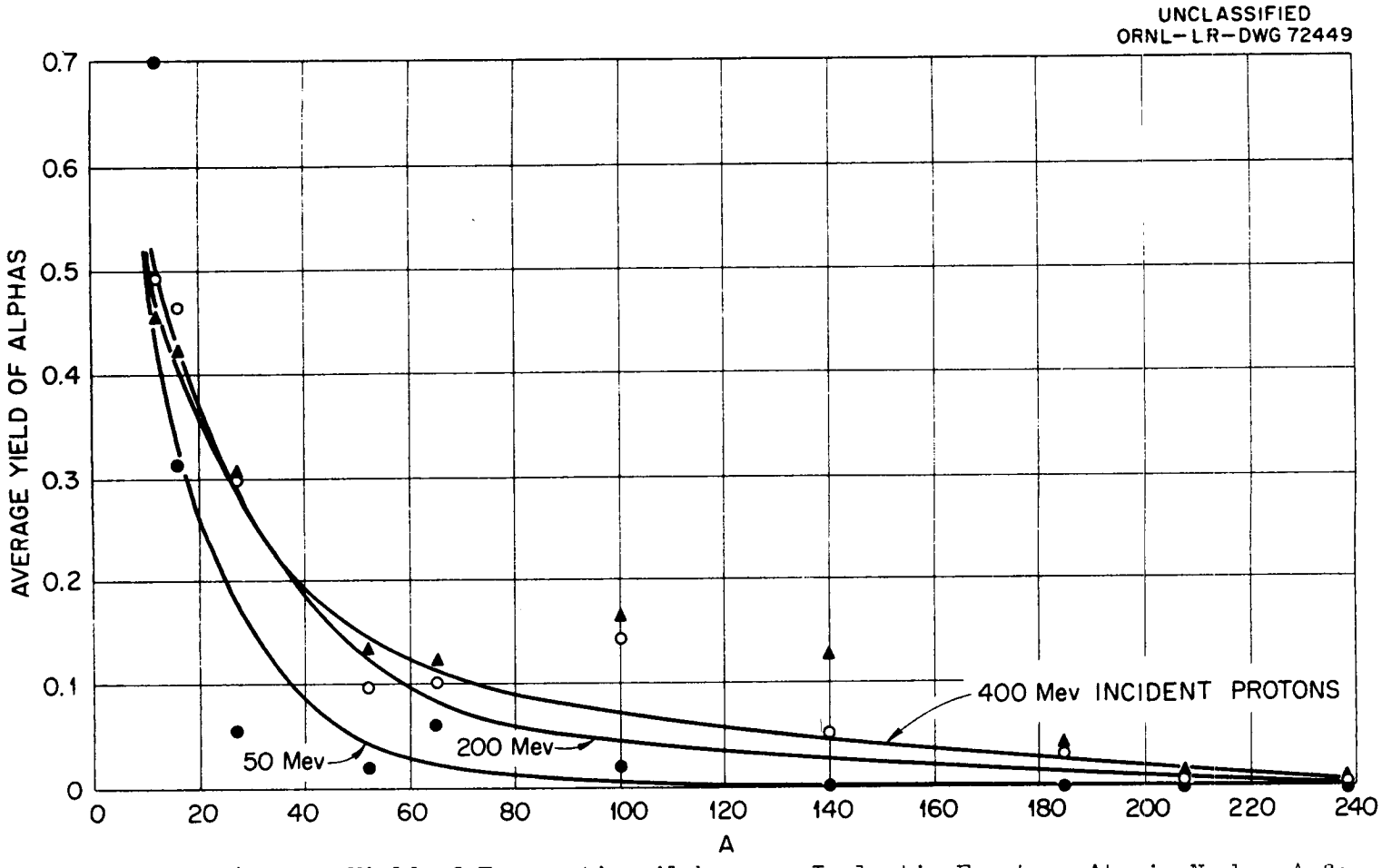

Fig. 71. Average Yield of Evaporation Alphas per Inelastic Event vs Atomic Number A for Incident Protons.

collisions.[11] This model assumes that a T = 3/2, J = 3/2 isobar (excited nucleon state) occurs as a collision product which subsequently decays into a pion and a nucleon; T is the isotopic spin quantum number and J is the total angular-momentum quantum number. In nucleon-nucleon collisions two such isobars can be formed, leading to the decay of two pions and two nucleons. If sufficient energy is available, the model allows for the formation of a T = 1/2 isobar, which can decay into one pion and one nucleon or into two pions and one nucleon. A considerable amount of experimental data (not yet available) would have been required to fix the contribution of the T = 1/2 isobar, and hence this reaction mode was not considered. The data for the description of the production processes decided upon were scarce enough in certain areas, and rather drastic assumptions had to be made in those cases.

Pion Production in Nucleon-Nucleon Reactions

The type of production event, single or double production, in nucleon-nucleon collisions within the nucleus is determined by the free-particle cross section for that event. The data for p-p single production were taken from the paper by Fickinger et al.[12] and are illustrated in Fig. 72. The n-p single-production cross section was assumed to be one-half the p-p cross section for the following reasons: The isotopic spin part of the n-p wave function can be written as a combination of T = 0 and T = 1 isotopic spin states, each comprising one-half the total state. If single pion production occurs through the formation of a T = 3/2 isobar only, the T = 0 state cannot contribute. Therefore only one-half the total n-p state contributes to pion production via the composite T = 1 state, while all of the total p-p state (a pure T = 1 state) contributes.

The p-p double-production cross section[13] is illustrated in Fig. 73. Since double production is assumed to occur via the formation of two T = 3/2 isobars, the T = 0 part of the n-p isotopic spin state does contribute. The cross section for the formation of two isobars through the T = 0 state must be known for the isobaric states being formed to be determined. The cross section for formation of two isobars through the T = 1 state is known (i.e., the p-p double-production cross section). From the expression $\sigma_{T=0} = 2\sigma_{p-n} - \sigma_{p-p}$, the ratio of the total cross sections for n-p scattering in the T = 0 and T = 1 states can be calculated:

$$R = \frac{\sigma_{T=0}}{\sigma_{T=1}} = \frac{2\sigma_{n-p}}{\sigma_{p-p}} - 1.$$

This ratio was assumed to be the same for the formation of two T = 3/2 isobars. The n-p double-production cross section (illustrated in Fig. 73) can then be calculated.

---

11. R. M. Sternheimer and S. J. Lindenbaum, Phys. Rev. 123, 333 (1961); Phys. Rev. 109, 1723 (1958); Phys. Rev. 105, 1874 (1957).

12. W. J. Fickinger et al., Phys. Rev. 125, 2082 (1962).

13. W. O. Lock et al., Phil. Mag. 2, Ser. 8, 215 (1957); W. B. Fowler et al., Phys. Rev. 103, 1479 (1956); F. F. Chen, C. P. Leavitt, and A. M. Shapiro, Phys. Rev. 103, 211 (1956).

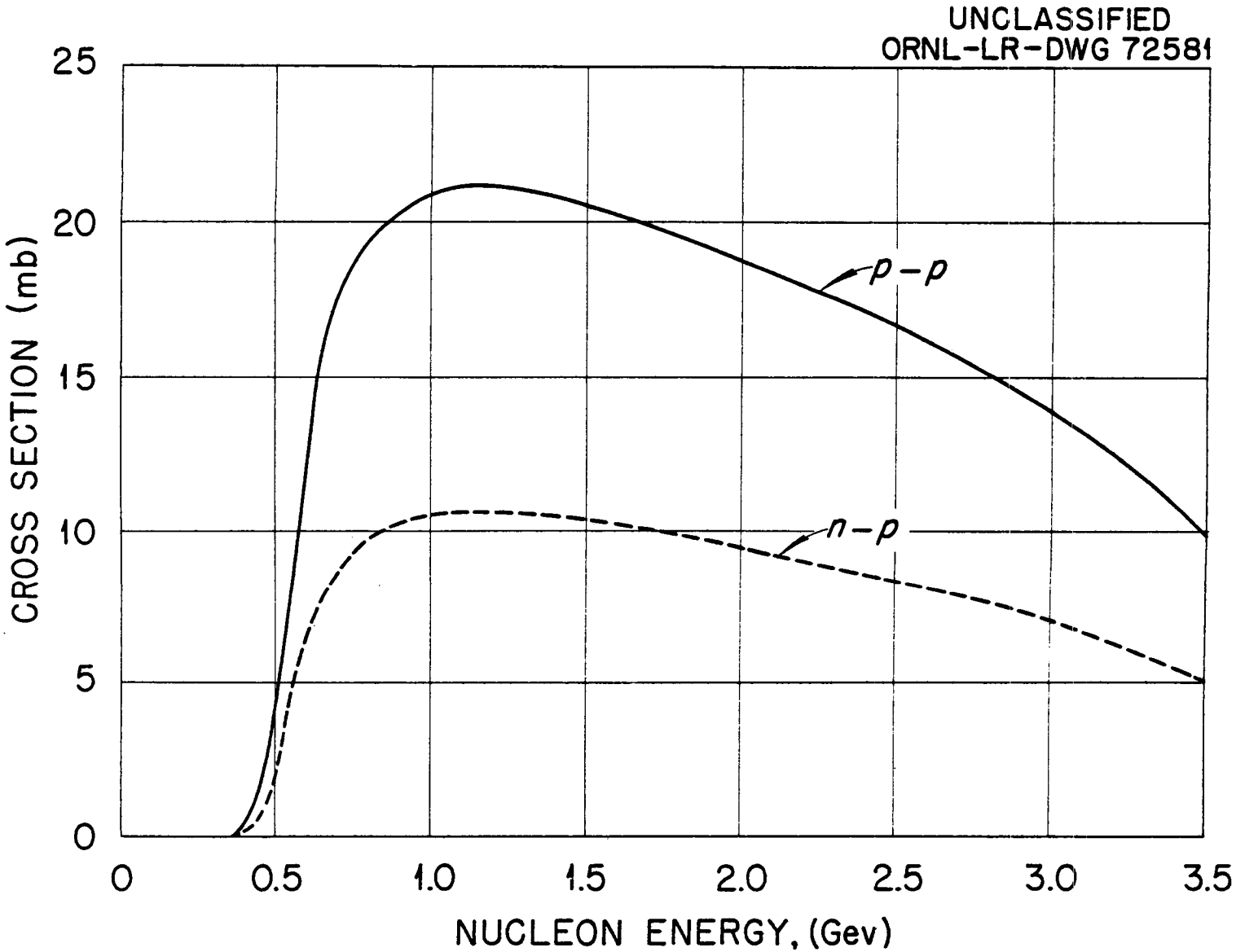

Fig. 72. Single Pion Production Cross Sections for p-p [from W. J. Fickinger et al., Phys. Rev. 125, 2082 (1962)], and n-p Collisions.

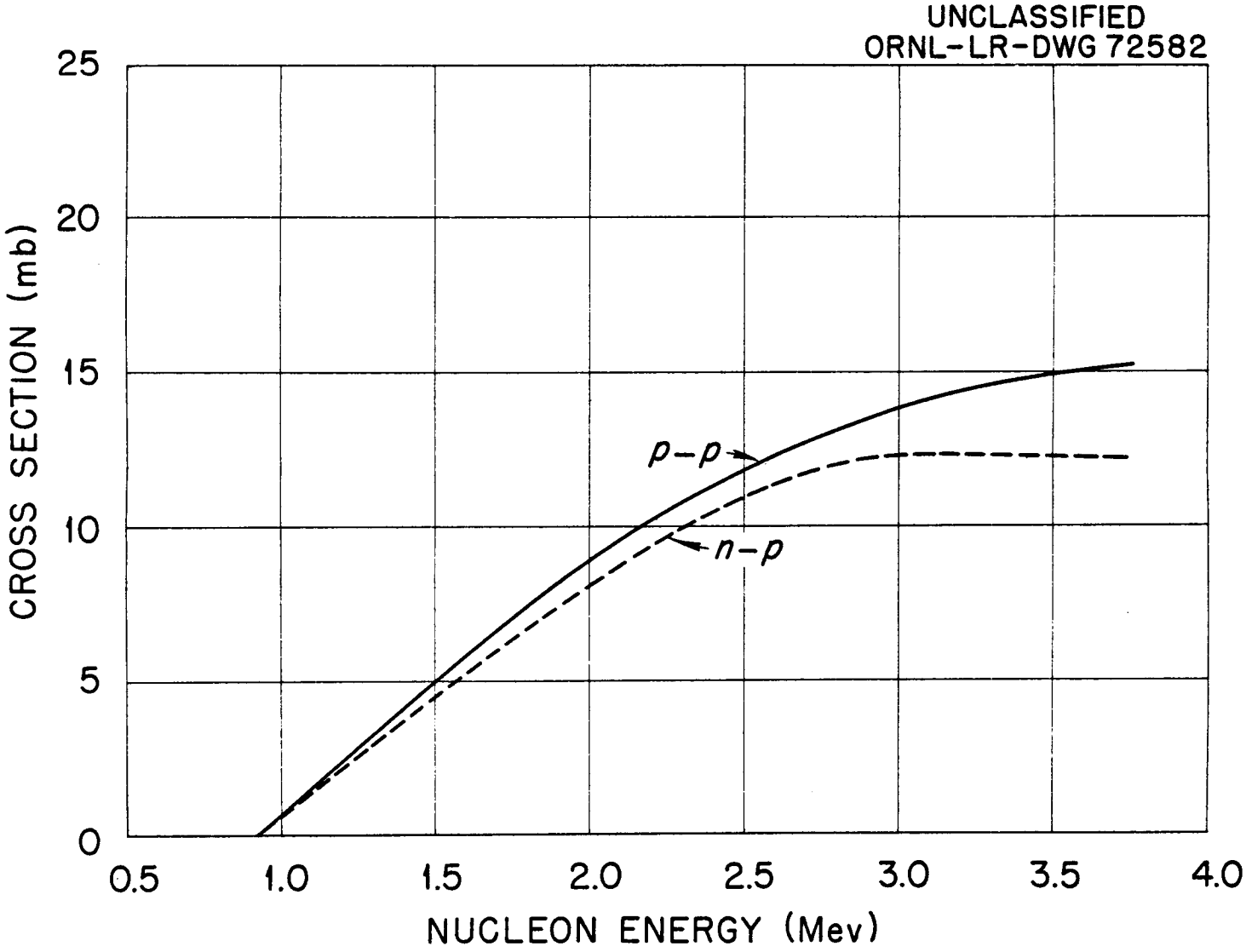

Fig. 73. Proton-Proton [from W. O. Lock et al., Phil. Mag. 2, Ser. 8, 215 (1957); W. B. Fowler et al., Phys. Rev. 103, 1479 (1956); F. F. Chen, C. P. Leavitt, and A. M. Shapiro, Phys. Rev. 103, 211 (1956)] and Neutron-Proton Double-Production Cross Section.

After the type of event is determined, it is necessary to calculate the mass, m, of the isobar. For single pion production this is done using the following expression, which is assumed to give the probability for formation of an isobar of mass m when the relative kinetic energy of the colliding particles is T_r:

$$P(m,T_r) = k\ \sigma_{3/2}\ F(m,T_r) \quad ,$$

where $\sigma_{3/2}$ is the pure T = 3/2 cross section (π^+ + p cross section), F is the phase space available to the isobar decay products, and k is a normalizing constant. This expression is a slight modification of the one given by Sternheimer and Lindenbaum.[11] For double pion production the expression

$$P(m_1,m_2,T_r) = k\ \sigma_{3/2}(m_1)\ \sigma_{3/2}(m_2)\ F(m_1,m_2,T_r) \quad ,$$

is used, where m_1 and m_2 are the masses of the two isobars.

When the isobar masses are known, the recoil angles of the isobars must be determined. The code is presently set up with any one of three options in this respect: Isobars are produced in either a forward or backward direction in the center-of-mass (C) system, isotropically in the C system, or in each of them 50% of the time. At present the latter alternative seems best,[14] but the others are included to determine their effects. Relativistic kinematics are used to determine the final momenta of the isobars, and they are allowed to decay isotropically in their own rest mass system to give the produced pions and decay or recoil nucleons.

The Clebsch-Gordon coefficients, in the framework of the isotopic spin formalism, are used to determine the final products.

Pion Production in Pion-Nucleon Reactions

The calculation of the production of pions in pion-nucleon collisions is carried out in exactly the same way as that for nucleon-nucleon collisions. Most of the data needed for these reactions are contained in an excellent article by Falk-Vairant and Vallados.[15] The inelastic cross sections that they give for π^+ + p and π^- + p reactions were assumed to be all single-production cross sections. These are given in Figs. 74 and 75.

The composite isotopic spin states involved in pion-nucleon collisions are generally the pure T = 3/2 and T = 1/2 state. Each of these can in turn be written in terms of the isotopic spin states of a recoil pion and a T = 3/2 isobar. Here both the composite T = 3/2 and T = 1/2 states contribute to the production process. The phase angle, ϕ, between the matrix

---

14. A. C. Mellissinos, Rochester University, private communication.

15. P. Falk-Variant and G. Vallados, Rev. Mod. Phys. 33 362 (1961).

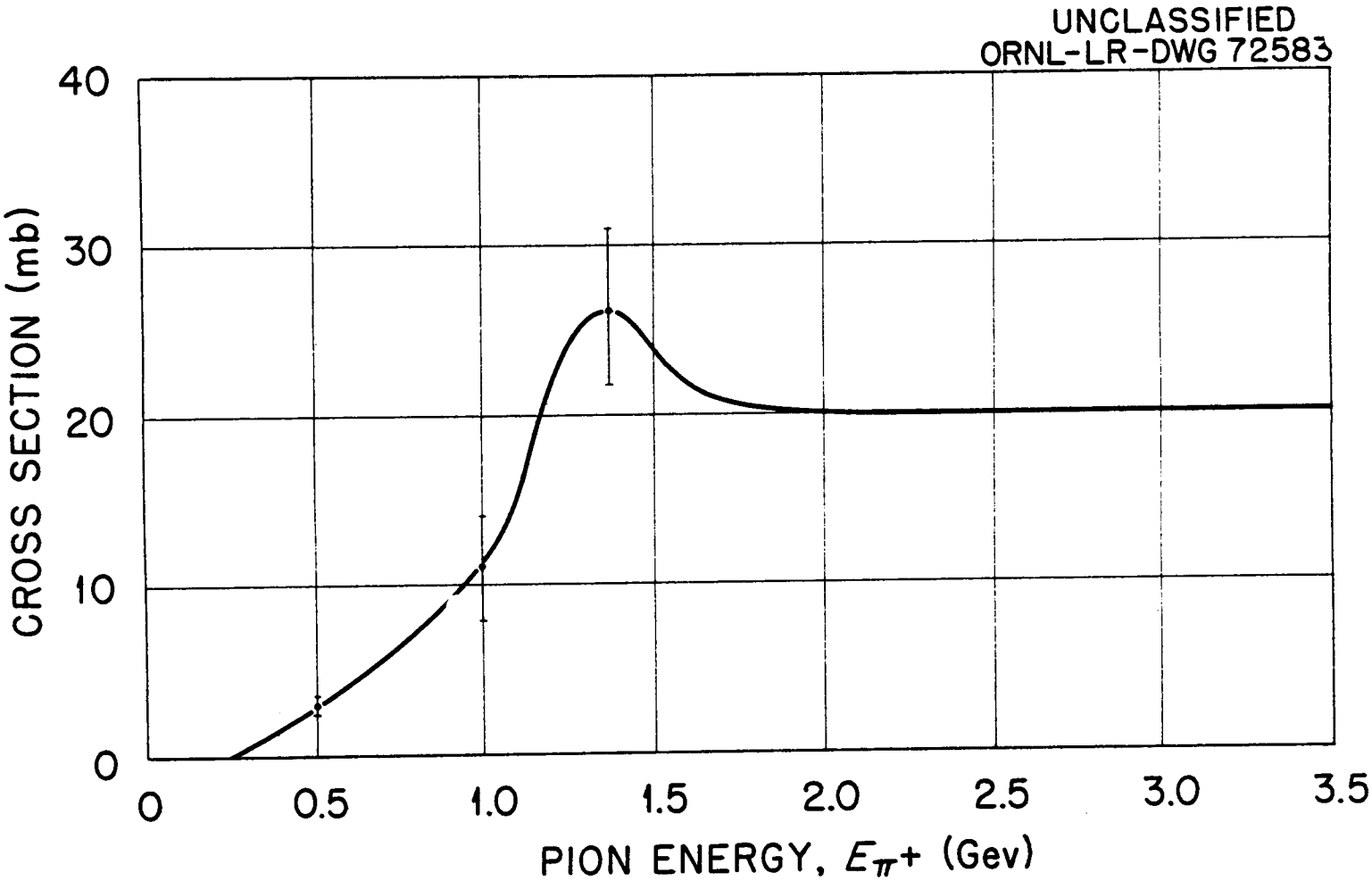

Fig. 74. π^+ + p Inelastic Cross Section [from P. Falk-Vairant and G. Vallados, Rev. Mod. Phys. 33, 362 (1961)].

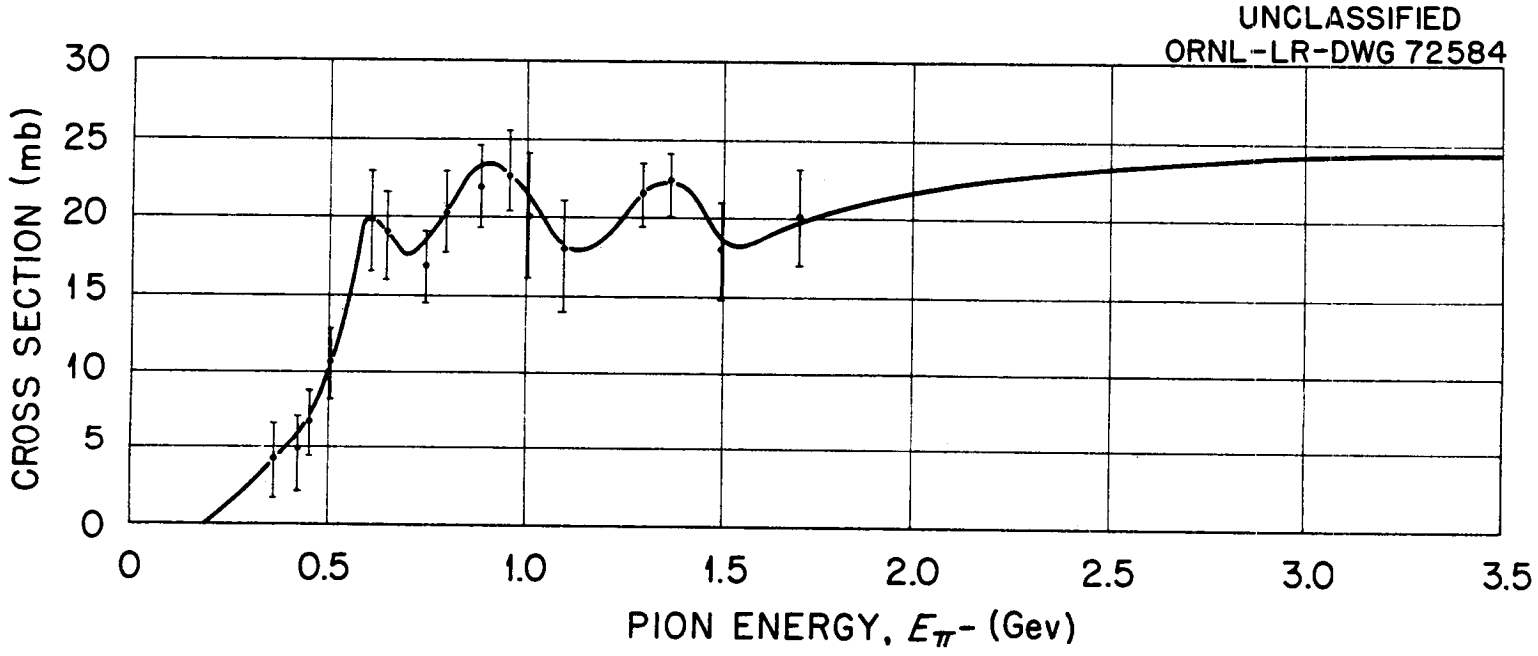

Fig. 75. π^- + p Inelastic Cross Section [from P. Falk-Vairant and G. Vallados, Rev. Mod. Phys. 33, 362 (1961)].

elements of the states and the ratio of the cross sections for production through each of these states must be known, as well as the single-production cross section, in order to determine the mode of formation of the isobar. By using the isotopic spin formalism, the single-production $\pi^- + p$ cross section can be written:

$$\sigma_{s.p.} = \frac{2}{3}\sigma_{11}(1 + \rho_1) \quad ,$$

where $\rho_1 = \sigma_{31}/2\sigma_{11}$, and σ_{31} and σ_{11} are the single-production cross sections for the pure $T = 3/2$ and $T = 1/2$ states, respectively. The $T = 1/2$ nonelastic cross section is given elsewhere.[15] This cross section was assumed to be all single production, and hence ρ_1 could be determined. By again making use of the isotopic spin formalism, the cross section for the reaction $\pi^- + p \rightarrow n + \pi^+ + \pi^-$ can be written

$$\sigma = \frac{2}{3}\sigma_{11}\left(\frac{5}{9} + \frac{26}{45}\rho_1 + \frac{7}{9}a\right) \quad ,$$

where $a = 2\sqrt{\rho_1/5}\cos\phi$, and ϕ is the phase angle mentioned before. The cross section is given by Perkins et al.[16] and by Walker,[17] and therefore a can be calculated. These quantities are sufficient for determining all the formation and decay modes of the $T = 3/2$ isobar for any pion-nucleon reactions.

Status

The coding for the extended intranuclear cascade calculation is nearing completion. Extensive checks must be made and the code debugged; then the code must be run so that extensive comparisons with experiment can be made. The estimated completion time for this portion of the work is about six months.

---

16. W. A. Perkins et al., Phys. Rev. 118, 1364 (1960).

17. W. I. Walker, Proceedings of the Sixth Annual Rochester Conference for 1956, p IV-16, Interscience, New York.

Paper D-4

EXPERIMENTAL TECHNIQUES FOR THE MEASUREMENT OF NUCLEAR SECONDARIES FROM THE INTERACTIONS OF PROTONS OF A FEW HUNDRED MEV

F. C. Maienschein, T. V. Blosser, H. R. Brashear,
W. R. Burrus, F. M. Glass, W. A. Gibson, N. W. Hill,
C. F. Johnson*, T. A. Love, V. A. McKay,
R. W. Peelle, R. T. Santoro, R. J. Scroggs,
T. F. Sliski, H. J. Stripling, and W. Zobel

Oak Ridge National Laboratory**

1514 over

Abstract

In this paper are described the preparations for a set of experiments which are designed to check space shielding calculations. The experiments are at an early stage and all information must be considered as preliminary. The approximate calculations of Alsmiller[1] have been used to estimate that spectral measurements are most important for secondary neutrons, protons, and gamma rays arising from the interactions of incident protons in the energy range from 20 to 600 Mev. Both "thin" and "thick" targets are needed to check the two pertinent types of calculations, those for the prediction of cross sections and secondary spectra for intranuclear cascades and those for transport through shields. Previous measurements exist only for thin targets and these are all limited in energy resolution or the range of energies and angles covered.

For the present experiments, the choice of spectrometers was conditioned by the need to move the equipment to several accelerators and the very stringent time schedule imposed by the need for shielding information for the Apollo mission to the moon. Thus, for neutron spectroscopy magnetic-deflection of proton recoils was not seriously considered. Three approaches have been followed with extensive development. Proton-recoil telescopes of two types have been studied but current emphasis centers on a dE/dx scintillation spectrometer for the energy range above 50 Mev. Neutron time of flight over a short path is being utilized to cover the energy range from a few Mev to ~50 Mev with reasonable resolution. Finally, a set of Bonner spheres is used for the energy range below 10 Mev.

---

*On assignment at Oak Ridge National Laboratory from General Dynamics, Fort Worth, Texas.

**Operated by Union Carbide Nuclear Company for the U. S. Atomic Energy Commission.

1. R. G. Alsmiller, Jr., and J. E. Murphy, "Space Vehicle Shielding Studies: Calculations of the Attenuation of a Model Solar Flare and Monoenergetic Proton Beams by Aluminum Slab Shields," ORNL-3317, 1962 (in press).

15140

For proton spectroscopy, the telescopes may be used by removing the hydrogenous radiator. The time-of-flight equipment may also be used for protons although the energy resolution from flight-time measurement becomes inferior to that available from energy absorption in a dE/dx scintillator above about 30 Mev. Flight time can be used to relieve the total absorption vs dE/dx ambiguity. For low-energy protons (less than ~10 Mev) no spectrometer, other than nuclear emulsions, is available nor is this energy region considered to be of particular importance.

Because of the complexity and size, Compton-recoil or pair magnetic deflection spectrometers were not considered for gamma rays. A sodium iodide scintillation spectrometer has an efficiency for neutrons comparable to that for gamma rays in the Mev region, and the resulting neutron-induced background was considered to be overwhelming. Thus a 3-NaI-crystal-pair spectrometer with a high inherent neutron rejection is used above 1.5 Mev. An anticoincidence scintillation spectrometer is used for lower energies.

The various spectrometers, together with dosimeters and threshold detectors have been tested in feasibility studies at the Harvard University Synchrocyclotron (156-Mev protons). Spectral measurements continue at that facility at this time, but the data await analysis. Results from the feasibility studies are discussed.

Introduction

As is discussed in papers by H. W. Bertini, W. E. Kinney et al., and R. G. and F. S. Alsmiller at this symposium, considerable calculational effort has been spent at the Oak Ridge National Laboratory to provide data pertinent to the shielding of space vehicles. The important sources of radiation which must be considered arise from protons trapped in the Van Allen belt(s) and from solar flares. The Van Allen protons will be most troublesome for vehicles with a slow rate of vertical ascent, such as those powered with ion-propulsion engines, while the solar-flare protons will be dangerous for occupants of any extraterrestrial spacecraft. The danger of solar flares is not accurately predictable, however, since their occurrence is statistical, the average rate varying periodically with time. Further, the calculations available, which take into account the production of secondary particles by the interactions of the protons, do not give consistent results for the dose which results from a single

flare.[1-3] Therefore, at present it is not possible to conclude whether the shields required for the approximately seven-day Apollo mission to the moon will be of sufficient thickness to make secondary nuclear interactions of importance. But it is clear that manned interplanetary flights will require shields of such thicknesses that the production of secondary particles must be accurately predicted, and the great cost of extraterrestrial transport emphasizes the need for accurate and not overly conservative calculations.

The calculations necessary for spacecraft shielding are of two basic types: those of cross sections and the spectra of secondary particles for intranuclear cascades and those of the transport of the secondary particles through shields. Energy losses by ionization are included in the transport calculation and are considered to be well understood, but serious uncertainties arise in other parts of the calculations which make experimental checks highly desirable. Thus preparations are under way for a series of experiments to provide such checks. The present status of the preparations is described herein; however, it must be understood that these experiments are at an early stage and that modifications in the equipment and plans may be necessary.

As an aid in determining which measurements would be most pertinent for spacecraft shielding, Alsmiller and Murphy[1] have performed preliminary calculations of the dose resulting from incident monoenergetic protons of various energies. Although these calculations contain many approximations, they represent the best information presently available and several conclusions may be drawn. For example, for shields thinner than the range of the incident protons the dose from the primary protons is dominant; the dose due to secondary protons decreases rapidly with increasing shield thickness, while the dose due to secondary neutrons drops slowly and becomes dominant for thicknesses greater than the incident proton range; and the dose due to secondary mesons is only a few percent of the total dose for any shield thickness appropriate for spacecraft. The dose due to secondary gamma rays was not considered by Alsmiller and Murphy,[1] but Alsmiller et al.[4] and Madey et al.,[5] who estimated the production of inelastic scattering gamma rays, indicate that there will be a significant

---

1. R. G. Alsmiller, Jr., and J. E. Murphy, ORNL-3317, op. cit.

2. R. I. Allen et al., Shielding Problems in Manned Space Vehicles, NR-140 (September, 1961).

3. R. K. Wilson et al., A Study of Space Radiation Shielding Problems for Manned Vehicles, FZK-144 (June 8, 1962).

4. F. S. Alsmiller, R. G. Alsmiller, Jr., and D. K. Trubey, Comparison of Primary Proton Dose with the Dose from Gamma Rays Produced by Inelastic Scattering of Solar Flare Protons, ORNL CF-62-10-29 (1962).

5. R. Madey et al., Trans. Am. Nuclear Soc. 5 (1), 213 (1962).

dose due to secondary gamma rays. In summary, then, it appears that the measurements most needed are for secondary neutrons, protons, and gamma rays. The energy spectra and angular distribution of these particles must be determined in order to provide definitive tests of the theory. (It is assumed that the spectra of the incident primary particles in space will be available from other sources.)

To determine the energies of the incident protons that are the most important, Alsmiller and Murphy[1] calculated two "importance functions." The second of these gives the total secondary dose as a function of incident proton energy and shield thickness for the solar-flare spectrum that occurred on May 10, 1959. The importance function for an aluminum shield of 0.5 collision length (~42 g/cm^2) appears to peak at about 300 Mev and to decrease by a factor of ~10 at 1 Bev. It would be desirable to know the importance function for lower energies, but, unfortunately, the lowest energy point given is at 200 Mev. For thicker shields the importance function is roughly constant from 200 to 600 Mev, with a small decrease at still higher energies. The production of gamma rays is expected to be most important at lower energies, where the proton intensities are highest. Thus the incident-particle energy range of most interest for space shielding lies below about 600 Mev, with a lower limit of perhaps 20 to 50 Mev (lower when secondary gamma rays from nuclear excitation are considered).

Finally, consideration must be given to the choice of target thickness. For checking the intranuclear cascade calculations, experiments are needed with a few "thin" targets with widely varying Z values. For checking the transport calculations, spectra at various angles must be obtained with one or more "thick" targets. Actually, the targets will not be thick with respect to a mean free path for nuclear interactions, but their thickness will be greater than the range of the incident protons.

Previous Research

A number of spectral measurements have been made with synchrocyclotrons, the type of accelerator that covers most of the energy range of interest. Table 1 summarizes the pertinent characteristics of some of these measurements, all of which cover a limited energy range for the outgoing particles, suffer from poor energy resolution, or are otherwise limited. In general, the proton spectra and the neutron spectra with the best resolution show effects of nuclear level structure. Perhaps the most surprising feature of the data is the apparent absence of an exchange peak in the neutron spectra observed at Harvard ($\leq$ 100 Mev) for elements heavier than beryllium. At other laboratories exchange peaks were observed for all Z with energies as low as 143 Mev.

The one set of spectra listed for deuterons and tritons indicates that cascade particles with Z > 1 are unlikely to give an effect of more than a few percent. The gamma-ray data, however, when considered together

1. R. G. Alsmiller, Jr., and J. E. Murphy, ORNL-3317, op. cit.

Table 1. References to Measurements of Spectra of Secondary Particles from High-Energy Proton Interactions

Observed Particle	Accelerator	Incident Proton Energy (Mev)	Spread of Incident Proton Energy (Mev)	Target Thickness	Materials	Observed Energy Range (Mev)	Observed Angles (deg)	Type of Spectrometer	Energy Resolution	Comments	References
Protons	Harvard	96		~8 Mev	C		3–90	Range telescope	~3 + (*a*)	Observed level structure in C	Strauch and Titus, *Phys. Rev.* 103, 200 (1956)
Protons	Harvard	96			17 elements from Li to Bi	30–90	40	Range telescope	3–17 Mev including target thickness	Level structure for lower Z	Strauch and Titus, *Phys. Rev.* 104, 191 (1956)
Protons	Harvard	160			Zn, Sn, Ta, Pb	5–23	60, 90, 120	Range telescope and magnetic deflection	Good	Peaks slightly below Coulomb barriers	Fox and Ramsey, *Phys. Rev.* 125, 1609 (1962)
Protons	LRL	190		Thin	C, Al, Ni, Ag, Au	~3–90	0–65, 100–180	Nuclear emulsions and magnetic deflection	Very large angular acceptance	Also measured d and α spectra	Bailey, UCRL-3334 (1956)
Protons	Rochester	240	±8	7 Mev	C	60–190	90	Nuclear emulsions	Poor		Temmer, *Phys. Rev.* 83, 1067L (1951)
Protons	LRL	340	11	4 Mev	H, D, C, O	100–350	30, 40	Magnetic deflection	(*a*)	Nucleon momentum distributions are deduced	Cladis, Hess, and Moyer, *Phys. Rev.* 87, 425 (1952)
Neutrons	Harvard	50	Large		Li, Be, C, Pb	35–70	0, 5, 10, 16	Telescope	(*a*)	Li and Be indicate exchange reactions; C and Pb do not	Hoffman, Harvard thesis, 1952
Neutrons	Harvard	100	Large	0.125 in.	Be, C	40–110	0	Telescope	(*a*)	Li and Be indicate exchange reactions; C and Pb do not	Bodansky and Ramsey, *Phys. Rev.* 82, 831 (1951)
Neutrons	Harvard	95	~20		D, Li, Be, C, Al, Cu, Pb	50–110	0, 5, 10, 16, 28	Telescope	8–10 Mev and (*a*)	Li and Be indicate exchange reactions; C and Pb do not	Hoffman and Strauch, *Phys. Rev.* 90, 449 (1953)
Neutrons	Harwell	143	3	2.5–7.0 Mev	D, Li, Be, C, Al, Cu, Pb, U	15–140	~0	Time-of-flight	$0.07 \leq (\Delta E/E)_n \leq 0.14$	Measurements all relative; high-energy peak for all Z	Bowen *et al.*, *Nuclear Phys.* 30, 475 (1962)
Neutrons	Harwell	171		1–2 g/cm^2	Be, C, Al, U	50–200	2.5	Range telescope	(*a*)	High-energy peak for all Z	Cassels *et al.*, *Phil. Mag.* 44, 425 (1953)
Neutrons	Rochester	244		~0.3–1.0 in.	Be, C, Pb	120–240	0, 15	Telescope	$0.10 \leq (\Delta E/E)_n \leq 0.15$	High-energy peak for all Z	Nelson *et al.*, *Phys. Rev.* 88, 1 (1952)
Neutrons	LRL	190	±15	4.7–14.6 Mev	C, Al, Ni, Ag, Au, U	0.5–12	45, 90, 135	Nuclear emulsions	(*a*)	Primarily evaporation neutrons	Gross, UCRL-3330 and UCRL-3337 (1956)
$Z \geq 1$	ORSAY	154			Au^{197}	>30	15, 30, 60	$(dE/dx - E)$ telescope	±20%	$d/p \approx 1/10$, $t/p \approx 1/20$	Genin *et al.*, *J. Phys. Radium* 22, 615 (1961)
Gamma rays	Harvard	35	Large		LiH, Be, B, C, Mg, Al, Si, Cu, Au	~3–~20	90	NaI scintillation		Pulse-height spectra only; serious neutron-induced backgrounds	Culler, Harvard thesis, 1956
Gamma rays	Harvard	24, 56, 90	Large		C, Al	~3–~20	90	NaI scintillation		Pulse-height spectra only; serious neutron-induced backgrounds	Culler, Harvard thesis, 1956
Gamma rays	Harwell	150		20–40 Mev	Li, Be, B, C, N	<15	90	NaI scintillation			Clegg *et al.*, *Proc. Phys. Soc.* 78, 681 (1961)
Gamma rays	Harwell	150		20 Mev	O, F	<15	90	NaI scintillation			Foley *et al.*, *Nuclear Phys.* 31, 53 (1962)
Gamma rays	Harwell	150		20 Mev	Na, Mg, Al, Si, P, S	<15	90	NaI scintillation			Foley *et al.*, *Nuclear Phys.* 37, 23 (1962)
Gamma rays	LRL	30–340			C	8–22	90	180° pair spectrometer		Studied C^{12} level at 15.2 Mev	Cohen *et al.*, *Phys. Rev.* 96, 714 (1954)

(*a*) Energy resolution limited by energy spread of incident beam.

with one lower energy measurement,[6] are of quite limited value. None of the previous studies were made with a target "thick" from the transport point of view.

Planned Experiments

As described in a previous report,[7] experiments are planned with the primary goal of determining energy spectra at selected angles for secondary neutrons, protons, and gamma rays. Preliminary or feasibility studies were made at the Harvard University Synchrocyclotron (156-Mev protons) in May and August, 1962. The object of these studies was not to produce spectral data but to determine the necessary beam intensities, to measure backgrounds, and to check the operation of the spectrometers. Substantial modifications to the equipment were required after each test. The test results have not been analyzed in detail for all spectrometers, and the comments presented in this paper are all tentative. Further measurements were performed at Harvard in October, 1962, and continue at the time of this symposium.

The arrangement of the targets and spectrometers at the Harvard accelerator is described in the next section. Also discussed are the measurements of the proton-beam average intensity and spatial extent, as well as the necessary studies of the complex time behavior of the beam. The use of targets thicker than the range of the primary protons simplifies many experimental problems, especially for measurements near the forward direction. However, both thin and thick targets will be studied (as feasible) in order to check the two types of calculations (cross sections and transport). Targets will be chosen from Be, C, Al, Co, Bi, and H_2O. Copper and lead were used in the preliminary studies. The change to cobalt and bismuth will provide single isotopes, a potential advantage in interpreting nuclear level effects.

The choice of spectrometers was dictated by the need to move the equipment to several accelerators and the stringent time schedule imposed by the need for shielding information for the Apollo mission to the moon. Thus for neutron spectroscopy, magnetic deflection of proton recoils was not seriously considered, but three other approaches have been followed with extensive development. Proton-recoil telescopes of two types have been studied, with current emphasis centering on a dE/dx scintillation spectrometer for the energy range above 50 Mev. Neutron time of flight over a short path is being utilized to cover the energy range from a few Mev to ~50 Mev with reasonable resolution, and, finally, a set of Bonner spheres is used for the energy range below 10 Mev. These three systems are described in Sections II, III, and IV.

---

6. T. Wakatsuki et al., J. Phys. Soc. Japan 15, 1141 (1960).

7. W. A. Gibson, W. R. Burrus, and T. A. Love, Neutron Phys. Div. Ann. Prog. Rep. September 1, 1961, ORNL-3193, p. 325.

In connection with the interpretation of the Bonner sphere data (Section IV) and their extension to higher energy, several threshold detectors were tried. These depended upon fission reactions or $C^{12}(n,2n)C^{11*}$ activation. It was decided not to use these detectors, basically because of their inability to differentiate between neutron- and proton-induced reactions.

In a cooperative effort with the Fort Worth Division of General Dynamics, nuclear emulsions of varying thickness and sensitivity were exposed in the feasibility studies.[8] It has been determined that appropriate exposures were achieved for many of the plates, but they have not yet been subjected to detailed scanning. The separation of proton tracks from neutron-induced proton-recoil tracks is quite difficult at the energies considered here, and the efficacy of the approach remains to be demonstrated. If successfully used, the emulsions should give useful data up to about 25 Mev.

For proton spectroscopy the telescopes may be used by removing the hydrogenous radiator. The time-of-flight equipment may also be used for protons, although the energy resolution from flight-time measurements becomes inferior to that available from energy absorption in a dE/dx scintillator above about 30 Mev. Flight time can be used to relieve the ambiguity between total absorption and dE/dx. For low-energy protons (less than ~10 Mev) no spectrometer, other than the nuclear emulsions, is available; nor is this energy region considered to be of particular importance.

Because of their complexity and size, Compton-recoil or pair magnetic deflection spectrometers were not considered for gamma rays. A NaI(Tl) scintillation spectrometer has an efficiency for neutrons comparable to that for gamma rays in the Mev region, and the resulting neutron-induced background was considered to be overwhelming. Thus a three-crystal (NaI) pair spectrometer with a high inherent neutron rejection was chosen and is described in Section V.

As stated previously, the major goal for the experiments is to provide accurate spectral data for comparison with calculations. A further check may be provided by determining the distribution in depth of the dose resulting in a spherical phantom from the interaction of all secondary particles. Fractionation of the dose with respect to the type of radiation would require dosimeters which are not available. The "integral" dose measurement described in Section VI will, if successful, test whether the interactions of secondary particles in water (or tissue) and the integrations over angle required by the complex geometry can be handled by the calculation.

The electronics for the various spectrometer systems is located in two mobile laboratories so that it may be transported to the accelerators of interest. Connecting cables ~200 feet long permit operation of the experiment from the mobile laboratories. The photograph on page 531 shows

8. Sponsored by the U. S. Air Force, Wright Air Development Division.

part of the 17 relay racks of equipment which is largely transistorized. The design, purchase, fabrication, test, and assembly of the apparatus were possible in the short time available only through the extraordinary efforts of the electronic design, counter, and mechanical design groups of the Instrumentation and Controls Division of ORNL. The tests at Harvard University were greatly facilitated by the cooperation afforded by the synchrocyclotron group, particularly A. M. Koehler and W. M. Preston. Use of the electronic components is described in Sections I - VI. Detailed descriptions of individual components designed for this experiment but of general interest will be prepared for publication elsewhere.

I. Proton Intensity Measurements

The series of experiments currently in progress at the Harvard University Synchrocyclotron[9] has been outlined in the Introduction. For a meaningful interpretation of the experimental data, the detector position as a function of angle and distance from the experimental target must be accurately known. In addition, the spatial and time distributions of protons incident upon the target, as well as the absolute intensity of the proton beam, must be known. Solutions to these problems are individually discussed below.

Experimental Arrangement

The general experimental arrangement is shown in Fig. 1. The Harvard University 95-in. synchrocyclotron is a frequency-modulated machine capable of producing unpolarized protons at an energy of 156 Mev, with an energy spread of 2 Mev, and fluxes up to 5×10^{10} protons/sec. Its frequency range is from 23 to 30 Mc/sec, modulated by a rotating condenser. The nominal beam area is ≤ 7 cm^2. The permanent shield of the machine consists of from 3 to 8 ft of ordinary concrete.

The proton beam emerging from the machine passes through a vertical slit, which was introduced late in the experiments to reduce the effects of backgrounds observed in dosimetry measurements. It is then deflected by the steering magnet and focused by the quadrupole magnet, after which it continues through the beam tube and impinges onto the target. The lead bricks shown were added to further reduce backgrounds.

The target and detector-holding device is shown in the photograph on page 533. The apparatus is first centered on the proton beam by adjustment of the alignment posts at either end. Polaroid film is used as the beam-locating sensor. The target holder and detector arms are then positioned by using an alignment bar extending between the alignment posts. The detectors are rotatable through large angles about the target axis and can be varied in distance from the target up to 100 cm, depending upon which arm is used. All three arms can be used independently, permitting three simultaneous experiments to progress at three different angles and distances.

---

9. F. T. Howard, Cyclotrons and High-Energy Accelerators, ORNL-2644 (January, 1959).

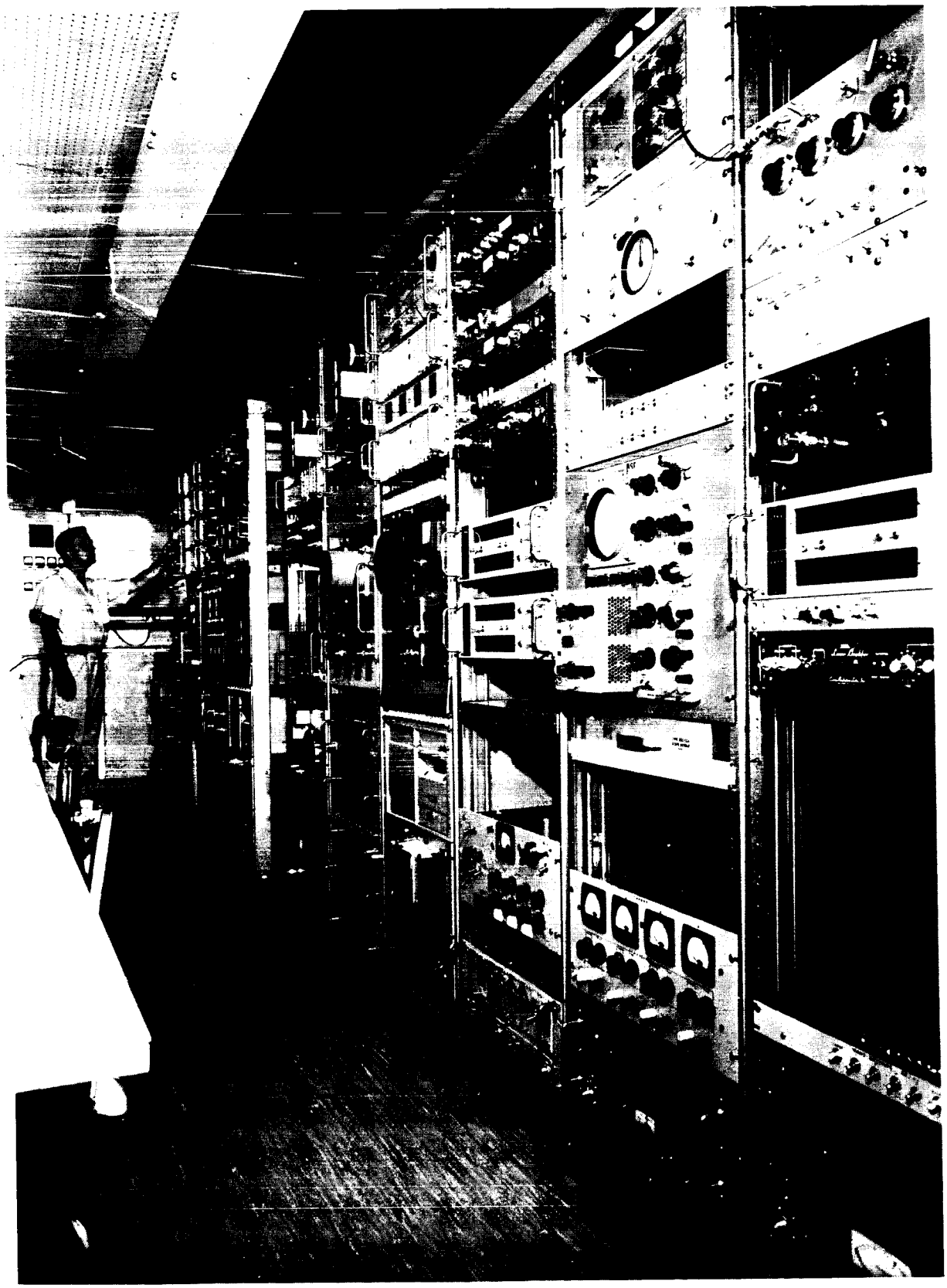

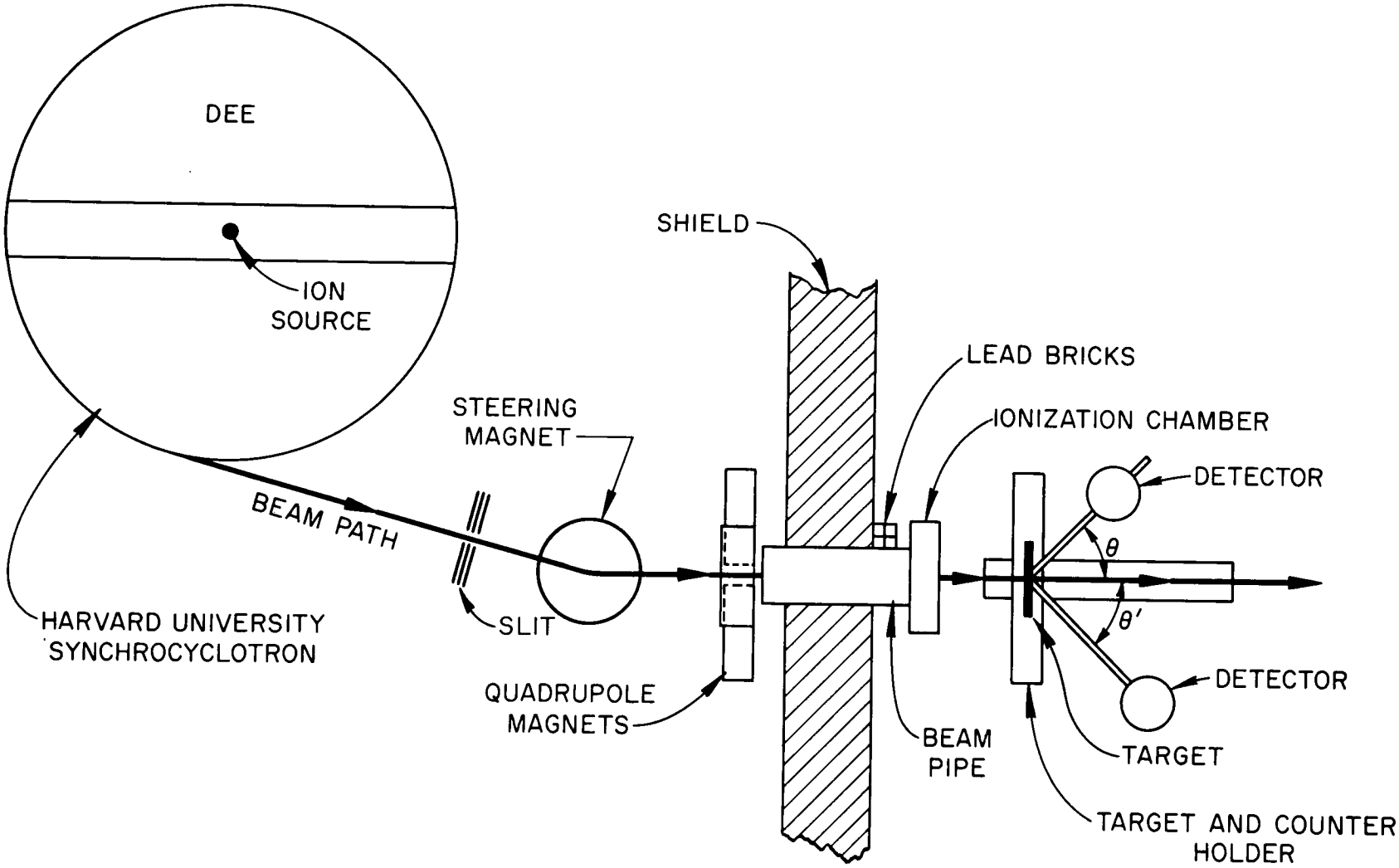

Fig. 1. Experimental Arrangement at Harvard University Synchrocyclotron.

Proton Distribution Over the Beam

Film Studies. The intensity distribution in a plane perpendicular to the beam, called the beam profile, was determined from Polaroid film exposures in the beam at several distances from the beam pipe. The shape of the image was indicative of the condition of focus. Because of the shape of the slit, the ideal cross section should have been a vertically elongated rectangle. In practice, however, the image attained was an oval, with its major axis horizontal. The contradiction is believed to be due to difficulties in adjustment of the quadrupole focusing magnet.

An attempt was made to determine a correlation between the density of Polaroid film negatives exposed in the beam and the number of protons per unit area causing the exposure. A nitrogen-filled ionization chamber at the beam pipe monitored the beam protons while the films were exposed approximately 1 m from the end of the pipe. Densitometer readings of the developed images showed a linear relationship between density and proton flux over the range from 5×10^8 to 1.6×10^{10} protons. Figure 2 shows a graph of relative beam intensity as a function of image width, but sufficient information is not available from the film to accurately determine a density-proton relationship.

Profile Telescope. The need for a more accurate device with which to analyze the distribution of protons in the beam led to the construction of a profile telescope. The profile telescope, diagrammed in Fig. 3, consists of two small cylindrical crystals, with their z axes coincident and parallel to the axis of the proton beam. The signals from the crystals are in coincidence, so that it is possible to count only those protons which pass through both crystals and to minimize the effects of noise, gamma-ray background, and neutron-induced counts present in the individual counters.

The telescope is used to scan the beam horizontally and vertically, counting the number of protons across the beam profile. Figure 4 plots the proton distribution as a function of beam width for both horizontal and vertical profiles. The difference in focus, described above, is clearly shown in these data.

Beam Monitoring

The proton beam was monitored by a Faraday cup and two helium-filled ionization chambers. The Faraday cup was the absolute beam monitor, providing the basis for calibration of the ionization chambers.

The chambers, calibrated in the region of 10^7 to 10^{10} protons per second, gave the values of 74 ± 1.3 and 79 ± 1 ion pairs per proton. The difference in performance is probably due to the variation in plate spanning, gas pressure, or gas composition between the two chambers. Figure 5 shows the performance of ion chamber #2 over a range of nominally 3.5 decades of beam intensity.

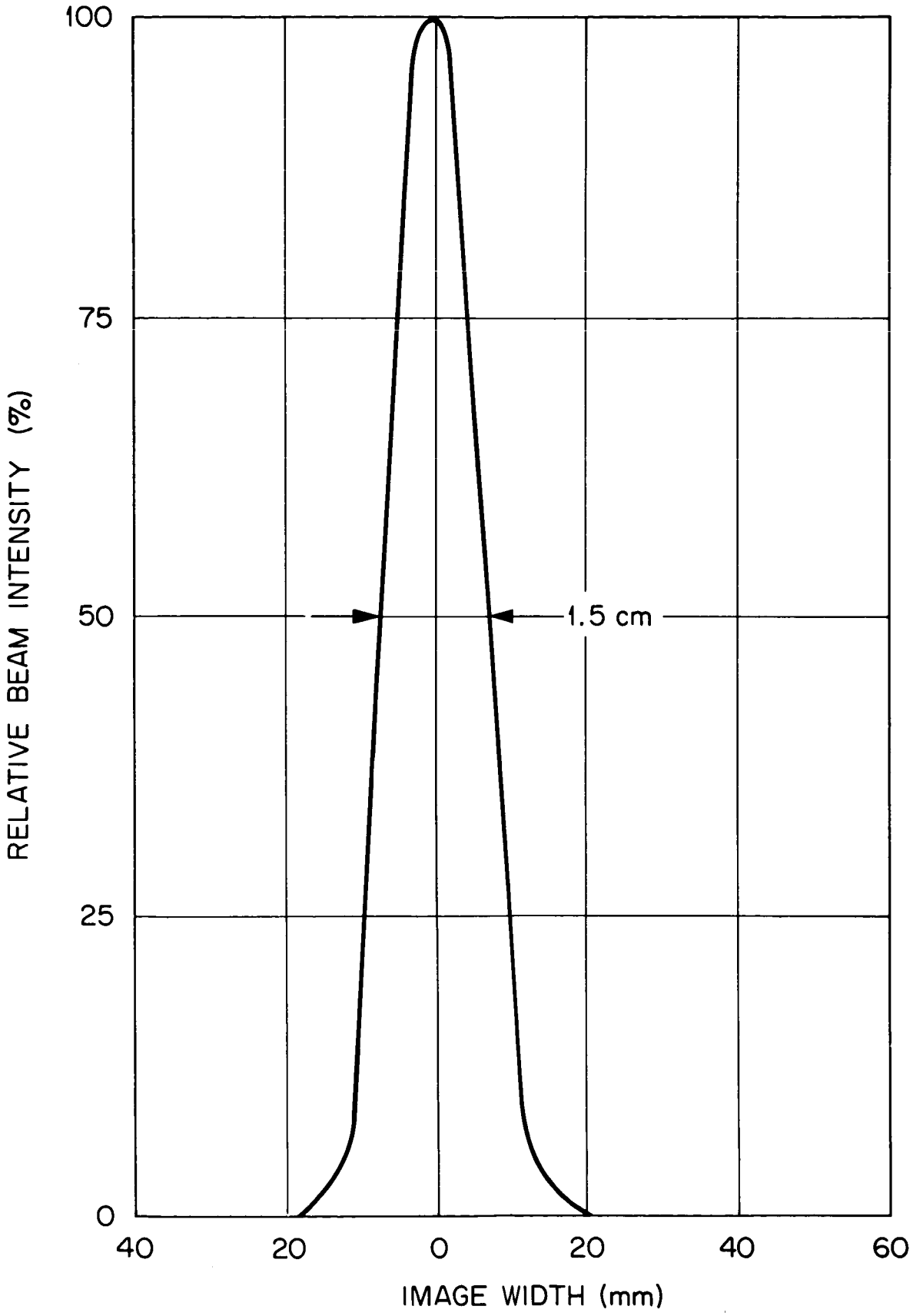

Fig. 2. Relative Beam Intensity as a Function of Image Width.

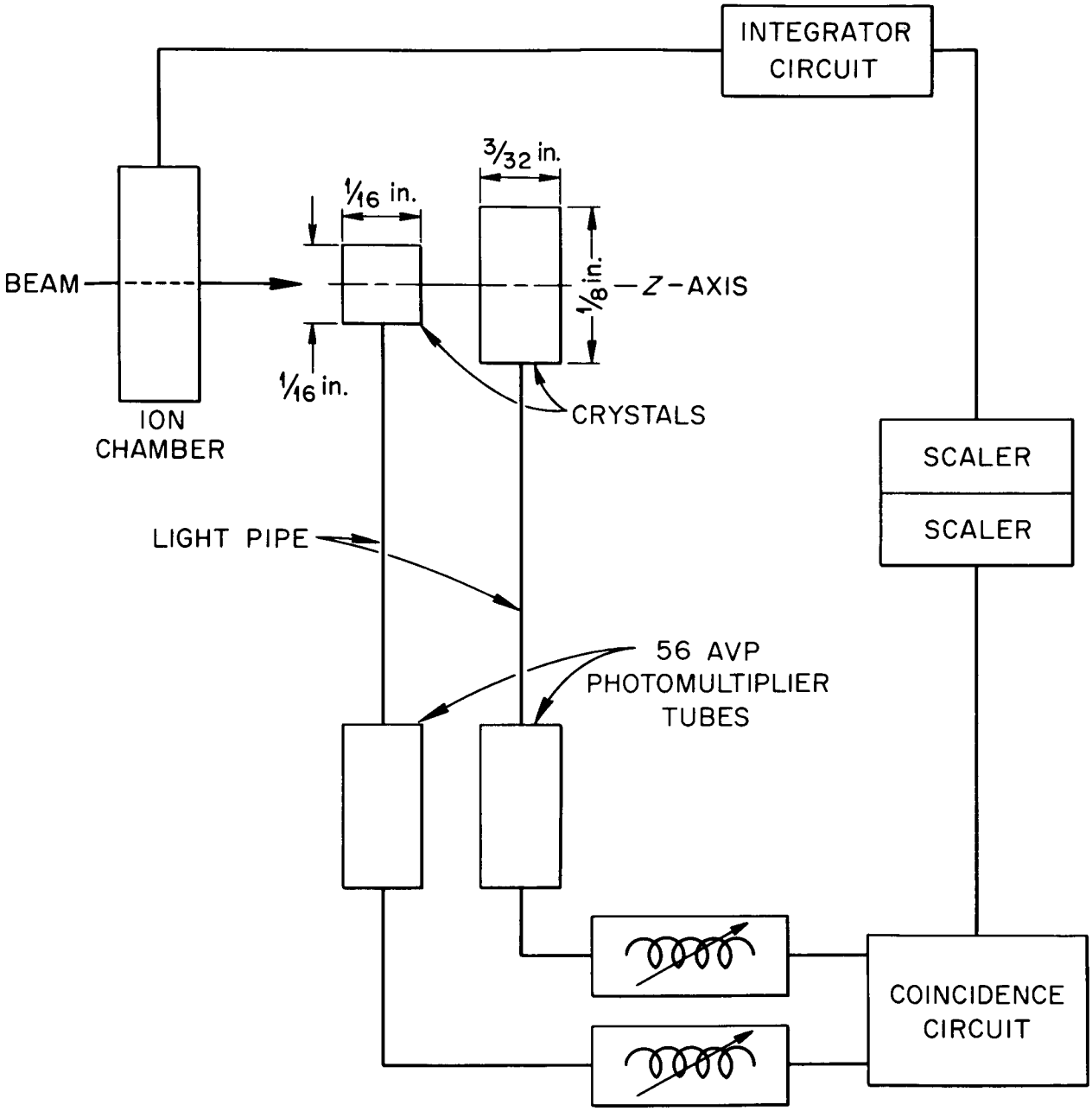

Fig. 3. Schematic of Profile Telescope.

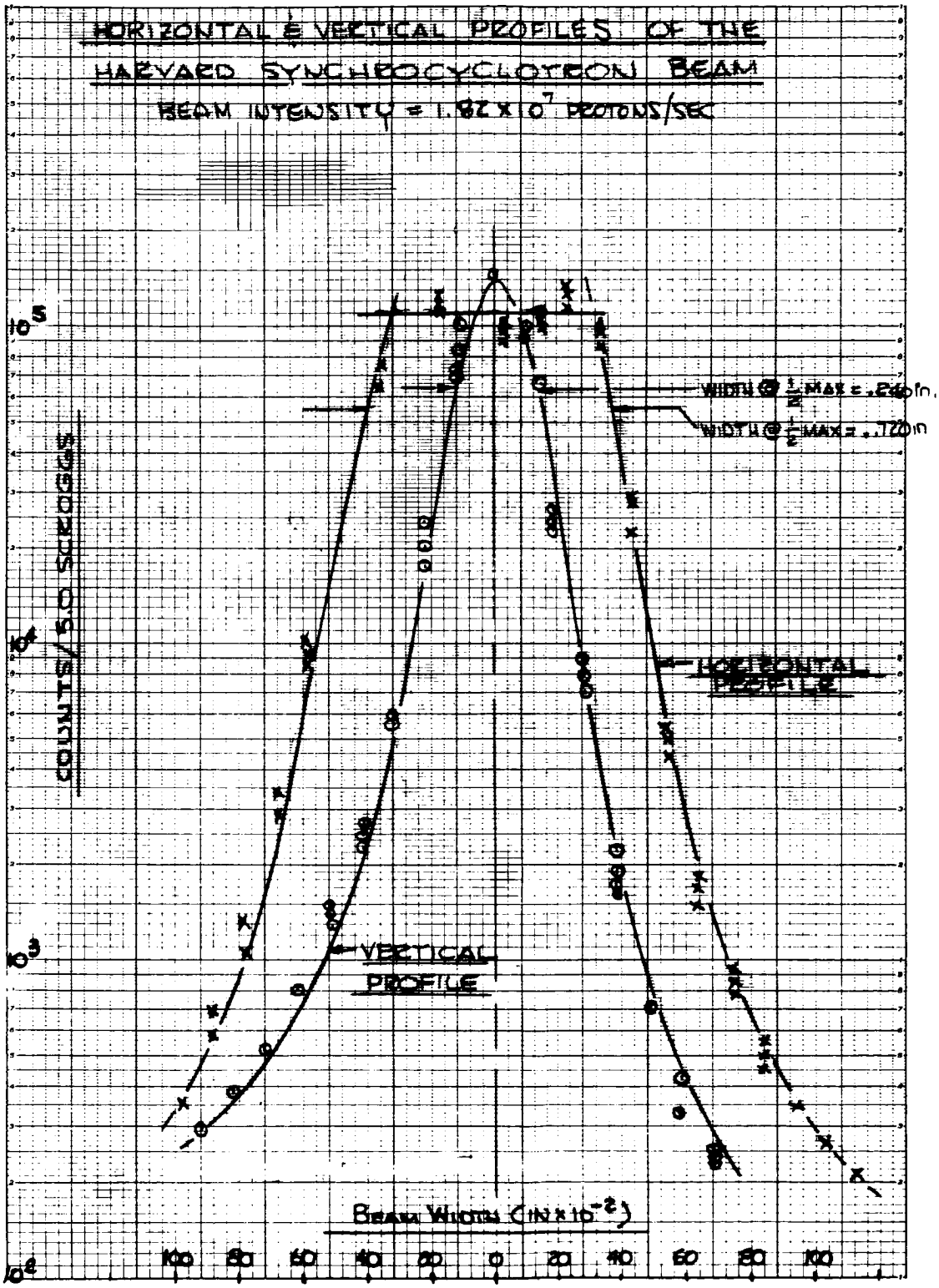

Fig. 4. Horizontal and Vertical Profiles of the Harvard University Synchrocyclotron Beam.

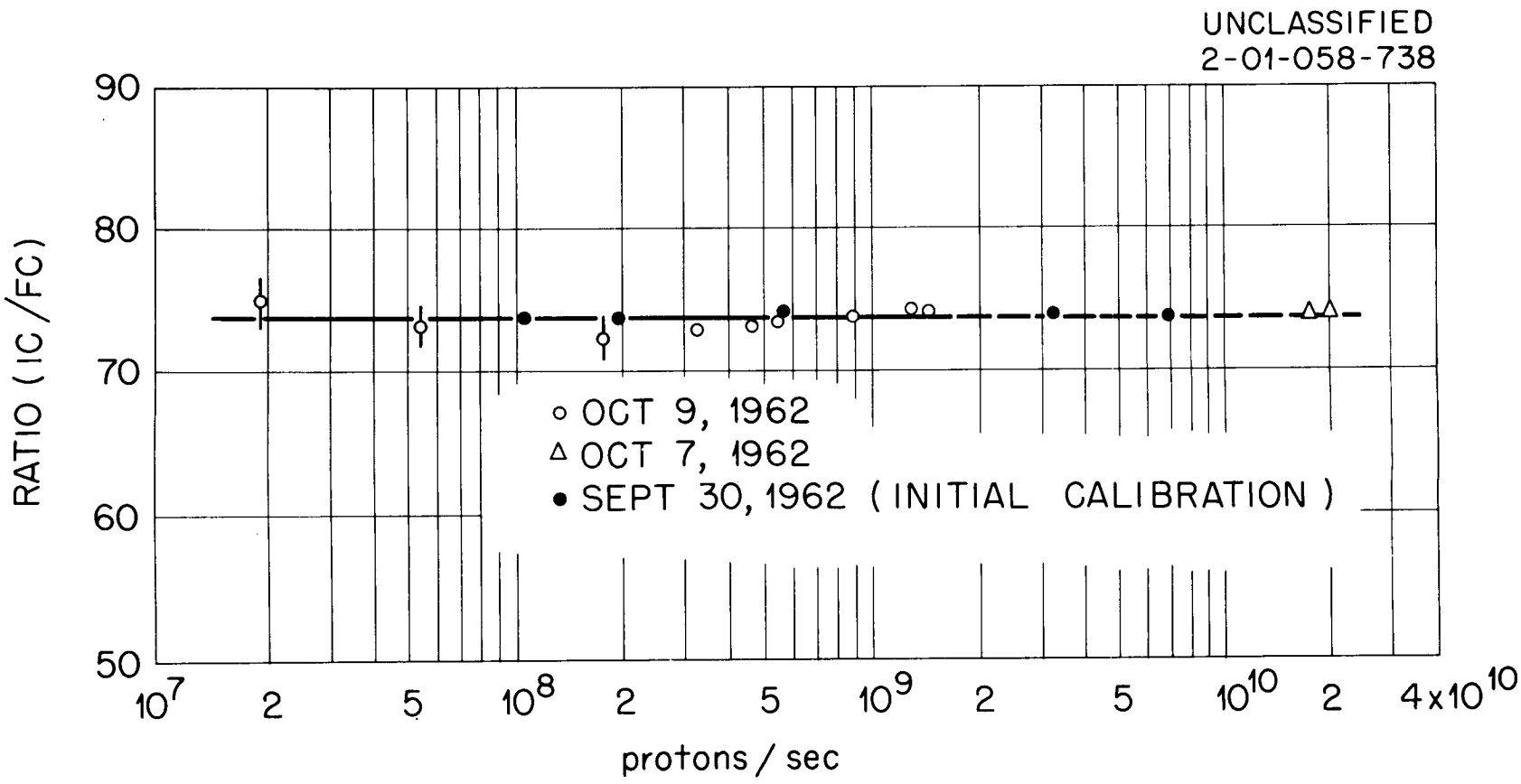

Fig. 5. Performance Curves for Ionization Chamber No. 2.

Time Dependence of the Proton Beam

Protons can be extracted from a synchrocyclotron only when the frequency of the accelerating voltage lies within narrow limits, that is, at the extraction frequency. To minimize the corrections required for random counts in experimental data, it is desirable to extract the beam for as long a period as possible (a continuous beam would be ideal). It is important, therefore, to understand how the duration of the beam is affected by the adjustment of cyclotron parameters and also to have a knowledge of the shape of the individual bursts.

Frequency modulation in the Harvard machine is accomplished with a 16-tooth rotating condenser, which rotates at about 20 rps. There is one proton burst per tooth per revolution, or 320 bursts/sec. The 320-burst/sec modulation is defined as the macrostructure. There is an additional modulation which takes place at the accelerating voltage frequency due to bunching of protons in phase with the accelerating field.

Because of the limited time available in the preliminary studies, the examination of the macroburst was restricted to a feasibility study.

A study of the structure was made for one synchrocyclotron setting. The circuit employed is shown in Fig. 6. The detector, an organic scintillator, was positioned so as to obtain a count rate of somewhat less than one count per macroburst. A marker pulse was obtained on the downswing of the frequency modulation cycle just before proton extraction. The elapsed time between the marker pulse and a proton signal from the scintillator was then analyzed and stored. Since there is a variation from tooth to tooth of the condenser (due to fabrication differences, eccentric alignment, wobble in the mechanical support, etc.), a gate was used which permitted analysis of only the pulse from each sixteenth tooth. The tooth with the widest frequency swing was arbitrarily designated tooth No. 7. As shown in Fig. 6, it was possible to implement all of the necessary gating by using a dual-sweep oscilloscope. The main sweep was set for 500 μsec; the delayed sweep was synchronized to the condenser rotation. Figure 7 shows intensity versus time profiles for teeth 1 and 9. It is evident that the burst shape varies with individual teeth.

A quicker and less detailed determination of the "duty factor," d, for the cyclotron can be obtained from a measurement of the chance coincidence rate, N_{BC}, which is given by:

$$N_{BC} = \left[\frac{(B-B^S)(C-C^S)}{d} + B^S C^S \right] \tau_{BC}$$

where:

$B = B^S + B^P d$ = average count rate in channel B;
B^S = steady count rate when beam is off;
B^P = peak count rate when beam is on; and
τ_{BC} = resolving time of coincidence circuit.

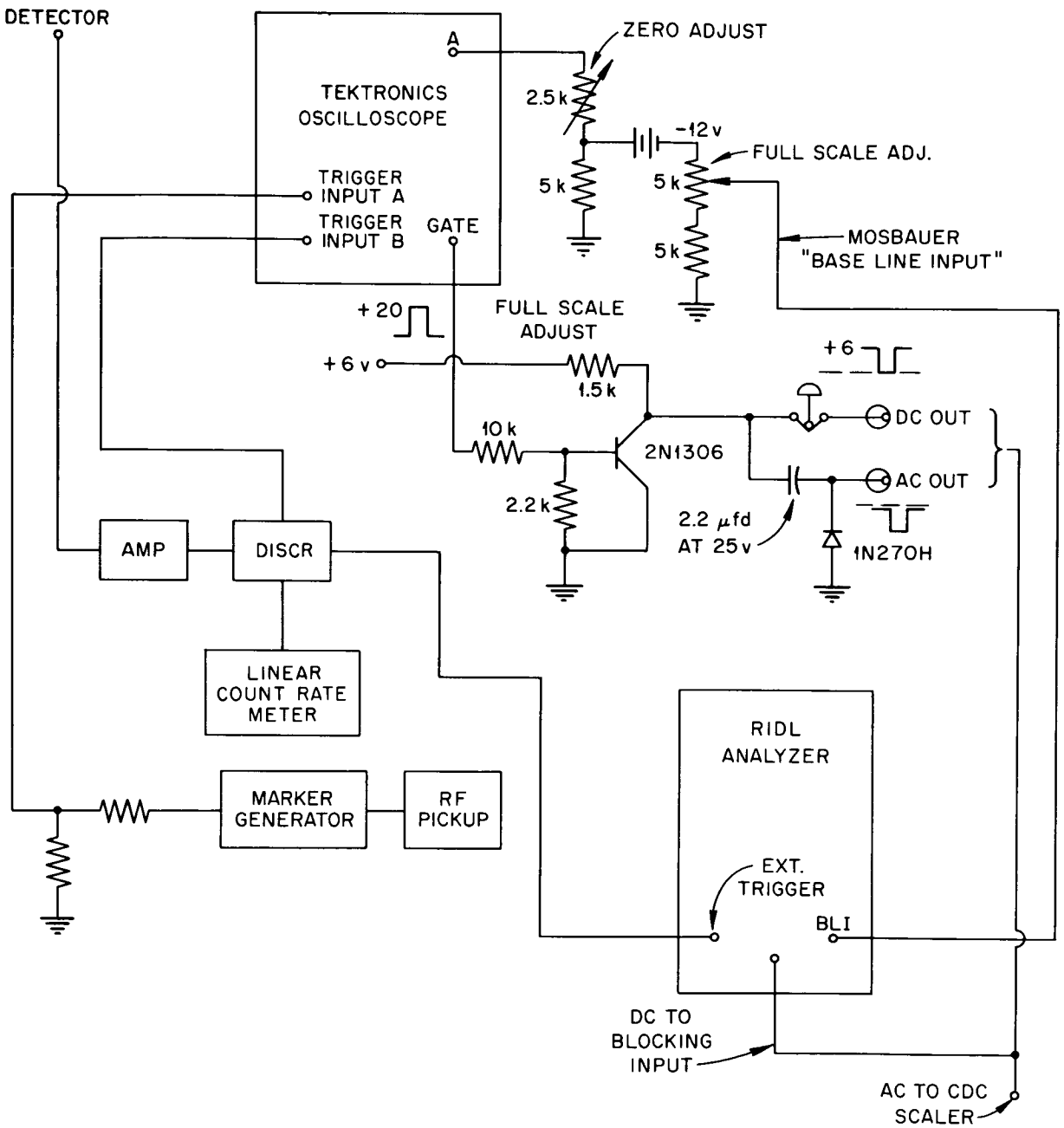

Fig. 6. Circuit Used in Macroburst Studies.

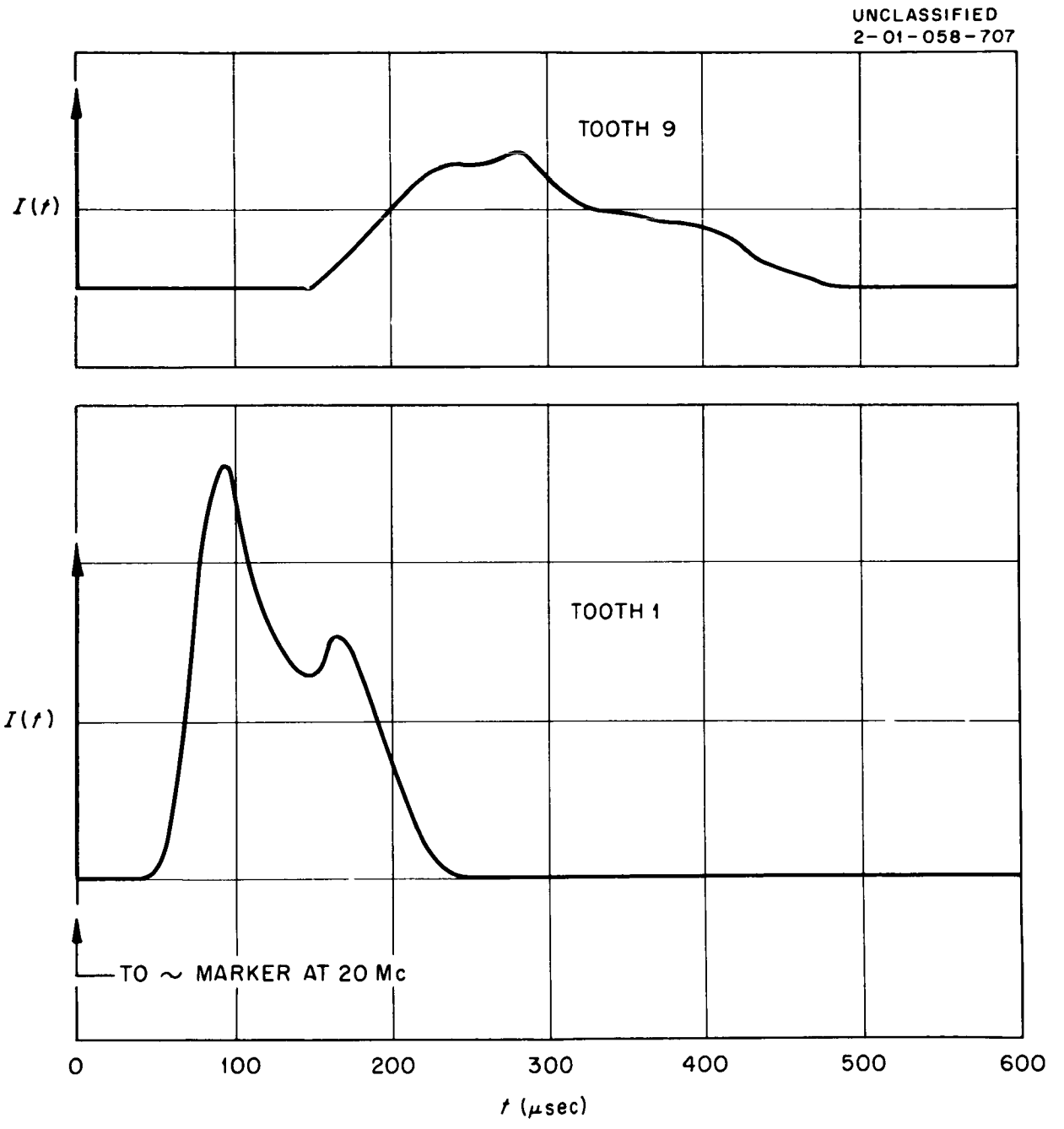

Fig. 7. Intensity as a Function of Time for Teeth 1 and 9.

Measurements using this method are routinely made during the gamma-ray spectral measurements at Harvard using $\tau_{BC} = 3.7 \times 10^{-7}$ sec. However, the NaI(Tl) crystals used give rise to a considerable B^S term due to activation and the neutron flight time. The effect of the B^S term is largely eliminated by using a time gate open only during a cyclotron pulse, but correction for the remaining contribution is difficult. In practice, B^S and C^S are taken as equal to zero and the duty factor determined is an upper limit. Typical values range from 3 to 5%.

A closer analysis of the macroburst shows that it is composed of a series of finer bursts, the microstructure. The fine structure of the beam was analyzed by observing the pulses from an organic scintillator with an oscilloscope. It was also determined by using two detectors placed equal distances from the cyclotron, one in the left corner of the beam and one in the right. Coincidences would be random and at a uniform rate in time were it not for the microstructure. A time calibration against an Ad-Yu delay line gave about 0.755 ns/ch with some nonlinearity. The time interval between the first two peaks in Fig. 8 measures 43.2 ns and between the second pair 43.4 ns, corresponding to about 23.2 mc. The time width of the bursts is shown to average 6.7 ns, and 90% of the protons in the peaks appear to be within a time range of 10 ns. Since both start and stop signals are chosen at random from the microbursts, these time widths would be about 70% as wide in "cyclotron time." Instrument resolving time does not contribute to the width.

The data were very greatly distorted in the valley regions by a now-understood pulse pile-up problem in the time-to-pulse-height converter. Depending on the assumed gross duty factor, 30-40% of the pulses were misplaced in time, enough to explain the valley shown. Anticipated random coincidences would fall about a decade lower. Photographs of a few hundred pulses failed to show any pulses appreciably removed in time from the microbursts. Another effect of the pile-up smearing is to broaden the times listed in the paragraph above.

The first peak shown is higher and perhaps narrower than the others, presumably because it includes a few prompt coincidences from scattered protons, etc. The second and third peaks have the same area, and the apparent difference in width is believed caused by statistical fluctuation.

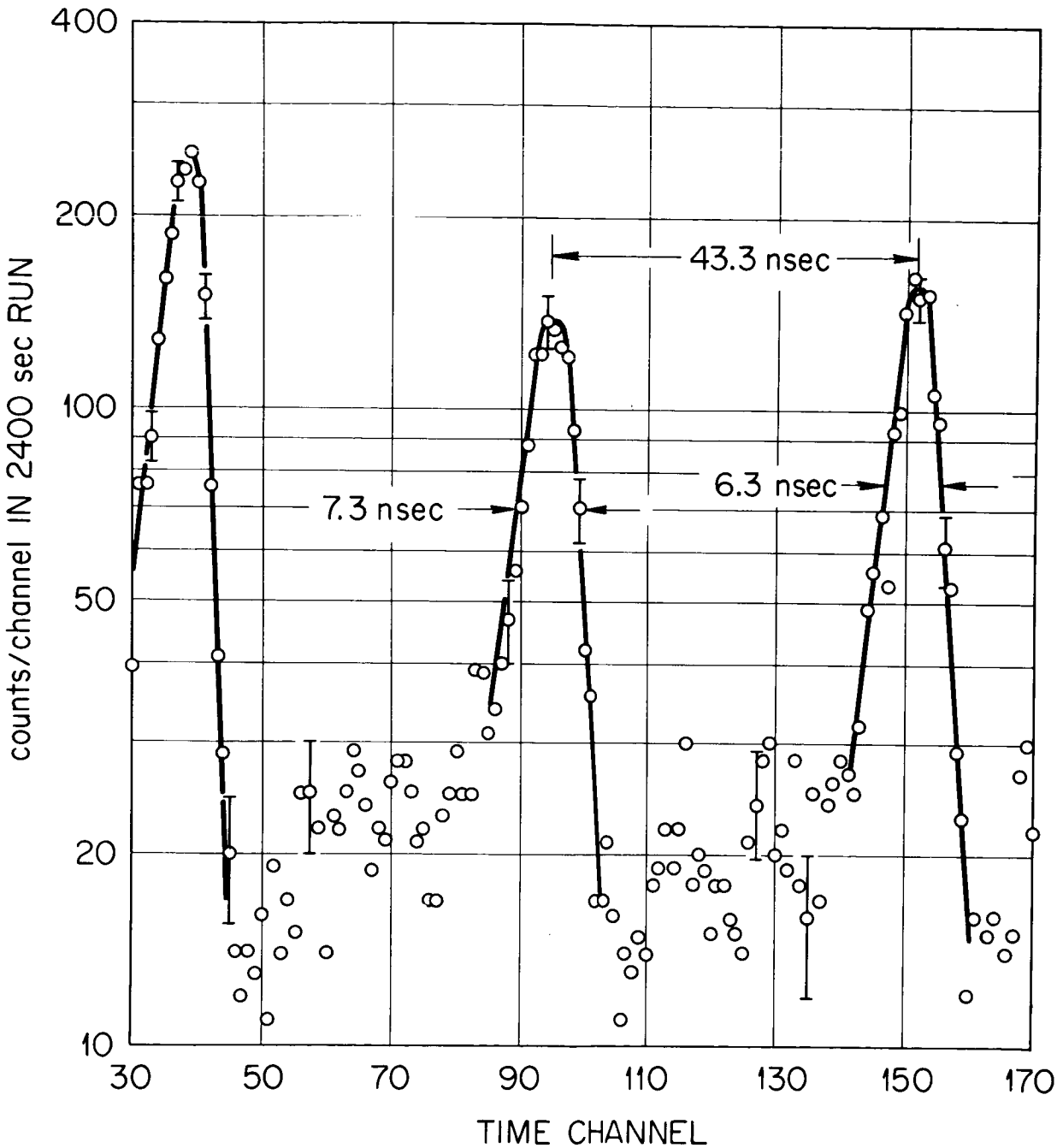

Fig. 8. Beam Microstructure Study Using A and B Counters Intercepting Different Sections of the Beam.

II. Proton-Recoil Telescopes for Spectral Measurements of Neutrons and Protons with Energies > 10 Mev

A brief description of the proton-recoil telescopes proposed for measurements of the energy spectra of neutrons with energies from ~8 Mev to several hundred Mev was given previously,[10] and the efficiency for neutron detection was calculated for neutron energies between 8 and 50 Mev. These instruments have now been constructed and tested in the preliminary experiments at Harvard (see p. 4) on the spectra of neutrons arising from the bombardment of a thick copper slab by 156-Mev protons. The results of these tests and the suggested constructional changes are discussed below.

Spectral Measurements of 8- to 50-Mev Neutrons

The telescope used for the ~8 to 50-Mev neutron range consists of a polyethylene radiator followed by two proportional counters and a NaI crystal. All three counters are placed in coincidence, and a recoil proton originating from the radiator produces pulses in coincidence which gate on a multichannel pulse-height analyzer that records the total energy deposited in the NaI crystal (see Fig. 9). A CsI crystal in front of the radiator is placed in anticoincidence with the other three counters and eliminates counts from protons present in the incident flux. Backgrounds are measured by replacing the polyethylene radiator with a carbon radiator containing the same amount of carbon as the polyethylene.

In the preliminary runs, adequate neutron counting rates were obtained and the single rates in the individual counters were reasonable. However, more than 60% of the triple coincidences representing neutron counts were background. On closer inspection it appeared that these counts were coming from high-energy (n,p) events in the structure of the proportional counters and surrounding material. The bodies of the proportional counters are now being rebuilt to reduce the mass of the counters and hopefully the background.

Spectral Measurements of 50- to 150-Mev Neutrons

The recoil telescope for the 50- to 150-Mev neutron range consists of a polyethylene radiator followed by two organic scintillators and a NaI crystal (see Fig. 10). All three crystals are placed in coincidence and a coincidence pulse from these counters gates on the multichannel analyzer to analyze the pulse from the NaI crystal. An anticoincidence crystal is placed in front of the radiator to eliminate counts from protons in the incident flux.

The NaI crystal is thin (1.5 g/cm^2) compared to the range of a 50-Mev proton and hence the dE/dx of the recoil proton is measured rather than its total energy.[11] The energy deposited in the crystal by the proton is calculated from the pulse height recorded by the multichannel analyzer. For

---

10. W. A. Gibson, W. R. Burrus, and T. A. Love, Neutron Phys. Div. Ann. Prog. Rep. Sept. 1, 1961, ORNL-3193, p. 325.

11. G. L. Guernsey et al., Rev. Sci. Instr. 23, 476 (1952).

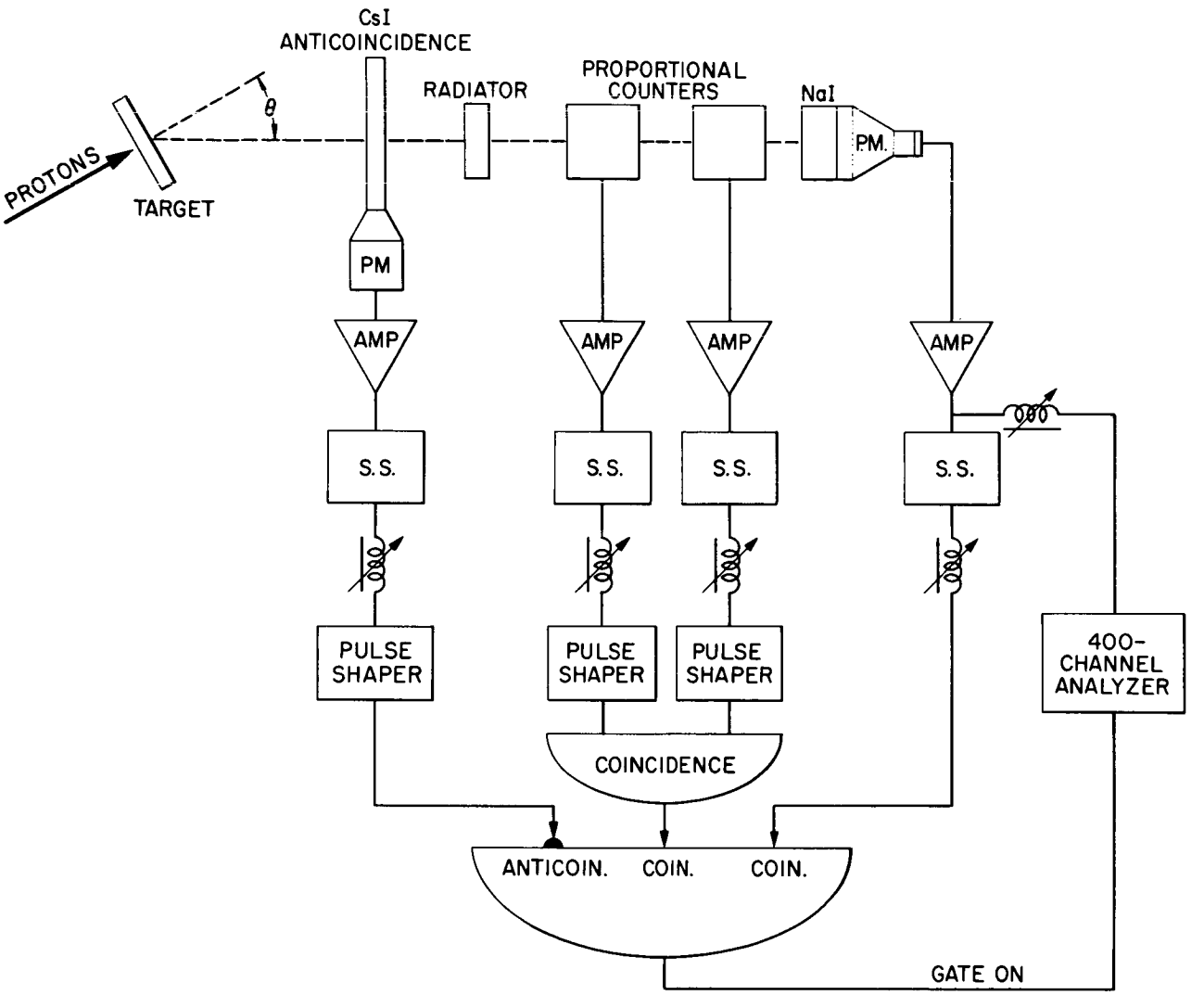

Fig. 9. Block Diagram of Proton-Recoil Telescope Proposed for Measurements of Neutron Spectra Over 8- to 50-Mev Range.

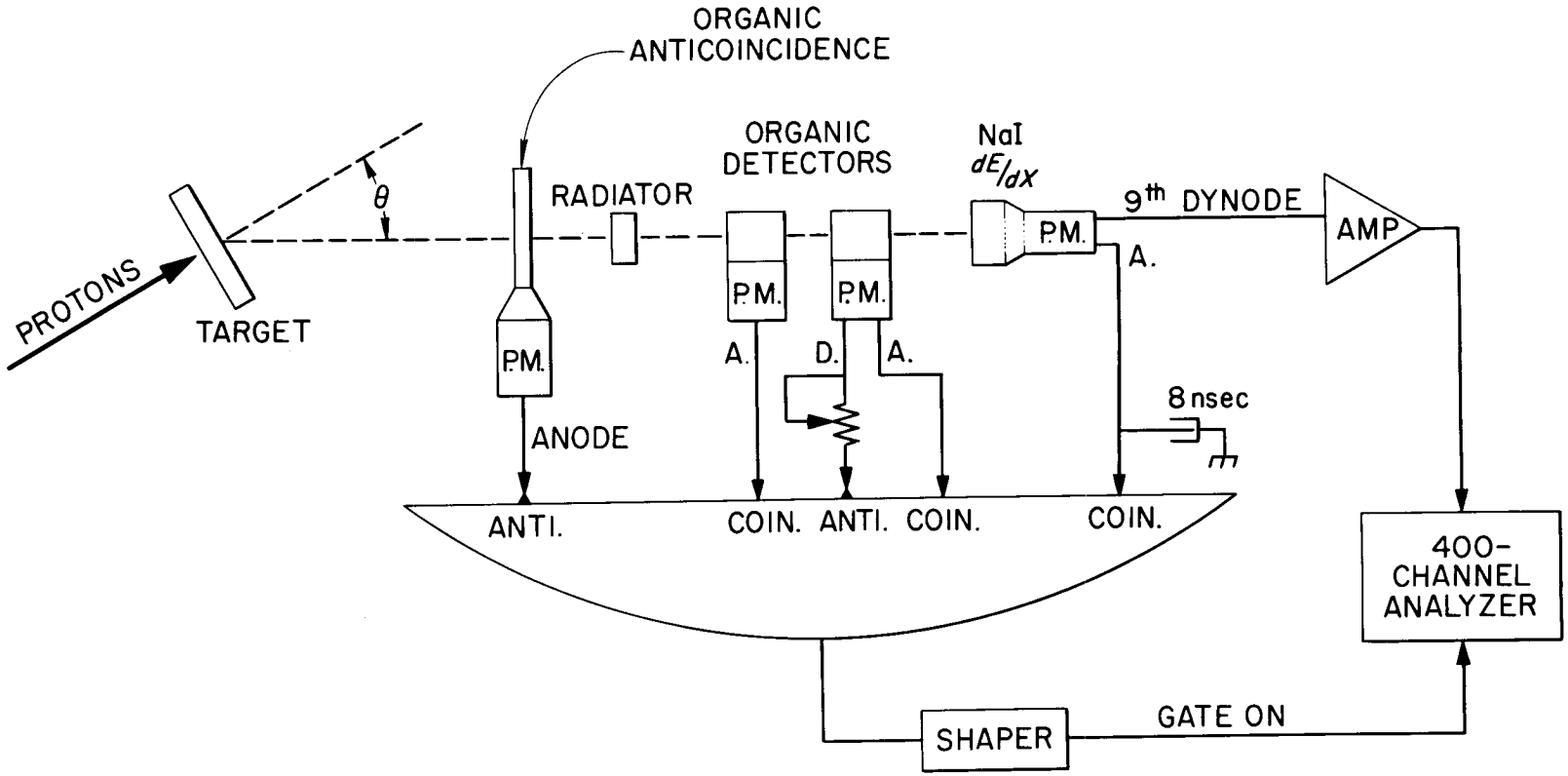

Fig. 10. Block Diagram of Proton-Recoil Telescope Proposed for Measurement of Neutron Spectra Over 50- to 150-Mev Range.

protons which penetrate the NaI crystal, the energy deposited is a direct measure of the dE/dx of the recoil proton and is a unique function of energy for proton energies below the minimum energy for ionization; hence the total energy of the proton is determined from the curves relating dE/dx to energy.

The two major disadvantages of an energy determination by a dE/dx measurement are:

1. For the higher energies the dE/dx changes only slowly with energy and therefore the error in determining the total energy of the proton is much larger than the error in measuring dE/dx.

2. Statistical fluctuations in the energy lost by protons as they pass through the thin NaI crystal (known as the Landau effect[12]) introduce a spread in the pulse-height spectrum obtained for a monoenergetic beam.

The width of the resolution function has been calculated for the crystal used on this telescope and the full widths at half maximum for 50- and 156-Mev protons are 6% and 18%, respectively. The resolution obtained experimentally on the 156-Mev beam supports the calculation.

The advantages of using a thin crystal are that the probability of nuclear interaction is reduced to a negligible value and the geometric effects introduced by a finite thickness crystal are small.

A NaI crystal was chosen rather than an organic scintillator for the dE/dx measurement because of the greater light output of the crystal and because its scintillation efficiency increases with increasing dE/dx below 10 Mev g^{-1} cm^{-2}.[13] Since the dE/dx decreases with increasing proton energy, the two effects add to accentuate the inverse relation between the light output of the crystal and the energy of the proton.

Figure 11 is a plot of the efficiency of the recoil telescope as a function of energy. The solid line is the efficiency for a continuously increasing radiator thickness and a 10% geometric energy resolution, and the dotted lines show the efficiency for radiators of constant thicknesses. The intrinsic resolution of the telescope is approximately 15%. That is, the radiators are chosen so that the lowest energy proton being analyzed loses 10% of its energy in passing through the thickness of the radiator, and the geometries are chosen so that 10% uncertainty in the energy is introduced by variations in the scattering angle of the recoil proton.

Figure 12 is a plot of pulse height as a function of the energy of protons incident upon the NaI crystal. It is seen that a particular energy deposition in the crystal does not correspond to a unique incident proton energy, since a low-energy proton that just stops in the crystal will result in the same size pulse as that produced by a higher energy proton

---

12. Bruno Rossi, High Energy Particles, Prentice Hall, New York (1952), p. 29.

13. R. B. Murray and A. Meyer, Phys. Rev. 122, 815 (1961).

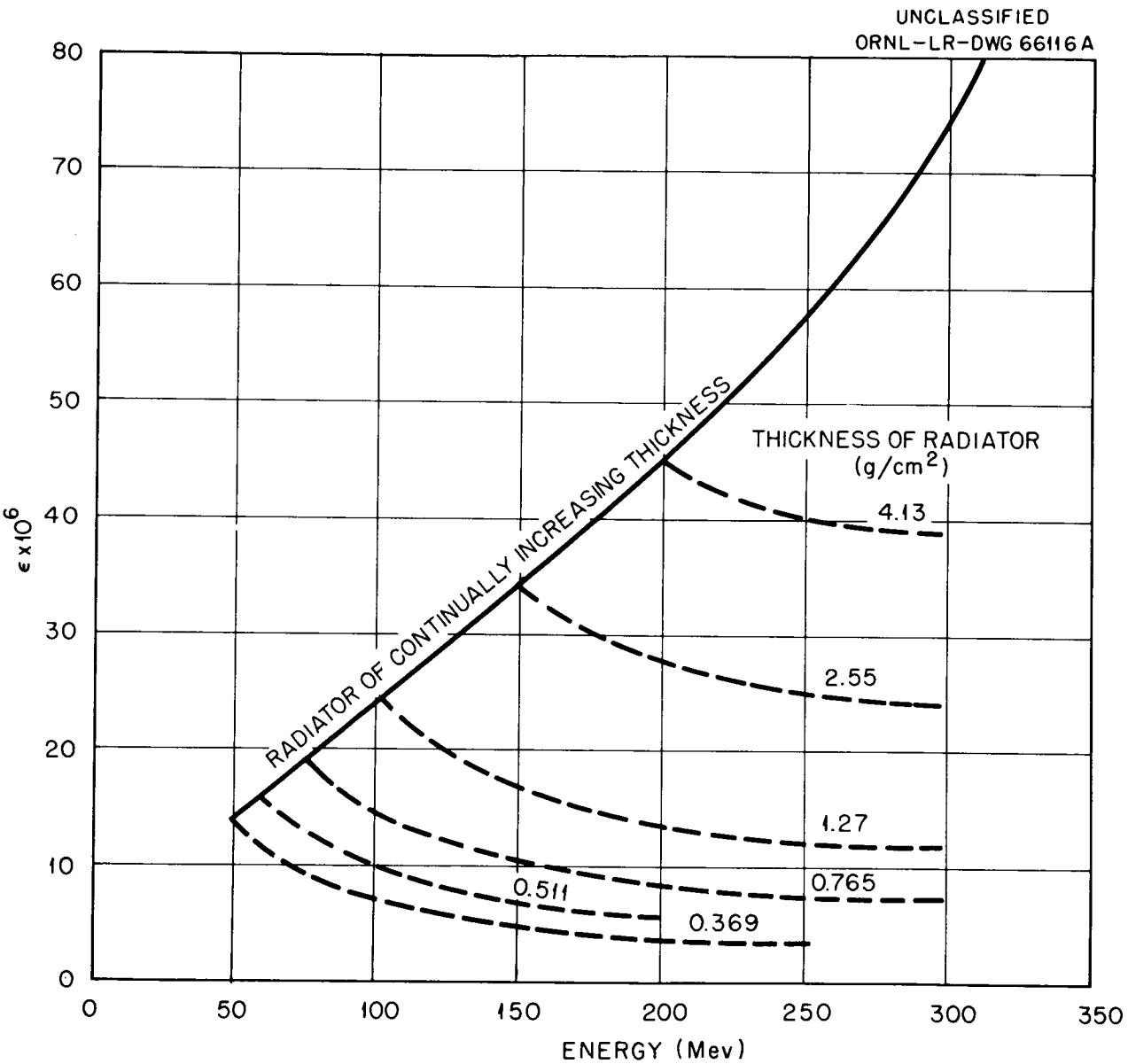

Fig. 11. Calculated Efficiency of High-Energy Proton-Recoil Telescope as a Function of Energy.

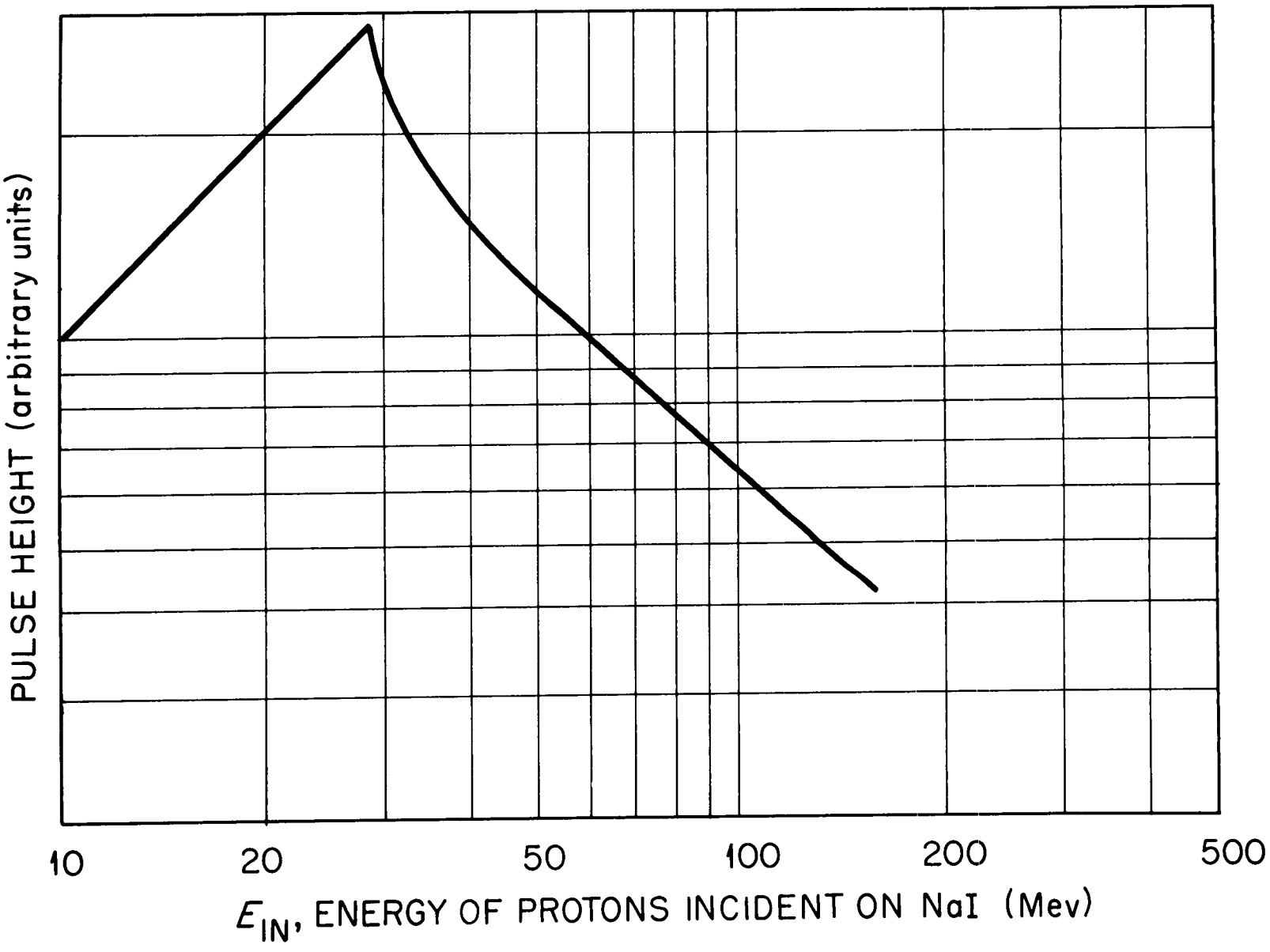

Fig. 12. Pulse Height, as a Function of Incident Proton Energy, for a 0.161-in.-thick NaI Crystal in the Telescope Shown in Fig. 2.

passing through the crystal. The straight-line portion of the graph at low energies results from those protons that stop in the crystal.

To overcome this ambiguity, it is planned to place an upper level discriminator on the organic scintillator preceding the NaI crystal in order to identify the low-energy protons which will stop in the last crystal (the low-energy protons will have a larger dE/dx and therefore deposit more energy in the crystal preceding the NaI crystal than will the higher energy protons).

Figure 13 shows the pulse-height spectrum from the dE/dx crystal with both the background and an estimated contribution from low-energy neutrons subtracted. Figure 14 is a graph of the neutron spectrum obtained by calculating the total energy of the recoil protons from the pulse-height spectrum of Fig. 13. Because of the uncertainty in estimating the low-energy neutron contribution and the large errors in the data, this curve is only indicative of the expected shape of the spectrum.

Since fast decay times are characteristic of organic scintillators, high counting rates were obtained and the operation of the telescope, except for the ambiguity introduced by the low-energy neutrons, was satisfactory. The background was about 10% of the foreground.

Spectral Measurements of Protons

The telescopes described will also be used for measurements of proton spectra, in which case the hydrogenous radiator and the anticoincidence crystal preceding the radiator will be removed and the telescopes will look directly at the target.

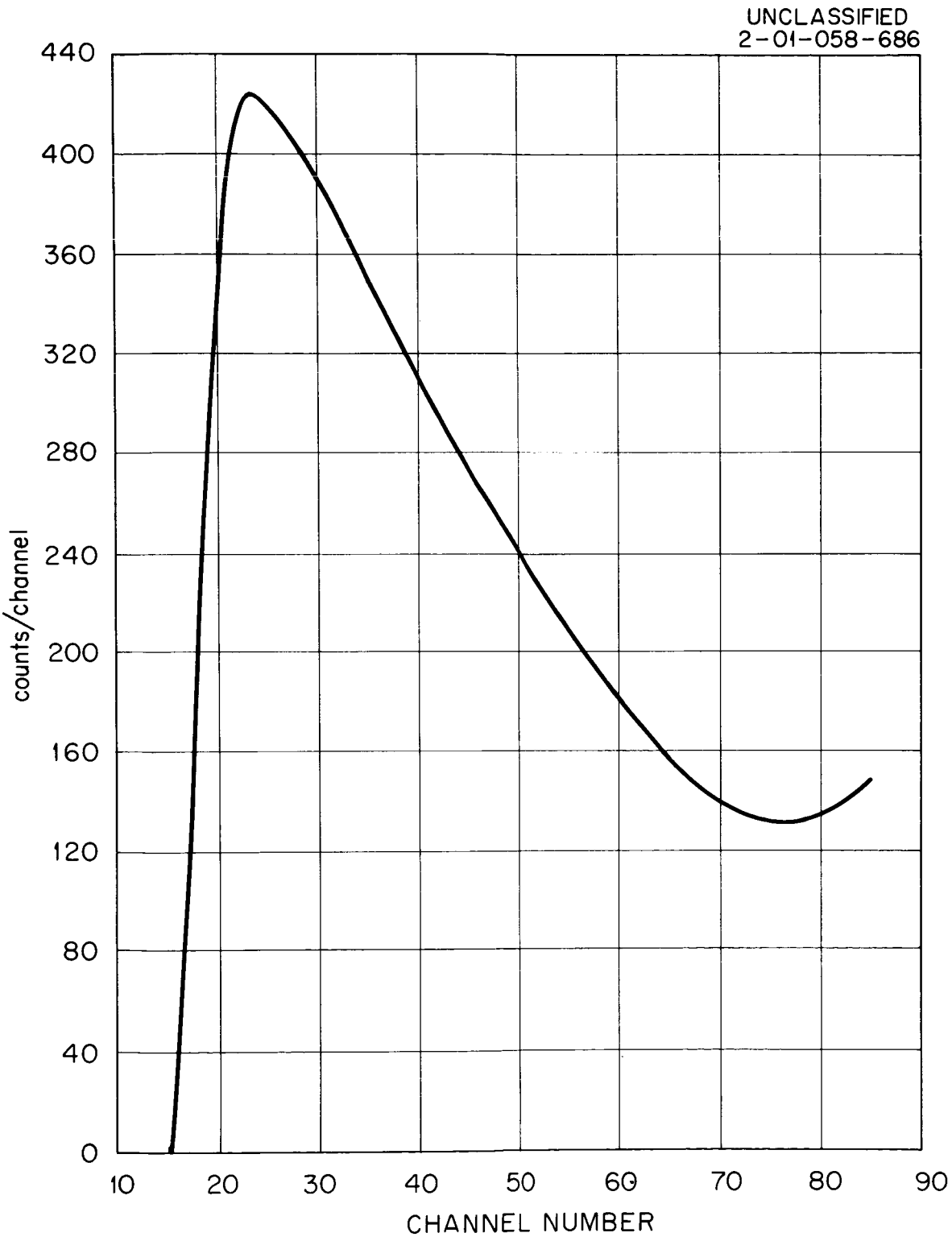

Fig. 13. Pulse-Height Distribution of Neutrons from 31.8-g/cm^2 Copper Target Bombarded by 156-Mev Protons. Curve corrected for background and an estimated correction made for low-energy components.

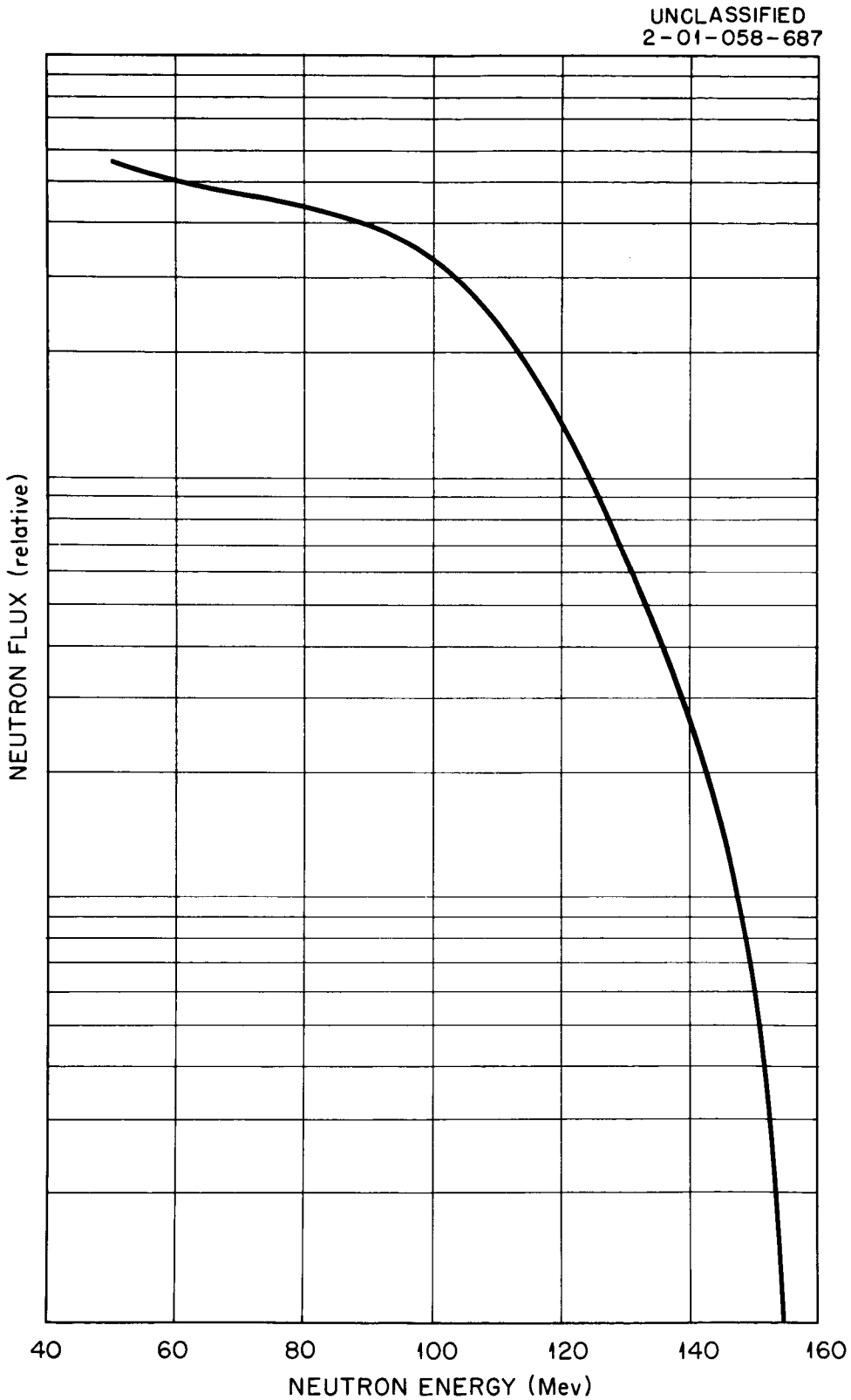

Fig. 14. Spectrum of Neutrons Emitted Forwardly from a 31.8-g/cm^2 Copper Target Bombarded by 156-Mev Protons. Computed from data of Fig. 5.

III. Flight-Time Spectroscopy for Neutron and Proton Yields from Nuclei Bombarded by Protons

The deduction of energies of fast neutrons from measurements of their velocities is a common procedure for the energy region below 20 Mev, even for neutrons resulting from neutron-induced reactions. This "flight-time" method has also been used for very high energies, an example being its recent application at Harwell for neutrons produced in reactions of 143-Mev protons incident on nuclei.[14] Therefore, it was natural to consider flight-time spectroscopy for measuring thick target yields and differential cross sections for interactions of 50- to 700-Mev protons with nuclei.

To measure the velocity of a secondary neutron in the Mev range, the time required for it to travel from the target to a fast-neutron detector, usually a plastic or liquid scintillator, is measured. Thus the pulse from the phototube attached to the scintillator determines one end of the flight-time interval. Either of two systems can be employed for timing the other end of the interval:

1. Particles in the beam can be bunched to an extent consistent with required resolution, and the time that the entire group is incident upon the target can be determined by methods depending on the experiment in question. A neutron chopper is a simple example of this system.

2. The time of each individual incident particle can be determined, as in the associated-particle method in which a timing pulse representing an individual incident fast neutron is derived from a charged particle produced in the reaction with the neutron. For instance, the associated alpha particles may produce timing pulses for fast neutrons from the $D(T,\alpha)n$ reaction.

The first system was used at Harwell[14] by utilizing a natural phase bunch in the cyclotron internal beam once during each cycle of the modulation frequency. At least at the lower end of the range of interesting incident-proton energies, a like system could be used on an external beam provided that a special electrostatic deflection system could be employed to eliminate counts from most of the microstructure bursts. Since the time resolution of the proton burst probably could not be shorter than 4 nsec, a large target room would be required for such a method. Although with this system electronic timing problems would be simpler and there would be less stringent requirements on the detector and target thicknesses, it seems to be out of the question for the experiments required in this program since they must be conducted at other laboratories. Thus the second system has been adopted, and the time that each incident proton reaches the target is deduced from a pulse produced in a detector placed in the beam. This system leads to considerable difficulties with resolution and counting rates, but it is flexible enough that any available external proton beam which can be adjusted to the correct intensity can be used.

---

14. P. H. Bowen et al., Nuclear Phys. 30, 475 (1962).

Experimental Method

Figure 15 shows a plan schematic of the detector apparatus required for neutron-producing reactions, along with a simplified block diagram of the associated electronic apparatus. Detector A consists of a thin (1- or 2-mm) plastic scintillator placed a convenient distance from the target. Since the protons have essentially uniform velocity, the time the proton reaches the target can be inferred from the timing of the light flash in this scintillator. The 5-in.-diam detector B, generally 1-in. thick, is for detection of neutrons originating in the target. At energies below 10 Mev, detection is primarily by means of the recoil protons from n-p scattering, while above 20 Mev various charged-particle reactions with the carbon of the scintillator surely dominate. Detector C, which takes the form of a thin cup surrounding all but one side of detector B, is used in coincidence with the latter to label the detection of charged particles. Coincidences between detectors B and C cause the corresponding time measurement to be stored separately.

The simplified electronic diagram indicates several of the most important features required:

1. The strength of the incident beam is required to put the experiment on an absolute basis and is determined by actually counting the individual protons detected. The time between the pulse from B and the delayed pulse from A is converted to a pulse amplitude and fed into a standard multichannel pulse-height analyzer for storage.

2. The time-to-pulse-height converters deemed appropriate for this experiment are of the general variety which measure the time between "start" and "stop" signals. Since the output of this converter is 1 μsec or so in length, the number of "start" signals must be as small as possible. For this reason the time scale is reversed by delaying the pulse from A.

3. At the beam strength corresponding to a reasonable counting rate, there will be an important (~10%) fraction of cases in which B-A time intervals should not be recorded because two or more protons reach the target so closely spaced in time that one cannot be sure which proton produced the observed pulse in B. Control of such cases is a function of the supervisory circuitry.

4. Additional supervisory circuitry is required to set the lower energy threshold of detector B and to sort the true neutron-produced pulses from those which cause coincidences between detectors B and C. The B counting threshold is very important because it determines the neutron efficiency.

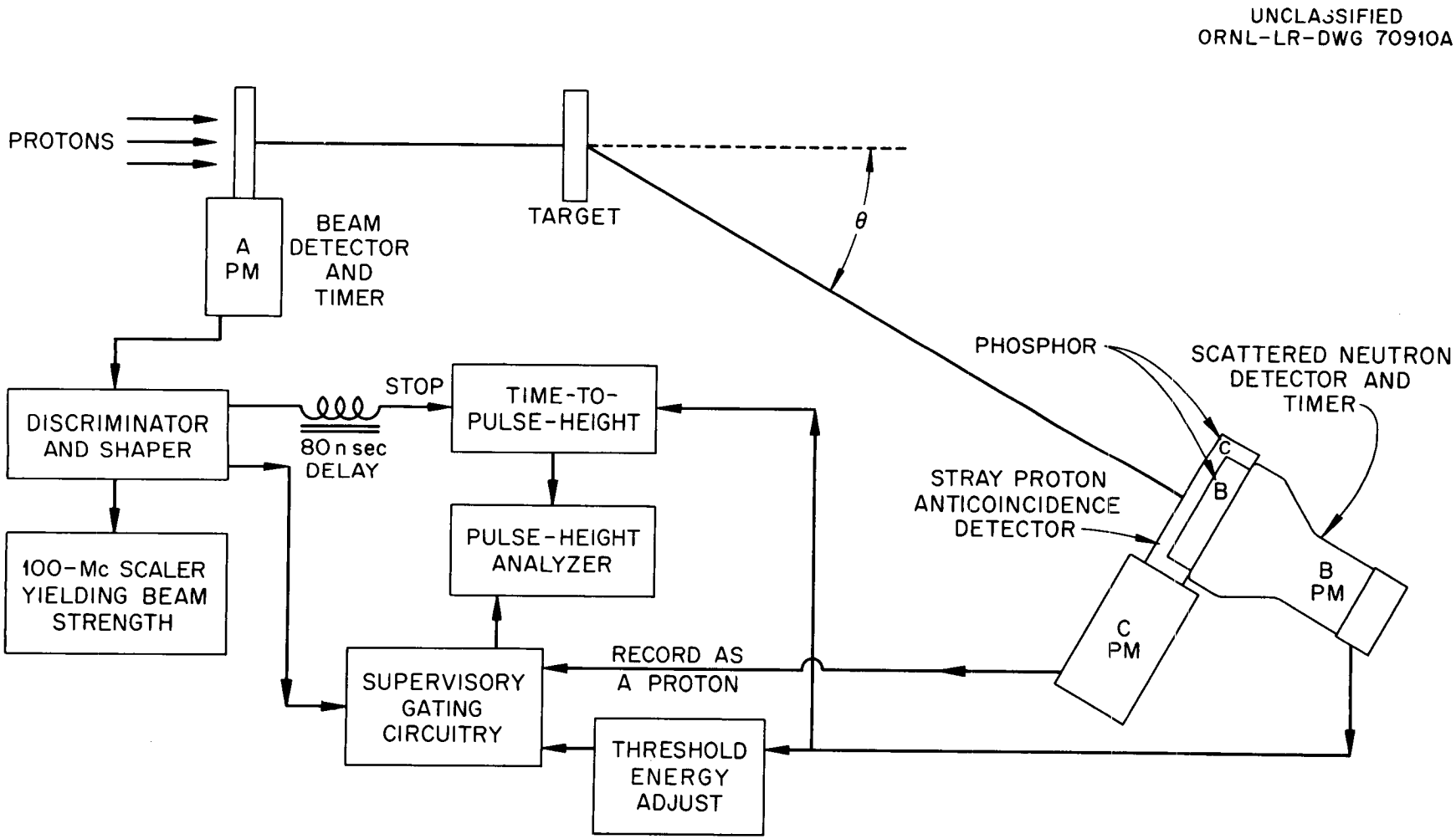

Fig. 15. Detector Plan View and Simplified Block Diagram for Neutron Time-of-Flight Spectrometer.

Two main types of background are likely to be encountered, assuming that detector A responds only to protons from the beam. Gamma rays that do not come from prompt reactions in the target can be detected in B. These lead to a flat background of time-interval measurements. The other important background arises from neutrons generated by the beam. The presence of the beam microstructure synchronizes this background to a certain extent with the protons observed in detector A, and so this background must be expected to be time dependent. The component that results indirectly from reactions in the target is virtually impossible to measure, but that from the floor and perhaps the cyclotron shield can readily be measured by removing the target. Except for gamma rays from radioactivity in the target, the random gamma-ray background is also eliminated by subtracting the target-out counts from those obtained with the target in.

Some understanding of intensity problems can be gained by study of the estimated efficiency curve, Fig. 16, plotted for a scintillator thickness of about 1 in. and a detector bias of just over 1 Mev. If clumsy arrangements involving multiple B detectors are avoided and detector B is placed ~70 cm from the target, the scintillator subtends a fractional solid angle of $\sim 2 \times 10^{-3}$. If one neutron is produced in the target for every ten protons, then in the case of an isotropic yield there would be about one fast neutron detected for some flight time for each 10^5 incident protons. As is developed below, a plausible intensity is $2 \times 10^6 \times f$, where f is the gross duty factor, about 4% at the Harvard synchrocyclotron. Thus, in a typical case it can be anticipated that about 1 count/sec will correspond to some energy of interest. Rates actually observed in tests using a 25-g/cm^2 copper target were two or three times this value.

Table 2 will aid in understanding the time resolution problem. It shows the time required for a 70-cm flight by neutrons of various energies. For the assumed time-measuring system with resolution of about 1 nsec, the best available time resolution for a 50-Mev neutron is 12%, leading to an energy resolution of 25%. The target and detector thicknesses must also be considered. They typically limit energy resolution to 15% by making uncertain the precise length of the flight path. Thus with reasonable target-detector spacings, the equipment can be operated to detect neutrons over 50 Mev only for very low resolution work. Fortunately, the efficiency of Fig. 2 does not seem to vary much in the higher energy region. Table 2 also indicates that at 70 cm the spectrum can be carried down to about 0.5 Mev if an 80-nsec period is allotted to each time measurement. If a 0.5-Mev bias is employed on detector B, efficiency will be reasonably well known for neutrons above 1 Mev. The considerations of this paragraph lead to the energy range limitation for secondary neutrons.

Since if two protons should arrive on the target during an 80-nsec period it is difficult to know which has generated a detected secondary particle, part of the supervisory circuitry is designed to eliminate such proton pairs from consideration. If in the macroburst (see Section I) the intensity averages about 2.2×10^6 protons/sec, and if the microstructure is definite, there is roughly a 0.74 chance ($e^{-0.3}$) that a given pulse will

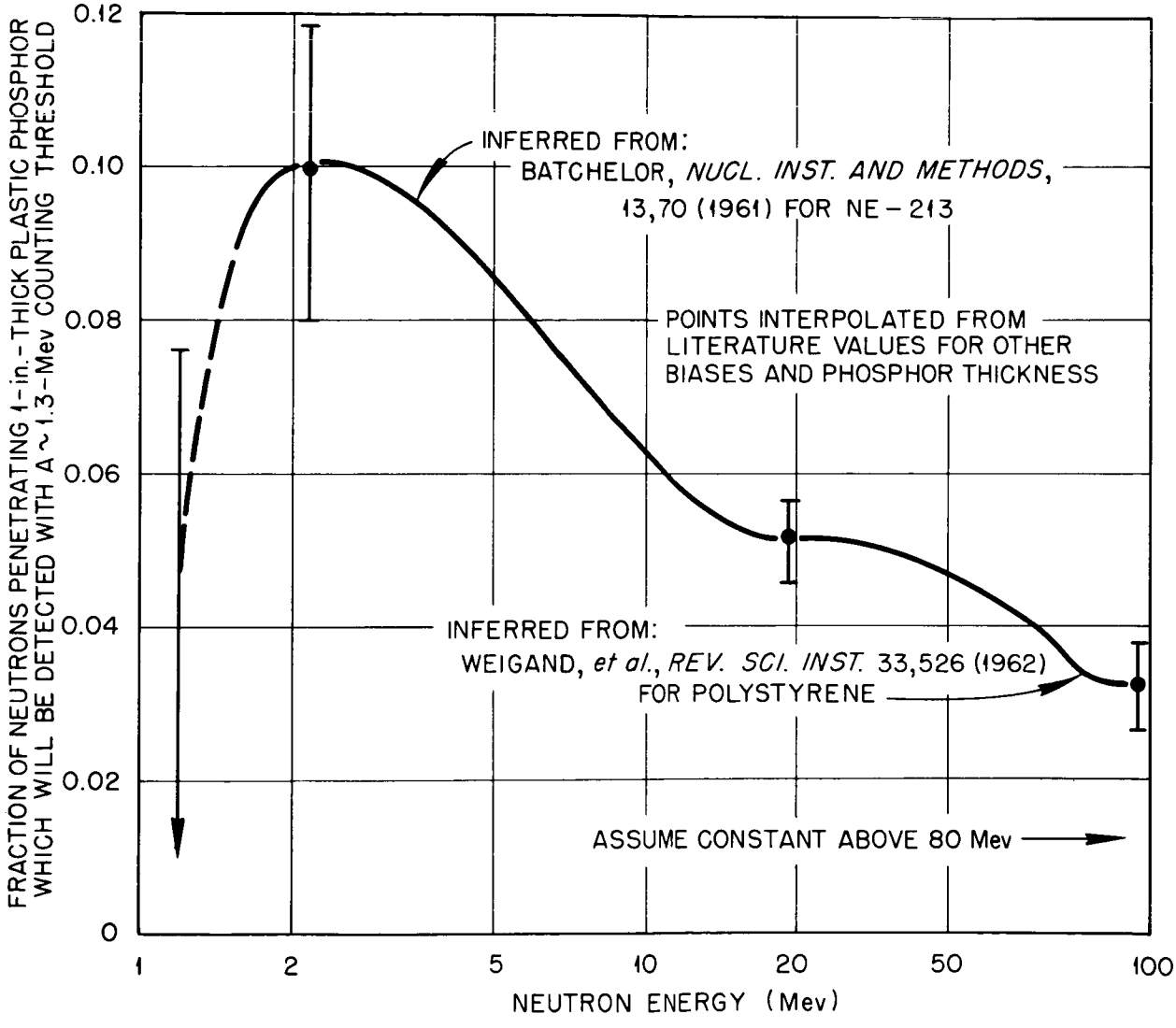

Fig. 16. Estimated Counting Efficiency of the Scattered-Neutron Detector.

Table 2. NEUTRON FLIGHT TIME AND ENERGY RESOLUTION FOR A 70-cm FLIGHT PATH

Kinetic Energy of Secondary Neutron (Mev)	Neutron Velocity (cm/nsec)	Flight Time for 70-cm Path (nsec)	Energy Resolution for 1-nsec Time Resolution[a] (%)
0.5	0.98	71	3
1.0	1.38	51	4
2.0	1.95	36	6
4.0	2.76	25	8
8.0	3.89	18	11
16.0	5.46	13	15
30	7.4	9.5	23
60	10.2	6.8	32
100	12.8	5.5	40
150	15.2	4.6	50

[a]Energy resolutions quoted are for a limitingly thin target and detector and are based on a hypothetical 1.0-nsec time resolution of the system.

be adequately isolated from its neighbors. This probability would lead to a 25% correction by the supervisory electronics to a net counting rate of about 1.5×10^6 protons/sec during the macrobursts. Perhaps a gross microburst intensity as high as 3.3×10^6 protons/sec could be considered, which would give a net rate of 2.1×10^6 protons/sec after correction. It is doubtful if larger corrections by the supervisory circuitry should be allowed, and little counting intensity remains to be gained if the 80-nsec interval is maintained. If there were no microstructure, a clear time interval of $\pm$ 80 nsec around each accepted proton must be provided, which has a probability per proton given by $\exp(-160 \times 10^{-9} \times 2.2 \times 10^6) = e^{-0.35} = 0.70$ for the case of a gross microburst intensity of 2.2×10^6 protons/sec. Therefore, the sharp microstructure helps slightly in utilizing the beam, provided that the amount of free time required is just less than in integral number of cyclotron rf periods.

Preliminary Measurements

An apparatus of the type described above was tested in May, 1962, with protons from the ~156-Mev external beam of the Harvard University Synchrocyclotron. This section discusses very briefly the instrumentation used and shows some of the preliminary results obtained.

Detector A was a single 2-mm-thick polystyrene-based plastic scintillator which gave an ~40% pulse-height resolution from the ~1-Mev energy loss from a single proton. No protons produced pulses of less than half the average pulse height. The bias for pulses to be counted as part of the beam was set just below the half-average pulse-height level by use of a tunnel diode discriminator which fed an amplifier capable of producing a pulse of appropriate shape for the 100-Mc scaler used. Detector B showed 14% resolution (on integrated pulses) for the ~15-Mev energy losses by the primary beam protons.

Light collection in detector C was inadequate, so the resolution for the 1-Mev energy loss from the full-energy beam was about 100%.

Integral lower-bias levels on B and C signal channels were set using conventional slow (1 μsec) electronic circuitry, and the necessary conditions for storage of a pulse were determined in a slow gating circuit. This circuit was operated at much higher than design counting rates because of failure of some of the other supervisory circuitry. In practice, except for a few trial runs, mutually interfering events in the A channel were held to a minimum by operating at a beam strength during the macrobursts of about 0.5×10^6 protons/sec.

Timing signals were formed at the photomultiplier bases in the B and C signal channels by tunnel diode discriminators. The time-to-pulse-height converter formed a voltage pulse by integrating a fixed current during the time between the output signals from these discriminators.

Figure 17 indicates the timing resolution available under the ideal conditions of the full-energy proton beam traversing both the A and B detectors. Artificial delays account for the channel in which the peak appears. For the broad spectrum of pulse heights resulting from a monoenergetic neutron incident on detector B the sharp resolution of the ideal case (~1.2 nsec) is not expected to exist. Figure 18 shows a typical calibration curve for the time-to-pulse-height converter; it was obtained by varying a delay line in the "start" signal channel. A nonlinearity is observable at small pulse heights. Velocity measurements were made by comparing the channel in which the pulse appeared against that in which was centered the full-energy proton peak with the target removed and the detector at 0°. Other distance and delay parameters were, of course, held constant.

Figure 19 shows a typical pulse-height spectrum, obtained at a 10° scattering angle from a copper target 25.2 g/cm^2 thick. The background with the target removed is plotted on the same scale and includes essentially the same random background as the target-in data. Figure 20 shows the same 10° data plotted on a neutron/Mev vs Mev basis. The data were reduced by a computing machine program[15] based on the detector efficiency illustrated in Fig. 16. The spectrum observed at 60° is shown on the same plot. The 120° data (not plotted) appear consistent with that shown for 60°, and the 30° spectrum falls between the two shown. The efficiencies used in reduction of the data should not be catastrophically in error at energies over 3 Mev. The peak in the neighborhood of 6 Mev, which appears at least at 60° and 120°, is unexpected. Because of beam-counting and dead-time difficulties, absolute magnitudes are uncertain by at least 25% plus the undetermined percentage due to efficiency uncertainties.

While the apparatus automatically recorded "proton spectra" for each case studied, it was found that BC coincidences in the apparatus shown were inadequate to assure that the observed charged particles originated in the target. For this reason the proton spectra obtained are interesting but not helpful for estimating the actual proton spectra.

Table 3 gives gross observed counting rates during the entire series of short runs. The values should be helpful in estimating counting rates for future experiments, even though the present runs were too short to produce meaningful spectra. As indicated above, effective proton beam strengths of the order of 1.5×10^6 protons/sec are contemplated during future gross duty-cycle bursts, so at the Harvard cyclotron with a 4% gross duty cycle the apparatus can handle about 2×10^8 protons/hr. Adequate data should be obtainable at low resolution for a limited number of cases.

---

15. The program was designed by R. L. Cowperthwaite, co-op student from the Missouri School of Mines, Rolla, Missouri.

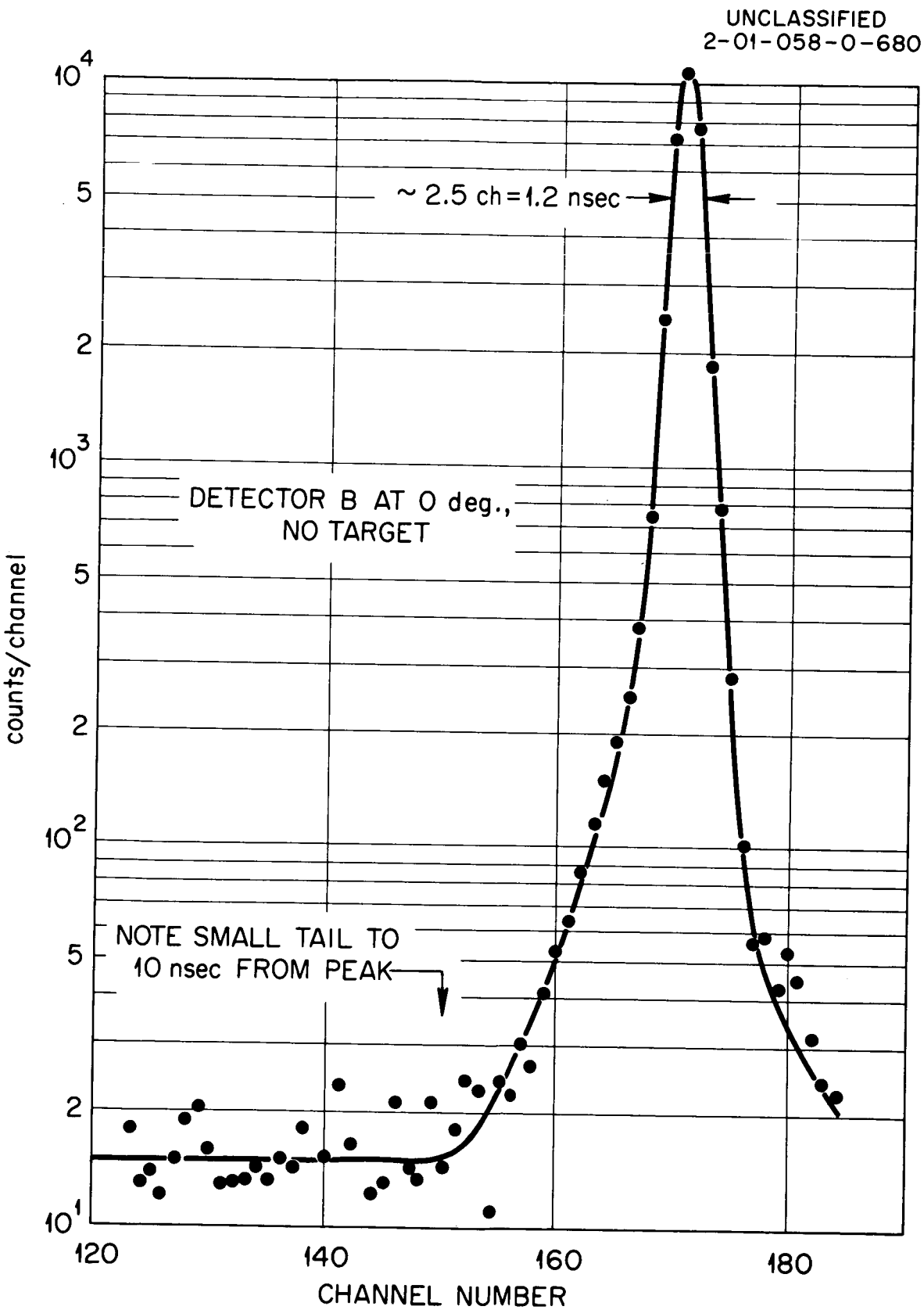

Fig. 17. Time Resolution of Spectrometer System at 0.45 nsec/channel.

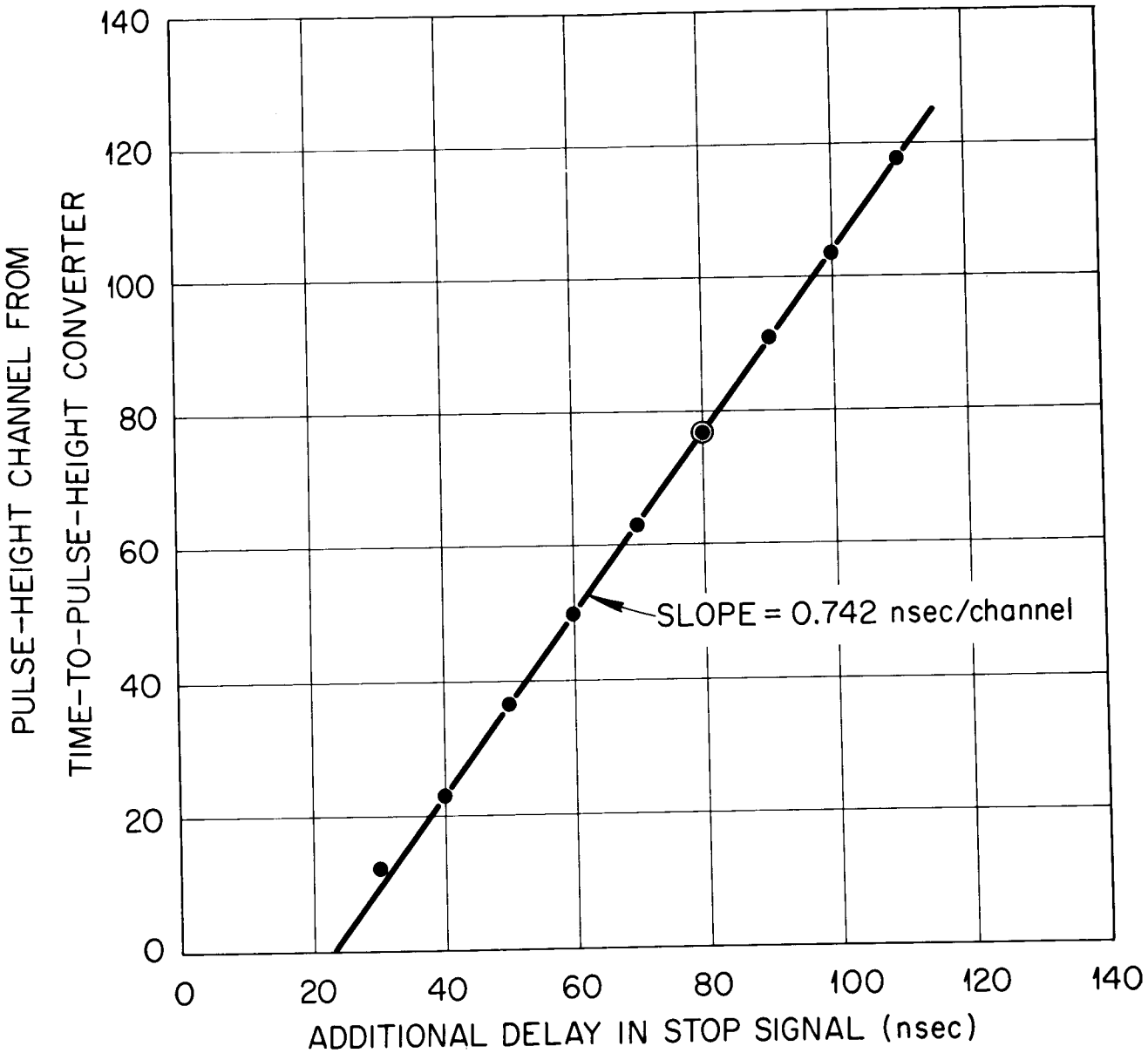

Fig. 18. Typical Calibration Curve of Time-to-Pulse-Height Converter.

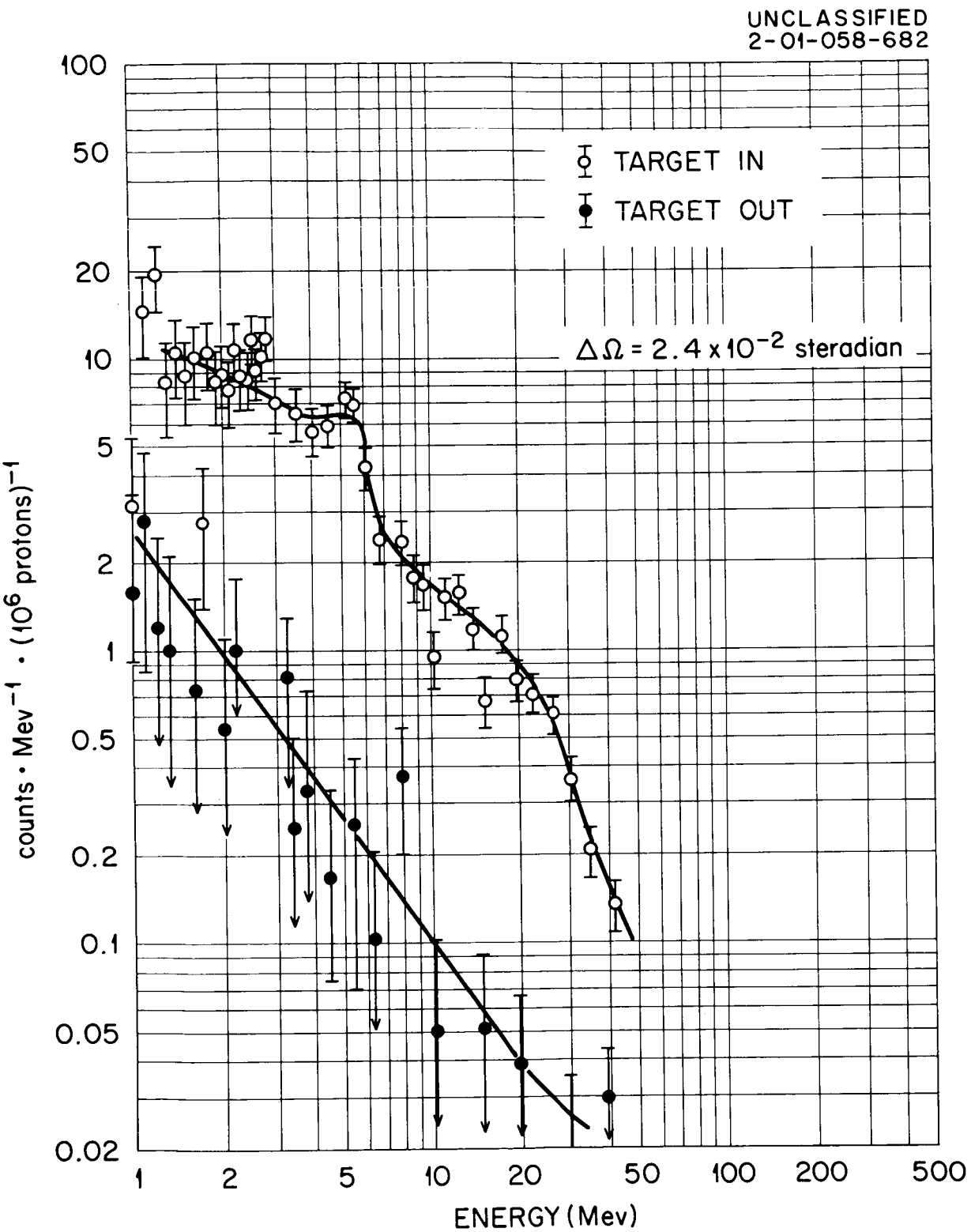

Fig. 19. Neutron Count Spectrum and Target-Out Background for 156-Mev Protons on 25.2 g/cm^2 Thick Copper Target.

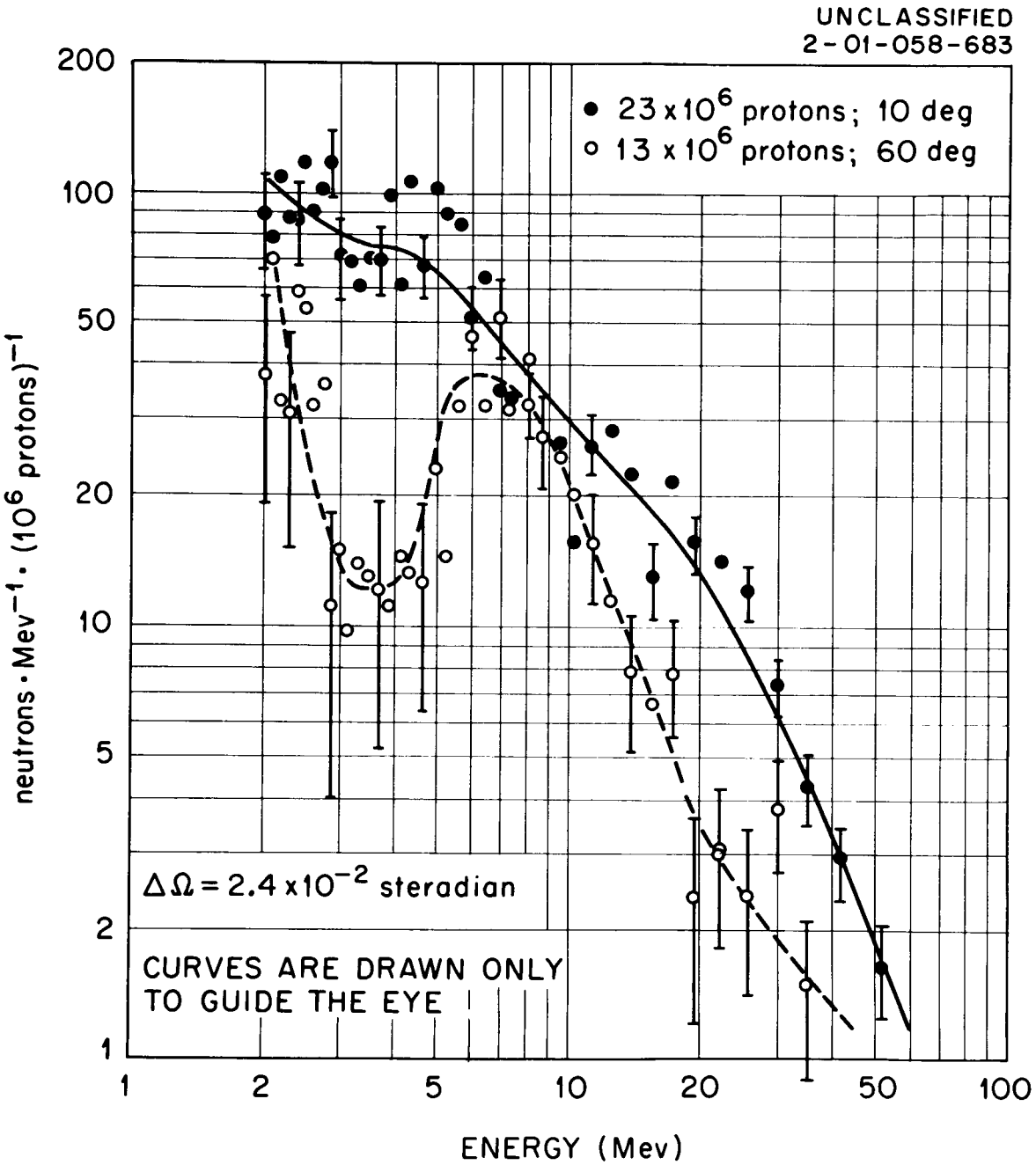

Fig. 20. Neutron Spectrum at Scattering Angles of 10 and 60° from a 25.2 g/cm^2 Copper Target.

Table 3. Summary of Gross Counting Information

Copper Target Thickness (g/cm^2)	θ, Angle from Beam (deg)	Total Protons in Beam	Average Beam Strength (protons/sec)	Total Counts in Time-of-Flight Spectrum	Neutron Counts/10^6 Protons in Energy Bins Shown[a]				
					2–5 Mev	5–10 Mev	10–20 Mev	20–70 Mev	>70 Mev
		$\times 10^6$	$\times 10^3$						
25.2	10	22.7	14	1725	25 ± 1	14 ± 1	11 ± 0.6	9.5 ± 0.6	1.7 ± 0.3
8.6	10	8.1	16	1710[b]	15 ± 1	19 ± 1.5	7.6 ± 1	59[b]	19[b]
0	10	21.9	15	110	0.6 ± 0.1	0.6	0.5	1 ± 0.2	0.4
25.2	30	26.5	53	1690	10.7 ± 0.6	12.8	9.3 ± 0.5	8.8	0.5 ± 0.04
8.6	30	12.9	13	160	1.9 ± 0.4	2.2 ± 0.4	1.7	2.2	1.4
0	30	14.4	14	77	0.8	0.5	0.4 ± 0.2	0.8	0.2
25.2	60	13	13	510	6 ± 0.7	12 ± 1	4	3.5	3.0
8.6	60	8	16	83	3.5 ± 0.7	5.7 ± 0.8	4.0 ± 0.8	3.5	0.7
0	60	15	15	47	0.3	0.2	0.1	0.2	0.3
25.2	120	15	15	406	4.2 ± 0.6	9.8 ± 0.8	3.4	1.6	2.3 ± 0.4
8.6	120	8	16	73	1.2 ± 0.4	3.1	0.9	0.6	0.2 ± 0.1
0	120	16	16	46	0.2	0.3	0.2	0.1	0.1

[a] Representative errors shown are based on counting statistics.

[b] Many protons accidentally registered here as neutrons.

Development of Improved Instrumentation

In the period since the preliminary measurements, efforts have been made to improve the original apparatus in the following ways:

1. The ambiguity in the definition of the incident beam is to be resolved by using two A detectors in fast coincidence with each other.

2. All the electronics in the A-channel, dealing with the incident beam, will be fast.

3. The time isolation of the incident protons used will be more positively assured by using an "isolated signal detector" which yields output pulses for protons isolated from their neighbors by at least 60 nsec. The complementary logic was used during preliminary measurements.

4. Pulse-shape-discrimination methods will be used to insure that random gamma-ray backgrounds are not seriously large. To employ these methods, a Ne-213 liquid scintillator[16] will be employed for the B detector.

5. Fast circuitry will be employed in the scattered particle detectors, B and C, so that measurements can be made at quite small angles with thin targets under conditions such that a substantial portion of the beam passes through these detectors.

6. A separate detection scheme will be employed to allow observation of proton spectra. The scheme includes an arrangement with minimum mass in the scattered beam path and a thin (0.5 mm) plastic detector (C') placed about halfway between the target and the scattered-particle detector (B') to create a telescope arrangement.

7. The anticoincidence detector, C, will be formed from thicker (4 mm) plastic, and an improved light pipe will be used so that effective anticoincidence action will be assured.

Figure 21 shows a block diagram of the equipment to be used in the next trials. It is expected that only minor changes will remain to be made to attain fully satisfactory operation after final testing of the arrangement shown.

Most of the fast circuits shown are in the final design or laboratory testing stage. The circuitry will be based largely on tunnel-diode univibrator designs similar to those described by Whetstone.[17] Adequately

16. Product of Nuclear Enterprises, Ltd., Winnipeg, Canada.

17. A. Whetstone and S. Kounoso, Rev. Sci. Instr. 33, 423 (1962).

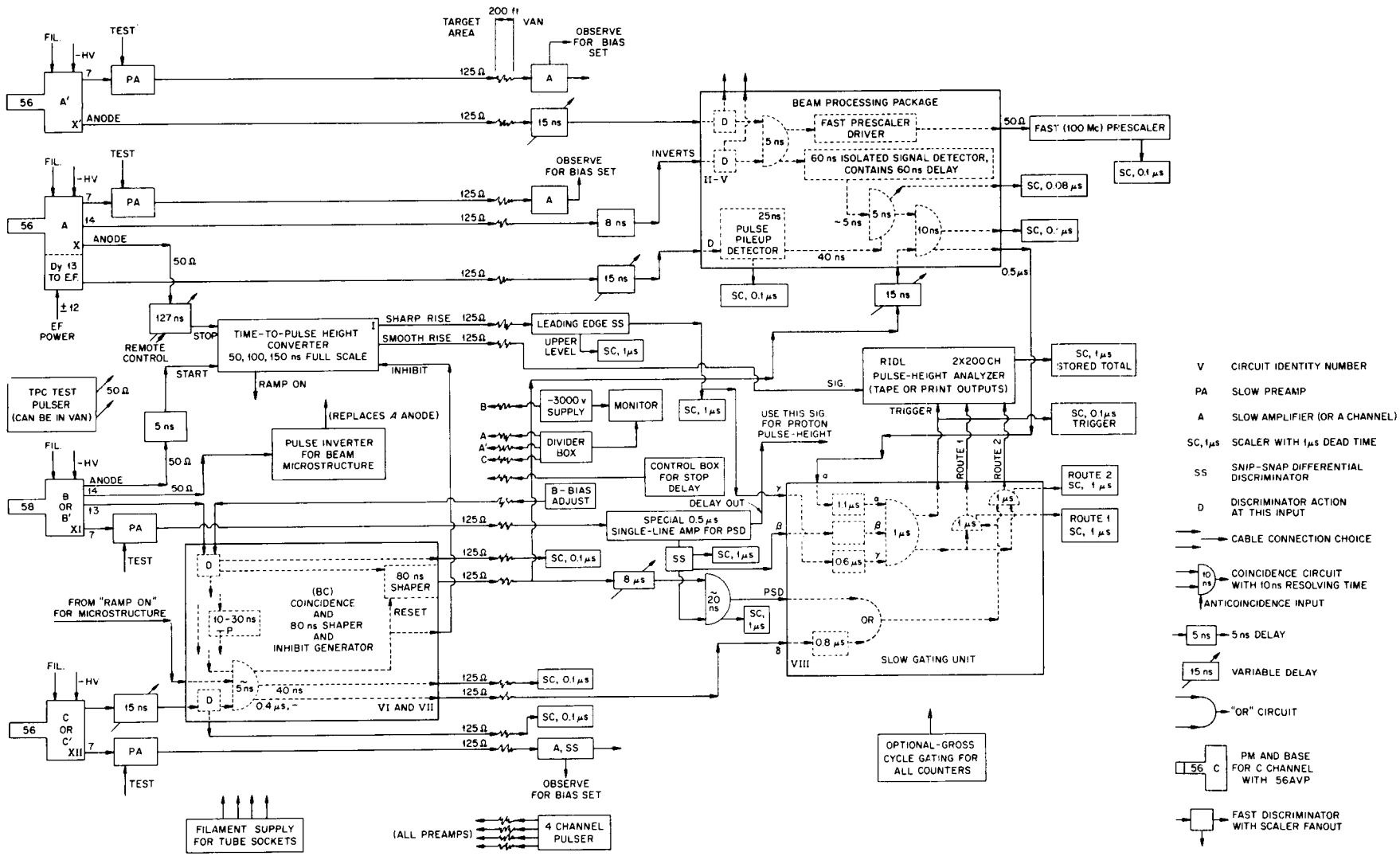

Fig. 21. Block Diagram of Neutron Time-of-Flight Spectrometer.

small propagation delays and rise and fall times can be attained, though some difficulty with dead times is anticipated. Only in the time-to-pulse-height converter will there be a problem caused by "walk" as a function of pulse amplitude from detector B.

If neutron spectra are to be measured over a range from 0.5 to 155 Mev, the light pulses in a 1-in.-thick plastic phosphor will have a dynamic range of 470:1. Since the minimum electronic pulse will be a few milliamperes at its peak, and since under the conditions of the experiment the 58-AVP photomultiplier is capable of producing maximum pulses of only about 0.5 amps, the dynamic range of electronic pulses will be smaller than that of the light pulses. Nevertheless, the electronic pulse range is unusually large, and it is felt that this factor is the source of the major design problems in developing a time-to-pulse-height converter with 1-nsec resolution.

IV. Bonner Spheres and Threshold Detectors for Neutron Spectroscopy

The variety of neutron spectrometers required to encompass the wide range of energies considered in the space vehicle shielding problem is pointed out in the Introduction. For neutron energies < 10 Mev, the use of so-called "Bonner spheres" has been investigated during preliminary experiments at the Harvard University Synchrocyclotron, and the feasibility of augmenting the Bonner sphere data above 10 Mev by threshold detector techniques has been examined. Bonner-sphere data have been obtained for a variety of configurations.

Experimental Procedure - Bonner Spheres

A Bonner sphere[18] basically consists of a thermal-neutron detector surrounded by a spherical mass of polyethylene moderator. For the present work the plans of Bonner have been followed as closely as possible, so that counting efficiency calibrations determined by him could be used. The thermal-neutron detector is a $Li^6I(Eu)$ scintillation crystal, essentially totally absorbing at thermal energies and "transparent" to energies > 100 ev. It is therefore predominantly sensitive to low-energy neutrons. As moderating material is added and the sphere diameter is increased, sensitivity to higher energy neutrons is increased. Table 4 gives the counting efficiencies used, over a neutron energy range from 0.01 ev to 160 Mev, for spheres of five different diameters, as well as for the $Li^6I(Eu)$ detector both with and without a 30-mil-thick cadmium cover. The data from thermal energies to 15 Mev were compiled from large-scale graphs supplied by Bonner and are quoted to be accurate to about 6%. From 15 to 160 Mev, the data represent a crude extrapolation by the author.

A diagram of the simple experimental arrangement for the preliminary experiments is shown in Fig. 22.

---

18. R. L. Bramblett, R. I. Ewing, and T. W. Bonner, Nuclear Instr. and Methods 9, 1 (1960).

Table 4. Counting Efficiencies for Bonner Spheres

Neutron Energy (ev)	Counting Efficiency (counts n^{-1} cm^{-2})						
	Bare Detector	Cd-Covered Detector	2-in.-diam Sphere	3-in.-diam Sphere	5-in.-diam Sphere	8-in.-diam Sphere	12-in.-diam Sphere
1.0 (−2)[a]	0.122	0.000	0.0820	0.0740	0.0420	0.0100	0.0040
1.6 (−2)	0.122	0.000	0.0850	0.0768	0.0448	0.0116	0.0041
2.5 (−2)	0.120	0.000	0.0880	0.0796	0.0476	0.0132	0.0043
4.0 (−2)	0.118	0.000	0.0930	0.0824	0.0504	0.0148	0.0044
6.3 (−2)	0.116	0.000	0.0960	0.0852	0.0532	0.0164	0.0045
1.0 (−1)	0.114	0.000	0.0980	0.0880	0.0560	0.0180	0.0046
1.6 (−1)	0.110	0.000	0.0990	0.0924	0.0600	0.0200	0.0047
2.5 (−1)	0.102	0.000	0.1000	0.0968	0.0640	0.0220	0.0048
4.0 (−1)	0.116	0.116	0.1000	0.1012	0.0680	0.0240	0.0050
6.3 (−1)	0.110	0.110	0.1008	0.1056	0.0720	0.0260	0.0051
1.0 (0)	0.084	0.084	0.1016	0.1106	0.0762	0.0282	0.0052
1.6 (0)	0.076	0.076	0.1020	0.1146	0.0806	0.0300	0.0054
2.5 (0)	0.068	0.068	0.1030	0.1194	0.0850	0.0318	0.0057
4.0 (0)	0.060	0.060	0.1040	0.1224	0.0896	0.0336	0.0059
6.3 (0)	0.052	0.052	0.1000	0.1262	0.0940	0.0354	0.0062
1.0 (1)	0.042	0.042	0.0940	0.1302	0.0986	0.0372	0.0064
1.6 (1)	0.036	0.036	0.0892	0.1338	0.1032	0.0390	0.0067
2.5 (1)	0.028	0.028	0.0862	0.1374	0.1076	0.0408	0.0070
4.0 (1)	0.020	0.020	0.0804	0.1410	0.1120	0.0426	0.0072
6.3 (1)	0.010	0.010	0.0776	0.1446	0.1164	0.0444	0.0075
1.0 (2)	0.002	0.002	0.0746	0.1482	0.1208	0.0462	0.0078
1.6 (2)	0.000	0.000	0.0712	0.1500	0.1258	0.0480	0.0080
2.5 (2)	0.000	0.000	0.0678	0.1520	0.1308	0.0498	0.0083
4.0 (2)	0.000	0.000	0.0646	0.1516	0.1358	0.0516	0.0085
6.3 (2)	0.000	0.000	0.0614	0.1510	0.1408	0.0534	0.0088
1.0 (3)	0.000	0.000	0.0582	0.1500	0.1458	0.0552	0.0090
1.6 (3)	0.000	0.000	0.0548	0.1478	0.1514	0.0574	0.0092
2.5 (3)	0.000	0.000	0.0516	0.1446	0.1570	0.0596	0.0095
4.0 (3)	0.000	0.000	0.0484	0.1412	0.1626	0.0618	0.0097
6.3 (3)	0.000	0.000	0.0452	0.1378	0.1682	0.0640	0.0100
1.0 (4)	0.000	0.000	0.0420	0.1346	0.1740	0.0660	0.0102
1.6 (4)	0.000	0.000	0.0386	0.1290	0.1798	0.0724	0.0116
2.5 (4)	0.000	0.000	0.0354	0.1236	0.1856	0.0790	0.0132
4.0 (4)	0.000	0.000	0.0322	0.1182	0.1914	0.0856	0.0148
6.3 (4)	0.000	0.000	0.0290	0.1126	0.1972	0.0920	0.0164
1.0 (5)	0.000	0.000	0.0258	0.1072	0.2032	0.0986	0.0180
1.6 (5)	0.000	0.000	0.0222	0.0986	0.2082	0.1148	0.0222
2.5 (5)	0.000	0.000	0.0180	0.0900	0.2136	0.1320	0.0274
4.0 (5)	0.000	0.000	0.0132	0.0780	0.2152	0.1578	0.0394
6.3 (5)	0.000	0.000	0.0098	0.0618	0.2118	0.2022	0.0618
1.0 (6)	0.000	0.000	0.0066	0.0596	0.1930	0.2240	0.0900
1.6 (6)	0.000	0.000	0.0044	0.0350	0.1580	0.2250	0.1360
2.5 (6)	0.000	0.000	0.0026	0.0230	0.1240	0.2120	0.1600
4.0 (6)	0.000	0.000	0.0016	0.0148	0.0880	0.1800	0.1650
6.3 (6)	0.000	0.000	0.0010	0.0092	0.0630	0.1640	0.1840
1.0 (7)	0.000	0.000	0.0008	0.0064	0.0420	0.1012	0.1252
1.6 (7)	0.000	0.000	0.0008	0.0056	0.0320	0.0800	0.1040
2.5 (7)	0.000	0.000	0.0008	0.0060	0.0260	0.0680	0.0880
4.0 (7)	0.000	0.000	0.0008	0.0060	0.0260	0.0600	0.0780
6.3 (7)	0.000	0.000	0.0008	0.0060	0.0260	0.0540	0.0720
1.0 (8)	0.000	0.000	0.0008	0.0060	0.0260	0.0520	0.0680
1.6 (8)	0.000	0.000	0.0008	0.0060	0.0260	0.0520	0.0660

[a]Digit in parentheses denotes power-of-ten multiplier.

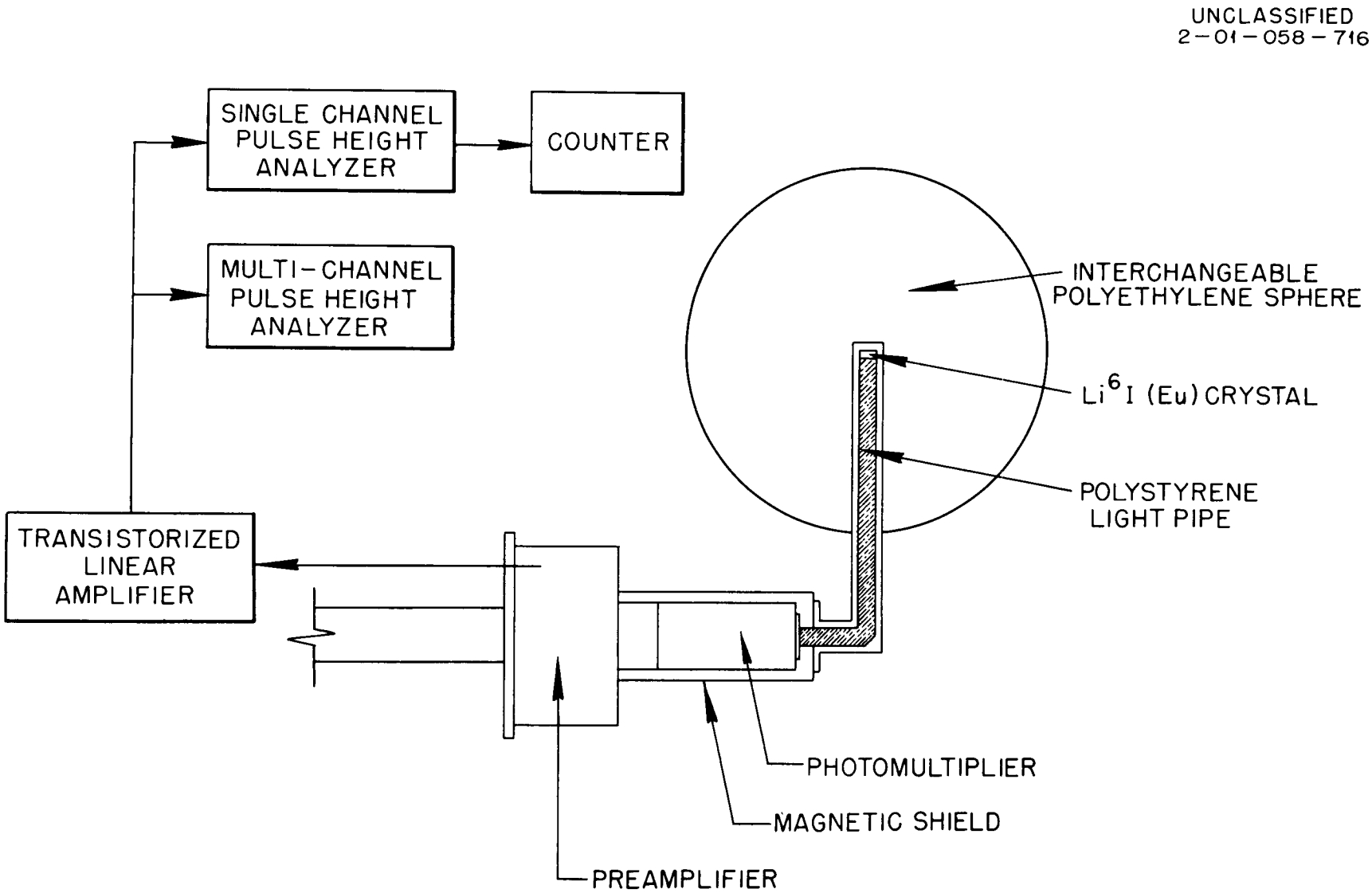

Fig. 22. Experimental Arrangement for Bonner Sphere Tests.

Experimental Results - Bonner Spheres

Pulse-height distributions obtained with 2- and 8-in.-diam polyethylene spheres are shown in Figs. 23 and 24, respectively. In both cases the particles incident on the target were 156-Mev protons, and the Bonner sphere was located 40 cm from the target on a line 30° from the beam-target axis. The target in the case of the 2-in.-diam sphere was a copper disk with a hole punched through its center, while for the 8-in.-diam sphere it was a solid copper disk. Both targets had a thickness of 31.8 g/cm^2. A considerable background is evident in the data from the smaller sphere and punched-out target, mostly due to protons scattered from the primary beam. It should be possible to subtract the background satisfactorily by recording the entire pulse-height distribution and performing a least-squares analysis for the area of the thermal peak. Few pulse-height spectra were recorded in these tests since no significant background had been anticipated.

Net counts recorded for various sphere diameters are shown in Table 5. The values represent the total counts less background for ~10^{10} protons incident on the copper target. Similar data are available but not yet analyzed for a total of 76 configurations. Table 6 lists the targets and angles studied.

Table 5. Total Counts in Thermal Peak for Bonner Spheres of Various Diameters

Detector	Net Counts[a]
Bare $Li^6I(Eu)$	~200[b]
Cd-covered $Li^6I(Eu)$	~ 50[b]
2-in. sphere	300
3-in. sphere	1300
5-in. sphere	3800
8-in. sphere	4900
12-in. sphere	3400

a. ~10^{10} 156-Mev photons incident on 31.8-g/cm^2-thick copper target. Detector 40 cm from target and 30° from beam axis. Beam-off background and counting loss corrections negligible.

b. Background estimated from similar experiments in which aluminum targets were used and pulse-height distributions recorded.

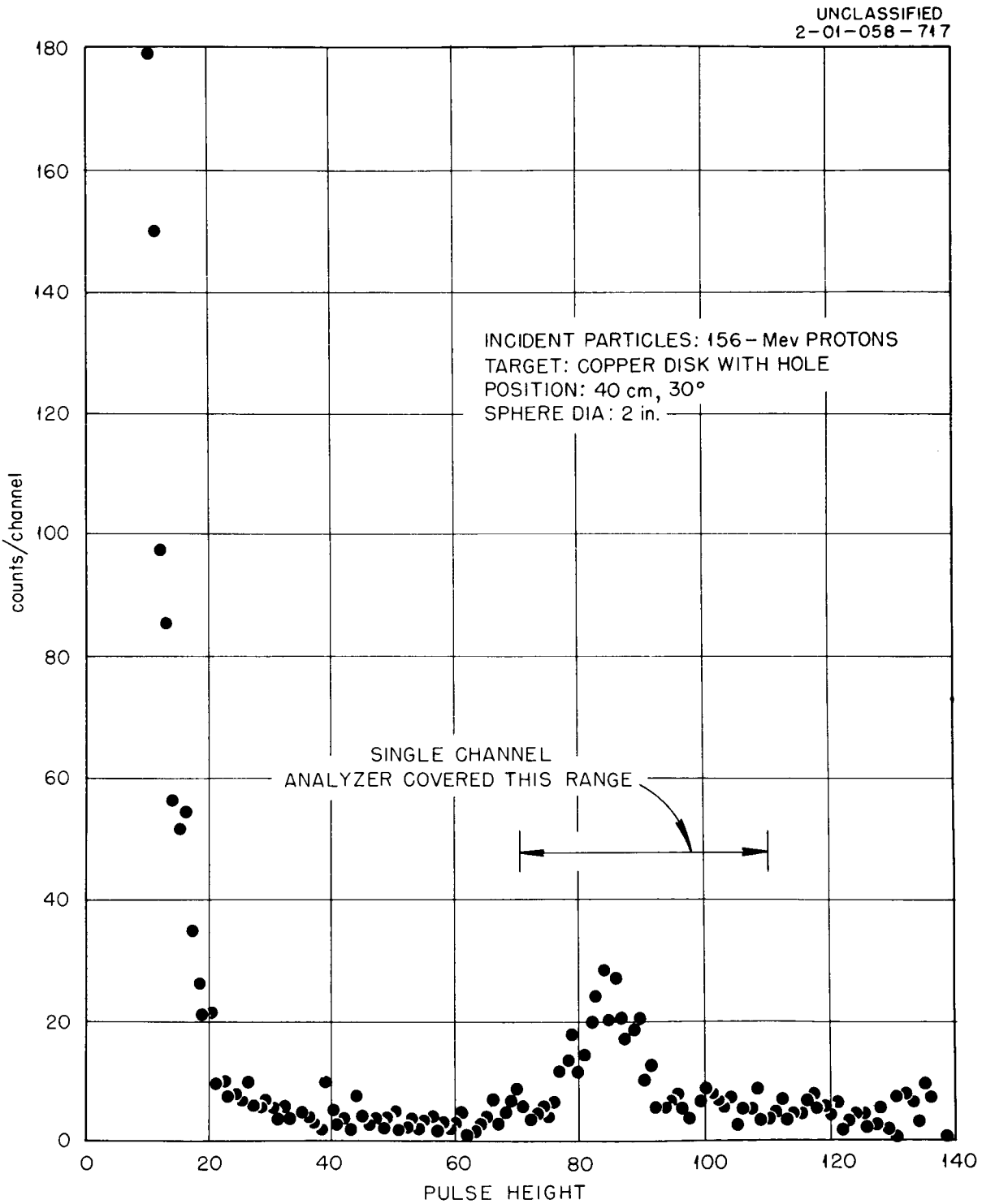

Fig. 23. Pulse-Height Distribution of Neutrons Resulting from 156-Mev Protons Incident Upon Copper, as Detected by a 2-in.-diam Bonner Sphere.

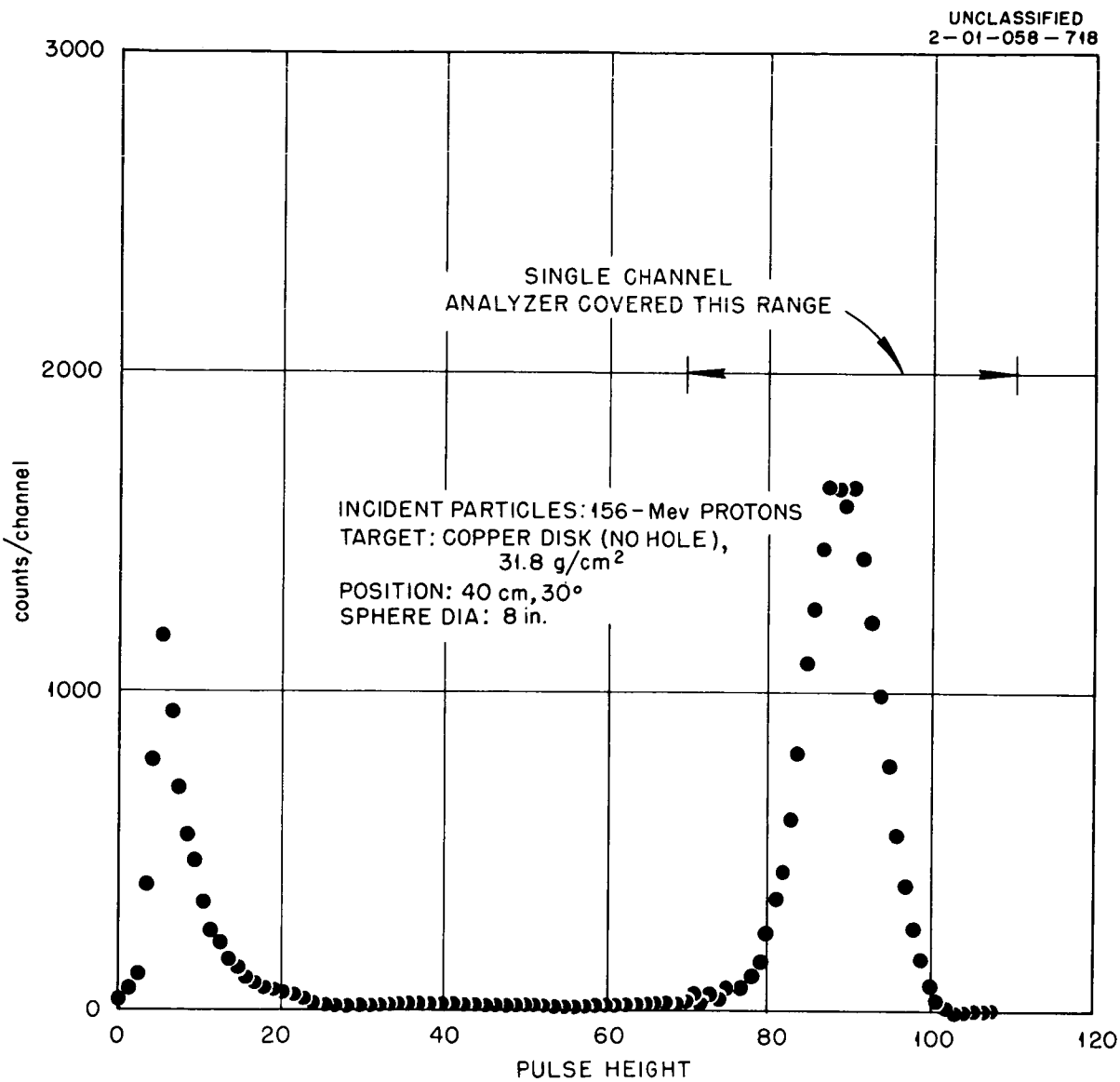

Fig. 24. Pulse-Height Distribution of Neutrons Resulting from 156-Mev Protons Incident Upon Copper, as Detected by an 8-in.-diam Bonner Sphere.

Table 6. Target Configurations for which Bonner Sphere Data were Obtained

Nominal $E_p \approx 156$ Mev

1.2-Range Targets	Angles	12-Mev Targets	Angles
H_2O	0°	Blank Can	30°
C	30°	H_2O	45°
Al	45°	D_2O	60°
Co	60°	Be	135°
Cu	135°	C	
Bi		Al	
Pb		Co	
None		Bi	
		None	

Experimental Procedure - Threshold Detectors

Three threshold detectors were tested to determine their usefulness for neutron energies > 10 Mev. Two were spiral fission chambers containing ~150 mg of U^{238} and ~150 mg of bismuth. A block diagram of the arrangement is shown in Fig. 25. The organic scintillator shown was used in anticoincidence with the fission chamber to discriminate against proton-induced fission.

The third threshold detector employed the $C^{12}(n,2n)C^{11}$ reaction by measuring the 20.5-m β^+ activity induced in 2 by 2-in. cylinders of Polyfluor plastic scintillator. The cylinders, after exposure to the neutrons, were counted on a conventional pulse-height analyzer using a 6655A photomultiplier. Cross sections used to compute efficiencies for all detectors are given in Table 7.

Experimental Results - Threshold Detectors

The results obtained with the detectors described above are listed in Table 8. Because of the difficulty noted below, the fission chamber counts were taken without the anticoincidence guard. The possibility of proton interaction is reflected in the large errors quoted. The U^{238} fission chamber data, of dubious value, were not used.

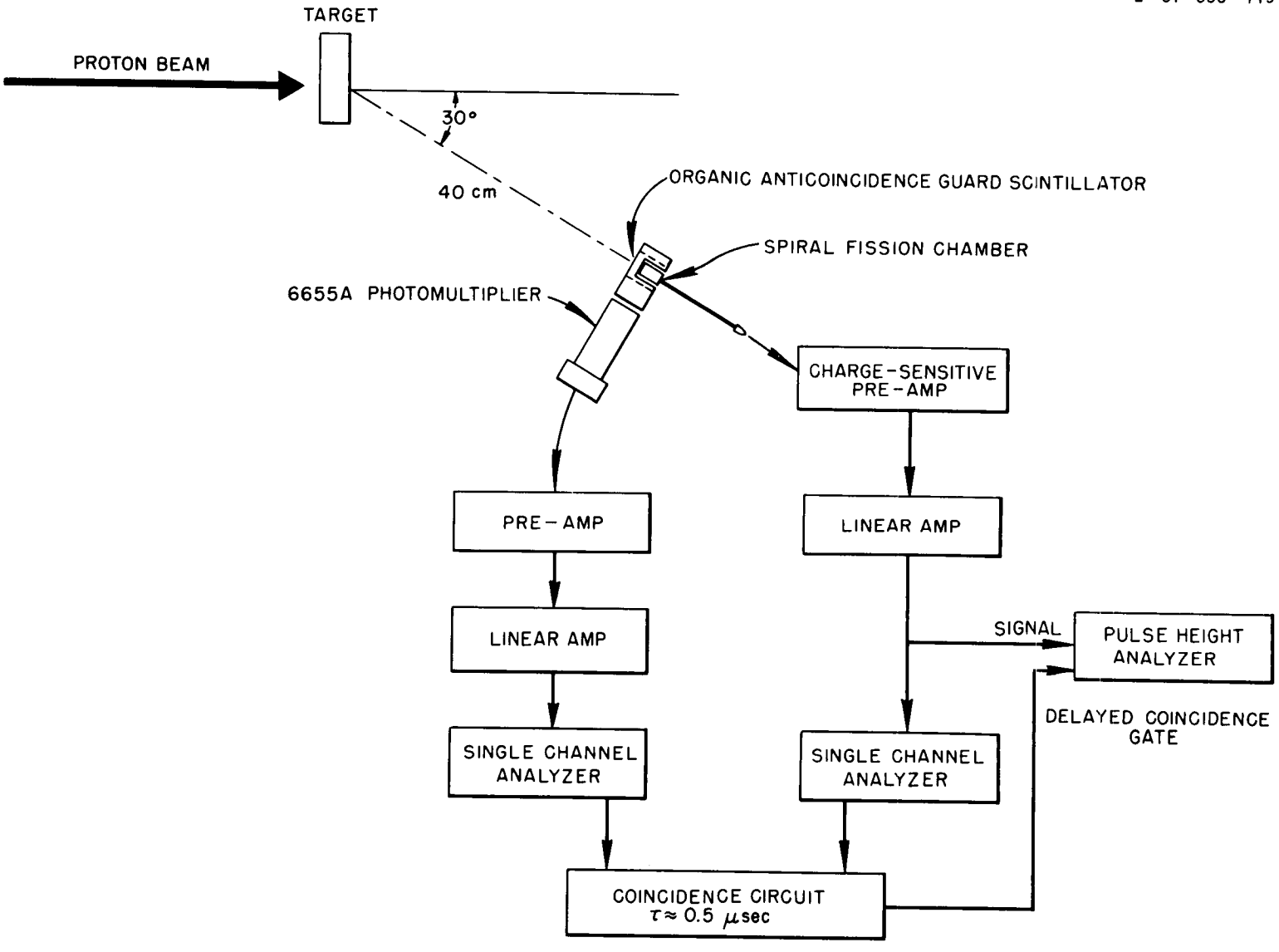

Fig. 25. Arrangement for Threshold Detector Experiments.

Table 7. Cross Sections Used for Threshold Detectors

Energy (Mev)	U^{238} (n,f) (barns) [a]	Bi (n,f) (barns) [b]	C (n,2n) (barns) [c]
0.40	0.000		
0.63	0.001		
1.00	0.18		
1.6	0.30		
2.5	0.58		
4.0	0.56		
6.3	0.70		
10	1.01		
16	1.30		
25	1.60	0.000	0.000
40	1.60	0.007	0.025
63	1.60	0.022	0.030
100	1.60	0.095	0.033
160	1.60	0.150	0.033

a. Accurate within 5% for energies below 16 Mev and probably within 20% for energies up to 160 Mev.

b. Probably accurate within a factor of 2 for energies up to 100 Mev and within a factor of 3 for energies up to 160 Mev.

c. Probably accurate within 30%.

Table 8. Experimental Results for Threshold Detectors

Detector	Number of Atoms in Sensitive Region	Number of Counts[a] per 10^{11} Incident Protons
U^{238} spiral fission chamber (FS-110)	$N_U = 3.8 \times 10^{20}$	$1250 \pm 80\%$
Bi spiral fission chamber (FS-109)	$N_{Bi} = 3.66 \times 10^{20}$	$25 \pm 40\%$
2 by 2-in. Polyfluor cylinder	$N_C = 5.06 \times 10^{24}$	$1.2 \times 10^4 \pm 50\%$[b]

a. Indicated errors include allowance for possible proton interaction. U^{238} data were not used in analysis.

b. Value listed is total activation based on β^+ counting.

It was difficult to obtain satisfactory data with the threshold counters. If the primary proton beam intensity was adjusted so that a count rate of a few counts per second was obtained in the fission counters, then the anti-coincidence guard crystal was jammed. Trouble was also encountered in using the $C^{12}(n,2n)C^{11}$ reaction because of the competing $C^{12}(p,pn)C^{11}$ reaction in the detector. Further development might eliminate these difficulties, but since the energy range above 10 Mev presumably will be adequately covered by other devices, the use of threshold detectors has been abandoned.

Calculation of Neutron Spectra

The raw material from which the neutron spectrum was calculated consisted of the efficiencies of Table 4, the cross sections of Table 7, and the experimental counting rates of Tables 5 and 8. It was known from published measurements and from theoretical calculations of the evaporation neutron spectrum that the neutron spectrum should be fairly slowly varying. This "regularity" of the spectrum was taken into account by assuming that the spectrum $\phi(u)$, where $u = \log_{10}(E/1\ \text{Mev})$, could be expressed as a positive combination of smooth functions,

$$\phi(u) = \sum_{k=1}^{m} q_k R_k(u),$$

where $q_k \geq 0$ and $R_k(u)$ are suitable slowly varying functions. Several typical $R_k(u)$ functions are shown in Fig. 26. Fifty-two such functions were used in the present calculation.

An approximate spectrum was then obtained by solving for the q_k's by the method of optimal combinations.[19] Briefly, the method consists of arbitrarily specifying the response function of a fictitious crude spectrometer and then trying to fit the response function with the counting efficiency functions of the actual detectors. The fictitious spectrometer chosen had a resolution (full width at half maximum) of 0.8 decade in energy.

Results

The results of the present preliminary experiments have been analyzed in the manner described above to give the tentative differential neutron energy spectrum shown in Fig. 27. The choice of the fictitious spectrometer with its resolution of 0.8 decade is reflected in the resolution shown in the figure.

Having obtained the approximate spectrum, one may then calculate the biological dose resulting from such a spectrum. Alternatively, the biological dose may be calculated directly by the method of optimal combinations. It was decided to calculate the entire distribution function, or "importance function," for biological dose, that is, the fraction of the total biological

19. Although not specifically identified by this name, this is the method described by W. R. Burrus, Neutron Phys. Div. Ann. Prog. Rep. Sept. 1, 1961, ORNL-3193, p. 44.

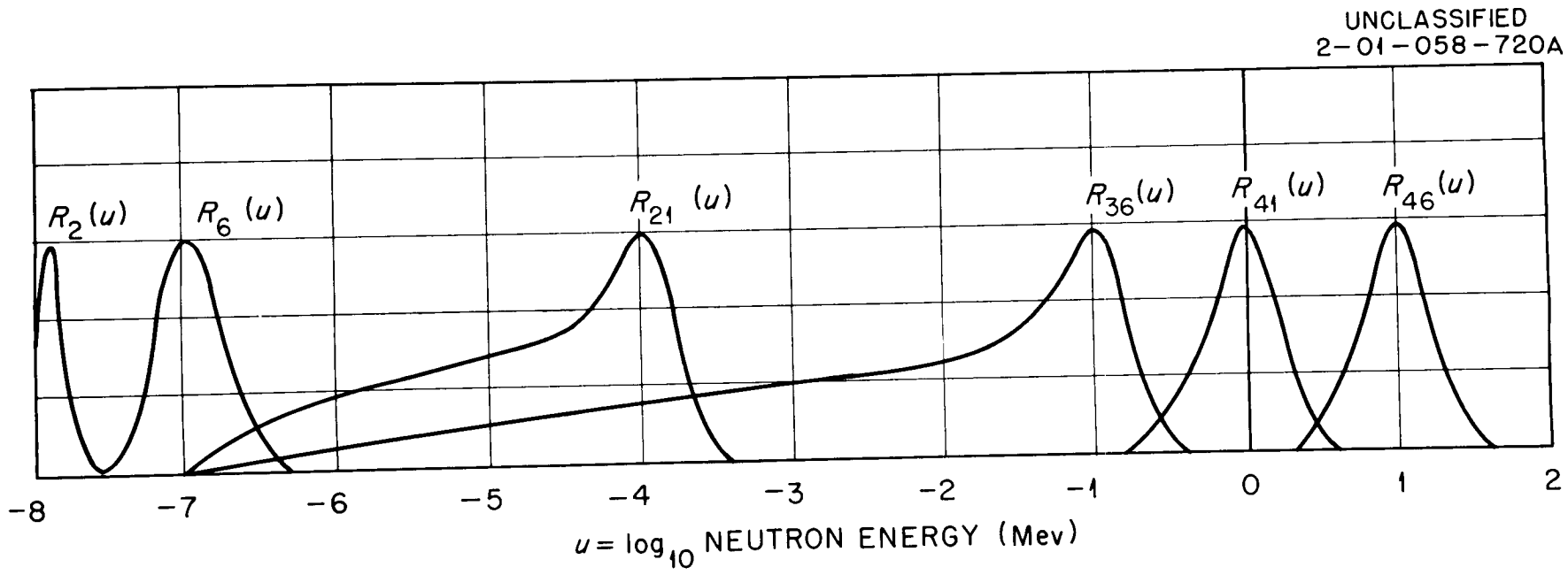

Fig. 26. Six Typical $R_k(u)$ Functions.

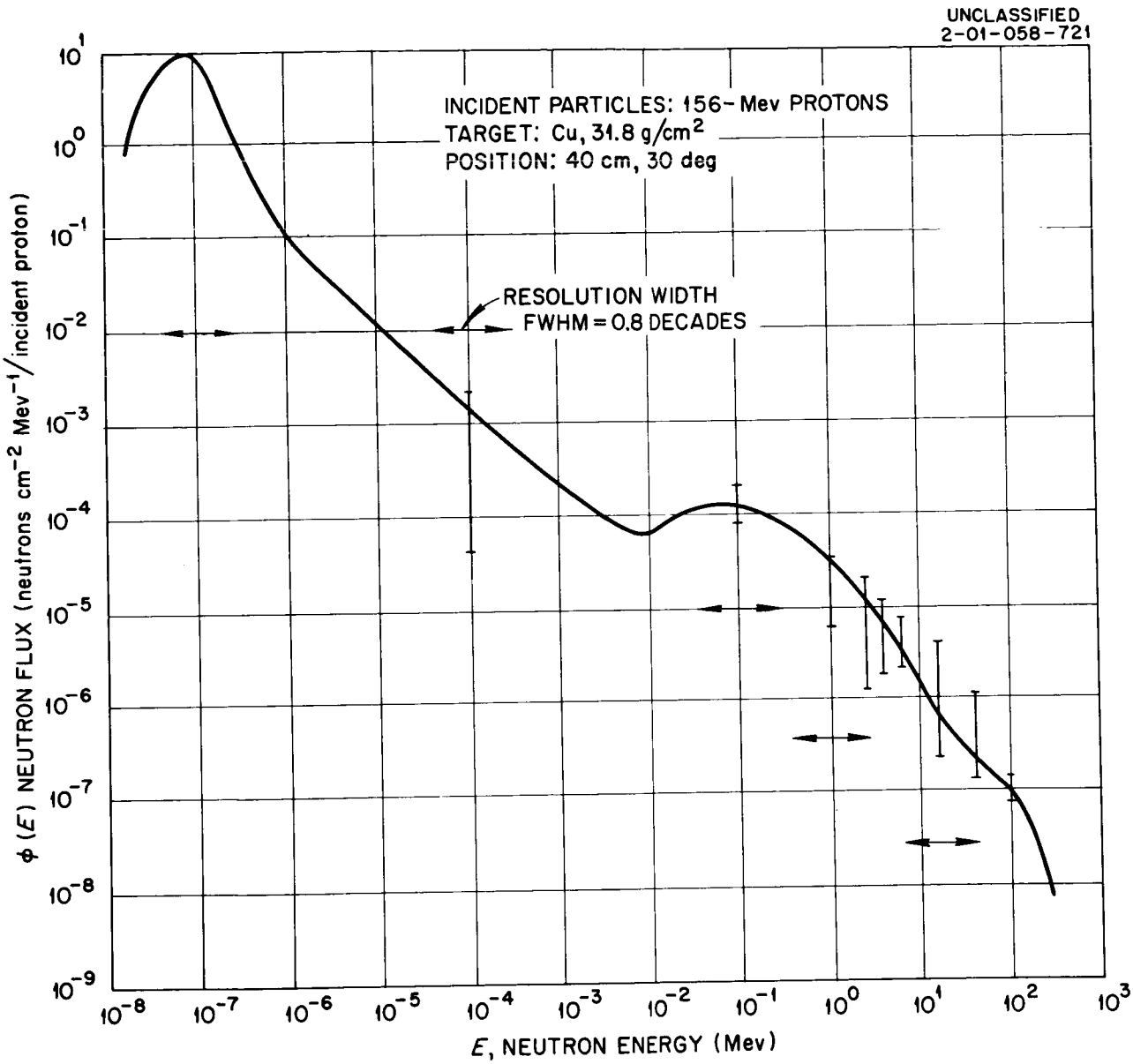

Fig. 27. Differential Neutron Energy Spectrum from 156-Mev Protons on Copper.

dose due to neutrons with energy above E. The result is shown in Fig. 28. From this curve an idea as to which part of the spectrum is most important from a biological damage viewpoint can be obtained. Somewhat unexpectedly, the present work shows that one-half the dose comes from neutrons with energies > 20 Mev and that only ~20% is due to neutrons with energies < 4 Mev.

The relation between biological dose and neutron flux is fairly complicated. In calculating the dose due to the neutron spectrum of the present work, values were taken from NBS Handbook 63[20] for that part of the spectrum below 10 Mev. These values are based on the energy deposited in a 30-cm-thick slab of tissue. They were weighted by a relative biological effectiveness (RBE) taken from NBS Handbook 69[21] and based on the linear energy transfer of the elementary event. Above 10 Mev the assumption was made that the product of the effective RBE and the effective buildup remained constant at the value of 6.5 found for 10 Mev, and the energy removal curve of Gibson[22] was used in lieu of the first collision dose curve. The resulting curves for biological dose and first-collision dose are shown in Fig. 29. The data of Fig. 29, which result in an integrated dose rate of 1.8×10^{-12} (±40%) rem per incident proton, are probably reliable within a factor of ~3 at 160 Mev.

Problems in Use of Bonner Spheres

No measurements of the efficiencies of Bonner spheres in the energy region above 15 Mev are available. Efforts are under way to determine the sensitivity of results to errors in the efficiency in the region from 15 to 160 Mev. In the event that such errors are important, a Monte Carlo calculation of the high-energy response of the spheres appears feasible.

Although direct proton response may be subtracted from the thermal-neutron response peak, secondary neutrons produced within the moderator by p,n interactions are indistinguishable from target neutrons. Additional experiments, with the proton beam directly incident on the sphere, have been performed to estimate the importance of this effect.

Variations in the size of commercially furnished $Li^6I(Eu)$ crystals and small differences in techniques used to analyze the thermal-neutron peak cause slight discrepancies from published calibration values. The spheres to be used in future experiments are being calibrated against a recently obtained standardized Am-Be neutron source.

If dose distributions, such as the curve of Fig. 28, are to be important in future work, better values of flux-to-dose conversion ratios must be sought. It may be more plausible to base conversions on a tissue sphere rather than a tissue slab.

---

20. Protection Against Neutron Radiation up to 30 Million Electron Volts, NBS-63 (1957).

21. Maximum Permissible Body Burdens and Maximum Permissible Concentrations of Radionuclides in Air and Water for Occupational Exposure, NBS-69 (1959).

22. W. A. Gibson, Energy Removed from Primary Proton and Neutron Beams by Tissue, ORNL CF-61-6-48 (June, 1961).

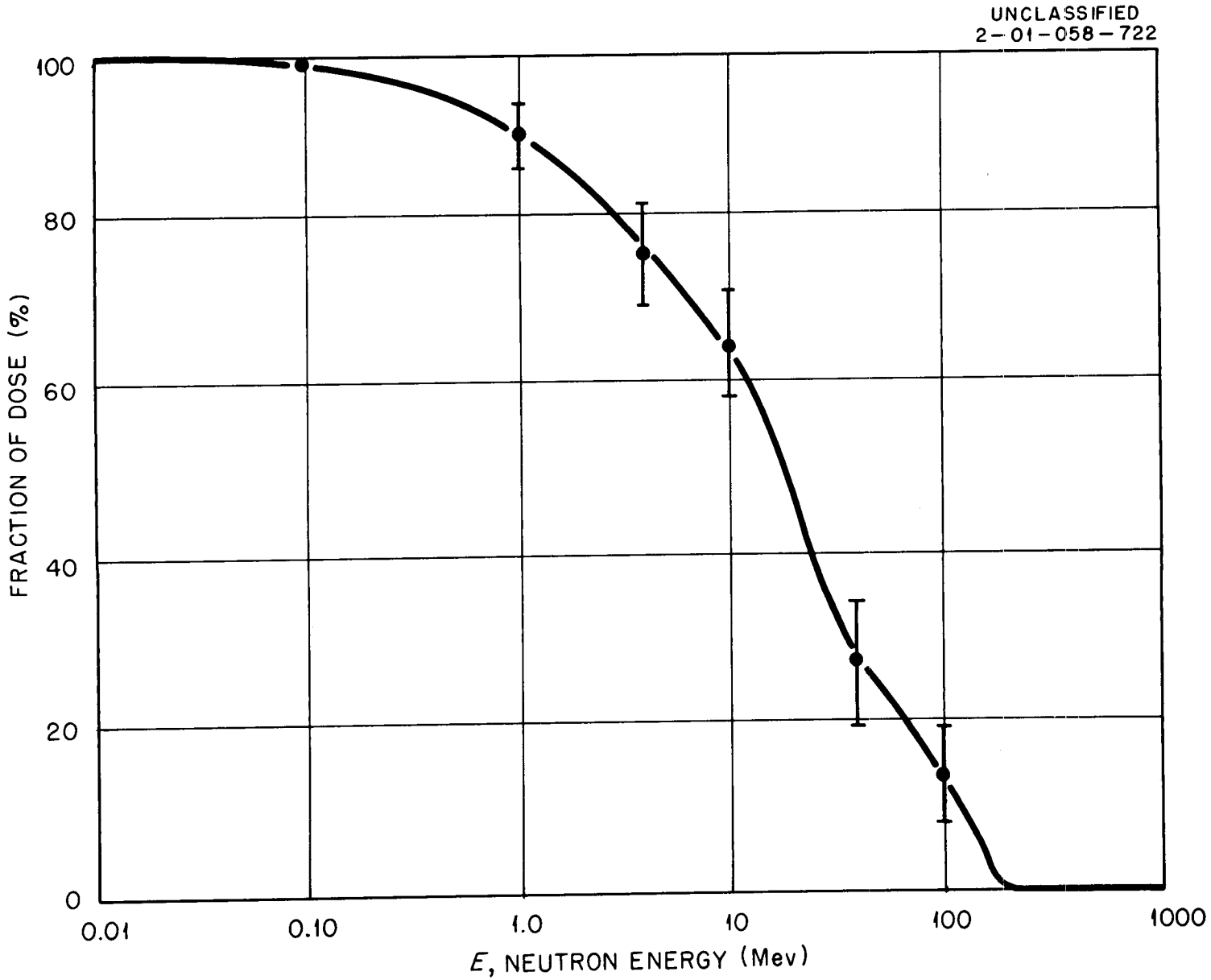

Fig. 28. Biological Dose Distribution.

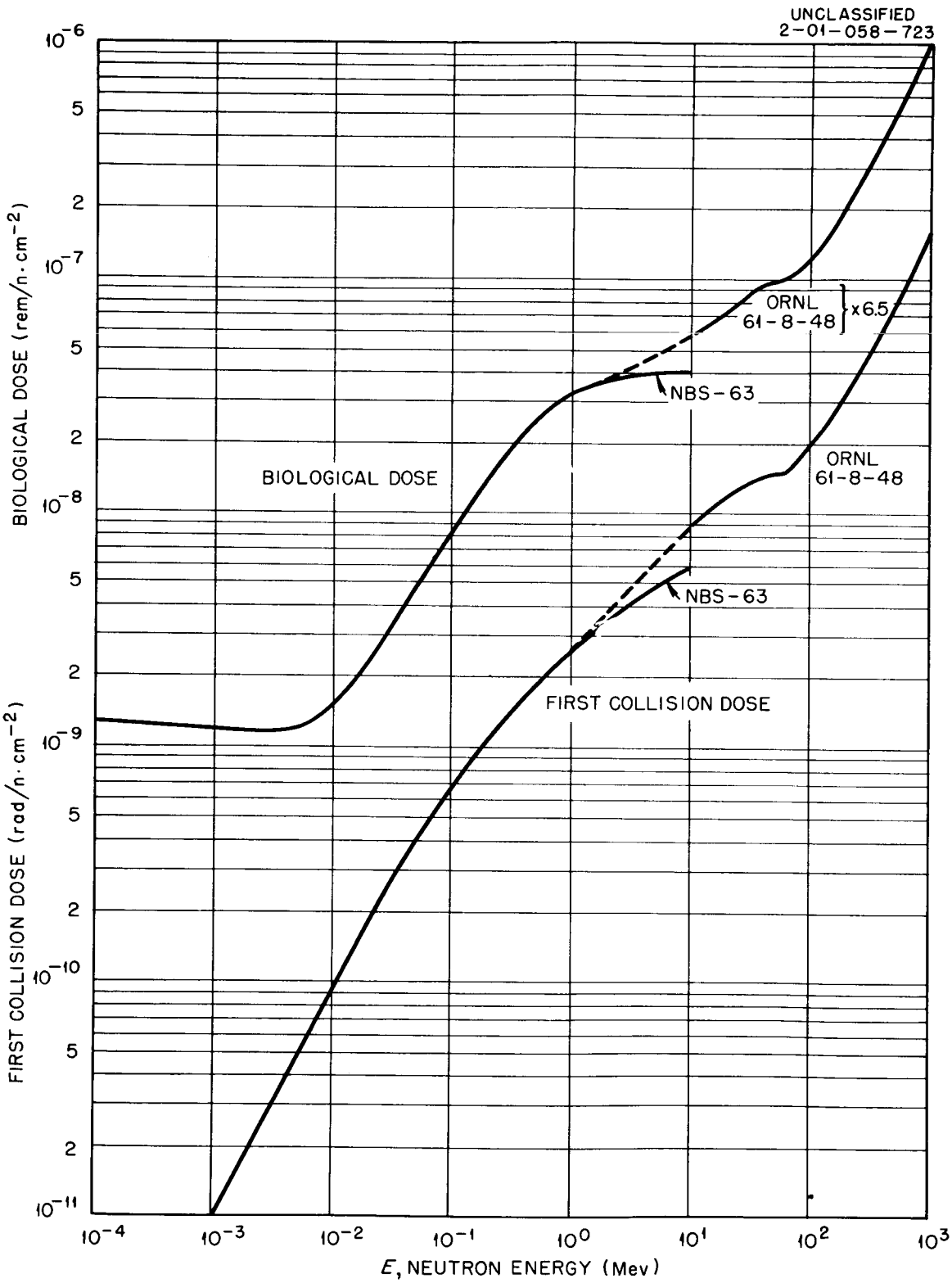

Fig. 29. Biological Dose and Removal Dose as a Function of Neutron Energy.

V. Spectrometry for Gamma Rays From Proton-Bombarded Nuclei

The spectrometer chosen for the preliminary measurements of secondary gamma rays produced by the bombardment of nuclei with ~156-Mev protons was a multicrystal spectrometer. For low-energy (< 2 Mev) photons it will be used as a total-absorption spectrometer, and for photons with energies above 2 Mev, as a pair spectrometer. Multicrystal spectrometers in use at ORNL have been described previously;[23] however, to improve the efficiency, the side crystals were redesigned so that the solid angle subtended by them at the center of the central crystal was greatly increased. The resulting configuration is shown in the photograph on page 586. Each side crystal is a frustum of a cone, with a base diameter of 4.000 in., a top diameter of 3.000 in., and a height of 1.871 in. A semicircular groove is cut into the base along a diameter. Both side crystals are mounted in a thin-walled aluminum can and are optically decoupled. A 3-in. photomultiplier tube, Du Mont Type K-1846, views each side crystal as shown. The central crystal, 1 in. in diameter and $1\frac{1}{2}$ in. in length, fits into the cylindrical hole formed by the semicircular grooves.

A simplified block diagram of electronics, as used for the pair configuration, is shown in Fig. 30. The central crystal is labelled A, the side crystals B and C. The amplifiers are Cosmic Radiation Labs., Inc., Model 901. The introduction of the snip-snap crossover pick-off single-channel analyzers eliminated the requirement for a slow coincidence circuit. The triple coincidence circuit used had a resolving time of ~130 nsec.

For use as a total absorption spectrometer, the snip-snaps in the B and C channels are used as integral discriminators. Their outputs are placed in anticoincidence with the output of the A channel, and the resulting signal is used as the 400-channel analyzer gate.

The detectors are enclosed in a lead housing 6-in. thick on the side nearest the target and at least 4-in. thick on all other sides. During part of the preliminary runs an additional 8-in.-thick layer of lithiated paraffin, intended to reduce the neutron-induced background, surrounded the lead. A collimator through the target side of the housing permits radiation to fall on the central crystal only.

During the initial runs with the pair spectrometer, in which an aluminum target was used, it became apparent that a large background existed that was connected with radiation emanating from the target. The collimator was replaced by a solid lead plug and lithiated paraffin, but the coincidence counting rate was reduced only by about a factor of 2. Removal of the paraffin from the shield did not appear to influence the coincidence counting rate, but removal of the aluminum target reduced it by a factor of more than 10. Similar results were observed later when a copper target was used in the proton beam. The proper functioning of the spectrometer, however, was demonstrated by the data from a carbon target, shown in Fig. 31. It

23. T. A. Love, R. W. Peelle, and F. C. Maienschein, Electronic Instrumentation for a Multiple-Crystal Gamma-Ray Scintillation Spectrometer, ORNL-1929 (Oct. 25, 1955).

Crystals and Photomultipliers of the Gamma-Ray Spectrometer.

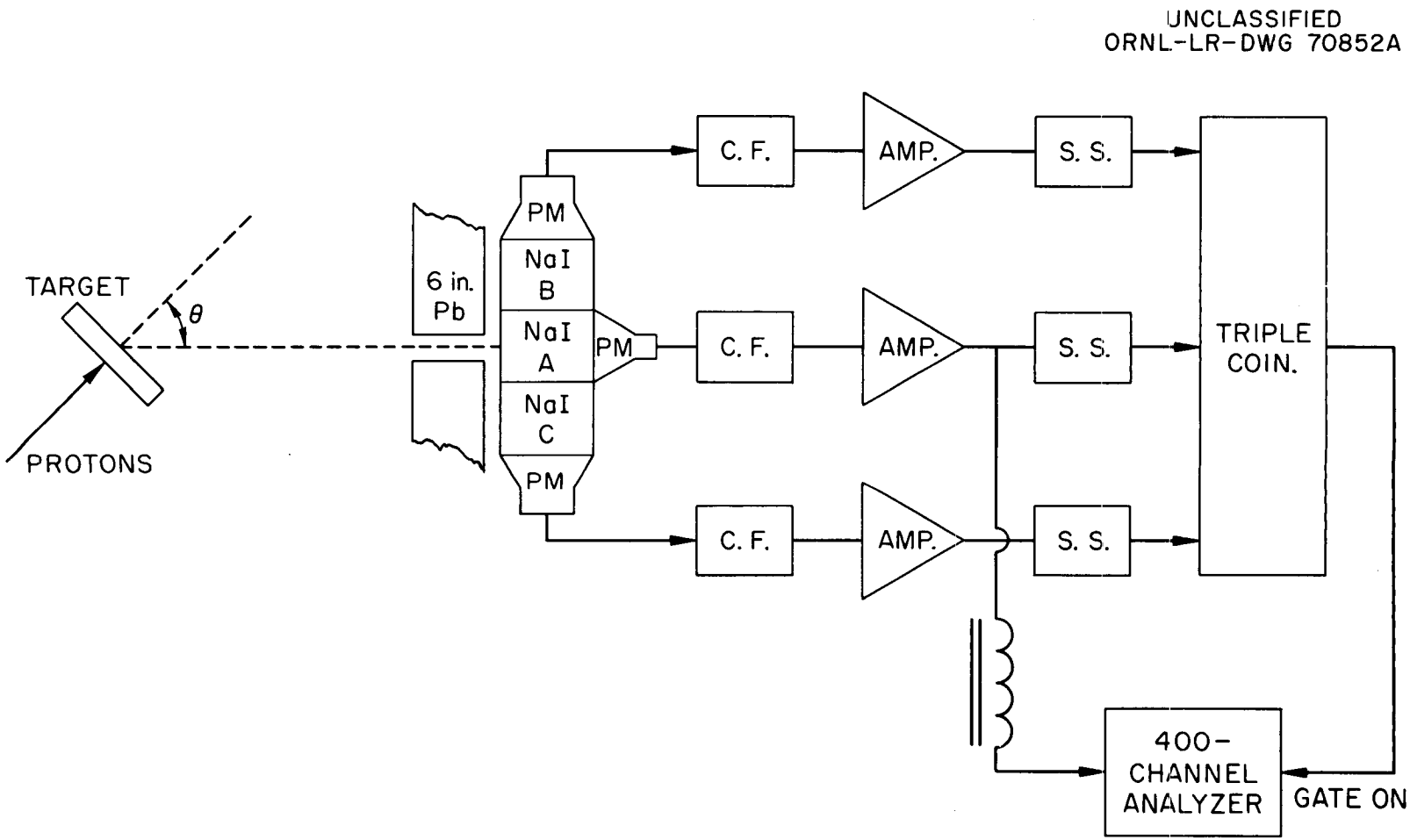

Fig. 30. Original Arrangement of Spectrometer Components in Pair Configuration.

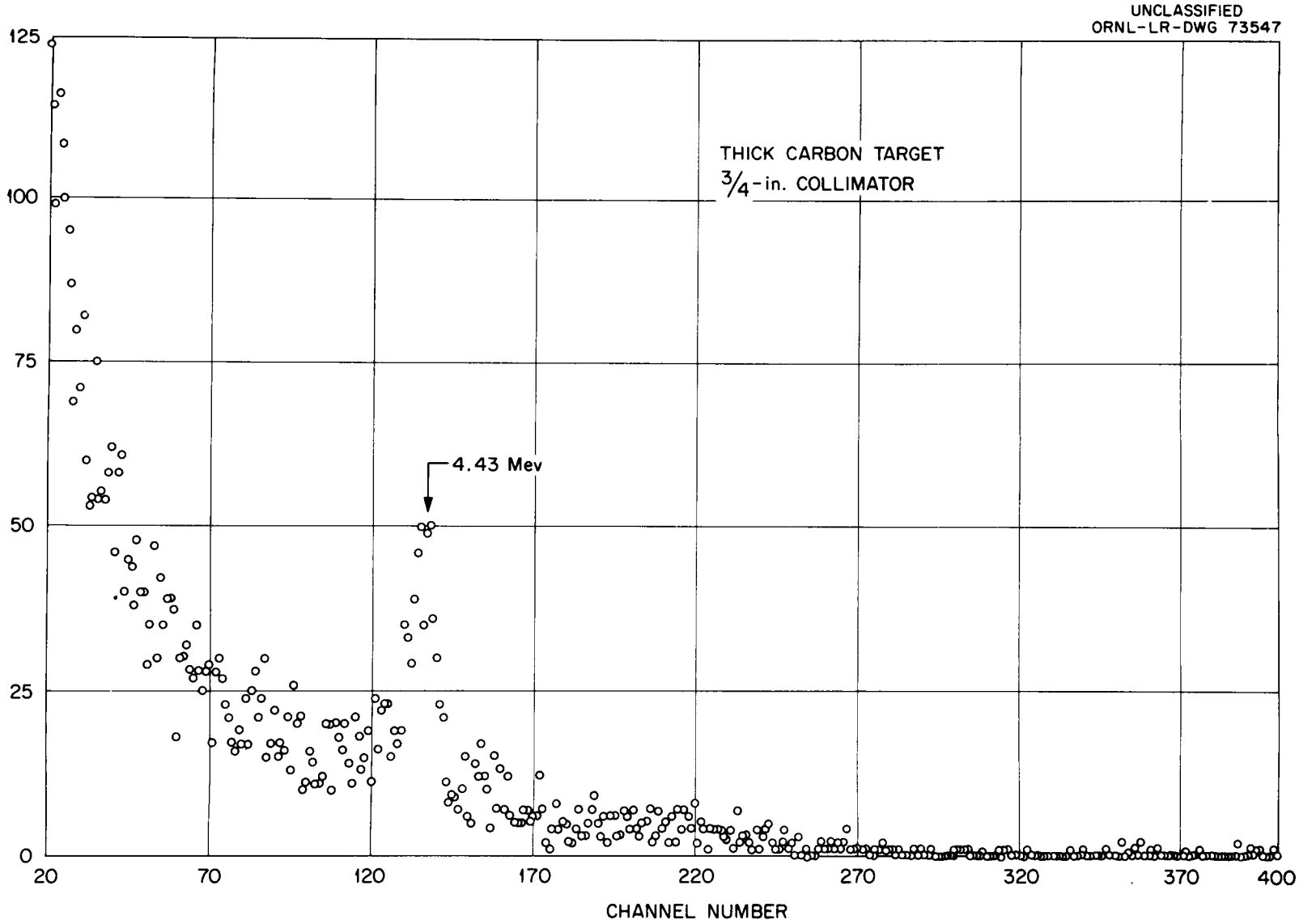

Fig. 31. Uncorrected Pulse-Height Spectrum of Gamma Rays Resulting from Bombardment of a Thick Carbon Target by ~156-Mev Protons.

should be noted that these data are of a very preliminary nature, with no corrections of any type applied. Based upon a rough energy calibration, the very prominent peak appearing at about channel 136 corresponds to a gamma-ray energy of 4.5 Mev. This is in good agreement with the well-known 4.43-Mev gamma ray from carbon.

The results of the trials suggest that the large background is due to neutron-induced radiation. To verify this hypothesis and to minimize the background, several modifications have been made. The shield around the spectrometer has been changed to a greater thickness of lead and a successful attempt was made to reduce the neutron-induced background by using time-of-flight techniques. A block diagram of the revised electronics is shown in Fig. 32. The method depends on the experimental observation that the protons are produced in the machine in bursts, with a frequency depending on the rf of the accelerating voltage. A thin (~1 mm) plastic scintillator detects the beam, and only those gamma rays detected in coincidence with the beam are accepted.

In Fig. 33 is shown the time dependence of the counts recorded in the tunnel diode (TD) fast coincidence circuit of Fig. 32 with the spectrometer viewing a 1.2-proton-range carbon target at 129° and ~145 cm. The peak width of ~12 ns is consistent with the detection of gamma rays in the A crystal. The counting rate at the minimum indicates a small neutron background. At 0°, the neutron background is much larger as would be expected. Figure 34 shows the results at 0° for a distance of ~226 cm.

Preliminary runs were made with the anticoincidence spectrometer and thin (12 Mev) targets of Be, C, and Al. The results for Al, shown in Fig. 35, give peaks at energies corresponding to those previously reported.[24]

24. K. J. Foley et al., Nuclear Phys. 37, 23 (1962).

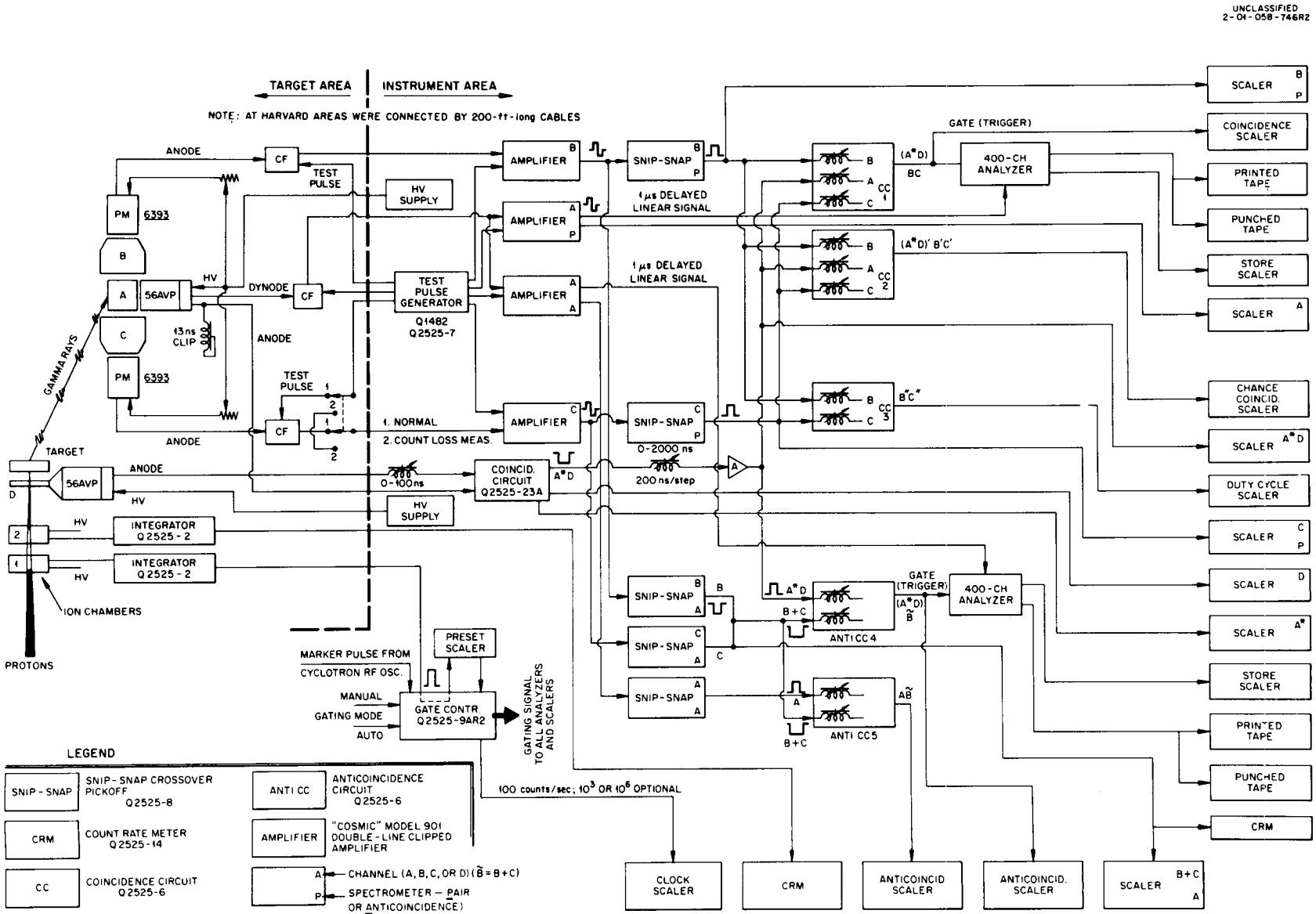

Fig. 32. Block Diagram of Modified Gamma-Ray Spectrometer

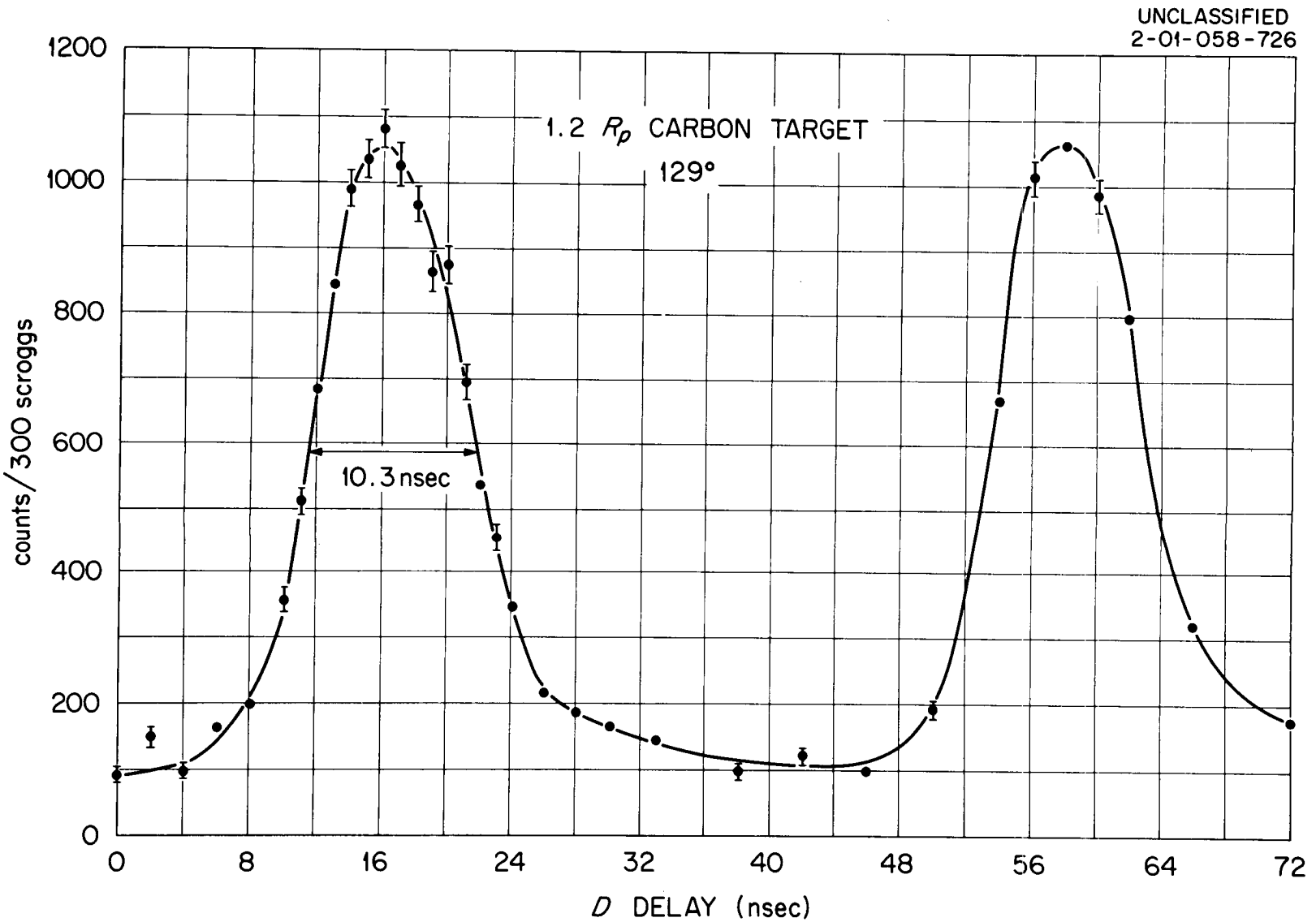

Fig. 33. Delayed Coincidences Between Channel D (Beam Detector) and Channel A (Central Crystal) for a 1.2 R_p Carbon Target at 129° and ~145 cm.

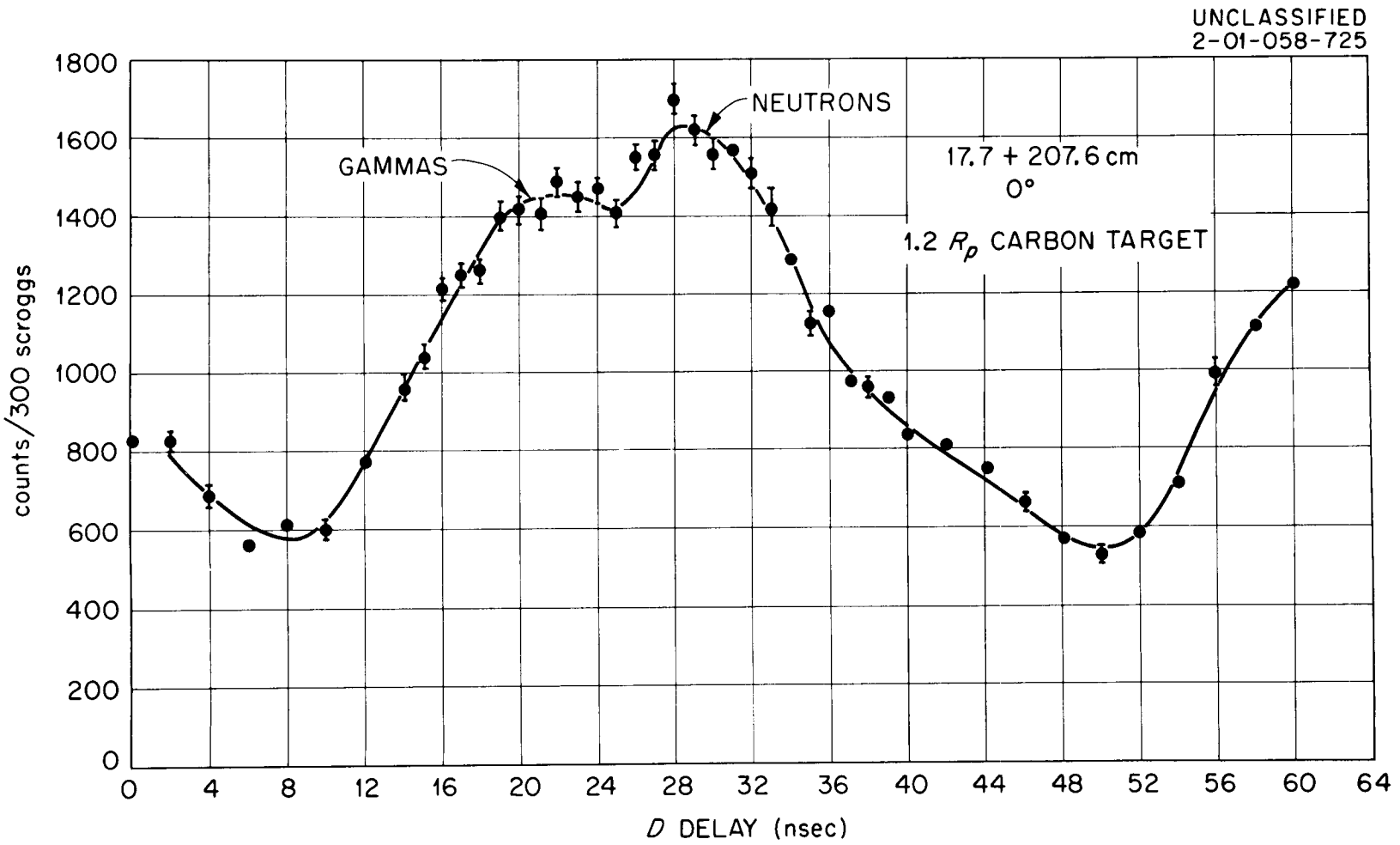

Fig. 34. Delayed Coincidences Between Channel D (Beam Detector) and Channel A (Central Crystal) for a 1.2 R_p Carbon Target at 0° and ~226 cm.

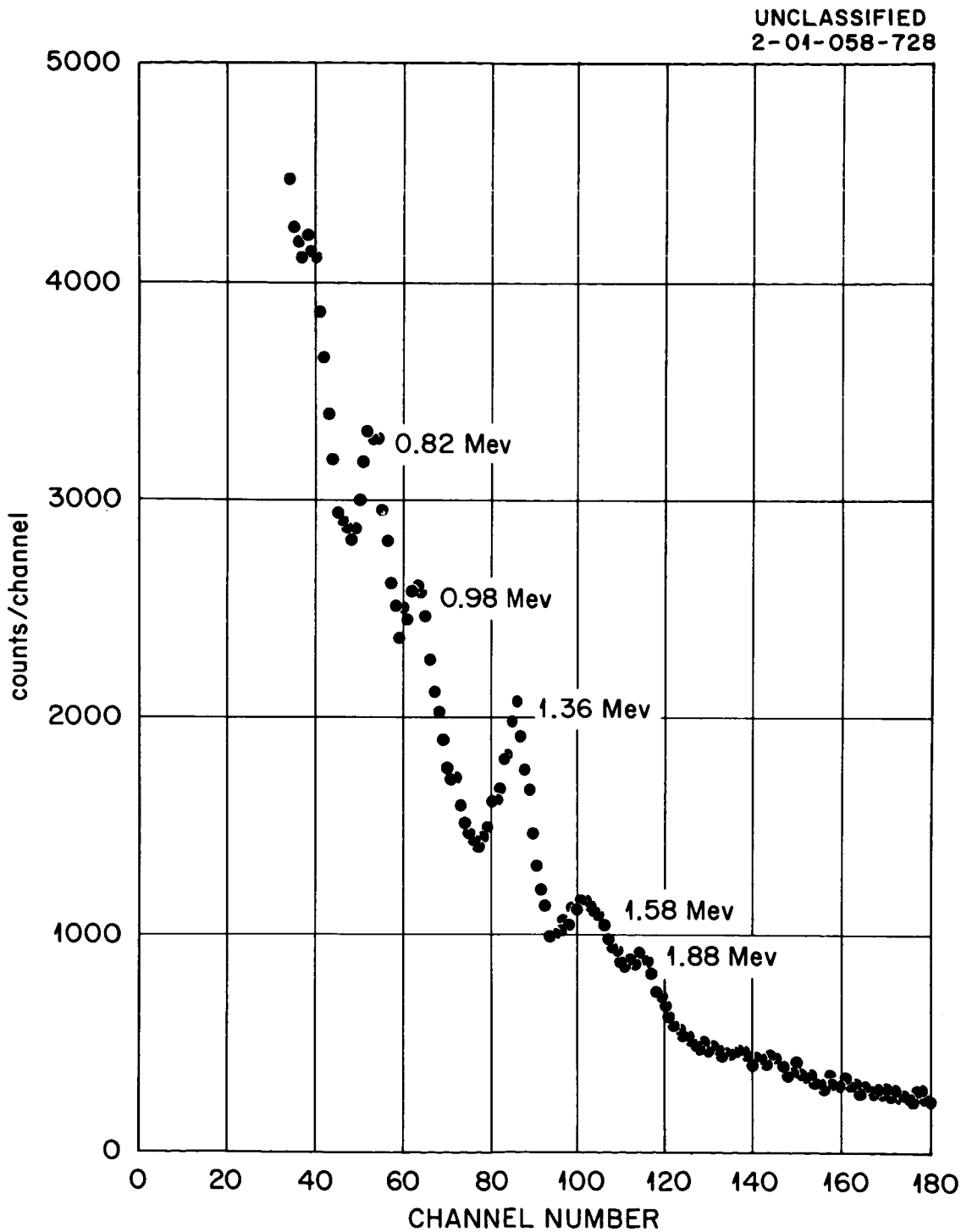

Fig. 35. Gamma Rays from 156-Mev Protons on a 12-Mev-Thick Aluminum Target.

VI. Dosimetry

Measurement of the physical dose resulting from the secondary particles from high-energy reactions would make additional demands upon the calculations. The proper conversion from flux to dose would be required, while for a large object, such as a man or phantom, the penetration through the object and integration over the incident angular distribution would have to be properly taken into account.

The instruments presently used to measure dose from reactor radiations are the results of lengthy development efforts. They measure either the total dose delivered to tissue or the separate contributions from neutrons and gamma rays to the dose.[25] Instruments of either type are not directly useful in the energy range of tens or hundreds of Mev, and another considerable development program will be required to provide dosimeters suitable for such energies. The present effort does not include such a program.

In one of the preliminary experiments at the Harvard accelerator, however, an attempt was made to use dosimeters of the type developed for reactor use in order to obtain very approximate results. A RADSAN, which is a Hurst proton-recoil counter with pulse-height analysis,[26] was used as a neutron dosimeter, and a small, halogen-filled GM counter[27] was used as a gamma-ray dosimeter. The GM counter gives only a single count for any charged particle passing through it, no matter how heavily ionizing, and thus discriminates against proton recoils. Unfortunately, both these instruments respond to high-energy protons with an undetermined efficiency. On a qualitative basis, the walls of the RADSAN were thick enough to stop protons with energies below about 35 Mev. For the relatively thin-walled GM tube, the pertinent parameter in considering the counting efficiency is the reciprocal of the energy loss per unit length, dE/dx. The dE/dx for a 150-Mev proton is roughly equal to that for a 60-kev electron, or three times the dE/dx for an electron in the energy range from ~0.5 to ~10 Mev. Therefore, the efficiency for high-energy protons should be only a few times less than that for recoil electrons produced by gamma rays.

Because of their nondirectional response and low-energy bias, the dosimeters are more responsive to background than are the spectrometers discussed in other sections of this report. Most of their use in the preliminary experiments at Harvard was in attempting to eliminate extraneous room background. As was noted in Section I, backgrounds were reduced by using a slit to restrict the beam and by addition of lead shielding at the point where the beam pipe penetrated the cyclotron shield. The "target-out" background in the horizontal plane of the cyclotron beam was nevertheless

---

25. G. S. Hurst et al., Measurement of Absorbed Dose of Neutrons, and of Mixtures of Neutrons and Gamma Rays, NBS-75, Sec. 3 (1961).

26. E. B. Wagner and G. S. Hurst, Rev. Sci. Instr. 29, 153 (1958).

27. E. B. Wagner and G. S. Hurst, Health Physics 5, 20 (1961).

very large for the gamma-ray dosimeter. This may be noted in Fig. 36. The target-out background increases rapidly as the angle between the beam axis and target counter axis is decreased, that is, as the beam is approached. The effect of shielding by the target at small angles may be seen in the target-in data. Background diminished rapidly as the detector was dropped below the plane of the beam.

In Table 9 are shown the results of measurements with the neutron and gamma-ray dosimeters at 40 cm from 20-cm-diam disk-shaped targets. The scattering angle was 40° for the neutron dosimeter and 50° for the gamma-ray instrument. The values listed, nominally in terms of tissue rad per incident proton, are quantitatively meaningless because of the proton background and are shown only to give an order of magnitude.

Table 9. Response of Dosimeters to Secondary Radiation from 156-Mev Protons Incident on Various Targets

Target	Thickness (g/cm^2)	Dose Rates (see text)	
		Neutrons	Gamma Rays
		($\times 10^{-14}$)	($\times 10^{-14}$)
H_2O	22.2	3.6	0.8
C	23.4	7.2	0.5
Al	26.5	8.9	2.0
Cu	29.4	16.0	2.8
Pb	44	28.0	1.0
none	0	3.8	5.3

Because of their high-energy proton response, the above dosimeters will not be used in future work. However, one dose measurement will be attempted. An ionization chamber will be used in a 42-cm-diam spherical water-filled phantom to determine the response due to all secondaries, regardless of type. The chamber will be moved throughout the phantom to determine the distribution in depth of the response of the ion chamber. The ionization current collected may be related to a physical dose, since the energy required to produce an ion pair depends but little on the type of particle or energy. Correlation with a biological dose, however, is clearly not possible unless the relative biological effectiveness is identical for all of the types of secondaries.

It is estimated that a 20-cc atmospheric-pressure ion chamber with polyethylene walls will yield about 10^{-11} to 10^{-12} amps, depending on position in the phantom, for a beam containing 10^{10} protons (150 Mev) per second. Such a current should be measurable with existing remote-reading electrometers. Determination of backgrounds will require "target-in," "target-out" subtractions. A serious additional background problem will be presented by reflection of secondaries from the laboratory floor.

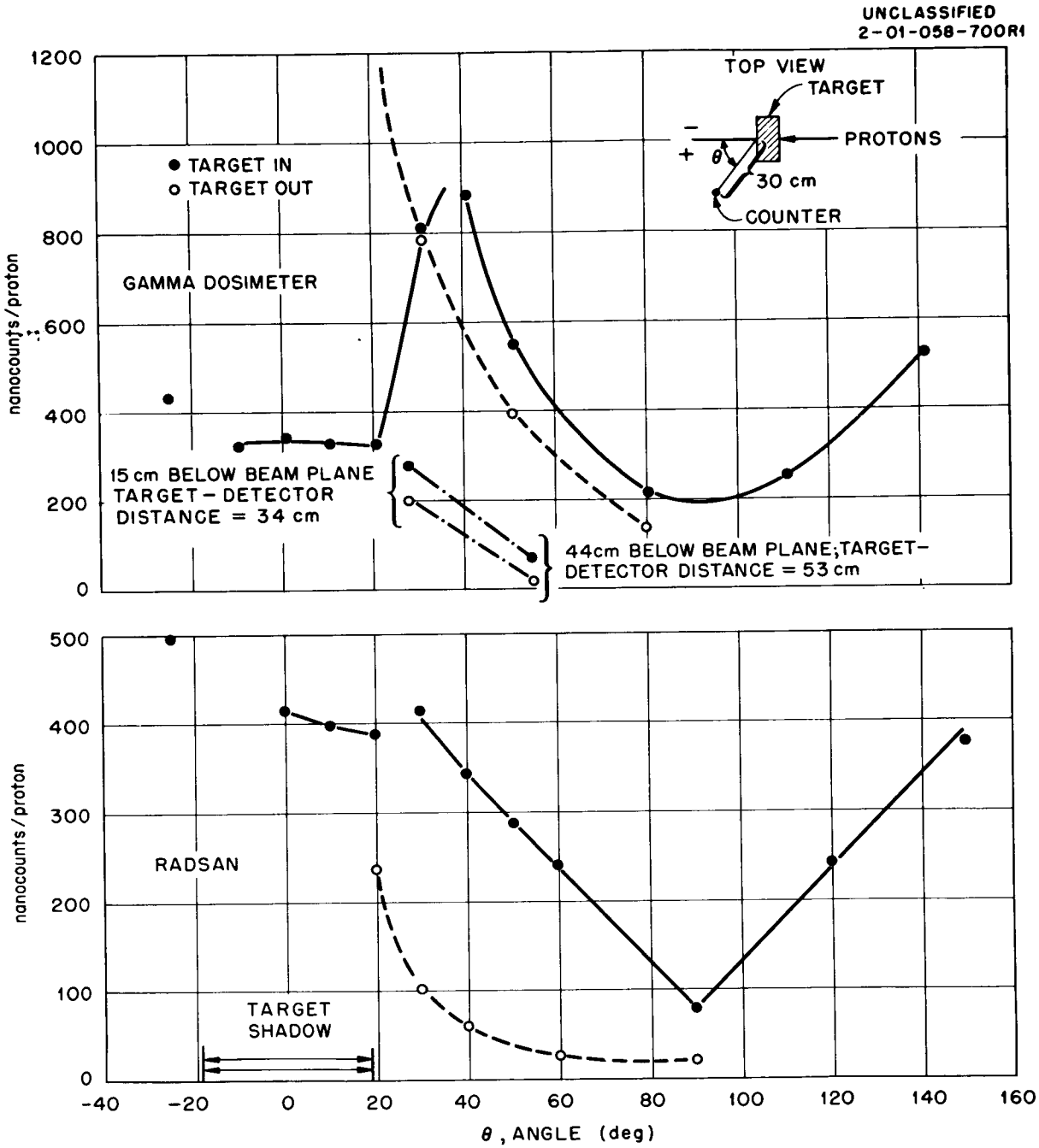

Fig. 36. Angular Distributions with Neutron (RADSAN) and Gamma-Ray Dosimeters Responding to Secondary Particles from a 20-cm-diam by 3.4-cm-thick Cu Target Bombarded by 156-Mev Protons. The target shadow indicates the angular displacement corresponding to the target at the 30-cm radius.

Paper D-5

SECONDARY-PARTICLE DOSE CONTRIBUTIONS INDUCED BY SOLAR PROTON RADIATION*

R. K. Wilson and R. A. Miller
General Dynamics/Fort Worth

15142

Abstract

A study was made to determine the biological hazard due to secondary radiation components produced in bulk shielding by high-energy extra-terrestrial protons. An idealized shield system - spherical-shell shield with a differential-volume water-target at the center - was chosen for the study. A comparison was made of the physical dose due to primary protons penetrating the shield and the secondaries produced in the shield. It was found that (1) shield-target geometry and target model greatly influence the ratio of primary proton-to-secondary component dose, and (2) secondaries may well be important for shield thicknesses greater than about 10 gm/cm^2 in the case of an aluminum shield and a solar-flare proton spectrum.

Introduction

With the prospects of manned flight in cislunar space within this decade, the question arises concerning the potential magnitude of the extraterrestrial radiation hazard to which man will be exposed. Soon after the discovery of the regions of trapped high-energy charged-particles encircling the earth, calculations indicated that no major hazard exists for short transit through these regions. However, the documentation of solar flare effects near the earth indicates that high-energy protons ejected by some solar flares may present a serious radiation hazard to cislunar flight.

Until the questions are answered about the time history and magnitude of the solar cosmic-ray source term, the shielding requirements for a manned space vehicle remain somewhat clouded. However, an area of study which initially requires only a limited amount of source term input - determination of the relative importance of the shielding-produced

*Work supported in part by NASA-MSFC under Contract NAS5-1093.

secondary components - can be considered with some success. Determination of the relative magnitude of the resultant secondary component doses may serve in the future as guidelines for the selection of materials and arrangements for primary component shields.

Dose Components

It should be agreed at the outset that, for such a study of the radiation hazard due to secondary components, a simple geometry be chosen for the shielded system. With this in mind, a spherical-shell shield (Fig. 1) was chosen to represent the system with a point target (differential volume of water) placed at the center. In addition to defining the relative importance of secondaries, a study based on this geometry may serve to define "importance areas" which will require consideration in realistic geometries.

Primary-Proton Component

In order to maintain the simplicity of the system, a point dose for primaries $D_{pp}(T)$ was calculated (Eq. 1) for comparison purposes with the secondary doses. The primary proton dose equation is given by

$$D_{pp}(T) = \int_{E^*(T)}^{E_{max}} dE \left\{ \Phi_p(E) \exp\left[- \int_0^T dx' \sigma_p(E,x') \right] \right\} S_p(E_T), \qquad (1)$$

where $\Phi_p(E)$ is the omnidirectional proton flux in free space as a function of energy E (protons/cm^2-sec-Mev),

$\exp\left[- \int_0^T dx' \sigma_p(E,x') \right]$ is the intensity attenuation due to nuclear collisions, and

$S_p(E,T)$ is the flux-to-dose conversion factor for protons (rads/proton/cm^2) as a function of the energy E_T, with $E_T = g(E,T)$ determined from range-energy curves for the shield material.

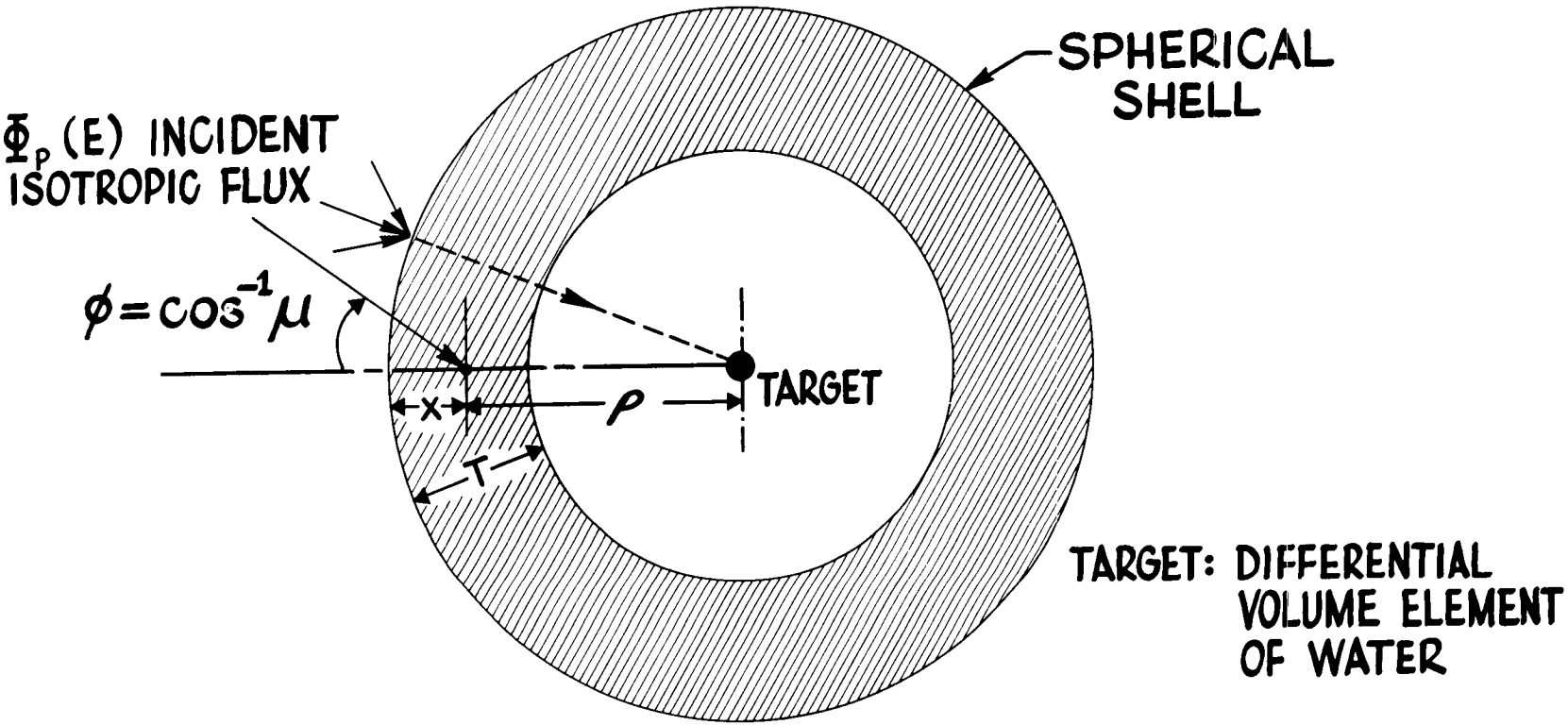

FIGURE I. RADIATION SHIELDING SYSTEM

As indicated by H. J. Schaefer's work[1], the point-target dose may not be the best method for defining shielding requirements; however, all we wish to determine, at this point, is the relative importance of secondaries. In the results section, a comparison of secondary and primary doses will be made on both the point-target and body - phantom basis of defining primary-proton dose received. A body phantom, as the term is used in this paper, is a finite size target representing the astronaut in a "curled-up" position. By using the body phantom method of determining dose, the shielding afforded by other parts of the body is considered in the calculation of the dose at a particular location in the body.

The flux-to-physical dose conversion functions for protons and neutrons shown in Fig. 2 are inferred from results of W. A. Gibson[2]. These curves represent only removal of energy from a particle beam by all processes and not necessarily the deposition of the energy in the body. However, they are presently the best material available for the purpose of representing dose.

Secondary-Particle Component

The type s secondary particle contribution $D_s(T)$ to the total dose can be classically represented by a volume integral of the secondary sources in the shield is given by

$$D_s(T) = \int d\vec{r} \int d\vec{\Omega}' \int dE' \; N_s(\vec{r}, E', \vec{\Omega}') \frac{\Lambda_s(\vec{r}, E', E_t, \vec{\Omega}')}{|\vec{r}|^2} S_s(E_t), \tag{2}$$

where

$N_s(\vec{r}, E', \vec{\Omega}')dE'd\vec{\Omega}'$ is the number of type s secondaries produced as the result of a given primary spectrum per unit volume at $\vec{r}$ in the energy interval dE' about E' and the solid angle interval $d\vec{\Omega}'$ about $\vec{\Omega}'$;

---

1. H. J. Schaefer, Dosimetry of Proton Radiation in Space. U. S. Naval School of Aviation Medicine, Pensacola, Florida, Report No. 19, (June 1961).

2. W. A. Gibson, Energy Removed From Primary Proton and Neutron Beams by Tissue. ORNL-3260 (September 1962).

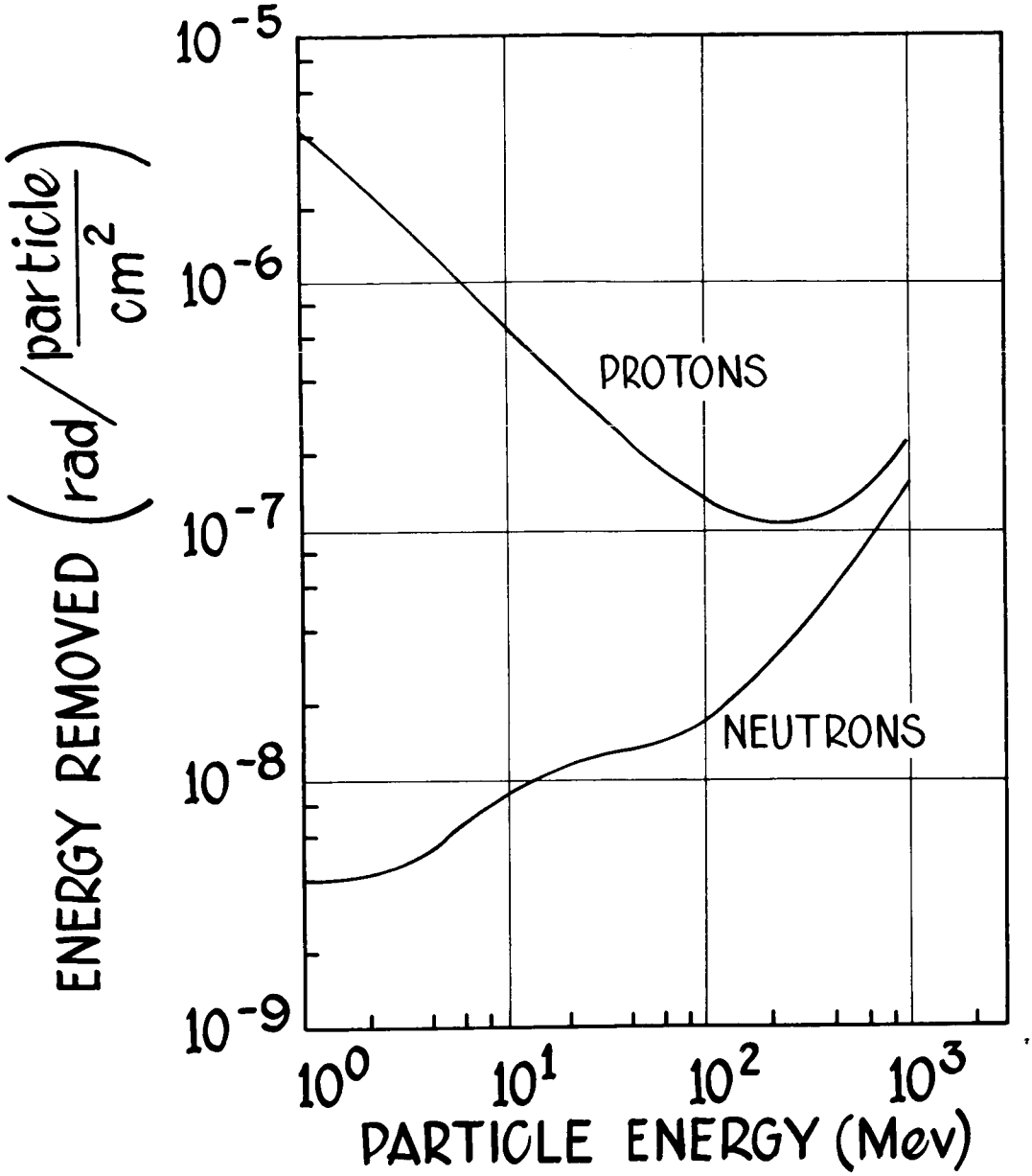

FIGURE 2. ENERGY REMOVED FROM PRIMARY-PROTON AND -NEUTRON BEAMS BY TISSUE

$\Lambda_s(\vec{r}, E', E_t; \vec{\Omega}')$ is a transfer function which considers the type s particle transport from secondary source location, $\vec{r}$, to the target (the term ideally would consider the energy degradation, tertiary production, and angular dependence of the secondary source);

$S_s(E_t)$ is the flux-to-dose conversion factor for type s secondaries which reach the target with degraded energy E_t;

$d\vec{r}$ is the volume (for the spherical shell, $d\vec{r} = \rho^2 d\rho\, d\mu\, d\phi$); and

$|\vec{r}|$ is the distance from the secondary-source location to the target (for the spherical shell, $|\vec{r}| = \rho$).

The secondary-particle source term is given by the equation

$$N_s(\vec{r}, E'', \vec{\Omega}') = \int d\vec{\Omega} \int_{E_s^*(x)}^{E^+} dE'' \left\{ \Phi(x, E'', \vec{\Omega}) \exp\left[- \int_0^{x/\mu} dx' \sigma_R(E'', x') \right] \right.$$

$$\left. \sigma_s^R(E'')\, \bar{n}_s(E'') f_s(E'', E; \vec{\Omega}, \vec{\Omega}') \right\}, \qquad (3)$$

where

$\Phi(x, E'', \vec{\Omega})$ is the primary-proton flux (energy degraded, but not attenuated in intensity) at the secondary-source location x, energy E";

$\exp\left[- \int_0^{x/\mu} dx' \sigma_R(E'', x') \right]$ is the intensity attenuation factor for a proton which arrives at the point x, making an angle $\cos^{-1}\mu$ with the radius, and with energy E";

$E_s^*(x, \mu)$ is the minimum-energy proton at x that can cause a reaction resulting in a type s secondary;

E^+ is some arbitrary upper limit to the energy spectrum;

$\sigma_s^R(E'')$ is the reaction cross section for type s secondary production at the location x by a proton of energy E"; and

$\bar{n}_s(E")$ is the average number of type s secondaries produced per reaction by a proton of energy E";

$f_s(E",E;\vec{\Omega},\vec{\Omega}')$ is the type s secondary energy and angular distribution function so normalized that

$$\int_{4\pi} d\vec{\Omega}' \int dE\ f_s(E",E;\vec{\Omega},\vec{\Omega}') = 1 \qquad (4)$$

Simplifications. An obvious question at this point concerns the assumptions which can be made in order to simplify these equations. One approach which has been used by several investigators[3,4] has been to assume that only primary protons moving initially in the direction of the target produced secondaries which would contribute to the dose. This assumption is based on the fact that high-energy secondaries* are given off essentially in the direction of the incident, reaction-producing proton. However, low-energy secondaries are produced with an angular distribution which is more nearly isotropic, and the "straight-ahead" approximation cannot be used without some modification in the "spirit" of its use (see Fig. 3).

If this "straight-ahead" assumption is to be used for all secondary components, it is necessary to determine some approximate secondary-source intensity in the direction of the target for each secondary component. One approach is suggested by considering the reaction rate R (reactions/gm-Mev) of protons with energy E" at the location x as given below:

---

3. J. H. Tolan, Ed., Shielding Problems in Manned Space Vehicles. Lockheed Nuclear Products (Marietta, Ga.), Report NR-140 (September 1961).

4. R. G. Alsmiller, Jr., et al., Nuclear-Meson Cascade Calculations: Traverse Shielding for a 45-Gev Electron Accelerator (Part 1). Oak Ridge National Laboratory Report ORNL-3289 (1962).

* High-energy secondaries are defined here as those secondaries which are produced essentially in the direction of the primary (fairly well approximated by an energy limit of $E_s > 20$ Mev).

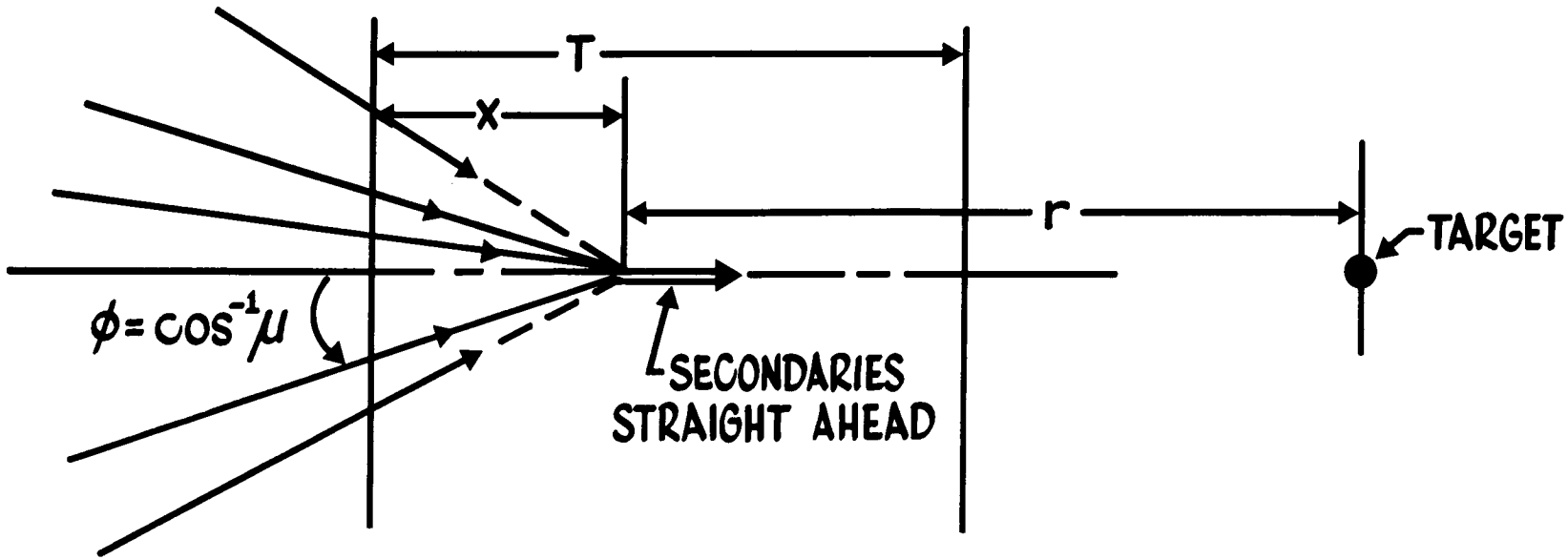

FIGURE 3. SECONDARY-PARTICLE STRAIGHT-AHEAD GEOMETRY

$$\sigma_s^R(E'')\int d\vec{\Omega}\ \Phi(x,E'',\vec{\Omega}) = R. \tag{5}$$

The question is: How can the type s secondary flux in the direction of the target be related to the reaction rate, R_o, due to primary protons moving initially in the inward radial direction? The answer is found in the ratio $A(x,E'')$ of the normalized secondary flux to the reaction rate R_o (Eq. 6):

$$A(x,E'') = \frac{\sigma_s^R(E'')}{R_o}\left\{\int_{2\pi} d\vec{\Omega}\ \Phi(x,E'',\vec{\Omega})\int_0^{E''} dE\ f_s(E'',E;\vec{\Omega},\vec{\Omega}_o)\right\} \tag{6}$$

Ultimately, $A(x,E'')$ serves as a "weight" function which allows the explicit integration over $\vec{\Omega}$ to be dropped in the secondary source term (Eq. 3).

For the region of the shield from which most of the secondaries are produced near the incident face (in the case of a "typical" flare spectrum), $A(x,E'')$ is reasonably constant as a function of x. The energy dependence of $A(x,E'')$ is considered through the type of secondary component which the primary produces, i.e., evaporation or cascade particles. On the basis of the above remarks, it can be seen that not much generality is lost in assuming that $\bar{A}$ (an average A) can be determined for each of the secondary components. For cascade neutron and proton particles, which are the result of direct high-energy interaction in the nucleus, A is found to be approximately equal to 1. It was found that an $\bar{A}$ equal to 1/4 could be used to weigh the source intensities for evaporation and low-energy cascade particles.

As a result of these several approximations, the secondary-component dose equation can be written in the form

$$D_s(T) = \bar{A}\int_0^T dx\int dE'\left\{\int_{E_s^*(x)}^{E} dE\,\Phi_p(E)\,\exp\left[-\int_0^x dx'\sigma_R(E,x')\right]\right.$$
$$\left.\sigma_s^R(E'')\,\bar{n}_s(E'')g_s(E'',E)\right\}\Lambda_s(x,E',E_t)S_s(E_t) \tag{7}$$

where the terms not defined previously are

$\Phi_p(E)$ is the omnidirectional-proton flux incident on the system in terms of the free-space proton energy E (protons/cm^2-sec-Mev),

$\exp\left[-\int_0^T dx'\sigma_R(E,x')\right]$ is the intensity attenuation due to nuclear-collision removal, and

$g_s(E'',E)$ is the type s secondary-particle energy distribution function.

Results of Dose Calculations

The secondary-component-dose equations were solved as a function of shell thickness for several incident-proton spectra and material compositions[5]. Figure 4 shows the variation of the physical dose rate with thickness of an aluminum shield for the 10 May 1959 flare spectrum[6] (measured 33 hours after onset). In order to appreciate the relative significance of the secondary components, the primary-proton dose contribution is given in terms of both the point-target and body-phantom (52-cm-diam sphere of water, representing a man in the fetal position) volume dose, evaluated 5 cm below the surface of the phantom. If the secondary-component doses are compared to that due to the primaries evaluated in terms of the body-phantom model, one observes that the secondaries are indeed significant*. The relative flatness of the neutron-dose curve as a function of shield thickness can best be explained by the realization that the low-energy portion of the flare spectrum generates the majority of the secondaries. From the spectrum shown in Fig. 4, one can see that more than 95% of the particles incident on the shield are removed by ionization losses before they penetrate 10 gm/cm^2 of aluminum. Some of these particles, however, undergo neutron-producing reactions before they are stopped through energy degradation by ionizing losses.

5. R. K. Wilson, R. A. Miller, and R. L. Kloster, A Study of Space Radiation Shielding Problems for Manned Vehicles. GD/FW Report FZK-144 (June 1962).

6. J. R. Winckler and P. D. Bhavsar, J. Geophys. Res. 65, (1960) 2637.

* If the respective RBE (relative biological effectiveness) values were used to determine biological dose, the secondary component doses would doubtlessly appear even more important; however, the RBE values for the high-energy secondaries presently are only estimated.

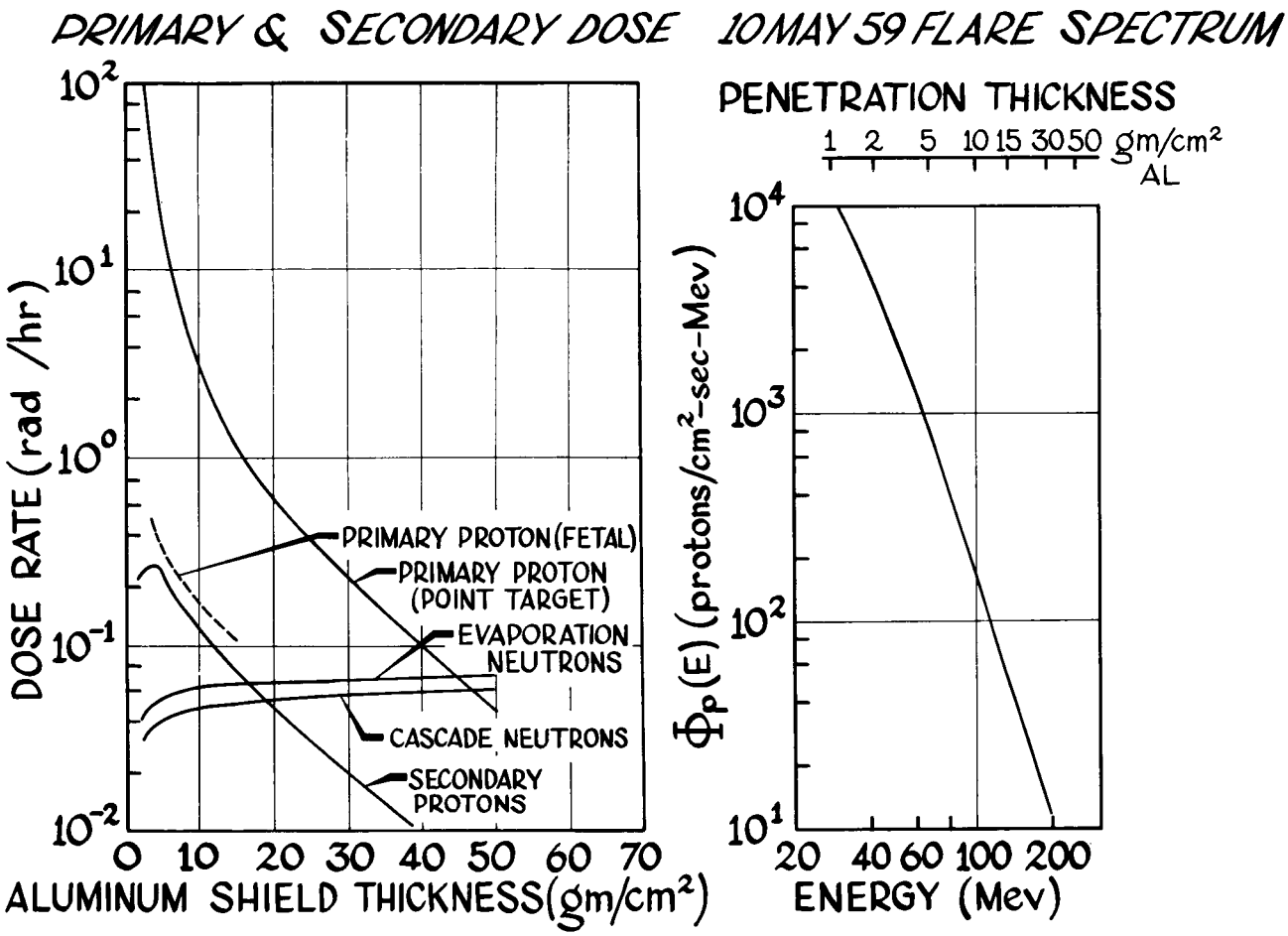

FIGURE 4. CALCULATED DOSE COMPONENTS FOR THE 10 MAY 1959 SOLAR-FLARE PROTON SPECTRUM AS MEASURED 32 HOURS AFTER ONSET (SHIELD GEOMETRY SHOWN IN FIGURE 1)

Thus, it is seen that the greater portion of the secondaries are formed near the outer surface of the shield. This would suggest the need for selection of a low-secondary-producing outer surface of a vehicle.

The order of magnitude difference in the two methods of defining dose for a particular thickness of shielding gives some idea of the problems encountered in defining the radiation dose an astronaut would receive. This difference in primary-proton dose is principally a problem of geometry and the consideration of a finite size target. The geometry of a space capsule can thus be seen to affect greatly the dose received.

The dose-rate curves shown in Fig. 5 for the same shield and the Van Allen inner-belt proton spectrum[7] indicate the secondary contribution is much less significant for this spectrum. This result is primarily due to the much harder inner belt spectrum (Fig. 5). With the hard spectrum, the secondaries are formed rather uniformly across the shield and not just at the surface.

Conclusion

It can be concluded from the results presented that, under the assumption a solar-flare primary-proton hazard exists for manned-space flight, the secondary-particle production in the vehicle skin must be considered. Certainly it should not be inferred that the secondaries will be an all-consuming problem, but rather that they warrant further study and consideration in the selection and arrangement of shielding materials.

---

7. S. C. Freden and R. S. White, Phys. Rev. Letters 3, 9 (1959).

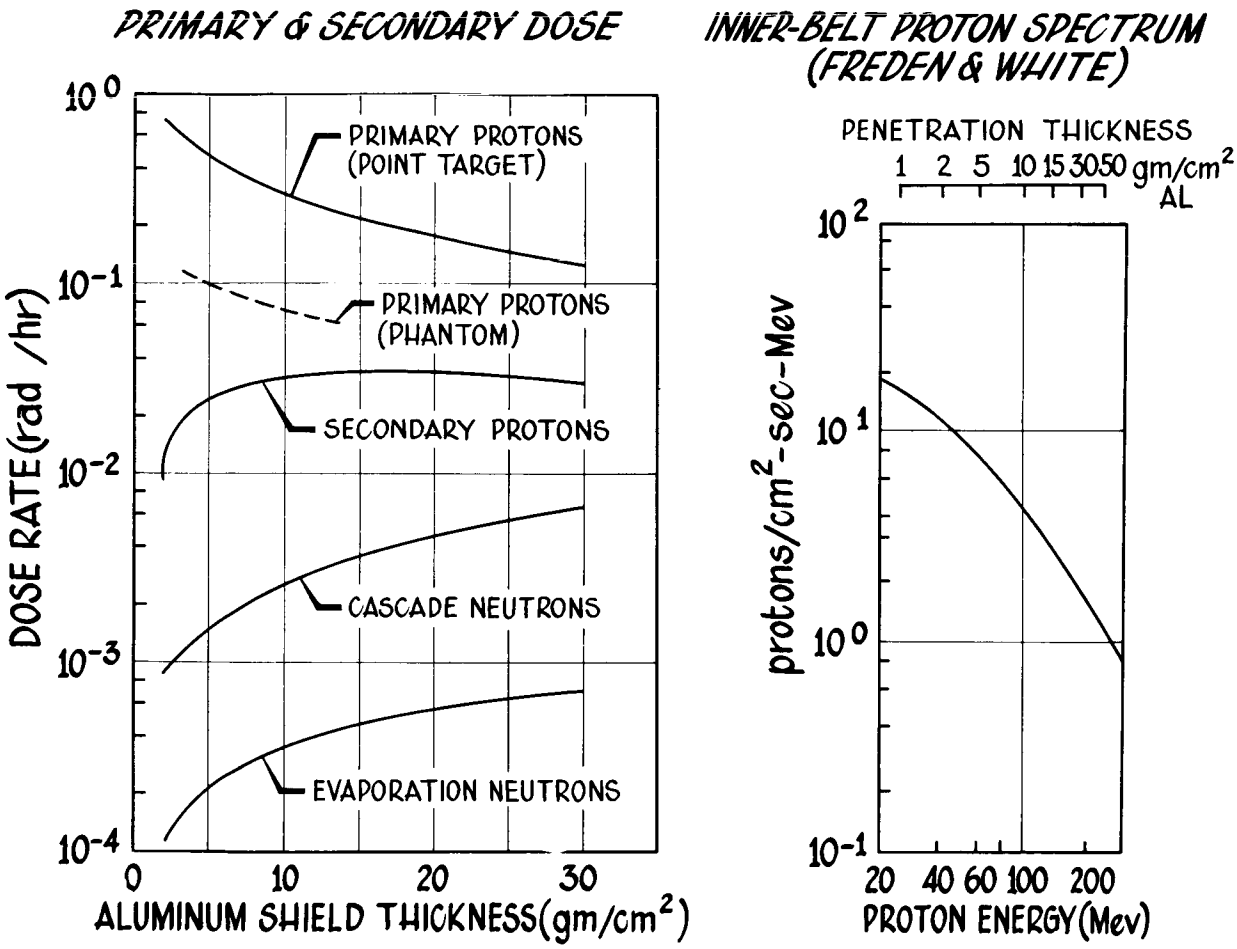

FIGURE 5. CALCULATED DOSE COMPONENTS FOR THE INNER VAN ALLEN BELT PROTON SPECTRUM (SHIELD GEOMETRY SHOWN IN FIGURE 1)

Paper D-6

A SERIES OF MONTE CARLO CODES TO TRANSPORT NUCLEONS THROUGH MATTER

W. E. Kinney, R. R. Coveyou, and C. D. Zerby
Oak Ridge National Laboratory

Abstract 15743

A series of Monte Carlo codes for the IBM-7090 computer has been written to transport nucleons of energy less than 400 Mev through complex configurations composed of four or fewer materials. The nucleons above 50 Mev are treated by a high-energy transport code which uses an intra-nuclear cascade subroutine to compute the production of secondary nucleons. Below 50 Mev, protons are allowed to proceed straight ahead with no nuclear interactions and neutrons are transported by the already existing 05R code. Doses in tissue behind aluminum slabs of varying thickness estimated from 1940 400-Mev source protons and their descendants showed the primary beam dose to be more than a factor of two larger than the dose due to all secondaries.

The interaction of a high-energy nucleon with the material of a radiation shield initiates a complex avalanche of lower energy secondary particles which proceeds through the shield, increasing in population and decreasing in total energy. It is essential to the design of a space vehicle shield to know the behavior of such an avalanche as a function of energy and shield thickness.

In general, a high-energy nuclear interaction produces first of all several secondary nucleons which are due to direct interactions of the incident particle with the nuclear constituents and which have energies ranging from a few Mev to a large fraction of the incident particle energy. There is left a highly excited recoiling nucleus which rids itself of most of its excess energy by evaporating nucleons and heavy particles of relatively low energy of the order of a few Mev.

A calculational method which may include as much detail as desired and which is relatively easy to program for a computer is the Monte Carlo method. It performs an idealized experiment on a system whose properties are completely known with counters of known resolution and 100% efficiency. As with any counting experiment, however, it is subject to counting uncertainties and so a balance must be struck between counting statistics and the cost of a calculation.

The Monte Carlo method has been used in 05R,[1] a code for the IBM computers to treat neutron transport at fission energies and below. At energies greater than fission, two circumstances prevent a high-energy nucleon transport code from being a simple extension of 05R. First, nuclear interactions absorb the parent nucleon and produce a number of secondary nucleons. In 05R a neutron never disappears by absorption at a collision but rather continues with its statistical weight multiplied by the nonabsorption probability at the energy of the collision. Secondly, protons lose energy in flight due to ionization collisions, and account must be taken of this effect. For these reasons, then, the nucleons are transported by a separate code down to some appropriate boundary energy, while below the boundary protons are transported straight ahead and neutrons are treated by 05R. A suitable boundary energy is 50 Mev since that is an energy below which most evaporation particles are emitted, the direct interaction calculational model does not apply, and the proton range is small.

The series of codes will first be described in a general way. The high-energy transport and 05R source preparation codes will next be discussed in some detail. Finally some typical results will be presented and future plans indicated.

A General Description

The series of codes, all written for the IBM-7090, will transport nucleons of energies up to 400 Mev through arbitrary complex configurations containing four or fewer media each of which may be composed of as many as ten isotopes. A very schematic flow chart of the code series is given in Fig. 1. The nucleons are introduced into the system and transported through the 400- to 50-Mev region by the high-energy transport code. When a nucleon escapes from a medium, has a collision, or slows down past 50 Mev, details of the event such as the position and velocity of the nucleon at the time of the event are recorded on a history tape. The only task assigned to the code is the tracing of particle paths in phase space and recording information at significant points along the paths. This method was originally used in 05R to allow freedom in the manner of analyzing the particle trajectories and also to allow saving the data for possible future reanalysis for additional information.

The 05R source preparation routine uses the history tape from the high-energy transport code to do four things: (1) estimate the desired high-energy nucleon distributions, (2) complete the intra-nuclear cascades by evaporating additional nucleons from the highly excited residual nuclei, (3) estimate the distribution of protons below the boundary energy, and (4) prepare a neutron source tape for 05R of neutrons below the boundary energy.

---

1. R. R. Coveyou, J. G. Sullivan, and H. P. Carter, "The 05R Code: A General Purpose Monte Carlo Reactor Code for the IBM-704 Computer," Codes for Reactor Computations, p. 267, International Atomic Energy Agency, Vienna, 1961.

05R transports neutrons below 50 Mev starting them according to the source tape from the source preparation routine. The position of collisions and escapes and the velocities of the neutrons before and after collisions are recorded on the 05R history tape. Finally, the 05R analysis code uses the 05R history tape to estimate the desired distributions of neutrons below 50 Mev.

The High-Energy Transport Code

A general flow chart of the high-energy transport code is given in Fig. 2. The calculation starts by specifying the upper and lower energy limits of the calculation, the atomic number, atomic weight, nuclear density, and effective ionization potential for each isotope of each medium, the desired number of source particles to be treated, a description of the geometry of the problem, and any source information required by the source subroutine.

A range table is then prepared containing values of the range at 101 equally spaced values of the energy between the upper and lower energy limits. An inverse range or energy table containing values of the energy corresponding to 101 equally spaced values of the range from the maximum range to zero range is also computed. Quantities in both tables are assumed to vary linearly between entries.

Flexibility in the geometry is achieved by using Irving's general purpose geometry subroutine.[2] Briefly, it subdivides space into a number of parallelepipeds each of which may be further subdivided by several quadratic surfaces. Given the end points of a line, the subroutine gives the coordinates of the point of intersection of the line with the nearest intervening surface, if any.

The repetitive portion of the code starts by calling the source subroutine to select a source particle. This subroutine is arbitrary and is written to satisfy the requirements of the problem at hand.

A flight distance, d, is next selected from the distribution $\Sigma e^{-\Sigma d}$, where Σ is the total macroscopic geometric cross section.* If the particle being treated is a proton, its energy at the end of the flight is computed by interpolation in the inverse range table. If a proton has crossed the lower energy limit within the distance d or if the particle, proton or neutron, has escaped from the system, the position of the energy or spatial boundary crossing is recorded on the history tape and interest in the particle ceases for this code. If the particle has

---

2. D. Irving, Neutron Physics Division Annual Progress Report for Period Ending September 1, 1962, Oak Ridge National Laboratory Report ORNL-3360, p. 230 (1962).

*The largest proton cross section in the energy range, the n-p cross section at the lower energy limit, plays the role of a geometric cross section for hydrogen.

neither slowed past the energy boundary nor escaped, it suffers a nuclear interaction. The jth nucleus is selected as the target nucleus by the requirement that

$$\sum_{i=1}^{j-1} (\Sigma_i/\Sigma) < R < \sum_{i=1}^{j} (\Sigma_i/\Sigma),$$

where R is a random number uniform on the unit interval, Σ_i is the ith isotope geometric macroscopic cross section and

$$\Sigma = \sum_{i} \Sigma_i .$$

If the target is not hydrogen, Bertini's cascade subroutine[3] is given the energy and type of incident particle and the atomic weight and number of the target and it returns the number, type, energy, and direction cosines of the cascade products. The subroutine has built into it an energy variation of the interaction cross sections and allows the passage of the incident particle through the nucleus with no interaction whatever. Collisions with hydrogen are treated by storing the n-p and p-p cross sections as functions of energy. A random number R is tested against $[\sigma_{np}(E)/\sigma_{max}]$ or $[\sigma_{pp}(E)/\sigma_{max}]$ for incident neutrons or protons, respectively, where $\sigma(E)$ is a microscopic cross section at energy E and σ_{max} is the pseudo-microscopic geometric cross section for hydrogen. If R is less than the ratio, a scattering takes place as an apparent cascade with two particles emitted. If R is greater than the ratio, the particle continues with no collision.

When there is a nuclear collision, the following details are recorded on the history tape:

1. The type of colliding particle, neutron or proton,
2. the position, energy, and velocity of the colliding particle at its birth,
3. the position of the collision and the energy of the colliding particle at collision,
4. the number, type, energy, and velocity of the product nucleons having energies above the lower energy limit,

---

3. H. W. Bertini, Neutron Physics Division Annual Progress Report for Period Ending September 1, 1961, Oak Ridge National Laboratory Report ORNL-3360, p. 137 (1962).

5. the number, type, energy, and velocity of the product nucleons having energies below the lower energy limit,

6. the atomic number and weight, and the excitation and recoil energies of the residual nucleus.

The data for the product nucleons with energies above the lower energy limit are saved in the fast memory as well as being put on the history tape so that they may be transported in turn. The colliding particle, of course, disappears and the question is asked whether or not all the descendants of the starting source particle with energies above the lower energy limit have been treated. If they have not, the next descendant is chosen as the transported particle, a flight distance is selected, and the entire process is repeated. When all the descendants have been treated, a test is made to see whether or not the desired number of source particles have been considered. If they have not, another source particle is selected by calling the source subroutine and the steps are repeated from point 1 in the flow chart.

The 05R Source Preparation Routine

The functions of the 05R source preparation routine are summarized in Fig. 1 and the flow chart shown in Fig. 3 indicates how they are performed. A record is first read into the memory from the high-energy transport history tape and an arbitrary Analysis I subroutine is called to analyze the particle history and determine its contribution to whatever distributions are being estimated.

If the record was that of a particle which escaped from the system, the code has no further interest in the particle. If the record shows the particle (necessarily a proton) slowed down past the lower energy limit of the high-energy code, the arbitrary "Analysis II" subroutine is called to treat protons below that energy limit. If the record is one of a particle interaction then the code determines whether there are any product nucleons below the lower energy limit and, if there are, treats protons with the "Analysis II" subroutine and writes the neutron data on the 05R source tape. Finally, particles are evaporated from the excited residual nucleus by calling a subroutine version of Dresner's evaporation code[4] with the resulting protons being referred to "Analysis II" and the neutron data being put on the 05R source tape. Provision is also made in the code to record the spatial distribution of evaporated heavy particle energy and final residual nucleus energy.

The 05R Code and Its Analysis Routine

The 05R code has been described elsewhere.[1] For its application here, provision was made to treat nonelastic events by means of an

4. L. Dresner, EVAP - A Fortran Program for Calculating the Evaporation of Various Particles from Excited Compound Nuclei, Oak Ridge National Laboratory Report ORNL-CF-61-12-30 (Dec. 19, 1961).

abbreviated version of Dresner's evaporation subroutine which allows only nucleon and alpha particle emission. (It should be pointed out that a present limitation in 05R is the restriction of elastic scattering to a P_1 center-of-mass angular distribution.) 05R writes a history tape similar to that of the high-energy transport code, recording the details of the neutron paths in phase space. The 05R analysis routine has been left entirely open to be written as the needs of a particular problem dictate.

Typical Results

Some results from the series of codes treating 400-Mev protons incident normally on infinite slabs of aluminum are shown in Fig. 4. The partial dose rates in rads per hour per unit incident current in a thin tissue slab behind aluminum shields of varying thickness are plotted as a function of thickness. The flux-to-dose conversion factors were those used by Alsmiller[5] and are shown in Fig. 5. It is of interest to notice that the contribution of all the secondary doses never comes up even to one-half the primary dose contribution. The statistical fluctuations are not indicated but become quite large for the secondary protons at thicknesses larger than 50 cm. The results were obtained from 1940 incident protons and the machine time required was 32 minutes in the high-energy transport code, 18 minutes in the 05R source preparation routine, 18 minutes in 05R, and 20 minutes in the 05R analysis.*

Future Plans

It is planned to raise the upper energy limit of the code above the present 400 Mev as Bertini's intra-nuclear cascade calculation is improved to apply to the higher energies. It will then become necessary to include pions as well as nucleons. 05R is in the process of being changed to accommodate a more general elastic scattering angular distribution than is presently allowed.

---

5. R. G. Alsmiller, Jr., F. S. Alsmiller, and J. E. Murphy, Nucleon-Meson Cascade Calculations: Transverse Shielding for a 45-Gev Electron Accelerator, Part I, Oak Ridge National Laboratory Report ORNL-3289 (1962).

*The machine times go down as (1) the medium thickness decreases, (2) the atomic weights of the elements in the medium decrease thus yielding fewer secondaries in a nuclear interaction, (3) the incident nucleon energy decreases, and (4) the analysis routines simplify. To compute partial doses as a function of depth in 30 cm of tissue using 2000 400-Mev protons required 11 minutes in the high-energy code, 9 minutes in the 05R source preparation routine, 14 minutes in 05R, and 2 minutes in the 05R analysis.

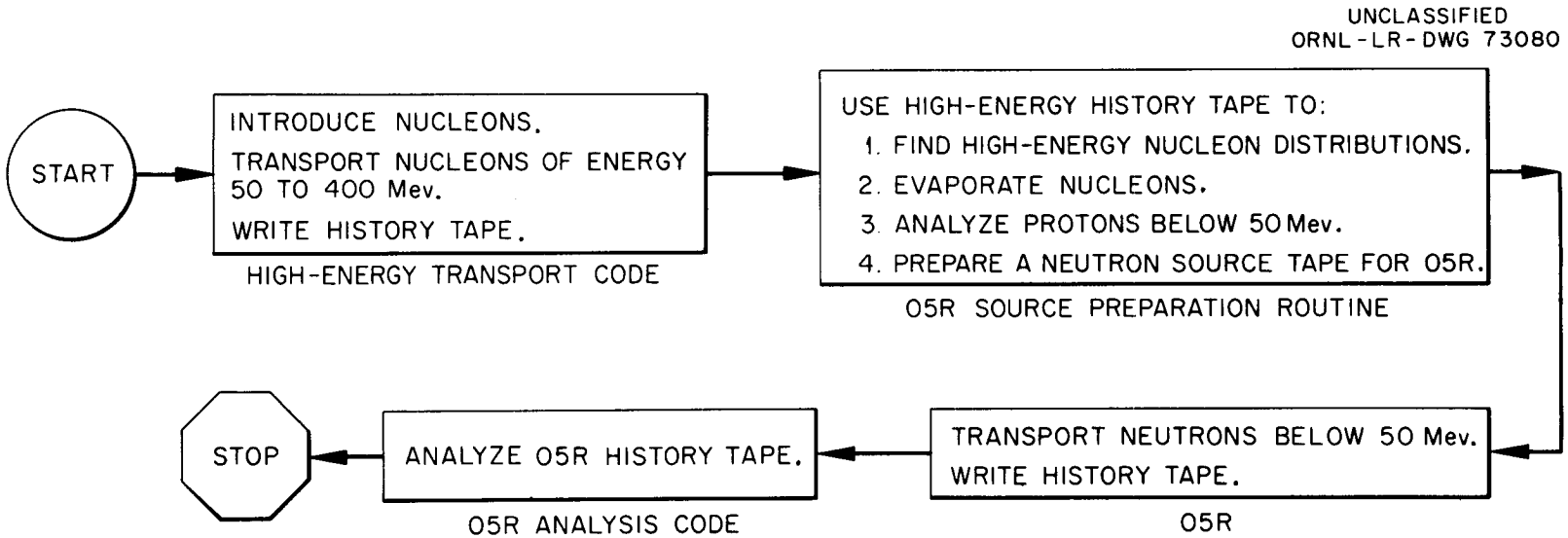

Fig. 1. A Flow Chart for the Series of Nucleon Transport Code.

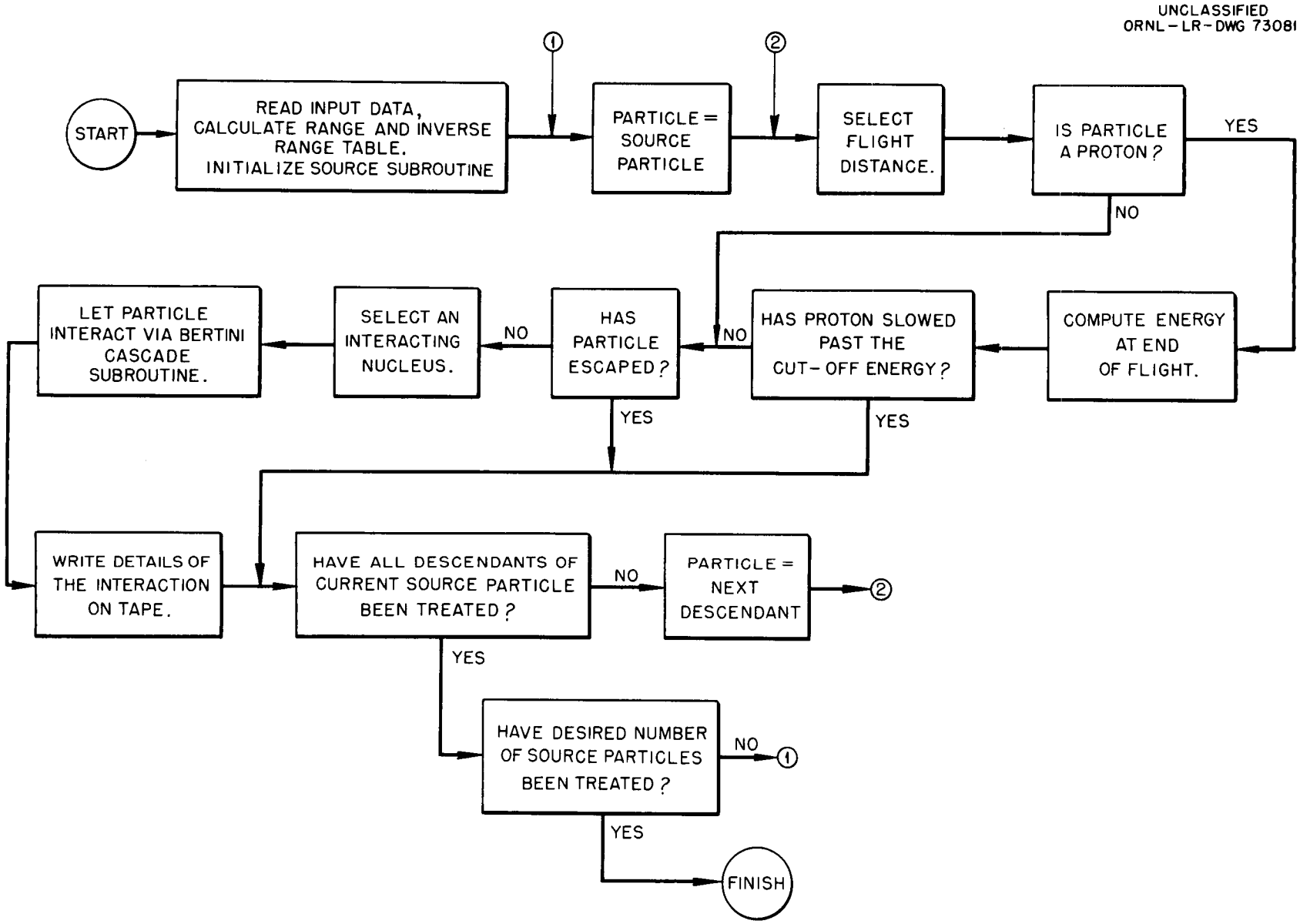

Fig. 2. A Flow Chart for the High-Energy Transport Code.

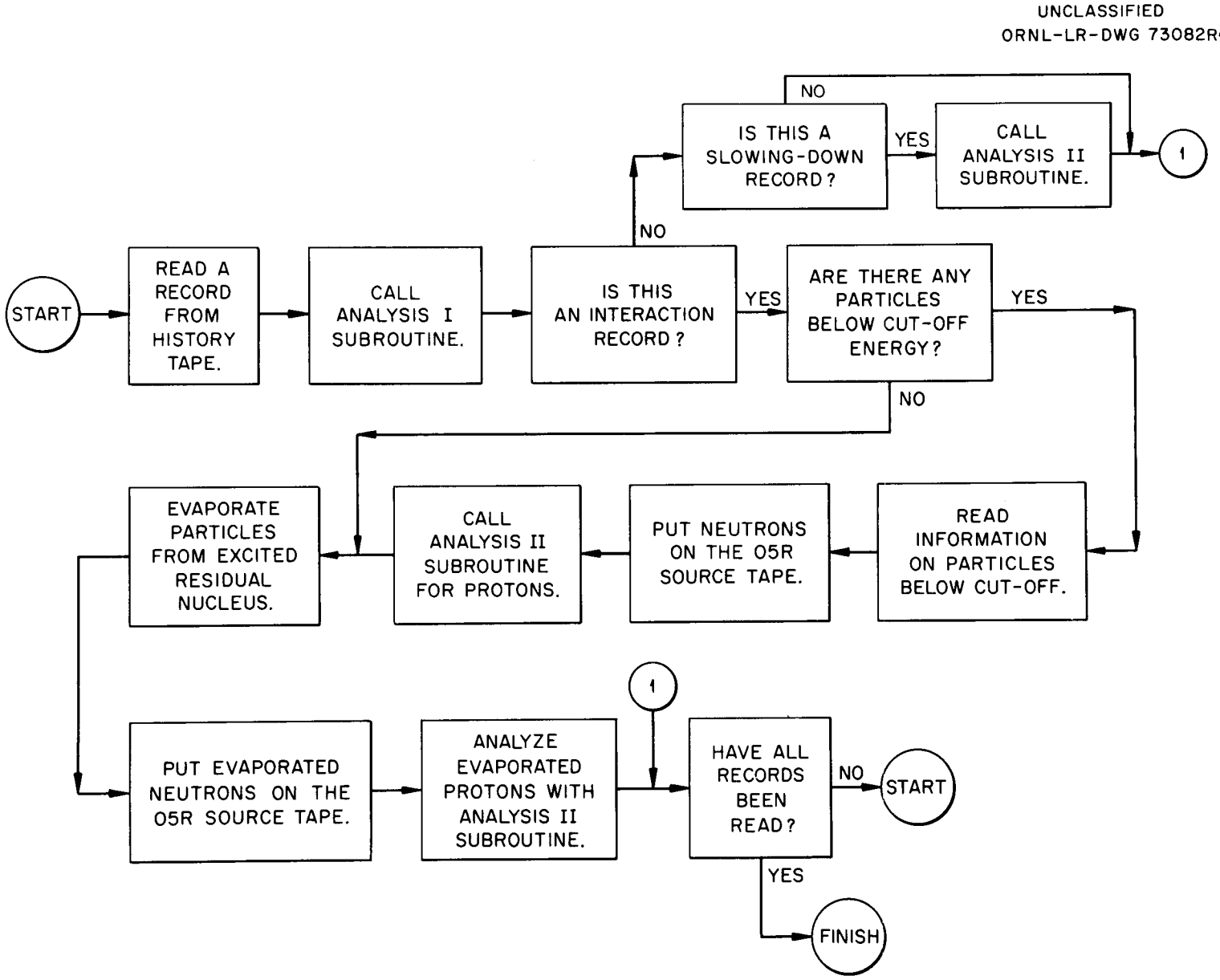

Fig. 3. A Flow Chart of the 05R Source Preparation Routine.

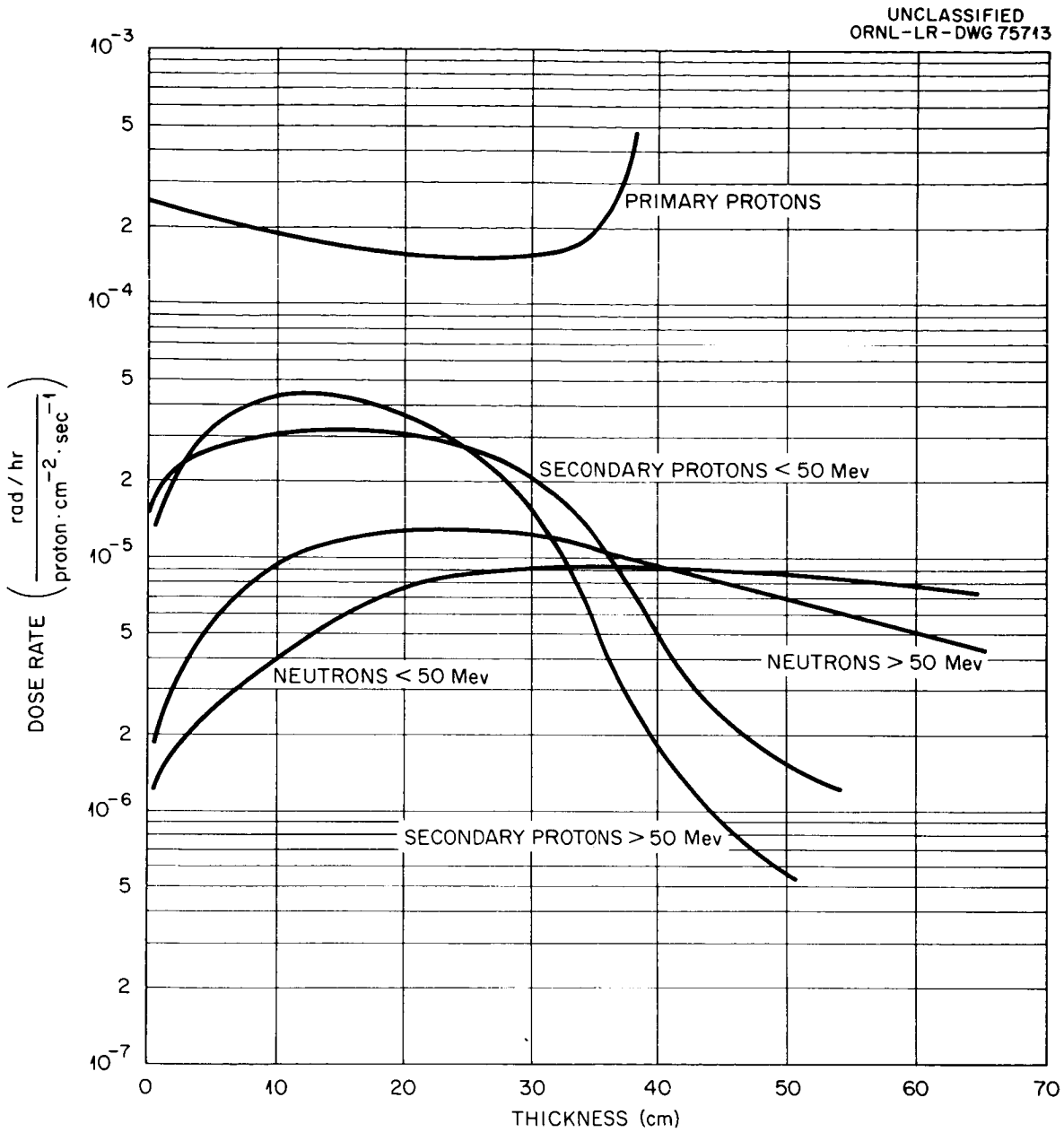

Dose Rate vs Thickness: 400-Mev Protons on Aluminum.

Fig. 4. Partial Tissue Dose Rates Behind Aluminum Slabs vs. Slab Thickness for 400-Mev Incident Protons.

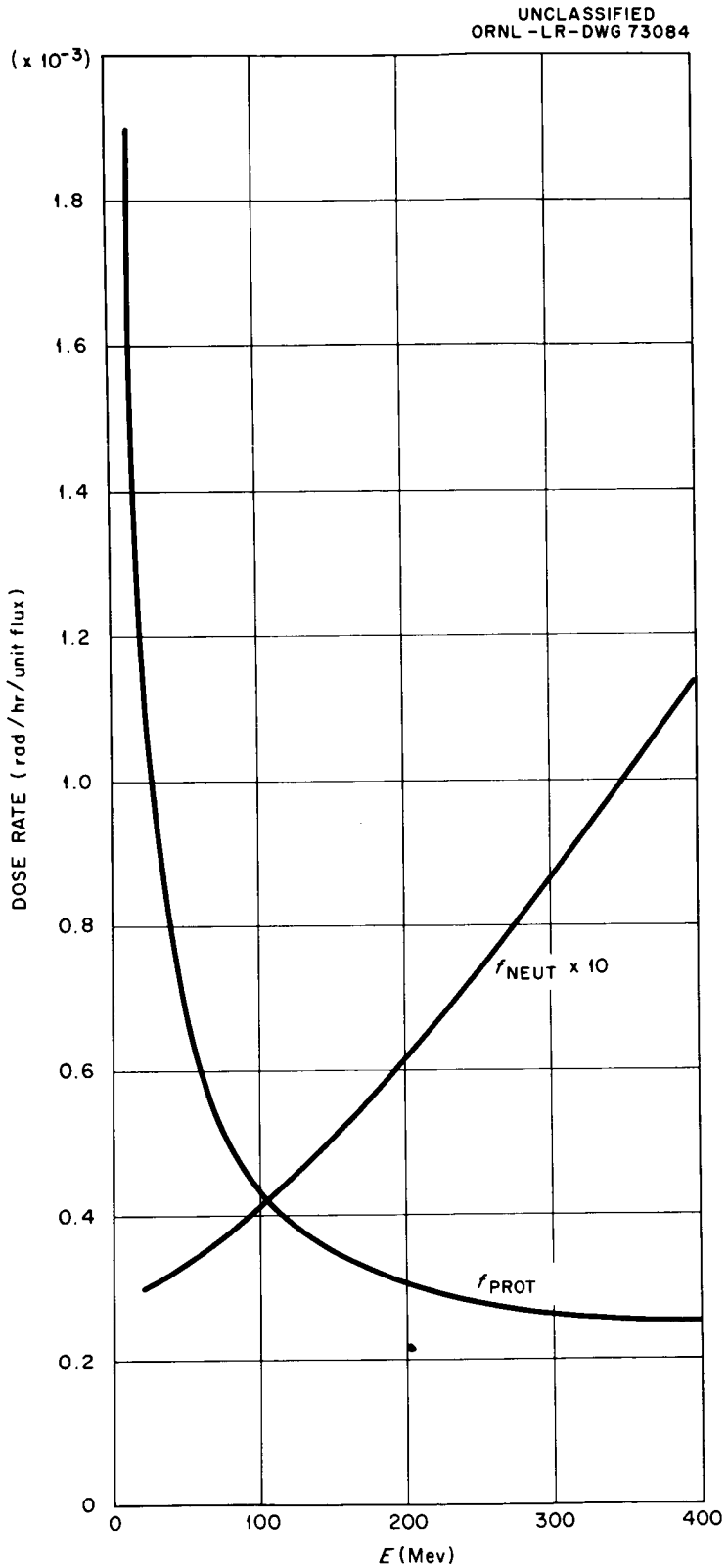

Fig. 5. Neutron and Proton, Flux-to-Dose Conversion Factors vs. Energy.

Paper D-7

THE CALCULATION OF RADIATION DOSE IN TISSUE FROM HIGH-ENERGY PROTONS*

J. E. Turner, J. L. Feuerbacher, C. D. Zerby, W. E. Kinney,
J. Neufeld, W. S. Snyder, and R. L. Woodyard
Health Physics Division and Neutron Physics Division
Oak Ridge National Laboratory**
Oak Ridge, Tennessee

15144

Abstract

The Oak Ridge National Laboratory is developing Monte-Carlo calculations for the paths and interactions of particles of various kinds and energies and for secondary particles they produce when incident on phantoms of a given composition, i.e., for materials and combinations of materials of given atomic number Z and mass number A. These calculations provide histories of the particles involved, as described in the preceding paper. For the estimation of dose from high-energy radiation, particle histories have been analyzed in a tissue slab of thickness 30 cm from normally incident protons with energies of 100, 150, 200, 250, 300, 350, and 400 Mev. Calculations at still higher energies are in progress. The results of the calculation of rad and rem dose as a function of depth in the tissue slab are presented. Also shown at each incident energy is the relative contribution of recoil nuclei (and other particles with mass number $A > 1$) to the total absorbed energy per unit mass. For the purpose of estimating rem dose, the recommendations of the National Committee on Radiation Protection and Measurements (NCRP) published in NBS Handbook 59 were used. For values of linear energy transfer (LET) greater than those considered in Handbook 59 (viz., for LET > 1750 Mev/cm) an RBE (relative biological effectiveness) value of 20 was used. A method for analyzing particle histories is utilized which will later permit computations of rem dose curves under very general assumptions about the dependence of RBE on LET. The rem dose as presented here uses the estimation of LET as formulated by Neufeld and Snyder and is calculated using their methods.

---

* Supported by National Aeronautics and Space Administration.

** Operated by Union Carbide Corporation for the U. S. Atomic Energy Commission.

This paper presents results which are available at this time on the calculation of radiation dose due to high-energy protons incident on tissue. The highest incident proton energy considered here is 400 Mev, which is the maximum energy at which the presence of pions is not being considered. Calculations up to several Bev incident nucleon energy are in progress. Assuming the charge independence of nuclear forces, one can apply much of the data from nuclear interactions discussed below for incident protons directly to incident neutrons of the same energies. The essential difference between the penetration of high-energy protons and high-energy neutrons through matter arises through the circumstance that protons lose energy by ionization as well as in nuclear interactions.

The calculations of the penetration of high-energy incident protons and the secondary particles to which they give rise are described elsewhere.[1,2] The information from these studies from which energy deposition per unit mass in a medium can be calculated is summarized by the example shown in Fig. 1. The figure represents the history of one incident proton and secondaries, derived on the basis of the above mentioned Monte-Carlo calculations. The line (1) represents the path of a proton incident normally at a point P on a tissue slab 30 cm thick having infinite extension in space in directions perpendicular to the velocity vector of the incident proton. (The distribution of dose in such a slab will approximate the expected dose distribution in man; calculations will be modified later to treat other geometries.) The incident proton (1) penetrates the slab to some point A at which a nuclear interaction takes place. (Depending upon the incident proton energy, a certain fraction of incident protons will not experience a nuclear interaction.) In the example in Fig. 1 the interaction between the incident proton (1) and a nucleus in the tissue slab gives rise to a proton (2) and two neutrons (3) and (4); the track (5) represents the recoiling residual nucleus following the nuclear interaction. Proton (2) is stopped in the slab, neutron (3) escapes, and neutron (4) interacts at B with another nucleus, giving rise to a proton (6), a neutron (7), and another recoiling nucleus (8). Proton (6) comes to rest; neutron (7) is elastically scattered at C and subsequently escapes from the slab. For each nuclear track shown in the figure, the following information is given:

type of particle,
position coordinates of particle at birth,
energy at birth,
direction cosines of velocity vector at birth,
position coordinates of particle at next interaction.

---

1. H. W. Bertini, "Monte-Carlo Calculations on Intranuclear Cascades," this Symposium.

2. W. E. Kinney, R. R. Coveyou, and C. D. Zerby, "A Series of Monte-Carlo Computer Codes to Compute the Transport of Nucleons Through Matter," this Symposium.

The nuclei remaining after the cascade and evaporation processes are identified, and the initial kinetic energy of recoil and the residual excitation energy of each nucleus are given. It should be pointed out that Fig. 1 schematically represents particle trajectories which, of course, are calculated in three dimensions.

For the calculation of radiation dose in the tissue slab, the particle histories for a number of incident protons are analyzed. For analysis, the slab is divided into a number of sub-slabs parallel to the slab faces, and the total energy deposited in each sub-slab from all events involving the incident protons and their products is first calculated. By symmetry, the total energy deposited in any sub-slab from one incident particle at P is equal to the energy deposited per unit volume in that sub-slab from a uniform, normally incident broad proton beam having unit flux. Consequently, the calculation of the total energy deposited in a given sub-slab from a number of normally incident protons at the single point P on the slab boundary provides directly the energy absorbed per unit mass, or rad dose, in that sub-slab from a broad beam of normally incident protons.

Results of the calculation of rad dose as a function of depth in tissue slabs for incident protons of energies 100, 150, 200, 250, 300, 350, and 400 Mev are presented in Figs. 2-8. The figures show both the total rad dose and the rad dose due to heavy particles (i.e., particles with mass number $A \geq 2$, which arise as recoil nuclei and as nuclear evaporation products.) At each energy 1000 incident protons were used, and the energy deposition was calculated in each of 150 successive sub-slabs of thickness 2 mm. The total rad dose is generally quite uniform throughout the slabs in which the primary protons do not come to rest (Figs. 5-8). For the energies 200 Mev and below, protons coming to rest show the familiar Bragg peak.* At depths beyond the peak there is a small dose arising from interactions of secondary neutrons with nuclei of the slab. This dose was calculated and found to be about two orders of magnitude less than the dose at depths on the other side of the Bragg peak. Accordingly, in Figs. 2-4 it should be realized that there is a small dose beyond the straight-ahead depth of penetration of primary protons which come to rest in the slab.

While the rad dose is of interest, presumably the important quantity for radiation protection purposes is the rem dose, which considers explicitly the relative biological effectiveness (RBE) of the various components contributing to the absorbed energy per unit mass, or rad dose. The rem dose estimations for each incident proton energy are also shown in Figs. 2-8. Presently available values of RBE are based upon the rate of linear energy transfer (LET) of radiation in tissue and apply to low-level chronic exposure to radiation. The current recommendations of the National Committee on Radiation Protection and Measurements (NCRP) for exposures under these conditions are incorporated

*A smoothing routine was used in the calculation, which produces the smooth variation of dose shown over the otherwise discontinuous analytic expression for dose at the end of the proton range.

in Fig. 9.[3] The highest value of LET for which recommendations are given is 1750 Mev/cm path length. For the rem dose estimations the value RBE = 20 was used for particles having a LET greater than this, corresponding to the dashed portion of the curve shown in Fig. 9. All of the recoil nuclei in the present calculation have LET values greater than 1750 Mev/cm.[4]

Inasmuch as the LET for all recoiling nuclei (except hydrogen) arising in tissue exceeds the maximum value considered by the NCRP, an estimation of rem dose even within the framework of the existing recommendations for RBE for chronic, low level exposure cannot be completely made. From the results presented in Figs. 2-8 one can make quick estimates of rem dose from rad dose by considering the rem dose as due, approximately, to two distinct groups: (1) protons and (2) heavy particles (i.e., all particles with $A \geq 2$). For the first group, the RBE is essentially unity. For example, with reference to Fig. 9, the LET for protons of energies greater than about 20 Mev is less than 40 Mev/cm, and so, to a first approximation, most of the total proton dose can be considered to have RBE = 1. (In Figs. 2-8 the total proton dose is represented by the difference of the total rad dose and heavy particle dose curves.) For this group, then, the rad and rem doses are approximately numerically the same. In the second group, a large fraction of the energy deposited comes from recoiling nuclei, for which RBE = 20 has been used at all energies. For this group, then, the rem dose is numerically approximately 20 times the rad dose. Thus, for an order of magnitude estimate, one has

$$\text{Rem Dose} \cong (\text{Proton Rad Dose}) \times 1 + (\text{Heavy Particle Rad Dose}) \times 20.$$

One sees in Figs. 2-8 that this approximate relationship is borne out.

The question of appropriate RBE values to use for exposure conditions anticipated in space missions remains an outstanding problem in space dosimetry at the present time.[5] The problem arises both through (1) the different conditions of exposure encountered in space missions

---

3. Taken from Table 3, p. 48, Permissible Dose from External Sources of Ionizing Radiation, Recommendations of the National Committee on Radiation Protection and Measurements, National Bureau of Standards Handbook 59, Washington, D. C., 1954.

4. J. Neufeld and W. S. Snyder, "Estimates of Energy Dissipation by Heavy Charged Particles in Tissue," Selected Topics in Radiation Dosimetry, pp 35-44, Bruder Rosenbaum, Vienna, 1961.

5. W. S. Snyder, "Some Data on the Relationship of RBE and LET," this Symposium.

as opposed to the exposure conditions previously dealt with and through (2) the relatively large fraction of the dose deposited at LET values which are orders of magnitude larger than those encountered previously in most work in radiation dosimetry. An investigation of these problems will be made from an analysis of the LET spectrum based upon accumulating biological evidence. The incorporation of RBE in the dose codes has been made in a way which will permit a wide range of RBE values to be considered without repeating the entire calculation. The method employs a polynomial expansion of expressions for rem dose in powers of energy, the coefficients of the polynomial corresponding to a particular choice of RBE values.

Acknowledgments

The contributions of H. A. Wright and K. Katoh in various phases of the dose calculations are gratefully acknowledged. The present calculations have made use of several previous calculations which were constructed through the efforts of many people. In particular, we would like to recognize the contributions of R. R. Coveyou, H. W. Bertini, and L. Dresner..

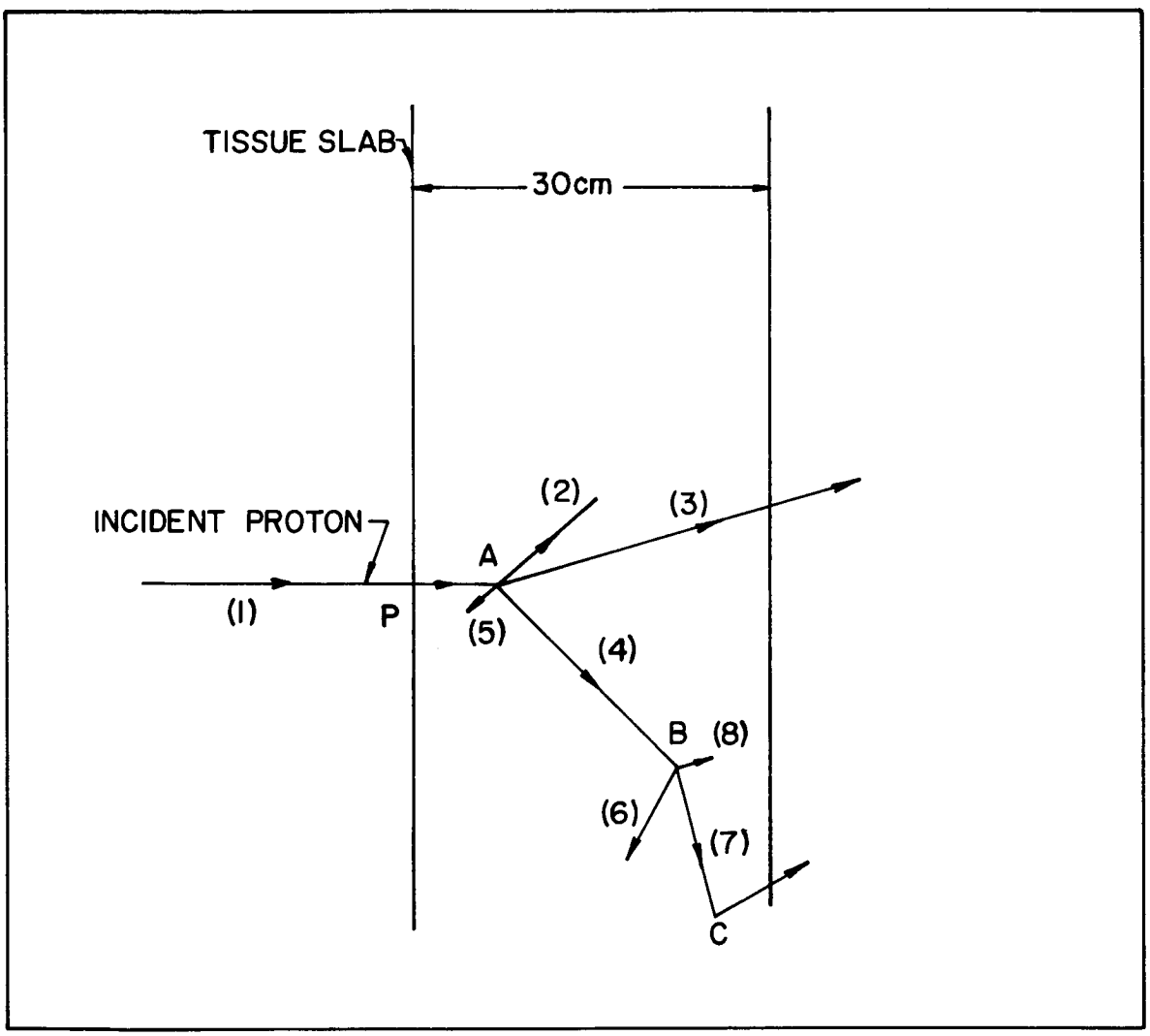

FIG. 1 SCHEMATIC REPRESENTATION OF TYPICAL PRIMARY AND SECONDARY PARTICLE TRAJECTORIES

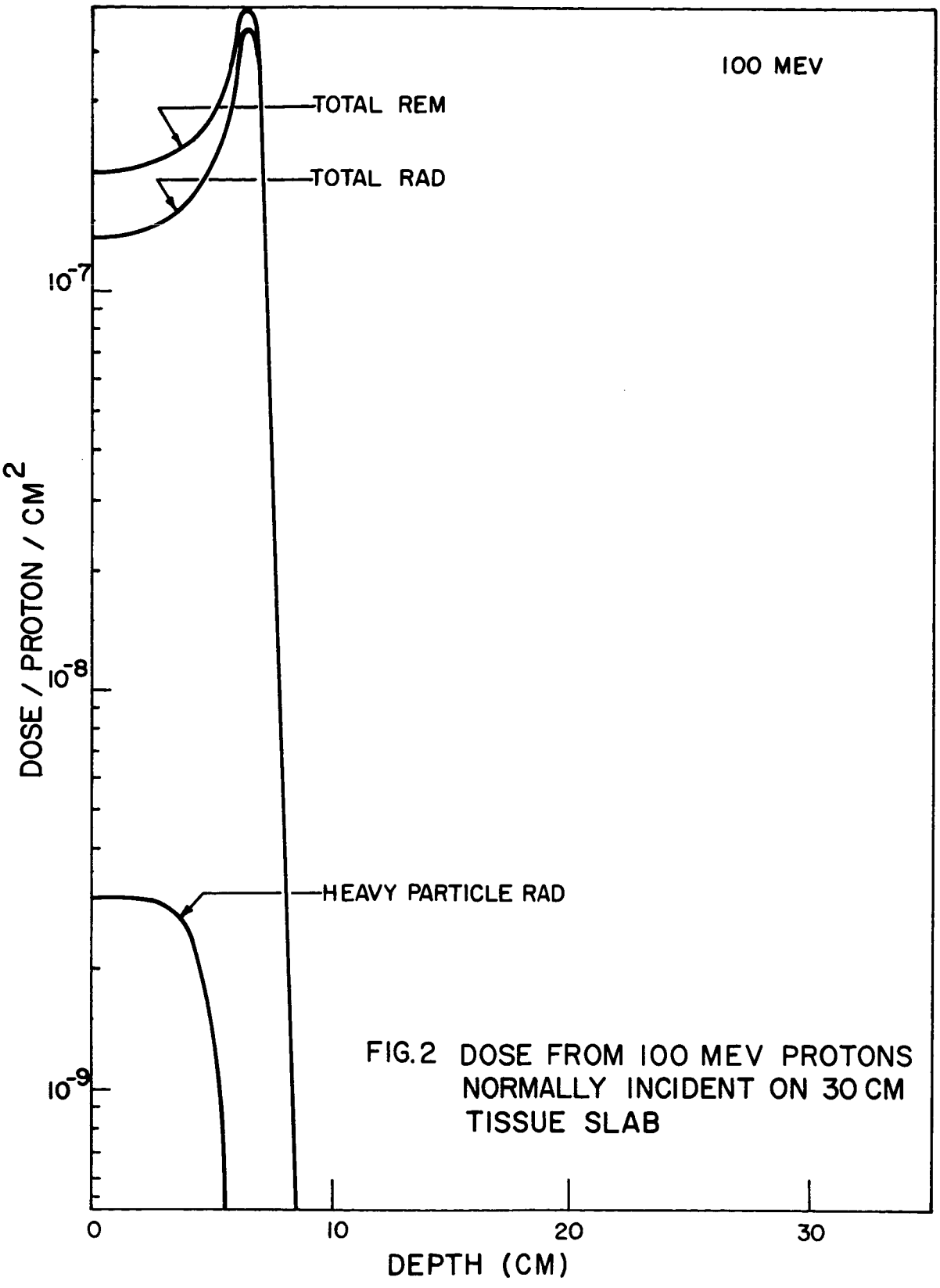

FIG. 2 DOSE FROM 100 MEV PROTONS NORMALLY INCIDENT ON 30 CM TISSUE SLAB

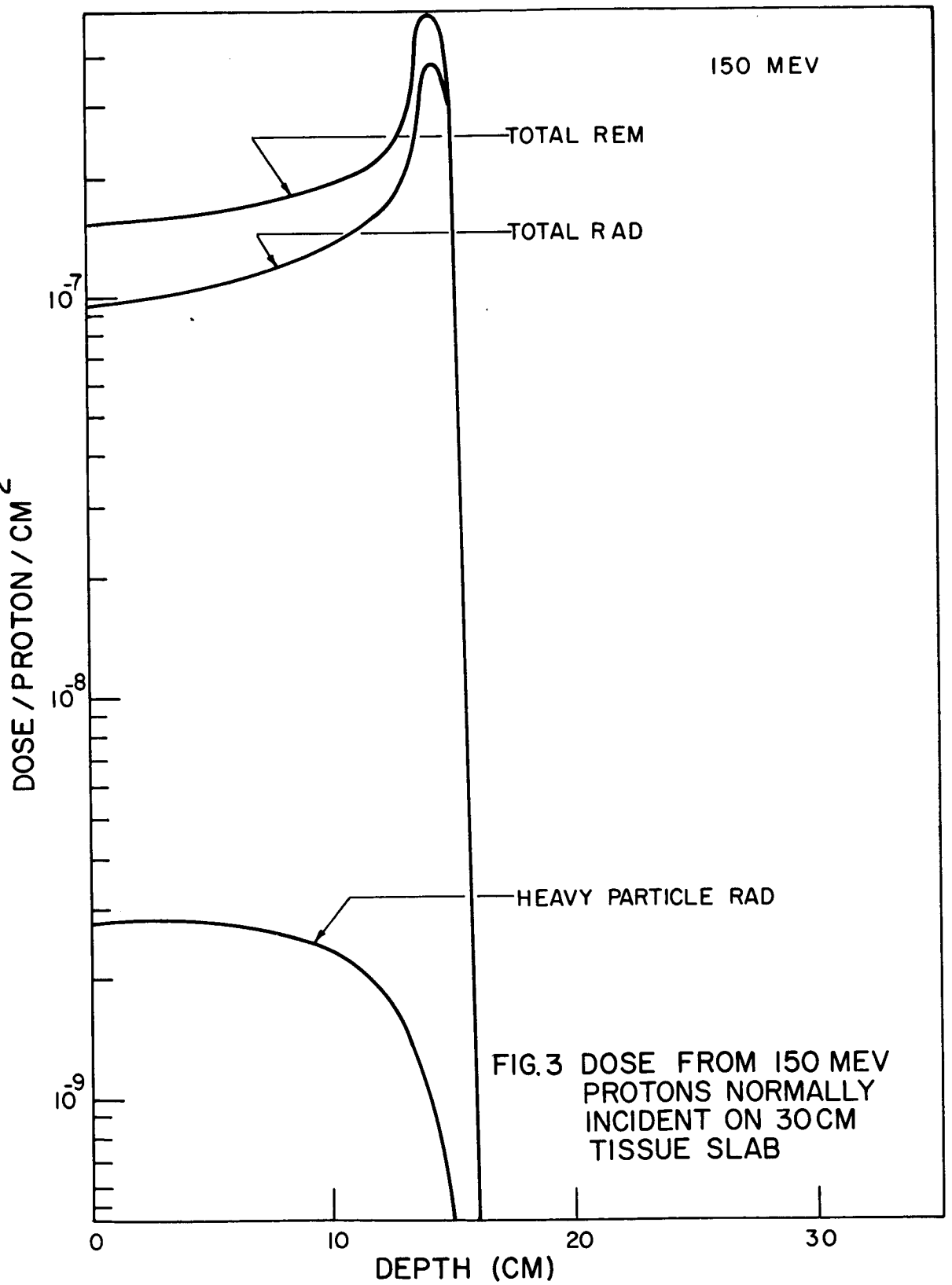

FIG. 3 DOSE FROM 150 MEV PROTONS NORMALLY INCIDENT ON 30 CM TISSUE SLAB

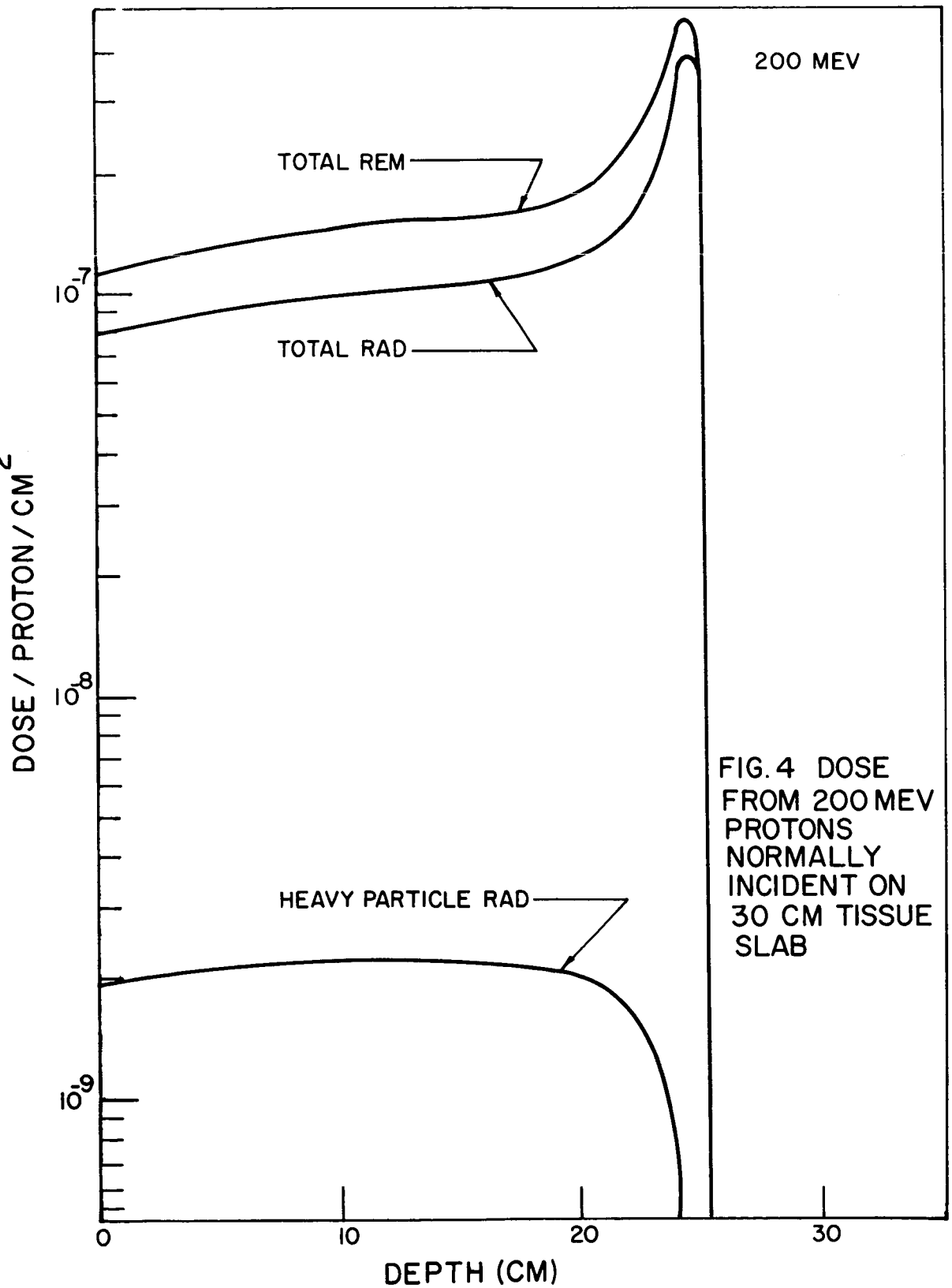

FIG. 4 DOSE FROM 200 MEV PROTONS NORMALLY INCIDENT ON 30 CM TISSUE SLAB

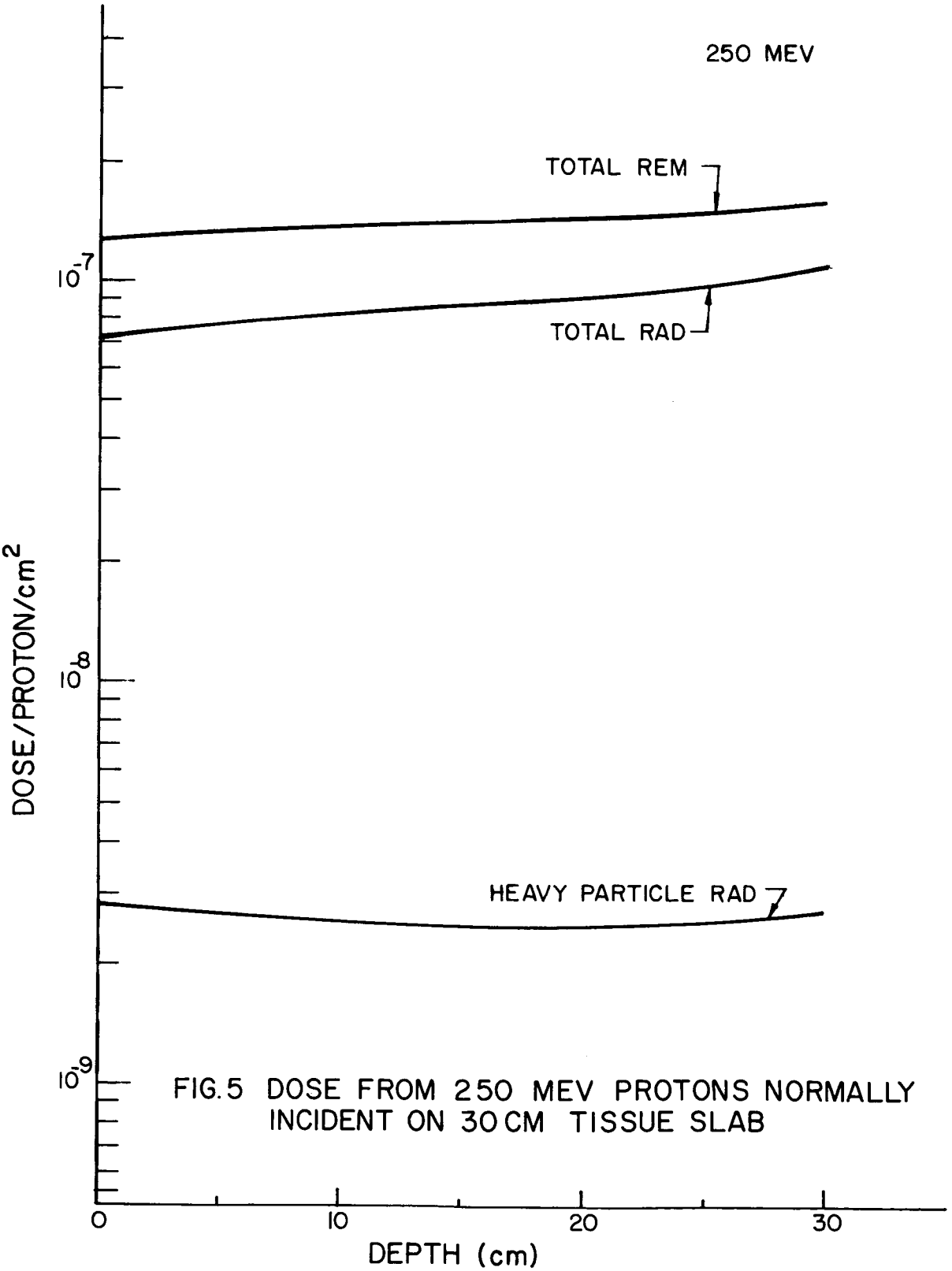

FIG. 5 DOSE FROM 250 MEV PROTONS NORMALLY INCIDENT ON 30 CM TISSUE SLAB

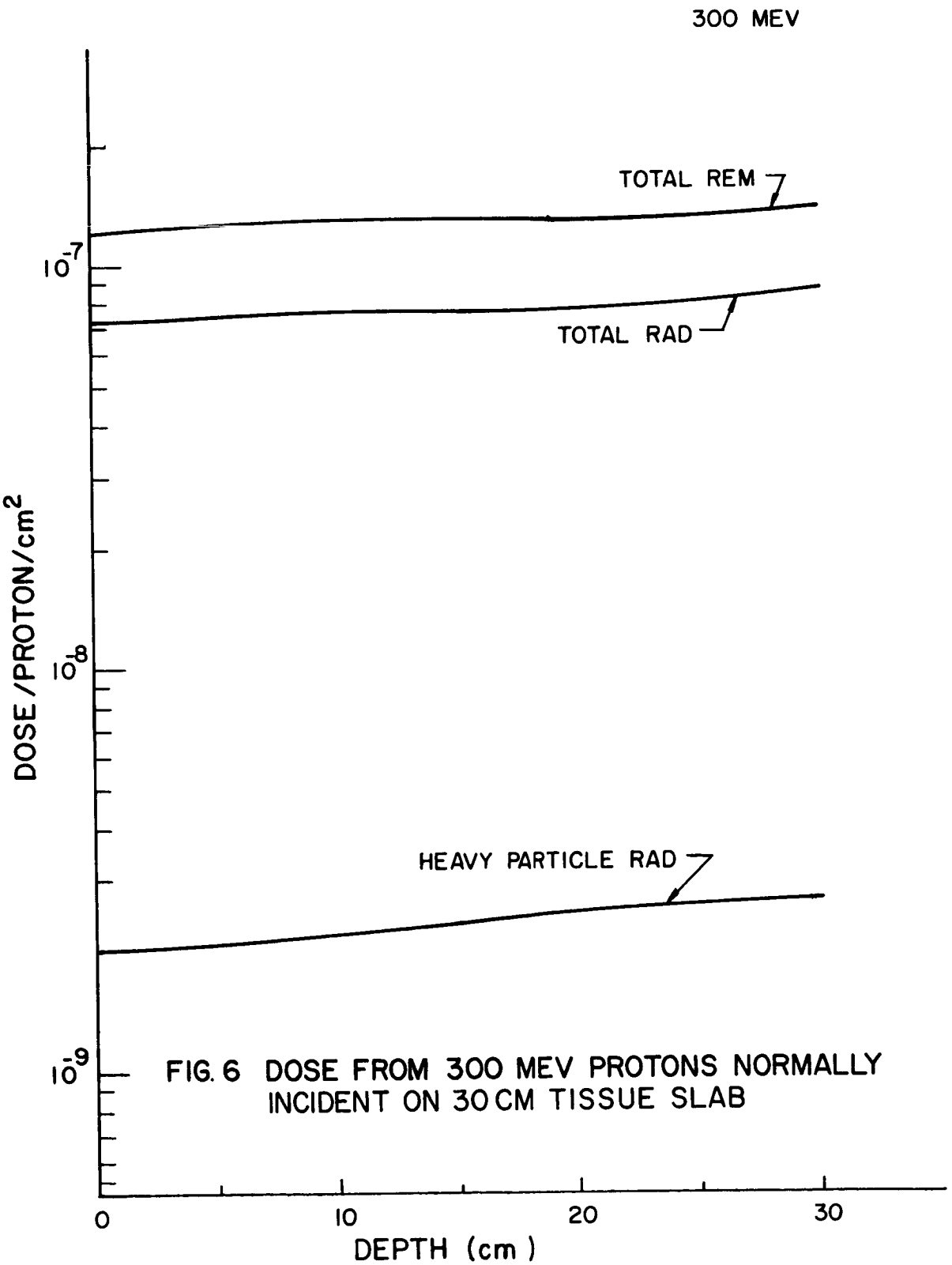

FIG. 6 DOSE FROM 300 MEV PROTONS NORMALLY INCIDENT ON 30 CM TISSUE SLAB

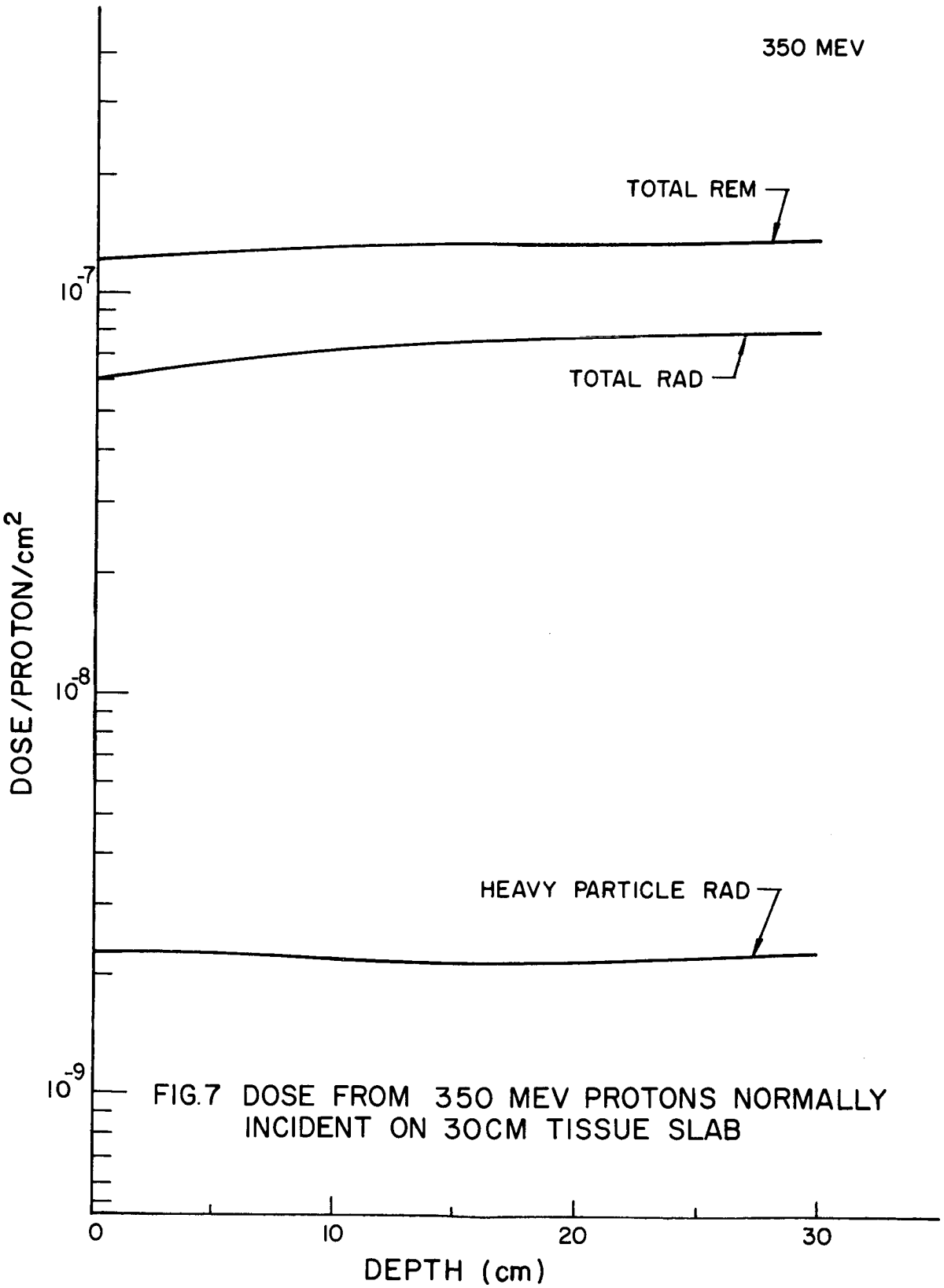

FIG.7 DOSE FROM 350 MEV PROTONS NORMALLY INCIDENT ON 30CM TISSUE SLAB

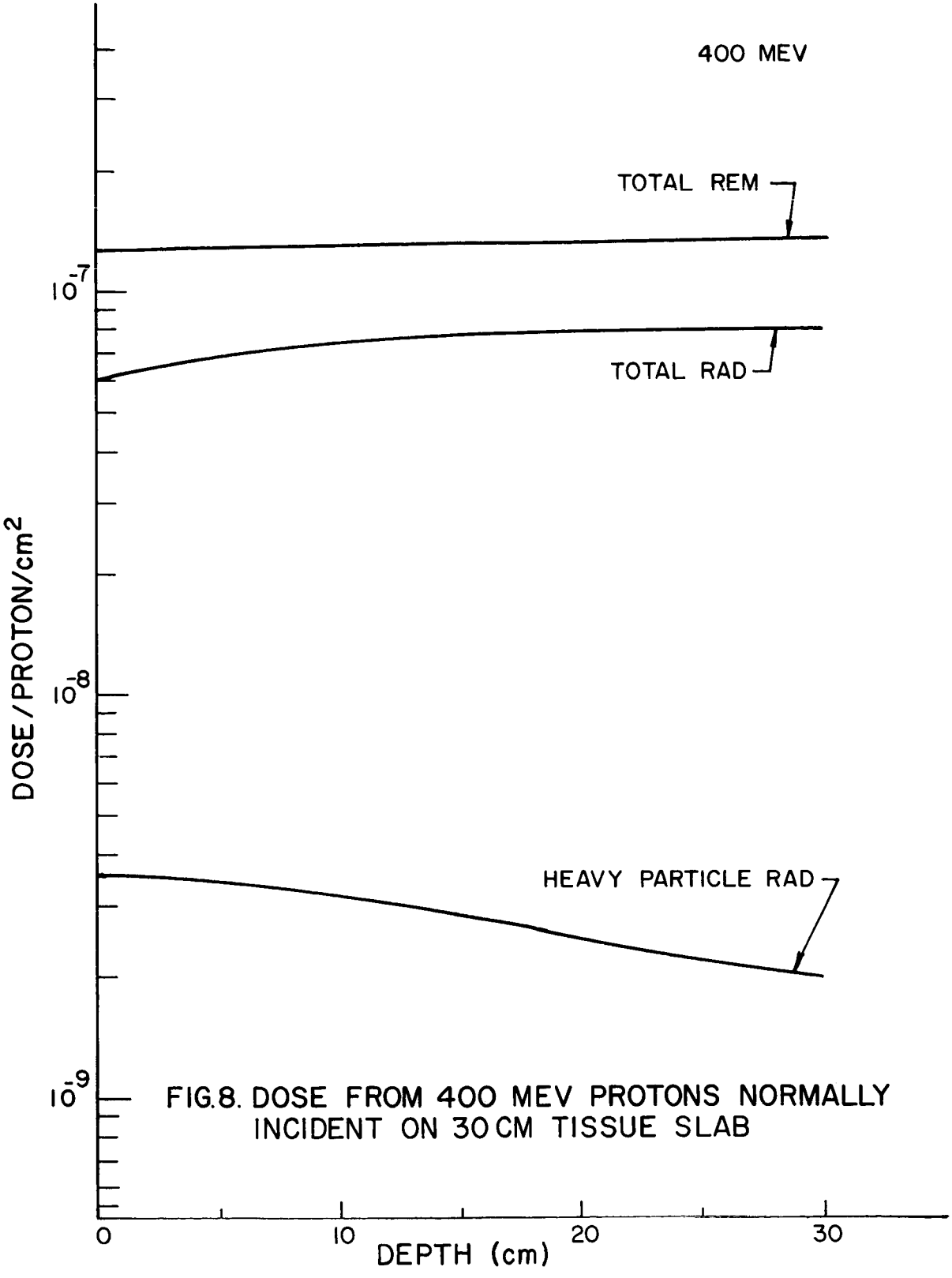

FIG.8. DOSE FROM 400 MEV PROTONS NORMALLY INCIDENT ON 30 CM TISSUE SLAB

UNCLASSIFIED
ORNL-LR-DWG.69771R

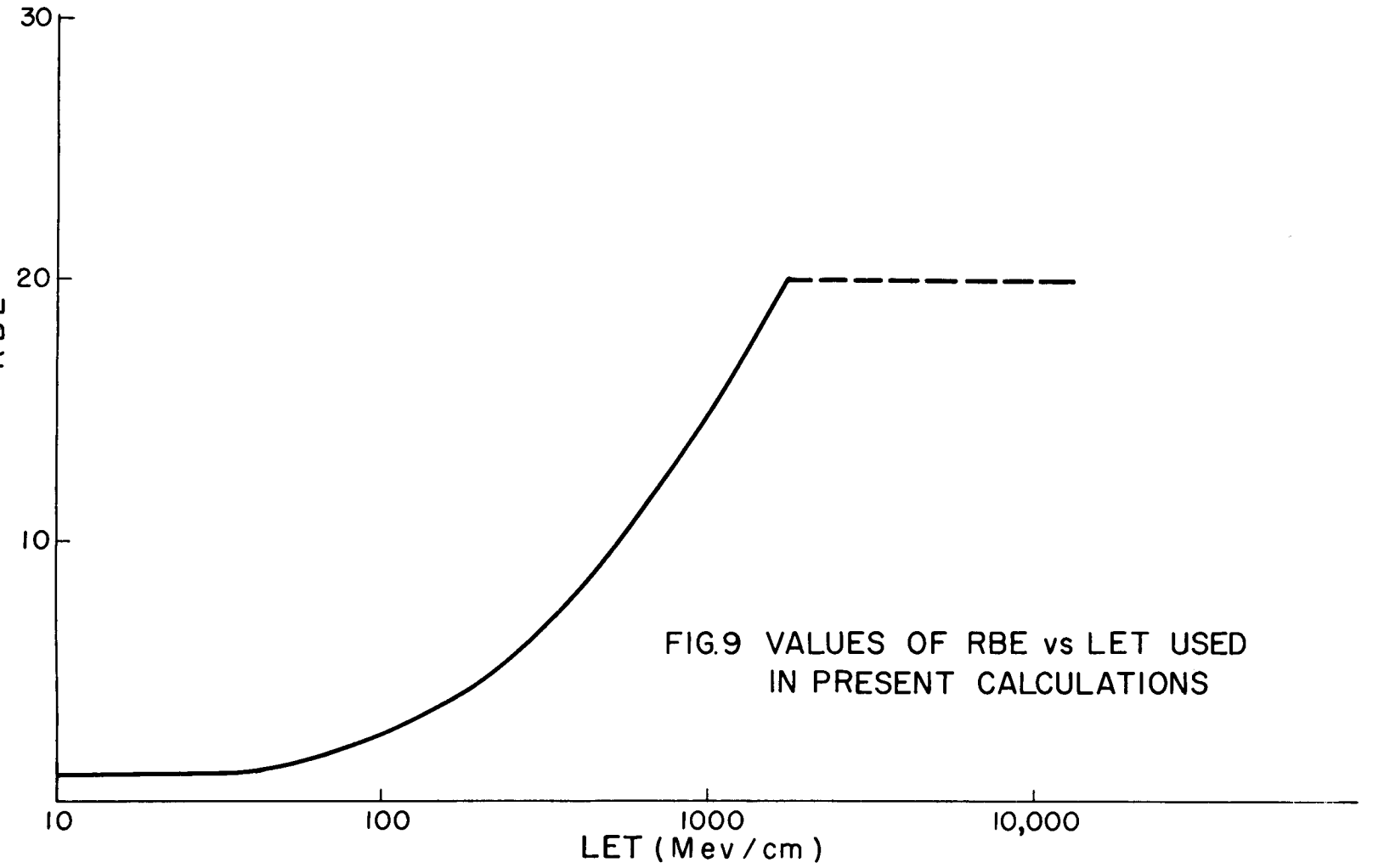

FIG.9 VALUES OF RBE vs LET USED IN PRESENT CALCULATIONS

15145

Paper D-8

SPACE PROTON DOSES AT POINTS WITHIN THE HUMAN BODY

David L. Dye
The Boeing Company

15145 cont

Abstract

Distribution patterns of absorbed dose influence the radiation response of a mammalian system, because of differing radiosensitivities of different organ systems. In a man exposed to space radiations; e.g., an astronaut, body self-shielding produces nonuniform dose distributions which depend upon external shielding configurations and the incident radiation parameters. In this paper are presented the doses at twelve specific points in the body of a seated man exposed to isotropic incident space protons, where the man is inside various thicknesses of external vehicle shell shielding. The body points, selected for their radiobiological interest, are in (or on) sternum, chest skin, femur, spinal column, eye, central gut, and a series at various lateral depths on the waist. The protons reaching these specific points from all directions traverse tissue thicknesses that were determined from scale drawings of a statistically standard man (75-percentile). The proton penetration, secondary radiation generation, and total dose delivered to each specific body point was calculated using an IBM (Fortran) computer code.

For feasibly thin aluminum shields and typical spectra, the secondary dose is a small fraction of the total proton dose for most of the body points. The doses at a given point vary with both spectral shape and external shielding, as well as point to point. Power law spectra, $E^{-n}dE$, normalized to one proton/cm^2-sec of $E > 100$ Mev, with $2 \leq n \leq 5$, and the Freden and White trapped proton spectrum, were considered. Resulting dose values for n = 3 to 4 (a

typical solar flare-associated proton spectrum) vary from about 10^{-4} to 10^{-8} rad/proton/cm^2 > 100 Mev for the various body points for a 1 gm/cm^2 external shield, and from 10^{-7} to 10^{-8} rad/proton/cm^2 > 100 Mev for a 10 gm/cm^2 external shield.

Introduction

Dose distribution patterns in a biological system have an important influence on the radiation effects in that system. In the human body exposed to a typical space proton environment, there is some self-shielding that reduces the body interior doses with respect to the skin doses and thus affords some measure of radiation protection. Previous studies have been made of the depth-dose patterns resulting from several simple proton spectra impinging on slab shields and penetrating into tissue slabs.[1,2] These early results show the dependence of depth-dose on spectral shape and exterior shielding, but the simplified geometry used leaves one still wondering just what the absorbed doses are inside a biologically interesting shape such as the human body.

The earlier results were calculated by means of an IBM 7090 computer code.[2] A slightly modified version of this same program was used in part of the present calculation. A principal feature of the present program is that it calculates a series of dose values due to penetrating protons in a set of slab geometries, then sums these dose values, weighted as necessary by the fractional solid angles subtended by each slab problem, to obtain the proper total dose at an interior point. For the work here reported, the seated human (75-percentile male) body was used, with various spherical shells around it. Doses were computed at a number of body-interior points: femur, sternum,

---

1. D. L. Dye and J. C. Noyes, Biological Shielding for Radiation Belt Particles, J. Astron. Sci. VII, 64 (1959).

2. D. L. Dye and G. Butler, Computer Calculations of Doses from Protons in Space, J. Astron. Sci. IX, 63-71 (1962).

backbone, eye lens, central gut, and at waist level.[3] The results of these computations are tabulated here and show a dependence on spectral and shielding parameters similar to the earlier results. However, these values now represent useful doses (per isotropic incident proton/cm^2 of E > 100 Mev) at the specific body points. If the incident isotropic flux and spectrum is known exactly--an unlikely eventuality--then the proton ionization dose at any of these points may be known accurately.

The dose due to secondaries generated in nuclear interactions has been estimated variously [4,5] but it is small for thin shields. A computer program has been developed to determine the tissue doses due to the secondaries generated by the incident primary protons in the shielding material. The secondary component includes inelastic scattering-produced gamma rays, low-energy evaporation nucleons, and high-energy knock-on nucleons. Part of the tertiary neutron and gamma effects were included, by adding the secondary proton spectrum to the primary at every point, so the total was used in interior sublayers. The results justify the usual procedure of neglecting the secondaries from incident space protons of typical energy spectra.

The Computer Programs

Primary Dose Code

Spectral Modification. In the present version of the primary proton dose calculation, an incident proton spectrum is degraded through shielding layers according to formulas 1 to 3 of Ref. 2. However, instead of interpolating between tabulated range-energy points, as was

---

3. D. L. Dye, A Geometrical Analysis of the Seated Human Body for Use in Radiation Dosage Calculations, The Boeing Company, D2-90107, (1962).

4. R. I. Allen, et al., Shielding Problems in Manned Space Vehicles, Lockheed Aircraft Corp., NT-140, (1961).

5. R. K. Wilson, et al., A Study of Space Radiation Shielding Problems for Manned Vehicles, General Dynamics Corp., FZK-144 (1962).

done in Ref. 2, we have made a least squares fit to those tables[6] to obtain analytic expressions for proton range as a function of energy and energy as a function of range. Thus, the proton range function is defined empirically to be:

$$\text{RNGEF}(E) = \exp(A1 + A2 \log E + A3 \log^2 E), \tag{1}$$

and the proton energy function is (by quadratic inversion):

$$\text{ENGYF}(R) = \exp\left[\frac{-A2 + \sqrt{A2^2 - 4A3(A1 - \log E)}}{2A3}\right], \tag{2}$$

where E is proton energy, R is proton range, and the A's are coefficients of the fit which depend on the shielding material. Equation 1 was chosen as the form to which to fit by least squares the range-energy tables because range is approximately a power law function of energy; that is,

$$R = kE^n, \tag{3}$$

with k and n slowly varying functions of E over the range of interest, $1 \lesssim E \lesssim 1{,}000$ Mev.

Use of an analytic range function provides simply for the solution to the spectral modification with penetration into shielding material. It also allows one readily to compute the output spectrum on a specified energy grid, so that spectra are easily added at an interior point.

If a monodirectional proton spectrum P(E)dE is incident on a shield layer of thickness X, then the penetrating spectrum P'(E')dE' may be computed by means of the recipe:

$$E' = \text{ENGYF}(\text{RNGEF}(E) - X), \tag{4}$$

$$P'(E')dE' = P(E)dE(dE'/dE), \tag{5}$$

and

$$(dE'/dE) = \frac{(dR/dE)_E}{(dR/dE)_{E'}} \tag{6}$$

---

6. M. Rich and R. Madey, Range Energy Tables, UCRL-2301 (1954)

where the subscripts mean that the derivative is evaluated at E and E', respectively.

In the present IBM code, an output energy grid E'(K) is specified, so the E(K) values needed to obtain it are computed by Eq. 4. Then the incident specified spectrum P(K) is rearrayed, by interpolation, onto this input energy grid. Then the "energy spread factor", determined by Eq. 6, is multiplied into the spectrum P to obtain the output spectrum P' arrayed on the specified output energy grid E'(K), according to Eq. 5.

This spectrum degrading process is repeated for each layer of shielding material until the point of interest for dose calculation is reached. The actual dose computation is done as it was earlier in versions of this code; namely, by:

$$\text{DOSE} = \int_{1}^{1{,}000\ \text{Mev}} P'(E')\ \text{DOSF}(E')\ dE' \qquad (7)$$

where DOSF(E) is proportional to dE/dX for tissue.

Vehicle Analysis. It is desired to compute a dose absorbed by some material such as tissue, within a complicated arbitrary shielding configuration such as a space vehicle or a human body, due to an arbitrary angular distribution of incident protons. The way this is done may be seen by referring to Fig. 1. Briefly, the three-dimensional material configuration is analyzed in a large number of one-dimensional problems, so that the code just described can solve the three-dimensional problems.

Looking outward from an interior point P in all directions, one sees various solid angular regions $\Delta\Omega$, over each of which the shielding layers are approximately the same. If the radiation reaching P is direct, or primary and unscattered, then we may approximate the dose at P by the sum:

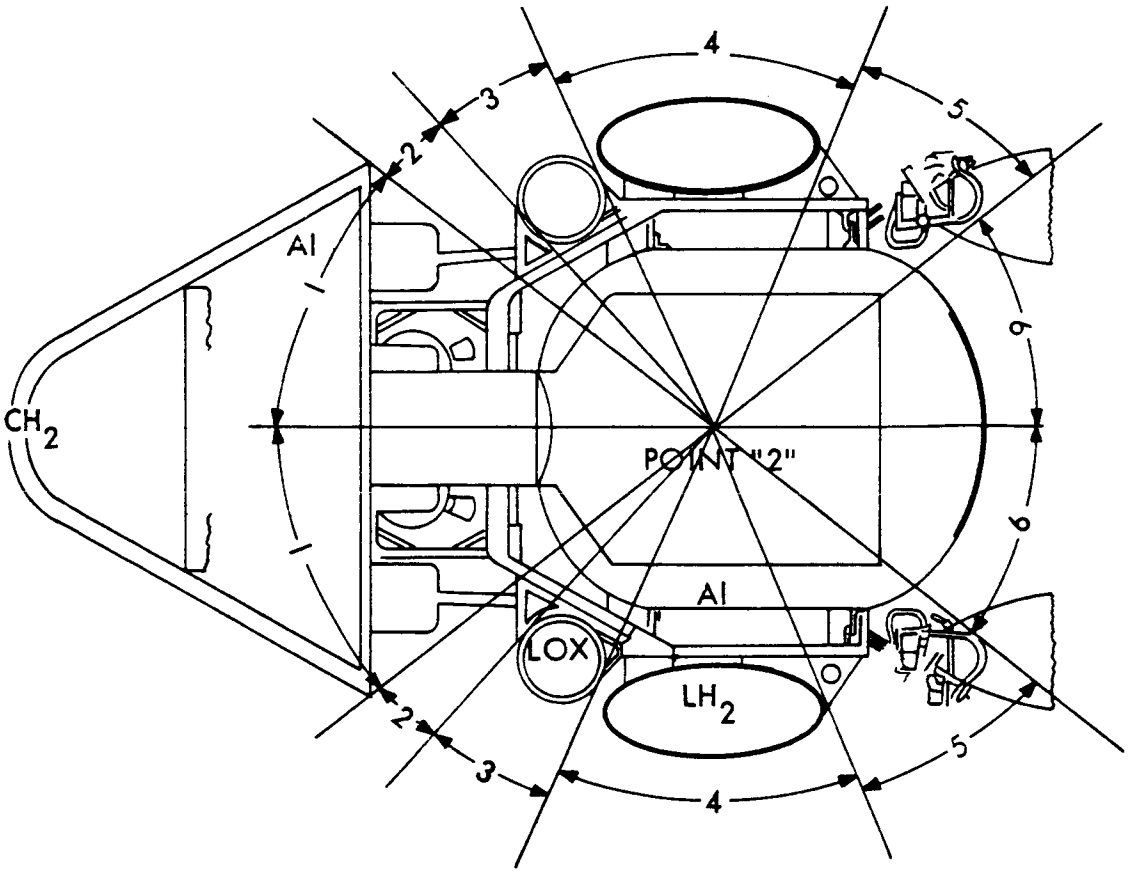

REGION	FRACTIONAL SOLID ANGLE	SHIELDING IN REGION
1	.10	3" CH_2 +4.7" Al
2	.07	1.25" Al
3 (with fuel)	.14	.02" Al +15" O_2 +1.5" Al
3 (without fuel)	.14	1.52" Al
4 (with fuel)	.4	.02" Al +18" H_2 +1.6 Al
4 (without fuel)	.4	1.62" Al
5	.13	2.2" Al
6	.18	3.1" Al

TYPICAL SPACE VEHICLE SHIELDING THICKNESS ANALYSIS

FIGURE 1

$$\text{DOSE}(P) = F \sum_{IP=1}^{NP} \left[\text{DOSE}(S_{IP})\right] \left[\text{ANG}(IP)\right] \left[\Delta\Omega_{IP}\right], \qquad (8)$$

where: $\text{DOSE}(S_{IP})$ is the absorbed dose computed behind a layer shield S_{IP},

S_{IP} represents the one-dimensional shielding configuration of whatever layers, materials, and thicknesses specified for the solid angular region indexed by IP,

ANG(IP) is the fraction of the flux coming from the IP direction, calculable from the angular distribution of the incident radiation, and normalized to be a constant unity value for isotropic flux,

F is the incident flux assumed suitably normalized,

$\Delta\Omega_{IP}$ is the fractional solid angle subtended about the point of interest P by the constant shielding region IP, and

NP is the total number of such regions needed to complete the full solid angle, so that the vehicle shielding is analyzed into sufficiently small angular regions to obtain the desired accuracy.

In Fig. 1, six regions were chosen to illustrate the concepts, but an actual analysis might use more. In the body point results reported here, 15 to 25 regions were used in most cases. It was found that little change in the final dose answer is obtained with larger numbers of subregions than this; that is, the dose calculation converges with relatively large $\Delta\Omega$ values for practical cases.* Equation 8 describes the method of calculating a dose to an interior point due to incident primary, straight-through, radiation of arbitrary incident angular

*See the paper by J. W. Keller, this symposium, for some further comments on the need for an adequately fine analysis.

distribution. Because in practice a space vehicle is likely to be drifting or slowly tumbling, the results computed and here reported are for isotropic distributions. Also, DOSE(S) was normalized to one proton/cm^2 of energy $E > 100$ Mev (for power law spectra), so the normalization of F, incident flux, must be compatibly defined.

Thus, in a vehicle shielding design problem, a geometrical analysis is made of the proposed design to determine a number of "constant-shielding" regions about an interior point. The dose at that point is calculated, one-dimensionally, for each of the constant-shielding regions and the weighted sum, Eq. 8, is performed using the dose values and the fractional solid angles for each region. The vehicle analysis part is a drafting board problem, and can be done quickly and with adequate accuracy for most practical vehicle configurations. But the power of this method is in the fact that any complex arrangement can be analyzed in these terms. The dose results presented here apply to specific points inside a very complex shielding arrangement--the tissue of the human body.[3]

Secondary Dose Code

Secondary Radiation Components. In addition to the dose due to primary penetrating protons, there is some energy deposition by the secondary radiations generated by the incident protons. These secondaries include gamma rays, and evaporation and knock-on nucleons. The neutrons and protons are generated in nuclear reactions where an incident proton excites a shield material nucleus. Some neutrons and protons of high energy (up to about the incident proton energy) can theoretically be produced. The bulk of the secondary neutrons and protons, perhaps with ten times the intensity of the high energy tail, are produced by evaporation from the excited nucleus. These evaporation nucleons are generated isotropically and have energies of 5 to 25 Mev, and proton numbers are roughly one half the neutron numbers. The statistical theory of the nucleus, which formally describes the excitation and evaporation processes, is invalid for the low atomic number

nuclei, such as carbon or aluminum, so the proton interaction probabilities were not computed using that theory. Rather, experimental data[7] were used to estimate the total neutron production probabilities as a function of incident proton energy.

Gamma rays emerge from excited nuclei, having energies depending on the specific nuclei and excitation levels. The excitation may be residual from a higher energy nucleon-producing interaction, or it may be from an inelastic scattering process in which the incident proton loses a relatively small amount of energy to the nucleus. From either cause, a discrete gamma ray spectrum results from the passage of high energy protons through matter.[8]

The secondary dose code was developed to compute, for all three components, the secondary fluxes and spectra generated in successive layers of the shielding, the secondary flux and spectra penetrating through the material between the generation layer and the interior point of interest, and the total absorbed dose at the interior point.

Description of the Code. The secondary code will not be described here in detail, as it is to be reported elsewhere.[9] Only enough discussion will be given to indicate how the preliminary results depend on the assumed secondary radiation production data, since these data are likely to be better known as more nuclear physics research is done. Then, presumably, better results will be obtained.

---

7. W. E. Crandall and G. P. Millburn, Neutron Production at High Energies, J. Appl. Phys. 29,698 (1958).

   See also R. Wallace and C. Sondhaus, (especially Figs. 12-16) this symposium, and UCRL-10439.

8. R. Madey, A. G. Duneer, Jr., and T. J. Krieger, Gamma Dose from Solar Flare Protons Incident on an Aluminum Shield, Trans. Am. Nuc. Soc. June 1962 meeting.

9. D. L. Dye, Space Proton Doses at Points Within the Human Body, The Boeing Company, D2-90106 (1962).

GENERATION AND TRANSMISSION OF SECONDARY RADIATIONS

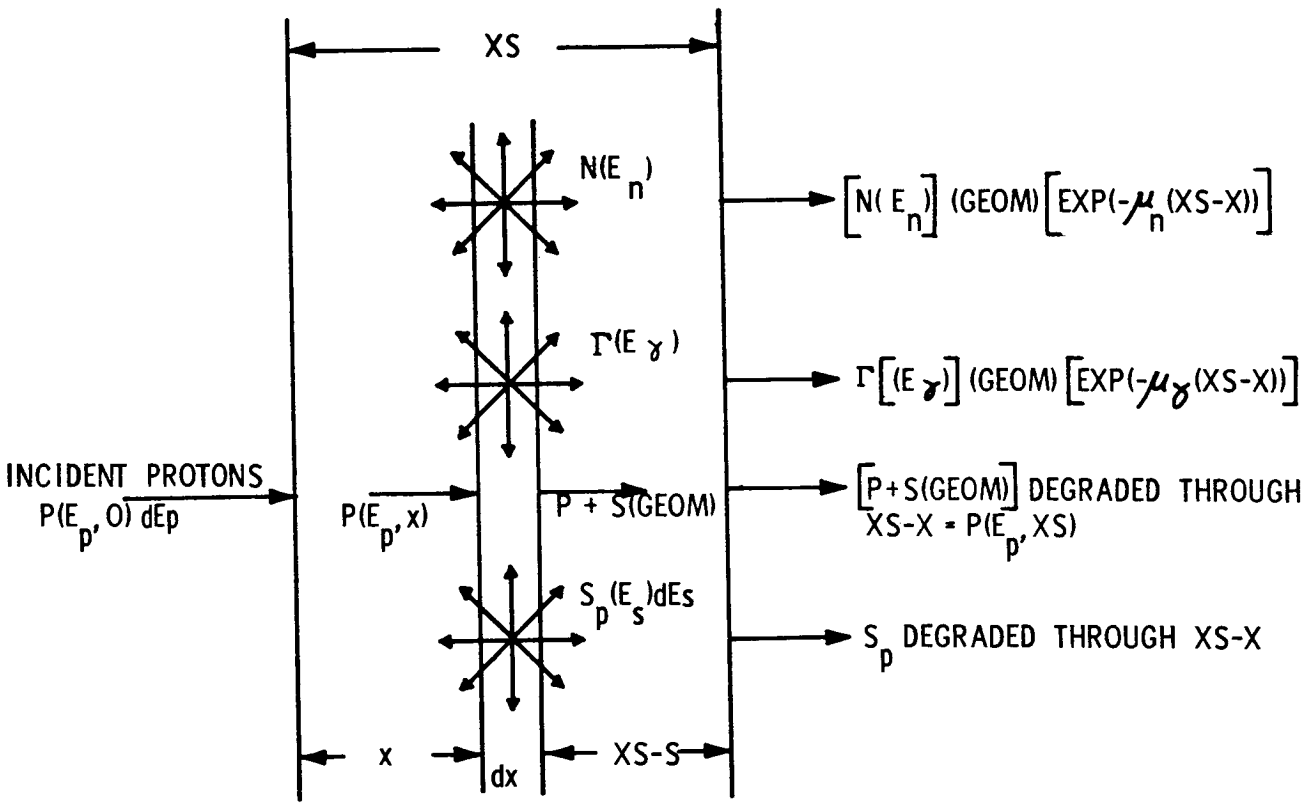

FIGURE 2

Consider a layer of shielding material, Fig. 2, of total thickness XS. At a depth X, in a layer dX thick, the secondary radiation is being generated according to:

$$N(E_n) = \frac{6 \times 10^{23} dX}{A} \int P(E_p,X)\ XNMULT(E_p,E_n)\ \sigma_n(E_p)\ dE_p, \qquad (9)$$

$$\Gamma(E_\gamma) = \frac{6 \times 10^{23} dX}{A} \int P(E_p,X)\ XGMULT(E_\gamma)\ \sigma_\gamma(E_p)\ dE_p, \qquad (10)$$

and

$$S_p(E_s)E_s = \frac{6 \times 10^{23} dX}{A} \int P(E_p,X)\ XPMULT(E_p,E_s)dE_s\ \sigma_s(E_p)\ dE_p. \qquad (11)$$

Where: A is atomic number of the shield material,

$N(E_n)$ is the flux of neutrons generated in an energy group having energy E_n,

$\Gamma(E_\gamma)$ is the flux of photons generated having energy E ,

$S_p(E_s)dE_s$ is the differential energy distribution of secondary protons generated having energy E_s to $E_s + dE_s$,

$P(E_p,X)dE_p$ is the proton energy spectrum at depth X, the flux having energy between E_p and $E_p + dE_p$,

$XNMULT(E_p,E_n)\ \sigma_n(E_p)$ is the yield of neutrons having energy E_n, per incident unit flux of protons having energy E_p,

$XGMULT(E_\gamma)\ \sigma_\gamma(E_p)$ is the yield of gamma rays having energy E_γ (due to inelastic scatter or other processes) produced per incident unit proton flux of Energy E_p. XGMULT depends primarily on the nuclear levels of the struck nucleus, while σ_γ is the cross section for an interaction,

$XPMULT(E_p,E_s)dE_s\ \sigma_s(E_p)$ is the differential yield of secondary protons having energy E_s to $E_s + dE_s$ from processes induced by incident protons of energy E_p.

The multiplicity factors (XNMULT, XGMULT, XPMULT) are normalized to one "particle" produced so that experimentally determined total yield cross sections may be used.[7,10]

---

10. T. Watasuki et al., Gamma Rays from Several Elements Bombarded by 10 and 14 Mev Protons, J. Phys. Soc. Japan 15, 1141 (1960).

A geometrical weighting factor (GEOM) is assigned to the radiation generated in any given material layer. This factor depends upon the angular distributions of the secondaries and upon the relative sizes of the vehicle shield and the dose point of interest. The fraction of the secondaries produced in a given sublayer within the shielding that is directed toward the interior dose point is given by multiplying N_s, Γ_s, or S_p by GEOM for that layer.

The neutrons and gamma rays are assumed to be absorbed by intervening shielding according to exponential laws. The protons generated in dX are added to $P(E_p,X + dX)dE_p$. (This is the reason we needed the differential energy distribution for $S_p(E_p)$). Thus, the spectrum for the next dX is enhanced by the secondary protons generated in previous sublayers.

In the actual code computation, the layer XS thick is broken up into NSL finite-thickness sublayers, where NSL is determined by a specified maximum sublayer thickness, except that NSL never exceeds another specified parameter, NSUBL. This last restriction saves computer time for thick shields.

The absorption of the neutrons and gammas is carried through all intervening shielding layers to the dose point inside, and the dose there calculated using well-known dose conversion factors. The code is dimensioned for 10 different materials and/or layers. The secondary protons are also carried through the intervening shielding separately from the total (primary plus secondary) proton flux, so as to show secondary proton dose separately. For this, the proton spectrum modification and dose code described in the previous section is used. After the absorbed doses, in rads, are computed at the interior point for each secondary component, these doses are individually converted to biological dose, in rem, by multiplying by the appropriate, specified, RBE. The individual component, as well as the total, secondary biodose is then read out. Finally, the weighted sum, Eq. 8, is done to obtain total dose from all directions at the point.

Data Used in the Secondary Dose Computation. In addition to the proton range-energy tables used in the primary dose computation, a number of nuclear and other parameters are needed in the secondary code. These include: the yield cross sections σ_n, σ_γ; the multiplicities XNMULT, XPMULT, and XGMULT; the discrete gamma ray energies generated in the specific shielding materials, designated EGAM; the gamma and neutron absorption coefficients and dose conversion factors for these energies; the angular distribution factors, GEOM, for each layer; and the maximum sublayer thickness, XLMAX, for each material. Neutron yield cross sections were found from the empirical relation

$$\sigma_n = C_1 E^{0.4}$$

which fits the experimental data[7] for aluminum and carbon (assumed the same as tissue) with $C_1 = 0.07$ and $C_1 = 0.035$, respectively. (For iron, $C_1 \simeq 0.3$.) Gamma ray yield cross sections and energies were also inferred from reported experiments [10,11] and the σ_γ values used are plotted, along with σ_n, in Fig. 3. Two different σ_γ curves were used, one in which σ_γ approaches σ_{total} at high energies, and one in which it is held constant at its low energy maximum (~ 2 barns) at high energies. This latter case is labelled "upper limit". The inelastic scatter gamma ray energies, EGAM, and multiplicities, XGMULT, for aluminum and tissue, and the NBS Handbook dose conversion coefficients, are given in Table 1.

The secondary nucleon energy distributions are somewhat less well known, and as better data become available, better dose values can be obtained by using them in this code. For the present calculation, an evaporation hump ranging from 5 to 25 Mev for secondaries was assumed for all incident proton energies above 25 Mev, and a high-energy tail was assumed to extend out to 0.5 the incident proton energy,

---

11. G. Schrank et al., Inelastic Scattering of 17-Mev Protons, Phys. Rev. 127, 2159 (1962). This paper gives many references to experimental determinations.

Table 1. Gamma Ray Energies, Multiplicities, and Dose Coefficients Assumed for the Secondary Dose Computation

Material	EGAM (Mev)	XGMULT	DOSGAM (Tissue) (rad/proton/cm^2)
Aluminum	1.4	0.45	4.8×10^{-9}
	2.2	0.19	4.0×10^{-9}
	3.0	0.25	3.5×10^{-9}
	5.0	0.08	3.3×10^{-9}
	8.0	0.03	3.2×10^{-9}
Tissue	4.4	0.88	3.0×10^{-9}
	6.1	0.06	2.9×10^{-9}
	7.0	0.06	2.9×10^{-9}

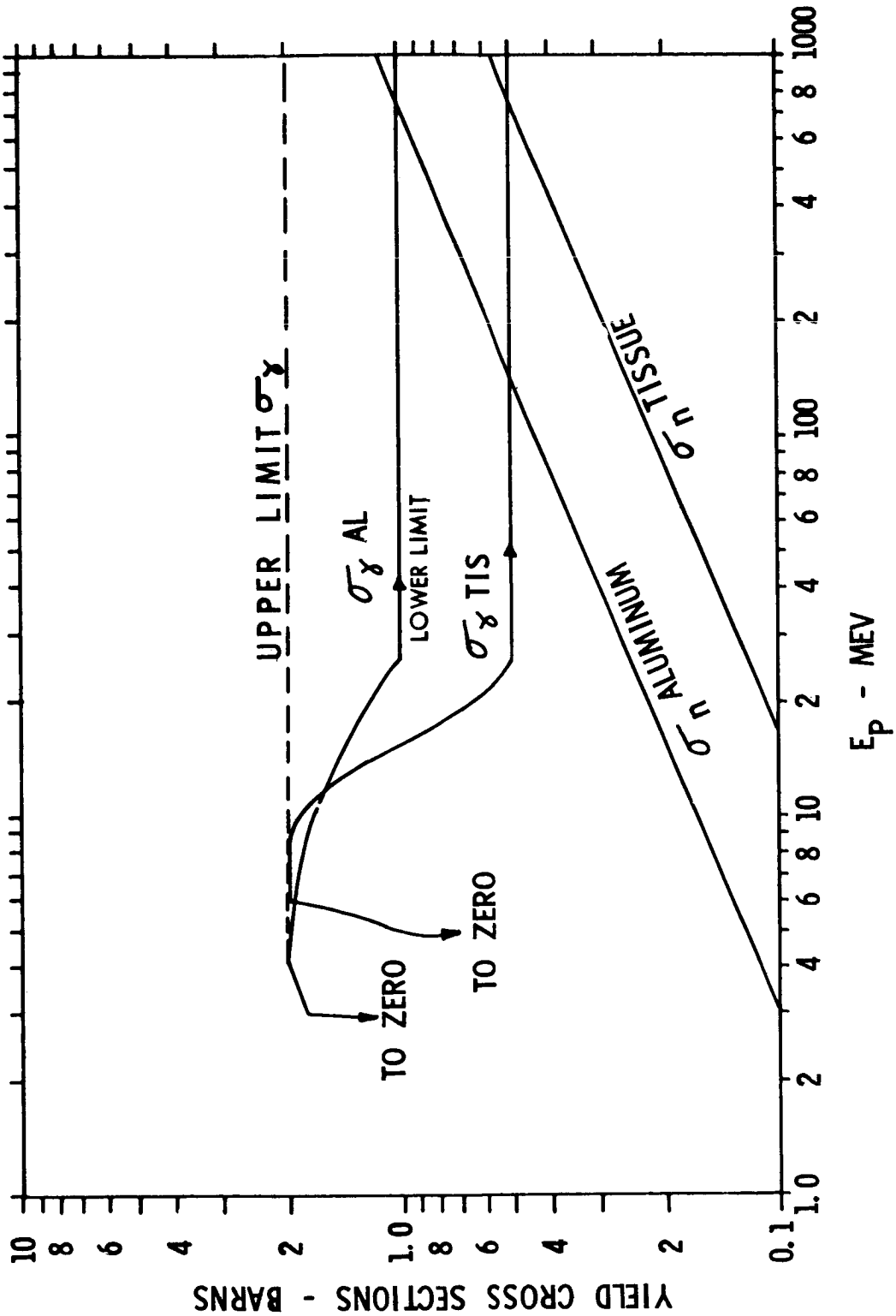
YIELD CROSS SECTIONS - BARNS
10
8
6
4
2
1.0
8
6
4
2
0.1
1.0
2
4
6
8
10
2
4
6
8
100
2
4
6
8
1000
E_p - MEV
UPPER LIMIT σ_γ
σ_γ AL
LOWER LIMIT
σ_γ TIS
TO ZERO
TO ZERO
σ_n ALUMINUM
σ_n TISSUE

FIGURE 3

containing about 10 percent of the total secondary nucleons.* The secondary spectrum was normalized, for each incident proton energy in the integration of Eq. 11, to one nucleon over the whole energy range $1 < E_s < E_p/2$. More detail is given elsewhere.[9]

The GEOM factors were assumed to be constant for each shielding layer, and were taken as 0.5 for both outer aluminum and inner tissue layers in the results to be given here.

Human Geometry

The absorbed dose at each of several points in a seated astronaut is desired. The points of specific interest are those that are parts of radiosensitive physiological systems, such as hematopoetic and spinal marrow, gut, and eye lens. Twelve such body points were chosen, located as indicated in Table 2, on a 75-percentile seated man. This body geometry is based on data given[12] in an anthropometric study of Air Force personnel. (Seventy-five percent of the men had smaller body measurements than those used.) Scale drawings of this composite astronaut's body were made and used to determine the tissue thicknesses around each of the selected body points in all directions.[3] For each specific body point listed in Table 2, this descriptive geometry problem was solved; the point is taken as the center of a large sphere on which isothickness contours are projected. These contours mark out a set of solid angular regions; a region's projected area on the sphere divided by the total sphere area is the fractional solid angle of that region. Depending on the accuracy required, one may choose any set of regions to define the fractional solid angles for the human geometry problem.

The isothickness contours are obtained by drawing a series of cross sectional views of the body at different angles ϕ from the

---

12. Hertzberg, Daniels, and Churchill, Anthropometry of Flying Personnel--1950, WADC Technical Report 52-321 (1954).

*The form of this secondary nucleon distribution is not unlike that given in this symposium by Dr. K. Strauch as a "hypothetical particle spectrum", built-up on the high energy end to account for secondary angular distributions.

TABLE 2. DESCRIPTION OF BODY POINTS ANALYZED

BODY POINT	LOCATION	SYMBOL
CENTRAL GUT	10 CM UP FROM SEAT, AND 10 CM FORWARD FROM BACK OF SEAT.	GUT
CHEST CENTER	ON THE SKIN SURFACE, 55 CM UP FROM SEAT.	CHEST 0
CHEST CENTER	2 CM IN FROM THE SKIN, IN STERNUM, 55 CM UP FROM SEAT, NEGLECTING LUNGS.	CHEST 2
CHEST CENTER	2 CM DEEP, IN STERNUM, AS BEFORE, TAKING ACCOUNT OF AIR IN LUNGS.	CHEST 2 L
SPINAL CORD REGION	55 CM UP FROM SEAT, 2 CM DEEP IN BODY.	BACK 2
FEMUR	LEG CENTER, 38 CM FORWARD FROM BACK OF SEAT, 9 CM UP FROM SEAT LEVEL (NEGLECTING BONE).	FEMUR
FEMUR	SAME POINT AS BEFORE, TAKING ACCOUNT OF BONE STRUCTURE	FEMUR B
EYE LENS	RIGHT EYE SURFACE, NEGLECTING FACIAL AND CRANIAL BONY STRUCTURE.	EYE
WAIST, RIGHT SIDE	ON THE SKIN, 25 CM UP FROM SEAT LEVEL.	WAIST 0
WAIST, RIGHT SIDE	25 CM UP FROM SEAT LEVEL, 1 CM IN FROM SKIN, ON THE MID-SAGGITAL LINE.	WAIST 1
WAIST, RIGHT SIDE	25 CM UP FROM SEAT LEVEL, 4 CM IN FROM SKIN, ON THE MID-SAGGITAL LINE.	WAIST 4
WAIST, RIGHT SIDE	25 CM UP FROM SEAT LEVEL, 6 CM IN FROM SKIN, ON THE MID-SAGGITAL LINE.	WAIST 6
WAIST, RIGHT SIDE	25 CM UP FROM SEAT LEVEL, 8 CM IN FROM SKIN, ON THE MID-SAGGITAL LINE.	WAIST 8

anterior-posterior plane; and by drawing a series of horizontal cross sectional views at various planes above and below the point of interest. A tissue thickness is then obtained by determining the true distance from the point to the body surface along every (latitude) direction θ in the ϕ plane. Figure 4 illustrates the method for a specific point. The result of this descriptive geometry problem is a map on the projection sphere showing lines of constant tissue thickness between the point of interest and the body exterior along the θ, ϕ direction. Figure 5 shows a typical isothickness contour for a body point, in the spinal column. In this procedure, the human body is assumed to be a homogeneous tissue mass except for certain cases below.

Conceptually simple, but computationally tedious, extensions of the interior body point dose calculations for the STERNUM, FEMUR, WAIST 4, and EYE LENS positions were also analyzed with slight geometric variations. These variations were intended: (1) to solve more realistic problems that include bones and lung absorption effects, (2) to give an idea as to the dose error made in neglecting bones and lungs; i.e., in assuming the body to be homogeneous, (3) to assess the shielding effectiveness of partial body shielding built in as a chair, and (4) to assess the effect of goggles in eye protection.

Incident Proton Spectra

Five different incident proton spectra were considered; four having power law forms, the other approximating the Van Allen belt spectrum. The power law forms, normalized to one proton/cm^2 of E > 100 Mev, are given by:

$$N(E)dE = (n - 1)(100)^{n-1} E^{-n} dE \text{ for } 20 \text{ Mev} \leq E \leq 1{,}000 \text{ Mev}$$

for the parameter n with values 2, 3, 4, and 5. They are flat at the 20 Mev value for the interval $1 \leq E \leq 20$ Mev. The Van Allen spectrum is normalized to one proton/cm^2 of E > 40 Mev, and has an E^{-2} form above 100 Mev, with the lower energy part of Hess's theoretical form matched to it at 100 Mev.

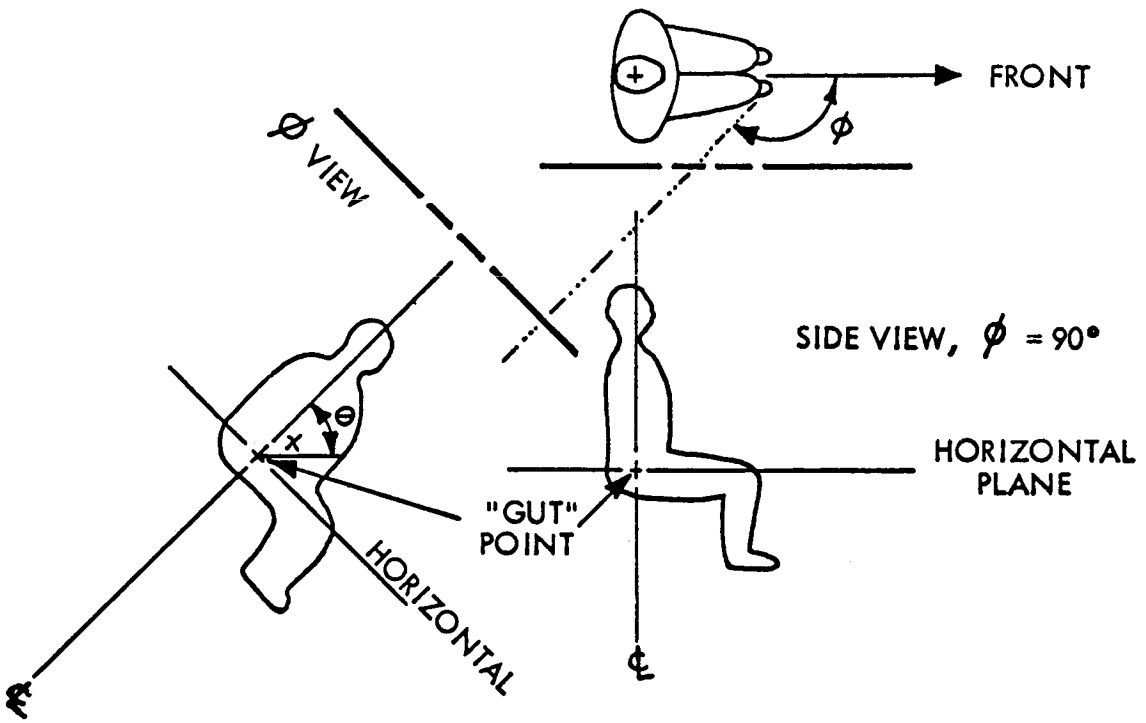

FIGURE 4

℄ IS VERTICAL AXIS, PASSING THROUGH THE POINT OF INTEREST

ϕ IS LONGITUDE ANGLE

θ IS LATITUDE ANGLE

x IS THICKNESS, A FUNCTION OF θ AND ϕ FOR THIS POINT

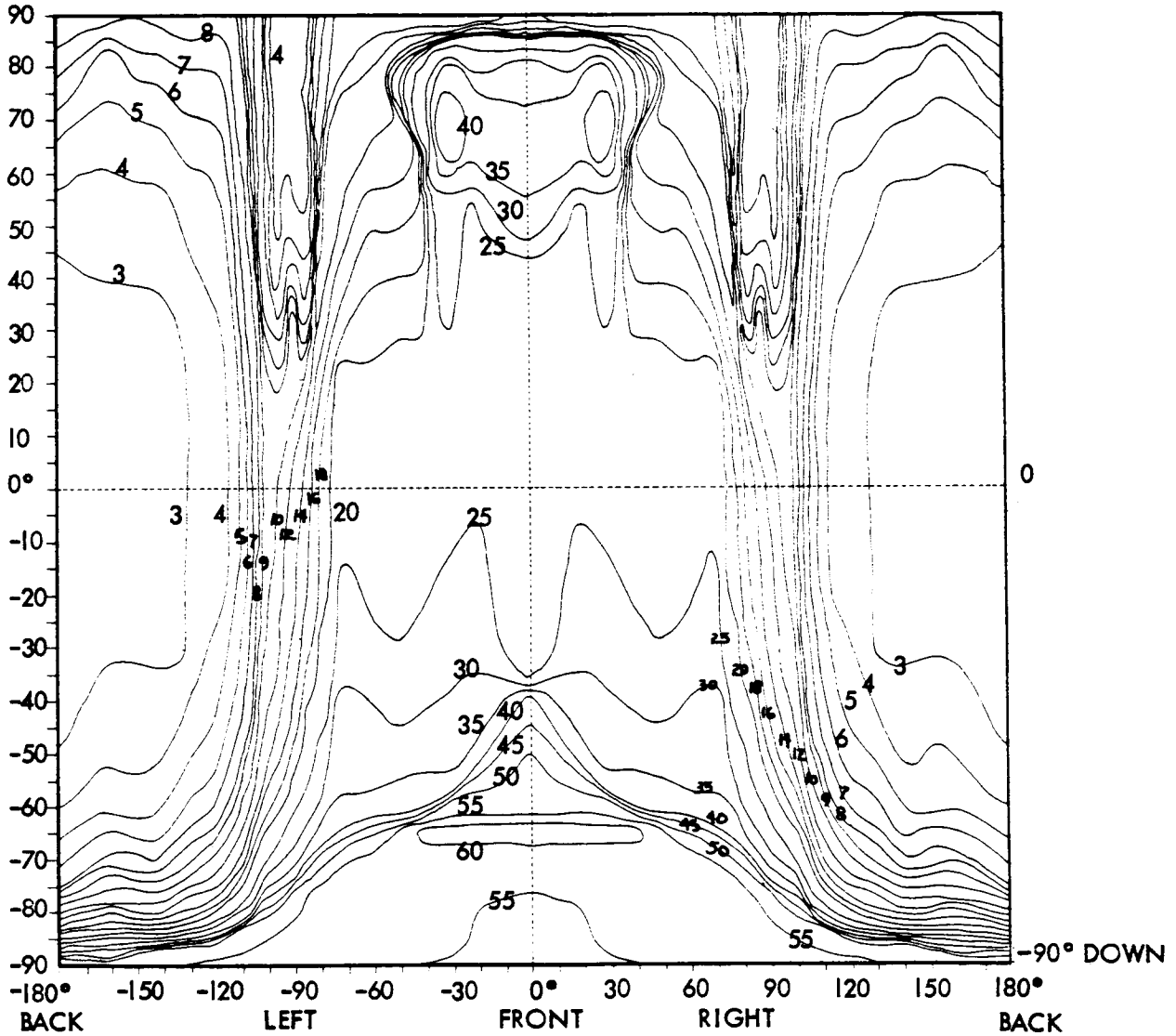
90
80
70
60
50
40
30
20
10
0°
-10
-20
-30
-40
-50
-60
-70
-80
-90
0
-90° DOWN
-180° -150 -120 -90 -60 -30 0° 30 60 90 120 150 180°
BACK
LEFT
FRONT
RIGHT
BACK
SPINAL COLUMN

FIGURE 5

Dose Results

Figure 6 shows the penetrating primary proton dose and the secondary dose plotted separately for the E^{-3} spectrum and for one-dimensional cases. It is seen that the nuclear data assumptions made here lead to a relatively small secondary radiation dose, even with "upper limit" inelastic scatter cross sections. It should be noted that for steeper primary spectra the primary absorption is greater, so that the secondary dose is a larger fraction of the primary than for spectra having smaller n values.[9] However, the secondary dose is clearly a small fraction of the primary proton dose for tissue thicknesses up to 20 gm/cm^2 and aluminum shields of up to 10 gm/cm^2, for typical space proton spectra. Further, the solid angle subtended by tissue thickness greater than 20 gm/cm^2 around the deepest body points considered (GUT, WAIST 8) totals only about 20 percent[3], and it is even less for most radiosensitive organs. Thus the total dose to these organs is essentially equal to the primary proton dose, computed by Eq. 8, for feasibly thin external aluminum shields.

Tables 3 through 7 show the total doses at each of the body points considered for a variety of aluminum shells for the E^{-2}, E^{-3}, E^{-4}, E^{-5}, and Van Allen spectra, respectively. The units are tissue rad per incident isotropic proton/cm^2 having $E > 100$ Mev. These values utilize the three-dimensional human geometry analyses, Eq. 8, and the solid-line cross section data of Fig. 3. The nuclear data used are thus reasonable composites of published experimental information.

In addition to the twelve body points with only external shell shielding, four special cases are listed. In the case WAIST 4S, a shielding chair of either 2 gm/cm^2 or 4 gm/cm^2 polyethylene is considered with three outer aluminum shell values. The line labelled FEMUR B is a 72-region case in which the structure of the bone was considered. The line labelled EYE G is a case in which 0.25 cm of lead glass was added to the zero tissue thickness region of the EYE analysis; that is, to the front of the eye lens. The case CHEST 2

PRIMARY & SECONDARY DOSES DUE TO E^{-3} SPECTRUM PROTONS MONODIRECTIONAL FLUX, NORMALIZED TO 1 PROTON / CM^2 OF E > 100 MEV

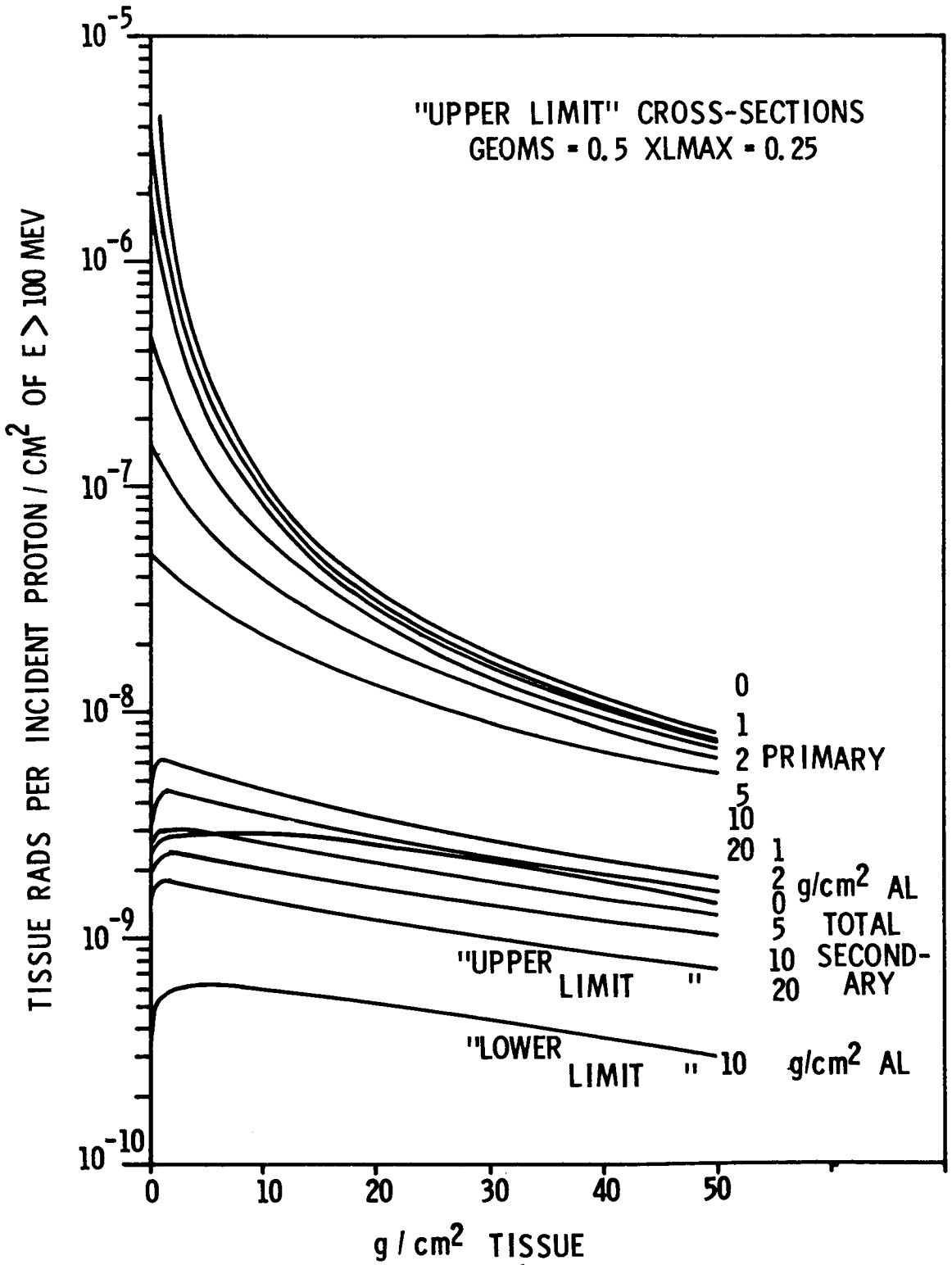

FIGURE 6

Table 3. Doses at Specific Body Points Due to Incident Isotropic Proton Flux with n = 2 Spectrum, for Various Aluminum Shell Shield Thicknesses (rads per proton/cm^2 of E > 100 Mev)

Body Points	Aluminum Shell Thickness (gm/cm^2)						
	0	1	2	4	6	8	10
GUT	5.4×10^{-8}	5.1×10^{-8}	4.8^{-8}	4.3×10^{-8}	3.9×10^{-8}	3.6×10^{-8}	3.3×10^{-8}
CHEST 0	3.0×10^{-6}	6.5×10^{-7}	3.3×10^{-7}	1.7×10^{-7}	1.2×10^{-7}	8.9×10^{-8}	7.3×10^{-8}
CHEST 2	1.3×10^{-7}	1.1×10^{-7}	9.2×10^{-8}	7.2×10^{-8}	6.1×10^{-8}	5.2×10^{-8}	4.6×10^{-8}
CHEST 2L (Sternum)	1.4×10^{-7}	1.2×10^{-7}	1.0×10^{-7}	8.0×10^{-8}	6.7×10^{-8}	5.8×10^{-8}	5.1×10^{-8}
BK 2 (Spinal Column)	1.4×10^{-7}	1.1×10^{-7}	9.5×10^{-8}	7.5×10^{-8}	6.2×10^{-8}	5.4×10^{-8}	4.7×10^{-8}
WAIST 0	2.4×10^{-6}	5.2×10^{-7}	2.7×10^{-7}	1.4×10^{-7}	1.0×10^{-7}	7.9×10^{-8}	6.5×10^{-8}
WAIST 1	1.3×10^{-7}	1.1×10^{-7}	9.5×10^{-8}	7.5×10^{-8}	6.2×10^{-8}	5.4×10^{-8}	4.7×10^{-8}
WAIST 4	7.6×10^{-8}	6.9×10^{-8}	6.3×10^{-8}	5.4×10^{-8}	4.8×10^{-8}	4.3×10^{-8}	3.9×10^{-8}
WAIST 6	6.1×10^{-8}	5.7×10^{-8}	5.3×10^{-8}	4.7×10^{-8}	4.2×10^{-8}	3.8×10^{-8}	3.5×10^{-8}
WAIST 8	5.5×10^{-8}	5.2×10^{-8}	4.9×10^{-8}	4.3×10^{-8}	3.9×10^{-8}	3.6×10^{-8}	3.3×10^{-8}
WAIST 4S (2 gm/cm^2 CH_2chair)	6.6×10^{-8}		5.6×10^{-8}		4.4×10^{-8}		
(4 gm/cm^2 CH_2chair)	5.9×10^{-8}		5.1×10^{-8}		4.4×10^{-8}		
FEMUR	8.0×10^{-8}	7.2×10^{-8}	6.6×10^{-8}	5.7×10^{-8}	5.0×10^{-8}	4.5×10^{-8}	4.1×10^{-8}
FEMUR B	8.0×10^{-8}	7.3×10^{-8}	6.7×10^{-8}	5.8×10^{-8}	5.2×10^{-8}	4.7×10^{-8}	4.5×10^{-8}
EYE	2.5×10^{-6}	5.6×10^{-7}	3.1×10^{-7}	1.7×10^{-7}	1.2×10^{-7}	9.1×10^{-8}	7.5×10^{-8}
EYE G (2.5 mm glasses)	1.1×10^{-6}	4.4×10^{-7}	2.6×10^{-7}				

Table 4. Doses at Specific Body Points Due to Incident Isotropic Proton Flux with n = 3 Spectrum, for Various Aluminum Shell Shield Thicknesses (rads per proton/cm^2 of E > 100 Mev)

Body Points	Aluminum Shell Thickness (gm/cm^2)						
	0	1	2	4	6	8	10
GUT	5.6×10^{-8}	5.0×10^{-8}	4.6×10^{-8}	3.9×10^{-8}	3.4×10^{-8}	2.9×10^{-8}	2.6×10^{-8}
CHEST 0	2.8×10^{-8}	3.5×10^{-6}	1.2×10^{-6}	3.9×10^{-7}	2.1×10^{-7}	1.3×10^{-7}	9.5×10^{-8}
CHEST 2	2.8×10^{-7}	2.0×10^{-7}	1.5×10^{-7}	9.9×10^{-8}	7.3×10^{-8}	5.6×10^{-8}	4.6×10^{-8}
CHEST 2L (Sternum)	2.9×10^{-7}	2.1×10^{-7}	1.6×10^{-7}	1.1×10^{-7}	8.2×10^{-8}	6.4×10^{-5}	5.2×10^{-8}
BK 2 (Spinal Column)	3.0×10^{-7}	2.1×10^{-7}	1.6×10^{-7}	1.0×19^{-7}	7.6×10^{-8}	5.8×10^{-8}	4.7×10^{-8}
WAIST 0	2.2×10^{-5}	2.7×10^{-6}	9.2×10^{-7}	3.2×10^{-7}	1.7×10^{-7}	1.1×10^{-7}	8.1×10^{-8}
WAIST 1	2.9×10^{-7}	2.0×10^{-7}	1.6×10^{-7}	1.0×10^{-8}	7.5×10^{-8}	5.8×10^{-8}	4.7×10^{-8}
WAIST 4	1.1×10^{-7}	9.0×10^{-8}	7.7×10^{-8}	5.9×10^{-8}	4.8×10^{-8}	4.0×10^{-8}	3.4×10^{-8}
WAIST 6	7.2×10^{-8}	6.4×10^{-8}	5.7×10^{-8}	4.6×10^{-8}	3.9×10^{-8}	3.3×10^{-8}	2.9×10^{-8}
WAIST 8	6.0×10^{-8}	5.3×10^{-8}	4.8×10^{-8}	4.0×10^{-8}	3.4×10^{-8}	3.0×10^{-8}	2.6×10^{-8}
WAIST 4S (2 gm/cm^2 CH_2 chair)	8.3×10^{-8}		6.3×10^{-8}		4.1×10^{-8}		
(4 gm/cm^2 CH_2 chair)	7.0×10^{-8}		5.4×10^{-8}		3.7×10^{-8}		
FEMUR	1.1×10^{-7}	9.3×10^{-8}	8.0×10^{-8}	6.3×10^{-8}	5.1×10^{-8}	4.2×10^{-8}	3.6×10^{-8}
FEMUR B	1.1×10^{-7}	9.4×10^{-8}	8.2×10^{-8}	6.4×10^{-8}	5.3×10^{-8}	4.4×10^{-8}	3.8×10^{-8}
EYE	2.2×10^{-5}	2.9×10^{-6}	1.0×10^{-6}	3.6×10^{-7}	2.0×10^{-7}	1.3×10^{-7}	9.6×10^{-8}
EYE G (2.5 mm glasses)	7.1×10^{-6}	1.9×10^{-6}	8.3×10^{-7}				

Table 5. Doses at Specific Body Points Due to Incident Isotropic Proton Flux with n = 4 Spectrum, for Various Aluminum Shell Shield Thicknesses (rads per proton/cm^2 or E > 100 Mev)

Body Points	Aluminum Shell Thickness (gm/cm^2)						
	0	1	2	4	6	8	10
GUT	6.3×10^{-8}	5.6×10^{-8}	4.7×10^{-8}	3.8×10^{-8}	3.1×10^{-8}	2.6×10^{-8}	2.0×10^{-8}
CHEST 0	2.2×10^{-4}	1.7×10^{-5}	3.9×10^{-6}	8.4×10^{-7}	3.3×10^{-7}	1.7×10^{-7}	1.1×10^{-7}
CHEST 2	5.7×10^{-7}	3.4×10^{-7}	2.3×10^{-7}	1.3×10^{-7}	8.1×10^{-8}	5.6×10^{-8}	4.4×10^{-8}
CHEST 2L (Sternum)	5.9×10^{-7}	3.6×10^{-7}	2.4×10^{-7}	1.4×10^{-7}	8.8×10^{-8}	6.2×10^{-8}	4.7×10^{-8}
BK 2 (Spinal Column)	6.0×10^{-7}	3.6×10^{-7}	2.5×10^{-7}	1.4×10^{-7}	8.5×10^{-8}	6.1×10^{-8}	4.7×10^{-8}
WAIST 0	1.6×10^{-4}	1.3×10^{-5}	2.8×10^{-6}	6.3×10^{-7}	2.6×10^{-7}	1.4×10^{-7}	9.4×10^{-8}
WAIST 1	5.7×10^{-7}	3.5×10^{-7}	2.4×10^{-7}	1.4×10^{-7}	8.6×10^{-8}	6.0×10^{-8}	4.5×10^{-8}
WAIST 4	1.5×10^{-7}	1.1×10^{-7}	8.9×10^{-8}	6.2×10^{-8}	4.6×10^{-8}	3.5×10^{-8}	2.9×10^{-8}
WAIST 6	8.3×10^{-8}	7.0×10^{-8}	5.8×10^{-8}	4.3×10^{-8}	3.4×10^{-8}	2.7×10^{-8}	2.3×10^{-8}
WAIST 8	6.4×10^{-8}	5.5×10^{-8}	4.7×10^{-8}	3.6×10^{-8}	3.0×10^{-8}	2.4×10^{-8}	2.0×10^{-8}
WAIST 4S (2 gm/cm^2 CH_2 chair)	1.0×10^{-7}		6.6×10^{-8}		3.8×10^{-8}		
(4 gm/cm^2 CH_2 chair)	8.3×10^{-8}		5.7×10^{-8}		3.3×10^{-8}		
FEMUR	1.4×10^{-7}	1.2×10^{-7}	8.9×10^{-8}	6.3×10^{-8}	4.8×10^{-8}	3.8×10^{-8}	3.1×10^{-8}
FEMUR B	1.3×10^{-7}	1.1×10^{-7}	8.9×10^{-8}	6.5×10^{-8}	5.0×10^{-8}	3.9×10^{-8}	3.1×10^{-8}
EYE	1.7×10^{-4}	1.4×10^{-5}	3.0×10^{-6}	6.1×10^{-7}	3.1×10^{-7}	1.8×10^{-7}	1.2×10^{-7}
EYE G (2.5 mm glasses)	3.9×10^{-5}	8.4×10^{-6}	2.3×10^{-6}				

Table 6. Doses at Specific Body Points Due to Incident Isotropic Proton Flux with n = 5 Spectrum, for Various Aluminum Shell Thicknesses (rads per proton/cm^2 of E > 100 Mev)

Body Points	Aluminum Shell Thickness (gm/cm^2)						
	0	1	2	4	6	8	10
GUT	5.8×10^{-8}	5.4×10^{-8}	4.2×10^{-8}	3.3×10^{-8}	2.5×10^{-8}	2.2×10^{-8}	1.9×10^{-8}
CHEST 0	1.6×10^{-3}	7.8×10^{-5}	1.0×10^{-5}	1.4×10^{-6}	4.8×10^{-7}	2.3×10^{-7}	1.2×10^{-7}
CHEST 2	1.1×10^{-6}	6.2×10^{-7}	3.4×10^{-7}	1.6×10^{-7}	8.7×10^{-8}	5.9×10^{-8}	4.2×10^{-8}
CHEST 2L (Sternum)	1.1×10^{-6}	6.0×10^{-7}	3.6×10^{-7}	1.7×10^{-7}	9.7×10^{-8}	6.5×10^{-8}	4.7×10^{-8}
BK 2 (Spinal Column)	1.1×10^{-6}	6.0×10^{-7}	3.7×10^{-7}	1.7×10^{-7}	1.0×10^{-7}	6.4×10^{-8}	4.9×10^{-8}
WAIST 0	1.2×10^{-3}	6.0×10^{-5}	7.9×10^{-6}	1.1×10^{-6}	3.8×10^{-7}	1.8×10^{-7}	1.0×10^{-7}
WAIST 1	1.0×10^{-6}	5.4×10^{-7}	3.3×10^{-7}	1.5×10^{-7}	8.9×10^{-8}	5.8×10^{-8}	4.1×10^{-8}
WAIST 4	1.8×10^{-7}	1.3×10^{-7}	9.8×10^{-8}	6.3×10^{-8}	4.4×10^{-8}	3.3×10^{-8}	2.6×10^{-8}
WAIST 6	8.3×10^{-8}	5.7×10^{-8}	5.9×10^{-8}	4.1×10^{-8}	3.1×10^{-8}	2.5×10^{-8}	2.2×10^{-8}
WAIST 8	6.8×10^{-8}	5.9×10^{-8}	4.7×10^{-8}	3.3×10^{-8}	2.7×10^{-8}	2.2×10^{-8}	19.0×10^{-9}
WAIST 4S (2 gm/cm^2 CH_2 chair)	1.1×10^{-7}		6.7×10^{-8}		3.4×10^{-8}		
(4 gm/cm^2 CH_2 chair)	8.9×10^{-8}		5.4×10^{-8}		3.0×10^{-8}		
FEMUR	1.7×10^{-7}	1.4×10^{-7}	9.9×10^{-8}	6.3×10^{-8}	4.5×10^{-8}	3.4×10^{-8}	2.7×10^{-8}
FEMUR B	1.5×10^{-7}	1.3×10^{-7}	9.6×10^{-8}	6.4×10^{-8}	4.7×10^{-8}	3.7×10^{-8}	2.75×10^{-8}
EYE	1.2×10^{-3}	6.2×10^{-5}	8.3×10^{-6}	1.2×10^{-6}	4.2×10^{-7}	2.0×10^{-7}	1.1×10^{-7}
EYE G (2.5 mm glasses)	1.9×10^{-4}	3.7×10^{-5}	5.5×10^{-6}				

Table 7. Doses at Specific Body Points Due to Incident Isotropic Proton Flux with Van Allen Spectrum, for Various Aluminum Shell Shield Thicknesses (rads per proton/cm^2 of E > 40 Mev)

Body Points	Aluminum Shell Thickness (gm/cm^2)						
	0	1	2	4	6	8	10
GUT	3.1×10^{-8}	2.9×10^{-8}	2.8×10^{-8}	2.5×10^{-9}	2.3×10^{-8}	2.1×10^{-8}	1.9×10^{-8}
CHEST 0	3.8×10^{-7}	1.3×10^{-7}	1.0×10^{-7}	7.5×10^{-8}	6.0×10^{-8}	5.0×10^{-8}	4.2×10^{-8}
CHEST 2	6.0×10^{-8}	5.4×10^{-8}	4.9×10^{-8}	4.1×10^{-8}	3.5×10^{-8}	3.0×10^{-8}	2.7×10^{-8}
CHEST 2L (Sternum)	6.7×10^{-8}	6.0×10^{-8}	5.4×10^{-8}	4.6×10^{-8}	3.9×10^{-8}	3.4×10^{-8}	3.0×10^{-8}
BK 2 (Spinal Column)	6.2×10^{-8}	5.6×10^{-8}	5.0×10^{-8}	4.2×10^{-8}	3.6×10^{-8}	3.1×10^{-8}	2.7×10^{-8}
WAIST 0	3.1×10^{-7}	1.2×10^{-7}	9.4×10^{-8}	6.9×10^{-8}	5.5×10^{-8}	4.5×10^{-8}	3.8×10^{-8}
WAIST 1	6.4×10^{-8}	5.7×10^{-8}	5.2×10^{-8}	4.3×10^{-8}	3.7×10^{-8}	3.1×10^{-8}	2.8×10^{-8}
WAIST 4	4.4×10^{-8}	4.0×10^{-8}	3.7×10^{-8}	3.2×10^{-8}	2.8×10^{-8}	2.5×10^{-8}	2.3×10^{-8}
WAIST 6	3.6×10^{-8}	3.3×10^{-8}	3.1×10^{-8}	2.7×10^{-8}	2.4×10^{-8}	2.2×10^{-8}	2.0×10^{-8}
WAIST 8	3.2×10^{-8}	3.0×10^{-8}	2.8×10^{-8}	2.5×10^{-8}	2.3×10^{-8}	2.1×10^{-8}	1.9×10^{-8}
WAIST 4S (2 gm/cm^2 CH_2 chair)	3.8×10^{-8}		3.3×10^{-8}		2.5×10^{-8}		
(4 gm/cm^2 CH_2 chair)	3.4×10^{-8}		3.0×10^{-8}		2.4×10^{-8}		
FEMUR	4.5×10^{-8}	4.2×10^{-8}	3.8×10^{-8}	3.3×10^{-8}	2.9×10^{-8}	2.6×10^{-8}	2.4×10^{-8}
FEMUR B	4.7×10^{-8}		4.0×10^{-8}		3.0×10^{-8}		
EYE	3.3×10^{-7}	1.3×10^{-7}	1.0×10^{-7}	7.7×10^{-8}	6.2×10^{-8}	5.1×10^{-8}	4.3×10^{-8}
EYE G (2.5 mm glasses)	1.5×10^{-7}	1.0×10^{-7}	8.6×10^{-8}				

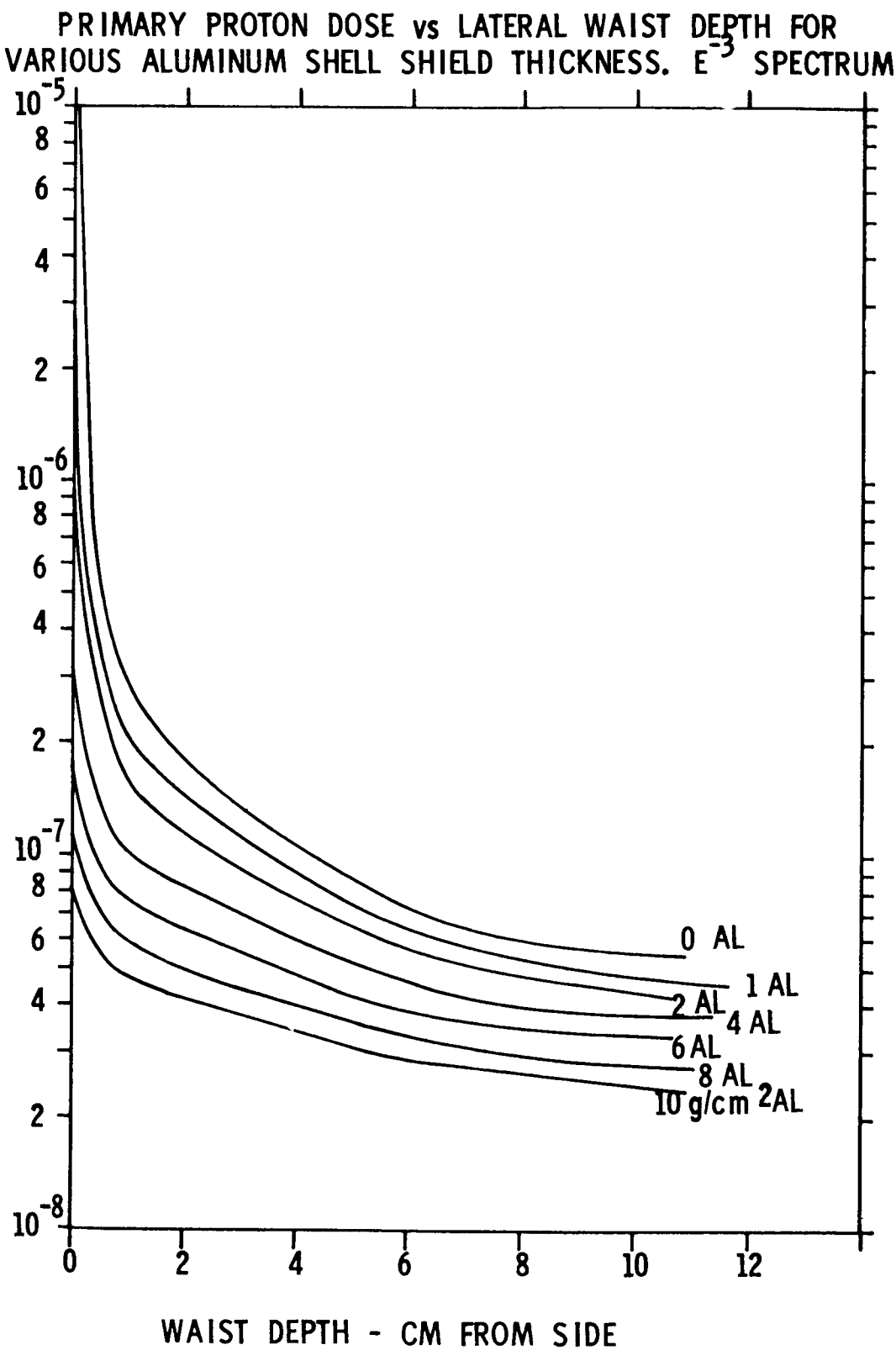
PRIMARY PROTON DOSE vs LATERAL WAIST DEPTH FOR VARIOUS ALUMINUM SHELL SHIELD THICKNESS. E^-3 SPECTRUM
10^-5
8
6
4
2
10^-6
8
6
4
2
10^-7
8
6
4
2
10^-8
0 AL
1 AL
2 AL
4 AL
6 AL
8 AL
10 g/cm 2AL
0
2
4
6
8
10
12
WAIST DEPTH - CM FROM SIDE

FIGURE 7

Paper E-1

LONG RANGE NASA SHIELDING REQUIREMENTS

J. Warren Keller
Headquarters, National Aeronautics and Space Administration
Washington, D.C.

Abstract

The NASA being confronted with the relatively short range problem of shielding for Project Apollo is faced with the task of developing a shielding technology which can be applied not only to Apollo but to future manned or unmanned missions as well. This task is the responsibility of the Office of Advanced Research and Technology working through the NASA centers and their contractors.

Future missions will present in many cases much more severe shielding problems than those encountered in Apollo, primarily because of their longer duration in affected regions in space. In this paper several types of future missions are discussed in a quite general manner to establish the magnitude of the shielding problems that may exist. Also, some of the uncertainties in environmental data and shielding calculations are discussed in an effort to clear up some misconceptions which exist as to the need for a significant shielding effort with respect to future missions.

It is obvious that the available on-board mass in the form of equipment, fuel, etc., must be utilized as shielding where possible. However, high effectiveness in the utilization of such mass may be difficult. The importance of accurate determination of such effectiveness is pointed out.

An effort is made to outline a general approach to the space vehicle shielding problem.

Introduction

All space vehicles will, to some degree, be exposed to particulate radiation fields in space. Consequently, the NASA, besides being confronted with the relatively short range problem of radiation shielding for Project Apollo, is faced with the task of developing a shielding technology which can be applied not only to Apollo but to future manned or unmanned missions as well. This task is the responsibility of the

ignores air in the lungs and bilateral asymmetry due to the heart; CHEST 2L takes these into account. It is seen from Tables 3 through 7 that to take account of lung air or bone structure is hardly worth the extra analysis effort and computing time for the proton dose.

The depth-dose pattern in the human body is felt to be of special significance[13] and so the doses at points laterally along the waist are plotted in Fig. 7 to show the representative pattern. It is seen from Fig. 7 and the tabulated values that a midline dose of 15 to 30 percent the skin dose is typical, dpending on shielding and spectrum in obvious ways.

Because of the normalization used in the values reported here, they may readily be applied to environment data. If a trajectory is known, the trapped proton flux of $E > 40$ Mev may be computed and integrated over the orbit.[14] If a specific solar flare proton event is estimated to have a spectrum denoted by n and size in protons/cm^2, both parameters integrated over the whole event, (or instantaneous flux in protons/cm^2-sec), then total dose (or dose rate) may be determined to any of the body points. An estimated flare size-probability curve can be converted to significant dose-probability[15] using these data and vehicle shielding assumptions. By simple descriptive geometry techniques and the codes here reported, the shielding required in specific vehicle designs may be computed so as to maintain a desired lower probability limit for specified organ tolerance dose.

---

13. K. L. Jackson, The Lethal Effectiveness of a Solar Flare-type Dose Distribution Delivered to the Rat, this symposium.

14. F. C. Perry, Proton Fluxes Along Trajectories Through the Inner Van Allen Belt, this symposium.

15. E. L. Chupp, D. L. Dye, B. W. Mar, L. O. Oncley, and R. W. Williams, Analysis of Solar-Flare Hazards to Manned Space Systems, The Boeing Company, D2-11608 (1961)

Office of Advanced Research and Technology, within NASA Headquarters, working through the various NASA centers and their contractors.

The importance of the radiation portion of the total vehicle environment will depend to a very large extent upon the given mission. While the Apollo vehicle may be exposed to each of the major components of the indigenous radiation in space, future missions will present, in many cases, much more severe shielding problems for man and equipment, primarily because of their longer duration in the affected regions.

The purposes of this paper are:

(1) to outline, in a general sense, the nature and possible magnitude of the radiation shielding problem for several categories of future missions,

(2) to discuss some of the uncertainties in environmental data and shielding calculations and some of the reasons for wide variations in the results of dose calculations,

(3) to attempt to clear up some misconceptions as to the need for a significant shielding effort with respect to future space vehicle missions, and

(4) to outline a general approach to the space vehicle shielding problem.

A significant problem exists with respect to the protection of certain components of unmanned vehicles from damaging radiations in space. This problem, however, will not be considered in this paper, which is devoted primarily to the problem for manned missions. Also the problem of shielding against radiation leakage from on-board reactor power sources is not considered.

Mission Categories

Most future manned missions may be categorized, in a broad sense, into groups based on the nature of the radiation environment which will be encountered. In this section several such categories are discussed, in a quite general manner, to establish the nature and magnitude of the shielding problems that will exist.

The curves of dose as a function of shield thickness for each of the categories considered are for infinitesimally small samples of tissue located at the center of a spherical shield (model discussed later in this paper) and were derived primarily from data given in the sources below. [1-5]

---

1. Keller, J. W., A Study of Shielding Requirements for Manned Space Missions, Convair-Ft. Worth Report FZK-124 (1960).

2. Bailey, D. K., "Time Variations of the Energy Spectrum of Solar Cosmic Rays in Relation to the Radiation Hazard in Space" Journal of Geophysical Research, 67, pp 391-296 (1962).

References 3-5 continued on next page.

The curves should be considered only as approximations to the actual doses and should not be taken as definitive. However, they should be of sufficient accuracy to illustrate rather well the relative importance of the various components and the magnitude of the shielding problems. The curves for the solar protons are based on observations over a portion of the last solar cycle. There is, of course, no assurance that this represents the worst possible case.

Two-Week Lunar Mission- Figure 1, illustrates the radiation environment for a two week lunar mission such as Apollo and is included primarily as a point of comparison with the immediate short range shielding problem. The solar proton component is based on the occurrence of a single "typical" large event[2] which in itself is a rather unlikely happening. Even with the occurrence of such an event one is well below the dose limits[6] presently considered for Apollo if only quite thin shields are used. The galactic cosmic radiation and the Van Allen belts are seen to be of very little significance for this type of mission.

Interplanetary Missions- The radiation problem for interplanetary missions will depend to a large extent upon the manner in which the missions are carried out. Consequently these types of missions are divided into two categories for consideration of the radiation problem. The first category [Fig. 2(a)] represents those missions which are characterized by high thrust, rapid traversal of the Van Allen radiation belt of which the two-week lunar mission discussed previously may be considered a special case. The second category [Fig. 2(b)] on the other hand, is representative of missions accomplished with low thrust vehicles, such as those utilizing electric propulsion, which spiral slowly through the region of the trapped radiation. The curves for both cases are based arbitrarily upon a two to three year mission duration.

---

3. Malitson, H. H., and Webber, W. R., A Summary of Solar Cosmic Ray Events, Solar Proton Manual, Goddard Space Flight Center Report X-611-62-122, pp 1-17, (1962).

4. Schaefer, H. J., "Radiation and Man in Space", Advances in Space Science, Vol. 1, (edited by F. I. Ordway, III), Academic Press, New York (1959).

5. Tobias, C. A., Radiation Hazards in High Altitude Aviation, WADC Technical Report 52-119, May 1952.

6. Gill, W. L., "Shielding Requirements for Apollo", paper presented at symposium on "Protection Against Radiation Hazards in Space", Gatlinburg, Tennessee, Nov 5-7, 1962.

It is seen that the radiation problems encountered in these two categories differ. In the high thrust case the problem is primarily that resulting from solar protons while in the case of the low thrust trajectory the trapped radiation presents the major problem. This difference of course, arises not through any difference in the solar proton or galactic cosmic ray environments but from the difference in exposure time in the Van Allen belt. It is noted that whereas about 10 gm/cm^2 will reduce the dose to a few hundred rem in the high thrust case, 80-100 gm/cm^2 are required to accomplish a similar reduction in the low thrust case. Also for large shield thicknesses, as in the case of the low thrust mission, secondary production in the shield (not considered in the curve in Fig. 2(b)) will become important making the dose still greater than that indicated in the figure.

It is seen from the graphs that as long as the tolerant mission dose is kept above several 10's of rem the controlling components as far as the shielding problem is concerned are the solar protons and the Van Allen belt protons for the high thrust and low thrust cases respectively. On the other hand, if the tolerant dose were lowered below this level one would be faced with the problem of shielding against primary cosmic rays - a very difficult task. Unless one is forced to live with such low tolerant doses much more shielding will be required for the low thrust than for the high thrust missions. On the other hand, the low thrust vehicles are likely to be able to afford considerably more shielding (weight-wise) than those using high thrust propulsion techniques.

Another source of radiation which may be a factor in interplanetary missions but has not been included in the above considerations is the existence of radiation belts surrounding other planets having magnetic fields. Some attention has been given to this problem by others.[7]

The picture as presented in Fig. 2(a) would also be indicative of the shielding problem for personnel manning a lunar base.

Orbital Missions- The nature of the radiation problem for orbital missions in the region occupied by the trapped radiation belt is indicated in Fig. 3. Here the missions may be divided into two general categories- (1) those utilizing equatorial orbits [Fig. 3(a)] and (2) those calling for polar orbits [Fig. 3(b)]. The primary type of mission for which these categories would apply would be the manned space station. Since it would be highly desirable to be able to leave a crewman in such a station for a period of from six months to a year the curves in Fig. 3 are based on a one year period. Contracting

7. Singer, S. F., "Some Considerations of Expected Radiation Belts of Planets Mars and Venus", Advances in Astronautical Sciences, Vol. 6, The MacMillan Co., New York (1961).

or expanding this period, however, would not significantly effect the relative importance of the various components as indicated but would only change their absolute magnitude. The shaded areas indicated for the Van Allen belt radiation in Fig. 3 are representative of the variation in radiation intensity over altitudes from about ~900 to ~7500 km.

The chief difference in the radiation environment for the polar orbit as opposed to the equatorial orbit is the disappearance of the solar proton radiation in the latter case. This, of course, is due to the shielding afforded by the earth's magnetic field, as is the variation noted for the galactic cosmic radiation. Also a difference is noted in the magnitude for the trapped radiation component for the two cases since, in the case of the polar orbit, less time is spent in the region of high proton flux. For any orbital inclination between the two extremes represented in Figs. 3(a) and 3(b) the magnitudes of the components will lie intermediate to those shown for the two cases. The effects of the trapped electrons in the Van Allen belt are not indicated on the curves in Figs. 1, 2, or 3 since their effects to man are not comparable with those posed by the protons for shielding thicknesses of interest.

It is seen that for any manned orbital vehicle operating at altitudes between ~900 and ~7500 kilometers the Van Allen belt protons present the controlling component of the radiation as far as biological shielding is concerned and are of a magnitude so as to require rather thick shields if the desired staying times for space station crews are to be obtained. The sensitivity of the required shielding on altitude is illustrated quite well in Fig. 3 since the spread in shield thickness to attain the same dose varies by as much as ~100 gm/cm^2 over the range of altitudes considered.

Of course all orbital operations need not be in the regions between ~900 and ~7500 kilometers. For orbits at higher altitudes the shielding problem slowly approaches the case illustrated in Fig. 2(a) while those at lower altitudes approach those shown in Figs. 3(a) and 3(b) with the Van Allen component removed.

It is apparent from the foregoing discussion that for the early manned missions (missions in the category represented by Fig. 2(a), or space stations orbiting beneath the trapped radiation belts) the shielding problem will be governed primarily by the providing of protection from the solar proton environment.

It is also clear that missions will surely be undertaken in a later time period for which the governing radiation component as far as shielding is concerned will be the trapped protons. Based on observations to date the shielding problem for these missions will be much more severe (weight-wise) than those imposed by the solar protons due partially to the harder spectrum which characterizes the trapped

radiation. As was pointed out earlier such large shielding thicknesses give rise to the additional problem of secondary production. Indeed, in some cases, these missions will be relegated to the later time period principally because of the magnitude of the shielding problem.

Preliminary studies[8-9] have indicated that electromagnetic shielding (using superconducting magnets) may be superior to passive shielding in cases where a high energy cut-off is required and/or large volumes are to be shielded. Consequently, it appears that such systems may be particularly useful for these missions. Superconducting magnets of the nature needed for such an application are a number of years off since they represent a rather large advancement in the present state of the art, however, studies are continuing in this area. A detailed discussion of such systems is beyond the scope of this paper.

Discussion of Uncertainties

Before a logical approach to the problem of developing a technology for use in designing space vehicle shields can be formulated an assessment must be made of the uncertainties which exist in both the environmental data and existing techniques for shielding calculations. A detailed discussion of such uncertainties was given in an earlier paper.[10]

In this section several selected topics are discussed which may have an important influence on the proper approach to the shielding problem. It is hoped that some apparent misconceptions which have arisen recently concerning the magnitude of the shielding problem may be illuminated by these discussions.

Typical Solar Flare- During the last few months much attention has been directed toward the "typical" solar flare presented by Dr. D. K. Bailey.[2] This hypothetical solar proton event represented an attempt at correlating continuous radio observations with direct balloon, satellite, and rocket observations to arrive at a time history for a typical large event.

---

8. Levy, R. H., "Radiation Shielding of Space Vehicles by Means of Superconducting Coils" ARS Journal, 31, pp 1568-1570 (1961).

9. Dow, N. F., Shen, S. P., and Heyda, J. F., "Evaluation of Space Vehicle Shielding," General Electric Space Sciences Laboratory Report R62SD31, April 1962.

10. Keller, J. W., "Uncertainties in Space Radiation Shielding Calculations," paper presented at ARS Space Flight Report to the Nation, New York, N.Y., October 9-15, 1961.

A cross plot of Bailey's flux versus energy curves (time as a parameter) are shown in Fig. 4(a) in the form of integral flux as a function of time with energy as the parameter. The dashed portion of the curves represent extrapolations in time beyond that given by Bailey. The dotted curve in Fig. 4 represents a curve derived by Fichtel, Guss, and Ogilvie[11] to envelope the highest integral fluxes >100 Mev which have been experimentally observed for solar proton events to date and is included for comparison with the Bailey "typical" event.

The time integrated integral and differential spectra derived from the curves in Fig. 4(a) are shown in Fig. 4(b) while the time integrated dose (for the entire event) is given as a function of shield thickness in Fig. 5(a). The curve in Fig. 5(a) again represents the dose in an infinitesimally small tissue sample at the center of a spherical shield.

Shortly after Bailey's paper was published the tolerance dose values[6] which are proposed for project Apollo became known. These dose values are more liberal (and perhaps more realistic) values than many persons had allowed themselves to consider in the past. Using Bailey's flare, Schaefer[12] made depth-dose calculations in a spherical phantom wrapped by shielding[12] (model to be discussed later) which yielded values which were of little concern (i.e. skin dose of 19r behind 8 gm/cm^2 of shielding) when compared to the allowable dose values. It has since that time, been generally accepted in many quarters that the Bailey model flare has resulted in greatly reduced doses compared to earlier calculations based on direct observations.

If the earlier dose calculations are compared with dose calculations for the Bailey flare which are made in the same manner (i.e. dose in infinitesimally small sample of tissue at the center of a spherical shield) the agreement is quite striking. Fig. 5(b) is a comparison in this manner with the earlier calculations of Foelsche[13] based on direct experimental measurements for three large events. Foelsche's curves are very nicely bracketed by those based on Bailey's typical flare (solid dots) and his estimates of possible upper limits for observed flares (triangles and circles).

It is evident, that the magnitude of the shielding problem has been somewhat reduced by the appearance of liberal tolerant doses and not by the acceptance of the Bailey "typical" flare. It would not

---

11. Fichtel, C.E., Guss, D. E., and Ogilvie, K. W., Details of Individual Solar Particle Events, Solar Proton Manual, Goddard Space Flight Center Report X-611-62-122, pp 19-54 (1962).

12. Schaefer, H. J., "Protection Against the Solar Flare", Astronautics Vol 7, No. 8, pp 24-25 (1962).

13. Foelsche, T., "Radiation Hazards in Space" paper presented at Fall General Meeting of the AIEE, Detroit, Michigan, October 15-20, 1961.

be wise at this point, however, to feel that dose tolerances for all future missions will be as liberal as those proposed for Apollo. It seems certain that as weight becomes less of a problem the question will change from what can be tolerated to what would we like to tolerate. Also since the length of time over which detailed observations of solar proton events have been made is quite small and our statistics are few it cannot be said with any degree of certainty that we have observed the largest events which are possible. Also, it appears quite improper to correlate size or frequency of events with any other physical phenomena such as sun spot cycles when one considers that detailed observations have been made during but one cycle.

Models For Dose Calculations- Consider now the problem which has been referred to earlier- the selection of models for dose calculations. Much of the disagreement among dose calculations made by different persons results from differences in the models used. Three general types of models are depicted in Figs. 6(a) and 6(b) and 6(c). The pictured rays are for skin dose. The model in Fig. 6(a) involves the calculation of the dose in an infinitesimally small sample of tissue at the center of a spherical shield while in Fig. 6(b) a spherical tissue phantom is surrounded immediately by the shield. Figure 6(c) depicts a model similar to Fig. 6(b) where an attempt is made to assess the relative sizes of the man and the shielded volume. Figure 6(c), of course, represents a more accurate type of calculation than the others but requires knowledge of the vehicle dimensions which is not practical unless calculations are being made for a specific vehicle. Model (b) has the advantage of lending itself easily to depth-dose calculations while (a) can be used only for calculating a quantity which is representative of skin dose but should, in most cases be divided by roughly a factor of from one and one-half to two to allow for self-shielding.

It should be noted that the skin dose calculated using model (b) will always be less than that for (a) since the path length traversed by the radiation in penetrating the shield in (b) is greater than or equal to that for (a) at all angles. The same is true for (b) and (c) with the depth dose in (b) being less than that for (c) at every point except the center. It is obvious that the value for skin dose obtained for (c) will tend toward that for (a) as the shielded volume becomes large with repsect to the phantom. As an example of the different values which may be obtained by using (a) and (b), the skin dose for the Bailey "typical" flare behind 10 gm/cm^2 is$\sim$53/2=26 R for (a) and 10 R for (b). The correct value should lie between these values. The importance of making clear the techniques which are used in arriving at dose values is clearly seen.

On-Board Mass As Shielding- In arriving at a minimum weight vehicle-shield system one must make maximum use of any on-board mass (for other purposes) as shielding. There will always be a considerable amount of such mass on board a manned space vehicle and, indeed there are some persons who are expressing the rather naive viewpoint that the whole shielding program should be eliminated since the on-board equipment can more than take care of all the shielding problems for manned space flight by offering $\sim$10 gm/cm^2 of protection. It is obvious from the discussions in an earlier section that there probably exist more formidable problems than those resulting from solar protons unless we are willing to rule out, for manned operations, rather large regions of space near the earth as well as the use of some methods of propulsion without even trying to solve the problem. It has been shown that many more than 10 gm/cm^2 are involved in these cases.

The utilization of on-board mass as shielding is an area of consideration which, no doubt, will always appear more attractive than it turns out to be in practice. The most efficient use is hampered considerably by the fact that all vehicles can not be shields first and operational vehicles second. Also the types of equipment which are involved are far from being homogeneous in their mass distribution thus surely leaving relatively thin spots, or holes, in the protective shielding. The effects of such holes and the importance of detailed geometry in making penetration calculations are illustrated in Fig. 7.

The plots in Fig. 7 show the distribution of shielding thicknesses for a hypothetical spherical shield as a function of solid angle. The first example in the figure is that of a constant thickness shield having a thickness of 10 gm/cm^2. A dose calculation for the point at the center of the sphere using Bailey's "typical" flare yields a value of 53 Rads. The second distribution shows the effect of making 9% of the solid angle have a 2 gm/cm^2 thickness while 18% of the solid angle is increased to 14 gm/cm^2. While the average shield thickness for this case is still 10 gm/cm^2 the dose is now almost doubled or 103 Rads. For a vehicle where one is utilizing on-board mass as shielding the thin areas or holes will, without doubt, be scattered about more in the manner illustrated in the third distribution in Fig. 7. Here the total percentage distributions are the same as in the previous case with an average of 10 gm/cm^2. In this type of situation one must be careful how he makes his penetration calculation. The dose rate has been calculated by dividing the shield into different numbers of equal increments of solid angle, calculating the penetration through each, based on its average thickness, and summing over the increments. The results are given in the table in Fig. 7 for each of several numbers of increments chosen. From these results it is obvious that significant errors may be encountered unless one takes increments, at least in the

region of the irregularities, which are comparable to the dimensions of the irregularities. Also it should be noted that the effect of "holes" in a shield upon the dose received will be a strong function of position within the shielded region. Procedures for calculating dose rates within a vehicle should be capable of handling quite detailed geometry if they are reliable.

Secondary Radiation- From the curves shown earlier one must conclude that in future missions the use of quite thick shields, $\sim$60-100 gm/cm^2, may be needed to afford protection from Van Allen belt protons. On the other hand, based on the observations to date and present conceptions of tolerable doses shields well under 20 gm/cm^2 may suffice for the cases where solar protons are the controlling component. The question then arises as to the importance of secondary radiation production in the shield.

Figure 8 shows the relative importance (on a Rad basis) of the secondaries to the primaries as a function of shield thickness for the trapped protons (a) and the solar protons (b).[14] It appears from these curves that the secondaries will not be of major importance in cases where solar protons are the major component however, their importance in the case of the thick shields which may be needed for protection from Van Allen belt protons is obvious. Consequently, work devoted to the determination of data on secondary production must be continued in support of the long range problem.

General Approach to Shielding Problem

Figure 9 is a flow chart showing how the various parts of the long range space vehicle shielding program within the NASA fit together to yield a final vehicle shield design.

The blocks entitled Detailed Transport Calculations (and associated experiments), and Conceptual Studies (and associated experiments) fit properly into the Advanced Research and Technology area as does general work on the methods to be used in the block titled Dose Calculations. In these areas work is carried out on a continuing basis in support of the more specific work on particular vehicles signified by the blocks titled Space Vehicle Geometry, Shield Design, and Experimental Shield Verification as well as the more specific aspects of the Dose Calculations.

The detailed transport calculations should supply basic data for the dose calculations which, for the reason discussed in the previous section, should probably be restricted to rather simple transport considerations so as to accomodate rather complex geometries. The detailed transport techniques, on the other hand, could be developed to the point that they could be used to handle detailed geometry in special regions of a shield as is indicated. Conceptual Studies is

---

14. Allen, R. I. et al, Shielding Problems in Manned Space Vehicles Lockheed Nuclear Products Report No. 104 (1960)

a rather broad heading given to those studies which yield information on such subjects as the selection of shield materials, proper ordering of materials, weight optimization, general techniques for efficient utilization of on-board mass, methods for shield verification, and at this point studies of active shielding techniques. The experimental checks which are indicated include the generation of basic data as well as the verification of analytical techniques.

The results of the conceptual studies are, of course, fed into both the preliminary determination of the vehicle geometry and the block called Shield Design which is essentially the iteration process in arriving at a shield design. The final shield is then verified experimentally as the final step.

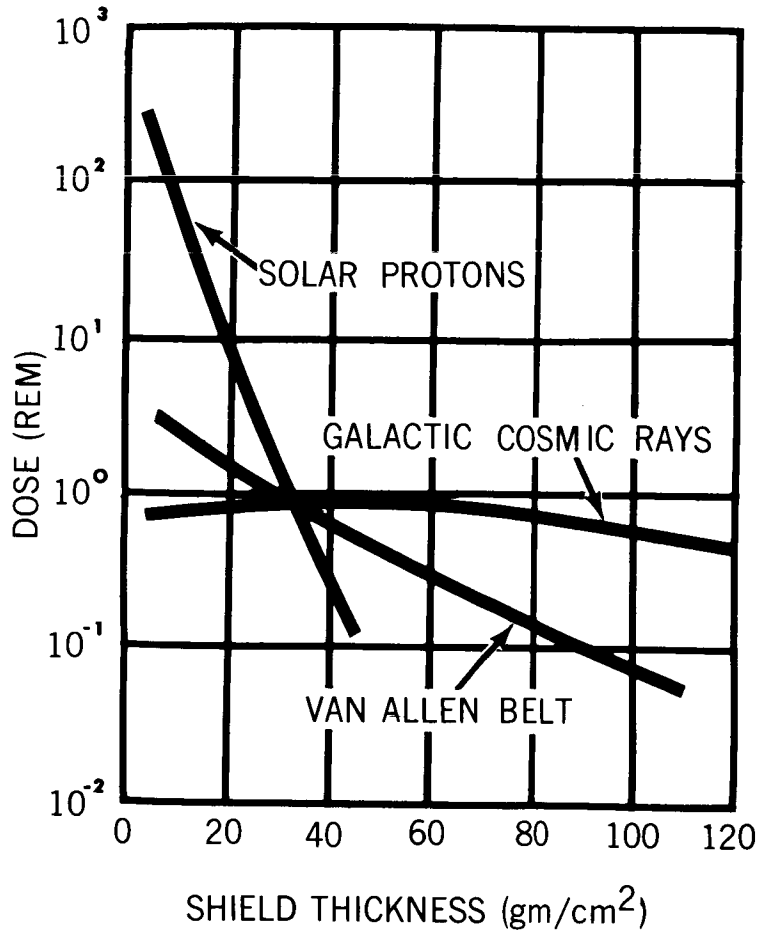

FIGURE 1

RADIATION ENVIRONMENT FOR TWO WEEK LUNAR MISSION

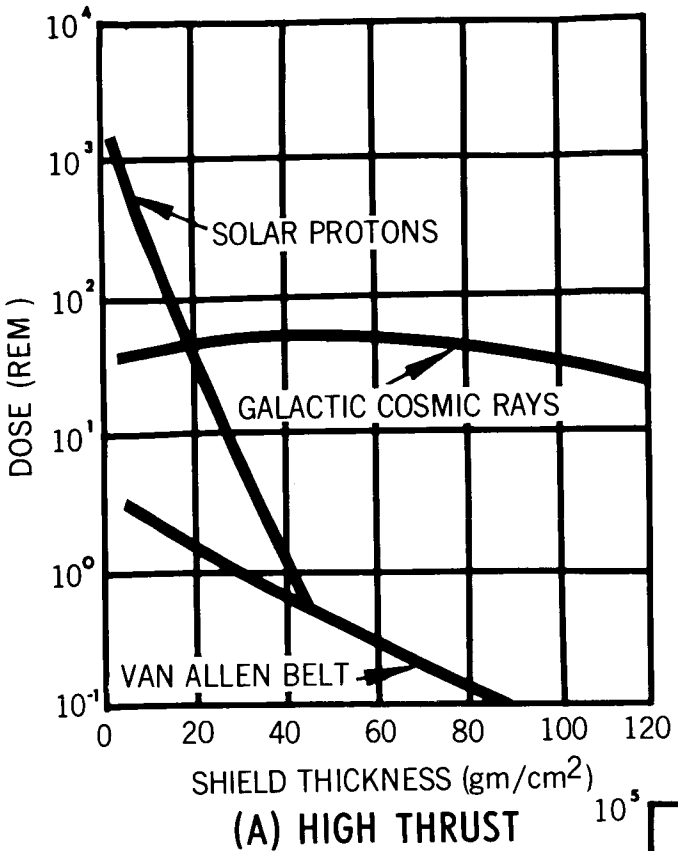

(A) HIGH THRUST

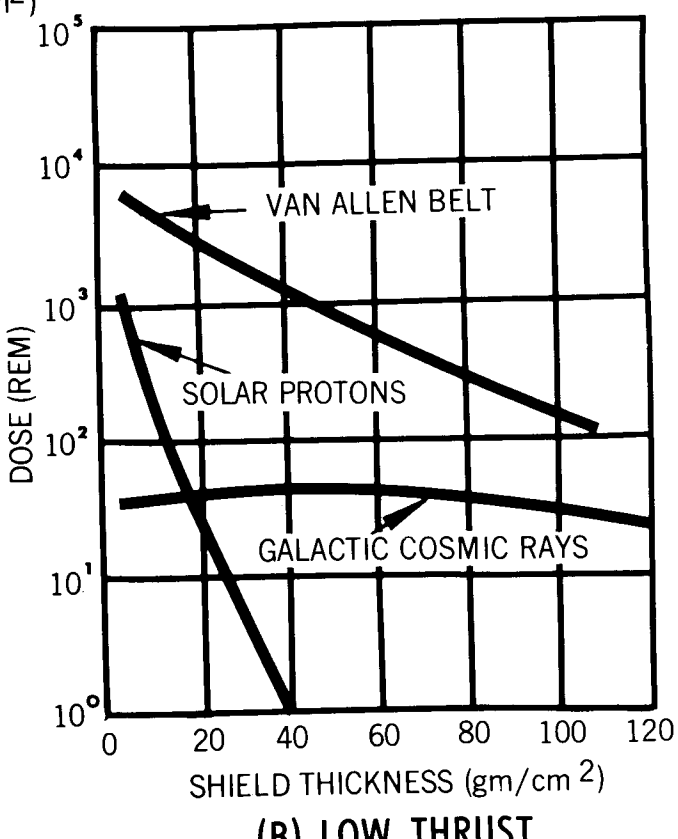

(B) LOW THRUST

FIGURE 2

RADIATION ENVIRONMENT FOR INTERPLANETARY MISSIONS

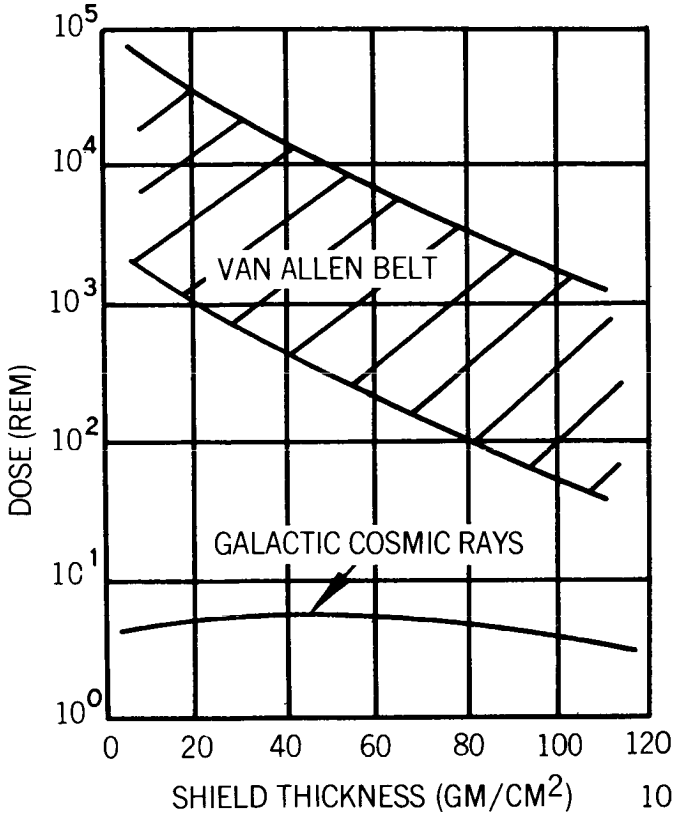

(A) EQUATORIAL ORBIT

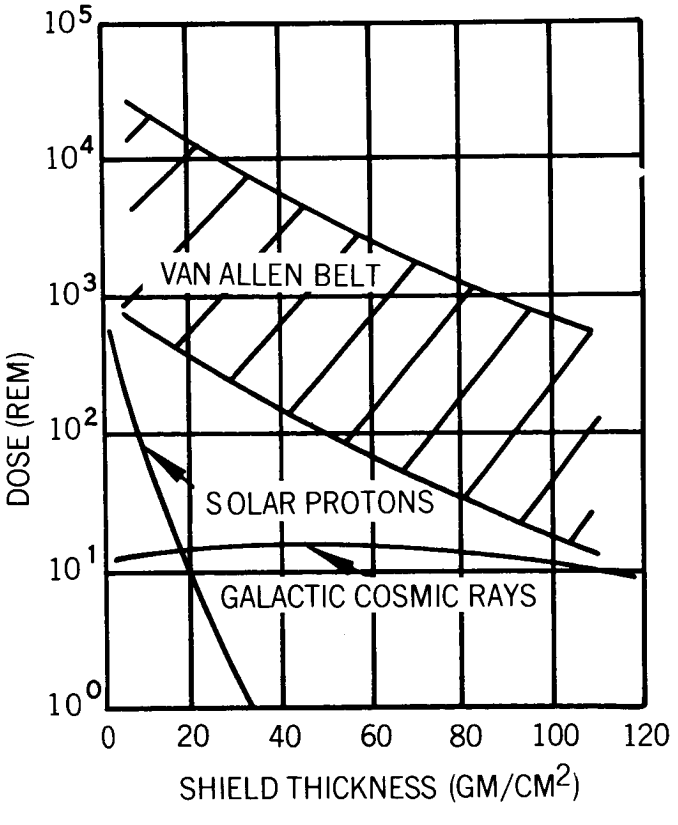

(B) POLAR ORBIT

FIGURE 3

RADIATION ENVIRONMENT FOR VEHICLES ORBITING IN VAN ALLEN BELT

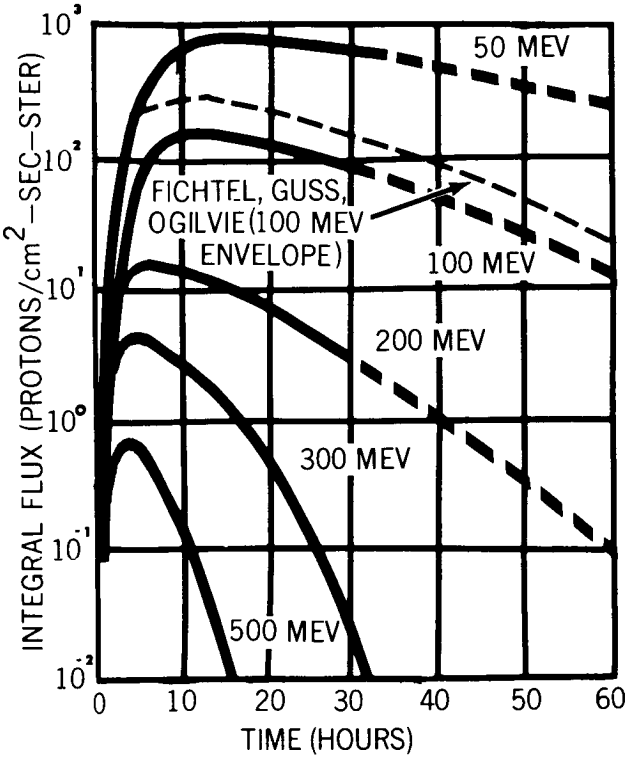

(A) TIME VARIATION OF INTEGRAL FLUX

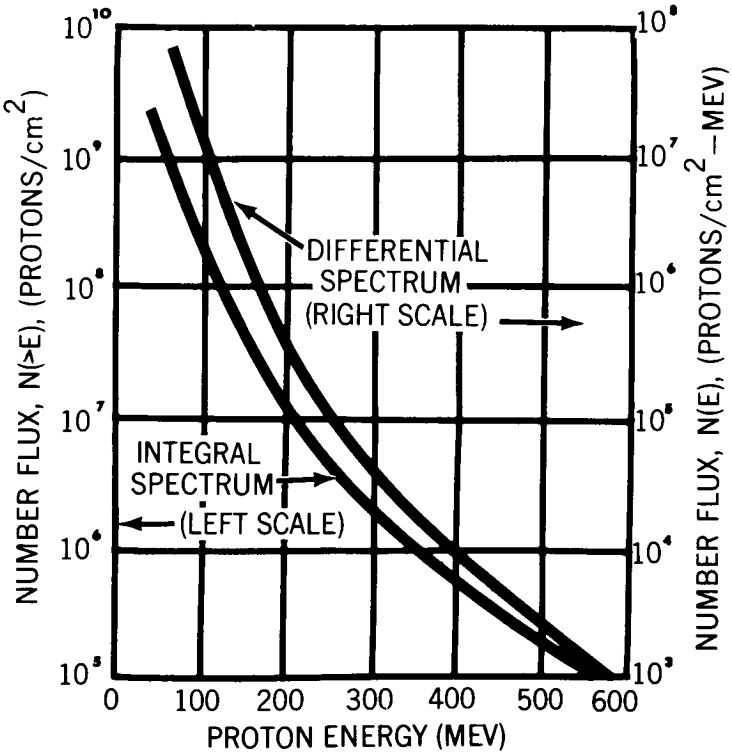

FIGURE 4 (B) TIME INTEGRATED SPECTRA

SPECTRAL CHARACTERISTICS OF BAILEY'S "TYPICAL" FLARE

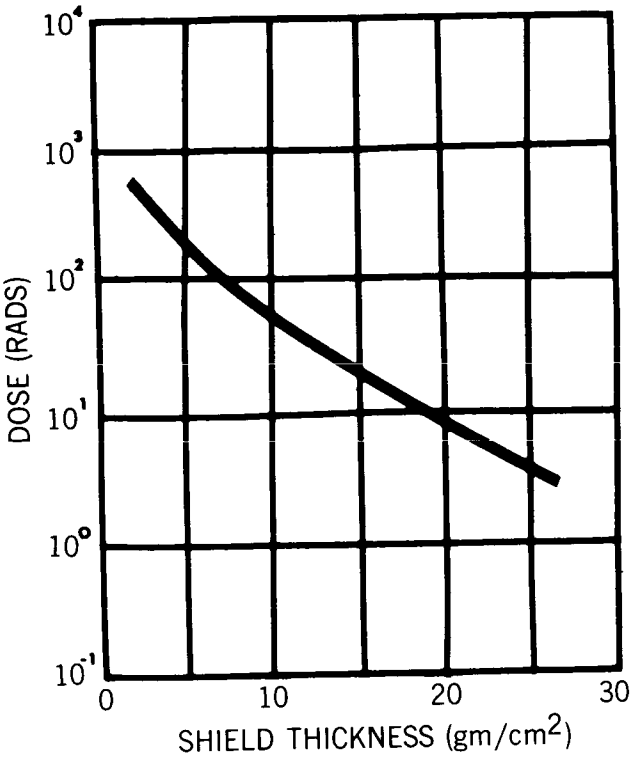

(A) EFFECT OF SHIELDING)

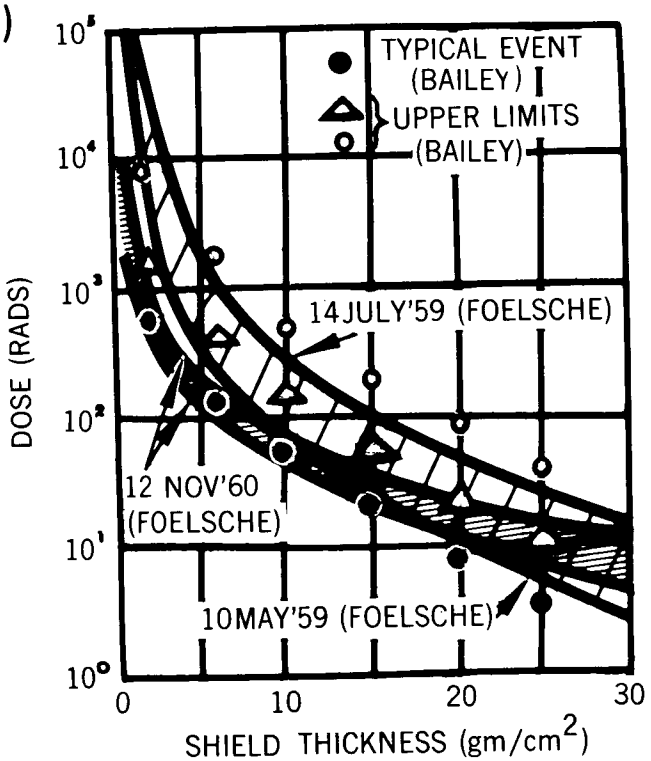

(B) COMPARISON WITH EARLIER ESTIMATES

FIGURE 5

DOSE FROM BAILEY'S "TYPICAL " FLARE

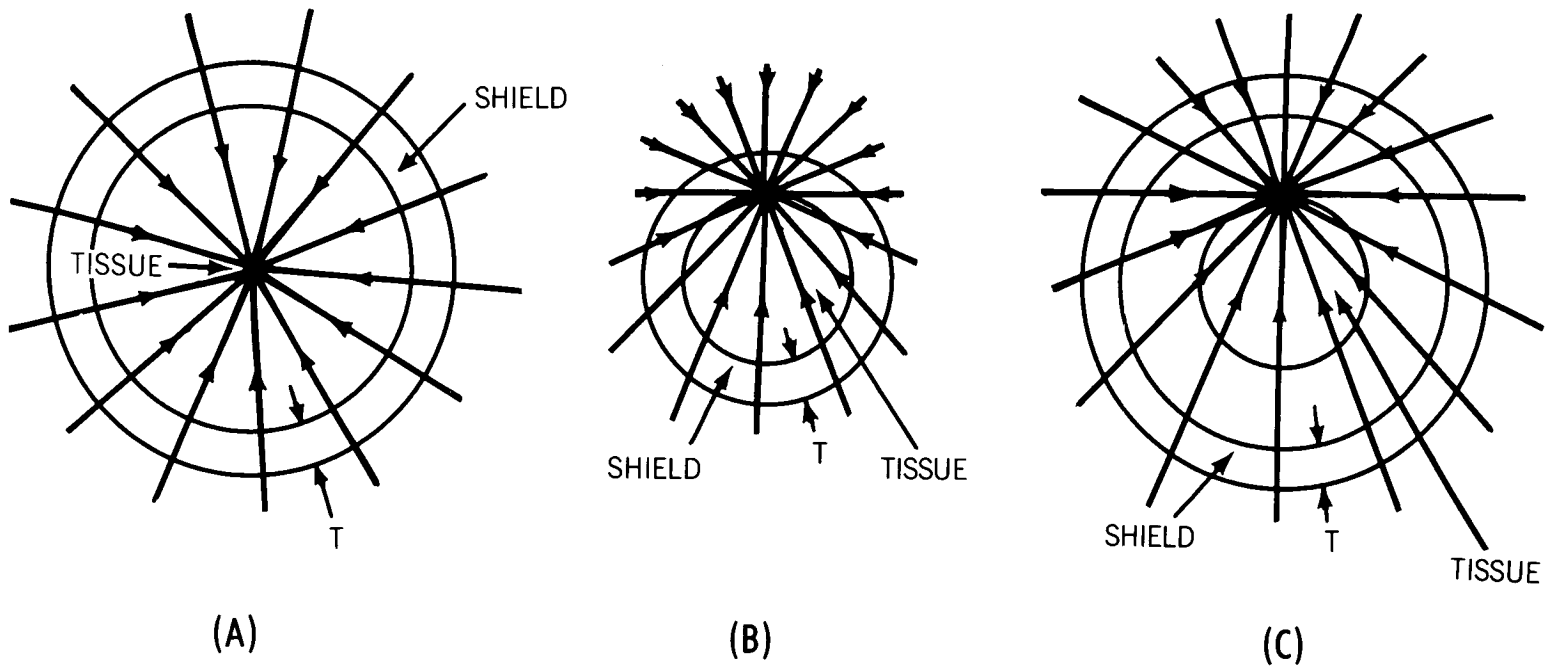

FIGURE 6

MODELS FOR CALCULATING DOSE

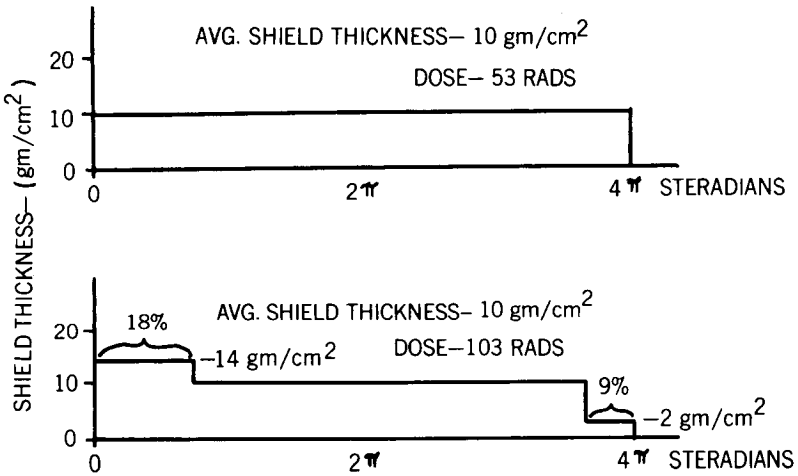

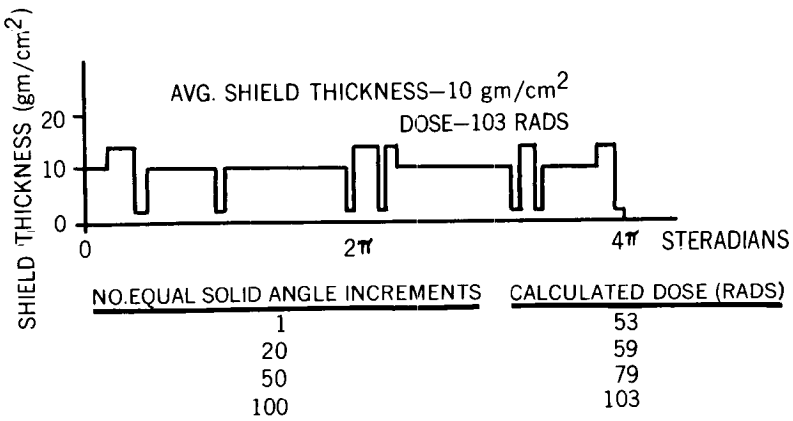

NO. EQUAL SOLID ANGLE INCREMENTS	CALCULATED DOSE (RADS)
1	53
20	59
50	79
100	103

FIGURE 7

UTILIZATION OF ON-BOARD MASS AS SHIELDING

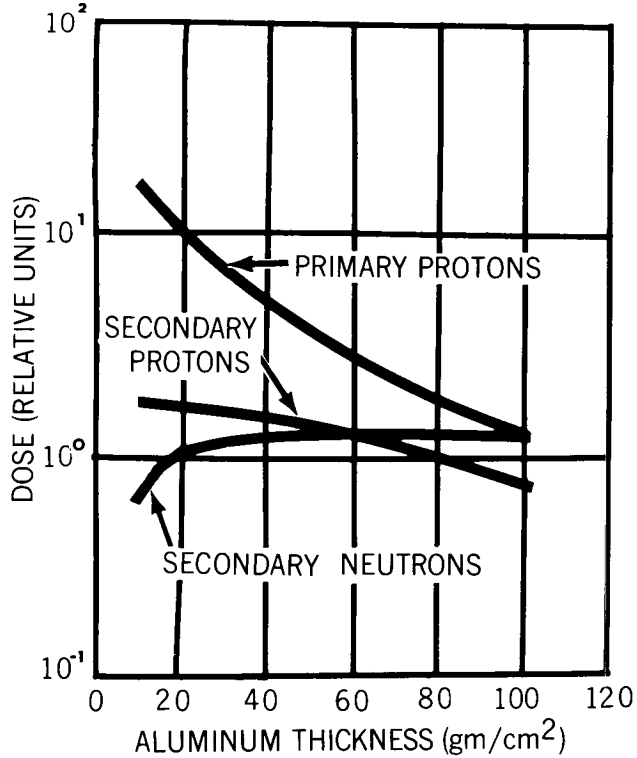

(A) TRAPPED PROTONS

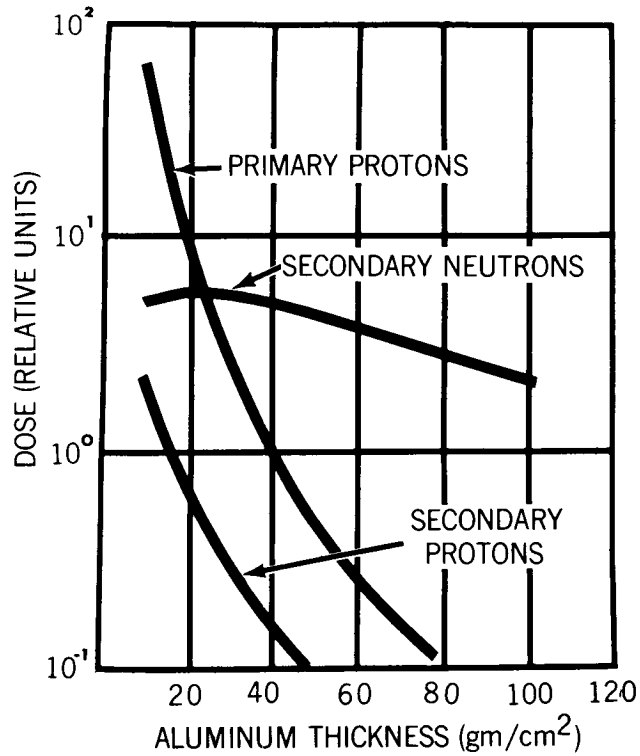

(B) SOLAR PROTONS

FIGURE 8

IMPORTANCE OF SECONDARY RADIATION

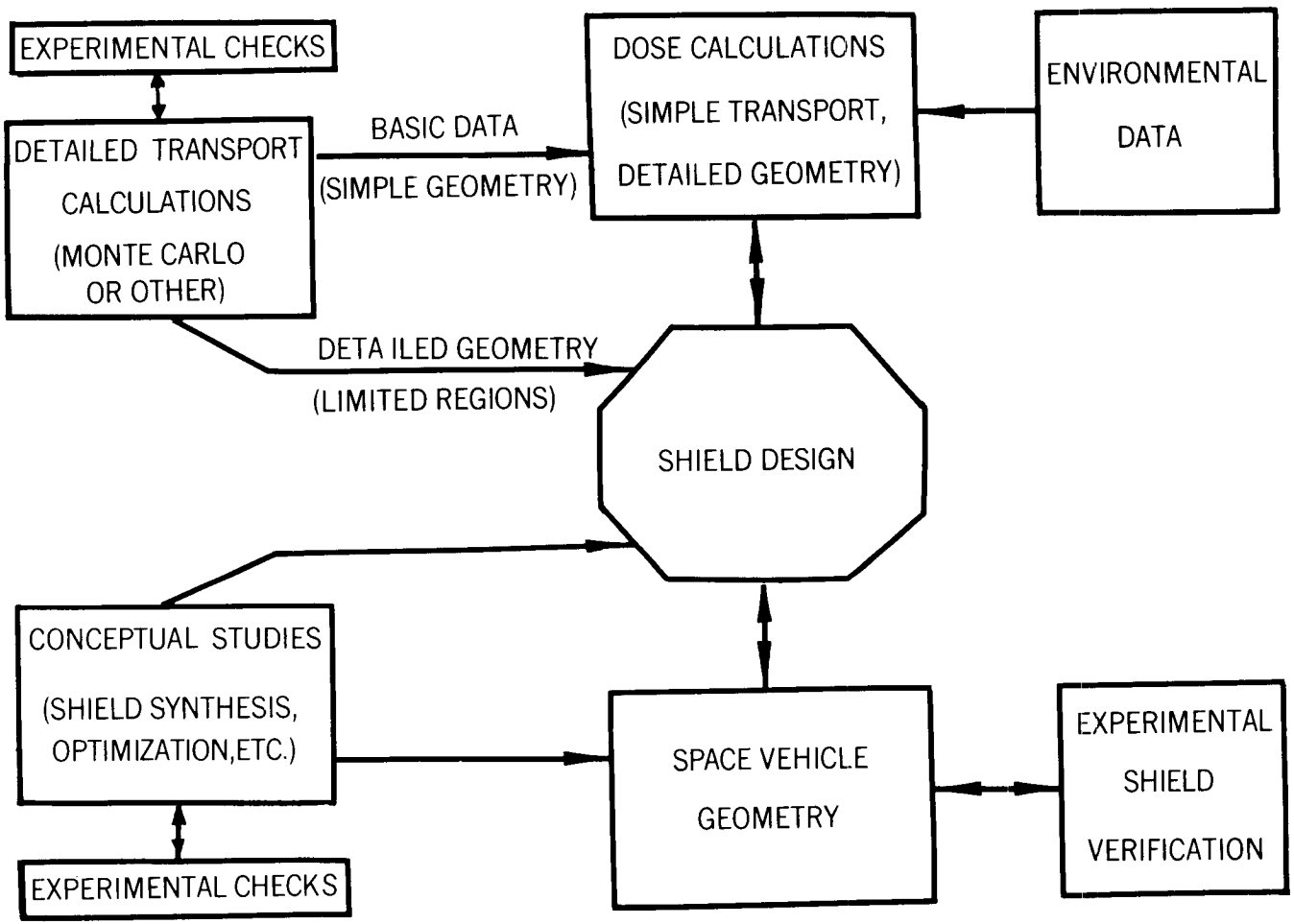

FLOW CHART FOR SPACE VEHICLE SHIELDING WORK

FIGURE 9

Paper E-2

COMPARISON OF MONTE CARLO AND IONIZATION CALCULATIONS FOR SPACECRAFT SHIELDING

K. A. More and O. L. Tiffany
Bendix Systems Division

ABSTRACT

Various methods have been used to calculate shield designs for manned space vehicles. The methods differ in the approximations used to describe the spacecraft geometry and the physical interactions of the space particles in the vehicle shield. Since calculation time is least for the methods with the most approximations, it is desirable to know what degree of approximation is permissible in designing shields. This paper compares the results of shield calculations using the Monte Carlo method and the more approximate ionization loss method.

The Monte Carlo method calculates the physical interactions following nuclear collisions and ionization loss. The ionization loss method considers only ionization loss of the incident protons. On a short-term mission the required shield is thin and the number of nuclear collisions by the incident protons is small. Therefore, both the increase in dose due to secondary particles from nuclear collisions and the decrease in dose due to nuclear absorption are small, and the dominant physical interaction is ionization loss. On the other hand, thick shields are required on long-term missions during which a large number of nuclear collisions will occur. The contribution to the astronaut's dose from the nuclear collision particles, especially the contribution from secondary neutrons, cannot be neglected. Consequently, there is a critical thickness in shield design at which shielding calculations must account for nuclear collisions.

To find this thickness, calculations were performed on a spherical shell aluminum spacecraft. The Monte Carlo code was basically the same one used in previous calculations, there

being added a subroutine for nuclear evaporation. The nuclear evaporation subroutine was patterned after the evaporation model used by Allen et al. The ionization loss calculation was taken directly from that part of the Monte Carlo program that computes ionization loss. Since the Monte Carlo calculation used the multigroup energy approximation, our ionization loss calculation also includes the multigroup approximation. While this method decreases the accuracy of an ionization loss calculation, its use here permits more direct comparison.

INTRODUCTION

During the last several years, different methods for calculating the radiation inside spacecraft have been tried. These methods have ranged from consideration of only the ionization loss of the protons to Monte Carlo treatments which take into account the three-dimensional processes in nuclear cascades. These calculations have been performed for geometries ranging from simple, one-material, spherical shell spacecraft to asymmetrical, multi-layered, spacecraft. But, because of the limitations of available computers it has been found necessary to limit calculations on complex geometry to simple calculation methods and to limit complex calculations to simple geometries. Thus, in order to perform calculations on the detailed designs of actual spacecraft, it has been necessary to develop approximate methods that give nearly the same results as the more exact methods. For this reason this paper aims to find how the simple calculation involving ionization loss compares with the complex Monte Carlo calculation for the simple, one-material, spherical shell, spacecraft geometry.

INPUT SPECTRA

The results presented in this paper are limited to missions of one year duration. The reason for this assumed duration was to smooth out the effects of solar flare fluctuations and to point out the differences in thick shields needed for long missions where the differences in calculation methods become consequential. The input proton spectra used in making the comparison between calculation methods were the expected yearly averages of cosmic protons during both periods of solar maximum and solar minimum. These averages were taken from data for spectra near the earth but outside of the man-made and natural radiation belts. The averages for solar flare

protons during solar maximum were obtained by normalizing the idealized spectrum derived by Bailey[1] to the average values[2] for the number of protons above 30 Mev and 100 Mev per year. These average values were an average of the three highest values reported by NASA for the years 1956, 1959, and 1960. The galactic cosmic ray spectra during solar maximum and solar minimum were taken from Bailey's paper. The input spectra used are shown in Figure 1.

METHOD OF CALCULATION

The Monte Carlo calculations were basically the same that we have used in the past[3]. The computer program was revised to include neutrons from evaporation and to include a different method for obtaining the dose inside the spacecraft. The approximate evaporation model developed by Allen et al[4] was incorporated as a subroutine in our program. We considered evaporation of both excited nuclei left after the intranuclear cascade and from compound nuclei formed by low-energy particle absorption. Since the limited data on intranuclear cascades prevented our considering cascades initiated by protons and neutrons below 150 Mev, we treated all collisions by particles below 150 Mev as producing compound nuclei.

The most significant modification to our previous calculations was in our method of obtaining the dose inside the spacecraft. In our previous calculations we found the radiation flux inside the spacecraft, assuming the inside was a vacuum. We then converted the radiation flux to dose by considering only the ionization loss this flux would have in plexiglass, the nearest material to tissue on which data were readily available for ionization loss.

Gibson[5] has computed the rate of energy removal of high-energy protons and neutrons in tissue as a function of particle energy. These energy removal rates include both ionization and nuclear collision mechanisms. We used his data in order to find the amount of energy removed by tissue inside the spacecraft from the neutrons and protons passing through the interior. Since no equivalent data were available for charged pions, only the ionization loss of the pions as they passed through the tissue was recorded. It should be noted that the energy removed from the particle beam is not necessarily deposited in the same location and no attempt was made at this time to determine the location at which the energy was absorbed. This can only be done when intranuclear cascade data are available for tissue. Our results can be interpreted as rads only if one assumes that

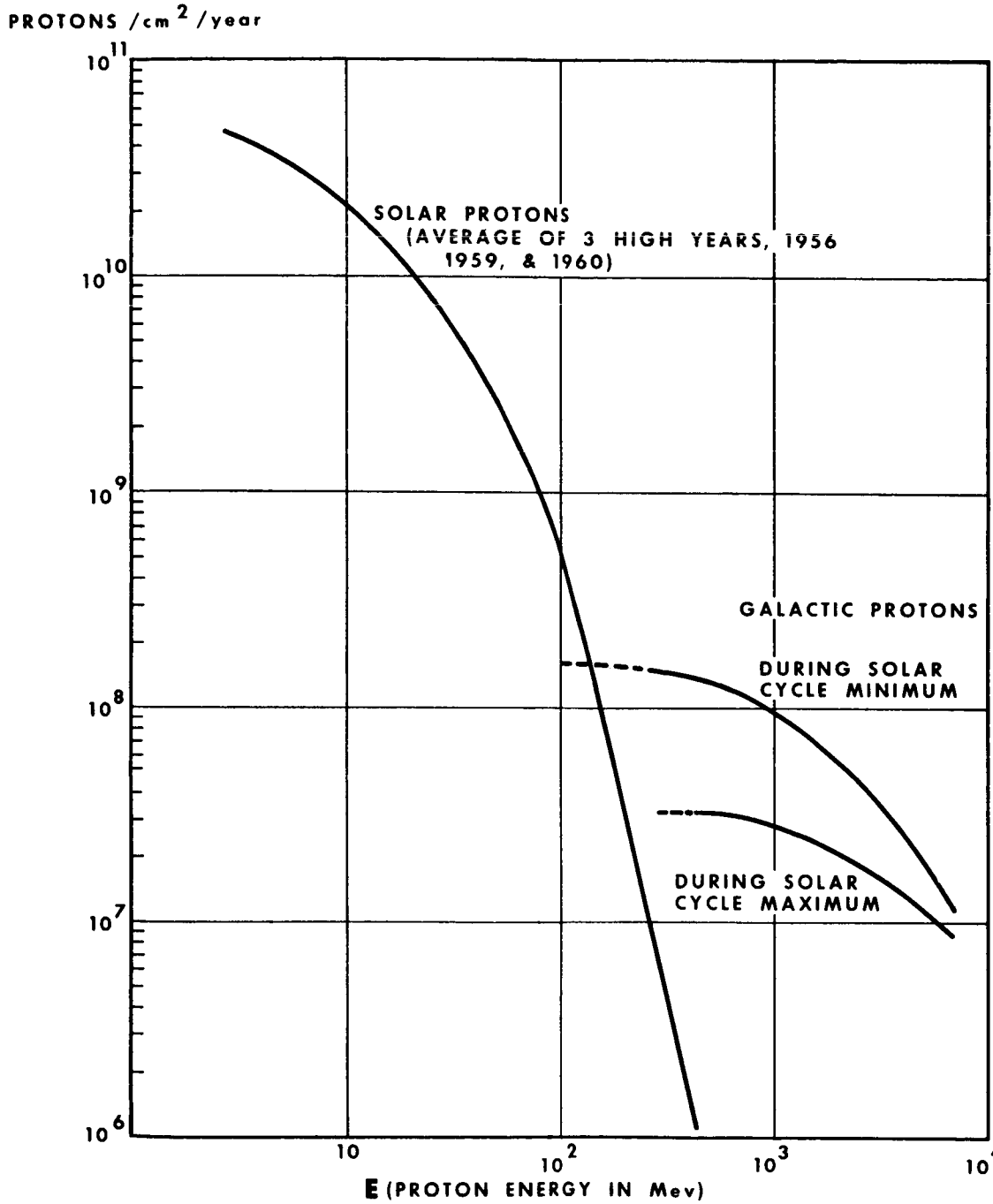

Figure 1 Omnidirectional Integrated Proton Flux. Number of Protons Having an Energy Greater Than E.

all the energy removed was absorbed in the tissue. In order to avoid any confusion on this subject, we have labeled our results energy removal dose and we define energy removal dose as the energy removed from a beam of particles by a gram of material.

The changes to our previous Monte Carlo computer program (to find the energy removal dose in tissue) were chosen to minimize the necessary modifications to the program while giving us enough information to compare ionization and Monte Carlo calculations and to account for the partial absorption of particles by the astronauts.

With the model used for this calculation it was assumed the inside of the spacecraft was homogeneously filled with tissue. The average energy lost by the particle in traversing the tissue was found by using Gibson's data for neutrons and protons, and ionization loss for pions. After summing all of the energy losses incurred by all the particles, the average energy loss per gram of tissue was found by dividing the total energy loss by the mass of tissue.

We began our calculations with a spherical shell spacecraft having inside dimensions comparable to the Apollo command module (inside diameter of 9 feet). The mass of tissue was taken to be 225 kg, which is roughly equivalent to the weight of three astronauts. This gives a density of .021 gm/cm^3 for the homogeneous tissue. Since this tissue density is thin, calculations were also carried out for a spherical shell spacecraft surrounding the same mass of tissue but having a density of one (inside radius of spacecraft equal to 37.33 cm). It will be seen that qualitatively the same conclusions are reached using either of these models for the tissue inside the spacecraft.

The ionization calculation used the ionization loss subroutine of the Monte Carlo program. This subroutine requires the incident proton spectrum to be divided into energy and angular groups. It is possible to treat ionization loss continuously by approximating the incident proton spectrum and proton range with power laws, and thus avoid energy groups. However, the use of the ionization subroutine was chosen here because it has the same approximations that were used in the Monte Carlo calculation. We believed this would give a sounder basis for comparing the two calculation methods.

Calculations were made for eighteen energy groups for the thin tissue and ten energy groups for the unit density tissue. The incident energies for these groups ranged from 10 Mev to 4000 Mev. The incident proton current, due to an assumed isotropic flux, was divided into 50 angular groups. The spacecraft walls were considered to be solid aluminum and the wall thickness was varied from 2 cm to 55.15 cm. The calculations were carried out on the Bendix G-20 computer.

DISCUSSION OF RESULTS

Three general conclusions can be drawn from our calculations: (1) For very thin spacecraft the predicted energy removal dose is nearly the same whether calculated by ionization loss or Monte Carlo. (2) The ionization loss calculation always predicted a higher energy removal dose than Monte Carlo. (3) For moderately thick spacecraft the energy removal dose for missions longer than a year was predicted to be higher during periods of solar minimum than solar maximum. These general conclusions were drawn from Figures 2 through 5. *

The first conclusion, that ionization loss and Monte Carlo should give nearly equal results for thin spacecraft was expected: because the probability of a nuclear collision in thin spacecraft is small so that the dominant shielding mechanism is ionization loss.

The second conclusion, that Monte Carlo results for the energy removal dose should be lower than for ionization loss was not predictable. There are two energy absorption processes: ionization loss and nuclear collisions. However, most of the nuclear collisions generate low-energy secondary particles and the dose from these low-energy secondaries may be higher than it would have been had the original particle passed through the tissue. Also, due to the energy difference between the parent particle and the secondary particles, the parent and secondary particles fall on different parts of the energy removal curve. Because of the nature of this curve, a high-energy proton may lose more energy per gm/cm^2 of path than low-energy secondaries. But, since there may be several secondary particles,

*Due to a question raised at the Gatlinburg conference on how Monte Carlo calculations compare with calculations based on ionization loss and exponential attenuation of the beam by nuclear collisions, the calculations for the latter case have been carried out and were added to Figures 2 through 5.

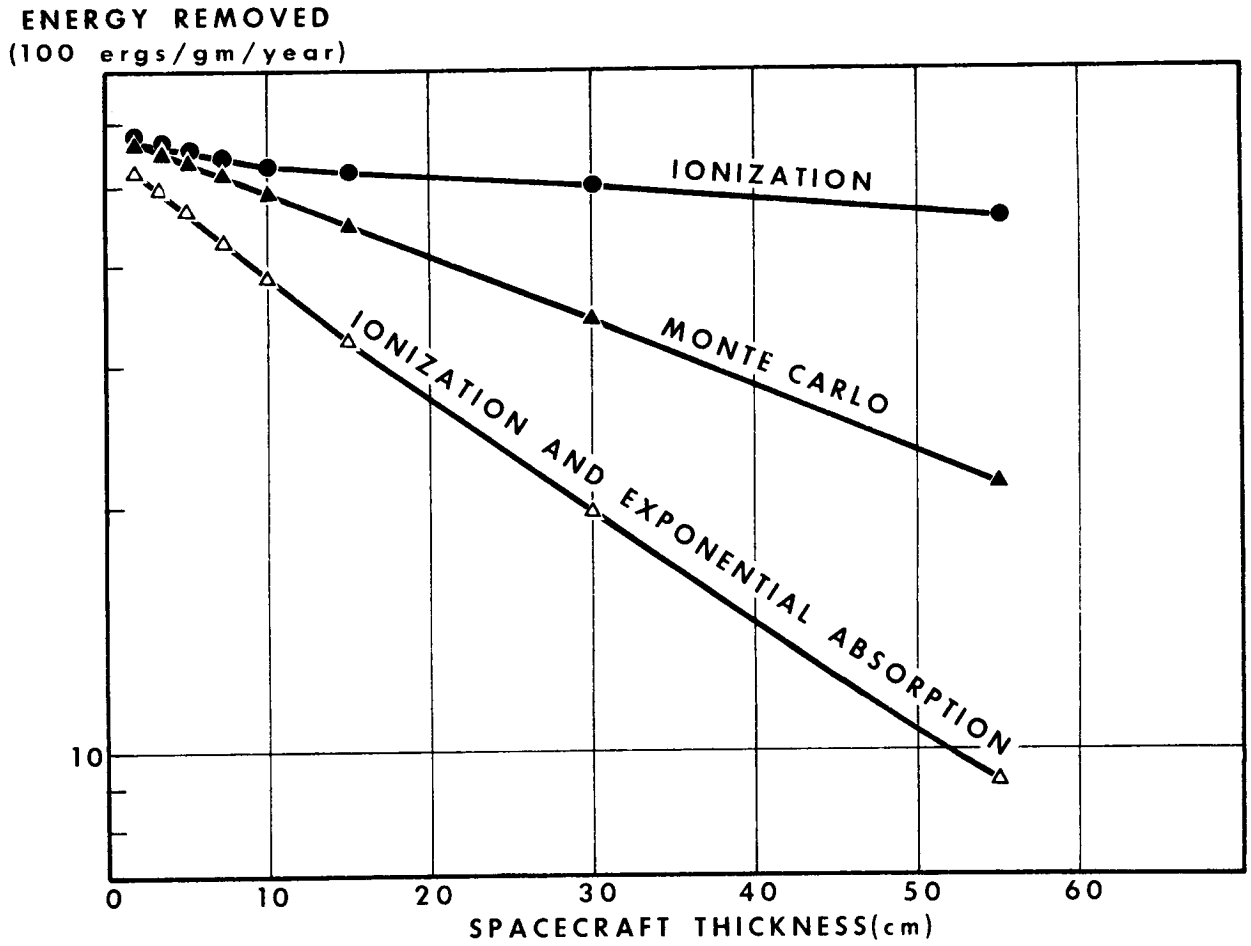

Figure 2 Comparison of Monte Carlo and Ionization Results for Aluminum Walled Spacecraft During Solar Minimum. Thin Tissue ($\rho = .021$)

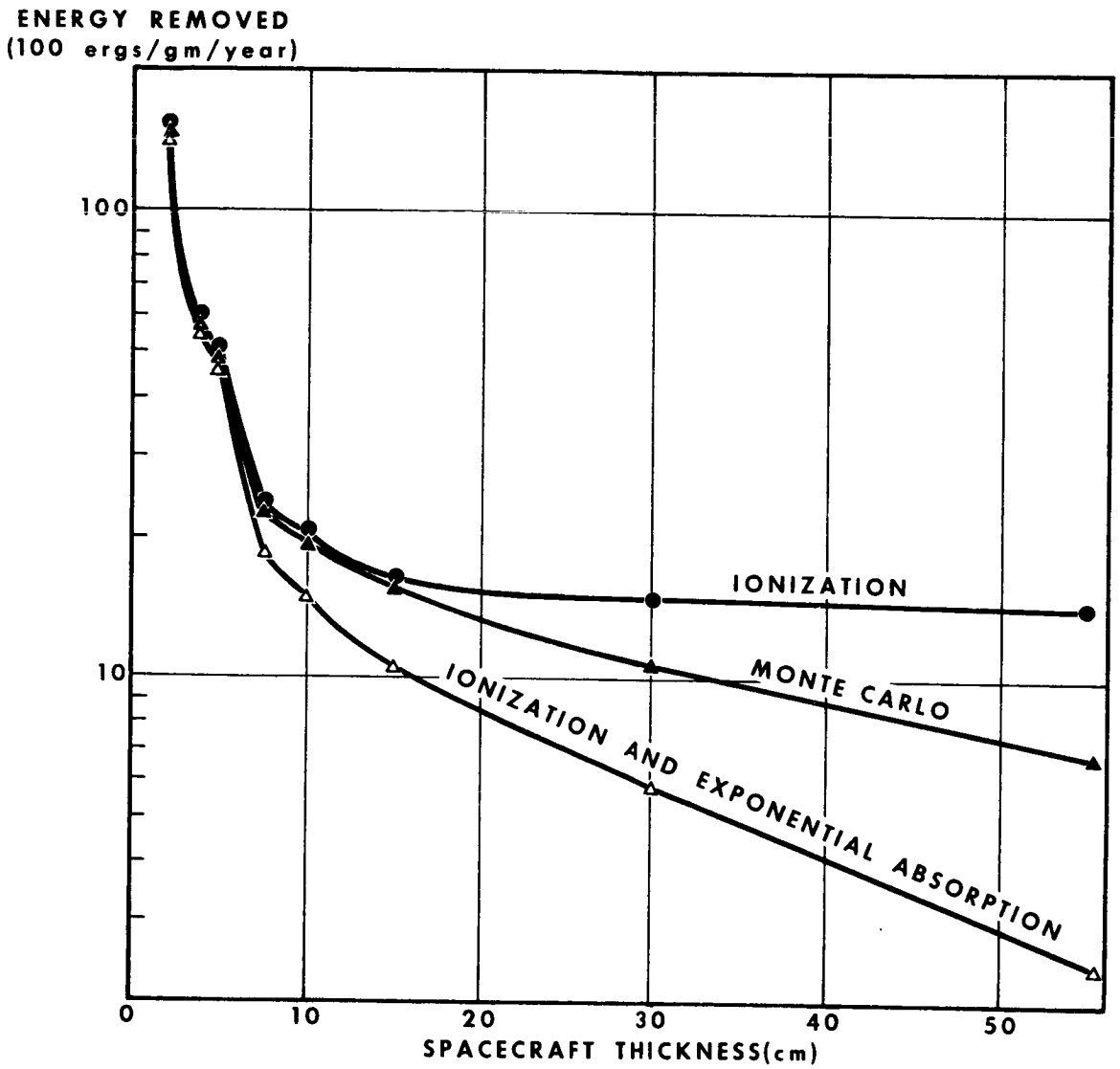

Figure 3 Comparison of Monte Carlo and Ionization Results for Aluminum Walled Spacecraft During Solar Maximum. Thin Tissue ($\rho = .021$).

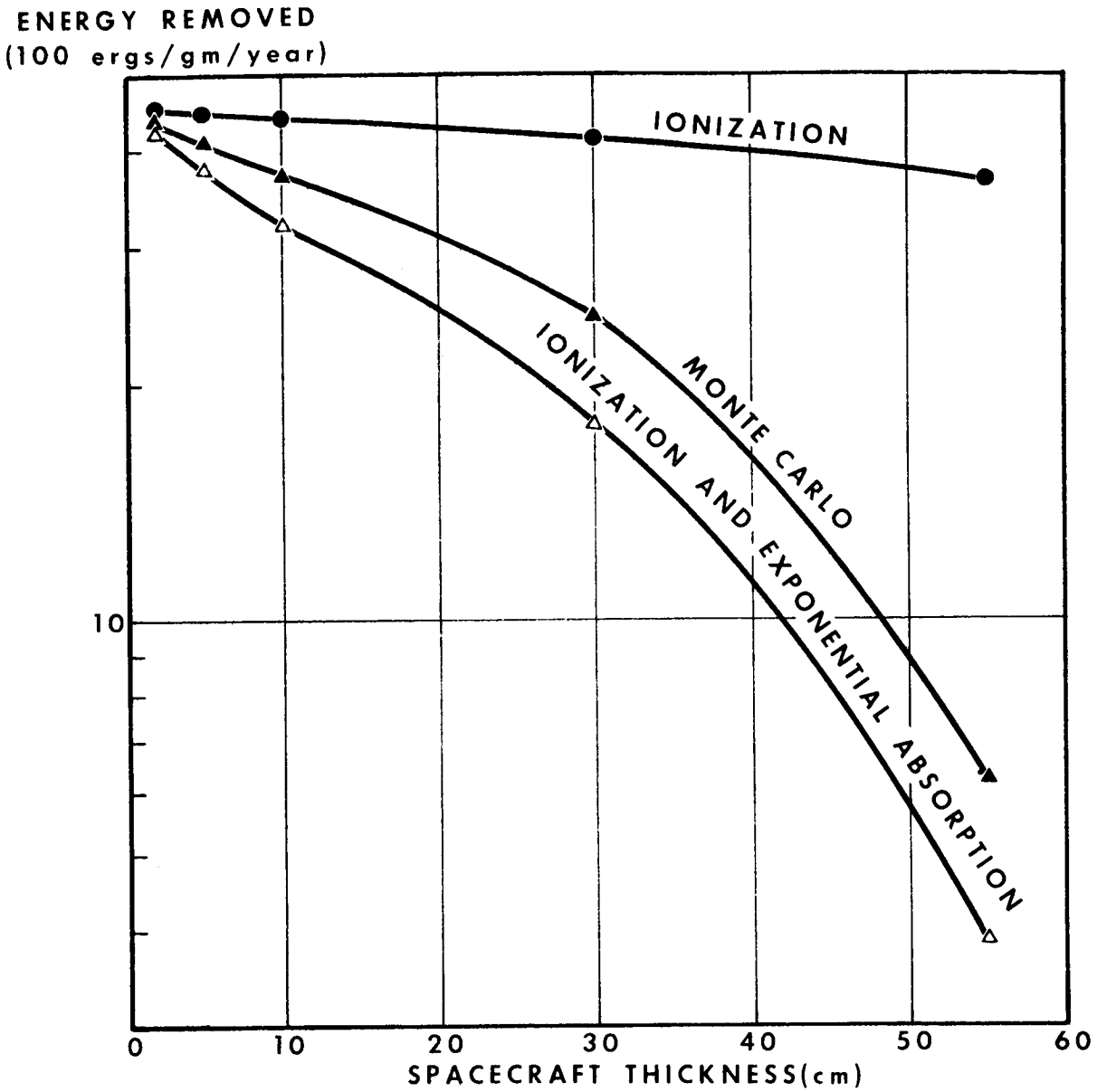

Figure 4 Comparison of Monte Carlo and Ionization Calculations for Aluminum Walled Spacecraft During Solar Minimum Normal Tissue (ρ = 1).

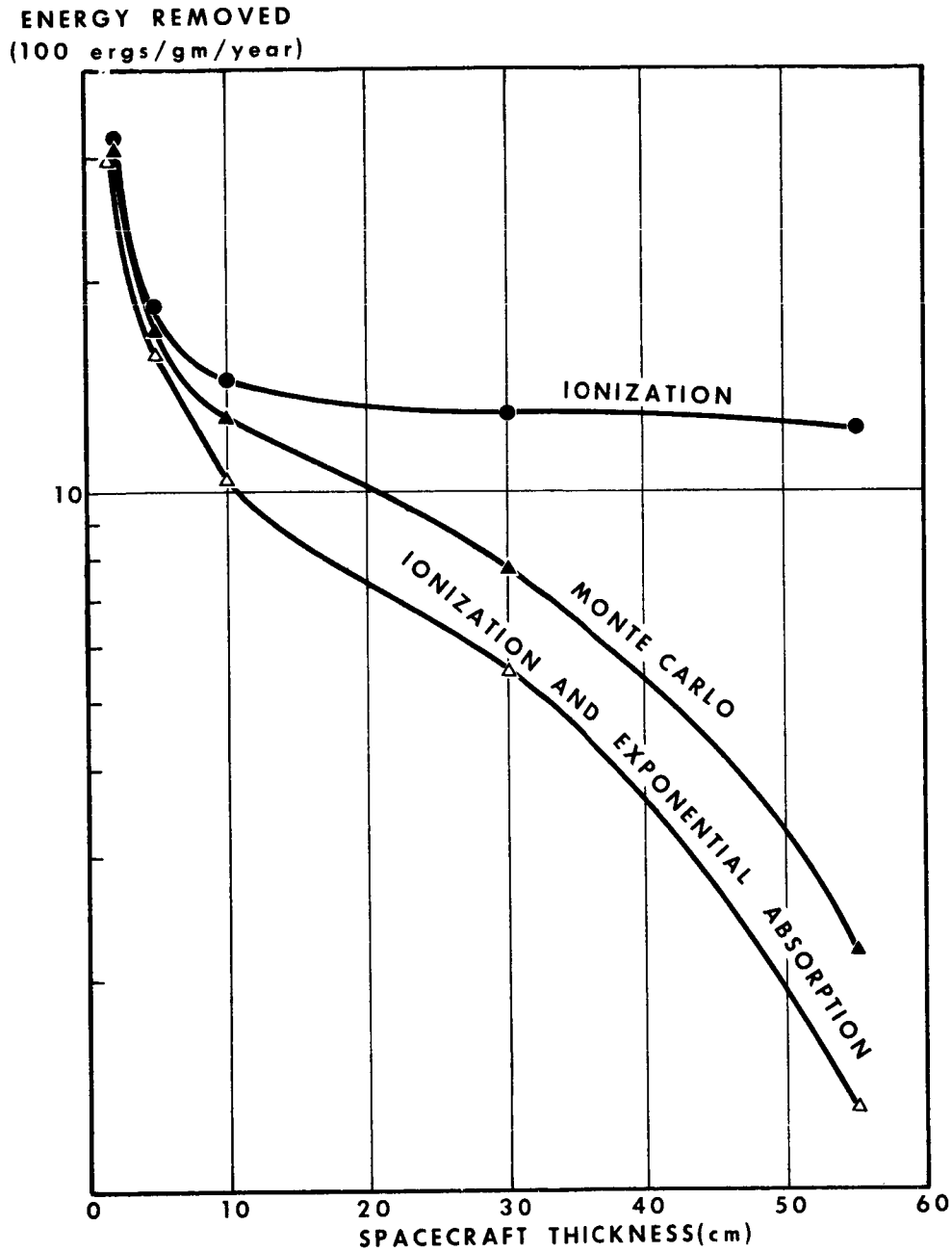

Figure 5 Comparison of Monte Carlo and Ionization Results for Aluminum Walled Spacecraft During Solar Maximum. Normal Tissue (ρ = 1).

the energy removal dose from all of the secondaries may be greater than it would have been had the parent particle passed through the tissue. Thus, with all of these mechanisms varying the energy removal dose, the only way to determine whether Monte Carlo results would be higher or lower than ionization results was to carry out the calculation.

The third conclusion, that the yearly energy removal dose for moderately thick spacecraft would be lower during solar maximum than solar minimum (see Figure 6), can be explained by the Forbush decreases during solar maximum and the large energy removal rates for high-energy particles. The Forbush decreases remove a considerable fraction of the galactic cosmic rays below 1 Gev, causing a considerable reduction in the energy removal dose. Moderately thick spacecraft, on the order of 5 cm thick, remove most of the solar flare particles below about 150 Mev. The solar flare protons above this energy that do penetrate the spacecraft fall into the minimum of the energy removal curve so that they contribute only a small dose. This can be seen in Figure 7 which shows the rapid attenuation of the energy removal dose from solar flare protons. Since the solar flare protons produce a minor dose and since there is a reduced number of cosmic rays during solar maximum, the dose should be higher during solar minimum, as our calculations show.

In the process of carrying out a Monte Carlo calculation, part of the results are the dose from both evaporation and secondary neutrons, and from pions. The pion dose that we found on the basis of only ionization loss of charged pions was two orders of magnitude less than the total energy removal dose, and therefore is of little interest. The neutron energy removal dose was an appreciable fraction of the total dose for all but the very thin spacecraft. During solar maximum, the evaporation neutron energy removal dose is higher than the secondary neutron dose for thin spacecraft (see Figure 8). The reason for this is the low production rate of secondary neutrons in thin spacecraft, and the high production rate of evaporation neutrons by solar flare protons in the 10 to 100 Mev energy range. In thicker spacecraft many of the evaporation neutrons are absorbed and more secondary neutrons are produced. This results in a nearly constant neutron energy removal dose with increasing spacecraft thickness.

The absence of low-energy protons during solar minimum changes this effect. During solar minimum the energy removed from evaporation neutrons was always less than from secondary neutrons (see Figure 9).

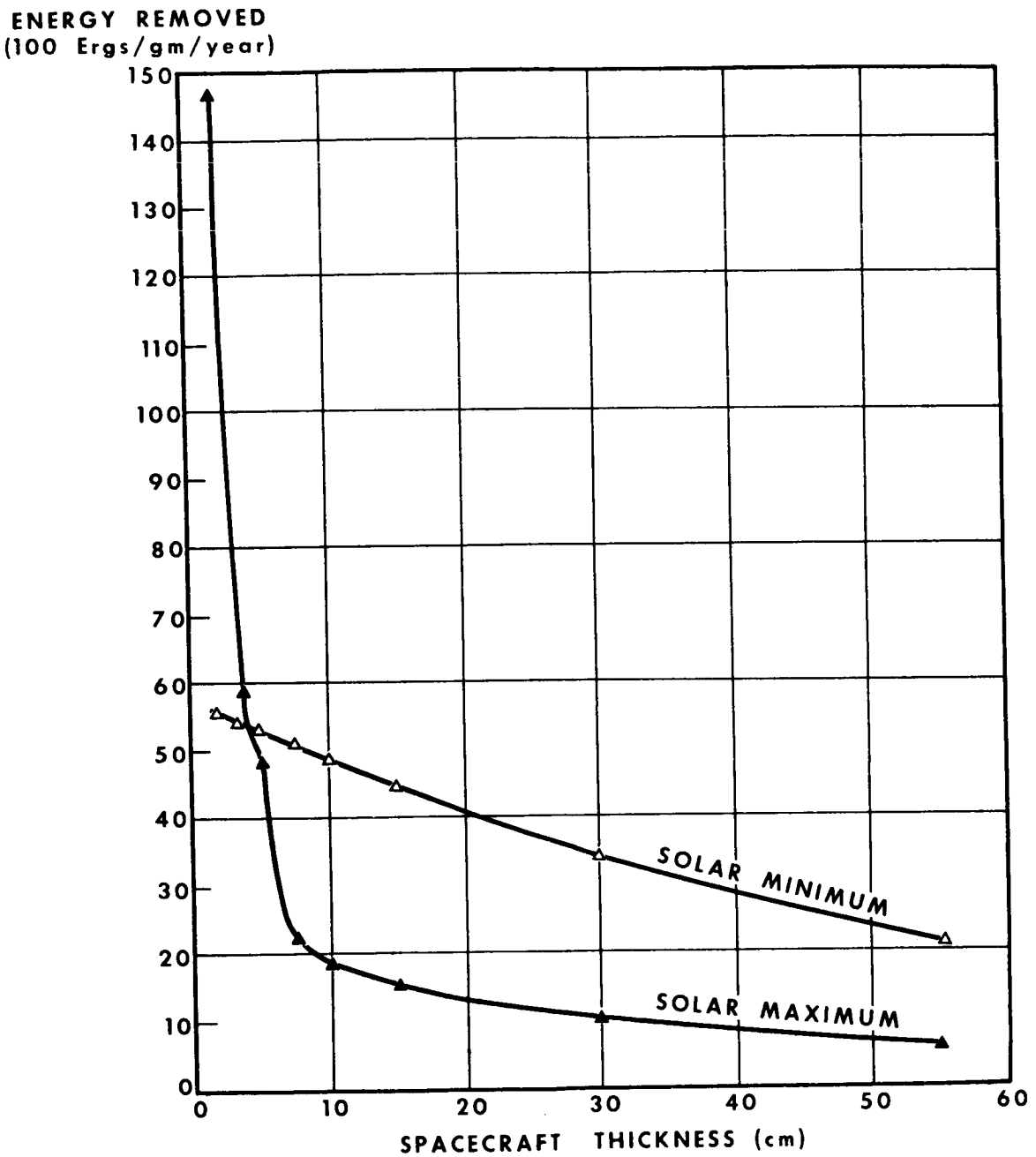

Figure 6 Comparison of Monte Carlo Results for Solar Cycle. Thin Tissue (ρ = .021).

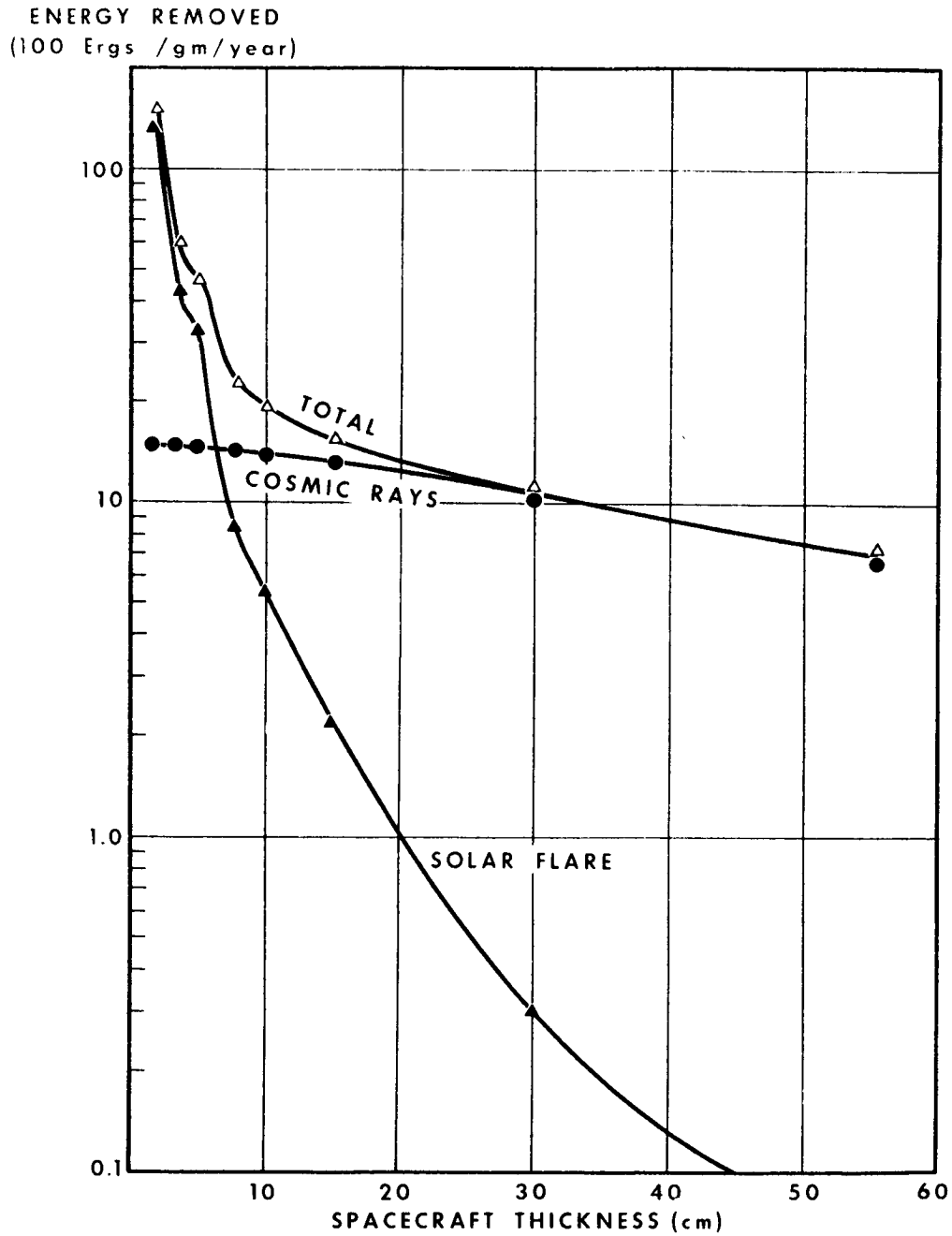

Figure 7 Monte Carlo Results for Solar Flare and Cosmic Ray Radiation in Spacecraft During Solar Maximum. Thin Tissue ($\rho = .021$).

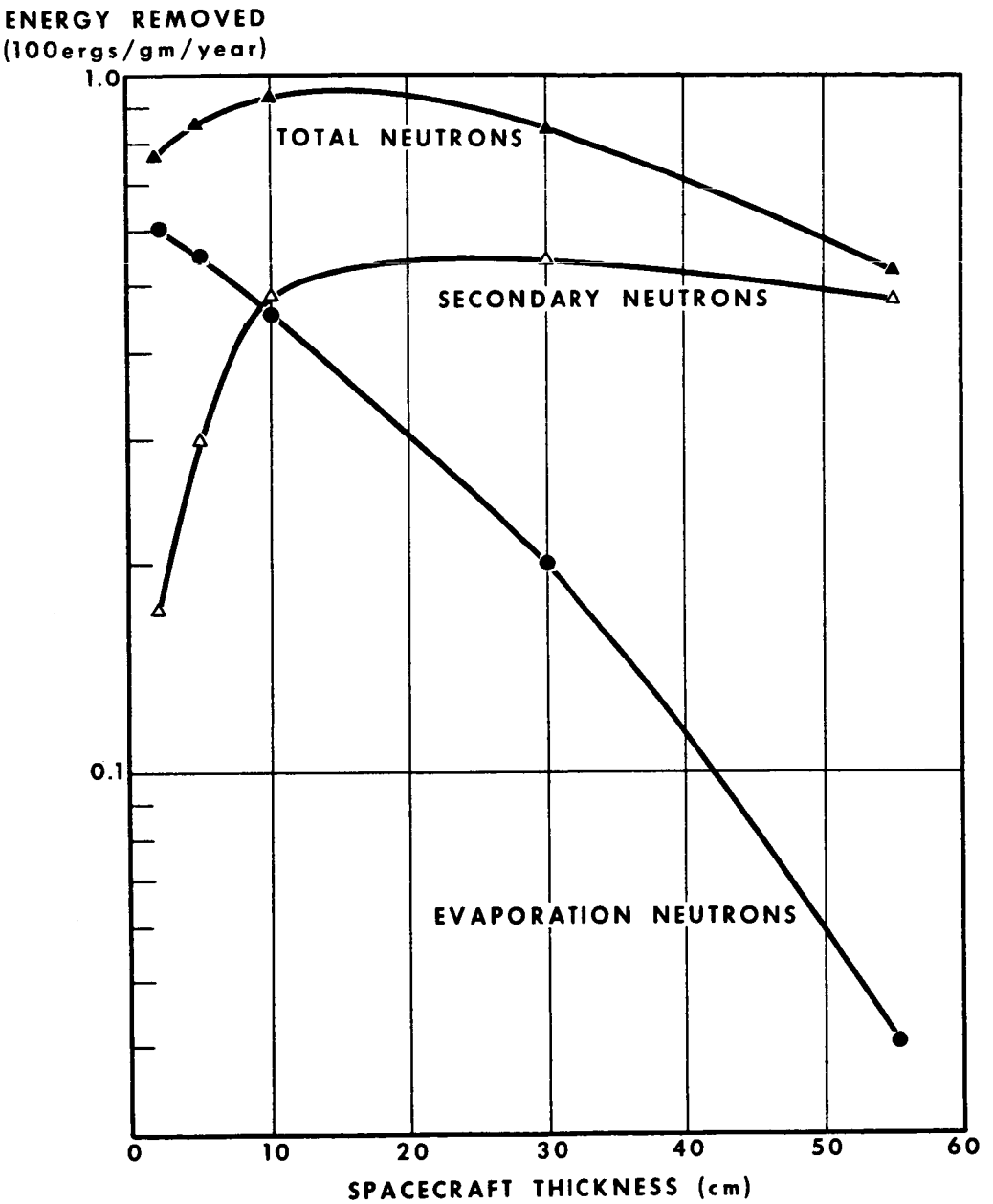

Figure 8 Energy Removed by Normal Tissue (ρ = 1.0) From Neutrons Produced in Aluminum Walled Spacecraft by Protons During Solar Maximum.

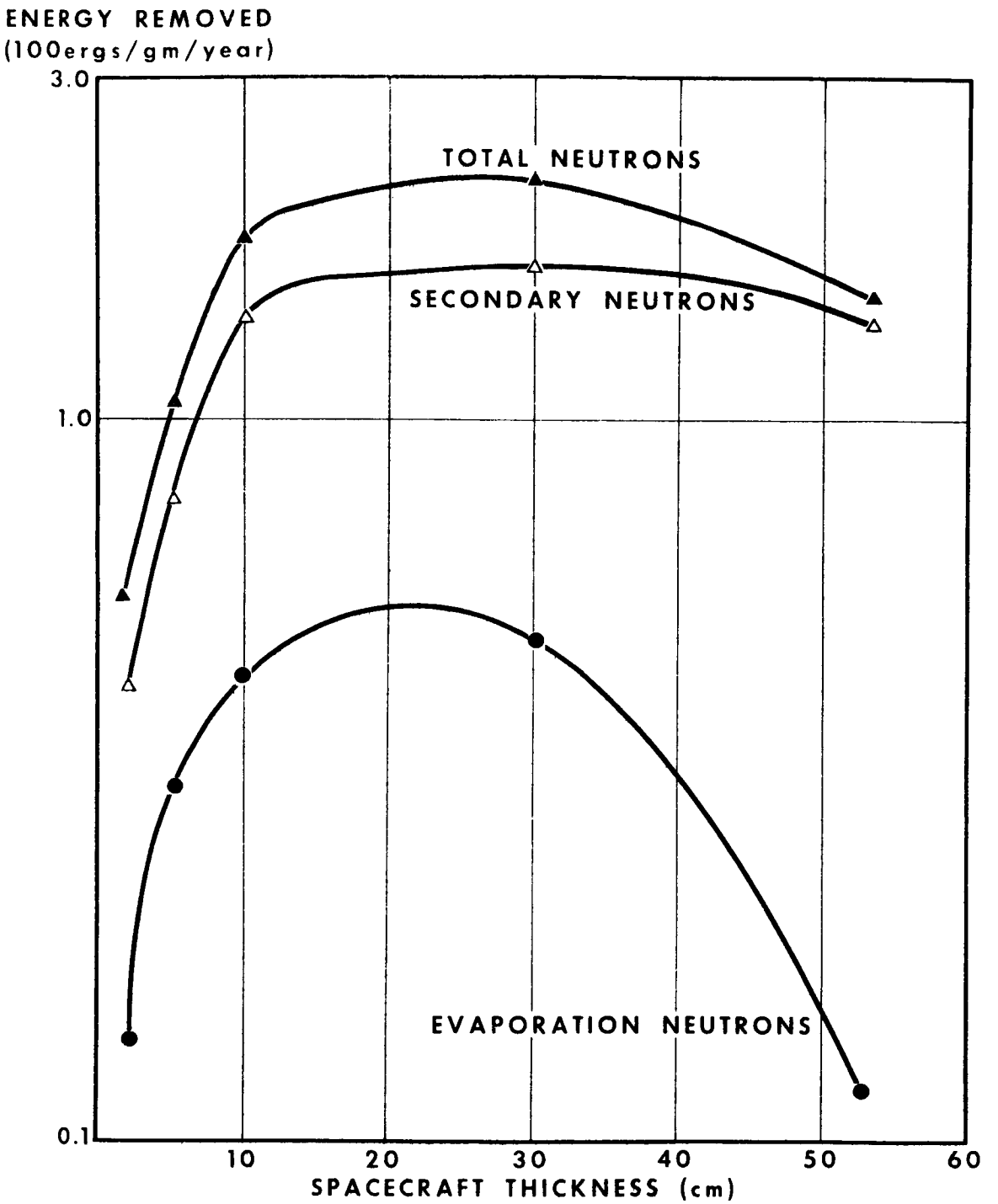

Figure 9 Energy Removed by Normal Tissue From Neutrons Produced in Aluminum Walled Spacecraft by Protons During Solar Minimum.

REFERENCES

1. Bailey, D.K., "Time Variations of the Energy Spectrum of Solar Cosmic Rays in Relation to the Radiation Hazard in Space," Journal of Geo. Rev., 67, No. 9, p. 391.

2. "Solar Proton Manual," edited by F. B. McDonald, X-611-62-122, NASA, Goddard Space Flight Center, Greenbelt, Md.

3. More, K.; Tiffany, O. L.; and Wainio, K., "Cosmic Ray Shower Production in Manned Space Vehicles," Chapter 8, Proceedings of the Conference on Medical and Biological Problems of Manned Space Flight, Nassau Conference, Nov. 1961, New York: Academic Press (In Publication 1962).

4. R. I. Allen et al, "Shielding Problems in Manned Space Flight," Annual Report - 1960, NASA Contract NAS 8-879, Lockheed Aircraft Corporation, Marietta, Georgia.

5. Gibson, G. A., "Energy Removed from Primary Proton and Neutron Beams by Tissue," ORNL-3260 Oak Ridge National Laboratory (1962).

ACKNOWLEDGEMENTS

We would like to acknowledge the continued support of I. H. McLaren and B. H. Colmery of the Bendix Systems Division. We would also like to thank Tom Cline, Arley Ferguson, and Harry Stigall of the Bendix Systems Division Data Processing Department for their invaluable assistance during the course of this investigation.

Paper E-3

NUCLEON-MESON CASCADE CALCULATIONS IN THE STRAIGHT-AHEAD APPROXIMATION

R. G. Alsmiller, Jr.
F. S. Alsmiller
J. E. Murphy*
Oak Ridge National Laboratory

Abstract

Nucleon-meson cascade calculations have been carried out for monoenergetic proton beams incident on aluminum shields. The results are used to obtain information for shielding against a solar flare proton spectrum.

A comparison between the one-dimensional cascade calculations and the more rigorous Monte Carlo calculations has been made. The two calculations are in very approximate agreement.

An IBM-7090 code which is being written to solve the nucleon-meson cascade equations is described.

In order to design shielding experiments for manned space vehicles, such as those being conducted at ORNL, it is necessary to know what energy regions are most important in the shielding problem. In order to give a preliminary answer to the question, nucleon-meson cascade calculations have been carried out in the straight-ahead approximation.

The method of calculation as well as the data used are given in detail in an ORNL report,[1] so only the results will be given here.

Let

$d(E_i,r)$ = the total dose rate per unit incident flux at a shield depth r from a monoenergetic proton beam of energy E_i

$d_s(E_i,r)$ = dose rate from secondary particles only per unit incident flux at a shield depth r from a monoenergetic proton beam of energy E_i.

---

*Central Data Processing Facility of the Oak Ridge Gaseous Diffusion Plant.

1. R. G. Alsmiller, Jr. and J. E. Murphy, Space Vehicle Shielding Studies: Calculation of the Attenuation of a Model Solar Flare and Monoenergetic Proton Beams by Aluminum Shields, ORNL-3317.

Using these functions, two "importance" functions, $I_1(E_i,r)$ and $I_2(E_i,r)$, are defined by

$$I_1(E_i,r) = d(E_i,r)\ F(E_i)$$

$$I_2(E_i,r) = d_s(E_i,r)\ F(E_i)$$

where

$F(E_i)$ = a solar flare proton spectrum.

If F is an isotropic angular flux incident on a spherical shell shield of thickness r, the importance functions must be multiplied by 4π steradians to obtain the total and secondary dose rates per unit incident energy range at the center of the spherical shell. If F is an isotropic angular flux incident on a slab shield, the importance functions must be Gross transformed[1] to obtain the dose rates per unit incident energy range at any given shield thickness. Since integrations over incident energies are required to obtain the dose rates from the flare, F, it is clear that the magnitude of I_1 is a measure of the importance of a given energy region in the incident spectrum for the determination of the total dose rate. Similarly, the magnitude of I_2 is a measure of the importance of a given energy region in the incident spectrum for the determination of the dose rate from secondary particles.

The importance functions for the case of a May 10th flare[2] on an aluminum shield are shown in Figs. 1 and 2. The dotted portions of the curves are drawn only for purposes of continuity and are, of course, not meant to be exact.

There are, of course, no discontinuities as shown in Fig. 1, rather, there is a very rapid variation in the regions where the discontinuities are shown. For a given curve (i.e., a given r) the discontinuity occurs at an energy such that the proton range at this energy is equal to r. To the right of the discontinuity the primary beam is contributing to the dose while to the left of the discontinuity only the secondary particles are contributing. It is clear that if one integrates under the curves in Fig. 1, most of the contribution to the integral will come from the region just to the right of the discontinuity, and thus, the primary dose is considerably more important than the secondary dose. It is clear that no single energy region can be singled out as being most important; rather the energy region of importance varies with the shield thickness. For a given shield thickness the energy region of most importance is that for which the proton range at this energy is just greater than the shield thickness.

---

2. W. L. Gill, Statement on the Approach to the Radiation Problem for Apollo, (submitted to National Academy of Sciences, Space Science Board, Working Group on Radiation Problems in Space Flight, Jan. 12-13, 1962).

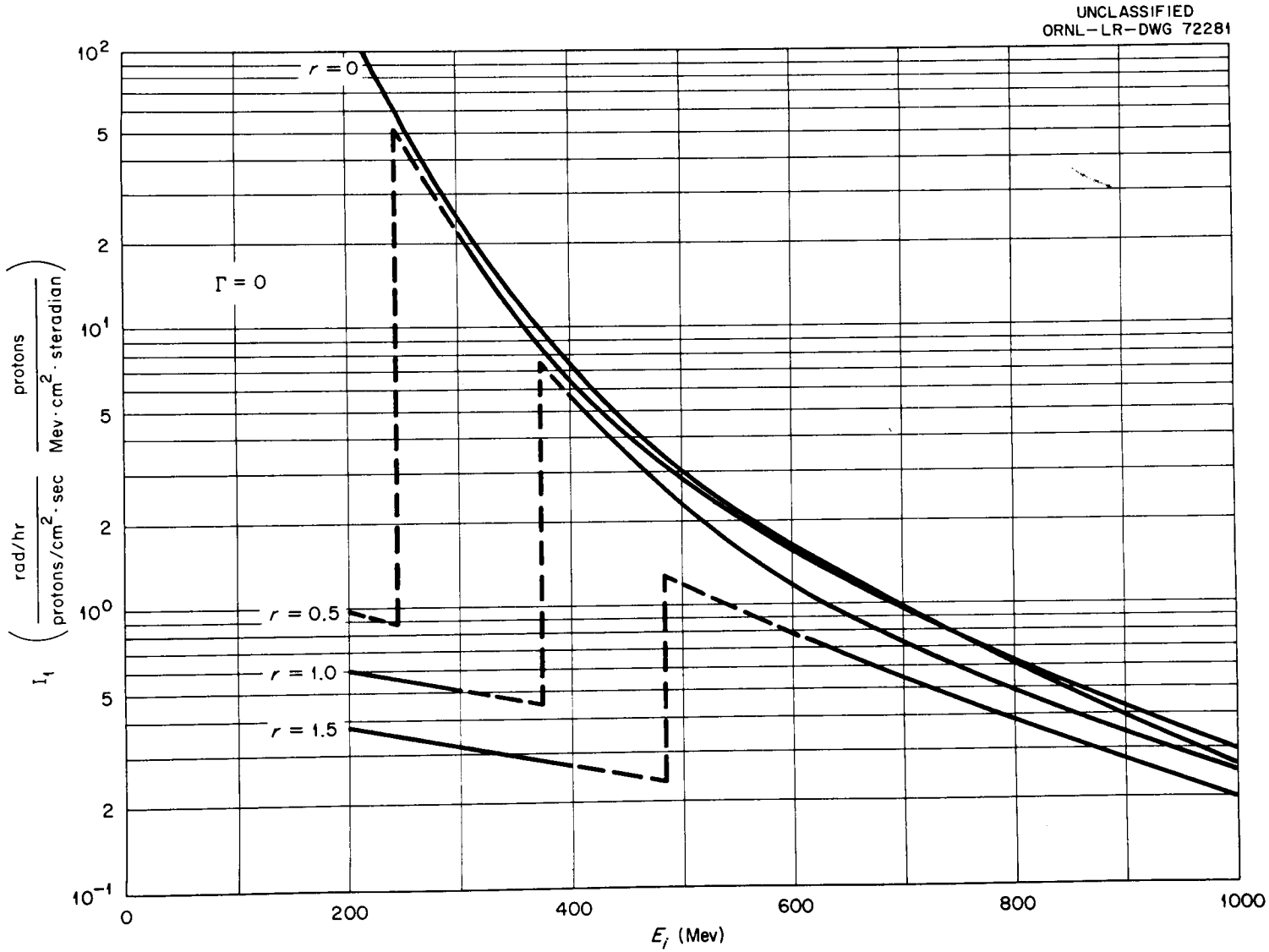

Fig. 1. First Importance Function vs Incident Energy
(r is measured in collision lengths = 93.80 g/cm²)

The second importance function shown in Fig. 2 is of more interest since it is the secondary particles which will be the primary concern of the experimentalist. The curves in Fig. 2 are essentially flat over the energy region from 200 to 600 Mev. This is, of course, not precisely true,but the evaluation is not considered accurate enough to make the peaks significant.* Above 600 Mev the curves begin to fall off and thus these higher energies tend to be less important. No results are given for incident energies of less than 200 Mev because the computational method becomes very unreliable at the lower energies.

In general all energies from 200 to 600 Mev are of approximately the same importance in determining the dose from secondary particles. It must be understood that this statement is dependent on the particular flare used and could conceivably change if a very different flare spectrum were to be considered.

The straight-ahead approximation may not give accurate results at the low energies of interest in the shielding of manned space vehicles. The calculations discussed above were meant to give only preliminary answers until the more refined calculations of H. Bertini[3] and W. E. Kinney et al.[4] become available. These calculations are beginning to be available so it is now possible to obtain an estimate of the validity of the results discussed above.

In Fig. 3 the results for a 400 Mev proton beam incident on a slab as obtained in reference 1 are compared with the Monte Carlo calculations of W. E. Kinney et al.**,+ It must be emphasized that the data concerning high energy interactions used in the two calculations was not the same so the disagreement shown in the figure is not entirely due to the straight-ahead approximation. Also, the flux-to-dose conversion factors were taken to be the same in the two calculations, so the very approximate nature of these

---

3. H. W. Bertini, "Monte Carlo Calculations for Intranuclear Cascades," this report.

4. W. E. Kinney, "A Series of Monte Carlo Codes to Transport Nucleons Through Matter," this report.

*Note that the thinnest shield shown is 47 gm/cm^2. For thinner shields the peak in the curve becomes somewhat more pronounced and occurs at a lower energy.

**We wish to thank W. E. Kinney and his collaborators for allowing us to use their work prior to its publication.

+The pions and muons were included in all of the calculations in reference 1. They are not shown in Fig. 3 because for this low energy case they may be neglected.

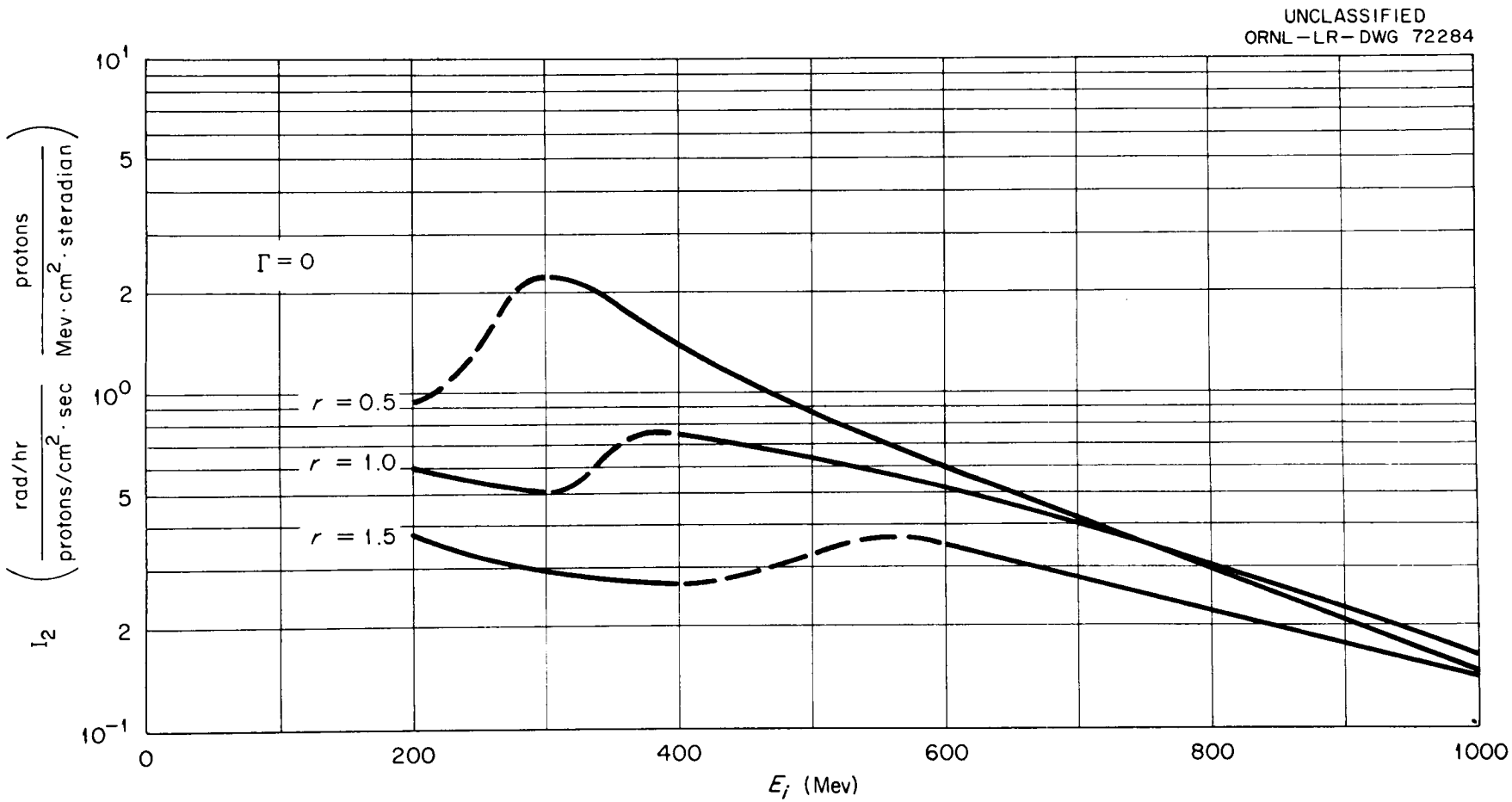

Fig. 2. Second Importance Function vs Incident Energy
(r is measured in collision lengths = 93.80 g/cm^2)

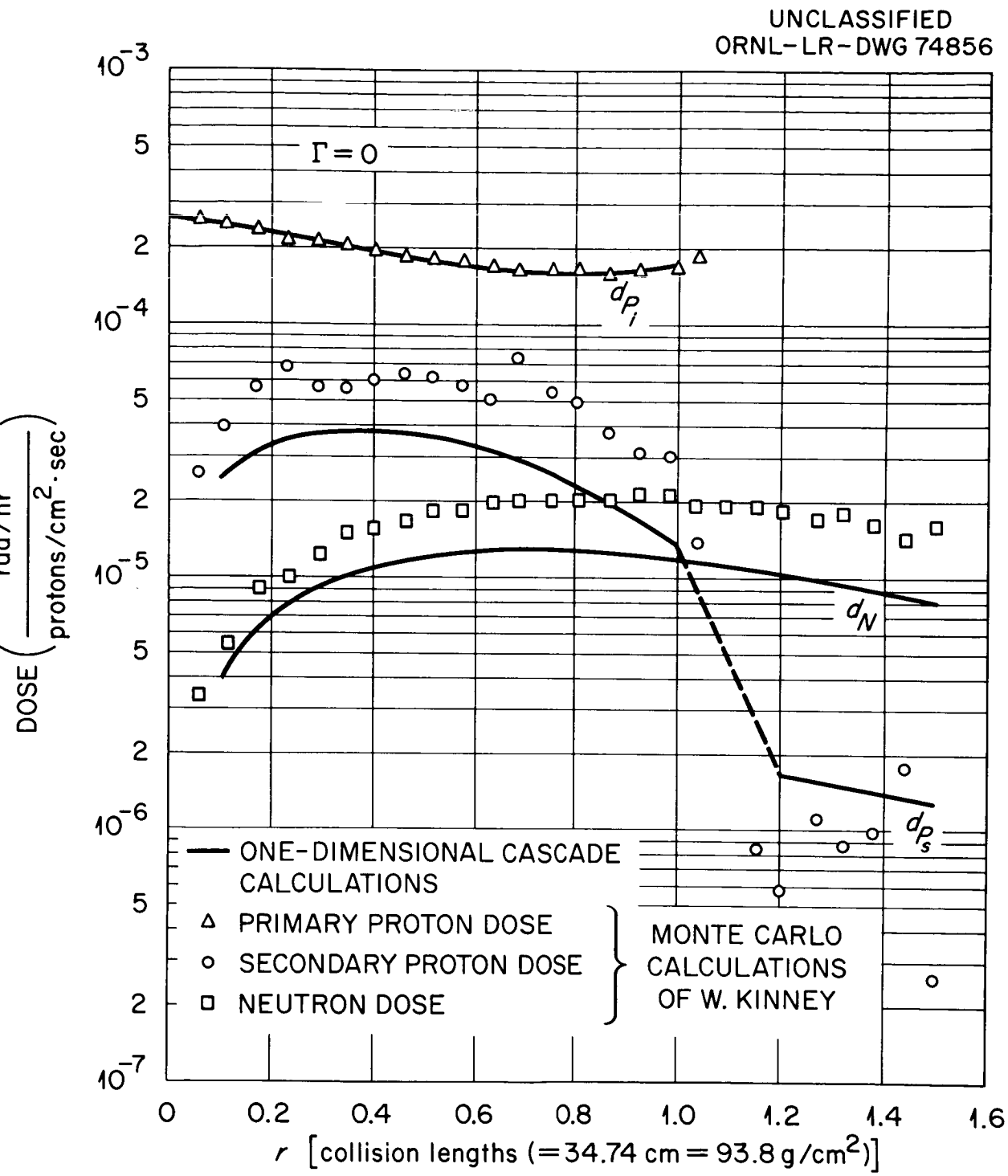

Dose vs Distance; 400-Mev Protons Incident.

Fig. 3.

conversion factors are incorporated in the Monte Carlo results.[1]

The two calculations are in good agreement insofar as the primary dose is concerned, but the Monte Carlo calculation gives a higher dose from both secondary protons and secondary neutrons. It is not possible to say how much of the discrepancy is due to the difference in data and how much is due to the straight-ahead approximation.

In general the results from the one-dimensionsl treatment leave much to be desired, but they are perhaps not so inaccurate as to invalidate the general conclusions drawn from Figs. 1 and 2.

Primarily because there is a lack of data concerning high-energy interactions, the IBM-7090 code written to solve the cascade equations included several approximations. Before long theoretical results for high-energy interactions will become available and make use of these approximations unnecessary; hence, a new code is being written which does not impose them.* At the same time several new features are being included so that the new code will be not only more accurate but also more efficient and more versatile.

The major improvements in the code are listed below:

1. Each of the secondary energy distributions, $F_{jk}(E',E)$, that is, the number of particles per unit energy of type j produced with energy E when a particle of type k and energy E' induces a nuclear reaction, may be an arbitrary function of E and E'. (The subscripts j and k take values N, P, and π corresponding to neutrons, protons, and pions.)

2. Monoenergetic sources, in addition to sources with a continuous energy distribution, may be considered.

3. The density of the medium in which the cascade takes place may be an arbitrary function of depth. (This allowance for density variation was introduced so that the propagation of cosmic rays in the atmosphere could be considered.)

4. The production of muons from the decay of pions is treated more rigorously.

5. A provision has been made for including neutron-proton elastic scattering in hydrogenous media. The slowing-down effect of this elastic scattering on the cascade neutrons is included, as is the introduction of the recoil protons into the cascade, but the method used is very approximate.

The basic approximation, the one-dimensional cascade treatment, is retained in the new code. The cascade components considered are neutrons,

---

*The coding is being done by R. G. Mashburn of the Central Data Processing Facility of the Oak Ridge Gaseous Diffusion Plant.

protons, charged pions, and charged muons; no distinction is made between positive and negative pions or positive and negative muons.

For numerical convenience all calculations will be done in terms of a lethargy variable u defined by

$$u = \ell n \frac{E_o}{E} ,$$

where E is the particle kinetic energy and E_o is an arbitrary energy which defines the zero of lethargy. However, the code will be written in such a way that all inputs (e.g., initial flux, secondary energy distribution, etc.) must be specified as a function of energy, and all outputs be given in energy.

The primary particle fluxes may be given analytically, and thus in the numerical calculation it will be convenient to separate the primary, $\phi_{ij}(E,r)$, and secondary, $\phi_{sj}(E,r)$ components.

The equations for the primary fluxes, to which we give the solutions, are the same as the equations for the secondary fluxes with the right-hand side set equal to zero. Although the equations will be coded in terms of lethargy, for clarity they are written here in terms of energy. The neutron, proton, and pion equations are:

$$\phi_{ij}(E,r) = \phi_j(E,0)(1 - C_j)\, e^{-Q_j(E)r} + Q_j(E_j,0)\, C_j \frac{S_j(E_j)}{S_j(E)}$$

$$\times \exp\left\{ - \int_E^{E_j} \left[\frac{Q_j(E') + \delta_{\pi j}\, Q_{\pi D}(E',r')}{S_j(E')} \right] dE' \right\} \quad , j = N,P,\pi, \qquad (1)$$

where

$$C_N = 0, \text{ or } 1;$$

$$C_P = 1;$$

$$C_\pi = 1;$$

$$\int_E^{E_j} \frac{dE'}{S_j(E')} = r; \text{ that is, } E_j = E_j(E,r),$$

$$\int_{E'}^{E_j} \frac{dE''}{S_j(E'')} = r'; \text{ that is, } r' = r'(E_j,E'),$$

$$\delta_{\pi j} = 1 \text{ if } j = \pi$$
$$= 0 \text{ if } j \neq \pi,$$

$$Q_{\pi D}(E,r) = \frac{C_\rho \lambda_o}{\rho \Lambda_\pi(E)} + \frac{(1 - C_\rho)\ \lambda_o}{\rho_c(r)\ \lambda_\pi(E)},$$

in which

$$\frac{1}{\Lambda_\pi(E)} = \frac{m_\pi}{\tau_\pi} \left[\frac{1}{E(E + 2m_\pi)} \right]^{1/2},$$

$$C_\rho = 0, \text{ or } 1$$

$$\frac{\partial}{\partial r} \phi_{sj}(E,r) + \left[Q_j(E) + \delta_{\pi j}\ Q_{\pi D}(E,r) \right] \phi_{sj}(E,r) - C_j \frac{\partial}{\partial E} \left[S_j(E)\ \phi_{sj}(E,r) \right]$$

$$= \sum_k \int_E^{E_{max}} F_{jk}(E',E)\ Q_k(E') \left[\phi_{ik}(E',r) + \phi_{sk}(E',r) \right] dE'$$

$$+ \delta_{Pj}\ H_R(E,r) + H_j(E,r), \qquad j,k = N,P,\pi, \tag{2}$$

where

$\phi_{iN}(E,r) = N_i(E,r)$

= primary neutron flux per unit energy from a neutron source at r = 0 with a continuous energy spectrum;

$\phi_{sN}(E,r) = N_s(E,r)$

= secondary neutron flux per unit energy;

$\phi_N(E,r) = N_i(E,r) + N_s(E,r)$

= total neutron flux per unit energy when there are no monoenergetic sources present; since $N_s(E,0) = 0$, then $\phi_N(E,0) = N_i(E,0)$ is one of the initial values which must be specified.

ϕ_{iP}, $\phi_{i\pi}$, etc. have similar definitions. Furthermore,

r = dimensionless distance variable defined by the relation $r = (\rho/\lambda_o)R$ if the density of the medium, ρ, is a constant, and by $r = [x(t) - x_o]/\lambda_o \cos\theta$, where $x(t) = \int_o^t \rho_c(t')\,dt'$, if the density of the medium, ρ_c, is a function of depth;

θ = angle of the flux with respect to the vertical; this angle is introduced so that the propagation of the cascade can be considered in a direction other than the vertical;

ρ = density of the medium, g/cm^3, if this density is constant;

R = distance in the direction θ, cm;

λ_o = an arbitrary constant with dimensions g/cm^2 which determines the units in which the dimensionless variable r is measured;

x_o = pressure, g/cm^2, at the point from which r is measured;

$\rho_c(t)$ = density of the medium, g/cm^3, as a function of position;

t = depth, cm;

C_j = constant which takes the value 0 or 1; the quantities C_P and C_π are always unity, but C_N may be 0 or 1; if $C_N = 1$, neutron slowing down (e.g., by elastic scattering from protons) is included; when $C_N = 0$, neutron slowing down is omitted;

$$Q_j(E) = \frac{\lambda_o N_o}{A}\,\sigma_j(E);$$

$\sigma_j(E)$ = nonelastic cross section for particles of type j in the medium being considered;

N_o = Avogadro's number;

A = atomic weight of the nuclei in the medium;

$S_j(E) = \frac{\lambda_o N_o}{A} \epsilon_j(E)$;

$\epsilon_j(E)$ = atomic stopping cross section for particles of type j in the medium;

C_ρ = constant which takes value 0 or 1; when a medium of constant density is considered, $C_\rho = 1$; when a medium of variable density is considered, $C_\rho = 0$;

m_π = rest mass of the charged pion, Mev;

τ_π = mean life of the charged pion, sec, multiplied by the velocity of light, cm/sec;

$F_{jk}(E',E)dE$ = the number of secondary particles of type j in the energy interval E to E + dE produced by the nonelastic collision of a particle of type k of energy E'.

Still to be discussed are the source terms H_R and H_j. The equations without H_j are satisfactory if only sources with continuous energy distributions are to be considered; however, monoenergetic sources are most conveniently handled by introducing H_j. By utilizing the fact that the primary flux from a monoenergetic source may be calculated analytically, the number of secondary particles per unit energy range per unit volume, H_j, produced per second by the primary flux may be written

$$H_j = \sum_k F_{jk}(E'_k,E)\, Q_k(E'_k)\, \phi_{k\delta}(r)\, \Theta(E'_k - E), \quad j,k = N,P,\pi \tag{3}$$

where

$$E_k' = E_{ok}(1 - C_k) + E_{Rk}\, C_k,$$

$$\phi_{k\delta} = \phi_{k\delta o}(1 - C_k)\, e^{-Q_k(E_{ok})r} + \phi_{k\delta o}\, C_k \exp\left\{ - \int_{E_{Rk}}^{E_{ok}} \left[\frac{Q_k(E') + \delta_{k\pi}\, Q_{\pi D}(E', r')}{S_k(E')} \right] dE' \right\}$$

$$\int_{E_{Rk}}^{E_{ok}} \frac{dE'}{S_k(E')} = r,$$

$$\int_{E'}^{E_{ok}} \frac{dE''}{S_k(E'')} = r',$$

$$\Theta(E_k - E) = 1 \text{ if } E_k - E \geq 0$$

$$= 0 \text{ if } E_k - E < 0,$$

$$\phi_{N\delta}(r) = N_\delta(r)$$

= flux strength of source neutrons which reach position r when a flux of $N_{\delta o}\delta(E - E_{oN})$ source neutrons start at the origin with energy E_{oN},

$N_{\delta o}$ = strength of neutron monoenergetic source,

E_{oN} = energy of monoenergetic neutron source,

E_{RN} = energy of monoenergetic source neutrons when they reach position r.

The other quantities, $\phi_{P\delta}$, $P_{\delta o}$, etc., have similar definitions.

The Θ functions are introduced into H_j to indicate that a particle of energy E' cannot produce secondary particles of energy greater than E'. The physically correct functions F_{jk} have the property

$$F_{jk}(E',E) = 0 , \qquad E \geq E' ,$$

so that the Θ functions are superfluous when these functions are used. In some cases, however, we use approximations to the F_{jk}'s which do not have this property,[5] and then it is necessary to introduce this property through the Θ functions.

The three terms in H_j correspond to the production of secondary particles of type j by the three kinds of monoenergetic sources allowed—neutrons, protons, and pions. The code will be written so that monoenergetic and continuous sources for all three types of particles may be considered simultaneously.

The term $H_R \delta_{jP}$ is introduced for the purpose of including recoil protons from neutron-proton elastic scattering in hydrogenous media. Assuming that when a neutron-proton collision takes place the neutron transfers, on the average, a given portion of its energy to the proton,

$$H_R = C_s \frac{S_N(KE)}{E} [N_i(E,r) + N_\delta(E,r)]$$

$$+ C_s \frac{K S_N[E_{RN}C_N + E_{oN}(1 - C_N)]}{E_{RN}C_N + E_{oN}(1 - C_N)} G[E_{RN}C_N + E_{oN}(1 - C_N),E]$$

$$\times N_\delta(r) \Theta[E_{RN}C_N + E_{oN}(1 - C_N) - E] , \qquad (4)$$

where

C_s = 0 or 1 and is introduced so that the recoil proton terms may be omitted; note that since C_s and C_N are specified separately it is possible to include the recoil protons and at the same time neglect the effects of elastic scattering on the neutrons;

5. R. G. Alsmiller, Jr. F. S. Alsmiller, J. E. Murphy, Nucleon-Meson Cascade Calculations: Transverse Shielding for a 45-Gev Electron Accelerator (Part I), ORNL-3289 (1962).

$1/K$ = fraction of the neutron's energy which on the average is given to the proton when a neutron-proton elastic scattering occurs;

$G(E',E)$ = energy distribution of the recoil proton when a neutron of energy E' is scattered by a proton; to be consistent with the first term in H_R we should have $G(E',E) = \frac{1}{K}\,\delta(E' - KE)$, but because of the difficulties associated with introducing a delta function into the equation we shall use an analytic function which approximates the delta function.

In writing Eq. 4 we assumed that $S_N(E)$ is given by

$$S_N(E) = n_P\,\sigma_E(E)\,\frac{E}{K} \quad ,$$

where n_P = number density of protons in the medium, and σ_E = elastic scattering cross section.

The muon equations are similar to those for the other cascade particles, but differ in one important way: since the small muon nuclear interactions are neglected, the muons do not produce neutrons, protons, or pions and thus do not take an active part in the cascade.

The muon equations are[6]

$$\mu_i(E,r) = \mu_i(E_\mu,0)\,\frac{S_\mu(E_\mu)}{S_\mu(E)}\,\exp\left[-\int_E^{E_\mu}\frac{Q_{\mu D}(E',r')}{S_\mu(E')}\,dE'\right] \qquad (5)$$

where

$$\int_E^{E_\mu}\frac{dE'}{S_\mu(E')} = r,$$

6. The form of the muon source term from pion decay is discussed in detail in Appendix 3 of Ref. 2. The secondary muon equation may be solved in quadrature, but in the present code the differential equation was found to be more convenient to use than the solution.

$$\int_{E'}^{E_\mu} \frac{dE''}{S_\mu(E'')} = r',$$

$$Q_{\mu D}(E,r) = \frac{C_\rho \lambda_o}{\rho \Lambda_\mu(E)} + \frac{(1 - C_\rho)\lambda_o}{\rho_c(R)\,\Lambda_\mu(E)},$$

$$\frac{1}{\Lambda_\mu(E)} = \frac{m_\mu}{\tau_\mu}\left[\frac{1}{E(E + 2m_\mu)}\right]^{1/2};$$

and

$$\frac{\partial}{\partial r}\mu_s(E,r) + Q_{\mu D}(E,r)\,\mu_s(E,r) + \frac{\partial}{\partial E}\left[S_\mu(E)\,\mu_s(E,r)\right]$$

$$= \int_{E_{\mu 1}}^{E_{\mu 2}} dE'\, F(E')\, Q_{\pi D}(E',r)\left[\pi_i(E',r) + \pi_s(E',r)\right]$$

$$+ \begin{cases} \pi_\delta(r)\, F(E_{R\pi})\, Q_{\pi D}(E_{R\pi},r), & E_{\mu 1} \le E_{R\pi} \le E_{\mu 2}, \\ 0, & E_{\mu 2} < E_{R\pi} < E_{\mu 1}, \end{cases} \qquad (6)$$

where

$$F(E') = \frac{\left(\frac{m_\pi}{m_\mu}\right)E'}{2U_2[E'(E' + 2m_\pi)]^{1/2}},$$

$$E_{\mu 1} = \frac{m_\pi}{m_\mu}\left\{U_1(E + m_\mu) - U_2[E(E + 2m_\mu]^{\frac{1}{2}}\right\} - m_\pi,$$

$$E_{\mu 2} = \frac{m_\pi}{m_\mu}\left\{U_1(E + m_\mu) + U_2[E(E + 2m_\mu)]^{\frac{1}{2}}\right\} - m_\pi.$$

Paper E-4

TRANSPORT CALCULATIONS FOR PROTON SHIELDING *

Gerald Litton, Rubin Goldstein, and Roger Wallace

Lawrence Radiation Laboratory
University of California
Berkeley, California

15149

Abstract

To calculate the dose rate and integrated dose behind a layer of material that shields against a proton flux it is necessary to know the effect of the shield on the incident flux. The work reported here investigates that effect.

The analysis takes into account both proton ionization energy loss and secondary-particle production, using the transport method of successive generations. The secondaries considered are protons, neutrons, and π mesons.

Introduction

The system chosen for analysis is a one-dimensional slab of width a, upon which is incident a uniform and isotropic proton flux with an arbitrary spectrum. An expression is developed for the uncollided proton flux, termed the primary flux, as a function of energy, angle, and position in the slab.

The first-generation secondary flux, i.e., the flux due to direct nuclear collisions of the primary flux, is then calculated. Similarly, a second-generation secondary flux, due to nuclear collisions of the first-generation flux is calculated. Succeeding generations of the secondary flux are calculated until the magnitude of the flux in a particular generation is sufficiently small to be neglected.

The secondary flux is subdivided into protons, neutrons, and π mesons, each of which is considered individually in the calculations.

---

* Work done under the auspices of the U. S. Atomic Energy Commission, and the Joint Atomic Energy Commission—NASA Space Radiation Program.

Primary Proton Flux

The primary or uncollided proton flux is given as

$$\phi_p^{(0)}(x, E, \mu) = \frac{1}{2\pi} \phi_0(E_0) \exp\left\{ - \int_E^{E_0} \frac{\Sigma_p(E')}{f(E')} \, dE' \right\}, \qquad (1)$$

where $\phi_0(E_0)$ = incident proton flux,

$\Sigma_p(E)$ = total macroscopic proton cross section of the slab medium,

$f(E)$ = ionization energy loss of the slab medium.

The relation between E and E_0 is given as

$$E_0 = E + \int_0^{x/\mu} f(E') \, dx' \, , \qquad (2)$$

which states that the initial proton energy E_0 is equal to the energy E at x plus the energy lost by ionization.

The exponential term in Eq. 1 represents the proton attenuation due to nuclear interactions.

Data on ionization energy loss are well known for a large number of elements. Similarly, low-energy proton cross sections are known. Unfortunately, only a small amount of high-energy cross-section data is available. Some estimates[1] and some experimental measurements[2] have been made. A useful approximation is the equivalence of neutron and proton cross sections at high energies, allowing the use of high-energy neutron cross-section data.[2]

Because of the complex form of f(E), the integration in Eqs. 1 and 2 must, in general, be performed numerically. The calculations are minimized by noting that the primary flux may be expressed as a function of two independent variables: E and x/μ.

Secondary Particle Fluxes

For the sake of brevity, meson fluxes are not discussed in the following sections. It is pertinent to note that the equations describing π^0 mesons are analogous to those describing neutrons. A similar correspondence exists for $\pi^{\pm}$ mesons and protons.

First-Generation Fluxes

The flux of particle i at some point $\vec{r}$, where i may represent protons or neutrons, is calculated by considering the production of i particles by proton interactions within a volume element at $\vec{r}'$, which contribute to the flux at $\vec{r}$, and then integrating over all $\vec{r}'$. The results for slab geometry are

$$\phi_i^{(1)}(x, E, \mu) = \frac{2\pi}{|\mu|} \int_{-1}^{1} d\mu' \int dE' \int_0^a dx' \, G(x';\mu) \Sigma_p(E') \, \phi_p^{(0)}(x', E', \mu') \cdot N_{ip}(E' \rightarrow E_0, |\mu''|) \cdot \exp[-h_i(E, x', x)] \tag{3}$$

with the following definitions:

The term μ'' is the cosine of the difference in angle between the direction fo the initial proton and the direction of the final particle i. It is related to μ and μ' by

$$\mu'' = \mu\mu' + \sqrt{[1 - (\mu)^2][1 - (\mu')^2]} \, . \tag{4}$$

The quantity E_0 is that energy which the particle i must have at x' so as to arrive at x with energy E. For neutrons, E_0 is identically E, but for protons, E_0 is greater than E by an amount equal to the ionization energy loss experienced by the proton in migrating from x' to x. The relationship between E and E_0 in this case is

$$E_0 = E + \int_0^{|(x'-x)/\mu|} f(E'') \, dx'' . \tag{5}$$

The function $G(x', \mu)$ serves to set the limits on the x' integration, and is defined by

$$G(x', \mu) = \begin{cases} 1 \ldots 0 < x' < x, & \text{for } \mu > 0, \\ 0 \ldots x < x' \leq a, & \text{for } \mu > 0, \\ 0 \ldots 0 \leq x' < x, & \text{for } \mu < 0, \\ 1 \ldots x < x' \leq a, & \text{for } \mu < 0. \end{cases} \tag{6}$$

The quantity $\exp[-h_i(E, x', x)]$ is the fraction of particles i that travel from x' to x without undergoing any nuclear interactions. The term $h_i(E, x', x)$ is given by

$$\begin{aligned} h_i(E, x', x) &= \Sigma_N(E) \frac{x'-x}{\mu} && \text{-- for neutrons,} \\ h_i(E, x', x) &= \int_E^{E_0} \frac{\Sigma p(E'')}{f(E'')} \, dE'' && \text{-- for protons,} \end{aligned} \tag{7}$$

where Σ_n = total macroscopic cross section for neutrons.

The superscripts attached to the fluxes denote generation number, with the primary proton flux being defined as the zero-order generation.

The function $N_{ij}(E' \rightarrow E_0, |\mu''|)$ represents the number of particles i with energy E_0 and direction μ produced per interaction of a proton of energy E' and direction μ'.

Higher-Generation Fluxes

The calculation of the higher-order fluxes is analogous to that for the first-generation fluxes, with one difference. Particles i may be produced not only by nuclear interactions of protons, but also from secondary neutrons and mesons. The expressions for the nth-generation fluxes are

$$\phi_i^{(N)}(x, E, \mu) = 2\pi \int_{-1}^{1} \frac{d\mu'}{|\mu|} \int dE' \int_0^a dx' \exp\left[-h_i(E, x', x)\right] G(x', \mu) \cdot \sum_j \phi_j^{(N-1)}(x', E', \mu') \Sigma_j(E') N_{ij}(E' \rightarrow E_0, |\mu''|) . \tag{8}$$

The summations in Eq. 8 extend over proton, neutron, and meson interactions.

Integral Evaluation

The integrals appearing in Eqs. 3 and 8 must be evaluated numerically for several reasons, the strongest of which is the complex form of the functions N_{ij}. Furthermore, the primary flux is in general specified as numerical data, as previously discussed.

At present, direct triple numerical integration of these equations appears to be the most likely method of attack.

Secondary-Particle Production

One of the major difficulties is the great lack of information about the function $N_{ij}(E' \rightarrow E_0, |\mu''|)$. The data that are available are due primarily to Metropolis[3] and Wallace and Moyer.[4]

The function N_{ij} represents the angular, energy, and number distributions of secondary particles j, and is, therefore, quite complicated. It is expected that more complete data on this function will be made available in the future.

Conclusions

The primary and secondary fluxes can, in principle, be determined to a high degree of accuracy by means of the foregoing analysis. In practice, however, there are two limitations on the obtainable accuracy, the more important by far being the lack of accurate data on high-energy cross sections and secondary-particle production.

The second limitation arises from truncation errors produced in the numerical integrations. The magnitude of these errors is determined by the sizes of the coordinate differences, which are unfortunately limited by computer capacities.

The desired end result is the fluxes of the various particles at the inner surface of the slab. A detailed knowledge of these fluxes is of major importance in determining the dose away from the inner slab surface.

REFERENCES

1. Burton J. Moyer (Lawrence Radiation Laboratory), Data Related to Nuclear Star Production by High-Energy Protons, unpublished data, 1961.

2. T. Coor, D. A. Hill, W. F. Hornyak, L. W. Smith, and G. Snow, Phys. Rev. 98, 1369 (1955).

3. N. Metropolis, R. Bivins, M. Storm, A. Turkevich, J. M. Miller, and G. Friedlander, Phys. Rev. 110, 185 (1958); and 110, 204 (1958).

4. R. W. Wallace and B. J. Moyer, Shielding and Activation Considerations for a Meson Factory, Lawrence Radiation Laboratory Report UCRL-10086, April 11, 1962 (unpublished).

Paper E-5

COMPARISON OF PRIMARY PROTON DOSE WITH THE DOSE FROM GAMMA RAYS PRODUCED BY INELASTIC SCATTERING OF SOLAR FLARE PROTONS

F. S. Alsmiller
R. G. Alsmiller, Jr.
D. K. Trubey
Oak Ridge National Laboratory

Abstract 15150

The primary proton dose resulting from solar flare (May 10, 1959) protons incident on an aluminum shield is compared with the dose from gamma rays produced by inelastic collisions of the primary protons. Both spherical shell and slab shields are considered.

Most of the radiation dose behind thin shields exposed to solar flare protons can be attributed to the primary protons. However, the possible importance of secondary gamma rays produced in proton non-elastic collisions has been pointed out recently by Madey et al.[1] They computed the gamma dose rate at the center of an aluminum spherical shell, as a function of shield thickness, and found it comparable to the primary proton dose at a thickness of about 12 cm. These results are based on the use of experimental values of the gamma spectrum and yield for 14-Mev protons[2] which were assumed to be the same for all proton energies above the Coulomb barrier up to 50 Mev.

---

1. R. Madey, A. G. Duneer, Jr., and T. J. Krieger, Gamma Dose from Solar Flare Protons Incident on an Aluminum Shield, Presented at the Annual Meeting of the American Nuclear Society, June 18-21, 1962 Boston, Mass.

2. T. Wakatsuki et al., J. Phys. Soc. Japan 15, 1141 (1960).

tables[6] based on experimental values for E < 2 Mev. The proton total nonelastic collision cross section was taken mostly from the Monte Carlo calculation of Bertini above 30 Mev (see Paper D-3) and from Howerton's[7] compilation of neutron nonelastic cross sections for neutron energies below 15 Mev, using the same approximation as in Eq. 1; i.e.,

$$\sigma_{p,\text{nonel}}(E') = \sigma_{n,\text{nonel}}(E' - V_c). \qquad (3)$$

In the calculations for spherical shell shields, the photons are assumed to be produced by primary protons only, to have the same direction as the incident proton, and to be attenuated[8] exponentially through the shield. Photon flux-to-dose conversion factors for tissue were taken from ref 9.

The numerical differences in the estimates of the gamma dose rate shown in Fig. 1 are consistent with the differences in the assumed gamma spectrum. Fig. 1 also shows a comparison of the primary proton dose rate, $d_{P,dE/dx}$, calculated considering only the proton ionization energy losses in tissue,[10] with the results of Madey et al. No crossing between the gamma and proton curves occurs in our calculations; the gamma dose rate is less than 10% of the proton dose at a thickness of 25 g/cm^2 (9.3 cm).

The spherical shell calculations were repeated for the time-integrated May 10 solar flare spectrum,[11]

$$\begin{aligned} P(E,0) &= 0 && (0 \leq E < 5 \text{ Mev}) \\ &= 2.5 \times 10^{11} E^{-2.07} && (5 \text{ Mev} \leq E \leq 60 \text{ Mev}) \\ &= 5.486 \times 10^{14} E^{-3.95} && (60 \text{ Mev} \leq E \leq 10^3 \text{ Mev}) \end{aligned} \qquad (4)$$

---

6. American Institute of Physics Handbook, McGraw-Hill Book Co., Inc., 1957.
7. R. J. Howerton, Semi-Empirical Neutron Cross Sections, UCRL-5351 (1958).
8. G. W. Grodstein, X-ray Attenuation Coefficients from 10 Kev to 100 Mev, NBS Circular 583 (1957).
9. B. J. Henderson, Conversion of Neutron or Gamma-Ray Flux to Absorbed Dose Rate, XDC-59-8-179 (1959).
10. W. S. Snyder and J. Neufeld, Radiation Research 6, 67 (1957).
11. W. L. Gill, Statement on the Approach to the Radiation Problems for Apollo, submitted to the National Academy of Sciences, Space Science Board, Working Group on Radiation Problems in Space Flight, Jan. 12-13, 1962, NASA Manned Spacecraft Center, Life Systems Division.

Since many questions remain, we have performed several further calculations for both spherical shell and infinite slab aluminum shields. The gamma spectrum is constructed from theoretical estimates of the gamma production cross sections[3] which are available for inelastic (n,n') neutron scattering in aluminum, for neutron energies from 0.9 to 18 Mev. We assume the gamma production cross sections for proton inelastic scattering can be approximated with sufficient accuracy by the relation

$$\sigma_{pp'\gamma}(E,E_\gamma) = \sigma_{nn'\gamma}(E - V_c,E_\gamma) \qquad (V_c \leq E \leq 22.3 \text{ Mev})$$

$$= \sigma_{nn'\gamma}(22.3 - V_c,E_\gamma) \quad (22.3 \text{ Mev} \leq E \leq E_{c_{max}}) , \qquad (1)$$

where V_c is the Coulomb potential barrier, E the incident proton energy, and E_γ the photon energy; $E_{c_{max}}$ is an upper limit on the proton energy, taken variously as 22.3 and 50 Mev.

In Fig. 1 we compare our curve of the gamma dose rate, d_γ, versus spherical shell thickness, with the result of Madey et al. for an isotropically incident differential proton flux,

$$P(E,0) = 3.1 \times 10^9 E^{-4.6} , \qquad (85 \text{ Mev} \leq E \leq 45 \times 10^3 \text{ Mev})$$

$$= 1.0 \times 10^6 E^{-2.8} , \qquad (5 \times 10^{-2} \text{ Mev} \leq E \leq 85 \text{ Mev}) , \qquad (2)$$

where P(E,0) has the units of protons cm^{-2}-sec^{-1}-steradian^{-1}-Mev^{-1}. The primary proton flux is calculated as a function of distance through the shield in the usual manner;[4] the proton stopping power in aluminum was computed from Sternheimer's[5] formula for E > 2 Mev, and from

---

3. E. S. Troubetzkoy, Fast Neutron Cross Sections of Iron, Silicon, Aluminum, and Oxygen, NDA-2111-3, Vol. C, 38,39.

4. R. G. Alsmiller, Jr., F. S. Alsmiller and J. E. Murphy, Nucleon-Meson Cascade Calculations in the Straight-Ahead Approximations, Paper E-3 this symposium.

5. R. M. Sternheimer, Phys. Rev. 115, 137 (1959).

(units are protons cm^{-2}-steradian^{-1}-Mev^{-1}), and are shown in Fig. 2. The curve labeled d_p is a total proton dose, in which not only the ionization losses but also the energy deposition by proton absorption in tissue is roughly accounted for by a method similar to that used by Gibson.[12]

The effect of varying the upper limit, $E_{c_{max}}$, on the energy of protons assumed capable of producing gamma rays, from 22.3 Mev to 50 Mev, is about a factor of two. At 25 g/cm^2 the gamma dose is less than 5% of the proton dose in Fig. 2.

These factors are changed very little in Fig. 3 in which we plot the dose results for the May 10 flare incident isotropically on an infinite slab shield. This is true even though three changes were made in the calculation. First, the photons were more realistically assumed to be emitted isotropically, rather than in the direction of the incident proton. Second, photon transport through the shield was calculated by means of the OGRE-P2 Monte Carlo code[13] which takes build-up of the photon flux into account. A major part of the gamma dose at the larger shielding distances is due to the "collided" photon flux, as opposed to the "uncollided" flux; only the latter was considered in the spherical shell cases.

Third, the primary proton flux is calculated as a function of position by taking into account the variation of path length with angle of incidence, and integrating over all angles; i.e., a Gross transformation is carried out. It is worth noting that the geometry effect is rather important, since the change from a spherical shell to a slab decreases the primary proton dose by almost a factor of 10.

On the basis of so few calculations, only very tentative conclusions can be drawn. In general, we find that with our cross sections the gamma dose is not so important as the calculations of Madey et al. would indicate. By comparing Figs. 1 and 2, it is clear that the ratio of the gamma dose to the primary proton dose at larger shield thicknesses is very dependent on the shape of the incident flare spectrum.

Finally, comparing the results of this paper with calculations of secondary neutron and proton dose,[4] it seems that in general the gamma rays are neither more nor less important than secondary nucleons.

---

12. W. A. Gibson, Energy Removal from Primary Proton and Neutron Beams by Tissue, ORNL-3260 (1962).

13. D. K. Trubey, S. K. Penny, and M. B. Emmett, OGRE-P2 - A Monte Carlo Program for Computing Gamma-Ray Leakage from Laminated Slabs Containing Distributed Sources, Neutron Physics Div. Ann. Progr. Rep. Sept. 1, 1962, ORNL-3360.

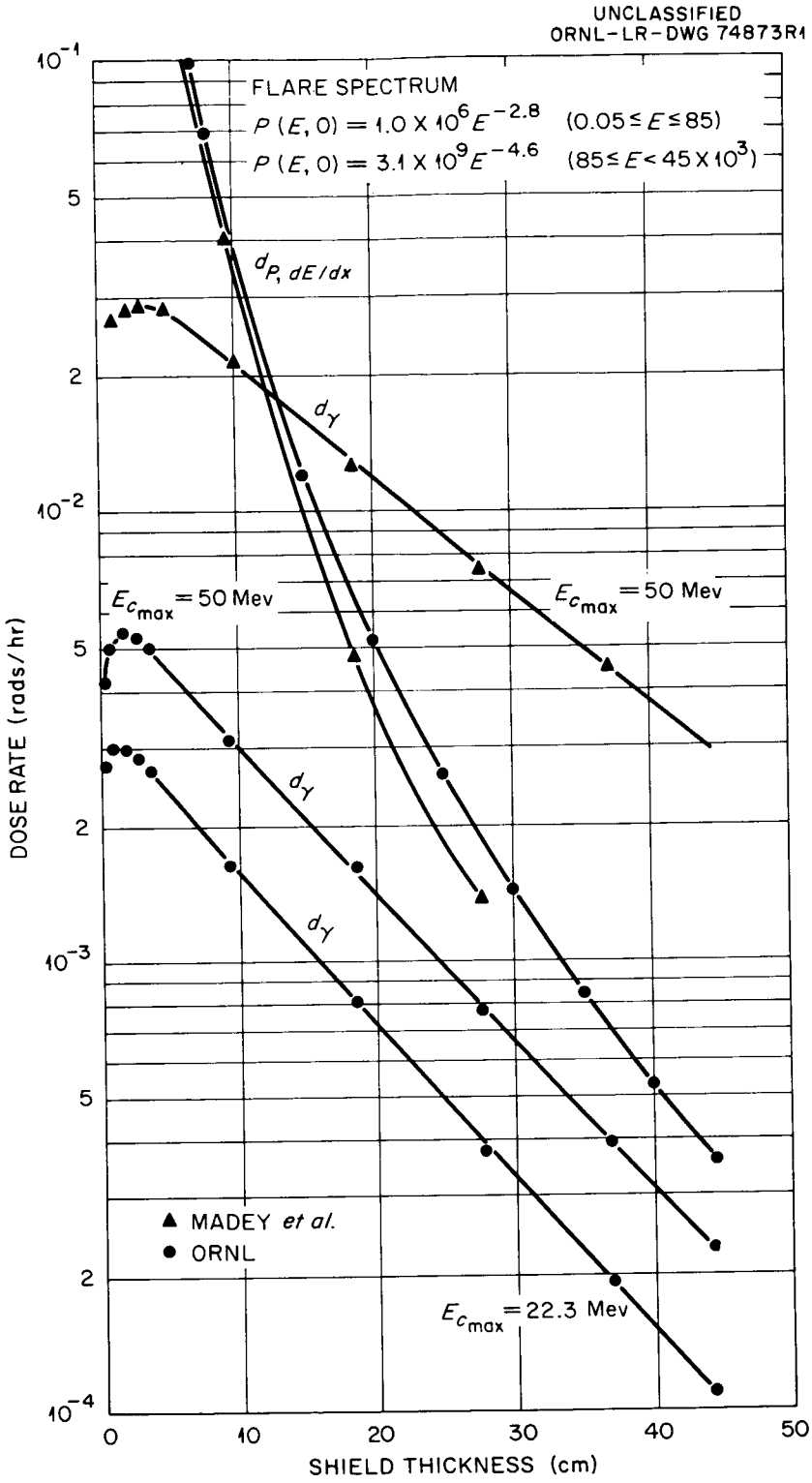

Fig. 1. Gamma and Primary Proton Dose Rates at the Center of a Spherical Aluminum Shell from Solar Flare Protons.

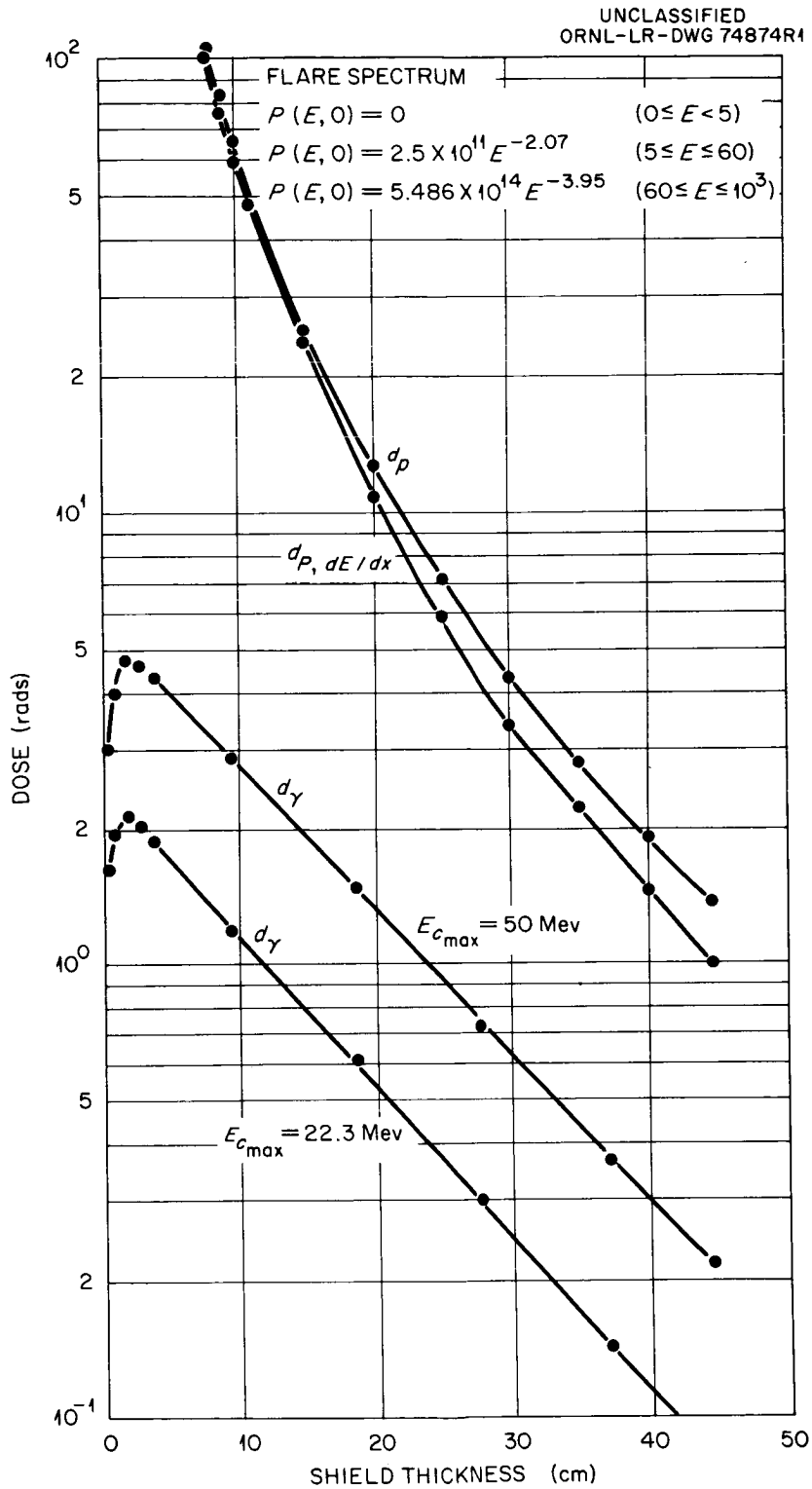

Fig. 2. Gamma and Primary Proton Doses at Center of Spherical Aluminum Shell from Solar Flare (May 10, 1959) Protons.

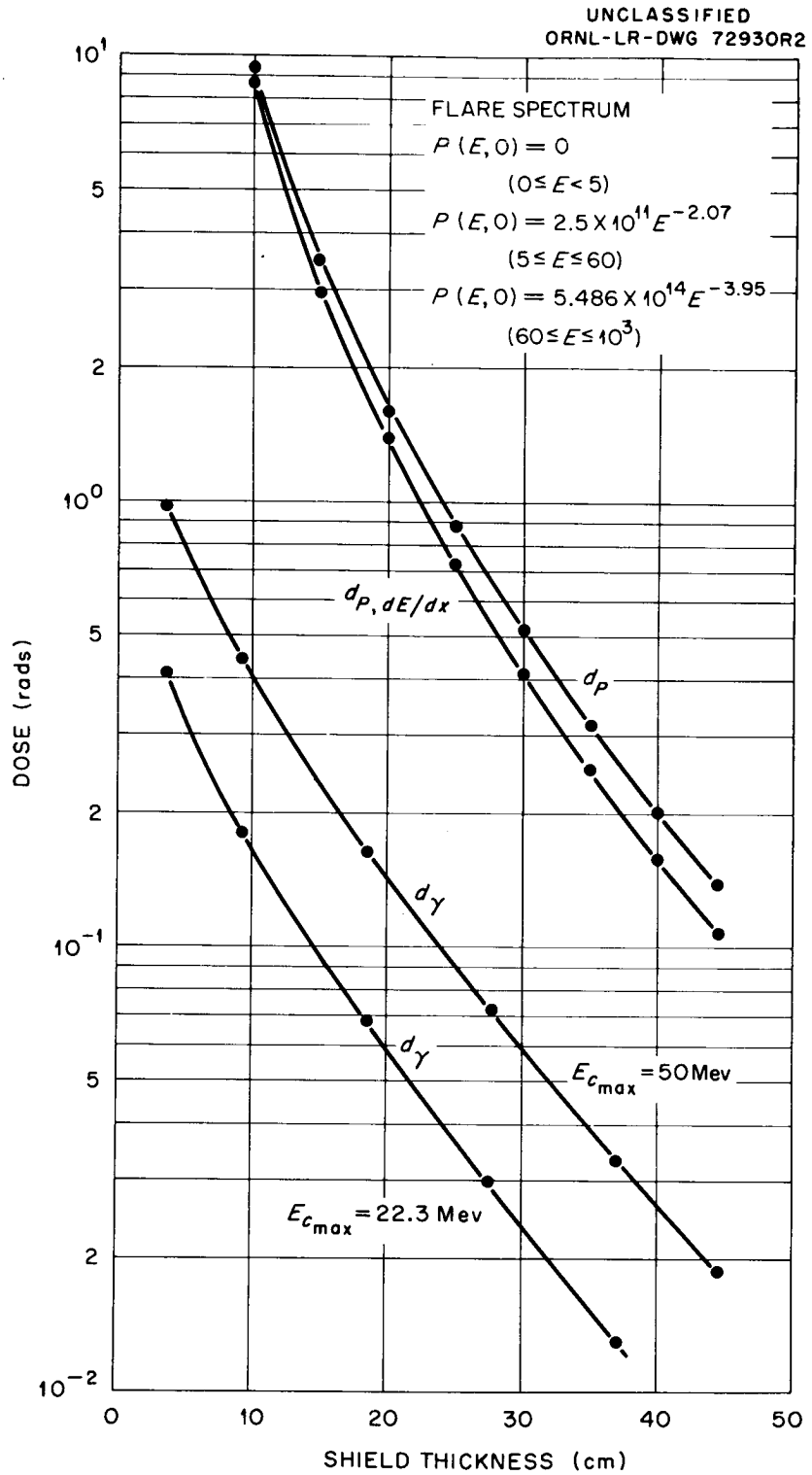

Fig. 3. Gamma and Primary Proton Doses from Solar Flare (May 10, 1959) Protons Incident on Aluminum Slab Shield.

Paper E-6

PROTON FLUXES ALONG TRAJECTORIES THROUGH THE INNER VAN ALLEN BELT

F. C. Perry
Aero-Space Division
The Boeing Company

1515 over

Abstract

A method is formulated to calculate, by means of high-speed digital computing equipment, the total time-integrated proton flux for an arbitrary trajectory through the inner Van Allen belt. To this end, a map of the inner belt proton flux has been prepared in the (B,L) coordinate system, where B is computed from the 48-term spherical harmonic expansion of the earth's magnetic potential due to Finch and Leaton[1] and L is the McIlwain parameter.[2] This map is feasible, since the high-energy trapped proton component is generally quite stable with respect to geomagnetic activity.

The major souces of error inherent to the proton map in the (B,L) coordinate system are not to be found in the mathematical description of the geomagnetic field, but rather are to be found in positional inaccuracies of raw counting rate data, ambiguities connected with discrimination between protons and electrons, and time variations in the low energy proton component. This is especially true for large values of L ($L > 1.6$). Of interest are the marked differences between these proton flux contours and the proton flux contours calculated from the neutron albedo hypothesis.[3] Such differences indicate that other source mechanisms may well be important for populating the inner belt.

---

1. H. F. Finch and B. R. Leaton, The Earth's Main Magnetic Field - Epoch 1955.0, Monthly Notices R. Astron. Soc., Geophysical supplement, Vol. 7, 1957, pp 314-17.

2. C. E. McIlwain, J. Geophys. Res. 66, 3681-91 (1961).

3. A. M. Lenchek and S. F. Singer, J. Geophys. Res. 67, 1263 (1962).

15151

Values of the flux as a function of B and L are stored in a computer. Utilizing these values and given r, θ, and φ as a function of time for a trajectory of specified mission, the computer is programmed to (1) calculate B and L, (2) interpolate to obtain integral proton flux, and (3) integrate with respect to time along the trajectory to get the total integrated proton flux. The integrated proton flux can then be inserted, along with an appropriate differential spectrum, into a program[4] to calculate the total radiation dose received by the vehicle, components, and personnel (as modified by shielding). This is one of several computer programs which have been developed to assess the problem of radiation in space environment.

Introduction

In this paper the analysis leading to a calculational procedure to get integrated proton fluxes along trajectories is described in four sections. First, the general approach to the problem and its rationale are pointed out. Second, something is said about the coordinate system employed in developing a map of the inner belt protons. Third, a description is given of how the map was put together, the data utilized, and sources and magnitudes of possible errors; also, a comparison is made with a theoretical result based upon the cosmic-ray neutron albedo source mechanism. Fourth, the actual steps of programmed computation are delineated and examples are given of proton fluxes calculated along a few trajectories through the Inner Van Allen Belt.

General Approach to the Problem

As is well-known, the region of the inner belt is comprised of highly energetic protons of several million electron volts and thereby constitutes a possible radiation hazard to many space missions. The basic motivation in going to the trouble of developing a computer code to assess this radiation hazard is the feeling that the variety and complexity of space systems and subsystems warrant such an approach. For example, a question that may be asked by persons connected with space system hardware is "How long can transistor X be expected to

---

4. See paper by D. L. Dye in Session D.

function properly in space mission Y where the space mission is, say, characterized by a vehicle orbiting for 30 days at a certain inclination, etc.?" Due to the asymmetries inherent to the natural radiation belts, such a question (without the aid of automation) would entail a very laborious calculation to come up with even an order of magnitude estimate of the radiation. However, with a computer code the answer in terms of the total number of energetic protons per square centimeter can be estimated (in most cases to within much better than an order of magnitude) in a few minutes.

For the purpose of evaluating the radiation hazard to components and personnel, it would be desirable to know the differential energy spectrum of penetrating protons at every point of the inner belt (also, of course, as a function of time). Unfortunately, the spectrum itself has been measured at only a few positions in the region generally thought to be occupied by high energy protons. On the other hand, there has been a fair accumulation of counting rate data from satellites employing Geiger tubes. These detectors were sensitive to protons with energies above a specific threshold, and they detected radiation over a substantial volume of space. Therefore, our approach to the problem was to develop a spatial distribution of radiation based upon counting rate information (accounting separately for time variations), and then to make certain assumptions about the shape of the spectrum to be used in dose calculations.

The Coordinate System

To accomplish this task, a map of the inner belt proton flux has been prepared in the (B,L) coordinate system, where B is a representation of the earth's magnetic field[1] and L is the McIlwain parameter[2]. Several years ago it was realized that a dipole representation of the geomagnetic field was not adequate to systematize flux data[5]. As a result of this fact and attempts with other systems, the (B,L) coordinate system has been adopted as a standard in the systematization of measurements of the trapped corpuscular radiation.

The L parameter was invented by C. E. McIlwain and is the physical analog of the geomagnetic equatorial distance to a field line in the case of a dipole field. Figure 1 shows a typical example of surfaces of constant L and B. From the theory of adiabatic invariants as

---

5. S. Yoshida , G. H. Ludwig, and J. A. Van Allen, Distribution of Trapped Radiation in the Geomagnetic Field, J. Geophysical Research, 65, 807-813, 1960.

B.L. COORDINATE SYSTEM

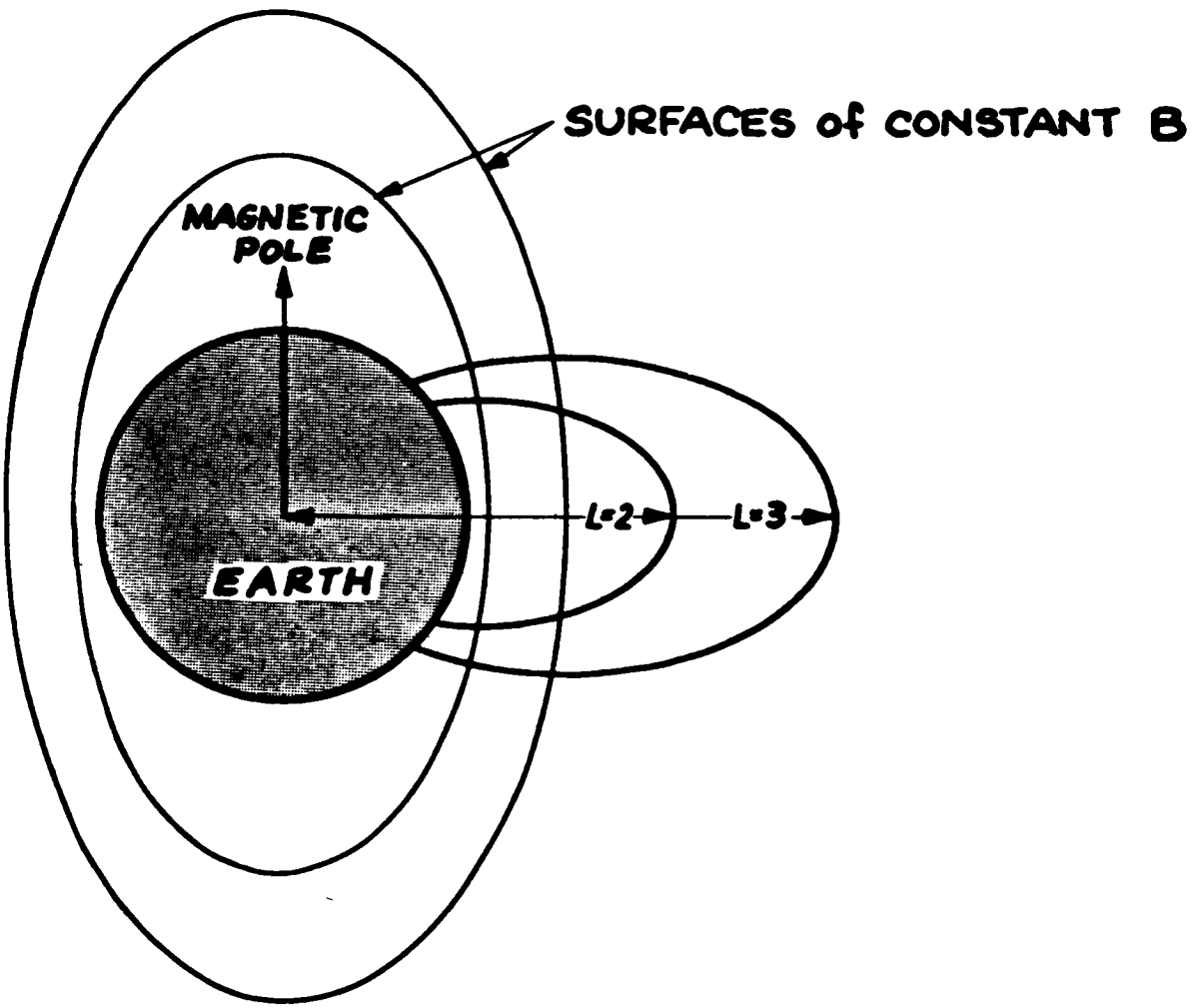

Figure 1

applied to particles trapped in the earth's magnetic field[6], we know, when the invariants are preserved, that the particle omnidirectional intensity is constant (to a good approximation) along loci of constant magnetic field and the longitudinal invariant. Since L is defined as a function only of B and I (longitudinal invariant), the same condition holds for particle intensity along loci of constant B and L. It also turns out, as one would expect from the definition of L, that the L parameter is approximately constant along magnetic field lines[2]. These facts imply, for our purposes, that geographic asymmetries will be smoothed out in a transformation from spherical spatial coordinates to the (B,L) coordinates, and our problem has been reduced from three to two dimensions (where computer interpolation is feasible).

Our procedure to compute B and L is as follows. The magnetic field is calculated from the 48-term spherical harmonic potential whose gaussian coefficients were computed by Finch and Leaton for epoch 1955.0 data[1]. The L parameter is calculated via the method of McIlwain from this magnetic field and the longitudinal invariant (also based upon the Finch and Leaton field). The longitudinal invariant itself is computed from a spherical harmonic expansion on shells of constant magnetic field. This expansion was devised by E. C. Ray and the coefficients were determined by fitting the series to values of I previously computed by Vestine.[7]

The method of computing B and L was not a critical factor in our analysis. The reasons for this are twofold: First, in the region where adequate flux data was available, comparisons were made between the values of B and L computed from a 512-term expansion kindly supplied by AFSWC[8] and the 48-term expansion[1]. The computed values always lay within the scatter deviation of points constituting isoflux contours. Second, in the region of scarce data, other errors by far exceeded those attributable to the (B,L) computational procedure (this will be explained in the next section).

In order to obtain the fullest advantage from a magnetic field representation, the coefficients should be updated every 10 years or

---

6. J. G. Northrup and E. Teller, Stability of the Adiabatic Motion of Charged Particles in the Earth's Magnetic Field, Phys. Rev. 117, 215-225, 1960.

7. E. C. Ray, NASA Goddard Space Flight Center, private communication, 1962.

8. D. C. Jensen and W. A. Whitaker, Spherical Harmonic Analysis of the Geomagnetic Field (abstract), J. Geophys. Research, 65, 2500, 1960.

less. A more recent magnetic field[9] should be used in an analysis such as the one presented here whenever better and more up-to-date flux data are available.

Data, Map, Errors, and Comparison with Theory

We discuss now the data that were used in the preparation of the inner belt proton map. Data in the form of true counting rates and spatial positions were taken from the satellites and space probes whose trajectories passed through the inner belt. The available information included the true counting rates of the unshielded 302 Geiger tube of Explorer IV already plotted in (B,L) coordinates by McIlwain,[2] and the Pioneer III[10] and IV[11] true counting rates. In all these vehicles the Anton 302 Geiger counter was the major information source, and the shielding was such as to make detection possible for directly penetrating protons with energies exceeding 30 Mev and directly penetrating electrons with energies exceeding about 2 Mev.

Counting rate data were also available from the detectors flown in the Explorer I[12] and Explorer VII[13] satellites. Both of these information sources were discarded for preparation of the present map for the reasons that: (1) the Explorer I counters saturated at the high counting rates and (2) the Geiger tube used on Explorer VII had an 18 Mev threshold for penetrating protons so that too many assumptions would have to be made in connection with the proton spectrum at low energies.

---

9. D. C. Jensen and J. C. Cain, An Interim Geomagnetic Field (abstract), J. Geophys. Research, 67, 3568-3569, 1962.

10. J. A. Van Allen and L. A. Frank, Radiation around the Earth to a Radial Distance of 107,400 km, Nature, Vol. 183, pp 430-434, February 14, 1959; IGY Satellite Report, Number 11, June 1960.

11. J. A. Van Allen and L. A. Frank, Radiation Measurements to 658,300 km with Pioneer IV, Nature, Vol. 184, pp 219-224, July 25, 1959; IGY Satellite Report, Number 11, June 1960.

12. SUI 61-3, Volumes I-V, Radiation Observations with Satellite 1958 Alpha (Explorer I).

13. G. Pizzella, C. E. McIlwain, and J. A. Van Allen, Time Variations of Intensity in the Earth's Inner Radiation Zone, October 1959 through December 1960, J. Geophys. Research, 67, 1235-1253, 1962.

The lower fringe of the inner belt was taken to be the McIlwain plot of Explorer IV true counting rates.[2] These counting rates were converted to omnidirectional proton flux ($E > 30$ Mev) by using the omnidirectional factor supplied by the Iowa group. Other experimental evidence which corroborates the Explorer IV fluxes derived in this manner are the Freden and White spectrum measurements[14], the Armstrong and Heckman spectrum measurements[15], and the Naugle and Kniffen experiment[16] (all of these utilizing emulsions and all measurements taken in the lower fringe of the inner belt).

In order to specify the peak and outer fringe of the high energy proton belt it was necessary to use the results of the space probes Pioneer III and IV. Both the trajectory of Pioneer IV and the outbound leg of the Pioneer III trajectory passed through a high latitude section of the inner belt, while the inbound leg of Pioneer III passed through the outer fringe of the inner belt very close to the geomagnetic equator. Counting rate data terminated at about 10,000 km geocentric distance on the inbound leg of Pioneer III; this point is believed to be close to the peak flux values in the inner belt. Omnidirectional fluxes were obtained from the equation given by Van Allen, namely $J = 1.6\,R$, where R is the true rate.

When flux positions for the outbound Pioneer III and IV trajectories were transformed to the (B,L) coordinates, marked inconsistencies were noted. The flux positions in (B,L) space for the inbound leg of Pioneer III were used to extrapolate the Explorer IV contours to the geomagnetic equator. The resulting contours seemed to average out the apparent inconsistencies between the Pioneer III and IV outbound legs in the outer fringe of the belt. The contour of maximum flux was taken to be 30,000 protons per square centimeter per second, based upon the work of Lenchek and Singer[3]. The result of these machinations is the plot of iso-proton flux contours shown in Fig. 2.

---

14. S. C. Freden and R. S. White, Trapped Proton and Cosmic-Ray Albedo Neutron Fluxes, J. Geophys. Research, 67, 25-29, 1962.

15. H. H. Heckman and A. H. Armstrong, Energy Spectrum of Geomagnetically Trapped Protons, J. Geophys. Research, 1255-1262, 1962.

16. J. E. Naugle and D. A. Kniffen, The Flux and Energy Spectra of the Protons in the Inner Van Allen Belt, J. Physical Society of Japan, Vol. 17, Supplement A-II, 118-122, 1962.

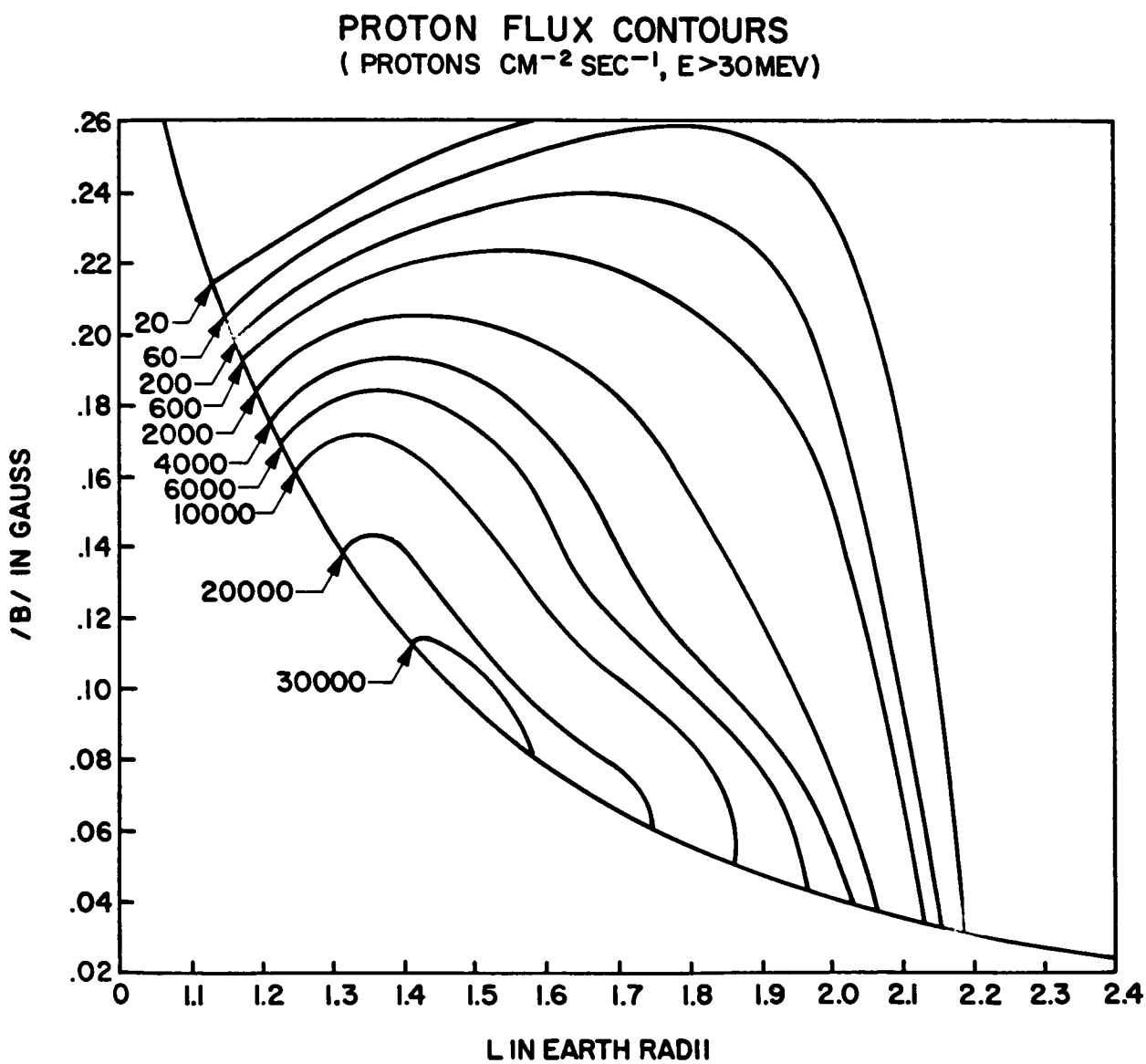
PROTON FLUX CONTOURS
(PROTONS CM⁻² SEC⁻¹, E>30MEV)
/B/ IN GAUSS
.26
.24
.22
.20
.18
.16
.14
.12
.10
.08
.06
.04
.02
20
60
200
600
2000
4000
6000
10000
20000
30000
0
1.1
1.2
1.3
1.4
1.5
1.6
1.7
1.8
1.9
2.0
2.1
2.2
2.3
2.4
L IN EARTH RADII

Figure 2

Now we discuss briefly the sources and magnitudes of possible errors inherent to this plot. There are several.

1. A major source of error is in the trajectory of Pioneer III (inbound leg). Van Allen estimates[10] the accuracy during the re-entry phase to be of the order of 1000 km. This amounts to a 10 percent error at the maximum of the belt. If all this error were to be found in the radial direction, it would amount to 1500 gamma in the magnetic field and .16 in the L parameter at the center of the belt. These, of course, are maximum errors. At the center of the belt this corresponds to believing the flux within about a factor of two. At larger values of L, i.e., toward the outer fringe of the belt, a 10 percent error in L may amount to flux errors of greater than an order of magnitude. Again this is undoubtedly a maximum estimate. More detailed knowledge is required to definitely establish the nature of the contours in the outer fringe region.

2. Errors in converting counting rates to omnidirectional flux. Van Allen estimates an uncertainty of ± 20 percent[10] in the omnidirectional factor of the 302 Geiger tube in Pioneer III; the Pioneer IV counter is supposed to be the same ± 10 percent[11]. For Explorer IV the error in conversion is not known but is presumed to be smaller.

3. Errors in determination of the nature of the radiation - discrimination between protons and electrons. The Iowa group estimates[13] tentatively on the basis of Explorer XII and other satellite information that the 302 Geiger tube aboard Explorer VII was counting the following particles:

   a. For $L < 1.8$, penetrating protons, $E > 18$ Mev.

   b. For $1.8 < L < 2.2$, comparable contributions of electrons and protons.

   c. For $L > 2.2$, penetrating electrons.

   Due to the somewhat different characteristics between the Geiger tubes aboard Explorer VII and the Pioneer probes, a pure proton contribution was ascribed to the Pioneer counting rates up to about $L = 2.0$. Above $L = 2.0$ the contours were arbitrarily joined to the equator in a manner symmetric to the lower fringe. Errors in the flux amounting to factors of two or three are possible here.

4. Errors from using the assumption of isotropic flux. There is practically no experimental information concerning the angular

distribution of inner belt protons, but certainly anisotropies exist.

5. Errors due to time variations in the belt. Investigations in this area using the Explorer VII data (Pizzella, et al.)[13] have indicated that there are time variations amounting to factors of two or three over a period of slightly more than a year when the data is averaged in a particular way. They found that some correlation may exist between magnetic storms (and accompanying solar proton events) and an enhancement of the inner belt protons. The picture is not clear to us yet, since the 302 Geiger tube in Explorer IV had a higher detection threshold than the tube in Explorer VII. This means that differences in counting rates may be due to either time variations or the different detection characteristics or a combination of both. If the changes are mainly attributable to low energy ($E < 40$ Mev) protons, perhaps from neutron albedo of solar protons arriving at the polar caps, then we are not in such bad shape (insofar as the radiation hazard is concerned). Such protons could be accounted for in the spectrum by looking at the 40 Mev threshold Geiger tube in Explorer IV.

A factor that should be remembered is that we are using 1958-59 data systematized by a magnetic field valid for 1955. It is felt that secular changes in the field up to the present time are of less importance than errors attributable to the data itself. A general conclusion regarding the errors in the proton map is that if in the heart of the belt the spectrum does not change radically from the one measured by Freden and White and others in the lower fringe (and this presumes that the cosmic-ray neutron albedo source mechanism is a likely source for the higher energy protons), then in this region the flux may be off by a factor of two or three. At larger values of L and at lower flux values (toward the slot), we may be off by an order of magnitude.

Of interest is a comparison between the proton map and a spatial distribution of inner belt protons calculated from the cosmic-ray neutron albedo source mechanism. Such a comparison is indicated in Fig. 3. The dashed distribution was originally computed by Lenchek and Singer[3] in spatial dipole coordinates, and it was then transformed to (B,L) coordinates. The neutron albedo-proton contours were computed for a 75 Mev threshold, so there should be some differences. In the regions near the geomagnetic equator the number of $E > 75$ Mev protons is less than the number of $E > 30$ Mev protons, as one might predict. At higher latitudes the number of $E > 75$ Mev protons exceeds that of the $E > 30$ Mev protons, which is contrary to expectation. If some low energy particles are due to the solar proton-neutron albedo mechanism, then one would expect that such a population would be most evident in the higher latitude regions of the inner belt. At any rate one can see that mechanisms other than the cosmic-ray neutron albedo may well be operative in the inner belt.

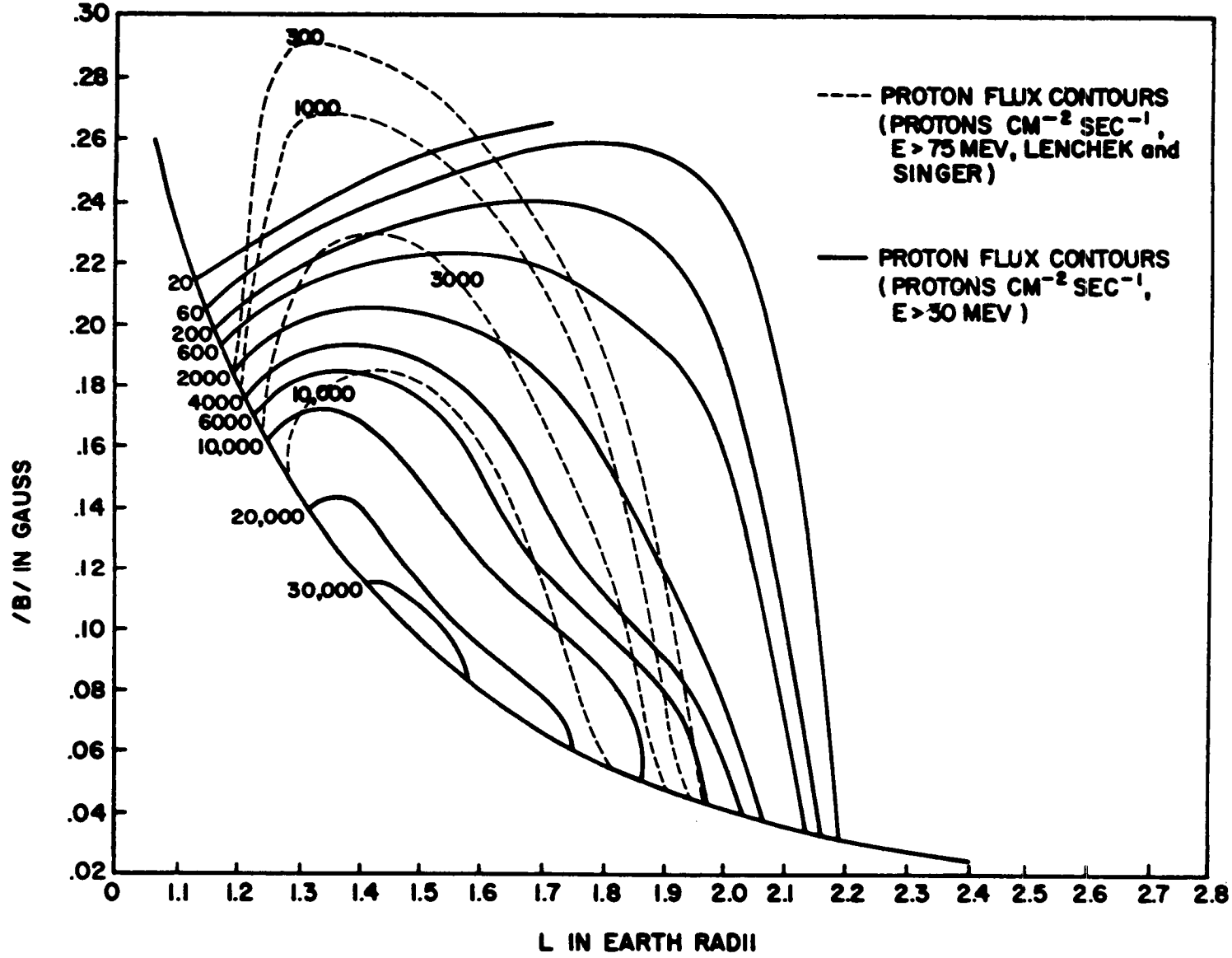
PROTON FLUX CONTOURS
(PROTONS CM⁻² SEC⁻¹,
E > 75 MEV, LENCHEK and
SINGER)
PROTON FLUX CONTOURS
(PROTONS CM⁻² SEC⁻¹,
E > 30 MEV)
300
1000
3000
10,000
20,000
30,000
20
60
200
600
2000
4000
6000
10,000
/B/ IN GAUSS
L IN EARTH RADII
.30
.28
.26
.24
.22
.20
.18
.16
.14
.12
.10
.08
.06
.04
.02
0
1.1
1.2
1.3
1.4
1.5
1.6
1.7
1.8
1.9
2.0
2.1
2.2
2.3
2.4
2.5
2.6
2.7
2.8

Figure 3

Calculation of Integrated Proton Flux and Examples

Utilizing the previously described map of the inner belt, a method has been developed to calculate the integrated proton flux for an arbitrary trajectory. Values of the flux at magnetic field increments of 400 gamma and L parameter increments of .02 earth radii have been stored in a computer. These values (of flux) were obtained by logarithmic interpolation between the contours specified on the map. The computer program is designed to perform the following steps: (1) given a trajectory specified by the coordinates r, θ , φ , t (altitude, latitude, longitude, time), compute B and L at each point, (2) interpolate (linearly) in the stored flux values to get a flux at each point, and (3) integrate with respect to time along the trajectory to get the total proton flux for the duration of the mission.

The spectrum shape to be used along with the integrated flux in dose calculations is the latest one measured by Freden and White[14]. This spectrum is considered valid down to about 40 Mev. At lower energies and at higher latitudes there is some evidence for a steepening in the spectrum[16], possibly the result of protons from the solar proton-neutron albedo. The gammas as a function of B and L (assuming a power-law spectrum) have been computed[17] for energies between 30 and 40 Mev from counting rate data taken from the Explorer IV shielded Geiger tube, and these can be used in dose calculations if desired. However, it should be borne in mind that the lower energy component may well be subject to strong time variations.

In Fig. 4 are shown two examples of vehicle trajectories through the inner belt. The dashed curves represent a single polar circular orbit at an altitude of 1000 nautical miles; the total integrated flux per orbit was computed to be 2.5×10^7 protons per square centimeter. The dotted curves represent firstly the trajectory en route to an equatorial circular orbit, and secondly (the lopsided figure eight) a single equatorial circular orbit at an altitude of 2000 nautical miles; total integrated flux en route to orbit and per orbit are 5×10^7 and 2.7×10^8 protons per square centimeter, respectively.

Conclusions

1. Within the limits of available information a map of the high energy ($E > 30$ Mev) trapped protons has been prepared in the (B,L) coordinate system.

2. Errors in the proton map have been discussed. It is concluded that in the heart of the belt the flux is known to a factor of two

---

17. F. C. Perry and L. A. Oncley, to be published.

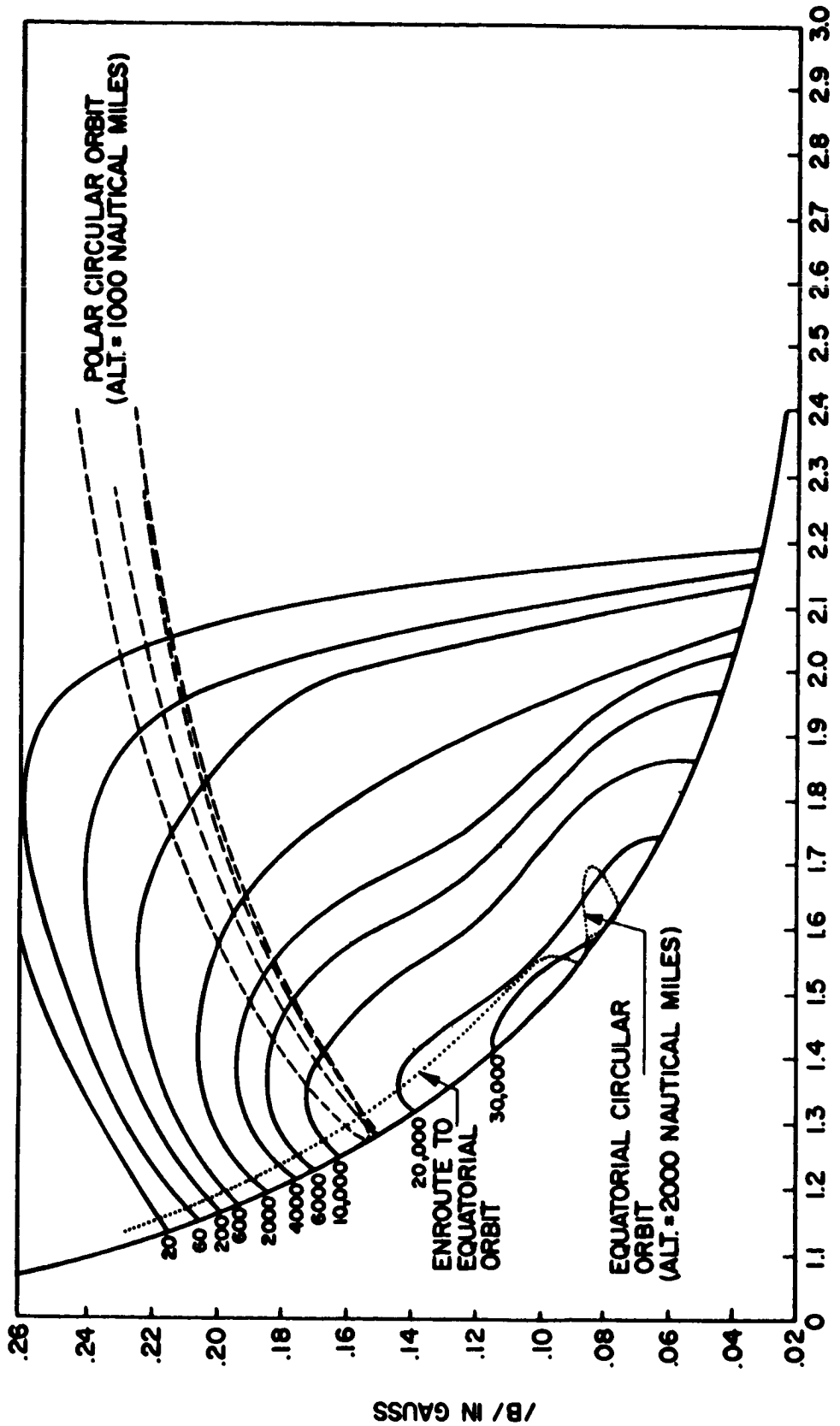
POLAR CIRCULAR ORBIT
(ALT.= 1000 NAUTICAL MILES)
20
60
200
600
2000
4000
6000
10,000
20,000
30,000
ENROUTE TO
EQUATORIAL
ORBIT
EQUATORIAL CIRCULAR
ORBIT
(ALT.=2000 NAUTICAL MILES)
L IN EARTH RADII
/B/ IN GAUSS
.26
.24
.22
.20
.18
.16
.14
.12
.10
.08
.06
.04
.02
0
1.1
1.2
1.3
1.4
1.5
1.6
1.7
1.8
1.9
2.0
2.1
2.2
2.3
2.4
2.5
2.6
2.7
2.8
2.9
3.0

Figure 4

or three; at larger L values we may be off by an order of magnitude.

3. Comparison of the proton map with a distribution based upon the cosmic-ray neutron albedo source mechanism, indicated that other sources may contribute to the trapped proton population.

4. The procedure to calculate the integrated proton flux along an arbitrary trajectory was outlined and a few examples given.

Paper E-7

A CALCULATIONAL PROCEDURE FOR ESTIMATING SPACE RADIATION EXPOSURE DURING LUNAR MISSIONS

R. A. Miller and W. Cranford
General Dynamics/Fort Worth

15152

Abstract

One problem concerned with manned space missions is the determination of shielding requirements for the protection of man from the hazards of space radiation. A space trajectory radiation exposure procedure (STREP) has been developed to estimate the magnitude of this radiation hazard by calculating the time-integrated spectra incident on a vehicle on a simulated trajectory during missions in cislunar space. STREP will calculate the dose received from radiation penetrating a thin shield. A brief description is given for the trajectory and radiation computational techniques. Some results are given for calculations of the integrated spectra and dose incident on a vehicle subjected to trapped radiation, cosmic radiation, and solar flare radiation during a lunar mission of about seven days.

Introduction

The problem described in this paper is concerned with one phase in determining the requirements for the protection of man from the hazards of space radiation. A computer program[1], STREP, has been developed at General Dynamics/Fort Worth under Air Force sponsorship to determine the magnitude of the radiation hazard to which manned space vehicles are exposed while on missions in cislunar or lunar space. The results of calculations of the time-integrated spectra incident on the vehicle from the various radiation components can be used as input for another procedure to compute the dose inside a shielded crew compartment. The computations made with STREP

1. W. Cranford, R. F. Falkenbury, and R. A. Miller, A Space Trajectory Radiation Exposure Procedure for Cislunar Missions. General Dynamics/Fort Worth Report FZK-9-178 (31 July 1962).

for two lunar missions - one in which the vehicle is beyond the earth's magnetic field during a solar flare, the other in which the vehicle is in a 24-hour orbit during the solar activity period - are described. Some results from calculations of the secondary components of the dose within a shielded crew compartment are shown as a function of polyethylene thickness.

Hazards to Space Missions

The discovery of ionizing radiations surrounding the earth has emphasized the existence of a hazard which must be assessed before manned space flight is feasible. From balloon observations, satellite measurements and earth-based monitoring systems, it is evident that the intensities of charged particles, both protons and electrons, are sufficiently great to create a radiation hazard.

The penetrating radiations to which a manned space vehicle will be exposed may be divided into four broad classifications: primary galactic cosmic radiation, trapped radiation, solar-flare radiation, and miscellaneous extraterrestrial radiation (Fig. 1). Of these categories, the greatest hazards to crews on lunar missions will be due to the solar-flare protons. The effects of solar flares within the vicinity of the earth are illustrated in Fig. 2.

Solar flares have an extreme time variability, which may depend to some extent on sunspot activity, since the flare frequency apparently varies roughly as the sunspot number with a period of approximately 11 years. During the peak sunspot cycle, Class 3+ flares may average one or more per month; however, during July 1959, three Class 3+ flares were observed within six days. The energy spectrum, measured 32 hours after onset, and other data for the 14 July 1959 flare are listed in Table 1. These data were used in the example described later in the paper.

Table 1. Solar Flare Data

Event	Spectrum (protons/cm^2-sec)	Energy Range (Mev)	Decay (hr)	Flare Duration (hr)
7-14-59	$1.5 \times 10^7 E^{-3.9}$	$30 < E < 1000$	t^{-2}	55.5

PRIMARY COSMIC RADIATION
- PROTONS
- HEAVY PARTICLES

TRAPPED RADIATION
- PROTONS
- ELECTRONS

SOLAR FLARE RADIATION
- PROTONS
- HEAVY PARTICLES
- GAMMAS
- ELECTRONS

MISCELLANEOUS RADIATION
- ALBEDO NEUTRONS
- AURORA BOREALIS GAMMAS

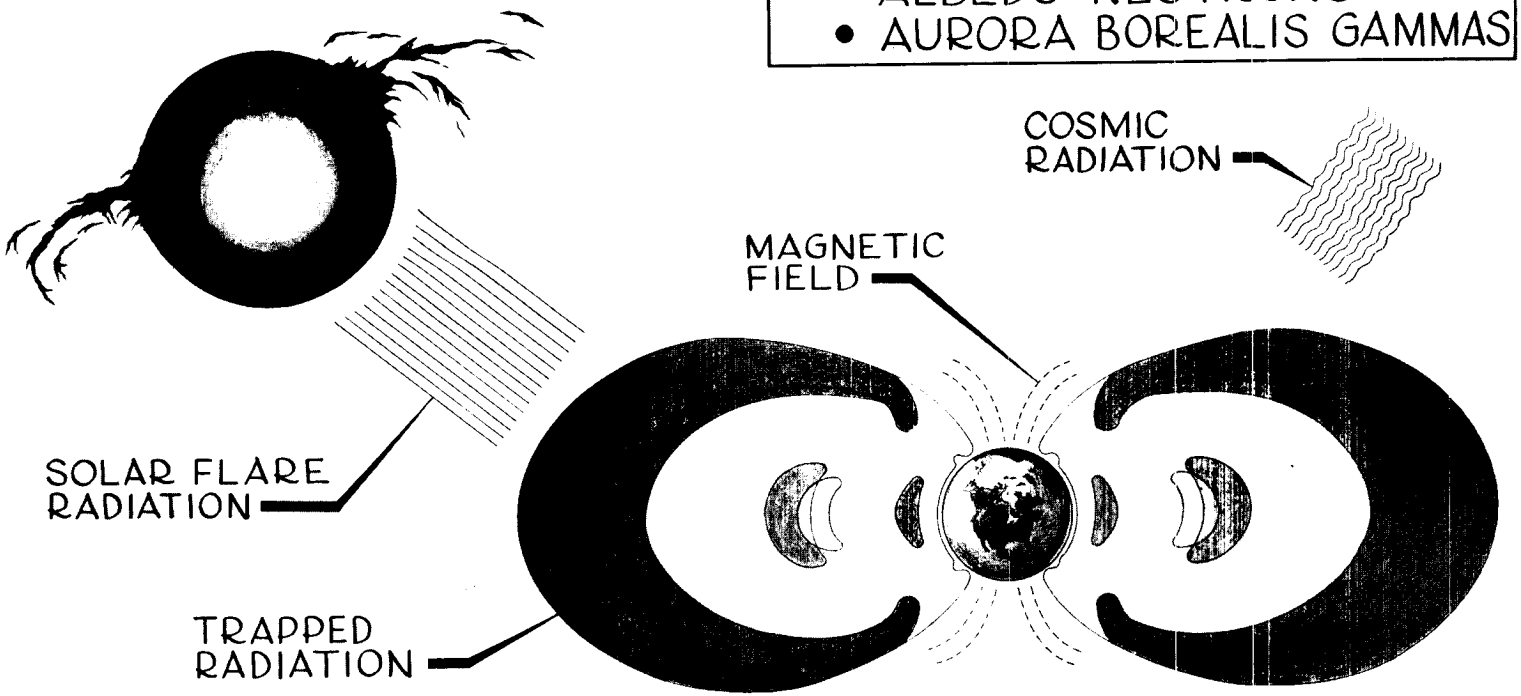

FIGURE 1. RADIATION HAZARDS TO SPACE MISSIONS

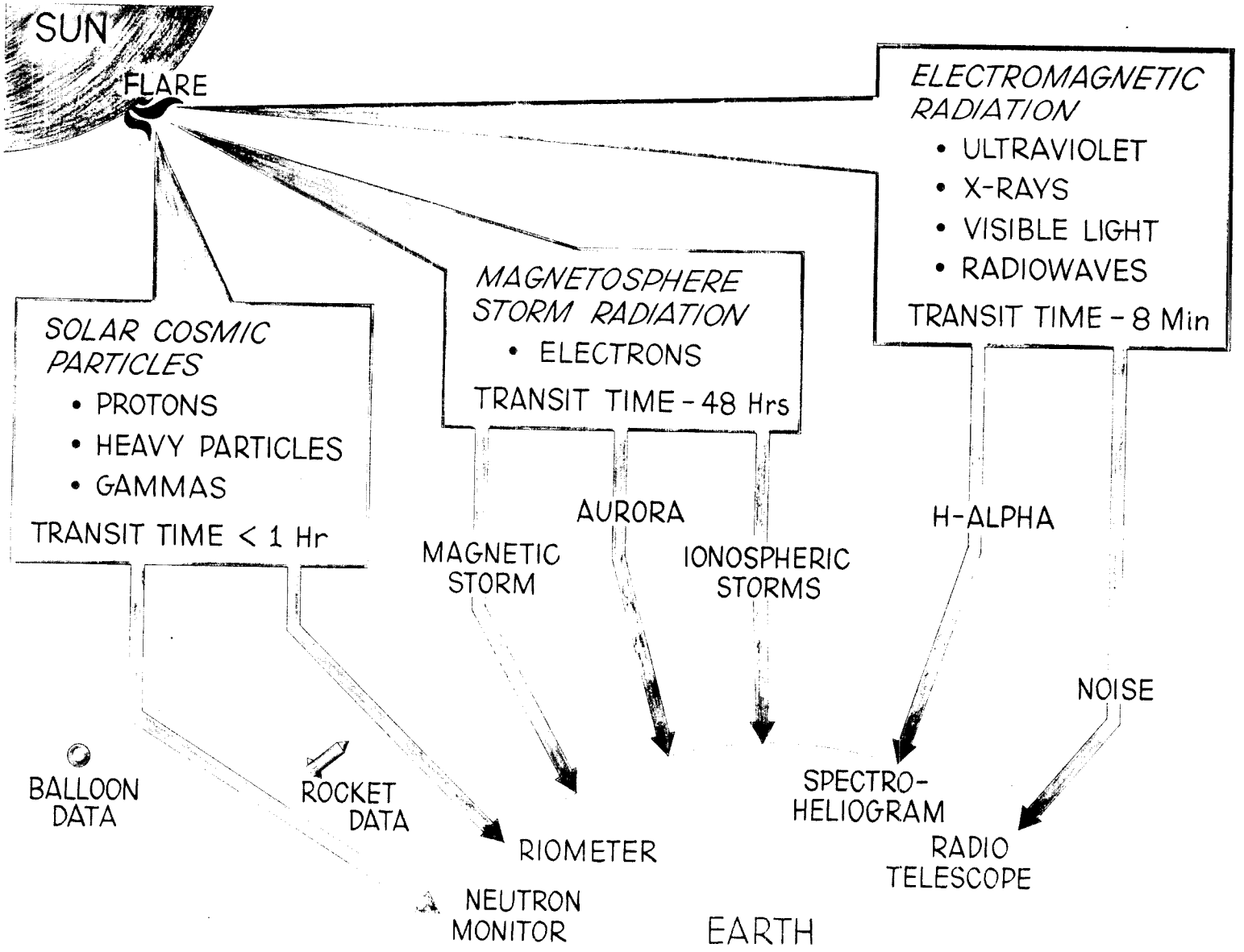

FIGURE 2. SOLAR FLARE EFFECTS

Calculation of Radiation Exposure

A procedure (STREP) which calculates the time-integrated spectra for mission trajectories will be described in the following sections. These spectra can be used in a second computer program (PAP) to calculate the primary and secondary proton and secondary neutron dose components within a shielded vehicle. STREP was designed to compute the time-integrated spectra for any combination of the several components of space radiations in lunar space. These components include the following: trapped protons and electrons; solar-flare protons, gammas, electrons, and heavy particles; cosmic-radiation protons and heavy particles; albedo neutrons; and aurora-borealis gamma radiation. The program will calculate the dose behind a thin shield at any time after the start of the mission.

Trajectory Calculations

General Considerations

The integration of the space-radiation spectra over a vehicle mission with experimental data for the radiation fields requires numerical integration with respect to time. Thus, this requirement infers the knowledge of the vehicle position as a function of time. The number and spacing in the set of positions in space, as well as the time required to obtain the desired accuracy under the assumption of accurate knowledge of the radiation field, influence the general approach to the trajectory computation problem. The spatial separation of the required points along the trajectory is governed by the gradients of the radiation field.

Since the problem has been confined to cislunar space and since no spatial dependence of the radiation components is known to exist in the vicinity of the moon, consideration is given only to the gradients induced by the earth. Such gradients are known to exist out to approximately ten earth radii, thereby defining a sphere of influence corresponding to the earth's magnetosphere. Outside this sphere of influence in cislunar space all types of radiation are assumed to be independent of position; however, time variation of the components, such as solar flares, will influence the integration. The greatest gradients are those associated with the trapped radiation regions. In practice, short time steps in integration are required inside the sphere of influence, whereas longer steps may be used for positions outside this region.

Trajectory Constraints

Since most of the space missions of immediate interest involve either close approach to an astronomical body other than the earth or several earth orbits, more than two points on the trajectory are necessary as input information for two-body calculations. The present version of STREP requires a number of positions, with associated times, determined by an external source which may include perturbation results. In order to reduce the number of positions required for input, the procedure solves the two-body problem by using an initial-position vector, estimated initial-velocity vector, and elapsed time to reach a second position. It computes the parameters of the free-fall orbit necessary to reach the second position at the proper time. The initial input velocity is used only to resolve the ambiguity of the direction of traversing the orbit. Once these parameters are established, STREP can compute any position along this trajectory leg which may be required by the radiation integration procedure. In this manner, a fast and efficient method for interpolation between known points on an accurately determined trajectory is provided, subject only to the restriction that the elapsed time is less than one orbital period in duration.

For free-fall trajectories inside the earth's magnetosphere, positions can be given at time intervals of less than one period. However, for thrust positions of the trajectory inside the sphere of influence, positions must be given every thirty seconds to maintain accurate integration. Outside the sphere of influence, for either thrust or free-fall legs, the positions must be given only when a change from thrust to free-fall, or vice versa, is evident. At each initial position of a free-fall orbit leg, an estimate of the velocity at this position must be given unless the previous leg was free-fall. The time from midnight of the day before the start of the mission must be specified with each position. Any number of thrust and free-fall legs may be used to describe the trajectory, with the required positional data given in any one of several different coordinate systems.

Time-Step Selections

For a trajectory in which burnout occurs below the inner radiation belt, calculations are begun from burnout as the first point. The first two points (P_1,P_2), shown in Fig. 3, and the elapsed time are used to compute orbit parameters for the first orbit leg of the trajectory. The radiation intensities are evaluated at the first point, P_1. A time step is calculated from the initial point by the equation

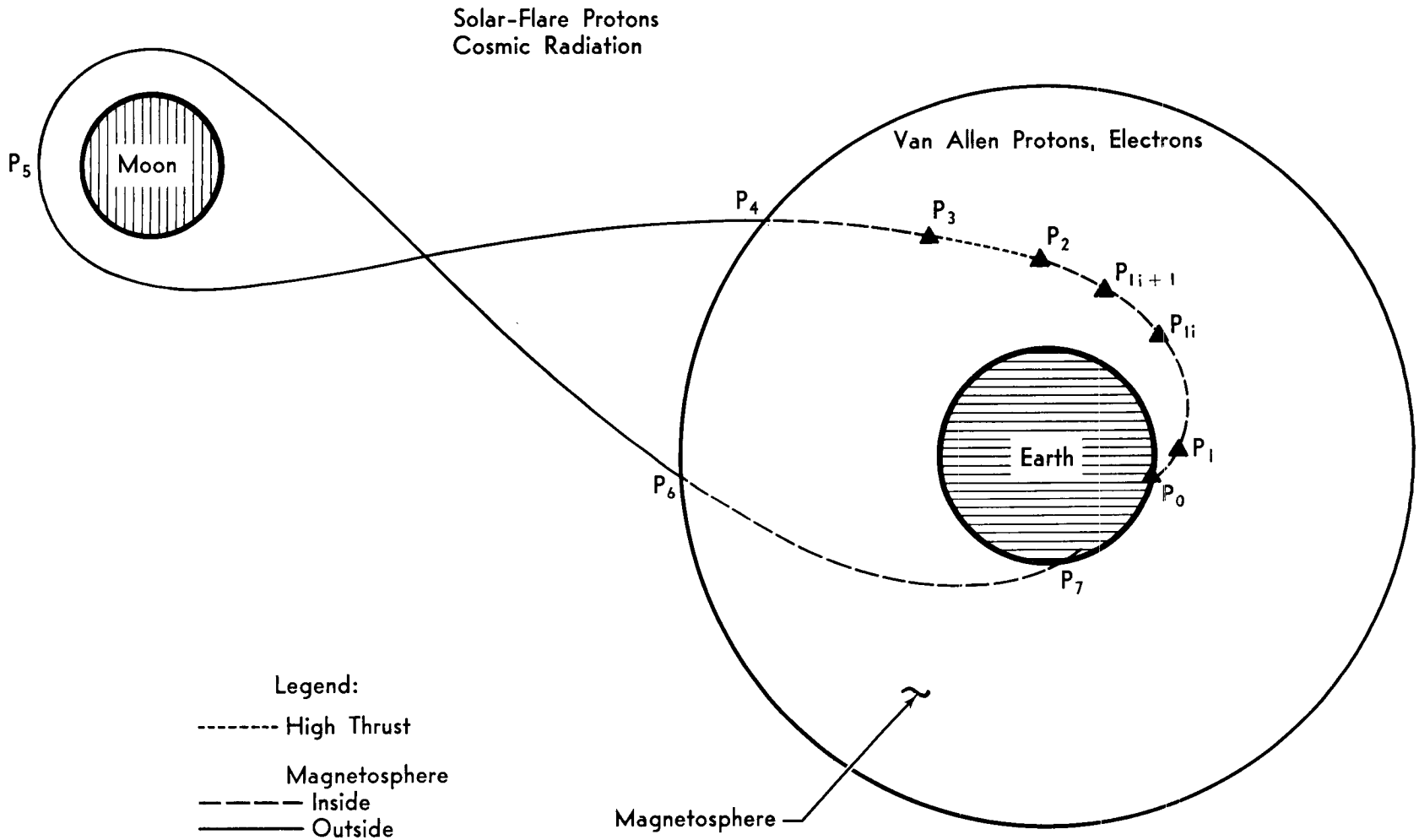

FIGURE 3. TRAJECTORY CHARACTERISTICS

$$\Delta t_i = K\, r_e^{3/2}, \qquad (1)$$

where r_e is expressed in earth radii and K is an empirically determined constant. The radiation integration is performed with the integrand as a product of the intensity at the initial point and the time interval. The position at the end of the time interval is computed, the radiation intensities re-evaluated, and the radiation integration continued by adding the contribution from the new position. After a new time interval is found from the new position, the radiation integrals are increased by the contribution from the second step. This process is continued with the new position, P_{1i} until the end (P_2) of the orbit leg is reached. The velocity at the end of this first leg is computed and is used as the initial estimate for parameters on the second leg (P_2,P_3). If the vehicle leaves the magnetosphere and the rest of the leg is entirely outside the sphere of influence, the remainder of the orbit leg is covered in one time step. This interpolation process is continued until the vehicle is outside the magnetosphere or else enters a high-thrust leg condition as indicated by a control number. In either of these cases, the two-body interpolations are not used until the vehicle is back within the magnetosphere or is on a low-thrust leg. Figure 4 shows the computational procedure in STREP.

Radiation Calculations

In addition to positions along the trajectory, data must be given to define the expected radiation environment for the mission. Although STREP does not predict the time of occurrence of solar flares or magnetic storms, any combination of these events with the associated times from the start of the mission may be used in describing the radiation environment. A maximum of ten changes - e.g., a total of ten different solar flares - could be programmed for each mission.

In general, the radiation environment is space-dependent. STREP considers cislunar space to be divided into two major domains by virtue of the earth's magnetic field. The first region is assumed to be a sphere with its center at the geomagnetic center. Inside this region all charged-particle radiation is modified by the effect of the earth's magnetic field on charged-particle intensities. An approximation is acquired through the reduction of the intensity at each energy by the solid-angle effect imposed by the cutoff energy and the distance from the earth's center. Outside this inner region, all types of radiation are assumed to be independent of space.

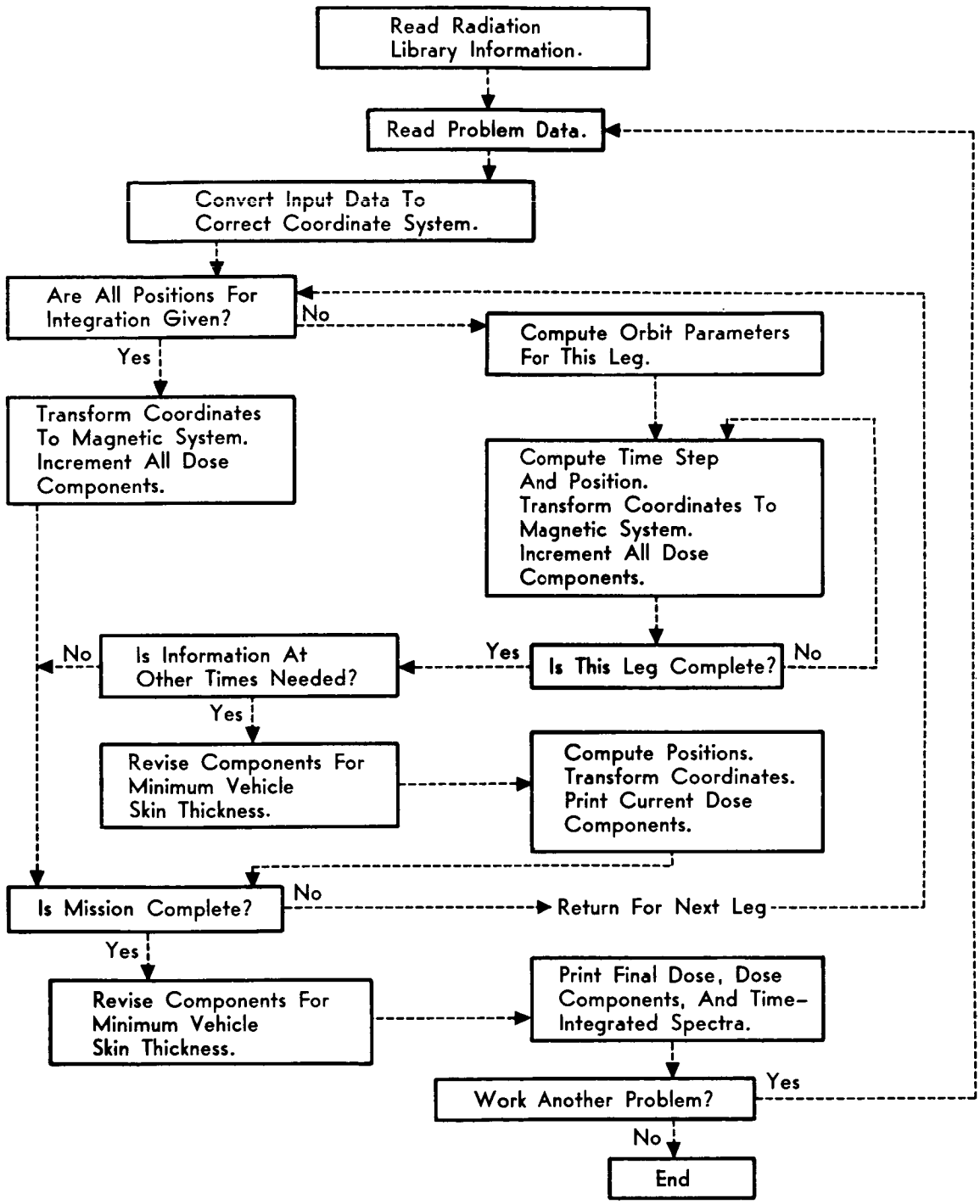

FIGURE 4. STREP FUNCTIONAL CHART

Trapped Radiation

The trapped radiation is assumed to be symmetric about an axis perpendicular to the equatorial plane and also symmetric with respect to the geomagnetic equator in a geomagnetic coordinate system. Under these assumptions, the data defining the space-dependent intensities are used in the form of a two-dimensional array in distance from the geomagnetic center and geomagnetic latitude. The intensity at a specified time is secured by linear interpolation with natural logarithms of the array, after transformation of the position to the geomagnetic coordinate system. Additional data required to define the spatial distribution of the trapped radiation are a maximum radius, minimum radius, and maximum latitude angle. After the intensity is calculated, the spectrum is computed from an expression of the form

$$\psi(E) = N_1 e^{-k_1 E} + N_2 E^{-k_2}, \qquad (2)$$

where the four parameters N_1, N_2, k_1, and k_2 are space-dependent. Provision is made to expand and contract the belts in case of a magnetic storm by insertion of new data at the proper time. After the activity has ceased, the original data may be re-inserted. The data for each component of the trapped radiation are secured from a separate library deck. In this manner, changes may be made in one component without modification of the other. A numerical integration is performed to secure the time-integrated spectra.

Solar-Flare Radiation

The spectra for solar-flare electrons, protons, and heavy particles are all computed by a formula similar to $\psi(E)$ with a decay factor t^{-k} and a normalization constant secured by an integration over the energy range. Inside the sphere of influence the integration with respect to time is numerical, since the intensities at each energy are modified by the effect of the geomagnetic field. A maximum of ten sets of constants for each flare is permissible, and as many as ten flares can be used during a mission to compute the radiation components. Outside the earth's magnetosphere, the spectra are integrated analytically in contrast to the numerical integration required by effects of the geomagnetic field on the charged-particle intensities.

Cosmic Radiation

The range of galactic particles is represented by protons for hydrogen and three types of heavy particles, namely:

Type A, (Helium); Type B ($2 \leq Z \leq 10$); and Type C ($Z > 10$). The spectra for protons and the heavy particles are computed by the formula

$$\phi(E) = H(E)\, C_1\, (C_2 + E)^{-k}, \tag{3}$$

where C_1, C_2, and k are determined from data for each type of spectral data, and H(E) is the modification produced on the spectra by the earth's magnetic field. Outside the sphere of influence, H(E) = 1.

Dose Calculations

The dose calculations are made for a vehicle skin with a thickness of 2 gm/cm^2. The charged-particle contributions are not attenuated through the skin of the vehicle. The portion of the spectrum which will not penetrate the skin is removed. The dose, for all charged particles except electrons, is calculated with the formula

$$D = A \int_{E_{cutoff}}^{E_{max}} \phi(E)/F(E)\, dE, \tag{4}$$

where A is constant to convert Mev to rads, $\phi(E)$ the time-integrated spectra, and F(E) an effective flux-to-dose conversion factor. The electron spectra are converted to gamma dose in the bremsstrahlung calculation by the formula

$$D_\gamma = \int_{E_{emin}}^{E_{max}} \phi(E_e) \int_0^{E_e} \frac{\psi(E_\gamma)\, e^{-u(E_\gamma)x}}{F(E_\gamma)}\, dE_\gamma E_e, \tag{5}$$

where $\psi(E_\gamma)$ is the gamma spectrum due to Wu[2], $\phi(E_e)$ the electron spectrum, E_e the electron energy, E_γ the gamma energy, $F(E_\gamma)$ a flux-to-dose conversion factor, and $e^{-u(E_\gamma)x}$ an attenuation factor for skin thickness x.

Radiation Calculations for a Lunar Mission

Trajectory and Environmental Data

The exposure of a shielded manned space vehicle to several radiation components while on two arbitrarily selected

---

2. B. T. Price, C. C. Horton, and K. T. Spinney, Radiation Shielding. New York: Pergamon Press (1957), 76

versions of a lunar mission was calculated with STREP to provide a functional evaluation of the procedure.

A trajectory of 149.2 hours duration[3] from the point of injection to the point of re-entry was used as a model. In the first trajectory, the vehicle was permitted to traverse the Van Allen regions, to proceed about the moon while exposed to a solar flare of the 14 July 1959 type, and then to return through the belts to the re-entry point. In this case, the flare was of 55.5 hours duration and was timed to begin onset at 12 hours after injection of the vehicle into its trajectory. The data for the solar-flare event is that listed in Table 1.

In the second case, the vehicle traversed the belts, proceeded beyond the magnetosphere, and received warning of probable flare activity six hours prior to onset. The vehicle returned to circle the earth in a 24-hour orbit (22,400-mile altitude) for 60 hours and then completed the lunar mission. A schematic drawing of these trajectories is shown in Fig. 5. The trajectory specifications[4] and radiation exposure conditions are listed in Table 2.

Table 2. Trajectory Specifications

Conditions	Trajectory 1	Trajectory 2
Radiation Exposure (hours after injection)		
Proton belt (exit)	.82	.82
Electron belt (exit)	3.4	3.4
Circular orbit (enter)		10.0
Solar Flare (onset)	12.0	12.0
Solar Flare (end)	67.5	67.5
Circular orbit (end)		70.0
Re-entry		
Time from injection (hr)	149.2	209.2
Altitude (miles)	75.77	75.77

3. J. P. Gapcynski and D. S. Woolston, Characteristics of Three Precision Circumlunar Trajectories for the Year 1968, NASA Report TN-D-1028 (March 1962).

4. Ibid.

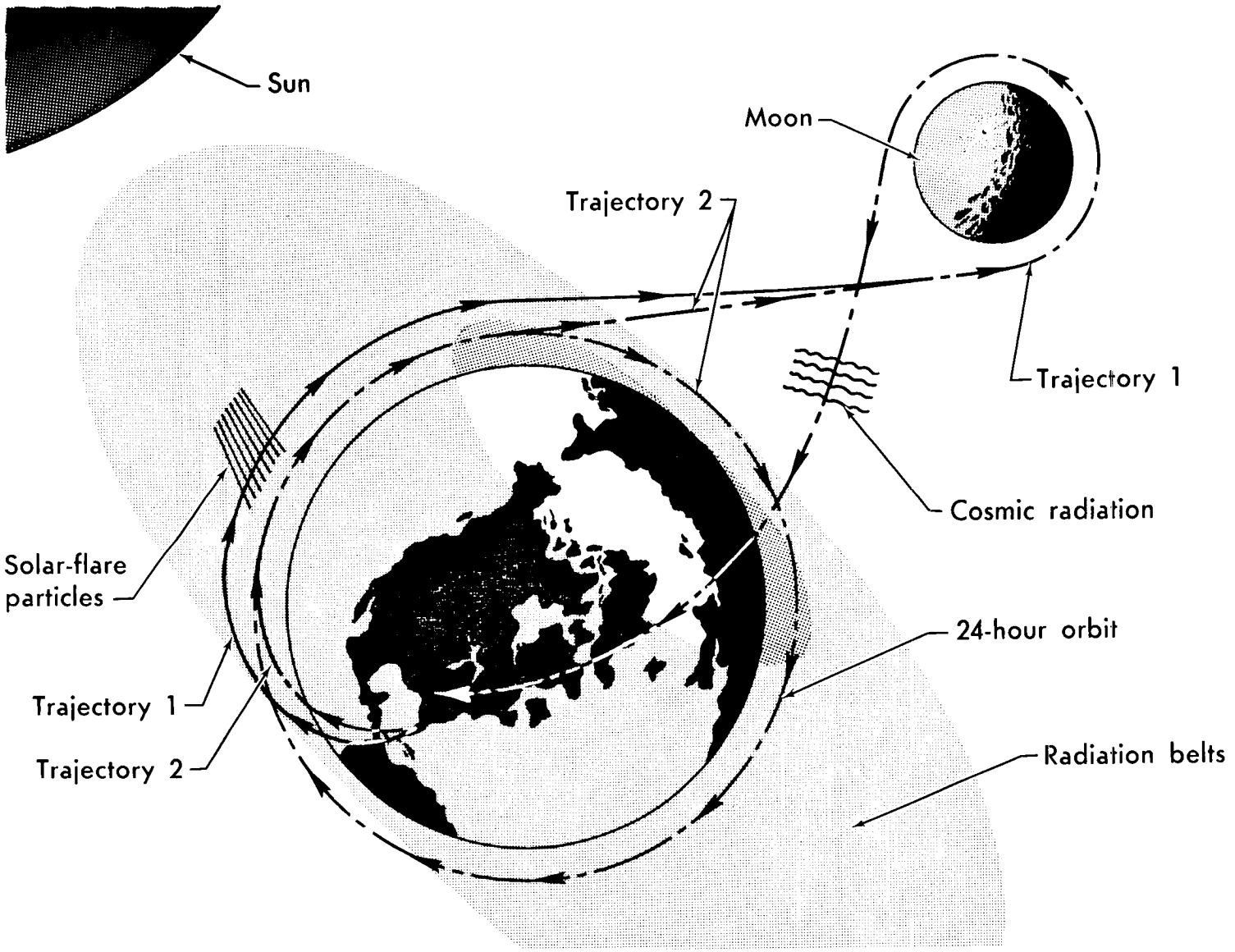

FIGURE 5. LUNAR TRAJECTORIES

A modification of Trajectory 1 consisting of a change of 30° in the longitude of the end point of the first leg after injection is designated by Trajectory 3. A portion of Trajectory 1 and Trajectory 3 through the Van Allen proton belt is shown in Fig. 6. This judiciously chosen alternate trajectory essentially avoided the radiation belts.

Some indications of the accuracy of STREP calculations of the required velocity can be seen from a comparison of the results in Table 3.

Table 3. Velocity Comparisons

Time (hr)	Velocity (ft/sec)	
	Reference 3	STREP
0	36,167	35,805
7.9	8,077	8,109
136.1	6,485	6,478
149.2	36,082	36,071

Spectra and Dose Calculations

The time-integrated spectra incident on the unshielded vehicle from solar-flare protons, Van Allen protons, and cosmic radiation for the trajectories are shown in Fig. 7. It will be noted that the solar-flare spectrum for Trajectory 2 is lower than that for Trajectory 1 in the energy range of from 30 to 300 Mev. This decrease for the lower-energy particles will reflect a decrease in the dose from secondary particles within a shield. Figure 8 shows the time-integrated spectra from Trajectory 1 for the three different types of heavy particles represented in STREP. A comparison of the time-integrated spectra for electrons during Trajectory 1 and Trajectory 2 is shown in Fig. 9. A slight increase of the electron spectrum, the heavy-particle spectrum, and cosmic-radiation spectrum was calculated for the 60 hours spent in the 24-hour orbit.

The results of the unshielded-dose calculations behind an aluminum skin of 2 gm/cm^2 thickness are summarized in Table 4 for the three trajectories. It may be noted that the dose from the Van Allen belt shows a decrease of from 14.3 rad for Trajectory 1 to 2.9 rad for Trajectory 3. It may be remarked that a geomagnetic equatorial orbit selected at about 2½ earth radii would have eliminated the contributions to the dose from the flare.

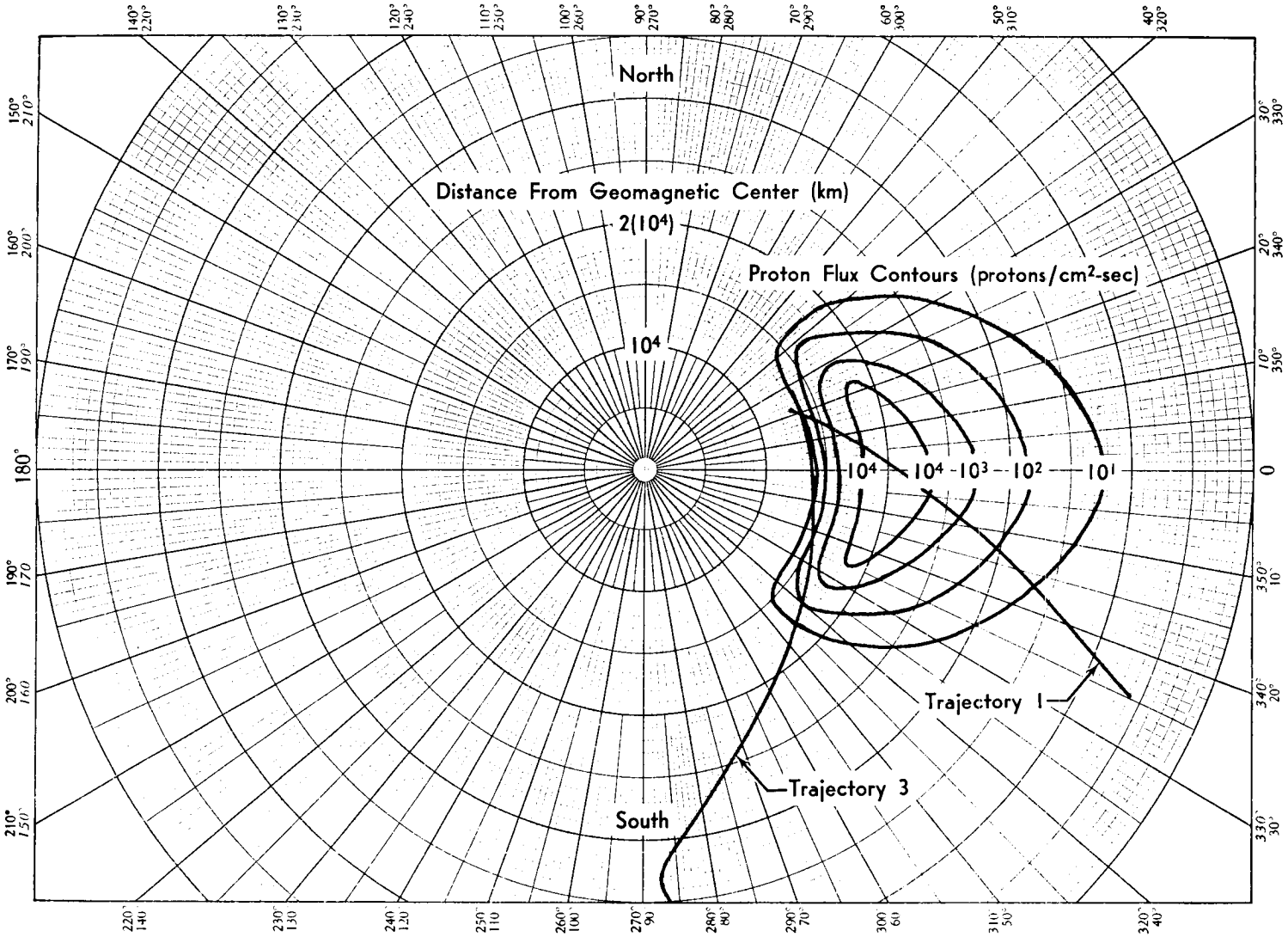

FIGURE 6. TRAJECTORIES THROUGH VAN ALLEN FROTON BELT

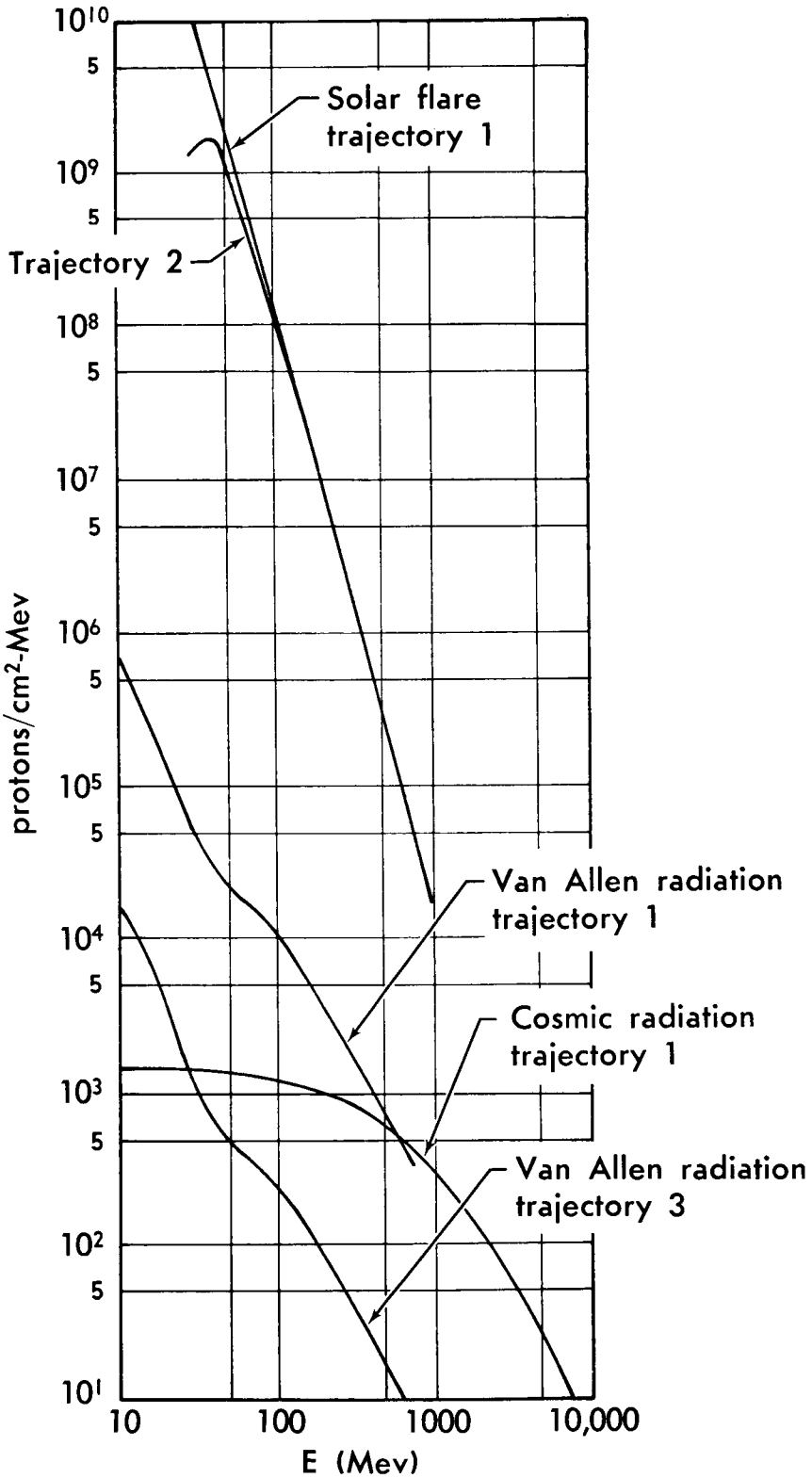

FIGURE 7. PROTON TIME-INTEGRATED SPECTRA

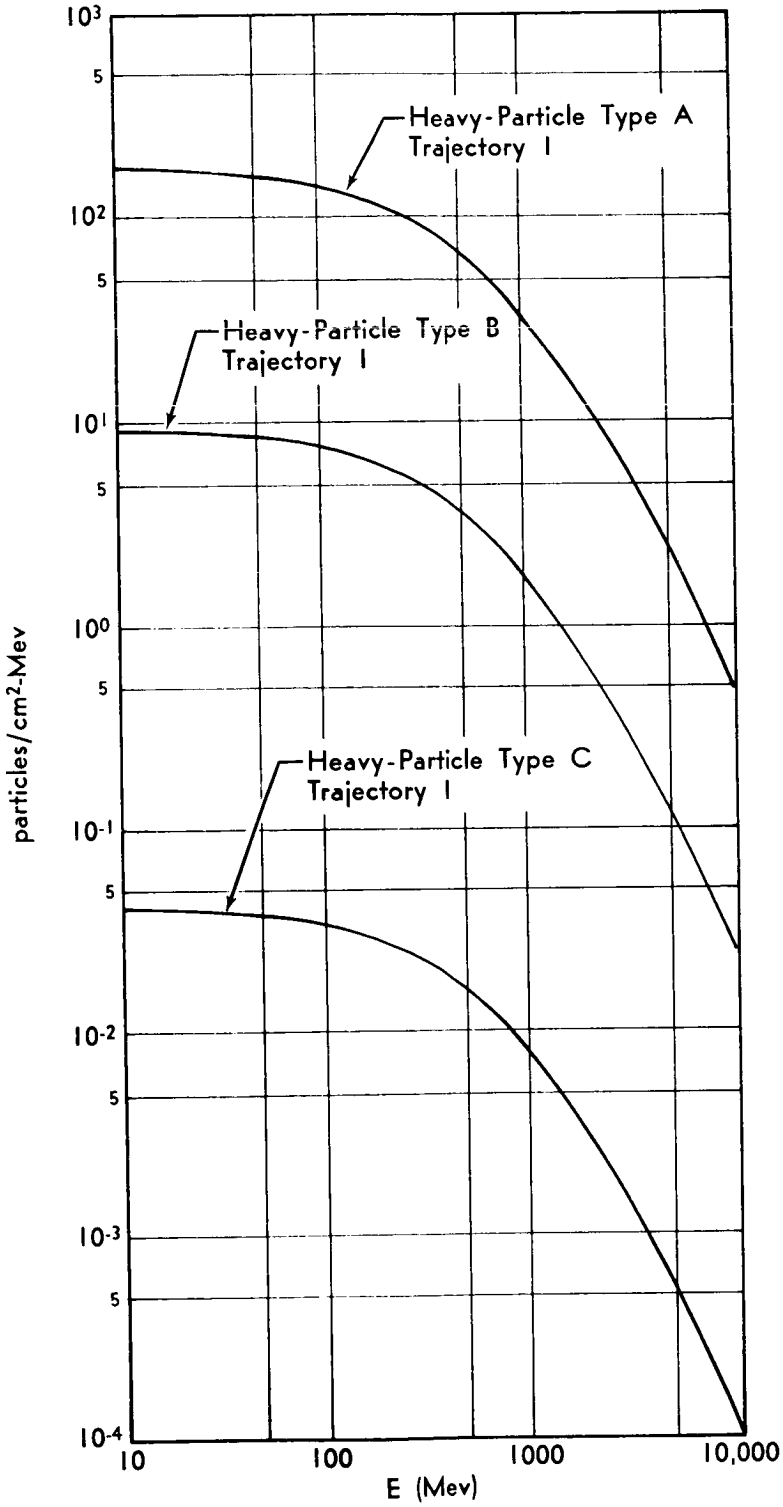

FIGURE 8. HEAVY-PARTICLE TIME-INTEGRATED SPECTRA

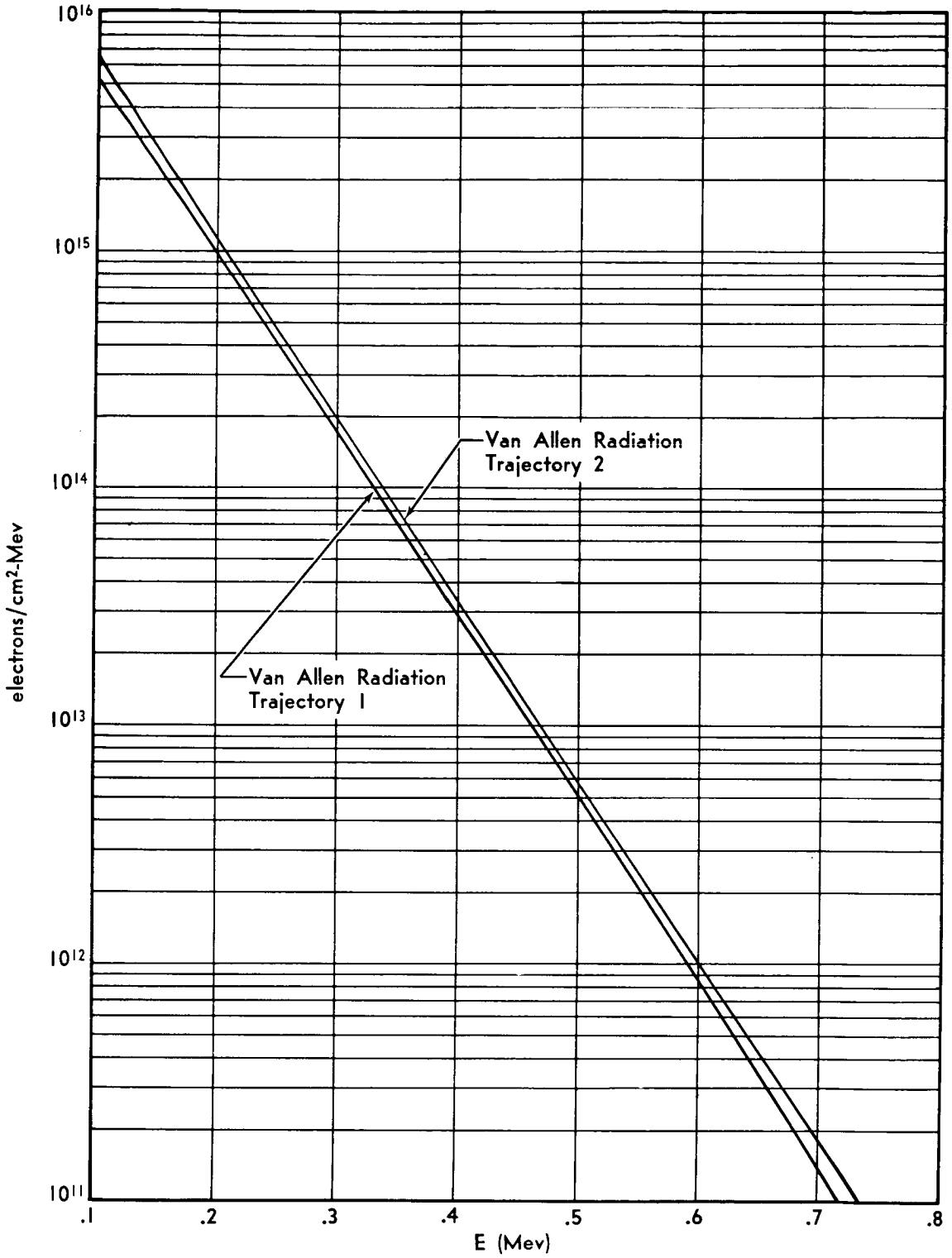

FIGURE 9. ELECTRON TIME-INTEGRATED SPECTRUM

Table 4. Unshielded-Dose Calculations

Component	Dose (rad)		
	Trajectory 1	Trajectory 2	Trajectory 3
Van Allen Protons	$3.1(10^{-1})$	$3.1(10^{-1})$	$6.8(10^{-3})$
Solar Flare Protons	$2.2(10^{4})$	$9.4(10^{3})$	$2.2(10^{4})$
Cosmic Protons	$6.2(10^{-2})$	$8.2(10^{-2})$	$6.2(10^{-2})$
Heavy Particle A	$2.7(10^{-2})$	$3.8(10^{-2})$	$2.7(10^{-2})$
Heavy Particle B	$7.9(10^{-3})$	$1.1(10^{-2})$	$7.9(10^{-3})$
Heavy Particle C	$2.5(10^{-5})$	$3.5(10^{-5})$	$2.5(10^{-5})$
Van Allen Electrons	$1.4(10^{1})$	$1.7(10^{1})$	$2.9(10^{0})$
Albedo Neutrons	$1.3(10^{-4})$	$2.7(10^{-4})$	$1.8(10^{-4})$

These dose values are for an essentially unshielded vehicle. The results of using the spectra output in another procedure[5] (PAP) are shown in Fig. 10 for lunar Trajectory 1. A fixed shield of 6 gm/cm^2 of aluminum backed with a variable thickness of polyethylene was assumed. The several components of the dose, primary and secondary, are shown as functions of the polyethylene thickness. It should be noted that the contribution to the dose from the secondary components begins to play an increasing role with increasing thickness of the shield. This contribution from the secondary component has been characteristic of other calculations for thick shields[5]. It is clear that for this flare a dose of 100 rads would be received under a composite shield of 6 gm/cm^2 of aluminum and 25 gm/cm^2 of polyethylene. The magnitude of this dose value indicates that for a flare with the characteristics of the 14 July 1959 event, considerable shielding will be required on lunar missions.

5. R. K. Wilson, R. A. Miller, and R. L. Kloster, A Study of Space Radiation Shielding Problems for Manned Vehicles. GD/FW Report FZK-144 (June 1962).

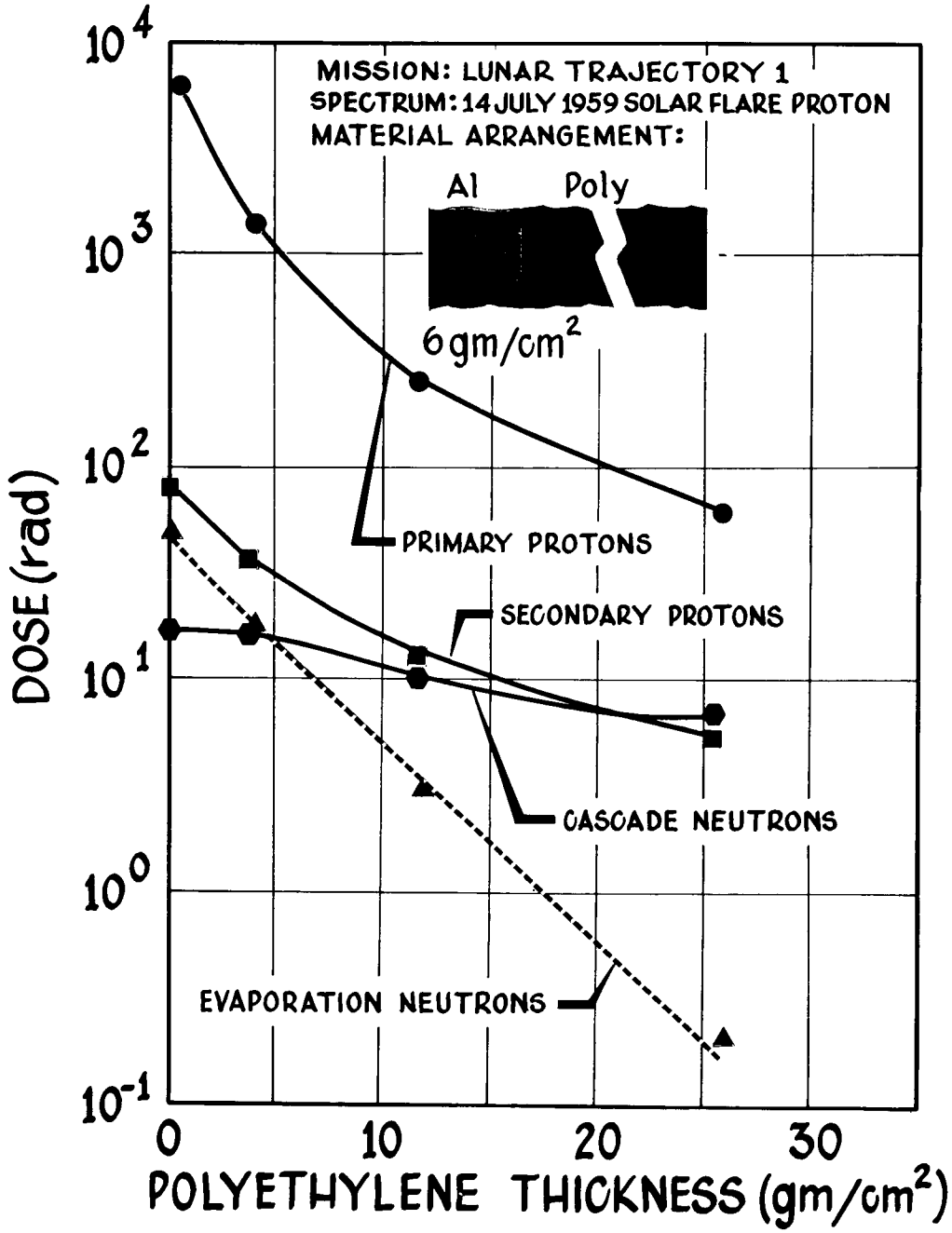

FIGURE 10. COMPOSITE-SHIELD DOSE

Paper E-8

RADIATION DOSAGES FROM ELECTRONS AND BREMSSTRAHLUNG IN THE VAN ALLEN BELTS

S. L. Russak
The Martin Company
Baltimore 3, Maryland

Abstract 1513

Radiation dose rates have been calculated for six electron spectra. The decrease in dose rate with shielding was determined--and in each case the electron dose becomes insignificant with 2 to 6 gm/cm^2 of aluminum. Electron bremsstrahlung dose rates versus absorber thickness were also calculated. Detailed dosage calculations for an Apollo-type spacecraft were made and mission dosages for four lunar trajectories are given, to show the effects of trajectory selection. These are compared with the dosages from protons and secondary neutrons in the Van Allen Belt. Doses as a function of orbital altitude, of inclination and of absorber thickness are also presented for the latest version of the inner belt.

Discussion

Over the past few years, a number of representations of the spectral distribution and intensity of geomagnetically trapped electrons have been evolved. We had had occasion to evaluate the radiation dosage that would result from exposure to these electrons and this paper reports on dosages from the six spectra shown in Fig. 1, namely: (1) the inner and (2) the outer zone integral spectra given by Van Allen[1] in 1959; (3) a composite inner and outer spectrum from the experimental data of Holley[2], together with Dessler's[3] interpretation of Walt's[4] data;

1. Van Allen, J. A., "The Geomagnetically Trapped Corpuscular Radiation," Journal of Geophys. Research, Vol. 64, No. 11, p 1683, 1959
2. Holley, F. E., "Radiation Measurements to 1500 Kilometers with Atlas Pods," Air Force Special Weapons Center, TR 60-9, 1960
3. Dessler, A. J., "Letters to the Editor," Journal of Geophys. Research, Vol. 65, No. 10, p 3487, 1960
4. Walt, M., Chase, L. F., Cladis, J. B., Imhof, W. L. and Knecht, D. J., "Energy Spectra and Altitude Dependence of Electrons Trapped in the Earth's Magnetic Field," Proceedings of First International Space Science Symposium, Nice, 1960

Summary

The procedure, STREP, may be utilized as a generation tool for a source of time-integrated spectra incident on a space vehicle during lunar missions. Since input requirements on the trajectory are positions and associated times, the procedure is independent of a particular calculational method for trajectories. The results from problems of interest indicate that the present version is adequate for lunar missions, provided a radiation field does not exist in the vicinity of the moon.

The calculations for a lunar mission during the active period of a particular solar flare indicate that an excessively high radiation dose may be received within a shielded vehicle. These calculations are predicated on the assumption that the radiation spectra as currently reported are reasonably correct. The results indicate the necessity of planning missions during quiet solar periods to avoid excessive shield weights to provide adequate protection.

(4) the outer zone peak spectrum given by Van Allen in the Space Flight Report to the Nation; (5) an inner belt spectrum given recently by the SUI[5] group; and (6) the fission spectrum believed to be representative of the electrons at the peak of the artificial radiation belt[6].

For Spectra (3) and (5), the peak fluxes were extrapolated to the peak of the electron zone. The small detector dose rates from each of these distributions (evaluated between 0.001 and 5.0 Mev) are shown in Fig. 2, as a function of aluminum thickness. The rates vary from about 2×10^3 to 2×10^5 rad/hr under 0.03 gm/cm^2--with the electrons completely extinguished between 2 and 6 gm/cm^2. If we divide by the peak flux, J_o, we find that the highest dose per electron (remembering that J_o is the integral between 0.020 and 5 Mev) at absorber thickness above 0.1 gm/cm^2 comes--as expected--from the very flat fission spectrum.

Figure 3 shows the bremsstrahlung dose rates from these six spectra under aluminum thicknesses between 0.03 and 10 gm/cm^2. At 0.03 gm/cm^2 the dose rates extend from about 3 to 2500 rad/hr--considerably below the electron dose rates at that thickness. At 6 gm/cm^2 the X-ray dose rate extends from less than 0.1 rad/hr, for the new outer belt, to about 30 rad/hr for the fission electrons of the artificial belt. Quite a bit more can be obtained from further examination of these first three figures--for example, note the pronounced rising dose rate for the fission spectrum. It is less pronounced for the steeper Spectra (3) and (5) and no longer seen at 0.03 gm/cm^2 for the remaining, softer, electron spectra.

Let it suffice to say that the wide variation in form, or slope and intensity, of these spectra results in dose rates that are significantly different. In the case of thin absorbers, the electron dose rates are much more important than the X-rays. As we increase the absorber, the X-rays become more important--with the cross-over point varying among the different spectra.

---

5. Pizzella, G., Laughlin, C. D. and O'Brien, B. J., "Note on the Electron Energy Spectrum in the Inner Van Allen Belt," Journal of Geophys. Research, Vol. 67, No. 9, p 3281, 1962

6. Zerby, C. D. and Moran, H. S., "Tissue Dose Rate from Bremsstrahlung Radiation Behind an Idealized Apollo Vehicle Wall Exposed to Electrons in the Artificial Radiation Belt," presented at the Symposium on the Artificial Radiation Belt, Washington, D. C., September 1962

There is only a very limited amount of practical information that can be obtained with homogeneous spheres or slabs and peak fluxes. The next set of data is for a detailed Apollo configuration along several lunar trajectories. The method of analyzing the spacecraft shape and construction is illustrated in Fig. 4. This analysis was used over 200 area elements to define the command module. The electron fluxes at one longitude are shown in Fig. 5. A trimetric view of part of the inner zone is shown in Fig. 6.

The belts are symmetrical with respect to the position of the dip equator and magnetic intensity (B) as determined by using the AFSWC field solution of Jensen. The development of the radiation belt models is described in the last reference[7]. We are now setting up models in B, L coordinates for use with McIlwain's B, L program--and would welcome any recent spectral data in either B, L or World Map coordinates.

Bremsstrahlung doses on four Apollo trajectories from Cape Canaveral (bracketing the lunar month) are shown in Fig. 7. The first column, for the old inner and outer belts, shows total doses between 0.37 and 0.49 rad made up of between 0.08 and 0.15 rad from the inner and 0.29 to 0.41 rad from the outer region. The dose rate within the Apollo at the belt peak is shown along the top of the table. It is seen that traversal of the inner region along different trajectories gives from about 8% to 15% of one hour's exposure at the peak. For the outer belt, these values are between 38% and 53%.

The second column, for the composite outer and inner belt spectrum, gives total doses between 0.10 and 0.14 rad--depending on the trajectory selected. These calculations did not consider electrons above 1 Mev and it is estimated that these electrons would increase the doses by factors of 1.1, 3.3 and 1.3, for Spectra (1), (2) and (3)--respectively. This configuration carried 700 pounds of personal shielding--and electrons with incident averages as high as 5 Mev were extinguished before passing through all the materials. The bremsstrahlung dose time histories corresponding to the values of the first column are shown in Fig. 8. For comparison, the Van Allen Belt proton doses, as well as secondary neutron doses, are shown.

Note that the least favorable trajectory for protons results in doses comparable to the bremsstrahlung doses. The most favorable trajectory is an order of magnitude less--and neutron doses are still another order of magnitude lower.

---

7. Beck, A. J., Divita, E. and Russak, S. L., "Evaluation of Space Radiation Safety Procedures in the Design and Operation of Some Early Manned Lunar Vehicles," Proceedings of the Sixth Symposium on Ballistic Missile and Aerospace Technology, Academic Press, New York, 1962

Based upon these last data, some reasonable estimates may be made of the lunar mission dose, using the more recent inner and outer regions--Spectra (5) and (4). If we assume that the Apollo command module has some regions as thin as 2 gm/cm^2 of aluminum, the total inner belt dose on the least favorable trajectory would be less than 0.00001 rad from electrons and 0.295 rad from bremsstrahlung.

Corresponding outer belt doses would be 0.181 rad from electrons and 0.031 rad from X-rays--or a total of about 0.5 rad. For that portion of the command module having 6 gm/cm^2, only X-rays would be seen and the inner and outer belt dosages, respectively, would be 0.198 rad and 0.014 rad--or a total of less than 0.25 rad.

Also of interest, are the doses that would be received within an orbiting spacecraft. We have not yet analyzed a specific orbital spacecraft, but have made a series of calculations for aluminum spheres. This is of value in showing how the doses vary with the orbital parameters. Figure 9 shows dosages for 12 hours in the inner belt--Spectrum (5). The doses increase with altitude, such that the ratio of equatorial orbital doses at 300, 400, 600 and 1000 n mi to the dose from a stationary 12-hour exposure at the peak of the belt are--respectively--0.0063, 0.016, 0.091 and 0.36. Within each altitude, the effect of orbital inclination gives ratios to the equatorial orbit dose of 0.31 and 0.15, for 40° and 90°, respectively. The effect of increasing absorber has already been discussed.

If we look at the middle column in Fig. 9, assuming that orbiting laboratories might be no thicker than 1 gm/cm^2 over a considerable solid angle, then--at 300 n mi--a 50-rad dose would be received in about 110 days in an equatorial orbit and in about 2 years in a polar orbit. However, at 1000 n mi, these times are only about 2 and 4-1/2 days, respectively.

Therefore, depending on the position and duration of the mission, inner belt bremsstrahlung doses could be a factor in the design and operation of manned orbital laboratories.

Acknowledgements

The author would like to acknowledge the work of his colleagues at the Martin Company--Andrew Beck and Edward Divita--who developed the computer programs used to obtain the data reported upon. Credit is also due to Frank Roth and Leo Kossa, who coded these programs for the IBM 7090 machine.

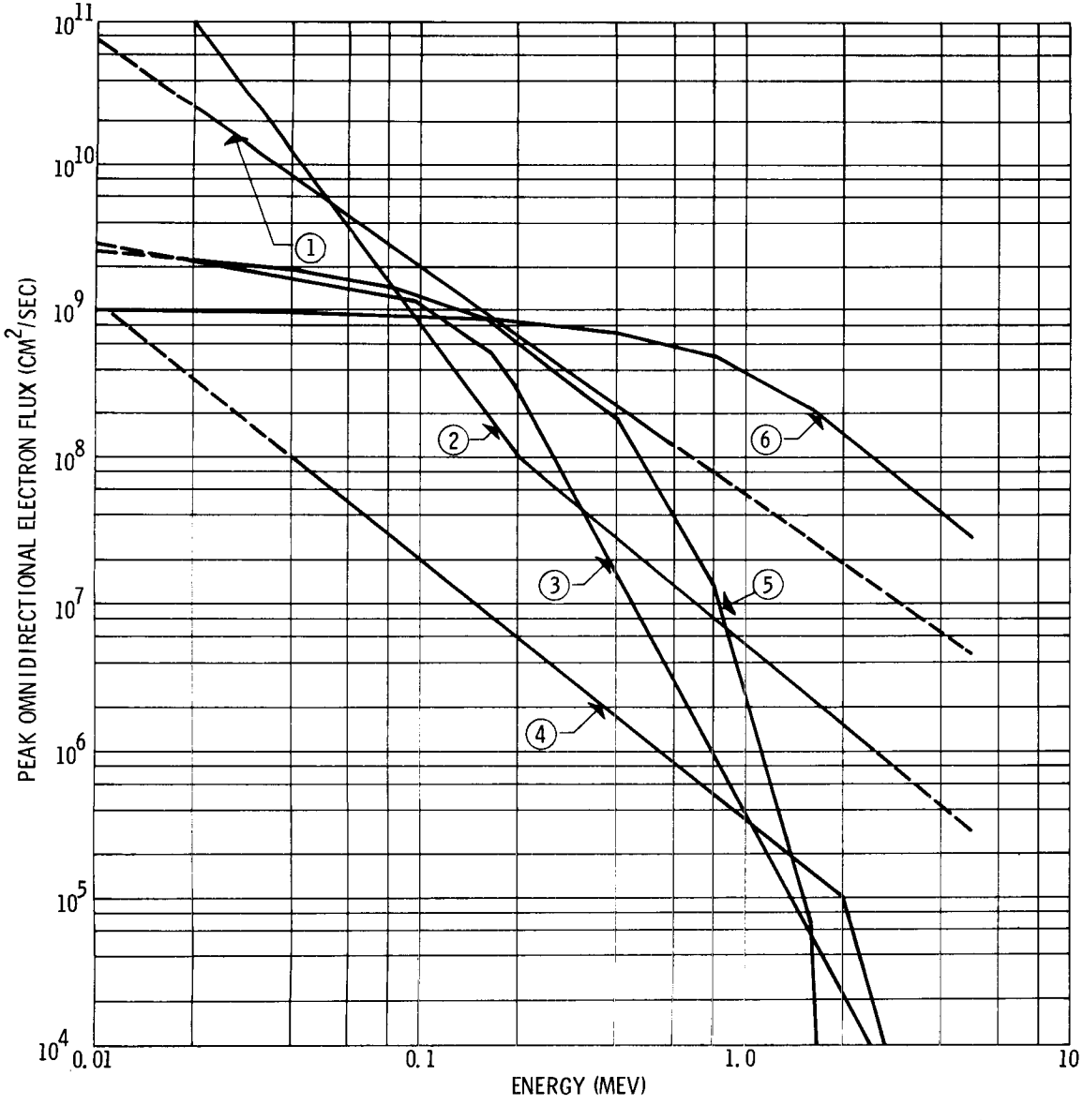

① 1959 INNER BELT, $J_0 = 2.5 \times 10^{10}$ (VAN ALLEN)

② 1959 OUTER BELT, $J_0 = 10^{11}$ (VAN ALLEN)

③ 1960 COMPOSITE, $J_0 = 2.2 \times 10^{9}$ (DESSLER; HOLLEY; WALT, ET AL.)

④ 1961 OUTER BELT, $J_0 = 3.2 \times 10^{8}$ (VAN ALLEN)

⑤ 1962 INNER BELT, $J_0 = 2.2 \times 10^{9}$ (PIZZELLA, LAUGHLIN & O'BRIEN)

⑥ FISSION SPECTRUM, $J_0 = 10^{9}$ (ZERBY AND MORAN)

Fig. 1. Integral Electron Kinetic Energy Spectra

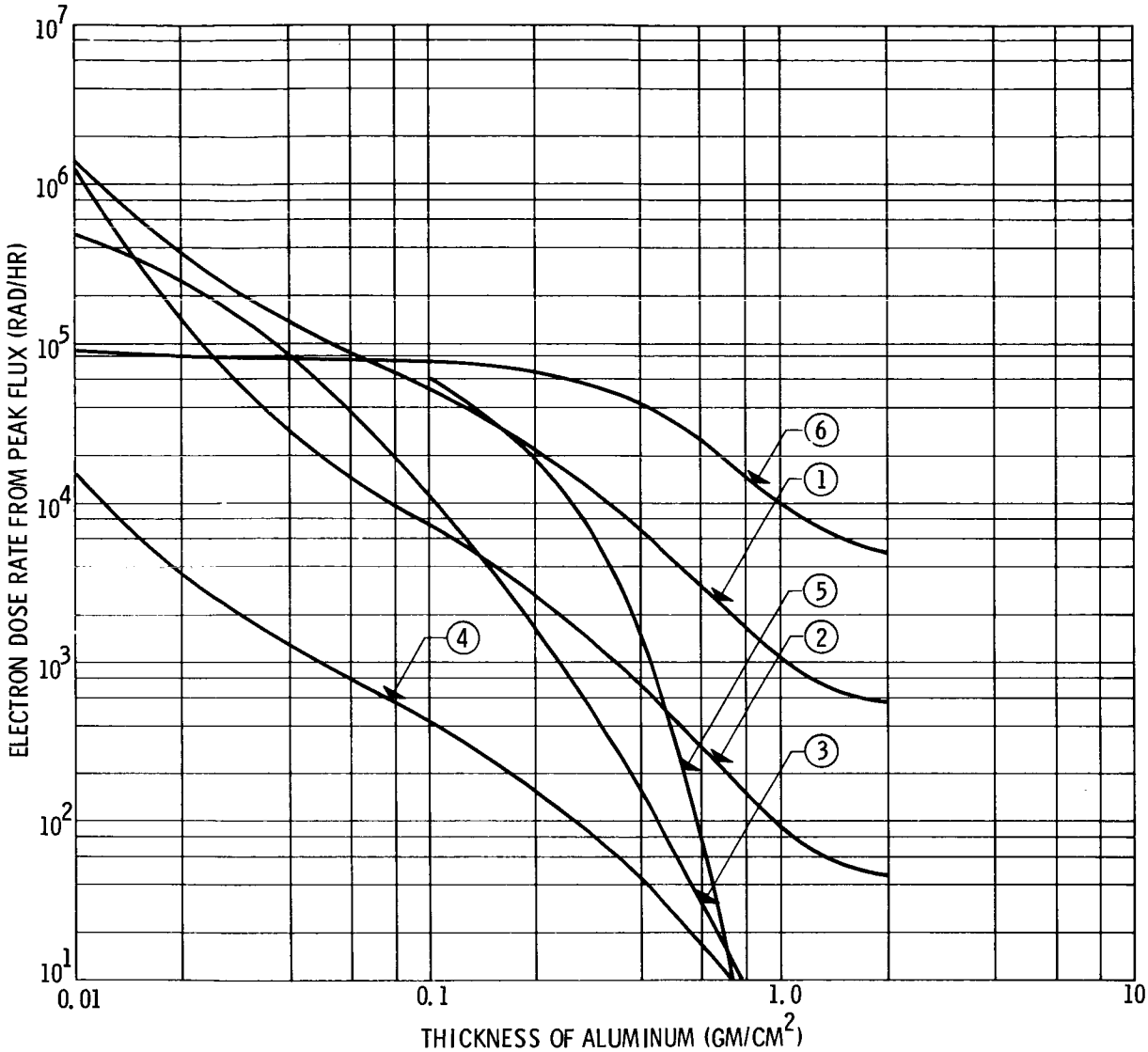

Fig. 2. Electron Dose Rates

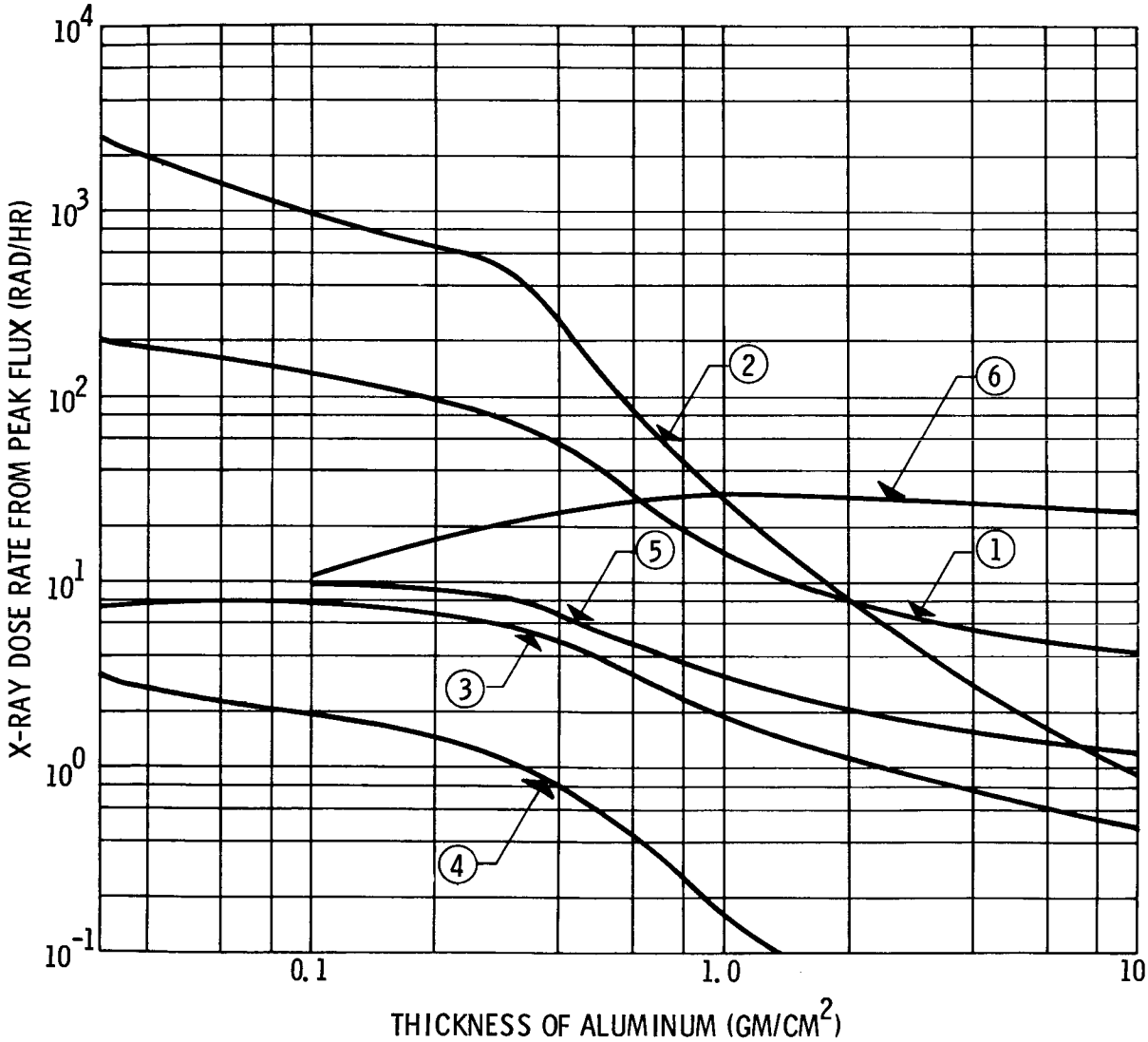

Fig. 3. X-Ray Dose Rates

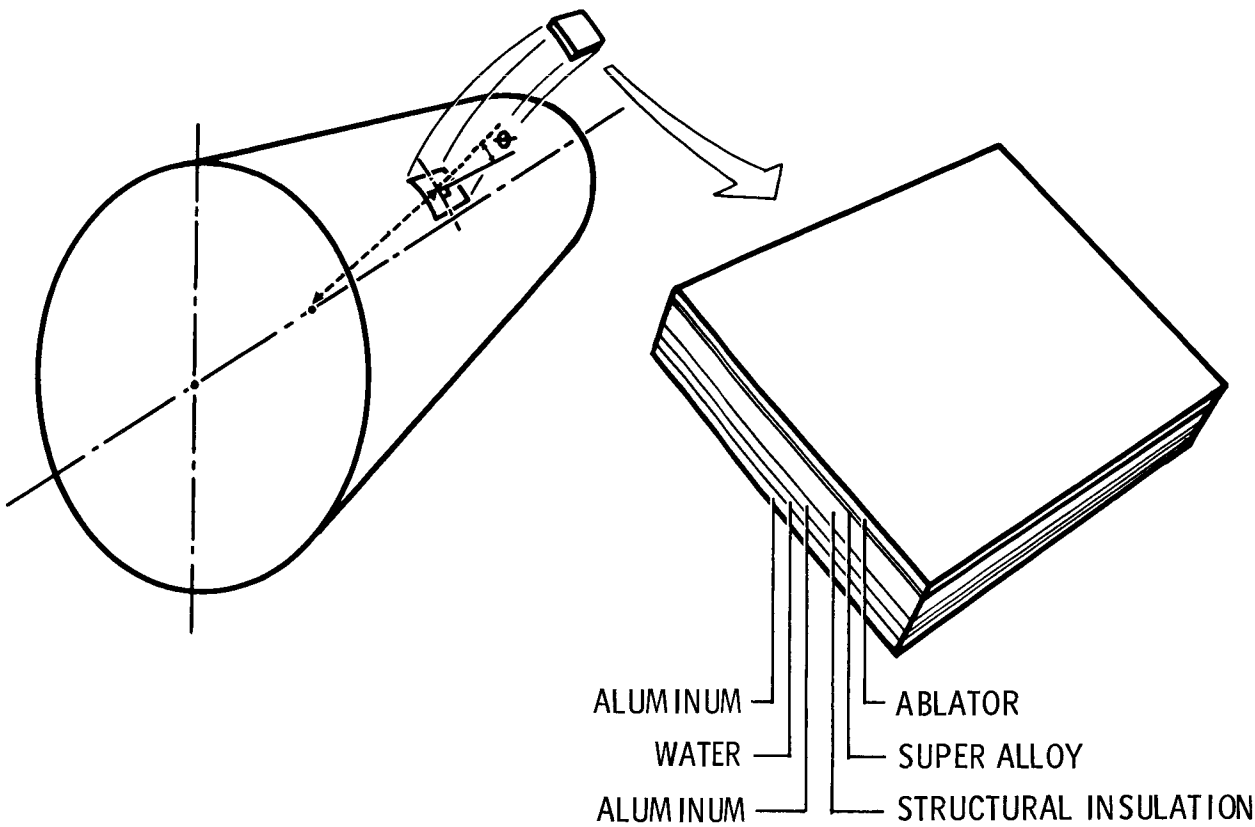

Fig. 4. Radiation Dose Calculation Schematic

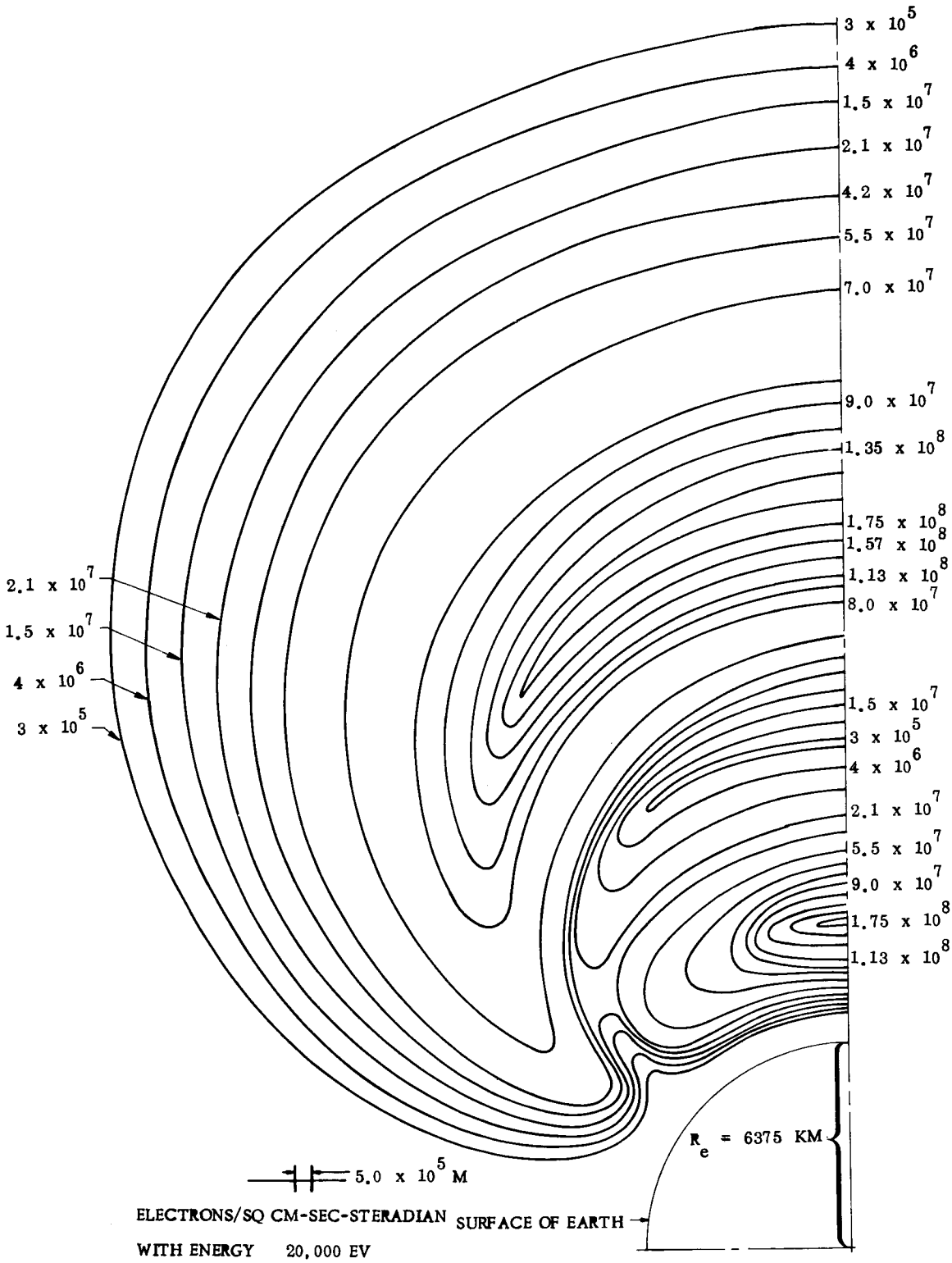

Fig. 5. Flux of Electrons at One Longitude in the Van Allen Belts

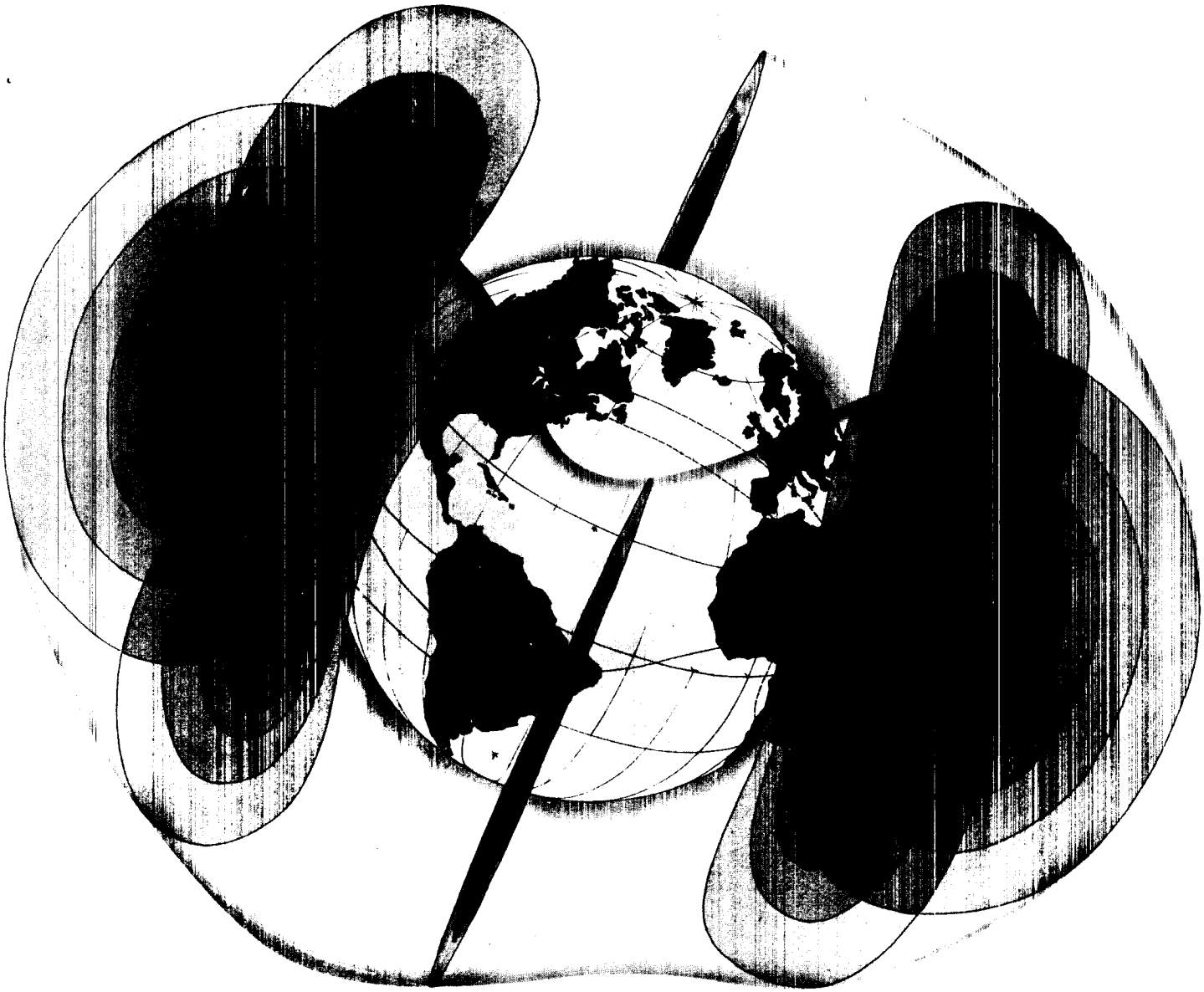

Fig. 6. Shape of Inner Van Allen Belt

LATITUDE AND LONGITUDE OF INJECTION POSITION	SPECTRUM NUMBER & PEAK DOSE RATE	
	① ② 1.0437 R/HR 0.7685 R/HR	③ ③ 0.24037 R/HR
-21.753^{0}	0.1531	0.0353
-102.524^{0}	0.3174	0.0923
	0.4705	0.1276
$+166.394^{0}$	0.0843	0.0194
$+31.953^{0}$	0.4053	0.1179
	0.4896	0.1373
-5.98^{0}	0.1529	0.0352
-127.23^{0}	0.3407	0.0992
	0.4936	0.1344
5.13^{0}	0.0815	0.0188
-141.599^{0}	0.2891	0.0841
	0.3706	0.1039

Fig. 7. Bremsstrahlung Radiation Doses Within Apollo Spacecraft on Four Lunar Trajectories

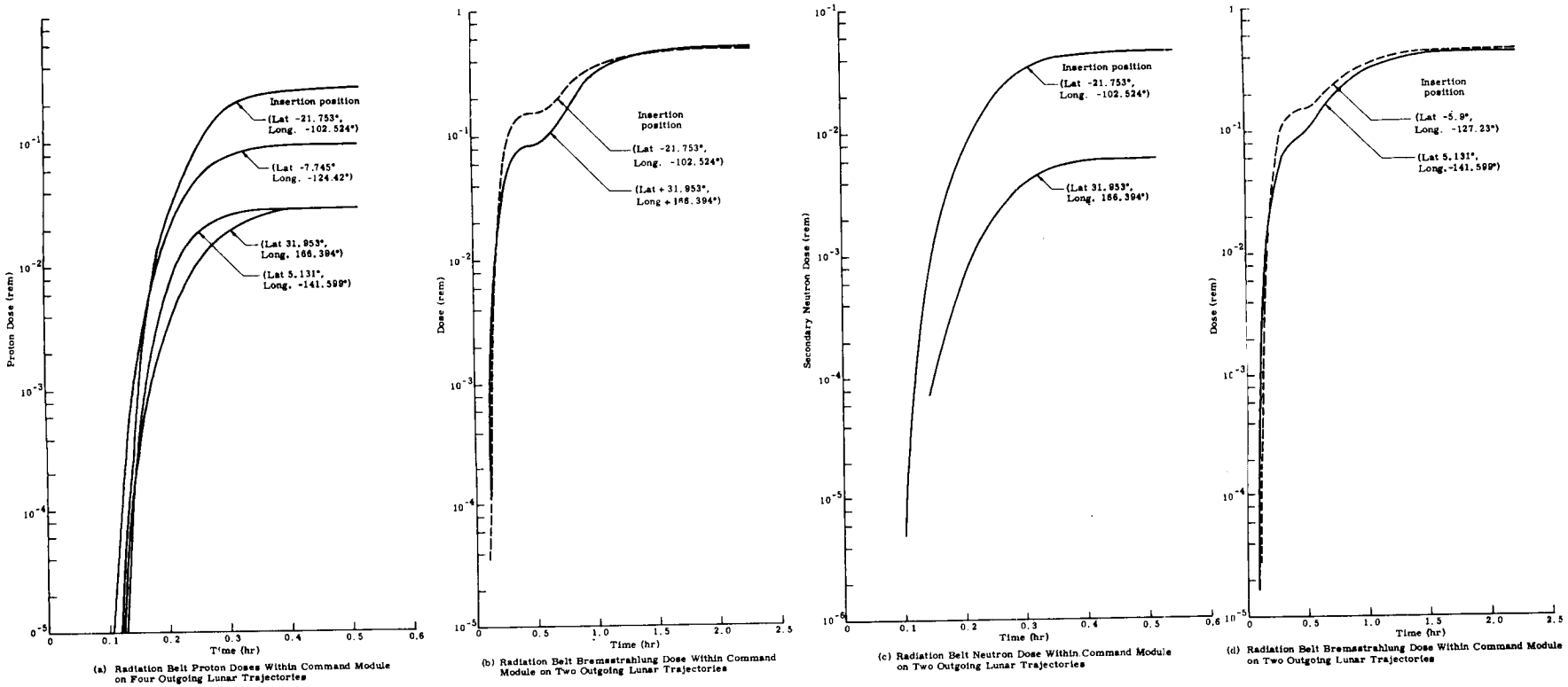

Fig. 8. Radiation Dosages Along Various Trajectories for an Apollo Configuration in the Van Allen Belt

ALTITUDE (N MI)	ORBITAL INCLINATION (DEG)	ALUMINUM SPHERE THICKNESS (GM/CM^2)					
		0.1		1.0		2.0	
		ELECTRONS	X-RAYS	ELECTRONS	X-RAYS	ELECTRONS	X-RAYS
300	0	4.598×10^{3}	0.7569	1.137×10^{-3}	0.2301		0.1575
	40	1.444×10^{3}	0.2377	3.574×10^{-4}	0.0723	$<10^{-5}$	0.0494
	90	6.811×10^{2}	0.1121	1.686×10^{-4}	0.0341		0.0233
400	0	1.1690×10^{4}	1.9241	2.892×10^{-3}	0.5849		0.4003
	40	5.046×10^{3}	0.8306	1.248×10^{-3}	0.2525	$<10^{-5}$	0.1728
	90	3.693×10^{3}	0.6078	9.136×10^{-4}	0.1848		0.1264
600	0	6.634×10^{4}	10.9197	1.641×10^{-2}	3.3196		2.2716
	40	4.129×10^{4}	6.7964	1.021×10^{-2}	2.0661	$<10^{-4}$	1.4138
	90	2.359×10^{4}	3.8825	5.835×10^{-3}	1.1803		0.8077
1000	0	2.625×10^{5}	43.2147	6.495×10^{-2}	13.1373	1.803×10^{-4}	8.9898
	40	2.088×10^{5}	34.3755	5.166×10^{-2}	10.4502	1.434×10^{-4}	7.1510
	90	1.097×10^{5}	18.0597	2.714×10^{-2}	5.4901	7.534×10^{-5}	3.7569

Fig. 9. Twelve-Hour Orbital Dose (rad) Within Van Allen Belt

Paper E-9

SYNTHESIS OF MINIMUM WEIGHT PROTON SHIELDS*

A. D. Krumbein, P. S. Mittelman, E. S. Troubetzkoy,
F. Nakache, and J. Celnik
United Nuclear Corporation
Development Division – NDA
White Plains, New York

15154

Abstract

A shield optimization technique originally developed for reactor shields has been applied to proton shields. The cases of both spherical and nonspherical shields have been studied and the effects of certain special constraints and of secondary neutrons have been included in the analysis. The method indicates which materials should go into making up the minimum weight shield and what their order and the thickness of each material should be. The amount of weight saved is found to be a function of the radius of the shielded void and of the specified attenuation required.

Introduction

Recently a technique for the synthesis of minimum weight reactor shields has been developed at the United Nuclear Corporation in connection with advanced shielding work being carried out for the AEC. This technique had its origin in a series of suggestions made by Gale Young which were given mathematical verification by M. Slater. A fairly complete account of this theory can be found in Reference 1. This

---

*Work sponsored by National Aeronautics and Space Agency, Huntsville, under contract NAS8-2658.

1. E. S. Troubetzkoy, Minimum Weight Shield Synthesis, UNC-5017 (Part A) (1962).

shield synthesis technique has now been applied to the design of minimum weight proton shields. Starting with the radiation environment and given all the materials available which might be suitable as proton shields, and a specified allowable total dose in the shielded region, the synthesis technique indicates the proper materials and their disposition so as to obtain the minimum weight shield.

Minimum Weight Spherical Shields

For shielding against incident protons only, the problem is equivalent to designing a shield that will eliminate all protons below a given energy. This energy is so chosen that the dose from protons above that energy is below design levels. In the energy range from about 50 to 500 Mev one can write an approximate expression for the rate of energy loss per cm in a given material as:

$$\frac{dE}{dr} = A_i f(E), \tag{1}$$

where f(E) is the energy dependence of the proton stopping power of a reference material. In this work aluminum was chosen as the reference and A_i is then defined as the ratio of the proton energy loss with distance in the i^{th} material to the same loss in aluminum. A is called the proton relative stopping power. Figure 1 shows a plot of A vs energy for many materials of interest to space shielding. It is seen that the values of A are indeed fairly constant over the energy range indicated.

If a shield consisting of concentric spherical shells of radii r_0, r_1, ..., r_N, where r_0 is the void radius, and containing materials with relative stopping powers A_1, A_2, ..., A_N, has to stop protons with energies up to E_0, the following relationship has to be satisfied

$$\sum_{1}^{N} A_i (r_i - r_{i-1}) = \int_0^{E_0} \frac{dE}{f(E)} = K(E_0). \tag{2}$$

The last equality defines K, which is the equivalent aluminum thickness of the shield.

It can be shown that the choice of materials for the minimum weight shield can be obtained by the following prescription:

All materials available are plotted on a plane, the ordinate being A_i and the abscissa, the material density, ρ_i. Now one constructs for $\rho \geq 0$, the shortest curve $A = A(\rho)$ which lies above the material points. This curve will be a broken line whose vertices are the origin and certain pairs (A,ρ). The minimum weight shield will be made up only of materials whose coordinates are vertices of the broken line, the outermost shell being made up of the material vertex closest to the origin, the next outermost by the next material vertex, and so on. In general all materials will not be used but only some initial sequence governed by the restriction that the inner radius of the shield be equal to r_0. If $r_0 = 0$, all the materials on the broken line will be used. Figure 2 shows such a curve, which we call a "Young Diagram." The materials at the vertices are CH_2 (polyethylene), carbon, iron, and copper. As can be seen several other plastic materials might easily be used in place of polyethylene.

The method of Lagrange multipliers is used to locate the radii of the various layers of the minimum weight shield. From Eq. 2, the attenuation of the shield is:

$$K = \sum_{1}^{N} A_i \, (r_i - r_{i-1})$$

or

$$K + r_0 A_1 = \sum_{1}^{N} r_i \, (A_i - A_{i+1}) = K' \tag{3}$$

and the shield weight for the spherical case is given by:

$$W = \frac{4}{3} \pi \sum_{1}^{N} \rho_i \, (r_i^3 - r_{i-1}^3)$$

or

$$\frac{1}{4\pi} W = \sum_{1}^{N} \frac{r_i^3}{3} (\rho_i - \rho_{i+1}) - \frac{r_0^3}{3} \rho_1 \, . \tag{4}$$

What is now required is to minimize the shield weight subject to the condition of Eq. 3. We therefore construct the Lagrangian.

$$L = \frac{1}{4\pi} W - \mu K', \tag{5}$$

where μ is the Lagrangian multiplier.

The radii of the various layers of the minimum weight shield will then be obtained by minimizing L with respect to each r_i. Setting the derivatives of L with respect to each r_i equal to zero, we obtain:

$$r_i = \sqrt{\mu}\ \frac{(A_i - A_{i+1})^{1/2}}{(\rho_i - \rho_{i+1})^{1/2}} \ . \tag{6}$$

μ can then be obtained by substitution in Eq. 3 giving the following expression for the radius of each layer of a spherical shield:

$$r_i = \frac{K_0 + r_0 A_1}{\left[\sum_1^N \frac{(A_n - A_{n+1})^{3/2}}{(\rho_n - \rho_{n+1})^{1/2}}\right]} \ \frac{(A_i - A_{i+1})^{1/2}}{(\rho_i - \rho_{i+1})^{1/2}} \ . \quad i = 1, 2, \ldots, N \tag{7}$$

In order to investigate the application of the theory to a spherical shield, the parameter K/r_0 is used. The abscissa in Fig. 3 shows how different shielding materials enter the minimum weight shield as K/r_0 varies. For example, for the smallest practical value of void radius r_0 which can be considered, i.e., 25 cm or a small man-sized shield, a shield having a shielding equivalent of 20 g/cm^2 ($K/r_0 = 0.3$) would consist of iron, carbon and polyethylene in that order. If a shielding equivalent of 30 g/cm^2 ($K/r_0 = 0.44$) is desired, copper would also be a component of the minimum weight shield. On the other hand, if the shielded volume has a radius of 100 cm, below a shielding equivalent of about 22 g/cm^2 ($K/r_0 = 0.08$), the minimum weight shield consists only of polyethylene. Carbon must be added if higher shielding equivalents are desired but iron is not included in such a shield till a shielding equivalent of 55 g/cm^2 ($K/r_0 = 0.20$) is specified.

Conditionally Optimized Shields

The shield synthesis technique has been extended to include certain constraints which make the configurations more realistic. Two cases in particular have been considered:

1. The shield includes up to a certain volume, V, of a given material which primarily serves purposes other than shielding, e.g., electronic gear.
2. The shield must contain a shell of a given thickness of a given material, e.g., an aluminum "skin."

For the first case where the given material to be included is simulated by aluminum, Fig. 3 shows how the makeup of the shield changes both as a function of the amount of aluminum required and of K/r_0. The parameter used for the ordinate, the cube root of V over $4/3\,\pi r_0^3$, is essentially the ratio of the radius of the sphere of Al required, to the radius of the shielded void.

For the second case, for shielded regions of reasonable size with the necessary inclusion of an aluminum or titanium layer 1 cm thick, the minimum shield will consist of the metallic layer lying inside a layer of polyethylene. For both the special constraints we have discussed, the position of the required material in the shield is determined by its place on the "Young Diagram." However, depending on the value of K/r_0 and the amount of the required material to be included, one or another of the materials in the "Young sequence" may be omitted.

Treatment of Secondary Neutrons

Theory

It is believed that a significant contribution to the total dose inside a shielded vehicle traversing a proton flux region will be due to secondary neutrons arising from the interaction of the protons with the shielding material. We have, therefore, extended our shield optimization technique to include the effect of secondary neutrons. The model which was used is based on the following assumptions:

1. The secondary neutron flux inside the shielding material is a function of the incident proton flux at the outside of the shield and must be calculated explicitly for each proton environment. It is also obviously a function of the shielding material.

2. A power law dependence is assumed both for the impinging proton spectrum (Eq. 8) and for the proton attenuation in aluminum (Eq. 9), i.e.,

$$P_0(R,E') = C_1 [E'^{M} + \alpha]^{-1} \text{ , and} \tag{8}$$

$$\frac{dE}{dr} = C_2 E^{-N} , \tag{9}$$

where C_1, M, and α are constants determined by the particular proton environment and C_2 and N are determined by the properties of aluminum. For the solar flare of May 10, 1959, for example, we have taken $C_1 = 3.19 \times 10^{17}$ and M = 5. With $\alpha = 0$, this is an approximation to the Winckler spectrum[2] for that flare though in practice we have cut it off at about 7 Mev, the threshold of the (p,n) cross section for aluminum. When α is set equal to 5×10^6, the impinging proton spectrum is an approximation to the NASA spectrum[3] for that flare. Both of these calculated spectra are shown in Fig. 4.

From this, and using the previously given definition of K(r), viz.,

$$K(r) = \int_E^{E'} \frac{dE}{f(E)} = \int_r^R A(r)\, dr, \tag{10}$$

one can calculate the proton flux, P(r,E), throughout the shield as a function of position and energy. P(r,E) has the form:

$$P(r,E) = \frac{C_1 \left\{C_2[N+1]\, K(r) + E^{N+1}\right\}^{-\frac{N}{N+1}} E^N}{\left[C_2(N+1)\, K(r) + E^{N+1}\right]^{\frac{M}{N+1}} + \alpha} . \tag{11}$$

From this proton flux the secondary neutron source can be obtained from the expression:

---

2. J. R. Winckler and P. S. Bhavsar, J. of Geophys. Res., 65, 2637 (1960).

3. J. R. Winckler, Primary Cosmic Rays, Proceedings of Conference on Radiation Problems in Manned Space Flight, edited by G. J. Jacobs, NASA TN-D588, Appendix A (1960).

$$S\,[K(r)] = \int_0^\infty P(r,E)\ \sigma_{eff}(E)\,dE, \tag{12}$$

where $\sigma_{eff}(E)$ is the effective (p,n) cross section which takes into account multiple neutron production. The effective (p,n) cross sections as used were composed of two parts, those for the production of isotropic "evaporation" neutrons and those for the production of straight ahead "cascade" neutrons. The cross sections for evaporation were multiplied by 3/8 to take into account the isotropy of those neutrons. Figure 5 shows a typical curve of S[K(r)]. The point marked r = 0 is the asymptotic value of S for zero shielding thickness. S[K(r)] in any material is assumed proportional to the secondary neutron production in aluminum, viz.,

$$S[K(r)] = z(r)\ S_{Al}\,[K(r)]\,, \tag{13}$$

where z(r) is a function only of the material at r.

Finally, the total neutron production, $\Sigma\,[K(r)]$, is calculated from S [K(r)] by

$$\Sigma[K(r)] = \int_0^{K(r)} S\,[K(r')]\,dK(r')\,. \tag{14}$$

It turns out that relatively large differences in the shapes of the curves of the effective (p,n) cross section as a function of energy result in relatively small differences (< 10%) in the shapes of the capital sigma curves. This has been borne out for Al, C, and Cu, the only elements for which we could find sufficient (p,n) data. Figure 6 shows a typical curve of the total neutron production for an approximation to the NASA spectrum for the flare of May 10, 1959, for which $\alpha = 5 \times 10^6$. For this case more than half of the neutrons are produced in the first few millimeters of aluminum.

The final assumption in the complete model is the exponential attenuation of the secondary neutrons using a parameter y(r) which is a function of material only. Because of lack of data on the energy spectrum of secondary neutrons from proton bombardment, the neutron

attenuation parameters used were calculated from the removal cross sections for fission neutrons.

Whereas in the pure proton case we had only two parameters A and ρ, when production and attenuation of secondary neutrons is included, we have four parameters, z and y being the additional ones. The materials defined by these four parameters are now to be plotted in a four-dimensional space, all the materials and their mixtures lying either inside or on a hypersurface P. This hypersurface is defined by a collection of tetrahedra, each tetrahedron in turn being defined by a set of four material points in the four-dimensional coordinate system A, y, z, ρ. This replaces the two-dimensional graph which was described previously, and which led to the "Young Diagram." Mixtures of materials are now possible since it was shown by Troubetzkoy[1] that up to an (n-1) material mixture is possible where n is the number of parameters used. Hence, for proton attenuation alone, only pure material layers are allowed, whereas for the present four parameter case, shielding layers consisting of up to three materials are possible.

The method of Lagrange multipliers is again used to determine the shield configurations and requires that the total weight be minimized with respect to the four parameters subject to the constraints that:

1. the total dose (both from primary protons and secondary neutrons) to the inside of the shield be equal or less than a certain specified dose $\overline{D}$, and
2. a point (A,y,z,ρ) lies inside or on the hypersurface P.

The results show that:

1. in joining two regions in the optimum shield, it is permissible to add or delete only one material;
2. the innermost and outermost regions must be composed of pure materials.

Figures 7 and 8 give the possible shield configurations for 2, 3, 4, 5, and 6 region shields. The actual materials used in the optimum shields, however, are functions of r_0 and $\overline{D}$. The following comments can be made on these configurations:

1. All materials in adjacent regions must lie on the same tetrahedron of the hypersurface.

2. Three material regions can occur only in relatively complex shields containing five or more regions. Even in a five-region shield such a mixture is contained in only one of six possible configurations. In a six-region shield, three material mixtures are contained in only two of ten possible configurations.

Numerical Results

Because of a lack of sufficient data on (p,n) cross sections, we have only been able to calculate, according to this model, shields containing Al, C, and CH_2. The results of some sample calculations are given in Table 1. The weight savings for the minimum weight configuration for this flare proton spectrum, as can be seen, are small. Aluminum, and presumably iron and copper if they had been included in the calculations, do not enter into the optimum shields for these permitted dose values and void radii. For decreased values of $\overline{D}$, i.e., for heavier shielding requirements, the optimum configuration will be expected to represent an increasingly substantial saving over a one-material shield. Another point to be noted is that for this proton spectrum the dose inside the lightest weight shields is contributed mainly by protons. The materials used, C and CH_2, though they have low values of A_i, produce only small numbers of secondary neutrons. Therefore, for a fairly soft proton spectrum, such as we have used here, their proton attenuation is sufficient to make them the most desirable materials for the optimum shield within the permitted dose requirements we have set. For harder spectra, such as the Van Allen belt or the giant flare of Feb. 23, 1956, better proton attenuators will be required in the optimum shield and other materials besides C and CH_2 will come in.

Extension to Other Geometries

Slater[4] has shown that the shield optimization technique has validity in geometries other than spherical as long as the volume function is a convex function of some typical dimension. As before, one considers the condition that at every point on the shield the cutoff energy for protons is constant. This was originally interpreted as allowing the design of a shield for protons normally incident as this was believed to lead

4. M. Slater, Private Communication.

Table 1. Optimum Spherical Shields for the May 10, 1959 Flare – Effect of Secondary Neutrons is Included

Void Radius, cm	Materials	Total Dose Requirement, rem	Proton Dose, rem	Neutron Dose, rem	Total Weight, kg
0	Al	70	39	31	0.37
0	C	70	64	6	0.16
0	CH_2	70	67	3	0.51
0	C + CH_2	70	65	5	0.15
20	Al	70	39	31	50.9
20	C	70	64	6	32.8
20	CH_2	70	67	3	30.0
20	C + CH_2	70	66.5	3.5	29.9
20	Al	24.3	5.1	19.2	215
20	C	24.3	19.0	5.3	74.5
20	CH_2	24.3	22.3	2.0	70.6
20	C + CH_2	24.3	21.3	3.0	68.3

An RBE of 1.3 is assumed as the average over the energy range of the protons.

to a conservative result since protons entering normally would be attenuated less than protons coming from any other direction. This turned out not to be strictly true for certain shield regions but the errors involved have been calculated and turn out to be extremely small (fractions of a percent).

The problem of the minimum weight shield was solved for the general case of a convex volume void assuming normally incident particles, again using the method of Lagrange multipliers. The particular cases of the right cylinder, cone, and truncated cone were investigated. For the particular case of the right cylinder of inner radius r_0 and height h_0, the radius of the i^{th} circular shell in the shield is given by:

$$r_i = \left[\frac{K + r_0 A_1}{\sum_{1}^{N} \frac{(A_n - A_{n+1})^2}{(\rho_n - \rho_{n+1})}} \right] \left(\frac{A_i - A_{i+1}}{\rho_i - \rho_{i+1}} \right) . \qquad (15)$$

The same expression gives the radii of the various conical shield regions for a cone of the same height and base radius as the right cylinder, if for r_0 in Eq. 15 we substitute S_0, the normal distance from the axis of the cone to the void surface. In the conical shield each shield layer is bounded by a conical surface and the number of materials required varies with S_0, decreasing for a complete cone, from the total number available from the Young Diagram, at the top of the cone, to a smaller number as one proceeds toward the base. For truncated cones, the number of materials used even at the top of the cone can be less than the total number available and depends on the relative values of the upper and lower radii of the cone.

Table 2 compares several convex optimum shields of different shapes and sizes with all aluminum and all polyethylene shields. It is seen that, as in the case of spherical shields, the percentage weight saved by using an optimum configuration increases with decreasing void radius and with increasing prescribed attenuation.

Some attempts have been made to ease the constraint that the shield be required to remove all incident protons of energy below a certain specified energy, particularly for volumes near the bottom of the cone. In the calculations carried out thus far, additional weight savings have been achieved and by applying the method to other less important portions of the shielded volume still lighter shields may be obtained.

Table 2. Optimum Convex Shields of Several Types

Type of Void	Height, cm	Radius, cm	Attenuation, cm of Al	Shield Weights: Optimum, kg	Shield Weights: All Al, kg	Shield Weights: All CH_2, kg	% Savings
Conical	200	50	3.7	338	439	362	7
Conical	200	50	11.1	1195	1573	1470	23
Conical	200	25	11.1	621	813	857	31
Cylindrical	200	25	11.1	1102	1366	1312	19
Cylindrical	100	10	11.1	266	360	430	35
Cylindrical	200	50	11.1	2112	2644	2218	5
Truncated conical	200	Lower 100 Upper 50	11.1	3478	4555	3792	9
Conical	100	100	11.1	2090	3258	2788	33

Conclusion

Though for usable voids (25 cm in radius or greater), the optimization method for the spherical case reveals that a simple one- or two-layer carbonaceous shield is best, the method can provide much useful information for space shield design for the more practical nonspherical shapes and special constraints. In addition, as more shielding is required, say for longer space voyages, the method should also prove useful.

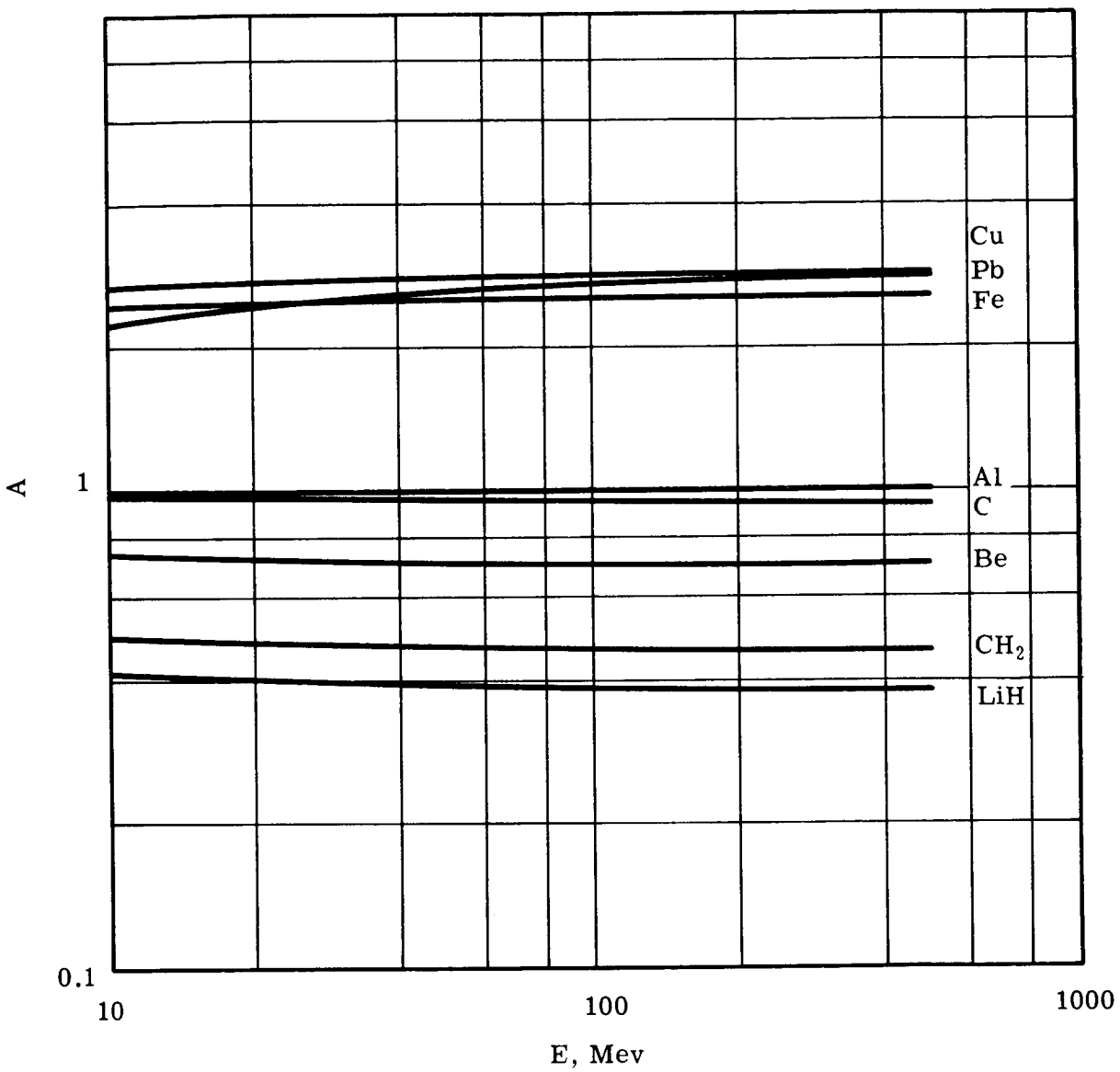

Fig. 1 — The Proton Relative Stopping Power as a Function of Proton Energy for a Number of Elements and Compounds (Al is taken as the standard)

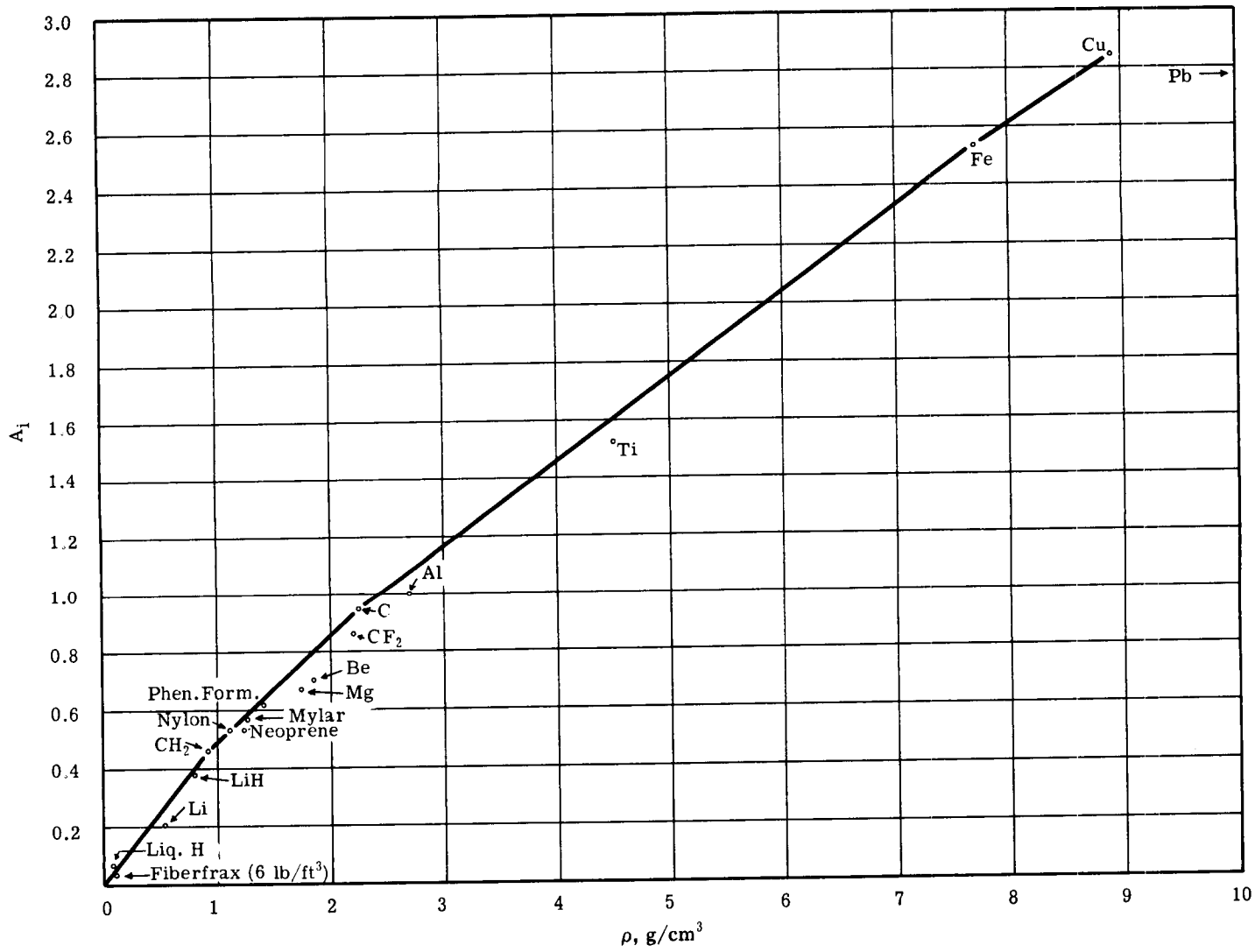

Fig. 2 — Proton Relative Stopping Power (calculated for 300 Mev protons), as a Function of Material Density for a Number of Elements and Compounds

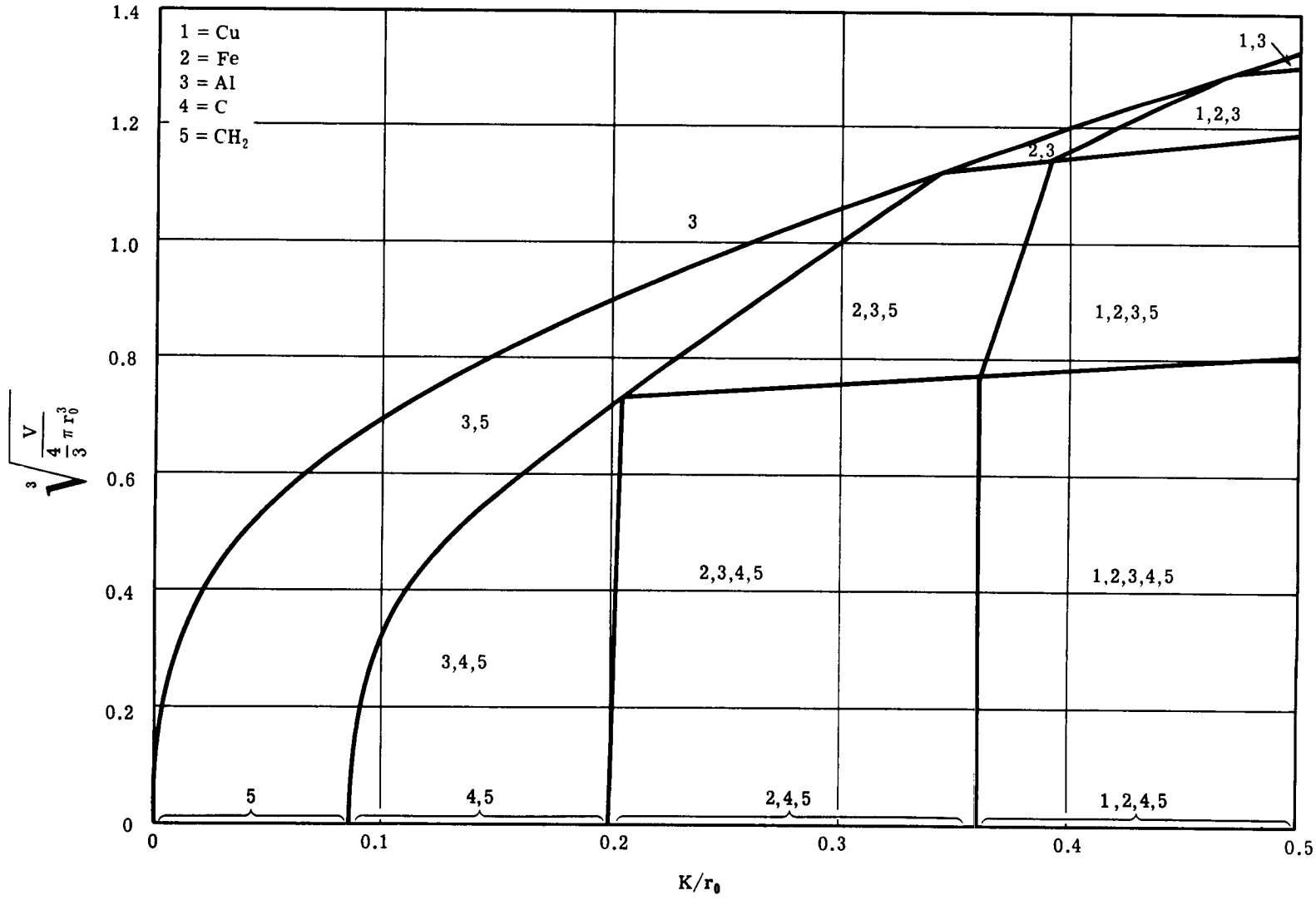

Fig. 3 — Materials to be Included in an Optimized Spherical Shield as a Function of K/r_0 and Required Amounts of Aluminum

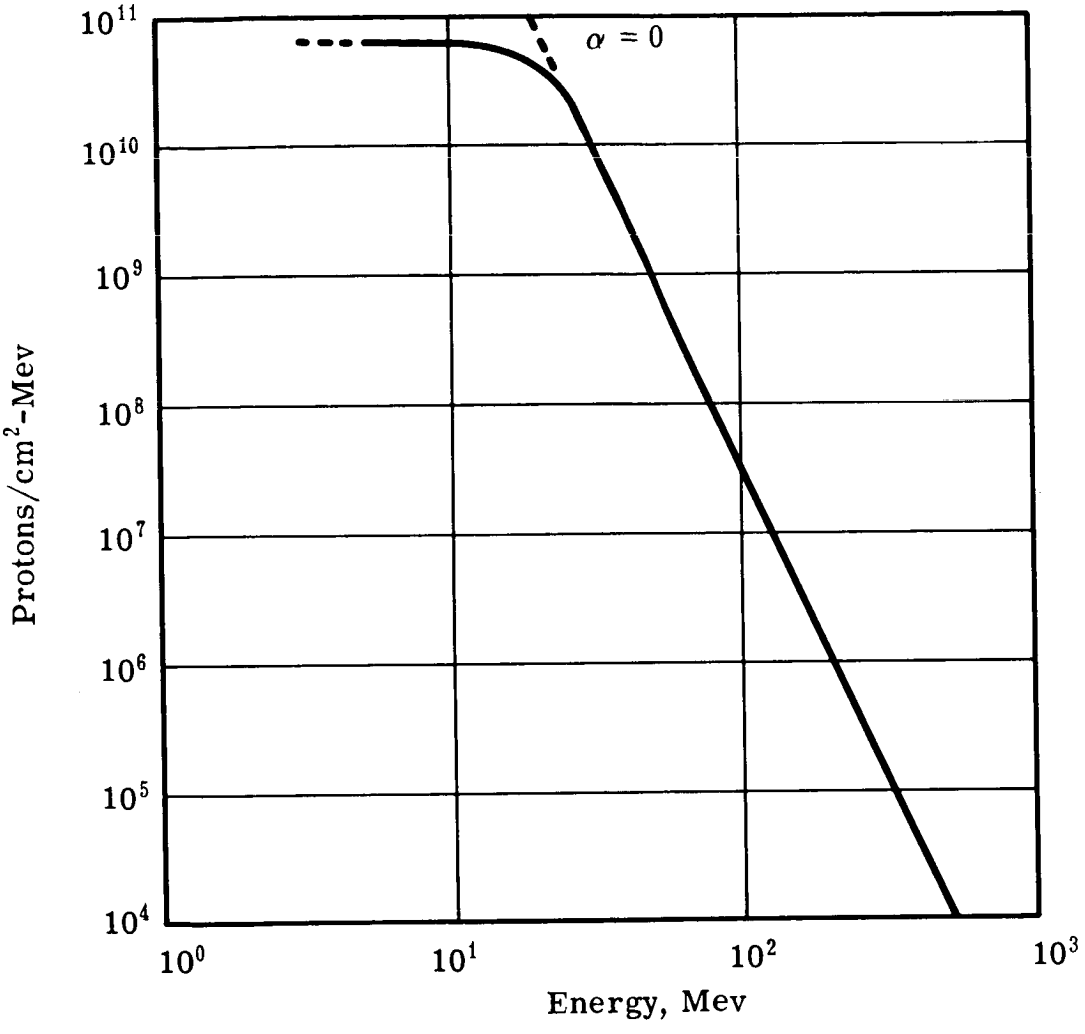

Fig. 4 — Calculated Approximation to the Proton Spectrum of the Flare of May 10, 1959; $\alpha = 0$ – Winckler Spectrum; $\alpha = 5 \times 10^6$ – NASA Spectrum.

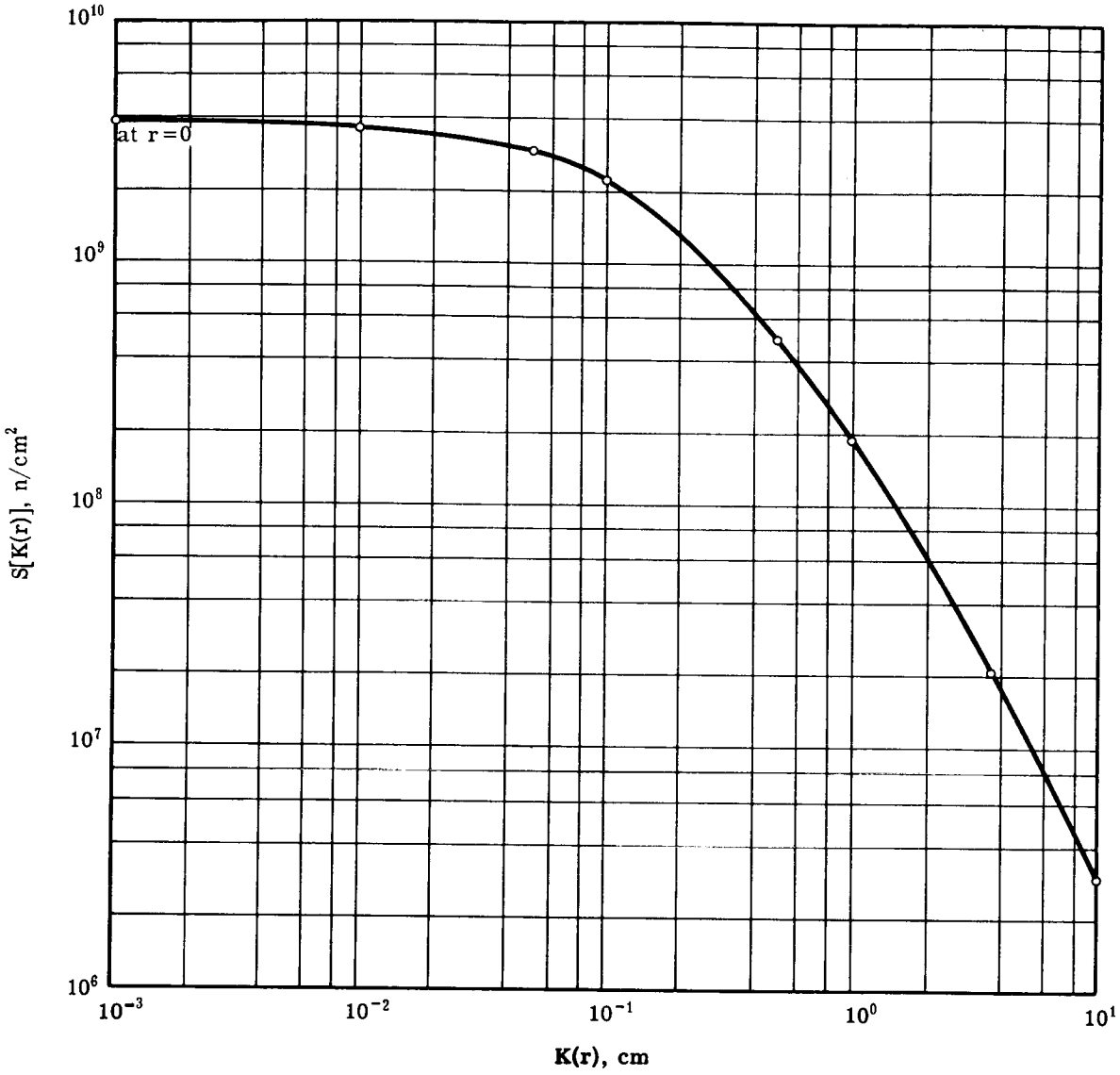

Fig. 5 — Secondary Neutron Source Inside the Shielding Material as a Function of the Equivalent Depth into Aluminum for the May 10, 1959 Flare – NASA Spectrum

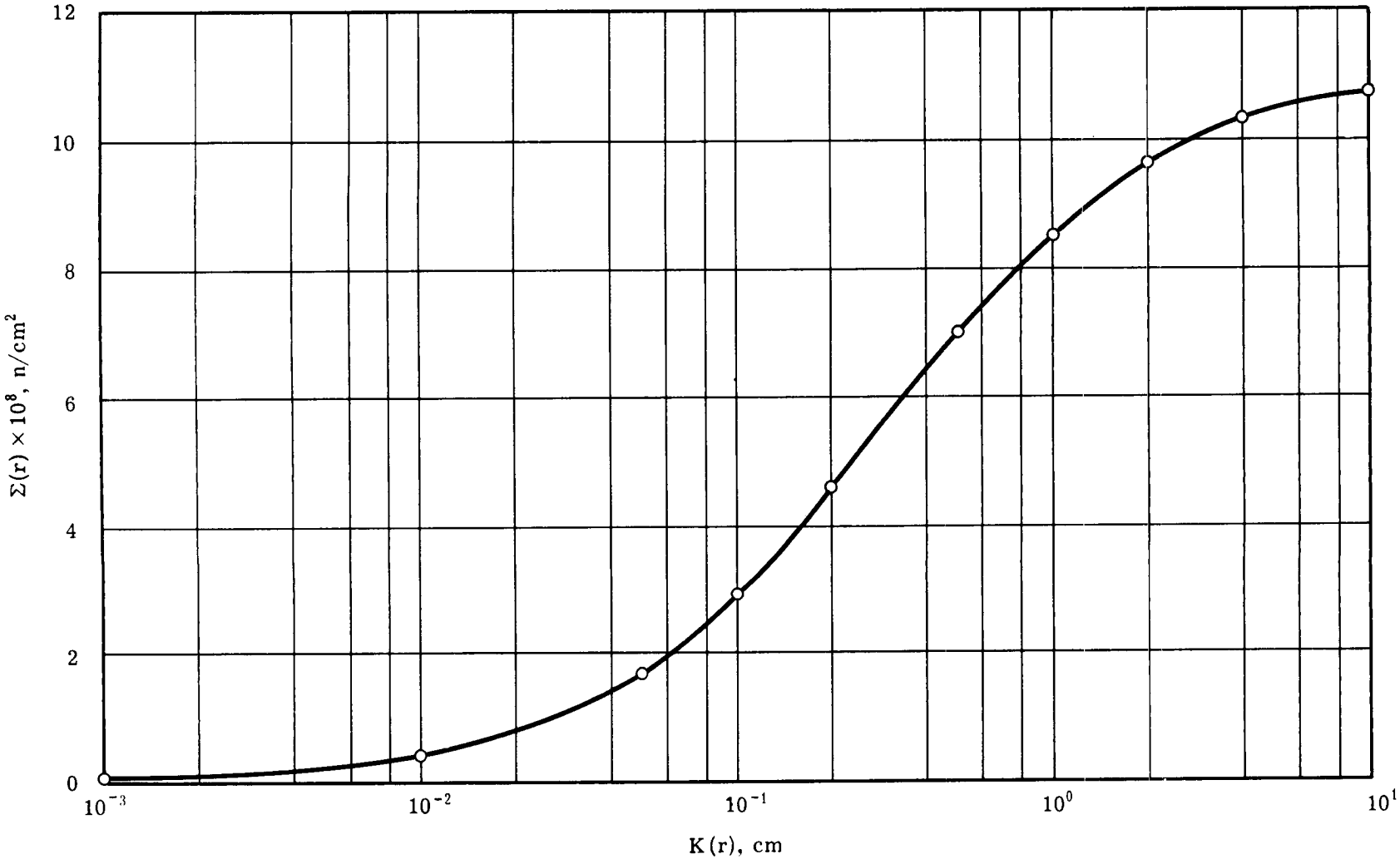

Fig. 6 — Total Secondary Neutron Production as a Function of Equivalent Thickness of Aluminum for May 10, 1959 Flare – NASA Spectrum

Two-region shield

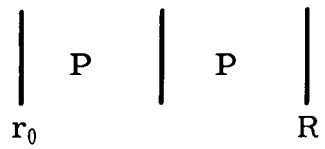

P = pure material
2M = two-material mixture
3M = three-material mixture

Three-region shield

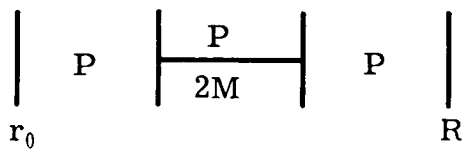

Four-region shield

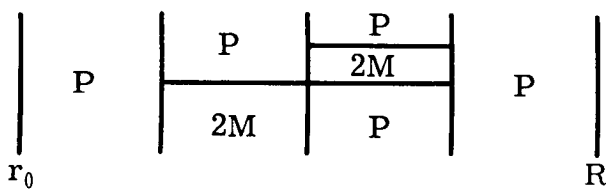

Five-region shield

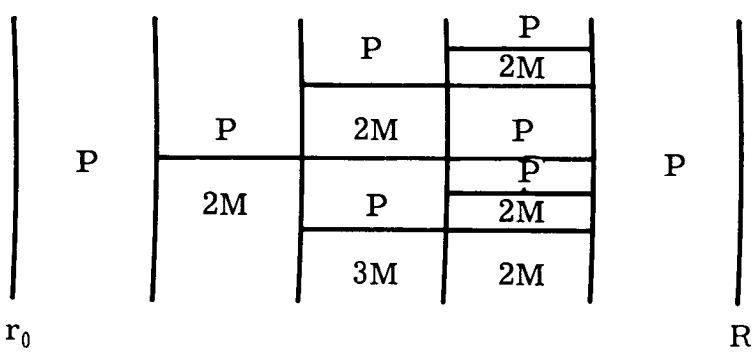

Fig. 7 — Possible configurations for shields containing from 2 to 5 regions

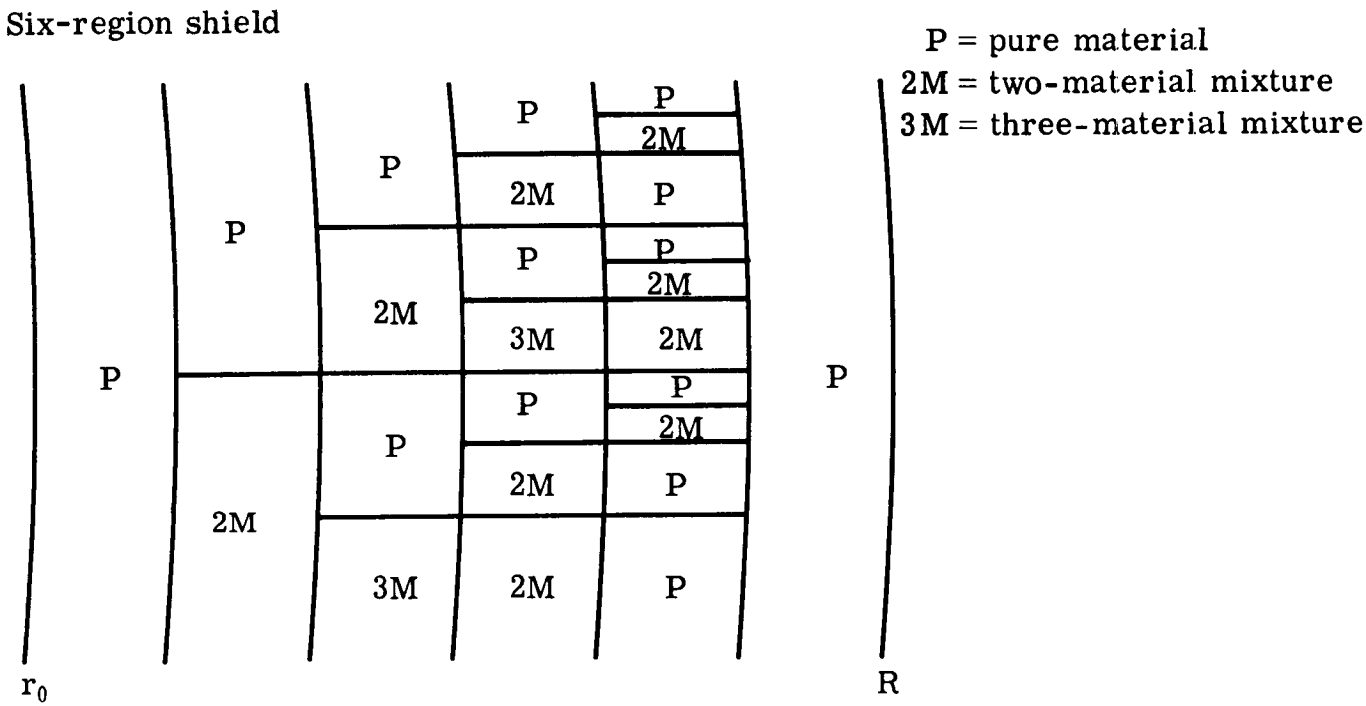

Fig. 8 — Possible configurations for shields containing 6 regions

Paper F-1

THE PROSPECTS FOR ACTIVE SHIELDING*

R. H. Levy**

Avco-Everett Research Laboratory
Everett, Massachusetts

I. Introduction

Shielding the astronaut against the various forms of penetrating radiation likely to be encountered on a space trip is one of many difficult problems facing the space ship designer. Perhaps it is fair to say that at this stage it is the most uncertain of all the environmental factors which must be considered in the design.

Estimates of the shielding required for the first travelers to the moon are low, but as permissible doses decline, the shielding requirement will increase. Again, we may anticipate a desire to fly extended missions in those regions near the earth (or other planets) where substantial fluxes of trapped radiation are to be found, thus imposing a severe shielding requirement on the designer. Interplanetary travel involving substantial transit times will make the occurrence of large solar flares during the trip virtually certain, and here again a sizable shielding problem is involved. Finally, for any mission, as the number of individuals undertaking it increases, permissible radiation doses will decrease, so that shielding will inevitably grow in importance as the era of space flight progresses.

It is the purpose of this note to make some general remarks on various methods of shielding which might be used other than the standard one of interposing a substantial amount of matter between the astronaut and the radiation. The importance of such methods is directly related to the

* This work was supported by the Office of Naval Research, Department of the Navy, under Contract No. Nonr-2524(00).

** Principal Research Scientist.

weight involved in bulk shielding. We shall in this note consider only the radiation hazard due to high energy protons since it appears at present that such protons constitute the most important natural source of danger to the astronaut.

II. Electrostatic Shielding

In order to stop a proton with an electrostatic field, the necessary potential rise in the field (in volts) must be numerically equal to the energy of the proton (in electron volts). Thus, one must at once consider potentials in the order of 10^7 to 10^9 volts.

Two methods of obtaining such potentials may be discussed. In the first, one maintains a positive charge on the space ship such that its potential relative to infinity has the required value V. This has the immediate result that electrons will bombard the ship, each having an energy equal to V electron volts. Thus, one has exchanged one form of radiation for another. Since the stopping of electrons with such energies will involve substantial production of highly penetrating bremsstrahlung, the advantage of such a method is not obvious. Furthermore, in order to maintain the potential, one would have to accelerate electrons away from the ship with this same energy V. This operation is quite difficult by itself, but, in addition, will consume a substantial amount of power.

An alternative method of generating the required potential drop would be to maintain it between, say, two concentric spherical shells. The achievement of the necessary potentials in this way is at present beyond the reach of ground based machines; and the space environment would not appear to make the problem any easier, especially since the conductors would both be essentially unshielded against galactic cosmic rays.

III. Magnetic Shielding

Magnetic shielding using superconducting field coils appears to offer an attractive shielding method provided only that the engineering problems involved in the construction of the large coils involved prove to

be tractable. It has been shown[1] that in such a shield the heaviest item by far would be the structure required to contain the magnetic stresses. In this note we shall use a theorem[2] on the minimum (ideal) weight of this structure to estimate the minimum (ideal) weight of a magnetic shield. In this way we will obtain some impression of the gains which are potentially available in a magnetic shield.

The structural weight theorem states that if it is required to confine a magnetic field containing energy E_M by using a structural material having density ρ and allowable stress σ, the mass of material required (M_s) is always greater than $E_M (\rho/\sigma)$,

$$M_s \geq \frac{\rho}{\sigma} \quad E_M \tag{1}$$

The equality holds only if each element of the structure is in tension and at its allowable stress. The quantity ρ/σ is a property only of the structural material. For our purposes it is conveniently quoted in kilograms of structure per joule of stored magnetic energy, but may be more familiar when quoted as a specific strength in inches, being the length of a wire of the material that could support itself under gravity. Two examples are quoted in Table I, the one for aluminum being somewhat conservative, and the one for titanium being somewhat optimistic.

Table I

Strength of Materials

	Aluminum	Titanium (-423°F)
Stress	50,000 psi	230,000 psi
Strength to Weight	7.8×10^{-6} kg/joule	2.9×10^{-6} kg/joule
	$.52 \times 10^{6}$ inches	1.4×10^{6} inches

An extremely simplified view of the shielding problem is shown in Fig. 1. We consider the surface of a shielded region. Outside this surface we have a uniform magnetic field B parallel to the surface; the thickness of the magnetic field is Δ. Now it is clear at once that if proton trajectories are to be strongly affected by the magnetic field, the thickness of the

magnetic field must be of the order of the proton Larmor radius. A more detailed study shows that the "worst" proton is the one that approaches in the direction illustrated in Fig. 1. To shield against this proton it is clear that Δ must be one Larmor diameter. Thus, $\Delta = 2p/eB$ where p/e is the momentum to charge ratio of the incident proton. Now, the energy in the field per unit surface area is just $(B^2/2\mu_o) \cdot \Delta$, and with this surface distribution of energy we can (by the structural theorem) associate a structural mass per unit surface area. This mass per unit area can be regarded as a "range" in the same sense that once calculates the "range" of a proton in a solid material. Denoting it by R_B we find

$$R_B = \frac{\rho}{\sigma} \quad \frac{B^2}{2\mu_o} \cdot \Delta = \frac{\rho}{\sigma} \quad \frac{(2p/e)^2}{2\mu_o} \cdot \frac{1}{\Delta} \qquad (2)$$

With this formula we can now compare, say, aluminum as a bulk material for stopping protons and aluminum as a structural material for supporting field coils for stopping protons. This comparison is shown in Fig. 2 for a value of ρ/σ between the two values quoted in Table I.

The first thing to note from this figure is that magnetic shielding improves as we go to larger sizes and lower fields. Of course, at some point it is no longer reasonable to neglect the contributions of the superconductor, insulation, etc. to the total mass; but the general trend of the numbers is certainly correct.

Since the results shown in Fig. 2 appear to be encouraging, it is appropriate here to list the idealizations which led to them, and which will be violated, more or less, in a real system.

1. Every element of the structure is in tension, and the cross section of each element is such that the tension is the maximum allowable.
2. The magnetic field is uniform and parallel to the surface of the shielded region.
3. The weight of the system is entirely in the structure required to support the magnetic stresses.

We will not in this note proceed to more detailed consideration of the errors involved in these assumptions; we will, however, define the

limit on how much progress can be made in the direction of reducing the weight of a magnetic shield simply by increasing its size and decreasing the field strength.

It is clear that one cannot expect to gain much beyond the point where Δ becomes of the order of the size of the shielded region. We will make this point quantitatively by resorting to a further idealization. We imagine a spherical shielded region or radius R, as illustrated in Fig. 3, surrounded by a magnetic field of thickness Δ. Now this configuration is topologically impossible since div B = 0 and a magnetically shielded region must always be multiply connected. Thus, in considering the results we will obtain from the idealization of Fig. 3, we will have to bear in mind that there is a topological factor to be considered in estimating real weights; or, alternatively, some part of the surface must be shielded by solids. With this limitation in mind we proceed by noting that Δ must still be one Larmor diameter. The volume occupied by the magnetic field is

$$\frac{4\pi}{3} (R + \Delta)^3 - \frac{4\pi}{3} R^3 \tag{3}$$

so that the minimum structural mass is, from Eq. (1),

$$M_s = \frac{\rho}{\sigma} \frac{1}{2\mu_o} \left(\frac{2p}{e}\right)^2 \frac{4\pi}{3} \left[\frac{3R^2}{\Delta} + 3R + \Delta\right] \tag{4}$$

The last term in this expression clearly has a minimum when $\Delta = \sqrt{3}\, R$ verifying our assertion that Δ should be of the order of magnitude of the size of the shielded region. With this value of Δ, the minimum weight is

$$M_s = \frac{\rho}{\sigma} \frac{1}{2\mu_o} \left(\frac{2p}{e}\right)^2 \frac{4\pi}{3} (3 + 2\sqrt{3})\, R \tag{5}$$

and this quantity is shown in Fig. 4 for various values of the proton energy. Also shown in Fig. 4 are the corresponding weights for solid spherical shields having thicknesses appropriate to the proton energy. It is seen that here again for all reasonable sizes of the shielded volume and energies of the incident proton stream there is an advantage to be realized by shielding magnetically. However, this is, as has been pointed out, an idealized

calculation. It is not possible at present to estimate with much precision just what penalty is involved in going from the idealized situation of Fig. 4 to some real situation. However, in Fig. 5 a shield is illustrated for which the weight was calculated in Ref. 1. For 100 m^3 shielded volume and for 1 Bev protons the weight was found to be about 3×10^5 kg, and this point is marked on Fig. 4 as a "Real Magnetic Calculation." The difference between this weight and the ideal weight of 10^4 kg can be interpreted as a measure both of the prospects for magnetic shielding and of the ingenuity which has to date been exercised in the design of such shields. Further study of magnetic shields is clearly warranted and some effort should be made to pin down the real weight and operating problems involved with actual hardware. In this connection it is worth pointing out that each kg of structure in Fig. 4 corresponds to something on the order of a megajoule of stored magnetic energy. The superconducting coil with the largest energy storage known to the author to be presently functioning[3] has an energy storage of 45,000 joules, at leat three orders of magnitude smaller than anything that might be useful for radiation shielding.

IV. Explosive Shielding

One final method of shielding seems worthy of mention, although its operation is many orders more undertain than those discussed. Furthermore, the reason for discussing it is chiefly to point out that it apparently cannot be done.

The method in question is illustrated in schematic form in Fig. 6. The principle is as follows: An explosion with a yield in the megaton range takes place in an ionized medium containing a weak magnetic field. A large fraction of the energy released in the explosion is tied up in the kinetic energy of the debris of the bomb, its case, etc. All this material can be expected to be ionized, and in its expansion it will interact with the ambient magnetic field in such a way as to make a large bubble empty of both field and plasma. In this way the field lines in the interplanetary plasma will be bent around the outside of the bubble, and individual high energy protons might be expected to follow these field lines around the outside of the hole.

The difficulty with this method is not in protecting the space ship from the effects of the explosion, for the size of the bubble must be many times the radius of the earth and the bomb could easily be exploded a safe distance from the ship. In fact, it seems likely that such a bubble could be made and might persist for some minutes. However, the magnetic field produced in this way cannot exclude the high energy protons even in the extreme case where the size of the bubble is large compared to the Larmor radius of the incident protons. For it is easy to find proton paths which go through the bubble. The existence of such paths, when taken together with the form of Liouville's theorem suitable for the motion of charged particles in a magnetic field,[4] guarantees that the flux in the interior is just the same as that in the exterior. Thus, no advantage appears possible from this method.

In conclusion it may be worth pointing out that this is a fortunate circumstance. For if it were not so, one might expect the magnetosphere to act somewhat like the bubble described above, in that the interplanetary field lines to some extent go around it. Then, if there were a shielding effect, we would have to conclude that measurements of the flux of solar protons made within the magnetosphere were suspect and that the intensity of these protons in free space might be much higher than suspected. There is, at present, no evidence of such an effect, although there is not much evidence from beyond the magnetosphere.

Acknowledgment

The author wishes to thank Dr. H. Petschek for the many helpful discussions in the course of this work.

REFERENCES

1. Levy, R. H., "Radiation Shielding of Space Vehicles by Means of Superconducting Coils," Avco-Everett Research Laboratory Research Report 106, April, 1961; ARS Journal, Vol. 31, p. 1568, November, 1961.
2. Levy, R. H., "Author's Reply to Willinski's Comment on 'Radiation Shielding of Space Vehicles by Means of Superconducting Coils,'" ARS Journal, Vol. 32, p. 787, May, 1961.
3. Electronics, p. 56, November 16, 1962.
4. Lemaitre, G., "Contributions A La Theorie Des Effets De Latitude Et D'Asymetrie Des Rayons Cosmiques," Ann. Soc. Sci. de Bruxelles, A54, p. 162, 1934.

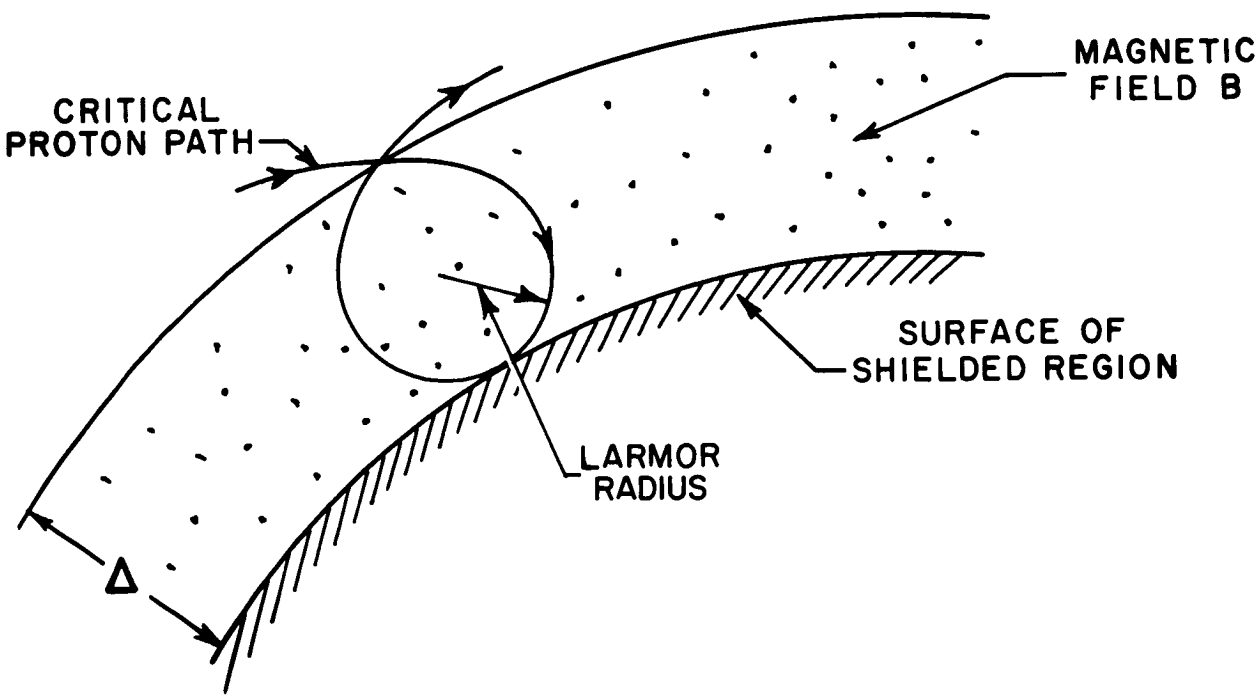

Fig. 1 This figure illustrates in a schematic manner the way in which a surface may be shielded against charged particle radiation with a magnetic field which is parallel to the surface.

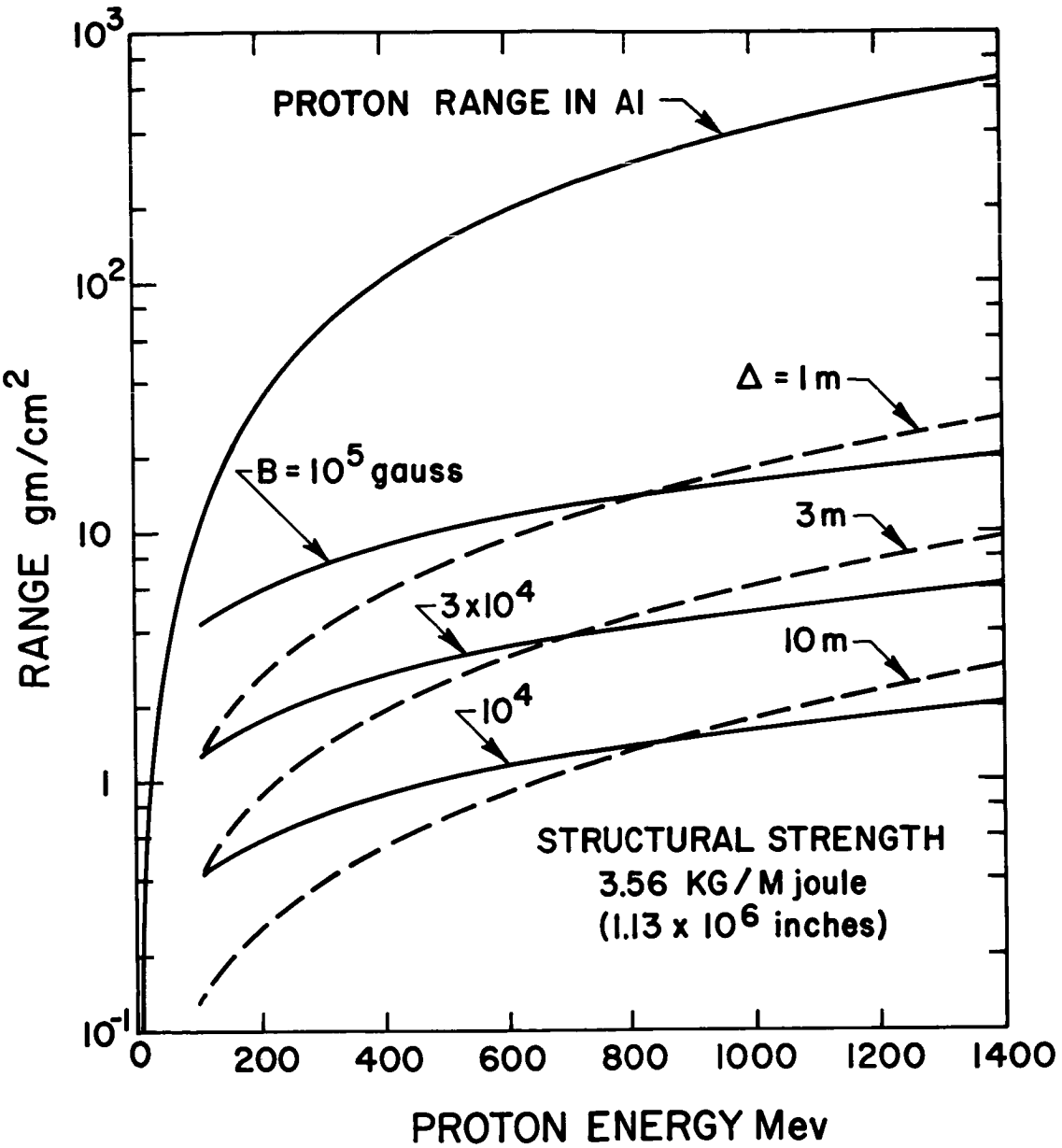

Fig. 2 This graph gives the mass per unit area (under idealizing assumptions) of a magnetic shield and compares it with the mass per unit area of a bulk shield for various field strengths and sizes.

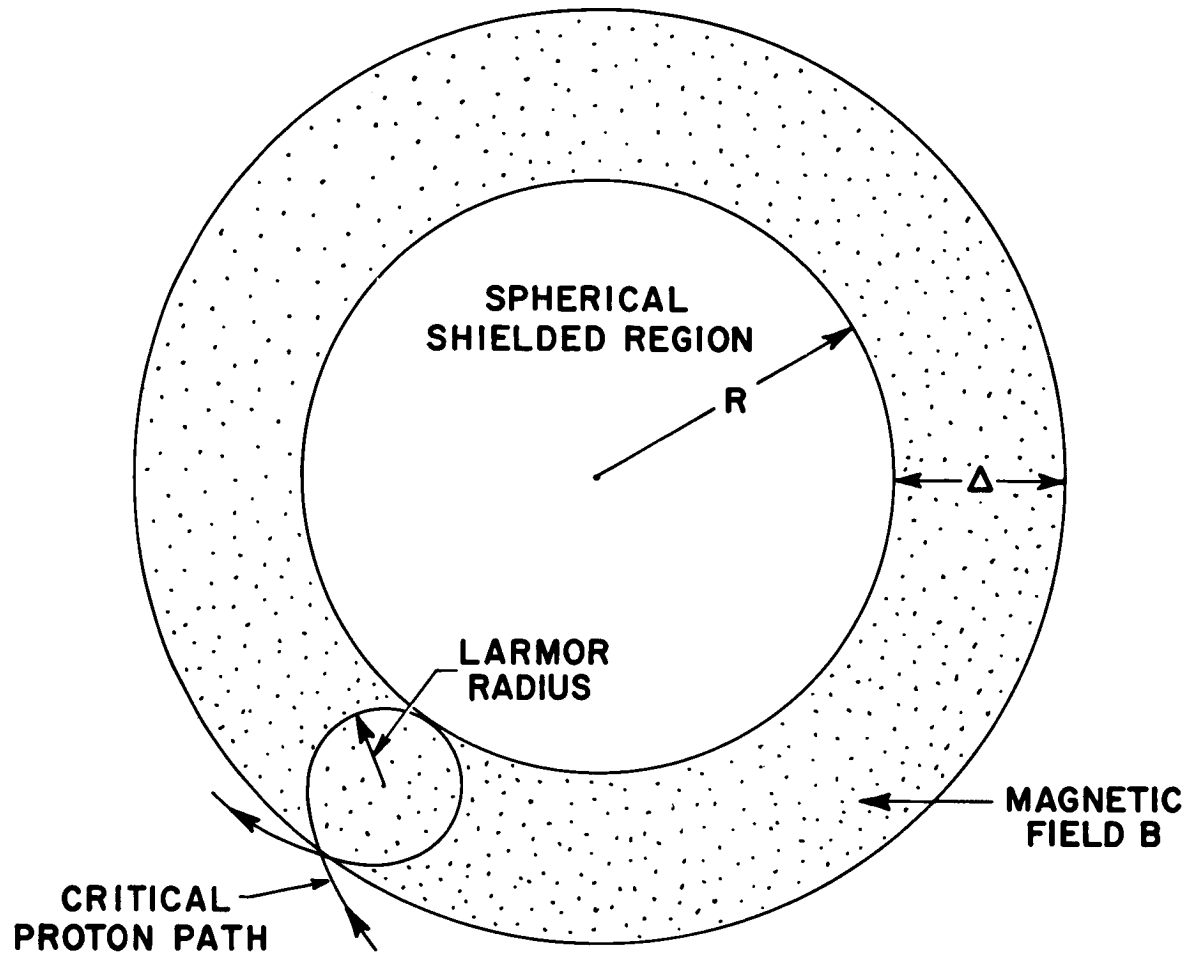

Fig. 3 This figure illustrates in a schematic manner the way in which a spherical cavity might be shielded with a magnetic field. Note that the field configuration shown is impossible; it does, however, represent a reasonable idealization of a practical configuration.

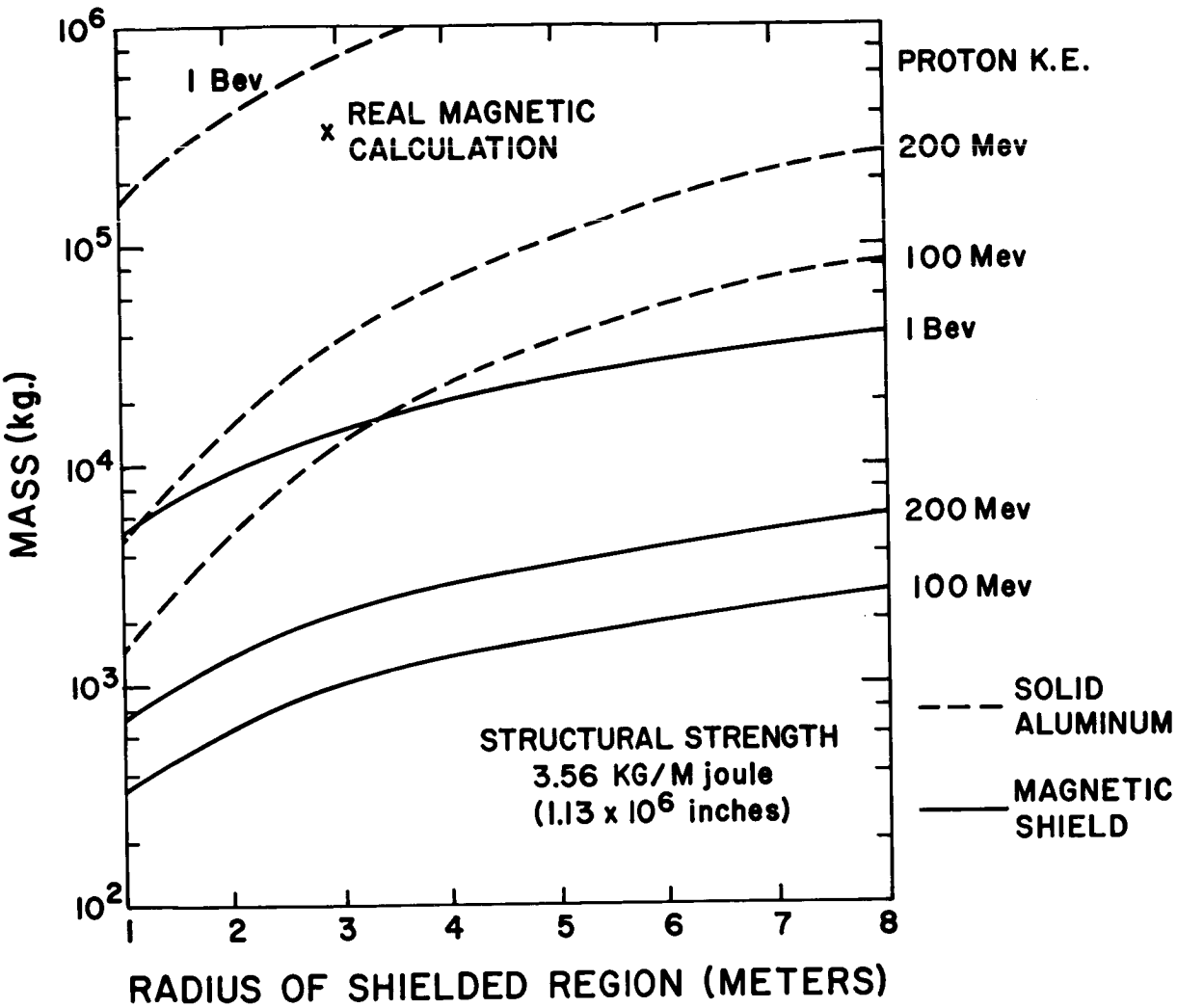

Fig. 4 This graph gives the mass (under idealizing assumptions) of the magnetic shield illustrated in Fig. 3. It also gives the mass of the bulk shield required to perform the same task, not counting secondaries, and, in addition, a more realistic calculation of a magnetic shield from Ref. 1.

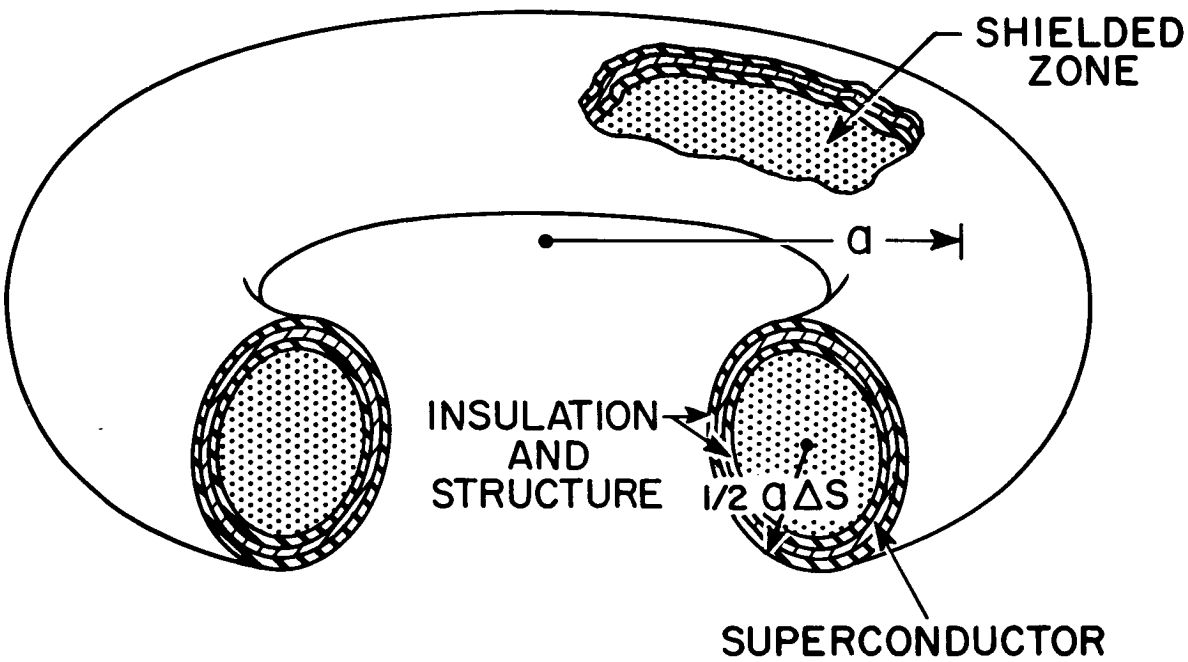

Fig. 5 This magnetic shield was discussed in Ref. 1. The shielded volume is tubular in shape, and the magnetic field is confined to the exterior of the shielded volume.

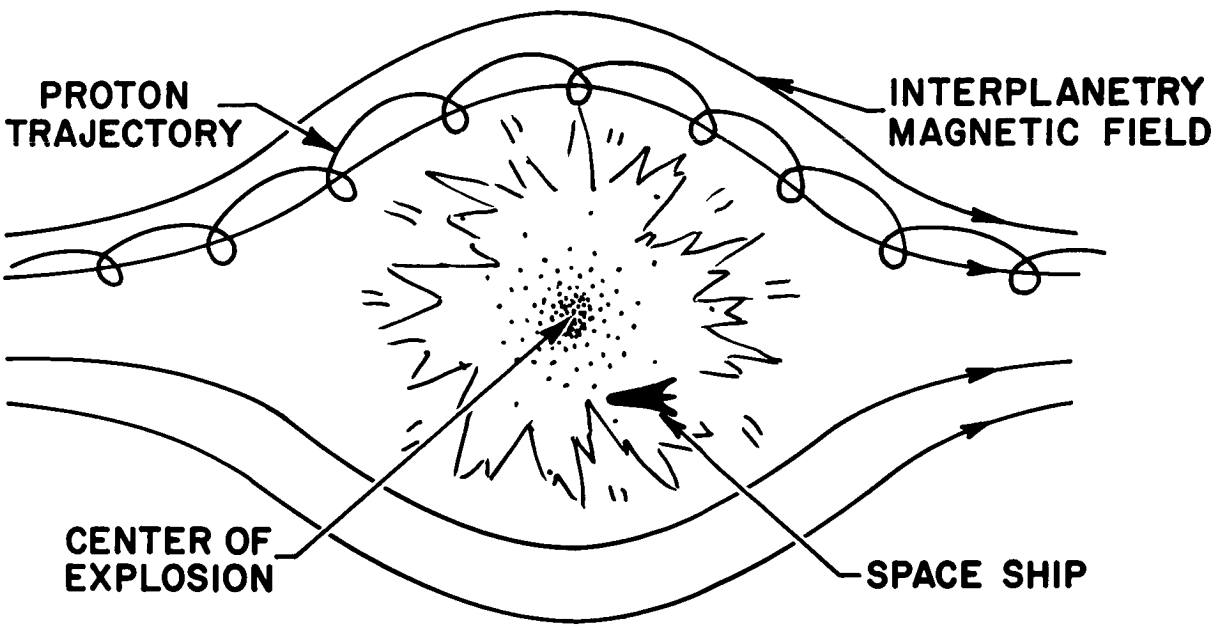

Fig. 6 This figure illustrates the explosive method of shielding discussed in the text. The size of the hole made in the magnetic field should be greater than the Larmor radius of the incident protons.

Paper F-2

SHIELDING OF SPACE VEHICLES BY MAGNETIC FIELDS

N. Edmonson, C. D. Verwers and F. L. Gibbons
General Dynamics/Fort Worth

Abstract

Protons emitted by solar flares represent a significant radiation hazard to crew members of an interplanetary space vehicle. Shielding the vehicle from charged particles by the use of magnetic fields is an obvious possibility. Reduction of secondary radiation otherwise produced in bulk shielding is an added incentive to study magnetic shielding. The feasibility of this type of shielding was reported by R. H. Levy, who utilized the properties of new superconducting materials. A program has been initiated at General Dynamics/Fort Worth to study various aspects of magnetic shielding of space vehicles. In one phase of the program, a procedure has been formulated and coded for the IBM-7090 computer for rapidly computing the field of an optimized superconducting solenoid.

In another phase, samples of NbZr wire have been irradiated with neutral particles from two sources. Preliminary results are now available. Irradiation with 10^{11} neutrons per cm^2 from the D-T reaction showed no change in the critical current versus magnetic field curve. Irradiation with 10^{16} neutrons (>2.9 Mev) per cm^2 showed a slight downward shift in the critical current. It is difficult to say whether this shift was due to the irradiation or due to the environment during the irradiation.

Introduction

A program for studying the magnetic shielding of space vehicles against charged space radiations was initiated approximately a year ago at the NARF facility of General Dynamics/Fort Worth. Two assumptions are basic in this program:

1. Magnetic shielding against charged space radiations is feasible for space vehicles;

2. Superconductors even more effective than existing superconductors will be developed.

The first assumption was based on a study by R. H. Levy[1]. The second assumption was made after a survey of the literature[2,3] and after conferences with many active research workers in the field of superconductivity.

This program was broken down into the subdivisions:

1. Design of optimized superconducting magnets;

2. Shielding effects of magnetic fields against charged particles;

3. Optimized solenoid configurations for shielding prescribed volumes;

4. Structural support design, refrigeration, and power sources for a superconducting electromagnet system;

5. Protection of the superconducting magnet system against quenches;

6. Experimental investigation of the effects of different kinds of radiations, particularly neutrons and protons on the properties of superconducting materials.

Work is being actively carried out on phases 1, 2, and 6. In this paper, a discussion is given of the analytical and experimental activities at GD/FW.

---

1. R. H. Levy, Radiation Shielding of Space Vehicles by Means of Superconducting Coils. Avco-Everett Research Laboratory (April 1961, Contract AF04(647)-278.

2. J. E. Kunzler, "Superconductivity in High Fields." Rev. of Mod. Phys., 33, 4 (October 1961).

3. J. J. Haak, G. D. Cody, P. R. Aron, and H. E. Hitchcock, (RCA Labs, Princeton, N. J.), "Some Physical Properties of Deposited Nb_3Sn." High Magnetic Fields, MIT Press (Cambridge) and John Wiley and Sons, Inc., (New York), 1962.

Problems and Computational Techniques for Superconducting Magnets

For a given temperature in the temperature range for which a given material is superconducting, there is for any transverse magnetic-field strength within a definite range of magnetic-field strengths a current I_c, the critical current, so that for currents less than I_c the superconductor behaves as a superconductor and for currents greater than I_c the superconductor behaves as a conventional or normal conductor. The superconductor goes normal or quenches at $I = I_c$. This experimental fact is added to the classical methods for computing the magnetic fields arising from current-carrying circuits to develop methods for computing the fields due to superconducting electromagnets. For example, at a given location within the windings of a superconducting solenoid, the transverse magnetic field would be the vector sum of the transverse external magnetic field and the field generated by the solenoid. The current carries by the superconducting winding at this point would be fixed from above by this total transverse magnetic-field strength. Methods for computing the magnetic-field intensities generated by superconducting solenoids have been developed by a number of workers[4,5]. These methods are discussed in Reference 6.

To apply these methods, it is necessary to have procedures for rapidly computing the field due to a superconducting solenoid both within and without the solenoid structure.

A IBM-7090 computer FORTRAN code, MAGFI, based on classical formulae for solenoids having a rectangular cross section, has been prepared. This code, furnishes a very fast means for mapping the field of a solenoid.

---

4. R. W. Boom, and R. S. Livingston, "Superconducting Solenoids." 1961 Western Electronics Show and Convention, San Francisco, August 22-25, 1961.

5. W. F. Gauster and C. E. Parker, "Some Concepts for the Design of Superconducting Solenoids." High Magnetic Fields. pp. 3-13. MIT Press (Cambridge) and John Wiley and Sons, Inc. (New York), 1962.

6. N. Edmonson, Magnetic Field Shielding Against Charged Space Radiations. GD/FW Report FZK-9-181 (to be published).

If the magnetic field of a solenoid is mapped by MAGFI, the solenoid requirements for superconducting material and structural support for the superconductors can be reduced in the following way. In general, the maximum field of a rectangular solenoid occurs at the longitudinal midpoint of the inner surface of the solenoid. The field decreases in all directions from this point. Thus, if the solenoid were wound in ring-shaped segments, the number of turns in each segment could be reduced and the current raised in accordance with the critical current-magnetic field relation of the superconducting material, so as to keep the ampere-turn constant. This technique would lead to a reduction in material and size for the solenoid for the same magnetic field strength. An optimization procedure is currently being developed for the IBM-7090.

Shielding Effects of a Magnetic Field

The shielding effect of a magnetic field is investigated by use of Störmer's concept of "forbidden regions" and by computations of the orbits of individual charged particles in a magnetic field.

The basic concepts of Störmer's theory are given in References 7 and 8. Both of these references are concerned with geomagnetic effects on charged particles. The geomagnetic field is approximated by a dipole. For the much smaller space vehicle, the dipole approximation is not sufficiently accurate. A more realistic approach is to compute the vector potential of a loop current. The equivalent solenoid may then be computed. Perhaps a more realistic procedure is to compute a solenoid optimized as described earlier and then to compute the vector potential of each one of the ring-shaped segments of the solenoid. Then the total vector potential of the solenoid is the result of a summation of the elementary vector potentials. The computations of the vector potential of a ring-shaped current is a classical procedure to be found in any advanced treatise on electromagnetism[9]. Its application to the determination of regions open to charged particles and closed (or forbidden) to charged particles is discussed in References 1 and 6.

---

7. M. S. Vallarta, "Theory of Geomagnetic Effects," Handbuch der Physik, Band XLVI/1, 88, Springer, Gottingen, 1961.

8. C. Störmer, Polar Aurora, Clarendon Press, Oxford, 1955.

9. W. R. Smythe, "Static and Dynamic Electricity," 2nd Ed., New York; McGraw-Hill Book Co., (1950).

In applying the Störmer procedure to shielding problems, a shut-off energy is selected, so that the total dose for all charged particles having energies above this shut-off energy is tolerable. For more exact information about the effects of charged particles in the neighborhood of this pre-selected shut-off energy orbit, computations may be necessary. Such computations are classical[7-10].

The Experimental Program

A major goal of the present experimental program at GD/FW is to investigate the effects of neutral particle irradiation on a superconducting material. At present, the principal interest in superconductors at GD/FW is for use in producing a large volume magnetic field for shielding a space vehicle. Clearly, magnetic shielding is not effective against neutral particles; however, in the event that the space vehicle is nuclear-powered, it is essential to determine whether neutral radiation will affect the superconducting properties of the material. The techniques developed during the phase of neutral irradiation can be used during the later phase of charged-particle irradiation.

The maximum current density of a superconducting material or alloy is not only a function of the environmental conditions during its use, but also its purity, crystal structure, and the manufacturing process used to produce the material. Work-hardening during the manufacturing process makes some materials better superconductors. For example, the maximum current density of extruded NbZr wire increases by 50% between 20- and 10-mil wire. Since it is known that irradiating a material can change the structural strength and crystal structure, one may expect a change in maximum current density after irradiation. Changes are particularly expected at low temperatures, where lattice defects may remain frozen in the material.

---

7. Ibid.
8. Ibid.
9. Ibid.
10. L. Paige, Electrodynamics, New York, Van Nostrand.

Measurement of the critical current (I_c) as a function of an applied external magnetic field is the method selected to observe changes due to irradiation. The critical current is described as the current necessary to cause a small resistive voltage to appear across the sample. All measurements are made in liquid helium at ambient pressure (approx. 4.2°K) and in a magnetic field of 10 to 15 Kgauss.

NbZr wire being used in the experiment is 0.014 inch in diameter, hard drawn (>99% reduction), and of a Nb 25 at. % Zr alloy.

The Dewar used is a conventional liquid-nitrogen-jacketed, glass, helium Dewar with a liquid helium capacity of approximately one and one-half liters. Current leads are brought into the dewar through liquid nitrogen to decrease liquid-helium boiloff. This setup allowed about 45 minutes working time. (See Fig. 1.)

The circuit used to measure the critical current is shown in Fig. 2. A Keithly Model 149 millimicrovoltmeter is used to measure the voltage across the sample. Its output is attached to the y axis of a Sylvania Type B-281 x-y recorder with the x axis attached to a precision resistor through a D-C amplifier to record the current. The current is supplied by two large storage batteries and controlled through a transistorized series amplifier.

The sample holder (see Fig. 3) is cut so that it will fit into the 5/8-in.-diam Dewar tip and hold the sample in the center of the Dewar. The sample is mounted parallel and coincident to the center plane midway between the poles of the magnet. All samples are copper-plated, except for three lengths between the four contact points. The contact between the superconductor and current lead is made by winding 12 inches of wire around the current lead and then soft-soldering with 60/40 lead-tin or indium. The contact resistance with these junctions was on the order of 5×10^{-6} ohms.

Two pieces of NbZr wire were irradiated at ambient temperature in the Ground Test Reactor and compared with control samples. The total neutron flux was 10^{17} neutrons (>2.9 Mev) per cm^2. X-ray diffraction and optical magnifications to x 1000 showed no observable change in the crystal structure. The micro-hardness test, using a Knoop micro-hardness tester and converting the readings to the Rockwell "c" hardness scale, showed a change of from 30.5 to 28.6 on the hardness scale after irradiation. Another sample that was completely annealed by heating changed from 30.8 to 25.1. Due to the dependence of the current density on work-hardening these

measurements indicate a plausible explanation for any possible change in the critical current due to irradiation.

Three different samples have been irradiated in the Ground Test Reactor at ambient temperature, with a total flux of $>10^{16}$ neutrons (>2.9 Mev) per cm^2. Preliminary results of several measurements of the critical current before and after irradiation are shown on the bottom curve of Fig. 4.

Effects of neutron irradiation are being studied by irradiating samples with 14.2-Mev neutrons from the D-T reaction using a Cockcroft-Walton type accelerator. The critical current as a function of the magnetic field is measured before, during, and after irradiation with the sample temperature kept at $4.2^{o}K$ during the experiment. Preliminary results of this irradiation are shown by the top curve of Fig. 4.

Summary of Experimental Results

The upper curve of the accelerator irradiation shows no significant change, but the lower curve with reactor irradiation is suggestive of a downward shift in the critical current curve. One other sample was irradiated at the accelerator and two other samples were irradiated with the reactor. Those data show similar trends. However, the reproducibility from one run to the next and between samples leaves something to be desired. The spread in the points is comparable to the apparent effects observed with the reactor irradiation. Note that the accelerator exposure was only 10^{11} neutrons compared to more than 10^{16} from the reactor.

The data then seem to suggest that there may be an effect at the higher exposures, but our experimental techniques must be improved to reach a firm conclusion. This will be the next step in this current phase in the experimental program at GD/FW. Beyond that, the next phase in the overall program will include the construction and testing of optimized magnets.

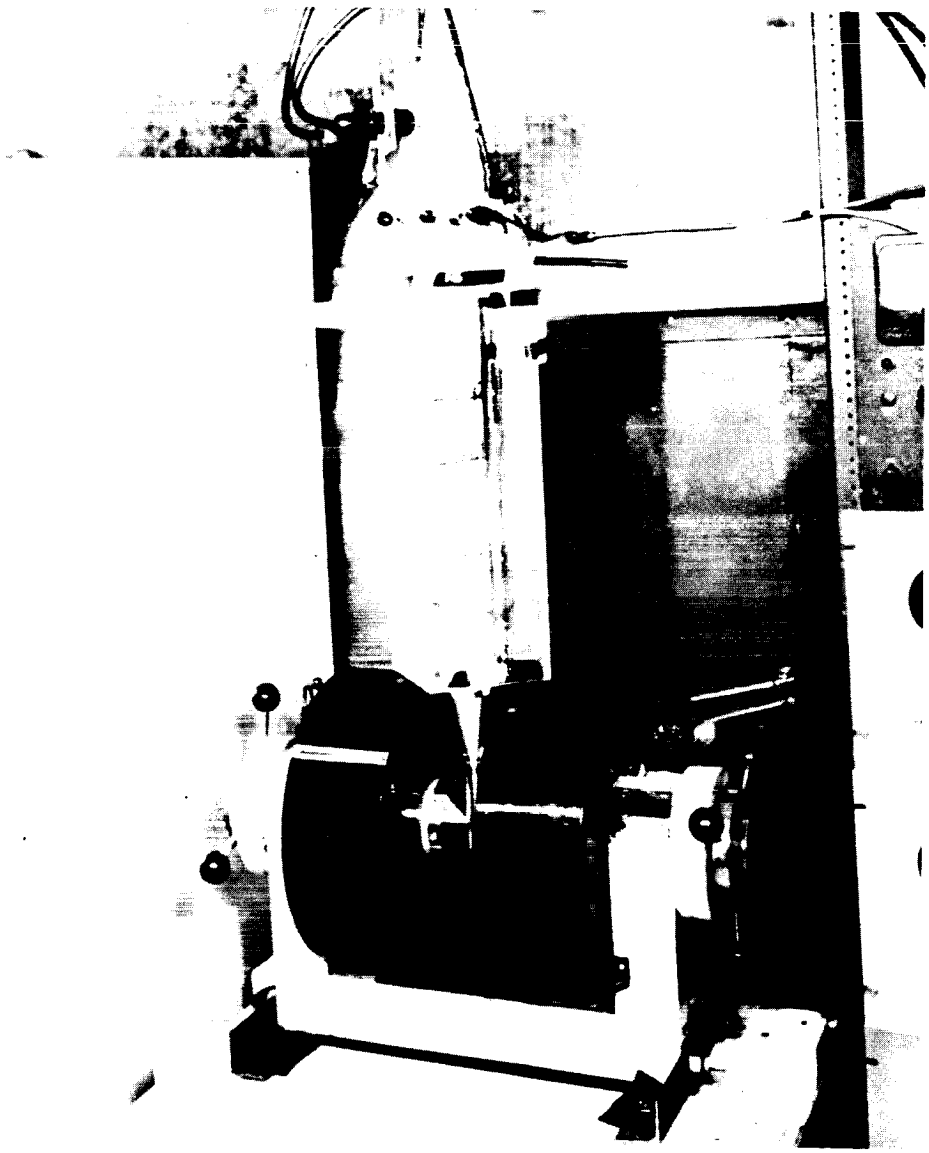

FIGURE 1. DEWAR AND MAGNET

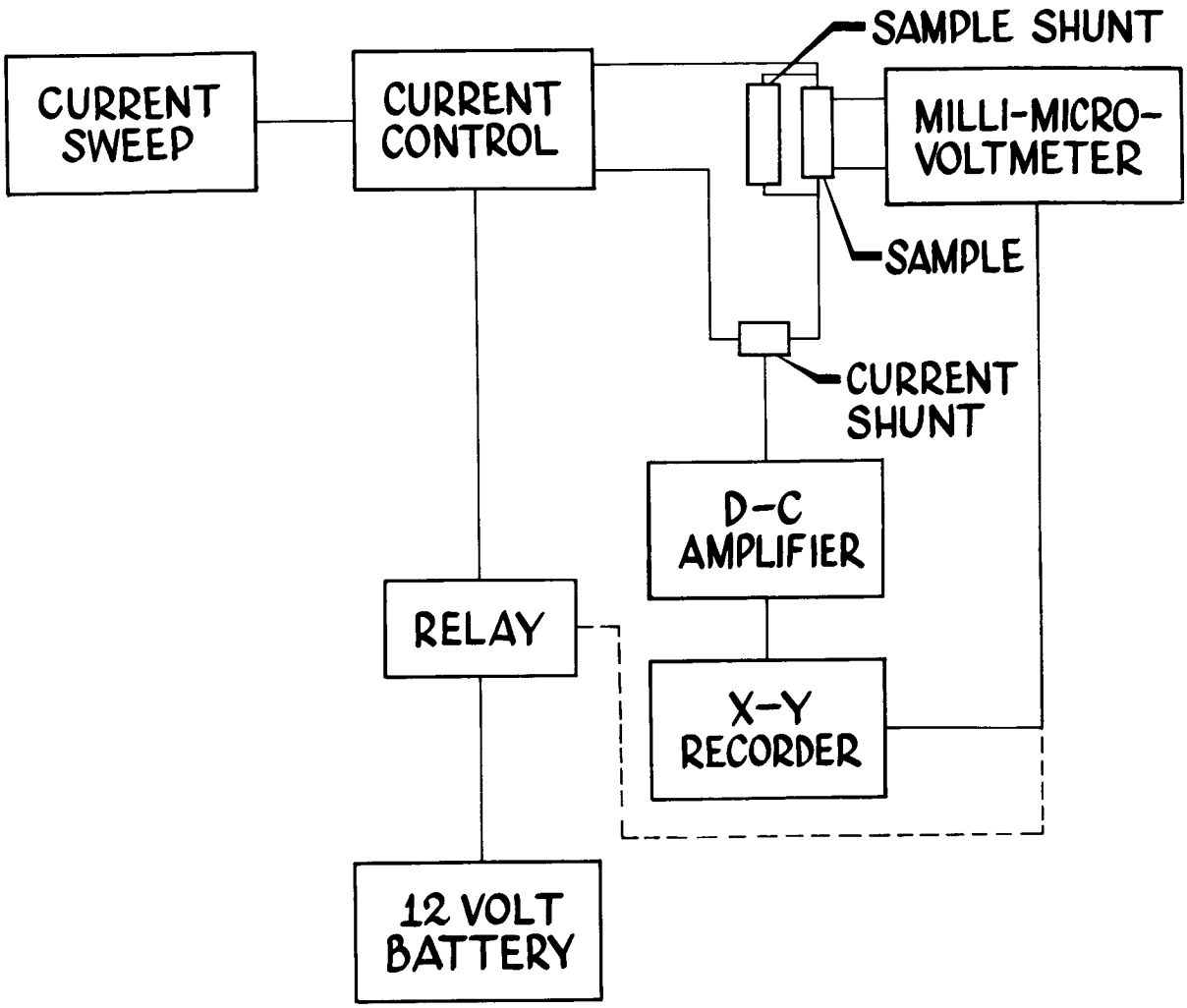

FIGURE 2. BLOCK DIAGRAM OF ELECTRICAL CIRCUIT

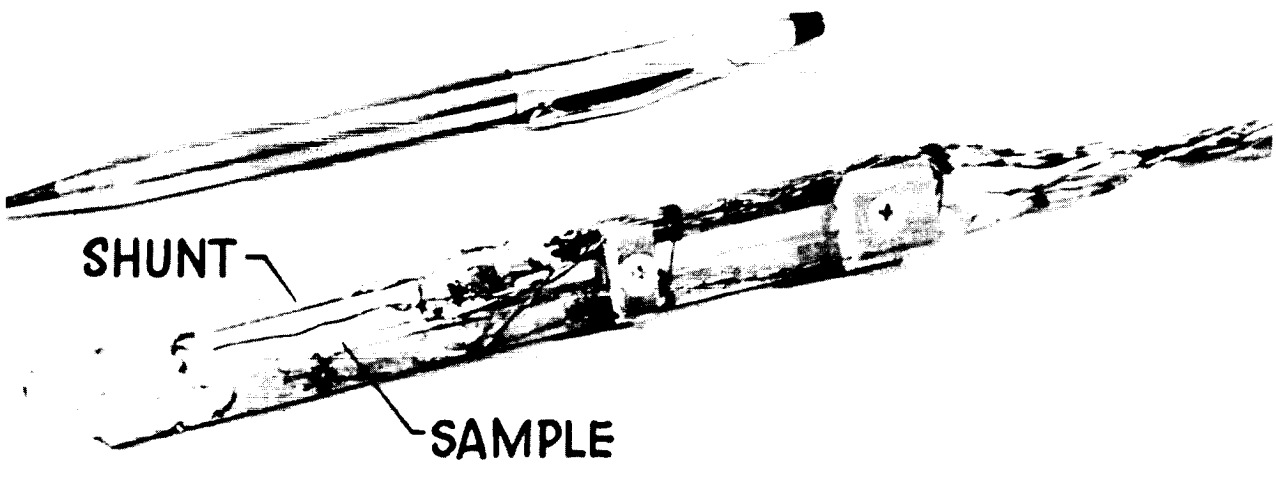

FIGURE 3. SAMPLE HOLDER WITH NbZr SAMPLE

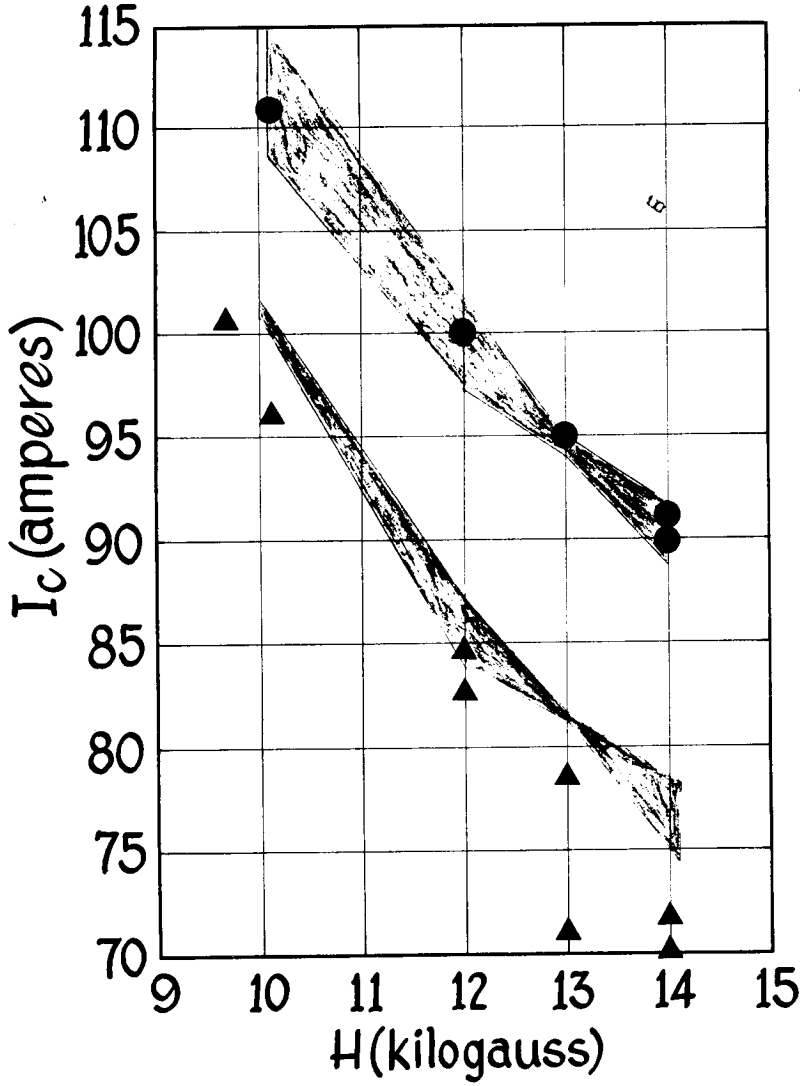

Nb Zr SAMPLE "C"
14 Mev NEUTRON IRRADIATION

▩ PRE-IRRADIATION
(DATA SPREAD IN 4 RUNS)
JUNCTION RESISTANCE-5.3$\mu\Omega$

● POST IRRADIATION-1.2×10^{14} n/cm^2
JUNCTION RESISTANCE-8.3$\mu\Omega$

NbZr SAMPLE "B"
REACTOR IRRADIATION

▩ PRE-IRRADIATION (2 RUNS)
JUNCTION RESISTANCE-5.6$\mu\Omega$

▲ POST-IRRADIATION >10^{16} n/cm^2
JUNCTION RESISTANCE-15$\mu\Omega$

FIGURE 4. PRELIMINARY RESULTS

Paper F-3

THE COMBINATION OF ACTIVE AND PASSIVE SHIELDING

J. M. Norwood
General Dynamics/Fort Worth

15156

Abstract

It is conceivable that improved shielding of space vehicles against high-energy charged-particle radiation can be obtained by combining active and passive shielding. Methods of shielding calculations and some preliminary observations pertaining to active-passive shielding are given. An analysis based upon the field of a magnetic dipole indicates that weight savings in bulk shielding can be accomplished.

Introduction

A space vehicle can, of course, be protected against high-energy, charged-particle radiation by either a passive bulk shield or an active magnetic shield. The weight, however, of a passive shield may be excessive[1], and magnetic shielding apparently provides inadequate protection against charged particles incident from certain directions and no protection from neutrons and gamma rays. It is conceivable that improved shielding with reduced weight can be obtained by combining the two shielding methods. Possibly, thick bulk shielding will be required only in regions of the magnetic field which provide weak active shielding, with relatively thin bulk shielding being sufficient elsewhere. These possibilities warrant examination, thus a limited investigation has been undertaken for that purpose. Some preliminary observations and shielding calculation methods are presented.

The Mathematical Formulation of the Problem

The combination active-passive shielding problem can be separated into two parts: (1) the passive shielding problem with the complication of a magnetic field, and (2) the active

---

1. R. K. Wilson, R. A. Miller, and R. L. Kloster, A Study of Space Radiation Shielding Problems for Manned Vehicles. GD/FW Report FZK-144 (June 1962).

shielding problem which must be solved to find the magnetically shielded regions and to determine the charged-particle intensity on the surface of the bulk shield in the unshielded regions. The intensity of incident charged particles is assumed to be known, and the dose calculation problem is ignored. Preliminary information pertaining to the feasibility of active-passive shielding can be obtained without dose calculations by computing the total number of particles which penetrate the shield.

Passive Shielding

Motion Through Bulk Material. Those particles of primary radiation which penetrate the magnetic field into the bulk shield move through the bulk material under the influence of the magnetic field and a slowing down force. If it is assumed that the slowing-down force is directed backwards along the trajectory, that it is independent of the magnetic field and of the path, and that there is no straggling, the path can be computed from the following equations:

$$\frac{d\vec{R}}{ds} = \vec{\Omega} = \frac{\vec{v}}{v}, \tag{1}$$

$$\frac{d\vec{\Omega}}{ds} = \frac{q\sqrt{1-\beta^2}}{m_p c^2 \beta}\,\vec{\Omega} \times \vec{B}, \tag{2}$$

the Bethe-Bloch equation[2]

$$-\frac{dE}{ds} = \frac{4\pi e^2 q^2 NZ}{m_e v^2}\left[\ell n \frac{2m_e c^2}{I(Z)} + \ell n \frac{\beta^2}{1-\beta^2} - \beta^2\right], \tag{3}$$

and the relativistic kinetic energy equation

$$U + m_p c^2 = \frac{m_p c^2}{\sqrt{1-\beta^2}} = E. \tag{4}$$

$\vec{R}$ is the particle position vector, s the arc length of the path, $\vec{\Omega}$ a unit vector along the path, $\vec{v}$ particle velocity, c the speed of light, m_p and q particle mass and charge, respectively, and $\vec{B}$ the magnetic field vector. E is particle energy, m_e and e electron mass and charge, respectively, Z

---

2. S. K. Allison and S. D. Warshaw, Rev. Mod. Phys. 25, (1953), 779.

the atomic number of the shielding material, N the number of atoms of shielding material per cubic centimeter, I(Z) the mean excitation potential (approximately equal to 12.5 Z electron volts), and $\beta = v/c$. If the bulk shield is composed of more than one element, dE/ds is assumed to equal the sum of a set of equations of the form of Eq. 3, one equation for each element.

The Differential Form of The Transport Equation. The transport theory formulation of the passive shielding problem in terms of the integro-differential equation is

$$\vec{v} \cdot \nabla_R N(\vec{R},\vec{P}) + \left[q\vec{v} \times \vec{B} + \frac{\vec{v}}{v}\frac{dE}{ds}\right] \cdot \nabla_P N(\vec{R},\vec{P})$$

$$+ v(\sigma_t - \sigma_{sl}) N(\vec{R},\vec{P}) = \int \sigma_s(\vec{P}' \rightarrow \vec{P}) v' N(\vec{R},\vec{P}') d^3\vec{P}'. \qquad (5)$$

$N(\vec{R},\vec{P})$ is the particle density in phase space at the point in phase space $(\vec{R},\vec{P})$, where $\vec{R}$ and $\vec{P}$ are position and momentum vectors, respectively; ∇_R and ∇_P are the usual ∇ operators, but the former denotes differentiation with respect to the space coordinates and the later with respect to the momentum coordinates. The parameter σ_t is the total cross section, and $\sigma_s(\vec{P} \rightarrow \vec{P})$ is the usual function denoting the probability that a charged particle of momentum $\vec{P}'$ will undergo a nuclear collision at the point $\vec{R}$ and give rise to a charged particle of momentum $\vec{P}$. Equation 5 is written in terms of only one type of particle, but it can, of course, be generalized to include all types.

The parameter σ_{sl} is an abbreviation for the expression

$$\sigma_{sl} = -\frac{1}{v P^2}\frac{d}{dP}\left\{P^2 \frac{dE}{ds}\right\} \qquad (6)$$

and arises from the fact that volume in phase space is not conserved within the bulk material because of inelastic collisions with electrons. An expression for σ_{sl} derived from the Bethe-Bloch equation is

$$\sigma_{sl} = \frac{8\pi e^2 q^2 NZ}{m_p m_e c^4}\frac{\sqrt{1-\beta^2}}{\beta^2}\left[\ell n \frac{\beta^2}{1-\beta^2} + \frac{1}{\beta^2} + \ell n \frac{2m_e c^2}{I(Z)} - 1\right]. \qquad (7)$$

Values of σ_{sl} and σ_t for carbon are compared in Table 1.

Table 1. Comparison of Parameters for Carbon

U (Mev)	σ_{sl} (cm^{-1})	σ_t (cm^{-1})
100	0.034	0.019
200	0.015	0.017
500	0.006	0.018

The Integral Form of The Transport Equation. The transport equation for active-passive shielding can also be formulated as an integral equation, and as such its functional form is unaltered by the presence or absence of the magnetic field. With N in terms of $\vec{R}$, $\vec{E}$, and $\vec{\Omega}$, the integral equation is

$$vN(\vec{R},E,\vec{\Omega})S(s) = v_oN(\vec{R}_o,E_o,\vec{\Omega}_o)S(o)e^{-\ell(o,s)}$$

$$+\int_o^s\left[\iint\sigma_s\left\{E'',\vec{\Omega}''\rightarrow E(s'),\vec{\Omega}(s')\right\}\ v''N\left\{\vec{R}(s'),E'',\vec{\Omega}''\right\}dE''\ d\Omega''\right]$$

$$x\ S(s')e^{-\ell(s',s)}\ ds'\ , \qquad (8)$$

where

$$S(s) = \frac{dE(s)}{ds} \qquad (9)$$

and

$$\ell(s',s) = \int_{s'}^{s}\sigma_t\left\{E(s'')\right\}ds'' \ . \qquad (10)$$

Integration of Eq. 8 is carried out along the path of a particle in the increment of volume in phase space of $d^3\vec{R}dEd\Omega$ as the volume increment moves along the arc from point $\vec{R}_o$ to $\vec{R}$ (Fig. 1).

The arc can be obtained by integrating Eqs. 1 through 4. The first term on the right of Eq. 8 represents the primaries which enter the shield at $\vec{R}_o$ with energy E_o and direction $\vec{\Omega}_o$ and which reach $\vec{R}$ with energy E and direction $\vec{\Omega}$. The second term represents secondaries which reach $\vec{R}$ with energy E and direction $\vec{\Omega}$ from all points $\vec{R}(s'')$ along the arc $0 \leq s'' < s$. Terms of the form $e^{-\ell}$ represent attenuation due to nuclear processes.

Shielding calculations are performed for a given shield configuration by summing the total number of particles which

reach the interior of the bulk shield from all possible paths through the shield. That is, the total number I of particles, which cross the inner surface is calculated by integrating $\vec{\upsilon} \cdot \vec{\Omega}\ v\ N(\vec{R},E,\vec{\Omega})$ over the inner surface of the shield, over all directions $\vec{\Omega}$ into the shield, and over all energies E; $\vec{\upsilon}$ is a unit normal to the inner surface and $v\ N(\vec{R},E,\vec{\Omega})$ is given by Eq. 8.

$$I = \int dS \int d\Omega \int_0^\infty dE\ \vec{\upsilon} \cdot \vec{\Omega}\ v\ N(\vec{R},E,\vec{\Omega}). \tag{11}$$

If desired, dose calculations can be performed by including a flux-to-dose conversion factor behind the energy integral. However, dose calculations are ignored in this paper.

It can be shown by a modification of Liouville's theorem[3] that if the incident charged-particle flux is isotropic and homogeneous at infinity (an assumption which is adequate for present purposes), it is isotropic and homogeneous everywhere in a magnetic field except in magnetically shielded regions, where it is zero. Thus, if secondaries can be neglected in Eq. 8, then Eq. 11 can be written as

$$I = \int dS \int d\Omega \int_{E^*(\vec{R},\vec{\Omega})}^\infty dE_o\ \frac{1}{4\pi}\ \Phi(\vec{R},E_o,\vec{\Omega})\ \vec{\upsilon} \cdot \vec{\Omega}\ e^{-\ell\{E_o,E(\vec{R},E_o,\vec{\Omega})\}} \tag{12}$$

where

$$\Phi(\vec{R},E_o,\vec{\Omega}) = \Phi(E_o) \text{ in non-shielded regions}$$
$$= 0 \text{ in shielded regions.} \tag{13}$$

Magnetic shielding will be discussed in the next section. $E^*(\vec{R},\vec{\Omega})$ is the minimum energy required of particles at the outer bulk shield surface to reach the inner surface at $\vec{R}$ with direction of motion $\vec{\Omega}$. The parameter ℓ is written in terms of E_o and E instead of s' = 0 and s' = s.

Evidently, active-passive bulk shielding calculations are executed in the same manner as passive shielding calculations with zero magnetic field. Active-passive bulk shielding calculations are much more complicated, however, because of nonlinear particle paths through the bulk material. Speci-

---

3. W. F. G. Swann, Phys. Rev. 44, 224 (1933).

fically, loss of symmetry due to nonlinear particle paths results in the necessity of performing more integrations, or conversely, linear paths lead to symmetry which renders certain integrations trivial.

Active-Passive Shielding

A realistic solution to the combined active-passive shielding problem is dependent upon the geometry chosen for the shielding configuration. Since such a configuration has not been selected at this time, only investigations of a preliminary nature can be undertaken. Indeed, one object of such investigations is to determine optimum active-passive configurations.

The tentative analysis to follow is based upon the Störmer analysis of a dipole field[4,5]. According to the Störmer analysis, a volume of space at the magnetic equator of the dipole field is completely shielded from charged particle radiation of a given energy. Outside this volume, there is a region of space which is shielded against all particles except those which possess directions of motion inside a given cone of directions (the Störmer cone). Since the sizes of the partially and completely shielded regions are functions of energy and since these regions decrease in size as incident-particle energy decreases, the position of the magnetically-shielded regions relative to the position of the bulk shield is a function of energy.

For a fixed passive shield, the boundary of the completely magnetically shielded region will lie outside the bulk shield for low-energy particles and inside for very-high-energy particles. Thus, the active shield will stop the low-energy particles, while the passive shield must stop the high-energy particles. But if the bulk shield is to stop the high-energy particles, it will be quite thick, in which case its presence will negate the usefulness of the magnetic shield.

This analysis applies to the volume about the magnetic equator. At the magnetic poles, the component of $\vec{\Omega}$ parallel to the axis of the field, $\vec{\Omega}_{//}$, is not affected by the field, since by Eq. 2, $d\vec{\Omega}_{//}/ds = 0$. Consequently, $\vec{\Omega}_{//}$ is constant, and by Eq. 1 the component of $\vec{R}$ in the $\vec{\Omega}_{//}$ direction is

---

4. L. Janossy, Cosmic Rays. Oxford, (1950), Chap. VII.

5. R. F. Tooper and W. O. Davies, Electromagnetic Shielding of Space Vehicles. Armour Research Foundation, IAS Paper No. 62-156 (June 1962).

$\vec{R}_{\parallel} = s\vec{\Omega}_{\parallel}$. Thus, the necessary thickness of the bulk shield at the poles is independent of the presence or absence of the magnetic field.

It appears that thick bulk shielding is needed everywhere, thus rendering the active shield useless. But the preceding analysis ignores several things. First, the dipole field is not very realistic, although one is led to believe that it represents many of the shielding properties of any magnetic field; second, it ignores the fact that the magnetic field bends the path of a charged particle as it traverses the bulk shield; and third, it neglects the partially shielded region.

In the partially shielded region at the magnetic equator, the solid angle subtended by the cone of allowed directions (which opens to the east) decreases in size as energy decreases. After consideration is given to take advantage of this fact and the turning effect of the magnetic field, an active-passive shield with reduced bulk shield weight can be constructed so that no particle of energy less than a maximum energy can penetrate it. The shield is designed so that lower-energy particles have directions of incidence which lie closer to the bulk shield surface and their paths inside the bulk shield tend to bend away from the inner surface (Fig. 2).

Computational Results. Calculations were made for a spherically shaped bulk shield and a magnetic field independent of position within the bulk shield. A dipole field was assumed to exist outside the bulk shield. The outer diameter of the bulk shield was taken as 2 meters and the magnitude of the magnetic field intensity within the material was 37,500 gauss. At points on the magnetic equator, it was found that a shield thickness of 5.3 gm/cm^2 of polyethylene would completely stop protons of energy of 100 Mev or less; at the poles, where the effect of the magnetic field is minimum, the necessary thickness is 7.1 gm/cm^2. No calculations were made at magnetic latitudes other than at the equator and at the poles, but if it is assumed that the inner surface of the bulk shield is an ellipsoid of revolution (the shielding being thinner at the equator) as opposed to a spherical inner surface, the weight saving in shielding material is some 1200 lb or 16% of the whole.

Conclusions

Although it appears that active-passive shielding may be a useful concept, a more comprehensive study is indicated. Calculations for more realistic geometries would be desirable. For example, an active shielding analysis for a large diameter circular loop or solenoid would be more reasonable as a basis for active-passive shielding calculations. Another possible geometry is Levy's torus with concentric windings centered on the axis of symmetry[6].

6. R. H. Levy, Radiation Shielding of Space Vehicles by Means of Superconducting Coils. Avco-Everett Research Laboratory, Research Report 106 (April 1961).

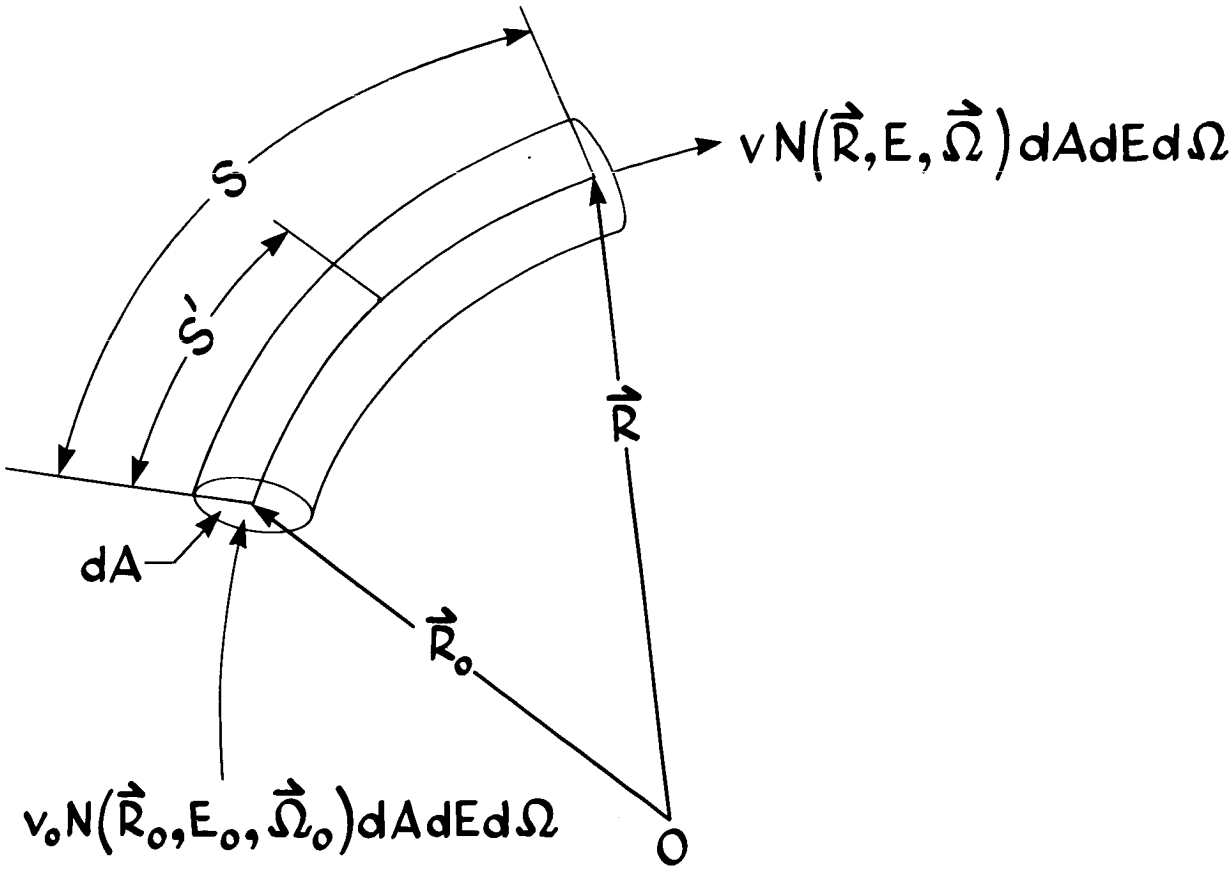

FIGURE 1. CHARGED PARTICLE FLUX ALONG AN ARC

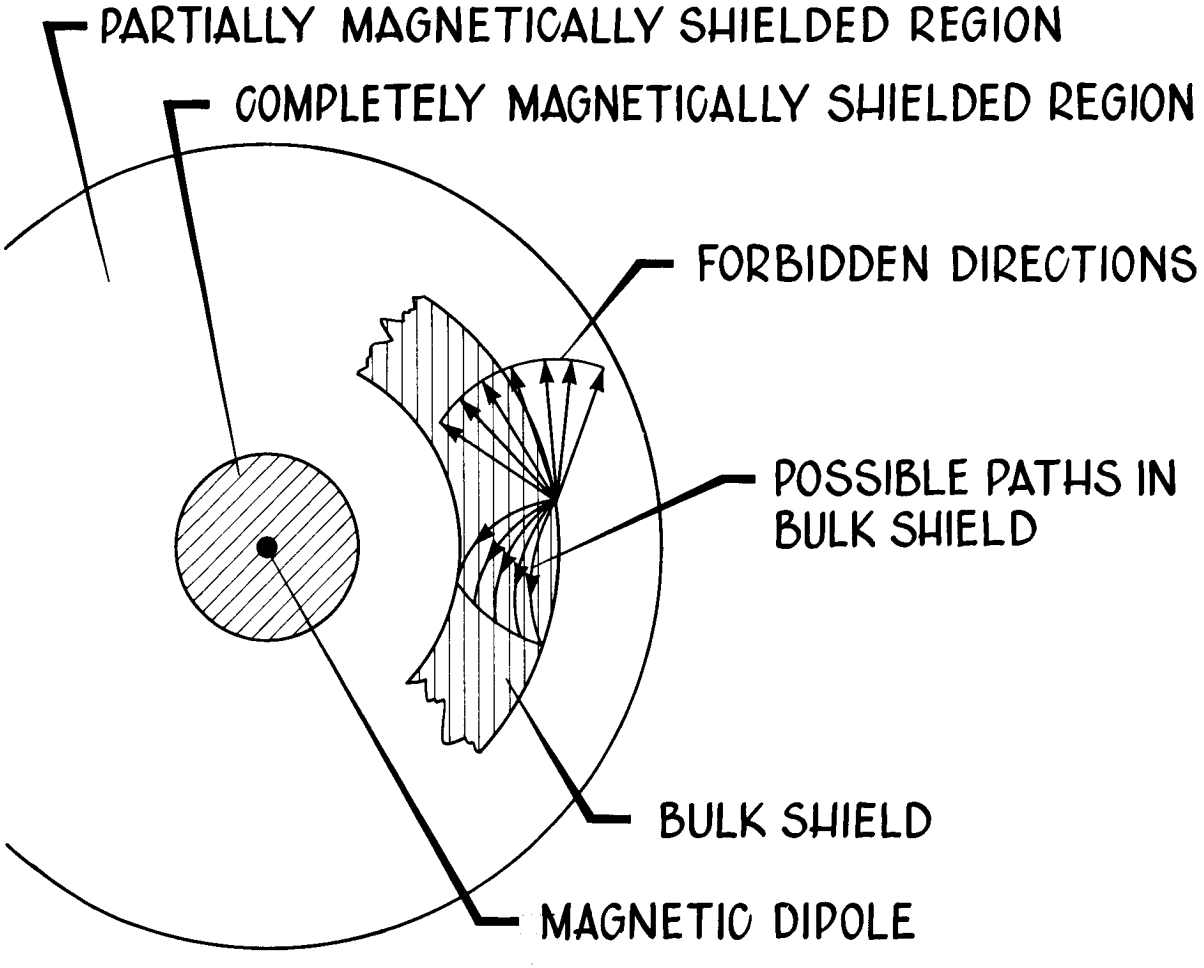

FIGURE 2. SHIELDING IN THE EQUATORIAL PLANE

Paper F-4

TECHNIQUES USED IN SHIELDING CALCULATIONS FOR HIGH-ENERGY ACCELERATORS: APPLICATIONS TO SPACE SHIELDING*

Roger Wallace and Charles Sondhaus

Lawrence Radiation Laboratory
University of California
Berkeley, California

15157

Abstract

The prediction for the secondary neutron spectrum produced inside of a thick shield is described. The multiplicity of cascade and evaporation secondaries as well as subsequent moderation of the secondary spectrum is described quantitatively. Experimental thick-target neutron yields, as well as Monte Carlo cascade data, are the basis for these estimates.

Introduction

The principle differences between shielding a man in space and shielding the crew of a large accelerator are that the tolerance levels for the space ship are higher, and the integrated incident dose is lower. This reduces the thickness of shield in the space ship relative to that in the accelerator. The detailed investigation of this difference is not the subject of this paper. We only attempt to show how approximate estimates for the shielding of accelerators can be made. These methods and the data used in them are applicable to the space-ship problem.

The spectrum of protons incident on a space ship is both continuous and somewhat softer than the monoenergetic protons that would emerge from a high-energy accelerator in the several-hundred-MeV region. This difference tends to reduce greatly the number of secondary neutrons produced and emphasizes the role of primary protons that may actually penetrate the space-ship wall. Such wall penetration by protons is not characteristic of accelerator-shield situations. The companion paper by Sondhaus and Wallace[1] describes the penetration of a thick shield by protons, whereas this paper is largely limited to neutron considerations. For high-energy accelerators it has been found that the gamma-ray dose outside of a very thick shield is only a modest fraction of the neutron dose. This conclusion may not be true in the case of space shielding where the shield may be somewhat thinner and the gamma-ray dose a more important fraction of the neutron dose.

*Work done under the auspices of the U. S. Atomic Energy Commission, and the Joint Atomic Energy Commission--NASA Space Radiation Program.

The technique generally used to estimate shielding is that developed by B. J. Moyer.[2a, 3, 4] While each proton produces a variety of particles as it undergoes collision in the shield, only the neutrons are of biological significance. For protons striking an extended thick target, the total neutron production as a function of energy for carbon, aluminum, copper, and lead is shown in Fig. 1. This total neutron production consists of two parts: "cascade" and "evaporation" neutrons. There are also cascade protons. The cascade particles that are knocked out during the immediate passage of the incident proton by direct interactions between the proton and the individual nucleons in a target nucleus have been extensively treated by Metropolis.[5] The cascade particles, because of momentum conservation, are strongly concentrated in the forward direction relative to the incident-proton direction. Due to their long mean free paths only those cascade particles having energies above 150 MeV need be considered in shielding. Cascade particles would be rather unimportant as secondaries from protons below 100 MeV.

The remainder of the secondary particles are produced by evaporation from the nucleus after the initial proton passage as a result of the excitation energy that is left behind in the nucleus. The evaporation process gives off neutrons isotropically. There has been some augmentation of these curves to allow for a plural cascade within the target nucleus.

The cascade yields of neutrons and protons resulting from either neutron or proton bombardment are shown in Fig. 2. The synthesis of the resulting secondary neutron spectrum results from three parts:

(1) the cascade neutrons above 20 MeV,

(2) the evaporation-neutron spectrum that is peaked in the few MeV region, and

(3) the resulting thermal spectrum which arises from the degradation of the energy of the other two neutron sources.

This three-part synthesis is a natural division of this otherwise far too complex problem for a simple estimate. Of course, the problem is not too complex for a computer approach. The cascade neutrons above 150 MeV are the only part of the spectrum which must initially be considered in the evaluation of the thickness of the shield. This results from the neutrons of lower energy having attenuation lengths substantially shorter than those above 150 MeV. It is only this penetrating high-energy component that controls the shield thickness, as can be seen in Fig. 3. There is a plateau in the half-value thicknesses of concrete shielding above 150 MeV. The conclusions that one reaches about concrete are also applicable to most other materials (with the exception of hydrogen) on a gram for gram basis. A thick shield made of liquid hydrogen would need special consideration.

There is, of course, a buildup and an establishment of equilibrium in the secondary neutron spectrum in the first few outer layers of the shield. After equilibrium is established in one or two half-value layers, no further change in the shape of the neutron spectrum occurs with depth in the shield, only an attenuation of the entire spectrum as the highest-energy primaries are attenuated.

Cascade Particles

The spectra of cascade particles computed by Metropolis are shown in Fig. 4 for 460 and 1840 MeV incident protons on aluminum. These spectra seem not to differ very much from each other except of course at the highest energies. These spectra are characteristic of somewhat lower energies as well. These spectra, multiplied by the appropriate normalization factors (given in Fig. 7), are shown in the energy region above 50 MeV on Fig. 5 for incident proton energies of 450, 600, and 850 MeV. It is seen that below about 100 MeV the cascade spectra are essentially the same. These spectra have not yet been degraded by passage through hydrogenous material, therefore no thermal peak is present.

The angular distribution of the cascade particles of Metropolis et al. [5] has been augmented by Moyer using data on the angular distribution of the prongs of nuclear-emulsion stars from the Bevatron and from cosmic rays. Such an angular distribution is shown in Fig. 6. The distribution shown is normalized for 6.2-GeV protons on copper; however, the angular distribution is not sensitive to energy. It is hoped that the extremely valuable work of Metropolis et al., which has served as a basis for so many shielding calculations, will soon be augmented by additional Monte Carlo computations from the Oak Ridge Group.

The number of cascade neutrons per incident proton as a function of proton energy for a variety of target materials is given in Fig. 7. It is seen that for the high energies there is a monatonic increase in the number of cascade neutrons with A, whereas for the energy region below 200 MeV the low-A materials actually have a higher neutron production than the high-A materials.

The number of cascade protons per incident proton as a function of proton energy and target A is shown in Fig. 8. These curves bear a resemblance to those for neutron production in Fig. 7 and the same conclusion can be drawn with respect to production in the light elements. It should be noted that in the energy region near 500 MeV the Fig. 8 cascade-proton curves are in the reverse order with the highest proton production coming from the low A's and the lowest proton production coming from the high A's in contrast to the Fig. 7 cascade-neutron case. Above 1000 MeV the low-A curve does cross over the others but the others still remain in the inverted order. This particular fact is of only minor importance to our present problem since cascade protons have a very limited range and it is really the cascade neutrons that one must consider.

After the shielding thickness becomes quite thick, a similar set of curves could be provided giving neutrons per incident neutron and protons per incident neutron as a function of A and energy. These additional curves would only be useful for some specialized accelerator-shielding situations. In the space-vehicle case we do not have a sufficient number of incident neutrons to concern us and the incident proton case is overwhelmingly dominant.

Evaporation Particles

The most important source of neutrons is the evaporation process. Several authors[6-9] have treated the evaporation of nucleons from nuclei that have been excited by very high-energy neutrons or protons. These evaporation neutrons will provide the low-energy end of our spectrum. Nuclear evaporation is somewhat analogous to the evaporation of the liquid on an atomic scale. The resulting particle spectra are obtained by estimating an excitation energy E_1 for the nucleus as a whole. This estimation, due to Moyer,[3] is shown in detail for A from 20 to 220 in Fig. 9. This set of curves gives the "excitation" energy E_1 left behind in a nucleus by a proton or neutron of energy E. This energy is then considered as a thermal kinetic-energy source for eventual evaporation.

The nuclear temperature produced by the deposition of energy E_1 in a nucleus A by an incident neutron or proton is shown in Fig. 10. Note that nuclear temperatures for the light elements have plateaus in the region of several hundred MeV, making the change in temperature in this region with incident proton energy quite small.

The excitation energy is related to the square of an effective nuclear "temperature" by an empirical parameter[6] (A/10); thus we have

$$E_1 = (A/10)\tau^2, \tag{1}$$

where E_1 is the nuclear excitation in MeV, and A is the atomic weight of the nucleus. This empirical equation is shown in Fig. 11 for four different values of A. It is seen that the light elements have higher nuclear temperatures than heavy elements for a particular excitation energy. Figures 9, 10, and 11 represent a three-dimensional surface in a space whose coordinates are the total nuclear excitation energy, nuclear temperature and bombarding-proton energy.

The evaporation spectrum itself is given by Eq. (2). The E in front of the exponential instead of the usual $E^{1/2}$ which appears in the

$$N(E)dE = (E/\tau^2)e^{-(E/\tau)}dE \tag{2}$$

Maxwellian energy distribution is necessary to account for the fact that N(E) is a flux density rather than a numerical density.

To estimate the complete spectrum penetrating the shield, it is now necessary to fit this modified Maxwellian low-energy evaporation end of the spectrum to the Metropolis cascade high-energy tail. This transition fit is made after the area under each individual spectrum has been normalized to the estimated total production of each spectrum's particular component (as given in Table I for the case of aluminum or shown for other A's and E's in Figs. 1, 7, and 12). Note that in Table I it is appropriate for the sum of "cascade" and "evaporation" neutrons to not equal the "total" neutrons. The "total" production is per incident particle on a thick target. The "cascade" and "evaporation" production are per inelastic collision at the quoted energy. The sum of these two productions can be either less than or greater than the "total," depending on the ratio of inelastic-collision proton removal to electromagnetic dE/dx proton energy loss. The total neutron production per inelastic collision and the ratio of the evaporation to the cascade process both as a function of energy and A are given in detail in Figs. 13 and 14. The electromagnetic energy loss changes with proton energy, while the inelastic cross sections are quite constant with energy above 100 MeV as seen in Fig. 15. It is seen that for the lightweight elements the number of evaporation neutrons is quite constant at about one neutron per proton over a wide energy range.

More details of this process are available, such as the suppression of the low-energy particles by the Coulomb barrier, as treated by Dostrovsky[6] and Le Couteur.[7] Particles other than neutrons, such as H, H^2, and H^3, as well as multiple-charged particles, such as He^3 and He^4 can also be estimated as given in Figs. 16 through 20. The doubly charged particles have their evaporation spectrum peaks at about twice the energy of the proton spectrum peak for a nucleus of the same excitation. The angular distribution of the particles emitted in connection with nuclear evaporation is of course isotropic. The evaporation particles produced in an internal target have no chance of their own of penetrating the main shield directly, except for the inner one or two mean free paths of the shield. Therefore, evaporation particles are mainly of interest with regard to the radioactivity that they may induce in the accelerator hardware. This problem is probably not of particular importance for space-craft shielding. The evaporation particles are far more important for inducing radioactivity than are the cascade neutrons, since evaporation particles are considerably more numerous and their energy is more favorable for capture. More extensive data is available on evaporation particles.

Attenuation of the Total Spectrum

Generally the fit between the two parts of the spectra as shown in Fig. 5 is done by eye. Greater accuracy is not appropriate to the degree of approximation which we are making. Direct measurements of shield thickness required for a given attenuation factor, using beams of restricted width, have been made for concrete, water, and a few other materials, but probably not for the materials of interest in

space-craft shielding. Light-weight elements, such as contained in concrete, have shielding values very little different for different A's; this value is mainly proportional to the number of grams of shield per cm^2. A thick shield provides neutron attenuation by absorbing, degrading, or deviating the neutrons by nuclear collisions. At the high energies characteristic of cascade particles, elastically scattered particles are so strongly peaked in forwardly directed diffraction patterns that essentially no geometric deviation or energy loss occurs. Thus, as the incident neutron energy is increased from values characteristic of the evaporation region to values associated with the cascade region, the value of the effective removal cross section for neutrons by a shield decreases from the value of the total cross section to the value of the inelastic cross section. This effect is shown in Tables 2, 3, and 4, from Patterson,[2b] as applied to the elements present in concrete. It is seen that $n\sigma_a(cm^{-1})$ is a figure of merit for the efficiency of each element in the concrete. Table 4 emphasizes the importance of the heavier elements as the neutron energy is raised. Several points calculated from these data for concrete, by Patterson, are plotted in Fig. 21 together with several experimental values for energies from 1 MeV to 4.5 GeV. The agreement between the experimental and calculated values is quite good. The same data appeared in CGS units in Fig. 3. These data only apply to thick shields and poor geometry situations. The companion paper presented by C. Sondhaus[1] will outline some deviations from this which are characteristic of somewhat thinner shields where the proton beam may be considered to survive in a geometrical fashion.

The measurements of σ_{total} and $\sigma_{reaction}$ for various nuclei as a function of neutron energy up to 5 GeV are given by Coor et al.[10] and Atkinson et al.[11] and are shown in Lindenbaum[12] (see Fig. 21). This experimental work shows that the attenuation of neutrons in the high-energy region is essentially constant.

Radiation Emerging from the Shield

Now that the spectrum and angular distribution of the neutrons produced in the target and accelerator hardware by the primary protons have been estimated, a secondary calculation can be made of the penetration of the outer shield by these neutrons. This can be done by using similar data for cascade and evaporation particles produced by neutrons, instead of protons as shown in Figs. 2, 9, 10, 12, and 16 through 20, secured from the same sources as that given earlier for incident protons. The evaporation data are the same as those for incident protons, whereas the cascade values are not. As would be expected, the neutrons are more numerous in neutron-induced cascades than in proton-induced cascades, and vice versa for proton-induced cascades. Cascade-produced mesons gradually increase in importance from 500-MeV incident energy on up. They do not become a controlling factor in the energy range considered in space shielding.

The flux of particles present inside the space-ship shield or outside the accelerator shield now consists of (a) directly transmitted primary neutrons of energy > 150 MeV (from the spectra shown in Fig. 5), and (b) evaporation fragments produced by the high-energy neutrons that suffer inelastic collisions in the last layers of the shield. The number of cascade neutrons making evaporation neutrons and protons by inelastic collisions within a last layer of the shield wall of thickness x is

$$N = N_o(e^{x/\lambda}-1), \tag{3}$$

where x is measured in from the shielded side of the shield, and λ is the mean free path for inelastic collisions of the cascade neutrons. Assume that half of the evaporation neutrons emerge. This is an obvious overestimate of the number of evaporation neutrons but it will to some extent be compensated for by the further multiplication of a fraction of the cascade neutrons in secondary collisions which again increases the number of evaporation neutrons emerging from the shield. Few of the protons produced in the cascade events in the early part of the shield will emerge from the shield, because of range limitations. There will, however, be protons arising from the evaporation processes emerging from the shield.

Considering a final layer of the shield $x = \lambda$, one mean free path thick, and using the spectra shown in Fig. 5 and values of λ shown in Fig. 15 from Lindenbaum,[12] we estimate that in a particular case each cascade neutron produced in the outer shield will be accompanied by 0.6 fast neutrons and 0.3 protons when it emerges from the shield.

There may also be a small flux of thermal neutrons and gamma rays. The gammas come from thermal neutron capture by the H of the shield (if present) and also from nuclear de-excitations associated with evaporation processes. Typically, the numerical value of the thermal neutron flux is only a few times that of the fast neutrons, so the relative dosage from the thermal neutrons is negligible, if we take RBE values into account, in comparison with the fast neutrons. Ionization-chamber measurements of the gamma-ray dosage are typically one-quarter or less than that arising from fast neutrons.

If one wishes to make an estimate of the spectrum of epithermal neutrons that will be produced by moderation of the cascade and evaporation neutrons and will extend below the evaporation peak, the slowing down spectrum can be approximated by assuming that each emission increment $Q(E_1)\Delta E_1$ gives rise to a flux increment with spectrum $1/E-1/E_1$. Thus, by integration, the slowing down flux has the spectrum

$$\phi(E) = K_1 \int_E^{E_{max}} Q(E_1)\left(\frac{1}{E} - \frac{1}{E_1}\right) dE_1 . \tag{4}$$

This slowing down flux spectrum is joined by continuity of slope of the thermal spectrum,

$$\phi_{th} = K_2 E^{1/2} e^{-(E/kT)}, \tag{5}$$

which are normalized by requiring the integral from zero energy to 1/2 eV to give the value[13]

$$\phi_{th} = 1.25 \frac{Q}{S}, \tag{6}$$

where Q is the total source strength of fast neutrons and S is the surface area over which they are thermalized (in cm^2).

Conclusions

The data that is presently available and pertinent to the shielding of high-energy proton accelerators has been presented. An approximate method for estimating the neutrons produced in the shield and released into the cabin has been outlined. The production curves for heavier secondaries have been given. Data for meson production, although available, are not included. Should the shield consist of liquid hydrogen, some revision of the data would be necessary since the lowest atomic weight included is A = 20 and the production of neutrons in a liquid hydrogen shield arises through different processes. Neither cascade nor evaporation are possible for H. Various modes of meson production accompanied by neutron production are the only sources of neutrons from H. While data for this type of neutron production is available it has not been accumulated and converted to a useful form for shielding purposes. It is probably true however that neutron production from the hydrogen shield would be considerably reduced relative to that from a shield of higher atomic weight. In general, on a weight basis, a hydrogen shield should be considerably more effective than an equal mass per cm^2 of any other type of material; this difference might be a factor of 2. This is probably not enough to dictate the use of liquid hydrogen relative to other shielding materials, unless it happens to be unusually convenient for propulsion and energy storage reasons, since its low density and temperature make its storage very difficult.

References

1. C. Sondhaus and R. Wallace, Solar Proton Exposure Simulation with the 184-Inch Cyclotron, Lawrence Radiation Laboratory Report UCRL-10447, November 1962 (unpublished).

2a. B. J. Moyer, Method of Calculation of the Shielding Enclosure for the Berkeley Bevatron, in First International Symposium on Protection Near Large Accelerators, Saclay, France, January 1962 (to be published).

2b. H. Wade Patterson, The Effect of Shielding on Radiation Produced by the 730-MeV Synchrocyclotron and the 6.3 GeV Proton Synchrotron at the Lawrence Radiation Laboratory (UCRL-10061, January 1962, in First International Symposium on Protection Near Large Accelerators, Saclay, January 1962 (to be published).

3. B. J. Moyer, Data Related to Nuclear Star Production by High-Energy Protons, Lawrence Radiation Laboratory, June 20, 1961 (private communication).

4. B. J. Moyer, Shielding and Radiation Calculations for USNRDL Cyclotron, Lawrence Radiation Laboratory, October 11, 1960 (private communication).

5. N. Metropolis, R. Bivins, M. Storm, A. Turkevich, J. M. Miller, and G. Friedlander, Phys. Rev. 110, (1958) pp. 185 and 204.

6. I. Dostrovsky, P. Robinowitz, and R. Bivins, Phys. Rev. 111, 1659 (1958).

7. K. J. Le Couteur, Proc. Phys. Soc. (London) A63, 259 (1950).

8. Y. Fujimoto and Y. Yamaguchi, Progr. Theoret. Phys. (Kyoto) 4, 468 (1950); ibid., 5, 787.

9. R. W. Deutsch, Phys. Rev. 97, 1110-23 (1955).

10. T. Coor, D. A. Hill, W. F. Hornyak, L. W. Smith, and G. Snow, Phys. Rev. 98, 1369 (1955).

11. J. H. Atkinson, W. N. Hess, V. Perez-Mendez, and R. Wallace, Phys. Rev. 98, 1369 (1955).

12. S. J. Lindenbaum, Shielding of High-Energy Accelerators, in Ann. Rev. Nucl. Sci. 11, 213 (1961).

13. H. W. Patterson and R. Wallace, A Method of Calibrating Slow-Neutron Detectors, Lawrence Radiation Laboratory Report UCRL-8359, July 1958 (unpublished).

Table 1. Secondary cascade and evaporation-particle production, nuclear excitation energy and temperature for aluminum targets in proton beams of three different energies.

Proton energy (MeV)	Total neutron thick target yield (n/p)on Al	No. cascade[a] neutrons per incident proton on Al per inelastic collision	No. cascade[a] protons per incident proton on Al per inelastic collision	Total[a] no. cascade nucleons per incident proton on Al per inelastic collision	Residual[a] nuclear excitation E_1 (MeV)	Residual[a] nuclear temperature τ (MeV)	No. evaporation neutrons per incident neutron or proton per inelastic collision
450	1.3	1.30	1.85	3.15	63	4.3	1.30
600	2.1	1.40	2.05	3.45	72	4.5	1.50
850	3.3	1.55	2.25	3.80	88	4.9	1.60

a. See ref. 3.

Table 2. N atoms/cm^3 for Berkeley concrete ($\times 10^{22}$).

O	4.73
H	1.73
Si	1.57
Ca	0.26
Al	0.17
Fe	0.053
Na	0.028
K	0.028
Mg	0.013

Table 3. Assumed relation between σ_a, the neutron-attenuation cross section, and σ_{tot}, the total neutron cross section

(MeV)	
1	$\sigma_a = 1.00\ \sigma_{tot}$
5	$\sigma_a = 0.65\ \sigma_{tot}$
14	$\sigma_a = 0.055\sigma_{tot}$
$\geqslant 150$	$\sigma_a = 0.50\ \sigma_{tot}$

Table 4. $N\sigma_a(cm^{-1})$ for various elements ($\times 10^{-2}$).

	1 MeV	14 MeV	270 MeV
O	16	4.4	0.89
H	7.8	0.64	0.026
Si	4.7	1.7	0.41
Ca	0.78	0.33	0.10
Al	0.51	0.16	0.05
Fe	0.16	0.045	0.028

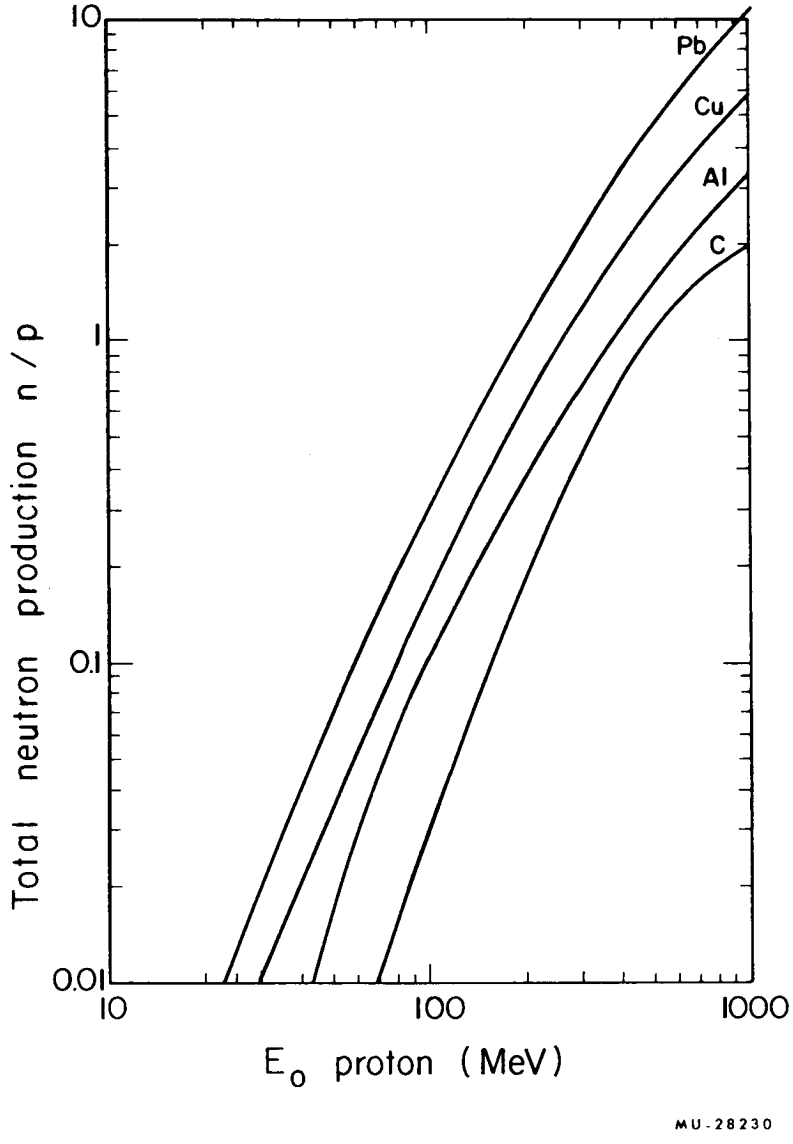

Fig. 1. Measured total neutron yields per proton stopping in a thick target for C, Al, Cu, and Pb, from Moyer.

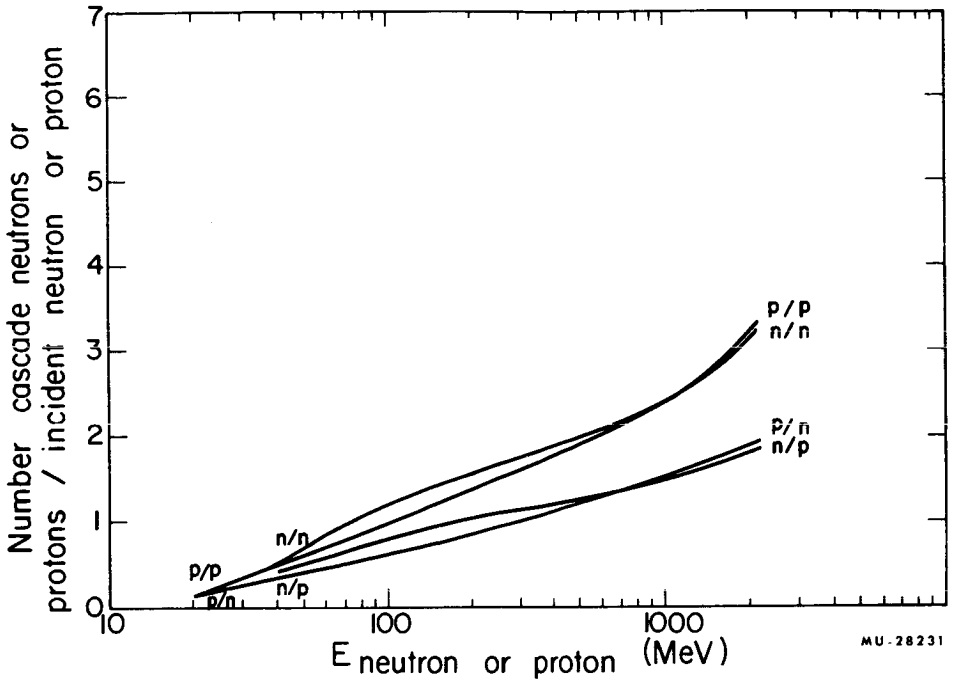

Fig. 2. Estimated cascade neutrons and protons produced by incident neutrons or protons of energy E_n on nuclei near A = 20 per incident particle per inelastic collision, from Metropolis et al. [5]

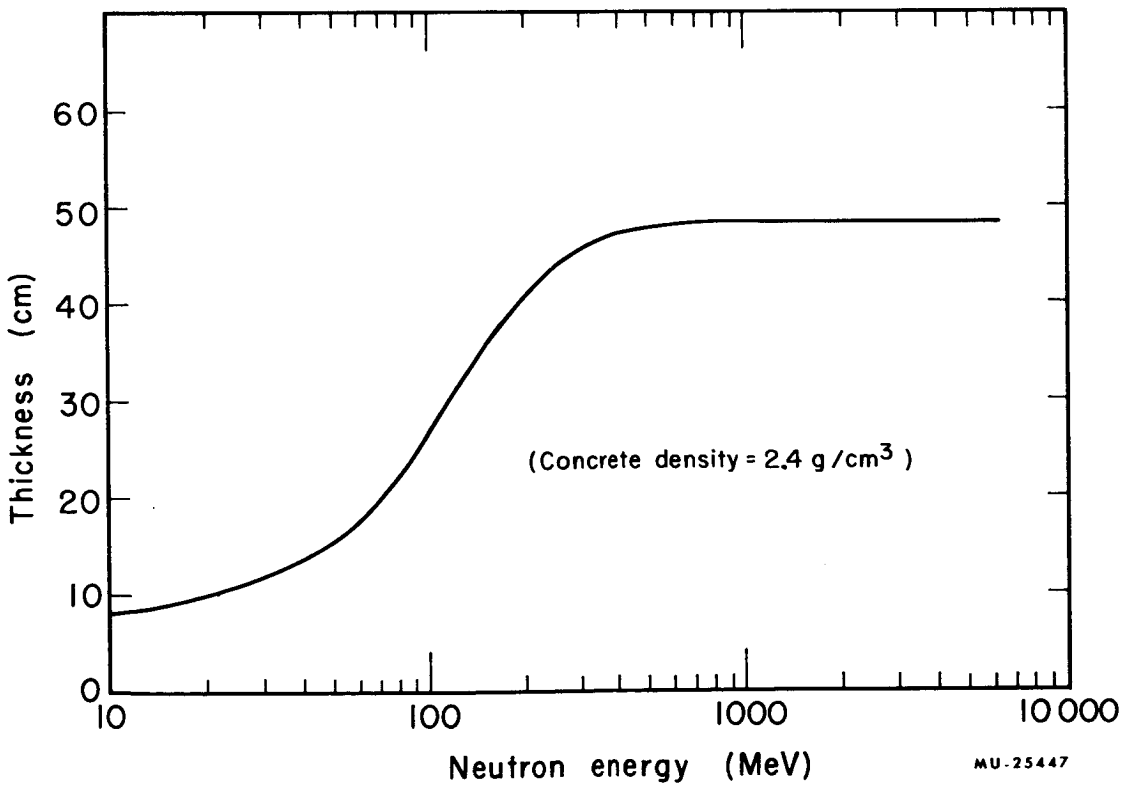

Fig. 3. Half-value reduction thickness for high-energy neutrons in ordinary concrete.

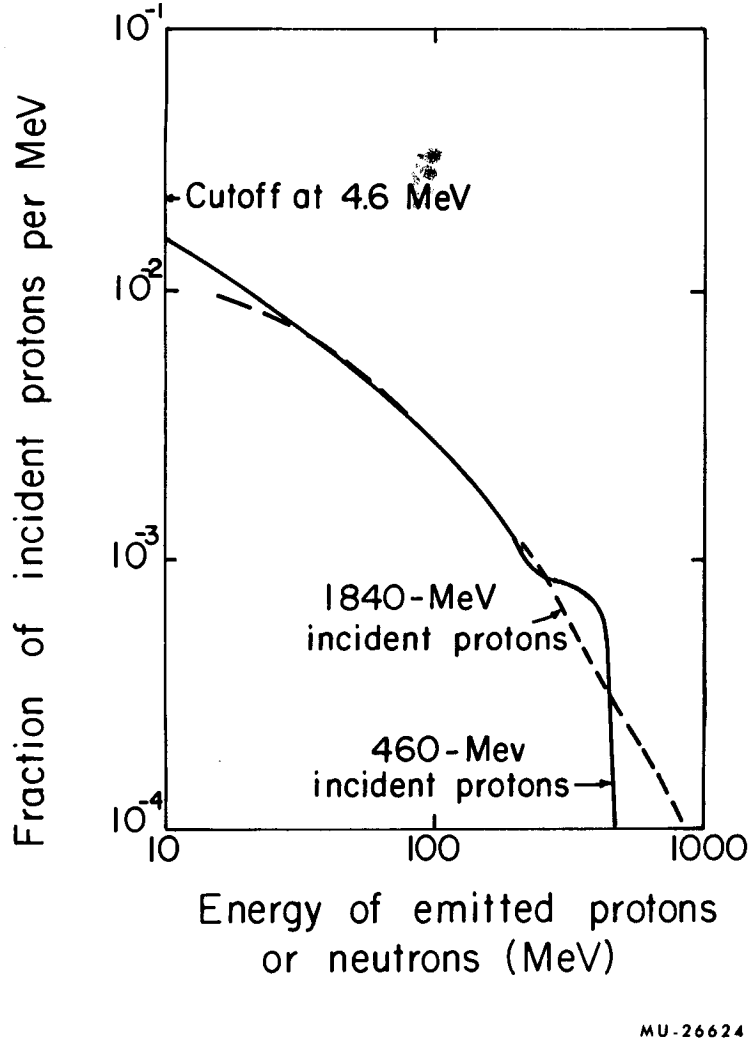

Fig. 4. Energy spectra of cascade nucleons emitted from aluminum, from Metropolis et al.[5]

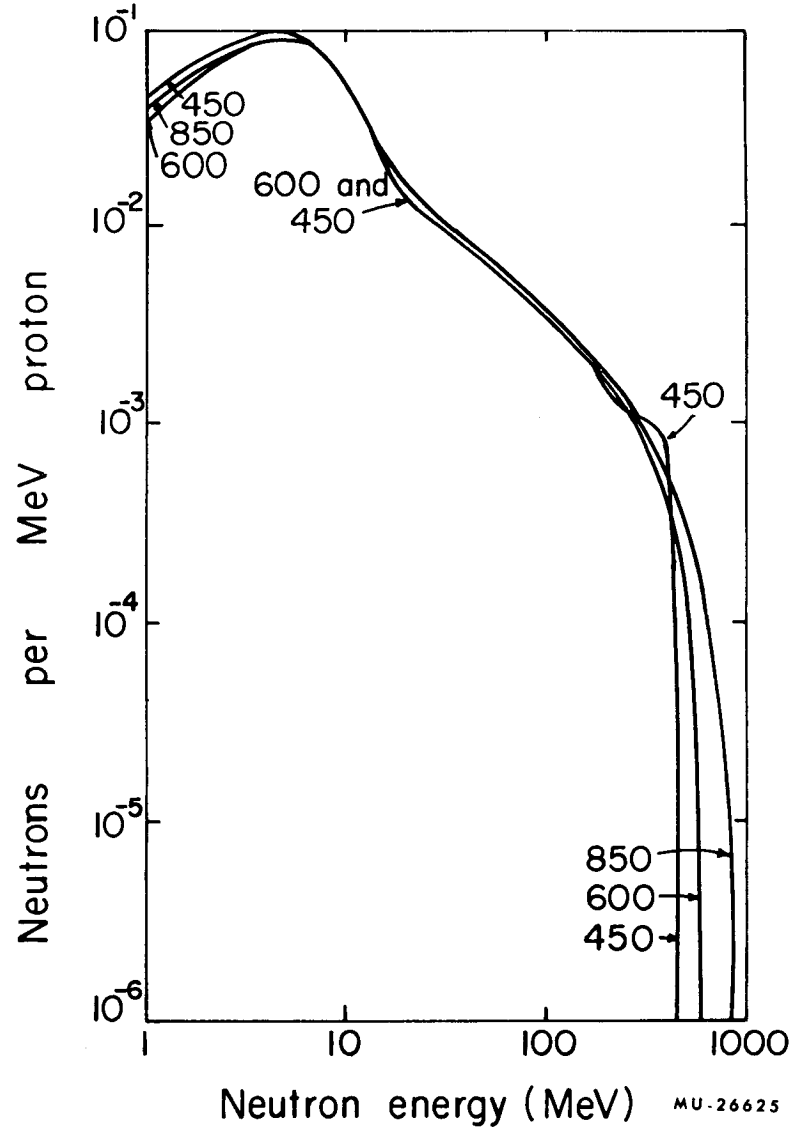

Fig. 5. Cascade and evaporation-neutron emission spectra from 450-, 600-, and 850-MeV protons on aluminum, per incident proton.

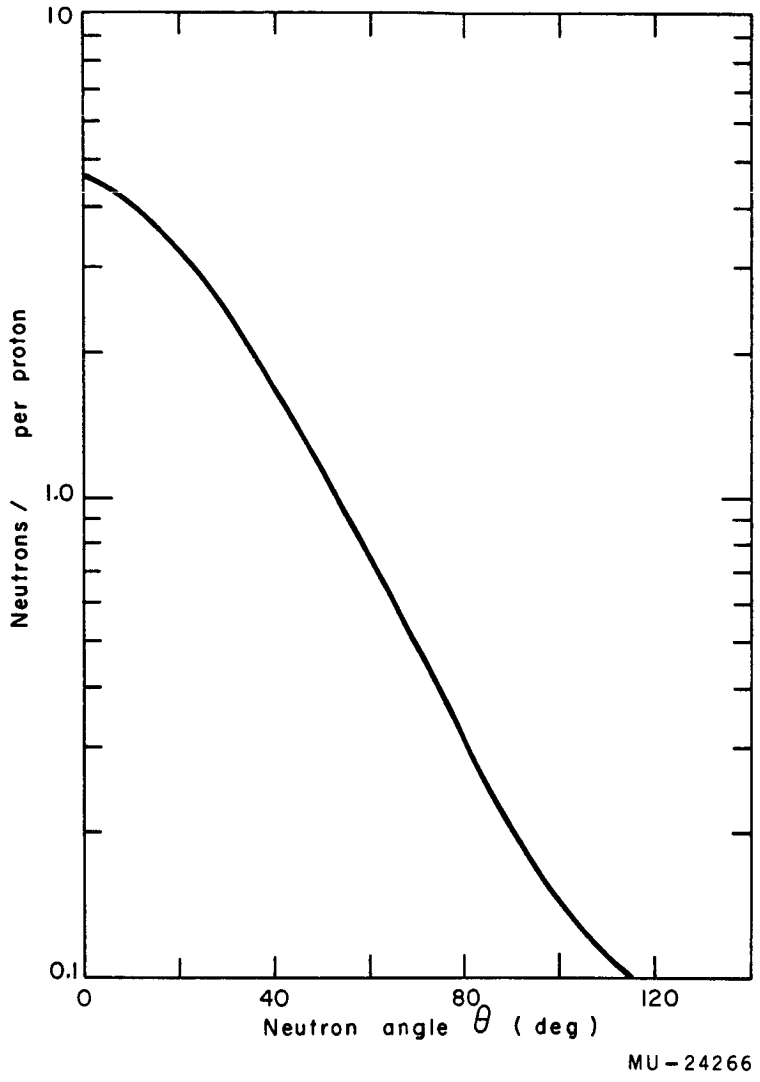

Fig. 6. Angular distribution of neutrons, over 150 MeV in energy, from a single collision in Cu by 6.3-GeV protons (normalized to 8 neutrons/proton), from Metropolis et al. [5]

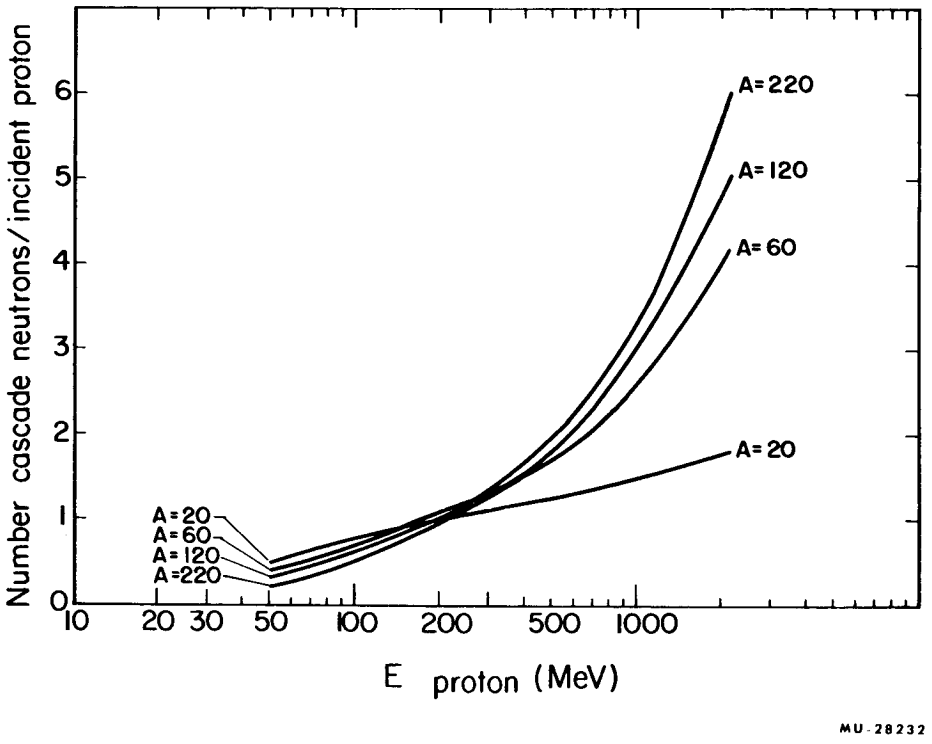

Fig. 7. Number of cascade neutrons per incident proton as a function of proton energy and target A, from Metropolis et al. [5]

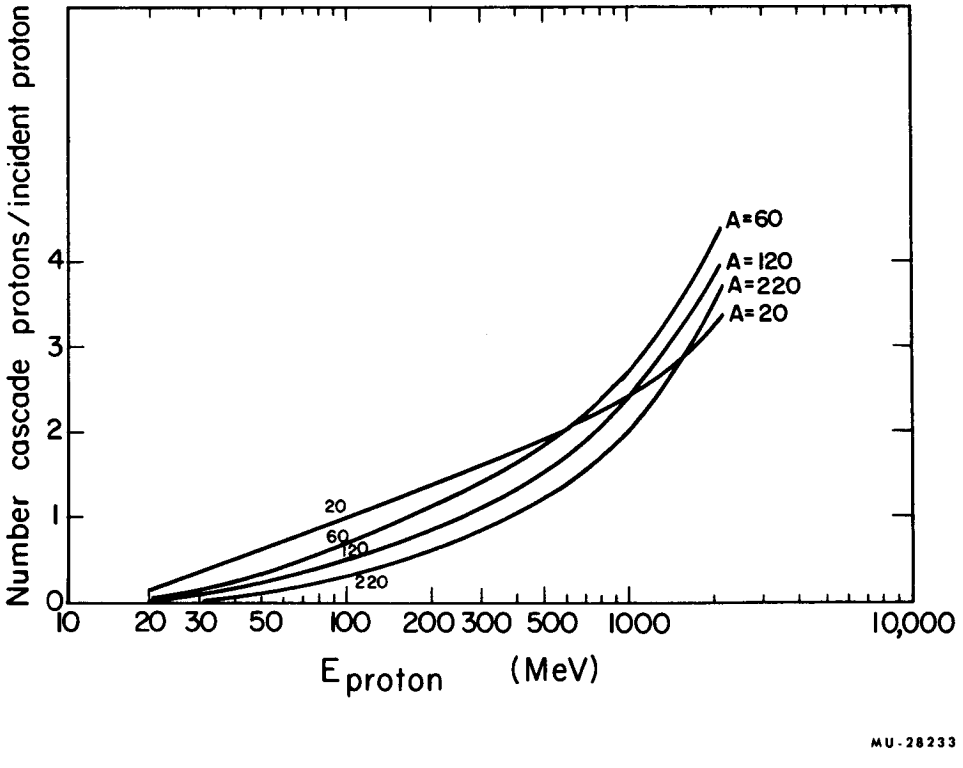

Fig. 8. Number of cascade protons per incident proton per inelastic collision as a function of proton energy and target A, from Metropolis et al. [5]

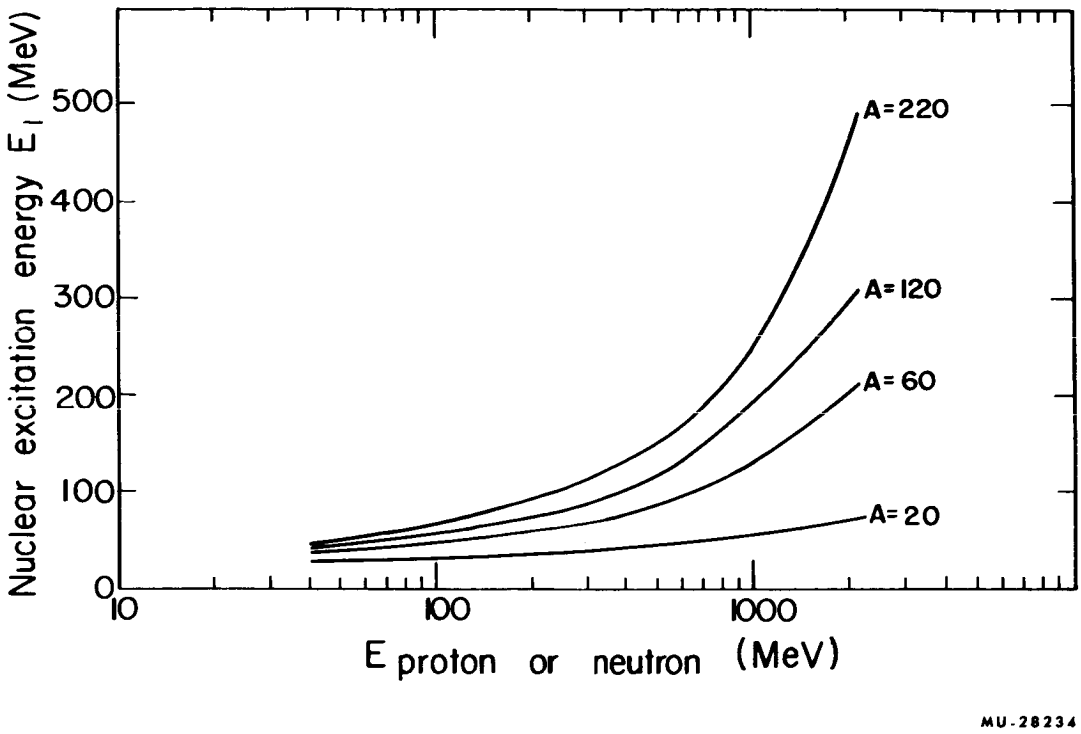

Fig. 9. Average nuclear excitation energy E_1 deposited in nucleus A by an incident neutron or proton of energy E in one inelastic collision.

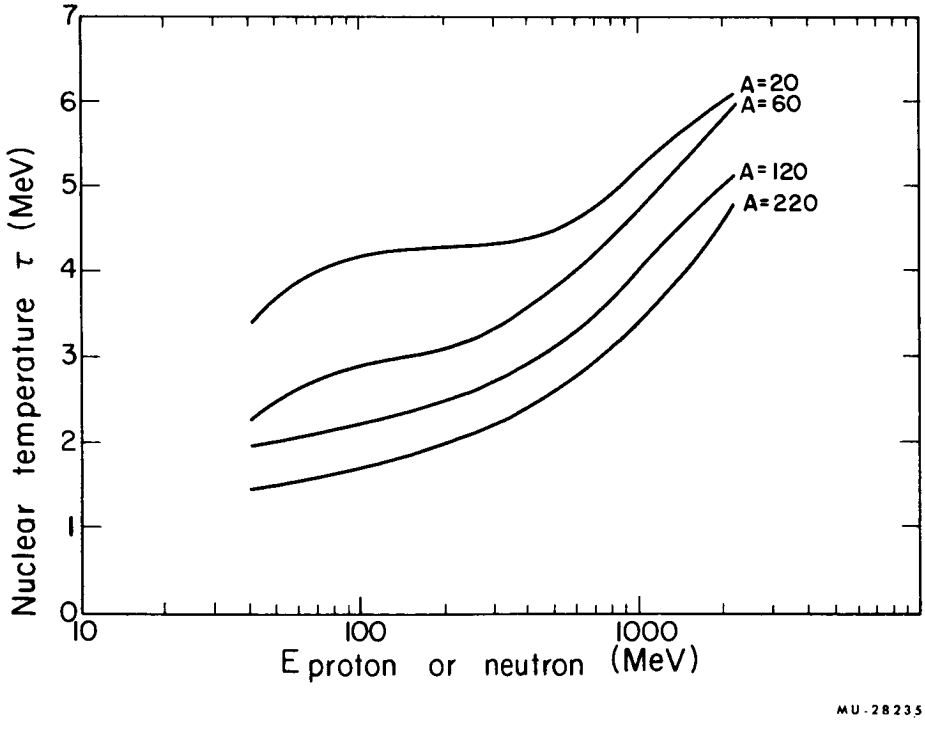

Fig. 10. Estimated residual nuclear temperature produced in nucleus A after excitation by a neutron or proton of energy E in one inelastic collision, from Metropolis et al. [5]

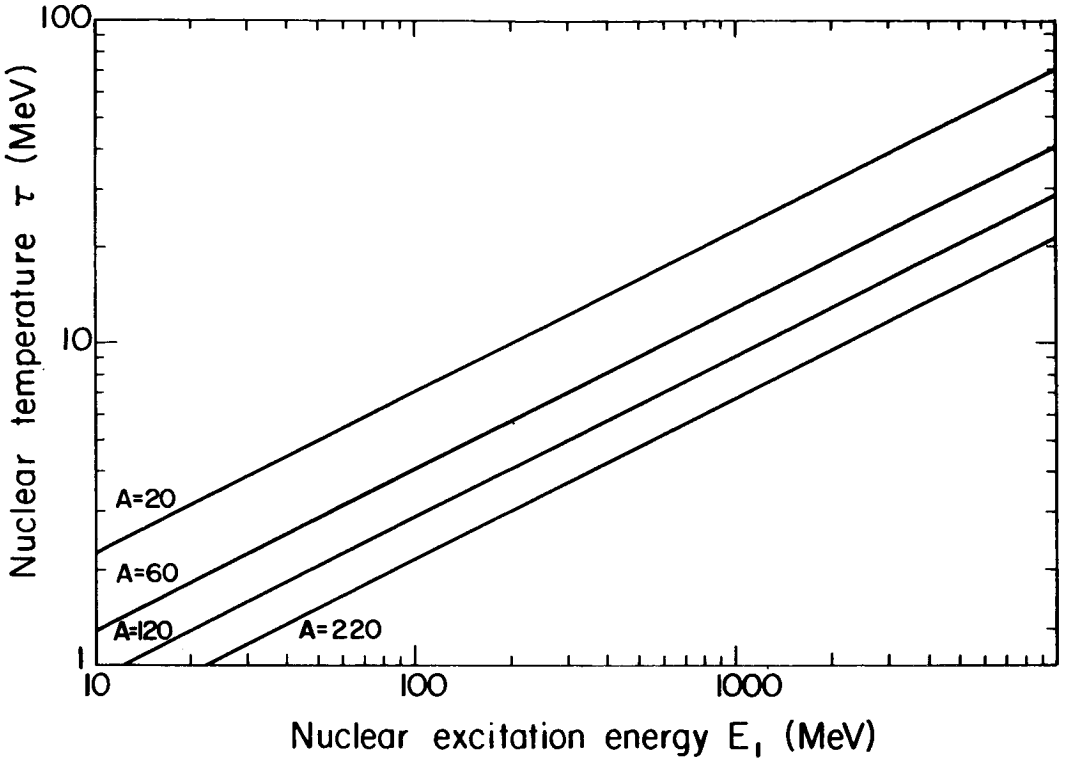

Fig. 11. Nuclear temperature τ vs nuclear excitation energy E_1 for various A's.

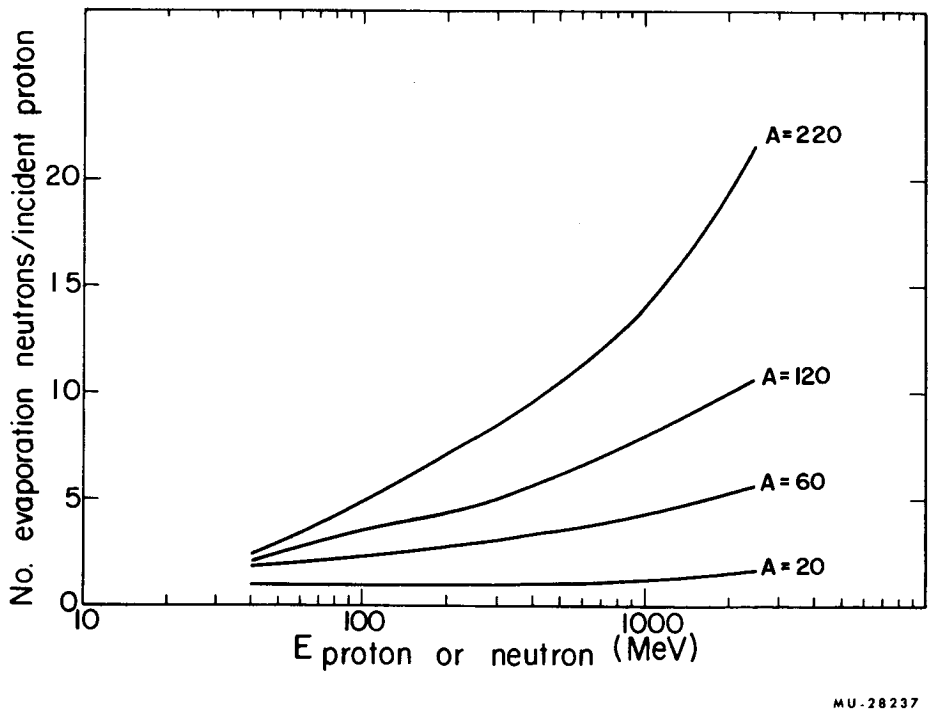

Fig. 12. Estimated number of evaporation neutrons produced per incident neutron or proton of energy E per inelastic collision, from Metropolis et al.

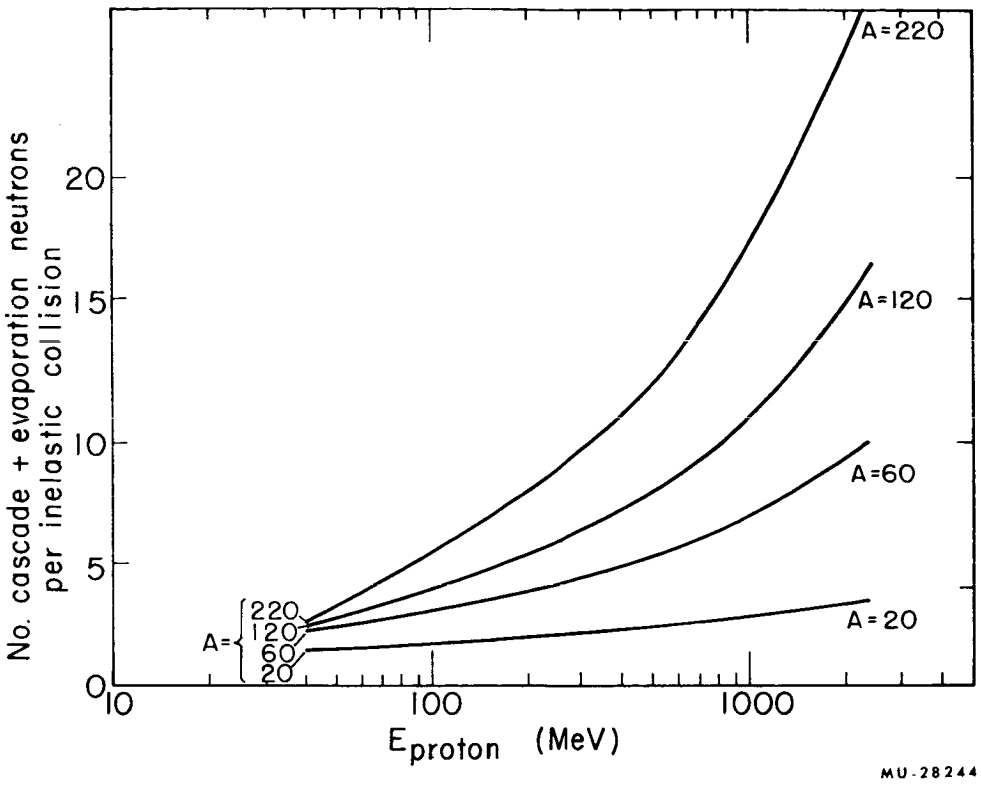

Fig. 13. Average number of evaporation protons per incident proton or neutron on various A's per inelastic collision vs energy of the incident particle, from Metropolis et al.

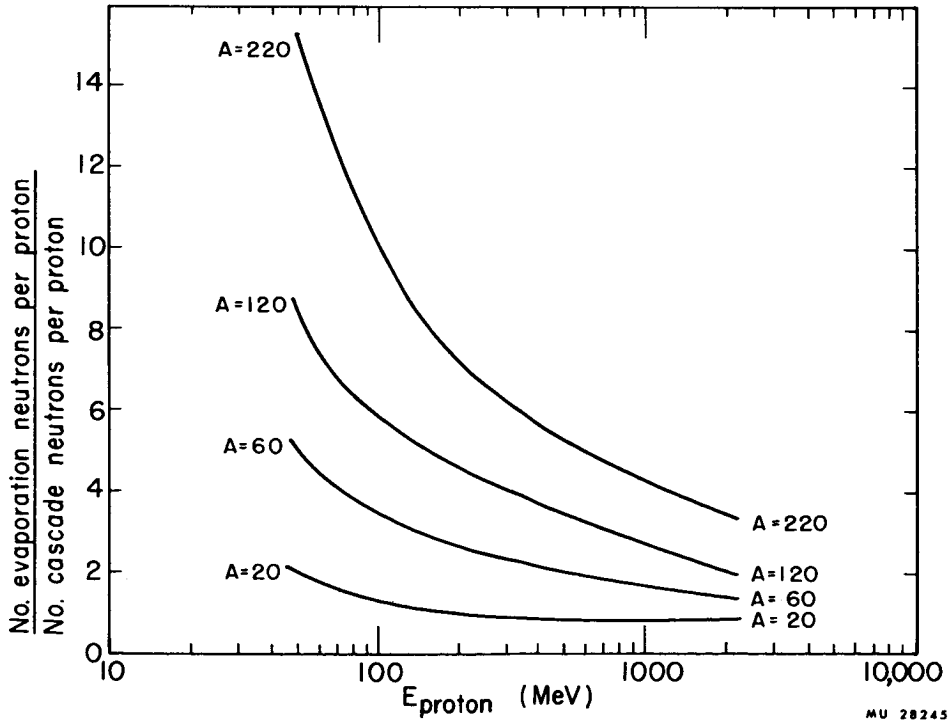

Fig. 14. Average number of evaporation H^2 per incident proton or neutron on various A's per inelastic collision vs energy of the incident particle, from Metropolis et al.

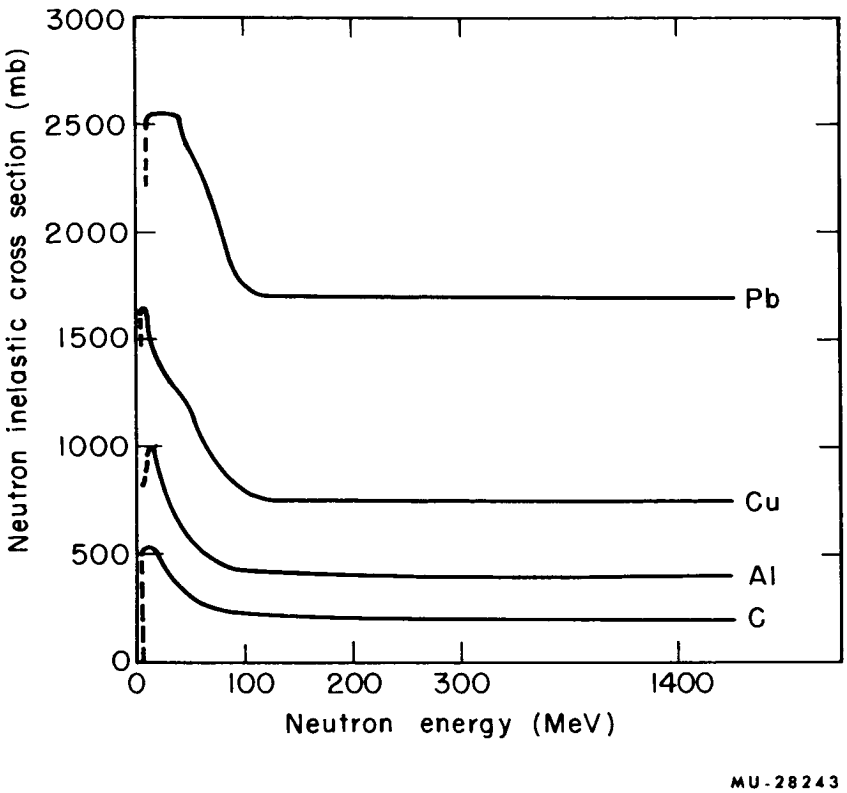

Fig. 15. Average number of evaporation H^3 per incident proton or neutron on various A's per inelastic collision vs energy of the incident particle, from Metropolis et al.

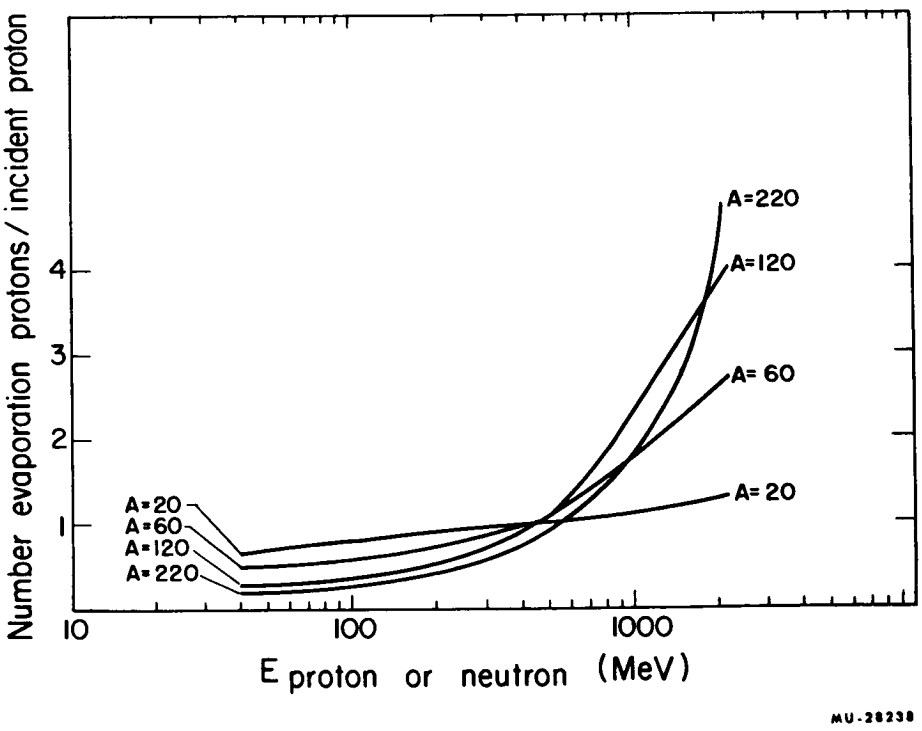

Fig. 16. Average number of evaporation He^3 per incident proton or neutron on various A's per inelastic collision vs energy of the incident particle, from Metropolis et al.

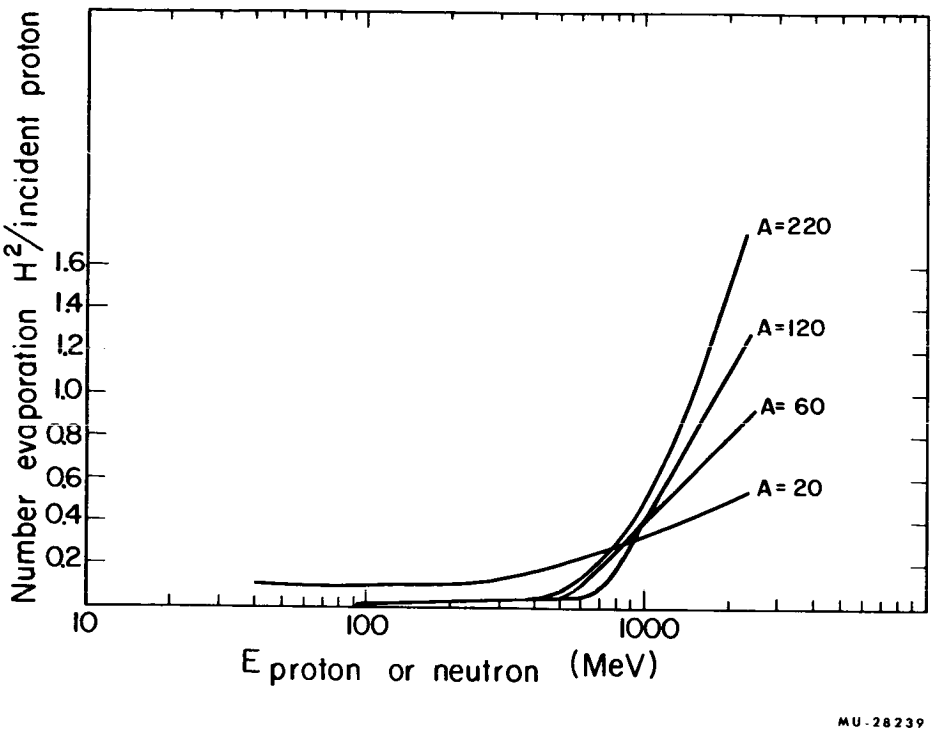

Fig. 17. Average number of evaporation He^4 per incident proton or neutron on various A's per inelastic collision vs energy of the incident particle, from Metropolis et al.

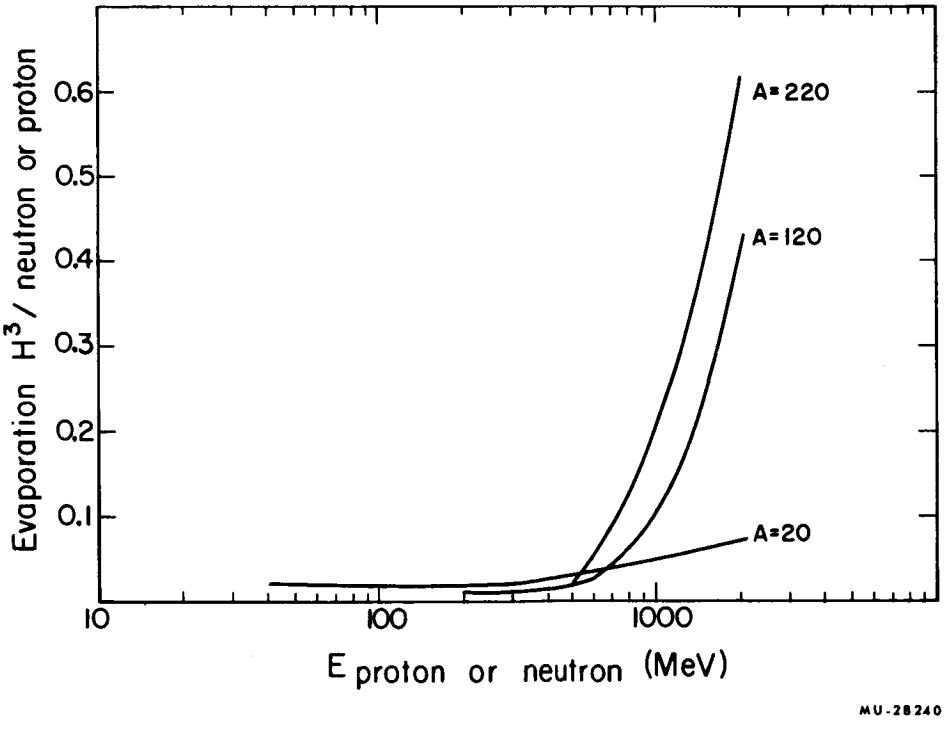

Fig. 18. Neutron inelastic cross-sections for C, Al, Cu, and Pb vs incident neutron energy, from Lindenbaum. [12]

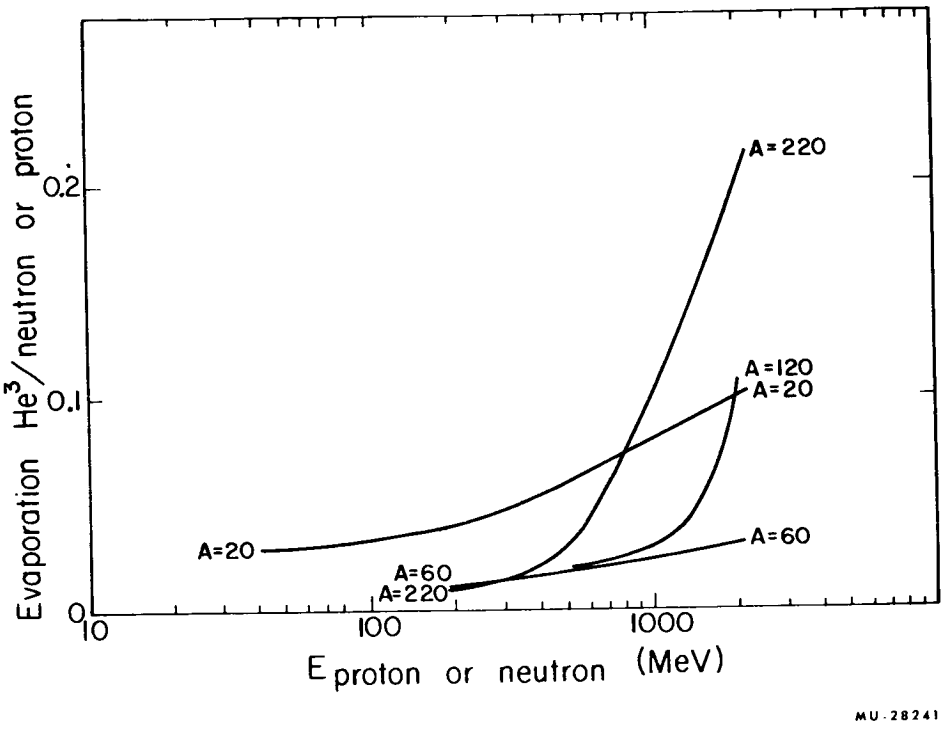

Fig. 19. Attenuation of neutrons in ordinary concrete. At 90 and 270 MeV, measurements were made at the 184-Inch 340-MeV cyclotron. At 4.5 GeV the measurement was made at the Bevatron.

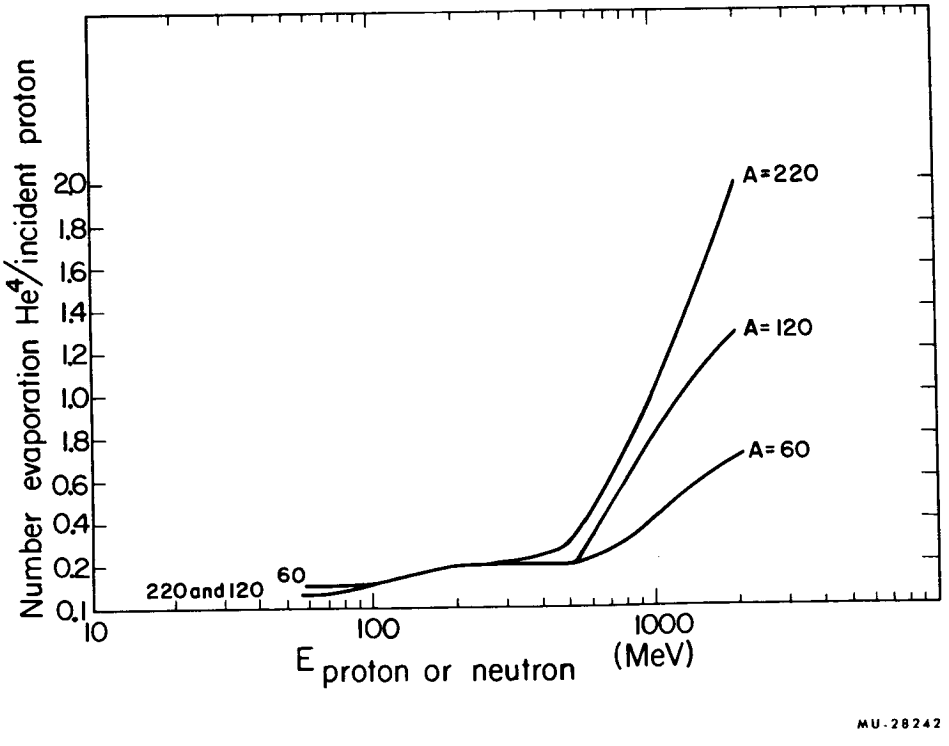

Fig. 20. Total neutron production per inelastic collision = cascade + evaporation as a function of the incident proton energy.

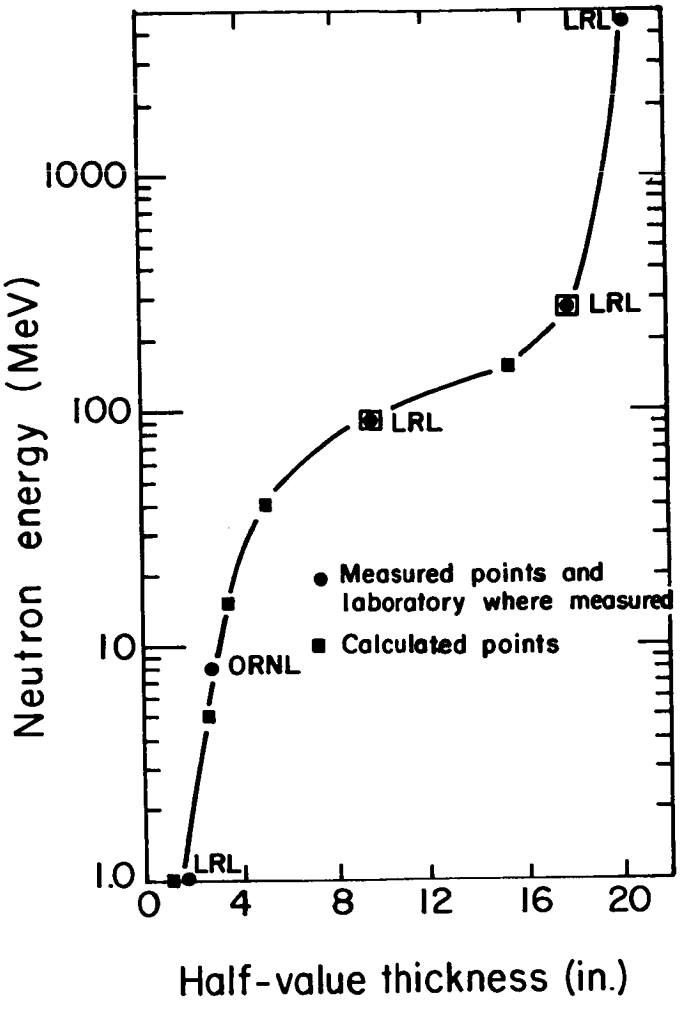

Fig. 21. Ratio of evaporation neutrons to cascade neutrons per inelastic collision as a function of the incident proton energy.

Paper F-5

SOME EXPERIMENTS ON THE PASSAGE OF HIGH-ENERGY PROTONS IN DENSE MATTER

S. P. Shen

Department of Physics, New York University
University Heights, New York, New York

Abstract

15158

A series of experiments designed to study the nuclear cascade resulting from the passage of 1 to 3 GeV protons in matter has been in progress at the Brookhaven Cosmotron. Preliminary results on the fluxes of fast neutrons (upper limits) and of strongly-interacting particles above 50 MeV are summarized here (Fig. 1 and Table 1). The four cases studied are: 1-GeV protons on Fe, on chondritic material, and on $C_5H_8O_2$, and 3-GeV protons on Fe.

I. Introduction

The passage in matter of low-energy radiation up to about 0.1 GeV (1 GeV = 10^9 eV) has been studied almost throughout the history of nuclear physics.[1] The passage in matter of particles of extremely high energy (above 100 GeV) has been studied in recent years in connection with Auger showers in the atmosphere and "jet" showers in nuclear emulsions.[2] In the intermediate region, viz., from about 0.1 to 100 GeV (hereafter referred to as the "high-energy" region), interest has been less pronounced although considerable data do exist for the case of average cosmic rays passing through the atmosphere.[3] Recently, interest in this energy range has been given renewed impetus by three superficially distinct but basically identical problems: (1) depth variation of nuclide production by cosmic rays in the atmoshpere, in meteorites, and in other astonomical objects, (2) depth dosimetry of high-

energy particles in tissue and in other absorbers, and (3) shielding of energetic particles in space and of the radiation emerging from particle accelerators.

The passage of high-energy protons differs from that of protons of lower energy mainly in that the former survive far enough in the absorber for inelastic nuclear interactions to take place. These interactions give rise to secondaries, and often to a succession of secondaries constituting what is known as a nuclear cascade. Thus, the study of the passage of high-energy protons consists largely in the study of the accompanying nuclear cascade. The nuclear cascade has been reviewed and discussed from the shielding standpoint elsewhere.[4]

Here, we will summarize briefly for this symposium several recent experiments on the passage in dense matter of monoenergetic protons of 1 and 3 GeV. The use of a narrow beam of artificially accelerated protons in these experiments made possible the study of their passage under well-defined conditions not available in cosmic-ray experiments. The reader should also refer to the nuclide-production experiments of Fireman and Zaehringer,[5] Goel, Rayudu, and Shedlovsky,[6] Shedlovsky,[7] and Honda,[8] to the shielding experiments of Tinlot,[9] and Citron, Hoffmann and Passow,[10] and those reviewed by Lindenbaum,[11] as well as to the dosimetric experiments of Shal'nov[12] and Sondhaus.[13] Some of the questions dealt with here are discussed in greater detail from the shielding standpoint in a forthcoming review article.[14]

II. Nuclear-Cascade Studies at the Cosmotron

A series of joint irradiations at the external beam of the Brookhaven Cosmotron involving several institutions was initiated in the fall of 1961. Since then, four irradiations have taken place. This section briefly summarizes some preliminary results on the nuclear-cascade experiments undertaken during these irradiations. Full details and discussions of these experiments will appear elsewhere.

In all these experiments, the basic arrangement has been the same. A narrow (< 3 cm^2 area) and nearly parallel beam of 1 or 3 GeV protons impinges perpendicularly on the center of the face (usually 1 ft by 1 ft) of a thick absorber

made of either iron, chondritic material,* or $C_5H_8O_2$ ("Plexiglas").

At various depths of interest inside the absorber are "sandwiched" very thin Al foils (usually 1 ft by 1 ft by 0.0025 g/cm^2 thick), with their flat faces normal to the beam direction. After the irradiation, which varies from 10 to 90 min in duration, the Al foils are removed, and the F^{18} and Na^{24} activities induced in each foil counted, without chemistry, by means of calibrated counters. F^{18} and Na^{24} can be produced in Al by the following reactions:

$$Al^{27}(N, X)\ F^{18},$$

$$Al^{27}(N, X)\ Na^{24},$$

and $$Al^{27}(n, \text{alpha})\ Na^{24},$$

where N stands for strongly-interacting particles (nucleons and charged pions) exceeding about 50 MeV, n stands for neutrons below 50 MeV, and X for the particles emerging from the reactions. From the measured F^{18} activity, one can deduce roughly the flux of N, which in turn allows the flux of n to be found, again roughly, from the measured Na^{24} activity. Henceforth, the symbols N will stand for the flux of strongly-interacting particles exceeding about 50 MeV, and n for the flux of fast neutrons between about 7 and 20 MeV. This method of measuring separately N and n when both types are present is described together with its variations and present limitations in detail elsewhere. Although at present the results obtained in this way are only approximate, it is felt that they are nevertheless of some interest in view of the current lack of data on the nuclear cascade.

Figure 1 ("intensity-depth curves") shows the smoothed variation of N and n with depth in the absorber for the four

---

* Material whose composition closely simulates that of chondrites, a common type of stone meteorite. Chief constituents are roughly, by weight: 35% O; 25% Fe; 20% Si; 15% Mg. The Moon is probably chondritic. We are indebted to Dr. J. P. Shedlovsky and his colleagues for providing the chondritic absorber and for permitting us to conduct our experiment in it in conjunction with theirs.

cases studied. The fours cases and the total thickness (T_o) of each absorber are listed, respectively, in the first and second columns of Table 1. Since, for each case we also made measurements (not shown here) of the lateral spread of the cascade at several depths, it has been possible to correct for the loss of particles through the sides of the absorber at great depths. This correction has already been made for the curves in Fig. 1, so that these in effect represent the integral N or n (the integration being taken over an infinite plane normal to the beam) found at various depths in an absorber of the specified total thickness but of infinite lateral extension.

Note that the ordinate in Fig. 1 is logarithmic, and is expressed in units of particles per incident primary proton. The F^{18} and Na^{24} counting rates are such that the statistical counting error is almost always negligible. For the N-curves, we estimate that the absolute values given by the ordinate have an overall error not exceeding 25%. On the other hand, the relative heights of points within each N-curve are subject to a much smaller error. The absolute values given for the n-curves should be regarded as upper limits; this is not because such neutrons were not detected (they were), but because we have chosen to use, in these preliminary results, a weighted average cross-section for Al^{27} (n, alpha) Na^{24} that we know to be too low for our cases and therefore very "safe". Thus, the four n-curves are too high by about the same factor. Note, however, that even these upper limits are interestingly low for chondrite and $C_5H_8O_2$. The relative heights within each n-curve should be quite accurate for depths greater than the maximum in the curve; for smaller depths, the relative heights may be altered slightly when the upper limits are later converted to actual values. Each curve in Fig. 1 represents the average behavior of the individual cascades induced by at least 8×10^{12} incident protons, and in one case by as many as 8×10^{13} protons. The total number of incident primaries for the 3-GeV bombardment of Fe is still somewhat uncertain at this writing; for this case, therefore, the ordinate gives upper limits for both N and n.

III. Parameters of the Intensity-Depth Curves

We now consider the intensity-depth curve in general, intorduce some parameters for specifying its more salient features, and finally use these parameters to specify the curves in Fig. 1.

Suppose an idealized detector detects the flux (or ionization, or energy deposition, etc.) of some arbitrarily chosen component (e.g., 7-MeV gamma rays; protons above 14 MeV) at every depth inside a dense absorber bombarded by high-energy protons. Consider the function

$$f_{det}(x, T_o),$$

where f, for the moment, stands for the flux, the subscript "det" stands for the detected component (so that f_{det} is the flux of the detected component), the variable x is the depth in the absorber, and T_o the fixed total thickness of the absorber. Now, in analogy with the curves shown in Fig. 1, one would expect the function $f_{det}(x, T_o)$ to assume the general shape shown by the curve so labelled in Fig. 2.

There is however, no need to restrict ourselves to the flux. Henceforth, let the symbol f stand for either flux, or energy deposition, or RBE dose, etc. (each of these quantities of course is ultimately some function of the flux of the component in question). One would expect that $f_{det}(x, T_o)$, even in this larger sense, would still take on the general shape of the curve so labelled in Fig. 2.* The dashed straight line labelled $f_{prim}(x)$ represents f due to the primaries alone. The detected component of course may or may not include the primaries.

It is convenient to regard the intensity-depth curve $f_{det}(x, T_o)$ as composed of four regions (see Fig. 2): pre-maximum, approach (to equilibrium), equilibrium, and exit.

---

* The exact shape of $f_{det}(x, T_o)$ of course depends on the functional form of f. In addition, Sondhaus[13] has observed, superposed on the nuclear cascade, the effect of the small fraction ($< 10\%$ for 730-MeV primaries) of electromagnetically-stopped primaries.[4] On the other hand, no effect due to electromagnetically-stopped primaries is obvious in the nuclide-production curves of Goel, Rayudu, and Shedlovsky[6] at 440 MeV, where such stopped primaries should account for some 20% of the incident beam. This is understandable, since one would expect the stopped primaries to show themselves in a much more pronounced manner when the total ionization is measured, as in Sondhaus' case, than when some quantity directly related to the flux is measured, as in the case of Goel et al.

The pre-maximum region may not exist if the detected component includes the primaries themselves. The equilibrium region may not be strictly reached in some cases save at very great depths where the radiation is no longer detectable.

Imagine now our finite absorber to be indefinitely extended in both the front and rear directions (i.e., the absorber is now infinitely long), then the intensity-depth curve would no longer have the shape of $f_{det}(x, T_o)$, but would instead assume the shape of a straight line identical or parallel (depending on the primary flux) to the line labelled $f_{det}(x,\infty)$. The deviation of the actual intensity-depth curve $f_{det}(x, T_o)$ from this straight line except in the equilibrium region can be thought of as due to the "missing" front and rear parts of the absorber. Thus, the "missing" front part fails to supply the forward-moving particles that would fill the area between $f_{det}(x,\infty)$ and $f_{det}(x, T_o)$ near the front; similarly, the "missing" rear part of the absorber fails to supply the backward-moving (albedo*) particles that would fill the corresponding area in the exit region. This deviation, in shape, of $f_{det}(x, T_o)$ from $f_{det}(x,\infty)$ is called the transition effect, a term used here in a more extended sense than usual. One may say that the pre-maximum and approach regions together constitute the entrance transition, and the exit region constitutes the exit transition.

If, instead of the fixed thickness T_o, we were to use an absorber of variable thickness T and detect the chosen component behind the absorber, then the "intensity-thickness" curve $f_{det}(T)$ should be expected to assume the general shape of the curve so labelled in Fig. 2. Obviously, the intensity-thickness curve can be derived from the intensity -depth curve $f_{det}(x, T_o)$ by subtracting from the latter the appropriate albedo flux at every depth x (except in the exit region, where part of the albedo is already absent). No attempt is made here to derive the intensity-thickness curves in this way from the empirical intensity-depth curves shown in Fig. 1, although this should be achievable provided one has a rough

---

* The backward-moving or albedo particles come from the backward moving secondaries emerging from the inelastic nuclear interactions. The flux of albedo particles for a given detected component is of course different for different depths x.

idea of the albedo flux as a function of depth, e.g., from the calculations in progress[15] at Oak Ridge.**

Quantities of interest in Fig. 2 are:

(a) Attenuation mean free path λ_{att}: it is customary to fit regions more or less below the transition maximum with a single exponential with exponent x/λ_{att}. Sometimes the approach region takes on a straight-line appearance only because the experimental points are few and far apart;

(b) Location of the transition maximum or "optimum depth" (term borrowed from electron-photon cascade theory): x_{max};

(c) Surface albedo per primary, defined as $f_{det}(0, T_o) - f_{prim}(0)$ if the detected component includes the primaries, or $f_{det}(0, T_o)$ if the detected component does not include the primaries;

(d) "Maximum-to-surface" ratio: $f_{det}(x_{max}, T_o)/f_{det}(0, T_o)$;

(e) "Maximum-to-primary" ratio: $f_{det}(x_{max}, T_o)/f_{prim}(0)$;

(f) Build-up factor:[17] $f_{det}(x, T_o)/f_{prim}(x)$;

** Even from the shielding standpoint, it is not certain that intensity-thickness curves are indispensable. For even when one knows in detail the radiation emerging from behind a shield, one will still be confronted with the problem of depth dosimetry of this complicated radiation. It seems that the ultimate day-to-day handling of the space-radiation shielding problem must rely on estimates based on calculations in which the shield, tissue, and even the air in between could be treated as a continuous absorber. At present, nuclear-cascade calculations have few empirical data with which to compare results. If the purpose of cascade calculations is (from the space radiation shielding standpoint) to check the validity of cascade calculations, then comparison of intensity-depth curves alone would probably suffice. From the standpoint of the physics of the nuclear cascade also, $f_{det}(T)$ is as a rule neither more nor less interesting than $f_{det}(x, T_o)$, provided T_o is not too small. On the other hand, intensity-thickness curves can be measured in far greater detail and with far more elaborate detectors[16] than intensity-depth curves.

(g) $f_{det}(x, T_o)/f_{det}(0, T_o)$;

(h) $f_{det}(x, T_o)/f_{prim}(0)$;

(i) "Critical" depth x_c, defined such that $f_{det}(x_c, T_o)/f_{prim}(0) = 1$ and $x_c \neq 0$.

Quantities (h) and (i) are of particular interest to shielding and dosimetry of high-energy particles. Thus, if f stands for the total RBE dose, then, for monoenergetic primaries, any shield thinner than x_c would be meaningless and in fact harmful.

Table 1 lists the values of some of the above parameters for the intensity-depth curves of Fig. 1. N and n have the same meansings as before. Note that, in Table 1, f stands for the flux, and not for some function of the flux. An attenuation mean free path has been arbitrarily fitted even to cases where much of the decrease is obviously not exponential. The $C_5H_8O_2$ curves in Fig. 1 are examples of the exit region merging into the pre-maximum region, resulting in an apparent maximum which is not the transition maximum of Fig. 2. In such cases, the "maximum" in Table 1 refers to this apparent maximum. Upper limits are indicated by an asterisk.

IV. Remarks

We will not here enter into any detailed discussion of the results shown in Fig. 1 and Table 1 beyond noting the following points of interest to high-energy shielding and dosimetry:

(a) The variation, with primary energy and with absorber mass number, of the quantities listed in Table 1 is generally in qualitative agreement with even the crudest of cascade theories, such as the energy-independent one based on the work of Martin.[18, 4] Quantitative comparison with detailed calculations based on transport theory is not yet feasible at present.

(b) The value of x_c and the apparent λ_{att} ($\gtrsim 110$ g/cm^2) (see Fig. 1) of the N-curve for chondritic material suggest that chondrites are poorer cosmic-ray shields than sometimes assumed. Bearing in mind that there are many cosmic rays above 1 GeV and that meteorites

are bombarded isotropically (both facts tend to make shielding far less effective than shown in Fig. 1), the result in Fig. 1 further reduces the possibility that shielding might explain the abnormally low Ne^{21} and Al^{26} contents of the two chondrites recently discussed by Anders.[19] It also makes less puzzling the nearly constant Al^{26} content of most chondrite specimens examined,[20, 21] and sets a lower limit on the pre-atmospheric mass of those chondrites whose various specimens do show dissimilar Al^{26} contents.[20]

(c) The components measured in these experiments, viz., N and n, are suitable bases for dose estimates. The quantity $N(x, T_o)$ is, in effect, the backbone of the nuclear cascade. From it, one can readily obtain the rate of inelastic nuclear interactions in the absorber material itself or in some other material (e.g., emulsion, tissue). From the interaction rate, one could then estimate as a function of depth the dose due to the interactions, including local absorption of the recoil nuclei and light fragments (e.g., He, Li, Be, B). Furthermore, adopting a fast-neutron spectral shape,[22] one can extrapolate the values of n (7 to 20 MeV) to include the flux in the dosimetrically-interesting range of, say, 1 to 30 MeV. One can then calculate, as a function of depth, the dose and RBE dose due to the fast neutrons by using the usual flux-to-dose factors.

(d) Despite the hydrogen deficiency of $C_5H_8O_2$ as compared to tissue ($C_5H_{40}O_{18}N$), the N and n measured here should be roughly valid for a true tissue absorber. This is because hydrogen deficiency should not seriously affect the development of the higher-energy components of the cascade, including fast neutrons; rather it would affect mainly the slow-neutron flux and the fast-neutron energy deposition, neither of which is directly measured here. Of course, when one now tries to calculate the fast-neutron dose in tissue from the measured n, the correct tissue composition should be used (i.e., use the usual flux-to-dose factors for tissue).

(e) The $C_5H_8O_2$ curve in Fig. 1 gives 0.12 as the maximum number of 7 to 20 MeV neutrons (per primary) emerging from the 30 g/cm^2 (10-inch) thick slab bombarded by 1-GeV protons. The maximum number of slow neutrons below 2 eV emerging from this slab was also measured, but data reduction is still incomplete at this writing. This

type of information is of some interest to the interpretation of measurements of fast cosmic-ray neutrons in the atmosphere and in space using BF_3 counters surrounded by a hydrocarbon moderator.[23]

---

1. See, e.g., H. A. Bethe and J. Ashkin, "Passage of Radiations Through Matter," Experimental Nuclear Physics, edited by E. Segre, Vol. 1, p. 166, John Wiley & Sons, New York, 1953.

2. See, e.g., papers in J. Phys. Soc. Japan 17, Suppl. A-III (1962) (Proc. Int'l. Cosmic-Ray Conf.).

3. See, e.g., R. K. Soberman, Phys. Rev. 102, 1399 (1956); W. N. Hess, H. W. Patterson, R. Wallace, and E. L. Chupp, Phys. Rev. 116, 445 (1959).

4. S. P. Shen, Aerospace Med. 32, 901 (1961); Astronautica Acta 8, 228 (1962).

5. E. L. Fireman and J. Zaehringer, Phys. Rev. 107, 1695 (1957).

6. P. S. Goel, G. V. S. Rayudu, and J. P. Shedlovsky, Progress Report (Nuclear Chemistry) Dept. of Chemistry, Carnegie Institute of Technology, Pittsburgh, Pa., 1959-60 (p. 38), 1960-61 (p. 74), 1961-62 (pp. 60, 67).

7. J. P. Shedlovsky (to be published).

8. M. Honda, J. Geophys. Research (to be published).

9. J. H. Tinlot, Brookhaven National Laboratory Internal Report 750 (T-276) (Mu-p No. 18) (1961).

10. A. Citron, L. Hoffmann, and C. Passow, Nucl. Instr. and Meth. 14, 97 (1961).

11. S. J. Lindenbaum, Annual Review of Nuclear Science 11, 213 (1961).

12. M. I. Shal'nov, Soviet J. Atomic Energy 4, 735 (1958).

13. C. A. Sondhaus, these Proceedings.

14. S. P. Shen, Astronautica Acta (to be published).

15. Papers by the Oak Ridge groups in these Proceedings.

16. F. C. Maienschein t al., these Proceedings.

17. B. J. Moyer, "Build-up Factors," Proceedings of the Conference on the Shielding of High-Energy Accelerators, TID-7545, p. 96 (1957).

18. G. R. Martin, Geochimica et Cosmochimica Acta 3, 288 (1953).

19. E. Anders, Science 138, 431 (1962), and references 1, 2 and 3 therein.

20. M. W. Rowe, "Quantitative Measurement of Gamma-Ray Emitting Radio nuclides in Meteorites," preprint, 1962.

21. S. P. Shen and G. R. Laurer, unpublished results of a gamma-spectrometric survey (in progress) of meteorite specimens in New York museums.

22. R. Wallace and C. A. Sondhaus, these Proceedings.

23. S. A. Korff and R. B. Mendell, private communication.

Acknowledgements

We wish to thank Professor S. A. Korff for his continued interest and hospitality. We are indebted to Drs. R. Davis, Jr., J. P. Shedlovsky, and R. W. Stoenner for their generous and invaluable help during these experiments, and to Dr. W. H. Moore and the Cosmotron staff for their cooperation. The joint irradiations were ably coordinated by Professor Shedlovsky, representing Carnegie Institute of Technology. The interest of Dr. F. W. Wendt is also much appreciated. This work was supported in part by the NASA, the AFOSR, and the Research Corporation.

Table I. Parameters of the Intensity-Depth Curves of Fig. 1.

	T_o (g/cm^2)	x_{max} (g/cm^2)		λ_{att} (g/cm^2)		"Max.-to-surface" ratio		"Max.-to primary" ratio		x_c (g/cm^2)		Surface albedo (particles per primary)	
		N	n	N	n	N	n	N	n	N	n	N	n
1-GeV on Fe	740	40	70	120	120	1.3	2.5*	1.3	-	120	-	0	0.3
1-GeV on chondrite	120	35	45	-	-	1.3	2.7*	1.3	-	85	-	.045	.089
1-GeV on $C_5H_8O_2$	30.4	22	22	-	-	1.25	4.10*	1.25	-	-	-	.027	.032
3-GeV on Fe	703	60	90	200	200	3	3*	6.8*	-	400*	-	0.8*	1*

*Upper limit.

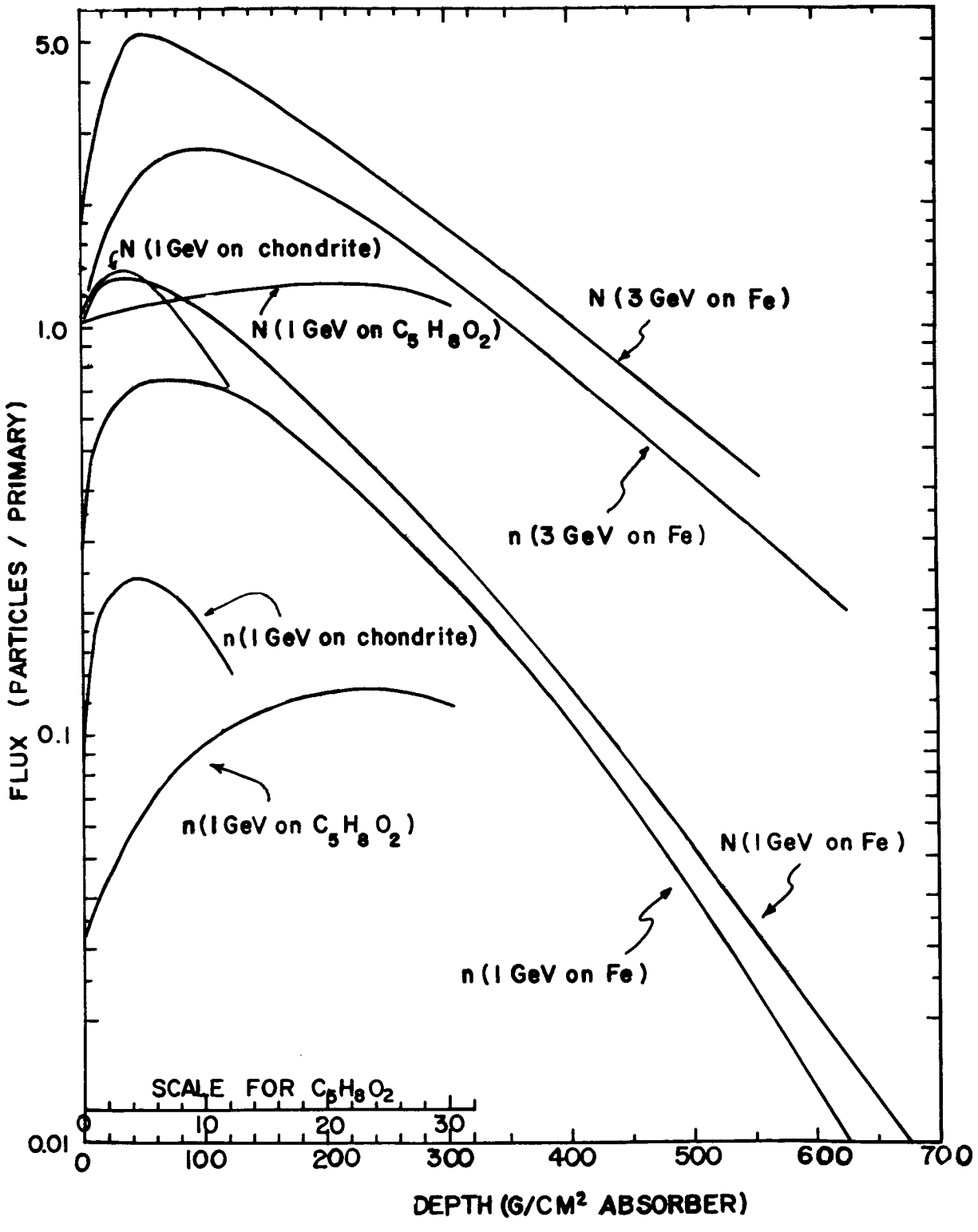

Fig. I Intensity - depth curves for N and n (n-curves are upper limits; see text). Note the expanded abscissa scale for $C_5H_8O_2$.

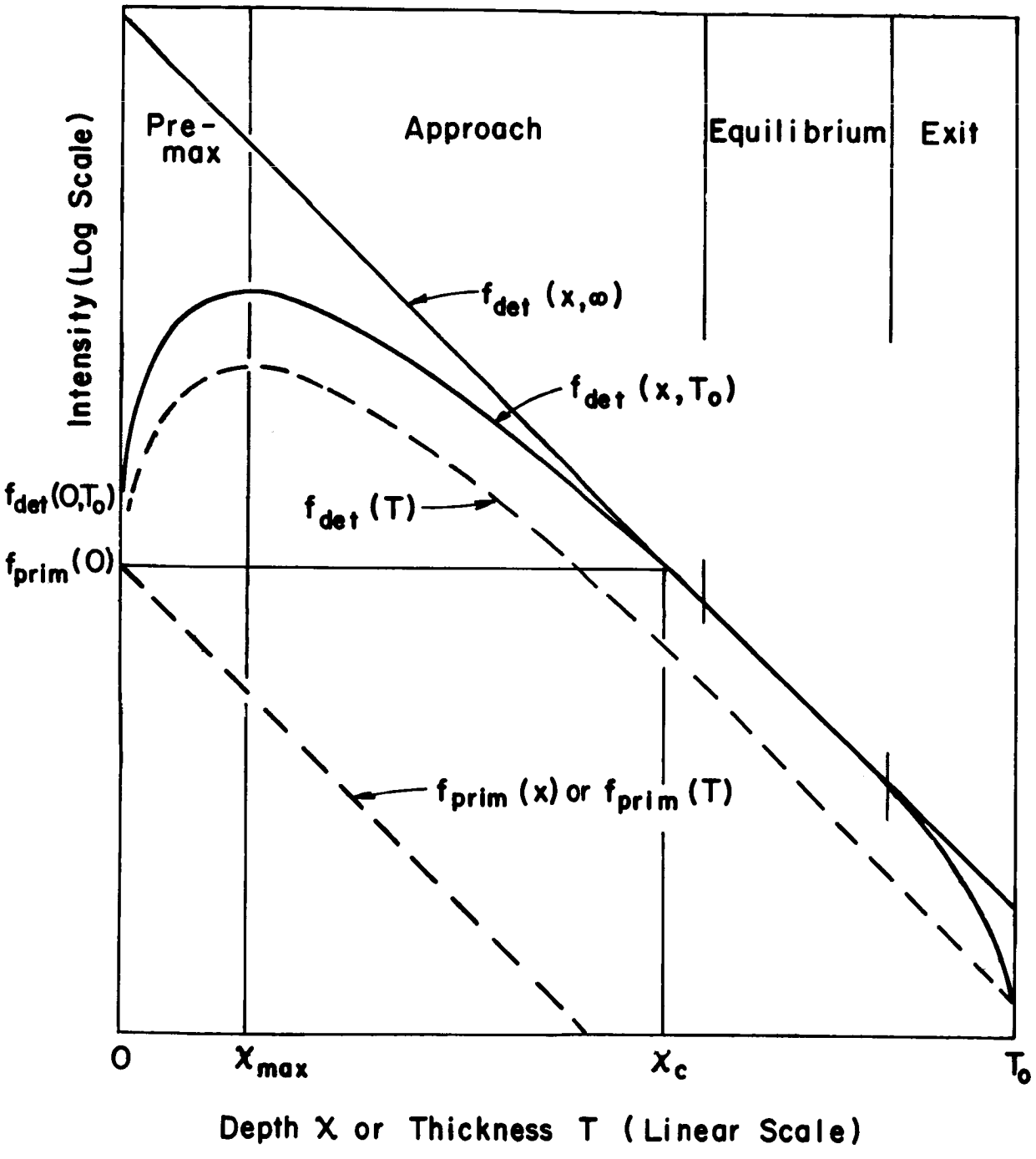

Fig. 2 Some idealized intensity - depth and intensity - thickness curves.

Paper F-6

THE BIOLOGICAL HAZARDS OF π AND μ MESONS

B.L. Murphy, P. Kitching and H.B. Knowles
Yale University

Abstract

15159

The biological hazard of both kinds of π and μ mesons has been very roughly evaluated for the purpose of estimating shielding about a meson factory. Certain processes relative to the probable interactions of stopped mesons are discussed in detail because of their relevance to shielding against high energy proton fluxes. In particular, stopping π^- mesons appear to be of the order of ten times more dangerous than neutrons of the same energy, and the importance of this ratio is noted for the case of thin space shields. Techniques for an improved calculation of the hazard are considered.

Introduction

As the last paper of this conference, it seems appropriate to remark that a number of our ideas have been revised in the last three days. In addition, our results are no more than a very rough estimate of the personnel hazard induced by mesons necessitated by a particular problem. It is hoped that these results will be revised in the near future when a proper computer Monte Carlo calculation is made.

Our interest in this problem has been connected with the design of a 750 Mev proton linear accelerator with a very high beam intensity, specifically, 1 milliampere

average current of high energy protons with suitable targets and magnetic optical devices, we expect to produce meson beams of the intensities shown in Table I. Justification for these values is given in a recent design study status report.[1]

Table 1. Expected Meson Beams $\Delta p/p = 1\%$

Meson	Intensity (number/sec)
π^+	10^9
π^-	10^8
μ^+	$\sim 10^8$
μ^-	$\sim 10^7$

It will be noted that these beams are analyzed and thus have a relatively narrow energy spread. This is not the case with the pions produced by a white spectrum of protons such as might be found in the inner Van Allen belt. It should be remarked that most nuclear physicists have assumed that rather large intensities of high energy protons were to be found in many space environments; many of the papers presented here have presented evidence to the contrary, and it is therefore not certain how pertinent the behavior of mesons is to the space radiation hazard problem, however important it may be to the designers of a meson factory. However, the findings are presented in the hope that they will be re-examined and incorporated into calculations relating to problems of radiation hazard during passage through regions of intense high energy proton fluxes.

Electromagnetic Interaction of Mesons with Tissue

If the human body is taken to be 30 cm thick, mesons of all kinds with kinetic energies above approximately 100 Mev penetrate the body and behave much as do protons in energy loss by ionization. One significant difference should be indicated: π mesons have a mass about one-seventh, and μ mesons a mass about one-ninth that of a proton. As Dr. H. J. Schaefer pointed out in his very informative talk, the tissue dose from protons is not localized because so many high energy delta rays are produced and the energy loss is diffused by these. Because the mesons will in general, produce delta

rays of maximum energies nine and seven times those produced by protons, their ionization loss will result in an even more diffuse tissue dose. No account was taken of this effect in the calculations to be presented here; an early modification of this study will be the calculation of an L.E.T. spectrum of the sort that Dr. Schaefer presented.

Mesons stopping within the body also exhibit a different stopping power behavior from that of heavy charged particles. If compared to protons, directly, a pion has one seventh and a muon one-ninth the residual range as a proton of the same velocity. Thus, π^+ and μ^+ mesons should reproduce the L.E.T. vs range curve of the proton in miniature, including the recombination effects, known to set in at about 40 kilovolts proton kinetic energy. In the terminology of Dr. Schaefer, the "thin-down" region is reduced to 1/7 or 1/9. The negative particles do not recombine and therefore rise to a higher value of L.E.T. These effects are shown schematically in Figure 1, in which the proton Bragg curve is approximately compared to that of the four kinds of mesons and also to that for the alpha particle. The latter undergoes double recombination and therefore has a peak of ionization only about 2.5 times that of the proton, rather than the 4 times expected on the simple theory. Figure 1 thus indicates some of the peculiarities of mesons. If the abscissa is noted, one might infer that the mesons would be less dangerous than protons for cells of order of 5 to 10 microns diameter, and about equally dangerous for cells of the order of one micron, which is the size of the meson thin-down region. On the left hand vertical scale are plotted some rbe values recommended by the NCRP (as functions of L.E.T. only); it is seen that the rbe is even harder to evaluate in this case than is usual, because the stopping mesons differ from protons first, in that their delta rays are more energetic, second, in that the effect more critically depends on all size, and third, in that the negative mesons behave quite differently in the last fraction of a micron than do the positive mesons. We chose an rbe of 5 for stopping mesons on a very conservative basis.

Terminal Interactions of Mesons With Tissue

After depositing their kinetic energy in tissue and coming to rest, mesons also differ from other charged particles in that they proceed to deposit some significant fraction of their rest energy. The negative mesons again differ from the

positive mesons by undergoing capture by the Coulomb field of a nucleus. If we note that tissue is well represented by $C_7H_{70}O_{32}N_2$ [2] capture on hydrogen would appear to be common, but if this should occur the neutral mesic hydrogen atom undergoes a sufficient number of thermal collisions to cause mesons always to be captured in the stronger Coulomb potential of one of the heavier nuclei. Details of this process are not well known; it is possible that the proton receives some of the capture energy. Once the negative meson is in the 2s level of, for example, an oxygen atom, its optical transitions rate [3] is much smaller than its Auger transition, as shown in Table 2. The latter is just large enough to permit the π^- to get to the 1s orbit before it decays.

Table 2 Lifetimes and Transition Probabilities For π^- and μ^- Mesons In Oxygen

	π^-	μ^-
Mean Life	2.5×10^{-8} sec.	2×10^{-6} sec
Transition Probabilities		
Optical		
2s ⟶ 2p*	1×10^{4}/sec	2×10^{4}/sec
2p ⟶ 1s	5×10^{15}/sec	1×10^{15}/sec
Auger		
2s ⟶ 1s	1×10^{8}/sec	2×10^{9}/sec

* The 2s meson level lies slightly above the 2p level because of the penetrating s orbit together with the small meson-nucleus radius.

However, this particular meson interacts strongly with the nucleus and is always absorbed by it in about 10^{-18} sec. The μ^- in the 1s orbit interacts so weakly that it undergoes nuclear absorbtion in water only about 17 per cent of the time. [4] The positive mesons undergo normal decay processes, as shown in Table 3. The complicated capture products of π^- mesons were taken from the emulsion data of Van der haeghe and Demeur, using only the oxygen stars.

Table 3 Behavior of Stopped Mesons in Tissue

MESON	TERMINUS	PRODUCTS	COMMENT
μ^+	Decay	34 Mev e^+ (Avg.)	e^+ annihilation
μ^-	**Decay - 83%	34 Mev e^- (Avg.)	
	Capture - 17 %	2 to 3n,	Excited nucleus $\bar{E}_n$ = 20 Mev
π^+	Decay	4.14 Mev μ^+	μ^+ decays
π^-	**Capture	(a) C^{12*} + p+3n (68%)	$\bar{E}_\alpha$ = 7 Mev
	(O^{16} only noted)	(b) 3 α + p+3n (17%)	$\bar{E}_p$ = 8 Mev
		(c) 2 α + 3p + 5n, etc.	$\bar{E}_n$ = 20 Mev

** Auger electrons also emitted

Calculation of Energy Deposition and Dose

The various processes indicated in Table 3 are evaluated on a very elementary basis. For energy deposition W' (Mev/cm) we write

$$D(\text{rads/particle/cm}^2) = \frac{1.6\ 10^{-6}\ \text{ergs/mev}}{100\ \text{ergs/g-rad} \times 19/\text{cm}^3}\ W'\ (\text{Mev/cm})$$

and approximate W' by

$$W' = \frac{W\ (\text{total Mev deposited})}{30\ \text{cm}}$$

The latter equacion is extremely crude and is particularly inaccurate when the energy of the mesons lost to range is considered for the worst case (π^-) the error is of less significance, as will be shown. We can thus calculate the energy deposition in rads per hour per unit flux as a function of incident meson kinetic energy as shown in Figure 2.

(a) energy loss by ionization
(b) electrons from $\mu^\pm$ decay
(c) neutrons from μ^- capture

(d) muons from π^+ decay
(e) neutrons from π^- capture
(f) protons from π^- capture
(g) alpha particles plus heavy fragments from π capture.

These are now to be evaluated by use of an rbe and added for each process. We have elected the NCRP values of rbe because we are dealing with chronic exposures, although the validity of these values for this problem is, as noted, not at all clear. In particular for the energy loss process (a), rbe = 5 is used for meson energies below 100 Mev and, rbe = 2 for penetrating mesons (refer to Fig. 1). For process (b) rbe = 1 is used, and for processes (c), (d), (e) and (f) a nominal rbe value of 10 is used. Progress (g) is assigned an rbe of 20, the usual value for particles above mass four. From these values, the rem for each particle at each energy can be evaluated and these are plotted in Fig. 3. Also shown, for comparison, is the equivalent value for neutrons.

Discussion

The extremely flat characteristic of the low energy π^- dose curve is the most significant feature of Fig. 3, and it indicates that the proton, neutron, and heavy particle fragments are of particular hazard following the capture of a π^- meson. The hazard may be worse than shown, in that all of these star fragments are very localized (in a more microscopic sense than that used by Schaefer) and a monoenergetic negative pion beam could produce a very serious internal radiation burn. With respect to space applications Metropolis, et. al show that protons near an energy of 700 Mev produce about 10 neutrons per inelastic collision, compared to about 0.5 of a negative pion.[6] Because the data of Fig. 3 suggests that the negative pions are each about 10 times more dangerous to a human than are neutrons, the negative pion flux behind a thin shield may be of the order of 30 to 50 per cent as dangerous as are the neutrons. Neither will be as serious as are the penetrating protons, but the π^- secondaries from inelastic processes should not be neglected, because of the extremely localized nature of the biological damage.

1. Internal Report Y-6 A Progress Report On The Design Of A Very High Intensity Linear Accelerator For Protons At An Energy Of 750 Mev. Yale University October 30, 1962.

2. W. A. Gibson, Energy Removed from Primary Proton and Neutron Beams by Tissue, ORNL 61-6-48 p. 5 (1961).

3. Table adapted from R. E. Marshak Meson Physics Chap. 5, p. 178, McGraw Hill, New York (1952).

4. H. K. Ticho, Phys. Rev. 74, 1337, (1948).

5. G. Van der haeghe and M. Demeur, Nuovo Cim 4 (Series 10), 931 (1956 Suppl.).

6. N. Metropolis, R. Bivins, M. Storm, J. M. Miller, G. Friedlander and Anthony Turkevitch, Phys. Rev. 110, 204, (1958).

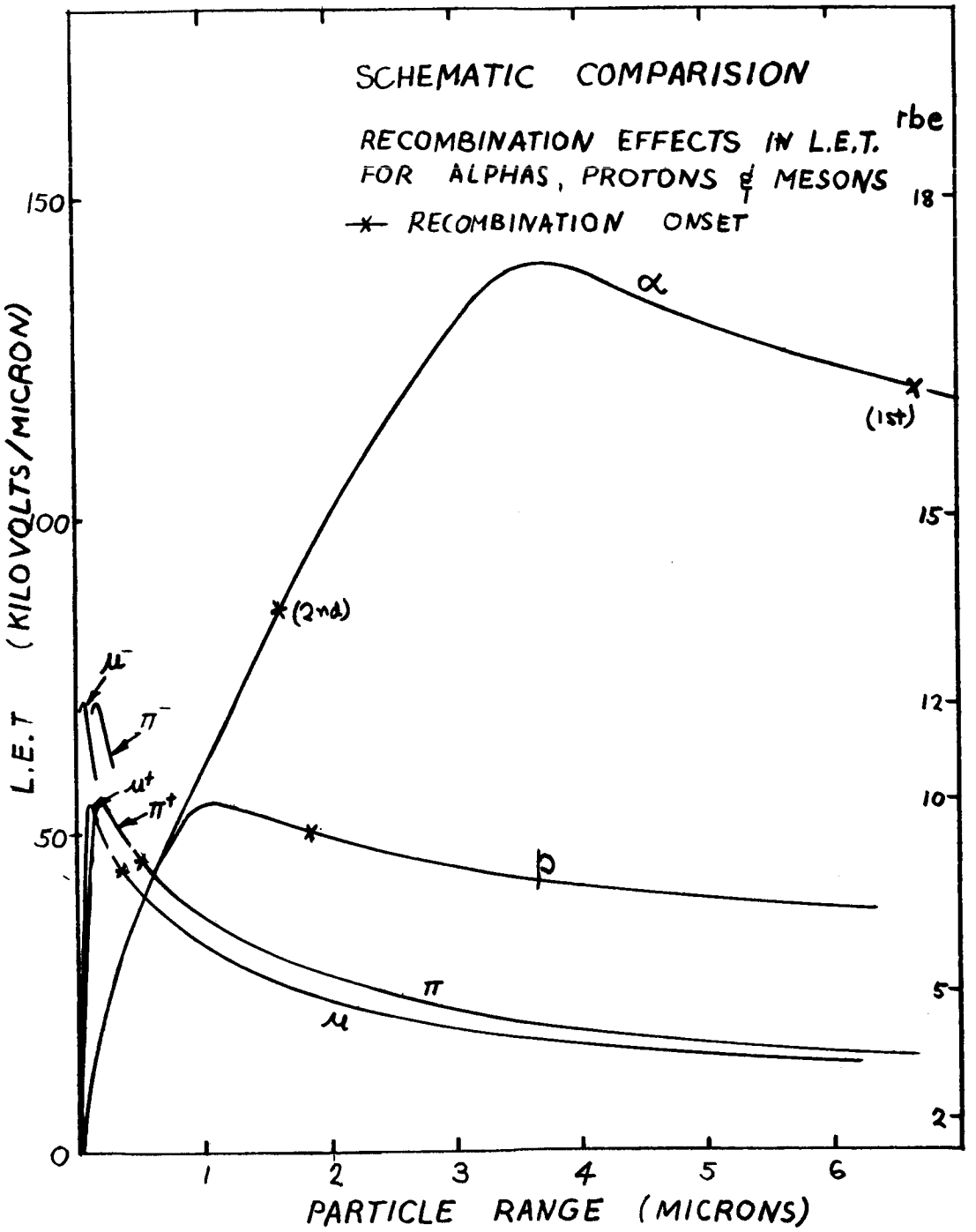
SCHEMATIC COMPARISION
RECOMBINATION EFFECTS IN L.E.T.
FOR ALPHAS, PROTONS & MESONS
RECOMBINATION ONSET
rbe
L.E.T (KILOVOLTS/MICRON)
PARTICLE RANGE (MICRONS)
150
100
50
0
18
15
12
10
5
2
1
2
3
4
5
6
α
(1st)
(2nd)
p
π
μ
μ⁻
π⁻
μ⁺
π⁺

FIG. 1

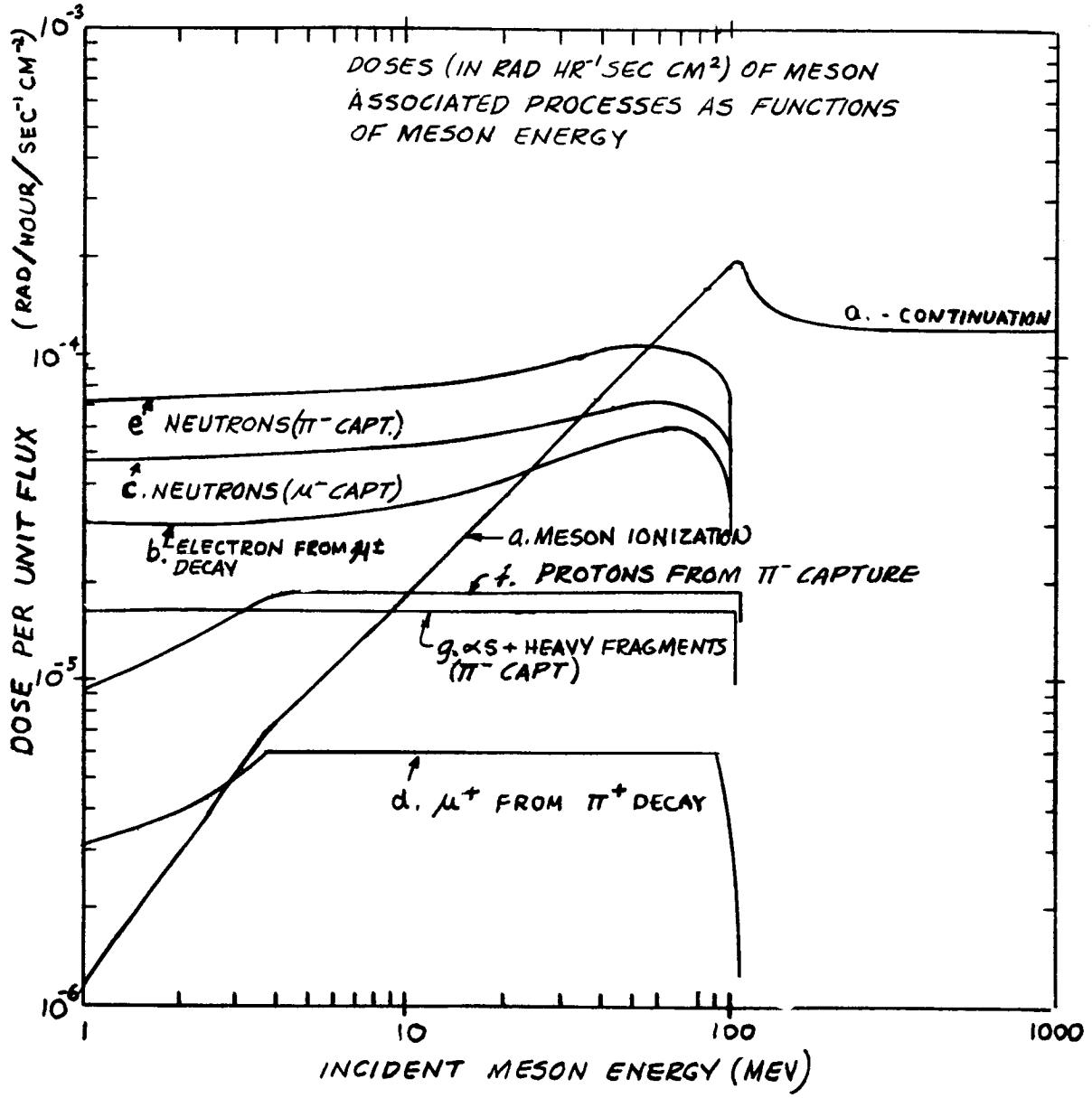
DOSES (IN RAD HR⁻¹ SEC CM²) OF MESON ASSOCIATED PROCESSES AS FUNCTIONS OF MESON ENERGY
DOSE PER UNIT FLUX (RAD/HOUR/SEC⁻¹ CM⁻²)
10⁻³
10⁻⁴
10⁻⁵
10⁻⁶
a. - CONTINUATION
e. NEUTRONS (π⁻ CAPT.)
c. NEUTRONS (μ⁻ CAPT)
b. ELECTRON FROM μ± DECAY
a. MESON IONIZATION
f. PROTONS FROM π⁻ CAPTURE
g. αS + HEAVY FRAGMENTS (π⁻ CAPT)
d. μ⁺ FROM π⁺ DECAY
1
10
100
1000
INCIDENT MESON ENERGY (MEV)

FIG. 2

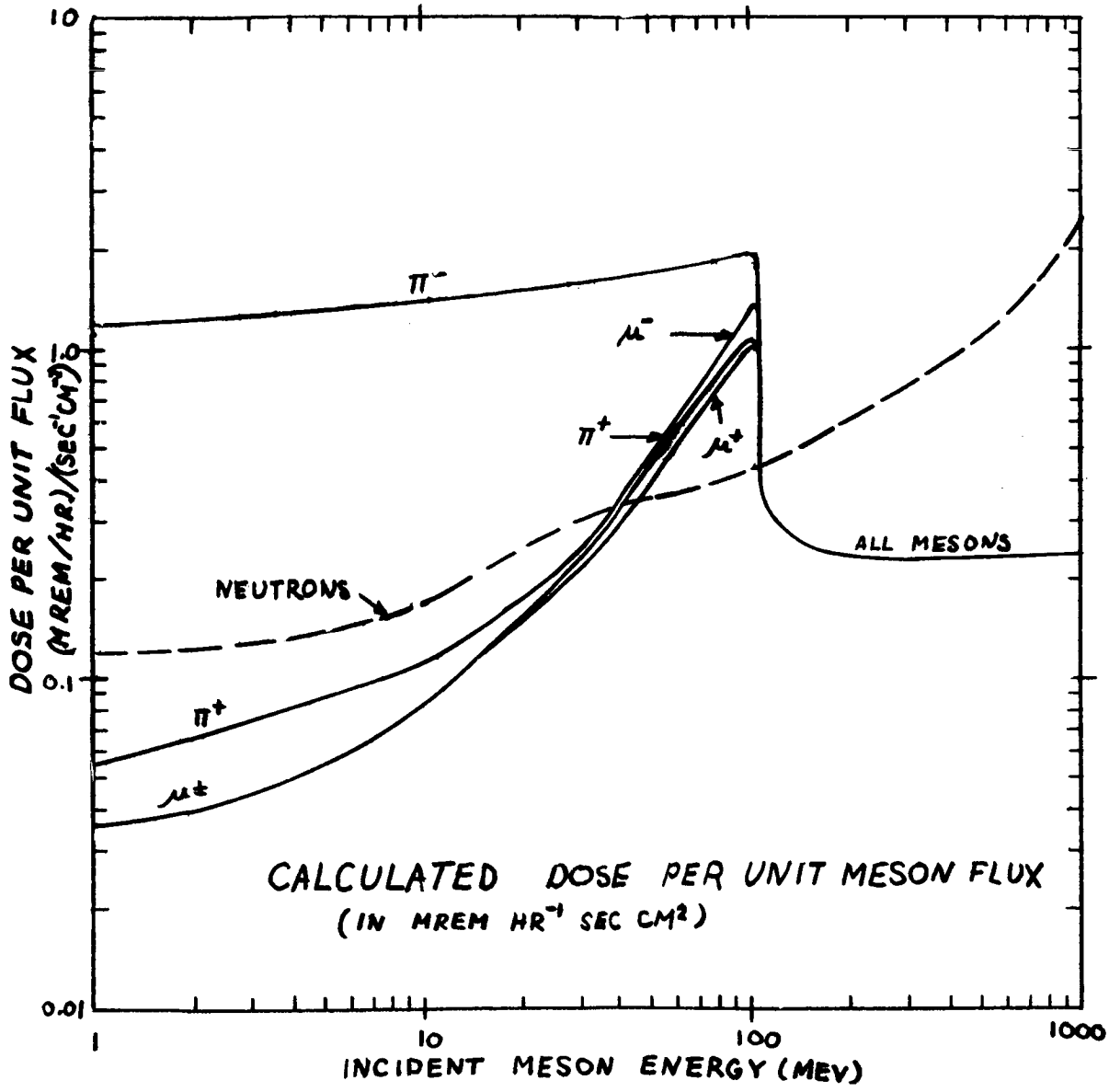
10
0.1
0.01
1
10
100
1000
DOSE PER UNIT FLUX
(MREM/HR)/(SEC⁻¹CM⁻²)
INCIDENT MESON ENERGY (MEV)
π⁻
μ⁻
π⁺
μ⁺
ALL MESONS
NEUTRONS
π⁺
μ±
CALCULATED DOSE PER UNIT MESON FLUX
(IN MREM HR⁻¹ SEC CM²)

FIG. 3.